AGARD-CP-386

AGARD-CP-386

AGARD

ADVISORY GROUP FOR AEROSPACE RESEARCH & DEVELOPMENT

7 RUE ANCELLE 92200 NEUILLY SUR SEINE FRANCE

AGARD CONFERENCE PROCEEDINGS No.386

Unsteady Aerodynamics-Fundamentals and Applications to Aircraft Dynamics

NORTH ATLANTIC TREATY ORGANIZATION

DISTRIBUTION AND AVAILABILITY ON BACK COVER

DISCLAIMER NOTICE

THIS DOCUMENT IS BEST QUALITY PRACTICABLE. THE COPY FURNISHED TO DTIC CONTAINED A SIGNIFICANT NUMBER OF PAGES WHICH DO NOT REPRODUCE LEGIBLY.

COMPONENT PART NOTICE

THIS PAPER IS A COMPONENT PART OF THE FOLLOWING COMPILATION REPORT:

TITLE: Unsteady Aerodynamics-Fundamentals and Applications to Aircraft Dynamics. Conference Proceedings of the Joint Symposium of the Fluid Dynamics and Flight Mechanics Panels held in Goettingen, Federal Republic of Germany on 6-9 May 1985.

TO ORDER THE COMPLETE COMPILATION REPORT, USE AD-A165 045.

THE COMPONENT PART IS PROVIDED HERE TO ALLOW USERS ACCESS TO INDIVIDUALLY AUTHORED SECTIONS OF PROCEEDING, ANNALS, SYMPOSIA, ETC. HOWEVER, THE COMPONENT SHOULD BE CONSIDERED WITHIN THE CONTEXT OF THE OVERALL COMPILATION REPORT AND NOT AS A STAND-ALONE TECHNICAL REPORT.

THE FOLLOWING COMPONENT PART NUMBERS COMPRISE THE COMPILATION REPORT:

AD#: P005 009 AD#: P005 043

AD#: AD#:

AD#: AD#:

REPORT DOCUMENTATION PAGE

1. Recipient's Reference	2. Originator's Reference	3. Further Reference	4. Security Classification of Document
	AGARD-CP-386	ISBN 92-835-0382-1	UNCLASSIFIED

5. Originator Advisory Group for Aerospace Research and Development
North Atlantic Treaty Organization
7 rue Ancelle, 92200 Neuilly sur Seine, France

6. Title

UNSTEADY AERODYNAMICS-FUNDAMENTALS AND APPLICATIONS TO AIRCRAFT DYNAMICS

7. Presented at

the joint Symposium of the Fluid Dynamics and Flight Mechanics Panels held in Göttingen, Federal Republic of Germany, 6—9 May 1985.

8. Author(s)/Editor(s)	9. Date
Various	November 1985
10. Author's/Editor's Address	**11. Pages**
Various	644

12. Distribution Statement This document is distributed in accordance with AGARD policies and regulations, which are outlined on the Outside Back Covers of all AGARD publications.

13. Keywords/Descriptors

Vortices
Boundary layer
Aerodynamics
Turbulent flow
Turbulence

14. Abstract

The dynamic behaviour of aircraft in high performance manoeuvres is greatly affected by various unsteady flow phenomena, particularly at high angles of attack, where extensive regions of separated flow and several systems of symmetric or asymmetric vortices are often present. Such flows, already rather complex in steady flight, become even more involved in oscillatory or high rate-of-turn flight, where the time lags associated with the various vortical and separated flows become a significant factor affecting profoundly both the static and the dynamic aerodynamic parameters of the aircraft. A good understanding of the unsteady aerodynamics is also important for design of advanced flight control systems, prediction of wing structural and manoeuvre loads and buffet prediction.

The aim of this symposium was to examine the recent advances in many countries in the methods for experimental and computational prediction of non-linear flow phenomena in unsteady aerodynamics and of stability parameters required to describe adequately the dynamic behaviour of aircraft with special emphasis on high-angle-of-attack situations. The programme comprised parts on (1) Unsteady Aerodynamics, (2) Dynamic Stability Parameters, and (3) Applications to Aircraft Dynamis. In the first part, topics such as unsteady boundary layers, unsteady separation and stall, buffeting and unsteady airloads were discussed. The second part covered wind-tunnel and flight-test techniques, with special emphasis on the measurement of non-linearities, aerodynamic cross-coupling, hysteresis and time-dependent effects. Finally, in part three the various applications of the above to the actual prediction of aircraft dynamics were described, including topics such as mathematical modelling, bifurcation theory, prediction of wing rock, advanced control systems, etc.

NORTH ATLANTIC TREATY ORGANIZATION

ADVISORY GROUP FOR AEROSPACE RESEARCH AND DEVELOPMENT

(ORGANISATION DU TRAITE DE L'ATLANTIQUE NORD)

AGARD Conference Proceedings No.386

UNSTEADY AERODYNAMICS – FUNDAMENTALS AND APPLICATIONS TO AIRCRAFT DYNAMICS

Papers presented and discussions held at the joint Symposium of the Fluid Dynamics and Flight Mechanics Panels held in Göttingen, Federal Republic of Germany, 6—9 May 1985.

THE MISSION OF AGARD

The mission of AGARD is to bring together the leading personalities of the NATO nations in the fields of science and technology relating to aerospace for the following purposes:

- Exchanging of scientific and technical information;
- Continuously stimulating advances in the aerospace sciences relevant to strengthening the common defence posture;
- Improving the co-operation among member nations in aerospace research and development;
- Providing scientific and technical advice and assistance to the Military Committee in the field of aerospace research and development (with particular regard to its military application);
- Rendering scientific and technical assistance, as requested, to other NATO bodies and to member nations in connection with research and development problems in the aerospace field;
- Providing assistance to member nations for the purpose of increasing their scientific and technical potential;
- Recommending effective ways for the member nations to use their research and development capabilities for the common benefit of the NATO community.

The highest authority within AGARD is the National Delegates Board consisting of officially appointed senior representatives from each member nation. The mission of AGARD is carried out through the Panels which are composed of experts appointed by the National Delegates, the Consultant and Exchange Programme and the Aerospace Applications Studies Programme. The results of AGARD work are reported to the member nations and the NATO Authorities through the AGARD series of publications of which this is one.

Participation in AGARD activities is by invitation only and is normally limited to citizens of the NATO nations.

Published November 1985

ISBN 92-835-0382-1

Printed by Specialised Printing Services Limited
40 Chigwell Lane, Loughton, Essex IG10 3TZ

THEME

The dynamic behaviour of aircraft in high performance manoeuvres is greatly affected by various unsteady flow phenomena, particularly at high angles of attack, where extensive regions of separated flow and several systems of symmetric or asymmetric vortices are often present. Such flows, already rather complex in steady flight, become even more involved in oscillatory or high rate-of-turn flight, where the time lags associated with the various vortical and separated flows become a significant factor affecting profoundly both the static and the dynamic aerodynamic parameters of the aircraft. A good understanding of the unsteady aerodynamics is also important for design of advanced flight control systems, prediction of wing structural and manoeuvre loads and buffet prediction.

The aim of this symposium was to examine the recent advances, in many countries, in the methods for experimental and computational prediction of non-linear flow phenomena in unsteady aerodynamics and of stability parameters required to describe adequately the dynamic behaviour of aircraft with special emphasis on high-angle-of-attack situations. The programme comprised parts on (1) Unsteady Aerodynamics, (2) Dynamic Stability Parameters, and (3) Applications to Aircraft Dynamics. In the first part, topics such as unsteady boundary layers, unsteady separation and stall, buffeting and unsteady airloads were discussed. The second part covered wind-tunnel and flight-test techniques, with special emphasis on the measurement of non-linearities, aerodynamic cross-coupling, hysteresis and time-dependent effects. Finally, in part three, the various applications of the above to the actual prediction of aircraft dynamics were described, including topics such as mathematical modelling, bifurcation theory, prediction of wing rock, advanced control systems, etc. All papers were obtained by invitation.

Due to the multi-disciplinary character of the subject, the Symposium was organized jointly by the Fluid Dynamics Panel and the Flight Mechanics Panel of AGARD. This was reflected in the composition of the Programme Committee.

CONTENTS

Reference

THE FOLLOWING PAPERS WERE PRESENTED DURING AN OPEN (i.e. INFORMAL) SESSION AT THE END OF THE CONFERENCE PROGRAMME

*Not available at time of printing

UNSTEADY FLOWS.- FUNDAMENTALS AND APPLICATIONS

by
B. Laschka
Institut für Strömungsmechanik
Technische Universität Braunschweig
Bienroder Weg 3, 3300 Braunschweig, Germany

ABSTRACT

An introductory overview about the fundamental equations describing the special features of unsteady flows is presented. Starting with the full Navier-Stokes-Equations, different stages of reductions down to linear potential theory are evaluated, their scope of validity is discussed. For viscous flows attention is given to the incompressible case whereas for inviscid flows compressibility has been retained.

SYMBOLS

A	cross area
a	speed of sound
c_D	drag coefficient
C_p	specific heat capacity
c_p	pressure coefficient
D	drag
d	thickness ratio or any body extent given by incidence or amplitude normal to the wing
Ec	Eckert number
f_c,$\pm f_d$	camber line, thickness line
F	fluid flow field quantities
Fr	Froude number
g	constant of gravity
k	reduced frequency
L	acceleration number
l	characteristic length
M	Mach number
P	potential
p	pressure
Pr	Prandtl number
Q	volume flux
q	source strength
R	elliptic or hyperbolic radius
r	cylinder coordinate
Re	Reynolds number
S	surface
s	span or streamline coordinate
Sr	Strouhal number
T	static temperature
t	time
U	free flow in x-direction
u,v,w	local flows in x,y,z-direction
W_i,W_j	velocity vector (u,v,w)
x,y,z	cartesian coordinates
x_i,x_j	(x,y,z)
α	cross area ratio A_2/A_1 or angle of attack
δ,δ^*	boundary layer thickness, displacement ~
η	propulsion efficiency
Φ	velocity potential
φ	velocity perturbation potential or cylinder coordinate
Ψ	acceleration potential
$\varkappa$	isentropic exponent
λ	heat conductivity
μ	dynamic viscosity or Mach dependent factor M_∞/β^2
ω	circular frequency
ρ	density of fluid
σ	entropy
τ_{ij}	stress tensor,$(=(\tau_D)_{ij}/\rho_R.W_R^2)$
ν	kinematic viscosity

Subscripts

D	dimensional quantities
i	1,2,3 denoting line
j	1,2,3 denoting column
n	normal to ...
R	reference quantities
∞	free flow conditions
δ	conditions on b.l. edge
l	lower side
u	upper side

1. Introduction

Probably one of the first considerations concerning unsteady flows were directed towards the outflow velocity at an orifice from a container filled with a liquid, see Fig. 1. Two fundamental equations are needed to solve this problem. The conservation of mass along a rigid stream tube gives us the continuity equation

$$(1) \quad Q(t) = W(t,s) \cdot A(s)$$

and - forgetting mechanical losses - the conservation of energy yields to

$$(2) \quad \frac{\rho}{2} W^2(s,t) + p(s,t) + g\,\rho\,z(s) + \int_{(s)} \frac{\partial W(s,t)}{\partial t}\,ds = f(t)$$

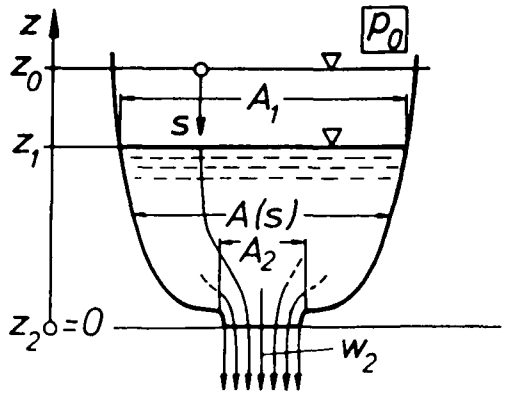

Fig. 1: Discharge of a fluid from a container

It was probably Johann Bernoulli already in 1842 who formulated this basic time dependent interrelation between velocity W, pressure p and geodetic position z along a streamline in his "Nouvelle Hydraulique", Ref. 1. $\partial W/\partial t$ is the local acceleration in streamwise direction. If we neglect this term we get the "quasisteady" formulation. We now denote all quantities which refer to the fluid surface with the subscript "1; and to the exit with the subscript "2" and introduce the boundary conditions:

(3a) $p_1 = p_2 = p_0 = const.$

(3b) $W_1(z_1 = z_0) = 0 \quad at \quad t = 0$

For a quasisteady treatment we simply have two algebraic equations in connection with the boundary condition Eq. (3a) to solve. For arbitrary container cross areas we easily get the exit velocity as

(4a) $W_2 = -\sqrt{\dfrac{2 \cdot g \cdot z_1}{1-\alpha^2}}$ with $\alpha = \dfrac{A_2}{A_1}$ quasisteady flow

For the full unsteady flow we have to solve an integral equation with making use of the initial condition Eq. (3b), in addition. The solution is not easy to obtain. The container cross area distribution is essential for it. After some calculations we get a nonlinear second order differential equation for the surface position $s_1(t)$, a linear first order differential equation for the square of the exit velocity $W_2(t)$, see Ref. 2. For a cylindrical container we finally receive

(4b) $W_2 = -\sqrt{\dfrac{2 \cdot g \cdot z_1}{1-2\alpha^2}\left[1-\left(\dfrac{z_1}{z_0}\right)^{\frac{1-2\alpha^2}{\alpha^2}}\right]}$ unsteady flow

The unsteady flow results referred to the quasisteady values over the instantaneous surface position are shown in Fig. 2. We realize first a time lag changing into an overshoot with decreasing surface geodetic position. This is the more pronounced, the bigger the area ratio α is, quasisteady flow is obtained for vanishing orifice area ($\alpha \to 0$) only. What can we learn for unsteady flows from this simple example when compared to quasisteady considerations:

(a) The complexity of solving the equations is markedly increased.

(b) We need initial conditions.

(c) We observe time lags and time leads.

(d) Quasisteady results may be accepted with caution only.

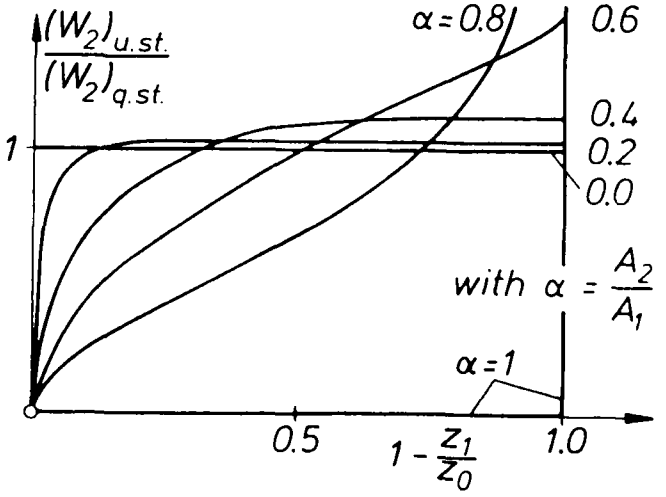

Fig. 2: Discharge velocity from a container for an incompressible fluid.

The just described kind of basic unsteady flow has innumerable applications, it has drawn attention just recently at wide body aircraft. The pressure inside of a passenger aircraft is controlled by an appropriate law. Passenger and cargo compartment are separated by a floor. In case of a sudden hole at the cargo compartment side a time-dependent decompression starts. A pressure difference between both compartments is being built up which may cause a break down of the floor, damaging all the supplies which have been installed underneath. By this way a DC 10 has lost its flight control due to breaks of hydraulic ducts, when a cargo door opened in flight. FAA, therefore, raised requirements to cover the occurence of sudden 20 ft^2 holes. A quasisteady assessment usually gives to high, that means to pessimistic loads, as may also be expected from Fig. 2 consequently penalizing the structure.

Actually the real conditions are much more complicated because several connected compartments may exist, they may have an intricate shape, e.g. by different container loadings; viscosity and compressibility have to be accounted for. Either experiment or a full three dimensional flow calculation might be necessary; full Navier-Stokes-Equations could be the appropriate tool, only.

2. Basic Equations For Continuum Flows (Newtonian Fluids)

A continuum flow of a perfect fluid is usually defined by eight fluid field quantities.

(5) $$(W_i, p, T, \varrho, \mu, \lambda) = F(x_j, t)$$

A flow is called unsteady if it depends besides on the space coordinates x_i also on time t. The required eight equations are received from mass conservation, momentum flux, energy balance, thermodynamic state equation, and material laws for viscosity and heat conductivity. Taken e.g. from Ref. 3 and changing into index notation we get (without gravitational forces):

(6) $$\frac{\partial \varrho}{\partial t} + \frac{\partial (\varrho W_j)}{\partial x_j} = 0$$ mass (continuity)

(7-9) $$\frac{\partial (\varrho W_i)}{\partial t} + \frac{\partial (\varrho W_i W_j)}{\partial x_j} = -\frac{\partial p}{\partial x_i} + \frac{\partial \tau_{ij}}{\partial x_j}$$ momentum (Navier-Stokes)

(10) $$C_p \left(\frac{\partial (\varrho T)}{\partial t} + \frac{\partial (\varrho T W_j)}{\partial x_j} \right) - \frac{\partial p}{\partial t} - W_j \frac{\partial p}{\partial x_j} = \tau_{ij} \frac{\partial W_i}{\partial x_j} + \frac{\partial}{\partial x_j} \left(\lambda \frac{\partial T}{\partial x_j} \right)$$ energy

(11) $$p = \varrho \cdot R \cdot T$$ equation of state

(12), (13) $$(\mu, \lambda) = f(p, T) \approx f(T)$$ material quantities

In Eq. (7) to (10) τ_{ij} means the stress tensor given by

(14) $$\tau_{ij} = \mu \left(\frac{\partial W_i}{\partial x_j} + \frac{\partial W_j}{\partial x_i} \right) - \frac{2}{3} \mu \, \delta_{ij} \frac{\partial W_l}{\partial x_l}$$

The noticeable unsteady terms are the local differential terms $\partial F / \partial t$. One has to bear in mind, however, that all field quantities $F(x_j,t)$ are time dependent, that means the convective, the pressure and the viscosity terms as well.

The Navier-Stokes partial differential equations are of first order concerning the momentum and pressure terms, and of second order concerning the viscosity terms. The second order terms imply two boundary conditions. For an interaction of the flow with a solid wall it is given by the compliance condition, which means, that at the wall the flow has the same velocity as the wall surface itself.

(15) $$(W_i)_{Fluid} = (W_i)_{Wall}$$ kinematic flow conditions, wall conditions

That gives actually two conditions, referring to the

(15a) unsteady normal wall velocity (tangential flow condition)
(15b) unsteady tangential wall velocity (no-slip condition)

Furtheron because of the time dependence initial conditions

(16) $$F(x_j, t) \quad for \quad t = t_0$$

are needed. Other conditions may have to take care of the kinematic and dynamic qualities of the undisturbed flow, of the boundary surfaces of liquid and gaseous fluids, the wall temperature, etc.

We have to bear in mind that a series of assumptions were needed for the derivation of the basic equations, e.g. the molecular mean free length is small to body lengths, the relations between stresses and deformations are isotropic, linear and instantaneous, the Stokes relation between the dynamic and bulk viscosity is valid, consequently the arithmetic mean value of the normal stresses is equal to the thermodynamic pressure, the van-der-Waal forces are neglected. Nevertheless there is manifold evidence that many fluids are represented properly by these assumptions. This holds for subsonic, transonic, and supersonic, for laminar and turbulent, for attached and separated, for irrotational and rotational, for discontinuous vortex sheet and discontinuous shock wave unsteady flows.

The basic equations may be rewritten in a nondimensional form by using reference quantities indicated by subscript R

$$W_R, \varrho_R, \mu_R, \lambda_R, T_R \quad and \quad l_R, t_R$$

For the subsequent denominations we will use

- the subscript D for dimensional values, e.g. W_{iD}, μ_D
- no subscript for nondimensional values, e.g. $W_i = \frac{W_{iD}}{W_R}$, $\mu = \frac{\mu_D}{\mu_R}$

The Eqs. (6) to (12) then contain a series of characteristic numbers.

For steady flows we get the well known characteristic numbers of Reynolds, Prandtl and Eckert

$$(17)\quad Re = \frac{W_R \cdot l_R \cdot \varrho_R}{\mu_R}\ ;\ Pr = C_p \frac{\mu_R}{\lambda_R}\ ;\ Ec = \frac{W_R^2}{C_p \cdot T_R}$$

They characterize the influence of viscosity, heat conduction and kinetic heating (at gaseous fluids), respectively. For unsteady flows we find in connection with the time differential term $\partial/\partial t$ one additional number, the "Strouhal number Sr.", (and for harmonically oscillating flows the "reduced frequency k").

$$(18)\quad Sr = \frac{l_R}{t_R \cdot W_R}\ ;\ t = \frac{t_D}{t_R}\ ,\ \left(k = \frac{\omega \cdot l_R}{W_R}\right)$$

It is a measure of the grade of unsteadiness of the flow. The characteristic numbers are also the flow dominating similarity parameters, that means, that in the case of unsteady flow simulating the Strouhal number plays the essential role.

There is no solution for the Navier-Stokes-Equations known up to now, in which the full interaction between the inertial and viscosity terms has been accounted for. Therefore, either numerical computational methods or justified simplifications to the N-S-Equations have to be adopted. At present the computational methods are in a rapid process of development and it is referred to the many existing references such as Ref. 4 to 6. Very briefly it should be mentioned that with the finite difference or finite element schemes a number of errors are introduced. They have to be assessed in the same sense as errors from mathematical modelling the physics of fluids as mentioned before or errors involved in experimental data. At finite difference equations there are errors from round-offs, from approximations in satisfying boundary conditions, and from truncations inherent in the difference scheme itself. The deviations between the solutions of the differential and the difference equation can formally be interpreted as higher order derivatives of a modified partial differential equation. They cause errors in magnitude and phase of the solution and are called dissipative and dispersive errors. Any finite difference scheme must prove
(a) consistency, that is the governing and the modified equations become identical when the time and spatial steps (Δt and Δx_i) tend to zero in an arbitrary manner
(b) stability, that is the errors in the numerical solution do not become unbounded when the number of time steps is increased.
Both conditions are needed for the convergence towards the exact solution (Lax' equivalence theorem).

First and higher order explicit, implicit, and hybrid schemes are applied, approaches to treat e.g. the inertial terms by explicit schemes and the viscosity terms by implicit ones have been proposed. Sophisticated schemes for sizing space and time steps have been evaluated, adapted to regions in which different physical effects predominate, such as near field and far field regions, or viscous and inertial forces governed areas. The benefits from explicit vs. implicit schemes may be coarsely summarized as follows: The explicit schemes are simpler to code, the storage requirements are less severe, incorporation of turbulence models is easier. They need, however, more computation time, because the stability of their solutions is conditioned by ratios of overall minimum time and spatial steps expressed by the "Courant-Friedrichs-Lewy Number (CFL)". Unsteady flows are usually treated by marching in time, starting from an initial phase. Oscillatory aerodynamic data are consequently received as the time-asymptotic values.

The maximum time steps Δt to be chosen depend on the required resolution of the unsteady phenomenon. One approach according to Ref. 6 is to compare spatial wave lengths Λ of disturbances propagating at velocities v with wave lengths from a governing unsteadiness, e.g. from a wing oscillation with reduced frequency $k = \omega_D \cdot l_R / U_R$. The smallest spatial wave lengths that can be resolved by steps Δx or Δt are $\Lambda \sim 2\Delta x \sim \Delta t \cdot v$. We then assess for the number n of time steps per cycle of the wing oscillation $n = 2\pi/k \cdot \Delta t = 2\pi\, v/k\Lambda$. Disturbances of interest are of high frequency ($v = 1 \pm M, \lambda \sim 2\Delta x$) and of low frequency moving slowly ($v = 1 - M, \lambda \sim 1$). The highest number of time steps is required for the resolution of high frequency downstream moving disturbances.

3. Turbulent flows (Reynolds-averaged N-S Eq.)

As was stated before, there exists no real doubt that the N-S equations are valid for turbulent unsteady flows, too, though speculations have been raised, that the assumption of linear isotropy may be the reason for defaults of understanding this phenomenon. The positive attitude is advocated by the consideration that the smallest significant eddies are composed by a big number of molecules; they still represent a continuum flow. The molecule mean free path should therefore be small when compared to the eddy size. Eddy lengths and time scales vary over a wide range especially at high Reynolds numbers. One reasonable assumption is that under flight conditions one has to retain eddies of the size of 10^{-5} based on the boundary layer thickness, Ref. 7. This implies that in finite difference calculations one has to operate with 10^6 nodes for 1 cm^3 flow, at least, consequently overcharging present computer capability.

According to O. Reynolds, Ref. 8, a turbulent flow may be split into the mean flow quantities $\bar{F}$ superimposed by the turbulent fluctuation F_i'. F stands here for any flow quantity, including products between each of them. Usually, the mean value is received by time averaging the flow quantities.

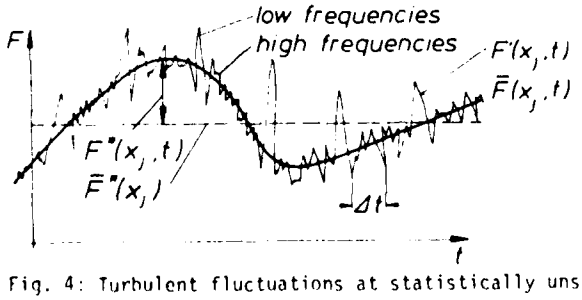

Fig. 4: Turbulent fluctuations at statistically unsteady flows.

$$(19)\quad F(x_j,t) = \bar{F}(x_j,t) + F'(x_j,t)$$

$$(20)\quad \bar{F}(x_j,t) = \frac{1}{\Delta t}\int_{(\Delta t)} F(x_j,t)\,dt\ ;$$

For statistically unsteady flows according to Fig. 4, however, the concept of time averaging has to be looked at cautiously. If the time scale of turbulence is sufficiently below to that of the unsteady mainflow, the averaging time step Δt can be taken such, that it is well apart from both sides. In this case it is assumed that the same turbulence models for steady and unsteady main flows can be applied, Ref. 9. Little is known for close proximities of time scales which may occur in separated flows.

When introducing Eq. (19) into Eq. (6) to (13) the new unknowns are instead of $W_i, \rho, p, T, \ldots$ now the averaged ones $\overline{W}_i, \overline{\rho}, \overline{p}, \overline{T}, \ldots$. They are furtheron supplemented by the mean values of the products of the fluctuating terms; for the momentum equation those are

for the time derivative term $\overline{\rho' W_i'}$

for the convective term $\overline{\rho' W_i'}, \overline{W_i' W_j'}, \overline{\rho' W_i' W_j'}$

When factured with $\overline{W}_i$ or $\overline{\rho}$ they represent the Reynolds stresses. They are themselves unknown and require additional equations (closure conditions), received by special semiempirical turbulence models, see e.g. Ref. 3,5,9,10. It may be noted that by the time derivative term only the mean fluctuation $\overline{\rho' W_i'}$ is introduced, which already occurs with the convective term in steady flow.

The boundary conditions as stated in Eq. (15) still hold for the mean velocities $\overline{W}_i$. The fluctuating parts W_i', i.e. any correlations have to vanish there, however.

(21a) $(\overline{W}_i)_{Fluid} = (W_i)_{Wall}$ (21b) $(W_i', \overline{W_i' W_j'}, \ldots\ldots) = 0$

The state of the art of unsteady flow turbulence modelling is still at its beginning. This holds for all parts of the layer, that means at the interface of the laminar sublayer, the intermediate as well as the region of intermittency; its wave length which is of the order of 2δ seems, however, to be well apart from unsteady mainstream motion. When Reynolds stresses are measured this is frequently performed via time derivatives which are converted to spatial derivatives by applying the space-time transformation. From P.S. Klebanoff's investigation in steady flow, Ref. 11, this seems to be valid for small scale flow motions only. Large scale motions have their own characteristics. Availability of unsteady flow turbulent data are thought to be limited. A compilation of all relevant experiments performed by L.W. Carr, Ref. 12, and sponsored by AGARD in 1981 revealed, however, that quite a lot of data are at hand. They are waiting to be analysed and condensed. They comprise flat plate, diffusor, pipe, airfoil, and cascade flows.

At present, quasisteady application of steady turbulence models are the only ones which have been used to some extent. Distinction is made between "zero-", "one-" or "two-equation models". The first one usually also called "algebraic" model is based on Prandtl's mixing length concept, the others are extended to two additional differential equations accounting for the turbulent energy k and dissipation ε, see Ref. 14. Their utilization for unsteady flows has been evaluated by several authors and it has been reviewed by D.P. Telionis in Ref. 13. No appraisal of all the suggested models seems to be possible at present.

A more refined approach is the "triple decomposition". The unsteady flow quantity $F(x_j,t)$ is assumed to be composed by

- a steady mean value $\overline{F}*(x_j)$
- an organized fluctuating term $F*(x_j,t)$
- a turbulent random fluctuating term $F'(x_j,t)$

$$F(x_j,t) = \overline{F}* + F* + F'$$

The organized oscillating frequency is assumed to be known from wing or any body motion and higher harmonics should be small. Introducing $F = \overline{F}* + F* + F'$ into the N-S Equations one gets in a similar way as has been shown before an averaged set of equations for turbulent mean flow and another set for turbulent organized fluctuation flow. This has been derived by H.L. Norris and W.C. Reynolds, Ref. 15. By this way additional stresses such as given by $W_i^* W_j^*$ from the organized motion have to be handled.

4. Stages of reducing Navier-Stokes-Equations

In Table 1 the full nondimensional N-S-Equations are rewritten. Subsequently several reductions are discussed. They give insight into first order dominated unsteady flow properties. For the viscous flow I will restrict myself to the incompressible case whereas for the inviscid flow compressibility will be retained. Simplifications can be received by

- assumptions of special types of flow for which certain terms of the N-S-Equations become zero
- assessment of the order of magnitude of different terms
- utilization of symmetry properties of the boundary conditions[+)]

4.1 Viscous, incompressible and isotherm flow (Eq. 22a to 22e)

4.1.1 Full N-S-Equations, Eq. (22a)

For incompressible, isotherm flow we take $\rho_D = \rho_R$ and $\mu_D = \mu_R$, what gives in Eq. (22)

(23) $\rho = 1 \quad and \quad \mu = 1$

The N-S-Equations are reduced markedly, see Eq. (22a). They remain nonlinear only in the convective term.

$$(24)\quad W_j \frac{\partial W_i}{\partial x_j} = \frac{1}{2} \frac{\partial W_i W_j}{\partial x_j} - \varepsilon_{kmi} w_m \varepsilon_{lij} \frac{\partial W_j}{\partial x_l}$$

[+)] Here one has to be very careful, because even with symmetric and steady boundary conditions the flow may be unsymmetric and unsteady, (see e.g. flow around a cylinder)

Navier-Stokes Equations (Stages Of Reduction)								Continuity Equation	Eq
	forces / mass	inertial: local	inertial: convective		press.	viscosity			
	Navier-Stokes-Eq. compressible (laminar and turbulent)	$Sr\frac{\partial w_i}{\partial t}$	$+w_j\frac{\partial w_i}{\partial x_j}$		$=-\frac{1}{\varrho}\frac{\partial p}{\partial x_i}$	$+\frac{1}{\varrho\,Re}\left[\frac{\partial}{\partial x_j}\left[\mu\left(\frac{\partial w_i}{\partial x_j}+\frac{\partial w_j}{\partial x_i}\right)\right]-\frac{2}{3}\frac{\partial}{\partial x_i}\left[\mu\frac{\partial w_j}{\partial x_j}\right]\right]$		$Sr\frac{\partial \varrho}{\partial t}+\frac{\partial}{\partial x_j}(\varrho w_j)=0$ **	22
viscous flow incompressible $\varrho=1$ isotherm $\mu=1$	Navier-Stokes-Eq. laminar and turbulent	$\frac{\partial w_i}{\partial t}$	$+w_j\frac{\partial w_i}{\partial x_j}$		$=-\frac{\partial p}{\partial x_i}$	$+\frac{1}{Re}\frac{\partial^2 w_i}{\partial x_j \partial x_j}$	$+0$	$\frac{\partial w_j}{\partial x_j}=0$	22a
	Reynolds - Eq. turbulent ($F_i=\bar{F}_i+F_i'$)	$\frac{\partial \bar{w}_i}{\partial t}$	$+\bar{w}_j\frac{\partial \bar{w}_i}{\partial x_j}$	$+\frac{\partial \overline{w_i' w_j'}}{\partial x_j}$	$=-\frac{\partial \bar{p}}{\partial x_i}$	$+\frac{1}{Re}\frac{\partial^2 \bar{w}_i}{\partial x_j \partial x_j}$	$+0$	$\frac{\partial \bar{w}_j}{\partial x_j}=0$	22b
	Parallel Flow $w_i=(u(y,z,t),\,0,\,0)$	$\begin{pmatrix}u_t\\0\\0\end{pmatrix}$	$+0$		$=-\frac{\partial p}{\partial x_i}$	$+\frac{1}{Re}\begin{pmatrix}u_{yy}+u_{zz}\\0\\0\end{pmatrix}$	$+0$	$u_x=0$	22c
	Creeping Flow $Re<1$, $w_j\frac{\partial w_i}{\partial x_j}=0$	$\frac{\partial w_i}{\partial t}$	$+0$		$=-\frac{\partial p}{\partial x_i}$	$+\frac{1}{Re}\frac{\partial^2 w_i}{\partial x_j \partial x_j}$	$+0$	$\frac{\partial w_j}{\partial x_j}=0$	22d
	Boundary Layer Fl. $Re\to\infty$, laminar; turbulent $w=\bar{w}$, $p=\bar{p}$	$\begin{pmatrix}u_t\\v_t\\0\end{pmatrix}$	$+w_j\frac{\partial}{\partial x_j}\begin{pmatrix}u\\v\\0\end{pmatrix}$	$+\begin{pmatrix}(\overline{u'w'})_z\\(\overline{v'w'})_z\\0\end{pmatrix}$	$=\begin{pmatrix}-p_x\\-p_y\\-p_z\end{pmatrix}$	$+\frac{1}{Re}\begin{pmatrix}u_{zz}\\v_{zz}\\0\end{pmatrix}$	$+0$	$\frac{\partial w_j}{\partial x_j}=0$	22e
inviscid flow compressible	Euler - Eq. $Re=\infty$	$\frac{\partial w_i}{\partial t}$	$+w_j\frac{\partial w_i}{\partial x_j}$		$=-\frac{1}{\varrho}\frac{\partial p}{\partial x_i}$			$\frac{\partial \varrho}{\partial t}+\frac{\partial}{\partial x_j}(\varrho w_j)=0$	22f
	Full Potential Flow $\varepsilon_{ij}\frac{\partial w_i}{\partial x_j}=0$	$\frac{\partial \Phi}{\partial t}$	$+\frac{1}{2}\left(\frac{\partial \Phi}{\partial x_j}\right)^2$		$=-\int\frac{dp}{\varrho}+f(t)$			$\frac{\partial^2 \Phi}{\partial x_j \partial x_j}-\frac{M^2}{a^2}\left[\frac{\partial}{\partial t}+\left(\frac{\partial \Phi}{\partial x_j}\right)_C\frac{\partial}{\partial x_j}\right]^2\Phi=0$ *	22g
	Potential Flow *** small disturbances, non linear $w_i=(1+\frac{\partial \varphi}{\partial x},\frac{\partial \varphi}{\partial y},\frac{\partial \varphi}{\partial z})$	φ_t	$+\varphi_x$		$=-(p-p_R)$			$\frac{\partial^2 \varphi}{\partial x_j \partial x_j}-M^2\left(\frac{\partial}{\partial t}+\frac{\partial}{\partial x}\right)^2\varphi=\begin{cases}(x+1)M^2\varphi_x\varphi_{xx}\\0\end{cases}$	22h
incom	Potential Flow *** incompressible $M=0$	Φ_t	$+\frac{1}{2}\left[\left(\frac{\partial \Phi}{\partial x_j}\right)^2-1\right]$		$=-(p-p_R)$			$\left(\frac{\partial^2 \Phi}{\partial x_j \partial x_j}\right)=0$	22i

Characteristic Numbers ***)

Strouhal	$Sr=\frac{l_R}{t_R\cdot W_R}$
Reynolds	$Re=\frac{W_R\cdot l_R\cdot \varrho_R}{\mu_R}$
Prandtl	$Pr=C_p\cdot\frac{\mu_R}{\lambda_R}$
Eckert	$Ec=\frac{W_R^2}{C_p\cdot T_R}$
Mach	$M=\frac{W_R}{a_R}$

Reference Quantities $l_R, W_R, a_R, \varrho_R, \mu_R, T_W, T_R, t_R, p_R$ Dimensionless Quantities $\vec{w}=\vec{w}_D/W_R$, $p=p_D/(\varrho_R W_R^2)$, $\varrho=\varrho_D/\varrho_R$, $a=a_D/a_R$, $\mu=\mu_D/\mu_R$, $T=T_D/T_R$

Dimensionless Coordinates $t=t_D/t_R$, x_i/l

*) Subscript C in eq. (22g) denotes that this term has to be treated as a constant with respect to $\partial/\partial t$ (Garrick's notation)

) In all the equations 22a to 22i the reference time $t_R=l_R/U_R$ has been chosen, giving $Sr=1$. *) undisturbed flow is taken for reference

The circular cylinder often serves as a test case for validation of N-S Equations based on numerical methods. One beautiful example for a low Reynolds number (Re = 9500) has been presented by Y. Lecointe and J. Piquet, Ref. 19. Details of primary, secondary and tertiary vortex developments as seen from experiment, Fig. 6, are predicted with impressive accuracy. Von Kármán vortex streets have been calculated, oscillations of the cylinder could be taken into account.

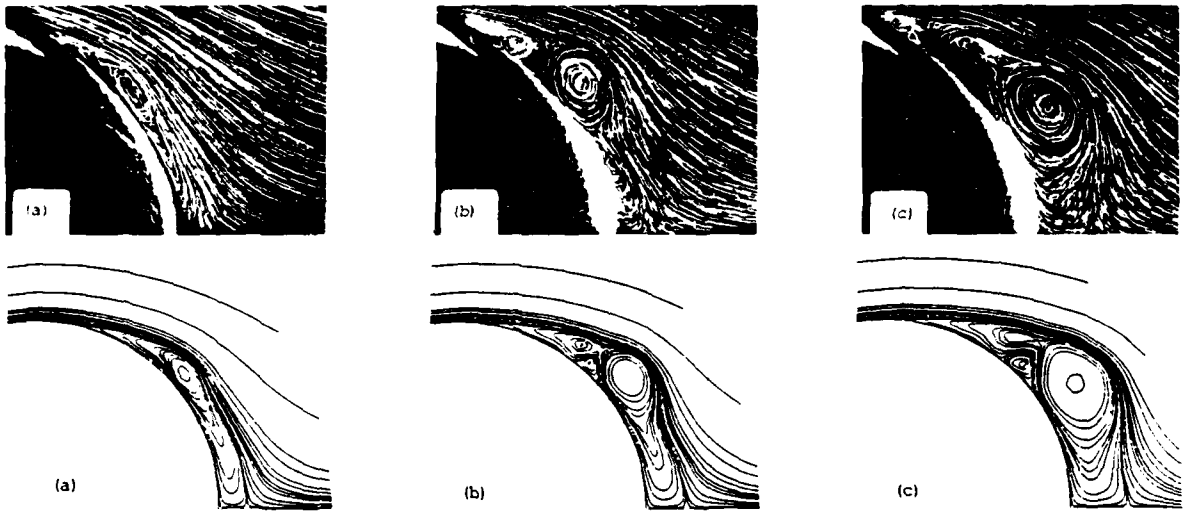

Fig. 6: Chronology of separation and vortex structure development.
Comparison between experiment and full N-S solution (from Ref. 19)

4.1.2 Reynolds-averaged N-S-Equations (turbulent flow), Eq. (22b)

The Reynolds stresses are given by six correlation quantities

(27) $\tau_{ij} = -\overline{W_i' W_j'}$

No fluctuation terms from the second order viscous terms contribute. Discussion on boundary conditions and turbulence modelling has been done already in a previous paragraph.

4.1.3 Parallel flows, Eq. (22c)

One class of unsteady flows which allows exact solutions is given by parallel flows. These are flows which can be represented by one velocity component only, whereas the other two are zero. An unsteady parallel flow with a gradient only normal to its direction belongs to it.

(28) $W_i = (u(y,z,t)\ ;\ v = 0\ ;\ w = 0)$

Introducing it into Eq. (22a) we find that the convective terms vanish and that, furtheron, only the equation in x-direction remains, which is now linear, see Eq. (22c). Several interesting flows of this kind have been investigated very early already. One result is presented:

Impulsive flow over a plate (1st Stokes problem, Ref. 20, Fig. 7)[+)]

Velocity: $u = u(z,t)\ ,\ v = 0\ ,\ w = 0$ N-S-Equation: $\dfrac{\partial u}{\partial t} = \dfrac{1}{Re}\dfrac{\partial^2 u}{\partial z^2}$

Boundary Condition: $\begin{cases} u = 0 \text{ for all } z \text{ at } t < 0 \\ u = 0 \text{ for } z = 0\ ,\ u = U_\infty \text{ for } z = \infty \text{ at } t > 0 \end{cases}$

Solution: $u = \dfrac{2H(t)}{\sqrt{\pi}} \int_0^\zeta \exp(-\zeta^2)\, d\zeta$ with $\zeta = \dfrac{z}{2}\sqrt{\dfrac{Re}{t}}$

H(t) means Heavyside Function. From the evaluation in Fig. 7 one may observe

- in the first moment there is no viscosity effect visible, the flow is uniform and irrotational (potential flow)
- with increasing time the boundary layer thickness increases to infinity according to $\delta \approx 4/\sqrt{Re\ t}$
- the wall shear stress proportional to $\partial u/\partial z$ is biggest at the start of the process
- the boundary layer of a flow starting impulsively is different to that of a steady flow starting from a plate leading edge (for the latter also convective terms contribute).

+) Reference Quantities: $U_\infty\ ,\ l_R = U_\infty \cdot 1\,\text{sec}\ ,\ Re = \dfrac{U_\infty \cdot l_R}{\nu}\ ;\ t = \dfrac{t_D \cdot U_\infty}{l_R}$

The convective terms give the reason that exact solutions retaining full interaction with the viscous parts have not been reached. Only for very special cases exact results could be received. The incompressible potential flow

$$(25)\quad W_i = \frac{\partial \Phi}{\partial x_i} \; ; \; \epsilon_{ij} \frac{\partial W_j}{\partial x_i} = 0 \; ; \; \frac{1}{Re} \frac{\partial^2}{\partial x_j \partial x_j} \left(\frac{\partial \Phi}{\partial x_i} \right) = 0$$

is an exact solution of the N-S-Equation because the viscous terms become zero, see Ref. 3. This holds, if besides the tangential flow condition also the no-slip condition is fulfilled. It implies a wall movement according to the potential velocity.

For an impulsive start of flow given by $W_j \cdot (x_j,t)\, H(t)$ it can easily be shown by integrating Eq. (22a) over a small time interval Δt that the convective and viscous terms do not contribute in the first moments as long as spatial velocity distributions can be assumed to be finite. We then receive

$$(26)\quad \frac{\partial W_i}{\partial t} = -\frac{\partial p}{\partial x_i} \; ; \quad w_i = -\frac{\partial}{\partial x_i} \int_{t_0}^{t_0+\Delta t} p \; dt = \frac{\partial \Phi}{\partial x_i}$$

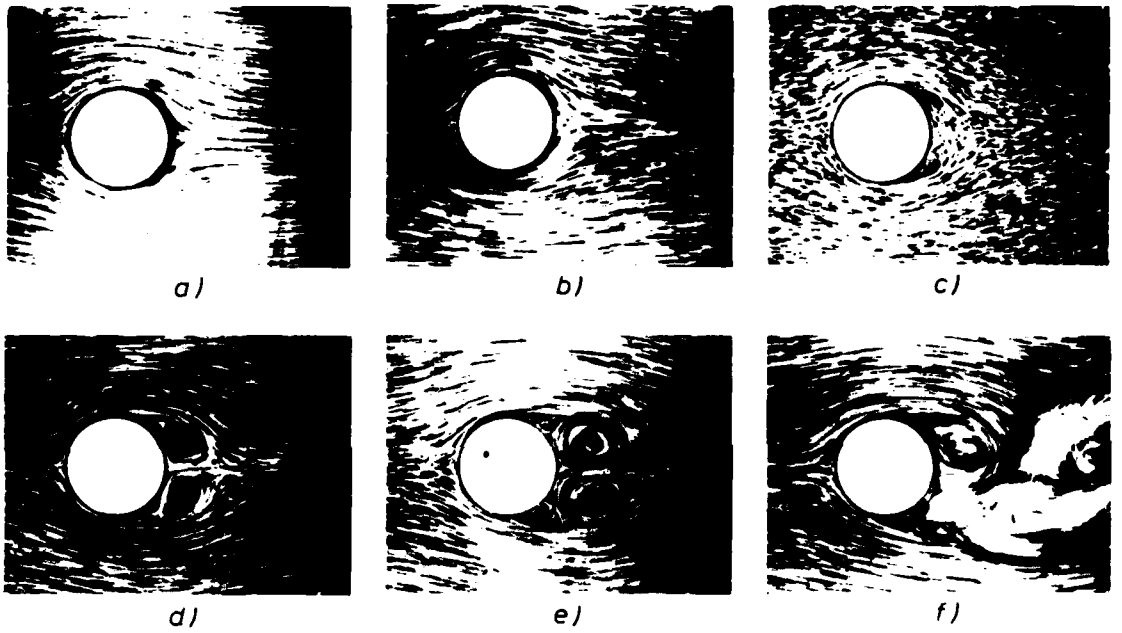

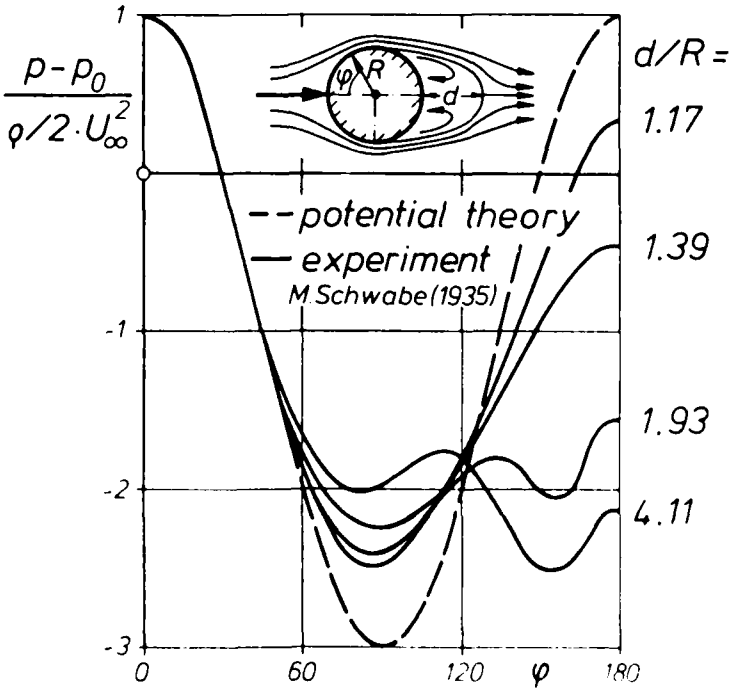

Fig. 5: Impulsive start of flow around a circular cylinder (Tietjens 1927), (Schwabe 1935)

One sees immediately that at the very start potential flow occurs, see Ref.16, (if no shock exists, this is also true for compressible flow). An experimental demonstration of this fact has been performed by Tietjens (1927), Ref. 17, for a variety of bodies including sharp edged plates. For the impulsive start of flow around a cylinder, Fig. 5, flow pictures show the sequence of patterns which develop successively at low Reynolds numbers. In the initial phase Fig. 5a, potential flow seems to be predominant. This is also substantiated by chronological pressure measurements from M.Schwabe, Ref. 18. After the start the boundary layer develops, separation starts in the vicinity of the downstream stagnation point, Fig. 5b. The separation point moves quickly upstream on both sides of the cylinder, leaving two at first still growing symmetrical vortices behind, Fig. 5e to 5d. They themselves cause the stagnation point to move downstream. In the further process the vortex formation becomes unstable and we reach a vortex street, the flow of which is unsymmetric and unsteady

It is not intended to review the unsteadiness of separated flows here. Reference is made e.g. to the excellent articles of McCroskey in AGARD-LS-94.

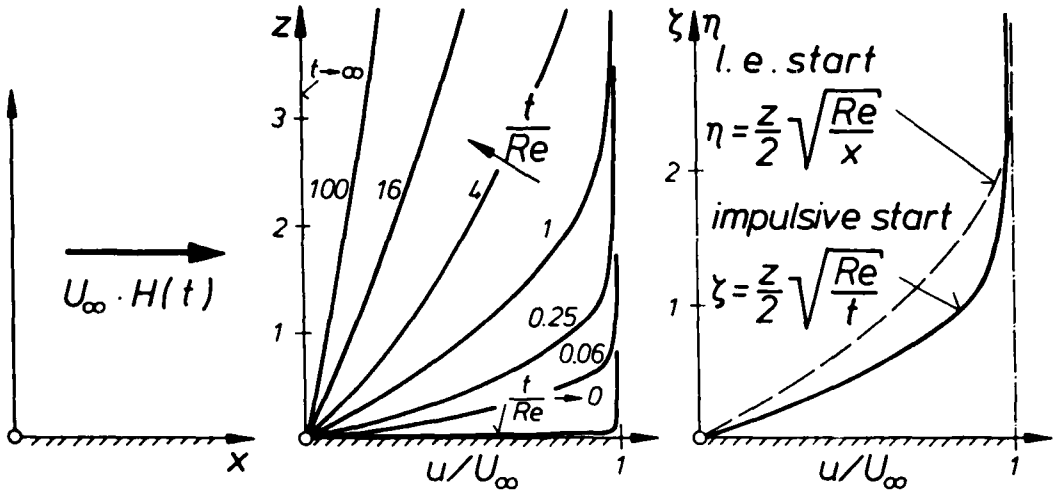

Fig. 7: Impulsive start of flow over an infinite flat plane

There are a variety of other exact viscous solutions, such as the impulsive start of flow in a duct. the decay of a vortex flow field, the in its plane oscillating plate (2nd Stokes problem), impulsive start of a Couette flow. An exact solution for a problem with not vanishing convective terms has been found for two-dimensional stagnation point flow (N. Rott), where the plate is moving in its plane. A comprehensive summary on this work may be found at H. Schlichting, Boundary Layer Theory, Ref. 3.

4.1.4 Creeping fluid flow (Re < 1), Eq. (22d)

In case the Reynolds number approaches small values (Re < 1), the convective terms, which are proportional to W^2 become small when compared to the viscous terms which are proportional to W. Neglecting the convection, gives a linear partial differential equation. The unsteady term is usually but not always necessarily small. Creeping flows have been applied to lubrication theories for bearings, where the gaps are narrow or to falling fog droplets, where the velocities are small. They are, however, also appropriate for treating particals moving with a slightly different velocity vector than the flow they are imbedded in. Unsteady phenomena have not been revealed to be important up-to-date.

4.1.5 Thin-layer N-S-Equation

Much more important than creeping flows are those at high Reynolds numbers. Nearly all flow phenomena in the context of flying aircraft belong to this category. As early as in 1904 L. Prandtl, Ref. 21, already proposed to consider a viscous layer near a solid wall and a nearly frictionfree flow outside of it. As this layer is thin the deceleration of the flow normal to the wall in order to meet the no-slip condition should be large. By reasons of reducing the requirements on computer capability the N-S-Equation has been simplified by dropping some or all of the viscous terms the derivatives of which are not taken normal to the wall. That means, the terms $\partial^2 W_i/\partial x^2$ and $\partial^2 W_i/\partial y^2$ are suppressed. The Eqs. are correct up to the second order terms. As a consequence the pressure through the layer is not constant as with the boundary layer assumptions and the Goldstein singularity at the separation point does not exist.

4.1.6 Boundary layer flow, B-L Eq. (22e)

For the case of $Re \to \infty$ L. Prandtl reduced the N-S-Eq. within the layer to some first order terms. Very strict derivations have been evaluated, e.g. by the method of asymptotic expansion. An easy way is to introduce characteristic reference lengths. These are streamwise and lateral body lengths, such as chord l and span s, respectively, but normal to a solid surface the boundary layer thickness δ. Furtheron the velocity components W_1, W_2 and their spatial derivatives are of first order when compared to W_3, and, finally the Reynolds number should be proportional to $1/\delta^2$ according to the flat plate results as found from the impulsive flow.

$$(29)\quad \bar{x}_i = x_i/\bar{l}_i \;;\; \bar{l}_1 = 1 \;;\; \bar{l}_2 = s \;;\; \bar{l}_3 = \delta \;;\; \delta \ll (1, s) \;;\; (W_1, W_2) = O(1) \;;\; W_3 = O(\delta) \;;\; Re = O(1/\delta^2)$$

Omitting all terms of higher order then one yields to the first order boundary layer equation. Eq. (22e). As a consequence - apart from getting rid of the $\partial^2/\partial x_1 \partial x_1$ and $\partial^2/\partial x_2 \partial x_2$ viscosity terms - the number of differential equations is reduced, by one and, because of

$$(30)\quad \partial p/\partial z = 0 \;;\; p = p(x, y, t)$$

The pressure through the boundary layer is constant and equal to that of the unsteady external flow at the matching point. For the external flow itself the viscosity plays no role. It can be calculated, therefore by crossing the viscosity terms in the N-S-Equations, as given in Eq. (22a), if it is appropriate, by any of its further reductions. For a boundary layer flow we can stress the following contributions to its unsteadiness, namely from

(a) the local momentum flux terms $\partial W_1/\partial t$, $\partial W_2/\partial t$ themselves

(b) the external unsteady flow received from inviscid considerations by fulfilling the tangential flow, the far field, and initial conditions

(c) the unsteady wall condition and here the no-slip in particular

The last two ones are the boundary conditions on the outer and inner side, respectively, of the viscous layer.

Turbulent boundary layers are also deduced in an analog manner as laminar layers using the Reynolds averaged Eq. (22b). Only two terms of the Reynolds stresses have to be retained consisting of the mean values $\overline{u'w'}$ and $\overline{v'w'}$.

a. Laminar boundary layers: The boundary layer equations can be solved by explicit or implicit schemes. In some cases also approximate or exact solutions using appropriate statements have been achieved. see Ref. 22 and 23. For two-dimensional flows beginning at time $t = t_0$ also successive methods have proven to work. The basic idea is to make use of the initial properties of the flow. The external inviscid unsteady flow is assumed to be known (W_{i0},p). From the impulsive start of flow over a flat plate we can judge, that because of the very thin shear layer in the first moments the viscosity terms overrule the nonlinear convective terms. The velocities W_i therefore can be split into an initial part W_{i0} and a higher order part W_{i1}. We then get two differential equations, each linear, to be solved successively taking the continuity equation and the boundary conditions into account.

$$(31)\quad W_i = W_{i0} + W_{i1} \quad ; \quad \frac{\partial U_0}{\partial t} = \frac{\partial U_\delta}{\partial t} + \frac{1}{Re}\frac{\partial^2 U_0}{\partial z^2}\,; \quad \frac{\partial U_1}{\partial t} + U_0\frac{\partial U_0}{\partial x} + w_0\frac{\partial U_0}{\partial z} = U_\delta\frac{\partial U_\delta}{\partial x} + \frac{1}{Re}\frac{\partial^2 U_1}{\partial x^2}$$

Subscript δ denotes the flow at the outer layer boundary. Several applications to circular and elliptic cylinders, to bodies of revolution, to spheres, to rotating disks etc. have been made.

Unsteady flows occur in many cases as organized small disturbances superimposed to a mean steady flow, e.g. as small oscillations. Any field quantities F, such as the flow velocities W_i may be written as

$$(32)\quad W_i(x_j,t) = \overline{W}_i(x_j) + W_i''(x_j,t)$$

When introduced into the boundary layer Eq. (22e) and separated into zero and first order terms one receives

(a) a set of steady boundary layer equations analog to Eq. (22e) where now, however, W_i has to be replaced by $\overline{W}_i$ and

(b) a second set of unsteady boundary layer equations for the disturbances W^*; here cross coupling terms $\overline{W}_j\,\partial W_i^*/\partial x_j$ and $W_j^*\,\partial\overline{W}_i/\partial x_j$ occur.

The advantage of this formulation is that the unsteady set of equations becomes linear, as the terms $W_j^*\,\partial W_i/\partial x_j$ are dropped because of their higher order, or are treated separately.

A comprehensive review of methods, results and references may be found in chapter XV of Ref. 3, written by K. Gersten, and in Ref. 5.

The unsteadiness influences the velocity profiles in several ways. They vary with time and they assume shapes, which are not familiar with steady flow. This may be shown for illustration for the case of a both in streamwise direction and temporally retarded external flow.

$$(33)\quad U(x,t) = U_\infty(1 - ax - bt)$$

(Williams/Johnson flow)

Eq. (33) is a Howarth's flow supplemented by the term bt. It has been investigated by J.C. Williams III and W.D. Johnson, Ref. 23. Evaluating their results the chronological development of the boundary layer profile at one selected point ax = 0.05 and at retardation conditions b/a = 0.2 have been plotted in Fig. 8a.

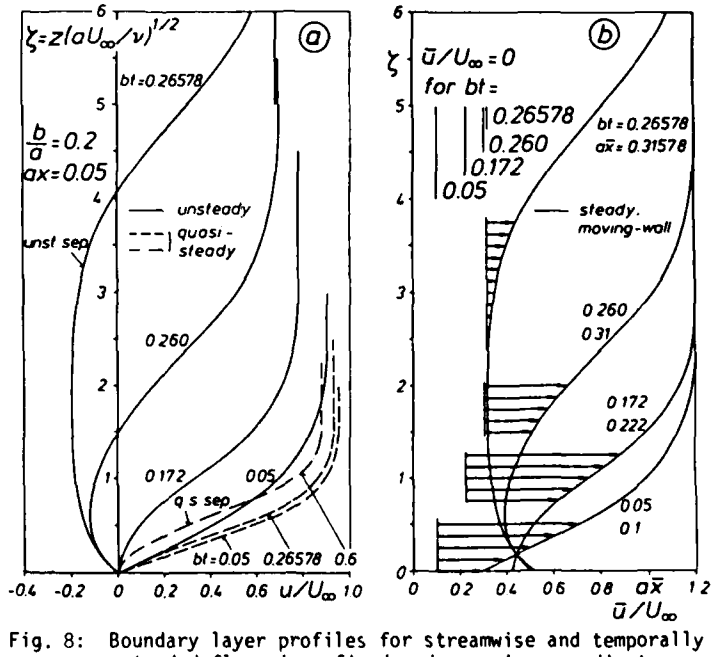

Fig. 8: Boundary layer profiles for streamwise and temporally retarded flows in a fixed and a moving coordinate system

At first (bt = 0,05) a profile very similar to that of steady flow develops until it reaches a vertical slope at the wall indicating vanishing shear at the wall (bt = 0,172). From steady flow consideration one would expect separation and a break down of calculations. This is, however, not the case. A dramatical change of the velocity profiles is received with further increasing time, revealing reverse flow in the boundary layer (bt = 0,26) and finally at bt > 0,266 a converged solution (for prescribed external flow boundary conditions) is no more obtainable. As will be explained later this signifies separated unsteady flow.

When compared to quasisteady results, which are also plotted in Fig. 8a, it is revealed that

(a) apart from the neighbourhood of bt = 0 the shapes of their profiles differ appreciably

(b) their boundary layer thickness may be bigger by multiples

(c) reverse flow without separation may occur

(d) the separation starts earlier, namely at bt = 0,266 instead of the quasisteady value bt = 0,6.

Quasisteady assumptions give consequently no reliable values for the case under consideration. One may speculate that the assumptions of small boundary layer thickness are more penalized than in steady flow. J.C. Williams and W.D. Johnson solved the unsteady boundary layer equation for the flow given in Eq. (33) not directly but rather after introducing a transformation.

$$(34)\quad \bar{x} = x + \frac{b}{a}t \;;\quad U_{Wall} / U_\infty = \frac{b}{a}$$

By this procedure the unsteady equations for a fixed wall boundary condition are transferred to steady equations with conditions for a wall moving with velocity b/a. Instead of changing velocity profiles with time at the point ax we then obtain fixed profiles at the different stations $a\bar{x}$ which will be reached by the fixed point ax of the body chronologically, see Fig. 8b. From this point of view we can interpret the present flow also as one at which velocity profiles of fixed shape move upstream with velocity -b/a.

b. Turbulent boundary layers: From the Reynolds averaged N-S-Eq. (22b) the turbulent B-L-Eqs. are deduced in the same way as it was done for laminar flow. For three-dimensional flow two of six fluctuation terms, namely $\overline{u'w'}$ and $\overline{v'w'}$, have to be retained, in two dimensions only the shear $\tau = -\rho\,\overline{u'w'}$ remains. For this case algebraic two-layer models have been proposed, $(\overline{u'w'})_I$ in continuation of the laminar sublayer, and $(\overline{u'w'})_E$ in transit to the frictionless external flow. As an example among other suggestions the following models have been checked by D.P. Telionis and D. Tsahalis, Ref. 24:

$$(35a)\quad (\overline{u'w'})_I = -l_m^2 \frac{\partial u}{\partial z}\left|\frac{\partial u}{\partial z}\right| ;\quad l_m = 0{,}41\, z\,(1-\exp(\frac{-z}{A}))$$

$$A = \frac{26}{Re\cdot|U_\tau|}\,(1-\frac{11{,}8}{Re\cdot|U_\tau^3|}\,\frac{\partial p}{\partial x})\quad \text{with}\quad U_\tau = \sqrt{\tau_w/\rho}\quad \text{and}\quad \tau_w = \tau_{WD}/\rho_R\, w_R^2$$

$$(35b)\quad (\overline{u'w'})_E = -0{,}0168\cdot U_\delta\cdot\delta^*\cdot\gamma\cdot\frac{\partial u}{\partial z}$$

l_m means Prandtl's mixing length, τ_w wall shear, U_τ friction velocity, δ and δ^* boundary layer thickness and displacement thickness, respectively, and γ is the intermittency factor. The unsteady flow is here introduced via the external flow velocity U_δ and the pressure gradient $\partial p/\partial x$.

4.1.7 Unsteady Separation

The common understanding on separation in two-dimensional steady flow over a wall in rest is based on Prandtl's concepts of a boundary layer having vanishing wall shear or - in other words - a vanishing velocity gradient normal to the wall, see Fig. 9a. If the external flow is specified, the boundary layer equations can be utilized down to the separation point. In this context separation is also characterized by the Goldstein singularity, Ref. 25. It states that the wall shear approaches the value zero in streamwise direction corresponding to the square root of its distance (This holds only if the B.L.Eqs. (22e) are used. When the N-S-Eqs. are used, the zero value is traversed with a finite slope, see Fig. 10, however.). This behaviour leads to a loss of convergence when difference methods are taken to solve the B.L.Eqs.; the observations of a rapid increase of a number of iterations till no more convergence is achieved, is accepted on the other hand as a sign that the separation point has been reached. We then have the following conditions, respectively flow behaviours, for the separation point:

$$(36)\quad u_{Wall} = 0\;;$$

$$\tau_{Wall} = \frac{1}{Re}\left(\frac{\partial u}{\partial z}\right)_{Wall} = 0\;;$$

$$\tau_{Wall} \sim \sqrt{x_{Sep} - x}\;;$$

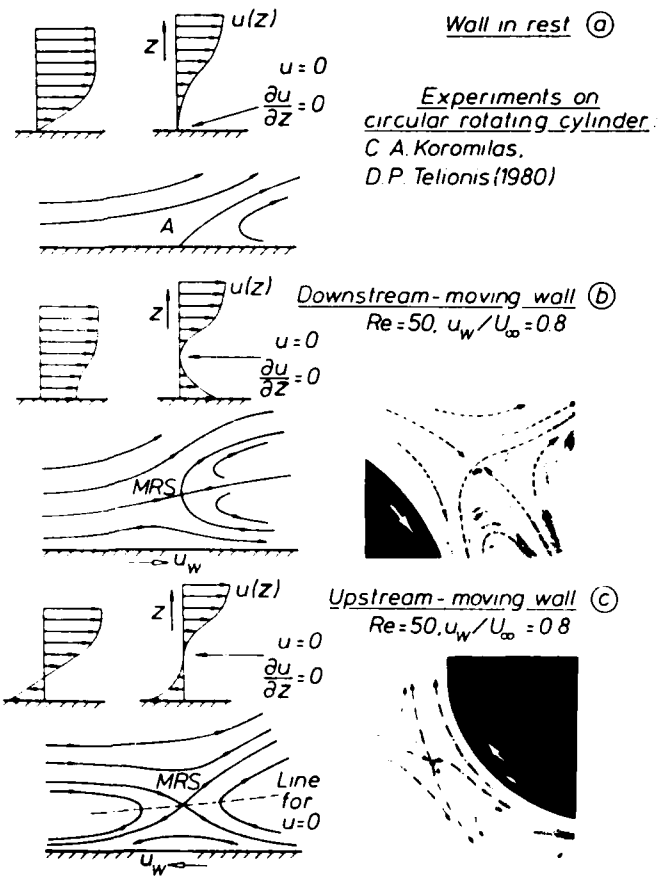

Fig. 9: Boundary layer separation over a non moving and moving wall, respectively.

Behind the separation point the layer between the wall and the separation line must have because of continuation reversed flow regions. The layer thickens up, the streamlines have finite curvatures, the pressure gradient through the layer is no more zero, the boundary layer assumptions may be hurt, and higher order terms have to be retained in the boundary layer equations. Calculations, however, are formally possible if instead of the external flow conditions now the displacement thickness or wall shears are specified (inverse method).

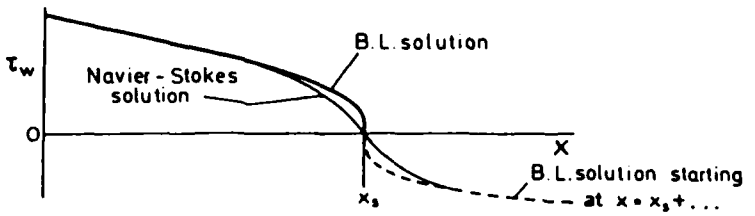

Fig. 10: Weakness of singularity at separation. (P. Bradshaw, Ref. 27).

After this excursion we return to unsteady flows. The Williams/Johnson flow as described before revealed for any station:

(a) The boundary layer in the $(\bar{x},z)$-coordinate system with downstream moving wall is steady. This case is analysed in more details in Fig. 9b. Due to the streamwise growing pressure in combination with the viscosity the velocity in the layer is reduced when going downstream. Its two boundaries are given by the external flow and the wall velocity. When the flow has become retarded to the point of vanishing wall shear no reverse flow appears causing separation from the wall (as would be for a wall at rest). Further retardation results in a negative wall shear, that means energy is transferred from the wall to the flow. The point of vanishing shear leaves the wall and moves into the layer, which forms an inward bow. Finally one streamwise station will be reached with zero velocity and reverse flow starts. This point must be a separatrix from which a bubble imbedded in the main flow develops. The corresponding flow field is also sketched in Fig. 9b, it has been experimentally proven on a rotating cylinder by Koromilas et al., Ref. 26. Simultaneously vanishing flow velocity as well as shear in a point of the layer causing a bubble with reverse flow may be considered as separation. The calculation, see Ref. 23, again reveals the Goldstein singularity to exist at this point and not at the wall zero shear point.

$$(36a)\quad u(x_s, z_s) = 0 \quad ; \quad \frac{\partial u(x_s, z_s)}{\partial z} = 0 \quad ; \quad \tau \sim \sqrt{x_s - x}$$

(b) The boundary layer in the (x,z)-wall-fixed-coordinate system is unsteady. Taking into account that we can transform the steady profiles into the unsteady ones by the simple Galilei-transformation given in Eq. (34) we can interpret the flow in the fixed system also as steady boundary layers moving upstream and passing each wall fixed station with the velocity b/a, resulting in a chronological sequence of different shapes. This holds also for the moving separation profile, which shows because of the transformation, reverse flow areas. For the Williams/Johnson flow in its generalization $U_\delta = f(ax + bt)$ one may state, that according to W.R. Sears

> "the unsteady separation point is defined by both vanishing shear and velocity in the layer in a flow seen by an observer moving with the separation point" and that it is also characterized by the Goldstein singularity when using boundary layer equations.

This statement has been postulated independently of each other by F.K. Moore, N. Rott and W.R. Sears, Ref. 28 to 30, in an intuitive way for arbitrary unsteady flows, it is also called "M-R-S Criterion". It should be noted that in general the movement of the separation point over a fixed wall is not known in advance.

The present considerations have been made for an upstream moving separation point i.e. downstream moving wall. The M-R-S Criterion is claimed to be valid also for a downstream movement i.e. upstream moving wall, see Fig. 9c. Streamline pattern is essentially different. Reverse flow in the vicinity of the moving wall is always existent, as well as a zero velocity line u = 0 in the layer because of matching the two boundaries. No unsteady calculation for prove has become apparent to the author. Nevertheless again waterflow visualization made by Telionis on a rotating cylinder substantiate the intuition. From these pictures one may better understand, why the unsteady boundary layer thickness according to Fig. 8 surmounts the quasisteady assessments.

Details of detachment of a two-dimensional unsteady turbulent boundary layer is even more a secret nowadays than it was with laminar ones. Steady turbulent separation itself is not a single event but rather a transition process from attached to detached flow over a distance in which increasing percentages of back mean flow occur. So the unsteadiness of the sublayer itself is part of the process and even in two-dimensional flow all three components of the turbulent time dependent motion near the wall have to be averaged and must result into a zero wall shear. This is fulfilled when the instantaneous fraction of forward and backward flow in the sublayer is around 50%, see Ref. 31 and 32. The interaction between moving walls, sublayer, turbulent layer, intermittency, and unsteady (phase shifted) external inviscid flow, when unsteady separation is approached and achieved, is a big research project for the future. The same holds for the three-dimensional unsteady case. Unsteady separation is a manifold event in applications, phenomena like dynamic stall, buffeting, rotating stall will not be understood by pure quasisteady deliberations.

4.2 Compressible Inviscid Flow

4.2.1 Euler-Equations (Eu-Eq. (22f))

Turning to inviscid flow means that the influence of molecular viscosity μ vanishes. The influence of heat conductivity λ then should also be neglected because both μ and λ have the same physical origin. According to the kinetic theory of gases the proportionality relation holds:

(37) $C_p \cdot \mu = (4 + 2f) / (9 + 2f) \lambda$ with f number of melocule degree of freedom

Consequently the Reynolds number becomes infinite. In the N-S-Eq. and in the energy Eq. (7) to (10) the terms with τ_{ij} and λ are cancelled. The N-S-Eqs. are reduced to the Eu-Eq. (22f) which is a nonlinear partial differential equation, now of first order. By losing the second order differential terms $\partial \tau_{ij} / \partial x_j$ one loses also one boundary condition. This is the no-slip condition which cannot be maintained anymore whereas the unsteady tangential flow condition remains. If the time-dependent loci of a body surface are denoted by

(38) $S(x_j, t) = 0$ then $\dfrac{\partial S}{\partial t} + w_j \dfrac{\partial S}{\partial x_j} = 0$ is the tangential flow condition.

The Eu-Eqs. are capable to describe for any speed

- any rotational or irrotational flow,
- it may be vortex dominated or not,
- it may have shock waves or not.

Shock waves and vortex sheets form discontinuities for the field quantities. Through the first ones there is a mass flux, through the second ones not. Special attention has to be given to the second law of thermodynamics which - for flows without heat transfer - states that along a particle path the entropy σ is constant, $d\sigma / dt = \partial\sigma / \partial t + W_j \partial\sigma / \partial x_j = 0$ with the exception of the entropy jump when crossing a shock. For unsteady flows locally the entropy can increase or decrease with time as is the case with moving shock waves. The entropy check is a mean to exclude physically not existent mathematical solutions, such as for compression and not existing "expansion" shocks or inconsistent numerical errors.

Vorticity in inviscid flows can be introduced by two ways, namely by free stream boundary conditions or by the occurrence of shocks. In addition, in real calculations - as mentioned in section 2 - small dissipative errors are inevitably introduced into the numerical flow field what has the effect of adding "artificial" viscosity. Especially when sharp edges exist they may create separation with appropriate vortex formations pretending viscosity. If the physical flow is not accounted for properly, the numerical flow field can be adjusted by introducing special edge conditions allowing for direction of edge velocities and velocity discontinuities (Kutta condition). Unsteady or steady vortex dominated flows as generated by slender bodies or highly swept leading edges are considered to be a good case for being treated by Euler-Equations. One has to bear in mind, however, that in the vortex core one finds a strong reduction of total mechanical energy due to dissipation. Their proper treatment would therefore require to retain the Reynolds stresses deducted from the convective terms even when the viscous terms - which themselves are responsible for turbulence - are dropped.

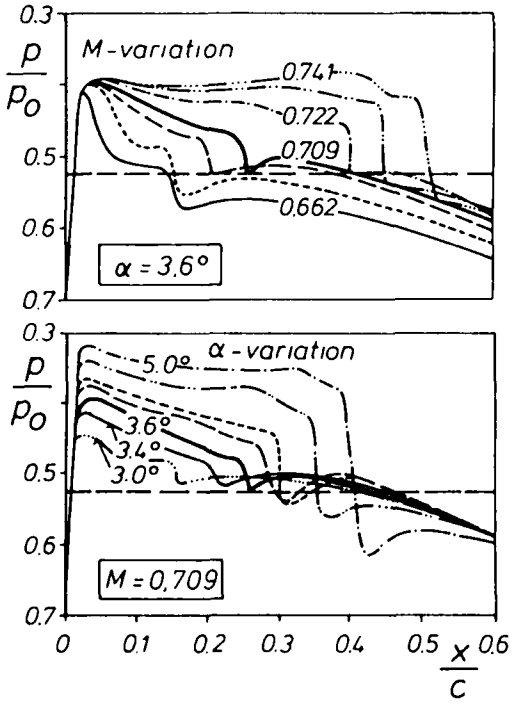

Fig. 11: Sensitivity of upper side wing pressures with respect to Mach number and angle of attack variations.

Disturbances in an inviscid fluid propagate spherically as weak ones with the speed of sound or as strong ones in specific shock formations. In the first case the entropy remains unchanged, in the second case not. Here the Mach number $M = W_R / a_R$ enters as a characteristic number. The Euler-Equation capability to calculate unsteady flows with shock waves of any strength from the transonic up to hypersonic speeds (excluding chemical reactions) has to be accentuated on the one hand, on the other hand it has to be relativated, too. It is quite evident that in the proximity of solid walls because of the no-slip condition an externally supersonic flow becomes subsonic. Before the shock terminates in the layer it diffuses. For a vertical shock approaching a laminar layer it is split in an upstream starting λ-type shock formation, its diffusion length may be up to 100δ. With a turbulent layer the shock becomes also bowed forward usually without being splitted, the diffusion length is around 10δ. Shock strength, location, inclination and formation in transit to a body surface is not dependent on Mach number alone but rather on Eckert and Reynolds number. For unsteady flows one has to add the Strouhal number. Boundary layer assumptions are violated. A crucial region is the transonic one though the shocks there are relatively weak. This is because of

- viscous - inviscid interaction as discussed,
- high sensitivity of the magnitude of flow field quantities to small changes in the kinematic flow condition or in Mach numbers,
- large phase shifts between the boundary conditions and the flow because of the low propagation disturbance velocities proportional to 1 - M.

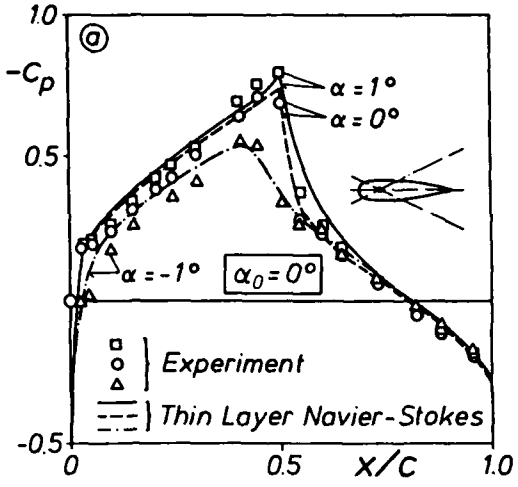

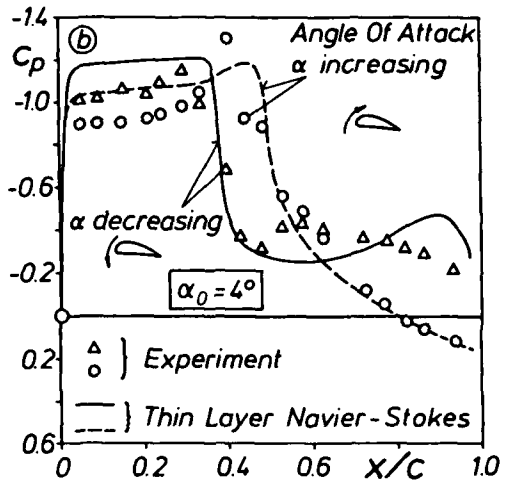

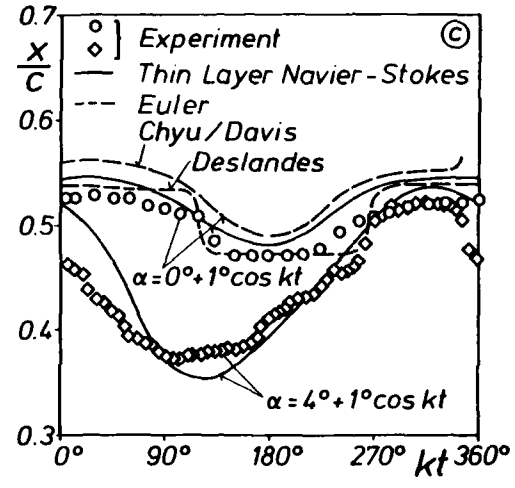

Fig. 12: Unsteady pressures during a cycle of oscillation of a NACA 64A10 airfoil for pitching motion ($M = 0,8$, $k = 0,2$, $Re = 12 \cdot 10^6$)
(a) upper surface pressures for $z = 1^0(x - 0,25) \cdot e^{ikt}$
(b) upper surface pressures for $z = 4^0 + 1^0(x - 0,25) \cdot e^{ikt}$
(c) shock location during one cycle
(taken from W.J. Chiu and S.S. Davis, Ref. 33)

This is evident already from quasisteady considerations as depicted in Fig. 11. At unsteady flows travelling shock waves characterize the physical properties. It is illustrated in Fig. 12, evaluated from Ref. 33, for a NACA 64A10 airfoil pitching harmonically about a 25% chord axis at two different mean angles $\alpha_0 = 0^0$ and $\alpha_0 = 4^0$, and an amplitude of $\alpha_1 = 1^0$. For the low mean angle the flow is attached, whereas for the high one separation behind the shock develops. Experiments at $Re = 12 \cdot 10^6$ as well as calculations based on Reynolds-averaged, thin layer, and Euler-Equations are available. For attached flows pressures (Fig. 12a) and shock excursions (Fig. 12c) are well predicted by Euler codes as well as by viscous methods. The convergence of calculation towards the experimental values for the shock location when viscosity has been accounted for may be misleading because Euler codes of other authors than given in the original reference show closer results. Naturally this is no more true for the oscillation about the high mean angle where the thin layer N-S-Eqs. prove their adequacy. Shock excursions are nearly 20% of wing chord.

Fig. 12b shows another interesting effect, namely hysteresis. For the upward movement through the neutral position of $\alpha_0 = 4^0$ no separation is observed whereas for the downpitch a break down of the flow can be recognized. This is in accordnace with low speed, high angle of attack observations and has to be seen in the context of unsteady separation.

Finally in Fig. 13 the first harmonic for the same NACA 64A10 airfoil, pitching about a mean angle of $\alpha_0 = 0^0$ has been plotted. Experiment from Ref. 33 and explicit Euler code calculation performed by R. Deslandes (MBB) show beautiful agreement even in this higher resolution. From a variety of further calculations there is some confidence that higher order harmonics are negligible even when shocks strongly determine pressures, as long as no separation occurs.

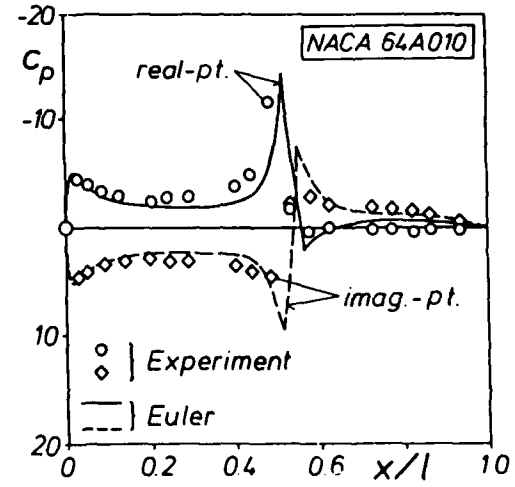

Fig. 13: First hamonic of unsteady pressure distribution of a pitching airfoil $k = 0,2$; $M = 0,8$; $z = \alpha_1(x-0,25)e^{ikt}$

4.2.2 Full Potential Equation (FP-Eq. (22g))

A further tremendous relief is given, if the inviscid flow field is irrotational. This is the case whenever the boundary and initial conditions do not introduce rotation and when weak shocks only exist. Edge conditions like Kutta condition which account for an infinite thin viscosity layer provide vortex sheets with discontinuities for the potential and its derivatives. Their introduction is essential for lift generation. Outside of the discontinuities the flow is isentropic and potential flow exists. Starting from Crocco's theorem we then have constant entropy in the flowfield and

(39a,b,c) $$\varepsilon_{ijj}\frac{\partial W_j}{\partial x_i}=0\ ;\ W_i=\frac{\partial \Phi}{\partial x_i}$$

$$c^2=\frac{dp}{d\varrho}=\left(\frac{\partial p}{\partial \varrho}\right)_\sigma=\frac{\varkappa p}{\varrho}\ ;\quad p/\varrho^{\varkappa}=const\ ;\quad \frac{1}{\varrho}\frac{\partial p}{\partial x_i}=\frac{\partial}{\partial x_i}\int_{p_0}^{p}\frac{dp'}{\varrho(p')}$$

ε_{ijj} denotes an operator as used in index notation ($\varepsilon_{ijj}\partial W_j/\partial x_i$ = curl $\vec{W}$). Because of Eq. (39b) the convective term $\varepsilon_{klm}W_m\varepsilon_{ijj}\partial W_j/\partial x_i$ in Eq. (24) vanishes. (The zero value is found not only for potential flow but also if the velocity vector W_i and the vorticity vector $\varepsilon_{ijj}\partial W_j/\partial x_i$ are parallel to each other, Beltrami flows). The main advantage is that instead of the first order Euler-Equation which is a vector differential equation we now get one scalar second order equation for the potential $\Phi(x_j,t)$ which is highly nonlinear, however, see Eq. (22g).

When comparing the relation between pressure and density for isentropic change of state with that given with a shock one may realize that the deviations are due to the third order terms. If shocks become essential for a flow these terms in the FP-Eq. do not improve the solution, they may be dropped without losing in accuracy. The FP-Eq. is able to handle all irrotational attached flows for the full boundary conditions, weak shocks are admitted.

4.2.3 Small Perturbation Potential Equation (SPP-Eq. (22h))

For transonic flow a reduced equation has been used very often by splitting into a main stream and a perturbation flow $\partial\varphi/\partial x_i$ such that $w_i = (1+\partial\varphi/\partial x\ ;\ \partial\varphi/\partial y\ ;\ \partial\varphi/\partial z)$. When only first order terms are retained Eq. (22g) results in a linear equation for subsonic and supersonic flow (LP-Eq.). For transonic flow $M\to 1$ the x-derivative $(1-M^2)\varphi_{xx}$ approaches zero and the linear equation has to be supplemented by the term $\varphi_x\varphi_{xx}$ which is nonlinear (TSP-Eq.). For small unsteady disturbances $\varphi(x_j,t) = \varphi_0(x_j)+\varphi_1(x_j,t)$ the nonlinearity enters into the unsteady TSP-Eq. via the steady mean values φ_{0x} and φ_{0xx} only. This gives the opportunity to apply either calculated or experimental steady values.

A further evaluation with respect to geometric and time properties can be made by introducing coordinates referred to characteristic lengths of the body and characteristic times t_R. This gives

(40) $$\frac{1}{l_1^2}\frac{\partial^2\bar{\varphi}}{\partial\bar{x}_i^2}-\left(Sr\frac{\partial}{\partial\bar{t}}+\frac{1}{l_1}\frac{\partial}{\partial\bar{x}}\right)^2\bar{\varphi}=\frac{1}{l_1^3}(\varkappa+1)M^2\bar{\varphi}_{\bar{x}}\bar{\varphi}_{\bar{x}\bar{x}}$$

with $\bar{x_i} = x_i/l_i\ ;\ l_i = (1, s, d)$

From this form we can judge e.g. for wings with l = 1 chord length, s as span and d as a measure for the vertical extent like angle of attack, thickness, camber, amplitude, etc., whatever is largest.

(a) large aspect ratio $s \gg 1$ drop φ_{yy} (c) small time scale $Sr^2 \gg Sr$ drop $\varphi_{xt}, \varphi_{xx}, \varphi_x\varphi_{xx}$

(b) small aspect ratio $1 \gg s$ drop $\varphi_{xx}, \varphi_x\varphi_{xx}$ (d) large time scale $Sr^2 \ll Sr$ drop φ_{tt}

We observe that the transonic nonlinear term obviously loses its importance already at moderate Strouhal numbers or at highly swept wings; for small time scales the SPP-Eq. reduces to the wave equation, etc. For a thorough investigation the present procedure can also be applied to the FP-Eq., see J.W. Miles Ref. 34. According to his findings full linearization is valid, if any of the following inequalities holds:

(41) $$|1-M| \gg O(d^{2/3})\ ;\ 1/s \gg O(d^{1/3})\ ;\ Sr \gg O(d^{2/3})$$

Only if all three inequalities turn jointly into equalities the nonlinear terms have to be included. For velocity and pressure perturbations both to be small the stringed requirements are:

(42) $$d \ll 1\ ;\ Md \ll 1\ ;\ Srd \ll 1\ ;\ Sr\,Md \ll 1$$

Local violations may be found at edges or stagnation lines.

5. Linear Potential Theory (LP-Eq.)

Complementary to the velocity potential Φ or φ with the property $w_i = \partial\Phi/\partial x_i$ there exists also an acceleration potential Ψ which reveals interesting features with respect to the pressure. For isentropic flow we get from Eq. (22f)

(43a,b,c,d) $$\frac{dW_i}{dt}=-\frac{1}{\varrho}\frac{\partial p}{\partial x_i}=-\frac{\partial}{\partial x_i}\int_{p_R}^{p}\frac{dp'}{\varrho(p')}=\frac{\partial\psi}{\partial x_i}\ ;\ \psi=-\int_{p_R}^{p}\frac{dp'}{\varrho(p')}\approx-\frac{p-p_R}{\varrho}$$

$$\psi=\frac{\partial\varphi}{\partial t}+\frac{\partial\varphi}{\partial x}\ ;\ \varphi(x,y,z;t)=\int_{-\infty}^{x}\psi(\xi,y,z;\,t-x+\xi)\,d\xi$$

The point relation between the acceleration potential Ψ and the pressure p, Eq. (43b), becomes very important for satisfying the pressure jump across a lifting surface.

5.1 Basic Solutions

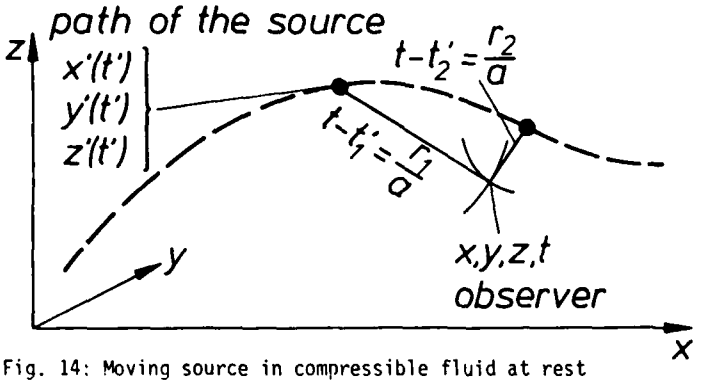

Fig. 14: Moving source in compressible fluid at rest

t' time at x' when impulse is emitted
t time at x when impulse is received

The prime benefit in the context of linear partial differential equations is that linear superposition of elementary solutions can be used to satisfy the boundary conditions. Application has found a variety of different solutions like unsteady sources, doublets, multiplets, vortices etc. As far as they are taken to describe the flow around lifting or non-lifting bodies they can be transformed to each other by proper devices. It is fully sufficient therefore to have knowledge of the simplest suitable solutions which is the unsteady source. In an ingenious way in 1940 by H.G. Küssner Ref. 35, and in 1951 by I.E. Garrick, Ref. 36, the unsteady source potential in uniform flow has been derived. Both start with the well known d'Alembert solution for a single source in rest $\varphi = q(t - Mr)/4\pi r$. Küssner argued that by simple application of the Lorenz-Transformation the moving source in a fluid at rest is received because of the invariancy of the wave Eq. to this transformation. Garrick on the other hand places sources along its path, see Fig. 14, and let each radiate one impulse $\delta(t - t')$, successively. By time integration over all impulses the moving source potential in a fluid at rest is received as

$$(44)\quad \varphi = -\frac{1}{4\pi}\int_{-\infty}^{t}\frac{q(t')\,\delta(t-t'-Mr(t'))}{r(t')}\,dt'$$

It is then Galilei transformed into a source-fixed coordinate system satisfying the linear potential Eq. (22h), see table 2. An observer watching in x_i may receive several signals generated at different times t' simultaneously at time t. This is evident from wave propagation pictures. It is familiar to us that for uniform flow there is one signal received in the subsonic case and there are two in the supersonic one. A more intricate case is a uniformly accelerated source. Starting at rest and accelerating to M = 2.5, the wave picture reveals three different areas, see. Fig. 15. They show time history for the

- one signal area from subsonicly or supersonicly
- two signal area from supersonicly
- three signal area from subsonicly and supersonicly as well as from purely supersonicly moving source

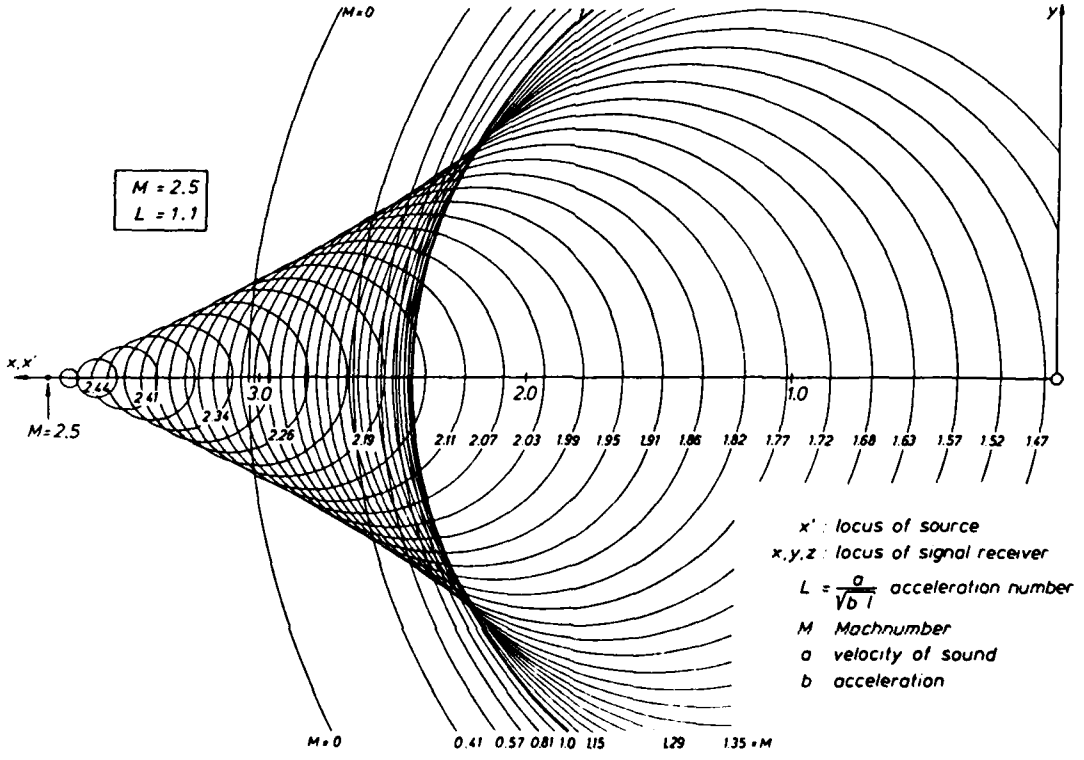

Fig. 15: Wave pictures of a uniformly accelerated source

	two-dimensional, arbitrary	two-dimensional, harmonic	three-dimensional
incompressible $M_\infty = 0$	$\frac{q(t)}{2\pi} \ln\sqrt{x_0^2 + z_0^2}$	$\frac{\bar{q}}{2\pi} e^{i\omega t} \ln\sqrt{x_0^2 + z_0^2}$	$-\frac{q(t)}{4\pi R}$
subsonic $0 \le M_\infty < 1$	$-\frac{1}{2\pi}\int_0^\infty \frac{q(t+\mu M_\infty x_0 - \mu R)}{R}\, dy_0$	$\frac{i\bar{q}\, e^{i\omega t}}{4\beta} e^{ik\mu M_\infty x_0} H_0^{(2)}(k\mu\sqrt{x_0^2 + \beta^2 z_0^2})$	$-\frac{1}{4\pi R} q(t+\mu M_\infty x_0 - \mu R)$
sonic $M_\infty = 1$	0 for $x_0 < 0$, otherwise $-\frac{1}{2\pi x_0}\int_0^\infty q(t - \frac{1}{2x_0}(x_0^2 + y_0^2 + z_0^2))\, dy_0$	0 for $x_0 < 0$, otherwise $-\frac{\bar{q}(1-i)e^{i\omega t}}{4\sqrt{k\pi x_0}} e^{\frac{ik(y_0^2+z_0^2)}{2x_0}}$	0 for $x_0 < 0$, otherwise $-\frac{1}{4\pi x_0} q(t - \frac{1}{2x_0}(x_0^2 + y_0^2 + z_0^2))$
supersonic $M_\infty > 1$	0 for $x_0 < \beta\lvert z_0\rvert$, otherwise $-\frac{1}{4\pi}\int_{-x}^{x} \frac{1}{R}\{q(t+\mu M_\infty x_0 + \mu R) + q(t+\mu M_\infty x_0 - \mu R)\}\, dy_0$	0 for $x_0 < \beta\lvert z_0\rvert$, otherwise $-\frac{\bar{q}\, e^{i\omega t}}{2\beta} e^{ik\mu M_\infty x_0} J_0(k\mu\sqrt{x_0^2 - \beta^2 z_0^2})$	0 for $x_0 < \beta\sqrt{y_0^2 + z_0^2}$, otherwise $-\frac{1}{4\pi R}\{q(t-\mu M_\infty x_0 + \mu R) + q(t-\mu M_\infty x_0 - \mu R)\}$

Notations

$\beta^2 = (1 - M_\infty^2)$

$\mu = \frac{M_\infty}{\beta^2}$

$R = \sqrt{(x - x_0)^2 + (y - y_0)^2 + (z - z_0)^2}$

$y_c = \frac{1}{\beta}\sqrt{(x - x_0)^2 - \beta^2(y - y_0)^2 - \beta^2(z - z_0)^2}$

$x_0 = x - x$

$y_0 = y - y$

$z_0 = z - z$

$x\ y\ z$ source location

$x\ y\ z$ field point

t time

ω circular frequency

$q\ \bar{q}$ source strength

$H_0^{(2)}$ Hankel function zero order second kind

J_0 Bessel function zero order

Table 2: Unsteady source potential in uniform flow

The beneficial properties of sources as elementary solutions are revealed if their continuous distribution along any curved surface is considered. The derivative normal to the source sheet of the corresponding potential P results in

(45) $$\frac{\partial P}{\partial x_n} = \frac{x_n}{|x_n|}\, q(x_1, x_2, t) + f(x_j, t)$$, see Fig. 16.

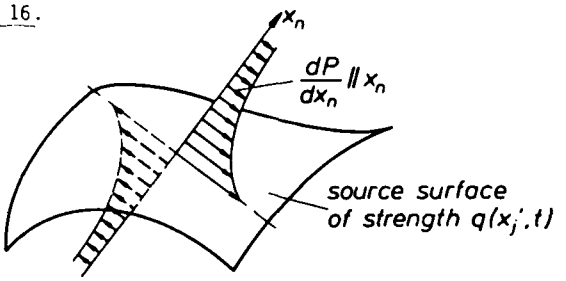

Fig. 16 : Discontinuity property of a source sheet

For wings or bodies this feature allows to fulfill the unsteady conditions comfortably, especially if full linearization of the tangential flow condition is accepted. In this case any wing motion is split into its symmetrical component, describing time variations of

- local thickness causing a displacement flow
- local incidence causing a lift producing flow

Linear superposition gives then the resulting flow.

5.2. Displacement Flow

The tangential flow condition Eq. (38) requires in its linearized form

(38a) $$w = \frac{z}{|z|}\left(\frac{\partial f_d}{\partial t} + \frac{\partial f_d}{\partial x}\right) \quad \text{with} \quad S_d = z - f_d(x, y, t) = 0$$

a discontinuity in the normal wash W_u, W_l across the symmetry plane of the pulsating body, Fig. 17.

According to Eq. (45) this can be fulfilled by representing the plan from by a source sheet. The corresponding potential is interpreted then as a velocity disturbance potential φ. E.g. for a pulsating wing in subsonic flow we receive with the aid of Table 2 and Eq. (45) and (38a) the simple integral relation

(46) $$\varphi = -\frac{1}{2\pi}\iint_{(S)} \frac{w(x', y', t + \mu M_\infty x_0 - \mu R)}{R}\, dx'\, dy'$$

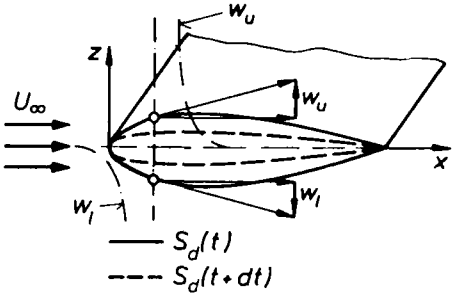

Fig. 17 Discontinuity condition for pulsating wing or body

If sonic or supersonic flow is to be considered the appropriate source solution must be taken.

For incompressible flow the potential Eq. (22i) always becomes linear and this gives sense to look at thick bodies. An example of such an exact solution is the flow around a cylinder of growing diameter, see Fig. 18. The unsteady potential may be found in Eq. (47).

(47) $$\Phi = r\cos\varphi + \frac{R^2(t)}{r}\cos\varphi + R(t)\frac{\partial R(t)}{\partial t}\ln r$$

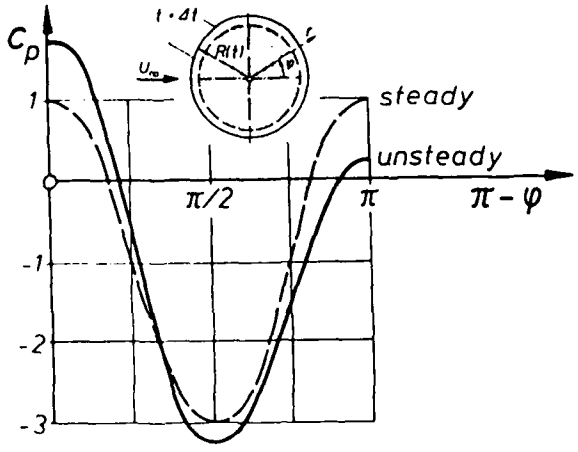

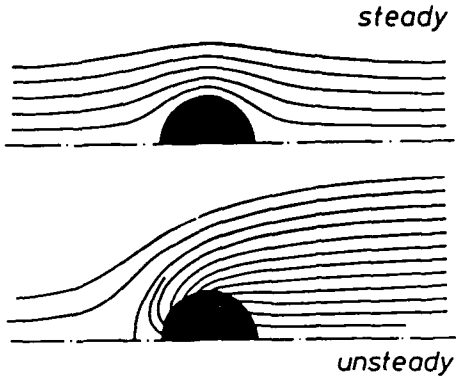

Fig. 18: Unsteady flow around a cylinder of growing diameter

The features of the unsteady flow when compared to the steady one reveal:

(a) There are characteristic differences between both flow fields in particular the positions of the stagnation points are moved upstream.

(b) The pressure in the front part is increased, in the hind part decreased.

(c) The drag is not zero but rather positive for an increase in diameter and negative for a decrease. ($c_D = D / q_\infty \cdot R(\tau) \cdot b = 2\pi \partial R(t) / \partial t$)

5.3 Lift Containing Flow

The condition for the wing to produce lift requires a pressure discontinuity between its lower and upper side, see Fig. 19, (dynamic boundary condition).

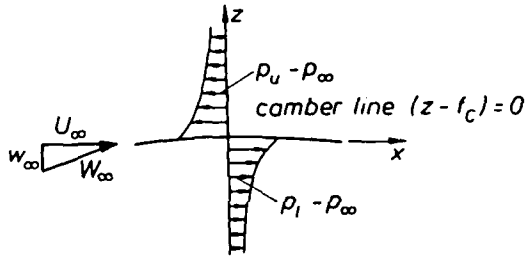

Fig. 19: Discontinuity for an unsteady lift producing wing.

Again according to Eq. (45) the source solution can be utilized, Remembering that the acceleration potential shows a point relation with respect to the pressure, Eq. (43b), the pressure jump $\Delta p = p_l - p_u$ now can be represented by the normal derivative of a source sheet (doublet sheet) which has to be interpreted now as an acceleration potential. The tangential flow condition at the unsteady camber line

$$(38b)\quad w(x,y,t) = \frac{\partial f_c}{\partial t} + \frac{\partial f_c}{\partial x}$$

is satisfied over the relation between velocity and acceleration potential, Eq. (43d).

Due to H.G. Küssner, Ref. 35, the velocity potential for arbitrary motions may be thus described for planar or non planar, for intersecting or otherwise discontinuous lifting surface elements. It results in an integral equation relating pressure and tangential flow condition on the wing. For an oscillating planar wing C.E. Watkins et al., Ref. 37, first have presented the kernel function in a suitable form. A thorough discussion of the subsonic kernels for arbitrarily spaced and inclined wing elements has first been made in 1963, Ref. 38. The subsonic flow integral equation for a planar surface lying in the plane z = 0 reads:

$$\varphi = \iint_{(S)} \Delta c_p(x', y') \cdot D(kx_0, ky_0, kz)\, dx'\, dy'$$

$$(48)\quad D = \frac{-\exp(ikx_0)}{8\pi} \frac{kz}{r} \left\{ \left[K_1(kr) + \frac{\pi i}{2} \left(I_1(kr) - L_1(kr) - \frac{2}{\pi} \right) \right] + \frac{x_0}{kr\,R} \exp\left[ik(x_0 - MR)/\beta^2 \right] - i \int_0^\infty \frac{\tau \exp(ikr\tau)}{\sqrt{1+\tau^2}}\, d\tau \right\}$$

K_1 mod. Bessel Function of 2. kind
I_1 mod. Bessel Function of 1. kind
L_1 Struve Function
$a = (x_0 - MR) / \beta^2 r$
$r^2 = y_0^2 + z^2$; $R^2 = x_0^2 + \beta^2 r^2$
$x_0 = x - x'$; $y_0 = y - y'$

For the subsonic flow three different approaches to solve the integral equation have shown to be successfull:

(a) The lifting surface method preferred by the author, Ref. 39, utilizes pressure functions which accurately account for all sensitive singularities at edges (leading edges, trailing edges, side edges, flap discontinuities, gaps, etc.) properly. The tangential flow condition is satisfied in a number of control points. Special benefits are attained if the control point location includes the leading and the trailing edge. In the status available today it utilizes surface modules which can be composed to represent any complex configurations. A complete review may be found in Ref. 40, see also H. Ashley, Ref. 41. It may be considered as the most refined solution to the integral equation with a minimum of handling complexity if the moduls are available.

(b) In the doublet lattice method as propagated mainly by W.P. Rodden et al., Ref. 42, the pressure of each lattice field is concentrated in a line placed at its 25% chordwise location. The tangential flow condition is fulfilled in the 75% midpoint of each field. The number of collocation points needed is much higher than with the lifting surface theory. Strong singularities are latently

introduced at the line locii. The doublet lattice method may be considered as a rough integration tool. It has proven, however, to give also very good results and it is appreciated because of its simplicity and versatility.

(c) The group of panel methods appears in different levels of refinement, for the most advanced version see W. Geissler, Ref. 42. Its general feature is that the pressure over a panel is taken as constant or (at least as a simple function). The kernel is approximated by a suitable set of simple functions which allow being integrated over a panel. Again the number of collocation points taken at the midpoint of each panel corresponds to the number of panels. Here logarithmic singularities are hidden at the panel edges, what can be circumvented by some smoothening devices.

The panel methods are frequently combined with the flow displacement calculation. Sources and source derived solutions can be placed also on the body surface itself instead of meanlines. The boundary conditions are directly satisfied. By this reason the panel method is best suitable to account for nonplanar configurations such as fuselages or fuselage/wing intersections. With regard to applications, such as flutter, these regions contribute only little to the generalized forces because the amplitudes there are small. Nevertheless it has to be kept in mind that an improvement in satisfying nonlinear boundary conditions in compressible flows is counteracted by the fact that the potential equation is linear, only.

For the supersonic flow the use of the integral equation formulation has been replaced by a "quasi"-inverse integral relation between pressure and downwash. It is easy to see that for all supersonic edges the lower side and the upper side of a lifting surface do not receive signals of each other. Both surfaces can be treated therefore independently. This is done in such a way that a fictive symmetrical motion pretending a pulsation is assumed. By this manner the lifting wing is reduced to the displacing wing. The potential can be formulated as described before by a source distribution placed over the wing planform and interpreted as velocity potential. This philosophy may also be extended to subsonic edges. In areas outside of the wing in which the flow velocity is not known the dynamic boundary condition, no pressure discontinuity to be permitted, has to be utilized. The equation for a planar wing is then received by the aid of Table 2 and Eq. (45) and (38a) as

$$(49)\qquad \begin{matrix} p(x,y,t) \\ \searrow \\ 0 \end{matrix} = \frac{-z}{2\pi|z|}\left(\frac{\partial}{\partial t}+\frac{\partial}{\partial x}\right)\lim_{z\to 0}\iint_{(forecone)}\frac{w(x',y',t-t_1)+w(x',y',t-t_2)}{R}\,dx'dy' \quad \begin{matrix} \nearrow \text{ on the wing} \\ \searrow \text{ outside of wing} \end{matrix}$$

The singularity is only of the order $1/\sqrt{x_0^2-\beta^2y_0^2}$ much lower than with the kernel function which is $1/y_0^2$. Box methods using quadratic, characteristic, Mach number adjusted rectangular or wing adjusted trapezoidal panels are well established, see e.g. Ref. 44. No difficulties in the treatment of complex nonplanar configurations occur.

5.4 Results

The present status of Eu- or FP-codes covers nearly without exclusion two-dimensional unsteady flows, only. Full aircraft configurations to be treated by non-linear methods are still at its very beginning. Therefore linearized three-dimensional theory still is the main engineering tool to assess flutter or loads.

Experiments compared with the lifting surface method of Ref. 39 and 40 have validated the linear theories beautifully as long as shock and viscous effects are not predominant. This is shown for two different cases (reduced frequency k is based on semispan). In Fig. 20 the applicability to high Mach numbers and control surfaces has been proven and in Fig. 21 the capability to predict interference effects such as wing-to-tail is demonstrated, Ref. 46. Aerodynamic

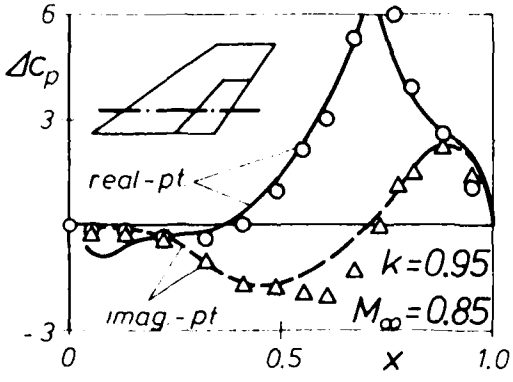

Fig. 20: Unsteady pressures for a control surface oscillation at transonic Mach numbers.

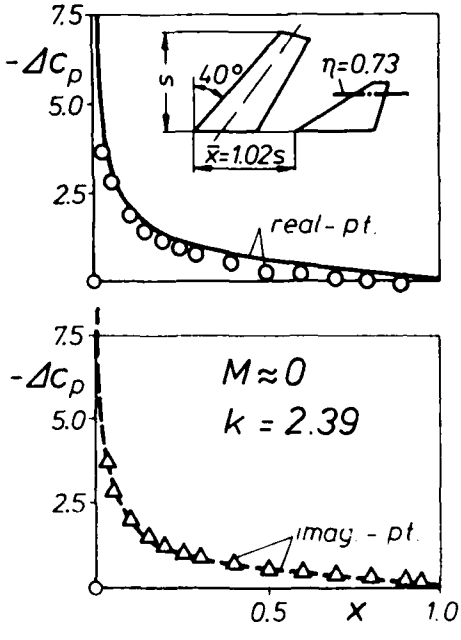

Fig. 21: Tail interference pressures due to a wing in pitching oscillations.

coupling to produce flutter could be demonstrated for the first time in Ref. 45.

Besides pressures, lift, moments or generalized forces moving wings produce also thrust or drag. This can easily be understood from translational oscillation, see Fig. 22. During one period of oscillation the unsteady normal force changes its sign, whereas the thrust does not. The thrust increases with frequency, efficiency drops down from $\eta = 1$ to $\eta = 0{,}5$. Interfering surfaces in tandem configurations can recover the maximum efficiency independently of frequency.

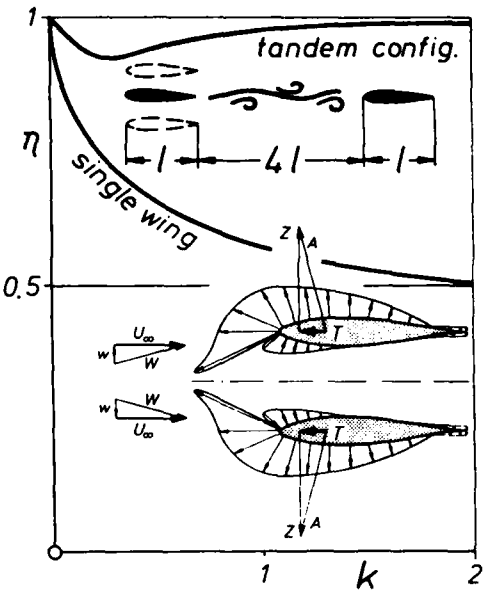

Fig. 22: Propulsion efficiency of wings in translational motion

6. Conclusions

1. Rapid progress in the numerical solution techniques of unsteady N-S-Eqs. gives good hope that for laminar flows stream patterns are predicted which represent most of the physical features. At present this holds for simple configurations at two-dimenional conditions.
2. Turbulent unsteady flows stand at its beginning of being understood. No profound knowledge exists about correct turbulence modelling. There are some good reasons to assume that quasisteady models hold as long as the time scales of turbulence and unsteady main flow are well apart. Unsteady turbulence measurements do exist to some extent, their analysis, however, is in a rudimentary state.
3. Laminar separation models for two-dimensional flows according to the M-R-S-Criterion have been substantiated by theory and experiment as long as upstream moving separations are considered. For downstream moving separations model calculations are still lacking. No detailed knowledge exists on turbulent two-dimensional unsteady separation. Investigations on three-dimensional unsteady separation both laminar and turbulent are not available.
4. The present state of calculations based on inviscid flow assumptions as given by the Eu-Eqs. accounts well for shocks over profiles at transonic speeds as long as the flow is attached. This also holds for the FP-Eq. which is, however, limited to weak shocks and irrotational flow. Three-dimensional results are extremely rare and directed towards low sweep, high aspect ratio wings. When looked at applications such as flutter, Eu- or FP-calculations have to be performed for each mode separately.
5. Linearized unsteady potential theory is well established. It will remain the prime tool to aerodynamicists for a long time. The advantages lie in
   - its easy applicability to complex three-dimensional configurations
   - its - when compared to steady conditions - less restrictive applicability to high subsonic flows
   - its superposition principle, e.g. allowing to calculate one influence matrix only independent of the number of modes.

REFERENCES

1. Johann Bernoulli: Nouvelle Hydraulique. Lausanne and Geneve, 1842.
2. E. Truckenbrodt: Fluidmechanik, Band 1. Springer-Verlag 1980.
3. H. Schlichting: Grenzschichttheorie. Verlag G. Braun, Karlsruhe, 8. Auflage, 1982.
4. R.W. MacCormack: Status and future prospects of using numerical methods to study complex flows at high Reynolds numbers. AGARD F.D.P. Meeting.
5. D.P. Telionis: Unsteady viscous flows. Springer Verlag, 1981.
6. W.F. Ballhaus, J.D. Bridgeman: Numerical solution techniques for unsteady transsonic aerodynamics problems, AGARD Rep. No. 679, 1980.
7. M. Rubesin: Subgrid or Reynolds Stress Modelling for Three-Dimensional Turbulence Computations. NASA SP-347, Part I, March 1975, pp. 317-339.
8. O. Reynolds: On the dynamical theory of incompressible viscous fluids and the determination of the criterion. Phil Trans. Roy. Soc. A 186 (1895), p. 123-164.
9. W.C. Reynolds, T. Cebeci: Turbulence (Edited by P. Bradshaw). Chapter on Calculations of turbulent flows. Springer-Verlag 1978.
10. T. Cebeci, A.M.O. Smith: Analysis of turbulent boundary layers. Academic Press 1974.
11. P.S. Klebanoff: Characteristics of turbulence in a boundary layer with zero pressure gradient. NACA Rep. 1247, 1955.
12. L.W. Carr: A compilation of unsteady turbulent boundary layer experimental data. AGARDograph No. 265, 1981.
13. D.P. Telionis: Analytical methods for prediction of unsteady turbulent boundary layers. AGARD Re. No. 679, entitled "Special Course on Unsteady Aerodynamics", 1980.

14. P. Bradshaw: Calculation of boundary layer development using the turbulent energy equation. VI. Unsteady flows. NPL Aero Rept. 1288.

15. H.L. Norris, W.C. Reynolds: Turbulent channel flow with a moving wavy boundary. Stanford University Technical Rep. No. TF-7, 1975.

16. H. Lamb: Hydrodynamics, Cambridge University Press, London and New York. 1932.

17. O. Tietjens: Entstehung von Wirbeln bei Wasserströmungen. Taken from a movie on "Vortex Generation in Water Flow". Available at Institute für Strömungsmechanik, Technische Universität Braunschweig, 1927.

18. M. Schwabe: Über Druckermittlung in der instationären ebenen Strömung. Ing. Arch. 6, 34, 1935.

19. Y. Lecointe, J. Piquet: Numerical solution of unsteady two-dimensional viscous flow around bodies. 3 rd Symp. Num. Phys. Aspects of Aerodynamic Flows. Long Beach,CA,Jan.1985.

19a. R. Bouard, M. Coutanceau: J. Fluid Mech., Vol. 101, pp. 583-607, 1980.

20. G.G. Stokes: On the effects of internal friction of fluids on the motions of pendulums. Trans. Cambr. Phil. IX,8, 1851.

21. L. Prandtl: Über Flüssigkeitsbewegungen bei sehr kleiner Reibung. Verhandlung d. III, Intern. Math. Kongr. Heidelberg, 1904, p. 484-491.

22. K. Stewartson: The theory of unsteady laminar boundary layers. Adv. Mech. VI, p. 1-37, 1960.

23. J.C. Williams III, W.D. Johnson: Note on unsteady boundary layer separation. AIAA Journal, Vol. 12, No. 10, 1974.

24. D.P. Telionis, D.Th. Tsahalis: Unsteady turbulent boundary layers and separation. AIAA Journal, Vol. 14, No. 4, 1976.

25. S. Goldstein: On laminar boundary layer flow near a position of separation. Quart. Journ. Mech. Appl. Math.1, 1948.

26. C.A. Koromilas, D.P. Telionis: Unsteady laminar separation; an experimental study. J. Fluid. Mech., Vol. 97, Cambridge University Press, 1980.

27. P. Bradshaw: Prediction of separation using boundary layer theory. AGARD LS No. 94 on "Three Dimensional and Unsteady Separation at High Reynolds Numbers", 1978.

28. F.K. Moore: On the separation of the unsteady laminar boundary layer. Boundary Layer Research, Springer Verlag Berlin, 1958 (edited by H.G. Görtler).

29. N. Rott: Unsteady flow in the vicinity of a stagnation point. Quaterly of Applied Mathematics. Vol. 13, 1956.

30. W.R. Sears: Some recent developments in airfoil theory. J. Aeron. Sci., Vol. 23, No. 5, 1956.

31. R.L. Simpson, J.H. Strickland, P.W. Barr: Laser and hot-film anemometer measurement in a separating turbulent boundary layer. J. Fluid Mech., Vol. 79, March 1971.

32. S.J. Kline, J.G.Bardina, R.C. Strawn: Correlation and detachment of two-dimensional turbulent boundary layers. AIAA Journ., Vol. 21, No.1, 1983.

33. W.J. Chyu, S.S. Davis: Numerical studies of unsteady transonic flow over an oscillating airfoil. AGARD SAM Panel Meeting, 2.-7. Sept. 1984, Toulouse, France.

34. J.W. Miles: Linearization of the equations of nonsteady flow in a compressible fluid. J. Math. and Phys. 33, 1954.

35. H.G. Küssner: Allgemeine Tragflächentheorie. Luftfahrtforschung 17, 1940.

36. I.E. Garrick: Moving sources in nonsteady aerodynamics and in Kirchoff's formula. Proc. First U.S. Natl.Congr.Appl.Mech., Chicago, 1951.

37. C.E. Watkins, H.L. Runyan, D.S. Woolston: On the kernel function of the integral equation relating lift and downwash distribution of oscillating finite wings in subsonic flow. NACA Rep. 1234, 1955.

C.E. Watkins, J.H. Bermann: On the kernel function of the integral equation relating lift and downwash distribution of oscillating wings in supersonic flow. NACA TR 1257. 1956.

38. B. Laschka: Das Potential und das Geschwindigkeitsfeld harmonisch oszillierender Tragflächen in Unterschallströmung (Potential and velocity field of harmonically oscillating lifting surfaces in subsonic flow). Z. Angew. Math. Mech. (ZAMM) 43, p. 325-333, 1963. - Erratum: ZAMM 47,p.284, 1967.

39. B. Laschka: Zur Theorie der harmonisch schwingenden tragenden Fläche bei Unterschallströmung. Z. Flugwiss. (ZFW) 11, Heft 7, 1963.

40. B. Laschka: Interfering lifting surfaces in subsonic flow. Z. Flugwiss. (ZFW)18, Heft 9/10, 1970.

41. H. Ashley: Unsteady Subsonic and Supersonic Flow. AGARD Conference on Unsteady Aerodynamics, Ottawa, Canada, 1977, AGARD CP-227, Paper 1.

42. E. Albano, W. Rodden: A doublet lattice method for calculating lift distribution on oscillating surfaces in subsonic flow. AIAA 6th Aerospace Sciences Meeting, New York, N.Y., Jan.22-24, 1968, Paper No. 68-73.

43. W. Geissler: Nonlinear unsteady potential flow calculations for three-dimensional oscillating wings. AIAA-Journal, Vol. 16, No. 11, Nov. 1978.

44. V.J.E. Stark:Calculation of aerodynamic forces on two oscillating finite wings at low supersonic Mach numbers. SAAB TN 53, 1964.

45. O. Sensburg, B. Laschka: Flutter induced by aerodynamic interference between wing and tail.

46. J. Becker: Interfering lifting surfaces at subsonic flows. - Comparison between theory and experiment. AGARD Rep. No. 614. For figure 20 see also MBB-Ottobrunn Rep. 403-69.

DYNAMIC STALL OF SWEPT AND UNSWEPT OSCILLATING WINGS

Franklin O. Carta
United Technologies Research Center
East Hartford, Connecticut 06108

SUMMARY

Recent unsteady tests on oscillating tunnel-spanning wings (representative of full scale helicopter blades) have shown that the dynamic stall phenomenon for a swept wing model is significantly different from that for an unswept wing. Several critical measurements and calculations relative to the behavior of the surface flow were made, including chordwise wave speed of the stalling vortex, the degree of pitch rate dependence of the vortex inception angle, and the ability of the cosine law for sweep to normalize unsteady post-stall behavior, even after reattachment occurs.

The vortex chordwise wave speed was found to be insensitive to sweep angle over the forward blade region, but was approximately half as large over the aft region for a sweep angle of 30 deg, relative to the unswept wing. It was also found that the vortex inception angle (which can be associated with dynamic stall inception) was virtually unaffected by changes in sweep angle. However, a change in Mach number (measured normal to the leading edge) from 0.3 to 0.4 caused a drop in vortex inception angle of about 4 deg, comparable to the change in quasi-steady stall angle for the same Mach number range. It was also found that the vortex inception angle varies linearly with reduced frequency, and appears to be independent of pitch rate at constant reduced frequency.

The traditional cosine law normalization for sweep is not applicable above the stall angle, either for steady or for unsteady behavior. As a corollary to this, it was determined that sweep causes a dynamic displacement of the lift response such that the unstalled portion of a C_L-α hysteresis loop (both prestall and post-stall) for the swept wing lies below that for the unswept wing. This result was totally unexpected and is as yet unexplained, although an examination of the Fourier components of the unsteady lift shows it to be primarily a first harmonic phenomenon.

Finally, an examination of hot film response data shows that the stagnation flow along the swept wing leading edge significantly alters the unsteady surface flow behavior in a narrow region along the leading edge when compared with data from the unswept wing. However, from approximately 15 percent chord and aft there appears to be no sweep effect, and the results from both wings are nearly indistinguishable.

LIST OF SYMBOLS

A	dimensionless pitch rate, Eq. (9)	q	dynamic pressure based on freestream velocity, newton/m^2, Eq. (3)
A_v	dimensionless pitch rate at vortex inception angle, Fig. 7	T	period, sec
a_∞	sound speed, m/sec, Eq. (2)	t	time, sec
c	Airfoil chord, m, Eq. (2)	t_0	vortex inception time, sec
C_L	lift force coefficient	V_c	chordwise velocity, m/sec, Eq. (4)
C_M	moment coefficient	V_∞	freestream velocity, m/sec
$C_p(\chi,\tau)$	pressure coefficient distribution, Eq. (3)	$\bar{V}_w$	average dimensionless wave speed, Eq. (4)
C_W	work coefficient , Eq. (11)	$\bar{V}_{wij}$	average dimensionless wave speed between stations i and j
f	airfoil pitching frequency, Hz, Eq. (2)	α	airfoil angle of attack, deg, Eq. (5)
k_c	chordwise reduced frequency, Eq. (2)	α_M	mean angle of attack, deg, Eq. (5)
M_c	chordwise Mach number, Eq. (1)	α_{ss}	steady state stall angle, deg
M_∞	freestreem Mach number, Eq. (1)	α_v	vortex inception angle, deg, Eq. (5)
m	slope, Eq. (6)	α_{v0}	constant used in Eq. (6), deg
$p(\chi,\tau)$	chordwise pressure distribution, newton/m^2, Eq. (3)	$\bar{\alpha}$	amplitude of pitching motion, deg, Eq. (5)
		β	dimensionless pitching axis, Eq. (11)

ϵ	data scatter parameter, deg, Eq. (10)	χ	dimensionless distance from airfoil nose
Λ	sweep angle, deg, Eq. (1)	ω	circular frequency, rad/sec, Eq. (5)
Ξ	dimensionless aerodynamic damping in pitch, Eq. (12)	$( )_R$	real part
τ	dimensionless time based on oscillation period, also fraction of period	$( )_u$	upper surface
τ_0	dimensionless vortex inception time based on oscillation period, Eq. (5)	$( )_\ell$	lower surface

INTRODUCTION

The need for unsteady aerodynamic data extending into the dynamic stall regime has long been recognized by helicopter designers, and many investigations have been performed to serve these needs. Early work at United Technologies Research Center (UTRC), Refs. 1 and 2, and at the Vertol Division of Boeing, Ref. 3, was specifically tailored to provide data over ranges of parameters typical of helicopter operation. More recently a series of tests were conducted at the NASA Ames Research Center, culminating in an examination of the unsteady stall behavior of eight airfoil sections (Ref. 4 and its related data reports). While all these tests yielded a great deal of detailed information on dynamic stall, they were restricted to unswept configurations. Sweep was not included in the early test programs for two main reasons. First, oscillating swept wing tests were probably beyond the achievable state-of-the-art for most investigators because of the prohibitive cost and the technical complication of the required facility. Second, it was felt for many years that the main emphasis should be the compilation of unswept wing data to serve as a basis for future investigations. Indeed, it was found that the use of basic unswept data in tabular form provided a substantial improvement in the ability to predict rotor blade dynamic response (Ref. 2).

Nevertheless, it is obvious that even under the simplest of inflow conditions, a helicopter rotor blade in forward flight is instantaneously unswept in only two positions; viz., at azimuth angles of 90 and 270 deg. Thus conventional, unswept, two-dimensional aerodynamic testing may not be completely adequate for helicopter rotor blade applications because of the wide variations in Mach number, sweep angle, and angle of attack over the plane of the rotor. As the requirements for improved dynamic predictions have increased, the need for unsteady dynamic stall data at nonzero sweep angles has become increasingly more important. To meet these needs, an oscillatory drive system capable of operating in both unswept and swept modes was developed at UTRC. The work reported on herein describes some of the results obtained from this experimental device, and is condensed from Refs. 5 and 6.

DESCRIPTION OF THE DATA BASE

The data base for the present study was obtained from aerodynamic experiments performed on an oscillating tunnel-spanning wing in both unswept and 30 deg swept configurations in the 2.44 m (8 ft) octagonal test section of the United Technologies Research Center (UTRC) Main Wind Tunnel (Fig. 1). Except for the hot film results, the data described herein were taken on a model whose chordwise profile, taken normal to the wing leading edge, is a NACA 0012 airfoil 40.6 cm (16 in.) in length. A detailed description of the test program can be found in Ref. 5, and an amplification of the material discussed here is presented in Ref. 6. The parameters for this test were the wing sweep angle, Λ, the amplitude of pitching motion, $\bar{\alpha}$, the mean angle of attack, α_M, the pitching frequency, f, and the approach Mach number, M_∞, and their ranges were chosen to be representative of the condition on the retreating blade of a helicopter rotor. The effect of sweep was accounted for in the normalization process by referring all data to the component of Mach number normal to the wing span,

$$M_c = M_\infty \cos \Lambda \tag{1}$$

where subscript c denotes the chordwise direction. Unsteady pressure data were obtained for sinusoidal pitching about the quarter chord axis at two values of M_c (0.3 and 0.4) for each value of Λ (0 and 30 deg), and two values of $\bar{\alpha}$ (8 and 10 deg) at four mean angles of attack α_M (0, 9, 12, and 15 deg). All angles were measured in a plane perpendicular to the span axis. Tests were conducted over a range of frequencies such that the chordwise reduced frequency

$$k_c = \frac{\pi c f}{a_\infty M_c} \tag{2}$$

was common for several f's at both sweep angles. The wind tunnel stagnation pressure was equal to atmospheric pressure, and for the 40.6 cm model at $M_c = 0.3$ the chordwise Reynolds number was approximately 2.8×10^6.

The effects of sweep on the pressure data were accounted for in Ref. 5 by normalizing the data with respect to the velocity component normal to the span to obtain the following expression for dimensionless pressure coefficient,

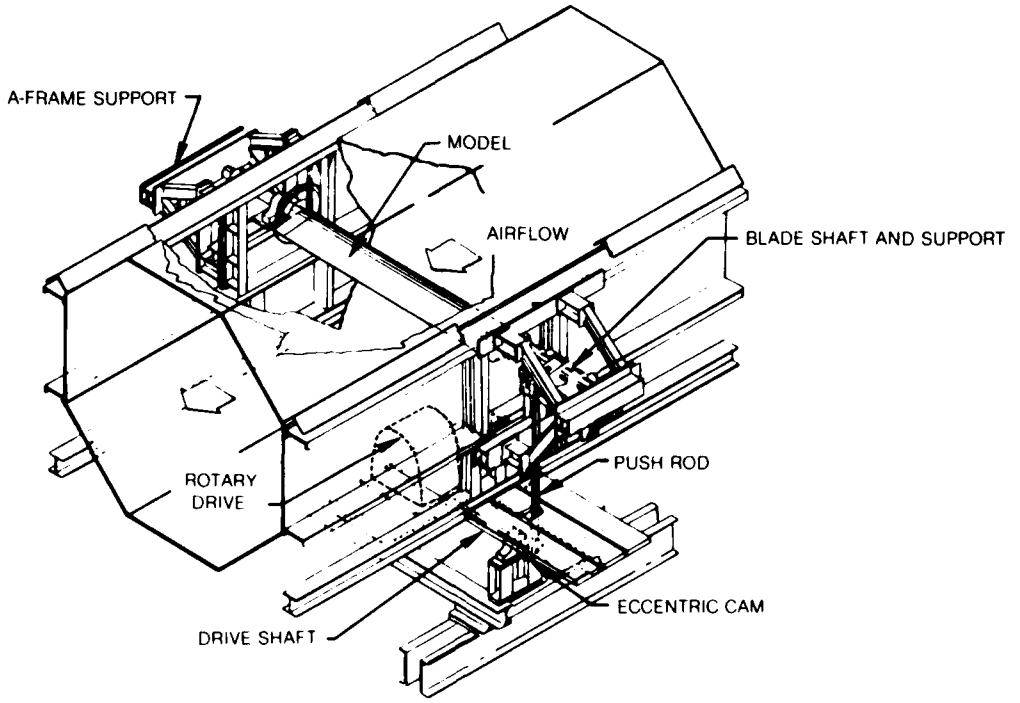

Fig. 1 UTRC Main Wind Tunnel Oscillatory Model System

$$C_p(\chi,\tau) = -\frac{p(\chi,\tau)}{q\cos^2\Lambda} \tag{3}$$

where χ is the dimensionless position along the chord and τ is dimensionless time. This nondimensionalization scheme is based on traditional steady-state sweep analysis which assumes the flow to be potential and the pressure distribution on the wing to be determined entirely by the magnitude of the normal velocity component, $V_\infty \cos\Lambda$. Note also that in this paper the pressure coefficient is defined as the negative of the normalized pressure, for convenience in relating positive integrated lift to a positive value of C_p.

NORMALIZATION PROCEDURE

Generally, the purpose of normalization is to consolidate data to a common reference. This is done to highlight the nonsimilar aspects of the data from case to case and thus to permit a more effective analysis of their dependence on the various test parameters. In well-behaved small disturbance problems, for example, the normalization process coalesces the data to a common curve so they become amenable to a general qualitative analysis. In the present investigation, however, the fluctuations in the measured pressures exceed what is normally considered "small disturbance" levels. In realization of this and the fact that much of the data was obtained within the stalled flow regime, the following discussion attempts to identify the limitations of the normalization procedure used in this paper.

An example of how well the normalization procedure works below stall with the current data base is depicted in Fig. 2a (left panel) in which unsteady data obtained from the 30 deg swept wing at $\bar{\alpha}$ = 8 deg, α_M = 0 deg, M_c = 0.40, and f = 8 Hz ($k_c = \pi cf/a_\infty M_c$ = 0.075) are compared with data similarly obtained at M_c = 0.30, and f = 6 Hz (also at k_c = 0.075). This example shows that the reduced frequency normalization procedure successfully coalesces the linear part (first harmonic component) of the chordwise amplitude response distribution to a common curve at low aerodynamic load (α_M = 0 deg). Conversely, Fig. 2b (right panel) shows some deterioration in similarity when results for the same combinations of Mach number and frequency are compared at α_M = 9 deg. Comparable results (cf. Ref. 6) were obtained for the first harmonic phase angle distribution. This would indicate that reduced frequency similarity deteriorates at high angles of attack.

As noted above in Eq. (1), wing sweep is accounted for in the normalization process by utilizing the component of freestream velocity normal to the span as the normalizing velocity. This simple approach is the same that has been traditionally used in the analysis of steady-state data. An example of the effectiveness of this approach to swept wing normalization in similarity analysis is shown in Fig. 3a (left panel) for the zero mean angle of attack case at f = 8 Hz, $\bar{\alpha}$ = 8 deg, and M_c = 0.40. Figure 3b (right panel) shows the same comparison but at α_M = 9 deg. As in Fig. 2b, it is seen that the higher mean angle of attack causes a deterioration in the sweep similarity between normalized data.

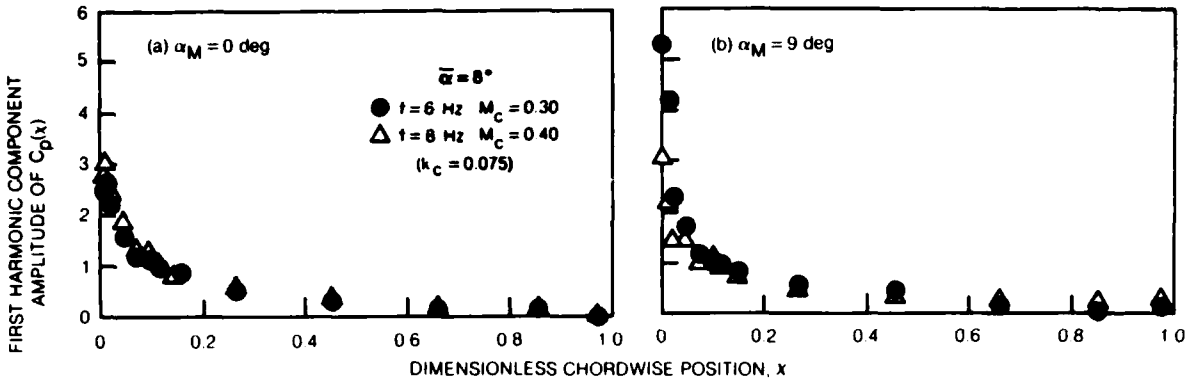

Fig. 2 Mach Number and Frequency Similarity Analysis of First Harmonic Component Amplitude Response Distribution for 30 deg Swept Airfoil

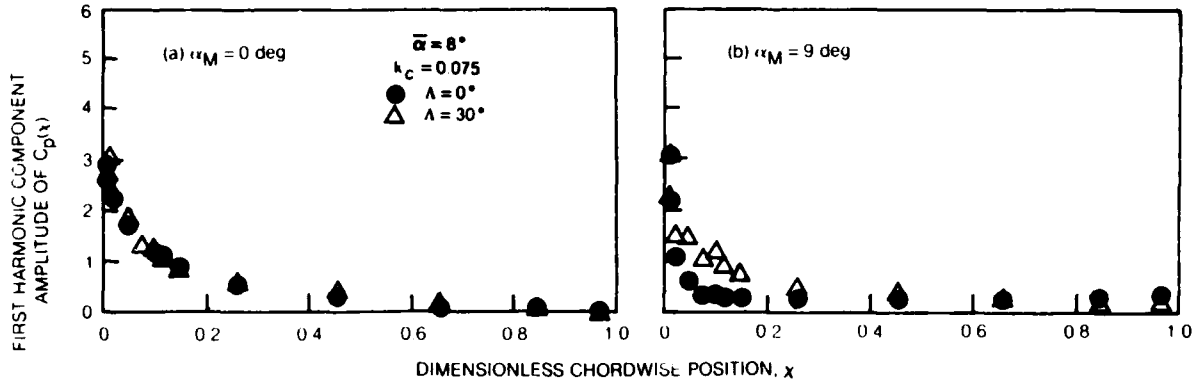

Fig. 3 Sweep Angle Similarity Analysis of First Harmonic Component Amplitude Response Distribution

On the basis of these examples, it would appear that the present normalization procedure is generally effective in highlighting the nonsimilar aspects of the data, and is thus useful in determining the effect of the various test parameters on the oscillatory stall phenomenon.

PRESSURE WAVE STUDY

Wave Speed Analysis

In Ref. 7 it was shown that plots of unsteady pressure versus both time and chordwise position could be analyzed to yield quantitative information on the chordwise propagation of pressure waves. That technique is applied herein, and in the example of Fig. 4a, the data are restricted to the first 15 percent of the chord for clarity. The vertical axis represents both the unsteady pressure coefficient level relative to steady state (left scale) and the chordwise location of the pressure measurement (right scale). The result is a pseudo three-dimensional plot of the $C_p(\chi,\tau)$ surface, referred to as a pressure carpet plot. To interpret this figure, refer each curve to its zero level at the appropriate χ-tic mark on the right scale, and use the left scale to measure the pressure relative to its zero level. The precipitous drop in C_p in the vicinity of τ = 0.17 to 0.2 is customarily associated with dynamic stall and is usually ascribed to the formation and chordwise passage of a stall cell or vortex.

For this carpet plot a set of constant pressure contours (isobars) was constructed in the χ,τ plane as shown in Fig. 4b. The numbers that are appended to each contour are values of unsteady C_p. As shown in Ref. 7, the direction of the family of contour extremes identifies the direction of wave propagation, and a simple estimate of the slope yields the wave speed.

Figure 4c concentrates on the first four tenths of the period, $0 \leq \tau \leq 0.4$. The connection between the contour extremum at the leading edge with the extremum at the 15 percent chord location (dashed line labeled "overall 15%") is used for estimating the wave speed over the forward 15 percent of the blade chord. This set of contour extremes moves toward increasing time as the chord is traversed from front to rear. The dimensionless wave speed was shown in Ref. 7 to be related to the ratio of chord extent to elapsed time by the formula

$$\bar{v}_w = \frac{c\Delta\chi}{V_c \Delta t} = \frac{k_c}{\pi} \cdot \frac{\Delta\chi}{\Delta\tau} \qquad (4)$$

using $t = \tau T = 2\pi\tau/\omega$, and $k_c = c\omega/2V_c$.

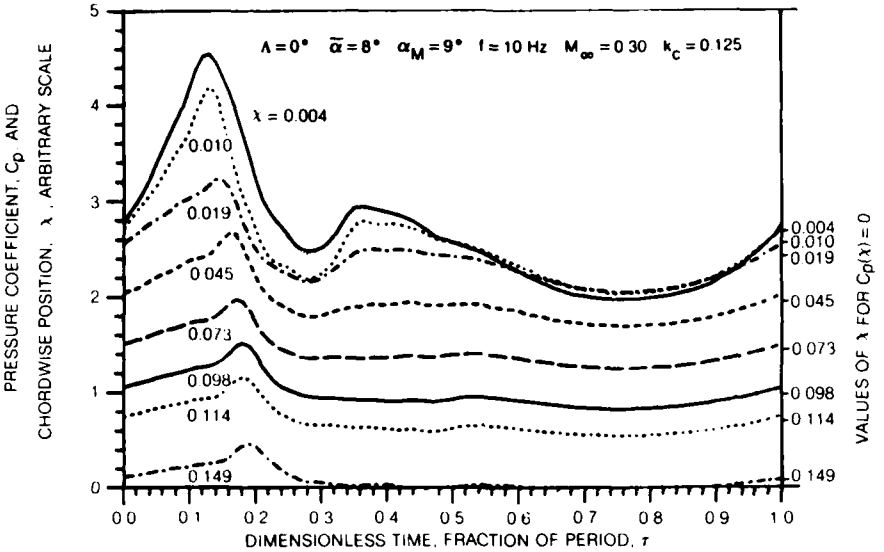

Fig. 4a Pressure Carpet Plot, Leading Edge Region

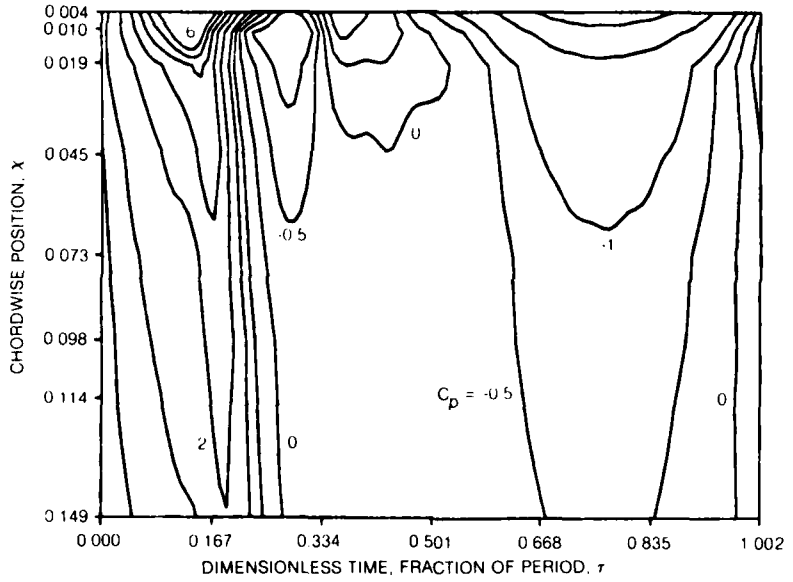

Fig. 4b Pressure Contour Map, Leading Edge Region

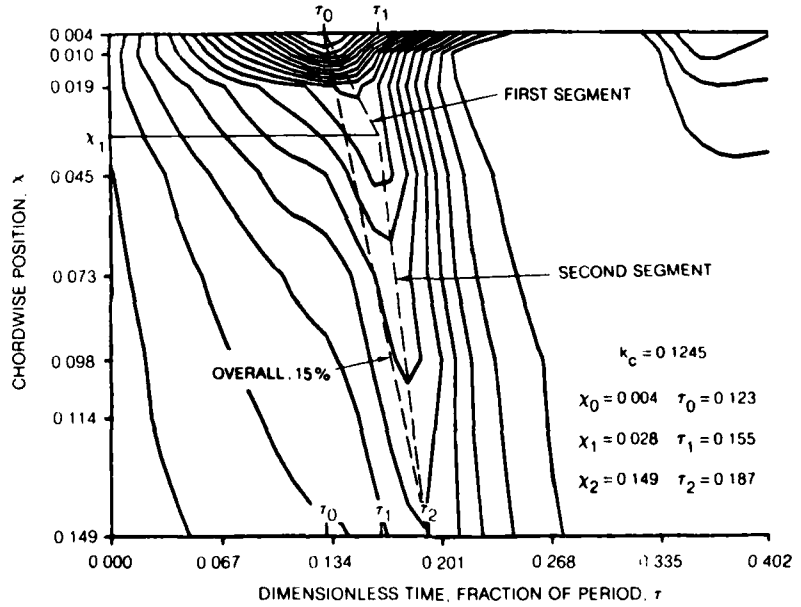

Fig. 4c Illustration of Segmented Wave Speed Near Leading Edge

In general, the locus of contour extremes is not linear but can be represented by straight line segments of different slopes. The end points of the first segment are denoted by (χ_0, τ_0) and (χ_1, τ_1) and those of the second segment by (χ_1, τ_1) and (χ_2, τ_2). Hence, there are *actually two distinct regions* within the first 15 percent of the chord that have different wave speeds. For this particular example, the coordinates of these regions are $(\chi_0, \chi_1, \chi_2) = (0.004, 0.028, 0.149)$, $(\tau_0, \tau_1, \tau_2) = (0.123, 0.155, 0.187)$, and with $k_c = 0.125$, application of the wave speed Eq. (4) yields $\bar{V}_{w01} = 0.035$ (first segment), $\bar{V}_{w12} = 0.146$ (second segment), and $\bar{V}_{w02} = 0.090$ (overall, 15%), where the wave speed subscripts match the subscripts of the initial and end-point coordinates of the segment in question. Furthermore, Fig. 14 of Ref. 6 for the entire chord shows that another discontinuity can be defined at the 15 percent chord station, separating the forward region from the aft region of the chord, implying additional speed changes along the chord. This last coordinate point is given by $(\chi_3, \tau_3) = (0.971, 0.284)$, and two additional wave speeds can be defined, $\bar{V}_{w23} = 0.326$ (third segment), and $\bar{V}_{w03} = 0.239$ (overall, 100%). It is seen that the wave is slowest in the region of high pressure gradient near the leading edge ($\bar{V}_{w01}$). This is the region characterized by the dense array of constant level contour lines in Fig. 4c. Conversely, the wave travels more rapidly over the second segment ($\bar{V}_{w12}$) where the chordwise pressure gradient is lower, and attains its highest speed over the last segment ($\bar{V}_{w23}$) where pressure gradient is minimal.

A study was performed to examine the effect of each of the test parameters on wave speed and the results are summarized in Fig. 5, in which the overall wave speed, $\bar{V}_{w03}$, is plotted versus reduced frequency, k_c. Mean angle of attack variation is depicted by the three symbols used (circle, triangle, and square) and the sweep variation is highlighted by the contrast between open and solid symbols. A comparison of the upper and lower panels (for effect of amplitude on wave speed) shows a negligible difference, and comparison of the left and right panels (for Mach number) shows a small difference, although Ref. 6 indicates that the effect of M_c on wave speed is inconsequential.

By far, the parameter that has the greatest effect on $\bar{V}_w$ is the sweep angle. In all four panels the overall wave speed for the unswept wing (open symbols) is consistently and significantly greater than that for the swept wing (solid symbols) by a factor of 1.5 to 2.0. This phenomenon of lower chordwise wave speed in swept flow has not been predicted by any previous analysis nor observed in any previous experiment.

In an effort to examine these trends more closely, wave speeds for the several segments (defined earlier) were computed and are displayed in Fig. 6 for $M_c = 0.3$. The three left hand panels are the three local wave speeds, $\bar{V}_{w01}$, $\bar{V}_{w12}$ and $\bar{V}_{w23}$, proceeding aft along the chord. The two right hand panels are the two average wave speeds, $\bar{V}_{w02}$ *over the first 15 percent of the chord, and* $\bar{V}_{w03}$ over the entire chord. (The latter is repeated from the upper left panel of Fig. 5.) It is clear that there is substantially no effect of sweep angle on the local wave speed over the forward 15 percent of the chord, either by examination of the panels for $\bar{V}_{w01}$ and $\bar{V}_{w12}$, or from the results for $\bar{V}_{w02}$. Virtually all of the sweep effect is perceived to occur in the aft portion of the chord (lower left panel), with factors of as much as 2 observed in unswept wing wave speed versus that for the swept wing. This result is representative of all cases examined. If the pressure wave is associated with the formation and chordwise transport of a vortex, these results would imply that the vortex motion along the chord is independent of sweep over the first 15 percent region of the chord, and is strongly dependent on sweep thereafter.

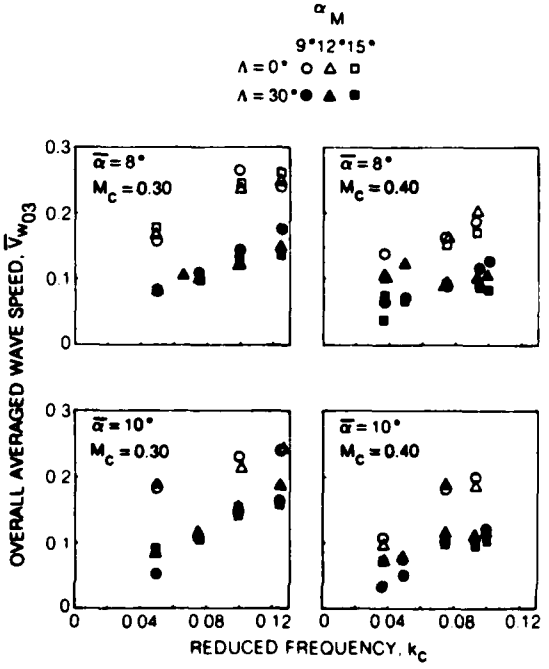

Fig. 5 Effect of Sweep Angle on Overall Wave Speed

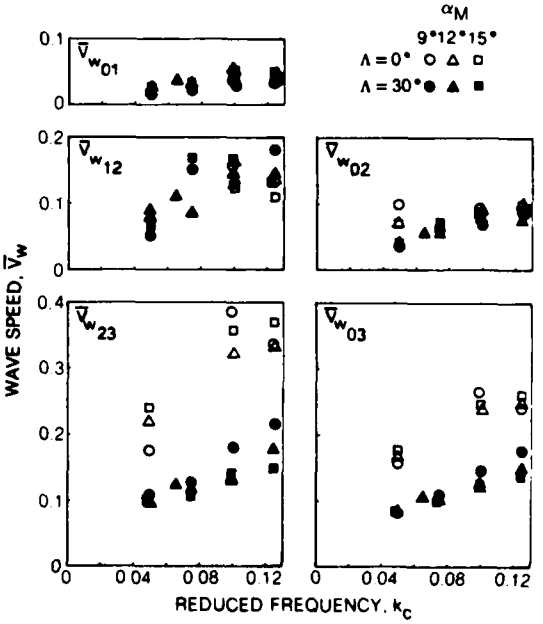

Fig. 6 Effect of Sweep Angle on Wave Speed at Several Chordwise Locations for $M_c = 0.30$ and $\bar{\alpha} = 8°$

Vortex Inception Angle Variation

In pursuing further the interpretation of the phenomenon just described as the formation of a vortex and its subsequent chordwise transport, the inception time can be studied and related to the vortex inception angle, α_v. A direct computation of α_v can be made by substituting the dimensionless inception time, $\tau_0 = \omega t_0/2\pi$ (cf. Fig. 4c), into the equation for instantaneous angular position.

$$\alpha = \alpha_M + \bar{\alpha} \sin \omega t = \alpha_M + \bar{\alpha} \sin 2\pi \tau_0 = \alpha_v \qquad (5)$$

The results are shown in Fig. 7 as plots of vortex inception angle versus reduced frequency. These plots also contain information on the steady state stall angle (triangular symbols on the left ordinate) and on the best linear fit to the data. The latter were obtained by a least squares procedure for each data group, and the former by estimating the steady state angle of attack at which $dC_M/d\alpha = 0$ in Figs. 14 through 17 in Ref. 5.

The vortex inception angle, α_v, varies linearly with k_c, as indicated by the good correlation of the linear least squares line

$$\alpha_v = \alpha_{v0} + mk_c \qquad (6)$$

with the measured data, and the narrow scatter range for each data set. (In this equation, α_{v0} is the zero frequency intercept and m is the slope.)

A comparison of the left and right panels of Fig. 7 shows that sweep has a tendency to delay vortex inception, but this delay is less than two degrees overall, and less than one degree in the majority of cases examined. In contrast to this result, the figure shows a substantial Mach number effect, with incipient vortex angle differences of as much as three or four degrees as M_c varies from 0.3 (open symbols) to 0.4 (closed symbols). The steady state stall angle based on zero moment slope, α_{ss}, is unaffected by sweep angle changes. (However, Figs. 14 through 17 of Ref. 5 show that the shape of the lift curve changes significantly in the direction of lift stall delay with increasing sweep, consistent with Fig. 3 of Ref. 8 which is based on the data of Ref. 9.) A comparison of the steady state stall angle with the zero frequency intercept of the least squares vortex inception line shows a two degree difference at $M_c = 0.3$, and a reasonably good correlation at $M_c = 0.4$.

A careful study of Fig. 7 reveals little or no effect of mean angle of attack on the incipient vortex angle. Specifically, at any constant value of k_c there is no discernable trend of α_v with α_M; there is only scatter. This is an observation that is directly concerned with the effect of pitch rate on α_v, which is addressed next.

A case to be considered in detail is represented by the open symbols at $k_c \cong 0.125$ in the lower right panel of Fig. 7 for $M_c = 0.3$, $\bar{\alpha} = 10$ deg, and $\Lambda = 30$ deg. In this instance the vortex inception angle is very nearly 16 deg for all three values of α_M. This is demonstrated in Fig. 8 which depicts three motion time histories for $\alpha_M = 9$, 12, and 15 deg versus dimensionless time, τ. A horizontal line at $\alpha_v = 16$ deg represents the observed insensitivity of the vortex inception angle to changes in α_M, and leads directly to a consideration of pitch rate effects. For a sinusoidal motion the instantaneous dimensional pitch rate is given by the time derivative of Eq. (5),

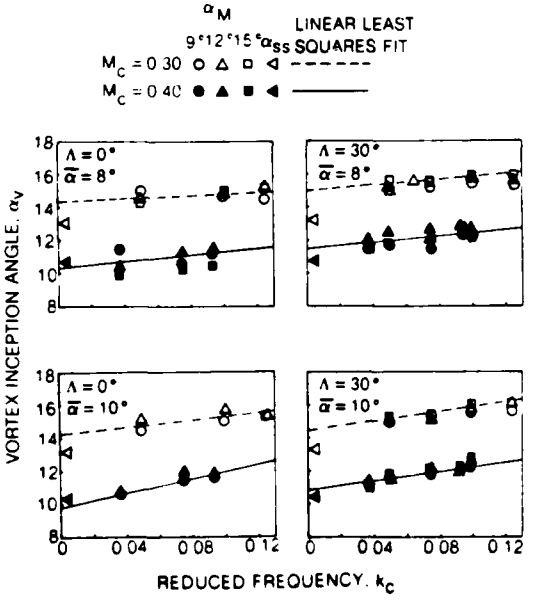

Fig. 7 Effect of Mach Number on Vortex Inception Angle Based on Initial Wave Propagation

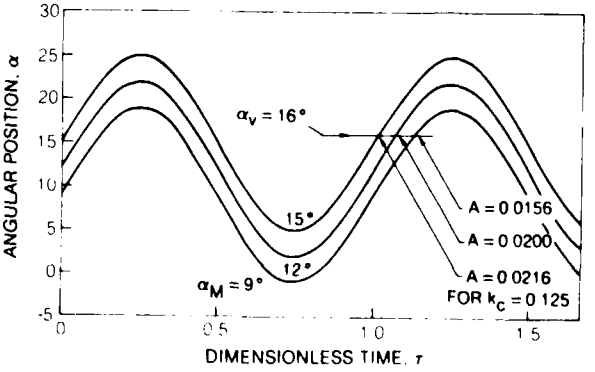

Fig. 8 Typical Motion Time Histories for Three Mean Angles of Attack

$$\dot{\alpha} = \omega\bar{\alpha}\cos\omega\tau = \omega\bar{\alpha}\sqrt{1-\sin^2\omega\tau} \tag{7}$$

A combination of Eqs. (5) and (7) yields

$$\dot{\alpha} = \omega\sqrt{\bar{\alpha}^2 - (\alpha - \alpha_M)^2} \tag{8}$$

which can be converted to the dimensionless pitch rate, A, by the formula (cf., Ref. 2)

$$A = \frac{c\dot{\alpha}}{2a_\infty M_c} = k_c\sqrt{\bar{\alpha}^2 - (\alpha-\alpha_M)^2} \tag{9}$$

The values of A for the intersections of the α_v= 16 deg line with the three motion curves in Fig. 8 are noted on the figure and are seen to vary from 0.0156 to 0.0216.

A direct examination of the effect of mean angle of attack variations on α_v with reduced frequency effects excluded is afforded by a return to the linear least squares fit of Eq. (6). The scatter of individual data points may be quantitatively evaluated by rewriting the equation in the form

$$\epsilon = \alpha_v - \alpha_{v0} - mk_c \tag{10}$$

where $\epsilon \equiv 0$ for an exact linear fit. In Fig. 9 a plot of this error function, ϵ, versus A_v emphasizes the irregularity of the scatter, and leads directly to the observation that the vortex inception angle is independent of the pitch rate when k_c is fixed. With the exception of a few isolated points the error, ϵ, is generally bounded by $|\epsilon| \leq 0.5$ deg, and never exceeds ± 1.0 deg. By virtue of the relationship in Eq. (9), it can be argued that the linear variation of α_v with k_c (Fig. 7) is equivalent to a corresponding variation of α_v with A, but of unknown functional form.

A question must be raised at this point on the possible relationship of the vortex inception angle, α_v, to the various dynamic stall angle concepts that have been cited in the literature. As far back as Halfman's 1951 report (Ref. 10) several authors have shown that the dynamic stall angle increases with both increasing reduced frequency and pitch rate. One of the more complete examinations is that of Gormont (Ref. 11). Here it is shown that the dynamic moment stall angle, based on ∂C_M (dynamic)/$\partial\alpha$ = 0, varies linearly with the square root of the pitch rate, and, for the thick V23010-1.58 airfoil, approaches the steady state stall angle as the zero pitch rate limit is reached.

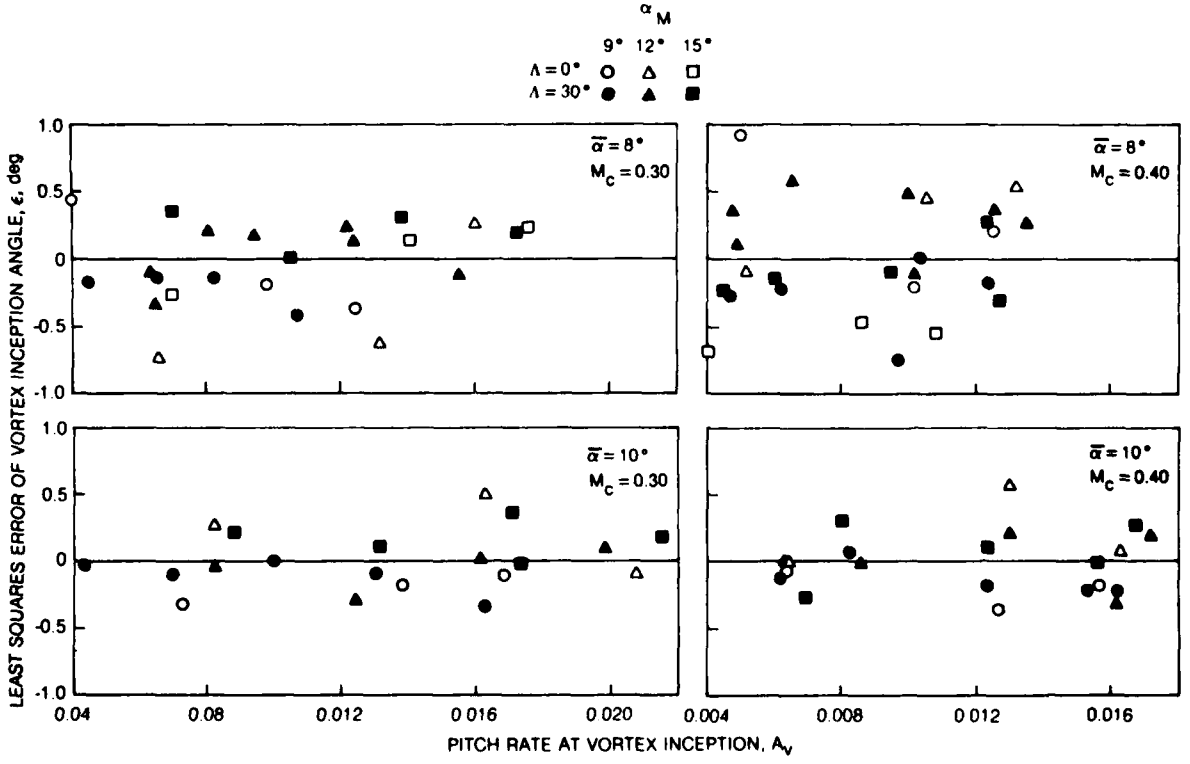

Fig. 9 Linear Least Squares Scatter Versus Pitch Rate

To permit a comparison of Gormont's linear fit of earlier dynamic stall angle results with the current data, the steady-state stall angle was removed from the vortex inception angle results of the present experiment, $\alpha_v - \alpha_{ss}$, and then plotted versus $\sqrt{A_v}$ in Fig. 10. The $M_c = 0.4$ linear fit to Gormont's thick airfoil moment stall results (lower left panel of Fig. 11 in Ref. 11) is shown plotted as dashed lines. Although there is considerable scatter of the present data, a linear trend is discernable for $\bar{\alpha} = 10$ deg. Gormont's linear fit for moment stall angle starts from the origin and lies roughly parallel to, and significantly above, the α_v data in the lower panel. If these data were linearly extrapolated to zero pitch rate, the intercept value would lie approximately 1.5 deg below the steady state stall angle, which is in direct contradiction to the results shown for $M_c = 0.4$ in the lower right panel of Fig. 7. This can be resolved by noting that a linear behavior of the data is observed for $\alpha_v - \alpha_{ss}$ plotted versus $\sqrt{A_v}$ in Fig. 10 or versus A_v in Fig. 11. The data are now more in keeping with the results in Fig. 7, and the original Gormont linear data fit is now a parabola. The apparent inconsistency lies in the lack of any data at low pitch rates (or reduced frequency).

INTEGRATED LOAD RESULTS

Aerodynamic Damping

The customary load integrations were performed on the measured pressure data and are reported in detail in Ref. 5. It is not surprising that sweep angle contributed to the observed differences in both unsteady lift and moment loops. For brevity, this paper will concentrate on the effects of sweep on the further integration of unsteady moment leading to work per cycle,

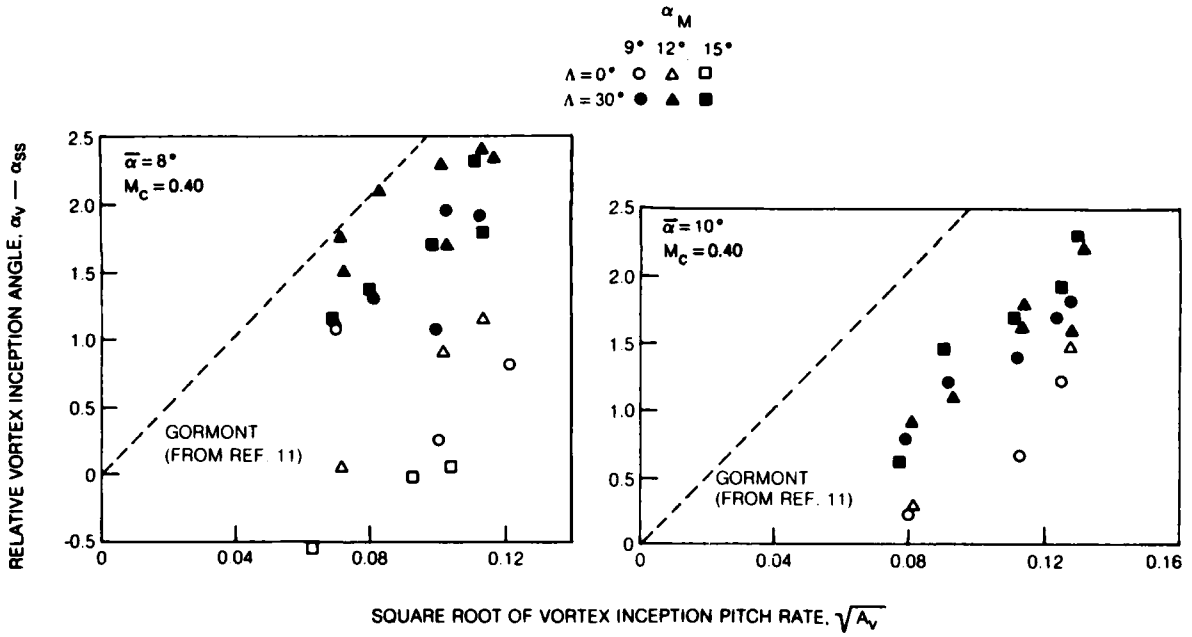

Fig. 10 Correlation of Relative Vortex Inception Angle with $\sqrt{A_v}$

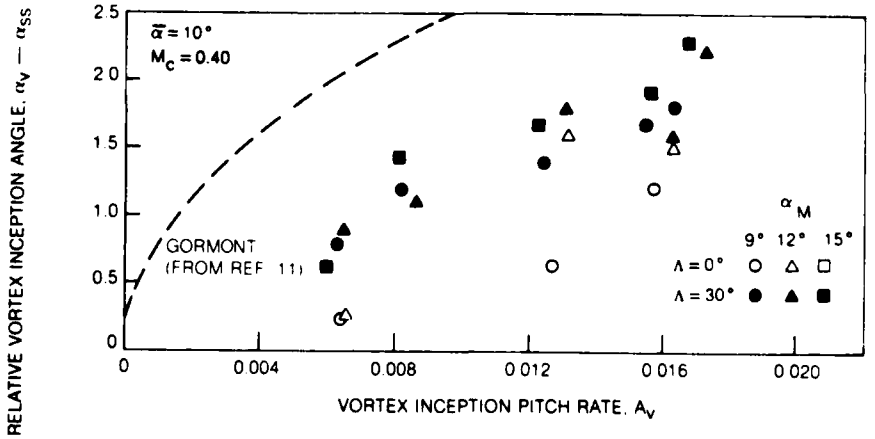

Fig. 11 Correlation of Relative Vortex Inception Angle with A_v

$$C_W = \oint C_{M_R}\, d\alpha_R = \oint \int_0^1 [C_{P_u}(\chi,t) - C_{P_\ell}(\chi,\tau)]_R (\chi-\beta) d\chi\, d\alpha_R \qquad (11)$$

and ultimately to aerodynamic damping in pitch,

$$\Xi = -\frac{C_W}{\pi \bar{\alpha}^2} \qquad (12)$$

which is positive for stable motions.

In Fig. 12 the aerodynamic damping is plotted versus chordwise reduced frequency for a variety of parameters. The circled points are for Λ = 0 deg and the triangular points for Λ = 30 deg, the open symbols are for M_c = 0.3 and solid symbols for M_c = 0.4. The measured damping for both sweep angles at α_M = 0 deg and M_c = 0.3 (open symbols, left panel) generally follow the theoretical linear prediction, $\Xi = \pi k_c/2$ (cf., Ref. 12); when M_c is raised to 0.4 the measured results deviate from theory as k_c is increased. When α_M is increased to 12 deg (right panel), blade sweep tends to reduce the stability margin of the airfoil. In terms of the moment loop results, this outcome implies a net decrease in the area bounded by a counterclockwise traverse path due to the cancellation effect of the destabilizing clockwise subloops that appear as a result of dynamic stall (see also the discussion of stability in Ref. 12). The moment loops shown in Fig. 13 are a good illustration of this event. At α_M = 12 deg the unswept result (solid line) represents a mixed condition in which some of the area at each end is enclosed counterclockwise. The central region represents that part of the cycle during which the airstream feeds energy into the motion, thus reducing the stability margin. Although sweeping (dashed line) is beneficial from the standpoint of reducing the nose down impulsive moment due to dynamic stall, it is seen that sweeping also increases the destabilizing central portion of the clockwise-traversed subloop.

Lift Loop Displacement

In the data analysis of Ref. 5 the customary hysteresis loop comparisons were made for unsteady lift, drag, and pitching moment to permit an examination of the effects of sweep on the unsteady lift, drag and moment components of the total force response. An unexplained feature in the results is the substantial displacement in the lift curve below stall between the unswept and swept wing results, especially at high

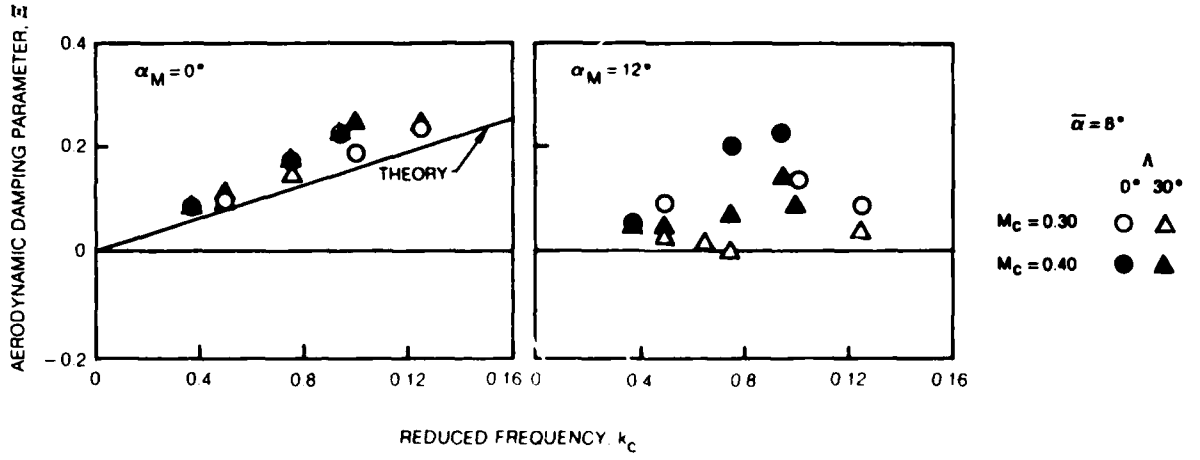

Fig. 12 Variation of Aerodynamic Damping Parameter with Reduced Frequency

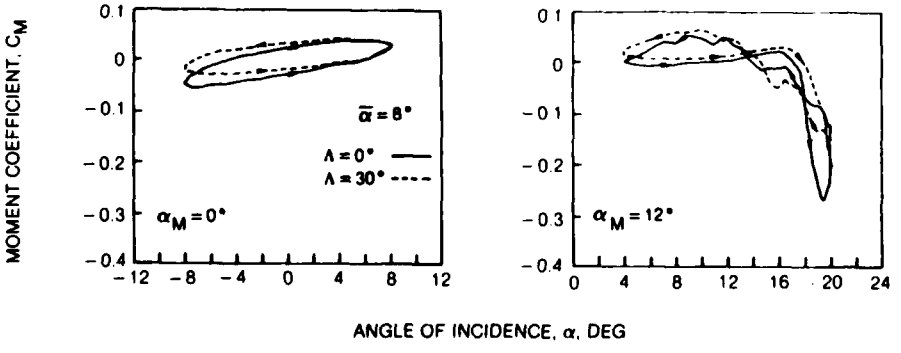

Fig. 13 Effect of Sweep and Mean Angle on Unsteady Moment Response for M_c = 0.30 and f = 8 Hz (k_c = 0.099)

mean angles of attack. A perspective on this displacement can be obtained from Figs. 14 and 15. Figure 14 shows that the normalized steady-state lift curves of the unswept and swept NACA 0012 airfoils are nearly coalesced below stall. This is not the case when viewing the unsteady comparisons in Fig. 15. Here it is seen that the upstroke portions of the unsteady lift below stall are significantly and increasingly displaced from one another as α_M increases.

It has been found that this displacement of the lift response is mainly associated with the first harmonic component. The time mean component of the lift response was removed in an attempt to bring the loops to closer alignment than shown in Fig. 15. The result is shown in the top row of Fig. 16 for the 15 degree mean angle of attack case where plot 16a is repeated from Fig. 15 and plot 16b is stripped of the time mean component. The resultant lack of change in the relative positioning of these loops indicates that the entire displacement is a sweep-induced unsteady phenomenon. A harmonic analysis of these loops was performed and it was found that the ultimate shape, displacement, and rotation of the lift loops of Fig. 16a are primarily governed by the first harmonic component ellipse. This is clearly illustrated in plot 16c where the midportion of the ΔC_L upstroke displacement is accounted for. The remaining comparisons in Fig. 16 (plots d through f) show how the addition of higher harmonic terms contributes in evolving the complete unsteady response without significant influence on the ΔC_L displacement at the midpoint of the upstroke.

HOT FILM RESPONSE

A preliminary, shakedown experiment was run in preparation for the swept wing work reported on in Refs. 5 and 6, and included a first effort into the study of sweep effects on hot film time histories. Because of the incomplete nature of this precursor work it was never published, but the indications from a small portion of the hot film response (shown below) are that there are significant changes caused by sweep in the surface flow of an oscillating wing. It should be noted that although the planform of this model was the same as that discussed above, the profile normal to the wing leading edge is a cambered airfoil, designated as the SC1095 (cf., Refs. 4 or 13 for profile coordinates and steady behavior). In the absence of comparable hot film data from the NACA 0012 airfoil, it cannot be determined if the observed swept/unswept results described below are generally applicable or are germane only to the SC1095 profile.

Although hot films have been used in the past by many investigators (e.g., Refs. 14 and 15) and the principles involved have been well-documented, it is useful to outline these principles and to use the schematic in Fig. 17 to illustrate the measurements that are possible with these devices. In brief,

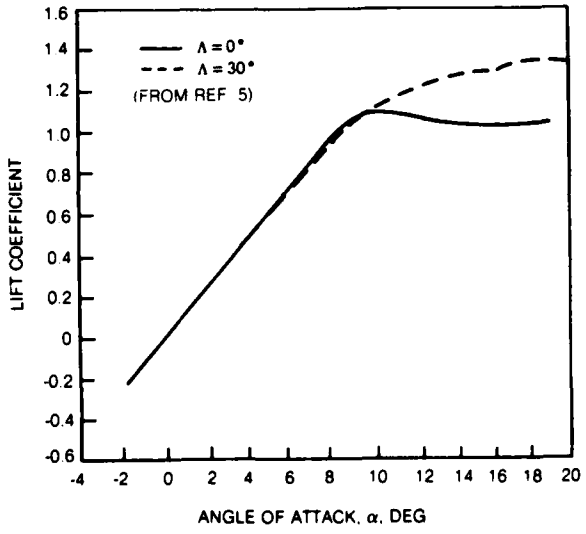

Fig. 14 Steady-State Lift Coefficient for NACA 0012 Airfoil at $M_c = 0.40$

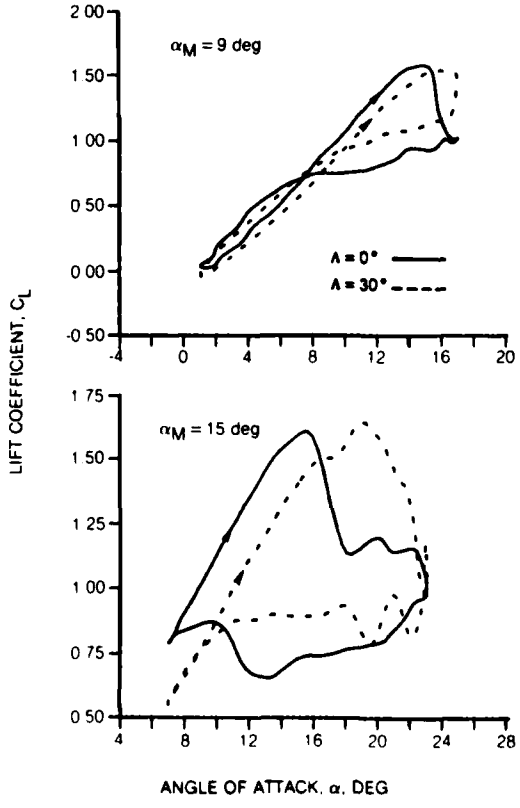

Fig. 15 Effect of Mean Angle and Sweep on the Lift Response at $k_c = 0.075$ (f = 8 Hz, $M_c = 0.40$), and $\bar{\alpha} = 8$ deg

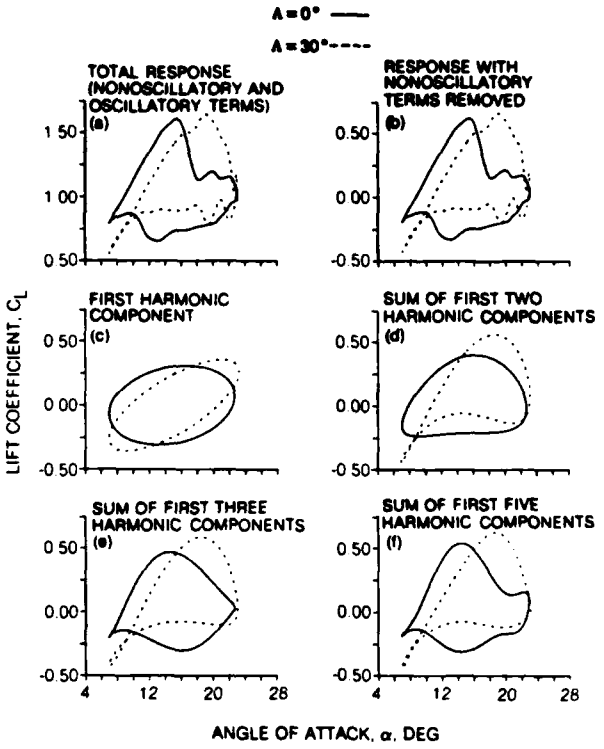

Fig. 16 Harmonic Analysis of the Sweep Effect on the Lift Response at $\alpha_M = 15$ deg, $k_c = 0.075$ (f = 8 Hz, $M_c = 0.40$), and $\bar{\alpha} = 8$ deg

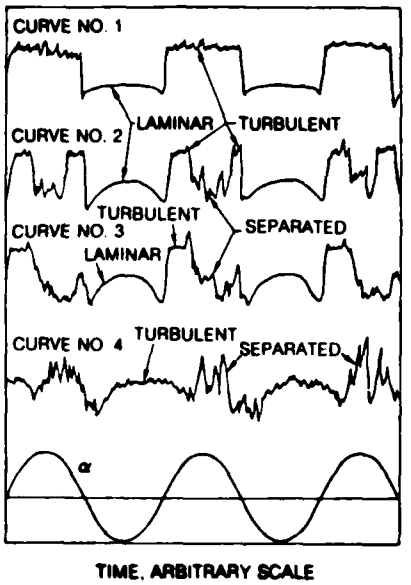

Fig. 17 Schematic of Hot Film Response

laminar flow is associated with low heat transfer and hence low output voltage. Further, the response will be smooth and somewhat rounded with time, as characterized in the first three curves of Fig. 17. Curve 1 also contains transition to turbulence, associated with high heat transfer, high output voltage, and noisy response, followed by relaminarization. Curves 2 and 3 are characteristic of a laminar-turbulent-separated flow combination. For separated flow the heat transfer varies over a wide range, indicated by large response fluctuations. In curve 2 the separated flow reattaches turbulently before relaminarization while in curve 3 it goes directly from a separated to a laminar condition. Finally, in curve 4, there is no laminar flow and the distinction between turbulent and separated flow can only be made by the intensity of the fluctuations. These events are related to the angle-of-attack variation, α, at the bottom of the figure such that the laminar or laminar/turbulent flow is associated with the low α region while the turbulent or turbulent/separated flow is associated with high α.

The hot films on the model were located at the 5, 15, 25, 45 and 65 percent chord locations near the center span, and arranged in a staggered array to prevent the soldered connections or any other local surface irregularities from affecting the downstream transducer response. No calibrations were taken to relate voltage output to either turbulence level or surface shear, and only the relative changes in signal level are considered herein. Furthermore, the subsequent computer processing involved removal of the mean value of each signal and self-scaling the remainder to a maximum amplitude of unity. Thus, some of these signals will appear artificially amplified relative to certain other comparable signals.

Figure 18 contains a selected group of hot film time histories which illustrate the effects of varying angle of attack and sweep angle on the surface flow phenomena for a nominal reduced frequency of $k_c = 0.077$ at $M_c = 0.3$ and $\bar{\alpha} = 8$ deg. Before examining these figures in detail, the format used in this set will be described.

Each panel represents a single chordwise location. The horizontal axis is a time scale with 0.1 sec duration marked for reference, and the uppermost trace is angular deflection, α, in arbitrary units. Maximum and minimum angular limits are denoted by tic marks, with increasing angle of attack in the upward direction. Below the angle of attack trace are either two or three pairs of curves which compare the unswept hot film response (solid curve) with the swept wing response (dashed curve). Each pair of curves is for a specific mean angle of attack, as designated by the appended value of α_M. The set of panels is logically arranged in increasing order of chordwise position, from 5 to 65 percent chord, but a discussion of the events at the 5 percent chord location (Fig. 18a) will be deferred to the end of this section because the response is atypical and its interpretation must be based on a comparison with other traces.

Figure 18b permits a comparison of hot film time histories for the unswept (solid line) and swept (dashed line) wing configurations at the 15 percent chord location. It is seen that the surface flow behavior at this chordwise location is substantially independent of sweep angle. For $\alpha_M = 0$ deg the flow is probably laminar over the negative angle of attack region, and turbulent over positive angle. (Note that α varies in this instance from -8 deg to +8 deg over the cycle. Note also that the filter

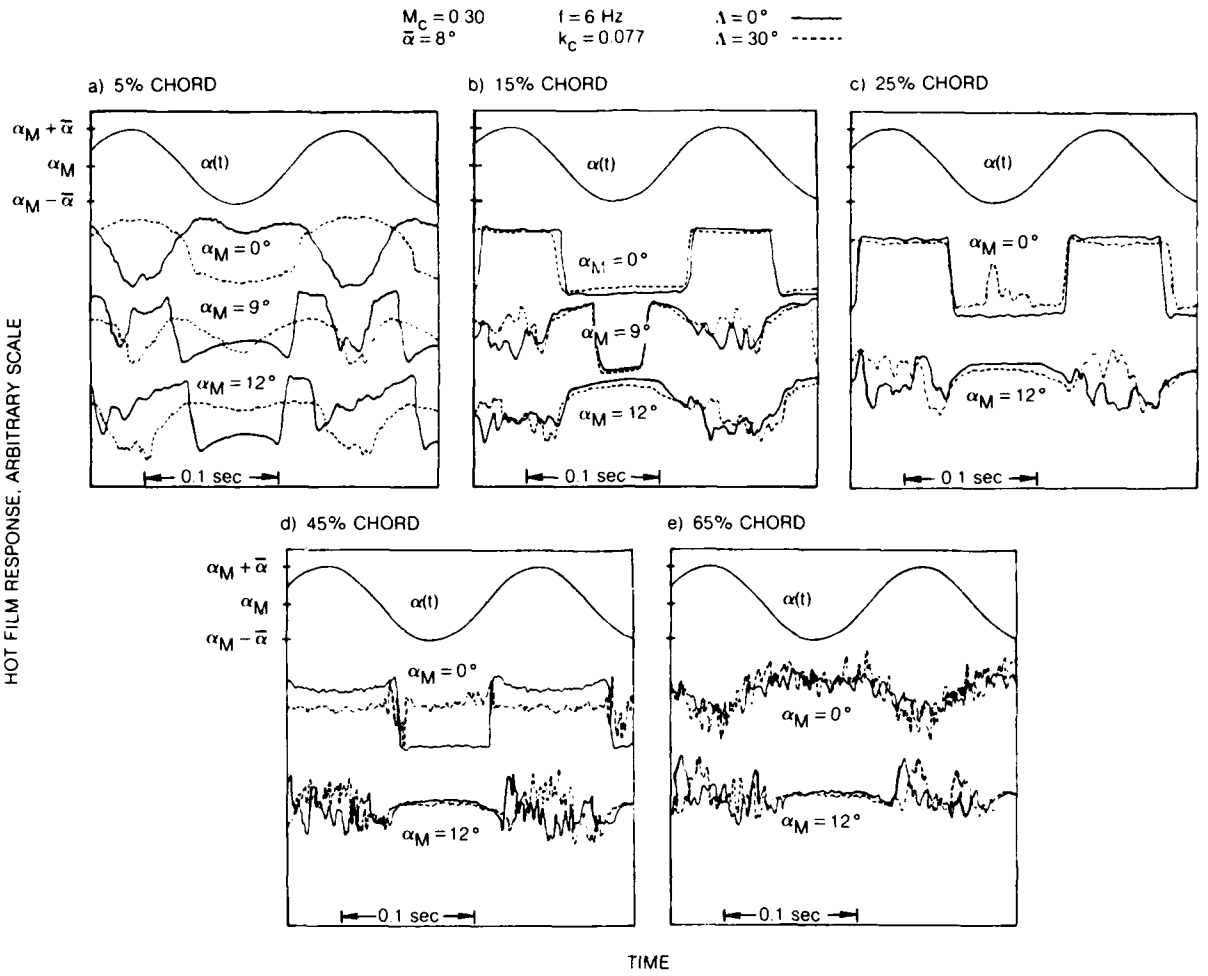

Fig. 18 Effect of Sweep on Hot Film Time Histories at Several Chord Locations

characteristics of this early data system [ca. 1975] were set for the low frequency pressure measurements, and virtually none of the high frequency noise usually associated with turbulence can be seen in these figures. Hence, in all of the time histories discussed in this section, there is some ambiguity between laminar and turbulent flow responses.) At α_M = 9 deg the flow is laminar in the neighborhood of α = 1 deg, becomes turblent as α increases, and separates (jagged response) at peak angle of attack. The flow then reattaches turbulently as α decreases, and once again becomes laminar as minimum angle is approached. At α_M = 12 deg there are only two flow regimes, turbulent at low angle and separated at high angle of attack.

The situation at 25 percent chord is similar (Fig. 18c) with the exception of minor bursts of turbulence (or perhaps laminar separation) at low angle of attack for the swept wing at α_M = 0 deg. Otherwise, the α_M = 0 and 12 deg traces here are identical to those in Fig. 18b for the 15 percent chord location. These swept wing bursts of apparent turbulence at α_M = 0 deg appear to have developed into fully turbulent behavior at the 45 percent chord location on the swept wing at α_M = 0 deg while the unswept wing continues to switch between laminar and turbulent flow (Fig. 18d). At α_M = 12 deg both wings retain the turbulent/separated character of the upstream stations. It is also seen in Fig. 18d that, for the swept wing at α_M = 0 deg, there are periodic sharp changes at times that appear to be associated with either transition or relaminarization of the unswept wing. In fact, these times correlate well with such changes at the upstream stations for both swept and unswept wings (cf., panels b and c at α_M = 0 deg). At the 65 percent chord location (Fig. 18e), the swept and unswept configurations are again behaving similarly. Self-scaling of the signal gives rise to large apparent variations at α_M = 0 deg, but this is believed to be a fully turbulent flow for both configurations. A consistent behavior at α_M = 12 deg with other chordwise locations is evident by comparison with panels b, c and d.

The change to 5 percent chord in Fig. 18a is, by contrast, remarkable. There appears to be no correlation at all between unswept and swept wing responses. To help understand what might be happening, first consider the unswept case for α_M = 12 deg (solid line) and refer it to its counterpart at 15 percent chord in Fig. 18b. In the vicinity of $\alpha \cong 4$ deg (minimum α) the flow at 5 percent chord is laminar. It obviously bcomes turbulent somewhere between 5 and 15 percent chord at this angle of attack. A simliar situation prevails at α_M = 9 deg in Fig. 18a, and for both values of α_M a repetitive pattern of laminar/turbulent/ separated/turbulent/laminar behavior occurs as α rises from minimum to maximum and decreases again. The swept curves (dashed lines) for these two angles are a bit more difficult to interpret because of the ambiguity of the signals, but it appears that the flow is never laminar at this

forward chord position, and it simply varies between turbulent and separated as the angle of attack varies. Finally, in the absence of a signal with greater frequency response, it is virtually impossible to fully interpret the results for $\alpha_M = 0$ deg. The unswept wing (solid curve) shows no evidence of laminar flow at low angle of attack, but instead appears to experience turbulence (high voltage signal) at low angle, and separation (low voltage) at high angle of attack, which leads to the conjecture that a small laminar separation bubble may exist ahead of the 5 percent chord location. At low unsteady angle (which is, in reality, a negative angle for $\alpha_M = 0$ deg) it may be further conjectured that the flow aft of the separation bubble is initially turbulent (at 5 percent chord) but thereafter the flow relaminarizes and remains laminar into the region of the midchord. At high unsteady angle the separation bubble encroaches upon the 5 percent chord location, followed by a reattachment to turbulent flow forward of the 15 percent chord, which persists over the remaining chord. Obviously, the swept wing has no comparable behavior at this forward location. On the basis of this evidence, it may be concluded that the leading edge region of the swept wing has a spanwise "stagnation flow" versus a traditional stagnation line for the unswept wing. As a result of this change in the nature of the leading edge flow, the unsteady characteristics of the flow are drastically different. However, somewhere between the 5 and 15 percent chord locations something happens to cause both flows to look remarkably similar.

SUMMARY OF RESULTS AND COMMENTARY

Summary

(Note that the first nine results highlighted below are for the NACA 0012 profile [Refs. 5 and 6] while the last two are from previously unpublished data on a SC1095 profile. Additional comments are appended to the end of this section.)

1. Traditional normalization procedures for both steady and unsteady phenomena work well below stall, but deteriorate as stall is encountered.

2. Mean angle of attack has little or no effect on wave speed, which in all cases increases uniformly with reduced frequency. Motion amplitude also has little or no effect on wave speed. Mach number has a small but consistent effect on wave speed, with higher Mach numbers yielding slightly smaller wave speeds.

3. Sweep angle has a dominant effect on wave speed. The overall wave speed for the unswept wing is consistently greater than that for the swept wing by a factor of 1.5 to 2.0. This represents a major failure above stall for the cosine law normalization which has been shown to be consistently valid below stall.

4. Mach number has a dominant effect on vortex inception angle and static stall angle, with a decrease in both angles as M_c increases.

5. Vortex inception is substantially independent of amplitude of motion and of mean angle of attack.

6. Local wave speed differences associated with sweep are confined to the region of the blade aft of the 15 percent chord. Wave speeds are substantially the same for both sweep angles forward of this chord location.

7. The vortex inception angle is independent of pitch rate when reduced frequency is fixed.

8. When α_M is increased beyond 9 deg, blade sweep tends to reduce the stability margin of the airfoil.

9. The main influence of sweep on the total integrated lift response is very strongly determined by the first harmonic term, and is characterized by a progressively greater displacement between the upstroke portions of unsteady lift loops as α_M increases.

10. The presence of a stagnation flow along the leading edge of the swept wing causes its surface flow phenomena near the leading edge to be entirely different from those of the unswept wing.

11. In contrast, surface flow phenomena from 15 percent chord aft towards the trailing edge tend to be strongly similar for both swept and unswept wings.

Commentary

This paper highlights the major differences in unsteady dynamic stall response that are associated with changes in sweep angle. Most of the information came from research performed on the NACA 0012 airfoil under NASA sponsorship. This was a well-documented program (Refs. 5, 6) which, from its inception, was designed to investigate the phenomenon of dynamic stall from several aspects. Even with sufficient preparation, however, some surprises still emerged, as in the case of lift loop displacement (item 9 above) which was initially believed to be a discrepancy, was ultimately proved to be a real effect, and is still not understood. In the course of this investigation on the NACA 0012 airfoil the

pressure wave propagation phenomenon was found to consistently be unaffected by sweep near the leading edge, and also to consistently exhibit a nearly 2:1 velocity ratio over the aft region of the chord (item 6 above).

The SC1095 experiments described here preceded the NACA 0012 tests by approximately 3 years, and were the first attempt to use the tunnel-spanning wing system in the UTRC tunnel as a dynamic drive for both swept and unswept wings. The objective of this early in-house effort was to proof-test the system and to prepare the way for later, more advanced work. The detailed re-examination of the hot film results described here was largely triggered by the realization that they were quite different from the NACA 0012 behavior described above. In contrast to these results, the SC1095 hot film evidence points to a leading edge flow dissimilarity and an aft region similarity associated with sweep (items 10 and 11 above). Without sufficient documentation of the SC1095 measurements, it is not possible to perform an in-depth data analysis to determine if the surface pressure wave phenomenon on this airfoil agrees or disagrees with the observed hot film response.

No apologies are offered, either for the apparent inconsistencies in the surface activity results of the two airfoils, or for the incomplete analysis of the SC1095 data. Indeed, these two sets comprise the only known data bank of swept versus unswept effects on large amplitude dynamic stall penetration, and represent our first efforts to move our experiments further towards the "real world". Based on these precursor tests, an ambitious experimental program is now being planned to address the questions raised in these earlier studies and highlighted herein.

REFERENCES

1. Carta, F. O.: Experimental Investigation of the Unsteady Aerodynamic Characteristics of an NACA 0012 Airfoil. United Aircraft Research Laboratories Report M-1283-1, August 1960.

2. Carta, F. O., G. L. Commerford, R. G. Carlson and R. H. Blackwell: Investigation of Airfoil Dynamic Stall and Its Influence on Helicopter Control Loads. USAAMRDL Technical Report 72-51, September 1972.

3. Liiva, J., F. J. Davenport, L. Gray, and I. C. Walton: Two-Dimensional Tests of Airfoils Oscillating Near Stall. Volume I, Summary and Evaluation of Results, USAAVLABS Technical Report 63-13A and Volume II, Data Report, USAAVLABS Technical Report 63-13B, April 1968.

4. McCroskey, W. J., K. W. McAlister, L. W. Carr, and S. L. Pucci: An Experimental Study of Dynamic Stall on Advanced Airfoil Sections. Volume 1, Summary of the Experiment. NASA Technical Memorandum 84245 (USAAVRADCOM TR-82-A-8), July 1982.

5. St. Hilaire, A. O., F. O. Carta, M. R. Fink and W. D. Jepson: The Influence of Sweep on the Aerodynamic Loading of an Oscillating NACA 0012 Airfoil. Volume I - Technical Report. NASA CR-3092, 1979.

6. St. Hilaire, A. O. and F. O. Carta: Analysis of Unswept and Swept Wing Chordwise Pressure Data From an Oscillating NACA 0012 Airfoil Experiment. Volume I - Technical Report. NASA CR-3567, March 1983.

7. Carta, F. O.: Analysis of Oscillatory Pressure Data Including Dynamic Stall Effects. NASA CR-2394, May 1974.

8. Harris, F. D.: Preliminary Study of Radial Flow Effects on Rotor Blades. Journal of the American Helicopter Society. Vol. 11, No. 3, July 1966.

9. Purser, P. E. and M. L. Spearman: Wind Tunnel Tests at Low Speed of Swept and Yawed Wings Having Various Plan Forms. NACA Technical Note 2445, December 1951.

10. Halfman, R. L., H. C. Johnson and S. M. Haley: Evaluation of High Angle-of-Attack Aerodynamic-Derivative Data and Stall-Flutter Prediction Techniques. NACA Technical Note 2533, November 1951.

11. Gormont, R. E.: A Mathematical Model of Unsteady Aerodynamics and Radial Flow for Application to Helicopter Rotors. USAAMRDL Technical Report 72-67, May 1973.

12. Carta, F. O. and C. F. Niebanck: Prediction of Rotor Instability at High Forward Speeds, Vol. III, Stall Flutter. USAAVLABS Technical Report 68-18C, February 1969.

13. Noonan, K. W. and G. J. Bingham: Aerodynamic Characteristics of Three Helicopter Rotor Airfoil Sections at Reynolds Numbers from Model Scale to Full Scale at Mach Numbers from 0.35 to 0.90. NASA Technical Paper 1701/AVRADCOM Technical Report 80-B-5, September 1980.

14. Carr, L. W., K. W. McAlister and W. J. McCroskey: Analysis of the Development of Dynamic Stall Based on Oscillating Airfoil Experiments. NASA TN D-8382, 1977.

15. Carta, F. O.: A Comparison of the Pitching and Plunging Response of an Oscillating Airfoil. NASA CR-3172, October 1979.

ECOULEMENT INSTATIONNAIRE DECOLLE D'UN FLUIDE INCOMPRESSIBLE AUTOUR D'UN PROFIL: UNE COMPARAISON THEORIE-EXPERIENCE*

par

O.Daube et Ta Phuoc Loc
LIMSI — CNRS
B.P. 30
91406 Orsay
France

et

P.Monnet et M.Coutanceau
LMF — Université de Poitiers
40 Avenue du Recteur Pineau
86022 Poitiers
France

I - INTRODUCTION

Les résultats présentés dans cet article concernent l'étude numérique et expérimentale de l'écoulement instationnaire d'un fluide visqueux incompressible autour d'un profil à forte incidence. Ce travail rentre dans le cadre d'un programme de recherche fondamentale sur les problèmes de décollements instationnaires. L'objectif de ce programme est d'analyser, par une simulation numérique et une étude expérimentale réalisée en parallèle, les conditions de validité des équations de Navier-Stokes aux nombres de Reynolds pouvant atteindre ceux correspondants à la transition. Jusqu'à maintenant dans le domaine des recherches en fluide visqueux par résolution des équations de Navier-Stokes, on peut distinguer deux classes d'approche: l'une concernant les écoulements laminaires à faibles nombres de Reynolds ($<2\ 10^3$) et l'autre relative aux écoulements complètement turbulents à très grands nombres de Reynolds. En fait, du point de vue de simulation numérique ces deux classes de problèmes sont analogues : en effet, par modélisation, on peut ramener le problème turbulent à grands nombres de Reynolds à celui de faibles nombres de Reynolds non uniformes (11). On peut remarquer que dans ces classes d'approche, les équations de Navier-Stokes sont toujours utilisées comme base. Il apparaît donc intéressant de contrôler si cette base reste valable quel que soit le nombre de Reynolds.

D'autre part, pour pouvoir comprendre les phénomènes d'instabilité et de transition, il est nécessaire de disposer de méthode numérique pouvant résoudre les équations-Stokes instationnaires aux grands nombres de Reynolds et de résultats expérimentaux suffisamment faibles pour contrôler leurs performances.

Les premiers résultats numériques et expérimentaux présentés ici correspondent à des nombres de Reynolds allant de 10^3 à 2.10^4. Des comparaisons qualitatives et quantitatives sur les structures de l'écoulement et sur les profils de vitesse obtenus par simulation numérique et par visualisation expérimentale montrent un excellent accord.

II - EQUATIONS PHYSIQUES - METHODE NUMERIQUE.

II.1. Equations physiques

La formulation fonction de courant et fonction de tourbillon des équations de Navier-Stokes instationnaires est utilisée avec une double transformation conforme. On peut en effet écrire :

$$\frac{\partial^2\psi}{\partial\eta^2} + \frac{\partial^2\psi}{\partial\xi^2} = g(\xi,\eta)\,\omega \qquad (1)$$

$$g(\xi,\eta)\frac{\partial\omega}{\partial t} + \frac{\partial}{\partial}\left(\omega\frac{\partial\psi}{\partial\xi}\right) - \frac{\partial}{\partial\xi}\left(\omega\frac{\partial\psi}{\partial\eta}\right) = \frac{2}{R_e}\left(\frac{\partial^2\psi}{\partial\eta^2} + \frac{\partial^2\psi}{\partial\xi^2}\right) \qquad (2)$$

avec $g(\xi,\eta)$ = module de la transformation conforme qui permet de ramener le domaine physique sur une bande semi-infini ($0<\xi<\infty$; $0<\eta<2$).

II-2.Méthode numérique.

Dans ce travail, on utilise une méthode précise d'ordre $O(h^4)$ proposée par L. COLLATZ (1), H.O. KREISS (2) et appliquée par R.S. HIRSH (3) à divers exemples notamment à l'écoulement dans une cavité carrée. Un point important de cette méthode est l'obligation d'imposer des conditions aux limites sur les fonctions inconnues ainsi que leurs dérivées premières et secondes. A cause des difficultés bien connues d'imposition de conditions aux limites sur la fonction-tourbillon, seule l'équation de Poisson de la fonction de courant est résolue par cette méthode précise d'ordre $O(h^4)$. L'équation de transport du tourbillon est résolue par un schema directionnel précis d'ordre $O(h^2)$ (4), (5).

---

* Recherche soutenue par la DRET - Ministère de la Défense

Ce choix est déterminé par le fait que toutes les conditions aux limites sur ω sont calculées à partir de la connaissance de Ψ : par conséquent une grande précision est nécessaire dans le calcul de Ψ . Les résultats numériques semblent confirmer cette constatation. En effet, les calculs que nous avons menés (7), ainsi que P. BONTOUX, B. ROUX (6), sur les problèmes de l'écoulement dans une cavité et autour d'un cylindre circulaire montrent que les résultats obtenus par cette méthode sont aussi précis que ceux donnés par une méthode complète d'ordre $O(h^4)$ et de toute façon beaucoup plus précis que ceux obtenus par un schéma précis d'ordre $O(h^2)$.

II-2.1 - Principe de la méthode hermitienne compacte $O(h^4)$.

L'avantage de cette méthode par rapport aux schémas classiques à cinq points est que la précision est obtenue à l'aide des relations simples des valeurs de la fonction f et de ses dérivées première et seconde en trois points.

Si on désigne par h le pas de discrétisation ; f_i, f'_i et f''_i la fonction inconnue et ses dérivées première et seconde au noeud i , ces relations tridiagonales s'écrivent :

$$f'_{i-1} + 4 f'_i + f'_{i+1} = \frac{3}{h} (f_{i+1} - f_{i-1}) + O(h^4) \qquad (3)$$

$$f''_{i-1} + 10 f''_i + f''_{i+1} = \frac{12}{h^2} (f_{i+1} - 2 f_i + f_{i-1}) + O(h^4) \qquad (4)$$

On a ainsi introduit deux nouvelles inconnues, la dérivée première f' et la dérivée f'' de la fonction inconnue f . Il apparait immédiatement que pour appliquer la méthode d'ordre $O(h^4)$ il est nécessaire de connaître les conditions aux limites non seulement sur f mais aussi sur f' et f''.

Si n est le nombre de noeuds du maillage, on aura donc en général un système de 3n équations à 3n inconnues à résoudre, ce qui peut apparaître comme un inconvénient.

Cependant, comme la précision d'ordre $O(h^4)$ permet de diminuer le nombre de noeuds du maillage, le gain en temps de calcul et occupation mémoire reste encore important.

II-2.2 - Résolution de l'équation de Poisson de la fonction de courant.

On a choisi la méthode d'ordre $O(h^4)$, dont le principe est exposé précédemment, combiné avec un schéma inspiré des méthodes de directions alternées implicites pour résoudre cette équation de la fonction de courant. Les avantages de cette méthode pour cette résolution résident dans la possibilité de prise en considération simultanée des conditions aux limites de Ψ'_ξ , Ψ'_η , qui sont des données du problème, ce qui n'est pas le cas des autres méthodes. L'utilisation des conditions aux limites sur $\Psi''_{\xi\xi}$ et $\Psi''_{\eta\eta}$ permet d'autre part un couplage "fort" entre la fonction de courant Ψ et le tourbillon ω .

Dans l'équation (1), n'apparaissent que les dérivées secondes $\Psi''_{\xi\xi}$, $\Psi''_{\eta\eta}$ on peut par conséquent en utilisant la relation (3), écrire pour chaque demi-pas de l'itération p les systèmes d'équations suivants :

$$\lambda_{ph} \Psi^{p+1/2}_{ij} - \Psi''^{\,p+1/2}_{\eta\eta\, ij} = - g_{ij}\, \omega^{n+1}_{ij} + \Psi''^{\,p}_{\xi\xi\, ij} + \lambda_{ph} \Psi^{p}_{ij}$$

$$\frac{12}{(\Delta\eta)^2} (\Psi^{p+1/2}_{ij+1} - 2 \Psi^{p+1/2}_{ij} + \Psi^{p+1/2}_{ij-1}) = \Psi''^{\,p+1/2}_{\eta\eta\, ij+1} + 10 \Psi''^{\,p+1/2}_{\eta\eta\, ij} + \Psi''^{\,p+1/2}_{\eta\eta\, ij-1}$$

et

$$\lambda_{pv} \Psi^{p+1}_{ij} - \Psi''^{\,p+1}_{\xi\xi\, ij} = - g_{ij}\, \omega^{n+1}_{ij} + \Psi''^{\,p+1/2}_{\eta\eta\, ij} + \lambda_{pv} \Psi^{p+1/2}_{ij}$$

$$\frac{12}{(\Delta\xi)^2} (\Psi^{p+1}_{i+1\, j} - 2 \Psi^{p+1}_{ij} + \Psi^{p+1}_{i-1\, j}) = \Psi''^{\,p+1}_{\xi\xi\, i+1\, j} + 10 \Psi''^{\,p+1}_{\xi\xi\, ij} + \Psi''^{\,p+1}_{\xi\xi\, i-1\, j}$$

où les inconnues sont

$$\Psi \quad , \quad \Psi''_{\eta\eta} \quad , \quad \Psi''_{\xi\xi}$$

Les λ_{ph} et λ_{pv} sont les coefficients optimums relatifs de 2^N itérations d'un schéma de directions alternées implicites appliqué à la résolution de l'équation de Poisson par une méthode d'ordre $O(h^2)$ donc utilisant des différences secondes centrées (8).

II-2.3 - Résolution de l'équation de transport du tourbillon

Pour résoudre l'équation de transport du tourbillon on a choisi une méthode directionnelle d'ordre $O(h^2)$. Ce choix est guidé par la recherche d'une simplicité dans l'affichage des conditions aux limites, des critères de stabilité moins restrictifs et d'un gain en temps de calcul.

Comme pour la résolution de l'équation de Poisson de la fonction de courant, l'algorithme des directions alternées implicites est utilisé. Chaque pas de temps va donc être résolu en deux demi-pas successifs avec une précision d'ordre $O(h^2)$ dans des variables spatiales.

Un pose

$$(\delta_\eta^+ f)_i = \frac{f_{i+1} - f_i}{\Delta\eta}$$

$$(\delta_\eta^- f)_i = \frac{f_i - f_{i-1}}{\Delta\eta}$$

les discrétisations décentrées de la fonction f au noeud i

$$v_{ij} = \psi'_{\xi\, ij} \qquad u_{ij} = \psi'_{\eta\, ij}$$

$$\alpha_{ij} = 1 \quad \text{si } v_{ij} > 0 \qquad \beta_{ij} = 1 \quad \text{si } u_{ij} > 0$$

$$= 0 \quad \text{si } v_{ij} \leqslant 0 \qquad = 0 \quad \text{si } u_{ij} \leqslant 0$$

1er demi-pas de temps - Intégration suivant η

On peut écrire l'équation du tourbillon sous la forme discrétisée suivante :

$$\frac{Re}{2}\left(g_{ij} \frac{\omega_{ij}^{n*} - \omega_{ij}^{n}}{\Delta t/2} + (\alpha_{ij}\delta_\eta^- + (1-\alpha_{ij})\delta_\eta^+)(\bar{v}_{ij}\,\omega_{ij}^{n*})\right) - \delta_{\eta\eta}^2 \omega_{ij}^{n*} =$$

$$-\frac{Re}{2}\left(((1-\beta_{ij})\delta_\xi^- + \beta_{ij}\delta^+)(\bar{u}_{ij}\,\omega_{ij}^{n})\right) + \delta_{\xi\xi}^2 \omega_{ij}^{n}$$

2ème demi-pas de temps - Intégration suivant ξ

$$\frac{Re}{2}\left(g_{ij} \frac{\omega^{n+1} - \omega^{n*}}{\Delta t/2} + (\beta_{ij}\delta_\xi^- + (1-\beta_{ij})\delta_\xi^+)(\bar{u}_{ij}\,\omega_{ij}^{n+1})\right) - \delta_{\xi\xi}^2 \omega_{ij}^{n+1} =$$

$$-\frac{Re}{2}\left((1-\alpha_{ij})\delta_\eta^- + \alpha_{ij}\delta_\eta^+)(\bar{v}_{ij}\,\omega_{ij}^{n*})\right) + \delta_{\eta\eta}^2 \omega_{ij}^{n*}$$

Suivant la précision recherchée en temps, d'ordre $O(\Delta t)$ ou $O((\Delta t)^2)$ on peut écrire

$$\begin{cases} \bar{u}_{ij} = u_{ij}^n \\ \bar{v}_{ij} = v_{ij}^n \end{cases} \quad \text{ou} \quad \begin{cases} \bar{u}_{ij} = \frac{1}{2}(u_{ij}^{n+1} + u_{ij}^n) \\ \bar{v}_{ij} = \frac{1}{2}(v_{ij}^{n+1} + v_{ij}^n) \end{cases}$$

On peut remarquer qu'en deux demi-pas de temps la précision spatiale des termes de transport est d'ordre $O(h^2)$. La prépondérance de la diagonale de la matrice tridiagonale est maintenue par cette technique qui permet d'éviter l'introduction de viscosité artificielle.

Comme dans le cas de l'équation de Poisson de la fonction de courant on a des systèmes tridiagonaux à résoudre par une technique de factorisation.

L'erreur de troncature du schéma combiné proposé est d'ordre

$$O(\Delta\tau, (\Delta\eta)^2, (\Delta\xi)^2)$$

A premiere vue l'introduction du schéma d'ordre $O(h^4)$ pour la resolution de l'équation de Poisson de la fonction de courant ne change pas l'ordre de precision global, qui est celui de l'equation de transport du tourbillon. Cependant il faut remarquer que la précision obtenue pour ω dépend de celle de ψ car toutes les conditions aux limites de ω sont déterminées à partir de ψ .

III – ETUDE EXPERIMENTALE

La complexite des phénomènes de décollements instationnaires impose à l'expérimentateur de s'entourer d'un maximum de garanties quant à la technique d'analyse qu'il emploie.

Nous avons donc :

1) élaboré un montage qui satisfait au mieux aux conditions imposees.
2) effectué des tests comparatifs avec d'autres installations et evalué la fiabilité des informations recueillies.

3) entrepris une étude systématique des tout premiers instants de l'écoulement autour d'une ellipse mince et d'un profil NACA 0012 placés dans un vent uniforme.

Les problèmes rencontrés lors de ces différentes phases sont analysés de façon à mettre en évidence les possibilités et les limites de notre appareillage.

Les visualisations que nous avons obtenues ont contribué à préciser les mécanismes de création et de transport des cellules tourbillonnaires aussi bien d'un point de vue qualitatif que quantitatif. A partir des clichés de visualisation nous avons en effet pu fournir une localisation spatio-temporelle des tourbillons et effectuer des relevés de champs de vitesses dans certains plans.

III-1 - Conditions expérimentales.

Pour générer une translation à vitesse constante et assurer l'instantanéité de la mise en mouvement, nous avons opté pour une "chute freinée" d'un chariot mobile, guidé par des glissières. La régulation de la vitesse est assurée par un verin à fuite d'un mètre de course ; une série d'ajustages autorise une gamme de vitesses allant de 1 cm/s à 20 cm/s. Le réglage fin entre deux ajustages est obtenu à l'aide de contrepoids. Le temps de mise en mouvement de l'amortisseur hydraulique, défini comme le temps nécessaire pour atteindre 99% de la vitesse finale, est inférieur 5/100ème s.

Les mobiles, arrimés au chariot, sont translatés dans une cuve de dimensions suffisamment grandes comparées à celles du profil, pour que les effets de paroi soient négligeables, tout du moins lors des tout premiers instants du mouvement.

- dimensions de la cuve : 150 x 100 x 80 cm^3
- profil NACA 0012 de 7 cm de corde.
- ellipse de rapport b/a = 1/10 et de 7 cm de corde.
- des profils homothétiques de 14 cm de corde ont aussi utilisés afin de préciser le détail des structures, mais les temps réduits t sont alors limités à 3.

Le déplacement de l'appareil photographique HASSEBLAD 500 EL/M de format 6x6 cm^2 est lié à celui des mobiles, de telle sorte que les photographies soient prises dans un repère lié à l'obstacle. Un plan lumineux d'une hauteur utile de 30 cm suit le profil dans son mouvement et garde une intensité constante toute la durée de la manipulation. Nous effectuons des séries de prises de vue en rafale avec un pas de temps réduit t variant de 0.5 à 0.8 suivant la vitesse de translation. Cette limitation est essentiellement dûe à des facteurs que l'on ne peut faire décroître, tels que le temps de réarmement de l'appareil photo, 1 s, ce qui est un minimum pour le format 6 x 6, et le temps de pose moyen, 0.07 en temps réduit. Le déclenchement de ces prises de vue est pré-programmé et fonction de l'altitude. Un codeur optique compte, par pas de 1 mm, la distance parcourue depuis l'instant initial ; le déclanchement et la durée des poses sont donc évaluées en mm de course avec arrondi au mm supérieur.

Nous utilisons une technique bien connue de visualisation par traceurs solides, et décrite dans (9) et (10). Le principe consiste à éclairer une section de l'écoulement par un plan lumineux mince. De fines particules solides, réfléchissantes ou diffusantes, en suspension dans le fluide dessinent pendant le temps de pose des éléments de trajectoires. Il suffit de photographier la section éclairée pour disposer d'une représentation complète de l'écoulement à un instant donné, ce qui est un avantage certain dans l'étude des phénomènes instationnaires. Les traceurs employés dans notre étude sont des grains de rilsan de taille comprise entre 80 et 150 . Des expériences ont montré que pour cette granulométrie, la vitesse moyenne de chute des particules est de l'ordre de 0.2 mm/s ; ce qui est suffisamment faible pour garantir la fidélité de la visualisation, le rapport (vitesse de chute/vitesse de translation) étant compris entre 1% et 1‰.

La datation de nos clichés évite toute ambiguité lors des dépouillements ; elle est double et donne à la fois la vitesse de référence et la référence d'altitude. Cette dernière est obtenue par le déplacement, lié à celui de l'appareil photo, d'une plaquette de 10 leds placées dans le plan objet et incrementées par le codeur optique. La référence de vitesse est constituée par une sucession de points lumineux régulièrement espacés, situés tout comme la plaquette de leds, dans le plan objet virtuel et photographiées, grâce à un jeu de miroirs, sur l'un des bords du film. L'espacement de ces points lumineux est tel que chaque cliche comporte au moins une référence.

III-2 - Essais qualitatifs du montage.

a) Problèmes rencontrés, fiabilité du montage.

Les premiers essais ont montré une légère accélération du chariot pendant la chute (8% d'augmentation de la vitesse sur 1 m). Elle est dûe à une faible conicité du vérin (0.5 mm sur 1 m) que nous avons pallié par l'utilisation d'un joint à lèvres et l'introduction d'une fuite centrale. Dans ces nouvelles conditions la vitesse est constante à mieux que 1% près sur toute la course.

Pour couvrir l'étendue de la gamme des vitesses, nous avons dû utiliser dans le vérin deux huiles de silicone de viscosité respective 50 cst et 1000 cst.

La déformation de la cuve de plexiglass sous la charge nous a contraint à la cercler, sans qu'il en résulte de gêne pour la visualisation, du moins tant que nous nous limiterons à l'étude d'écoulements plans.

Pour maintenir le profil en incidence sans entraver la visualisation, nous avons choisi de le bloquer entre deux joues en plexiglass. Ces dernières ont été profilées de manière à ce que l'augmentation de débit dûe à leur épaisseur soit

localisée entre elles et les parois de la cuve, et qu'ainsi l'écoulement ne soit pas trop perturbé entre les plaques. Dans le plan médian où nous visualisons, les essais effectués sans mobile (écoulement uniforme), avec et sans joues n'ont pas montré de différences significatives.

Une difficulté plus grande et non parfaitement résolue a été l'obtention d'un bon ensemencement en particules de la cuve. Celui-ci est réalisé par un puissant agitateur ; or on utilise de l'eau, et les dimensions de la cuve sont telles que l'amortissement des courants dû au brassage y est faible et il en subsiste encore après 30 mn d'attente. D'autre part, la vitesse moyenne de chute des particules étant de 0,2 mm/s, il est clair qu'après une attente de 30 mn la densité de particules est faible aux premiers instants puisque le mouvement démarre du haut de la cuve. De plus, les poudres restant en suspension sont les plus fines et les moins adaptées à une bonne visualisation, compte tenu du grandissement auquel nous opérons. Une solution serait de trouver des traceurs de masse volumique plus proche de celle de l'eau (densité du rilsan = 1.06). Les poudres de polystyrène que nous avons essayées sont plus légères (d = 1.04) mais ont un coefficient d'entraînement plus faible (plus grande taille et forme sphérique). Un autre remède consisterait à augmenter la densité du fluide par apport de sel ou de glycérine dans l'eau, mais cela pose un problème de stratification et de vieillissement optique (jaunissement). Nous avons donc adopté une solution de compromis avec un temps de repos moyen de 25 mn, tout en sachant bien que le décollement des cellules tourbillonnaires est peu stable et peut être provoqué ou retardé par un courant résistant ou portant.

b) Tests comparatifs

Outre les essais séparés des différents éléments du montage, nous avons testé ce dernier sur des écoulements étudiés par ailleurs, tels que ceux autour d'un cylindre ou d'une ellipse soumis à un départ impulsif et placés dans un vent uniforme. L'étude autour du cylindre a été effectuée pour deux nombres de Reynolds (Re = 1000 et 3000) et a donné lieu à des dépouillements de vitesse le long de l'axe de symétrie.

Les résultats obtenus montrent que pour deux séries d'expériences différentes réalisées avec ce nouveau montage ; la reproductibilité est bonne et la fiabilité est comparable à celle d'autres montages existants.

IV - RESULTATS

IV-1 - Résultats expérimentaux.

Trois nombres de Reynolds ont été étudiés (500-1000-3000) pour deux types de mobiles (ellipse mince de rapport 1/10 et profil NACA 0012)

Le processus de création et de transport des cellules tourbillonnaires est sensiblement le même sur toute la gamme étudiée. Néanmoins on observe une diminution de la vitesse de translation de la cellule principale (a) quand le Reynolds augmente. Parallèlement, la vitesse de rotation de ces cellules augmente.

On peut aussi noter comme caractéristique générale que le même tourbillon a une plus grande taille et se déplace moins rapidement dans le cas de l'ellipse que dans celui du profil NACA.

Outre ces relevés topographiques d'écoulements, nous avons effectué des mesures de champ des vitesses dans des plans particuliers.

Ce travail généralement trop lent et délicat pour être envisagé en dehors d'un axe de symétrie a été rendu possible grâce à l'adaptation à nos besoins de l'analyseur de film NAC.

IV-2-Résultats numériques.

Les calculs ont été réalisés pour Re = 10^3, 3.10^3 et 10^4 Les mêmes profils (ellipse de 10% d'épaisseur relative et profil NACA 0012) ont été choisis.

Pour des raisons d'encombrement en mémoire, on est obligé d'adopter un maillage de 61 x 61 noeuds quel que soit le nombre de Reynolds.

Le pas de temps adimensionnel choisi est égal à 0.01 pour le profil elliptique et à 0.005 pour le NACA 0012. Le temps de calcul nécessaire pour faire un pas de temps est environ 1,8 sec sur l'ordinateur UNIVAC 1110.

Les résultats obtenus, concernant le démarrage brusque d'un profil en incidence, sont comparés aux visualisations et mesures expérimentales réalisées dans les mêmes conditions. La comparaison se fait d'une part sur l'évolution spatio-temporelle de la structure d'ensemble de l'écoulement et d'autre part sur les profils de vitesse le long de la normale de l'axe du profil, passant par son centre. La confrontation est très satisfaisante aussi bien au point de vue qualitatif que quantitatif.

IV-2.1 - Profil de vitesse

Pour les écoulements simples présentant un axe de symétrie, nous avons effectué des relevés de champs de vitesse sur cet axe. Les courbes obtenues dans le cas de l'ellipse à incidence de 90° sont portées sur la figure 3 et correspondent au nombre

de Reynolds de 3000.

L'évolution de la composante Vx parallèle à la direction de l'écoulement général le long de la normale à l'axe du profil NACA et passant par son centre est donnée sur la figure 4, en fonction de la distance au centre du profil. On constate l'existence de survitesse dans la zone de recirculation comme dans le cas de l'ellipse ou du cylindre. Les résultats obtenus montrent une très bonne concordance entre calcul théorique et mesures expérimentales.

IV-2.2 - Structure de l'écoulement.

Observons, figures 4 bis à 12, l'évolution de la structure de l'écoulement autour du profil NACA 0012 pour Re = 1000 et une incidence α = 34°.

La position du starting vortex pour t = 0.8 montre que son détachement est quasi-instantané et que sa vitesse de translation est proche de celle de l'écoulement général.

Parallèlement se développe, au bord d'attaque, une zone de recirculation composée d'un tourbillon principal (a) et d'une paire de tourbillons secondaires (b) et (b').

Cette paire de tourbillons est stable et grossit régulièrement par apport du courant général pour (b) et de (a) pour (b').

A partir de t = 5.6, la cellule (a) se détache et naît au bord de fuite un tourbillon que nous appellerons (c). Ce dernier se développe rapidement, coalesce avec (b').

Sur les figures 13 et 14 on montre la comparaison calcul expérience relative à l'écoulement autour de l'ellipse pour une incidence α = 50°.

V - CONCLUSION-PERSPECTIVES

Cette étude a permis de dégager plusieurs conclusions :

- Les équations de Navier-Stokes instationnaires traduisent correctement les phénomènes étudiés. En effet on peut constater que pour des nombres de Reynolds inférieurs à 10^4 et dans le cas du phénomène de démarrage l'expérience et la simulation numérique fournissent des résultats dont la comparaison est très satisfaisante.
- L'installation expérimentale réalisée et la méthode numérique proposée sont fiables et adaptées à l'étude des phénomènes transitoires, en particulier le démarrage.
- Un progrès important est obtenu dans le domaine des dépouillements des visualisations permettant des comparaisons qualitatives et quantitatives.
- La méthode numérique proposée est performante en précision et en temps de calcul.
- Le mécanisme du décollement instationnaire autour d'un profil en incidence a pu être analysé d'une façon détaillée avec un maillage assez large (61 x 61).
- Le nombre de Reynolds, limité à 10^4, est dû à des contraintes informatiques (*encombrement en mémoire, vitesse de calcul...*).

Les comparaisons qu'on a réalisées au cours de cette étude ne concernent que des profils en incidence. Le montage relatif à un profil en mouvement oscillant est en cours de réalisation.

Des problèmes se posent au niveau de la génération des mouvements, l'automatisation des prises de vue et de dépouillement des résultats. Sur la photo 16 un premier résultat de la solution adoptée est donné.

Il sera intéressant de pouvoir procéder à des comparaisons sur les mouvements de base facile à réaliser expérimentalement, d'analyser expérimentalement l'influence des différences de paramètres (amplitude, fréquence, incidence) sur la formation des décollements et surtout sur la stabilité de l'écoulement.

Du point de vue de la simulation numérique on pense augmenter le nombre de Reynolds par utilisation de calculateur vectoriel ou parallèle. L'objectif est d'arriver à un maillage voisin de 100.000 noeuds à 2 dimensions.

REFERENCES

(1) - L. COLLATZ - "The numerical treatment of differential equations" Ed. Springer Verlag 1966

(2) - S. ORSZAG et M. ISRAELI -"Numerical simulation of viscous incompressible flows". Annual Rev. Fluid Mech., Vol. 6, 1974.

(3) - R.S. HIRSH - "Higher order accurate difference solutions of fluid mechanics problems by a compact differencing technique", J. Comput. Physics, Vol. 19, 1975.

(4) - O. DAUBE et TA PHUOC LOC - "A mixed compact hermitian method for the numerical study of unsteady viscous flow around an oscillating airfoil". Notes on Numerical Fluid Mechanics, Vol. 2, 1980.

(5) - TA PHUOC LOC et O. DAUBE - "Higher order accurate numerical solution of unsteady viscous flow generated by a transversely oscillating elliptic cylinder", WAM ASME - Chicago, November 1980.

(6) - B. ROUX, P. BONTOUX, TA PHUOC LOC, O. DAUBE - "Optimatisation of hermician methods for Navier-Stokes equations in vorticity and stream function formulation", Lecture Notes in Mathematics - Vol. 771, 1980.

(7) - O. DAUBE et TA PHUOC LOC - "Etude numérique d'écoulements instationnaires décollés de fluide visqueux incompressible", J. de Mécanique, Vol. 17, 1978.

(8) - E.L. WACHSPRESS - "Iterative solutions of elliptic systems", Ed. Prentice Hall 1966.
(9) - M. COUTANCEAU and R. BOUARD - "Experimental determination of the main features of the viscous flow in the wake of a circular cylinder in uniform translation - Part I - Steady flow", J. Fluid Mech. (1977) Vol 79 pp 231-256.
(10) - P. MONNET, C. MENARD, D. SIGLI - "Some new aspects of the slow flow of a viscous fluid though an axisymetric duct expansion or contraction - experimental part", Applied Scientific Research (1982) Vol 39 pp 233-248.
(11) - B.E. LAUNDER and D.B. SPALDING - Mathematical Models of Turbulence , Academic Press - NewYork

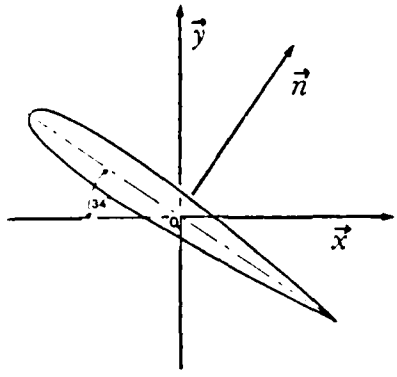

Figure 1

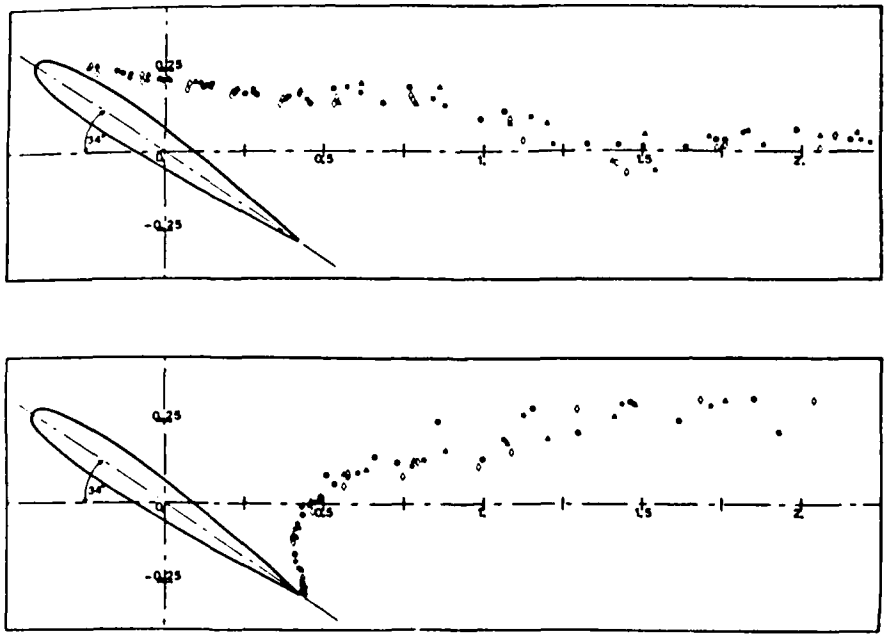

Figure 2 - Trajectoire des centres des premiers tourbillons principaux
Figure 2 - Paths of the centers of main first vortices

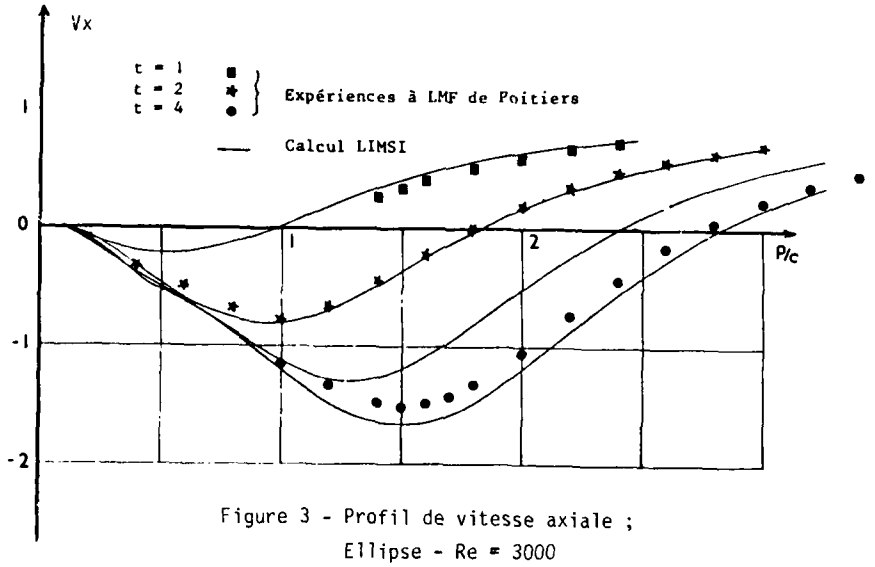

Figure 3 - Profil de vitesse axiale ;
Ellipse - Re = 3000

Figure 3 - Axial velocity profile ;
Ellipse - Re = 3000

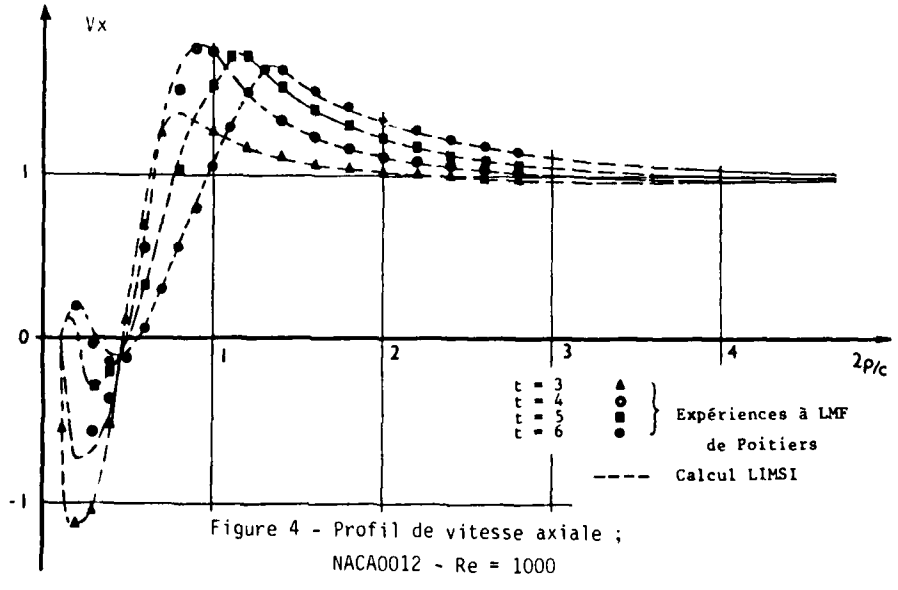

Figure 4 - Profil de vitesse axiale ;
NACA0012 - Re = 1000

Figure 4 - Axial velocity profile ;
NACA0012 - Re = 1000

Figure 4bis -NACA0012 - Re = 1000 - t = 0.8

Figure 4ter - NACA0012 - Re = 1000 - t = 3.2

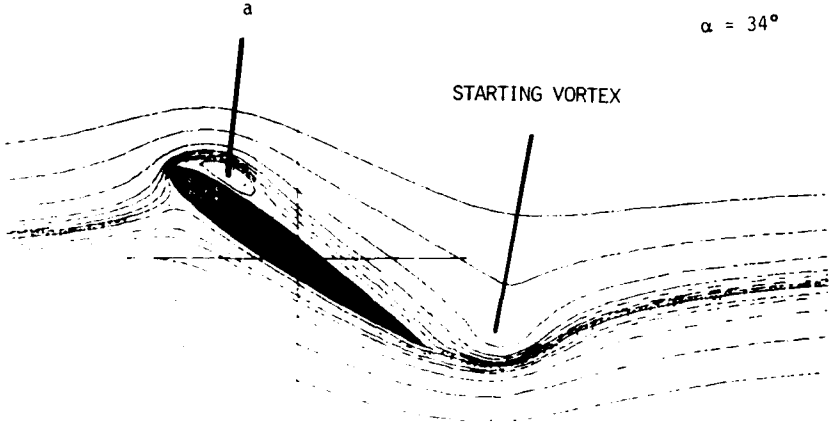

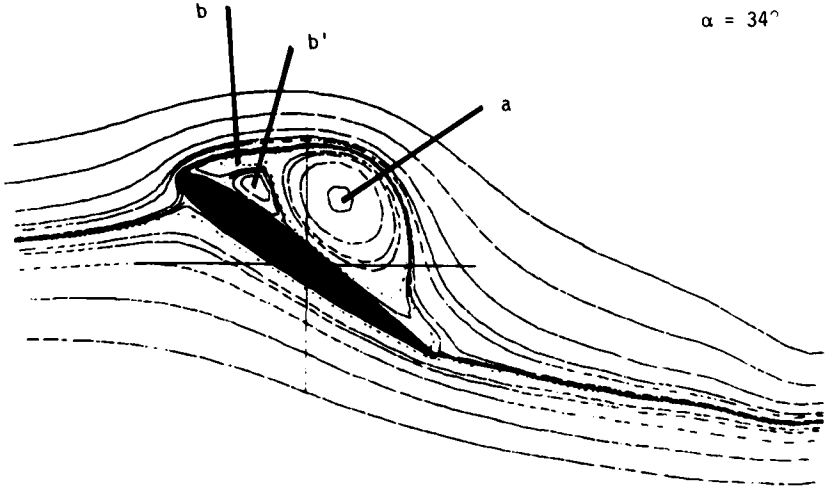

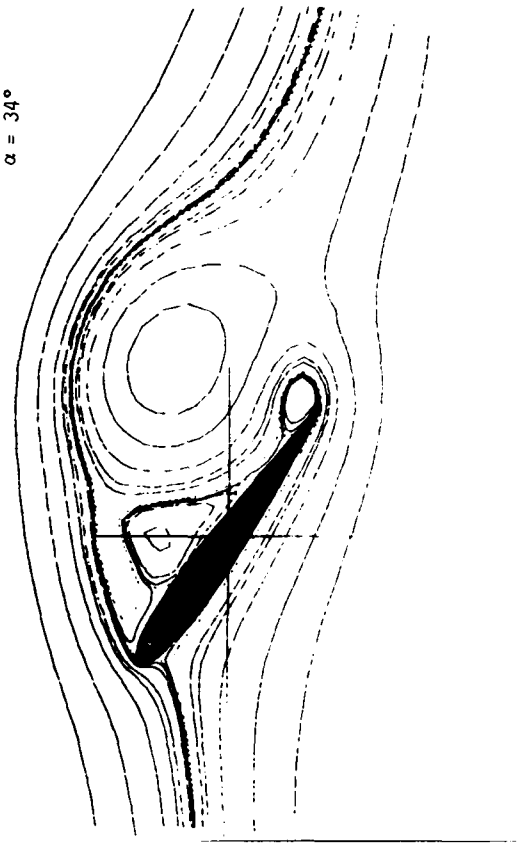

Figure 6 - NACA0012 - Re = 1000 - t = 6.4

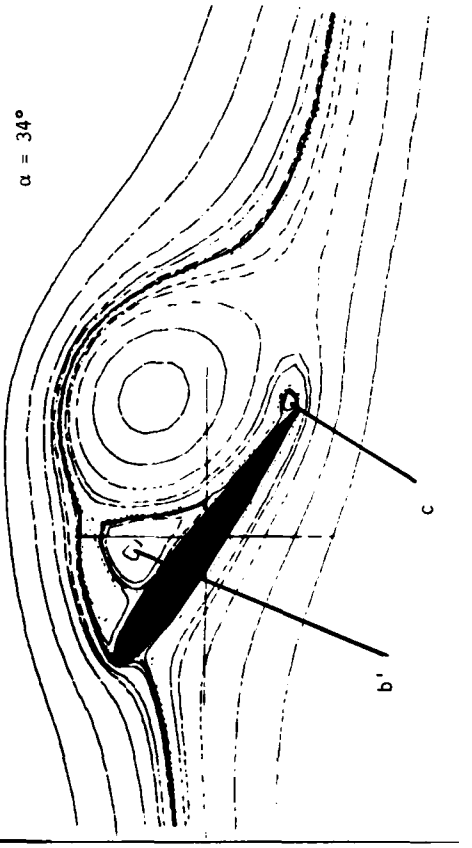

Figure 5 - NACA0012 - Re = 1000 - t = 5.6

Figure 7 - NACA0012 - Re = 1000 - t = 7.2

Figure 8 - NACA0012 - Re = 1000 - t = 8.

α = 34°

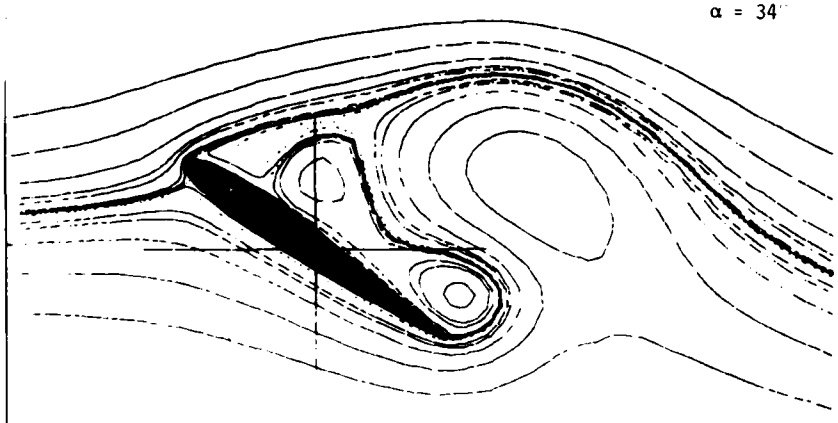

α = 34°

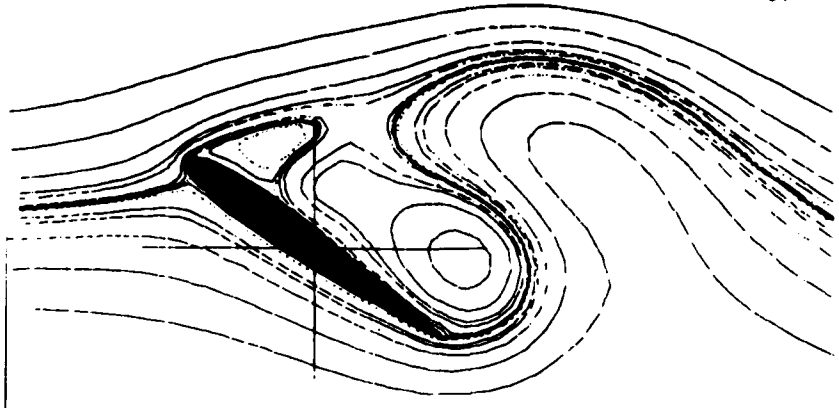

Figure 9 - NACA0012 - Re = 1000 - t = 8.8

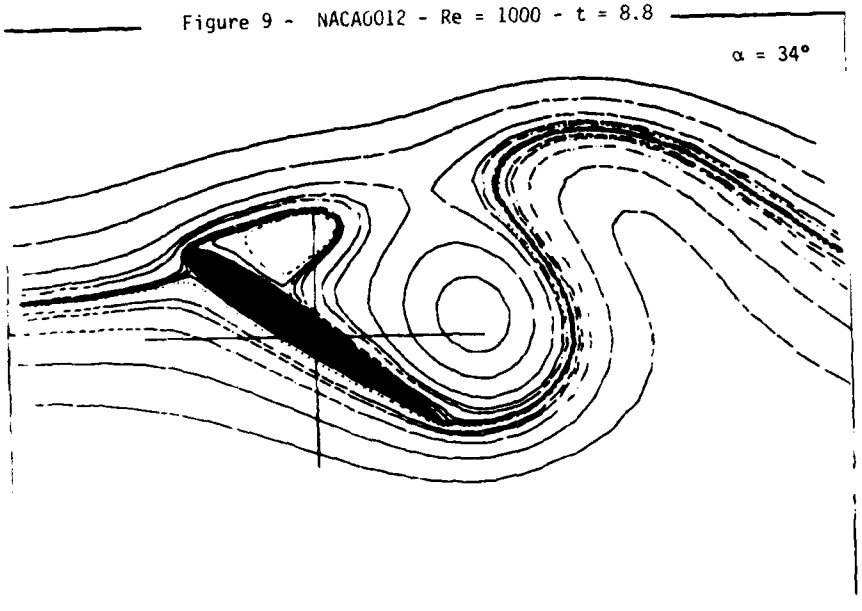

Figure 10 - NACA0012 - Re = 1000 - t = 9.6

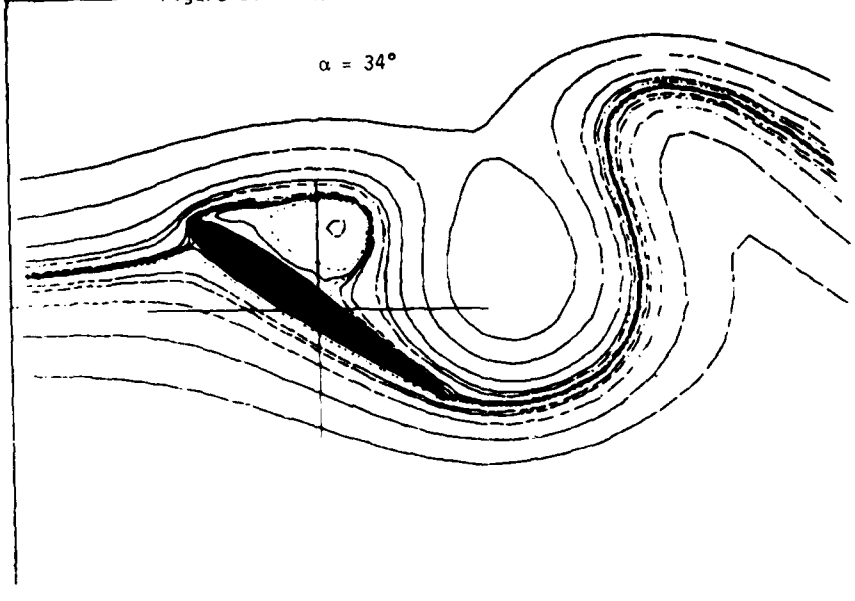

Figure 11 - NACA0012 - Re = 1000 - t = 10.4

α = 34°

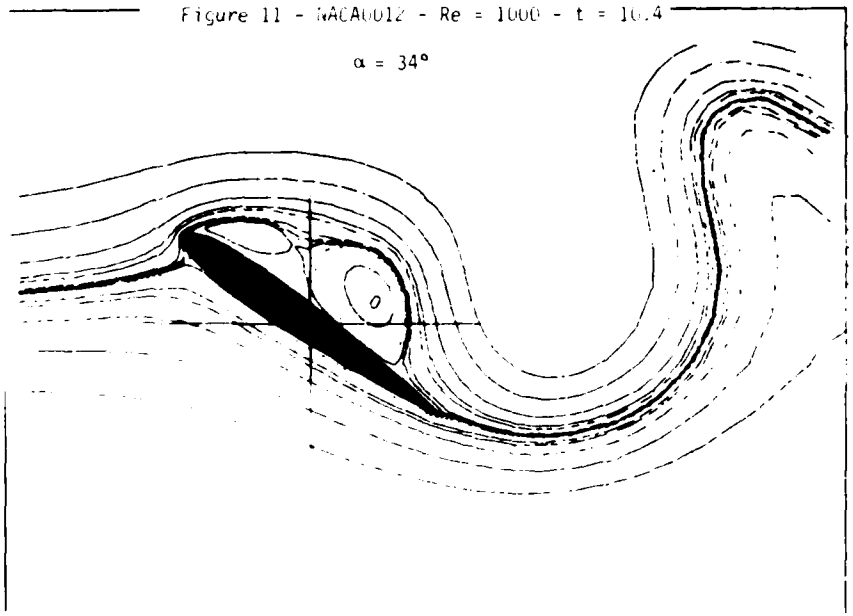

Figure 12 - NACA0012 - Re = 1000 - t = 11.2

α = 34°

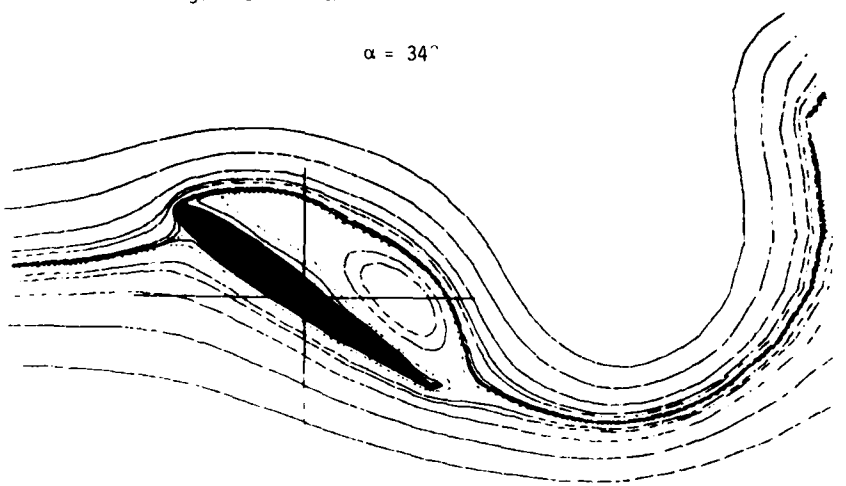

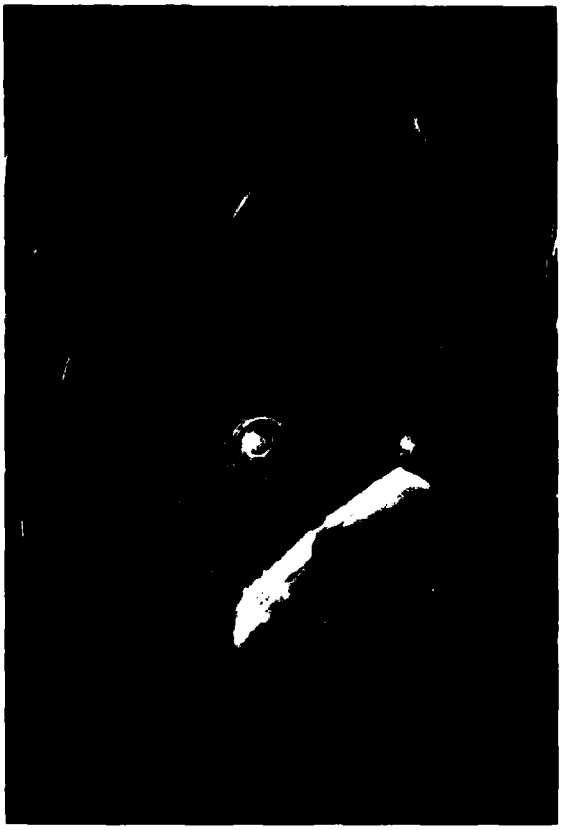

Figure 13 - Ellipse - Re = 1000 - t = 2

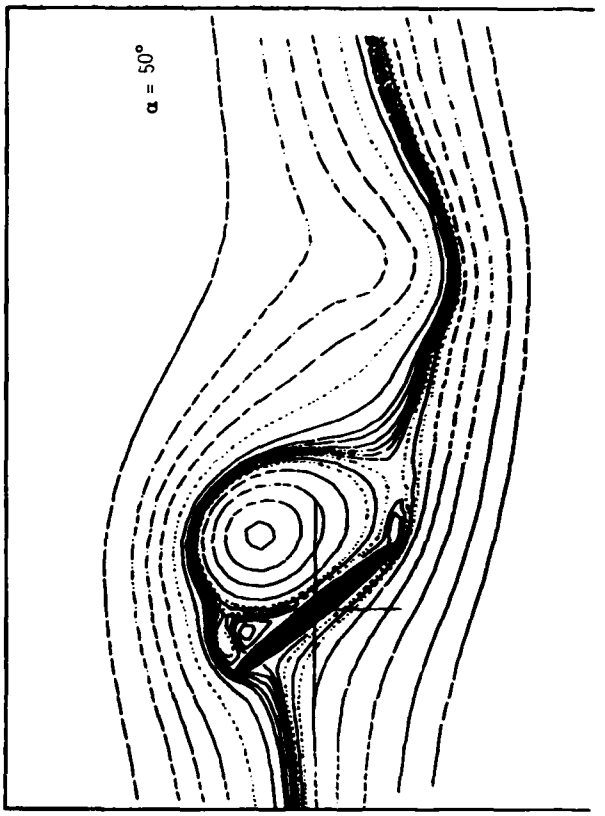

Figure 14 - Ellipse - Re = 1000 - t = 4

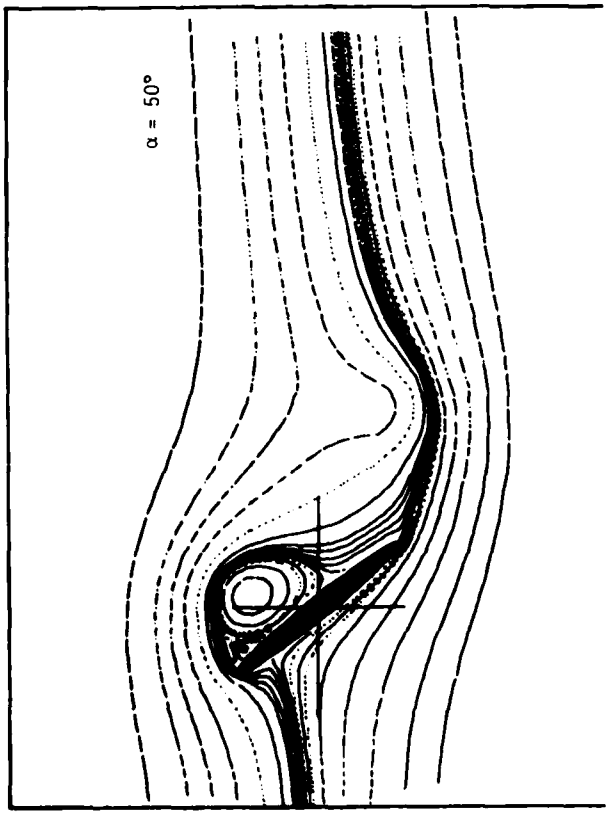

VELOCITY AND TURBULENCE MEASUREMENTS IN DYNAMICALLY STALLED BOUNDARY LAYERS ON AN OSCILLATING AIRFOIL

by

J. DE RUYCK and Ch. HIRSCH
Research ass. Professor

Vrije Universiteit Brussel
Dept. of Fluid Mechanics
Pleinlaan 2, 1050 Brussels
Belgium

SUMMARY

Detailed velocity and turbulence properties in the dynamically stalled boundary layer of an oscillating NACA 0012 airfoil have been measured. This airfoil oscillates around an axis at 25% distance from the leading edge with a sinusoidal motion. Measurements are performed at eight chordwise positions, in non stalled, stall onset and deep stalled flow conditions.

Instantaneous detailed flow and turbulence patterns of the periodic separation vortex are presented and discussed. Corresponding terms of the turbulent energy balance are derived and compared with flat plate boundary layer data. In particular, negative turbulent energy production is observed during the vortex development.

SYMBOLS

c	blade chord	u	chordwise velocity
f	phase angle	v	velocity normal to the wall
i	incidence	w	spanwise velocity
i_o	mean incidence	x	chordwise coordinate
k	reduced frequency $\omega c/2Q_\infty$	y	coordinate normal to the wall
Q_∞	free stream velocity	z	spanwise coordinate
q	velocity modulus	$\bar{}$	ensemble averaged value
		'	fluctuation from ensemble averaged value

1. INTRODUCTION

The verification of full unsteady Navier Stokes computations is presently limited by a lack of detailed experimental data. In the particular case of a pitching airfoil there is a need for quantitative measurements of velocity and turbulence fields, whereas mostly flow visualisations are available [1,2,3]. Computations of unsteady flows have been obtained during the last decade, but turbulence effects were in general not taken into account [4,5,6,7]

The experimental determination of velocity and turbulence fields in an unsteady, dynamic stalled flow is a most difficult task. In the present research project, a technique has been developed allowing th etermination of low speed high turbulent flows with arbitrary flow direction (2D). It has been applied to measure stalled boundary layers on a pitching NACA 0012 airfoil [8,9]. Measurements have been performed at eight chordwise positions along the blade chord. Results of five test configurations are available : an unstalled case, two cases with stall onset and two full stalled cases. Extensive wake measurements were made available in the past [10,11].

In the present paper, relevant results are discussed. The experimental turbulent energy balance has been analysed through the determination of production, transport and dissipation of turbulence. The unstalled turbulent energy balance is found to be very similar to the steady flow situations. Some negative turbulence production is found during the vortex development.

2. EXPERIMENTAL TECHNIQUES

The measurement of low speed flows with high turbulence and arbitrary flow direction is a difficult task in experimental fluid dynamics. Recently, some progress has been presented by Thompson and Whitelaw [12]. In this technique, called 'flying hot wire technique', the hot wire is in motion and a relative velocity is superimposed on the flow velocity to be measured. In this way, problems of zero velocity detection and arbitrary flow direction are solved. This technique is difficult to apply in the present context however.

A technique has been developed where reversed flows are measured from the angular calibration characteristics of a rotating slanted hot wire. This relatively simple

technique allows accurate measurements within the small sensing area of a single wire (1 mm) with no extra technical requirements. This technique has been presented in [8,9]. It can briefly be summarised as follows.

Velocity and turbulence determination

The method to determine main flow parameters as well as all non-zero Reynolds stresses with a single hot wire has its base in the work of Kool [13] and De Grande & Kool [14]. This technique has been improved by the authors, by increasing the resolution of the Reynolds stress measurements [10,11]. In principle, the flow properties are determined from the directional reponses of the wire which is rotated around its axis.

Reversed flow detection

The slanted wire is mounted as shown on figure 1. When rotating the wire over 360°, a response as shown on figure 2 is obtained. On this figure the anemometer voltage is shown as function of the rotational position. The minima indicate the flow direction. A correct and an adverse solution for the flow direction is thus found for each data point. The choice of the correct solution is based on the continuity in time of this flow angle, which is made possible by the large number of data points recorded over one period of oscillation (240 points).

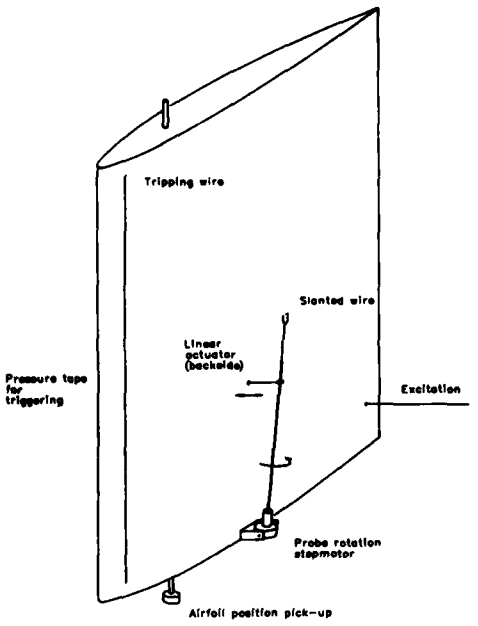

Figure 1 : experimental set-up

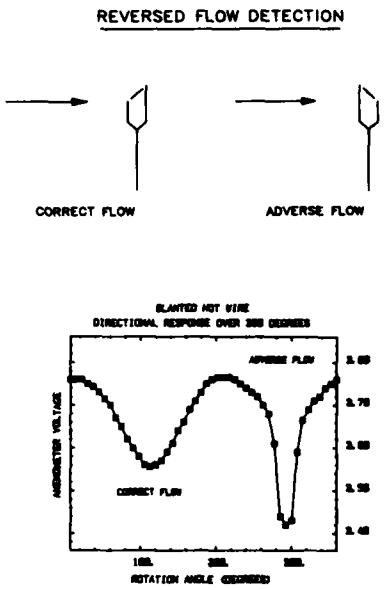

Figure 2 : angular hot wire calibration

Zero mean velocity determination

The splitting of a hot wire time signal into its mean value and a fluctuation term is essentially a one dimensional approach, assuming a turbulence which is small enough when compared whith the main flow velocity. When turbulence velocities become as large as the mean flow velocities, statistical corrections are to be made in order to determine the real mean velocity from the measured averaged anemometer voltage. When assuming a Gaussian probability distribution for the turbulence, following relation has been found for a one dimensional flow (v=w=0) [8,9]

$$\bar{q}_{meas} = \sigma \sqrt{2/\pi}\, e^{-\frac{1}{2}\left(\frac{\bar{q}_{real}}{\sigma}\right)^2} + \bar{q}_{real}\left[1 + \mathrm{erf}\left(\frac{\bar{q}_{real}}{\sqrt{2}}\right)\right] \qquad (1)$$

$$\sigma = \sqrt{\overline{q'^2}}$$

In the case of a two dimensional flow, a correction rule with a degenerate hypergeometric function Φ is found [8,9]

$$\bar{q}_{meas} = \sigma \sqrt{\pi/2}\; \Phi(3/2,1;\bar{q}^2_{real}/2\sigma) \qquad (2)$$

No expression has been found for a full three dimensional flow. It however appeared that both equations (1) and (2) yield quite similar and satisfactory results. To avoid unacceptable computing times, an approximation for equations (1) and (2) has been searched, as follows [8,9]

$$\bar{q}_{meas} = \bar{q}_{real} + K \sigma e^{-\frac{1}{2}\left(\frac{\bar{q}_{real}}{\sigma}\right)^2} \qquad (3)$$

$$K = 1.2$$

3. AVAILABLE TEST CASES

A tripping wire is used to trigger the turbulence. Incidence ranges were chosen in such a way that a clear distinction can be made between a non-stalled, stall onset and deep stalled case. Following test cases are available, all at an oscillation amplitude of +/- 5°.

Ident	incidence	reduced frequency	Reynolds number	
BLA5	5 to 15	0.48	178,000	stall onset
BL15	5 to 15	0.3	300,000	non stalled
BL16	6 to 16	0.3	300,000	stall onset
BL18	8 to 18	0.3	300,000	stalled
BL20	10 to 20	0.3	300,000	stalled

Test case BL15 is a non stalled case where the incidence ranges from 5° to 15°. When the reduced frequency is increased from 0.3 to 0.48 (BLA5), a flow separation near the leading edge occurs and a vortex is present during a small part of the oscillation period. When the frequency is kept constant but the mean incidence is increased by 1° (BL16), the flow separates at both the leading and the trailing edge. A very small vortex is present during a short time near the leading edge. When the incidence is further increased, the leading edge vortex developes into a large separation vortex and a full dynamic stalled flow results (BL18 and BL20).

Measurements were performed at 7° to 17° incidence, k=0.3. These conditions correspond to the transition between stall onset and stalled conditions : stall is sometimes initiated, sometimes not and no coherent results could be found.

4. RESULTS

Results are available at the chordwise positions x/c = 0.15, 0.24, 0.33, 0.41, 0.50, 0.60, 0.70 and 0.80. Data are available at 240 time steps (1.5° phase shift). This high density was required for the reversed flow detection, in particular near the vortex front which developes during a short time.

Relevant data are summarized on figures 3 to 7. The time step number (1 to 240), the instantaneous incidence (i) and the phase angle (f) are mentioned. The phase angle is defined through

$$i = i_o + 5° \sin f, \quad f = \omega t = 1.5° \text{ (time step - 1)} \qquad (4)$$

The scales are added below each figure. It is to be observed that no smoothing has been applied on velocity and velocity fluctuations. Smoothing on other results has moreover been done in the time domain only, not in space. It is important to observe that all the points at the same time step, as shown in the results, are completely independent of each other.

Turbulent energy balance

The balance of turbulent kinetic energy $\overline{q'^2}/2$ can be written as follows [15]

$$\frac{\partial}{\partial t}\frac{\overline{q'^2}}{2} = -u_i \partial_i \frac{\overline{q'^2}}{2} - \overline{u_i' u_j'}\,\partial_i \bar{u}_j - \partial_i \overline{u_i'\left(\frac{p'}{\rho} + \frac{q'^2}{2}\right)} + \nu\,\partial_i \partial_i \frac{\overline{q'^2}}{2} - \nu\,\overline{\partial_i u_j' \partial_i u_j'} \qquad (5)$$

LOCAL VARIATION | CONVECTION | PRODUCTION | DIFFUSION | DISSIPATION

Local energy variations, convection and production can be determined from the experimental data. Diffusion plus dissipation can be estimated from the energy balance

equation (5). Results are shown in a non-dimensional form, with the chord c and the velocity Q_∞ as references.

Incidence 5 to 15 degrees / k=0.3 / no stall

Figure 3 shows results when the maximum incidence has been reached. The unstalled case is shown at the left side. At that time, the boundary layer tends to separate in the last station, and it is believed that the boundary layer is lightly separated at the trailing edge. Turbulence levels at maximum incidence do not exceed 14% and minimum levels are comparable to the turbulence levels as found by Klebanoff on constant pressure flat plate experiments [15]. The Reynolds stress at maximum incidence reaches values of 0.008 Q^2 .

The unstalled turbulence profiles of case BL15 have been compared with data obtained by Klebanoff on a flat plate at constant pressure gradient [15]. On figure 4 the four non-zero turbulent stress profiles are compared at x/c = 0.60, at the minimum incidence of 5°. At this time the pressure gradient is the most favourable for the boundary layer and the results (squares) are quite close to the Klebanoff data (solid lines). At higher incidences, increased levels are observed, with maximum values in the most critical situation (figure 3). In this situation the Reynolds stress exceeds the Klebanoff profile by about 5 times. Maximum values in these profiles are shifted towards the middle of the boundary layer, which corresponds to a shift in the maximum velocity gradient $\partial u/\partial y$.

Some relevant contributions to the energy balance are shown on figure 5. At the lowest incidence, around 5°, profiles are found which are very close to the flat plate boundary layer data (dashed line). Local changes and convection are small. The turbulence production is compensated by dissipation. At the highest incidence, where the boundary layer is close to separation, the dominant terms are still production and dissipation. Although the flow is unsteady, local time variations and convection are still small when compared with the other terms. All the contributions are increased by about five times when compared with the flat plate data, however.

The present comparison indicates a good coherence with standard data such as those obtained by Klebanoff.

Incidence 5 to 15 degrees / k=0.48 / stall onset

The higher frequency case is shown on the central part of figure 3. The following differences with respect to the lower frequency case are observed :

The flow has less tendency to separate at the trailing edge, and it is believed not to separate at all at this place. Whereas the situation has improved at the trailing edge by increasing the reduced frequency, the situation has deteriorated at leading edge where a small vortex initiates at the maximum incidence time (not shown). This vortex affects the flow in the first two stations (figure 6) and it disappears at about 11° incidence.

The turbulence increases to about 0.2 Q for $\sqrt{u'^2}$ and 0.01 Q^2 for $\overline{u'v'}$ in all the stations when the critical stall onset incidence is reached. Peaks of resp. 0.35 Q and 0.05 Q^2 are observed in the first station.

Incidence 6 to 16 degrees / k=0.3 / stall onset

The stall onset case BL16 is shown on the right side of figure 3. The frequency is the same as for the unstalled case BL15 but the mean incidence has been increased by 1°.

A trailing edge separation initiates in the last station at an incidence of 15.8°. This separation must be present at the trailing edge at an incidence which is close to the static stall limit of 14°. During the following time steps this separation affects the flow further upstream, and the whole boundary layer flow tends to separate (figure 3). At the same time, a small but strong vortex is created close to the leading edge. This vortex however does not come to development and disappears, together with the trailing edge separation, as the incidence decreases towards its mean value. This vortex initiates at about 16.5° incidence. The flow is not fully reversed during the trailing edge separation, whereas a strong reversal is observed at the leading edge.

Turbulence intensities range from about 0.08 Q, which is close to the current levels as found by Klebanoff, to 0.18 Q in the trailing edge separated flow. Peak values of 0.37 Q are observed near the leading edge vortex. Maxima in the turbulence profiles in general correspond to the maxima in velocity gradients at any time, which is in accordance with the current turbulence models. Much scatter is present on the $\overline{u'v'}$ profiles in the leading edge vortex and these results should be considered as only indicative.

Incidence 8 to 18 degrees / k=0.3 / stalled

The stalled case BL18 is reported on figures 6 and 7. Figures 6.a to 6.d show a set of results at some representative times. On each figure are shown, from top to bottom : velocity field, chordwise fluctuations $\sqrt{u'^2}$, minus Reynolds stress $\overline{u'v'}$, local time variations of turbulent kinetic energy, convection, production and dissipation plus diffusion of turbulent kinetic energy. Each time step is discussed separately.

When the flow is separating, important scatter is observed on $\overline{w'^2}$ and $\overline{v'^2}$ in particular. As a consequence, no clear picture is obtained when deriving the turbulence energy convection and dissipation. In order to obtain a more clear picture of the turbulence balance, $\overline{q'^2}$ has therefore been approached by

$$\overline{q'^2} = K\,\overline{u'^2} \qquad (5)$$

$$K = \frac{\overline{u'^2}+\overline{v'^2}+\overline{w'^2}}{\overline{u'^2}} = 0.6$$

The value K = 0.6 was obtained as the best overall value for the present test case. The present approach does not affect the behaviour of the local variations and the convection of turbulent energy.

time 31 : separation onset (figure 6.a)

The boundary layer shows a tendency to separate from station 3 to 8. This separation initiates at the trailing edge when the static stall limit of 14° is exceeded (not shown). Increased levels of turbulence are observed (0.2 Q). The turbulence energy balance is still dominated by the production and the dissipation terms at the most downstream positions.

At the leading edge, the flow is going to separate. Peak values of turbulence are observed (up to 0.4 Q). Peculiar stress profiles are observed at this point : positive values of u'v', or negative Reynolds stresses appear. When looking to the corresponding turbulence production, some negative turbulence production is observed. This behaviour is also found during the further vortex development.

Local variations and convection of turbulent energy are significant at this point : the turbulence is rapidly increasing with time in the outer part of the layer. This is mainly due to a combination of diffusion, production and convection, which are all positive in the outer layer (first station, time 31). The positive convection indicates an important turbulence transport from the upstream flow which may already be separated. Important diffusion is present in the inner part of the layer at leading edge.

time 40 : leading edge and trailing edge separated (figure 6.a)

The situation at the trailing edge has not changed significantly within this short time. At the leading edge, the vortex is developing rapidly. The turbulence peaks are just above the separation line (see also figure 7). Positive values of $\overline{u'v'}$ are still observed, with a corresponding tendency towards negative turbulence production. The behaviour of the turbulent energy balance in the first station is changing rapidly.

The velocity is increased considerably in the central part of the boundary layer, between the leading and trailing edge separated flows. This portion of boundary layer is highly turbulent, although the boundary layer thickness and the turbulence production are small. This turbulence is mainly transported from the upstream flow.

time 49 : (figure 6.b)

This figure shows the further development of the leading edge vortex. The central high speed portion of the boundary layer is shifting towards the trailing edge and the low speed separated flow at trailing edge is blown away. Positive $\overline{u'v'}$ values and negative turbulence production are still observed in front and in the center of the leading edge vortex.

time 73 : leading edge vortex leaves (figure 6.b)

The incidence is now decreasing. The leading edge vortex has left the sensed area and is completely separated from the airfoil. The last stations are reversing abruptly the one after the other (station 7 is reversing). Negative stresses are still present under the separation line, and some corresponding negative production is still observed. From now on, changes in time are less abrupt and the local changes in turbulence have the tendency to be less significant than the other terms in the turbulent energy balance.

time 97 : creation of a second vortex (figure 6.c)

The large vortex observed at time 97 is a new one which came to development at its actual place, and which remains there for some time interval. The different terms of the turbulent energy balance become small in the separated area, whereas large values remain above the separation line. Although positive $\overline{u'v'}$ values are still observed, the tendency towards negative production has disappeared. The convection term becomes strongly negative along the separation line, indicating that the (strongly) produced turbulent energy is mainly blown away downstream, instead of being locally dissipated.

times 121, 145, 169 : blow-off of the separated flow (figures 6.c, 6.d)

As the incidence decreases, a normal boundary layer is going to be developed. This occurs through a gradual blow-off of the reversed flow area, as can be followed on times

121 to 169. The velocity as well as all the turbulence quantities gradually decrease. The vortex present at time 97 has 'diffused' into the flow seen at time 121, without moving away. The convection of turbulence is still strongly negative which is in accordance with the fact that the turbulence along the separation line is blown towards the trailing edge, rather than being dissipated locally.

The boundary layer which finally appears at the lowest incidence has a behaviour which is comparable with the unstalled flow case (not shown).

Comparison with computed data

Some computed results obtained by Mehta [4] are reproduced on figure 10. The test conditions for these results are different from the present ones. The Reynolds number is 10,000, the reduced frequency 0.25 and the airfoil oscillates from 0° to 20°. Some similarity with the present results is found however : the presence of two vortices is observed in the same way as in the present experiments and a similar acceleration between leading edge vortex and trailing edge separation is observed.

This similarity between the measured and computed flow configurations lends support to the negligible influence of the tripping wire on the measured flow structure. So more, that the length scale of the leading edge vortex is much larger than the scale of the tripping wire. It is to be observed that Mehta's computations are for a laminar flow.

5. CONCLUSIONS

A technique for velocity and turbulence measurements in dynamic stalled flows has been applied in the boundary layers of an oscillating airfoil. Measurements are made in unstalled, stall onset and full dynamic stalled conditions at 8 chordwise positions along the suction side of the airfoil. Detailed data about velocity, turbulence intensity, Reynolds stress and turbulent energy balance are available.

In the unstalled case, the turbulence structure behaves in accordance with current flat plate boundary layer data. At high incidence, a small trailing edge separation may be present.

In the stall onset cases, a vortex is created near leading edge, but it behaves as a bubble which disappears without separating fully. The stall onset can be obtained by increasing the reduced frequency, or by increasing the maximum incidence. Trailing edge separation is observed when the incidence exceeds the static stall limit of 14° at k=0.3. This effect is however reduced as the reduced frequency is increased.

Detailed pictures of leading edge vortices and trailing edge separations are presented in the deep stalled case. Negative Reynolds stresses and negative turbulent energy production are observed in front and in the center of the leading edge vortex. This may be an indicator for the coming vortex formation. Strong vorticities are observed at the leading edge, whereas the trailing edge separated flow is of low velocity.

Similarity is observed with computed results on different but similar conditions, although these computations are made without taking turbulence effects into account.

6. ACKNOWLEDGEMENTS

The present work has been supported by the U. S. Government through the U. S. Army Research & Standardization Group (Europe), contract nr DAJA 45-83-C-0021, and by the Belgian National Research Funds (NFWO).

7. REFERENCES

[1] MC ALISTER K.W., CARR L.W., "Water Tunnel Visualisations of Dynamic Stall" ASME Journal of Fluids Eng., Vol 101, 3, P377-380, 1979

[2] ROBINSON L.G., LUTTGES M.W., 1983, "Unsteady Flow Separation and Attachment Induced by Pitching Airfoils" AIAA Paper 83- 0131

[3] WERLE H., 1976, "Visualisation Hydrodynamique de l'Ecoulement Autout d'Une Pale Oscillante " Onera Rapport Technique 56/1369 An, 1976

[4] MEHTA U.B., 1978, "Dynamic Stall of an Oscillating Airfoil" Agard cp 227, Unsteady Aerodynamics, p 23-1,1978

[5] SUGAVANAM A., WU J.C., 1980, "Numerical Study of Separated Turbulent Flow Over Airfoils" AIAA Paper 80-1441, 1980

[6] SANKAR N.L., TASSA Y., 1980, "Reynolds Number and Compressibility Effects on Dynamic Stall of a Naca 0012 Airfoil" AIAA Paper 80-0010,1980

[7] HORIUTI K., CHYU W.J., BUELL D.A., "Unsteady Transonic Flow Computations for an Airfoil with an Oscillating Flap" AIAA paper 84-1562, 1984

[8] DE RUYCK J., HIRSCH C., "Instantaneous Flow Field Measurements of Stalled Regions on

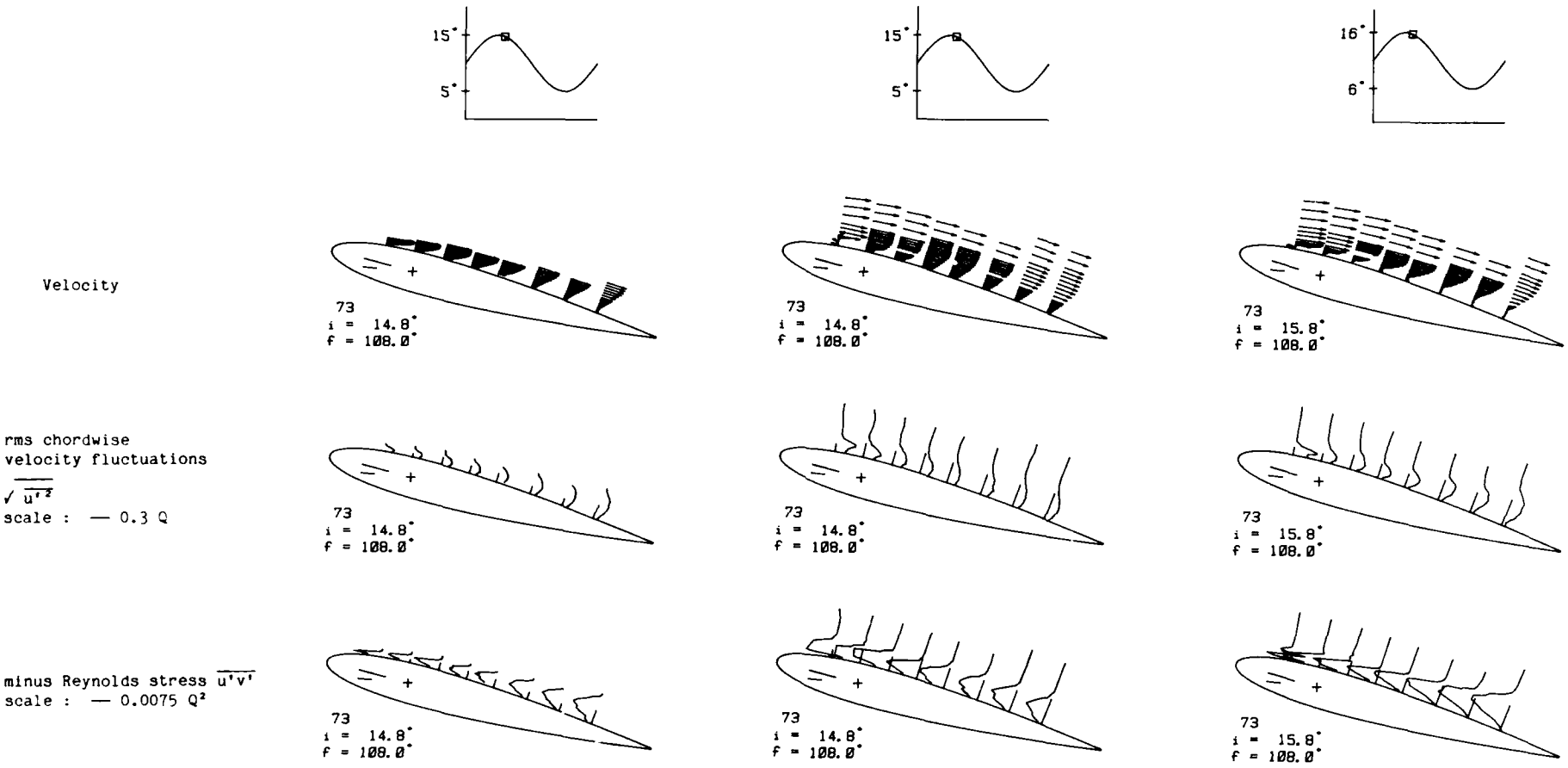

Figure 3 : left side : BL15, k=0.3, no stall
center : BLA5, k=0.48 stall onset
right side : BL16, k=0.3 stall onset

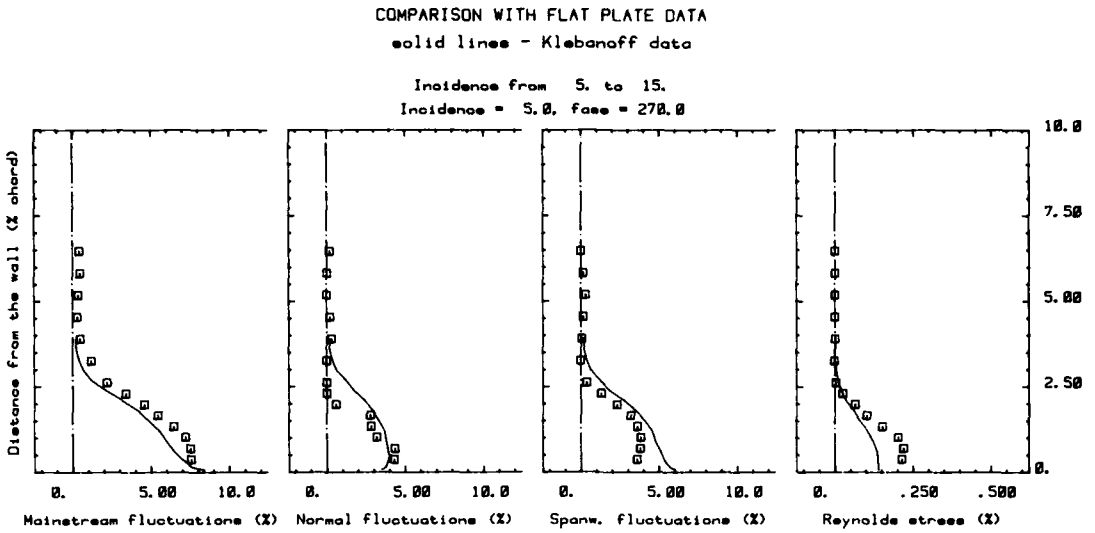

Figure 4 : Unstalled turbulence profiles
Squares : present experiment
Solid lines : Klebanoff data [15]

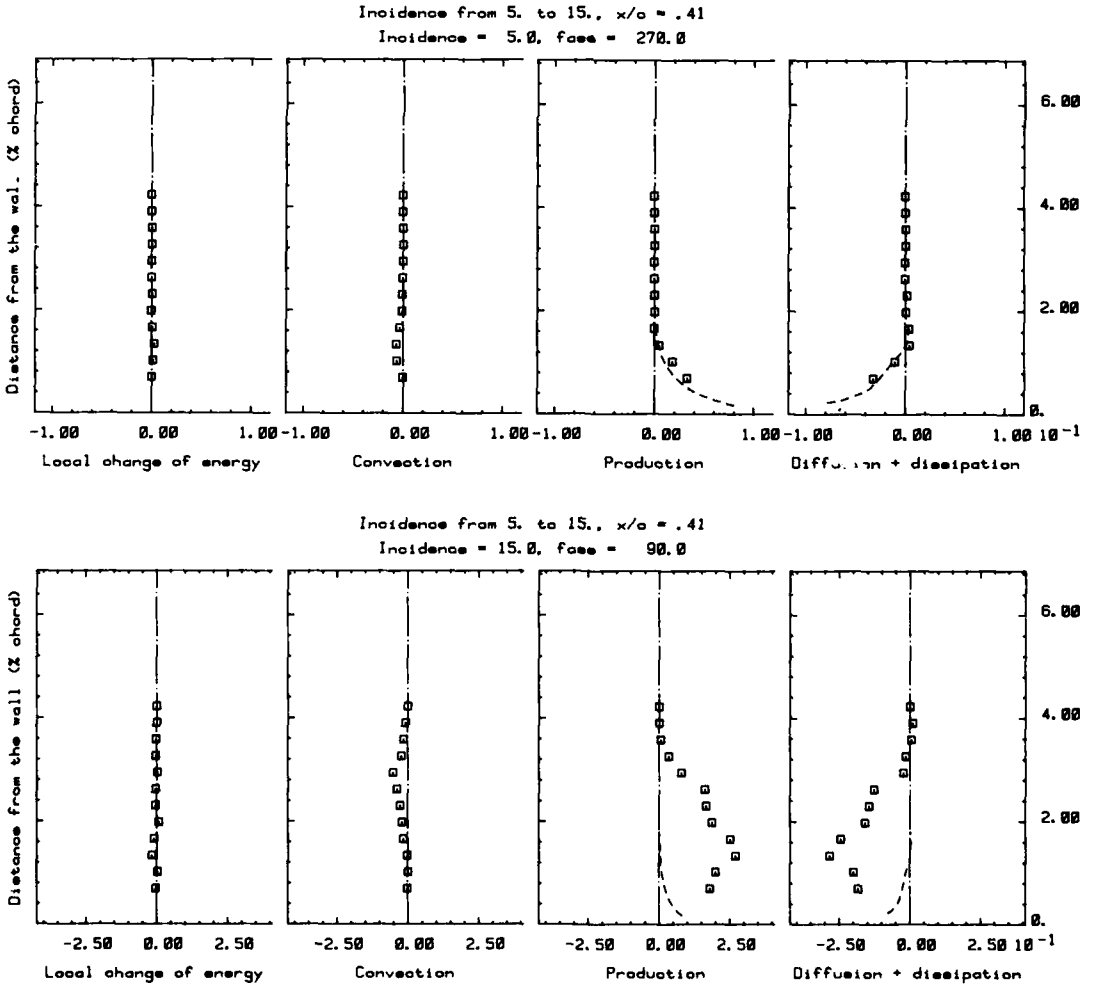

Figure 5 : Unstalled turbulent energy balance
Squares : present experiment
Solid lines : Klebanoff data [15]

Figure 6.a :
stalled testcase BL18
8° to 18°, k=0.3

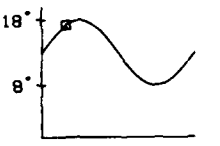

Velocity

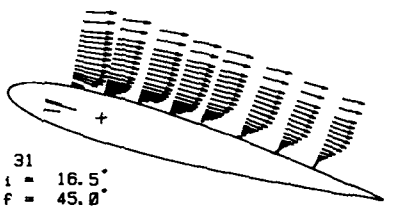

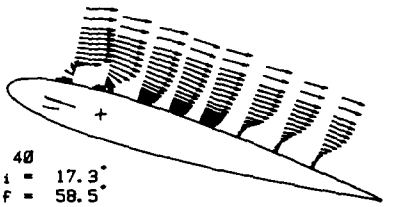

chordwise
fluctuations
$\sqrt{\overline{u'^2}}$
scale : — 0.3 Q

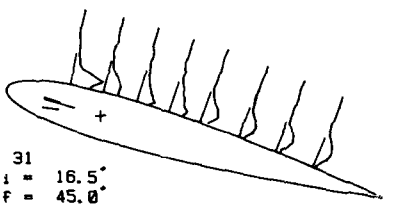

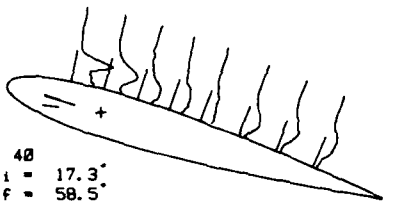

minus
Reynolds stress
scale : — 0.03 Q^2

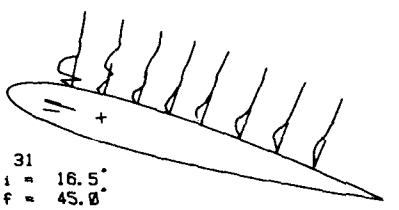

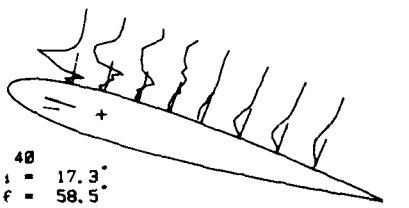

Local changes of
turbulent energy
scale : — 0.6

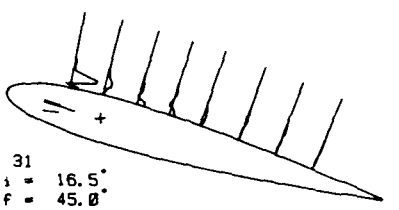

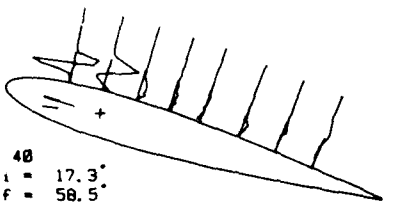

convection of
turbulent energy
scale : — 0.6

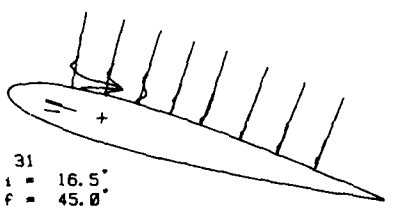

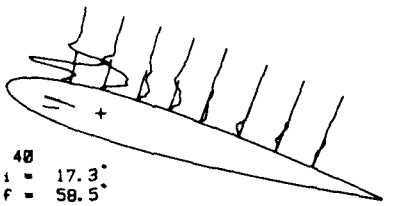

production of
turbulent energy
scale : — 0.6

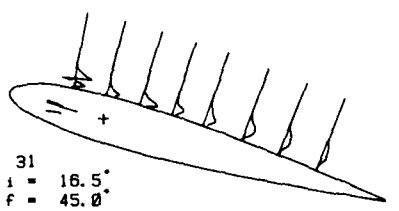

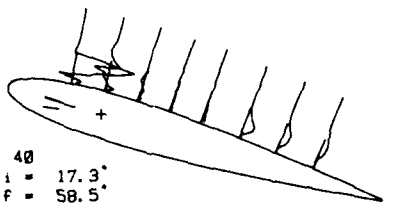

dissipation and
diffusion of
turbulent energy
scale : — 0.6

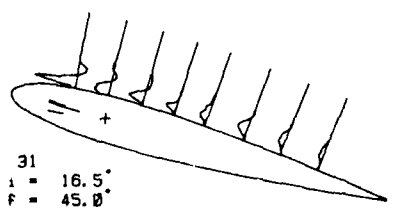

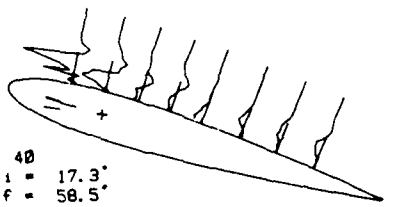

Figure 6.b :
stalled testcase BL18
8° to 18°, k=0.3

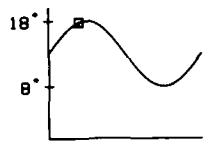

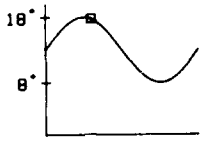

Velocity

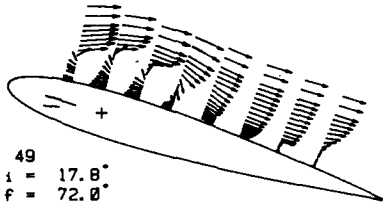

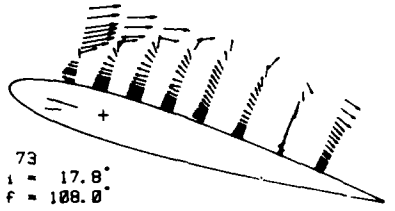

chordwise
fluctuations
$\sqrt{\overline{u'^2}}$
scale : — 0.3 Q

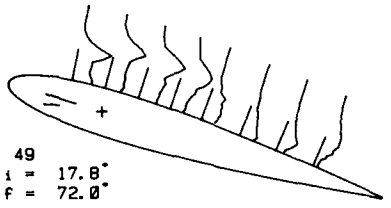

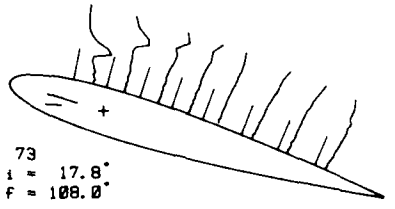

minus
Reynolds stress
scale : — 0.03 Q^2

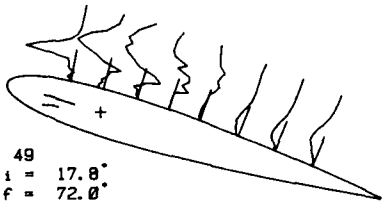

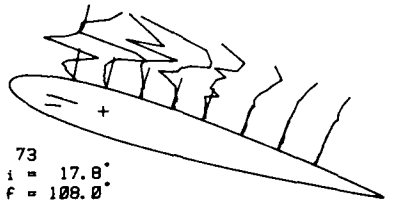

Local changes of
turbulent energy
scale : — 0.6

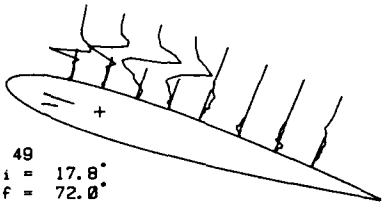

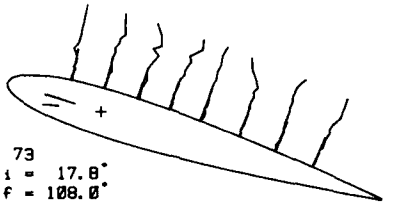

convection of
turbulent energy
scale : — 0.6

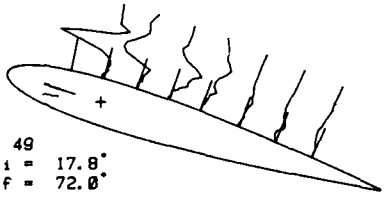

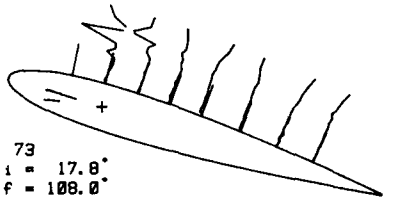

production of
turbulent energy
scale : — 0.6

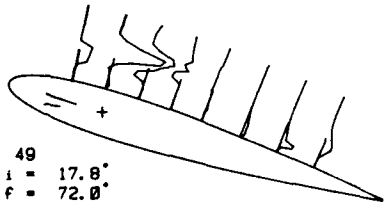

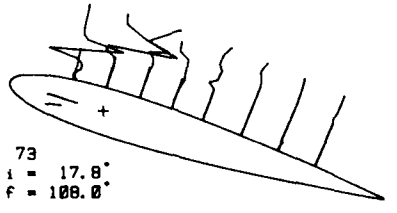

dissipation and
diffusion of
turbulent energy
scale : — 0.6

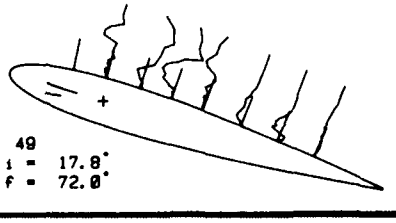

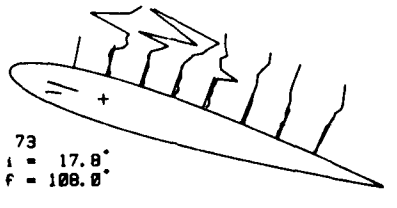

Figure 6.c :
stalled testcase BL18
8° to 18°, k=0.3

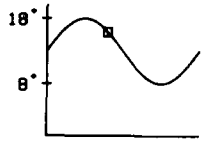

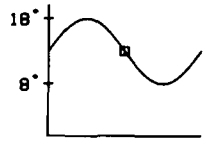

Velocity

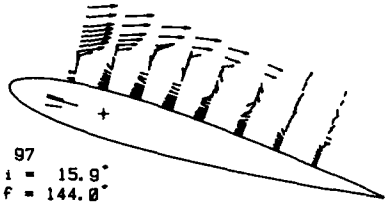

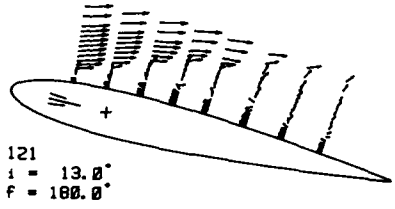

chordwise
fluctuations
$\sqrt{\overline{u'^2}}$
scale : — 0.3 Q

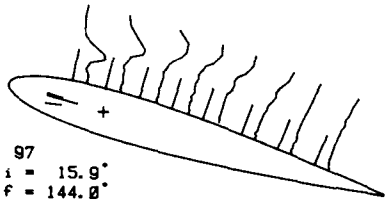

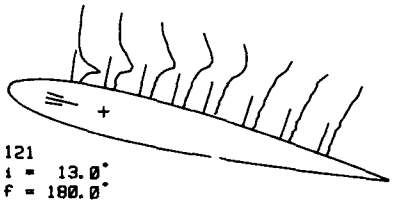

minus
Reynolds stress
scale : — 0.03 Q^2

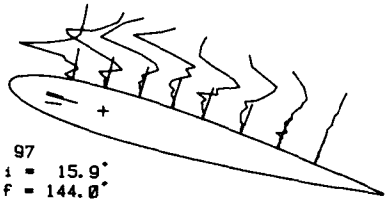

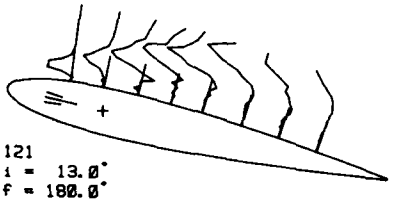

Local changes of
turbulent energy
scale : — 0.6

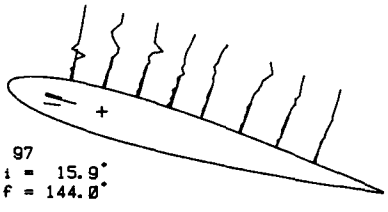

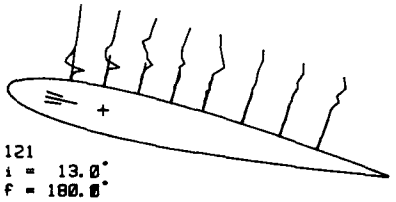

convection of
turbulent energy
scale : — 0.6

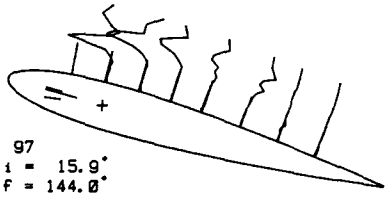

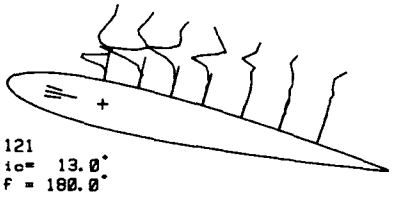

production of
turbulent energy
scale : — 0.6

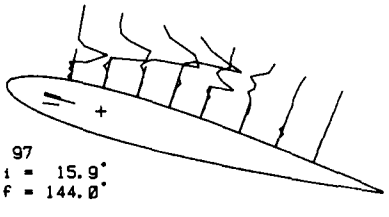

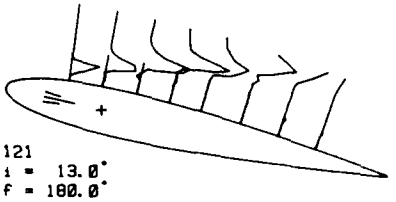

dissipation and
diffusion of
turbulent energy
scale : — 0.6

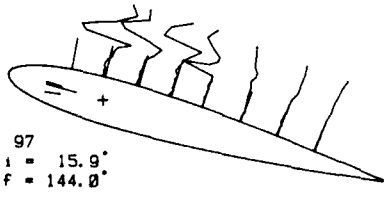

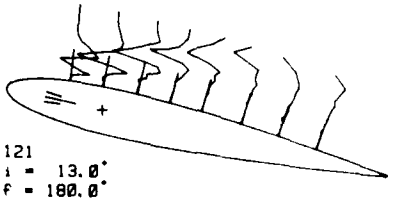

Figure 6.d :
stalled testcase BL18
8° to 18°, k=0.3

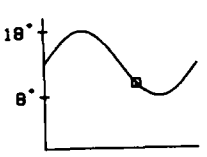

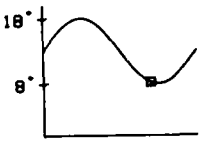

Velocity

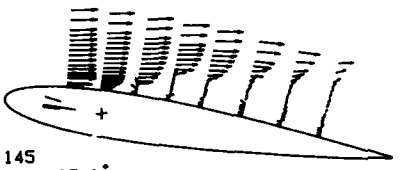

chordwise
fluctuations
$\sqrt{\overline{u'^2}}$
scale : — 0.3 Q

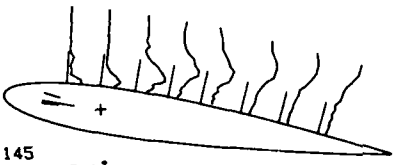

minus
Reynolds stress
scale : — 0.03 Q^2

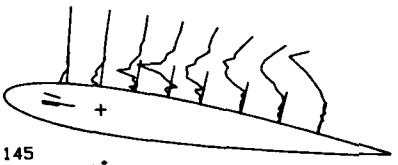

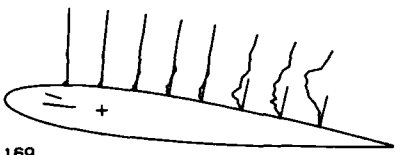

Local changes of
turbulent energy
scale : — 0.6

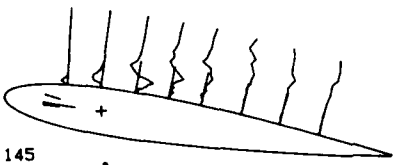

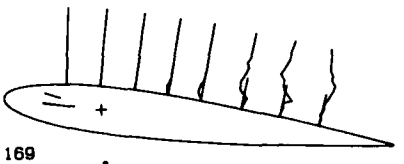

convection of
turbulent energy
scale : — 0.6

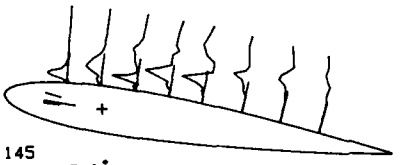

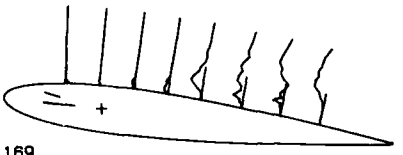

production of
turbulent energy
scale : — 0.6

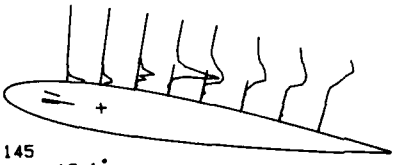

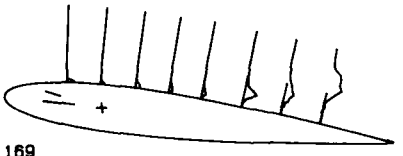

dissipation and
diffusion of
turbulent energy
scale : — 0.6

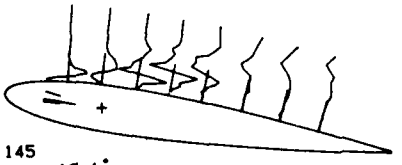

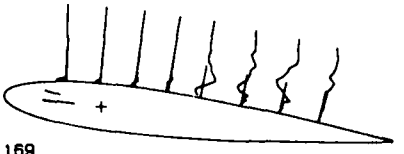

an Oscillating Airfoil" AIAA paper 84-1565, 1984

[9] DE RUYCK J., HIRSCH C., "Turbulence Structure in the Boundary Layers on an Oscillating Airfoil", Report VUB-STR-14, Vrije Universiteit Brussel, Dept of Fluid Mechanics, 1983

[10] DE RUYCK J., HIRSCH C., "Turbulence Structure in the Wake of an Oscillating Airfoil" Report Vub-Str-12, Vrije Universiteit Brussel, Dept of Fluid Mech., 1981

[11] DE RUYCK J., HIRSCH C., "Instantaneous Turbulence Profiles in the Wake of an Oscillating Airfoil" AIAA Paper 82-0353, 1982

[12] THOMPSON B.E., WHITELAW J.H., 1984, "Flying Hot Wire Anemometry" Experiments in Fluids 2, 47-55, 1984

[13] KOOL P., "Determination of the Reynolds Stress Tensor With a Single Slanted Hot Wire in Periodically Unsteady Turbomachinery Flow" ASME Paper nr 79-gt-130, 1979

[14] DE GRANDE G., KOOL P., "An Improved Experimental Method to Determine the Complete Reynolds Stress Tensor With a Single Rotating Hot Wire " Journal Phys. e. Sci. Instrum., Vol 14, P196-201, 1981

[15] SCHLICHTING H., 19.8, "Boundary Layer Theory" Mc Grew Hill Series in Mechanical Engineering, Mc Grew Hill Book Company p 512, 1968

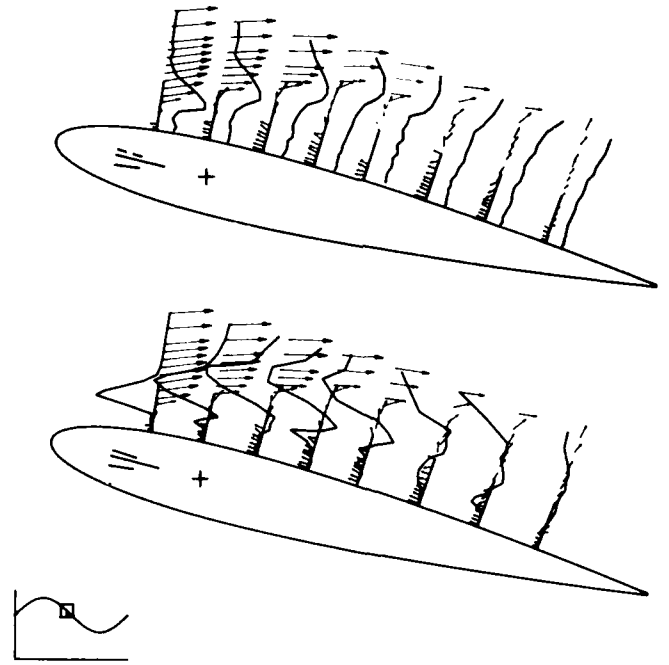

Figure 7 : Velocity and corresponding stress profiles
Testcase BL18, time step 104, fase = 142.5

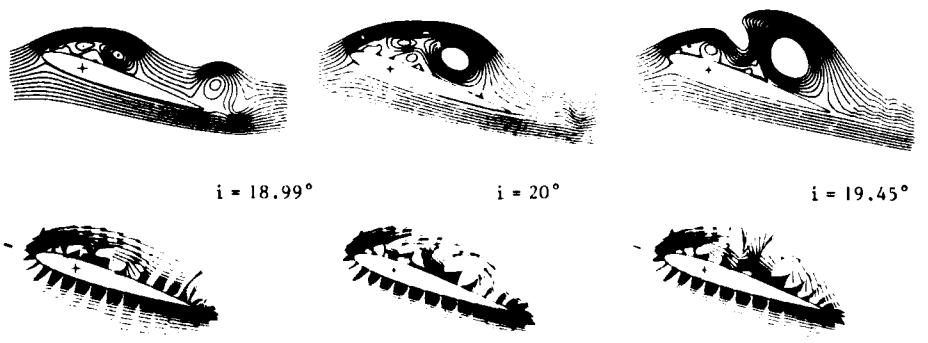

Figure 8 : Computed results obtained by Mehta (from [4])
Re = 10,000 / k = 0.25

PROFIL D'AILE EN DECROCHAGE SOUMIS A UN ECOULEMENT ALTERNATIVEMENT POTENTIEL ET A FORTE VORTICITE

C. MARESCA, Maître de Recherche au C.N.R.S.
D. FAVIER, Chargé de Recherche au C.N.R.S.

Institut de Mécanique des Fluides de Marseille
LA 03 du C.N.R.S.
1, rue Honnorat, 13003 Marseille, France

SOMMAIRE

Le comportement aérodynamique d'un profil d'aile soumis alternativement à un écoulement sain auquel succède un écoulement à forte vorticité est ici étudié expérimentalement. La simulation expérimentale consiste à placer un profil fixe, dans le sillage d'un profil qui oscille en incidence de décrochage parallèlement au vent infini. Les résultats montrent que les effets subis par le profil fixe, étudiés à partir de l'analyse conjointe des mesures instantanées d'efforts (P,T,M), de répartitions de pressions et de frottements pariétaux et de visualisations, peuvent être approchés théoriquement en considérant ce profil comme isolé dans un écoulement dont l'amplitude de la vitesse et l'incidence varient simultanément suivant des lois pré-établies.

A	Amplitude de l'oscillation (m)
C_0	Premier terme de la décomposition en série de Fourier
$C_1, C_2, \ldots, C_n$	Amplitudes des harmoniques de la décomposition en série de Fourier
C_N	Coefficient de force normale : $C_N = F_N / \frac{1}{2} \rho V^2 S$
C_T	Coefficient de force tangentielle : $C_T = F_T / \frac{1}{2} \rho V^2 S$
C_Z	Coefficient de portance instantané : $C_Z = P / \frac{1}{2} \rho V^2 S$
C_X	Coefficient de traînée instantané : $C_X = T / \frac{1}{2} \rho V^2 S$
C_M	Coefficient de moment instantané : $C_M = M / \frac{1}{2} \rho V^2 Sc$
$C_{Z\infty}$	Coefficient défini par : $C_{Z\infty} = P / \frac{1}{2} \rho V_\infty^2 S$
$C_{X\infty}$	Coefficient défini par : $C_{X\infty} = T / \frac{1}{2} \rho V_\infty^2 S$
$C_{M\infty}$	Coefficient défini par : $C_{M\infty} = M / \frac{1}{2} \rho V_\infty^2 Sc$
C_p	Coefficient de pression instantané : $C_p = (p-p_\infty) / \frac{1}{2} \rho V_\infty^2$
c	Corde des profils (m)
f	Fréquence de l'oscillation (Hz)
F_N, F_T	Force normale ou parallèle à la corde (N)
h	Envergure des profils (m)
k	Fréquence réduite $k = c\omega/2 V_\infty$
L,X	Distance séparant les deux ailes en tandem (m)
M	Moment de tangage par rapport au 1/4 avant de la corde (N.m)
N_c	Nombre de cycles d'oscillation
P	Portance instantanée (N)
p_∞	Pression statique de l'écoulement uniforme (Pa)
p	Pression statique instantanée (Pa)
Re_c	Nombre de Reynolds rapporté à c et à V_∞; $Re_c = V_\infty c/\nu$
S	Surface de l'aile, $S = h.c$, (m^2)
T	Traînée instantanée (N), ou période d'oscillation (sec)
t	Temps (sec)
V_∞, V	Vitesse à l'infini amont, et vitesse instantanée (m/s)
u,v	Composantes du vecteur vitesse dans le sillage (m/s)
V	Vitesse résultante $V^2 = u^2 + v^2$ (m/s)
(OXY)	Système d'axes défini sur la figure 1
α_f	Incidence induite dans le sillage (deg)
α_o, α	Incidence géométrique ou instantanée du profil (deg)
α_{SS}, α_{DS}	Incidence de décrochage statique ou dynamique (deg)
α_E, α_R	Incidence des profils amont et aval dans le système en tandem (deg)
δ	Angle entre l'axe d'oscillation et la direction de V_∞ (deg)
$\Delta\alpha$	Amplitude de l'oscillation d'incidence (deg)
$\Delta t, \Delta f$	Intervalle de temps (sec), ou de fréquence (Hz)
ω	Pulsation de l'oscillation, $\omega = 2\pi f$, (rd/sec)

ωt Phase de l'oscillation (deg)

λ Amplitude réduite, $= A_\infty / V_\infty$

ν Viscosité cinématique du fluide

ρ Densité du fluide

τ Tension de cisaillement instantanée

$\Phi_0, \Phi_1, \ldots, \Phi_n$ Déphasages des harmoniques de la décomposition en série de Fourier

Décomposition adoptée : $C_o + \sum_1^N C_n \cos (n \omega t + \Phi_n)$

Indice supérieur

- Moyenne sur une période d'oscillation

Indices inférieurs

St Régime stationnaire

inst Régime instantané

E,R Quantités relatives à l'émetteur ou au récepteur

1. INTRODUCTION

Les nombreuses études de base et appliquées menées sur l'aérodynamique des engins aéronautiques actuels afin d'en améliorer les performances, ont montré la place importante que tiennent, dans un grand nombre de configurations de fonctionnement, les effets instationnaires résultant de l'interaction entre les systèmes tourbillonnaires produits et les voilures.

Parmi les différents types d'interactions aérodynamiques rencontrés le plus fréquemment, quelques exemples significatifs sont à retenir, tels que : l'influence sur les empennages et dérives d'avions de combat des systèmes tourbillonnaires générés lors de manoeuvres rapides des volets de gouverne ; l'interaction intervenant entre des tourbillons d'extrémités d'ailes issus d'avions gros porteurs et des appareils plus modestes évoluant à proximité ; ou encore l'influence des sillages induits sur le stator par les décollements dynamiques engendrés sur les aubes du rotor, dans le cas d'écoulements en turbomachines.

Un autre exemple d'intérêts fondamental et pratique est fourni par l'aérodynamique des pales de rotors d'hélicoptères opérant dans différentes conditions de vol (point fixe, montée et descente verticales, avancement,...), et en particulier l'influence de l'écoulement résultant de la rotation de l'une des pales sur le comportement aérodynamique des pales suivantes. Dans ce dernier exemple, deux types d'interaction doivent être distingués suivant que le système tourbillonnaire a son axe orienté suivant une direction parallèle à celle de l'écoulement principal (tourbillon marginal issu de l'extrémité de pale), ou suivant une direction perpendiculaire à celle de l'écoulement principal (système tourbillonnaire issu du décrochage dynamique de la pale reculante) :

- En ce qui concerne l'interaction aérodynamique entre une surface portante et un tourbillon d'axe parallèle à la direction de l'écoulement, celle-ci a déjà donné lieu à un certain nombre d'études, tant en France à l'O.N.E.R.A. (1),(2),(3), qu'aux Etats-Unis (4),(5).

Ainsi la simulation expérimentale réalisée dans les essais conduits à l'O.N.E.R.A. a consisté à étudier, sur une demi-aile fixe montée à la paroi de la soufflerie, l'effet d'un tourbillon issu de l'extrémité libre d'une aile immobile également montée à la paroi en amont. Ces essais ont notamment montré que l'interaction tourbillonnaire engendrait une diminution de portance, et une augmentation sensible de traînée de la maquette réceptrice.

Dans la même optique, une simulation expérimentale de l'interaction profil - tourbillon d'extrémité de pale a été réalisée par Ham (4),(5), dans le cas où l'aile émettrice est de plus animée d'un mouvement de translation à faible amplitude suivant l'envergure de l'aile. Cette simulation est globalement équivalente à imposer au récepteur un mouvement de pilonnement à travers le tourbillon perturbateur. Dans ce cas, les résultats de Ham montrent que le récepteur interactionné enregistre un gain de portance au cours de la période ; ce gain étant proportionnel à l'intensité du tourbillon perturbateur.

- En ce qui concerne l'étude de l'interaction entre la surface portante et un tourbillon d'axe perpendiculaire à la direction de l'écoulement, très peu de recherches lui ont été consacrées. On peut citer la simulation réalisée au V.P.I. par Telionis et Poling (6), qui ont utilisé, dans un tunnel hydrodynamique, le mouvement de tangage à grande incidence du profil émetteur pour provoquer le décrochage dynamique, et par suite générer un sillage tourbillonnaire à l'amont d'un profil récepteur fixe. Bien que cette étude ait permis d'obtenir une bonne caractérisation du champ d'écoulement inter-maquettes, et des lignes de courant à différentes phases de l'oscillation (analyse de la validité de la condition de Kutta-Joukowsky en régime instationnaire), le comportement aérodynamique du récepteur interactionné n'a pas été envisagé plus avant dans cette recherche.

C'est pourquoi, en raison des motivations de nature fondamentale et pratique précédemment exposées et afin de mieux cerner les problèmes intervenant lors de la rotation d'un profil de pale d'hélicoptère en vol d'avancement, une étude approfondie du comportement aérodynamique d'un profil d'aile fixe soumis à un écoulement alternativement potentiel et à forte vorticité (de type sillage tourbillonnare) a été entreprise. La simulation expérimentale de ce problème d'interaction de base a donc été réalisée par l'intermédiaire d'une configuration 2D constituée de deux ailes émettrice (E) et réceptrice (R) disposées en tandem (voir fig. 1). L'émetteur (E) est animé en amont d'un mouvement de tamis dont les conditions d'oscillations permettent de générer un processus cyclique de décollement - recollement avec émission et propagation de tourbillons d'axe perpendiculaire à l'écoulement principal lors de la phase de décollement. L'écoulement incident sur R, qui lui demeure immobile, est alors constitué d'une zone tourbillonnaire à

forte vorticité, suivie d'une zone d'écoulement potentiel due à la phase de recollement sur E.

Au cours de cette étude, les effets instationnaires associés au processus d'interaction profil - sillage périodique ont ainsi pu être caractérisés (7) expérimentalement à partir de mesures globales et locales sur R (torseur aérodynamique, répartitions des pressions statiques et des frottements pariétaux), ainsi qu'à l'amont immédiat et autour du récepteur (champ de vitesse 2D, visualisations). L'étude paramétrique a plus particulièrement porté sur les incidences géométriques (α_E,α_R) des maquettes émettrice et réceptrice, ainsi que sur leur position relative axiale X/c. Le profil R pouvait en effet occuper en aval de la position moyenne de E, les 4 positions longitudinales X/c = 0,58 ; 1,0 ; 1,5 ; 2,0 suivant un axe parallèle à l'écoulement amont (Y/c = 0) et passant par le quart-avant de la maquette E (cf. Fig. 1).

Les résultats obtenus pour de telles configurations des maquettes E et R, ont fait apparaître une forte interaction avec des effets instationnaires intenses sur R au niveau du torseur aérodynamique, mais ont également révélé la complexité structurelle de l'écoulement ainsi généré dans le champ inter - maquettes. L'analyse expérimentale a montré en particulier que ces effets fortement non linéaires devaient être attribués aux grandes amplitudes de variations simultanées de vitesse et d'incidence, induites sur le récepteur par les systèmes tourbillonnaires d'extrados et d'intrados issus de E.

Dans le but de parvenir, par une approche uniquement théorique, à une modélisation aussi fidèle que possible des effets observés, il a été envisagé de considérer dans un premier temps, des configurations moins complexes de l'écoulement incident sur R; notamment celles obtenues en déplaçant transversalement la position aval du profil fixe R, de telle manière que le sillage perturbateur issu de E ne se développe principalement que d'un seul côté (intrados ou extrados) du récepteur.

L'objectif poursuivi a donc consisté à proposer un modèle de calcul susceptible de traduire les effets instationnaires observés et mesurés dans de telles conditions d'écoulement auxquelles correspondent les configurations les plus simples.

Après avoir rappelé les dispositifs et les moyens de mesure mis en oeuvre pour mener à bien l'étude expérimentale, le champ d'écoulement inter-maquettes est déterminé par la mesure des vitesses 2D instantanées juste en amont du profil récepteur, celui-ci pouvant occuper en aval de E différentes positions axiales et transversales (X/c variable ; Y/c $\neq$ 0).

La synthèse de ces champs de vitesses 2D jointe à des visualisations instantanées autour de R, conduit à définir les configurations d'écoulement les moins complexes, pour lesquelles une analyse détaillée du comportement aérodynamique de R a été effectuée (torseur aérodynamique, distribution de pressions et de frottements locaux).

L'approche théorique est ensuite abordée pour certaines de ces configurations d'écoulement (amplitudes de variations modérées de vitesse et d'incidence instantanées). Une démarche propre à la simulation concernée a été dégagée, et un modèle de calcul proposé. La limite de validité de ce modèle a été directement testée sur les résultats expérimentaux obtenus sur les variations de la portance du profil récepteur au cours de l'oscillation de E. Les perspectives d'amélioration et d'évolution de ce modèle sont également discutées.

2. ETUDE EXPERIMENTALE

2.1. Dispositifs expérimentaux, conditions et moyens de mesures

Les essais ont été conduits dans la soufflerie subsonique à refoulement S3 de l'I.M.F.M., de veine à section rectangulaire (3 x 1 x 0,5 m^3), et de faible turbulence naturelle (< 0,2 %). La configuration 2D d'ailes en tandem envisagée pour simuler le problème d'interaction est présentée sur la Figure 1.

Les deux maquettes émettrice (E) et réceptrice (R), géométriquement identiques, sont de forme rectangulaire (c = 0,30 m ; h = 495 m) et de profil symétrique NACA 0012. Elles sont montées verticalement dans la chambre d'expérience et s'étendent en envergure sur toute la hauteur de la veine. Les incidences géométriques α_E et α_R des deux maquettes peuvent être sélectionnées indépendamment de - 25° et + 25°, par l'intermédiaire de 2 dispositifs de mise en incidence autour du quart-avant de la corde avec une précision de 0,1°.

La maquette E est fixée sur deux mâts de supports solidaires d'un dispositif de sollicitation (8) qui communique à la maquette un mouvement de translation (X = - A sin ωt) suivant l'axe longitudinal de la veine d'essais (voir Figure 1), c'est-à-dire, dans la direction parallèle à celle du courant uniforme V_∞ (mouvement de tamis).

Les conditions d'oscillation de l'émetteur amont E ont été maintenues constantes pour tous les essais présentés dans cette étude, et sont définies ci-dessous :

- Incidence géométrique de E : $\alpha_E = 20°$
- Amplitude d'oscillation de E : A = 0,17 m, (λ = 0,524)
- Fréquence d'oscillation de E : f = 2,5 Hz, (k = 0,462)
- Vitesse du courant à l'amont de E : V_∞ = 5,1 m/s, ($Re_c = 1{,}02 \times 10^5$)

Il est à noter que la sélection de ces paramètres d'oscillation (α_E = 20° ; λ = 0,52 ; k = 0,46), pour le mouvement de tamis, conduit à générer sur E un décrochage dynamique intense qui se traduit par un processus de décollement - recollement de la couche limite, avec échappement tourbillonnaire le long de l'extrados de E puis dans son sillage (voir références (9),(10)).

En ce qui concerne le récepteur R, fixe en aval, son incidence géométrique peut être sélectionnée à α_R = 6° ou α_R = 20°, et sa position relative par rapport à la position moyenne de E (obtenue à ωt = 0°), fixée en l'une quelconque des 4 x 6 = 24 stations aval définies dans le repère OXY de la figure 1 corres-

pondant à 4 plans de coupe et à 6 positions transversales Y/c réparties symétriquement de part et d'autre de l'axe Y/c = 0 de la veine.

Dans ces conditions, le champ des vitesses longitudinale u et transversale v (voir figure 1) dans le sillage inter-maquettes, est déterminé à l'aide d'une sonde à fils chauds croisés à 90° (type DISA 55R51).

Dans chacun des 4 plans de coupe X/c = cste précédemment définis, et pour les 6 positions transversales Y/c = cste de la maquette (sauf pour X/c = 0,58 et Y/c = 0,25 ; - 0,25 ; - 0,50, où la distance trop rapprochée des deux maquettes ne permet pas le positionnement de la sonde), les mesures des composantes u et v sont réalisées suivant la ligne transversale située à 10 cm (soit c/3 environ) en amont du bord d'attaque de R. Le long de cette ligne, la mesure est réalisée en 21 points répartis entre $-10\text{ cm} < y < 10\text{ cm}$ (soit $\pm$ c/3) par incrément de 1 cm.

Le comportement aérodynamique du récepteur s'effectue à partir de l'analyse conjointe des grandeurs instantanées, globales et locales, obtenues par les différentes techniques de mesures instationnaires suivantes :

- La mesure des efforts de portance et de traînée, ainsi que celle du moment de tangage (par rapport au quart-avant de la corde du récepteur), sont réalisées à l'aide d'une technique antérieurement mise au point (8),(9), et basée sur l'utilisation de torsiomètres étalonnés en régimes statiques et dynamiques qui permettent de ramener la mesure d'une force à celle d'un moment par rapport à son axe passant par le centre de gravité de l'ensemble pesé. Les efforts et moments instantanés sont mesurés par cette technique avec une erreur relative inférieure à 4 %.

- Les distributions des pressions statiques le long de la surface du récepteur sont obtenues par l'intermédiaire de 11 capteurs piézorésistifs à membrane (type ENDEVCO 8507) montés suivant une seule des faces de la maquette R. Pour obtenir les distributions de C_p intrados et extrados, il suffit de placer les maquettes E et R suivant les incidences $\pm\,\alpha_E$ et $\pm\,\alpha_R$ (voir Figure 1), de sorte que la même série de capteurs fournit (dans le cas de ce profil symétrique), la distribution extrados pour les incidences $+\,\alpha_E$ et $+\,\alpha_R$ (profils hachurés sur la Figure 1), et la distribution intrados pour les incidences $-\,\alpha_E$ et $-\,\alpha_R$.

- Les répartitions des tensions de cisaillement pariétales le long de l'extrados et de l'intrados de R, sont mesurées à l'aide de jauges à film chaud conçues et fabriquées à l'I.M.F.M. Le principe de fonctionnement de ces jauges (film de Nickel déposés sur un support isolant) similaire à celui utilisé en anémométrie à film chaud classique, ainsi que leur technique de montage, sont également donnés dans les références (10) et (11).

Neuf jauges sont ainsi implantées sur R suivant les mêmes abscisses en corde que les capteurs de pression, sauf au bord d'attaque (X/c = 0) et à l'arrière du profil (X/c = 0,95).

L'ensemble des techniques de mesures précédentes est complété par un dispositif de visualisations par fumées blanches de chlorhydrate d'ammonium, émises à deux cordes en amont de E par l'intermédiaire d'une canne à sept émetteurs profilés.

En ce qui concerne l'acquisition des données, toutes les grandeurs à mesurer (efforts, moments, pressions, frottements, vitesses 2D) sont échantillonnées (256 échantillons par période), numérisées et enregistrées par un centralisateur de mesures (INTERTECHNIQUE, IN 110).

La synchronisation entre l'initiation de l'enregistrement et le mouvement d'oscillation de E, est assurée par une cellule photoélectrique montée sur le dispositif de sollicitation de E, laquelle délivre une impulsion au moment où la vitesse relative est maximum, i.e. à $\omega t = 0°$, (Cf. Figure 1 ; avec $V(t) = 1 + \lambda \cos \omega t$).

Toutes les grandeurs mesurées sont analysées en série de Fourier à l'ordre 4 sous la forme :

$$C = C_o + \sum_{n=1}^{4} C_n \cos (n\,\omega t + \Phi_n)$$

où C désigne une grandeur physique quelconque enregistrée en fonction du temps ; C_o la valeur moyenne de C au cours de la période ; C_n les amplitudes des harmoniques de la fréquence d'oscillation ; et Φ_n les déphasages de ces harmoniques par rapport au déplacement de l'émetteur.

Les mesures présentées ont été sommées (sauf mention contraire) dans chaque canal du centralisateur au cours de N_c cycles d'oscillations consécutifs (en général $N_c = 20$ cycles). Cette utilisation du mode d'enregistrement avec accumulation de N_c valeurs instantanées à chaque phase, présente l'avantage d'améliorer la précision des mesures et la qualité du rapport signal/bruit des enregistrements.

2.2. Champ d'écoulement inter-maquettes et sélection de configurations types

Avant d'étudier le comportement aérodynamique du récepteur, les caractéristiques du sillage issu de E sont analysées à partir de la mesure des composantes u et v en chacune des 24 positions (X/c, Y/c) possibles pour le récepteur. Pour une position aval donnée de R, les vitesses incidentes sont obtenues, juste en amont de R, en chacun des 21 points ($-1/3 \leqslant Y/c \leqslant 1/3$) de la grille de mesure précédemment définie.

Les champs de vitesse V et d'incidence α(induite ou résultante) sur R obtenus par les formules : $V = (u^2 + v^2)^{1/2}$ et $\alpha_i = \text{Arctg } u/v$, ont été analysés soit en grandeurs moyennes(régime stationnaire et régime instationnaire moyenné sur la période), soit en grandeurs instantanées.

- Champs stationnaire et moyen

L'analyse des résultats obtenus pour chacune des 24 positions aval du récepteur placé à $\alpha_R = 6°$ et 20°

ont montré que l'oscillation de E génère sur R un champ d'écoulement moyen beaucoup plus homogène que lorsque E est immobile. En effet, les déficits moyens de vitesse et des incidences induites moyennes sont nettement plus faibles. Par exemple à Y/c = - 0,25, l'incidence induite moyenne reste inférieure à 6° alors qu'elle est de l'ordre de 16° quand E est immobile.

- Champs instantanés d'écoulement (E oscillant)

Les répartitions spatio-temporelles (21 points sur la grille de mesure, et pour chaque point 256 valeurs échantillonnées au cours du temps sur la période) correspondant aux variations du module de vitesse $V = V(y, \omega t)$ et d'incidence résultante $\alpha = \alpha_R + \alpha_i(y, \omega t)$, ont été déterminées à l'amont de chacune des 24 positions sélectionnées pour la maquette réceptrice.

Les diagrammes de V et de α, représentés en fonction de ωt et Y/c et dont les figures 2 et 3 donnent un exemple, mettent en évidence, quelles que soient les conditions paramétriques (α_R, X,Y), la présence de fluctuations simultanées du module de vitesse et de l'incidence résultante, et permettent de localiser en fonction de la phase d'oscillation ωt, l'alternance de deux régimes distincts d'écoulement :

- un régime pratiquement laminaire, qui peut être observé par exemple pour la position (X/c = 1,5 ; Y/c = 0,5), aux phases $0° < \omega t < 130°$ (Fig. 2 à $\alpha_R = 6°$) ; et aux phases $0° < \omega t < 140°$ (Fig. 3 à $\alpha_R = 20°$). Pendant ce régime laminaire (correspondant à la phase de recollement dynamique le long de l'extrados de E), le module de vitesse s'accroît tandis que l'incidence induite décroît vers les valeurs négatives (tendant ainsi à diminuer l'incidence résultante sur le récepteur).

- un régime fortement perturbé, que l'on observe par exemple pour la même position : (X/c = 1,5 ; Y/c = 0,5), aux phases $\omega t > 130°$ (Fig. 2 à $\alpha_R = 6°$) ; et aux phases $\omega t > 140°$ (Fig. 3 à $\alpha_R = 20°$). Cet écoulement turbulent qui résulte de la propagation de la zone tourbillonnaire d'extrados issue du décrochage dynamique de bord d'attaque de E, provoque une première augmentation de V et de α sur les profils quel que soit le plan X/c = cste considéré. Durant cette partie de la période, la présence d'une seconde zone tourbillonnaire issue du bord de fuite de E (au moment de la décélération maximale du mouvement) provoque un nouvel accroissement du module de vitesse et de l'incidence résultante, d'autant plus marqué que l'on se rapproche de l'axe de symétrie de la veine (Y/c = 0).

De plus, l'analyse de l'ensemble de ces répartitions permet de conclure que pour une position transversale fixée Y/c = cste, l'évolution temporelle des profils de V et de α s'effectue de manière similaire dans tous les plans de coupe successifs X/c = cste du sillage. On observe en effet un déphasage des profils de V et de α qui est généralement de l'ordre de $\omega t \simeq 40°$ entre deux plans consécutifs distants de $\Delta X \simeq 0{,}5c$. A partir des résultats de V et α, la modélisation expérimentale de l'écoulement incident sur R, pour chaque configuration (X/c = cste, Y/c = cste) considérée, est déduite de la moyenne spatiale (suivant Y) des valeurs du module de vitesse et de l'incidence obtenues aux mêmes instants de la période. Pour une position donnée de R, cette moyenne spatiale est réalisée, à chaque phase ωt, le long d'une distance ΔY légèrement supérieure à la projection du maître-couple de R suivant l'axe Y,
(à savoir : $-0{,}11 < Y/c < 0{,}11$ pour $\alpha_R = 6°$, et $-0{,}26 < Y/c < 0{,}26$ pour $\alpha_R = 20°$).

Les variations au cours du temps du module de vitesse V, et de l'incidence résultante sur le récepteur ($\alpha = \alpha_R + \alpha_i$), ainsi moyennées spatialement à l'amont immédiat de R, sont présentées sur les Figures 4A,B et 5A,B (respectivement pour $\alpha_R = 6°$ et $\alpha_R = 20°$), dans chacune des positions aval du récepteur étudiées ($0{,}58 \leqslant X/c \leqslant 2{,}0$; $-0{,}75 \leqslant Y/c \leqslant 0{,}75$). Ainsi pour chaque position de R, l'écoulement incident sur le récepteur est synthétisé par l'intermédiaire de 2 profils $V = V(\omega t), \alpha = \alpha(\omega t)$, auxquels sont associées les deux décompositions en série de Fourier à l'ordre 4 correspondantes.

Quelle que soit l'incidence α_R du récepteur, les profils de V et de α présentés sur ces Figures font apparaître les caractéristiques suivantes :

- Pour une position Y/c = cste fixée de R, l'évolution des profils suivant la coordonnée axiale X/c confirme bien la présence d'un déphasage de l'ordre de 40° entre deux plans consécutifs distants de $\Delta X = 0{,}5c$.

- Pour un plan de coupe X/c = cste fixé de R, l'évolution des profils suivant la coordonnée transversale Y/c fait apparaître un accroissement des amplitudes de variations de V et de α lorsque $Y/c \to 0$.

- En outre, ces profils traduisent bien l'influence des deux zones tourbillonnaires issues successivement du bord d'attaque et du bord de fuite de E, au cours de l'oscillation. On observe par exemple sur les profils de V et de α des Figures 4A et 5A, considérés du côté de l'extrados de E ($0{,}25 \leqslant Y/c \leqslant 0{,}75$), l'apparition au cours du temps d'un maximum de V (coïncidant pratiquement avec le minimum de α), suivi d'un minimum de V (coïncidant pratiquement avec le maximum de α).

Parmi tous les champs d'écoulement précédemment décrits, et dans le but d'analyser des configurations où le sillage tourbillonnaire se développe principalement d'un seul côté de la maquette réceptrice, les configurations définies ci-dessous ont été choisies pour effectuer l'étude détaillée du comportement aérodynamique du récepteur :

- $\alpha_R = 6°$; X/c = 0,58 ; $Y/c = \pm 0{,}75$
- $\alpha_R = 20°$: X/c = 0,58 : $Y/c = \pm 0{,}75$

C'est en effet pour le premier des plans de coupe du sillage considérés (Y/c = 0,58) et pour les positions transversales les plus éloignées de l'axe de symétrie de la veine ($Y/c = \pm 0{,}75$), que les amplitudes de fluctuations de V et de α apparaissent les moins élevées : $-8° < \alpha < 17°$ (pour $\alpha_R = 6°$), et $10° < \alpha < 35°$ (pour $\alpha_R = 20°$).

2.3. Comportement aérodynamique du récepteur

2.3.1. Effets stationnaires et instationnaires moyens sur R

Le récepteur étant amené à occuper différentes positions successives en aval de E dans la veine d'essais, il a été vérifié, dans un premier temps, qu'en l'absence de E et en écoulement uniforme, les efforts

et les moments mesurés sur R étaient indépendants de la position transversale Y/c et de la distance axiale X/c. Par exemple, l'écart observé sur les portances mesurées entre le premier et le dernier plan de coupe X/c = cste reste inférieur à 3 % (c'est-à-dire inférieur à la précision de la mesure aux torsiomètres), quelle que soit la position transversale de R considérée (- 0,75 < Y/c < 0,75).

Dans le premier plan de coupe du sillage (X/c = 0,58) et pour les deux positions transversales Y/c=± 0,75, le comportement du récepteur a ensuite été analysé en fonction de sa propre incidence ($0° \leqslant \alpha_R \leqslant 24°$) dans les 3 configurations suivantes :

- cas a : configuration stationnaire (V_∞ = 5,1 m/s) en l'absence de E, ce qui correspond au cas de l'aile isolée.
- cas b : configuration stationnaire (V_∞ = 5,1 m/s) en présence de E immobile ($\alpha_E = 20°$).
- cas c : configuration instationnaire moyenne ($V/V_\infty = 1 + \lambda \cos \omega t$) en présence de E oscillant ($\alpha_E = 20°$; $\lambda = 0{,}524$; $k = 0{,}462$).

Les résultats ainsi obtenus sur les valeurs stationnaires du coefficient de portance et de distributions de pression et de frottement (cas a et b), sont comparés sur les Figures 6, 7, 8 aux valeurs instationnaires moyennes correspondantes ($\bar{C}_Z$, $\bar{C}_p$, $\bar{\tau}/\tau_{st}$), pour les 2 positions Y/c = ± 0,75 de R.

- Pour Y/c = - 0,75, où le récepteur est placé du côté de l'intrados de E, les valeurs de $(C_Z)_{st}$ obtenues en présence de E immobile (courbe continue sur la Figure 6) font apparaître un gain de portance par rapport au cas de l'aile isolée (représentée en pointillés). La pente $dC_Z/d\alpha_R$ est sensiblement modifiée en présence de E immobile dès que $\alpha_R > 4°$. De plus, le décrochage stationnaire se produit à une incidence de 10,5° légèrement inférieure à celle de l'aile isolée ($\alpha_{SS} = 12°$).

Lorsque l'émetteur est mis en oscillation, les valeurs moyennes de $\bar{C}_Z$ (cercles pleins sur la Figure 5) montrent que le récepteur n'enregistre un gain de portance, par rapport aux configurations stationnaires (cas a et b), que pour des incidences élevées ($\alpha_R = 20°$).

Ces résultats obtenus sur le coefficient de portance $\bar{C}_Z$ sont bien recoupés par les distributions moyennes de pression et de frottement présentées sur les Figures 7 et 8. En particulier les distributions de $\bar{C}_p$ relatives à $\alpha_R = 0°$ et 6°, traduisent également le déficit observé sur la portance moyenne par rapport au cas stationnaire avec E immobile (représenté en trait continu sur la Figure 7). De même, les répartitions du rapport $\bar{\tau}/\tau_{st}$ montrent qu'un accroissement du frottement extrados n'est observé, à partir du bord d'attaque, que pour l'incidence $\alpha_R = 20°$ pour laquelle se produit le gain de portance moyenne.

- Pour Y/c = 0,75, où le récepteur est positionné du côté de l'extrados de E, la courbe de $(C_Z)_{st}$, obtenue en présence de E immobile, met en évidence une perte de portance moyenne par rapport au cas de l'aile isolée. On peut remarquer que pour ce premier plan de coupe X/c = 0,58 un résultat du même type mais encore plus marqué (perte de portance moyenne de l'ordre de 70-80 %), avait été mis en évidence lorsque le récepteur était placé suivant l'axe de symétrie Y/c = 0 (Cf. Références (7),(12)).

D'une façon générale, les courbes de $(C_Z)_{stat}$ obtenues sur la Figure 6 en présence de E immobile, montrent que le récepteur interactionné se comporte également comme une aile d'allongement fini (dont la pente $dC_Z/d\alpha$ est inférieure à celle obtenue pour une aile isolée). Pour les parties linéaires, le $(C_Z)_{st}$ peut, en effet, être défini par les expressions ci-dessous (où α_R est exprimé en degrés) :

- Extrados de E, (Y/c = 0,75) : $(C_Z)_{st} = 0{,}092\ \alpha_R - 0{,}267$
- Aile isolée, (Y/c = 0) : $(C_Z)_{st} = 0{,}098\ \alpha_R$
- Intrados de E, (Y/c = -0,75) : $(C_Z)_{st} = 0{,}091\ \alpha_R + 0{,}100$

De plus, pour Y/c = 0,75, la courbe de la Figure 6 montre que la présence de E immobile tend à modifier la pente de $dC_Z/d\alpha_R$ dès que $\alpha_R > 9°$, et introduit un retard au décrochage stationnaire qui intervient dans ce cas à $\alpha_{SS} = 16°$ seulement (angle supérieur de 4° par rapport à l'aile isolée).

Les mesures moyennes de pression et de frottement relatives à Y/c = 0,75 sur les Figures 7 et 8, confirment également les effets observés sur la portance. Le gain par rapport au cas stationnaire (avec E immobile) est d'autant plus élevé que α_R est grand ($\bar{C}_Z/(C_Z)_{stat}$ = 1,005 ; 1,081 ; 1,553 respectivement pour α_R = 0° ; 6° ; 20°) comme l'indiquent les distributions correspondantes des coefficients C_p. Pour $\alpha_R = 0°$ et $\alpha_R = 6°$, les répartitions de frottement montrent également des accroissements (extrados et intrados) et $\bar{\tau}/\tau_{stat}$ nettement plus accentués qu'à Y/c = - 0,75.

2.3.2. Effets instantanés sur R placé à X/c = 0,58 et Y/c = 0,75

Le comportement instantané du récepteur a été analysé à partir des grandeurs globales et locales mesurées sur R en fonction de ωt.

2.3.2.1. Récepteur à faible incidence ($\alpha_R = 6°$)

Le récepteur étant placé à Y/c = 0,75 et $\alpha_R = 6°$, les variations, en fonction de la phase ωt, du module de vitesse et de l'incidence résultante du flux incident, sont représentées sur le haut de la figure 4A.

Les variations simultanées de V et de α subies par le profil R se déduisent alors des précédentes, en considérant que les perturbations se propagent axialement à la vitesse locale de l'écoulement. Le retard de phase qui s'introduit dans les variations de V et de α peut être calculé par les relations :

$$\Delta X = c/3 + c/2 = 0{,}25 \text{ m}$$

$$\Delta V = \bar{V} \cos \alpha$$

$$\Delta(\omega t) = f \cdot (\Delta X/\Delta V) \cdot 360° \qquad (\text{avec } f = 2{,}5 \text{ Hz})$$

où ΔX représente la distance axiale parcourue par la perturbation pour atteindre la mi-corde du profil ; et ΔV la vitesse locale moyenne de cette perturbation suivant OX.

Pour de telles variations de V et de α, la Figure 9 montre que le torseur aérodynamique suit une évolution dans le temps essentiellement imposée par les fluctuations d'incidence instantanées α. Le coefficient de portance rapporté à la vitesse amont V_∞ ($C_{Z\infty} = P/\frac{1}{2}\rho V_\infty^2 ch$), atteint sa valeur maximum pour $\omega t \simeq 270°$ qui correspond à la phase d'incidence maximum ($\alpha_{max} \simeq 16°$). Pour cette même phase, le coefficient de moment $C_{M\infty}$ subit un accroissement vers les valeurs négatives (correspondant à un moment piqueur).

On peut également noter que pour des phases telles que $60° < \omega t < 160°$, où α atteint des valeurs légèrement négatives, le coefficient de portance décroît et tend vers zéro, sans pour autant changer de signe, ce qui peut être attribué à l'effet d'accroissement du module de vitesse au cours de cette fraction de période. Il en résulte pour $C_{Z\infty}$ un accroissement de la valeur moyenne sur la période qui reste malgré tout assez faible ($(C_{Z\infty}/(C_Z)_{st} = 1{,}081$).

Ce comportement global du torseur instantané est parfaitement recoupé par les visualisations et les résultats de mesures locales.

Les visualisations réalisées aux phases $\omega t = 6°$; 124° ; 186° ; 194° ; 256°, montrent que l'écoulement reste recollé sur l'extrados de l'aile tout au long de la période d'oscillation, tout comme il l'était en écoulement stationnaire avec E immobile. Cet état recollé de l'écoulement est bien confirmé en particulier par les distributions de τ/τ_{st} qui font apparaître la présence d'une couche limite laminaire établie sur la plus grande partie de l'extrados ($0{,}04 < X/c < 0{,}70$).

2.3.2.2. Récepteur à grande incidence ($\alpha_R = 20°$)

Le récepteur est placé à grande incidence géométrique du côté de l'extrados de E ($Y/c = 0{,}75$), et subit des variations simultanées de V et de α dont les variations sont déduites de celles mesurées en amont de R dans le sillage (Figure 5A), par l'intermédiaire d'un déphasage qui, dans ce cas, est déterminé à $\Delta(\omega t) = 47°$ avec $\Delta V = \bar{V} \cos \bar{\alpha} = 4{,}803$ m/s. Les variations de α ainsi générées sur R, ($12° < \alpha < 35°$), recouvrent des incidences largement supérieures à l'angle de décrochage statique ($\alpha_{SS} = 16°$), à l'exception d'une petite fraction de la période où $\alpha < 16°$ (au voisinage de $\omega t = 90°$).

Dans ces conditions, la Figure 10 montre que les 3 composantes du torseur aérodynamique subissent un accroissement instantané important lors de la phase d'incidence croissante ($180° < \omega t < 270°$). Cette augmentation locale de $C_{Z\infty}$ et $C_{X\infty}$ (qui s'accompagne d'un moment $C_{M\infty}$ fortement piqueur pour $\omega t = 270°$), est suivie par une chute brutale de portance et de traînée lors des incidences décroissantes (pour $\omega t > 270°$). Un tel comportement mis en évidence et analysé lors d'études précédentes (7),(9) est typique du décrochage dynamique intense que subit le récepteur par variations de V et de α à des niveaux élevés ($\alpha >> \alpha_{SS}$).

Les visualisations et les mesures locales effectuées sur R traduisent bien le décrochage dynamique subi par le récepteur et permettent de suivre la chronologie de ce processus de décrochage en fonction de la phase ωt :

- Pour $\omega t = 30°$, la portance et la traînée sont voisines de leurs niveaux stationnaires respectifs, avec sur l'extrados une distribution pratiquement constante ($C_p \simeq -1$) caractéristique d'un écoulement décollé.
- Pour $90° < \omega t < 175°$, la portance s'accroît au-dessus du niveau stationnaire par l'intermédiaire de la formation d'un bulbe de bord d'attaque qui provoque un recollement local sur l'extrados.
- Pour $210° < \omega t < 270°$, la formation du bulbe donne naissance à un noyau tourbillonnaire de bord d'attaque qui crée un pic de succion sur la distribution des C_p lors des incidences croissantes. La propagation du tourbillon le long de l'extrados de R, pour des phases $265° < \omega t < 330°$, est clairement mise en évidence sur les distributions du frottement. Sa vitesse de propagation suivant la corde de R a pu être évaluée à 0,45 V.

2.3.3. Effets instantanés sur R placé à $X/c = 0{,}58$ et $Y/c = -0{,}75$

2.3.3.1. Récepteur à faible incidence ($\alpha_R = 6°$)

Le récepteur est dans ce cas placé du côté de l'intrados de E ($Y/c = -0{,}75$) et subit des variations simultanées de V et de α déduites de celles mesurées dans le sillage (Fig.4B) par l'intermédiaire d'un déphasage $\Delta(\omega t) = 52°$ (obtenu avec $\Delta V = \bar{V} \cos \bar{\alpha} = 4{,}328$ m/s). Le profil de α ainsi généré sur R ($-0{,}1° < \alpha < 10{,}1°$), montre que l'incidence instantanée demeure au cours de l'oscillation toujours inférieure à l'angle de décrochage statique obtenu sur R en présence de E immobile ($\alpha_{SS} = 10{,}5°$, Cf. Figure 6).

La Figure 11 présente l'évolution du torseur aérodynamique correspondant à ces variations de V et de α . On observe que les phases où se produisent les valeurs instantanées minimum et maximum de $C_{Z\infty}$ sont pratiquement les mêmes que celles où interviennent le minimum et le maximum d'incidence.

Il est à noter que pour l'incidence maximum ($\alpha_{max} = 10{,}1°$ à $\omega t \simeq 227°$), la portance instantanée ne dépasse que très légèrement le niveau stationnaire correspondant (mesuré à $\alpha_R = 6°$ en présence de E immobile) ; de même pour les faibles incidences ($\alpha_{min} = -0{,}1°$ à $\omega t \simeq 45°$), la portance tend vers zéro mais reste à un niveau strictement positif.

Bien que l'incidence évolue dans des limites de variations non décrochées pour un écoulement statique, ce comportement fait donc apparaître, en écoulement dynamique, un effet instationnaire marqué au niveau du torseur aérodynamique.

Comme en témoignent les clichés de visualisations et les distributions de C_p, durant la première demi-période de l'oscillation, l'écoulement est bien recollé sur l'extrados de R, et la portance s'accroît progressivement avec l'incidence croissante tout en restant largement inférieure au niveau stationnaire. Le niveau maximum de sustentation est obtenu après la phase $\omega t \simeq 180°$ et résulte d'une dépression extrados légèrement plus forte qu'en stationnaire.

Durant la fraction de période $230° < \omega t < 360°$, l'écoulement reste toujours recollé autour de R pour des incidences instantanées décroissantes. Au cours de cette phase décroissante de α, la perturbation issue de l'intrados de E influence très nettement l'extrados de R, sans modifier de façon sensible le côté intrados.

L'influence de cette perturbation tourbillonnaire émise depuis l'intrados de E (dont le sens de rotation s'oppose à celui de la circulation autour de R), a pour effet principal de réduire la dépression d'extrados sans affecter sensiblement la distribution d'intrados, et par suite de diminuer la circulation et la portance s'établissant sur R.

2.3.3.2. Récepteur à grande incidence ($\alpha_R = 20°$)

Les variations instantanées de V et de α imposées à R ($\alpha_R = 20°$; Y/c = - 0,75), sont déduites de celles présentées sur la Figure 5B par l'intermédiaire du retard de phase $\Delta(\omega t) = 57°$ ($\Delta V = \bar{V} \cos \bar{\alpha} = 3,919$ m/s). Pour cette configuration, l'oscillation d'incidence ($15° < \alpha < 29°$) s'effectue à des valeurs instantanées toujours nettement supérieures à l'incidence de décrochage statique de R ($\alpha_{SS} = 10,5°$ sur la Figure 6).

Dans ces conditions, la Figure 12 montre pour le torseur aérodynamique une augmentation importante des niveaux moyens par rapport à ceux mesurées en présence de E immobile ($\bar{C}_{Z\infty}/(C_Z)_{st} = 1,30$; $\bar{C}_{X\infty}/(C_X)_{st} = 1,10$; $\bar{C}_{M\infty}/(C_M)_{st} = 1,00$). De plus, à la phase $\omega t \simeq 292°$ (où est obtenue l'incidence maximum), des accroissements instantanés notables sont observés sur la portance et la traînée, tandis que le moment de tangage devient fortement piqueur.

Ce comportement instationnaire du torseur est caractéristique d'un décrochage dynamique généré sur R (aussi intense que celui observé pour $\alpha_R = 20°$; Y/c = 0,75), et dont la phénoménologie qui a pu également être analysée chronologiquement à partir des visualisations et des mesures locales, est analogue à celle décrite précédemment.

3. APPROCHE THEORIQUE

L'analyse expérimentale qui vient d'être exposée, montre que les variations simultanées de vitesse et d'incidence générées dans le sillage de l'émetteur jouent un rôle prépondérant sur le comportement aérodynamique du récepteur. L'intensité de l'interaction sillage - profil et l'instationnarité associée sont étroitement liées à la position transversale de R par rapport au sillage (Y > 0 ou Y < 0), à son incidence géométrique propre α_R, ainsi qu'à l'amplitude des fluctuations de vitesse et d'incidence induite générées dans le sillage de E ; celles-ci provoquant sur R des effets non linéaires plus ou moins intenses à la fois pour des configurations décollées ($\alpha > \alpha_{SS}$) ou non décollées ($0 < \alpha < \alpha_{SS}$).

A partir de ces constatations expérimentales, il est proposé de modéliser les effets non linéaires subis par R en supposant que ces derniers sont surtout dûs aux variations simultanées de vitesse et d'incidence. Il est donc possible de revenir à une configuration plus simple dans laquelle R est supposé isolé dans un écoulement pour lequel vitesse et incidence varient simultanément suivant une loi pré - établie (ΔV, $\Delta\alpha$ et k fixés).

3.1. Méthodes existantes

3.1.1. Configurations décollées

Dans le cas où α varie suivant des valeurs supérieures à α_{SS} simultanément au vecteur vitesse, aucune théorie ou modélisation numérique n'est en mesure, à l'heure actuelle, de résoudre ce problème dans son intégralité. Le travail le plus avancé à cet égard est celui effectué par l'O.N.E.R.A. (13), (14) qui concerne la modélisation du comportement du C_Z d'un profil soumis au décrochage dynamique résultant des oscillations d'incidence pure. Il s'agira ensuite de traiter le cas des oscillations de vitesse pure, et enfin de superposer ces deux types de variations élémentaires.

3.1.2. Configurations non décollées

Dans le cas où les variations considérées ne conduisent pas le profil à atteindre des incidences supérieures à α_{SS}, le calcul des effets instationnaires peut être envisagé par une méthode (10),(12) basée sur un écoulement de fluide parfait autour d'un profil d'aile animé d'un mouvement d'oscillation harmonique. Après transformation conforme, ce modèle (Euler 2D instationnaire) permet le calcul des distributions de pression surfaciques, et par intégration celui des efforts subis par le profil lorsqu'on le soumet à des variations de vitesse et d'incidence quelconques au cours du temps.

Dans un premier temps, le modèle de base proposé (sans effet additionnel de traîne tourbillonnaire) a été testé dans le cas d'un profil d'aile soumis par l'intermédiaire d'un mouvement d'oscillation oblique (10),(15) à des variations simultanées de vitesse et d'incidence définies par :

$$V(t) = V_\infty \{1 + 2\lambda \cos\delta \cos\omega t + \lambda^2 \cos^2 \omega t\}^{1/2}$$

$$\alpha(t) = \alpha_o - \text{Arctg} \{\lambda \sin\delta \cos\omega t / (1 + \lambda \cos\delta \cos\omega t)\}$$

où l'angle δ définit la direction d'oscillation du profil et α_o est son incidence géométrique.

A l'aide de ce type de mouvement propre du profil, il est possible de générer des variations de vitesse et d'incidence qui s'effectuent soit en phase (maximum de V coïncidant avec celui de α), soit en opposition de phase (maxima de V et de α déphasé de 180°). Des exemples de variations simultanées de vitesse et d'incidence ainsi réalisée, sont présentés sur les diagrammes du bas des Figures 13 et 14, dans lesquels les fluctuations d'incidence s'effectuent en dehors de tout décrochage.

Pour des oscillations de vitesse de l'ordre de 40 % de V_∞ et un paramètre de fréquence réduite k = 0,36, les variations d'incidence correspondantes (3° < α < 13°) sont considérées en phase sur la Figure 13, et en opposition de phase sur la Figure 14. Sur ces figures, sont également représentées, en fonction de α, les variations du C_Z calculées et mesurées sur le profil NACA 0012.

Dans le cas des variations en phase de V et de α(Fig. 13), la prévision par le calcul du comportement de C_Z dans le temps, traduit bien la présence d'effets non linéaires marqués, qui sont caractérisés par des écarts notables du C_Z instantané par rapport à l'état stationnaire (représenté en pointillés). La tendance des résultats expérimentaux est bien représentée par le modèle, de même que le sens du parcours de la boucle d'hystérésis qui indique que les variations de portance suivent celle de la vitesse. On notera également l'accroissement du niveau moyen de $\bar{C}_Z$ au cours de l'oscillation ($\bar{C}_Z/(C_Z)_{st} \simeq 1,2$) qui résulte (9),(15) de l'effet des variations de vitesse.

Dans le cas des variations en opposition de phase de V et de α (Fig. 14), les effets instationnaires sont relativement plus atténués que précédemment et sont correctement représentés par le modèle de calcul. Dans ce cas, de faibles écarts sont observés entre les courbes instationnaire et stationnaire, et les variations de C_Z suivent celles de l'incidence qui s'avèrent, dans ce cas, prédominantes.

Une amélioration du calcul précédent a été recherchée par l'intermédiaire de la méthode développée par l'E.S.T.E.P.-Orléans (16),(17), de même nature que celle utilisée à l'I.M.F.M. (Euler 2D instationnaire), mais qui de plus permet la prise en compte d'un échappement tourbillonnaire libre au bord de fuite, constituant une traîne déformable composée de tourbillons discrets qui évoluent dans le sillage de façon compatible avec les niveaux de circulation instantanés s'établissant sur le profil.

Un exemple de résultats obtenus par cette méthode en tenant compte de la traîne déformable, est présenté sur la Figure 15 dans le cas de l'oscillation oblique du profil (λ = 0,37 ; k = 0,36), de telle façon que les oscillations de V et de α s'effectuent en phase (α_0 = - 8,7°) ou en opposition de phase (α_0 = 8°), mais toujours en l'absence de décrochage (1,8° < α < 11,9°). La comparaison calcul - expérience de la Figure 15 montre que la traîne déformable conduit à une meilleure prévision pour les oscillations de V et de α s'effectuant en opposition de phase. Dans le cas en phase, bien que le calcul traduise correctement l'effet hypersustentateur moyen dû à la variation de vitesse, il sous-estime cependant les niveaux expérimentaux du C_Z pour la zone des valeurs élevées de V et de α. L'écart observé dans cette zone pourrait être attribué à des effets visqueux résultant de l'influence conjuguée des gradients de V et de α, qui ne sont pas considérés dans ce modèle d'écoulement potentiel.

Dans le cas d'interactions "aile - sillage", l'analyse expérimentale du paragraphe 2 a montré que les fluctuations simultanées de V et α imposées au profil récepteur R, sont périodiques mais non sinusoïdales. Dans cette configuration plus complexe, le calcul des effets instationnaires observés expérimentalement sur R a été abordé en supposant que le récepteur pouvait être assimilé à un profil isolé, placé en écoulement de vitesse moyenne $V_0 = \frac{1}{T}\int_0^T V(t)\,dt$, et soumis à des fluctuations de vitesse et d'incidence données par des décompositions en série de Fourier sous la forme :

$$V(t) = V_0 + \sum_{n=1}^{4} V_n \cos(n\,\omega t + \phi_n^V)$$

$$\alpha(t) = \alpha_0 + \sum_{n=1}^{N} \alpha_n \cos(n\,\omega t + \phi_n^\alpha)$$

Le calcul de l'écoulement potentiel autour du profil est effectué par intégration de l'équation d'Euler dans laquelle les fluctuations instantanées V(t) et α(t) sont données par les décompositions de Fourier à l'ordre 4 déterminées expérimentalement. En première approximation, la traîne tourbillonnaire utilisée dans ce modèle (18) a été limitée à l'harmonique 1. En outre, cette traîne est suppose être indéformable, rectiligne, et s'échappe à chaque instant depuis le bord de fuite et dans le prolongement de la corde du profil. Cette hypothèse implique en particulier que son influence au niveau des vitesses induites sur leprofil, n'est prise en compte que globalement par une formulation analogue à celle développée (19),(20) pour des oscillations sinusoïdales de V ou de α.

Un exemple de résultat préliminaire obtenu à l'aide de ce modèle simplifié, est comparé à l'expérience sur la Figure 16, qui est relatif à la position Y/c = - 0,75 ; X/c = 0,58 ; α_0 = 6° du profil récepteur et pour laquelle les fluctuations mesurées de V et α (voir Fig. 4B) sont représentées par les séries de Fourier à l'ordre 4 correspondantes. Ce premier résultat montre clairement l'amélioration apportée au calcul par l'effet de traîne(au niveau de la phase et de l'amplitude de la variation du coefficient de portance $C_{Z_0} = P / \frac{1}{2} \rho V_0^2 S$), même si elle n'est prise en compte ici que de façon globale et à l'harmonique 1. L'introduction d'une meilleure modélisation de l'effet de traîne, déformable, et déterminée pour chaque variation instantanée de V et de α (du type de celle proposée dans les références (16),(17)),devrait conduire à une prévision satisfaisante des efforts subis par le récepteur en présence du sillage périodique.

4 CONCLUSION

Les effets instationnaires résultant de l'interaction entre un écoulement tourbillonnaire périodique et une surface portante réceptrice immobile, ont été analysés dans le cadre de cette étude. Un tel écoulement a pu être simulé par l'intermédiaire du sillage tourbillonnaire (tourbillons d'axe perpendiculaire à l'écoulement principal) issu d'un profil oscillant en Tamis dans des conditions de décrochage dynamique.

L'écoulement incident sur R généré au cours d'une même période d'oscillation de E par l'alternance d'une zone d'écoulement potentiel et d'une zone à forte vorticité, a été caractérisé de façon précise par des fluctuations simultanées de vitesse et d'incidence induites dans le champ inter-profils. L'étude paramétrique de l'interaction a plus particulièrement porté : sur la distance relative longitudinale séparant E de R ; sur la position transversale de l'émetteur par rapport au récepteur (situé du côté extrados ou intrados de E, $Y/c = \pm 0,75$); ainsi que sur l'incidence géométrique propre de R.

Les éléments caractéristiques qui ont pu être dégagés au niveau du comportement aérodynamique du récepteur R, peuvent être résumés comme suit :

- Lorsque le récepteur est placé à grande incidence géométrique ($\alpha_R = 20°$), celui-ci subit toujours, quelle que soit sa position transversale ($Y/c = \pm 0,75$), un décrochage dynamique intense. La chronologie des effets associés à ce décrochage dynamique (typique des variations simultanées de V et de α) a pu être clairement mise en évidence sur le torseur aérodynamique, comme sur les grandeurs locales mesurées à la surface de R.

- Lorsque le récepteur est placé à faible incidence géométrique ($\alpha_R = 6°$), son comportement dépend plus étroitement de la position transversale considérée. Pour les deux positions $Y/c = \pm 0,75$, les oscillations de α générées sur R s'effectuent sans dépassement de l'incidence de décrochage statique correspondante ($\alpha_{SS} = 10,5°$ pour $Y/c = -0,75$; $\alpha_{SS} = 16°$ pour $Y/c = 0,75$).

Pour le récepteur placé du côte de l'extrados de l'émetteur ($Y/c = 0,75$), le tourbillon issu de l'extrados de E favorise l'accroissement de circulation autour de R et le torseur aérodynamique subit dans son ensemble une augmentation moyenne sur la période d'oscillation.

Au contraire, pour le récepteur placé du côté de l'intrados de l'émetteur ($Y/c = -0,75$), le tourbillon issu de l'intrados de E s'oppose à la circulation s'établissant sur R à chaque instant, ce qui conduit à une perte de portance moyenne sur la période. Les visualisations et l'analyse des grandeurs locales instantanées ont, en particulier, permis d'expliquer et de confirmer le comportement du torseur aérodynamique sur R.

A partir de cette analyse expérimentale, une tentative de modélisation théorique des effets non linéaires observés aux faibles amplitudes de variation de $\alpha (\alpha < \alpha_{SS})$ a été entreprise. Cette modélisation a consisté à considérer le profil récepteur isolé dans un écoulement potentiel périodique dont le module du vecteur vitesse et l'incidence varient simultanément à chaque phase de la période. La méthode a été testée sur des cas types pour lesquels ces variations (sinusoïdales) ont lieu soit en phase, soit en opposition de phase, puis étendue à un cas plus réaliste (4 harmoniques) prenant en compte les variations réelles de la vitesse et de l'incidence déterminées expérimentalement. Les calculs, menés en écoulement potentiel instationnaire, avec prise en compte de la traîne tourbillonnaire s'échappant du bord de fuite, ont été confrontés à l'expérience. Les résultats de la confrontation ont montré que le modèle adopté pouvait rendre compte avec une bonne approximation des phénomènes observés. L'amélioration de ce modèle de base est envisagée par le calcul, à chaque instant, du développement et de l'influence de la traîne émise à l'aval du récepteur.

REMERCIEMENTS. Cette étude a été effectuée avec l'appui financier du Service Technique des Programmes Aéronautiques, Division Etudes.

REFERENCES

(1) B. MONNERIE, A. TOGNET: "Etude de l'influence du tourbillon marginal issu d'une pale d'hélicoptère sur l'écoulement aérodynamique autour de la pale suivante", A.F.I.T.A.E., Lyon 1970.
(2) P. LAFON : "Etude en soufflerie de l'interaction tourbillonnaire sur une demi-aile à la paroi", Rapport technique O.N.E.R.A., N° 105/1369 AN, 1980.
(3) P. CERONI : "Etude expérimentale et théorique d'un tourbillon et de son interaction avec une demi - aile à la paroi", Rapport technique O.N.E.R.A., N°118/1369 AN, Novembre 1982.
(4) N.D. HAM : "Some preliminary results from an investigation of blade-vortex interaction", Journal of American Helico. Soc., Vol.19, N°2, pp.45-48, April 1974.
(5) N.D. HAM : "Some conclusions from an investigation of blade-vortex interaction", Journal of American Helico. Soc., Vol. 20, N°4, pp.26-31, October 1975.
(6) D.P. TELIONIS, D.R. POLING : "The response of airfoils to periodic disturbances - The unsteady Kutta condition", A.I.A.A. 22nd Aerospace Sciences Meeting, Reno, Nevada, January 1984.
(7) C. MARESCA, D. FAVIER : "Experimental study and modelling of the influence of a periodic wake on a lifting surface", A.I.A.A. 17th Fluid Dynamics, Plasma Dynamics and Lasers Conference, Paper 84-1660, Snowmass, June 1984.
(8) J. VALENSI, J. REBONT : "Efforts aérodynamiques sur un profil d'aile animé d'un mouvement harmonique parallèle à l'écoulement", AGARD-CP 111, paper N°12, Marseille, Septembre 1972.
(9) C. MARESCA, D. FAVIER, J. REBONT : "Experiments on an aerofoil at high angle of incidence in longitudinal oscillations", Journal of Fluid Mechanics, Vol.92, part 4, pp.671-690, June 1979.
(10) D. FAVIER : "Aérodynamique subsonique instationnaire d'un profil d'aile soumis à des variations de vitesse et d'incidence", Thèse de Doctorat es-Sciences, Université d'Aix-Marseille II, Octobre 1980.
(11) C. MARESCA, D. FAVIER, J. REBONT : "Techniques de mesure des pressions statiques et des tensions de cisaillement à la paroi d'un profil d'aile animé d'un mouvement harmonique parallèle ou perpendiculaire à l'écoulement non perturbé", EUROMECH Colloquium N° 90, L.E.M.T.A., Nancy, Juillet 1977.
(12) S.C. LEE : "Caractéristiques aérodynamiques d'un profil d'aile soumis à un sillage périodique", Thèse de Docteur- Ingénieur, Université d'Aix-Marseille II, Juin 1984.
(13) R. DAT, C.T. TRAN, D. PETOT : "Modèle phénoménologique de décrochage dynamique sur profil de pale d'hélicoptère", 16ème Colloque d'Aérodynamique Appliquée, A.A.A.F., Lille, Novembre 1979.
(14) D. PETOT : "Progress in the semi-empirical prediction of the aerodynamic forces due to large amplitude oscillations of an airfoil in attached or separated flow", Ninth European Rotorcraft Forum, Stresa, September 1983.
(15) D. FAVIER, C. MARESCA, J. REBONT : "Dynamic stall due to fluctuations of velocity and incidence", A.I.A.A. Journal, Vol.27, N°7, July 1982.

(16) M. MUDRY : "La théorie générale des nappes et des filaments tourbillonnaires et ses applications à l'aérodynamique instationnaire", Doctorat es-Sciences, Université de Paris VI, Juillet 1982.
(17) P. DEVINANT : "Numerisations fines d'écoulements fortement instationnaires autour de profils arbitraires", Thèse de 3ème Cycle, Université d'Orléans, Décembre 1982.
(18) D. FAVIER, C. MARESCA, J. REBONT : "Modelling of an airfoil empirical flow field below and through dynamic stall", J.M.T.A., Vol.3, N°1, pp.15-39, April 1984.
(19) T. VON KARMAN, W.R. SEARS : "Airfoil theory for non-uniform motion", Journal of Aeronautical Sciences, N° 10, pp.379-390, August 1938.
(20) J.M. GREENBERG : "Airfoil in sinusoïdal motion in a pulsating stream", NACA TN 1326, June 1947.

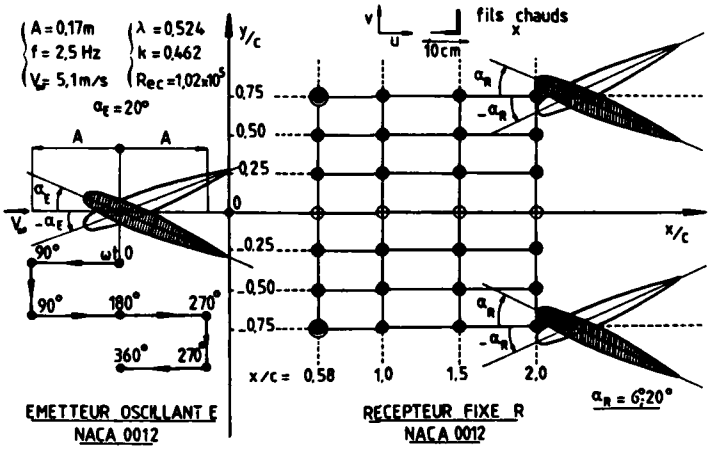

Fig. 1

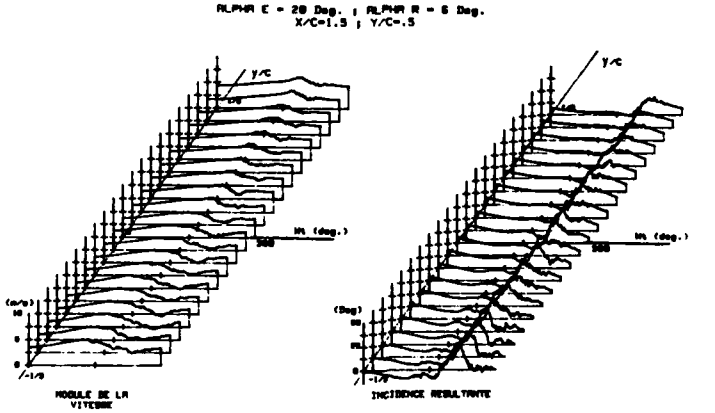

Fig. 2

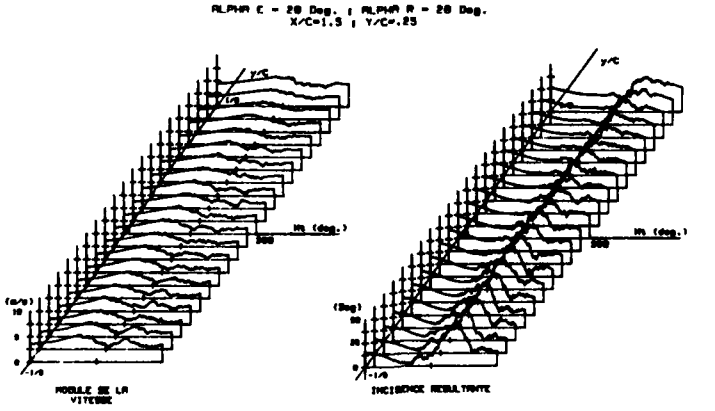

Fig. 3

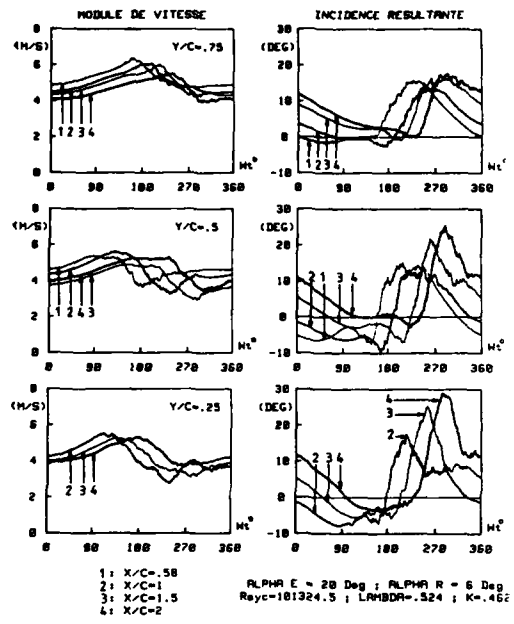

Fig.4A

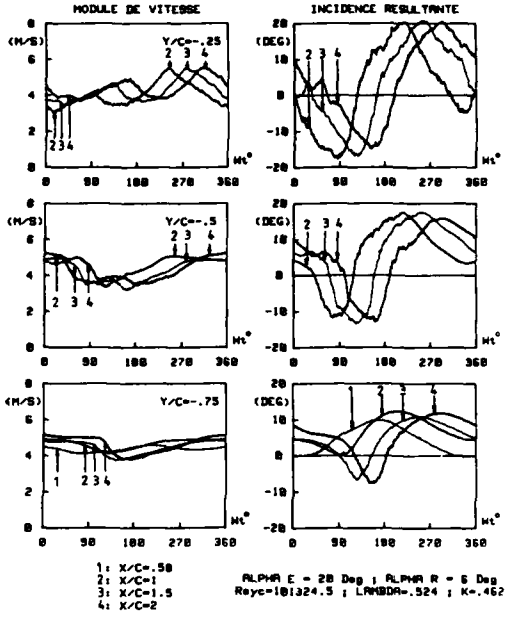

Fig.4B

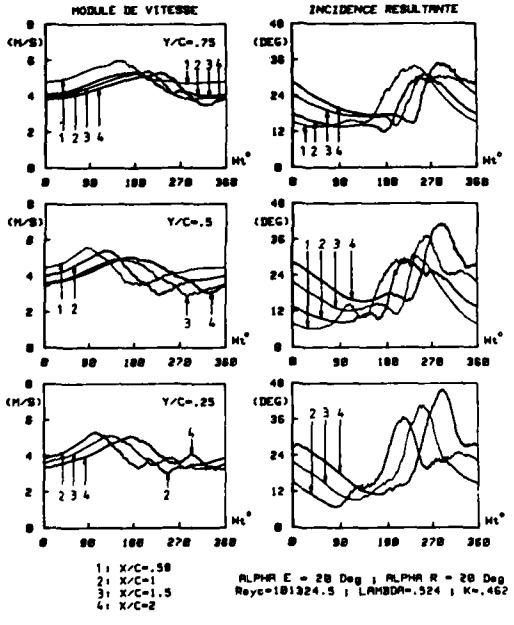

Fig.5A

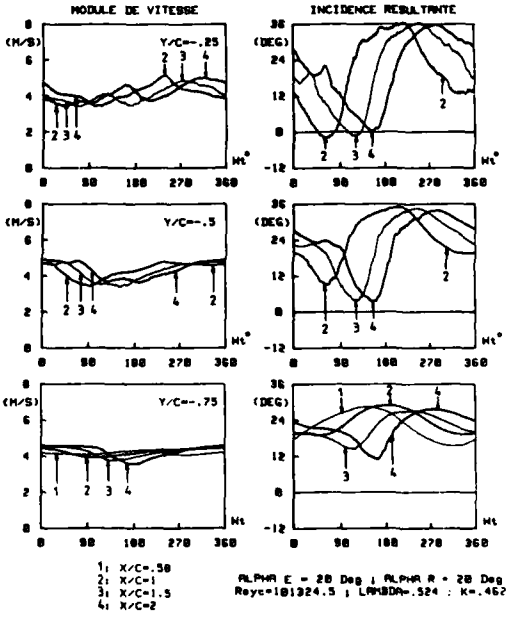

Fig.5B

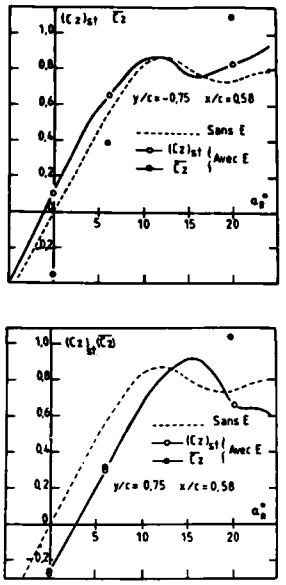

Fig.6

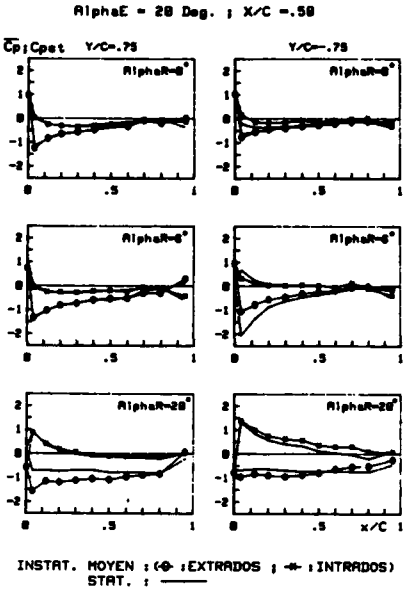

Fig. 7

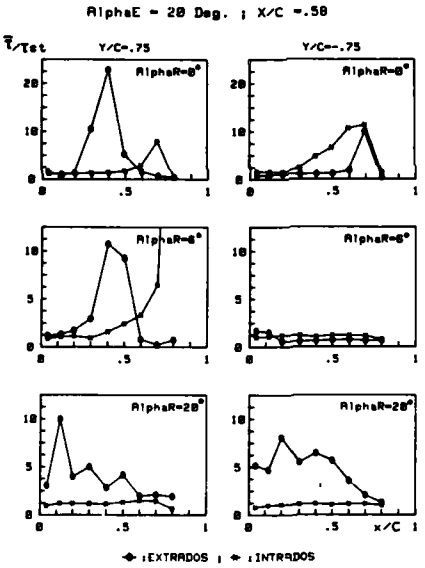

Fig. 8

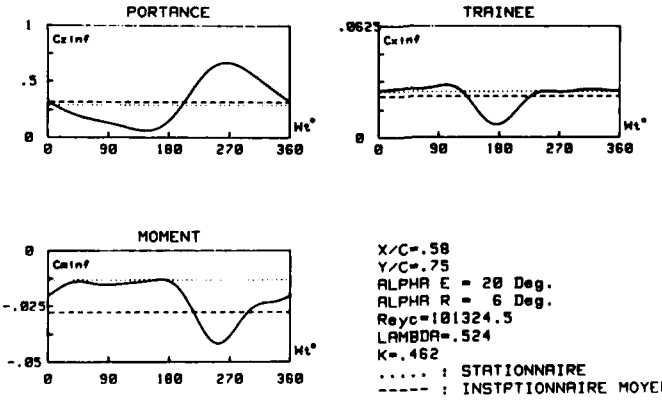

Fig. 9

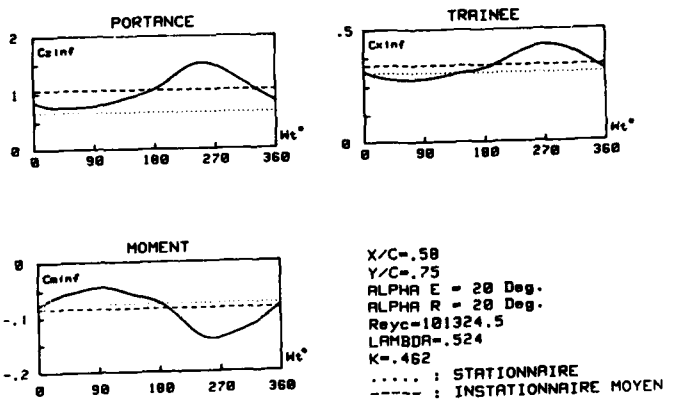

Fig. 10

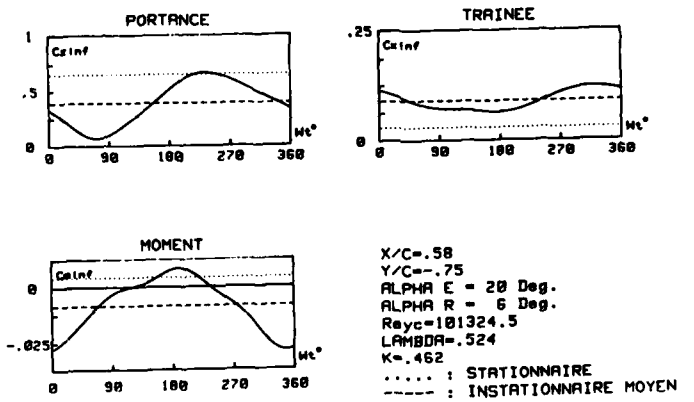

Fig. 11

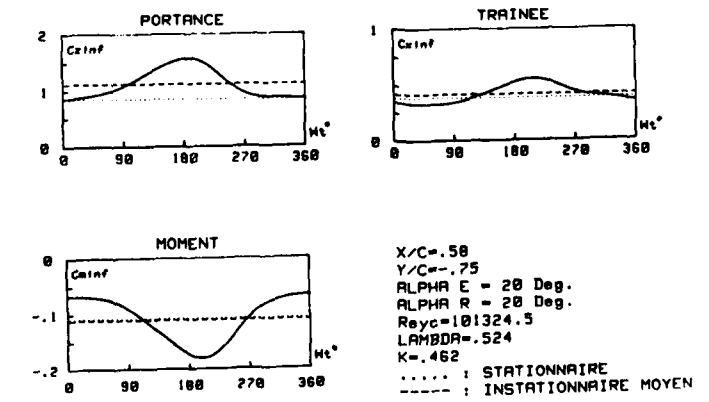

Fig. 12

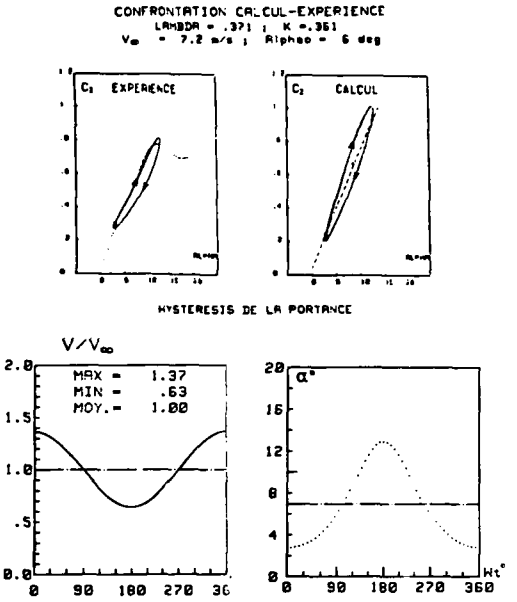

Fig. 14

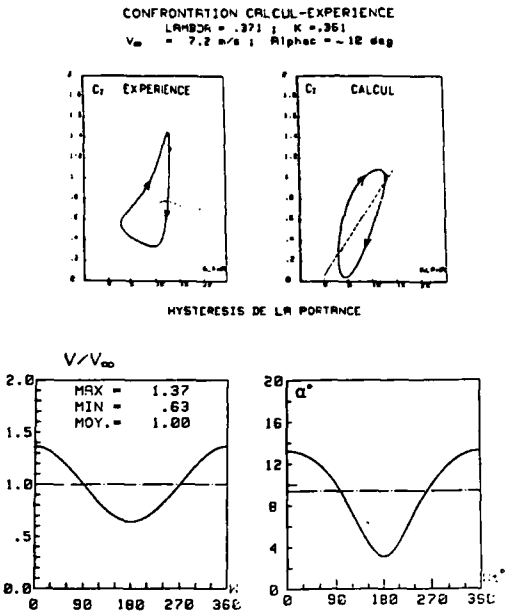

Fig. 13

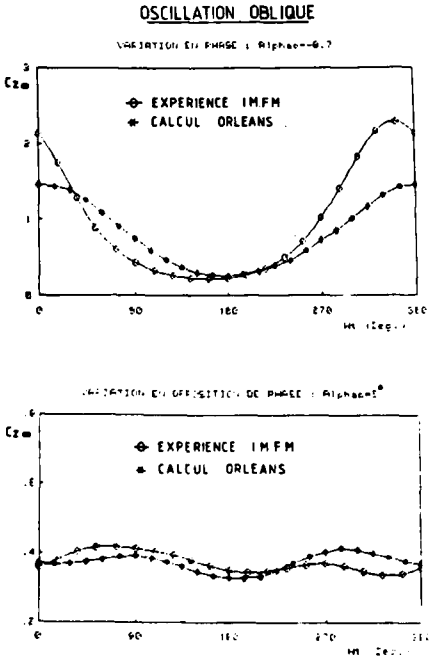

Fig. 15

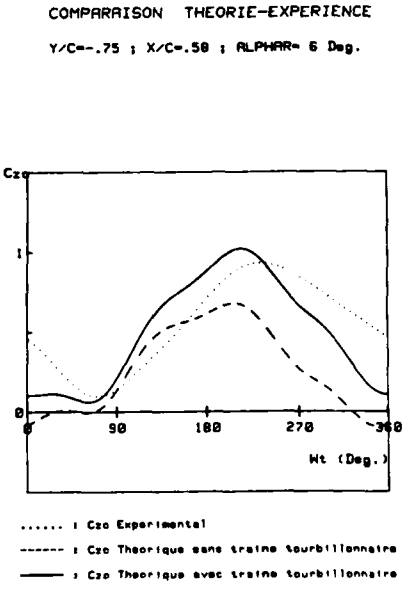

Fig. 16

A CRITICAL LOOK AT DYNAMIC SIMULATION OF VISCOUS FLOW

L. E. Ericsson
Lockheed Missiles & Space Company, Inc.
Sunnyvale, California 94086, USA

SUMMARY

A critical examination is made of the classic role of the wind tunnel as a tool for simulation of the free flight aerodynamics. That the equivalence concept established for steady flow is not valid for unsteady flow is no great surprise. More surprising, probably, is the fact that simulation of the relative velocity time history, which assures simulation of the inviscid unsteady aerodynamics, will in many cases not assure simulation of the unsteady viscous flow. In the case of flow separation and associated hysteresis the lack of simulation of the transient viscous flow can sometimes even generate the incorrect final steady state flow condition. Only close attention to the simulation of the unsteady boundary condition at the vehicle surface can assure the utility of experimental and numerical results for prediction of full scale unsteady viscous flow characteristics.

NOMENCLATURE

c	chord length
f	frequency
k	frequency parameter, $k = \bar{\omega}/2$
K_a	dynamic overshoot parameter, Eqs. (7)-(10)
l	sectional lift, coefficient $c_l = l/(\rho_\infty U_\infty^2/2)c$. $\bar{c}_l$ = time average value
m_p	sectional pitching moment, coefficient $c_m = m_p/(\rho_\infty U_\infty^2/2)c^2$
n	sectional normal force, coefficient, $c_n = n/(\rho_\infty U_\infty^2/2)c$
p	static pressure
P	stagnation pressure,
Re	Reynolds number based on chord length, $Re = U_\infty c/\nu_\infty$
t	time
U	horizontal velocity
V	resultant velocity, $V^2 = V_A^2 + V_\Omega^2 = U_\infty^2$
V_A	axial velocity
$V\Omega$	tangential velocity
W	vertical velocity
x	chordwise distance from the leading edge
z	translatory coordinate, positive downward
α	angle of attack
$\bar{\alpha}$	equivalent angular amplitude, $\bar{\alpha} = \lvert\dot{z}\rvert/U_\infty$
α_o	mean (trim) angle of attack
Δ	increment or amplitude
θ	perturbation in pitch
ξ	dimensionless x-coordinate, $\xi = x/c$
ρ	air density
ν	kinematic viscosity
ψ	azimuth (Fig. 2)
ω	angular frequency, $\omega = 2\pi f$

$\bar{\omega}$ reduced frequency, $\bar{\omega} = \omega c/U_\infty = 2k$

Subscripts

CG center of gravity or rotation axis

e boundary layer edge

g geometrically equivalent

G gust

LE leading edge

MAX maximum

MIN minimum

P plunging

s separation

w wall

1,2 numbering subscript

∞ freestream conditions

Derivative Symbols

$c_{l\alpha} = \partial c_l/\partial\alpha$

$\dot{\alpha} = \partial\alpha/\partial t$

1. INTRODUCTION

In earlier AGARD publications (Refs. 1-3) the problems of Reynolds number scaling and support interference have been reviewed. The present paper discusses the remaining question of how to apply dynamic test data to the full scale vehicle, assumming that the scaling and support interference problems have been resolved.

One of the great challenges facing the design engineer is how to use wind tunnel test data to assess the impact of dynamic stall on the performance of axial flow compressors and helicopter rotors. The standard procedure used so far has been to identify the instantaneous blade angle of attack and its rate of change, and to use wind tunnel test results for a pitching airfoil to estimate the effects of dynamic stall. Examples of this type of analysis (Refs. 4-6) will be examined in light of more recent detailed investigations of dynamic stall (Refs. 7-18) to determine to what extent the full scale unsteady flow characteristics have been represented. It is found that this approach to dynamic simulation is too crude, and that the classic free flight/wind tunnel equivalence concept remains valid only for steady flow. Further analysis shows that even the inviscid unsteady free flight/wind tunnel equivalence concept is invalid when considering unsteady separated flow characteristics, and can in some cases lead to the incorrect final steady state condition.

2. DISCUSSION

In an axial flow compressor (Ref. 4) the non-uniform inlet velocity distribution (Fig. 1a) generates a circumferentially varying angle of attack at the compressor blade (Fig. 1b). In transforming the actual velocity vector geometry in Fig. 1a to be represented by the geometric angle of attack α_g and the total relative velocity vector V all the characteristics for stationary flow are preserved. In the case of a helicopter rotor the axial velocity V_A in Fig. 1a is represented by the blade component $U_\infty \sin\psi$ of the forward speed of the helicopter. Adding to the sinosoidal α_g-variation obtained in this manner is the effect of the downwash from the preceding blade(s), generating a resultant angle of attack variation such as the one shown in Fig. 2 (Ref. 2). By adding the local time rate of change, $|\dot{\alpha}c/U_\infty| = \bar{\omega}|\bar{\alpha}|(\bar{\omega}=2k)$, to the local instantaneous angle of attack (Fig. 3), means are created for the use of experimental dynamic stall results for a pitching airfoil (Fig. 4) to predict the time rate of change of the blade loading on an axial flow compressor (Ref. 4) or a helicopter rotor (Refs. 5,6). Even when disregarding complex three-dimensional flow effects and the usual problem of Reynolds number scaling (Ref. 1), this approach to dynamic simulation is found to be highly questionable.

3. ANALYSIS

The pressure gradient of the external flow at the boundary layer edge is given by the Bernoulli equation for unsteady flow.

$$-\frac{1}{\rho_e}\frac{\partial p_e}{\partial x} = \frac{\partial U_e}{\partial t} + U_e\frac{\partial U_e}{\partial x} \qquad (1)$$

Or, with $\xi = x/c$

$$\frac{\partial p_e}{\partial \xi} = -\rho_e U_e\left[\frac{\partial U_e}{\partial t}\frac{c}{U_e} + \frac{\partial U_e}{\partial \xi}\right] \qquad (2)$$

That is

$$\frac{\partial p_e}{\partial \xi} = \left(\frac{\partial p_e}{\partial \xi}\right)_{\dot{U}_e=0} - c\,\rho_e\frac{\partial U_e}{\partial t} \qquad (3)$$

Equation (3) shows that the adversity of the pressure gradient, $dp_e/d\xi$, will be decreased by an accelerating external velocity, $\partial U_e/\partial t > 0$. Thus, the separation on the leeward side of an airfoil will be delayed in an accelerating free stream. Conversely, separation will be promoted in a decelerating free stream.

For an airfoil pitching in a constant velocity free stream, the leeside flow acceleration is induced by the change of angle of attack.

$$\partial U_e/\partial t = (\partial U_e/\partial \alpha)(\partial \alpha/\partial t) \qquad (4)$$

Thus, Eq. (2) can be written as follows for the pitching airfoil

$$\frac{\partial p_e}{\partial \xi} = \left(\frac{\partial p_e}{\partial \xi}\right)_{\dot{\alpha}=0} + \frac{\partial p_e}{\partial \alpha}\cdot\frac{c\dot{\alpha}}{U_e} \qquad (5)$$

The accelerated flow effect, $(\partial p_e/\partial \alpha)\,(c\dot{\alpha}/U_e)$, where $\partial p_e/\partial \alpha < 0$, permits a dynamic overshoot of the static adverse pressure gradient, $(\partial p_e/\partial \xi)_{\dot{\alpha}=0}$, before separation occurs, as has been discussed in detail (Refs. 8, 19, 20).

Thus, on a pitching airfoil the flow is accelerated on the leeward side when the angle of attack increases. In the case of axial flow compressors (Ref. 4) and helicopter rotors (refs. 5, 6) the increase of local angle of attack is associated with decelerating free stream flow, and, consequently, decelerating leeside flow on the airfoil. The importance of this difference will be examined next.

The acceleration-induced separation delay on the pitching airfoil gives a corresponding overshoot of static $c_{l\ max}$ (Ref. 8).

$$\Delta c_{l\ max} = c_{l\alpha}\ \Delta\alpha_{s1} \qquad (6)$$

$$\Delta\alpha_{s1} = K_{a1}\frac{c\dot{\alpha}}{U_e} \qquad (7)$$

Another mechanism for dynamic overshoot of static $c_{l\ max}$ by a pitching airfoil is the so-called "leading-edge-jet" effect (Refs. 8, 20 and Fig. 5). It causes an overshoot $c_{l\alpha}\ \Delta\alpha_{s2}$ of static $c_{l\ max}$, which in a first approximation is proportional to the leading edge plunging velocity (Refs. 8, 20).

$$\Delta\alpha_{s2} = -K_{a2}\ (\dot{z}_{LE}/U) \qquad (8)$$

Thus, combining Eqs. (7) and (8) one obtains for the airfoil pitching around its center of gravity (C.G.).

$$\Delta\alpha_s = K_a\ c\dot{\alpha}/U_e \qquad (9)$$

$$K_a = K_{a1} + K_{a2}\ \xi_{CG} \qquad (10)$$

Eqs. (6) and (9) forecast an undershoot of static $c_{l\ max}$ when the airfoil decreases angle of attack on the pitching "downstroke". Recent experimental results (Ref. 10 and Fig. 6) support this forecast, and indicate that the effect of decelerating leeside flow on dynamic stall could be as adverse as the accelerating flow effects are favorable.

Experimental results (Ref. 21) indicate that an accelerating free stream can generate large overshoot of static $c_{l\ max}$ (Fig. 7). An equally large overshoot is generated by accelerating the airfoil in longitudinal oscillations (Ref. 14 and Fig. 8). The figure shows the time average lift $\bar{c}_l(t)$ obtained for the complete pitch loop around α_0 (See Fig. 4 for loop examples). The reason why $\bar{c}_l(t)$ increases with increasing $\bar{\omega}$ and associated increasing $|U_\infty c/U_\infty|$ is that a leading edge vortex is spilled near the end of

the upstroke, generating lift during its travel from leading to trailing edge during the pitching downstroke (Ref. 22). When $\bar{\omega} > 0.656$ the flow will reattach at the leading edge before the "spilled" vortex passes downstream of the trailing edge (Ref. 20). This explains why $\bar{c}_1(t)$ lies above the extrapolated attached flow lift for $\bar{\omega}_2 = 0.656$, 0.926, and 1.314 in Fig. 8. Replotting the results against $|U_\infty c/U_\infty^2| = \bar{\omega}^2 \Delta x/c$ gives a data trend (Ref. 20) which is in agreement with that in Fig. 7, when considering the difference between time average and instantaneous lift just discussed (Fig. 9).

4. FREE FLIGHT/WIND TUNNEL EQUIVALENCE

It is clear from the results shown in Figs. 7-9 that the free flight/wind tunnel equivalence concept derived for stationary flow can not be applied to unsteady flow. However, the results show that the effect of accelerating the airfoil in a constant velocity stream is equivalent to accelerating the stream over a stationary airfoil. Thus, for inviscid flow effects, such as the boundary layer edge conditions discussed earlier, the free flight/wind tunnel equivalence concept derived for unsteady flow is valid. The next question is: can this inviscid unsteady flow equivalence concept be applied to viscous flow effects, in particular those associated with separated flow? The answer is "No", as will be shown.

The "leading edge jet" or "moving wall" effect, illustrated in Fig. 5, is the reason for the "No"-answer above (Fig. 10). In the free flight case the encounter of a vertical gust W_G will cause this velocity component to be added to the boundary layer edge velocity in the nose region of an airfoil. In contrast, in the wind tunnel, imposing a sudden plunging velocity W_p to the airfoil section will add the velocity component not at the boundary layer edge but at the airfoil surface. Thus, the perturbation effect on dynamic stall will be opposite in the two cases. In the free flight case the increased boundary layer edge velocity will delay flow separation, whereas the upstream moving wall effect in the wind tunnel test will promote separation, as has been discussed (Downstroke in Fig. 5). Thus, the general conclusion to be drawn is that in the case of unsteady viscous flow the unsteady flow equivalence between airfoil motion and free stream oscillation is not valid.

The so called moving wall effect is of significant magnitude only in the nose flow region where the boundary layer is thin (Refs. 8, 20, 23). That is, of course, why lateral or vertical translation generates large moving wall effects (Fig. 5). In contrast, longitudinal or horizontal oscillations will not generate significant moving wall velocities in the nose flow region. This is the reason why the inviscid unsteady equivalence concept is supported by the viscous experimental results in Figs. 7-9.

Some appreciation of the effect of the different unsteady boundary layer profiles shown in Fig. 10 can be obtained by comparing dynamic stall results for pitching and plunging airfoils, for which the moving wall effects are opposite (Fig. 5), delaying stall for a pitching airfoil (during the upstroke) and promoting stall for a plunging airfoil, which increases its effective angle of attack during the downstroke rather than during the upstroke.

An extensive experimental investigation has been performed by Carta (Ref. 11), comparing dynamic stall results for pitching and plunging airfoils, oscillating around the same trim angle of attack (α_0) with the same reduced frequency, $\bar{\omega} = 2k = \omega c/U_\infty$, and equivalent angular amplitude, $|\bar{\alpha}| = |\theta| = |\dot{z}|/U_\infty$. The results definitely show that there are great differences between the dynamic stall process experienced in pitching and plunging oscillations. In some cases the moment loops would agree, while the normal force loops were dramatically different (Fig. 11). In other cases the normal force loops agreed, while the moment loops disagreed greatly (Fig. 12). And there were also cases in which both c_n and c_m loops disagreed completely (Fig. 13).

While Carta's experimental results (Ref. 11) do demonstrate that the effects of pitching and plunging oscillations on dynamic stall are very different, the data show anomalies. So, for example, show Figs. 11 and 13 the plunging airfoil to experience the highest dynamic $c_{n_{max}}$, which is contrary to the expectations expressed earlier. The anomaly is caused by the complication introduced by the moving wall effects on transition.

It was discussed in Ref. 24 now the upstream moving wall effect could promote boundary layer transition and cause a reversal of the Magnus lift measured on a rotating cylinder (Ref. 25 and Fig. 14). Thus, the adverse "leading-edge-jet" effect on the plunging downstroke could cause earlier transition, thereby changing the flow separation from laminar to turbulent stall. Strong coupling between airfoil motion and boundary layer transition has been demonstrated for pitch oscillations (Ref. 26 and Fig. 15). The moving wall effects, favorable on the upstroke and adverse on the downstroke, cause transition to occur at $\xi = 0.10$ at $\alpha \approx 5^0$ for decreasing α compared to at $\alpha \approx 9^0$ for increasing α.

For plunging oscillations the effects are reversed, and the earlier transition would occur for increasing rather than for decreasing $\bar{\alpha}$ ($\bar{\alpha} = \dot{z}/U_\infty$). Carta's hot film response data (Ref. 11) tend to verify this (Fig. 16). Comparing the results for pitch and plunge it can be seen how the adverse moving wall effect $\dot{z}(t)$ promotes transition and causes the plunging airfoil to have a longer run of attached turbulent flow prior to stall. As a result the flow stays attached past 7.5% chord whereas flow separation occurs forward of 5% chord on the pitching airfoil. This explains how the plunging airfoil in Figs. 11 and 13 could have a higher dynamic $c_{n_{max}}$ than the pitching airfoil.

The effect of the upstream moving wall is similar to that of roughness, which in turn has an effect similar to that of an increase of the free stream turbulence or unit Reynolds number. Thus, the anomalous plunging effect can be visualized using the static data (Ref. 22) shown in Fig. 17. For example, the adverse "leading-edge-jet" effect on the plunging downstroke could elevate the maximum lift from that for Re = 0.33×10^6 to that for Re = 0.66×10^6 (The test data in Figs. 11 and 13 are for Re 0.3×10^6).

A comparison similar to that made by Carta (Ref. 11) has been performed by Maresca, Favier, and Rebont (Ref. 9). They did not encounter the transition complication experienced by Carta (Ref. 11) and their results show dynamic stall to occur at $\alpha \approx 16^\circ$ for the plunging airfoil compared to the delay of stall to $\alpha \approx 24^\circ$, measured for a pitching airfoil (Ref. 28 and Fig. 18). This agrees with the expectations expressed earlier and illustrates the problem addressed in the present paper, if one lets the pitching airfoil represent the case of the gust encounter (Fig. 10a).

5. TRANSIENT EFFECTS ON THE FINAL STEADY STATE AERODYNAMICS

In the experiment giving the results shown in Fig. 19, Maresca et al[15] found that after starting the oscillations at the stalled condition, E in Fig. 19, when they stopped the longituidnal oscillations the airfoil maintained the attached flow lift value, F in Fig. 19. The dashed line shows the lift measured in steady flow at the same angle of attack, $\alpha = 16^\circ$, exhibiting the Reynolds number hysteresis often present for flow separation/reattachment. Obviously, the accelerated flow effect, discussed in connection with the results in Fig. 8, brings about the flow reattachment for the oscillating airfoil, the action being similar to that of increasing the Reynolds number. Stopping the oscillation and thereby reducing the effective Reynolds number leaves the lift on the corresponding higher Re-branch of the hysteresis.

Results for oscillations in pitch, corresponding to those for longitudinal oscillations shown in Fig. 8, were obtained by Halfman et al (Ref. 29 and Fig. 20). At $\alpha_o = 22$ deg the minimum angle of attack is $\alpha_o - \Delta\theta = 15.92$ deg., well above the static stall angle, $\alpha_s < 12$ deg. The similarities in trends are obvious when comparing Figs. 8 and 20, and a result similar to that in Fig. 19 can also be expected for pitch oscillations. In the latter case it is the viscous moving wall effects (Fig. 5) that dominate the unsteady aerodynamics, not the inviscid boundary layer edge conditions, as was the case in Fig. 19. Thus, based upon the previous discussion of the flow sketches in Fig. 10, one can expect to find that the final steady state aerodynamics are dependent upon the preceding transient vehicle maneuver.

The flow separation on slender forebodies, with associated asymmetric vortex shedding at high angles of attack, has been found to be extremely sensitive to moving wall effects (Refs. 30 and 31). Consequently, one could expect the final vortex asymmetry to be determined by the preceding transient vehicle motion characteristics.

6. CONCLUSIONS

A critical examination of existing experimental results for unsteady separated flow has led to the following conclusions.

- The free flight/wind tunnel equivalence concept derived for stationary flow conditions cannot be applied to inviscid or viscous unsteady flow analysis.
- The free flight/wind tunnel equivalence concept derived for unsteady inviscid flow can in general not be applied to unsteady viscous flow because of the unsteady boundary condition at the airfoil surface, the so called moving wall effect.

7. ACKNOWLEDGEMENT

The author wants to acknowledge the contribution made by the absent co-author Peter Reding; who due to other commitments could not participate to the extent he considers commensurate with co-authorship. The author is also indebted to Nancy Behney, who with her usual skill transformed a stack of handwritten notes to a readable document.

8. REFERENCES

1. Ericsson, L. E. and Reding, J. P., "Scaling Problems in Dynamic Tests of Aircraft-Like Configurations", Paper 25, AGARD-CP-227, Feb. 1978.

2. Ericsson, L. E. and Reding, J. P., "Practical Solutions to Simulation Difficulties in Subscale Wind Tunnel Tests", Paper 16, AGARD CPP-348, AGARD FDP Symposium on Wind Tunnels and Testing Techniques, Cesme, Turkey, 26-29 Sept. 1983.

3. Ericsson, L. E., "Support Interference", Lecture 8, AGARD LS-114, March 1981.

4. Carta, F. O., "Unsteady Normal Force on an Airfoil in a Periodically Stalled Inlet Flow", J. Aircraft, Vol. 4, No. 5, Sept.-Oct. 1967, pp. 416-421.

5. Ham, N. D., "Helicopter Blade Flutter", AGARD Rpt. No. 607, Jan. 1973.

6. Carta, F. O., "An Analysis of the Stall Flutter Instability of Helicopter Rotor Blades", with comment by Ham, N. D., "Stall Flutter of Helicopter Rotor Blades - a Special Case of the Dynamic Stall Phenomenon", Annual Forum of the American Helicopter Society Washington, D.C., May 10-12, 1967.

7. McCroskey, W. J., "The Phenomenon of Dynamic Stall", NASA TM 81264 and Paper 2, VKI Lecture Series 1981-4, March 1981.

8. Ericsson, L. E. and Reding, J. P., "Dynamic Stall Analysis in Light of Recent Numerical and Experimental Results", J. Aircraft, Vol. 13, No. 4, April 1976, pp.248-255.

9. Maresca, C. A., Favier, D. J., Rebont, J. M., "Unsteady Aerodynamics of an Airfoil at High Angle of Incidence Performing Various Linear Oscillations in a Uniform Stream", J. Am. Helicopter Soc., April 1981, pp. 40-45.

10. Favier, D., Rebont, J., Maresca, C., "Profil d'Aile a Grande Incidence Animé d'un Mouvement de Pilonnement", 16ème Colloque d'Aérodynamique Appliquée, Lille, 13-15 November 1979.

11. Carta, F. O., "A Comparison of the Pitching and Plunging Response of an Oscillating Airfoil", NASA CR 3172, October 1979.

12. McCroskey, W. J., Carr, L. W., and McAlister, K. W., "Dynamic Stall Experiments on Oscillating Airfoils", AIAA Journal, Vol. 14, No. 1, Jan. 1976, pp. 57-63.

13. McCroskey, W. J., McAlister, K.W., Carr, L.W., Pucci, S.L., Lambert, O., and Indergrand, R.F., "Dynamic Stall on Advanced Airfoil Sections", J. Am. Helicopter Soc., July 1981, pp. 40-50.

14. Maresca, C. A., Favier, D. J., Rebont, "Experiments on an Airfoil at High Angle of Incidence in Longitudinal Oscillations", J. Fluid Mech., (1979), Vol. 92, Part 4, pp. 671-690.

15. Maresca, C., Rebont, J., and Valensi, J., "Separation and Reattachment of the Boundary Layer on a Symmetric Airfoil Oscillating at a Fixed Incidence in Steady Flow", Proc. Univ. Ariz/USAF OSR Symposium on Unsteady Aerodynamics, Kinney, R. B. ed., Tucson, 1975, pp. 35-54.

16. Carta, F. O., "Analysis of Oscillatory Pressure Data Including Dynamic Stall Effects", NASA CR-2394, May 1974.

17. McAlister, K. W., Carr, L. W. and McCroskey, W. J., "Dynamic Stall Experiments on the NACA 0012 Airfoil, NASA TP 1100, Jan. 1978.

18. McCroskey, W. J., McAlister, K. W. Carr, L. W., and Pucci, S. L., "An Experimental Study of Dynamic Stall on Advanced Airfoil Sections, Volume 1, Summary of the Experiment", NASA TM 84245, July 1982.

19. Ericsson, L. E. and Reding, J. P., "Unsteady Airfoil Stall, Review and Extension", J. Aircraft, Vol. 8, August 1971, pp. 609-616.

20. Ericsson, L. E. and Reding, J. P., "Unsteady Flow Concepts for Dynamic Stall Analysis", J. Aircraft, Vol. 21, No. 8, Aug. 1984, pp. 601-606.

21. Minkkinen, G. T., Wilson, T. A., and Beavers, G. S., "An Experiment on the Lift of an Accelerated Airfoil", AIAA Journal, Vol. 14, May 1976, pp 687-689.

22. Ericsson, L. E. and Reding, J. P., "Dynamic Stall at High Frequency and Large Amplitude", J. Aircraft, Vol. 17, No. 3, March 1980, pp. 136-142.

23. Ericsson, L. E. and Reding, J. P., "Analytic Prediction of Dynamic Stall Characteristics", AIAA Paper 72-682, June 1972.

24. Ericsson, L. E., "Karman Vortex Shedding and the Effect of Body Motion", AIAA Journal, Vol. 18, No. 8, August 1980, pp. 935-944.

25. Swanson, W. M., "The Magnus Effect: A Summary of Invesitgations to date", J. Basic Eng., Vol. 83, Sept. 1961, pp. 461-470.

26. McCroskey, W. J. and Philippe, J. J., "Unsteady Viscous Flow on Oscillating Airfoils", AIAA Journal, Vol. 13, No. 1, Jan. 1975, pp. 71-79.

27. Jacobs, E. N. and Sherman, A., "Airfoil Section Characteristics as Affected by Variations in the Reynolds Number", NACA Tech. Report 586 (1937).

28. Carr, L. W., McAlister, K. W., and McCroskey, W. J., "Analysis of Development of Dynamic Stall Based on Oscillation Airfoil Experiments", NASA TN D8382, 1977.

29. Halfman, R. L., Johnson, H. C., and Haley, S. M., "Evaluation of High-Angle-of-Attack Aerodynamic Derivative Data and Stall Flutter Prediction Techniques", NACA TN 2533, Nov. 1951.

30. Ericsson, L. E. and Reding, J. P., "Steady and Unsteady Vortex-Induced Asymmetric Loads on Slender Vehicles", J. Spacecraft and Rockets, Vol. 18, No. 2, March-April 1981, pp 97-109.

31. Ericsson, L. E. and Reding, J. P., "Dynamics of Forebody Flow Separation and Associated Vortices", AIAA Paper 83-218, Aug. 1983 (Accepted for publication in J. Aircraft, 1985).

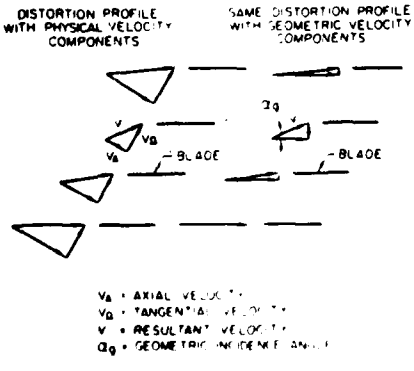

a. **Typical axial velocity distortion.**

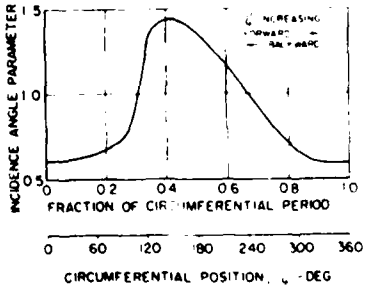

b. **Hypothetical distortion profile.**

Fig. 1 Dynamic Stall Analysis of Axial Flow Compressor (Ref. 4)

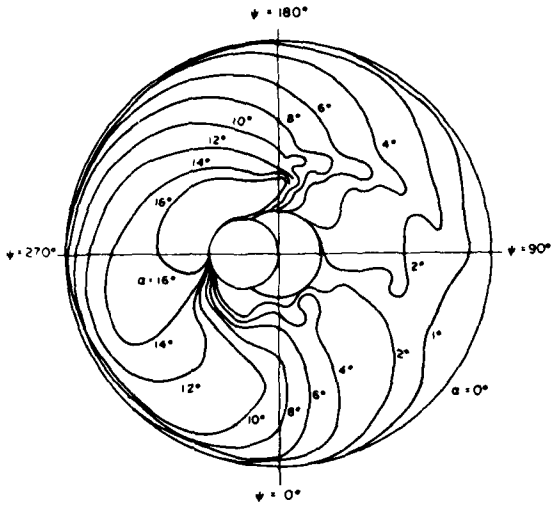

Fig. 2 Angle of Attack Map for a Helicopter Blade (Ref. 5)

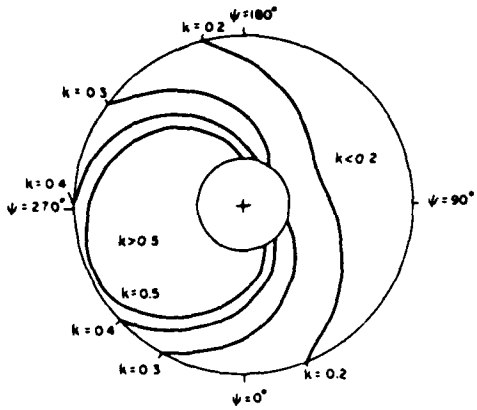

Fig. 3 Reduced Frequency Map for a Helicopter Blade (Ref. 6)

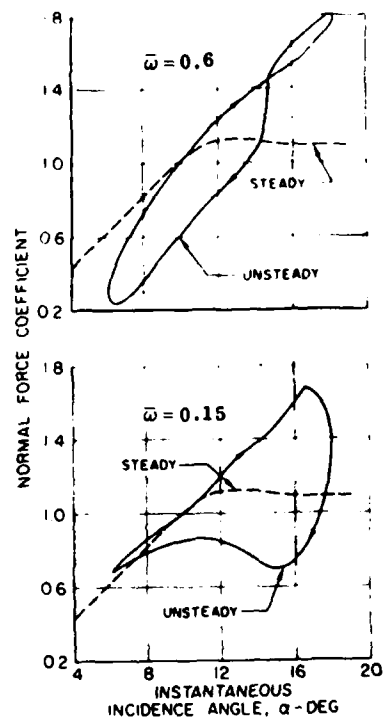

Fig. 4 Dynamic Stall Characteristics of NACA-0012 (Ref. 4)

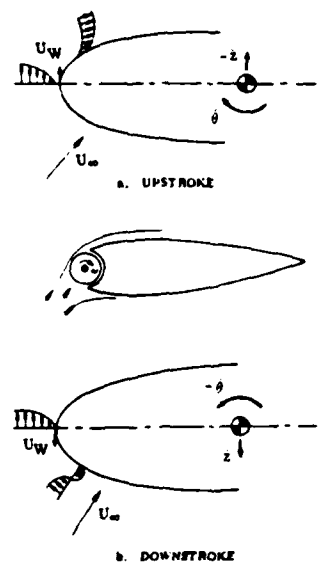

Fig. 5 "Leading Edge Jet" Effect

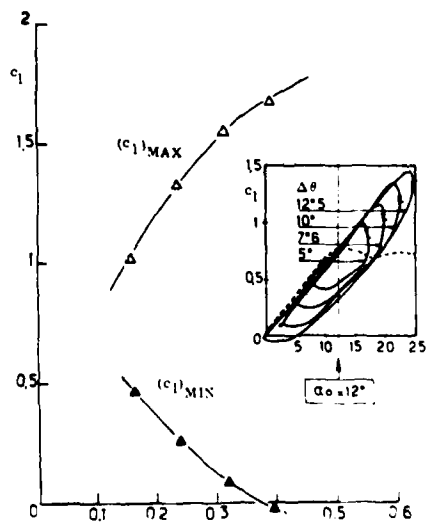

Fig. 6 Effect of reduced Frequency on Maximum and Minimum Lift (Ref. 10)

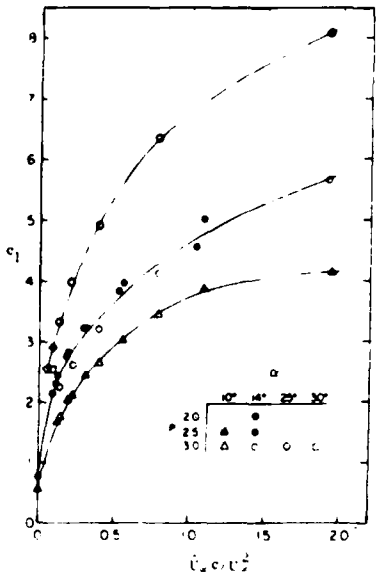

Fig. 7 Effect of Flow Acceleration on the Lift of NACA-0015 (Ref. 21)

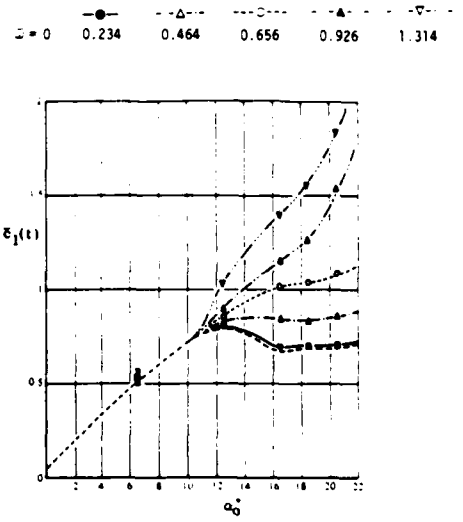

Fig. 8 Time Average Lift for Streamwise Airfoil Oscillation of Amplitude $\Delta x/c = 0.565$ (Ref. 14)

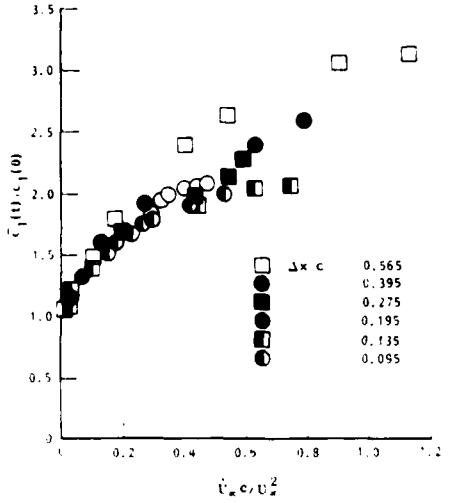

Fig. 9 Effect of Normalized Acceleration Parameter on Time Average Lift (Ref. 20)

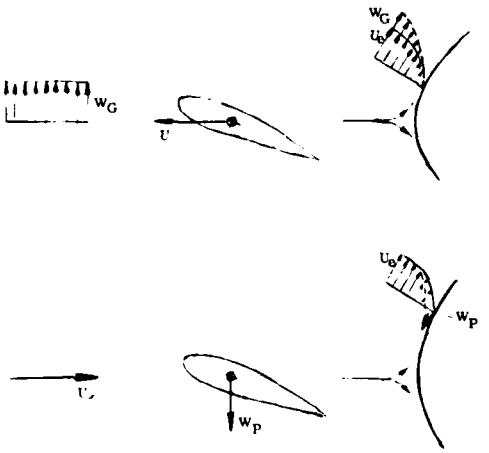

Fig. 10 Non-Equivalence Between Gust Encounter and Airfoil Plunging

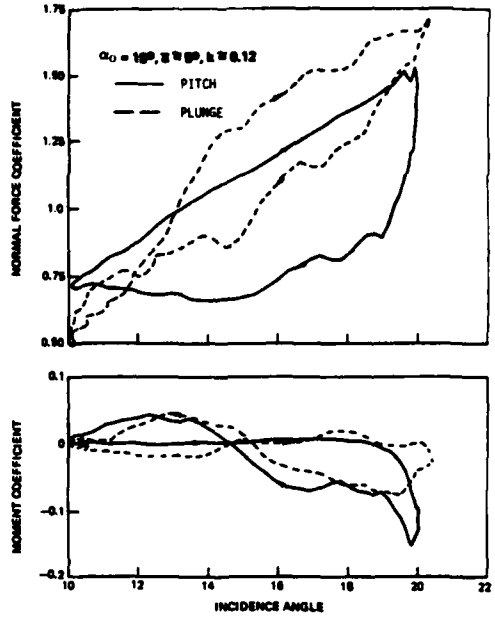

Fig. 11 Airfoil Characteristics in Plunge and Pitch, $\alpha_0 = 15^0$, $\bar{\alpha} \approx 5^0$, $\bar{\omega} \approx 0.24$ (Ref. 11)

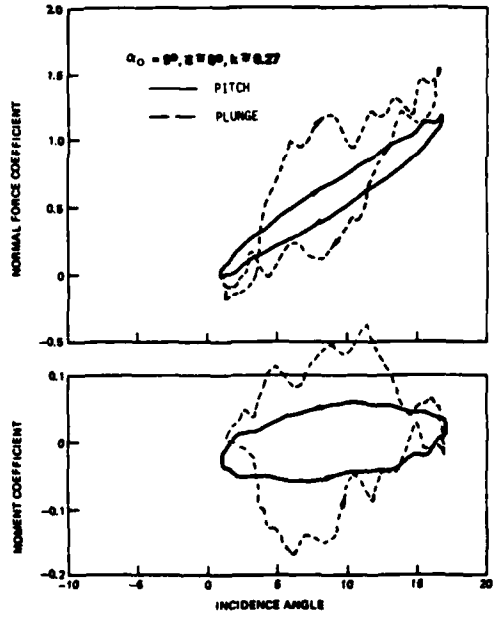

Fig. 13 Airfoil Characteristics in Plunge and Pitch, $\alpha_0 = 9^0$, $\bar{\alpha} \approx 8^0$, $\bar{\omega} \approx 0.54$ (Ref. 11)

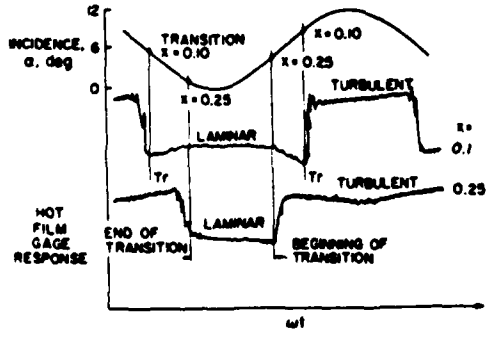

Fig. 15 Boundary Layer Transition on a Pitching Airfoil (Ref. 26)

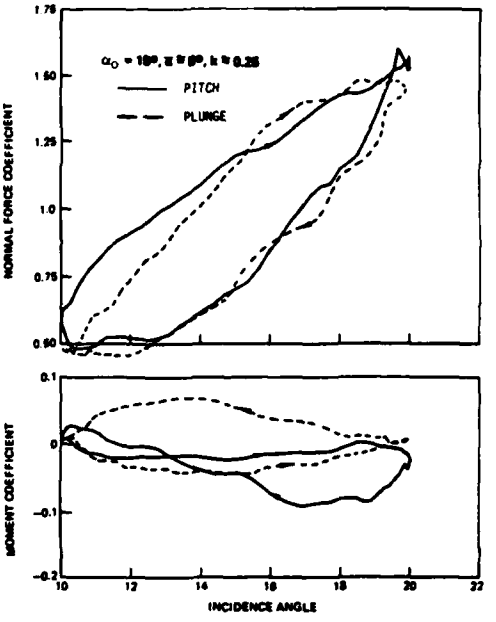

Fig. 12 Airfoil Characteristics in Plunge and Pitch, $\alpha_0 = 15^0$, $\bar{\alpha} \approx 5^0$, $\bar{\omega} \approx 0.5$ (Ref. 11)

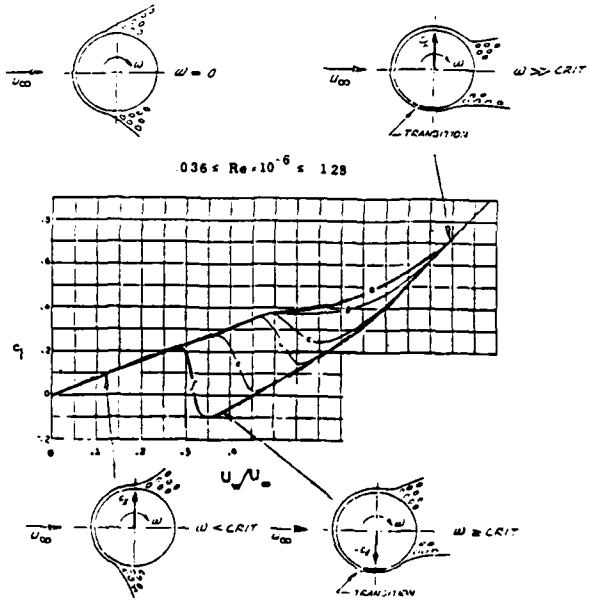

Fig. 14 Moving Wall Effects on a Circular Cylinder in Laminar Flow

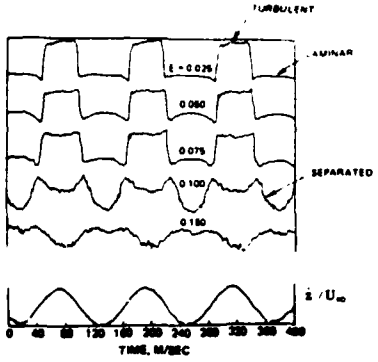

a Plunging

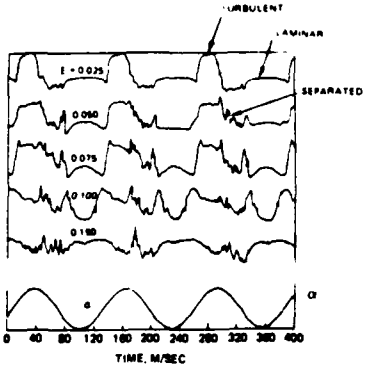

b. Pitching

Fig. 16 Hot Film Response for Pitching and Plunging Oscillations of a NACA-0012 Airfoil at $\alpha_o = 15^o$ $\bar{\alpha} = 5^o$, and $\bar{\omega} = 0.5$ (Ref. 11)

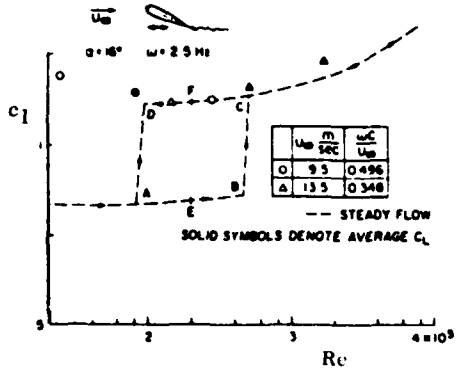

Fig. 19 Hysteresis Effects for an Airfoil Oscillating with a Streamwise Amplitude $\Delta x/c = 0.565$ (Ref. 15)

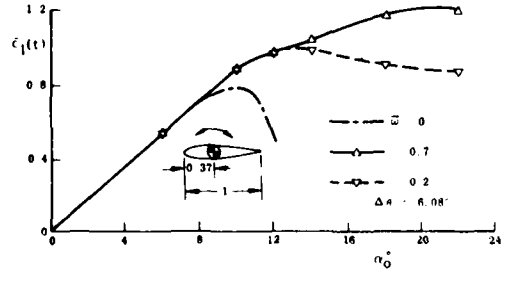

Fig. 20 Time Average Lift of a Thin Airfoil Describing Pitch Oscillations at $Re = 10^6$ (Ref. 29)

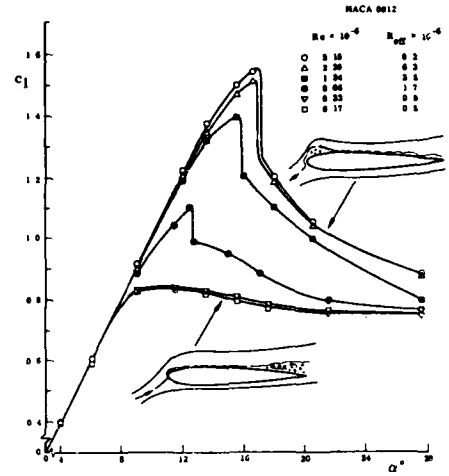

Fig. 17 Effect of Reynolds Number on the Lift Characteristics of the NACA-0012 Airfoil (Ref. 22)

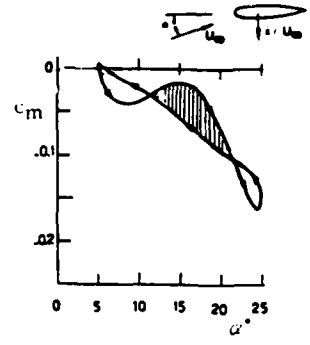

a. Plunging (Ref. 9)

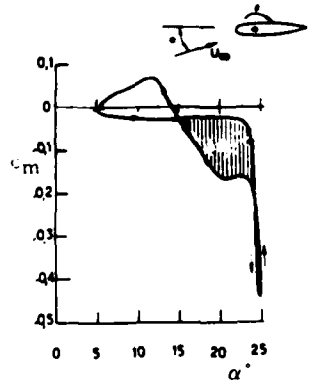

b. Pitching (Ref. 28)

Fig. 18 Moment Loops for Plunging and Pitching Oscillations of the NACA-0012 Airfoil

UNSTEADY BOUNDARY-LAYER SEPARATION ON AIRFOILS PERFORMING LARGE-AMPLITUDE OSCILLATIONS - DYNAMIC STALL -

by

W. Geissler
Institut für Aeroelastik, DFVLR-AVA
Bunsenstr. 10, D-3400 Göttingen
West Germany

SUMMARY

Experimental investigations have exposed a strong dependency of unsteady separation characteristics in the regime of dynamic stall on airfoil shape, Reynolds and Mach number, frequency and time-dependent incidence. A suitable prediction method should therefore be able to account for these various parameters. Coupling procedures between two-dimensional unsteady boundary layers and inviscid surface singularity methods (panel methods) have been developed for analytical investigation of unsteady turbulent separation. In the present study, the influence of various parameters on unsteady separation is discussed in detail and comparison with experimental data is made. The results show that, even for weak coupling between boundary layer and inviscid boundary conditions, good correspondence exists between theory and experiment with respect to the development of unsteady separation.

1. INTRODUCTION

Extensive experimental data in the dynamic stall regime have been measured by McCroskey et al [1] on eight different helicopter-relevant airfoil sections. Influence of airfoil shape, incidence variation, reduced frequency, Reynolds and Mach number on the dynamic stall characteristics is discussed in detail. For analytical treatment of this problem, a finite-difference procedure has been developed recently to calculate unsteady laminar boundary layers on oscillating airfoils [2]. Unsteady separation characteristics and the correspondence between two-dimensional unsteady and three-dimensional steady separation have been investigated. In the present study, this method is extended to unsteady turbulent boundary layers using the eddy viscosity formulation of Cebeci and Smith [3]. A new time-marching procedure has been developed to calculate the outer boundary condition for the unsteady boundary layer on the basis of a surface singularity method (panel method) [4]. Weak coupling between boundary layer and panel method serves as a first step. Subsequent extension of the method to include strong coupling in the time domain is straightforward.

The present investigation is a study of unsteady turbulent separation. It has already been found in the laminar case that reversed flow areas occur before the boundary layer separates. With the second-order central finite-difference procedure of the Crank-Nicolson type, it is possible to initiate the "marching-through" process in these areas. The calculations break down, however, due to a severe increase of the normal velocity inside the boundary layer. Variation of the mesh spacing in time and space has only a minor influence on the location of breakdown. The time-dependent breakdown locations are therefore interpreted as locations of separation. It will be shown that comparisons with experimentally-determined reversed flow areas (from Ref. [1]) are in good correspondence with calculated results.

2. INVISCID BOUNDARY CONDITION (PANEL METHOD)

A singularity method with a combination of sources and vortices on the real surface of the profile has been developed directly in the time domain. This time-marching procedure renders the method suitable for direct coupling with unsteady boundary-layer methods. Contrary to Ref. [5], the vorticity distribution is also placed on the profile surface instead of being arbitrarily distributed inside the profile. The vorticity strength on the profile is assumed to be constant per time step. The (vorticity) loading of the wake (γ_w) is determined by the time-dependent rate of change of the profile vorticity ($\gamma_p(t)$). The wake geometry is prescribed and subdivided into panels corresponding to the profile surface.

Using the notation of Figure 1, the relationship between surface vorticity and wake vorticity can be specified with

$$(1) \qquad \frac{\partial \Gamma_p}{\partial T}\, dT = \frac{\partial}{\partial T}\left(\oint_s \gamma_p\, ds\right) dT = \frac{\partial \gamma_p}{\partial T}\, dT\, s_p$$

as the time-dependent change of profile vorticity ($s_p \triangleq$ total arc length of profile) and

$$(2) \qquad \gamma_w = -s_p \frac{d\gamma_p}{dT} ; \qquad ds_w = dT\,(U_\infty = 1)$$

as the loading of a wake panel shed at nondimensional time T:

$$(3) \qquad T = \frac{t \cdot U_\infty}{c} .$$

It is assumed that the wake panels move downstream with the undisturbed flow velocity U_∞.

Adding the prescribed kinematic velocity $\vec{V}_{kin}$ due to the oscillatory movement of the profile and the induced velocities of source distributions ($\vec{v}_q$) on the profile surface and vorticity distributions ($\vec{v}_\gamma$) on both profile surface and wake, the kinematic flow condition (zero normal velocity) for control points on the profile can be expressed by

$$(4) \qquad \vec{\zeta}\,(\vec{V}_{kin} + \vec{v}_q + \vec{v}_\gamma) = 0 ; \qquad (\vec{\zeta} \triangleq \text{outer unit normal vector}).$$

The unknown source strengths of the surface panels can be determined by solving a large system of linear equations (corresponding to the number of panels). The vorticity strength $\gamma_p(t)$ is first set to unity and is later solved by application of the Kutta condition, assuming zero pressure difference between the two

control points adjacent to the trailing edge. The loading of the wake panels downstream of the first wake element is known from previous time steps. Finally, pressures are calculated from the unsteady Bernoulli equation

$$(5) \qquad c_p(\bar{T}) = -2\,\frac{\omega^*}{2\pi}\,\frac{\partial\phi}{\partial\bar{T}} + \vec{V}_{kin}\,\vec{V}_{kin} - \vec{w}\,\vec{w} \ ,$$

with

$$(6) \qquad \bar{T} = T\,\frac{\omega^*}{2\pi} \ ; \qquad \omega^* = \frac{\omega c}{U_\infty} \quad \text{(reduced frequency)} \ ; \qquad \phi \triangleq \text{velocity potential} \ .$$

$$(7) \qquad \vec{w} = \vec{V}_{kin} + \vec{v}_q + \vec{v}_\gamma$$

is the relative velocity vector at a surface control point.

The overall procedure starts with quasi-steady values at an arbitrary time T. Three calculation periods are sufficient to obtain a final solution. It should be mentioned at this point that the method can easily be modified to account for boundary-layer displacement. In this case, the right-hand side of Eq.(4) is no longer zero but is given by the blowing velocity:

$$(8) \qquad v_B = \frac{\partial}{\partial s}\,(\delta_1\,U_e)$$

($\delta_1 \triangleq$ boundary-layer displacement thickness; $U_e \triangleq$ edge velocity of the boundary layer), which can be interpreted as the effect of an additional surface source distribution with source strengths obtained from the boundary-layer calculation.

3. UNSTEADY TURBULENT BOUNDARY-LAYER CALCULATION

3.1 Equations (stagnation-point-fixed)

With the unsteady inviscid calculation procedure of Section 2 it is possible to determine the time-dependent locations of the front stagnation point. Figure 2 shows the coordinate (s_{sp}) as a function of time for the incidence variation

$$\alpha = 15° + 10° \sin\omega^* T \ ; \qquad \omega^* = 0.2 \ .$$

Curves are plotted for NACA 0012 and AMES-A01 airfoil sections. The movements of the stagnation points are 180° out-of-phase with respect to the movement of the profile and are nearly harmonic in time.

In order to have a well-defined starting point for the boundary-layer calculations on the upper and lower surface, the unsteady boundary-layer equations are transformed into a stagnation-point-fixed frame of reference. With this procedure a complicated upstream marching scheme [6] is avoided. The coordinate transformation from body-fixed to moving coordinates yields

$$(9) \qquad \begin{aligned} x_{1u} &= s - s_0 + d\,e^{i\omega^* T} \ , \\ x_{1\ell} &= -(s - s_0) - d\,e^{i\omega^* T} \ . \end{aligned}$$

Indices u and ℓ refer to the upper and lower surface, respectively; body-fixed coordinate s lies on the surface (see Fig.1). The kinematic velocity of the stagnation point (assuming harmonic time-dependency) is given by

$$(10) \qquad U_{1kin} = \frac{\partial x_1}{\partial T} = \pm\, i\omega^*\, d\, e^{i\omega^* T} \ .$$

In Eqs.(9) and (10), d is the amplitude of the oscillating stagnation point. With Eq.(10), the velocities within the boundary layer are transformed (index "1" $\triangleq$ stagnation-point-fixed) to:

$$\begin{aligned} u_1(\eta_1) &= u + U_{kin} \ , \\ (11) \qquad \bar{v}_1(\eta_1) &= \bar{v} \ : \qquad \bar{v} = v\sqrt{Re} \ : \qquad Re = \frac{U_\infty c}{\nu} \ \text{(Reynolds number)} \ , \\ \eta_1 &= \eta \ : \qquad \eta = y\sqrt{Re} \qquad \text{(coordinate normal to wall)} \ . \end{aligned}$$

All lengths in Eqs.(9-11) are referred to chord length c of the profile; all velocities are referred to the undisturbed main-flow velocity U_∞. With transformations (9)-(11), the two-dimensional unsteady boundary-layer equations in stagnation-point-fixed coordinates are

$$(12) \qquad \frac{\partial u_1}{\partial x_1} + \frac{\partial \bar{v}_1}{\partial \eta_1} = 0$$

$$(13) \qquad \frac{\partial u_1}{\partial T} + u_1\,\frac{\partial u_1}{\partial x_1} + \bar{v}_1\,\frac{\partial u_1}{\partial \eta_1} = \frac{\partial U_1}{\partial T} + U_1\,\frac{\partial U_1}{\partial x_1} + \frac{\partial}{\partial \eta_1}\left\{\left(1 + \frac{\varepsilon_1}{\nu}\right)\frac{\partial u_1}{\partial \eta_1}\right\} \ .$$

with the boundary conditions

$$(14) \qquad \begin{aligned} \eta_1 = 0 \ : \qquad & u_1 = \pm\, U_{1kin} = \pm\, i\omega^*\, d\, e^{i\omega^* T} \ : \qquad \bar{v}_1 = 0 \ . \\ \eta_1 \to \infty \ : \qquad & u_1 = U_1 \pm i\omega^*\, d\, e^{i\omega^* T} \ . \end{aligned}$$

Eqs.(12)-(14) represent final expressions which are then discretized and solved numerically. The upper/lower sign in Eqs.(14) refer to the upper/lower surface of the profile.

3.2 Initial conditions

To commence the numerical boundary-layer calculations, initial conditions must be specified at a given time T_0 for all x_1 and at a given x_1 for all T. Initial conditions at $T = T_0$ for all x_1 along the profile surface are obtained by solving the steady boundary-layer equations with $\partial u_1/\partial T$ and $\partial U_1/\partial T = 0$ in Eq.(13). Initial conditions at all time steps close to the front stagnation point at $x_1 = \Delta x_1$ are derived from the stagnation-point case (linear term) of the Falkner-Skan series. With

$$U_1(x_1,T) = cx_1 + U_{1kin}(T) \tag{15}$$

prescribed, the velocities inside the boundary layer yield

$$\begin{aligned} u_1(x_1,T) &= cx_1\, f'(\eta_1) + U_{1kin}(T)\ , \\ \bar{v}_1(x_1,T) &= -\sqrt{c}\, f(\eta_1)\ . \end{aligned} \tag{16}$$

The (steady-laminar) boundary-layer equations are then transformed into an ordinary differential equation

$$f''' - f'^2 + f\,f'' + 1 = 0 \tag{17}$$

with the boundary conditions

$$\begin{aligned} &\eta_1 = 0\ ; \qquad f = 0\ ; \qquad f' = U_{1kin}\ , \\ &\eta_1 \to \infty\ ; \qquad f' = U_1 + U_{1kin} \quad (U_{1kin} \text{ taken from Eq.(10)}). \end{aligned} \tag{18}$$

Eqs.(17) and (18) are solved for each time step, taking into account the corresponding time-dependent values of U_1 and U_{1kin}. Initial conditions in the time domain are therefore determined on a quasi-steady basis.

3.3 Eddy viscosity model, transition

To specify the eddy viscosity term ε_1 in the momentum equation (13), the first formulation appearing in Ref. [7] is used. To obtain ε, the boundary layer is subdivided into two regions: a region close to the wall with

$$\begin{aligned} &\frac{\varepsilon_{1i}}{\nu} = \left\{0.16\sqrt{Re}\,\eta_1^2 \left|\frac{\partial u_1}{\partial \eta_1}\right| \left[1 - e^{-y'/A}\right]^2\right\} \gamma_{tr}\ ; \qquad y'/A = \frac{\eta_1}{26}\, Re^{1/4} \left|\frac{\partial u_1}{\partial \eta_1}\right|_{max}^{1/2}\ , \\ &\left|\frac{\partial u_1}{\partial \eta_1}\right|_{max}^{1/2}\ , \end{aligned} \tag{19}$$

as the maximum value inside the boundary layer, and an outer region with

$$\frac{\varepsilon_{1o}}{\nu} = 0.0168\sqrt{Re}\, U_1\, \delta_1\, \gamma_{tr} \tag{20}$$

and

$$\delta_1 = \int_0^\infty \left(1 - \frac{u_1}{U_1}\right) d\eta_1 \tag{21}$$

as the boundary-layer displacement thickness. Both inner and outer regions are matched by the condition of continuity of the eddy viscosity formulas.

The expressions for ε_{1i} and ε_{1o} (Eqs.(19) and (20)) are each multiplied by the intermittency factor γ_{tr} which yields a smooth transition from laminar to fully-developed turbulent flow ([7]):

$$\begin{aligned} \gamma_{tr} &= 1 - e^{-E}\ , \\ E &= \frac{8.35\cdot 10^{-4}\, U_1^3}{(U_1 x_1)_{tr}^{1.34}}\, Re^{0.66}\, (x_1 - x_{1tr}) \int_{x_{1tr}}^{x_1} \frac{dx_1}{U_1}\ . \end{aligned} \tag{22}$$

x_{1tr} in Eq.(22) is the prescribed position of the beginning of the transition region. Although Eq.(22) is taken into account in the present calculation procedure, the influence of transition is not investigated here, see [8]). The beginning of transition is assumed always one step (Δx_1) behind the stagnation point with the laminar initial conditions obtained from Eqs. (15)-(18).

3.4 Finite-difference calculations

For both initial steady and unsteady solution procedures, second-order central differences of the Crank-Nicolson type are used for discretization of the various derivatives in Eqs.(12) and (13). The solution vector of the new level is obtained by solving a linear system of equations with a tri-diagonal coefficient matrix. The solution is carried out iteratively, starting with linear extrapolated initial values from the previous positions. For the eddy viscosity values in Eqs.(13), the known values from the previous iteration level are used. The iteration process is stopped until the wall shear-stress τ_w between two iterations is smaller than a prescribed small number

$$\left|\tau_w^i - \tau_w^{i-1}\right| < \varepsilon = 10^{-3}\ . \tag{23}$$

The detailed finite-difference expressions of Eqs.(12) and (13) are given in [9].

4. RESULTS

Some characteristic results of the experimental study [1] are displayed in Figure 3. The development of separation (and reattachment) for four different airfoil sections is represented by bold lines, including arrows which indicate the directions of the moving separation event. The thick supercritical NLR-7301 airfoil shows separation extending from the trailing edge toward the leading edge. For the thin NLR-1 profile, separation starts close to the leading edge and moves downstream. In the VR-7 case, separation areas develop at the leading edge moving downstream and at the trailing edge moving upstream. For the AMES-A01 profile, separation occurs on the entire profile surface extending in upstream and downstream directions. Reattachment takes place for all profiles from the leading to the trailing edge. Fig.3 shows also the various locations of the laminar separation bubbles which are not investigated further in the present study. The NACA 0012 and NLR-7301 profiles produce similar effects as long as the Reynolds number is not too low ($Re > 10^6$). To ascertain whether these complicated types of separation characteristics can be predicted analytically by the present method, the two airfoil sections NACA 0012 and AMES-A01 are investigated in detail for two incidence cases:

1) $\alpha = 15° + 6° \sin\omega^* T$ - light stall conditions ,

2) $\alpha = 15° + 10° \sin\omega^* T$ - deep stall conditions .

Reynolds numbers and reduced frequencies are varied for these cases and results are compared with experimental data.

4.1 NACA 0012, $\alpha = 15° + 6° \sin\omega^* T$

Figure 4 shows hysteresis curves of the unsteady separation and reattachment boundaries on the profile upper surface for three different Reynolds numbers. These curves must be followed in the direction indicated by the arrows. The coordinate x_1 has its origin at the stagnation point. For the case $Re = 10^6$, the calculated reversed flow area is displayed by the shaded region. Separation is indicated by the breakdown of the boundary-layer calculation due to a strong increase of the normal velocity inside the layer, as described above. Separation takes place during the upstroke at $15 \leq \alpha \leq 21°$. Reattachment ($18° \geq \alpha \geq 9°$, during downstroke) is approximated by the line $\tau_w = 0$. This part of the cycle is found by extrapolation of the boundary-layer velocity profile into the separated region. This procedure yields a certain numerical scattering which has been somewhat smoothed out in Fig.4.

It is interesting to note that an increase of the Reynolds number over one order of magnitude reduces the area of the hysteresis loop considerably. In this Reynolds number range, separation always takes place from the trailing edge continuously toward the leading edge. The steepness of the curves indicates the magnitude of the separation (and reattachment) velocities. In Fig.4, vertical (α = const.) and horizontal (x_1 = const.) arrow indicate locations where details inside the boundary layer are plotted.

Figure 5 shows contour plots of equal velocity u_1 (Fig.5a) and equal vorticity $\gamma = (\partial u_1/\partial \eta_1)$ (Fig.5b) in the x_1, η_1-domain for $\bar{T} = 1.15$ ($\alpha = 19.85°$, upstroke). The reversed flow area extending from the rear to the front, covering large parts of the profile upper surface, can be seen in Fig.5a. The region of negative wall shear reaches $x_1 = 0.45$ at this incidence. Similar to laminar results, the lines of equal vorticity form tongues extending downstream (Fig.5b). The dashed lines in Figs.5 indicate the median values of u_{1m} and γ_m for orientation purposes.

The situation along the horizontal arrow in Fig.4, i.e. for variable time $\bar{T}$ at a specific x_1-location ($x_1 = 0.35$), is given in the 3-d plots of Figures 6a and 6b (u_1-velocity and γ-vorticity, respectively). The velocity profiles of Fig.6a change from Blasius type at the beginning of the cycle ($\bar{T} = 0.75$) to s-shaped profiles with reversed velocities at the wall for the maximum of $\bar{T}$ ($\approx 1.16 \triangleq \alpha \approx 20°$↑). The vorticity distribution (Fig.6b) has a maximum at the wall at $\bar{T} = 0.75$ ($\alpha = 5°$). This maximum decreases rapidly and shifts away from the wall with increasing time. Finally, negative vorticity is produced in regions of reversed flow. The maximum value of x_1 in Figs.5 (right-hand margin) and the maximum value of $\bar{T}$ in Figs.6 coincide with the location of breakdown of the boundary-layer calculation (see end points of the vertical and horizontal arrows in Fig.4). The smooth behavior of the u_1-velocity and vorticity distributions in these areas do not directly indicate the reason for the breakdown. The reason is found in the behavior of the normal velocity $\bar{v}_1$, as will be shown below.

4.2 AMES-A01, $\alpha = 15° + 6° \sin\omega^* T$, $\omega^* = 0.5$

Corresponding results for the AMES-A01 airfoil section with the same incidence variation, reduced frequency and Reynolds number range are displayed in Figures 7 to 9. A notable difference occurs in Fig.7 compared to the NACA-0012 case in Fig.4: for the two lower Reynolds numbers (10^6, $3 \cdot 10^6$) a reversed flow area develops again at the trailing edge ending in separation which is moving slowly upstream. At a specific incidence during upstroke (for instance at $\alpha \approx 18.5°$↑, $Re = 10^6$), a second reversed flow area develops at about $x_1 = 0.3$. This area is extending very quickly towards the trailing edge and slowly towards the leading edge. Between these two reversed flow areas, the flow is directed downstream throughout the entire boundary layer. At a specific incidence ($\alpha \approx 19.9°$), breakdown occurs at $x_1 = 0.325$ (indicated by ⊛). For higher incidences it is not possible to extend the boundary-layer calculation beyond this point. A connection between the rear and front separation areas is therefore indicated in Fig.7 by a dashed line between the ⊛-points. Reattachment also takes place in one large discontinuous step, smoothing out at further reduced incidences. For $Re = 10^7$ the hysteresis loop looks almost identical to the NACA 0012 case. No front separation or front reversed flow area occurs in this case.

Fig.8 shows again velocity (Fig.8a) and vorticity (Fig.8b) contours along the vertical arrow ($\alpha \approx 19.4°$↑) of Fig.7. This section crosses the two reversed flow areas. Closed loops of equal velocity contour indicate a reversed flow area at about $x_1 = 0.35$, which is located very close to the wall. The rear reversed flow area has a similar form as seen in Fig.5a for the NACA 0012 case, but its extension upstream is limited: negative wall shear-stress is extended only to $x_1 \approx 0.75$. Interestingly, the contour lines of vorticity in Fig.8b show closed loops downstream of the reversed flow area. These loops are located around a vorticity maximum there. Marching against the separation line along the horizontal arrow in Fig.7 ($x_1 = 0.35$) the corresponding 3-d plots show similar behavior for velocity (Fig.9a) and vorticity (Fig.9b) distributions compared to Figs.6a and 6b of the NACA 0012 airfoil.

4.3 Normal velocities, separation criterion

Figures 10a (NACA 0012) and 10b (AMES-A01) display the variations of normal velocity $\bar{v}_1$ following the horizontal arrows of Figs.4 and 7, respectively (x_1 = const.). The normal velocities increase rapidly up to a steep maximum at $\bar{T}$. A breakdown of the numerical boundary-layer calculation occurs due to the severe steepening of the normal velocities in the outer region of the boundary layer. The typical behavior of $\bar{v}_1$ is therefore used as a separation criterion in the present method. All separation lines presented in this study coincide with numerical breakdown. It is quite obvious that such a numerically-derived separation criterion is not fully satisfactory. But, similar to steady three-dimensional separation, a simple analytical criterion in unsteady flow does not exist. The question whether the so-called Moore, Rott and Sears criterion [10] is applicable to these results has not been investigated. For such investigations, a transformation of the coordinates into a separation-point-fixed frame of reference must be achieved. But in the present method, the movement of the separation (reattachment) event is part of the solution. It is possible to perform the transformation in a second step (after the numerical calculation) but this is not straightforward. Fig.4 shows very complicated (and by no means harmonic) time-dependent movements of the separation point, which makes a transformation very difficult. In the case of the AMES-A01 profile (Fig.7), parts of the separation line (moving downstream, during upstroke) are even located in a "forbidden" zone and cannot be treated by the weak interaction procedure of the present method. In order to cover this part of the cycle as well, a strong interaction procedure combined with inverse boundary-layer calculations will be necessary, as outlined in a later section.

Figs.4 and 7, however, show that the experimentally-determined trends of separation movements (Fig.3) can be predicted quite well with the present numerical procedure. It will be shown below that the analytical results correspond also quantitatively quite well with experimental data.

4.4 NACA-0012, $\alpha = 15° + 10° \sin\omega^* T$, $\omega^* = 0.2$

Results of separation and reattachment for the high amplitude case are plotted in Figure 11. Reversed flow boundaries have been measured in Ref. [1] by means of reversed flow sensors, which are specially designed hot-wire probes. The results are given in Ref. [1] in profile-fixed coordinates and have been transformed into the stagnation-point-fixed frame (x_1), taking into account the instantaneous positions of the stagnation points in Fig.2. The experimental data are also indicated in Fig.11. For the two higher Reynolds numbers ($Re = 10^6$, $1.5 \cdot 10^6$) correspondence between theory and experiment is very good. One has to keep in mind that, on the one hand, flow reversal and separation are in close coincidence and that, on the other hand, a weak coupling procedure is used, where the pressure peak in the leading edge area is not changed during the cycle, although a breakdown of pressures takes place in the experiment due to dynamic stall. The largest deviation can therefore be observed in the leading edge region.

For the lowest Reynolds number ($Re = 0.5 \cdot 10^6$) the agreement is less satisfactory, although the trend is in the right direction. The experimental data even show a development of flow reversal from the leading to the trailing edge. Analytical results show a severe steepening of the separation curve. Reversed flow occurs over nearly 50% of the airfoil upper surface for this Reynolds number. The reversed flow area and separation line react quite sensitively to further reduction of the Reynolds number: for $Re = 10^5$ (not pictured in Fig.11) a similar trend can be observed as in the experimental results for $Re = 0.5 \cdot 10^6$. A reversed flow area now develops in the leading edge region as well at about $x_1 = 0.15$ and $\alpha \approx 15°$. Thus, at this low Reynolds number, similar behavior for the NACA-0012 airfoil is evident as was the case for the AMES-A01 airfoil: over part of the oscillatory cycle two reversed flow areas coexist. The difference between theory and experiment for the smaller Reynolds number may also be explained by simple treatment of transition in the calculation procedure (see Section 3.3).

4.5 AMES-A01, $\alpha = 15° + 10° \sin\omega^* T$, $\omega^* = 0.2$

Figures 12a-c display time-dependent separation and reattachment for the AMES-A01 profile at slightly different Reynolds numbers: $Re = 10^6$ (Fig.12a), $Re = 1.5 \cdot 10^6$ (Fig.12b) and $Re = 2.5 \cdot 10^6$ (Fig.12c). Corresponding experimental data for flow reversal are again indicated in the plots. For the two higher Reynolds numbers, the trend has now changed: reversed flow areas develop over the entire profile (at about $x_1 \approx 0.35$) and spread downstream. A breakdown of the boundary-layer calculation at the front reversed flow area (indicated by ⊗ in Figs.12) prevent the calculation to be extended farther downstream. In this case, however, it is quite obvious that the reversed flow areas and separation lines extend downstream as can be seen from the experimental data. Large deviations occur again in the leading edge region due to the same reasons discussed in Section 4.4 for the NACA 0012 airfoil.

4.6 NACA-0012, frequency variation

Finally, another important parameter for unsteady separation, frequency (i.e. the characteristic speed of the oscillatory movement), is investigated and presented in Figure 13. Frequency is made nondimensional in the usual manner by means of U_∞ and chord length c of the profile (see Eq.(6)). Fig.13 gives only the effects of frequency on the separation lines. The trend is a shift of separation lines to increasing incidences with increasing ω^*. Consequently, the curves steepen considerably. In the case $\omega^* = 1$, a reversed flow area develops again at about $x_1 = 0.2$ in addition to a corresponding rear reversed flow area at the same time. For this case a calculated reversed flow area extends over 76% of the wing's upper surface. Breakdown of the boundary layer takes place very abruptly from back to front.

Similar frequency influences are also observed for other flow cases and airfoils and have also been found experimentally.

4.7 Possible extension to strong coupling procedures

To investigate the behavior of some characteristic boundary-layer quantities, τ_w (wall shear-stress), δ_1 (boundary-layer displacement thickness) and v_B (blowing velocity)

$$(24) \quad v_B = \frac{\partial}{\partial x_1} (\delta_1 \cdot U_e)$$

are plotted in Figures 14 at the positions of the horizontal arrows in Fig.11 and Fig.12c. The wall shear-stress τ_W (Fig.14a) crosses the zero line in both cases. The calculation is extended through reversed flow regions until breakdown occurs at $x_1 \approx 0.61$ (NACA 0012) and $x_1 \approx 0.8$ (AMES-A01). Characteristic differences can be observed for both cases: for the NACA-0012 airfoil the wall shear-stress develops continuously throughout the reversed flow region until breakdown. For the AMES-A01 profile, the τ_W-curve falls from the leading edge region very steeply, reaches a minimum and then increases after a second minimum. At this incidence ($\alpha = 21.4°$) the wall shear-stress remains negative and decreases again at higher x_1-values until breakdown.

Fig.14b shows the boundary-layer displacement thicknesses for the same cases. Prominent in this instance is the s-shape of the δ_1-curve in the AMES-A01 case. The most severe steepening of the δ_1-curve coincides with the minimum wall shear-stress of Fig.14a.

Evaluation of the differentiation in Eq.(24) leads to the blowing velocity v_B displayed in Fig.14c. These curves have been smoothed to compensate for irregularities due to the numerical differentiation. A very strong double peak exists for the AMES-A01 profile which coincides again with the region of minimum wall shear in Fig.14a and with the steepening of the δ_1-curve in Fig.14b. A severe steepening of the v_B-curve is also observed toward breakdown. The behavior of the v_B-curves in the NACA-0012 case is much less dramatic. Nevertheless a maximum exists in the leading edge region but there is no severe increase toward breakdown.

The blowing velocities are indicative of the effect of the boundary layer on the external inviscid boundary condition. In further developments of the present coupling procedure, this effect of the boundary layer on the outer boundary condition should be taken sufficiently into account. To do so, the kinematic flow condition (Eq.(4)) is simply modified

$$(25) \quad \vec{\zeta}\,(\vec{V}_{kin} + \vec{v}_q + \vec{v}_\gamma) = v_B \,.$$

v_B is assumed to be simulated by a continuous source distribution on the profile surface such that the displacement effect of the boundary layer is taken into account. The magnitude of v_B is known by means of the boundary-layer calculation (Eq.(24)).

The interaction between boundary layer and inviscid outer boundary condition can be performed iteratively at a particular time $\bar{T}$, starting with v_B-values of the previous time-step as initial values. The iteration can also be done in an inverse boundary-layer calculation, modifying the outer boundary condition directly during the development of the boundary layer. It is hoped that, by this latter method, the calculation can be extended farther even into regions of separation as has for instance been shown for steady and unsteady trailing-edge separation using integral equation methods [11].

5. CONCLUSION

For the calculation of turbulent unsteady 2-d boundary layers, a finite difference procedure has been developed and combined with a 2-d inviscid surface singularity method for determination of the outer boundary condition. For investigation of the dynamic stall problem, the following four parameters have been evaluated:

- airfoil shape,
- Reynolds number,
- incidence variation and
- reduced frequency.

The influence of these parameters on separation and reattachment of the flow during a cycle of oscillation have been discussed. Details of the various flow quantities inside the boundary layer are presented. Comparison with experimental data shows good agreement with respect to the time-dependent location of separation. Extension of the present weak coupling procedure to include strong coupling is straightforward.

6. REFERENCES

[1] Carr, L.W., McCroskey, W.J., McAllister, K.W., Pucci, S.L., Lambert, O., An Experimental Study of Dynamic Stall on Advanced Airfoil Sections, NASA TM 84245, 1984; also: USA AVRADCOM TR 82-A-8, 198[illegible].

[2] Geissler, W., Unsteady Laminar Boundary-Layer Calculations on Oscillating Configurations Including Backflow. Part I: Flat Plate, Oscillating in Its Own Plane; Part II: Airfoil in High-Amplitude Pitching Motion - Dynamic Stall, NASA-TM 84319, 1983.

[3] Cebeci, T., Smith, A.M.O., Analysis of Turbulent Boundary Layers. New York: Academic Press, 1974.

[4] Geissler, W., Calculation of Unsteady Airloads on Oscillating Profiles by a Time-Marching Procedure, DFVLR Internal Report IB 232 - 84 J 05, 1984.

[5] Giesing, J.P., Nonlinear Two-Dimensional Unsteady Potential Flow with Lift, J. Aircraft, Vol.5, No.2, March/April 1968, pp.135-143.

[6] Cebeci, T., Carr, L.W., Prediction of Boundary-Layer Characteristics on an Oscillating Airfoil, NASA-TM 81303, 1981.

[7] Cebeci, T., Carr, L.W., Computation of Unsteady Turbulent Boundary Layers with Flow Reversal and Evaluation of Two Separate Turbulence Models, NASA-TM 81259, 1981; also: USA AVRADCOM TR 81-A-5, 1981.

[8] Cebeci, T., Carr, L.W., Calculation of Boundary Layers of Oscillating Airfoils, NASA-TM 8594[illegible], 1984; also: USA-AVSCOM TR 84-A-1, 1984.

[9] Geissler, W., Unsteady Turbulent Boundary-Layer Calculations on Profiles with High Amplitude Pitching Oscillations - Dynamic Stall, DFVLR Internal Report IB 232 84 J 04, 1984.

[10] Teliones, D.P., Unsteady Viscous Flows, Springer Series in Computational Physics, New York/Heidelberg/Berlin: Springer, 1981.

[11] Le Balleur, J.C., Girodroux-Lavigne, P., A Viscous-Inviscid Interaction Method for Computing Unsteady Transonic Separation, 3rd Symp. on Numerical and Physical Aspects of Aerodynamic Flows, Long Beach, USA, Jan. 21-24, 1985.

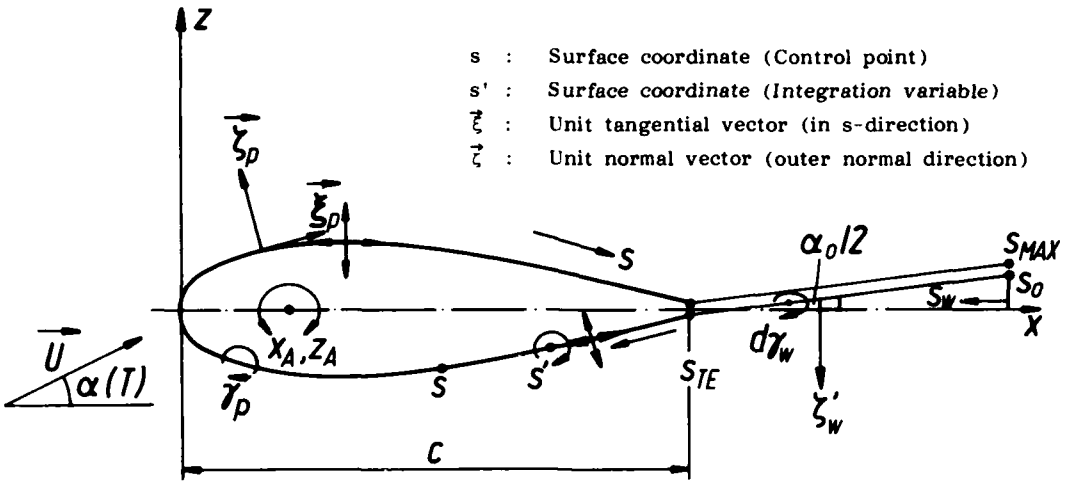

Figure 1: Geometry, nomenclature (inviscid method)

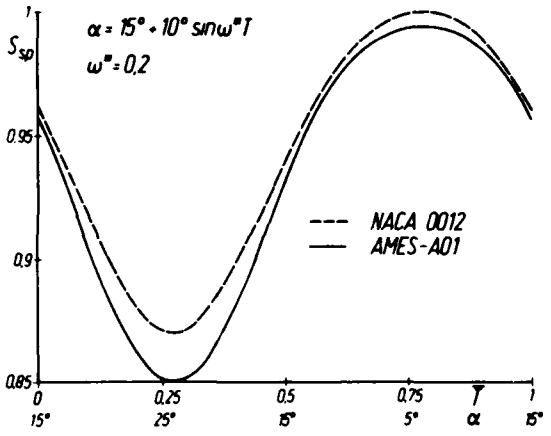

Figure 2: Displacement of stagnation point for NACA 0012 and AMES-A01 profiles; $\alpha = 15° + 10° \sin \omega^* T$, $\omega^* = 0.2$

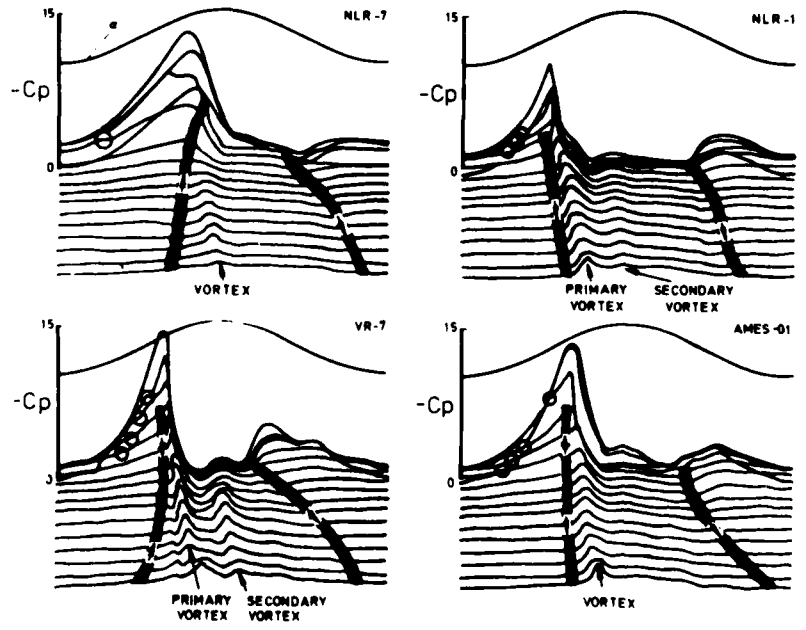

Figure 3: The important stall events for four different types of boundary layer separation (after [1]): Ma = 0.25, $\alpha = 15° + 10° \sin \omega^* T$, $\omega^* = 0.2$ (circles indicate laminar bubbles)

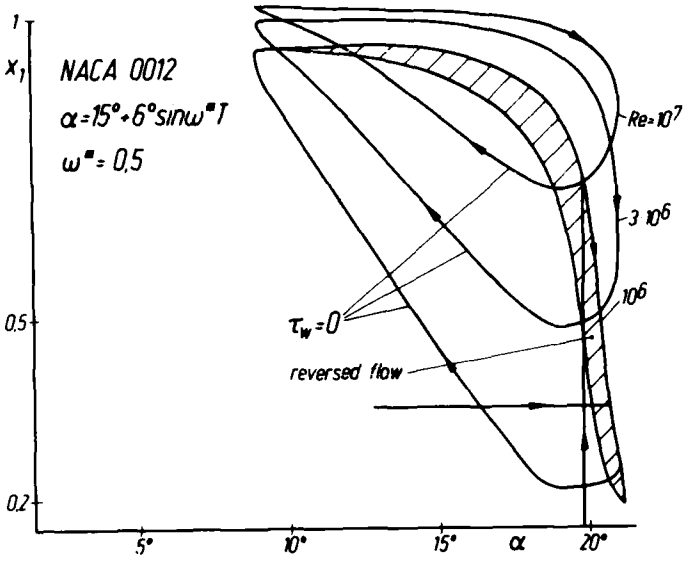

Figure 4: Separation and reattachment on the NACA 0012 airfoil; Re-number variation; light stall conditions

Figure 5: Contour lines of
a) equal u_1-velocities
b) equal vorticities
in the x_1, η_1-domain of Fig.4 (vertical arrow)

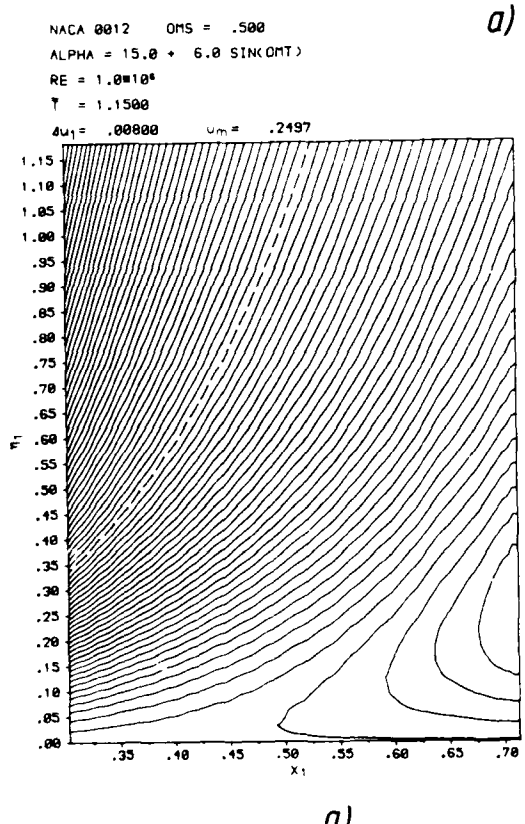

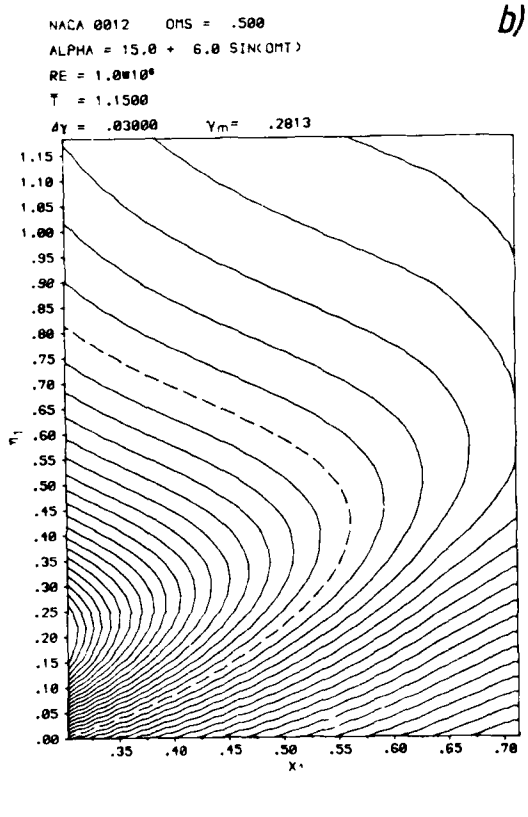

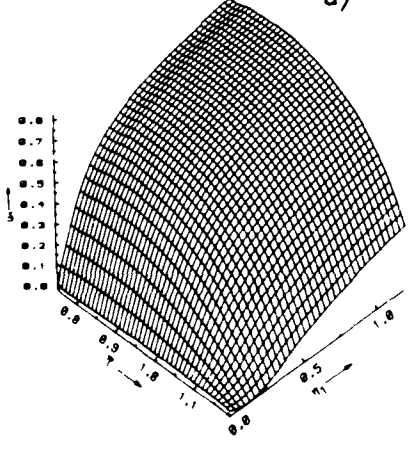

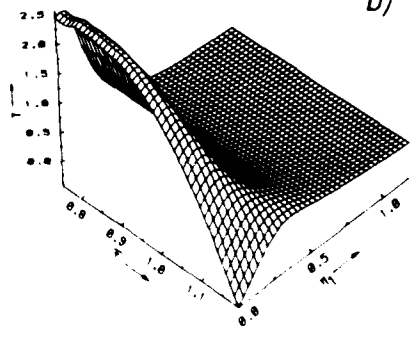

Figure 6: 3-d plots of
a) u_1-velocities
b) vorticities
in the $\bar{T}, \eta_1$-domain of Fig.4 (horizontal arrow): $x_1 = 0.3542$

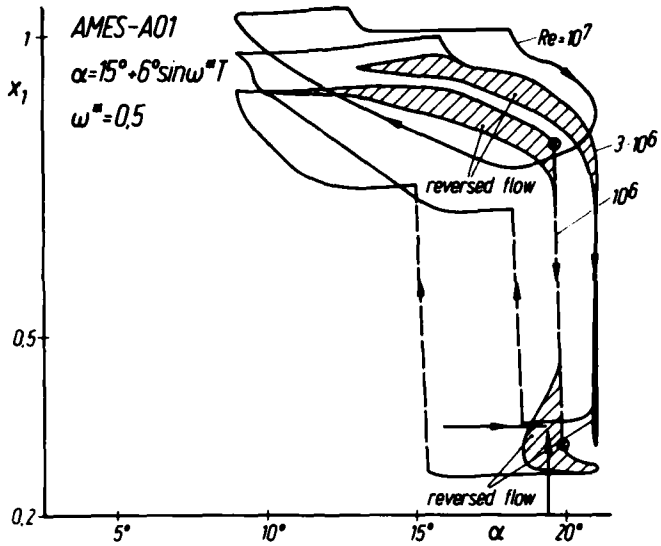

Figure 7: Separation and reattachment on the AMES-A01 airfoil; Re-number variation; light stall conditions

Figure 8: Contour lines of
a) equal u_1-velocities
b) equal vorticities
in the x_1, η_1-domain of Fig.7 (vertical arrow)

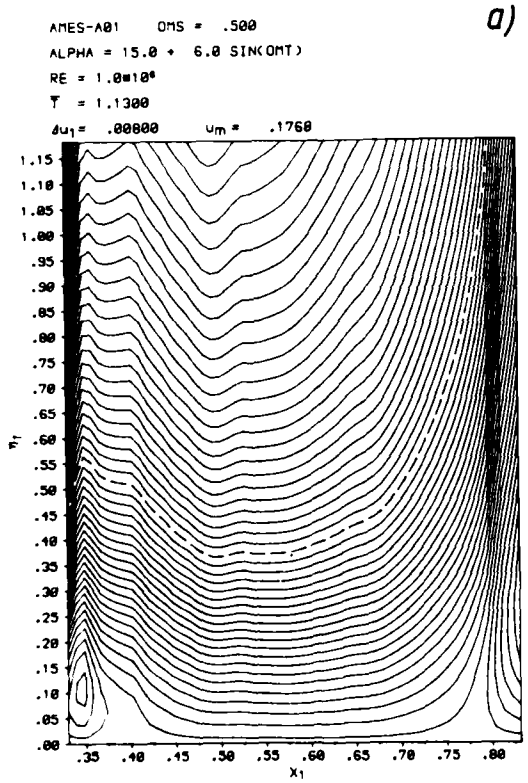

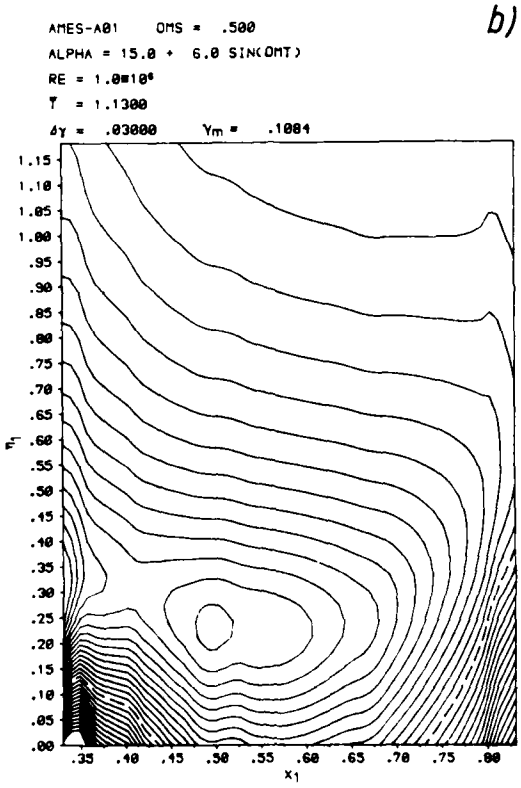

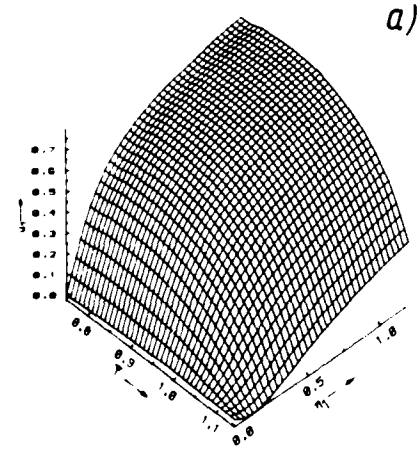

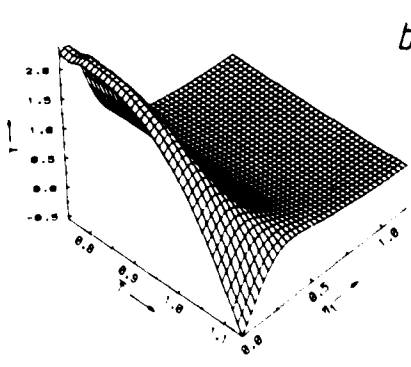

Figure 9: 3-d plots of
a) u_1-velocities
b) vorticities
in the $\bar{T}, \eta_1$-domain of Fig.7 (horizontal arrow):
$x_1 = 0.3538$

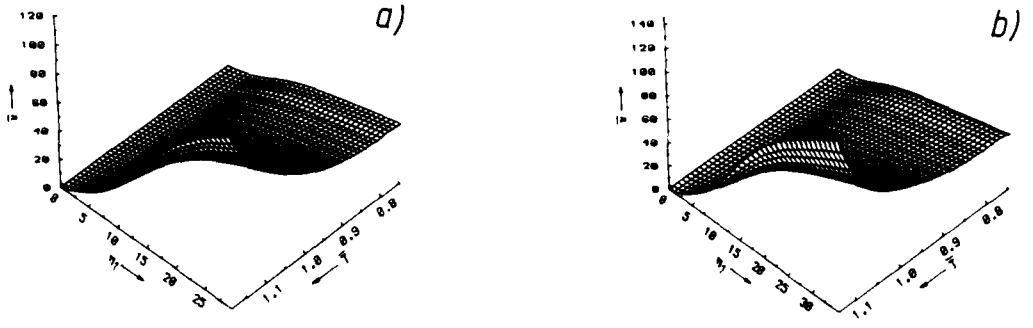

Figure 10: 3-d plots of
a) $\bar{v}_1$-velocities, NACA 0012 ($x_1 = 0.3542$)
b) $\bar{v}_1$-velocities, AMES-A01 ($x_1 = 0.3538$)
in the $\bar{T}, \eta_1$-domain of Figs. 4 and 7 (horizontal arrow)

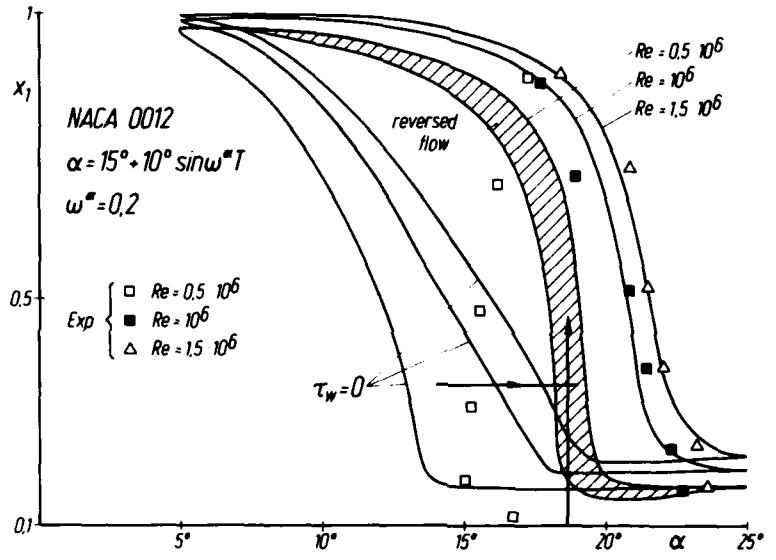

Figure 11: Separation and reattachment on the NACA 0012 airfoil and comparison with experimental data [1]; Re-number variation; deep stall conditions; arrows indicate constant x_1- and α-values for plots of Figs. 14

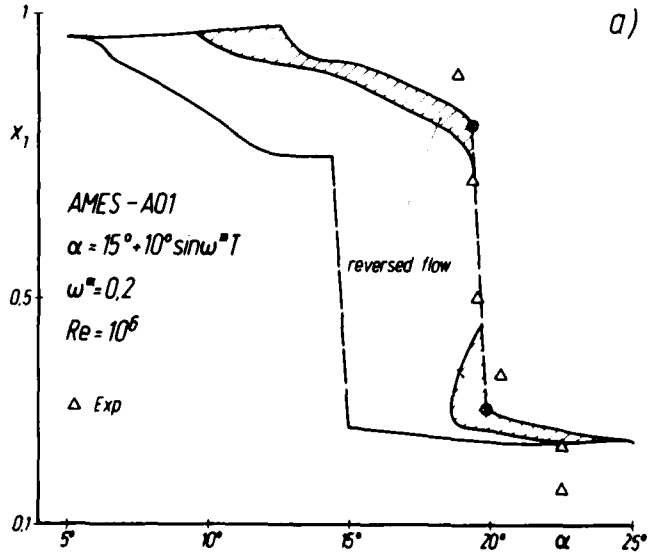

Figure 12: Separation and reattachment on the AMES-A01 airfoil and comparison with experimental data [1]; deep stall conditions
a) Re = 10^6

(arrows indicate constant x_1- and α-values for plots of Figs. 14)

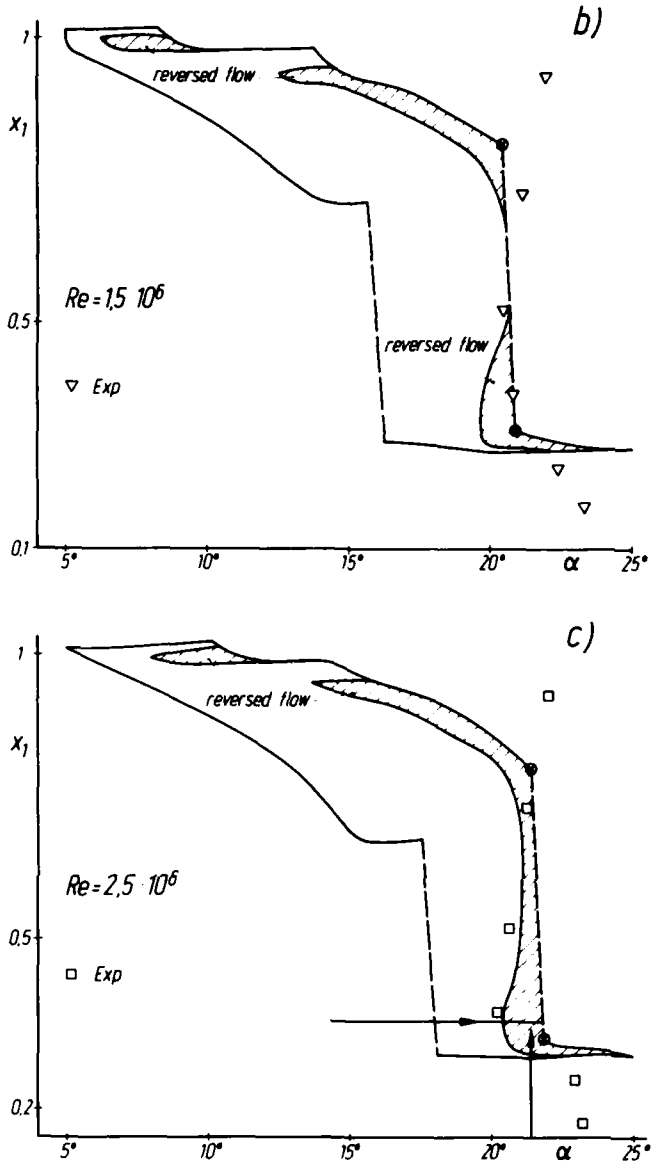

Figure 12: Separation and reattachment on the AMES-A01 airfoil and comparison with experimental data [1]; deep stall conditions
◀ b) Re = $1.5 \cdot 10^6$
◀ c) Re = $2.5 \cdot 10^6$
(arrows indicate constant x_1- and α-values for plots of Figs. 14)

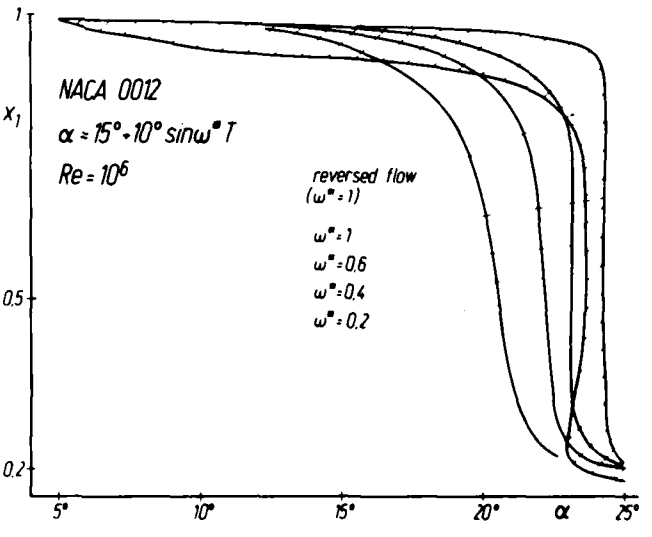

Figure 13: Influence of reduced frequency on unsteady separation (NACA 0012 airfoil); deep stall conditions; Re = 10^6

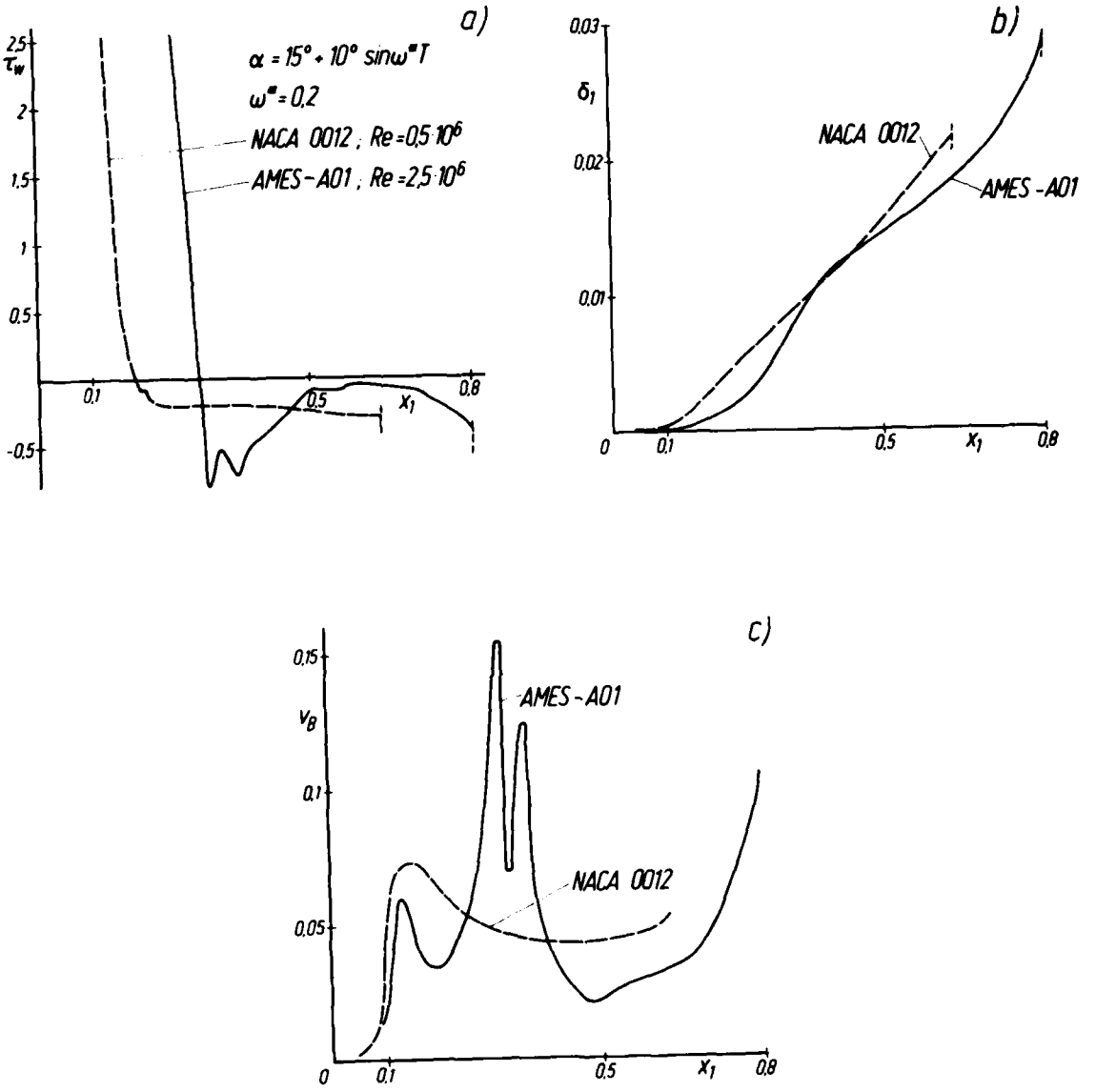

Figure 14: Behavior of
a) wall shear-stress
b) boundary-layer displacement thickness
c) blowing velocity $v_B = \partial/\partial x_1 (\delta_1 \cdot U_e)$ inside reversed flow areas of the NACA 0012 and AMES-A01 profiles

COMPUTATIONAL ASPECTS OF UNSTEADY FLOWS

by
Tuncer Cebeci
MDC Senior Fellow - Fluid Mechanics and Heat Transfer
Douglas Aircraft Company
3855 Lakewood Boulevard, Long Beach, California 90846, USA

L.W. Carr
Research Scientist, US Army Aeromechanics Laboratory
NASA Ames Research Center, Moffett Field, California 94035 USA

A.A. Khattab and S.M. Schimke
Research and Technology, Aircraft Configuration and Performance
Douglas Aircraft Company
3855 Lakewood Boulevard, Long Beach, California 90846, USA

SUMMARY

The paper is concerned with the calculation of unsteady flows and particularly with the development of numerical methods for solving unsteady boundary-layer equations and their application to the flows around practically important configurations such as oscillating airfoils. It provides a brief review of recent work and emphasizes the need for numerical methods which can overcome possible problems associated with flow reversal and separation. The zig-zag and characteristic box schemes are described in this context and, when embodied in a method which permits interaction between solutions of inviscid and viscous equations, the characteristic box scheme is shown to avoid the singularity associated with boundary-layer equations and prescribed pressure gradient. Calculations have been performed for a cylinder started impulsively from rest and oscillating airfoils and the results are presented and discussed. It is concluded, for example, that turbulence models based on an algebraic specification of eddy viscosity can be adequate, that location of transition is important to the calculation of the location of flow separation and, therefore, to the overall lift of an oscillating airfoil.

1.0 INTRODUCTORY REMARKS

Unsteady flows have been of interest for many years and early work, such as that of Lighthill [1] and Glauert [2], established the theory of laminar-flow problems. Physical knowledge of turbulent flows was provided by experiments such as those of Karlsson [3] in which a flat-plate boundary layer was subjected to a periodically varying freestream and of Carr, McAlister and McCroskey [4] who investigated flows around oscillating airfoils. As evidenced by the proceedings volume of Francis and Luttges [5] and the review of Reynolds and Carr [6], recent emphasis has been on the improvement of physical understanding and the need to develop a method to calculate the flows around oscillating airfoils has provided much of the stimulus. The theme of this paper is the calculation of unsteady flows and particularly the development of numerical methods for solving unsteady boundary-layer equations and their application to the flows around oscillating airfoils; other applications include flow over wings subjected to rapid change in orientation, turbine blades subjected to nonuniform onset flow which varies at blade passing frequencies and turboprops mounted on aircraft configurations.

The calculation of an unsteady boundary layer, with a known and spatially fixed initial profile and in the absence of separation, is comparatively straightforward; with increasing magnitude of flow reversal, however, calculations become more difficult and require special numerical procedure to overcome instabilities and allow accurate solutions. Flow reversal implies vanishing wall shear stress but not necessarily separation and the relationship between the two has been considered extensively in the literature, for example, see the reviews of [7] to [13]. The onset of boundary-layer separation raises the possibility of a singularity, which would lead to a breakdown of the calculations, and has been the subject of several investigations including those of, for example [14] to [34]. It is clear that many of the results of these investigators are a function of the particular numerical procedure and its implementation. The most recent study in [33] suggests that accurate solutions can only be obtained if the numerical mesh is related to the local velocity in a manner which satisfies the stability criterion of Courant, Friedricks and Lewey (CFL) [35]. The problem posed by the singularity can be overcome by interaction between solutions of the inviscid-flow and boundary-layer equations; the latter must be solved in an inverse method and with a procedure which satisfies the CFL condition.

The successes so far achieved with interaction methods, see for example [36] to [46], suggest that their extension to two- and three-dimensional unsteady flows is likely to provide the basis for a procedure which will represent oscillating airfoils over a wide range of angles of attack and frequency. In addition, they should also help in the representation of flows associated with the supermaneuverability requirements of fighter aircraft, see for example Herbert [47] which imply rapid changes in orientation and large flow separation. Useful reviews of the need for and principles of interaction have been reported, for example, by McDonald and Briley [48] and by Cebeci, Stewartson and Whitelaw [49], in the context of two-dimensional steady flows with separation.

Previous attempts to calculate the flow around oscillating airfoils include those of Mehta [50], Shamroth [51], Cebeci and Carr [52,53], Carr and Cebeci [54], Maskew and Dvorak [55] and Geissler [56] and range from the solution of inviscid-flow equations to the solution of a two-dimensional, time-dependent forms of the Navier-Stokes equations. The former can provide a useful approximation to lift but make no contribution to our knowledge of drag. The Navier-Stokes equations, on the other hand represent all transport processes within the limitations imposed by the averaged equations but their solution can be costly and subject to numerical truncation error. For flows with small separation, it is evident that interaction between inviscid and boundary-layer equations is the best compromise but the situation is less clear for large regions of separation. In principle, the Navier-Stokes equations should be required but the

comparatively low magnitude of the diffusion terms within large regions of separation, see for example Thompson and Whitelaw [57], suggests that the more economic and numerically accurate procedures based on inviscid and boundary-layer equations may be preferable. This is confirmed by the recent paper of Cebeci et al. [43] which shows that the use of an interactive procedure can lead to values of lift and drag coefficients in close agreement with experiment for angles of attack up to that which causes stall. As a consequence, the emphasis of this paper is on the solution of boundary-layer equations and their interaction with inviscid-flow equations: examples of the application of this form of interactive procedure to laminar and turbulent unsteady flows with separation are presented and discussed.

With any calculation procedure based on averaged equations, it is necessary to make use of a model to represent the Reynolds stresses and this must be guided by experimental information. A compendium of early experiments has been provided by Carr [58] and the review of Reynolds and Carr [6] is particularly helpful in that it categorizes unsteady flow investigations according to the nature of the investigation. It is clear from the investigation of attached boundary layers subjected to oscillating freestreams, see for example Karlsson [3], Cousteix and Houdeville [59], Simpson et al. [60,61], Parikh et al. [62] and Jayaraman et al. [63], that cycle mean characteristics are nearly independent of oscillations even when the amplitude is large. Covert and Lorber [64] show that the periodic component of the Reynolds shear stress can become significant with strong pressure gradients leading to separation, but the turbulent diffusion terms probably do not control the mean-momentum balance. A similar conclusion can be drawn from the separating boundary layer of Simpson et al. where the boundary layers are quasi-steady but some hysteresis was observed downstream of separation. With this experimental background, there is little justification for the use of a higher-order turbulence model with their uncertainties in the transport equations and boundary conditions and added complexity and cost. Consequently, an algebraic specification of length scale is preferred and a modified form of the eddy-viscosity formulation of Cebeci and Smith [65] has been used for all calculations. It is worthy of note that this model has been shown in references [66,67] to be equally able to represent the mean-flow characteristics of wall-boundary layers and wakes as a two-equation and a Reynolds-stress model. It is even possible that this approach will represent adequately strongly perturbed separated flows such as those of Francis et al. [68], Viets et al. [69] and Koga et al. [70] since the nature of the flow is that of a vortex with rotational inviscid characteristics, transported over a boundary layer and into a separated flow: again, the extent of the control exerted by turbulent diffusion is likely to be sufficiently small so that a simple description of turbulence is adequate. It remains to prove this conjecture and if it can be extended to oscillating airfoils subject to dynamic stall, such as that Carr et al [4] and Francis et al. [71]. The possibility is certainly worth pursuing since it will, when embodied in an interactive procedure, offer the real possibility of calculating the onset of stall and of representing the properties of a stalled flow.

The conservation equations associated with unsteady flows are considered briefly in the following section, which also considers appropriate boundary conditions. Section 3 describes numerical procedures for the solution of the boundary-layer equations in the contexts of flows without reversal, flows with reversal and the leading-edge region where special procedures are required to represent the movement of the locus of zero longitudinal velocity and the possibility of consequent instabilities. The Characteristic Box scheme, described by Bradshaw, Cebeci and Whitelaw [72] and by Keller [73] is shown to operate satisfactorily throughout the solution domains of the unsteady flows considered here. It examines the finite-difference grid in relation to the magnitude and direction of local velocity and reaches and implements a decision to ensure that the CFL condition is not violated.

The question of the singularity is addressed in Section 4 in the contexts of the laminar flows over a circular cylinder started impulsively from rest. The extension of the numerical scheme to include interaction between solutions of the inviscid- and viscous-flow equations is considered in Section 5 and results are presented for the leading edge of oscillating airfoil flow based on a thin ellipse. In Sections 4 and 5 the results and the related discussions correspond only to laminar flows since the arguments are of a mathematical nature and can be made independent of turbulence models. Section 6 considers the role of turbulence models and transition in the contexts of steady and unsteady flows with separation and the paper ends with a summary of conclusions and recommendations.

2.0 EQUATIONS, BOUNDARY AND INITIAL CONDITIONS

For two-dimensional incompressible unsteady laminar and turbulent boundary layers, the continuity and momentum equations are well known and can be written as

$$\frac{\partial u}{\partial x} + \frac{\partial v}{\partial y} = 0 \tag{2.1}$$

$$\frac{\partial u}{\partial t} + u\frac{\partial u}{\partial x} + v\frac{\partial u}{\partial y} = \frac{\partial u_e}{\partial t} + u_e\frac{\partial u_e}{\partial x} + \frac{1}{\rho}\frac{\partial \tau}{\partial y} \tag{2.2}$$

Here τ denotes the total shear stress given by

$$\tau = \mu\frac{\partial u}{\partial y} - \rho\overline{u'v'} \tag{2.3}$$

These equations are subject to the usual boundary conditions which, in the case of no mass transfer, may be written as:

$$y = 0 \qquad u = v = 0 \tag{2.4a}$$

$$y = \delta \qquad u = u_e(x,t) \tag{2.4b}$$

In addition to these boundary conditions, Eqs. (2.1) and (2.2) require initial conditions in the (t,y) and (x,y) planes and, depending on the unsteady flow problem under consideration, they may have to be calculated by special procedures.

The determination of the initial conditions is important and sometimes it can be arbitrary but in that event, the values of $\partial u/\partial t$ at $t = 0$ are nonzero; this implies an inviscid acceleration and, as a consequence, a slip velocity develops at the wall and is smoothed by an inner boundary layer initially of thickness $(\nu t)^{1/2}$ in which viscous forces are important. Thus a double structure develops in the boundary layer and may be treated by the numerical method described in [74]. However, if interest is centered on the solution at large times, this feature may be reduced in importance by requiring that the initial velocity distribution satisfies the steady-state equation with the instantaneous external velocity. In addition, it is necessary to smooth out the external velocity $u_e(x,t)$ so that $\partial u_e/\partial t = 0$ at $t = 0$ and then standard numerical methods may be used and are stable. The use of a smoothing function makes for some loss of accuracy at small values of t but the error soon decays to zero once the required value of u_e is specified.

The calculation of initial conditions in the (t,y) plane at some $x = x_0$ when the conditions at a previous time line are known, can introduce different problems. In principle, solutions can be determined at the next time-line by an explicit method but if, stability problems are avoided by the use of an implicit method, there arises the problem of generating a starting profile on the desired time-line. This requires the use of special numerical procedures, such as those discussed in [52] and later in this paper. Although approximate procedures involving quasi-steady assumptions can be utilized to calculate the initial conditions in the (t,y) plane and may be satisfactory, there are cases where a more accurate calculation procedure is required. This topic will be discussed in Section 3.3.

The presence of the Reynolds shear-stress term, $-\rho\overline{u'v'}$, introduces an additional unknown to the system of equations given by Eqs. (2.?) to (2.4) and can be satisfied by using several turbulence models. As long as the rate of change of Reynolds shear stress is not large, the ability of a turbulence model to predict unsteady flows can be gaged by its ability to predict steady flows. A comparison between the predictions of the algebraic eddy-viscosity formulation of Cebeci and Smith, (CS), [65] and the transport-equation model of Bradshaw, Ferriss and Atwell, (BF), [75], both developed for steady flows, yield almost identical results for unsteady flows which include pressure gradients strong enough to cause flow reversal across the layer. It appears from the studies conducted be Cebeci et al. [66] that for wall boundary layer flows in which the Reynolds shear stress and frequency do not change rapidly, the predictions of turbulent flows can be obtained satisfactorily by using simple algebraic eddy-viscosity expressions. On the other hand, when either the rate of change of shear stress or the frequency is large, it is not possible at present to calibrate appropriate turbulence models. In this paper we shall satisfy the closure condition by the eddy viscosity concept

$$-\rho\overline{u'v'} = \rho\varepsilon_m \frac{\partial u}{\partial y} \tag{2.5}$$

and assume that ε_m is given by the CS model, according to which ε_m is represented by two separate formulas. In the so-called inner region of the boundary layer $(\varepsilon_m)_i$ is defined as

$$(\varepsilon_m)_i = (0.4y[1 - \exp(-y/A)])^2 \left|\frac{\partial u}{\partial y}\right| \gamma_{tr} \qquad 0 \le y \le y_c \tag{2.6}$$

where

$$A = 26\nu u_\tau^{-1}, \qquad u_\tau = \left(\frac{\tau}{\rho}\right)_{max}^{1/2} \tag{2.7}$$

In Eq. (2.6) γ_{tr} is an intermittency factor that accounts for the transitional region that exists between a laminar and turbulent flow. It is given by

$$\gamma_{tr} = 1 - \exp\left[-G(x - x_{tr}) \int_{x_{tr}}^{x} \frac{dx}{u_e}\right] \tag{2.8}$$

Here x_{tr} is the location of the start of transition and the empirical factor G is

$$G = \frac{1}{1200} \frac{u_e^3}{\nu^2} R_{x_{tr}}^{-1.34} \tag{2.9}$$

The transition Reynolds number is defined as $R_{x_{tr}} = (u_e x/\nu)_{tr}$. In the outer region, $(\varepsilon_m)_o$ is defined as

$$(\varepsilon_m)_o = 0.0168 \left|\int_0^{\infty} (u_e - u)dy\right| \gamma_{tr} \qquad y_c \le y \le \delta \tag{2.10}$$

The boundary between the inner and outer regions, y_c, is established by the continuity of the eddy-viscosity formulas.

Here for brevity, we shall not discuss the use of similarity-type transformations, but use the definition of stream function

$$u = \frac{\partial \psi}{\partial y}, \qquad v = -\frac{\partial \psi}{\partial x} \tag{2.11}$$

to express Eqs. (2.1) and (2.2) as one third-order equation. For this purpose, with u_0 and L denoting a reference velocity and length, respectively, we define dimensionless variables

$$\tau = \frac{tu_o}{L}, \quad \xi = \frac{x}{L}, \quad \eta = \left(\frac{u_o}{\nu L}\right)^{1/2} y, \quad \psi = (u_o \nu L)^{1/2} f(\xi,\eta), \quad w = \frac{u_e}{u_o} \tag{2.12}$$

and by using the relation in Eq. (2.5), write the continuity and momentum equations and their boundary conditions in the following form:

$$(bf'')' + \frac{\partial w}{\partial \tau} + w \frac{\partial w}{\partial \xi} = \frac{\partial f'}{\partial \tau} + f' \frac{\partial f'}{\partial \xi} - f'' \frac{\partial f}{\partial \xi} \tag{2.13}$$

$$\eta = 0, \qquad f = f' = 0 \tag{2.14a}$$

$$\eta = \eta_e, \qquad f' = w \tag{2.14b}$$

Here primes denote differentiation with respect to η and

$$b = 1 + \varepsilon_m/\nu \tag{2.15}$$

The solution of the system, Eqs. (2.13) and (2.14), requires that b and w are known together with initial conditions in the (ξ,η) and (τ,η) planes.

3.0 NUMERICAL METHODS

A major problem in the calculation of boundary layers is to include regions of flow reversal. In two-dimensional steady flows over a fixed wall and driven by a prescribed external flow $u_e(x)$, the problem is associated with separation; in general the computations of the solution come to an end if and when the skin friction vanishes due to the appearance of a catastrophic singularity centered at the wall [76]. In three-dimensional steady flows under similar conditions, the problem is associated with crossflow reversals and with separation. The case of crossflow reversal is common in flows over wings, bodies of revolution, ship hulls, etc. Even though the flows remain attached in the generally accepted terminology and the solutions of the governing equations are not singular at the vanishing of zero cross-flow skin friction, numerical instabilities result from integration opposed to the flow direction and require that special numerical procedures be devised to obtain stable and accurate solutions. When the streamwise skin-friction vanishes at the wall, the computations of the solution, as in two-dimensional steady flows, come to an end due to the existence of a singularity, [77]. In general this situation occurs after regions of negative crossflow velocity in the flow and an accurate calculation of the flow under these conditions is crucial in defining the flow separation line in three-dimensional flows.

The computational problems associated with unsteady boundary layers are similar to those for three-dimensional steady boundary layers. In two-dimensional unsteady flows with no separation, the problem is roughly analogous to a three-dimensional reverse crossflow problem if we associate time with the direction of a mainstream with the unit velocity component. The unsteady boundary layer is then the crossflow velocity. As in three-dimensional steady flows, the computation of unsteady flows under these conditions requires the development of special procedures to avoid numerical instabilities which result from flow reversal. The flow separation, if there is one, again occurs after some regions of flow reversal develop within the boundary layer, and unlike steady two-dimensional flows, the breakdown of the solution does not always coincide with the vanishing of the skin friction nor it is centered at the wall. In this paper we shall refer to the occurrence of the singularity as separation [11], and discuss the importance of calculating unsteady boundary layers to properly define flow separation in time-dependent flows.

Unlike steady flows, the computation of unsteady three-dimensional boundary layers is in its infancy. We shall restrict the discussion to the numerical solution of unsteady two-dimensional flow equations. The extension of these methods to three-dimensional unsteady flows is likely to follow a path similar to that already followed for steady flows. There are several numerical schemes that can be used to obtain solutions [78], including the popular finite-difference methods of Crank-Nicolson [79] and Keller [80]. Either scheme can be used satisfactorily when there is no flow reversal across the boundary layer, although the Keller scheme has a number of more desirable features than the Crank-Nicolson scheme for turbulent flows. When reversal occurs, and for problems associated with initial conditions, the advantages of the Keller scheme becomes more pronounced and necessitate its use as we shall see in Sections 3.2 and 3.3.

3.1 Flows Without Reversal

One of the basic ideas of Keller's method is that Eq. (2.13) is written in the form of a first-order system. For this purpose we represent the derivatives of f with respect to η by new functions e and g defined by

$$f' = e \tag{3.1}$$

$$e' = g \tag{3.2}$$

and write Eq. (2.13) and its boundary conditions as

$$(bg)' + \frac{\partial w}{\partial \tau} + w \frac{\partial w}{\partial \xi} = \frac{\partial e}{\partial \tau} + e \frac{\partial e}{\partial \xi} - g \frac{\partial f}{\partial \xi} \tag{3.3}$$

$$\eta = 0, \qquad f = e = 0; \qquad \eta = \eta_e, \qquad e = w \tag{3.4}$$

To write the difference equations for the system given by Eqs. (3.1) to (3.4), we consider the net cube shown in Fig. 1 and denote the net points by

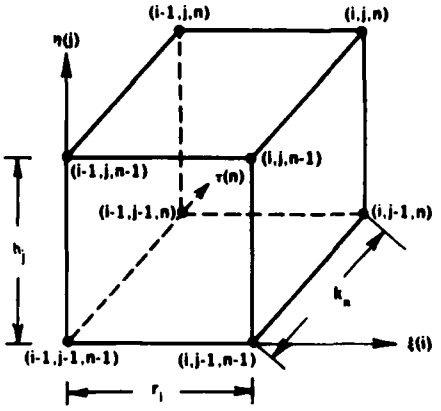

Fig. 1. Net cube for the difference equations.

$$\xi_o = 0, \quad \xi_i = \xi_{i-1} + r_i \qquad i = 1, 2, \ldots, I$$

$$\tau_o = 0, \quad \tau_n = \tau_{n-1} + k_n \qquad n = 1, 2, \ldots, N \tag{3.5}$$

$$\eta_o = 0, \quad \eta_j = \eta_{j-1} + h_j \qquad j = 1, 2, \ldots, J$$

where $r_i = \Delta\xi_i$, $k_n = \Delta\tau_n$ and $h_j = \Delta\eta_j$.

The difference approximations that are to represent Eqs. (3.1) and (3.2) are obtained by averaging about the midpoint $(\xi_i, \tau_n, \eta_{j-1/2})$,

$$h_j^{-1}(f_j^{i,n} - f_{j-1}^{i,n}) = e_{j-1/2}^{i,n} \tag{3.6a}$$

$$h_j^{-1}(e_j^{i,n} - e_{j-1}^{i,n}) = g_{j-1/2}^{i,n} \tag{3.6b}$$

where, for example,

$$e_{j-1/2}^{i,n} = \frac{1}{2}(e_j^{i,n} + e_{j-1}^{i,n}) \tag{3.7}$$

The difference approximations to Eq. (3.3) are obtained by centering all quantities at the center of the cube $(\xi_{i-1/2}, \tau_{n-1/2}, \eta_{j-1/2})$ by taking the values of each say q, at the four corners of the box, that is,

$$q_{j-1/2}^{i-1/2,n} = \frac{1}{2}(q_{j-1/2}^{i,n} + q_{j-1/2}^{i-1,n}) = \frac{1}{4}(q_j^{i,n} + q_j^{i-1,n} + q_{j-1}^{i,n} + q_{j-1}^{i-1,n}) \tag{3.8}$$

In terms of this notation, the finite-difference approximations to Eq. (3.3) can be written in the form:

$$h_j^{-1}[(\overline{bv})_j - (\overline{bv})_{j-1}] + \overline{\beta} = k_n^{-1}(\overline{e}_n - \overline{e}_{n-1})\, r_i^{-1}[\overline{e}_{j-1/2}(\overline{e}_i - \overline{e}_{i-1}) - \overline{g}_{j-1/2}(\overline{f}_i - \overline{f}_{i-1})] \tag{3.9}$$

where β denotes the pressure gradient term,

$$\beta = \frac{\partial w}{\partial \tau} + w\frac{\partial w}{\partial \xi} \tag{3.10a}$$

and where, for example,

$$\overline{e}_j = e_j^{i-1/2,n-1/2}, \qquad \overline{e}_n = e_{j-1/2}^{i-1/2,n}, \qquad \overline{e}_i = e_{j-1/2}^{i,n-1/2} \tag{3.10b}$$

The boundary conditions given by Eq. (3.4) become

$$f_o = e_o = 0; \qquad e_J = w_J \tag{3.11}$$

Sometimes it is more convenient to express Eq. (2.13) in a slightly different form, especially if we were to use the characteristic scheme to be discussed in the next section. For this purpose we define a new variable θ by

$$\theta = \frac{\partial f}{\partial \xi} \tag{3.12}$$

and write Eq. (3.3) as

$$(bg)' + \beta + g\theta = \frac{\partial e}{\partial \tau} + e\frac{\partial e}{\partial \xi} \tag{3.13}$$

In these new variables, e, g and θ, the solution of Eq. (2.13) by the standard box scheme is obtained by solving Eqs. (3.2), (3.13) and

$$\theta' = \frac{\partial e}{\partial \xi} \tag{3.14}$$

The difference approximations to these equations are obtained by centering all the variables except θ at the center of the cube $(\xi_{i-1/2}, \tau_{n-1/2}, \eta_{j-1/2})$ as before. The centering of θ is done by writing it as

$$\theta_{j-1/2}^{i-1/2,n-1/2} = \frac{1}{2}(\theta_j^{i-1/2,n-1/2} + \theta_{j-1}^{i-1/2,n-1/2}) \tag{3.15}$$

In terms of this notation, the finite-difference approximations to Eq. (3.14) can be written in the form:

$$h_j^{-1}(\theta_j - \theta_{j-1}) = r_i^{-1}(\overline{e}_i - \overline{e}_{i-1}) \tag{3.16}$$

where, for example,

$$\theta_j = \theta_j^{i-1/2,n-1/2} \tag{3.17}$$

The finite-difference approximations of Eqs. (3.2) and (3.13), except for the centering of θ in Eq. (3.13) are identical to those given by Eqs. (3.6b) and (3.9). The unknown variables in Eq. (3.16) correspond to e_j^n and $\theta_j^{i-1/2,n-1/2}$ so that e and g are computed at (i,n,j) and θ at $(i-1/2,n-1/2,j)$ when a solution of the system given by Eqs. (3.2), (3.13) and (3.14) is obtained. This modified centering procedure is necessary to avoid oscillations due to the form of the continuity equation given by Eq. (3.12) rather than that which allows Eq. (2.13) to be written as Eqs. (3.1) to (3.3).

The boundary conditions follow from Eq. (3.4) and can be written as

$$e_0 = \theta_0 = 0; \qquad e_J = w_J \tag{3.18}$$

The linearization of Eqs. (3.6), (3.9) and (3.11) is achieved with Newton's method and the equations are then solved by the block-elimination described, for example, by Bradshaw et al. [72].

3.2 Flows with Reversal

When there is flow reversal, it is necessary to modify the Standard Box of the previous section in order to avoid the numerical instabilities resulting from integration opposed to the flow direction. A convenient procedure is to include the zig-zag formulation of Krause et al. [81]. In common with the often-used Crank-Nicolson method, this scheme is easy to employ, particularly since the orientation of the numerical mesh is chosen a priori. This advantage has a corresponding and potentially dangerous drawback in the presence of large reverse flows since the mesh ratio must be related to the velocity according to the famous Courant, Friedricks, Lewey (CFL) condition [35] if stability is to be achieved. For a fixed grid chosen a priori, this condition may be violated as the flow velocities are determined in ever increasing computational domains. Thus a natural boundary limiting the domain in which stable computations can be made is also determined a priori.

One way to avoid the above limitation is to allow the grid to be determined along with the flow calculations and we shall describe a numerical scheme, Cebeci [33], which does this. The grid spacings and orientation are adjusted depending upon the magnitude and direction of the local velocity so that the CFL condition is satisfied. The scheme is thus in some sense intelligent in that it maximizes the domain in which the computations can be carried out. For completeness we shall first describe the zig-zag scheme and then proceed with the intelligent scheme which will be referred to as the Characteristic Box scheme.

To solve Eq. (2.13) by the zig-zag box scheme, we follow the procedure of Sec. 3.1 and express Eq. (2.13) by the first-order system given by Eqs. (3.1) to (3.4). The main difference between the standard and the zig-zag box schemes depends on how the difference equations are written for Eq. (3.3); the remaining two equations, Eqs. (3.6a,b), and boundary conditions, Eq. (3.5), remain unchanged.

To write the difference equations for Eq (3.3) centered at P (see Fig. 2), we use quantities centered at P, Q and R, where

$$P \equiv (\xi_i, \tau_{n-1/2}, \eta_{j-1/2}), \quad Q \equiv (\xi_{i-1/2}, \tau_n, \eta_{j-1/2}), \quad R \equiv (\xi_{i+1/2}, \tau_{n-1}, \eta_{j-1/2}) \tag{3.19}$$

Equation (3.3) is then written as

$$(bv)'(P) + \beta(P) = \frac{\partial e}{\partial \tau}(P) + \lambda_1 e(Q)\frac{\partial e}{\partial \xi}(Q) + \lambda_2 e(R)\frac{\partial e}{\partial \xi}(R) - \lambda_1 g(Q)\frac{\partial f}{\partial \xi}(Q) - \lambda_2 g(R)\frac{\partial f}{\partial \xi}(Q) \tag{3.20}$$

where

$$\lambda_1 \equiv \frac{\xi_{i+1} - \xi_i}{\xi_{i+1} - \xi_{i-1}}, \qquad \lambda_2 = \frac{\xi_i - \xi_{i-1}}{\xi_{i+1} - \xi_{i-1}} \tag{3.21}$$

The characteristic box scheme is based on the solution of governing equations along streamlines. It allows the step sizes in the τ and ξ directions to be automatically adjusted to ensure that the region of backflow determined by the local streamlines does not violate the CFL condition.

To solve Eq. (2.13) with this scheme, we use Eqs. (3.2), (3.13) and (3.14). Noting the definition of local streamlines, which in our notation,

$$\frac{d\tau}{1} = \frac{d\xi}{e} \tag{3.22}$$

If we denote distance in this direction by s and the angle that it makes with the τ-axis by α, then Eq. (3.13) can be written as

$$(bg)' + \beta + g\theta = \lambda \frac{\partial e}{\partial s} \tag{3.23}$$

where

$$\lambda = \sqrt{1 + e^2} \tag{3.24a}$$

$$\alpha = \tan^{-1} e \tag{3.24b}$$

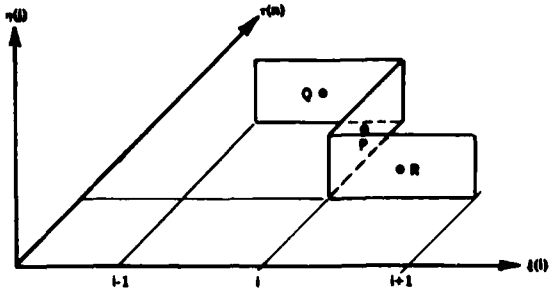

Fig. 2. Finite-differnce molecule for the zig-zag box.

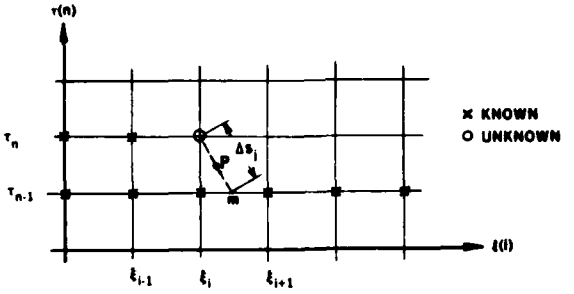

Fig. 3. Notation for the characteristic box scheme.

The finite-difference approximations to Eq. (3.23) are written along the streamline direction (see Fig. 3) at point P,

$$\frac{h_j^{-1}}{2}\left[(bg)_j^{i,n} - (bg)_{j-1}^{i,n}\right] + \frac{h_j^{-1}}{2}\left[(bg)_j^{m,n-1} - (bg)_{j-1}^{m,n-1}\right] + \beta^P + \frac{1}{2}\left(g_{j-1/2}^{i,n} + g_{j-1/2}^{m,n-1}\right)\theta_{j-1/2}^P = \frac{1}{2}\left(\lambda_{j-1/2}^{i,n} + \lambda_{j-1/2}^{m,n-1}\right)\frac{e_{j-1/2}^{i,n} - e_{j-1/2}^{m,n-1}}{\Delta s_{j-1/2}} \tag{3.25}$$

where

$$\Delta s_{j-1/2} = k_n/\cos\alpha_{j-1/2} \tag{3.26}$$

The finite-difference approximations to Eqs. (3.2) and (3.14) are again given by Eqs. (3.6b) and (3.16). The relation between $\theta_{j-1/2}^P$ and those values of θ centered at (i-1/2,n-1/2) and (i-3/2,n-1/2) are

$$\theta_{j-1/2}^P = \frac{\theta_{j-1/2}^{i-3/2} - \theta_{j-1/2}^{i-1/2}}{\xi_{i-3/2} - \xi_{i-1/2}}\left(\xi^P - \xi_{i-3/2}\right) + \theta_{j-1/2}^{i-3/2} \tag{3.27}$$

The solution of Eq. (3.13) by the characteristic scheme is achieved by solving the system, Eqs. (3.2), (3.13) and (3.14) by the standard scheme for all situations when there is no flow reversal. Where a calculation with the standard box reveals a flow reversal ($e_j < 0$) further iterations at that location make use of the characteristic scheme for $e_j < 0$ and the standard box for $e_j > 0$. This switch from one scheme to another continues to allow quadratic convergence and ensures that numerical instabilities are avoided provided the step lengths in the τ and ξ directions are "properly" selected. We shall discuss this point later in Section 4.

3.3 Special Problems Associated with Initial Conditions

There are several important problems in unsteady boundary-layer flows in which the calculation of initial conditions can be very important. Typical examples are flows in the stagnation region of an oscillating airfoil or a stator blade. In the latter case, the blade is stationary and the onset flow varies with time and location; with the oscillating airfoil, the onset velocity is uniform and the location of the airfoil surface varies. In either case, if we assume that the flow conditions on the body at t = 0 correspond to the steady state so that the initial conditions in the (x,y) plane can be obtained by solving the appropriate equations, in principle there is no difficulty in obtaining solutions on the next time line in the (t,y) plane at a specified x-location by an explicit method. However, if we wish to avoid the stability problems associated with such a method, we are immediately faced with the problem of generating a starting profile on the new time-line. Furthermore, the stagnation point varies across the shear layer at a given time and leads to profiles with flow reversal, so that a numerical scheme which avoids the numerical instabilities is required. An effective method for accomplishing these objectives is the characteristic scheme discussed in the previous section.

To illustrate the solution procedure for such problems, let us consider a thin oscillating airfoil and represent its external velocity distribution in the vicinity of the stagnation region by

$$\frac{u_e}{u_\infty} = \frac{\xi + \alpha_0(1 + A\sin\omega t)}{(1 + \xi^2)^{1/2}} \tag{3.28}$$

where A and α_0 denote parameters that need to be specified. By definition, u_e vanishes at the stagnation point and its location, ξ_s, based on the external streamlines, is given by

$$\xi_s = -\alpha_0(1 + A\sin\omega t) \tag{3.29}$$

Figure 4 shows the variation of the stagnation point with time for one cycle according to Eq. (3.29), with A = 1, $\omega = \pi/4$. We see that when t = 2, the stagnation point ξ_s is at $-2\alpha_0$ and when t = 6, it is at 0, etc. The grid points denoted by x's denote known solutions for all y.

The first velocity profile on either side of the "edge" stagnation point can be calculated by using the characteristic scheme on an iterative basis. To explain this further, consider the point denoted by 1 on the grid of Fig. 5 and assume that θ is known, say equal to $\theta^{i-1/2,n-1}$. This assumption decouples the continuity equation (3.14) from Eq. (3.13) and reduces the system given by Eqs. (3.2), (3.13) and (3.14) to one given by Eqs. (3.2) and (3.13) with e and g being the only unknowns. The finite difference

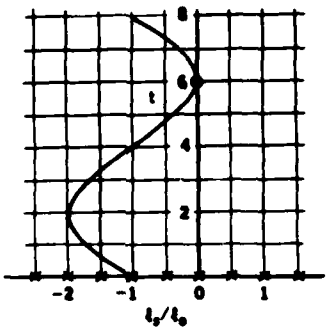

Fig. 4. Variation of stagnation point with time for one cycle according to Eq. (3.29), with $\bar{\omega} = \pi/4$, A = 1.

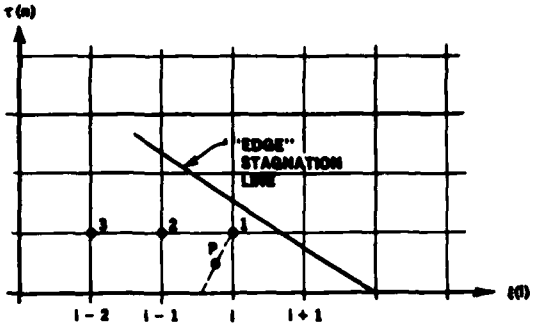

Fig. 5. Notation and finite-difference molecule for the characteristic box 2.

approximations to Eq. (3.13) are essentially the same as those given by Eq. (3.25). Furthermore, since there are only two unknowns, the matrices are 2 x 2 and the solution algorithm by the block elimination method is much easier. Once an approximate solution at point 1 is obtained, we solve the system given by Eqs. (3.2), (3.13) and (3.14) to obtain e_j and g_j at point 2 and θ_j at (i-1/2, n-1/2). This procedure is repeated at point 3 so that a new estimate for θ_j at P can be obtained from the computed values of θ_j at (i-3/2, n-1/2) and (i-1/2, n-1/2). The 2 x 2 system is then re-solved to obtain an improved solution at point 1. The procedure is repeated until the solutions converge and experience has shown that two to three iterations are required.

Figure 6 shows the computed velocity profiles in the immediate neighborhood of the stagnation region at different times when the external stagnation point varies with time according to Fig. 4. We note that for steady state the velocity profiles on either side of the stagnation point, defined by the vanishing of external velocity, behave "well" as expected. However, for unsteady flow, the stagnation point varies with both x and time and flow reversals begin to develop in the velocity profiles. The changes in the behavior of the velocity profiles on either side of the vanishing u_e become more drastic as t increases.

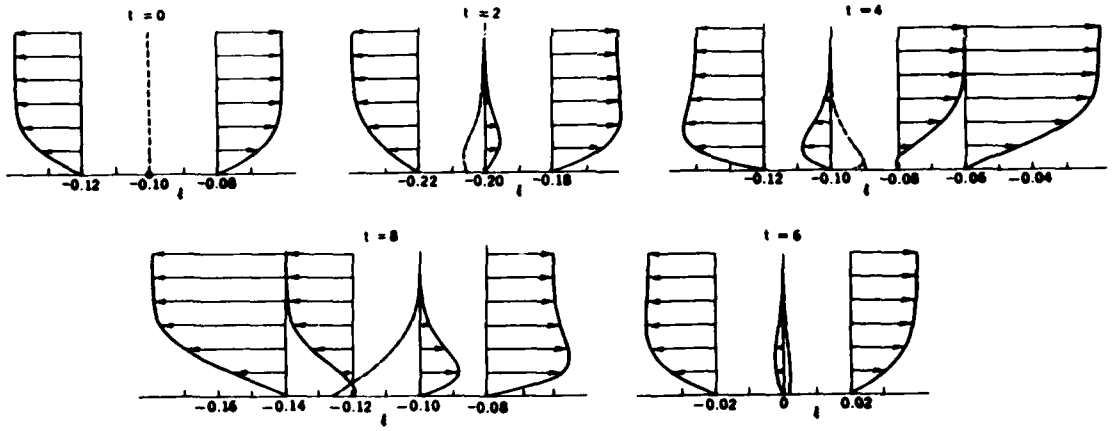

Fig. 6. Velocity profiles in the stagnation region of an oscillating airfoil. The dashed lines indicate the locus of zero u-velocity across the layer.

4.0 THE QUESTION OF SINGULARITY

It was suggested by Moore [82], Rott [83] and Sears [84] that the solution of the system of Eqs. (2.1) to (2.4) for laminar flows results in flow separation if and when there is a point $x_s(t)$, $y_s(t)$ in the flow field such that

$$u = \dot{x}_s, \quad \frac{\partial u}{\partial y} = 0 \tag{4.1}$$

i.e. $u = \partial u/\partial y = 0$ at the separation point when viewed by an observer traveling with the speed of separation. This condition referred to as the MRS criteria is consistent with the Goldstein singularity for a steady flow past a fixed wall but permits y_s to be nonzero. Its range of applicability was considered by the investigations of Telionis and Werle [17] and Williams and Johnson [19] in which the unsteady problems were reduced to steady problems with a moving wall. An important feature of their studies is that they solved a reduced form of Eqs. (2.1) to (2.4) obtained by letting $t \to \infty$ and assuming, in a sense, that $\partial/\partial t \to 0$. In taking this limit it is not necessarily assumed that x,y are held constant; instead, two combinations of x,y,t are fixed. Thus the relevance of the MRS was established by these computations in the limit $t \to \infty$.

A further generalization would be realized if, in any flow started from rest at t = 0, there exists a t^* such that the solution is smooth throughout the entire domain of integration in the x,y plane for $t < t^*$

and can only be found in a portion of the domain bounded in some way by a singularity in the solution for $t > t^*$. If this were so, and if the boundary is the line $y = y_s$ and the MRS criterion holds, there would be profound implications for the theory of high Reynolds-number flows. The classical view is that they evolve smoothly as t increases but the boundary layer grows exponentially with time in reversed-flow regions leading eventually to significant changes in the inviscid flow. This view would need to be changed and, for $t \geq t^*$, the boundary layer would abruptly make a noticeable impact on the external flow in a way which is not well understood but might well be by initiating a jet of fluid into it, as has been suggested by Shen [10]. These questions are also important from a practical point of view in the problem of dynamic stall. For example, Carr, McAlister and McCroskey [4] have observed large that eddies break away from the boundary of slowly oscillating airfoils after flow reversal has occurred in the boundary layer; they may be associated with the occurrence of a singularity in the solution of the unsteady equations.

These considerations have led to renewed interest in the laminar boundary layer on a circular cylinder moving with uniform speed after an impulsive start for which $u_e = \sin x$ in Eq. (2.4b). For this problem the steady-state solution has a singularity at $x = x_s = 1.82 = 104°$ and for $x_s < x < \pi$ it does not exist. The previous views of the unsteady solution were that it rapidly approached the steady state if $x < x_s$, but the boundary layer increased in thickness exponentially with time for $x > x_s$, the flow there being largely an inviscid eddy but with a thin subboundary layer below it moving fluid from the rear stagnation point at $x = \pi$ to $x = x_s$. A number of numerical studies have been conducted for this flow and include those of Refs. [12,14,15,16,18,21,26,28,29,31,32,33,34]. The study of Ref. [18] advanced the view of Sears and Telionis [7] that an evolving boundary layer can develop a singularity at a specific time, $t \simeq 1.30$ at a station $\theta \simeq 140°$ from the stagnation point. This result disagrees with the previous studies of Robins reported in Belcher et al. [14], of Collins and Dennis [16,17] and of Cebeci [26]: these authors found no singularity in the solution for $t < 2$.

While all the studies on this problem were conducted by using an Eulerian coordinate system, those of van Dommelen and Shen [28,29] were carried out with a Lagrangian coordinate method. Here x and y are taken as the dependent variables being functions of ξ, η, t where

$$x(\xi,\eta,0) = \xi, \qquad y(\xi,\eta,0) = \eta, \qquad \frac{\partial x}{\partial t} = u \tag{4.2}$$

They confirmed Cebeci's results [26] for $t < 2$ but found that for $t > 2$ a hump developed in the displacement thickness $\delta^*(x,t)$ in the neighborhood of $x = 2$, i.e. a little way into the reversed flow region. This evolved into a very sharp singularity at $t = 3.004$, $x = 1.937$. This result is surprising but it was obtained after a careful numerical study. Van Dommelen and Shen [28] have examined the analytic structure of the singularity and concluded that the MRS criterion is satisfied but that it is not of the Goldstein type.

Faced with this information, Cebeci extended his computations to times up to 2.75 and confirmed the results of van Dommelen and Shen [12] but the calculations had to be terminated because it proved to be impossible to select the step lengths required to satisfy the CFL condition in the presence of large flow reversal. Other attempts to use forms of the zig-zag scheme and the Eulerian formulation to calculate unsteady flows with large backflow have been plagued with the same difficulty. It appeared that all finite-difference methods using the Eulerian approach and some form of the zig-zag scheme procedure produced a singularity whose location was a function of the numerical method. The need to satisfy the CFL condition was not considered until recently when Cebeci [33] reported calculations using the characteristic box scheme of Section 3.2, which allows the orientation of the finite-difference mesh to vary across the shear layer, and the procedure for the automatic selection of time steps so as to maintain the angle

$$\alpha < \tan^{-1} \frac{r_j}{k_n} \tag{4.3}$$

The resulting values of k_n for the predetermined values of steps in the x-direction are shown in Table 1 and, as can be seen, they become extremely small at $\tau = 3.0$. These calculations made use of increments in ξ, η and τ of 101, 161 and 435, respectively and could have been extended beyond $\tau = 3.1$ but at considerable expense, as witnessed by the small and decreasing values of k_n. The values of k_n and r_j shown in Table 1, were subsequently used in conjunction with the zig-zag scheme, which had previously failed, Cebeci [12], to permit calculations for times greater than $\tau > 2.75$. The results were found to be identical to those presented here. The alternative approach of using the zig-zag scheme and the relationship

Table 1. The distribution of step sizes in τ and ξ.

τ	k_n	ξ	r_j
0 → 1	0.05	0 → 0.54	0.02
1 → 1.5	0.02	0.54 → 0.57	0.01
1.5 → 2.3	0.01	0.57 → 0.58	0.0025
2.3 → 2.73	0.005	0.58 → 0.60	0.0020
2.73 → 3.024	0.002	0.60 → 0.612	0.0015
3.024 → 3.1	0.001	0.612 → 0.64	0.0020
		0.64 → 0.67	0.0025
		0.67 → 0.72	0.01
		0.72 → 1.0	0.02

given by Eq. (4.3) was not, however, successful. This confirms that the selection of k_n must depend upon the direction of the local streamlines.

Figures 7, 8 and 9 display the variations of dimensionless displacement thickness, Δ^*, local skin-friction coefficient, c_f^* and dimensionless displacement velocity, $\bar{v}_w$ where these are defined, with $R_L = u_o L/\nu$, by

$$\Delta^* = \frac{\sqrt{R_L}}{L} \int_0^\infty (1 - \frac{u}{u_e}) dy$$

$$c_f^* = \frac{2\tau_w}{\rho u_o^2} \sqrt{R_L} \tag{4.4}$$

$$\bar{v}_w = \frac{v_w}{u_o} = \frac{d}{d\xi} (w\Delta^*)$$

It is of particular note that the displacement thickness is close to monotonic with the small maximum and minimum for $\tau = 3.1$ at which the calculations were terminated. The previous results of Cebeci [12] are also shown in the figure and reveal the maxima which stemmed from the use of a numerical scheme which did not meet the requirements imposed by the CFL condition.

The distributions of local skin-friction coefficients of Fig. 8 show trends which are similar to those of the previous results but with differences in magnitude consistent with those of Fig. 7. It should be noted that the results of Figs. 7 and 8 are identical with those previously obtained up to the value of θ at which the displacement thickness gradient reaches its maximum and for values of τ less than around 2.75. The differences for large values of θ and τ are associated with the numerical procedure and, in particular, with its ability to satisfy the CFL condition as discussed previously.

The dimensionless displacement velocity, $\bar{v}_w$, is shown in Fig. 9 together with the locus of points corresponding its maxima which increases with time and decreasing angle. At $\tau = 3.0$, the calculated value of θ is 111.5 and corresponds very closely to that determined by van Dommelen and Shen who terminated their calculations at this time. As the peak in the displacement velocity moves upstream with increasing time, the location at which the skin-friction coefficient becomes zero also moves upstream but at a slower rate and towards its steady-state value of 105° [65]. Figure 9 also shows that it is desirable to perform calculations at higher values of τ so as to confirm the conjecture that the only singularity is associated with the steady-state solution. To make a conclusive judgment, calculations should be performed up to $\tau = 4.1$ but, as Table 1 suggests, the required time steps are likely to be very small. The time required to obtain results in the range $\tau = 3.024$ to 3.1, which corresponds to 75 time-steps, was 7 hours on a CYBER 175. The computer time likely to be required to reach $\tau = 4.1$ is clearly excessive.

Corresponding velocity profiles are presented in Fig. 10 for $\tau = 2.75$ and 3.0. The general trends are in agreement with those of van Dommelen and Shen and the quantitative values agree closely up to 110°. The discrepancies at larger angles are probably due to the use of inappropriate time steps in the calculations.

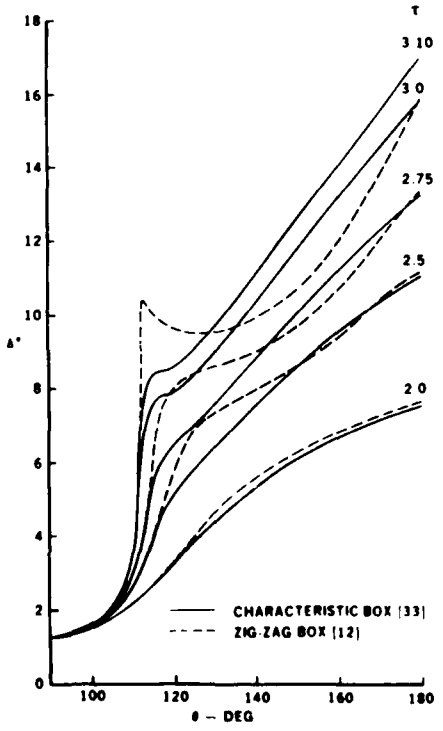

Fig. 7. Variation of displacement thickness for the impulsively started circular cylinder.

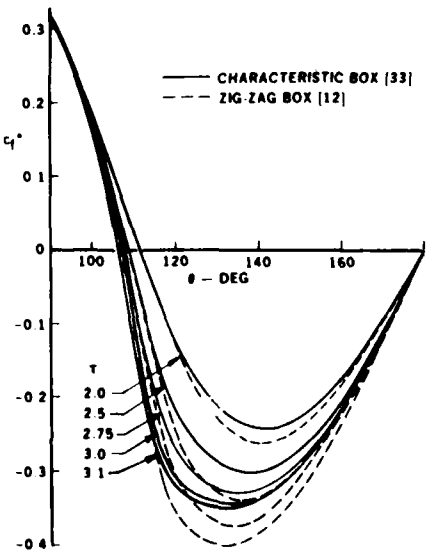

Fig. 8. Variation of local skin friction coefficient for the impulsively started circular cylinder.

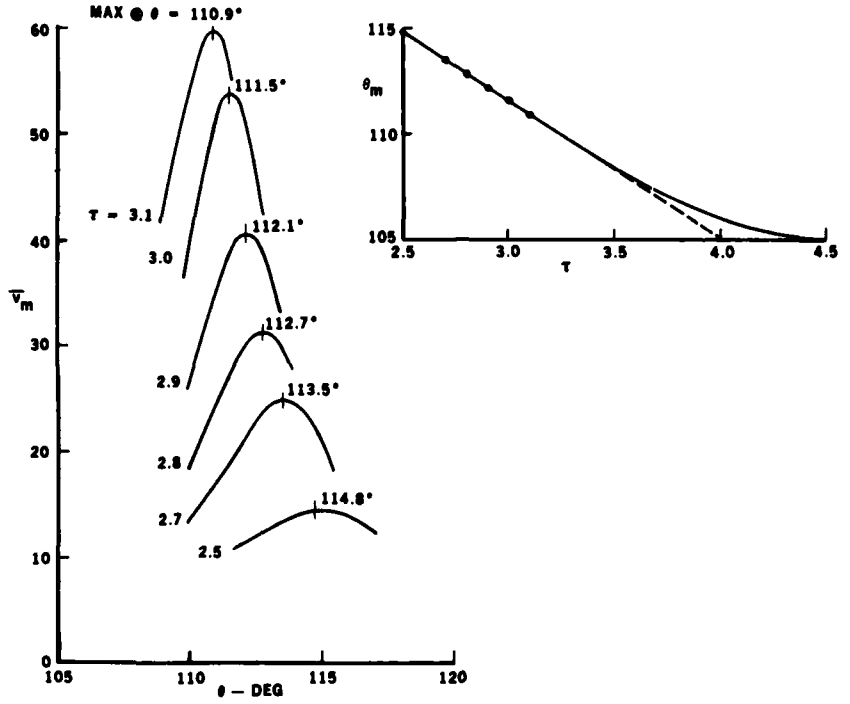

Fig. 9. Variation of displacement velocity for the impulsively started circular cylinder. The insert shows the variation of the location of maximum displacement velocity θ_m with circles indicating the computed values, the dashed lines indicate the linear extrapolation of θ_m and the solid line a conjectures variation of θ_m to steady state, Cebeci [33].

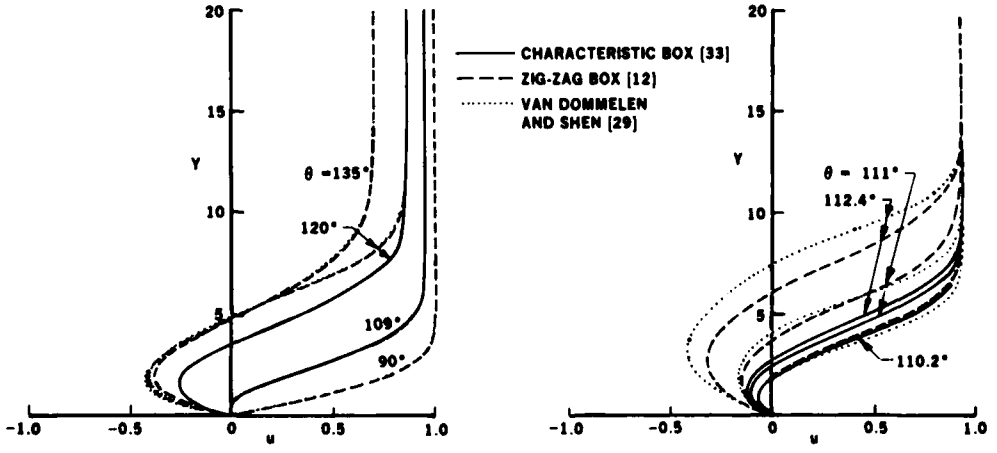

Fig. 10. Velocity profiles at different times. (a) $\tau = 2.75$. (b) $\tau = 3.0$.

It is clear that the characteristic box scheme has successfully permitted the calculation of the flow properties for the unsteady flow associated with a cylinder impulsively started from rest. The large reverse flow regions found with this model problem occur in the more practical application of oscillating airfoils as we shall see in Section 5.0. In particular, the use of the characteristic box scheme together with Eq. (4.3) leads to solutions which approach and pass the region of the singularity without numerical difficulty whereas the zig-zag scheme leads to solutions which oscillate and break down in the same manner experienced with the cylinder.

5.0 INTERACTION BETWEEN INVISCID AND VISCOUS FLOWS

5.1 Need for Interaction and Possible Approaches

An interpretation of a singularity in either two- or three-dimensional steady flows is that the external velocity distribution has been incorrectly chosen and that the boundary layer should not be considered separately from the external inviscid flow: instead, it is necessary to develop a theory and

devise special numerical methods which allow for the mutual interaction between the boundary layer and the inviscid flow. At this time there are two popular approaches for accomplishing this objective for two-dimensional steady subsonic and transonic flows. The first is due to LeBalleur [85] and Carter [86] and the second to Veldman [87]. In the first, the solutions of the boundary-layer equations are obtained for a prescribed pressure distribution and a displacement-thickness distribution $\delta_o^*(x)$ is determined. If this initial calculation encounters separation, $\delta_o^*(x)$ is obtained by extrapolation and one complete cycle of the viscous and inviscid calculation is performed. In general, this leads to two external velocity distributions, $u_{e_v}(x)$ obtained as part of an inverse boundary-layer solution in which the calculations are performed for a specified displacement thickness and $u_{e_i}(x)$ derived from the updated approximation to the inviscid velocity over the body with the added displacement thickness. A relaxation formula is introduced to define an updated displacement-thickness distribution,

$$\delta^*(x)^{\nu+1} = \delta^*(x)^{\nu} \{1 + \lambda_3 [\frac{u_{e_v}(x)}{u_{e_i}(x)} - 1]\}, \qquad \nu = 0, 1, 2, \ldots \tag{5.1}$$

where λ_3 is a relaxation parameter and the procedure is repeated with Eq. (5.1) until convergence is achieved.

In the second approach, the external velocity $u_e(x)$ and the displacement thickness $\delta^*(x)$ are treated as unknown quantities and the equations are solved simultaneously by an inverse boundary-layer method with successive sweeps over the body. For each sweep, the external boundary condition for the boundary-layer equation is written as

$$u_e(x) = u_{\ell}(x) + u_c(x) \tag{5.2}$$

where $u_{\ell}(x)$ is the inviscid velocity over the body and $u_c(x)$ is the perturbation velocity due to the displacement thickness and is given by

$$u_c(x) = \frac{1}{\pi} \int_{\xi_a}^{\xi_b} v_w(s) \frac{ds}{\xi - s} \tag{5.3}$$

where the interaction is confined between ξ_a and ξ_b and the transpiration velocity v_w is given by Eq. (4.4). This procedure has also been used by Cebeci and his associates in a number of studies relating to two-dimensional steady subsonic flows with separation as well as three-dimensional steady transonic flows [36,28,43,46].

The progress achieved with steady flows has not been matched with unsteady flows which have received comparatively little attention. Except for the contributions contained in the volume edited by Francis and Luttges [5] and for the papers [88-91] presented in the Third Symposium on Physical and Numerical Aspects of Aerodynamic Flows [92], and the very recent work, described in Section 5.2, interactive boundary-layer methods have not been used for unsteady flows with separation.

5.2 An Interactive Procedure

Recently the authors of this paper have developed an interactive boundary-layer method for calculating unsteady flows on oscillating airfoils. Studies were conducted to determine the relationship between unsteady separation and singularities in the solution, and to explore the possibilities of removing this singularity by interaction of the viscous and inviscid equations. In this section we present a brief outline of the interactive method and postpone the results to Section 5.3.

Usually the boundary-layer equations, (2.1) and (2.2), are solved subject to the boundary conditions given by Eqs. (2.4); we shall refer to this as the standard problem. In the interactive problem we determine $u_e(x,t)$ partly from inviscid flow theory and partly from the pressure distribution resulting from the blowing velocity $v_w(x)$ induced by the boundary layer. This can be done by writing Eq. (2.4b) in the form given by Eqs. (5.2) and (5.3) which, in terms of the dimensionless variables given by Eq. (2.12), can be written with $\varepsilon = 1/\pi\sqrt{R_L}$, as

$$w = \bar{u}_e^o + \varepsilon \int_{\xi_b}^{\xi_a} \frac{d}{d\xi} (\eta_e f_e' - f_e) \frac{d\sigma}{\xi - \sigma} \tag{5.4}$$

In an interactive boundary-layer method with separation, the external velocity w is unknown and must be obtained as part of the solution of Eqs. (2.13), (2.14) and (5.4) with known initial conditions. In the approach used by Cebeci and his associates, the Mechul function formulation is used for this purpose and, since w is independent of η, it is written as

$$w' = 0 \tag{5.5}$$

The solution of the system given by Eqs. (2.13), (2.14) and (5.5) can be obtained in a manner analogous to the standard methods described in Section 3.0. In regions where there are no flow reversals across the layer, we use the standard box scheme and in regions where there is flow reversal, we use either the zig-zag scheme or the characteristic box scheme. The main difference between the standard method and the inverse method lies in the procedure to include Eq. (5.4) in the "edge" boundary conditions. A discrete approximation was introduced into Eq. (5.4) and was written in the form [36],

$$w_e(\xi_i) - c_{ij}\varepsilon\Delta(\xi_j) = g_i \tag{5.6}$$

Here c_{ij} is the matrix of coefficients defining the relationship between the dimensionless displacement thickness Δ defined by

$$\Delta = \eta_e w_e - f_e \tag{5.7}$$

and external flow and the parameter g_i represents terms whose values are assumed to be known. It is given by

$$g_i = \bar{u}_e^0 + \epsilon \sum_{k=1}^{i-1} c_{ik}\Delta(\xi_k) + \epsilon \sum_{k=i+1}^{\ell} c_{ik}\Delta(\xi_k) \tag{5.8}$$

The solution of the inverse method is then obtained by solving the system given by Eqs. (2.13) and (5.5) subject to the boundary conditions given by Eqs. (2.14) and (5.6). As in the case of the standard problem and depending on the complexity of the flow, we can use either the standard box, zig-zag box or the characteristic box schemes. Except for the addition of one more equation, the solution procedure for the inverse problem is identical to that described for the standard problem.

5.3 Results for an Oscillating Airfoil

We now present results for a model oscillating airfoil based on a thin ellipse whose external velocity distribution corresponds to those found around the leading edge of thin airfoils and is given by Eq. (3.28). One part of the calculations was carried out for the standard problem by choosing $\alpha_0 = 1$, $A = -1/2$ and $\omega = 0.1$ [30]. With these choices, the maximum value of α_{eff}, defined by

$$\alpha_{eff} = \alpha_0 (1 + A \sin\omega t)$$

is sufficient to provoke separation with a strong singularity if the boundary layer were steady. Numerical calculations were made initially with the zig-zag box scheme and the results of Fig. 11 show that the boundary layer eventually separates, the flow remaining smooth. Immediately downstream of separation, however, it is evident that a singularity appears to develop in the neighborhood of $\xi = 2.12$ and $\omega t = 308.75°$ and that it is not possible to continue the calculation beyond this time with the standard formulation and the zig-zag scheme.

Figure 11a shows that the variation of the displacement thickness

$$\gamma_{\delta^*} = \frac{\delta^*}{a}\left(\frac{1+\tau}{\tau}\right)\frac{1}{\epsilon\pi} \tag{5.9}$$

is generally smooth except in the neighborhood of $\xi = 2.12$ and for $\omega t = 308.75°$. The first sign of irregularity is the steepening of the slope of δ^* when $\omega t = 300°$ and the local maximum of δ^* at $\xi = 2.12$ when $\omega t = 308.75°$. When the same results are plotted for a displacement velocity $(\bar{u}_e\delta^*)$, (Fig. 11b), we observe that the steepening of the displacement velocity near $\xi = 2.12$ is dramatic. For example the peak is at $\xi = 2.125$ for $\omega t = 300°$; at $\xi = 2.105$ for $\omega t = 305°$; at $\xi = 2.09$ for $\omega t = 307.5°$; and finally at $\xi = 2.08$ for $\omega t = 308.75°$. It should be noted that the maximum value of displacement velocity moves towards the separation point with increasing ωt as we observed previously with the circular cylinder discussed previously.

As shown in Fig. 11c, the wall shear parameter f_w'' shows no signs of irregularity for $\omega t \leq 308.75°$ but a deep minimum in f_w'' occurs near $\xi = 2.15$, i.e. near the peak of δ^*.

These results suggest that the solutions have a singularity in the neighborhood of $\xi = 2.12$ and $\omega t = 308.75°$ and that, as in steady flows, it is necessary to use an interactive theory to remove it. The procedure of Section 5.2 was used to investigate this possibly further for a specific value of R_L ($\equiv 10^5$). The standard method was used to compute the unsteady boundary layers up to $\xi = 0.5$ for all time and with

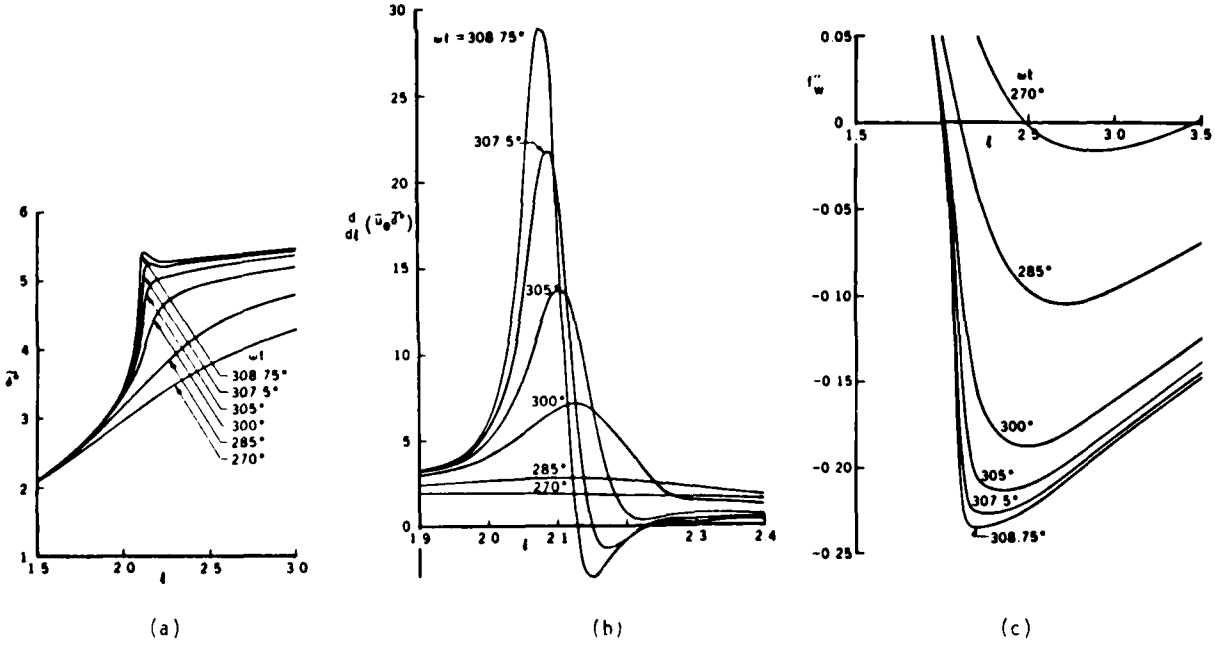

Fig. 11. Computed results for the oscillating airfoil, $A = -1/2$, $\bar{\omega} = 0.1$ using the zig-zag scheme. (a) Displacement thickness δ. (b) Displacement velocity, $d/d\xi(\bar{u}_e\delta^*)$. (c) Wall shear parameter f_w''.

these initial conditions and for each value of ωt, the inverse method was used to calculate the unsteady flow from $\xi = 0.5$ to $\xi = 5.5$. Since the system of equations is now elliptic, several sweeps in the ξ-direction were necessary to achieve a converged solution. Where flow reversal was encountered, as happens for values of $\omega t > 270°$ and $\xi > 2$, up to three sweeps were required; a single sweep was sufficient where separation did not exist.

Figure 12a shows the variation of displacement thickness $\tilde{\delta}^*$ and Fig. 12b the wall shear parameter f''_w as a function of nondimensional distance ξ and time and it is evident that the solutions are well behaved for values of $\xi < 2.5$. As expected, the displacement thickness increases with ξ for all values of time and reaches a maximum around $\omega t = 300°$ as a consequence of the change in the angle of attack. In the same range of ξ, the wall shear decreases for all values of ωt and reaches a minimum corresponding to the maximum in displacement thickness.

For values of $\xi > 2.5$, the solutions remain well behaved until around $\omega t = 290°$. The general trends are in accord with expectations and there is negligible difference between the results obtained with the standard and interactive methods for values of ωt up to the maximum for which the standard method allowed solutions. Although the calculations were carried out for one complete cycle, the solutions had wiggles for $\omega t > 295$ and several attempts to eliminate them by using different step sizes in time and space as well as Reynolds number were not successful. Indeed, in some cases the solutions broke down before the calculations achieved for one cycle.

Following the study conducted for the circular cylinder using the characteristic box [33], studies were then conducted for this model problem. At first calculations were made for the standard problem with the same net spacing used in the zig-zag scheme and the solutions broke down at $\xi = 2.12$ and $\omega t = 305°$ when the CFL condition given by Eq. (4.3) was not satisfied. As in the case of the circular cylinder problem, the original ξ-distribution was kept the same and the value of k_η was halved until the CFL condition was met. This allowed the calculations to be performed smoothly and without numerical problems for one complete cycle. More important, however, the solutions did not break down at $\omega t = 308.75°$ when the same calculations were repeated with the zig-zag scheme, and we were able to obtain them for one cycle. These results were also identical to those obtained with the characteristic box scheme indicating that with the "proper" net the predictions of both schemes are the same.

Figures 13 and 14 show the variation of displacement thickness $\tilde{\delta}^*$ and wall shear parameter f''_w, respectively. As expected, the new results up to flow reversal location are essentially the same as those in Figs. 11a and 11c, but substantially different in the region of flow reversal.

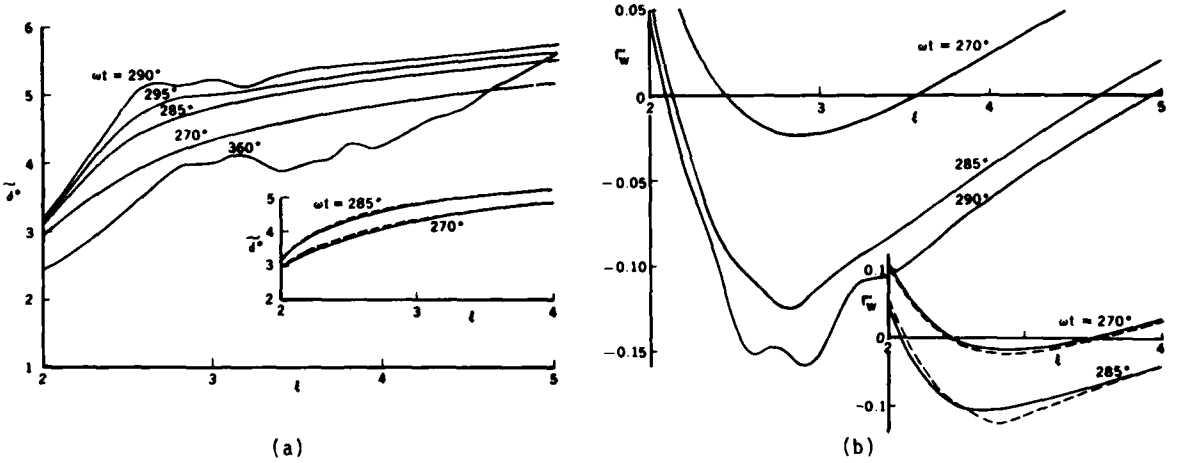

Fig. 12. Effect of interaction on the variation of (a) displacement thickness $\tilde{\delta}^*$, (b) wall shear parameter f''_w for an oscillating airfoil with $\varepsilon = 4.5 \times 10^{-3}$. Solid lines in the insert represent the results obtained by the standard method and dashed lines those by the inverse method. Calculations were made using the zig-zag box scheme.

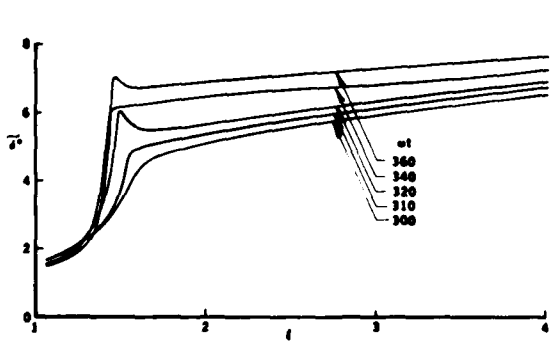

Fig. 13. Computed displacement thickness for the oscillating airfoil, $A = -1/2$, $\bar{\omega} = 0.1$ using the characteristic box scheme.

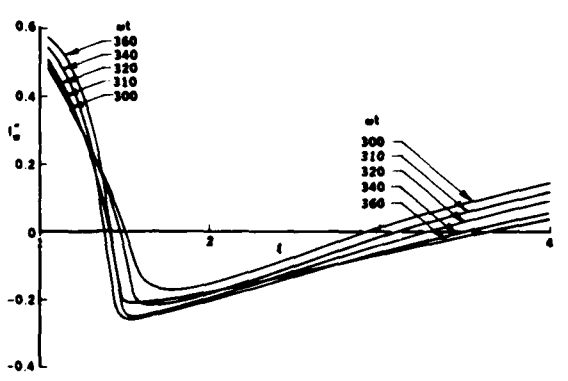

Fig. 14. Computed wall shear parameter, f''_w for the oscillating airfoil, $A = -1/2$, $\bar{\omega} = 0.1$ using the characteristic box scheme.

Calculations were also conducted using the unsteady interactive method for the net determined in the standard problem by the characteristic scheme. The results obtained with the zig-zag scheme are shown in Figs. 15 and 16 for Reynolds numbers, R_L, of 10^5 and 10^4. The results obtained by the interactive method are nearly the same as those obtained by the standard method prior to flow reversal and are substantially different when flow reversal is present. As expected, the difference between the predictions of two procedures (standard and interactive) increases as the Reynolds number decreases. We also note that the wiggles observed in the calculations with the "wrong" net are absent, and indicate that the rate of convergence is the same as in the standard problem.

6.0 THE ROLE OF TURBULENCE MODELS AND TRANSITION

6.1 Predictions of Two Turbulence Models

Except for the work of Patel and Nash [20], most methods for unsteady boundary layers use the simple eddy viscosity and mixing length concepts to satisfy the closure assumption. This choice, with Eq. (2.5) and with ϵ_m a function of the velocity field, allows the laminar boundary-layer methods to be extended to turbulent flows. Patel and Nash used a modified form of the Bradshaw, Ferriss and Atwell turbulence model [75] so that, unlike the Bradshaw et al. method which uses a single first-order partial differential equation for the Reynolds shear stress term, they used a second-order partial differential equation and solve it together with the continuity and momentum equations, Eqs. (2.1) and (2.2). Both methods neglect the contributions of laminar shear stress and apply the BF model only outside the viscous sublayer. Furthermore, the inner wall boundary conditions given in Eq. (4a) are applied outside the viscous sublayer, usually at $y = 50\ \nu(\rho/\tau_w)$, generally restricting the solution of the equations to problems with no flow reversal or separation. Their extension to account for flow reversal requires modification of the functional form of the law of the wall and the manner in which the wall shear is determined.

In this section, we discuss the role of turbulence models by considering two models for unsteady flows without flow reversal. Cebeci and Carr [93] performed calculations to determine whether the representation of unsteady flows with strong pressure gradient requires that account be taken of transport of turbulence quantities. They used the algebraic eddy viscosity formulation of Cebeci and Smith given by Eqs. (2.6) to (2.10) and the transport model of Bradshaw, Ferriss and Atwell and showed that the results with both models were nearly identical for both steady and unsteady flows with and without strong pressure gradients.

The test cases considered in their study correspond to cases 4 and 5, as reported in [58]. Case 4 corresponds to an unsteady Howarth flow and starts from a wellestablished steady flat-plate flow, on which a linear acceleration of u_e is imposed at $t = 0$. The external velocity distribution is given by

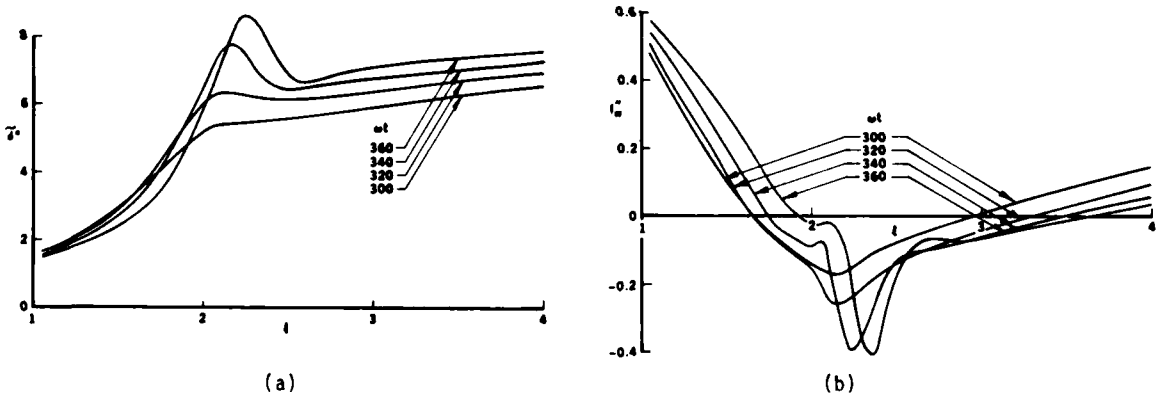

Fig. 15. Interactive solutions of (a) displacement thickness, and (b) wall shear parameter f''_w, for the oscillating airfoil, $A = -1/2$, $\bar{\omega} = 0.1$ obtained with the characteristic box scheme for $R_L = 10^5$.

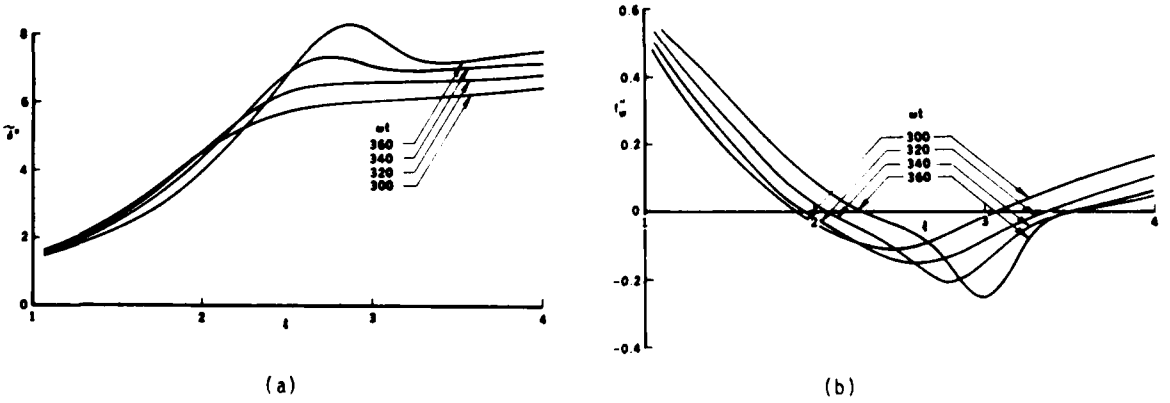

Fig. 16. Interactive solutions of (a) displacement thickness and (b) wall shear parameter f''_w, for the oscillating airfoil, $A = -1/2$, $\bar{\omega} = 0.1$ obtained with the characteristic box scheme for $R_L = 10^4$.

$$\frac{u_e}{u_\infty} = 1 - \bar{\alpha}(x - 1.24)t \qquad 1.24 < x < 4.69 \qquad (6.1)$$

where $\bar{\alpha}$ is a constant equal to 0.72 $sec^{-1}m^{-1}$. The flow was assumed to be steady up to x = 1.24m and the velocity distribution given by Eq. (6.1) was imposed as a function of x and t. According to the calculations of Cebeci and Carr [93], the wall shear vanishes first around t ≈ 0.22, x = 4.69. The computation of boundary layers for values of x in the range 1.24 ≤ x ≤ 4.69 for t > 0.22 depends on the specification of a velocity profile at x = 4.69 and Cebeci and Carr have assumed it is given by the extrapolation of the two velocity profiles computed for x < 4.69. This procedure in which the extrapolated station served as a downstream boundary condition, allowed the calculations to be continued in the negative wall shear region. Figures 17 to 19 show the calculated local-skin friction coefficient c_f, the shape factor H and the momentum thickness Reynolds number R_θ. There are no important differences between the predictions of the models, apart from a discrepancy in the shape factor which does not seem to be significant.

Calculations were also made for an external velocity distribution given by

$$\frac{u_e}{u_\infty} = 1 + [A^2 + (Bt)^2(\xi - \xi_0)^2]^{1/2} - [A^2 + (B\xi_0 t)^2]^{1/2} \qquad (6.2)$$

where A = 0.05, B = 3.4 sec-1, $\xi = (x - 1/24)/3.45$ and the range of x values are limited to 1.24 < x < 4.69. Figures 20 and 21 show the values of c_f and R_θ obtained with both turbulence models. Figure 22 shows the calculated velocity profiles for several t- and x-stations. Again, the predictions of both turbulence models are the same for all practical purposes.

Figure 23 shows the variation of wall shear parameter f_w'' as a function of x and t, and Fig. 24 the calculated velocity profiles, including the regions in which there is flow reversal across the boundary layer. These computations are done with the zig-zag scheme and the CS model and provide confirmation of the general trends in the test case 4, namely that the unsteady turbulent boundary layers thicken rapidly with increasing flow reversal as in laminar flows. A new feature is the dip in the graphs of f_w'' near x = 2.5 which develops as t increases towards 0.40. It is possible that a singularity occurs in the solution at a later time as in the case of unsteady laminar flow over an impulsively started circular cylinder, but we note that the most definite sign of its occurrence appeared in displacement thicknesses which showed spiky characteristics. Here the displacement thickness is fairly smooth but the skin friction becomes spiky.

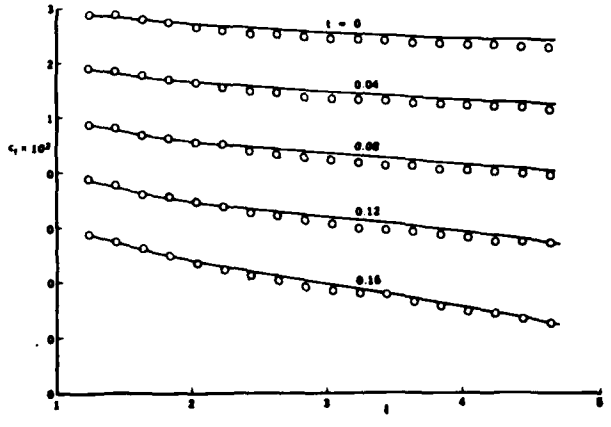

Fig. 17. Computed local skin-friction distribution for test case 4: ____, CS model; o BF model.

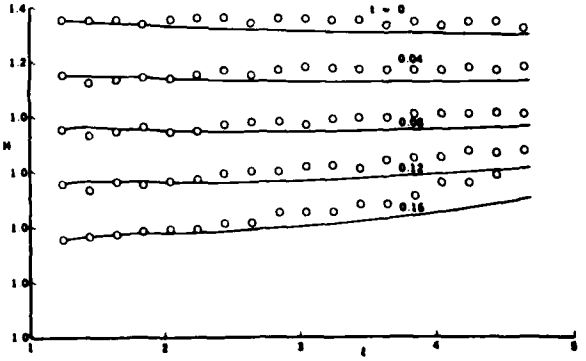

Fig. 18. Computed shape factor distribution for test case 4: ____, CS model; o, BF model.

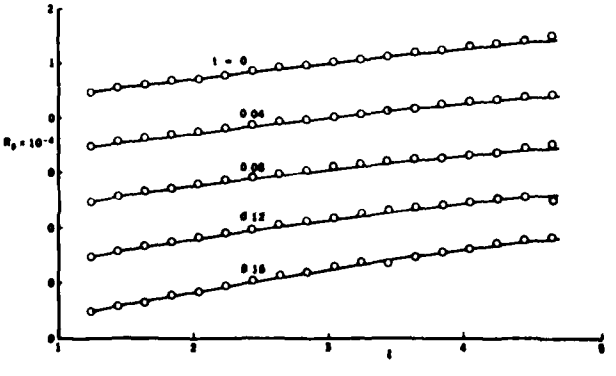

Fig. 19. Computed momentum-thickness Reynolds number for test case 4: ____, CS model; o, BF model.

6.2 Transition

The prediction of transition on stationary airfoils can be achieved, albeit in general terms and with limited range of accuracy from correlation formulas such as those of Michel [94], in which the Reynolds number based on momentum thickness, R_θ, and surface distance, R_x, are given in Cebeci and Bradshaw [95],

$$R_\theta = 1.174\ (1 + \frac{22{,}400}{R_x})R_x^{0.46} \qquad (6.3)$$

Where flow separation occurs before transition can be calculated from this formula, the location of laminar separation is taken to be the transition point. Studies on airfoils at high Reynolds numbers indicate that, in general, this procedure is reasonably accurate at low angles of attack, and the location of transition does not play a crucial role in determining its lift and drag characteristics, but

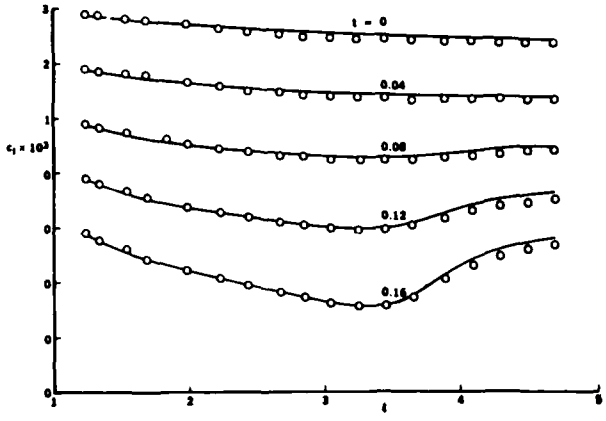

Fig. 20. Computed local skin-friction distribution for test case 5: ____ CS model; o, BF model.

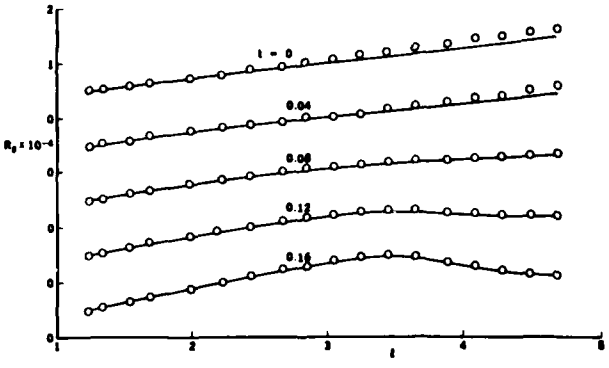

Fig. 21. Computed momentum-thickness Reynolds number for test case 5: ____, CS model, o, BF model.

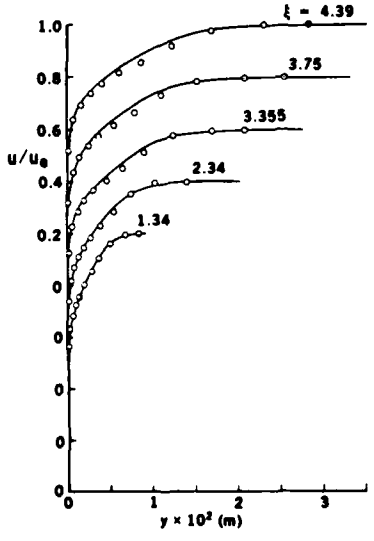

(a)

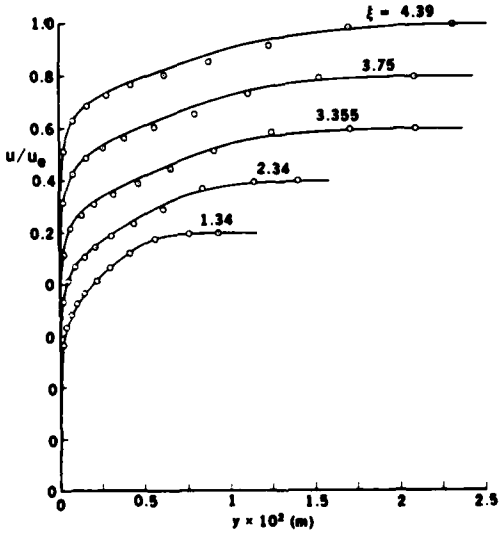

(b)

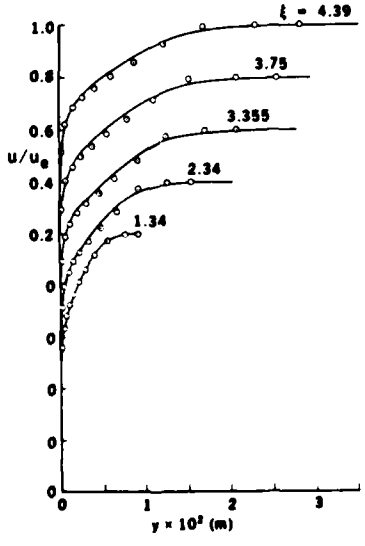

(c)

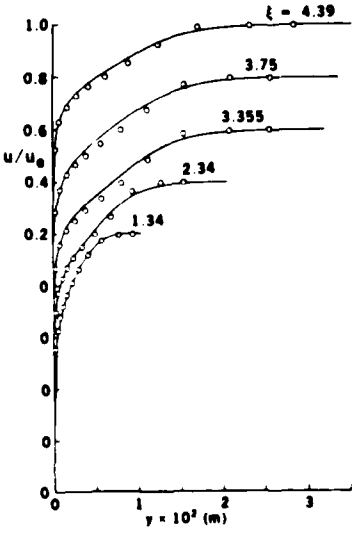

(d)

Fig. 22. Comparison of calculated velocity profiles for test case 5 with no flow reversal. ___ CS model; o, BF model. (a) t = 0.0, (b) t = 0.04, (c) t = 0.08, (d) t = 0.12.

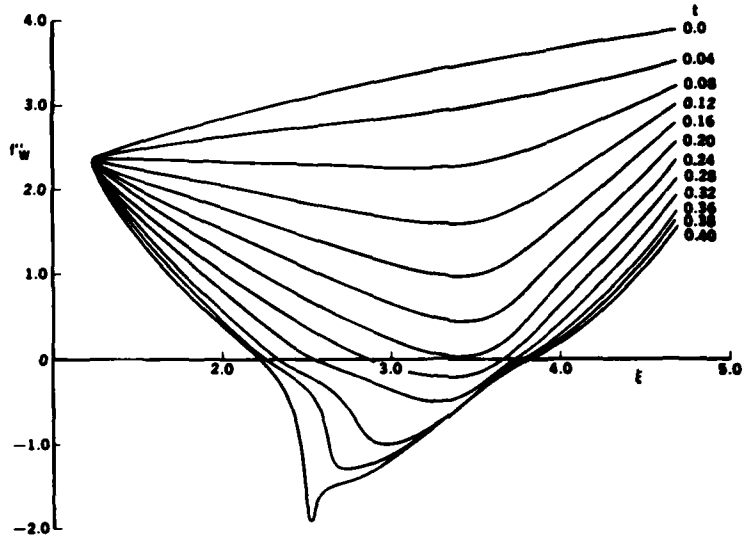

Fig. 23. Variation of wall shear parameter, f''_w, with distance, as a function of time for test case 5.

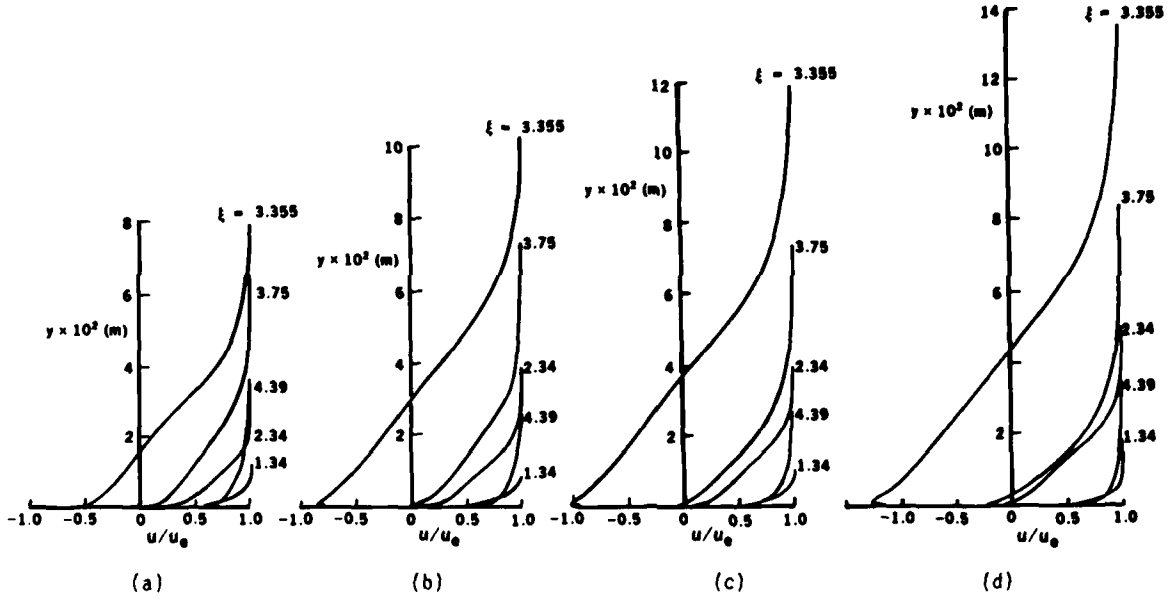

Fig. 24. Calculated velocity profiles including flow reversal by the CS models for test case 5.

this is not the case at angles of attack approaching stall conditions. The interactive boundary-layer studies of Cebeci et al. [43] indicate that, at high angles of attack, laminar separation usually takes place before the transition location can be computed from Eq. (6.3). With transition computed in this way, their calculations were continued well beyond the experimentally observed stall with no significant reduction in the lift curve slope. However, if the transition location is moved a small distance upstream, then the calculation predicts a stall angle which is in very close agreement with the experimental value. The importance of transition is further illustrated in Table 2, which shows the variation of the computed separation location and lift with transition location for $\alpha = 12°$ and $\alpha = 17°$: at the lower angle of attack, small changes in the transition location lead to small changes in the computed lift but, for $\alpha = 17°$, a small change in the specified transition location changes the computed lift by about 10%.

In addition to Eq. (6.3), transition can also be calculated by the so-called e^n-method developed independently by A.M.O. Smith [96] and by van Ingen [97]. This method makes use of the linear stability theory and, in general, gives good agreement with experiment. The method was proposed for attached flows, but it has the potential to be applied to separating flows by computing the boundary layers with an interactive boundary-layer method and analyzing the stability characteristics. Such work is in progress [98] with encouraging results.

Unlike steady flows, the prediction of transition in unsteady flows is in its infancy. Theoretical work is almost nonexistent and experimental data is scarce. The role of transition was known to be important but had not been quantified until the recent work of McCroskey et al. [99]. Their experiments show that, for an NACA 0012 airfoil, for two values of reduced frequency ($k \equiv 0.01$, 0.20) and for an angle of attack given by $\alpha = 8° + 10° \sin \omega t$, transition varies according to the results of Fig. 25. As can be seen, the transition location moves upstream with increasing angle of attack and is dependent on the direction of travel of the airfoil with transition occurring further downstream as the trailing edge moves upward. The transition location is dependent upon the reduced frequency so that, at low values of

Table 2. Effect of Transition on the Flow Properties of an NACA 0012 Airfoil, for $R_c = 6 \times 10^6$. (Computed Transition Location Corresponds to Laminar Separation.)

(a) $\alpha = 12°$. Experimental value of $c_\ell = 1.29$.

$(x/c)_{tr}$	c_ℓ	$(\frac{\delta^*}{c})_{t.e.}$	$(\Delta x/c)_{sep}$
-0.0030 (fixed)	1.270	0.0195	0.965∿TE
0.0025 (fixed)	1.283	0.0172	0.986∿TE
0.0083 (computed)	1.286	0.0167	0.986∿TE
0.0170 (fixed)	-	-	-

(b) $\alpha = 17°$. Experimental Value of $c_\ell = 1.42$.

$(x/c)_{tr}$	c_ℓ	$(\frac{\delta^*}{c})_{t.e.}$	$(\Delta x/c)_{sep}$
-0.0173 (fixed)	1.502	0.0768	0.56∿TE
-0.00925(fixed)	1.514	0.0737	0.60∿TE
-0.00250(fixed)	1.573	0.0615	0.66∿TE
0.000493(computed)	1.669	0.0453	0.77∿TE

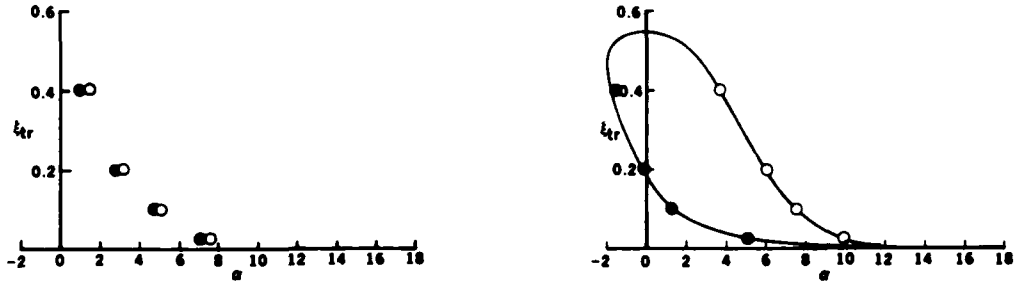

(a) k = 0.01 (b) k = 0.20

Fig. 25. Variation of transition location with angle of attack on the NACA 0012 airfoil at two reduced frequencies, according to the experimental data of McCroskey et al. [99]. The solid line in (b) denotes the fairing done by Carr and Cebeci [54].

frequency which approximate the steady-state condition, it is independent of the direction of travel of the airfoil: at the larger frequency, transition moves downstream of the near-stationary result for upwards travel of the trailing edge and upstream for downwards travel.

The effect of transition on the properties of oscillating airfoils was studied by Carr and Cebeci [54] for the NACA 0012 airfoil. The inviscid pressure distribution was obtained from Geissler's code [100] for two reduced frequencies, $k(\equiv \omega c/2u_0) = 0.01$ and 0.20 and for the angle of $\alpha = 8° + 10° \sin\omega t$. The experimental data indicates that the flow has a leading-edge separation bubble as well as an open trailing-edge separation. Its maximum angle of attack range falls in between light stall ($\alpha_{max} < 15°$) and deep stall ($\alpha_{max} < 20°$) with the magnitude of reduced frequency playing an important role in the performance of airfoil characteristics [101].

In the calculations, transition location was specified by two approaches. In the first, transition location was specified directly from experiment and in the second it was specified at the location of maximum pressure. The first assumption allows the evaluation of the numerical technique and the second is expected to be physically sound since the pressure distribution becomes increasingly peaky as the angle of attack is increased. It should be noted that the second assumption will become less appropriate as the peak in the pressure distribution diminishes with decreasing angle of attack.

Figures 26 and 27 show the results obtained for a chord Reynolds number of 3×10^6 with transition corresponding to maximum pressure peak. Approximately 100 stations were taken in the ξ-direction with 41 stations in the time direction. The steady-state conditions were obtained from the unsteady pressure distribution that corresponded to $\alpha = -2$ by taking $\omega t = 270°$ and the calculations for $t > 0$ were performed for increasing angle of attack. Since an unsteady pressure distribution is being used to calculate the initial conditions at $t = 0$ and since $\partial u/\partial t$ is not zero at $t = 0$, solutions indicate slight oscillation when unsteady-flow calculations are performed for the next time step. For this reason a smoothing procedure was applied to the calculated results at that time station and the next few stations.

The results show that for $k = 0.01$, the first traces of flow reversal occur near the trailing edge at $\alpha \simeq 8°$ and are limited to less than 1% of chord. As the angle of attack increases, the flow reversal region near the trailing edge increases becoming approximately 20% of chord for $k = 0.01$ and 15% for $k = 0.20$ at $\alpha = 18°$. Unlike experimental data, there is no leading-edge separation for either frequency. The results in Fig. 27 show that the calculations performed with higher frequency show differences between upward and downward strokes for the same angle of attack, indicating the unsteady effects. Those in Fig. 26 obtained for $k = 0.01$, on the other hand, exhibit the characteristics found in steady flows, indicating that the transition effects on the airfoil characteristics are similar to those of steady flows. This means that empirical relations such as those given by Eq. (6.3) can be used to calculate transition for

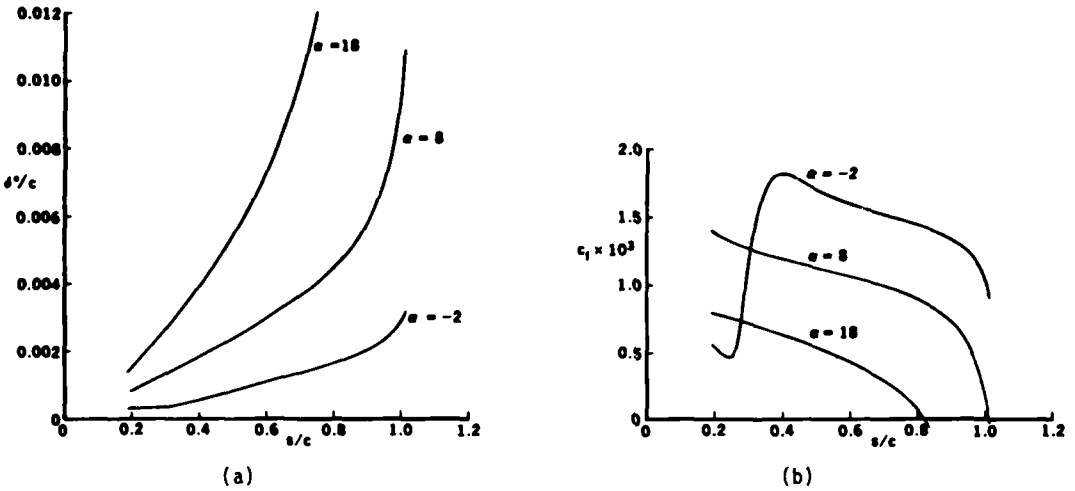

Fig. 26. Variation of (a) dimensionless displacement thickness δ*/c and (b) local skin-friction coefficient c_f for k = 0.01.

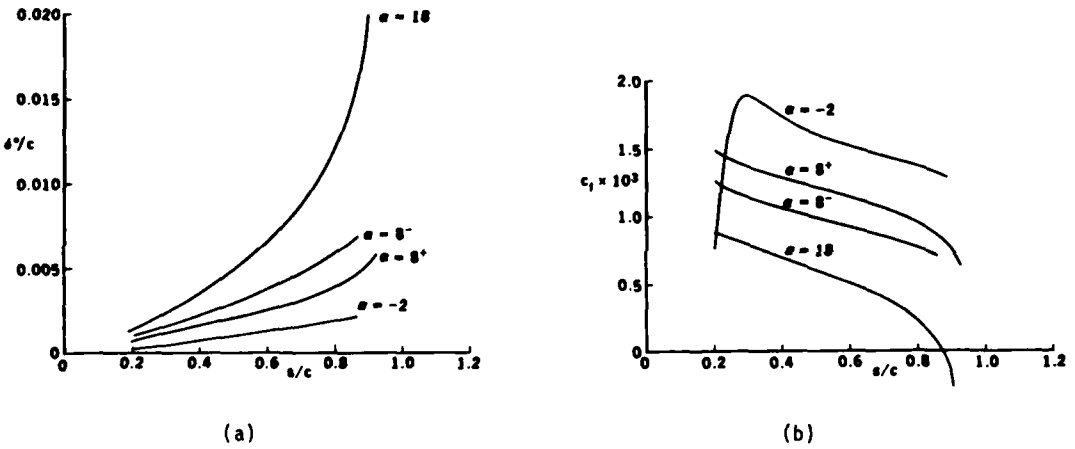

Fig. 27. Variation of (a) dimensionless displacement thickness δ*/c and (b) local skin-friction coefficient c_f for k = 0.20. Plus (+) and minus (-) on the angle of attack refer to upward and downward strokes, respectively.

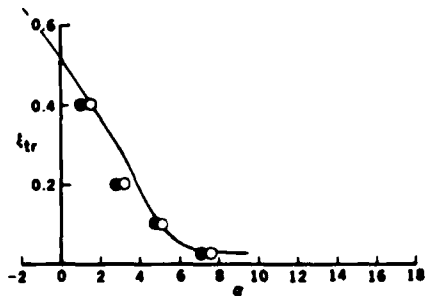

Fig. 28. Comparison of experimental (symbols) and calculated (solid line) transition locations for k = 0.01.

unsteady flows at low values of frequency. The results in Fig. 28 performed for the data of Fig. 25 confirm this expectation.

Figure 29 shows the results for k = 0.20 in which calculations were performed with transition specified from the experimental data, according to Fig. 25b. Again the calculations were started at the same angle of attack and continued in the upward stroke mode. In this case, however, the solutions broke down at $\alpha = 11.09°$. There was essentially no flow reversal and no signs of numerical difficulties until $\alpha = 9.56°$ when flow separation appeared around the trailing edge. At the next angle of attack, $\alpha = 11.09°$, a laminar leading-edge separation bubble appeared at around 4% chord and the solutions broke down shortly thereafter. Figure 29 also shows that while the computed displacement thickness distributions are smooth, those corresponding to local skin friction are not. The wiggles in the latter case are a result of transition locations specified at different angles of attack. For example, we see from Fig. 25b that for $-2° \leq \alpha < 0$, the transition location moves from $\xi_{tr} = 0.40$ to approximately $\xi_{tr} = 0.55$. This means that the laminar flow calculations for $\alpha = 0$ contain a combination of laminar and turbulent flow characteristics which originated at $\alpha = -2°$ where the laminar flow calculations terminated at $\xi_{tr} = 0.40$. It also points out that in order to obtain calculations free of wiggles, the angle of attack should be chosen in such a way that transition location moves in one direction during one stroke.

The results in Figures 27 and 29 clearly show that the location of transition plays an important role in obtaining the airfoil characteristics. The assumption that transition occurs at the location of

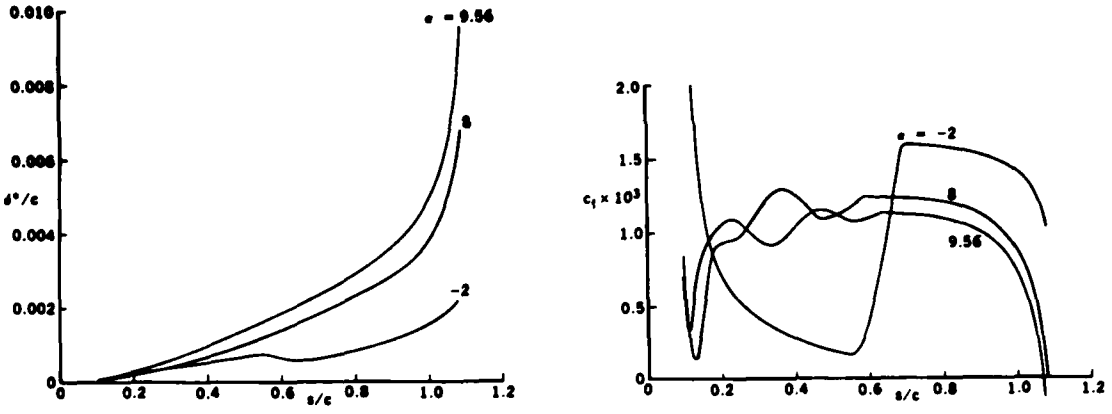

(a) (b)

Fig. 29. Variation of (a) dimensionless displacement thickness δ*/c and (b) local skin-friction coefficient c_f for k = 0.20 with transition specified according to the experimental data, Fig. 25b.

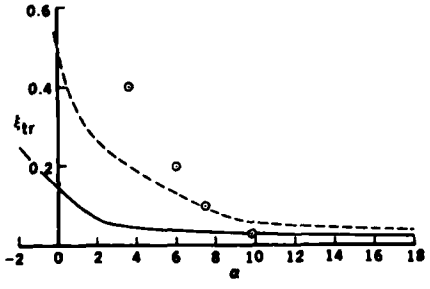

Fig. 30. Comparison of experimental (symbols) and calculated (dashed line) transition locations together with those corresponding to maximum pressure peak (solid line) for upward stroke, k = 0.20.

pressure peak leads to results which do not agree with the experimental observations. The calculations indicate that the airfoil characteristics at high angles of attack, as in steady flows, strongly depend on transition.

Figure 30 allows a comparison between the measured transition locations and those calculated from Eq. (6.3) during the upward stroke. It is clear that the use of this correlation, although imperfect, is to be preferred to the specification of transition at the location of the pressure peak. It is easy to understand why a formula such as Eq. (6.3) can represent the transition location on the upward stroke but not on the downward stroke of an airfoil oscillating at high frequencies. The basis for Eq (6.3) is laminar boundary-layer theory which works satisfactorily in situations where the transition occurs in a region of formerly laminar flow. This condition is satisfied in the upward stroke where the transition location moves upstream into a region where laminar flow previously existed. On the downward stroke, however, the transition moves downstream into a region previously characterized by turbulent flow and available correlation formulas do not take account of the effects of the residual turbulence.

7.0 CONCLUDING REMARKS

The following statements provide a summary of the more important conclusions which can be extracted from the preceding text, together with consequent recommendations.

1. The numerical solution of unsteady boundary-layer equations with large flow reversal across the layer requires proper numerical formulation which satisfies the CFL stability condition. If this condition is not satisfied, the schemes become numerically unstable leading to erroneous results regarding separation in unsteady flows. The characteristic scheme described here satisfies the CFL condition and suggests that for the problem of a circular cylinder started impulsively from rest, the unsteady separation corresponds to steady separation [33].

It is recommended that future calculations involving unsteady flows with separation make use of an intelligent numerical scheme such as the characteristic box.

2. The unsteady boundary-layer equations have been solved by using the characteristic box scheme for flow over an oscillating thin ellipse for a wide range of angles of attack. The inviscid and viscous flow equations have been interacted with a procedure developed by Cebeci et al. [43]. Convergence was achieved with a number of iterations which ranged up to three, depending on the existence and magnitude of any region of flow separation, and the procedure calculated through separated-flow regions without numerical difficulties.

It is recommended that the numerical procedure, involving interaction of solutions to the inviscid and boundary-layer flows be extended to oscillating airfoils, including their wake, first to allow quantitative evaluation over a wide range of flow parameters and secondly to predict the characteristics for flow and geometry parameters for which measured data is unavailable. The procedure should also be applied to the calculation of the flow over airfoils and wings (or blades) subjected to unsteady onset velocity and to rapid changes in orientation. A further important application is the installed performance of a turboprop. Because of their lower fuel consumption, turboprops are being seriously considered for future transport aircraft. While the flow about an isolated propeller may be steady in blade-fixed coordinates, when it is mounted on the airplane, the blades rotate through a nonuniform flowfield and thus encounter a time-varying flow environment.

3. Turbulence models and transition criteria have been evaluated. The algebraic eddy-viscosity formulation of Cebeci and Smith provides results which are sensibly identical to those from the stress model of Bradshaw et al. Transition, as in steady flows, is found to be very important at high angles of attack and the assumption that the maximum pressure peak location corresponds to transition is not satisfactory.

It is recommended that future turbulent-flow applications of the interactive procedure make use of an algebraic eddy-viscosity formulation such as that of Cebeci and Smith. New information is necessary to support procedures for the accurate determination of the location of transition in unsteady flow and must involve further experiment on oscillating airfoils as well as greater emphasis on the development of methods based on stability analyses and their extension to unsteady flows. Further calculations with the present interactive procedure should be made so as to guide the experimental and theoretical developments.

ACKNOWLEDGMENT

This research was supported under Air Force Office of Scientific Research contract F496720-82-C-0055.

8.0 REFERENCES

1. Lighthill, M.J., The response of laminar skin friction and heat transfer to fluctuations in the stream velocity, Proc. Roy. Soc. A 224, 1954, p. 1.

2. Glauert, M.B., The laminar boundary layer on oscillating plates and cylinders, J. Fluid Mech. 1, 1956, pp. 97-110.

3. Karlsson, An unsteady turbulent boundary layer, J. Fluid Mech. 5, 1959, pp. 622-636.

4. Carr, L.W., McAlister, K.W. and McCroskey, W.J., Analysis of the development of dynamic stall based on oscillating airfoil experiments, NASA TN D-8382, 1977.

5. Francis, M.S. and Luttges, M.W. (eds.), Workshop on Unsteady Separated Flows, 1984.

6. Reynolds, W.C. and Carr L.W., Review of unsteady driven, separated flows, AIAA Paper 85-0527, 1985.

7. Sears, W.R. and Telionis, D.P., Boundary-layer separation in unsteady flow, SIAM J. Appl. Math 28, 1975, p. 215.

8. Riley, N., Unsteady laminar boundary layers, SIUAM Rev. 17, 1975, p. 274.

9. Williams, J.C., III, Incompressible boundary-layer separation, Annual Rev. Fluid Mech. 9, 1977.

10. Shen, S.F., Unsteady separation according to the boundary-layer equations. Advances in Applied Mech. 18, 1978, pp. 177-200.

11. Telionis, D.P., Review - Unsteady boundary layers, separated and attached. J. Fluids Eng. 101, 1979, pp. 29-43.

12. Cebeci, T., Unsteady separation, Numerical and Physical Aspects of Aerodynamic Flows (T. Cebeci, ed.), Springer-Verlag, NY, 1982, pp. 265-277.

13. Cousteix, J., Three-dimensional and unsteady boundary-layer computations. To appear in Ann. Rev. of Fluid Mech., 1985.

14. Belcher, R.J., Burggraf, O.R., Cooke, J.C., Robins, A.J. and Stewartson, K., Limitless boundary layers, in Recent Research on Unsteady Boundary Layers, Proc. Int. Union Theoret. Appl. Mech. (G.A. Eichelbrenner, ed.), 1971, pp. 1444-1466.

15. Collins, N.M. and Dennis, S.C.R., The initial flow past an impulsively started circular cylinder. Quart. J. Mech. Appl. Math. 26, 1973, pp. 53-75.

16. Collins, N.M. and Dennis, S.C.R., Flow past an impulsively started circular cylinder, J. Fluid Mech. 60, 1973, pp. 105-127.

17. Telionis, D.P. and Werle, M.J., Boundary layer separation from downstream moving boundaries, ASME J. of Appl. Mech., 40, 1973, pp. 369-374.

18. Telionis, D.P. and Tsahalis, D.T., Unsteady laminar separation over cylinder started impulsively from rest, Acta Astronautics 1, 1974, p. 1487.

19. Williams, J.C., III and Johnson, W.D., Semi-similar solutions to unsteady boundary-layer flows including separation, AIAA J., 12, 1974, pp. 1388-1393.

20. Patel, V.C. and Nash, J., Unsteady turbulent boundary layers with flow reversal, in Unsteady Aerodynamics (Kinney ed.) 1, 1975, p. 191.

21. Bar-lev, M. and Yang, H.T., Initial flowfield over an impulsively started circular cylinder, J. Fluid Mech. 72, 1975, pp. 625-647.

22. Tsahalis, D.Th., Laminar boundary-layer separation from an upstream moving wall, AIAA J., 15, 1977, pp. 561-566.

23. Bodonyi, R.J. and Stewartson, K., The unsteady laminar boundary layer on a rotating disk in a counter-rotating fluid, J. Fluid Mech., 79, 1977, pp. 669-688.

24. Patel, M.H., On turbulent boundary layers in oscillatory flow, Proc. Roy. Soc, A 353, 1977, pp. 121-144.

25. Cebeci, T., An unsteady laminar boundary layer with separation and reattachment, AIAA J., 16, 1978, pp. 1305-1306.

26. Cebeci, T., The laminar boundary layer on a circular cylinder started impulsively from rest, . Comp. Phys. 31, 1979, pp. 153-172.

27. Bradshaw, P., Singularities in unsteady boundary layers, AIAA J., 17, 1979, p. 790.

28. van Dommelen, L.L. and Shen, S.F., The spontaneous generation of the singularity in a separating laminar boundary layer. J. Comp. Phys. 38, 1981, pp. 125-140.

29. van Dommelen, L.L. and Shen, S.F., The genesis of separation, Numerical and Physical Aspects of Aerodynamic Flows (T. Cebeci, ed.), Springer-Verlag, NY, 1982, pp. 293-311.

30. Cebeci, T., Khattab, A.A. and Schimke, S.M., Can the singularity be removed in time-dependent flows? In Workshop on Unsteady Separated Flow (M.S. Francis and M.W. Luttges, eds.), Colorado Springs, Colorado, 1984.

31. Cowley, S.J., Computer extension and analytic continuation of Blasius' expansion for impulsive flow past a circular cylinder, J. Fluid Mech. 135, 1983, pp. 389-405.

32. Ingham, D.B., Unsteady separation, J. Comp. Phys. 53, 1984, pp. 90-99.

33. Cebeci, T., Unsteady boundary layers with an intelligent numerical scheme. In review, 1985.

34. Matsushita, M., Shigeru, M. and Akamatsu, T., Studies on boundary-layer separation in unsteady flows using an integral method, J. Fluid Mech. 149, 1984, pp. 477-501.

35. Isaacson, E. and Keller, H.B., Analysis of Numerical Methods, John Wiley, N.Y., 1966.

36. Cebeci, T., Stewartson, K. and Williams, P.G., Separation and reattachment near the leading edge of a thin airfoil at incidence, AGARD CP 291, 1981, Paper 20.

37. LeBalleur, J.C., Numerical viscous-inviscid interaction in steady and unsteady flows. In Numerical and Physical Aspects of Aerodynamic Flows II (T. Cebeci ed.), Springer-Verlag, N.Y., 1984, pp. 259-284.

38. Cebeci, T. and Schimke, S.M., Calculation of separation bubbles in interactive boundary layers. J. Fluid Mech. 131, 1983, pp. 305-317.

39. Kwon, O.K. and Pletcher, R.H., Prediction of incompressible separated boundary layers including viscous-inviscid interaction, J. Fluid Eng., 101, 1979, pp. 466-472.

40. Gleyzes, C., Cousteix, J. and Bonnet, J.L., A calculation method of leading edge separation bubbles, in Numerical and Physical Aspects of Aerodynamic Flows II (T. Cebeci ed.), Springer-Verlag, N.Y., 1984, pp. 173-192.

41. Davis, R.L. and Carter, J.E., Analysis of airfoil transitional separation bubbles, AIAA Paper 84-1613, 1984.

42. Melnik, R.E., Rudman, S. and Brook, J.W., The computation of viscid/inviscid interaction on airfoils with separated flow, Third Symposium on Numerical and Physical Aspects of Aerodynamic Flows, Long Beach, California, 21-24 January 1985.

43. Cebeci, T, Clark, R.W., Chang, K.C., Halsey, N.D. and Lee, K., Airfoils with separation and the resulting wakes, Third Symposium on Numerical and Physical Aspects of Aerodynamic Flows, Long Beach, California, 21-24 January 1985.

44. Adair, D., Thompson, B.E., Whitelaw, J.H. and Williams, B.R., Comparison of interactive and Navier-Stokes calculations of separating boundary-layer flows, Third Symposium on Numerical and Physical Aspects of Aerodynamic Flows, Long Beach, California, 21-24 January 1985.

45. Wai, J.C, Baillie, J.C. and Yoshihara, H., Computation of turbulent separated flows over wings, Third Symposium on Numerical and Physical Aspects of Aerodynamic Flows, Long Beach, California, 21-24 January 1985.

46. Cebeci, T., Chen, L.T., Chang, K.C. and Peavey, C.C., An interactive scheme for three-dimensional transonic flows, Third Symposium on Numerical and Physical Aspects of Aerodynamic Flows, Long Beach, California, 21-24 January 1985.

47. Herbert, W.B., Supermaneuverability, In Workshop on Unsteady Separated Flow (M.S. Francis and M.W. Luttges eds.), Colorado Springs, Colorado, 1984.

48. McDonald, H. and Briley, W.R., A survey of recent work on interacted boundary-layer theory for flows with separation, in Numerical and Physical Aspects of Aerodynamic Flows II (T. Cebeci, ed.), 1983, pp. 141-162.

49. Cebeci, T., Stewartson, K. and Whitelaw, J.H., The calculation of two-dimensional flows past airfoils, Numerical and Physical Aspects of Aerodynamic Flows II (T. Cebeci, ed.), Springer-Verlag, N.Y., 1984, pp. 1-41.

50. Mehta, U., Dynamic stall of an oscillating airfoil, AGARD CP 227, 1977, Paper 23.

51. Shamroth, S.J., A Navier-Stokes calculation of the airfoil dynamic stall process, In Workshop on Unsteady Separated Flow (M.S. Francis and M.W. Luttges eds.), Colorado Springs, Colorado, 1984.

52. Cebeci, T. and Carr, L.W., Prediction of boundary-layer characteristics of an oscillating airfoil, In Unsteady Turbulent Shear Flows (R. Michel, J. Cousteix and R. Houdeville, eds.), Springer, 1981, pp. 145-158.

53. Cebeci, T. and Carr, L.W., Calculation of boundary layers near the stagnation point of an oscillating airfoil, NASA TM 84350, 1984.

54. Carr, L.W. and Cebeci, T., Boundary layers on oscillating airfoils, Third Symposium on Numerical and Physical Aspects of Aerodynamic Flows, Long Beach, California, 21-24 January 1985.

55. Maskew, B. and Dvorak, F.A., Prediction of dynamic separation characteristics using a time stepping viscid/inviscid approach, Third Symposium on Numerical and Physical Aspects of Aerodynamic Flows, Long Beach, California, 21-24 January 1985.

56. Geissler, W., Unsteady boundary-layer separation on airfoils performing large amplitude oscillations - dynamic stall, AGARD Symposium on Unsteady Aerodynamics, Fundamentals and Applications to Aircraft Dynamics, Göttingen, Germany, 1985.

57. Thompson, B.E. and Whitelaw, J.H., Flow characteristics of a trailing-edge flow with turbulent boundary-layer separation, to be published in J. Fluid Mech., 1985.

58. Carr, L.W., Standardization of computational experiments in unsteady turbulent boundary-layer flow, NASA TM-78-445, 1977.

59. Cousteix, J. and Houdeville, R., Couches limites instationnaires (unsteady boundary layers, English translation), CERT Technical Report 53/2259, ONERA, France, 1983.

60. Simpson, R.L and Shivaprasad, B.G., The structure of a separating turbulent boundary layer, Part 5. Frequency effects on periodic unsteady freestream flows, J. Fluid Mech. 121, 1983, pp. 319-340.

61. Simpson, R.L, Shivaprasad, B.G. and Chew, Y.T., The structure of a separating turbulent boundary layer, Part 4. Effects of periodic freestream unsteadiness, J. Fluid Mech. 127, 1983, pp. 219-262.

62. Parikh, P.G., Reynolds, W.C. and Jayaraman, R., Behavior of an unsteady turbulent boundary layer, AIAA J. 20, 1982, pp. 769-775.

63. Jayaraman, R., Parikh, P. and Reynolds, W.C., An experimental study of the dynamics of an unsteady turbulent boundary layer, Rept. TF-18, Dept. of Mech. Eng., Stanford University, 1983.

64. Covert, E.E. and Lorber, P.F., Unsteady turbulent boundary layers in adverse pressure gradients, AIAA J. 22, 1984, pp. 22-28.

65. Cebeci, T. and Smith, A.M.O., Analysis of Turbulent Boundary Layers, Academic Press, NY, 1974.

66. Cebeci, T., Chang, K.C., Li, C. and Whitelaw, J.H., Turbulence models for wall boundary layers, Mech. Eng. Rept. ME-84-2, California State University, Long Beach, to be published in AIAA J., 1985.

67. Chang, K.C., Bui, M.N., Cebeci, T. and Whitelaw, J.H., The calculation of turbulent wakes. Mech. Eng. Rept. ME-84-3, California State University, 1984, to be published in AIAA J., 1985.

68. Francis, M.S., Keese, J.E., Lang, J.D., Sparks, G.W. and Sisson, G.E., Aerodynamic characteristics of an unsteady separated flow, AIAA J. 17, 1979, pp. 1332-1338.

69. Viets, H., Palmer, G.M. and Bethke, R.J., Potential application of "forced unsteady flows," In Workshop on Unsteady Flow (M.S. Francis and M.W. Luttges, eds.), Colorado Springs, 1984.

70. Koga, D.J., Reisenthel, P. and Nagib, H.M., Control of separated flowfields using forced unsteadiness, IIT Heat Transfer and Fluids Rept. R-84-1, Illinois Institute of Technology, 1984.

71. Francis, M.S., Keese, J.E. and Retelle, J.P., Jr., An investigation of airfoil dynamic stall with large amplitude motions, FJSRL-TR-83-0010, F.J. Seiler Research Labs, Air Force Academy, Colorado Springs, Colorado, 1983.

72. Bradshaw, P., Cebeci, T. and Whitelaw, J.H., Engineering Calculation Methods for Turbulent Flows, Academic Press, London, 1981.

73. Keller, H.B., Numerical methods in boundary-layer theory, Ann. Rev. Fluid Mech. 10, 1978, pp. 417-433.

74. Cebeci, T., Stewartson, K. and Williams, P.G., On the response of a stagnation boundary layer to a change in the external velocity. SIAM J. Appl. Math. 36, 1979, pp. 190-199.

75. Bradshaw, P., Ferriss, D.H. and Atwell, N.P., Calculation of boundary-layer developments using the turbulent energy equation, J. Fluid Mech., 28, 1967, p. 593.

76. Goldstein, S., On laminar boundary-layer flow near a point of separation. Quart. J. Mech. and Appl. Math. 1, 1948, pp. 43-69.

77. Brown, S.N., Singularities associated with separating boundary layers. Phil. Trans. Roy. Soc. London A 257, 1965, pp. 409-444.

78. Blottner, F.G., Computational techniques for boundary layers. AGARD LSP-73 on Computational Methods for Inviscid and Viscous Two- and Three-Dimensional Flowfields, 1975.

79. Crank, J. and Nicolson, P., A practical method of numerical evaluation of solutions of partial-differential equations of the heat-conduction type, Proc. Cambridge Phil. Soc. 43, 1947, p. 50.

80. Keller, H.B., Accurate difference methods for two-point boundary-value problems, SIAM J. Numer. Anal. 11, 1974, pp. 305-320.

81. Krause, E., Hirschel, E.H. and Bothmann, Th., Die numerische integration der bewegungsgleichungen dreidimensionaler laminarer kompressibler grenzschichten, Bond 3, Fachtagung Aerodynamik, Berlin; D6LR-Fachlinchreike, 1968.

82. Moore, F.K., On the separation of the unsteady laminar boundary layer, in Boundary Layer Research (H. Gortler ed.), 1957, pp. 296-311.

83. Rott, N., Unsteady viscous flow in the vicinity of a stagnation point, Quarterly J. of Appl. Math., 13, 1956, pp. 444-451.

84. Sears, W.R., Some recent developments in airfoil theory, J. of Aero. Sci., 23, 1956, pp. 490-499.

85. LeBalleur, M., Couplage visqueux-non-visqueux analyse du probleme incluant decollements et ondes de choc, LeRech. Aerosp. 1977-6, 1977, p. 349, English trans. E5A-476.

86. Carter, J.E., A new boundary-layer inviscid interaction technique for separated flow. AIAA Paper 79-1450, 1979.

87. Veldman, A.E.P., New quasi-simultaneous method to calculate interacting boundary layers, AIAA J. 19, 1981, pp. 79-85.

88. Houwink, R., Computations of unsteady separated transonic flow about oscillating airfoils, Third Symposium on Numerical and Physical Aspects of Aerodynamic Flows, Long Beach, California, 21-24 January 1985.

89. Lorber, P.F. and Covert, E.E., Unsteady airfoil boundary layers - experiment and computation, Third Symposium on Numerical and Physical Aspects of Aerodynamic Flows, Long Beach, California, 21-24 January 1985.

90. LeBalleur, J.C. and Girodroux-Lavigne, P., A viscous-inviscid interaction method for computing unsteady transonic separation, Third Symposium on Numerical and Physical Aspects of Aerodynamic Flows, Long Beach, California, 21-24 January 1985.

91. Rothmayer, A.P. and Davis, R.T., Massive separation and dynamic stall on cusped trailing-edge airfoils, Third Symposium on Numerical and Physical Aspects of Aerodynamic Flows, Long Beach, California, 21-24 January 1985.

92. Proceedings of Numerical and Physical Aspects of Aerodynamic Flows, California State University, Long Beach, 21-24 January 1985.

93. Cebeci, T. and Carr, L.W., Computation of unsteady turbulent boundary layers with flow reversal and evaluation of two separate turbulence models, Proc. R. Soc. Lond. A 380, 1982, pp. 291-304.

94. Michel, R., Etude de la transition sur ler profiles d'aile; establissement d'un critere de determination de point de transition et calcul de la trainee due profile incompressible, ONRA Rept. 1/1578A, 1951.

95. Cebeci, T. and Bradshaw, P., Physical and Computational Aspects of Convective Heat Transfer, Springer-Verlag, NY, 1984.

96. Smith, A.M.O. and Gamberoni, N., Transition, pressure gradient and stability theory, Proc. IX Intl. Congress Appl. Mech., Brussels, 1956.

97. van Ingen, J.L., A suggested semi-empirical method for the calculation of the boundary-layer transition region, Rept. No. VTH71, VTH74, Delft, Holland, 1956.

98. Cebeci, T. and Wang, S.W., Transition prediction in flows with separation, paper in preparation, 1985.

99. McCroskey, W.J., McAlister, K.W., Carr, L.W. and Pucci, S.L., An experimental study of dynamic stall on advanced airfoil sections 1, 2, 3, NASA-TM-84245, 1982.

100. Geissler, W., Private communication, 1984.

101. McCroskey, W.J. and Pucci, S.L., Viscous-inviscid interaction on oscillating airfoils in subsonic flows, AIAA J. 20, 1982, pp. 167-174.

UNSTEADY TURBULENT BOUNDARY-LAYER EXPERIMENTS WITH RAPIDLY CHANGING FREE-STREAM CONDITIONS

G. J. Brereton
Stanford University
Stanford, California 94305, USA

L. W. Carr
Ames Research Center
Mountain View, California 94035, USA

and

W. C. Reynolds
Stanford University
Stanford, California 94305, USA

ABSTRACT

Selected data sets produced by the Stanford Unsteady Turbulent Boundary Layer Program are compared to analytic solutions of the Stokes equations for different kinds of imposed, organized unsteadiness. Good agreement is found, qualifying the facility as one that faithfully produces flows of different prescribed unsteady conditions. Data sets from the facility are therefore considered especially suitable for comparison with predictions of turbulence models for unsteady flows. New data describing the development of an unsteady separation bubble are presented.

NOMENCLATURE

$A_{1,U}$	Amplitude of fundamental frequency component of variable U.
E,e	Subscript used to denote free-stream value.
L	Length of test section.
L_s	Stokes layer thickness parameter.
$\tilde{P}$	Deterministic component of pressure.
$P_{1,U}$	Phase of fundamental frequency component of variable U.
S_x	Strouhal number based on the streamwise distance in the test section, and local mean free-stream velocity $[\omega(X-X_o)/\bar{U}_e]$.
S_δ	Strouhal number based on the local value of thickness of the mean boundary layer, and local mean free-stream velocity $[\omega\delta/\bar{U}_e]$.
t	Time.
t'	Time elapsed since the beginning of a ramp change in free-stream velocity.
$\tilde{U},\tilde{u}$	Deterministic component of streamwise velocity.
$\bar{U}_e$	Local mean free-stream velocity.
<U>	Phase-averaged value of streamwise velocity.
W	Streamwise acceleration.
X,x	Streamwise coordinate.
X'	Streamwise distance along the test section, normalized by total length of test section $[(X-X_o)/L]$.
Y,y	Surface-normal coordinate.
δ	Boundary-layer thickness.
ν	Kinematic viscosity.
ρ	Density.
ω	Circular frequency in radians/second.

INTRODUCTION

The Unsteady Turbulent Boundary Layer Program at Stanford University has been involved in experimental investigations for a number of years. The broad objectives of this program are twofold. Firstly they are to try to understand the characteristics of a particular kind of unsteady turbulent boundary layer. This is one which develops under steady, zero pressure gradient conditions and is then subjected to an organized form of free-stream unsteadiness. Secondly, the objectives are to provide an extensive and definitive data base, intended to be used for the development of and evaluation of turbulence-modeling schemes for unsteady flows.

Selected data sets obtained in this program, for which some independent comparison is available, are reviewed in this paper. The critiques used are the analytic solutions of the Stokes equation for boundary conditions corresponding to the different forms of imposed, organized unsteadiness. The intention is to establish the data sets created under this program as the results of "benchmark" experiments, suitable for the purposes of comparison with and development of models of turbulence for unsteady flows.

A second aspect of this paper is the presentation of some new and intriguing data as a possible target for turbulence-modeling schemes; the data describe the development of an unsteady, turbulent "separation bubble".

A recent and thorough overview of some experimental, analytic, and computational aspects of unsteady, turbulent boundary layers is given by Cousteix and Houdeville [1].

EXPERIMENTAL OVERVIEW

Experiments were performed in a closed-loop water tunnel, an illustration of which is shown in Figure 1. Water flows from a header tank through screens and a contraction, after which boundary layers are bled off. A new turbulent boundary layer is tripped on the top wall of the development section. Valves positioned below the development section permit sufficient flow to be removed to maintain a constant free-stream velocity and to prevent growth of a boundary layer on the bottom wall. Thus a steady, zero-pressure-gradient, turbulent boundary layer develops on the top wall. At the end of the development section, this steady, turbulent boundary layer is characterized by a free-stream velocity of 731 mm/sec. and a Reynolds number (based on momentum thickness) of 2800.

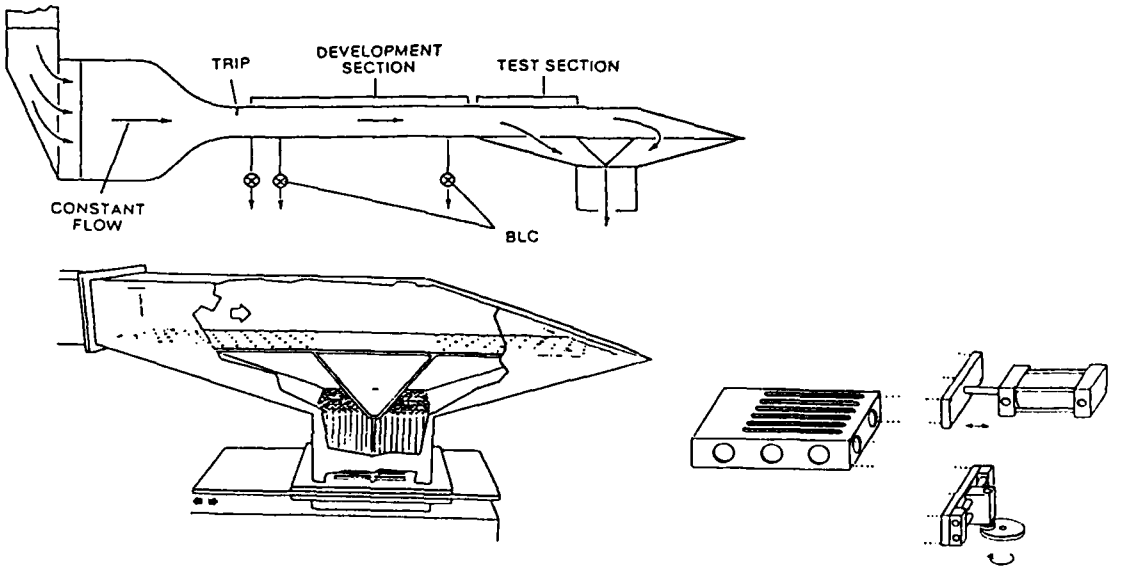

Fig. 1. The facility and its modes of operation.

It is in the test section that free-stream unsteadiness is controlled so that effects on the top-wall boundary layer may be studied. Water entering the test section may exit through either of two routes. Some may be bled off through the porous bottom wall of the test section. The remainder passes through to the recovery section and flows through its bottom wall. The proportion of flow exiting by each route is governed by the position of a gate valve. The gate valve always presents a constant area to the exiting flows so that, regardless of its position, the pressure drop across the valve should not vary. Thus the development-section flow is essentially unaffected by gate-valve movement.

With minimal disturbance to the flow in the development section, the position of the gate valve controls the fraction of water flowing through the bottom wall of the test section and so the decrease in free-stream velocity along the test section. The bottom of the test section consists of uniformly spaced holes. Consequently, when the gate valve is appropriately positioned, a nearly linear decrease in free-stream velocity along the test section results.

The ability to impose organized unsteadiness upon a turbulent boundary layer that has developed under steady, zero-pressure-gradient conditions is a unique and important feature of this facility, for several reasons. Firstly, it allows initial conditions present upstream of the point of introduction of unsteadiness to be clearly specified and easily documented. Secondly, it allows one to study the effects of unsteadiness on a turbulent boundary layer without regard for any complicating factors associated with transition. Thirdly, the introduction of only local unsteadiness will produce local, surface-generated vorticity. Were the boundary layer grown from a leading-edge in an already unsteady flow, leading-edge vorticity would convect downstream and its interaction with surface-generated vorticity might inhibit correct interpretation of experimental results.

Figure 2 shows the desired free-stream velocity distributions for two different experiments. The first involves oscillations in free-stream velocity about a flow of mean adverse pressure gradient (Figure 2a), while the second features abrupt changes between zero and adverse pressure-gradient flows (Figure 2b). The amplitude in the experiment featuring oscillating unsteadiness is the conventional one-half peak-to-peak amplitude at the end of the test section. In the second experiment, the amplitude is the magnitude of change in free-stream velocity at the end of the test section. In both cases it is useful to express these amplitudes as fractions of the free-stream velocity in the development section.

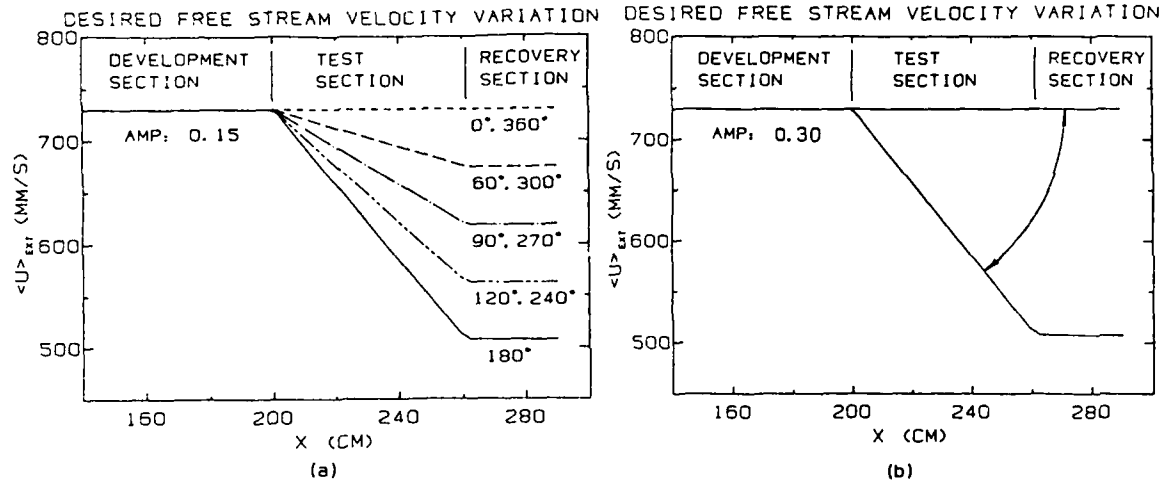

Fig. 2. Design-velocity distribution.

A scotch-yoke mechanism driven by motor provides the gate-valve movement to produce sinusoidal unsteadiness. Precise control of the motor speed allows the desired frequency of unsteadiness in the test-section flow to be imposed. For each cycle of this continuous, unsteady event, instantaneous streamwise velocity measurements were taken at each of 512 phases. A single-color, forward-scatter LDA system was used in conjunction with a frequency-tracker for these measurements. Typically, ten frequencies of oscillation were investigated in each experimental run.

In the second experiment, abrupt changes in free-stream velocity were achieved by displacing the gate valve with a double-acting pneumatic actuator. In order to bring the gate valve smoothly to rest at the limits of its travel, the appropriate exhaust port of the double-acting cylinder was closed just prior to the valve's reaching its end position. A mini-computer was programmed to energize the solenoid of the pneumatic actuator (and so initiate an abrupt decrease in free-stream velocity) and then make instantaneous velocity measurements at 20 millisecond intervals for the next ten seconds. The cycle was completed by de-energizing the actuator's solenoid and collecting data for the response to the complementary, abrupt velocity increase.

In both experiments, the unsteady events were repeated 500 times at as many as fifty positions across the boundary layer. Measurement of each unsteady profile took around one hundred hours. The processes of initiating unsteady events, of data acquisition, manipulation and storage, of positioning the LDA system and of controlling the temperature of water in the facility were therefore automated. The experiments were then repeated at other streamwise locations.

THE STOKES EQUATION

The particular flows of interest to this paper are those featuring rapid changes in free-stream velocity. Let us consider the decomposition of instantaneous values of pressure and velocity into three components, namely, a turbulent component, a deterministic component, and an initial mean or time-averaged mean component (whichever is the more relevant to the flow in question). Using this decomposition one can, after manipulations

of the Navier-Stokes equations, form "momentum" equations in terms of deterministic quantities (see Jayaraman et al. [2]). For sufficiently rapid changes in free-stream velocity, order-of-magnitude estimates imply that the streamwise momentum equation reduces to a Stokes equation in terms of deterministic quantities. That is,

$$\frac{\partial \tilde{u}}{\partial t} = -\frac{1}{\rho}\frac{\partial \tilde{P}e}{\partial x} + \nu \frac{\partial^2 \tilde{u}}{\partial y^2}$$

where "~" denotes a deterministic component.

A necessary criterion for reduction to this Stokes equation is that, in the streamwise momentum equation, the magnitude of the unsteady term is much greater than that of the convective terms. In the case of the first experiment, imposing sinusoidal unsteadiness, a suitable interpretation of this criterion is that the Strouhal number, S_x, is much greater than one. A similar criterion is found for the case of the second flow, but the Strouhal number's frequency term is replaced by the reciprocal of the time over which the abrupt change takes place. Since the length scales and velocity scales of these criteria are those one might associate with a large eddy in the outer part of the boundary layer, it is useful to draw the analogy between a Strouhal number much greater than one and the characteristic time scale of a large eddy much greater than that of the imposed unsteadiness. This might be interpreted as eddies passing by without sufficient time to adjust to the imposed unsteadiness.

A most desirable feature of the Stokes equation is that one can obtain analytic solutions for a variety of boundary conditions (and where applicable, initial conditions). A particular case of local, sinusoidal, variation in free-stream velocity and pressure gradient relates to the first experiment and its solution is discussed by Jayaraman et al. [2]. The case of an abrupt free-stream velocity change is, in our flow, very well modeled as a ramp or uniformly accelerated change, for which Goldstein [3] illustrates the relevant solution.

Good agreement between experimental measures of the deterministic velocity field and the appropriate analytic solution of the Stokes equation is of great importance. Firstly, it makes a strong case for using the experimental measurements of the velocity field as a reference against which computational models may be evaluated. Secondly, it provides a qualification that the experimental facility is indeed producing the desired flow. The value of a facility, from the point of view of providing such reference data, is further enhanced if this qualification can be made for several rather different experiments.

EXPERIMENTAL RESULTS - OSCILLATING FREE-STREAM VELOCITY

Jayaraman et al. [2] reported experimental results for a flow with imposed, sinusoidal unsteadiness about a mean, adverse pressure gradient in the test section of this facility. Careful attention was paid to thoroughly documenting the upstream conditions in the development section and the free-stream boundary conditions. The flow was found to be highly two-dimensional. Several of their experiments were conducted at Strouhal numbers which satisfy the criterion outlined earlier.

A Fourier analysis was performed on phase-averaged velocity measurements spanning the whole boundary layer, to find the deterministic response of the flow to the organized unsteadiness. Some results of this analysis are shown in Figure 3. In Figure 3a, the ordinate represents the amplitude of the fundamental frequency of oscillation in velocity at various Y points. This is normalized by the amplitude of the fundamental frequency of oscillation in free-stream velocity. The ordinate in Figure 3b is the phase-lead at a Y

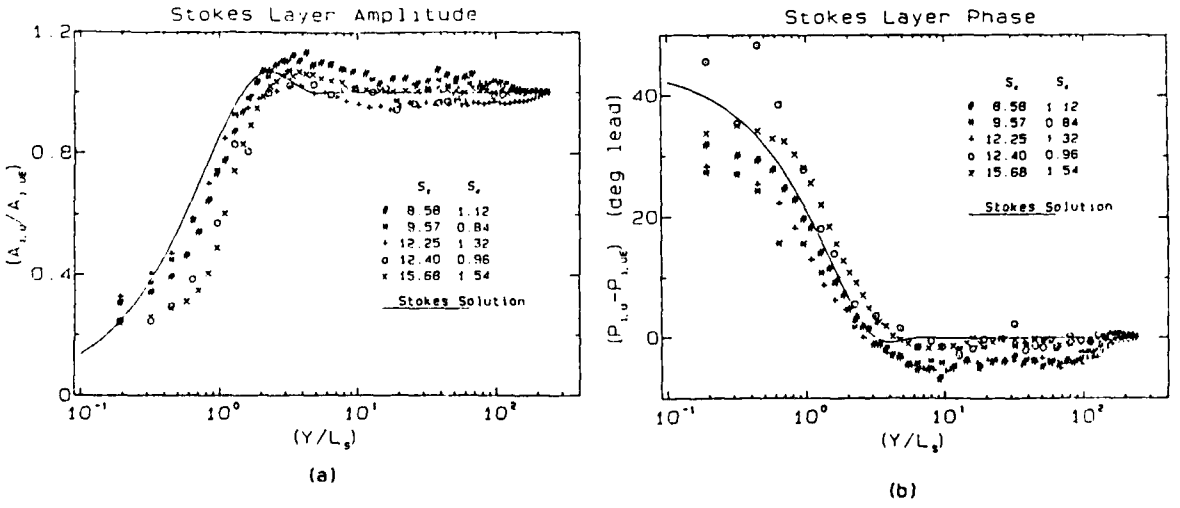

Fig. 3. Results of oscillating experiments for high values of Strouhal number.

position, relative to one in the free stream. The abscissa in each plot is Y divided by the Stokes-layer thickness parameter, a useful near-wall, unsteady length scale (Y/L_s is the dimensionless, independent variable of solutions to the Stokes equation for these oscillating boundary conditions). This Stokes layer thickness parameter is defined as

$$L_s = \sqrt{\frac{2\nu}{\omega}}$$

Clearly, good agreement is reached between the experimental data and the analytic solutions of the Stokes equation for values of S_x much greater than one (or for values of S_δ much greater than 0.1). The data sets presented are selected from flows of varying amplitudes of oscillation. Strouhal numbers based on distance from the beginning of the test section, and on boundary-layer thickness are tabulated for completeness.

For the case of this flow at significantly lower Strouhal numbers, the Stokes solution is not applicable. Computational predictions, however, have been made by Lyrio et al. [4], and the excellent agreement between their results and the data from this facility is most pleasing.

EXPERIMENTAL RESULTS - RAMP CHANGES IN FREE-STREAM VELOCITY

Recent experiments in this facility have featured abrupt changes in free-stream velocity between zero and adverse-pressure-gradient conditions. Figure 4a shows this change in free-stream velocity from a zero pressure-gradient flow to an adverse one at one particular location, almost at the end of the test section. It would seem that this change may be approximately modeled as a ramp function for a short period of time. The inset axes are for this deterministic function. One may set boundary conditions during this time period as

$$\tilde{u} = 0 \quad \text{at} \quad y = 0$$

and for $t' > 0$,

$$\tilde{u} = \tilde{u}_e = W(X) \cdot t' \quad \text{at} \quad y = \infty$$

where W is the free-stream acceleration during the ramp and t' is the time that has elapsed since the beginning of the ramp.

For sufficiently abrupt changes in free-stream velocity (say, the characteristic free-stream time scale, $L/\bar{U}_e$ or $\delta/\bar{U}_e$, greatly exceeding the time scale of the ramp), an analytic solution of the Stokes equation with these boundary conditions may then be found. The solution is a function of $Y/(2\sqrt{\nu t'})$; here Y/L_s is the dimensionless, independent variable for solutions to the Stokes equation for these boundary conditions.

Figure 4b shows the deterministic response of the boundary layer to this ramp change in free-stream velocity. The ordinate represents the change in velocity at a Y point during the ramp, normalized by the simultaneous free-stream velocity change. The abscissa is Y divided by the dynamic Stokes-layer thickness parameter, L_s. Again, good agreement is reached between the experimental data and the analytic solution of the Stokes equation for this flow.

The free-stream velocity undergoes deceleration from its steady state before the ramp function is assumed to begin. The resulting time-dependent effects would carry over into the time period for which the ramp function was presumed to describe the free-stream

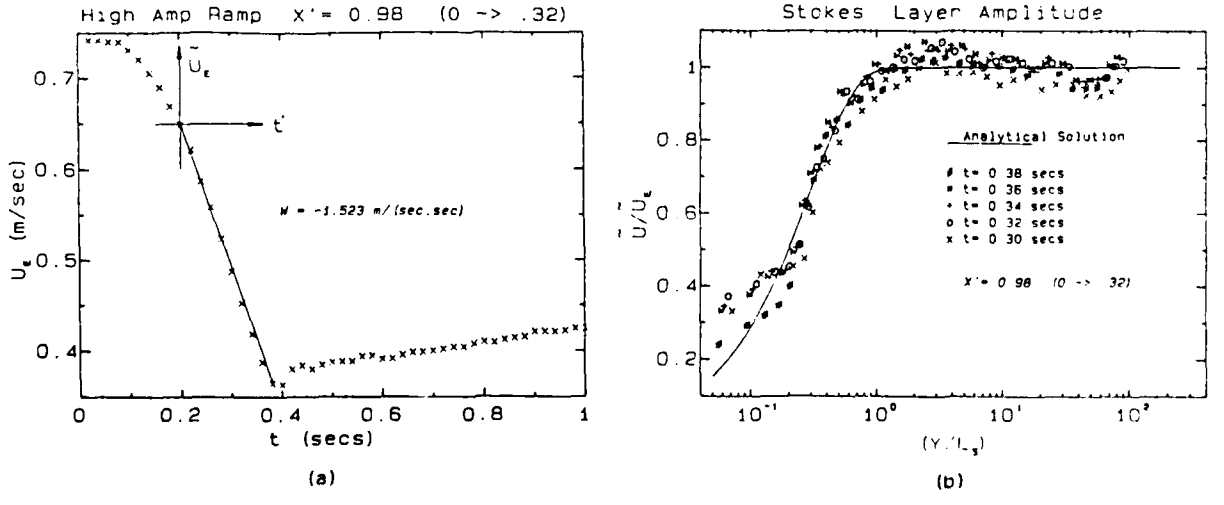

Fig. 4. Results of experiments for abrupt decrease in free-stream velocity.

velocity. Therefore, during the early part of the ramp, one would expect discrepancies between the data and this solution of the Stokes equation. For this reason, the times for which deterministic profiles are plotted are all during the later part of the ramp. Equally good agreement was found for similar experiments featuring different amplitudes of free-stream velocity change and converse abrupt changes from flows of adverse pressure gradient to flows of zero pressure gradient.

THE SEPARATION BUBBLE

In the recent series of experiments conducted in this facility, the pressure gradient experienced by the flow was rapidly changed from zero to adverse. After a period of recovery, it was abruptly changed back to zero, followed by another relaxation period. By careful choice of the amplitude of the abrupt change in free-stream velocity, it was possible to create what appears to be an unsteady "separation bubble". This phenomenon was observed during the period of relaxation following the change from a condition of zero pressure gradient to an adverse one.

Intermittency contours proved to be very useful for showing the character of the unsteady separation bubble. The intermittency of flow at a point is the percentage of measured ensembles for which the flow is in the downstream direction. This is the same intermittency measure for which Simpson [5] has proposed near-wall values as quantitative definitions of the state of detachment in steady, two-dimensional flows. If one makes intermittency measurements spanning the boundary layer at different streamwise locations, one can construct maps of contours of like values of intermittency. This exercise was performed for a sequence of discrete times during and after the abrupt change from zero to the appropriate adverse pressure gradient, and the results are shown in Figures 5 and 6.

The plots displayed in Figure 5 are for discrete times during and just after the ramp change in free-stream velocity, its behavior at an X' value of 0.98 shown in the graph inset in Figure 5a. Recall that free-stream behavior for the first second is described in Figure 4a. Data at seven streamwise locations in the test region are plotted, the abscissa representing the normalized distance of each location along the test section of the facility. Contour lines were fitted for clarity; only for the contour of 99% intermittency are the data points retained.

Figure 5a shows the earliest time for which a value of intermittency below 100% is measured at any significant distance from the wall. Figures 5b and 5c relate to discrete times in the middle of and near the end of the ramp. For each of these times, the contours for the various intermittencies appear to grow outwards with downstream distance as far as the end of the test section (X' equal to 1). Farther downstream, the intermittency contours appear to remain at approximately constant distances from the wall.

The intermittency values observed in the early stages of the development of the flow can be attributed to the existence of the eddy structure in the initially undisturbed flow near the top wall. This structure is essentially Gaussian in nature (Chien and Sandborn [6]) and results in a statistical chance for flow velocities to be instantaneously negative within the boundary layer near the wall. When the abrupt change in free-stream velocity is imposed on the existing flat-plate boundary layer, the outer portion of the layer reacts as a slug, with a "frozen" response in the streamwise turbulence field (Ramaprian and Tu [7], Jayaraman et al. [2]). This results in deceleration of the flow across the boundary layer by as much as 30%. When this is superimposed on the existing turbulent structure in the boundary layer, it greatly increases the chances of instantaneous negative velocities being measured. Consequently, momentary conditions are found during which statistically negative velocities can exist in the flow, as can be observed in Figures 5a, 5b, and 5c. Since the contours in these figures are all for data at points farther from the wall than one Stokes-layer thickness, the shape of the contours during this abrupt change reflects the imposed velocity field (Figure 2b); contours grow away from the wall as far downstream as the end of the test section, beyond which they remain at an approximately constant distance from the wall.

As the outer part of the boundary layer is convected out of the test region, the region of intermittent reversal becomes more closely confined to the wall at downstream positions (Figure 5d), indicating that part of the intermittent region is being removed from the test-region as the unsteady turbulent bubble appears. Thus, the initial intermittency is not governing the later development of the turbulent separation bubble, but can be considered to be an artifact of the suddenly imposed potential flow.

The developing character of the unsteady turbulent bubble is shown in Figures 5 and 6. The ordinate used is Y divided by the boundary-layer thickness at that time. In Figures 5d, 5e, and 5f, the nearly symmetric growth of the bubble is evident. The closed contour corresponding to an intermittency of 50% first appears after 1.44 seconds. After 1.60 seconds (Figure 6a) the bubble begins to lose its symmetric appearance; contours begin to move away from the wall at the downstream end. In Figure 6c (after nearly three seconds) the contour of 50% intermittency is no longer fully closed. For the purposes of providing test cases for computational models to try to emulate, the first few seconds of the development of this unsteady separation bubble seem well suited.

The interaction between the blockage effect of the boundary layer and the free-stream velocity is much milder for the last few seconds of this unsteady event. The change in boundary-layer structure is reflected in small changes in the shape of contours, a slight drifting of contours in the downstream direction, and reattachment and

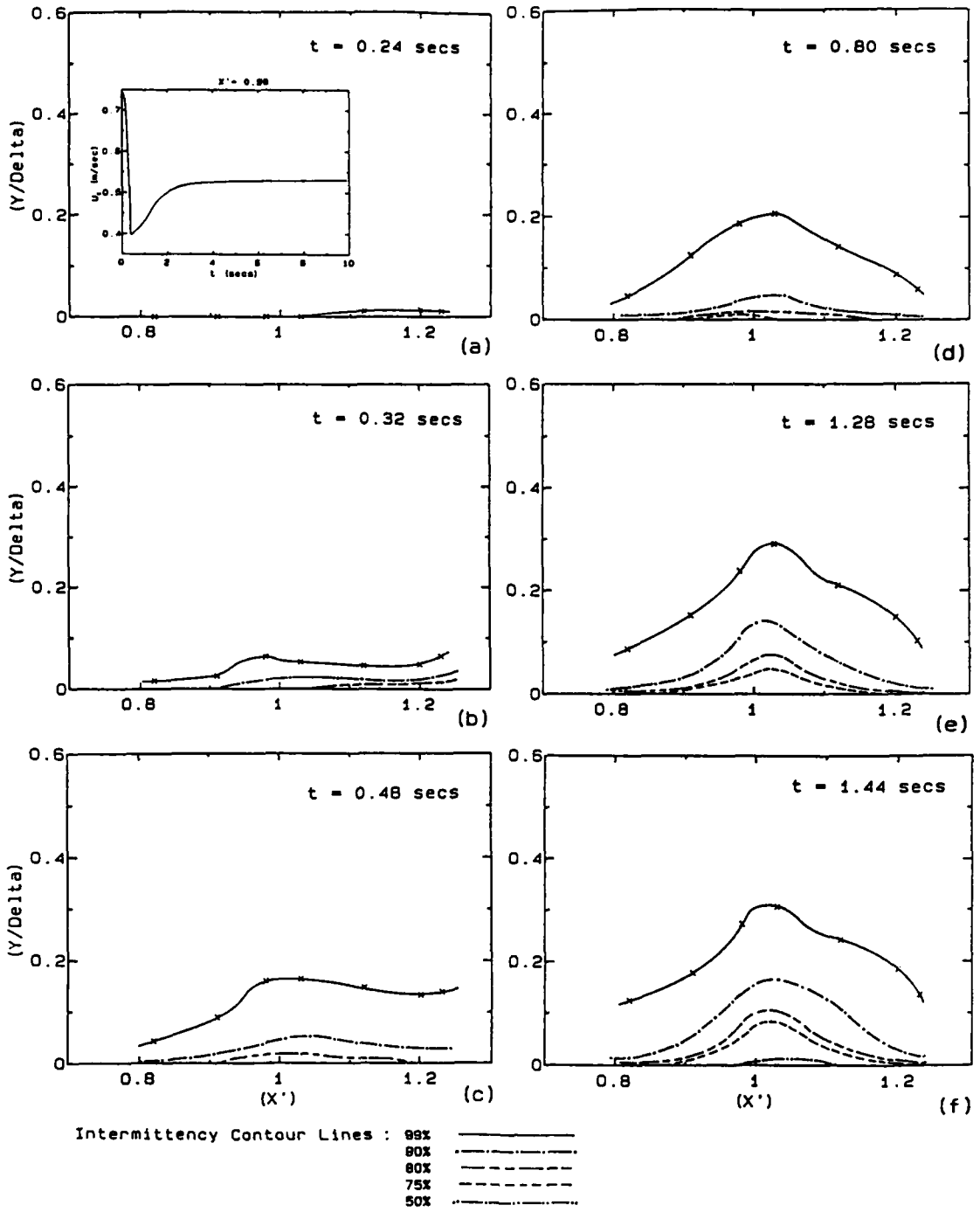

Fig. 5. Intermittency contours for development of unsteady "separation bubble".

decay of the contour of 50% intermittency (Figures 6c to 6f). After ten seconds, the flow is abruptly restored to one of zero pressure gradient. All intermittency contours disappear as the accelerating velocity field is superimposed on the existing turbulent structure--again an artifact of the suddenly imposed potential flow.

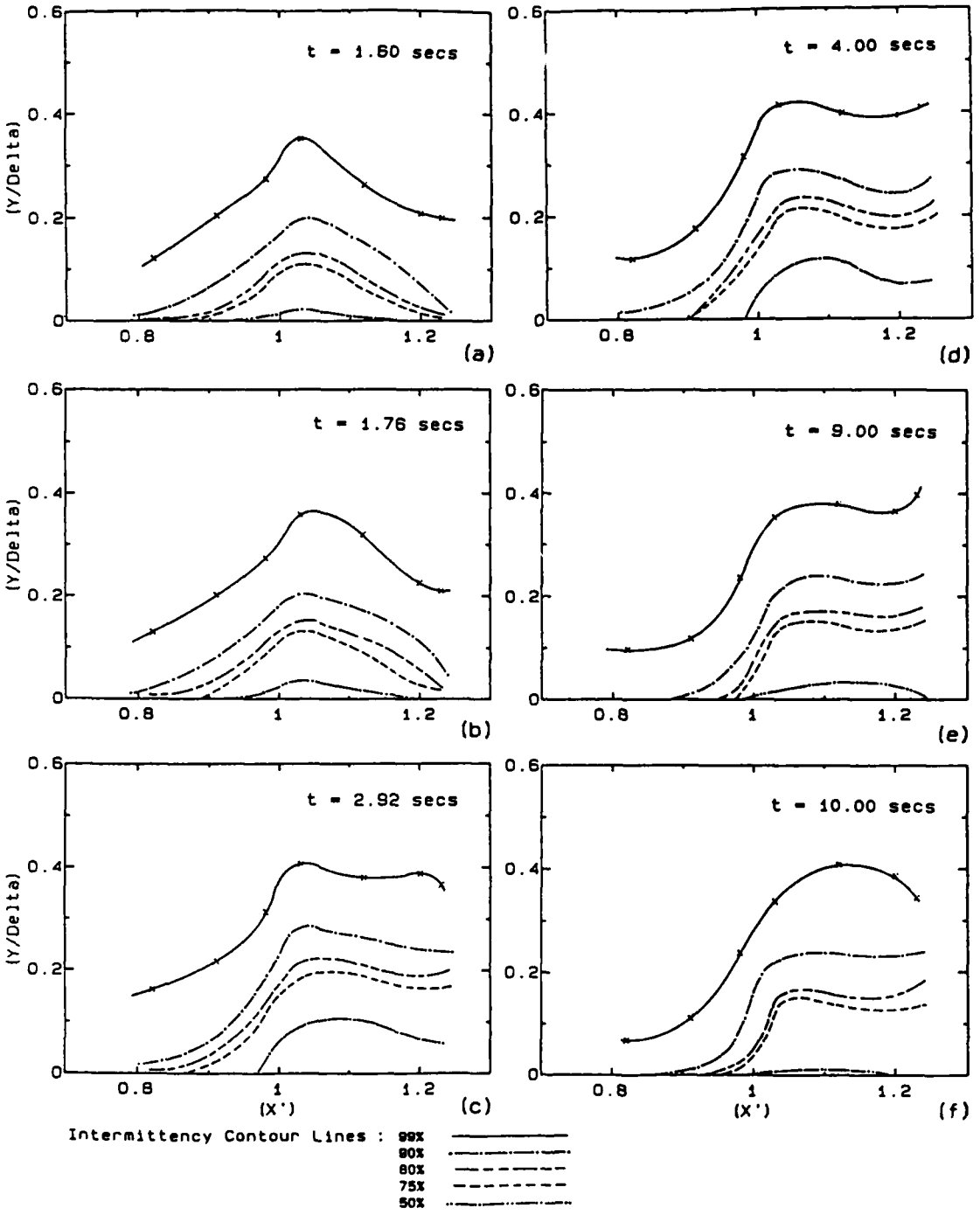

Fig. 6. Intermittency contours for decay of unsteady "separation bubble".

CONCLUSIONS

In this paper, experiments with different kinds of organized, imposed unsteadiness are described. Results are presented for flows with oscillating free-stream velocities at high values of Strouhal number and for flows with abruptly changing free-stream conditions. Both sets of results are shown to be in good agreement with the corresponding analytic solutions of the Stokes equation. Thus the facility is well qualified to produce the prescribed unsteady flows. Data sets from such experiments are therefore likely to be especially useful for the purposes of comparison with the predictions of turbulence models for unsteady flows.

Interesting data, in the form of intermittency contours, describing the development of an unsteady separation bubble are presented and partly explained.

REFERENCES

1. Cousteix, J. and Houdeville, R., "Couches Limites Instationnaires," 37/5004 DN, Jan. 1983, Departement d'Etudes et de Recherches en Aerothermodynamique, Centre d'Etudes et de Recherches de Toulouse, 2 Avenue Edouard Belin, Toulouse.

2. Jayaraman, R., Parikh, P., and Reynolds, W. C., "An Experimental Study of the Dynamics of an Unsteady Turbulent Boundary Layer," TF-18, Dec. 1982, Thermosciences Division, Department of Mechanical Engineering, Stanford University, Stanford, Calif.

3. Goldstein, S., Modern Developments in Fluid Mechanics, 1st ed., Vol. 1, Oxford, 1938, pp. 186-187.

4. Lyrio, A. A., Ferziger, J. H., and Kline, S. J., "An Integral Method for the Computation of Steady and Unsteady Turbulent Boundary Layer Flows, including the Transitory Stall Regime in Diffusers," PD-23, Mar. 1981, Thermosciences Division, Department of Mechanical Engineering, Stanford University, Stanford, Calif.

5. Simpson, R. L., Shivaprasad, B. G., and Chew, Y. -T., "The Structure of a Separating Turbulent Boundary Layer. Part 4. Effects of Periodic Free-stream Unsteadiness," Journal of Fluid Mechanics, Vol. 127, 1983, pp. 219-261.

6. Chien, H. -C., and Sandborn, V. A., "Aerodynamics - A Time Dependent Flow Model for the Inner Region of a Turbulent Boundary Layer," CER 80-81-HCC-VAS-45, Apr. 1981, Department of Civil Engineering, Colorado State University, Fort Collins, Colo.

7. Ramaprian, B. R. and Tu, S. W., "Periodic Turbulent Pipe Flow at High Frequencies of Oscillation," Unsteady Shear Flows (R. Michel, J. Cousteix and R. Houdeville, eds.), Springer-Verlag, West Berlin, 1981, pp. 47-57.

ACKNOWLEDGMENTS

This part of the program was supported by the Army Research Office, U.S.A., under Contract DAAG 29-83-K-0056, and monitored by Dr. Robert Singleton.

The authors would like to acknowledge the key contributions of Dr. Rangarajan Jayaraman and Dr. Pradip Parikh to this program.

ETUDE EXPERIMENTALE DE COUCHES LIMITES TURBULENTES INSTATIONNAIRES SOUMISES A DES GRADIENTS DE PRESSION MOYENS NULS OU POSITIFS

G. BINDER - S. TARDU - R. BLACKWELDER* - J.L. KUENY
Institut de Mécanique de Grenoble
b.p. 68 - 38402 Saint Martin d'Hères Cedex - France

RESUME

Des résultats expérimentaux sur des écoulements turbulents pariétaux pulsés réalisés sur une boucle à eau dans des gammes étendues de fréquence et d'amplitude sont présentés. Ces résultats comprennent les mesures de vitesse par vélocimétrie à laser et des mesures du frottement pariétal par film chaud.

On montre que dans le cas de l'écoulement en canal à gradient de pression nul que la vitesse et l'intensité turbulente moyennes sont insensibles aux oscillations forcées même à très forte amplitude, supérieure à 100 % localement. L'écoulement oscillant suit complètement la solution de Stokes à haute fréquence, mais à une fréquence intermédiaire ceci reste vrai pour l'amplitude mais pas pour le déphasage. Les oscillations périodiques de l'intensité turbulente sont très étouffées à haute fréquence. Les amplitudes et le déphasage du frottement dans des conditions très variées sont bien corrélés par le paramètre de similitude l_s^+ qui est la longueur visqueuse de Stokes exprimée en variables internes : le déphasage à haute fréquence ($l_s^+ < 10$) est proche de 45° ; l'amplitude rapportée à celle de Stokes croît progressivement lorsque $l_s^+ > 30$. Une vérification expérimentale est également apportée au critère d'apparition des courants de retour ($[\tilde{u}_e] = l_s^+/\sqrt{2}$) basé surla solution de Stokes.

Une première exploration d'écoulements pulsés soumis à un gradient adverse révèle des comportements très différents de l'écoulement oscillant par rapport à celui du canal

1. INTRODUCTION

1.1. Position du problème

Les couches limites qui se développent sous l'influence d'un écoulement libre dépendant du temps jouent un rôle pratique important. C'est notamment le cas lorsque cet écoulement a une composante sinusoïdale comme sur les pales d'hélicoptères, des turbomachines ou des hélices de bateaux et comme sur les organes de locomotion de nombreux animaux.

Les recherches sur les couches limites turbulentes instationnaires périodiques (CLT-I) se sont beaucoup développées depuis une décade après avoir marqué une longue pause à la suite des travaux de KARLSSON (1) à la fin des années 50 qui a ouvert la voie dans ce domaine. Les travaux portent aussi bien sur les couches limites se développant dans un gradient de pression moyen nul (2-7) que défavorable (8-9). Grâce à ces efforts s'est constitué un ensemble de données diversifié mais encore très épars duquel une image cohérente et incontestée a du mal à émerger. Très révélateur à cet égard est le manque de consensus entre chercheurs sur la similitude et les paramètres adimensionnels les plus appropriés dans diverses situations.

Ainsi pour le cas de figure le plus simple de la plaque plane ou du canal trois nombres adimensionnels ont été proposés : le nombre de Strouhal $\omega X/\bar{u}_e$ par COUSTEIX (8-9), REYNOLDS (8-9) et leurs collaborateurs, le nombre de Stokes turbulent $\omega\delta/u_\tau$ ou $\omega h/u_\tau$ par l'équipe d'IOWA de RAMAPRIAN (6-7) et le nombre de Stokes-Reynolds $l_s^+ = l_s u_\tau/\nu$, l_s étant la longueur de Stokes $\sqrt{2\nu/\omega}$, qui a été introduite par nous-mêmes (5). Aucun de ces trois nombres ne s'est encore indiscutablement imposé à l'ensemble des chercheurs dans ce domaine ne serait-ce que dans une gamme limitée des paramètres. De ce fait, dans certaines publications les fréquences des oscillations forcées sont seulement exprimées en unités physiques du hertz et les notions de haute ou basse fréquence peuvent correspondre à des écoulements intrinsèquement très différentes suivant les auteurs. La situation est encore bien plus confuse dans les CLT-I décélérées en moyenne car le nombre de paramètres qui interviennent est encore bien plus important que dans le cas de la plaque plane ou du canal.

La première raison de cet état de fait est l'évidente complexité des écoulements instationnaires qui introduisent automatiquement une variable indépendante supplémentaire, le temps, et deux paramètres supplémentaires par rapport aux écoulements permanents correspondants, à savoir une fréquence et une amplitude. Ainsi la couche limite turbulente sur plaque plane qui, en régime stationnaire, dépend seulement du nombre de Reynolds, devient une famille à trois paramètres où toute grandeur moyenne ou turbulente dépend en plus du temps. Il résulte de cette complexité que l'exploration expérimentale systématique d'une famille de CLT-I même en se limitant aux grandeurs essentielles est une tâche extrêment ardue, et en l'absence d'études systématiques, les similitudes sont difficiles à établir.

La deuxième raison est d'ordre pratique. Elle tient à la double difficulté, d'une part, celle de couvrir une large gamme de paramètres sur une même installation et, d'autre part, celle de mesurer certaines grandeurs essentielles comme le frottement turbulent ou le frottement pariétal et celle de pouvoir effectuer des mesures suffisamment près de la paroi. Ces dernières sont particulièrement sévères avec le vélocimètre à laser à cause de la dimension du domaine de mesure, la diminution de la qualité du signal Doppler due aux réflexions parasites, la faible fréquence de passage des particules diffusantes et le taux de turbulence élevé. Ainsi, la controverse sur le déphasage de l'écoulement au voisinage immédiat de la paroi serait réglée depuis longtemps sans ces difficultés d'instrumentation. Enfin, les mesures peuvent être affectées dans une proportion variable par des particularités de l'installation qui peuvent obscurcir les effets propres de l'instationnarité.

* En détachement (année sabbatique) de l'University of Southern California Los Angeles(USA)

1.2. Objectifs

Nos précédentes expériences (5) que nous désignons par la suite par I avaient montré que des variations forcées de vitesse de fréquence élevée ne produisaient pas d'interactions avec l'écoulement moyen conformément aux observations de la plupart des autres chercheurs. Un résultat plus original et plus frappant était que dans ces conditions, l'écoulement oscillant avait une épaisseur et des répartitions de l'amplitude et du déphasage conformes à celles de l'écoulement visqueux de Stokes, bien que l'écoulement moyen était pleinement turbulent. En particulier, l'extrapolation du déphasage jusqu'à la paroi conduisait à une valeur proche de 45°, typique de la couche de Stokes et analogue au résultat de LIGHTHILL (15) relatif à la limite des hautes fréquences des couches limites laminaires pulsées. D'autres investigations (3, 4, 7, 8) ont depuis trouvé des valeurs proches de 45° en écoulement turbulent. En s'appuyant sur ces résultats, nous avions conclu que le paramètre important était l'épaisseur de Stokes ℓ_s rapportée à ℓ_ν soit ℓ_s^+, conformément aux notations en usage. De plus, le régime des hautes fréquences avec un déphasage de 45° à la paroi semblait satisfaire au critère $\ell_s^+ < 10$ soit $f\nu/u_\tau^2 > 1/1000\pi$. Sur la base de l'écoulement de Stokes, on déduisant également un critère sur l'apparition de vitesses négatives. On arrivait donc à une conclusion assez surprenante d'une similitude visqueuse pour l'écoulement oscillant coexistant avec une similitude turbulente pour l'écoulement moyen, les deux écoulements étant complètement découplés à haute fréquence. Cette conclusion est en contradiction avec certaines idées voire des mesures selon lesquelles des interactions entre les oscillations forcées et la turbulence ont lieu lorsque leurs fréquences sont comparables (5, 6, 10, 11).

Nos précédentes expériences étaient critiquables par leur faible amplitude qui était seulement de 3 ou 5 % de la vitesse au centre du canal . De telles amplitudes peuvent paraître insuffisantes pour provoquer des interactions significatives avec la turbulence et l'écoulement moyen. De plus, aux faibles amplitudes la précision des mesures de l'écoulement oscillant $\tilde{u}(y, t)$ laisse à désirer surtout à proximité de la paroi où l'intensité turbulente est élevée. En effet, le rapport signal périodique sur bruit turbulent est faible et pour réduire la dispersion statistique des temps d'intégration extrêmement longs sont nécessaires. Par ailleurs, compte tenu des remarques qui précèdent, il a paru important d'étendre également le domaine des fréquences. Par conséquent, un nouveau pulseur qui permet d'atteindre des amplitudes de 80 % dans une large gamme de fréquences a été conçu et installé. De plus, à cause du rôle primordial joué par le frottement pariétal, sa mesure directe au moyen de films chauds a été mise en oeuvre.

Le premier objectif de ce travail était, grâce à ces moyens améliorés, de vérifier la similitude en ℓ_s^+ et d'en trouver les limites en fonction de la fréquence et de l'amplitude des oscillations forcées de l'écoulement en canal. Les aspects particuliers qui entrent dans ce cadre sont notamment l'effet de fortes amplitudes sur la vitesse moyenne, les répartitions d'amplitude et de déphasage de $\tilde{u}$, les conditions d'apparition des courants de retour, une étude systématique de l'évolution de l'amplitude et du déphasage du frottement pariétal.

Le deuxième objectif était de commencer l'exploration de CLT-I soumises à un gradient de pression adverse et de comparer leur comportement avec celui de l'écoulement en canal. L'étude du frottement pariétal qui est une indication très précieuse, est prévue mais n'a pas encore pu être menée à bien.

2. INSTALLATION EXPERIMENTALE

2.1. Le Canal

Les mesures sont effectuées sur un canal à eau alimenté par une cuve à niveau constant et est précédé d'une chambre de tranquillisation classique. Les dimensions du canal sont : longueur = 2600 mm, largeur = 1000 mm, hauteur = 2h = 100 mm. Le dernier mètre du canal qui constitue la section d'essai est installé à mi-hauteur d'un bassin de 2 m de haut. Les parois de ce tronçon du canal peuvent être inclinées par rapport à l'axe ce qui permet de réaliser un diffuseur bi-dimensionnel (de largeur 1000 mm) avec un angle d'ouverture réglable entre 0 et 30°. Les mesures avec un gradient de pression adverse rapportée ici ont été faites avec une divergence des parois de 6°.

La vitesse moyenne à l'entrée est réglable entre 0 et 50 cm/s , donc $(Re_h)_{max} = \bar{u}_{max} h/\nu = 25.10^3$ soit $(Re_\theta)_{max} \simeq 2,5.10^3$. Des rugosités tridimensionnelles de 5 mm à l'entrée du canal fixent la transition. Les mesures montrent que l'écoulement dans la section d'essai est pleinement turbulent jusqu'à $\bar{u} = 10$ cm/s. Ces nombres de Reynolds ne sont évidemment pas élevés, surtout pour $\bar{u} = 17$ cm/s où $Re_h = 8,5.10^3$ de certaines conditions d'essai, mais c'est le prix à payer pour pouvoir effectuer des mesures suffisamment près de la paroi. En effet comme dans ces conditions $u_\tau = \bar{u}_c/18$, si $\bar{u}_c = 17$ cm/s , $u_\tau \simeq 1$ cm/s et $\ell_\nu = 0,1$ mm et la mesure la plus proche de la paroi à y = 0,3 mm correspond à $y^+ \simeq 3$. Il est clair qu'à un Reynolds trois fois plus grand : $u_\tau \simeq 3$ cm/s, $\ell_\nu \simeq 0,03$ mm, et les mesures ne pourraient être faites qu'au-delà de $y^+ = 10$.

La longueur du canal est insuffisante pour avoir un écoulement pleinement développé même à ces nombres de Reynolds modérés puisque $L/2h = 26$. La longueur d'établissement L_e varie en fonction des conditions à l'entrée (14) et est atteinte d'autant plus rapidement que les perturbations initiales sont plus importantes. Dans ce dernier cas $L_e/2h$ peut être estimé à environ 45 pour $Re > 25000$. Des mesures faites sur notre installation montrent qu'à 6 h en amont de la station habituelle de mesure les vitesses moyennes diffèrent de moins de quelques pour cent à une même distance de la paroi. Par ailleurs, l'écoulement près de la paroi qui est contrôlé par τ s'établit beaucoup plus rapidement sur une distance estimée à 12 h environ (14). Nous avons effectivement vérifié que τ variait peu sur les derniers 20 h de la section d'essai. D'autre part, les profils de vitesse moyenne $u^+(y^+)$ (voir Fig. 6) et de $\sqrt{\overline{u'^2}}/u_\tau$ (5) sont tout à fait conformes aux mesures d'autres auteurs. Comme par ailleurs, les variations de l'écoulement périodique sont confinées près de la paroi, même une fréquence très faible comme f = 1/60 hz et, l'amplitude est constante dans la moitié centrale du canal. Le fait que l'écoulement moyen ne soit pas tout à fait établi dans cette partie, ne devrait donc pas avoir une grande influence sur l'écoulement périodique.

La bidimensionnalité de l'écoulement a été vérifiée ; elle est très bonne sur les 3/4 de l'envergure conformément à ce qu'on attend puisque l'élancement de la section est de 10. D'autre part, on a vérifié dans un cas que l'écoulement permanent et oscillant était symétrique par rapport à l'axe du canal.

2.2. Les déflections périodiques des parois de la section d'essai d produites par la pression p qui engendre l'écoulement oscillant induisent une oscillation de vitesse parasite $\tilde{u}_d$ en un point fixe qui ne se déplace pas avec la paroi. L'amplitude maximale de cette vitesse est :

$$[\tilde{u}_d] = \left(\partial\bar{u}/\partial y\right)_{y=0} [\tilde{d}] = \omega_\ell^+ [\tilde{d}]/\nu$$

Si la plus petite amplitude mesurable de la vitesse est $[u_\ell]/10$, l'erreur maximale est

$$\varepsilon_{max} = 10[\tilde{u}_d]/[u_\ell] = 10(u_\tau/[u_\ell])(u_\tau[\tilde{d}]/\nu) = 10(u_\tau/[u_\ell])[\tilde{d}]^+$$

Il est facile de voir que ε_{max} peut rapidement prendre des valeurs importantes supérieures à 10 % si $[\tilde{d}] > 1$ µm, même dans l'eau. Si on est loin de la résonnance de la paroi ce qui est souvent le cas surtout dans l'eau où les fréquences physiques sont faibles, $[\tilde{d}]$ doit être proportionnel à la force oscillante $\tilde{p}$ donc proportionnel à $\omega[u_\ell]$. ε_{max} est alors indépendant de l'amplitude $[u_\ell]$ et proportionnel à ω .

Pour minimiser les déflections périodiques, les parois de la section d'essai sont rigidement fixées sur le bâti du bassin. Les déflections ont toutefois été mesurées avec un capteur de déplacement à ultra-sons. Sa sensibilité sur les moyennes de phase était meilleure que 1 µm. Les résultats montrent que l'on a effectivement $[\tilde{d}] \propto \omega[u_\ell]$, plus précisément

$$[\tilde{d}]_{\mu m} = 2{,}1\ f_{he}\ [\tilde{u}_\ell]_{cm/s}$$

ce qui dans les conditions les plus défavorables conduit à $\varepsilon_{max} < 10$ %.

2.3. Le pulseur

Le nouveau pulseur est monté sur la conduite alimentant le caisson. Il est composé d'un tube cylindre intérieur muni de fentes (24 fentes de 5 x 200 mm) par lequel arrive l'eau et d'un tube cylindrique extérieur auquel on imprime un mouvement oscillant au moyen d'un excentrique. Dans la mesure où les effets d'inertie dans la conduite reliant la cuve à niveau constant au caisson sont faibles, le débit est proportionnel à la longueur des fentes laissées découvertes par ce cylindre extérieur. La position moyenne, l'amplitude et la période du mouvement du cylindre extérieur contrôlent donc les grandeurs correspondantes de la vitesse. Ces trois paramètres sont facilement réglables de manière continue ce qui confère une grande souplesse à ce dispositif. Les gammes pour l'amplitude et la période de la vitesse sont respectivement de (0- 80 %) et de (2,5s-∞). Des mesures ont été faites jusqu'à T = 120 s. Les périodes successives sont constantes à mieux que 0,2 % près.

La différence de niveau disponible pour engendrer l'écoulement est de 3,5 m. Compte-tenu de la longueur des tuyauteries, les effets d'inertie commencent à être visibles sur $\tilde{u}_\ell$ par la présence d'harmoniques lorsque $\bar{u}_\ell > 30$ cm/s et $[\tilde{u}_\ell]/\bar{u}_\ell > 0{,}5$ et $T > 80$ s. Mais en général l'écoulement oscillant au centre du canal était très proche d'une sinusoïde pure même à forte amplitude comme le montre la Fig. 1.

3. INSTRUMENTATION

3.1. Mesure des vitesses

On utilise un vélocimètre à laser différentiel, muni d'une cellule de Pockel pour produire un décalage de zéro pour la mesure de vitesses négatives. L'angle entre les faisceaux est de 6° et la taille de volume de mesure est de 0,4 mm lorsque la cellule de Pockel est montée. Un agrandisseur de faisceau est utilisé en l'absence de cette dernière, ce qui permet de réduire le diamètre à 0,08 mm. Il est possible d'effectuer des mesures jusqu'à $y \simeq 0{,}3$ mm de la paroi, ce qui pour une vitesse $\bar{u}_\ell = 15$ cm/s correspond à $y^+ = 3$.

La fréquence Doppler est mesurée par un compteur avec un système de validation qui compare la dernière période avec chacune des N précédentes ($N \leq 14$). Le flux de particules diffusantes étant proportionnel à la vitesse, les moyennes statistiques sont biaisées vers le haut. Si la vitesse d'acquisition n'est pas limitée par le système de traitement, le biais statistique peût être corrigé en tenant compte du temps de résidence d'une particule dans le volume de mesure. On peut montrer que, pour obtenir la vraie valeur de la vitesse moyenne, cette correction équivaut simplement à effectuer la moyenne des périodes et non pas des fréquences Doppler et en prenant une seule mesure par bouffée. Comme la vitesse d'acquisition et de traitement du microprocesseur utilisé est de 200 s^{-1} , la tension d'alimentation du photomultiplicateur est réglée pour maintenir le nombre de mesures validées au-dessous de 70 s^{-1} lorsque la vitesse est maximum. Ceci est important avec des amplitudes de pulsation de 60 % puisque le rapport entre vitesse maximum et minimum est de 4 et que les taux d'arrivée des bouffées sont dans le même rapport. Nous avons vérifié (Fig. 3) que le nombre de mesures faites pendant un temps donné était effectivement proportionnel à la vitesse. Le biais est modifié losqu'on décale la fréquence Doppler pour mesurer des vitesses négatives. On s'est assuré expérimentalement que les résultats n'étaient pas sensiblement affectés.

On effectue en définitive les moyennes $\langle T_D \rangle$ et $\langle f_D \rangle$ (ou en stationnaire $\overline{T}_D$ et $\overline{f}_D$) de la période et de la fréquence Doppler pour obtenir la moyenne de phase de la vitesse et de la turbulence puisque compte tenu du biais :

$$\langle u \rangle = d_f / \langle T_D \rangle \qquad \langle u^2 \rangle = (\langle u \rangle)^2 + \langle u'^2 \rangle = d_f \langle f_D \rangle$$

où d_f est l'interfrange.

Les moyennes de phase sont synchronisées avec le pulseur par un top électrique par période fourni par une cellule photoélectrique. Ces moyennes sont en général déterminées en 50 points répartis uniformément sur la période. Pour obtenir la moyenne au point i, on collecte dans le canal i toutes les valeurs arrivant dans l'intervalle (i - 1) T/50 et iT/50 à partir du top de synchronisation. La durée du temps d'intégration est variable et réglée pour obtenir une convergence statistique satisfaisante. Pour les mesures les plus difficiles près de la paroi, le temps d'intégration dépasse parfois 2 heures ce qui correspond à un temps d'intégration par canal de 2,5 mn. Malgré ce temps long, le nombre de valeurs par canal dépassait à peine 100 dans certains cas extrêmes. La convergence sur $\langle u'^2 \rangle$ est évidemment plus difficile à atteindre. L'exemple de la Fig. 2 montre que même près de la paroi, les variations périodiques de $\langle u'^2 \rangle$ ressortent clairement de la moyenne de phase.

3.2. Mesure du frottement pariétal

Le frottement pariétal en écoulement permanent $\tau/\rho = \nu (\partial \bar{u}/\partial y)_{y=0}$ pouvait être déterminé directement à partir des vitesses lorsque $\bar{u}_\ell < 20$ cm/s puisque le point de mesure le plus proche de la paroi était à $y^+ \simeq 3$ et $u^+(y)$ est linéaire jusqu'à $y^+ = 5$. Pour les vitesses plus élevées on déterminait et la position exacte de la paroi, en ajustant par moindres carrés le profil suivant : $u^+ = 14,5\ th(y^+/14,5)$ sur les mesures jusqu'à $y^+ \leq 14$. Cette expression est en excellent accord avec les mesures d'ECKELMANN (15). On souligne le fait que $\bar{\tau}$ est donc u_τ sont déterminés directement sans faire aucune hypothèse sur l'existence d'une couche logarithmique comme avec la méthode du tracé de CLAUSER.

Les caractéristiques instationnaires de $\tilde{\tau}$, amplitude et déphasage, ont été mesurées avec une sonde à film chaud (SFC) placée à même la paroi (sonde et anémomètre DISA). L'étalonnage était fait directement sur l'installation. Après avoir vérifié l'exactitude de la loi : $\bar{\tau} = C R_{e_h}^{-1/n} \frac{1}{2} \rho \bar{u}_\ell^2$ ($C = 0,048$) par des mesures de vitesses dans quelques cas, on l'a utilisée ensuite pour les étalonnages de la SFC puisqu'elle ne nécessite que la mesure de la vitesse au centre. A cause des dérives de la SFC, son étalonnage devait être fréquemment contrôlé et il était indispensable d'avoir une méthode rapide.

L'utilisation de la SFC pariétale dans cette étude soulève plusieurs problèmes, notamment celui de sa réponse en fréquence, de sa réponse lorsqu'il y a inversion de la vitesse près de la paroi et enfin de sa réponse moyenne lorsque l'écoulement est turbulent. Le premier a son origine dans l'inertie de la couche limite thermique (16-18) du fait de la faible valeur des vitesses près de la paroi. PEDLEY (17-18) met en évidence la fréquence adimensionnelle $\hat{\omega}_1$, qui, avec les présentes notations, prend la forme intéressante suivante :

$$\hat{\omega}_1 = \omega \left(\frac{L_f^2 \nu}{u_\tau^2} P_r \right)^{1/3} = \frac{2}{l_s^{+2}} \left(L_f^{+2} P_r \right)^{1/3}$$

où L_f est la largeur du film. Dans nos expériences $\hat{\omega}_1 < 0,06$, et la réponse du film au mouvement oscillant peut être considérée comme quasi-stationnaire à peu de choses près. Ceci est confirmé par l'aspect symétrique de $\langle \tau \rangle(t)$ (Fig. 4) entre les phases de décélration et d'accélaration. Rappelons qu'en régime convectif le transfert est lié à τ par la relation : $Q \propto \tau^{1/3}$. Cependant les fréquences des fluctuations turbulentes sont nettement plus élevées et la réponse de la SFC à la turbulence n'est plus quasi-stationnaire.

D'autre part, lorsque la vitesse près de la paroi change de signe le transfert de chaleur passe du régime convectif à un régime dominé par la diffusion. Le transfert reste non seulement de même signe, mais à cause de la diffusion il ne s'annule pas. D'après l'analyse de PEDLEY (19-20), la valeur minimale du transfert adimensionnel serait de 0,1. Nos mesures cependant, donnent systématiquement 0,3 (Fig. 4). La turbulence qui est présente accroît toujours le transfert. Or, les fluctuations du frottement sont très élevées et maximales, de l'ordre de 70 %, lorsque $\langle \tau \rangle$ est minimum (Fig. 5). La turbulence intervient donc de deux manières différentes, par sa fréquence qui est élevée par rapport à celle de la SFC et par son intensité qui est également élevée. Ces facteurs et la forte non-linéarité de la relation frottement-transfert pourraient expliquer les différences notées plus haut. Il ne semble pas que ce problème de la réponse la SFC en régime turbulent ait été abordé dans la littérature. Cette question est en cours d'étude et nous essayons d'en trouver une évaluation quantitative.

De manière pratique, lorsqu'on a un signal redressé comme celui de la figure 4 se pose alors la question : comment obtenir la courbe vraie $\langle \tau \rangle(t)$? c.a.d. par rapport à quelle ligne horizontale faut-il effectuer la symétrie de la partie redressée : la ligne AB, la ligne $\tau = 0,1$ ou l'axe $\tau = 0$? Les trois possibilités ont été essayées. Elles donnent toutes les trois pratiquement la même valeur du déphasage de $\tilde{\tau}$, mais évidemment des valeurs différentes de l'amplitude. On peut remarquer dans le cas de la Fig. 3 que la valeur minimum de $\langle \tau \rangle$ est suffisamment importante pour qu'elle ne soit pas appréciablement affectée par la diffusion. Ceci justifie la symétrie par rapport à $\tau = 0$. En procédant ainsi, après avoir supprimé quelques points autour des minima, on trouve pour $l_s^+ < 10$: $[\tilde{\tau}] \quad [\tilde{\tau}]_{Stokes} \simeq 0,9$, avec cependant une distorsion harmonique de 15 %. Si on prend simplement la symétrie par rapport à AB, on obtient $[\tilde{\tau}] \quad [\tilde{\tau}]_{Stokes} \simeq 0,7$ avec une distorsion très faible. Malgré la distorsion, la première solution semble plus logique, car on voit mal comment ce rapport peut être inférieur à un (cf. la discussion en 4.3.1). Cependant, les mesures de τ à faible amplitude et à haute fréquence, sans courants de retour, où donc $\langle \tau \rangle$ n'est pas redressé, donnent systématiquement 0,7 comme le montre la Fig. 10. Comme la symétrie par rapport AB donne un résultat plus cohérent avec les autres mesures, elle a pour cette raison été adoptée systématiquement. Il est clair qu'il y a donc une part d'arbitraire dans les valeurs de $[\tilde{\tau}] \quad [\tilde{\tau}]_{Stokes}$ de l'ordre de 30 % lorsqu'il y a inversion périodique de la vitesse. La valeur 0,7 de ce rapport à haute fréquence reste actuellement à expliquer. Comme remarquée ci-dessus, nous pensons qu'il résulte de l'effet de la turbulence.

3.3. Visualisations

Elles ont été faites avec des bulles d'hydrogène à l'aide de fils de platine de 100 µm placés soit parallèlement soit perpendiculairement à la paroi. Etant donné les faibles fréquences, l'observation directe à l'oeil est possible. L'existence de courants de retour pendant une partie de la période pouvait ainsi facilement même observée.

4. ECOULEMENTS PULSES EN CANAL

Les résultats ci-dessous sont présentés en fonction du paramètre de similitude ℓ_s^+ qui avait été introduit dans I et qui permettait de regrouper un certain nombre de résultats. Rappelons que ce paramètre est la longueur visqueuse de Stokes ℓ_s exprimée en variables internes de la couche limite turbulente stationnaire (CLT-S) à möeme vitesse moyenne au centre du canal (ou même R_{e_h}) En d'autres rermes, puisque l'épaisseur totale de la couche de Stokes est environ de $2\ell_s$ (le maximum de l'overshoot se situe à $2{,}2\,\ell_s$), $2\ell_s^+$ indique jusqu'où les variations de $\tilde{u}$ s'étendraient à l'intérieur de la couche pariétale stationnaire $u^+ = f(y^+)$ si la turbulence de cette couche n'influait pas sur $\tilde{u}$. Les résultats exposés ci-après confirment effectivement la similitude en ℓ_s^+ et justifient son utilisation.

4.1. Deux écoulements pulsés à forte amplitude

Les Figures 4 à 10 montrent les propriétés de deux écoulements soumis à une oscillation forcée de 64 % au centre du canal dont les périodes sont respectivement de 4 et 30 s, soit ℓ_s^+ de 8,1 et 23. Les mesures du frottement pariétal (Fig. 15 et 16) montrent que $\ell_s^+ = 8{,}1$ correspond au régime des hautes fréquences et $\ell_s^+ = 23$ à une fréquence intermédiaire où les déphasages sont faibles mais où les amplitudes ne sont pas encore sensiblement affectées par la turbulence.

La première question à examiner est l'effet d'oscillations d'une telle amplitude sur les caractéristiques moyennes $\bar{u}$ et $\sqrt{\overline{u'^2}}$. Rappelons que de nombreux auteurs, à l'exception de MIZUSHIMA et Al. (11, 12) et RAMAPRIAN et Al. (6) (encore que les résultats récents de cette dernière équipe (7) concernant des couches limites soient plus en accord avec les observations générales), ont trouvé que les caractéristiques moyennes étaient insensibles aux oscillations forcées. Ceci est tout à fait confirmé par les figures 6 et 7 : les profils de u^+ en régime instationnaire se confondent avec le profil universel du régime stationnaire et les écarts sur les profils de l'intensité turbulente $\sqrt{\overline{u'^2}}/u_\tau$ sont faibles et ne sont pas significatifs en égard à la dispersion habituelle de ces mesures près de la paroi. L'insensibilité des caractéristiques moyennes aux oscillatipns forcées est d'autant plus remarquable que près de la paroi les amplitudes relatives sont encore plus élevées qu'au centre du canal. La Fig. 8 montre que dans le cas $\ell_s^+ = 8{,}1$ haute fréquence, les vitesses deviennent négatives pendant une partiede la période sur une hauteur de plusieurs mm. Dans cette région, l'amplitude excède 100 % et elle atteint même 170 % ! Pour l'écoulement à moyenne fréquence $\ell_s^+ = 23$, on est juste à la limite des conditions produisant des courants de retour à la paroi et on atteint donc des amplitudes proches de 100 %. Compte tenu de ces ordres de grandeurs, la dispersion des points sur l'évolution de $\sqrt{\overline{u'^2}}/u_\tau$ paraît tout à fait insignifiante.

Dans I, nous avions spéculé que les oscillations forcées pourraient avoir une influence sur la turbulence et par ce biais sur l'écoulement moyen, si premièrement le gradient $\partial\langle\tilde{u}\rangle/\partial y$ devenait du même ordre que $\partial\bar{u}/\partial y$ pour que le mouvement oscillant puisse contribuer de manière significative à la production turbulente et si, deuxièmement la fréquence n'était pas trop élevée, afin que ceci se produise à une distance suffisante de la paroi pour que $-\langle u'v'\rangle$ atteinge une valeur voisine du maximum $\sim u_\tau^2$. La production étant maximum vers $y^+ = 12$, cette dernière condition ne serait pas satisfaite que pour des fréquences très élevées telles que $\ell_s^+ < 5$. Dans ces deux écoulements, ces conditions sont satisfaites et pourtant il n'y a pas d'effet sur l'écoulement moyen. En fait, ces conditions qui semblent nécessaires ne sont pas suffisantes. La production moyenne est en effet

$$-\overline{\langle u'v'\rangle \partial\langle u\rangle/\partial y} = -\overline{\tilde{u}\tilde{v}}\,\partial\bar{u}/\partial y - \overline{\tilde{u}\tilde{v}\,\partial\tilde{u}/\partial y}$$

Une contribution significative à la production exige donc également une variation périodique $-\tilde{u}\tilde{v}$ de la contrainte de cisaillement du même ordre que $-\overline{\tilde{u}\tilde{v}}$ et un déphasage entre $-\tilde{u}\tilde{v}$ et $\partial\tilde{u}/\partial y$ qui ne soit pas proche de la quadrature. En l'absence d'effet sur $\bar{u}$, on est tenté de conclure que ces dernières conditions ne sont pas satisfaites. Pour établir ce point, il serait évidemment très souhaitable de mesurer $-\tilde{u}\tilde{v}$ dans la région entre la paroi et $2\ell_s^+$ où se produisent les variations de $\tilde{u}$. Mais ceci est difficile à cause de la quasi impossibilité de mesurer v près de la paroi surtout avec la vélocimétrie à laser. Pour être complet, il faut ajouter que la production moyenne $-\overline{\tilde{u}\tilde{v}}\,\partial\bar{u}/\partial y$ pourrait elle-même être affectée par les oscillations forcées, mais celà ne semble pas être le cas. En effet, $\partial\bar{u}/\partial y$ clairement n'est pas affecté et comme $\overline{\tilde{u}^2}$ ne l'est pas non plus, il ne serait pas illogique qu'il en soit de même pour $-\overline{\tilde{u}\tilde{v}}$.

La figure 8 des profils instantanés dans le cas des hautes fréquences illustre l'importance considérable des variations de vitesse pendant la période près de la paroi et l'existence de vitesses négatives. De telles vitesses n'ont jusqu'à présent été constatées que par KARLSSON (1) à la fréquence la plus élevée qui correspondrait à une valeur $\ell_s^+ = 4{,}75$. La dispersion des points de mesure lorsque $\langle u\rangle < 0$ ne saurait étonner, car ces vitesses sont relativement faibles en valeur absolue et l'intensité turbulente à ces instants est très élevée.

L'amplitude $[\tilde{u}]$ et le déphasage $\{\tilde{u}\}$ par rapport à $\{\tilde{u}_1\}$ du mode fondamental de la vitesse décrit complètement cette dernière dans la mesure où les autres modes ont des amplitudes faibles par rapport au fondamental. Ceci était effectivement le cas pour ces deux écoulements : le premier harmonique était toujours inférieur à 5 % du fondamental. Les figures 9 et 10 représentent les évolutions de $[\tilde{u}]$ et $\{\tilde{u}\}$ en fonction de l'ordonnée adimensionnelle $y_1 = y/\ell_s$ ainsi que la solution de Stokes. Les résultats expérimentaux sont claires : à haute fréquence $\ell_s^+ = 8{,}1$ l'amplitude et le déphasage suivent la solution visqueuse de Stokes. A la fréquence intermédiaire $\ell_s^+ = 23$, l'amplitude coïncide exactement avec la solution de Stokes près de la paroi mais s'en écarte de 10 à 15 % plus loin. L'évolution de la phase, par contre, est tout à fait différente de cette solution : elle passe par un maximum de l'ordre de 10° et prend des valeurs négatives près de la paroi. L'extrapolation à la paroi -qui semble légitime vu la cohérence des mesures- donne un retard de phase d'environ 10°. On constate donc que le premier effet de la turbulence sur $\tilde{u}$ est de réduire de manière importante les déphasages. Ce qui est surprenant, c'est que près de la paroi où les effets visqueux dominent, le déphasage croît ici contrairement à l'évolution de la solution visqueuse.
D'autre part, l'influence faible de la turbulence sur l'amplitude mérite également d'être soulignée puisque la couche oscillante à $\ell_s^+ = 23$ pénètre loin dans la zone pleinement turbulente de la couche interne. Le gradient maximum $d[\tilde{u}]/dy$ se mantient nettement plus longtemps que celui de $d\bar{u}/dy$ et est errodé moins rapidement par la trubulence. Ces résultats confirment tout à fait nos résultats antérieurs à faible amplitude.

Le comportement de l'oscillation périodique de l'intensité longitudinale de la turbulence est illustré par les figures 11 et 12. On note symboliquement $\tilde{u}'$ défini par $\sqrt{\overline{u'^2}}$ (t) = $(\overline{\tilde{u}^2} + \tilde{u}'(t))$ L'amplitude $[\tilde{u}']$ rapportée à u_τ (Fig. 11) évolue de manière analogue à $\sqrt{\overline{\tilde{u}'^2}}/u_\tau$ avec notamment un maximum à la même distance $y^+ \simeq 20$. On note des différences importantes entre les deux écoulements : d'abord le maximum pour $l_s^+ = 23$ est deux fois plus important que pour $l_s^+ = 8{,}1$ et d'autre part cette amplitude tend vers zéro beaucoup plus lentement dans le premier cas. L'évolution de l'amplitude $[\tilde{u}']$ rapportée à l'amplitude locale de la vitesse $[\tilde{u}]$ (Fig. 12) est également très instructive. Les différences entre les deux écoulements sont encore plus importantes: une valeur maximum de l'ordre de 0,6 à la paroi pour $l_s^+ = 23$ et de 0,1 seulement pour $l_s^+ = 8{,}1$. Il semble que dans ce cas la trubulence soit véritablement étouffée. Si on compare ce rapport à $\sqrt{\overline{\tilde{u}'^2}}/u_\tau$ également tracé sur la figure, on conclut de même à une suppression de la modulation à haute fréquence d'oscillation, mais, par contre, à une amplification à la fréquence intermédiaire. Ces observations concordent avec celles faites antérieurement dans I à faible amplitude. La dispersion y était plus importante et les conclusions étaient de ce fait très réservées. Les faits concernant $\tilde{u}'$ ne concordent pas avec les idées (6, 11, 12) selon lesquelles il devrait y avoir des interactions fortes entre la turbulence et l'écoulement oscillant lorsque leurs fréquences deviennent comparables.

Les comportements des déphasages de $\tilde{u}'$ sont également très différents. On constate qu'à haute fréquence ce déphasage suit à peu près celui de la vitesse, alors qu'à la fréquence plus basse il y a une avance très importante de l'ordre de 155° qui décroît ensuite très lentement. Ce résultat est difficile à interpréter pour le moment.

4.2. Amplitude et fréquence critiques d'apparition de courants de retour

Des vitesses négatives apparaissent en un point lorsque $[\tilde{u}] \geqslant \bar{u}$, l'égalité correspondant aux conditions critiques. Comme $[\tilde{u}]$ (y) et $\bar{u}$ (y) sont des fonctions monotones et que la couche oscillante est plus mince que la couche permanente, la région des courants de retour commence presque toujours à se manifester en premier lieu à la paroi. On en a conclu dans I que la condition critique d'apparition de vitesses négatives était que $\left(d[\tilde{u}]/dy\right)_{y=0} = \left(d\bar{u}/dy\right)_{y=0}$ c.a.d. l'égalité des frottements :

$$\nu \left(d[\tilde{u}]/dy\right)_{y=0} = \bar{\tau}/\rho = u_\tau^2$$

Si $\tilde{u}$ suit la solution de Stokes : $\left(d[\tilde{u}]/dy\right)_{y=0} = \sqrt{2}\,[u_\xi]/l_s$ et dans ce cas le critère s'écrit :

$$[\tilde{u}_\xi]/u_\tau = l_s^+/\sqrt{2} \qquad \text{ou} \qquad [\tilde{u}_\xi]^+ = l_s^+/\sqrt{2}$$

Cette expression est remarquable par sa simplicité et parce qu'elle associe naturellement l'amplitude à la fréquence du mouvement oscillant. Dans des axes l_s^+ et $[\tilde{u}_\xi]^+$, la droite ci-dessus devrait séparer les régions avec ou sans courants de retour dans la mesure où $\tilde{u}$ obéit à la solution de Stokes. Inversement, si ce critère est vérifié expérimentalement, on confirme que $\tilde{u}$ suit la solution visqueuse de Stokes malgré la présence d'une turbulence importante. On remarquera que cette condition fait uniqement intervenir l'amplitude de $\tilde{u}$ mais pas le déphasage. D'après les mesures analysées plus haut, on peut s'attendre à ce que ce critère reste valable jusqu'à des valeurs relativement importantes de l_s^+ , puisque l'amplitude, surtout près de la paroi, s'écarte beaucoup plus lentement du profil visqueux que le déphasage.

La figure 12 rassemble des observations visuelles, des mesures de vitesse et de frottement avec la SFC. La conclusion d'ensemble qui se dégage de cette figure est que les résultats des trois types de mesures concordent et sont en accord avec le critère théorique. L'analyse plus détaillée fait apparaître quelques différences qui s'expliquent. En premier lieu, le fait que les points provenant des mesures de vitesse à l_s^+ = 7 et 12 soient à gauche de la droite limite est logique puisque la vitesse est toujours mesurée en un point situé à une certaine distance de la paroi ; on trouvera donc encore des vitesses négatives entre ce point et la paroi lorsqu'on diminue f c.a.d. lorsqu'on augmente l_s^+ . Les points de mesures à droite de ligne pour $l_s^+ = 23$ par contre, sont cohérentes avec le raidissement du gradient d $[\tilde{u}]/dy$ par rapport à la solution de Stokes lorsque l_s^+ s'écarte du régime des hautes fréquences (cf. § 4.3.). Les observations visuelles de courant de retour vers $l_s^+ = 10$ et à des fréquences inférieures au critère basé sur la solution de Stokes pourraient correspondre à la situation exceptionnelle où une zone de vitesse négative prend naissance à l'intérieur du fluide comme l'illustre le schéma de la Fig. 14. Ceci est possible parce que la partie linéaire du profil $[\tilde{u}]^+$ se prolonge nettement plus loin que celle du profil $\bar{u}^+$.

En conclusion, la prévision des conditions critiques d'apparition des courants de retour basée sur la solution visqueuse de Stokes est en bon accrod avec les observations jusqu'à $l_s^+ \simeq 20$. Au-dlà de cette valeur, les amplitudes au centre du canal nécessaires pour provoquer des vitesses négatives au voisnage de la paroi dépassent 70 % et deviennent difficile à rélaiser expérimentalement.

4.3. Les variations du frottement pariétal avec f et $[\tilde{u}_\xi]$.

Le frottement pariétal détermine entièrement l'écoulement près de la paroi, puisque

$$\tilde{\tau} = \rho\nu \left(\frac{d[\tilde{u}]}{dy}\right)_{y=0} \cos\left(\omega t + \{\tilde{u}\}_{y=0}\right)$$

Nous avons vu plus haut l'importance de $d[\tilde{u}]/dy$ et $\{u\}_0$ pour la description du mouvement périodique. Par ailleurs, les mesures de $\tilde{u}$ près de la paroi sont longues et difficiles. La mesure directe de τ par la SFC, malgré les problèmes qu'elle pose surtout en présence de courants de retour, est intéressante non seulement à cause des informations qu'elle apporte mais aussi parce qu'elle est rapide. Elle fournit en particulier un bon diagnostic de l'écoulement oscillant. Nous avons effectué des mesures de $\langle\tau\rangle$ dans une large gamme de fréquence et d'amplitude et également pour plusieurs valeurs de la vitesse moyenne $\bar{u}_\xi$. Les résultats sont rassemblés sur les figures 16 à 17. Les rapports $(\tau)_{instat.}/(\bar{\tau})_{stat.}$ à $\bar{u}_\xi$ constant se regroupent tous de manière satisfaisante autour de $\omega\nu$ (Fig. 14) : c'est une preuve supplémentaire de l'insensibilité de l'écoulement moyen aux oscillations forcées.

Les résultats les plus riches d'enseignements concernent la phase et l'amplitude de $\tilde{\tau}$ (Fig. 15 et 16). En premier lieu, ils confirment l'importance du paramètre de similitude l_s^+. La dispersion des mesures de phase autour d'une ligne moyenne est toujours inférieure à ± 5°. Or il faut remarquer la décroissance très rapide de l'avance de phase de 40° à presque 0° entre $l_s^+ = 10$ et 20. Une telle variation de s'obtient simplement en doublant la vitesse de frottement (ou approximativement la vitesse au centre) ou en divisant la fréquence par quatre. On note en passant que le déphasage à la paroi est plus sensible à une variation du nombre de Reynolds que de la fréquence. Sur la même figure sont également portés des résultats de COUSTEIX et Al. (4) qui sont bien corrélés avec les nôtres bien qu'ayant été obtenus dans des conditions expérimentales tout à fait différentes. Les points de RAMAPRIAN (7) sont plus bas ce qui pourrait être dû à la réponse en fréquence limitée de la SFC. L'amplitude $[\tilde{\tau}]$ est rapportée à celle de l'écoulement de Stokes $\sqrt{2}\,[\tilde{u}_e]/l_s$ (Fig. 17) pour mettre en évidence la conformité ou les déviations avec ce dernier. La dispersion des points autour d'une ligne moyenne est ici plus importante, mais il y a tout de même une tendance nette en fonction de l_s^+ qui se dégage.

En deuxième lieu, le déphasage tend vers 45° lorsque $l_s^+ < 10$ c.a.d. qu'aux hautes fréquences l'écoulement oscillant devient identique à l'écoulement visqueux de Stokes. D'autre part, l'existence de faibles retards de phase est confirmée. On s'attend au vu des mesures de $\tilde{u}$ (cf. 4.1.) à trouver un rapport $[\tilde{\tau}]/[\tilde{\tau}]_{stokes}$ égal à un à haute fréquence. Les valeurs qui sont systématiquement inférieures à un - et d'ailleurs relativement peu dispersées malgré les grandes différences en amplitude de $[\tilde{u}_e]$ - s'expliquent mal, car on ne voit pas bien comment la contrainte pourrait être moins importante que la contrainte visqueuse, sinon par l'influence de la turbulence sur la réponse du film comme on l'a montré plus haut. Plus positive est la constatation de l'accroissement de $[\tilde{\tau}]/[\tilde{\tau}]_{stokes}$ lorsque l_s^+ croît et qui traduit le raidissement du profil de $\tilde{u}$ à la paroi par la turbulence. Cet effet est semblable à celui de la turbulence sur l'écoulement moyen, puisque dans ce cas le gradient de vitesse passe de $\bar{u}_e/\delta$ à u_τ^2/ν soit un rapport $u_\tau \delta/\nu = R_e^+ u_\tau/\bar{u}_e \gg 1$. Mais cet effet sur le gradient de l'écoulement oscillant est beaucoup moins fort puisque le rapport équivalent n'atteint que 3 pour $l_s^+ = 50$.

Une autre représentation de l'amplitude $[\tilde{\tau}]$ pourrait être amenée par la recherche du régime quasi-stationnaire qui exigerait par exemple qu'une relation du type $u_\tau^2 = C\, R_{\delta_1}^{\alpha}\, \rho\, \tilde{u}_e^2$ reste valable à tout instant de la période. Dans ce cas, on aurait avec un développement au 1er ordre $\{\tilde{\tau}\} = \{\tilde{u}_e\}$ et

$$[\tilde{\tau}]/[\tilde{\tau}]_{quasi\text{-}stat.} = 4/7\,\left([\tilde{\tau}]/\bar{\tau}\right)\Big/\left([\tilde{u}_e]/\bar{u}_e\right)$$

Cette représentation conduit à une grande dispersion des points aux valeurs de $l_s^+ < 30$ comme on peut s'y attendre. Ce qui est plus surprenant est que le rapport reste de l'ordre de 1,3 donc nettement au-dessus de un lorsque $l_s^+ > 40$. Il ne semble pas que l'on puisse imputer cet écart entièrement aux défauts de la SFC. C'est comme si le régime quasi-stationnaire était difficile à atteindre.

5. ECOULEMENTS PULSES DANS UN GRADIENT DE PRESSION ADVERSE

Un gradient de pression adverse accroît la complexité de l'écoulement instationnaire bien plus qu'il ne paraît à première vue, car le gradient adimensionnel $\left(\delta/\tfrac{1}{2}\rho\bar{u}_e^2\right)\partial\bar{p}/\partial x$ n'est pas le seul paramètre nouveau. En effet, les dérivées longitudinales des gradients $\partial\bar{p}/\partial x$ et $\partial\tilde{p}/\partial x$ peuvent également jouer un rôle. La recherche présente a été commencée avec un gradient moyen modéré, engendré par une divergence de la section de 6°, qui ne provoquait pas de séparation en régime permanent. Le gradient de pression était $\left(\delta/\tfrac{1}{2}\rho\bar{u}_e^2\right)\partial\bar{p}/\partial x \simeq 10^{-2}$; les conditions expérimentales sont indiquées sur la figure 18. Ce travail est encore dans une phase exploratoire et les conclusions n'ont rien de définitif. Il s'agit pour le moment essentiellement de mettre en évidence des différences de comportement avec l'écoulement en canal. Si nous indiquons les valeurs de l_δ^+ c'est seulement pour faciliter la comparaison avec les écoulements correspondants en canal. Nous ne prétendons pas que l_δ^+ soit ici un paramètre de similitude approprié, les résultats étant encore bien trop partiels. Les mesures de frottement pariétal qui sont prévues devraient apporter un début de réponse au problème de la similitude.

Dans les conditions d'oscillation utilisées, il n'y avait pas d'effet significatif sur la vitesse moyenne, à savoir, les différences étaient inférieures à $u_\tau/2$ par rapport aux profils permanents. L'amplitude et le déphasage de $\tilde{u}$ reportés sur les figures 18 et 19 révèlent un comportement qui diffère de de manière frappante de celui de l'écoulement en canal. (On notera que sur ces figures l'échelle pour y_s est logarithmique). Seulement l'amplitude des cas $l_s^+ = 4.2$ et 11.7 suivent à peu près la solution de Stokes ; le maximum dans ce dernier cas est à $y_s = 10$ et le dépassement de la valeur externe de 20 %, ce qui est relativement faible par rapport à d'autres observations (3, 8, 10). L'amplitude pour $l_s^+ = 21$ croît très lentement. La nécessité d'élucider l'évolution près de la paroi apparaît clairement sur cette figure.

Les variations du déphasage qui reste positif sont également étalées sur une épaisseur bien plus grande qu'en écoulement en canal et très différentes de celles de l'écoulement de Stokes. On remarque que les déphasages ont une valeur presque constante de l'ordre de 45° jusqu'à $y_s \simeq 2$, une observation semblable à celle de SIMPSON et Al. (9). L'expérience à $l_s^+ = 21{,}1$ a été faite à une vitesse plus élevée sur l'axe ; certaines différences peuvent donc provenir du nombre de Reynolds.

6. CONCLUSIONS

Les résultats expérimentaux d'écoulements turbulents pulsés en canal présentés dans cette étude contribuent à accréditer l_s^+ comme paramètre de similitude. Dans la mesure où la couche oscillante ne s'étend pas au-delà de la région logarithmique de la vitesse moyenne, il est plausible que ce paramètre reste valable pour les couches limites turbulentes sur plaque plane. Cette conclusion s'appuie notamment sur la bonne corrélation de l'amplitude et du déphasage du frottement pariétal en fonction de l_s^+ dans des gammes étendues d'amplitude et de fréquence du mouvement oscillant et des variations du simple au double de la vitesse de frottement. Les régimes correspondants à $l_s^+ < 10$ peuvent être qualifiés de haute fréquence. Mais la valeur de l_s^+ au-delà de laquelle l'écoulement devient quasi-stationnaire n'est pas encore bien déterminée.

Les présentes observations confirment l'insensibilité de l'écoulement moyen aux oscillations forcées, même lorsque ces dernières atteignent de très fortes amplitudes locales supérieures à 100 %. A haute fréquence l'écoulement oscillant suit la solution visqueuse de Stokes : il y a un découplage complet entre l'écoulement moyen turbulent et l'écoulement oscillant visqueux, un fait qui avait déjà été esquissé dans I. A moyenne fréquence l'amplitude suit approximativement le même profil tandis que le déphasage est très différent : c'est la première manifestation de l'influence de la turbulence. A fréquence plus basse, les mesures de frottement pariétal montrent qu'il y a un raidissement de gradient de la vitesse oscillante par la turbulence. Ce raidissement par la turbulence est cependant nettement moins fort que celui de l'écoulement moyen, et sa partie linéaire s'étend plus loin : le profil visqueux de Stokes résiste mieux à la turbulence que le profil moyen. En résumé, à partir de $l_s^+ = 10$, il y a une interaction croissante à sens unique de la turbulence de l'écoulement moyen sur l'écoulement oscillant. Une vérification expérimentale est également apportée au critère d'apparition de courants de retour, $[\tilde{u}_\tau] = l_s^+/\sqrt{2}$. D'une manière générale, on ne constate pas d'effet spécifique de l'amplitude du mouvement oscillant forcé sur l'écoulement ; celle-ci intervient simplement de manière linéaire.

La modulation périodique de la turbulence apparaît comme très sensible à la fréquence : elle est faible par rapport à celle de u à haute fréquence et du même ordre que cette dernière aux fréquences intermédiaires. Il en est de même des déphasages, proches de ceux de $\tilde{u}$ à haute fréquence seulement.

Les premiers résultats obtenus dans des couches limites turbulentes décélérées, mais sans décollement permanent, révèlent, conformément à d'autres expériences, la profonde influence du gradient de pression adverse sur l'écoulement oscillant. Ce dernier perd toute ressemblance avec la solution de Stokes à des valeurs intermédiaires de l_s^+. La couche oscillante pénètre nettement plus loin dans l'écoulement turbulent moyen - toujours peu affecté ici par le mouvement instationnaire - sauf à très haute fréquence.

Pincipales Notations

d : déflection de la paroi
f, ω, T : fréquence et période des oscillations forcées
f_D, T_D : fréquence et période Doppler
$2h$: hauteur du canal
$l_s = \sqrt{2\nu/\omega}$: longueur de Stokes
$l_\nu = \nu/u_\tau$: échelle visqueuse interne
L_f : largeur du film chaud
L : longueur du canal
U : vitesse
u_τ : vitesse de frottement
y : distance à la paroi
$y_s = y/l_s$
$\tau = \rho u_\tau$ frottement pariétal
ν : viscosité cinématique

g : grandeur quelconque
g : $\overline{g} + \tilde{g} + g'$
$\overline{g}$: moyenne temporelle
$\tilde{g}$: oscillation périodique
g' : fluctuation turbulente
$\langle g \rangle$: $\overline{g} + \tilde{g}$: moyenne de phase
$[\tilde{g}]$: amplitude du fondamental de g
$\{g\}$: phase dufondamental de g
g_c : valeur au centre du canal
$(\,)^+$: longueur rapportée à l_ν ou vitesse rapportée à u_τ

REFERENCES

1. KARLSSON, S.K.F., "An Unsteady Turbulent Boundary Layer", J. Fluid Mech. 5, 622, 1959

2. COUSTEIX J., DESOPPER A., HOUDEVILLE R., "Structure and Devlopment of a Turbulent Boundary layer in an oscillatory external Flox". Turbulent Shear Flows I, édité par Durst & al., Spring Verlag, 1979.

3. COUSTEIX J., HOUDEVILLE, R., JAVELLE,J., "Response of a Turbulent Boudary Layer to a Pulsation of the External Flow with and without Adverse Pressure Gradient", Unsteady Turbulent Shear Flows, édité par Michel et al., Springer Verlag 1981, et Turbulent Shear Flow III, édité par Durst et al., Springer Verlag
1982.

4. HOUDEVILLE R., JULLEN J.E., COUSTEIX J., "Mesure du Frottement Pariétal par jauges à éléments chauds", La Recherche Aérospatiale, 1984

5. BINDER G., KUENY J.L., "Measurement of the Periodic Velocity Oscillations Near the Wall in Unsteady Turbulent Channel Flow". Unsteady Turbulent Shear Flows, édité par Michel et al., Springer Verlag, 1981 et Turbulent Shear Flow III édité par Durst et al., Springer Verlag, 1982.

6. RAMAPRIAN, B.R., T.U., S.W., "Fully Developed Periodic Turbulent Pipe Flow", J. Fluid Mech. 137, 31-81,1983.

7. MENENDEZ, A.N., RAMAPRIAN, B.R , "Study of Unsteady Turbulent Boundary Layers", IIHR Report N° 270, The University of Iowa, 1983.

8. JAYARAMIN, P., PARIKH, P., REYNOLDS, W.C., "An Experimental Study of the Dynamics of an Unsteady Turbulent Boundary Layer", Techn. Report N° TF-18, Dpt Mech. Engr., Stanford University, 1982.

9. PARIKH, P., REYNOLDS, W.C. JAYARAMAN, P., "Behaviour of an Unsteady Turbulent Boundary Layer", AIAA J. 20, 6, 769-775, 1982.

10 SIMPSON, R.L., SHIVAPRASAD, B.G., CHEN, Y.T., "The structure of a Separating Turbulent Boundary Layer-Effects of Periodic Free-Stream Unsteadyness", J. Fluid Mech. 127, 219-262, 1983. et "Frequency Effects of Periodic Unsteady Free-Stream Flows" - J. Fluid Mech. 131, 319-340, 1983.

11 MIZUSHINA, T., MARUYAMA, SHIOZAKI, Y, "Pulsating Turbulent Flow in a Tube", J. Chem. Engr Japan, 6, 487-494, 1973.

12 MIZUSHINA, T., MARUYAMA, HIPASAWA, H., "Structure of the Turbulence in Pulsating Pipe Flows", J. Chem. Engr Japan, 8, 210-216, 1975.

13 LIGHTHILL, M.J., "The Response of Laminar Skin Friction and Heat Transfer to Fluctuations in the Stream Velocity", Proc. Royal Society (London) Series A - 224, 1-23, 1954.

14 COMTE-BELLOT, G., "Ecoulement Turbulent entre deux Parois Parallèles". Publications Scientifiques et Techniques du Ministère de l'Air, 1965.

15 ECKELMAN, H., "The Structure of the Viscous Sublayer and the Adjacent Wall Region in a Turbulent Channel Flow", J. Fluid Mech. 65, 439-459, 1974.

16 FORTUNA, G., HANRATTY, T.J., "Frequency Response of the Boundary Layer on Wall Transfer Probes", Int. J. Heat Mass Transfer, 14, 1499-1507, 1971.

17 PEDLEY, T.J., "A Thermal Boundary Layer in a reversing Flow", J. Fluid Mech. 67, 209-225, 1975.

18 PEDLEY, T.J., "Heat Transfer from a Hot Film in a Reversing Shear Flow", J. Fluid Mech. 78, 513-534, 1976.

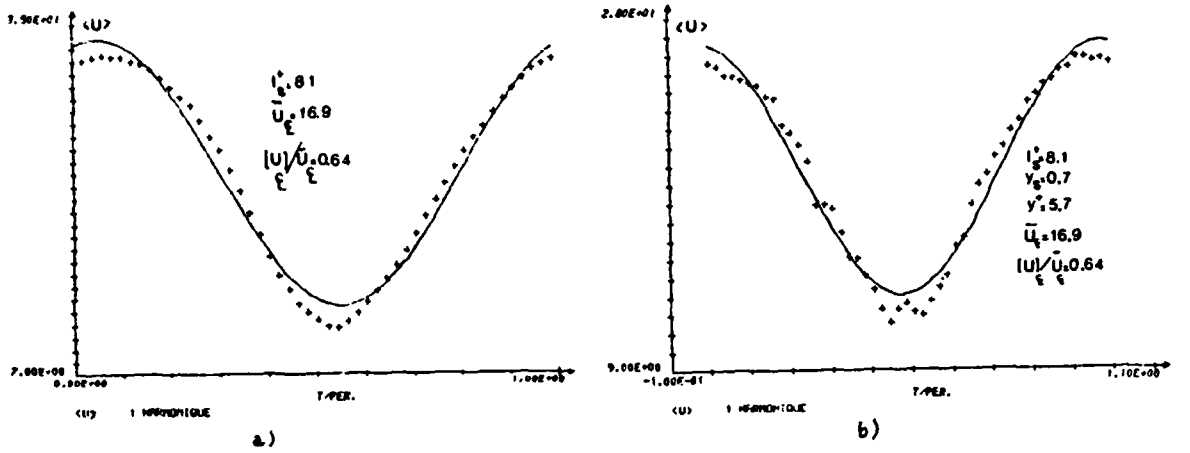

Fig. 1 - Moyenne de phase
a) vitesse au centre
b) vitesse près de la paroi

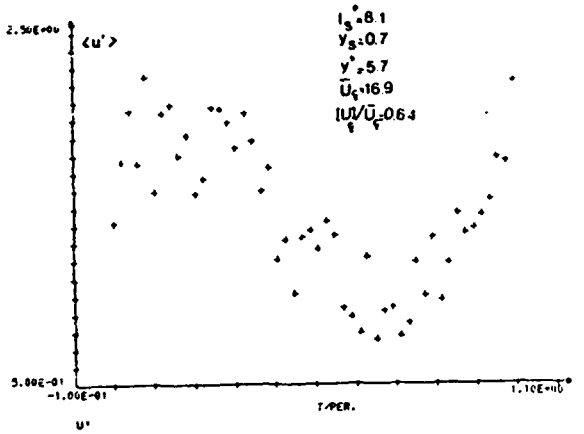

Fig. 2 - Moyenne de phase de l'intensité turbulente près la paroi.

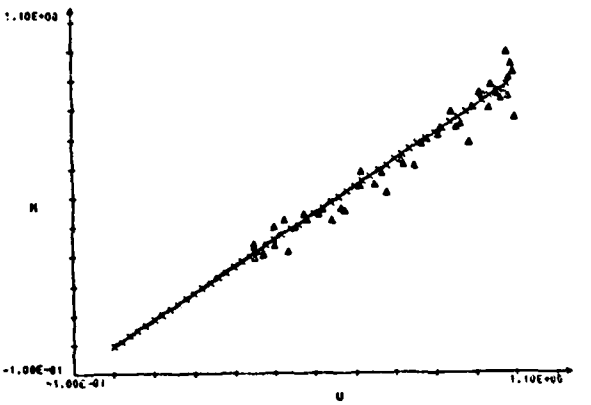

Fig. 3 - Répartition du nombre de mesures en fonction de la vitesse

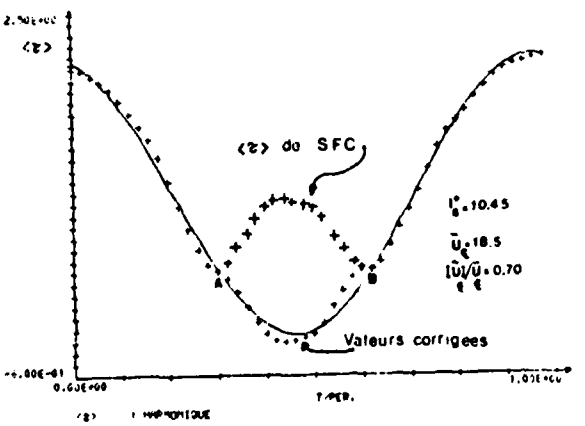

Fig. 4 - Moyenne de phase du frottement pariétal en présence de courants de retour. Signal redressé et signal corrigé

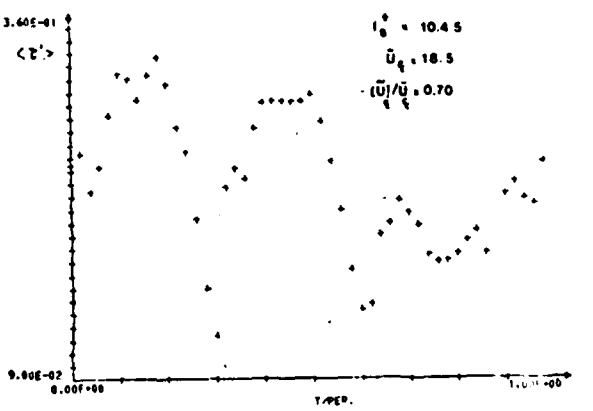

Fig. 5 - Fluctuations turbulentes du frottement pariétal

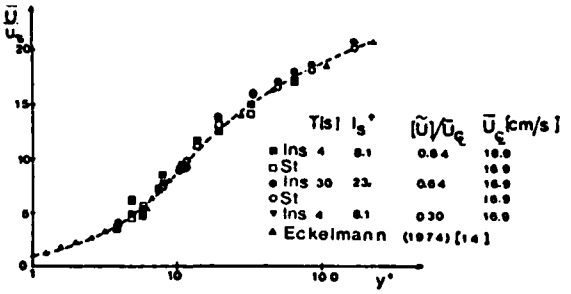

Fig. 6 - Vitesse moyenne en écoulement stationnaire et instationnaire

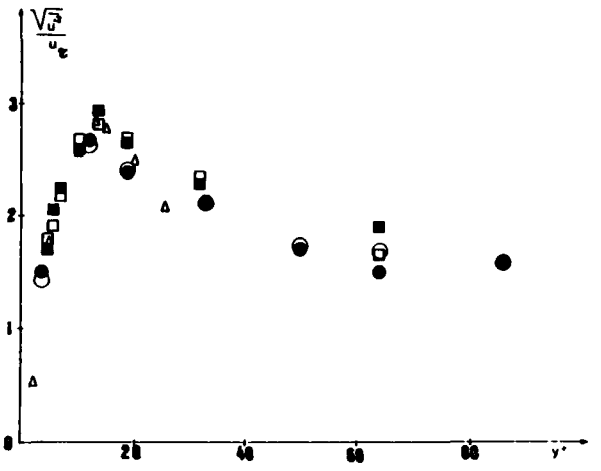

Fig. 7 - Intensité turbulente moyenne en régime stationnaire et instationnaire.
Symboles (voir Fig. 6)

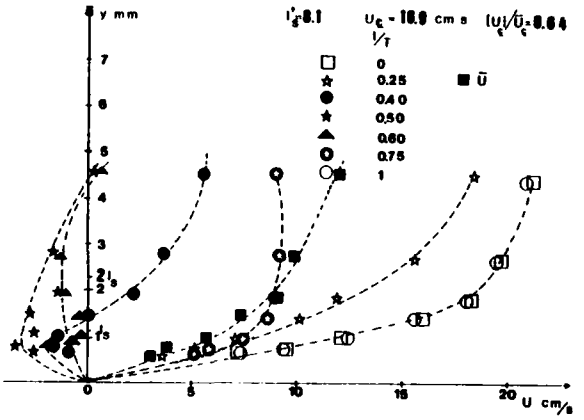

Fig. 8 - Profils de vitesse à différents instants de la période.
Symboles (voir Fig. 6)

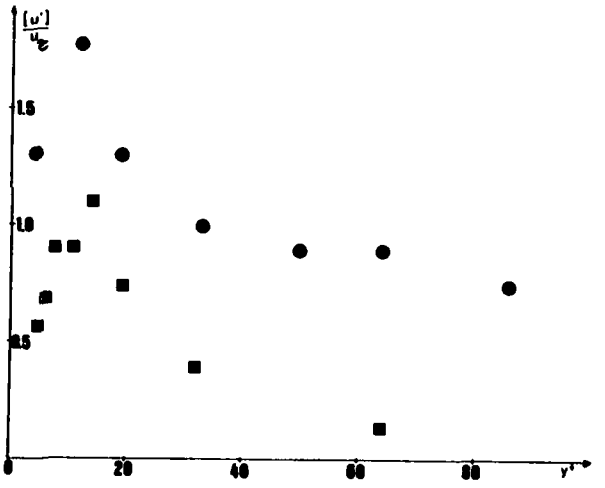

Fig.11 - Amplitude de la modulation de l'intensité turbulente.
symboles (voir Fig. 6)

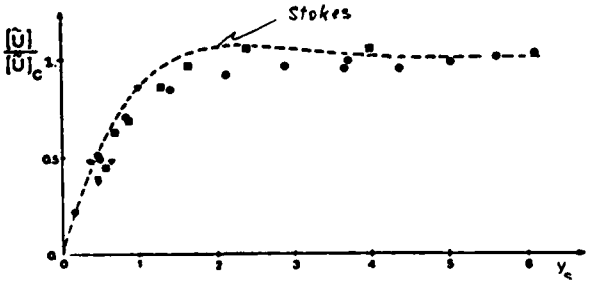

Fig. 9 - Répartition de l'amplitude de l'oscillation périodique de vitesse. Symboles (voir Fig. 6)

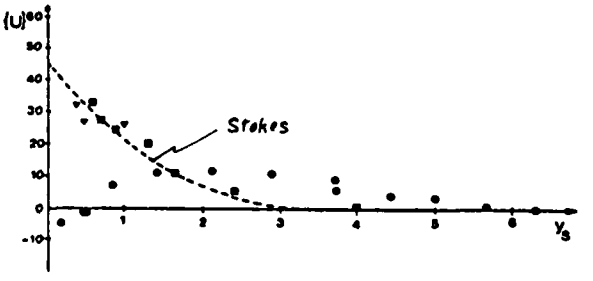

Fig.10 - Répartition du déphasage de l'oscillation périodique de vitesse. Symboles (voir Fig. 6)

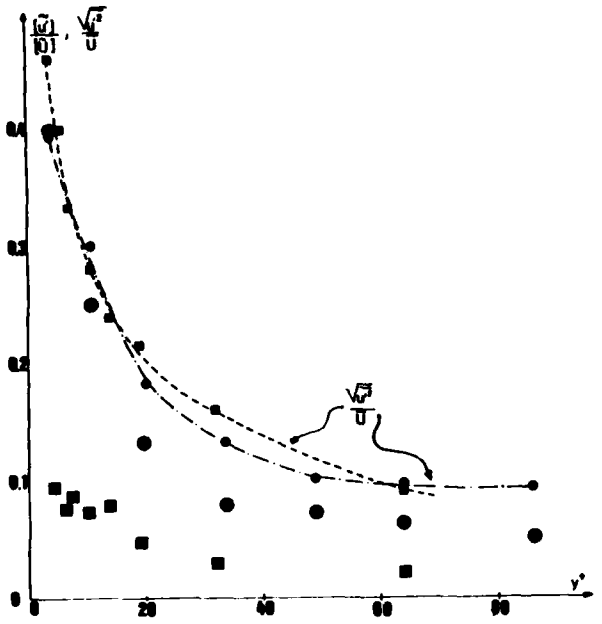

Fig.12 - Amplitude de la modulation de l'intensité turbulente rapport à l'amplitude locale de la vitesse. Symboles (voir Fig. 6)

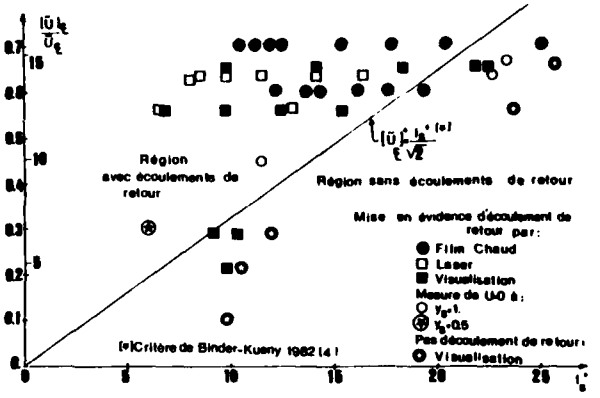

Fig.13 - Vérification du critère d'apparition des écoulements de retour

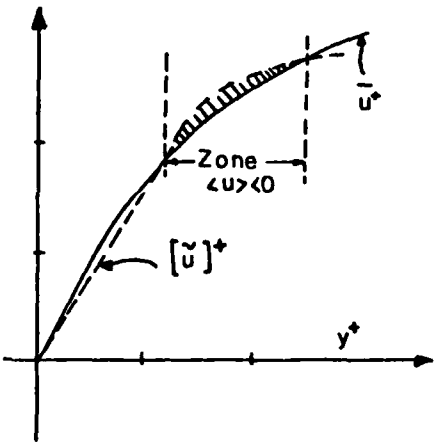

Fig.14 - Naissance de courants de retour à l'intérieur du fluide

Symbole	$\bar{U}_e$ cms	$[u]/\bar{U}_e$ (%)	T ts l
●	30	10	2.6÷15
■	28.5	13	2.6÷33
□	30	17	2.6÷61
○	19	19	3÷31
☆	30	27	2.6÷61
▣	26÷16	60	6
⊠	18.5	70	4÷132

■ ⊠ Points avec écoulement de retour.

Tableau I : Conditions expérimentales des mesures du frottement pariétal. Classification par ordre croissant de l'amplitude.

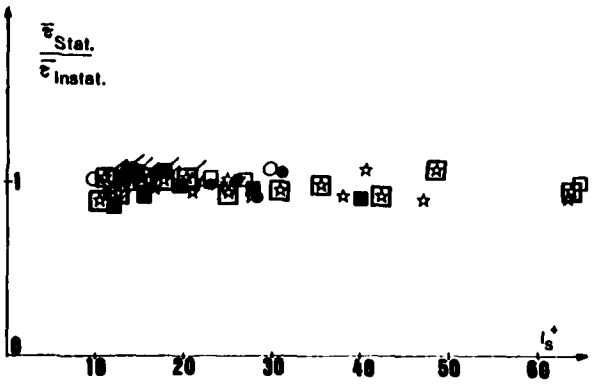

Fig.15 - Rapport des frottements moyens stationnaire et instationnaire. Symboles (voir Tableau 1)

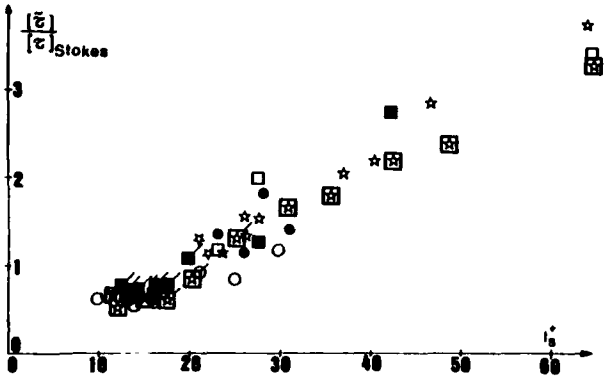

Fig.17 - Amplitude de l'oscillation périodique du frottement pariétal rapportée l'amplitude de l'écoulement de Stokes. Symboles (voir Tableau 1)

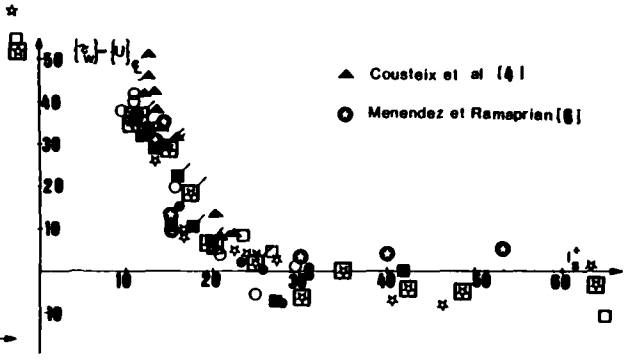

Fig.16 - Déphasage de l'oscillation périodique du frottement pariétal. Symboles (voir Tableau 1)

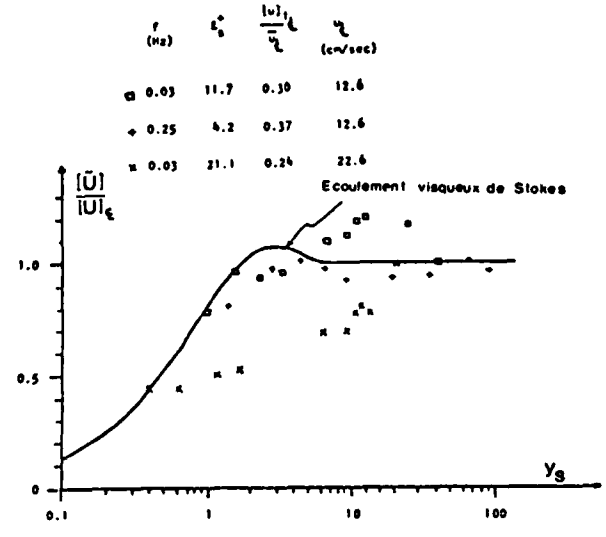

Fig.18 - Répartition de l'amplitude de l'oscillation périodique de vitesse. $dp/dx > 0$

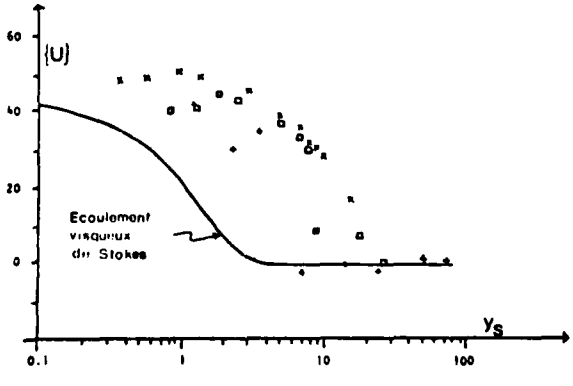

Fig.19 - Répartition du déphasage de l'oscillation périodique de vitesse. $dp\ dx > 0$ Symboles (voir Fig. 18)

COUCHE LIMITE TURBULENTE INSTATIONNAIRE : INVESTIGATIONS EXPERIMENTALE ET NUMERIQUE

J. COUSTEIX - R. HOUDEVILLE
ONERA/CERT
Département d'Etudes et de Recherches en Aérothermodynamique
2 avenue Edouard Belin - 31055 TOULOUSE Cedex - FRANCE

RESUME

L'étude expérimentale d'une couche limite turbulente soumise à une fluctuation périodique de l'écoulement extérieur est présentée. Deux cas sont ici considérés, celui d'une plaque plane et celui d'un gradient de pression positif conduisant au décollement. L'analyse des résultats repose sur la notion de moyenne de phase.

Une méthode intégrale de calcul ainsi qu'un modèle à trois équations de transport ont été utilisés. A grande valeur du paramètre de fréquence réduite, seule cette dernière méthode permet de retrouver la plupart des résultats expérimentaux.

L'étude de l'apparition d'une singularité dans les équations de couche limite instationnaire et sa relation avec le décollement est abordée analytiquement à partir des équations intégrales.

1 - INTRODUCTION

La prise en compte d'effets instationnaires dans différents problèmes pratiques d'aérodynamique ou d'hydrodynamique nécessite de disposer de moyens de calcul des régions visqueuses ou turbulentes et en particulier des couches limites. Des études expérimentales à caractère plutôt fondamental ont déjà été réalisées ou sont en cours de développement [1]. Elles devraient aboutir à une meilleure connaissance des phénomènes physiques, ainsi qu'à la réunion d'un ensemble de données assez important pour valider avec confiance les méthodes de calcul.

Sur le plan théorique, une question importante concerne l'apparition et la nature d'une singularité dans les équations de couche limite instationnaire et sa relation avec le décollement. De nombreuses études purement numériques ont déjà été consacrées à ce problème [2]. Afin d'éviter certaines ambiguïtés concernant l'interprétation de ces résultats, une étude analytique est présentée. Elle repose sur l'utilisation des équations globales de la couche limite avec un système de relations de fermeture simplifié, mais suffisamment représentatif.

2 - ECOULEMENT TURBULENT INSTATIONNAIRE - ETUDE EXPERIMENTALE

2.1. Moyenne d'ensemble - Turbulence

Les écoulements à considérer étant à la fois turbulents et instationnaires, la notion classique de grandeur moyenne doit être remplacée par celle de moyenne d'ensemble définie de la façon suivante :

$f_i(t)$ représentant l'évolution de la fonction f au cours de la ième réalisation d'un certain phénomène, la moyenne d'ensemble $\langle f \rangle$, fonction du temps, est donnée par :

$$\langle f \rangle = \frac{1}{N} \sum_{i=1}^{N} f_i$$

Pour les écoulements périodiques auxquels on s'intéresse, chaque période correspond à une réalisation particulière et donc $\langle f \rangle$ est définie entre 0 et T.

La composante turbulente de f se définit naturellement par :

$$f' = f - \langle f \rangle$$

et les traitements statistiques habituels s'appliquent à f_i'. Par exemple, la variance de f' s'obtient par la relation :

$$\langle f'^2 \rangle^{1/2} = \left(\frac{1}{N} \sum_{i=1}^{N} f_i'^2 \right)^{1/2}$$

2.2. Moyens de mesure

Mesure de la vitesse

L'effort expérimental a principalement porté sur la détermination de la composante longitudinale du champ de vitesse, aussi bien en ce qui concerne sa partie périodique que turbulente. Pour cela, l'anémométrie à fil chaud et la vélocimétrie laser ont été utilisées suivant la présence ou non d'écoulements de retour.

L'analyse statistique des résultats en termes de moyennes d'ensemble nécessite de disposer d'une base de temps. Celle-ci est très simplement fournie par un dispositif

photo-électrique lié au mécanisme de pulsation de l'écoulement (figure 1).

Mesure du frottement de paroi

Pour mesurer le frottement pariétal, la technique de l'élément chaud a été utilisée [3]. Originellement, une sonde de frottement consiste en un fil ou film mince collé à la paroi et maintenu à température constante. Le flux de chaleur cédé à l'écoulement dépend du frottement par la relation :

$$E^2 = E_o^2 + A(\varrho_p \mu_p \tau_p)^{1/m} \quad ; \quad m = 3$$

où E représente la tension aux bornes de l'élément sensible soumis au frottement τ_p et E_o sa valeur pour $\tau_p = 0$. Sous cette forme, la très faible bande passante de la sonde la rend inutilisable en écoulements instationnaires, aussi quelques modifications ont-elles été apportées. La principale consiste en la présence d'une petite cavité creusée sous l'élément sensible afin de l'isoler de la paroi (figure 2). Ceci a pour conséquence d'accroitre considérablement la bande passante, jusqu'à quelques kilohertz et, également, d'augmenter la sensibilité de la mesure et donc la précision des résultats [4]

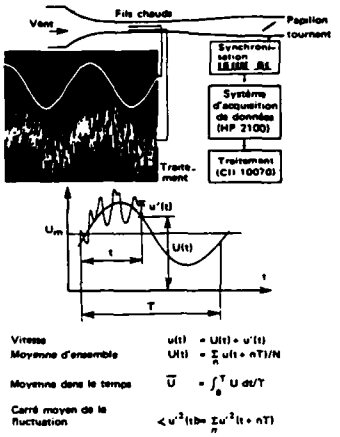

Fig. 1 - Etude expérimentale d'une couche limite turbulente - Traitement des mesures

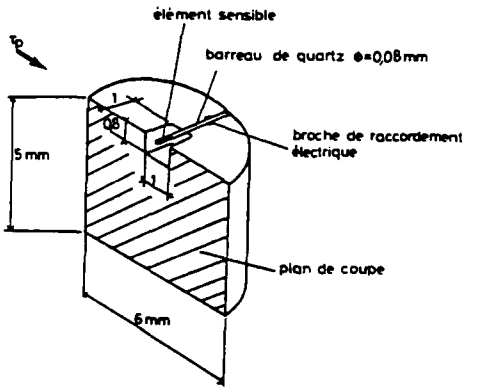

Fig. 2 - Sonde de frottement pour mesures en écoulement instationnaire - Vue en coupe

f (Hz)	$\bar{U}_e$ (m/s)	$\Delta U_e/\bar{U}_e$	$\omega X_o/\bar{U}_e$	$10^{-6} R_{X_o}$	u'_{max}/δ (s^{-1})	ℓ_s^+
38	21.9	0.15-0.1	1.52-8.35	0.2-1.1	350-120	25.2-21.9
62	16,8	0.12-0.05	3.2-17.8	0.15-0.87	270-90	15.9-13.8

Tableau 1 - Couche limite oscillante sans gradient de pression moyen [7]

2.3. Couches limites de plaque plane en écoulement pulsé

Montage expérimental

Pour des raisons de simplicité mécanique, la couche limite étudiée se développe sur une plaque plane fixe et c'est l'écoulement dans la soufflerie, de type EIFFEL, qui est modulé par un disque tournant placé en aval de la veine d'essais. Un tel dispositif induit une perturbation sinusoidale de la vitesse avec très peu d'harmoniques, à condition de se placer aux fréquences de résonance de l'installation [5].

La plaque plane, large de 22 cm, est longue de 70 cm. Son bord d'attaque est de section elliptique avec un allongement égal à 3. Un fil de 0,8 mm de diamètre, collé à 70 mm du bord d'attaque, déclenche la transition de la couche limite.

Paramètres de l'écoulement

En écoulement laminaire et pour des nombres de Reynolds assez grands, la structure de la couche limite dépend essentiellement du paramètre de fréquence réduite $\omega X/\bar{U}e$. Ce

paramètre est relié au rapport de l'épaisseur de la couche de BLASIUS où sont confinés les effets visqueux, à celle de la couche de STOKES correspondant aux effets instationnaires :

$$\frac{\delta_B}{\delta_S} \approx \frac{X/(\bar{U}eX/\nu)^{1/2}}{(\nu/\omega)^{1/2}} = \left(\frac{\omega X}{\bar{U}e}\right)^{1/2}$$

En écoulement turbulent, la signification du paramètre de fréquence réduite est moins évidente, mais il conserve néanmoins une grande importance. Une étude systématique de la couche limite a été faite pour des valeurs de $\omega X/\bar{U}e$ comprises entre 1,5 et 18, en ne considérant que deux fréquences différentes (tableau 1).

Un paramètre important pour caractériser les effets instationnaires en couche limite turbulente est le rapport de l'épaisseur de la couche de STOKES à celle de la sous-couche visqueuse [6] :

$$l_s^+ = \left(\frac{2\nu}{\omega}\right)^{1/2} \frac{U_\tau}{\nu}$$

Pour des valeurs de l_s^+ de l'ordre de 8 ou inférieurs, les effets instationnaires restent confinés dans la sous-couche, ce qui signifie que la vitesse et les grandeurs turbulentes évoluent sans aucun déphasage dans la plus grande partie de la couche limite. Compte tenu des conditions expérimentales, la valeur la plus faible obtenue pour l_s^+ dans l'étude présentée est de l'ordre de 14.

Grandeurs moyennes

Les profils de vitesse moyenne obtenus à différentes positions sur la plaque et présentés sur la figure 3 ne montrent pas d'influence notable des effets instationnaires. Ceci est confirmé par l'évolution des épaisseurs intégrales, figure 4, qui est comparée à celle obtenue en stationnaire à même valeur du nombre de Reynolds. Ces résultats s'accordent avec toutes les prévisions théoriques qui ne montrent pas d'effets dus à l'instationnarité de l'écoulement sur le développement du champ de vitesse moyenne, même pour des valeurs relativement élevées du taux de modulation de l'écoulement, voisin ici de 15 %.

Grandeurs périodiques

La figure 5 montre les profils d'amplitude réduite et de déphasage de la vitesse dans la couche limite à différentes abscisses sur la plaque et ceci pour la fréquence de 38 Hz. Aux premières stations de mesure, l'amplitude de fluctuation de vitesse ne dépasse que très légèrement dans la couche limite celle de la vitesse extérieure. Ce dépassement augmente vers l'aval pour atteindre un maximum de 20 % à X = 0,34 m ($\omega X/\bar{U}e \approx 4,2$). Plus loin en X, il disparaît complètement et, vers l'extérieur de la couche limite, un minimum d'amplitude apparaît. Aux deux dernières stations ($\omega X/\bar{U}e \approx 8,3$), le dépassement d'amplitude existe à nouveau. Un comportement analogue s'observe aussi dans l'étude à 62 Hz et traduit en fait une évolution périodique des profils d'amplitude avec l'augmentation suivant X de la fréquence réduite. Une telle évolution se retrouvera sur tous les paramètres de la couche limite.

La figure 5 présente également les profils de déphasage de la vitesse. Près de la paroi, existe un maximum positif correspondant à la région logarithmique des profils de vitesse. En supposant que la loi universelle de paroi reste valable en instationnaire, un développement en petites perturbations de cette loi montre que la phase de la vitesse devrait être constante dans cette région et égale à celle du frottement pariétal [7]. L'allure de l'évolution du déphasage pour y tendant vers zéro semble remettre en cause la validité en instationnaire d'une loi universelle de paroi.

Afin de mettre clairement en évidence la réponse de la couche limite à une perturbation périodique de l'écoulement extérieur, l'évolution en fonction du paramètre de fréquence réduite de l'amplitude et de la phase de l'épaisseur de déplacement est représentée sur la figure 6. L'ensemble des résultats obtenus à l'ONERA/CERT [7, 8] ainsi que ceux de KARLSSON [9] se regroupent remarquablement bien pour montrer une évolution quasi-périodique en $\omega X/\bar{U}e$ et ceci bien que les conditions expérimentales diffèrent d'une étude à l'autre : nombres de Reynolds variés, transition déclenchée ou naturelle. De plus, dans l'étude de KARLSSON, les mesures sont effectuées à une position donnée et la fréquence varie alors que les autres cas ne correspondent qu'à trois fréquences différentes avec X variable.

En terme de fréquence réduite, la périodicité de l'évolution de l'amplitude et de la phase de $\delta 1$ est voisine de 5. Cette évolution ainsi que la valeur de la période peuvent être retrouvées à partir d'un développement en petites perturbations de l'équation intégrale de quantité de mouvement en supposant une valeur constante pour le paramètre de forme des profils de vitesse et une loi de frottement ne dépendant pas explicitement du temps.

D'autre part, une telle périodicité en X se retrouve sur l'évolution de la turbulence dans la région externe de la couche limite.

Pour montrer cela, considérons la figure 7. Elle représente l'évolution en fonction du temps de l'intensité de turbulence, divisée par sa valeur moyenne, à différentes stations sur la plaque pour des valeurs de y correspondant à 0,8 δ. Les fluctuations de $\sqrt{\langle u'^2 \rangle}$ sont directement liées à celles de l'épaisseur de la couche limite puisque

$y/\delta = 0,8$ se situe dans la région d'intermittence. Les étoiles indiquent les instants dans la période des maximum de $\langle u'^2 \rangle^{1/2}$. La pente des droites joignant ces points donne une vitesse de convection de l'ordre de 0,85 $\overline{U}e$. Ceci montre que la frontière moyenne de la couche limite, au sens de moyenne d'ensemble, peut être représentée par une onde progressive de même célérité. La combinaison de cette vitesse de phase avec la fréquence de l'oscillation forcée conduit à une évolution spatiale quasi périodique des caractéristiques de la couche limite. En terme de paramètre de fréquence réduite, cette périodicité s'exprime simplement de la façon suivante :

$$\frac{\omega L}{\overline{U}e} = \frac{\omega}{\overline{U}e} \frac{0,85\ \overline{U}e}{f} = 2\pi\ 0,85 = 5,3$$

Cette valeur est très proche de celle notée sur l'évolution quasi périodique de l'épaisseur de déplacement ou des profils de vitesse.

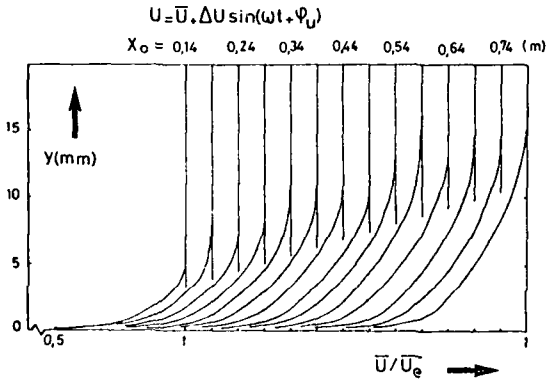

Fig. 3 - Profils de vitesse moyenne - F = 38 Hz

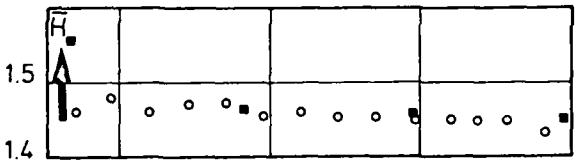

■ sondages stationnaires

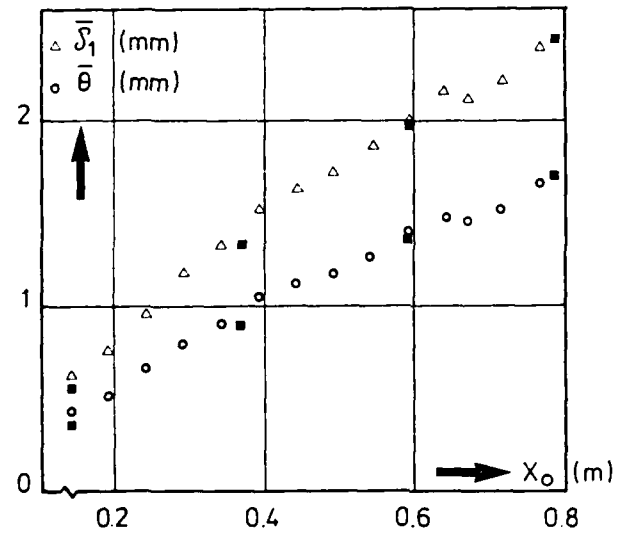

Fig. 4 - Epaisseurs intégrales et paramètre de forme moyen - F = 38 Hz

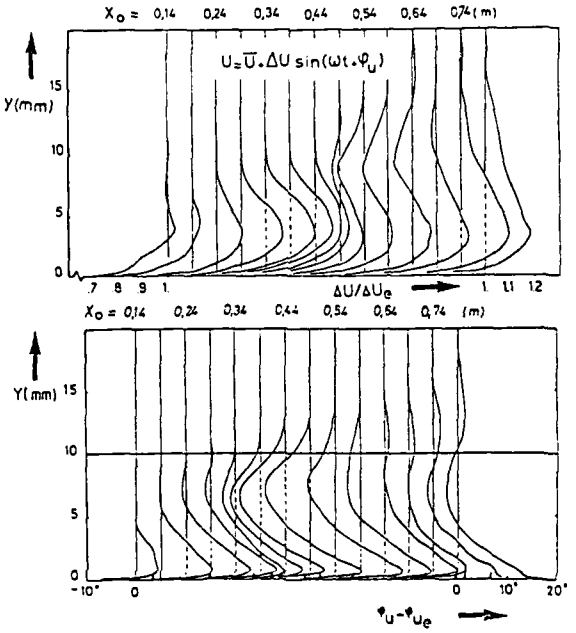

Fig. 5 - Profils d'amplitude réduite et de déphasage - F = 38 Hz

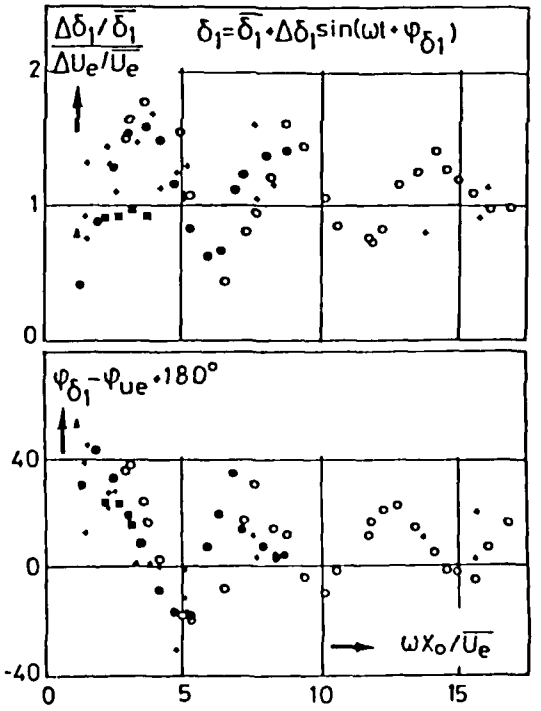

Fig. 6 - Analyse harmonique de l'épaisseur de déplacement
● F = 38 Hz ; o F = 62 Hz [7]
▲ F = 40 Hz ; ■ F = 43 Hz [8]
+ KARLSSON [9]

Frottement pariétal

L'évolution des profils de déphasage de la vitesse au voisinage de la paroi a déjà permis de soulever le problème de la validité de la loi universelle de paroi en écoulements isntationnaires. Pour préciser ce point, la figure 8 compare l'évolution de l'amplitude et de la phase du frottement mesurée par une sonde à élément chaud à celle déduite de la loi de paroi en supposant qu'à chaque instant, la relation valable en stationnaire reste inchangée :

$$\langle U^+ \rangle = 1/\chi \; Ln \langle y^+ \rangle + c$$

avec $\langle U^+ \rangle = \langle U \rangle / \langle U_\tau \rangle$; $\langle y^+ \rangle = y(\langle U_\tau \rangle / \nu)$; $U_\tau = \sqrt{\langle \tau_p \rangle / \rho}$

$\chi = 0,41$; $c = 5,25$

Pour l'étude à 38 Hz, les valeurs ainsi obtenues s'accordent assez bien avec celles mesurées, particulièrement en ce qui concerne l'angl de phase. Ceci correspond à des valeurs de $\omega X/\overline{Ue}$ inférieures à 7 et des valeurs de l_s^+ supérieures à 22. Pour le cas F = 62 Hz, $l_s^+ \approx 14$ et $\omega X/\overline{Ue}$ supérieur à 5, la phase du frottement déduite de la loi de paroi reste très faible alors que la mesure directe indique une avance pouvant dépasser 40° par rapport à la vitesse extérieure. Ces résultats doivent être rapprochés de ceux de BINDER-KUENY [6] obtenus dans l'eau pour des valeurs de l_s^+ plus faibles ainsi que de ceux de MENENDEZ-RAMAPRIAN [10]. L'ensemble des résultats expérimentaux s'accorde pour remettre en cause la validité de la loi universelle de paroi lorsque l_s^+ devient inférieure à une valeur comprise entre 15 et 20.

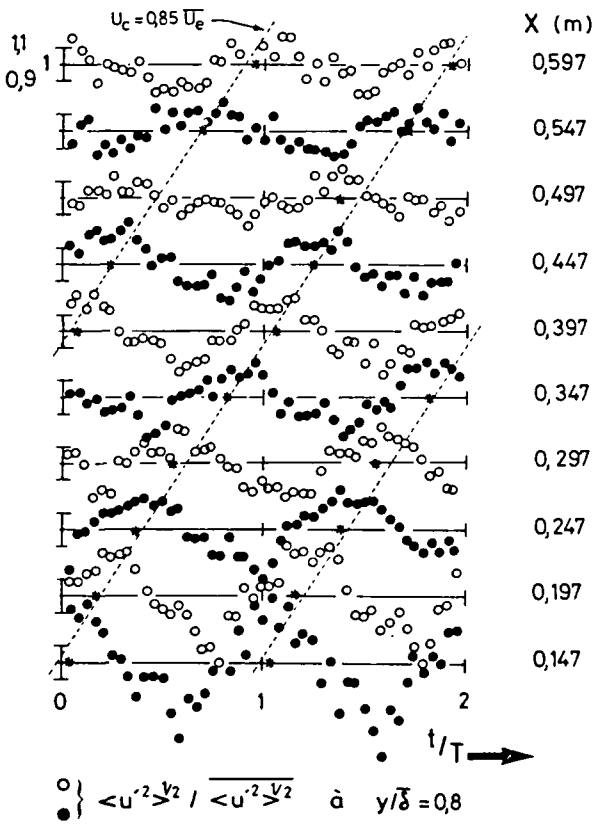

Fig. 7 - Evolution suivant X de l'intensité de turbulence à y/δ constant de l'ordre de 0,8 - F = 62 Hz

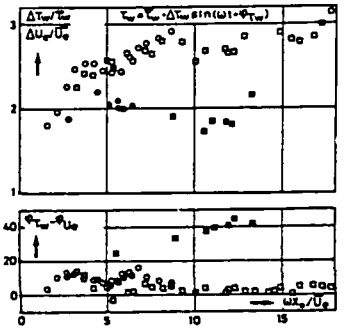

Fig. 8 - Analyse harmonique du frottement pariétal
o □ Déduit de la loi de paroi - F = 38 et 62 Hz
● ■ Mesure par jauge à élément chaud

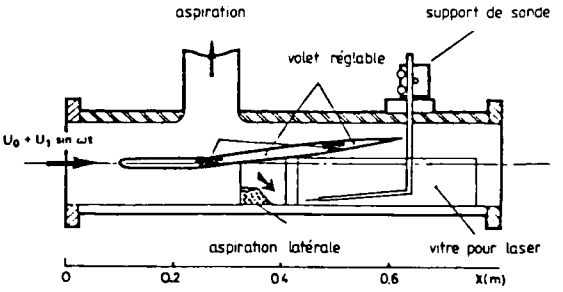

Fig. 9 - Couche limite pulsée avec gradient de pression moyen positif - Montage expérimental

2.4. Couche limite avec gradient de pression moyen positif

Montage expérimental et conditions d'essais

Cette étude avec gradient de pression moyen a été réalisée dans la même soufflerie et en utilisant la même technique d'analyse des résultats que pour celle de la plaque plane. Le gradient de pression positif est simplement créé par un corps profilé et la couche limite est mesurée sur le plancher de la veine (figure 9).

La figure 10 présente l'analyse harmonique de la vitesse extérieure suivant X. L'amplitude relative de fluctuation de Ue décroit de 20 à 8 % entre l'entrée et la

sortie de la veine alors que la phase varie de moins de 20 degrés.

Résultats expérimentaux

La figure 11 donne l'évolution suivant x de la valeur moyenne ainsi que celle de l'amplitude et du déphasage de l'épaisseur de déplacement. On retrouve la quasi périodicité suivant x de l'amplitude et de la phase de δ1 déjà observée dans le cas de la plaque plane. Cependant, au lieu d'un faible amortissement, on observe une augmentation importante de l'amplitude. La valeur de la quasi-période est ici voisine de 4, au lieu de 5 pour le cas sans gradient.

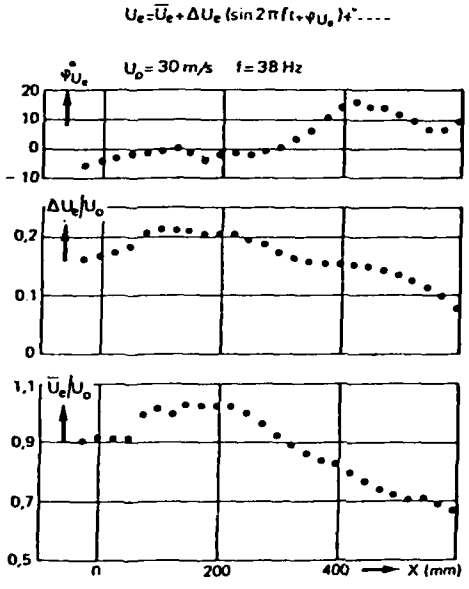

Fig. 10 - Couche limite pulsée avec gradient de pression moyen positif - Vitesse extérieure

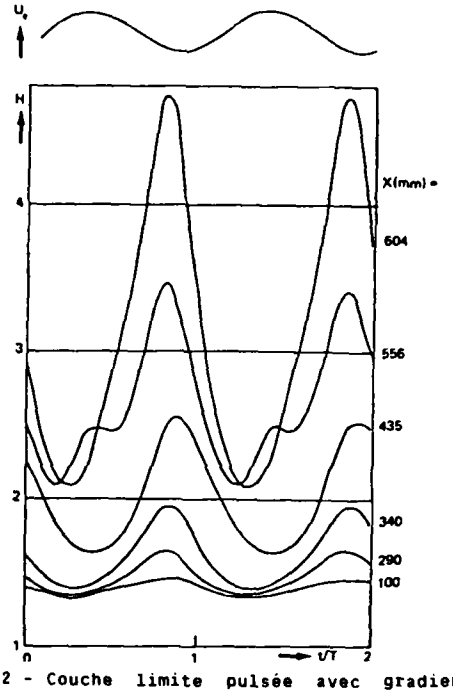

Fig. 12 - Couche limite pulsée avec gradient de pression moyen positif. Evolution du paramètre de forme en fonction du temps à différentes positions

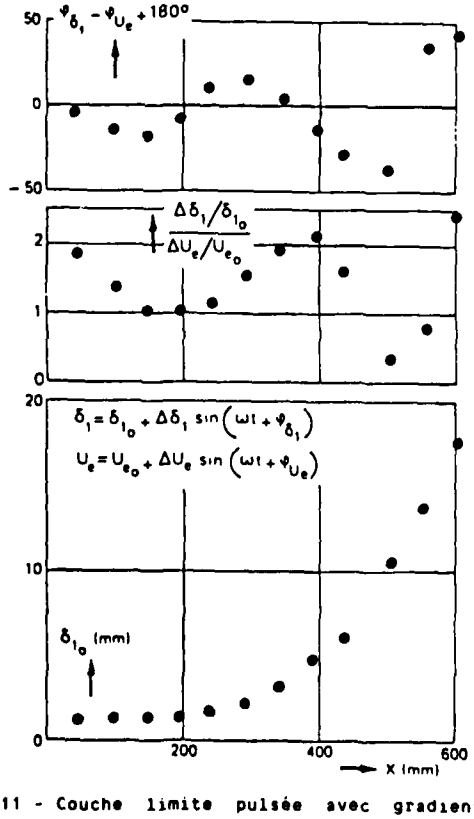

Fig. 11 - Couche limite pulsée avec gradient de pression moyen positif - Analyse harmonique de l'épaisseur de déplacement

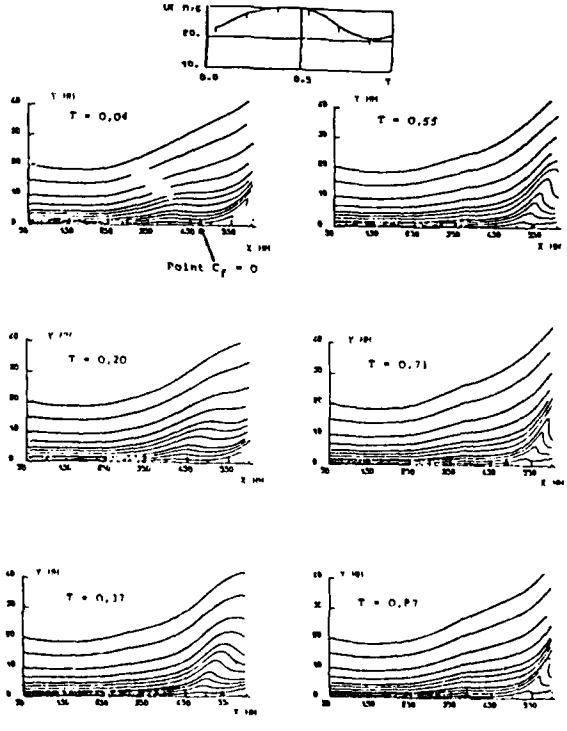

Fig. 13 - Couche limite pulsée avec gradient de pression moyen positif. Lignes d'émission à différents instants dans la période

Pour caractériser l'évolution des profils de couche limite en fonction du temps, considérons le paramètre de forme tracé pour deux périodes à différentes positions de sondage (figure 12). Jusqu'à X = 200 mm, en l'absence de gradient de pression moyen, son amplitude de fluctuation reste faible. Elle augmente dans la région avec gradient moyen pour devenir particulièrement importante quand des écoulements de retour prennent naissance. A la dernière station mesurée, H varie de 2,1 à presque 5, ce qui signifie qu'à certains instants, aucune vitesse négative n'existe. La position la plus avancée du point de frottement nul, correspondant à H ≈ 2,6, est égale à X = 435 mm. On note également l'apparition d'harmoniques en X = 556 mm. Ces harmoniques sont en fait plus marquées sur l'évolution de l'épaisseur de déplacement.

Pour interpréter les phénomènes rencontrés, les lignes d'émission de l'écoulement moyen (au sens de moyenne d'ensemble) ont été calculées. Pour cela, la composante verticale de la vitesse $\langle V(x,y,t)\rangle$ est déduite des valeurs expérimentales de $\langle U(x,y,t)\rangle$ par l'intermédiaire de l'équation de continuité. La figure 13 représente les images ainsi obtenues à six instants dans la période. La présence d'une région décollée déforme considérablement les lignes d'émission qui, partant d'une simple ondulation, tendent à former une structure de type tourbillonnaire.

3 - METHODES DE CALCUL

3.1. Méthode locale - Fermeture par équations de transport

Différents modèles de turbulence ont été utilisés pour intégrer les équations de couches limites instationnaires. Le plus intéressant utilise trois équations de transport pour k, ε et $\langle u'v'\rangle$. Il est déduit du modèle proposé par LAUNDER-REECE-RODI [11]

$$\frac{D}{Dt} k = - \langle u'v'\rangle \frac{\partial U}{\partial y} - \varepsilon + \frac{\partial}{\partial y} \left(\frac{\nu_t}{\sigma_k} \frac{\partial k}{\partial y}\right)$$

$$\frac{D}{Dt} \varepsilon = \frac{\varepsilon}{k} \left(- C_{\varepsilon_1} \langle u'v'\rangle \frac{\partial U}{\partial y} - C_{\varepsilon_2} \varepsilon\right) + \frac{\partial}{\partial y} \left(\frac{\nu_t}{\sigma_\varepsilon} \frac{\partial \varepsilon}{\partial y}\right)$$

$$\frac{D}{D} \langle u'v'\rangle = - C_{\tau_1} k \frac{\partial U}{\partial y} - C_{\tau_2} \frac{\varepsilon}{k} \langle u'v'\rangle + \frac{\partial}{\partial y} \left(\frac{\nu_t}{\sigma_\tau} \frac{\partial}{\partial y} \langle u'v'\rangle\right)$$

avec la relation $\nu_t = C\mu \frac{k^2}{\varepsilon}$

et les valeurs des constantes : $C_{\varepsilon_1} = 1,57$; $C_{\varepsilon_2} = 2$; $C_{\tau_1} = 0,137$; $C_{\tau_2} = 1,5$;

$\sigma_k = 1$; $\sigma_\varepsilon = 1,3$; $\sigma_\tau = 0,9$; $C\mu = 0,09$

Dans le modèle à deux équations de transport pour k et ε, l'équation pour $\langle u'v'\rangle$ est simplement remplacée par l'expression :

$$- \langle u'v'\rangle = \nu_t \frac{\partial U}{\partial y}$$

Près de la paroi, les équations ci-dessus, valables pour des régions pleinement turbulentes, sont remplacées par une formulation de longueur de mélange avec une fonction correctrice de sous-couche :

$$- \langle u'v'\rangle = F^2 l^2 \left(\frac{\partial U}{\partial y}\right)^2$$

$$\frac{l}{\delta} = 0,085 \tanh \left(\frac{\chi}{0,085} \frac{y}{\delta}\right)$$

$$F = 1 - e^{- \frac{1}{26\chi\mu} \sqrt{\tau\rho}} \qquad \chi = 0,41$$

Le raccord entre les deux schémas s'effectue à des valeurs de y^+ imposées, comprises entre 30 et 60, en assurant la continuité de $\langle u'v'\rangle$ et en posant :

$$k_r / - \langle u'v'\rangle_r = 2 a_1 \qquad a_1 = 0,15$$

3.2. Méthode intégrale

Cette méthode repose sur l'intégration des équations intégrales de continuité et de quantité de mouvement :

$$\frac{1}{Ue} \frac{\partial}{\partial x} (Ue (\delta - \delta 1)) = \frac{\partial \delta}{\partial x} - \frac{Ve}{Ue}$$

$$\frac{C_f}{2} = \frac{\partial \theta}{\partial x} + \theta \left(\frac{H + 2}{Ue}\right) \frac{\partial Ue}{\partial x} + \frac{1}{Ue^2} \frac{\partial}{\partial t} (Ue\, \delta 1)$$

Les relations de fermeture se déduisent de l'analyse de solutions semblables. Il a été montré que, pour un nombre de Reynolds infiniment grand, la famille des profils de vitesse obtenue n'était pas globalement modifiée par les effets instationnaires. Simplement, au coefficient de gradient de vitesse stationnaire $\beta x = (-\delta/U_\tau)\,(\partial Ue/\partial x)$, il faut ajouter un terme dû aux effets instationnaires : $\beta t = (-\delta/U_\tau\ Ue)\,(\partial Ue/\partial t)$ [12]. Comme au niveau des relations de fermeture, c'est le paramètre intégral de CLAUSER, G, qui est utilisé et non pas directement les paramètres de gradient de vitesse, les relations stationnaires s'appliquent aux valeurs instantanées. On a donc :

$$G = \frac{H - 1}{H\gamma} \qquad \text{avec} \qquad \gamma = \sqrt{\frac{C_f}{2}}$$

$$\frac{\delta_1}{\delta} = \gamma\, F_1(G) \quad ; \quad F_1 = 0{,}613\ G - \frac{1}{G}\left(3{,}6 + 76{,}86\left(\frac{1}{G} - 0{,}154\right)^2\right)$$

$$\frac{1}{\gamma} = \frac{1}{X}\,\mathrm{Ln}\,\frac{Ue\ \delta_1}{\nu} + D^*(G) \quad ; \quad D^* = 2G - 4{,}25\sqrt{G} + 2{,}12$$

$$C_E = \frac{\partial \delta}{\partial x} - \frac{Ve}{Ue} = \gamma\, P(G) - \frac{1}{Ue}\frac{\partial \delta}{\partial t} \quad ; \quad P = 0{,}074\ G - \frac{1{,}0957}{G}$$

Dans le coefficient d'entrainement, apparait un terme supplémentaire faisant intervenir la dérivée en temps de l'épaisseur de couche limite. D'autre part, la loi de frottement repose sur l'existence d'une loi universelle de paroi pour le profil de vitesse. Il faut donc limiter l'utilisation de cette méthode à des valeurs pas trop grandes du paramètre de fréquence réduite pour lesquelles la loi de paroi reste valable.

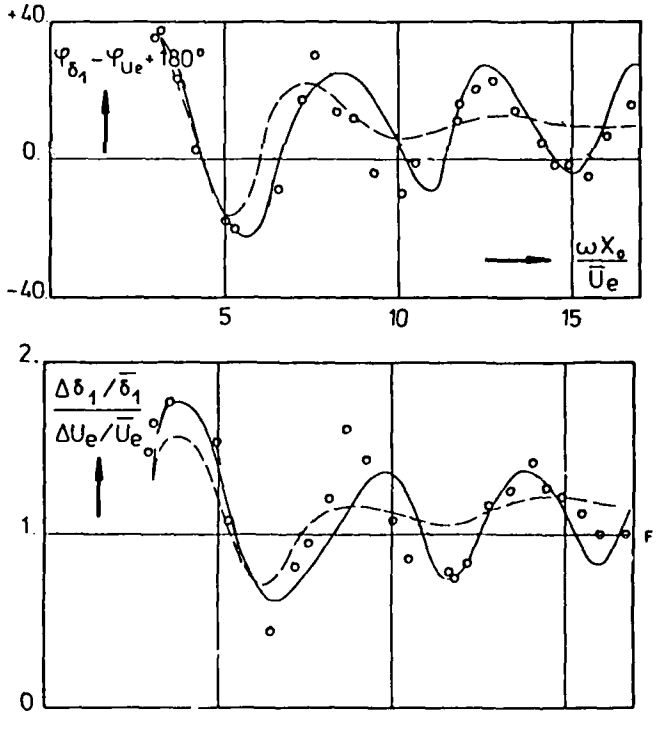

Fig. 14 - Couche limite de plaque plane - F = 62 Hz
——— Modèle à 3 équations de transport
----- Méthode intégrale

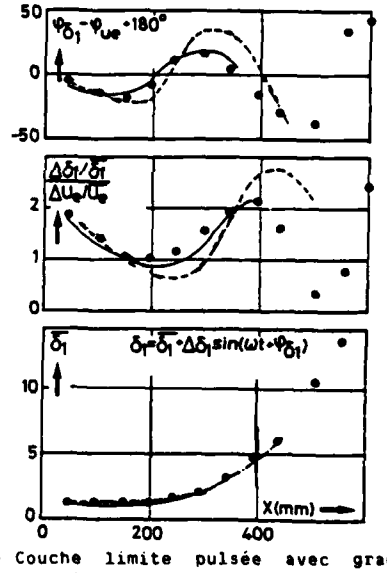

Fig. 15 - Couche limite pulsée avec gradient de pression moyen positif - Epaisseur de déplacement - ---- Méthode intégrale - ——— Modèle k-ε-⟨u'v'⟩

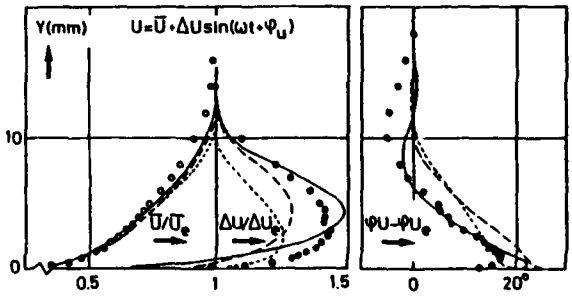

Fig. 16 - Couche limite pulsée avec gradient de pression moyen positif - Analyse harmonique de la vitesse - X = 0,39 m -
----- Longueur de mélange ;
_ _ _ Modèle k-ε ; ——— Modèle k-ε-⟨u'v'⟩

3.3. Comparaison aux cas expérimentaux

La figure 14 montre les résultats obtenus concernant l'analyse harmonique de l'épaisseur de déplacement pour le cas de la plaque plane. Pour des fréquences réduites inférieures à 5 environ, la méthode intégrale donne des résultats satisfaisants. Pour des valeurs supérieures, elle prévoit mal l'évolution quasi-périodique en X de l'amplitude et de la phase de $\delta 1$, contrairement au modèle à trois équations de transport.

Des conclusions analogues sont obtenues pour le cas avec gradient de pression moyen positif (figure 15). Pour cette configuration, des profils d'amplitude de la vitesse présentant un très fort dépassement par rapport à celle de la vitesse extérieure, allant jusqu'à 60 %, ont été obtenus. Seul le modèle à trois équations de transport pour k, ε, $\langle u'v' \rangle$ prévoit un tel phénomène (Fig. 16). En particulier, un modèle à deux équations de transport pour k et ε ne donne pas une amélioration sensible, comparé à un modèle de longueur de mélange [5].

4 - SINGULARITE LIEE AU DECOLLEMENT

Les équations de couche limite bidimensionnelle stationnaire présentent, au point de décollement, une singularité due essentiellement au fait que l'intégration des équations s'effectue avec une distribution de vitesse extérieure imposée. Ceci a été montré aussi bien par des études asymptotiques en triple couche que numériques [13]. Il est maintenant bien établi que la singularité de GOLDSTEIN peut être éliminée par un couplage entre le fluide parfait et la couche limite [14].

En écoulement instationnaire, l'analyse des éventuelles singularités est plus délicate et a été appréhendée le plus souvent numériquement ([2], [15], [16], [17], [18]). Une étude relativement simple de ce problème est cependant possible en considérant les équations intégrales de couche limite [19]. En stationnaire, elles permettent de retrouver la plupart des propriétés liées au décollement et se sont aussi révélées fort intéressantes pour l'étude du décollement tridimensionnel [20].

4.1. Discussion des équations intégrales

Les équations de base sont celles déjà présentées au paragraphe 3.2.. Elles sont ici réécrites en faisant apparaître le paramètre H^* défini à partir des épaisseurs de déplacement et de quantité de mouvement, ainsi que de δ, par : $H^* = (\delta - \delta 1)/\theta$. Ce paramètre est supposé uniquement fonction de H. Cette approximation est bien vérifiée en turbulent lorsque l'on s'approche du décollement [19]. En notant $H^{*\prime}$ la dérivée de H^* par rapport à H, les équations intégrales de continuité et de quantité de mouvement deviennent :

$$H^{*\prime} \frac{\partial \delta 1}{\partial x} + \frac{1 + H^{*\prime}}{Ue} \frac{\partial \delta 1}{\partial t} + (H^* - HH^{*\prime}) \frac{\partial \theta}{\partial x} + \frac{H^* - HH^{*\prime}}{Ue} \frac{\partial \theta}{\partial t} = A$$

$$\frac{1}{Ue} \frac{\partial \delta 1}{\partial t} + \frac{\partial \theta}{\partial x} = B$$

avec $$A = C_{ES} - \frac{\delta - \delta 1}{U} \frac{\partial Ue}{\partial x}$$

$$B = \frac{C_f}{2} - \theta \frac{H + 2}{Ue} \frac{\partial Ue}{\partial x} - \frac{\delta 1}{Ue^2} \frac{\partial Ue}{\partial t}$$

La nature de ce système aux dérivées partielles du premier ordre pour $\delta 1$ et θ s'étudie à l'aide de son équation aux directions caractéristiques qui s'écrit, pour la direction réduite $\lambda = dx/Uedt$:

$$\lambda^2 (H^* - HH^{*\prime}) + \lambda (1 - H^* + H^{*\prime}(1 + H) - H^{*\prime} = 0$$

En représentant H^* en fonction de H par la relation :

$$H^* = \frac{\beta H^2 + H}{H - 1} \quad \text{avec } \beta = 0,631$$

les deux racines sont données par :

$$\lambda 1 = \frac{1 + C}{H} \quad ; \quad \lambda 2 = \frac{1 - C}{H} \quad \text{avec} \quad C = (H - 1) \sqrt{\frac{\beta}{1 + \beta}}$$

Ces deux racines étant réelles et distinctes, le système est hyperbolique. L'une des directions caractéristiques reste toujours positive alors que l'autre, positive pour H inférieur à H_c, devient négative pour H supérieur à H_c, en s'annulant pour $H = H_c$. La valeur de H_c est voisine de 2,6. Compte tenu des relations de fermeture reliant le coefficient de frottement aux autres paramètres de la couche limite, une valeur du paramètre de forme voisine de 2,6 correspond pratiquement à une valeur nulle de C_f et donc à l'apparition de vitesses négatives à la paroi. On peut donc conclure qu'en instationnaire, le point de frottement nul n'est pas, en général, singulier, mais est lié à un changement de pente de l'une des directions caractéristiques. Ceci traduit une influence de l'aval sur l'amont et entraîne une modification des conditions aux limites

à imposer. Une conséquence importante est aussi que les schémas de discrétisation numérique doivent être adaptés pour respecter les règles de dépendance et d'influence.

4.2. Application à un cas théorique

L'exemple d'application présenté a été proposé par NASH-PATEL [21]. A l'instant initial, des conditions de plaque plane stationnaire sont imposées. La vitesse extérieure évolue ensuite comme indiqué sur la figure 17. Les équations globales, avec les relations de fermeture du paragraphe 3.2., s'intègrent par une méthode de différence finie en progressant en fonction du temps. Le schéma de discrétisation des dérivées en x est décentré amont ou centré suivant le signe de la seconde ligne caractéristique, afin de respecter les domaines de dépendance physique. En sortie du domaine en x, les pentes des deux lignes caractéristiques étant toujours positives, aucune condition aux limites n'est à imposer sur cette frontière.

Les deux familles des lignes caractéristiques calculées sont repréentées sur la figure 18. Les points de frottement nul correspondent à une tangente verticale pour les lignes λ2. Ils apparaissent à partir de t = 0,025 s sans qu'existe de singularité. Celle-ci se produit plus tard lorsque les lignes λ2 focalisent. Ceci se traduit sur l'évolution des épaisseurs intégrales de la couche limite par une variation de plus en plus brutale allant jusqu'à une quasi discontinuité, comme le montre la figure 19 pour l'épaisseur de déplacement.

Sur la figure 18 est aussi représentée la position du point Cf = 0 ainsi que celle de la singularité déterminée par NASH-PATEL comme un épaississement rapide de la couche limite et une région de fort gradient. L'accord entre les résultats obtenus par ces auteurs et la méthode intégrale présentée est bon, mais cet accord ne résulte que de l'utilisation de schémas numériques analogues et, en fait, nous allons montrer que ces résultats ne sont pas corrects.

Le système d'équations à intégrer étant hyperbolique, un schéma de discrétisation de type "prédicteur correcteur" (schéma de MacCORMACK), mieux adapté pour traiter ce problème, a été aussi utilisé. Les lignes caractéristiques correspondantes sont présentées sur la figure 20. Jusqu'à t = 0,035 s, instant où une singularité apparait, les résultats sont tout à fait analogues à ceux déjà obtenus. En revanche, la pente de la ligne singulière est très différente. Un calcul par une méthode de caractéristiques a confirmé les résultats obtenus par le schéma de MacCORMACK (figure 20). De plus, il est possible de montrer que le système des équations globales peut posséder une solution faible (ligne de discontinuité), ce qui confirme l'existence d'une singularité.

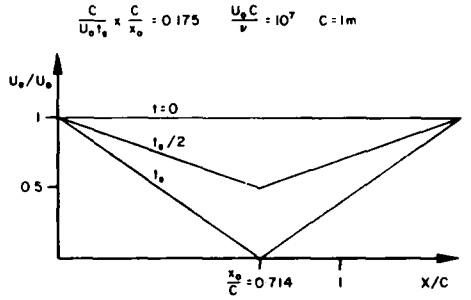

Fig. 17 - Singularité et décollement - Cas théorique de NASH-PATEL [21] - Evolution de la vitesse extérieure

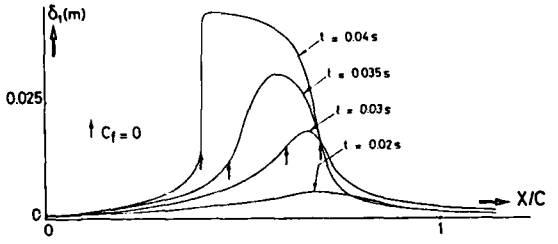

Fig. 19 - Singularité et décollement - Epaisseur de déplacement à différents instants - Schéma numérique de la figure 18

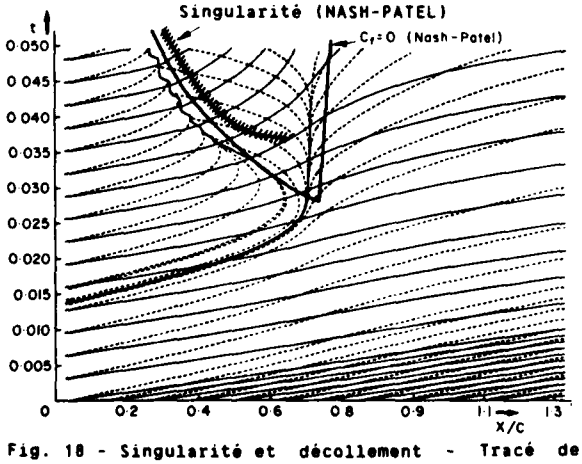

Fig. 18 - Singularité et décollement - Tracé des lignes caractéristiques —— λ1 ; --- λ2 - Schéma numérique décentré aval pour λ2 > 0, centré pour λ2 < 0

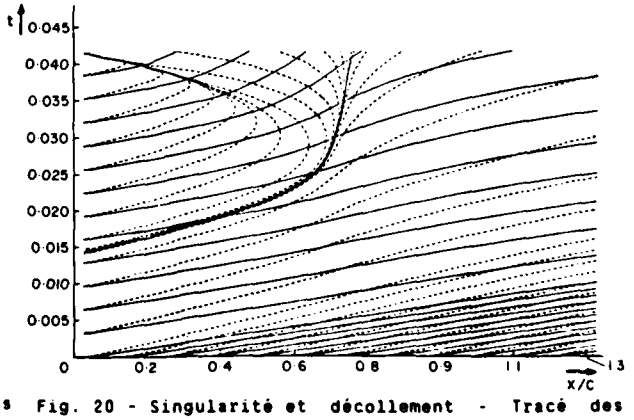

Fig. 20 - Singularité et décollement - Tracé des lignes caractéristiques —— λ1 ; --- λ2 - Schéma numérique de MacCORMACK

La cohérence des résultats obtenus, aussi bien analytiquement que numériquement, permet de conclure que le point de frottement nul n'est pas, en général, un point singulier en couche limite instationnaire. La singularité apparait à cause de l'existence d'une solution faible pour les équations de couche limite et se traduit par des variations très rapides des épaisseurs intégrales. Comme en stationnaire, la singularité provient de l'absence de couplage entre le fluide parfait et la couche limite.

4.3. Calcul en mode inverse

La présence d'une singularité lorsque l'on intègre les équations de couche limite en mode direct est essentiellement liée à la technique de résolution adoptée et un traitement approprié permet d'utiliser ces équations même dans des régions avec des vitesses négatives. Pour illustrer ceci, la figure 21 présente un calcul du cas avec gradient de pression moyen positif (paragraphe 2.4.) en mode inverse. Avec cette méthode, la donnée du problème est la distribution en fonction de x et t de l'épaisseur de déplacement. L'intégration des équations de couche limite permet de calculer la distribution de la vitesse extérieure ainsi que les autres paramètres de la couche limite. Non seulement aucune singularité n'existe pour ce mode de résolution, ce qui peut être montré analytiquement, mais, de plus, les résultats obtenus sont en bon accord avec ceux de l'expérience malgré la très grande amplitude de variation du paramètre de forme H, mesuré à X = 600 mm.

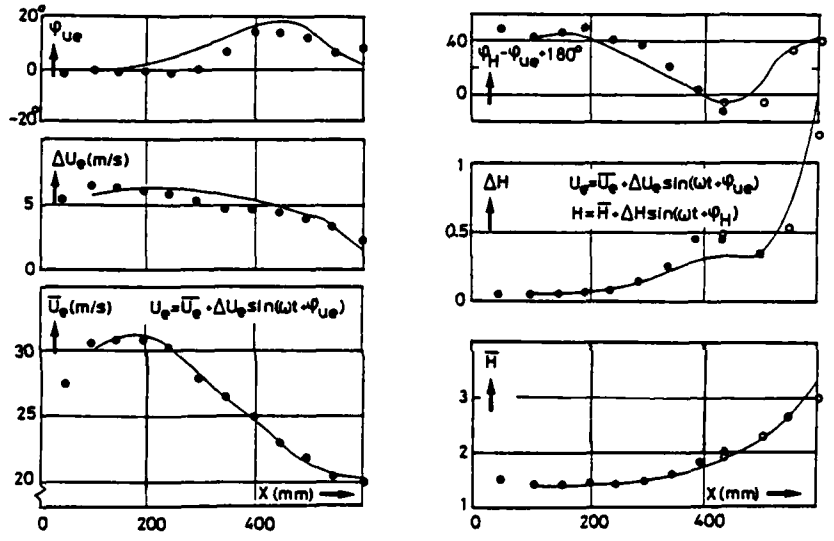

Fig. 21 - Couche limite pulsée avec gradient de pression moyen positif - Calcul en mode inverse - —— équations intégrales • expérience fil chaud
o expérience laser

5 - CONCLUSION

L'ensemble des résultats expérimentaux obtenus aussi bien pour une couche limite de plaque plane qu'en présence d'un gradient de pression moyen positif permet de dégager quelques idées essentielles.

L'écoulement moyen n'est pas affecté par les fluctuations forcées de l'écoulement extérieur, même pour des amplitudes assez fortes.

Les profils instantanés sont bien représentés par des profils stationnaires, sauf dans la région de paroi pour de faibles valeurs de l_s^+ où des effets instationnaires marqués existent.

En fonction du paramètre de fréquence réduite $\omega X/\overline{U}e$, la couche limite répond de façon quasi périodique avec un faible amortissement dans le cas de la plaque plane et une augmentation de l'amplitude en présence d'un gradient de pression positif. Dans ce cas, les effets instationnaires sont plus importants.

Le paramètre l_s^+ régit le comportement au voisinage de la paroi. Pour des valeurs faibles de l_s^+, de l'ordre de 5, les effets instationnaires restent confinés dans la sous-couche et la loi logarithmique de paroi ne permet plus de déterminer le coefficient de frottement.

Les méthodes intégrales de calcul des couches limites, qui utilisent une loi de frottement directement déduite de la loi de paroi, ne peuvent donner de bons résultats pour des valeurs faibles de l_s^+.

La réponse quasi périodique de la couche limite en fonction de $\omega X/\overline{U}e$ s'explique en partie par une interaction entre la convection de la turbulence dans la région extérieure et la pulsation forcée de l'écoulement.

Les méthodes de calcul utilisant trois équations de transport pour k, ε et <u'v'> prévoient assez bien le comportement de la couche limite instationnaire, même s'il subsiste des difficultés pour calculer le frottement de paroi.

REFERENCES

[1] L.W. CARR "A review of unsteady turbulent boundary layer experiments" - Unsteady Turbulent Shear Flows - Springer Verlag (1981)

[2] L.L. Van DOMMELEN, S.F. SHEN "The spontaneous generation of the singularity in a separating laminar boundary layer" - Journal of Computational Physics, 38, pp. 125-140 (1980)

[3] N.W. RUBESIN " A hot wire surface gage for skin friction and separation detection measurements" - NASA TM X 62 465 (1975)

[4] R. HOUDEVILLE, J.C. JUILLEN, J. COUSTEIX "Mesure du frottement pariétal par jauges à élément chaud" - La Recherche Aérospatiale 1984-1, pp. 67-79

[5] J. JAVELLE "Réponse d'une couche limite limite turbulente à une pulsation de l'écoulement général. Influence de la fréquence réduite" - Thèse ENSAE (1982)

[6] G. BINDER, J.L. KUENY "Measurements of the periodic velocity oscillations near the wall in unsteady turbulent boundary layers" - Unsteady Turbulent Shear Flows - Springer Verlag (1981)

[7] J. COUSTEIX, R. HOUDEVILLE, J. JAVELLE "Response of a turbulent boundary layer to a pulsation of the external flow with and without adverse pressure gradient" - Unsteady Turbulent Shear Flows - Springer Verlag (1981)

[8] J. COUSTEIX, A. DESOPPER, R. HOUDEVILLE "Structure and development of a turbulent boundary layer in an oscillating external flow" - Turbulent Shear Flows I - Springer Verlag (1977)

[9] S.K.F. KARLSSON "An unsteady turbulent boundary layer" - Journal of Fluid Mech., Vol. 5, pp. 536-622 (1959)

[10] A.N. MENENDEZ, B.R. RAMAPRIAN "Study of unsteady turbulent boundary layers" - IOWA Institute of Hydraulic Research - Report 270 (1983)

[11] B.E. LAUNDER, G.J. REECE, W. RODI "Progress in the development of a Reynolds stress turbulence closure" - journal of Fluid Mech., Vol. 68, Part 3, pp. 537-566

[12] J. COUSTEIX, R. HOUDEVILLE "Turbulent boundary layer calculations in unsteady flow" Numerical Methods in Applied Fluid Dynamics - Academic Press (1978)

[13] K. STEWARTSON "Multi-structured boundary layers on flat plates and related bodies" - Advances in Applied Mechanics, Vol. 14, pp. 145-239 (1974)

[14] J.C. LE BALLEUR "Calculs couplés visqueux-non visqueux incluant décollement et ondes de choc en écoulement bidimensionnel" - VKI AGARD LS-94 (1978) - T.P. ONERA 1978-5

[15] D. CATHERALL, K.W. MANGLER "The integration of two-dimensional laminar boundary layer equations past the point of vanishing skin friction" - Journal of Fluid Mechanics, Vol. 26, Part 1 (1966)

[16] W.R. SEARS, D.P. TELIONIS "Boundary layer separation in unsteady flow" - SIAM J. Appl. MAth., Vol. 28, N° 1 (1975)

[17] D.P. TELIONIS "Unsteady viscous flows" - Springer Series in Computational Physics (1981)

[18] T. CEBECI, L.W. CARR, P. BRADSHAW "Prediction of unsteady turbulent boundary layers with flow reversal" - Turbulent Shear Flow II (1979)

[19] J. COUSTEIX, J.C. LE BALLEUR, R. HOUDEVILLE "Calcul des couches limites turbulentes instationnaires en mode direct ou inverse, écoulement de retour inclus. Analyse des singularités" - La Recherche Aérospatiale 1980-3, pp. 147-157

[20] J. COUSTEIX, R. HOUDEVILLE "Singularities in three-dimensional turbulent boundary layer calculations and separation phenomena" - AIAA Journal, Vol. 19, N° 8, pp. 976-985

[21] J.F. NASH, V.C. PATEL "Calculation of unsteady turbulent boundary layers with flow reversal" NASA CR 2546 (1974)

[22] R.L. SIMPSON, J.H. STRICKLAND, P.W. BARR "Features of a separating turbulent boundary layer in the vicinity of separation" - JFM, Vol. 79, Part 3 (1977)

[23] R. HOUDEVILLE, J. COUSTEIX "Couches limites turbulentes en écoulement pulsé avec gradient de pression moyen défavorable" - La Recherche Aérospatiale N° 1979-1, pp. 33-48

REVIEW OF SMP 1984 SYMPOSIUM ON "TRANSONIC UNSTEADY AERODYNAMICS AND ITS AEROELASTIC APPLICATIONS"

Walter J. Mykytow
14 Old Stone Way (Unit 9)
Weymouth, Massachusetts 02189
U.S.A.

SUMMARY

The 59th meeting of the AGARD Structures and Materials Panel, was held on 3-7 September 1984, in Toulouse, France, It included a specialists' conference to discuss the latest methods of predicting transonic unsteady airloads for oscillating surfaces and flutter. Also considered were aeroelastic applications, many of which were made to standard configurations selected for the SMP cooperative program. This paper summarizes the 16 papers and the round table discussion in some detail for coordinations with AGARD's Fluid Dynamics Panel and Fluid Mechanics Panel.

INTRODUCTION

This specialists' meeting in Toulouse, France, in September 1984, could be considered the third of a series on transonic unsteady aerodynamics and aeroelastic applications.

The first AGARD SMP meeting was held in Lisbon, Portugal, in April 1977, and was entitled "Unsteady Airloads in Separated and Transonic Flow" (AGARD CP-226). Some of the subject matter concerned:

1. Reduced damping in bending during model tests of swept back wings.
2. Wing torsional buzz in flight and in model tests.
3. Reduction of flutter speeds due to leading edge vortex.
4. History of various aircraft flutter problems.
5. Wind tunnel wall porosity effects on flutter.
6. Unsteady pressure measurements on NLR-7301 airfoil.
7. Euler-viscous ramp calculations for NACA 64A-006 oscillating airfoil.
8. LTRAN applications to predict disappearing shocks, wall effects, coupled aero-structural response in pitch, and indicial aerodynamic parameters.
9. Euler calculations for pitching airfoil with boundary conditions on exact airfoil.
10. Garner's semiempirical method for computing transonic unsteady airloads.
11. Time-linearized relaxation methods for a rectangular wing.
12. Proper treatment of shock movements and jump conditions.
13. Numerical instabilities in the relaxation process.

The second AGARD SMP meeting was held in Aix-en-Provence, France, in September 1980, and was entitled "Boundary Layer Effects on Unsteady Airloads" (AGARD CP-296). Topics at this meeting included:

1. Demarcation of linear and nonlinear zones by a shock displacement criterion.
2. Application of TSP-viscous ramp method to NLR-7301 airfoil.
3. Levels of closure in unsteady turbulent flow. Transport equations and the inverse method
4. Unsteady Kutta condition, boundary layer displacement effects, gap flow for controls, and vortex effects.
5. Deduction of boundary layer effects versus frequency by comparison of experimental data and inviscid calculations. Weak coupling viscous effects for oscillating flap. Reversed shock movement in separated flow as flap angle increased. Aerodynamic resonance for NLR-7301 airfoil.
6. Application of the strong coupling method and TSP to oscillating flap in non-separated flow.
7. Application of Garner's semiempirical method to flutter model test data with success.
8. Application of Navier-Stokes method to airfoil with changing incidence at subsonic speeds.
9. Test data for airfoils with separated flow and Reynolds number effects. Anomalous behavior of unsteady airloads with frequency for separated flow.
10. The poor state of art for predicting unsteady airloads for control surfaces.
11. Flow instabilities over (nonmoving, rigid) thick, biconvex airfoils. Self-induced flow oscillations.
12. Boundary layers and cyclic pressure variations at subsonic speeds in a low speed tunnel.

The transonic region is the most critical one for aircraft static and dynamic aeroelastic problems. Reliable methods to predict unsteady transonic airloads had been lacking. However in 1977 it appeared practical to numerically simulate transonic unsteady physical phenomena for industrial applications. The AGARD Structures and Materials Panel therefore initiated a Working Group and a cooperative program. Standard configurations were selected for calculations and comparisons of computed transonic unsteady airloads. Seven conditions were selected for airfoils and five for 3-D wings (AGARD AR-156; AGARD AR-167; AGARD R-673; and AGARD R-702). Separated flow cases were not selected.

GENERAL COMMENTS ON SMP MEETING

The above background information then serves as a basis to judge the recent remarkable progress and the very noticeable success of AGARD SMP's cooperative program.

Sixteen papers were presented at this conference in Toulouse. Two of these concerned speed and memory capabilities of future computers. Milestones in unsteady CFD are mentioned together with limiting features and the possibilities for overcoming them. Dramatic time and cost reductions for future computations are forecast. With NASA's Numerical Aerodynamic Simulation Program, a 15-minute run before 1988 is quoted as possible for the application of the unsteady full potential method to a 3-D wing. Another optomistic hope, based on overcoming serious limitations, was that a reliable simulation of viscous transonic unsteady flow around a fighter might be possible in a decade.

Methods presented for predicting transonic unsteady airloads included time-linearized transonic perturbation, TSP, full potential and Euler methods for 2-D airfoils and 3-D wings. One report concerned applications of the 2-D Navier-Stokes method using an eddy-viscosity model based on simple steady flow experiments. Other modeling of viscous effects included matching of flow conditions by angle and Mach number changes, airfoil modifications, the viscous ramp, and weak or strong coupling of inner viscid flow and outer inviscid TSP flow. Several calculations were made for transonic separated flow on airfoils with some success. Two papers dealt with applications to supersonic flow fields.

One paper presented results of calculations for 2-D pitch-plunge flutter simulating the effects of a swept wing. The flutter calculations were made using TSP, linearized TSP, Euler, and corrected and uncorrected doublet lattice methods with noticeably different results. One other paper also presented 2-D flutter calculations. Five 3-D flutter calculations were also reported, several with rather good agreement with test data, indicating the initial transition of transonic unsteady aerodynamics from a research-scientific status towards industrial applications. One of the papers showed a second transonic flutter dip from model tests in separated flow. Inviscid 3-D methods were extended to highly swept wings of low aspect ratio.

Most of the calculated-test correlations are made for airfoils, but several applications were made to wings and control surfaces.

Some new test data were presented for airfoils in pitch or for flap rotation. More test data for plunge are now available. One paper presented data for an oscillating split-flap spoiler. Approximate calculations showed promise for rough prediction of subsonic unsteady spoiler loads.

Wall effect contamination of both quasisteady and low frequency test data was frequently mentioned. Also questioned several times were model surface conditions, low Reynolds number testing, and large model-wind tunnel dimensional ratios which caused interference. Reliable methods to predict wall effects are not available. Brief comments were made about the difficulty of such predictions and on tunnel resonances, unsteady wake effects, diffuser wall effects, corners, etc.

Higher nonlinear effects and larger, higher order harmonics were noticed in unsteady test data near oscillating strong shocks and separated flow. Their effects on flutter characteristics were not completely evaluated although previous investigations on airfoils under less severe conditions indicated that such higher order harmonics could be ignored in integrated airloads. Some evaluations of strongly nonlinear unsteady aerodynamic effects were deemed advisable to determine whether linear procedures in flutter analyses were still applicable.

Most numerical-test comparisons were made on the basis of unsteady pressure distributions. This data and other basic data are still required. More comparisons are needed on integrated sectional lift and moment coefficients, and are forthcoming from SMP's cooperative program. Comparisons of generalized aerodynamic forces used in typical flutter analyses were deemed highly desirable.

Information was presented for both conventional and supercritical airfoils. A few comments questioned the applicability of supercritical airfoils to fighter designs and to aircraft employing active controls and aeroelastic tailoring. High angle of attack information is needed for maneuvering fighters while aeroelastic deformations would be important boundary conditions for transports.

Two papers considered high angles. One treated ramping angular changes at constant rate. The other treated prediction of unsteady airloads for large pitch amplitudes.

The methods presented varied significantly in numerical complexity, computer time required, and cost. Some of the simpler methods could have runs of several minutes on modern computers. The more complex methods require hours per run.

Methods likely to be used in the future are difficult to predict. No doubt they will be the simpler and lower cost procedures which will develop in an evolutionary manner; but it was agreed that their acceptances must be validated and justified by comparisons with results from more complex methods and test data.

The selection of SMP standard flutter cases, preferably cases where reliable flutter model data existed, was recommended several times. The application to industrial type flutter problems would include calculation of generalized forces on the basis of given vibration modes and calculations of amplitude ratios and phases at the critical flutter point as well as dynamic pressure and flutter frequency.

There is an urgent need to develop low cost and quick turn around methods for preliminary design and first engineering stages to assure production of efficient aircraft with minimum weight and performance penalties from the start.

This meeting did describe the encouraging progress in predicting transonic unsteady aerodynamic effects such as shock location, movement, strength, and phase. Good qualitative agreement is achieved and trends compare quite reasonably with test data. In many cases, quantitative agreements between tests and calculations are good. Doublet lattice and kernel function methods neglect fundamental transonic effects and produce unconservative flutter speed predictions unless major modifications are made to key parameters. Other predicted data from these linear theories, such as flutter frequency, amplitude ratio and phase, are grossly incorrect frequently. Thus, the new transonic unsteady CFD methods will certainly be applied industrially in the near future.

PAPERS PRESENTED

A semidetailed summary of each paper has been prepared primarily for the appreciation of the new major contributions by the practicing flutter engineer. This summary is then followed by a description of the round table discussion, and finally by general conclusions and recommendations. Complete versions of the papers are given in AGARD SMP CP-374, "Transonic Unsteady Aerodynamics and Its Aeroelastic Applications."[1]

1. V. L. PETERSON: "Trends in Computational Capabilities for Fluid Dynamics"

Milestone developments in CFD, computer capability, cost trends, and future performance requirements were discussed for both inviscid and viscous steady and unsteady flows. The development for unsteady flows and for elastic surfaces has lagged since nonsteady calculations require larger computers and more time-consuming calculations. Real time must be simulated, the technology is more difficult, and fewer scientists are versed both in CFD and structural dynamics. Thus, the total level of effort is lower, and there is lesser availability of user-oriented codes.

The authors discussed progress versus time in levels of Navier-Stokes equation approximation. Linearized inviscid level I is mature for both steady and unsteady flows. Nonlinear inviscid level II has advanced, but aeroelastic applications are required. Reynolds-averaged Navier-Stokes level III is costly, and aeroelastic investigations are rare. Large eddy level IV and exact full Navier-Stokes level V are in the early research stages.

Milestones mentioned for inviscid unsteady transonic flow range from small perturbation methods for 2-D airfoils in 1975 to full potential unsteady methods for wings in 1981. Unsteady viscous flow applications were made to airfoil buffet, cavity aeroacoustics, turbulent flow plunge-pitch flutter, and aileron buzz from 1977-1979.

Relative computer costs have dropped markedly due to the rapid computer speed progress (millions of floating point operations per second) and the much lesser growth of rental costs (Figure 1-1). Furthermore, memory has grown 3 to 4 orders of magnitude in 20 years with 500 million words of memory expected about 1990. The improvement in relative costs is about two orders of magnitude in 15 years. With better algorithms, the compounded improvement in relative costs might be 1:100,000.

The authors mentioned that the operations per grid point are 50 times greater for unsteady calculations since 3 cycles of oscillation are generally used and since a factor of 15 is required to simulate time. The factor of 50 might be reduced to 5 with improved algorithms.

An advanced computational facility, NASA's Numerical Aerodynamic Simulation Program, has been proposed and would be available to the U.S. scientific and industrial aerospace community like wind tunnels. Estimates indicate about one minute of computer time would be needed to calculate unsteady viscous flows about 2-D airfoils. Figure 1-2 shows similar estimates for oscillating wings using 1984 algorithms. Simple wing-body combinations are a little more difficult.

The days to weeks of computer time for viscous calculations (Figure 1-2) suggest that near future unsteady aerodynamic and flutter calculations will be limited to nonviscous flows except for special cases or to simpler semiempirical approximations of the viscous effects.

NASA's experience has shown that computer time should be limited to 10 minutes per case if industry is expected to apply these methods in the design environment. Figure 1-3 shows memory-speed requirements for 15-minute computer runs. Unsteady calculations using the full potential method for wings should soon be possible, but unsteady, viscous, 3-D calculations by Reynolds-averaged forms will not be practical for some time to come.

Estimates were made for the time to compute a transonic flutter boundary using 5 Mach numbers, 4 reduced frequencies and 4 modes. An estimate of 37 hours was given using today's computers and inviscid methods. Very practical times of 1 to 2 hours might be achievable by 1988.

The authors emphasized the complementary aspects of combined computational and experimental investigations. Also emphasized was the capability of numerical investigations to provide salient data when experimental facilities were limited or lacking. The Jupiter probe studies were cited as an example.

2. H. TRIEBSTEIN AND R. VOSS: "Transonic Pressure Distributions on a Two-Dimensional NACA 0012 and Supercritical MBB-A3 Profile Oscillating in Heave and Pitch"

These experimental investigations concern effects of reduced frequency, Mach number, oscillation amplitude, angle of attack, separation, and Reynolds number. This paper deals mainly with results for the MBB-A3 airfoil. Results for the NACA 0012 airfoil were given at the September 1984 ICAS meeting.

All four walls of the wind tunnel are perforated. Solid disks were used at the sides of the model. The distance of the model was 1.7 chords from the upper (lower) wall. The design point is M = 0.765 at 1.5 degrees. No transition strips were used. A lambda shock results due to the laminar flow at lower wind tunnel Reynolds numbers.

Figure 2-1 shows the effects of Mach number for pitch oscillations. Typical subsonic trends result for M = 0.5. At M = 0.78, a strong shock peak occurs in the upper side pressure distribution. The real part changes sign due to separation near the trailing edge. The imaginary part changes sign at the shock. Heave oscillation tests show similar results but with imaginary part exchanged with real part relative to pitch. Leading edge (small bubble) flow separation is noticed for heave test data.

Unsteady real-part pressure peaks for pitch (M = 0.78; angle = 0.15 degrees) increase with increasing frequency. This trend is opposite to that expected from theory. The cause is suspected to be the influence of tunnel walls. For heave motions, elastic behavior of the model contaminated results for higher frequencies.

Larger pitch amplitudes decreased the height and increased the width of the unsteady pressure peaks near the shock. Higher harmonics are present near the shock due to the nonlinearity of shock movements and in separation areas. The higher harmonics disappear if the flow reattaches. Nonlinear effects are less evident with chordwise integrations of pressures.

Calculations were performed, for cases where flow was attached and shock strength moderate, by both the LTRAN 2 time integration method and the Geissler-Voss doublet-source, field panel, integral method for the time-linearized small perturbation equation.

The authors stress the need to first have a good prediction of the steady pressure distribution by varying both Mach number and angle to obtain good agreement on the shock position (or of the sonic line) and the supersonic plateau.

For the MBB-A3 airfoil in pitch at a subsonic Mach number of 0.7, agreement between unsteady test and theoretical data was good for the real part, but the zero crossing point for the imaginary part for theory was too far aft. The authors suspect wall interference effects rather than viscous effects.

For higher Mach numbers, the unsteady loading forward of the shock increases with increasing reduced frequency. Figure 2-2 shows results for the design condition at a higher reduced frequency. Notice the higher loading for test results forward of the shock. Wall interference effects may be responsible for this trend which is opposite to that from theory. The large shift towards positive imaginary peaks near the shock might be indicative of separation as shown by other tests and Navier-Stokes calculations. However, yet other data do not substantiate this. Thus, conclusions are not firm.

Results from the two theories differ in shock location and strength, and also in the Mach number and in the regional influence of the supersonic zone.

Agreement between theory and experiment for heave oscillations at design point conditions was not good due to wall effects, low heave loads, and model elasticity.

Pressure calculations for the MBB-A3 airfoil by the time-linearized field panel method for various frequencies at the design condition show chordwise waviness increasing with frequency due to the increasing wave number of the receding waves. Better damping of these upstream waves might result from the use of nonlinear codes and improved grid spacing. The integrated aerodynamic parameters shown in Figure 2-3 do not show these undulations. The values at higher reduced frequencies approach those of linear (flat-plate) theory.

Some Schlieren motion pictures were shown for the NACA 0012 airfoil in separated flow. For a nonmoving airfoil at 5 degrees and low Reynolds number, a lambda shock with separation occurs. A distinct low frequency flow oscillation is seen near the leading edge. Later

pictures show that the separation and lambda shock remain throughout the cycle of the oscillating airfoil. For 2 degrees, there is no lambda shock for the steady airfoil, but it appears at the higher angles when the model oscillates in pitch. The flow reattaches at lower angles. A phase lag of the shock relative to airfoil position is noticed.

This paper provided important new information and dramatically emphasized the effects of wind tunnel walls, separation and viscosity, and model elasticities. Future tests will include transition strips and different wall conditions.

3. W. J. CHYU AND S. S. DAVIS: "Numerical Studies of Unsteady Transonic Flow Over an Oscillating Airfoil"

Unsteady transonic pressures are computed using the 2-D Navier-Stokes equation and a time-varying grid for an oscillating airfoil. A two-layer, Cebici eddy-viscosity model, where mixing length scale is based on local vorticity, is used for turbulent flows.

Thin layer Navier-Stokes calculations are made for the NACA 64A010 airfoil at small incidences where weak shock-boundary layer interactions occur. The M = 0.8 calculations show reasonably good agreement with experimental instantaneous chordwise pressures for small pitch oscillations over the entire cycle. Negative pressures in front of the shock are overpredicted and wall effects are suspected. Nonlinear time histories of local pressures are well predicted by both thin layer and full Navier-Stokes codes, and almost as well by the Euler method. The chordwise shock location and its 7% motion are better predicted by the thin layer viscous code. Shock data for the full Navier-Stokes code were not shown. Viscous effects are small.

Figure 3-1 shows the first harmonic components of the pressure coefficients. Predictions are good except near the shock. Viscous calculations are better. Imaginary parts grow with increasing frequency and absolute values decrease with frequency in a consistent manner. This is in agreement with theory.

Calculations for pitch oscillations of the NACA 64A010 were also made about a higher mean angle (4 degrees) where strong shock-boundary layer interactions were present for most angles in the cycle. At the highest instantaneous angles (5 degrees) experimental data show slow pressure recovery aft of the shock and separation. As the instantaneous angle decreases to approximately 3 degrees and then up to 3.13 degrees, in an increasing manner, the aft pressure recovery is fast and the flow becomes attached.

While inviscid theory predicts the supersonic plateau reasonably well, the predicted shock is too far aft. Both full and thin layer Navier-Stokes methods show similar results and predict the chordwise instantaneous pressure distribution, shock location and shock (13% chord) travel reasonably well. Predicted suction levels in the plateau ahead of the shock are too high. The N. S. method predicted aft-pressure recoveries fairly well, but the transition angle between slow to fast recoveries (separated versus attached flow) is not well predicted. However, viscous calculations predicted an upstream (reversed) movement of the shock position with increasing angle as has been observed in experiments with separation.

Figure 3-2 shows the comparisons of the first harmonic components of the NACA 64A010 chordwise pressure distributions for a 4-degree mean angle. There are large and complex variations with frequency. The real (in-phase) peaks near the shock change sign with frequency. Real values near the trailing edge are high compared to the low angle, nonseparated flow case of Figure 3-1. Imaginary components also show high values near the trailing edge. Viscous calculations show that the complex trends are predicted qualitatively quite well even though quantitative agreement is not good near the peaks.

The blunt leading edge, 16.5% thick, supercritical NLR 7301 airfoil near the design condition (M = 0.75; angle = 0.37 degree) was the third case considered. Full Navier Stokes calculations were made for instantaneous chordwise pressures for airfoil pitch. Agreement was reasonably good between theory and experiment except near the compression. The test data showed a waviness ahead of the shock due to sensitivity of unsteady responses to the flow field. Figure 3-3 shows experimental and full Navier-Stokes calculations. The mean pressure shows a rapid compression but no shock, fast pressure recovery, and very little separation. The compression results in large real and imaginary first harmonic peaks. The imaginary component at low frequency is relatively large contrary to the result for the conventional airfoil at low angles. Overall, trends are qualitatively predicted. Phases along the chord between real and imaginary parts are reasonably well predicted. Tunnel walls, nonuniform free stream conditions, turbulence levels and airfoil shape tolerances are cited as possible reasons for differences. The tests and calculations show that the unsteady results for this blunt-thick supercritical airfoil are noticeably different than those for conventional airfoils and are sensitive to transonic flow conditions.

The authors conclude that thin layer and full Navier-Stokes methods gave similar results except near shocks and neither gave consistently better agreement. An improved turbulence model is required when viscous effects dominate.

4. R. G. DEN BOER AND R. HOUWINK: "Analysis of Transonic Aerodynamic Characteristics for a Supercritical Airfoil Oscillating in Heave, Pitch and with Oscillating Flap"

Unsteady pressure measurements were made covering a wide range of conditions for an oscillating, 12%-thick, supercritical airfoil. Test angles of attack were corrected for wall effects for the steady case. Wall effects were expected for unsteady tests, possibly giving a positive shift to lift phase angle and decreased lift at low frequency. Lesser effects should occur at higher frequencies.

Test data at the design point angle show increasing unsteady pressures at the trailing edge for the pitching airfoil and an unsteady boundary layer effect as Mach number increases.

Other tests for plunge or flap oscillations show pressure distributions as generally expected.

The effect of angle of attack on pitch oscillations is shown in Figure 4-1. Larger unsteady airloads result for the supercritical airfoil as design point conditions are approached (M = 0.75; angle = 0.75 degrees). Unsteady airload peaks become sharper near the strong shock for an angle of 1.5 degrees. Flow is attached. Finally, for 3.0 degrees, both the real and imaginary parts enlarge. High unsteady pressures are noticed near the trailing edge indicating large boundary layer variations. Flow is separated for the steady 3-degree case and for small changes about this position. The shock moves forward with increasing angle in the separated flow.

For 3 degrees, the peak unsteady pressure modulus increases with increasing frequency up to a reduced frequency of 0.25. (It decreases with increasing frequency for lower angles in unseparated flow.) The phase angle across the chord shows a completely different behavior. Pressures downstream of the shock and at the trailing edge also increase up to a reduced frequency of 0.25. The authors suggest an aerodynamic resonant phenomenon.

The following explanation was offered for one oscillation cycle. As the angle starts from 3 degrees, the flow is essentially attached; but with increasing instantaneous angle, the flow separates while the shock moves forward. The shock strength reaches a maximum three-eighths through the cycle, and the separation reaches a maximum half-way through the cycle when the perturbation angle (about 3 degrees) has reached zero. Negative perturbation angles (about 3 degrees) follow next. The shock moves back with decreasing angle and separation decreases. The cycle then repeats.

Figures 4-2 and 4-3 show the unsteady lifts and moments for this separated flow. These coefficients are much larger at M = 0.75 than for the attached flow. Other data show an influence of oscillation amplitude on real parts. Corresponding phase angles for attached and separated flow are different. All of the above differences have significant effects on flutter behavior.

The aerodynamic resonance at a reduced frequency of 0.25 is confirmed by a circle diagram plot of imaginary lift component versus real component at various frequencies. Power spectral analyses for lift fluctuations without airfoil motion show that an unsteady flow phenomanon is present. Minimum damping for this phenomenon occurs for angles where the shock motion reverses and when the reduced frequency is near 0.25. The aerodynamic resonance for separated flow has been noticed in NASA Ames data presented by Davis. Mabey has discussed flow instabilities over rigid, nonmoving, thick, biconvex airfoils at low angles.

Flutter model test results for a half-wing model show two transonic flutter speed dips. The lower speed dip occurs in attached flow with the flutter frequency close to the first (bending) mode as expected. The second dip, caused by the large changes in lift and moment, and the separated flow, occurs at a higher flutter frequency near the second (torsion) mode. The use of measured 2-D unsteady aerodynamic data, which include separation effects and information from 3-D steady tests in flutter analyses, predict the second torsional-buzz transonic dip.

Calculations were made using strong coupling between NLR's LTRAN 2 small perturbation method and Green's lag entrainment method for unsteady supercritical airfoil lift and moment data. These results agreed with test data much better than results from inviscid and weak coupling interaction methods as shown in Figure 4-4. Strong interaction viscous theory correctly produces a decrease in lift coefficient. Although viscous effects are too weak, the reversed sign of the lift phase angle is predicted as well as a point on the trend for the moment coefficient and its phase. Nonzero unsteady pressures at the trailing edge and the reversed shock motion shown in the tests were also predicted.

5. J. W. EDWARDS, S. R. BLAND, AND D. A. SEIDEL: "Experience with Transonic Unsteady Calculations"

The possibility of nonunique solutions for strong shock conditions was briefly discussed for several reduced frequencies.

The calculations presented are for inviscid flows although NLR viscous results were given for some comparisons. Methods used are the XTRAN2L 2-D and XTRAN3S 3-D small perturbation codes.

Steady and unsteady pressure distributions computed for the NACA 64A010 airfoil in pitch were in excellent agreement with experimental data for M = 0.50 and mean incidence of one degree. Agreement was also quite good for M = 0.796 where the computed steady flow shock was 2% too far aft and the unsteady peak was 10%-5% (as frequency increased) too far aft compared to measured values. Pressure differences are observable near shocks. Inviscid theory also predicted broader unsteady shock pulses with lower height due to shock movement as pitch amplitude increases in good agreement with experiment. Figure 5-1 shows the correct prediction of lift and moment coefficient trends with frequency. Viscous corrections improve agreements except for the imaginary part of lift due to pitch. Wall effects are expected at low frequencies.

Steady flow pressure calculations for the NACA 64A006 with oscillating flap show good agreement with experiment at lower Mach numbers. This is reflected in relatively good agreement with test data for predicted unsteady pressure distributions at M = 0.800 and 0.825. Separate unsteady shock pulse and hinge line singularity peaks are predicted. Both steady and unsteady calculated pressure distributions show differences compared to test data at M = 0.850 and 0.875. Trailing edge unsteady pressures agree with test data. Figure 5-2 shows the aerodynamic coefficients versus Mach number at a lower reduced frequency. Inclusion of viscous effects in theory gnerally improves agreement. Not shown in this summary is the much better agreement in unsteady coefficients and trends with Mach number at a higher reduced frequency of 0.24. This is due to the better agreement between calculated and experimental chordwise pressure distributions at the higher frequencies.

Inviscid unsteady calculations for the blunt leading edge, thick NLR-7301 airfoil oscillating in pitch at low Mach number (0.5) show reasonably good agreement with the experimental pressure distributions. Agreement was good for steady data although lower surface pressures were overpredicted. For the design point condition, the steady pressure distribution was not well predicted. The predicted chordwise unsteady pressure distribution shows features which are broadly similar to the experimental data so hope was expressed that viscous corrections in theory could show improvements. Both theory and experiment show the sensitivity of this supercritical airfoil to flow conditions.

The XTRAN2L inviscid small perturbation theory showed that reasonable and usable results could be provided below stall and separation (up to 8.5 degrees) for a NACA 0012 airfoil undergoing increasing angles from 0 to 15 degrees at constant rate. Instantaneous pressure distributions and lift agree reasonably well up to stall, which is delayed by a higher pitch rate. Figure 5-3 shows the good agreement between calculated and experimental lift coefficients at large angles. Moment coefficient data do not agree as well because of underprediction of loads near the leading edge and also separation. Large second harmonic components are present in moment coefficients and third harmonics are evident in Figure 5-3d.

Finally the results of comparisons between 3-D XTRAN3S (also a small perturbation method) data and test data were shown for a 12% supercritical, AR = 2, half-span model. Steady-state predictions were in reasonable agreement with test data at M = 0.70. Design Mach number is 0.8. The inviscid calculations showed poor agreement with test data for shock location at M = 0.825 so no unsteady data were shown. Figure 5-4 shows the unsteady results for M = 0.7. A viscous effect on the phase angle, due to lower surface pressures and geometry, is noticed at low frequency in test data. This effect disappears at higher frequency. The agreement between test and theory improves with increasing frequency and is better near midspan where shock effects are not overpredicted and tip effects are not pronounced. Agreement between calculated and experimental pressure distributions, both steady and unsteady, might be improved by the incorporation of better grids and viscous modeling.

Later calculations given in NASA TM 85817 show a broader 3-D shock pulse with increasing frequency in contrast to 2-D predictions.

6. D. J. SALMOND: "Calculation of Harmonic Aerodynamic Forces on Airfoils and Wings from the Euler Equations"

Since the Euler equations are the most accurate of inviscid methods and are likely to be more applicable for stronger shocks, lower aspect ratios, and higher sweep angles, the author extended these to subsonic-supersonic unsteady flows. The Pulliam and Steger steady flow method was used as a basis.

Applications of the fully conservative method were made to the NACA 64A010 airfoil in pitch. Steady calculations show very slightly different upper and lower pressure distributions due to slight asymmetry. For a lower reduced frequency, the agreement with test data for both real and imaginary parts of the first harmonic pressure distribution is good in front of and well behind the shock, but not as good at or near the shock. Results for a reduced frequency parameter of 0.404 are shown in Figure 6-1. Similar comments hold. The agreement for the real part is less good at an even higher frequency, but agreement between calculated and test data improves for the imaginary part.

Calculations are also made for the mid-semispan station of a very high aspect ratio wing and are compared with 2-D airfoil data. The 2-D and 3-D steady and unsteady results agree extremely well except for small differences near shock locations.

Subcritical flow calculations were made for the highly swept AGARD tailplane and are compared with experimental steady data in Figure 6-2 and unsteady in Figure 6-3. The full potential steady method (Arthur) and present Euler method data agree well with steady test data. The Euler method gives somewhat better agreement. Computed unsteady Euler results agree reasonably well with unsteady test data and are better than linear lifting surface results. (The frequency parameter is based on the root chord.)

Some new calculations for a free stream Mach number of M = 1.72 and frequency parameter of 0.543 were presented orally for pitch of the AGARD tailplane. Linear theory breaks down and results do not agree with test data especially near the leading edge region; the trend for the unsteady real part for the flat plate results is opposite to that of the Euler method and Mabey's test data near the airfoil nose. The real part from Euler results follows the experimental trend versus chord generally and agreement is better over the rear half of the airfoil. Flat plate unsteady imaginary components differ markedly in magnitude from test data, but Euler unsteady imaginary part results agree quite well with the experimental first harmonic chordwise pressure distribution. The leading edge is slightly supersonic at M = 1.72.

The unsteady calculations on the Cray 1S now take 2 minutes for 2-D calculations and 4 hours for 3-D calculations.

Future improvements will include implicit boundary conditions to permit larger time steps, will take advantage of characteristic directions, and will exploit improved grid locations and numbers. Flutter calculations will also be made for wings and conditions representative of industrial applications.

7. P. GIRODROUX-LaVIGNE AND J. C. LeBALLEUR: "Calcul D'Ecoulements Instationnaires Transsoniques Avec Decollements Par Interaction Visqueux-Non Visqueux"

A semiimplicit relaxation numerical technique having strong coupling for the interaction between inner viscous flow and outer small perturbation inviscid flow was described. It is consistent in space and time, and accounts for the downstream-upstream influence of viscous origins. Solutions of unsteady flows with shock-boundary layer interactions and with or without separation are possible. The (local) density of the mesh must be on a level or scale of the physical phenomena. Defect integral equations for the boundary layer and wake are closed by modeling the instantaneous velocity profiles (in a stationary sense) and by a set of turbulent transport equations.

Applications of the 2-D method were made to airfoils. Very interesting figures were presented which portrayed instantaneous iso-Mach lines and boundary layer parameters.

Results are given for the thick NLR-7301 airfoil where the small perturbation assumption is stretched and where viscous interactions occur near the trailing edge. Predicted steady pressure distributions are in good agreement with the experiment except near the blunt nose. Shock location and intensity are reasonably well predicted. Upper surface instantaneous pressure distributions for airfoil pitch at M = 0.75 are also quite reasonably predicted throughout the cycle as are the compression and shock disappearance. Figure 7-1 shows the satisfactory agreement between predictions and test data for pressure derivative due to pitch and its phase.

Similar calculations were conducted for an oscillating flap. Steady lift and leading-edge moment coefficients were overpredicted compared to experimental data. Calculated unsteady first harmonic pressure distributions for flap oscillations are qualitatively similar to test data but the predicted peak is much higher near the shock. Predicted phase angles versus chord show a trend very similar to experiment except near the trailing edge.

Calculations were also made for the NACA 64A010 airfoil at 4 degrees incidence using two equations of transport. A finer mesh than previously employed was used in order to properly simulate flows with large viscous effects. Agreement between test and calculated steady pressures is improved for the plateau in front of the shock and also towards the trailing edge. Computed viscous parameters show extended separation from shock foot and reattachment in the wake. Test and calculated instantaneous pressure distributions correlate better. Figure 7-2 shows the rather good qualitative agreements during a pitch cycle.

The first harmonic pressure derivative for pitch versus chord is shown in Figure 7-3. The authors report that differences for separated regions aft of the shock have been reduced. The predicted shock is a little too far aft. The correct prediction of the phase changes near the shock is noticeable. The steady lift coefficient was well predicted while the leading edge moment coefficient was 16% overpredicted. The unsteady first harmonic lift modulus was 85% of the test value while the leading edge moment coefficient was 73% of the test value. Calculated phase angles differed from the test data by 5 degrees.

Thick, circular arc, symmetric, rigid, nonmoving airfoils have shown flow oscillations at intermediate transonic Mach numbers. Periodic shock movements, oppositely phased on upper and lower surfaces, occur. The reduced frequency based on chord is near 1.0. The authors qualitatively predict the oscillating character of the flow. Flow dissymmetry amplifies near separation and ends with moving shocks near 60% - 85% chord. The present calculations predicted a decaying oscillation with a noticeably different reduced frequency of 0.27. However, the most critical Mach number might be higher. Other investigations

are required before firm quantitative conclusions can be drawn. The method does seem to predict a complex unsteady flow phenomenon, the same as Navier-Stokes approaches do. The authors hope that contributions might be made to buffeting phenomena.

The method presented has also been applied in an approximate fashion to predict pressure distributions for a 15% split flap spoiler near mid-chord and displaced into the subsonic (M = 0.6) stream by 10 degrees.

The predicted steady pressure distribution across the chord is in surprisingly reasonable agreement with measured data in shape and magnitude. The results for spoiler oscillations are shown in Figure 7-4. For upstream locations, the unsteady pressure data are in good agreement. Large differences are noticed over the spoiler and downstream. The spoiler had only a few measurement stations. The second large predicted peak is not evident in the test data. The calculated phase angle is in good qualitative agreement with the test data.

Mr. LeBalleur later stated that extensions to 3-D would require modifications to the coupling technique, closure condition, and inverse method.

8. M. J. GREEN AND D. LAMBERT: "A Semiempirical Unsteady Transonic Method with Supersonic Free Stream"

Garner developed an economic, temporary, semiempirical method for predicting transonic oscillatory loads for industrial use. The method was reasonably successful in predicting the transonic velocity dip of a flutter model. The authors extend the method to supersonic free streams. The Allen-Sadler linearized theory for low aspect ratio wings in a supersonic flow is employed to provide information on velocity potentials and their spacial derivatives at zero and nonzero frequencies. Pressure data and their variation with angle are obtained from steady theory or experiment. An important mode such as pitch is used as a reference mode and a basis.

The method, using steady measured pressure data, is applied to a low aspect ratio, highly swept AGARD taileron whose leading edge becomes sonic at 1.55. For M = 1.32, a frequency of 70 Hz, incidence of zero degrees, and 65% semispan station, the unsteady real-part pressure distribution versus chord from theory agrees very well with experiment. The imaginary part does not agree quite as well. Both parts are better than linear theory. Figure 8-1 shows results at incidence for the 65% semispan station. Again, the real test and calculated components tend to agree well. While the imaginary parts show disagreements, the Green-Lambert predicted trend is correct and is much better than linear theory. The cross flow is small at this station.

Figure 8-2 shows a section close to the outboard side edge. While the agreement between real parts from the Green-Lambert method and experiment is good, the imaginary parts differ from test data at the aft end. The one-dimensional Bernoulli approach was replaced by a new formulation taking cross flow into consideration. Since flow directional properties are not practically obtained from measured pressure data, information from steady Euler approaches was employed for cross flow and pressure data. The unsteady pressure distribution computed by the revised method shows close agreement with that computed without cross flow for the 65% span station. Real and imaginary components, with and without cross flow, agree reasonably well with experiment at this station.

The rate of change of steady pressure coefficient with incidence across the chord computed by the Euler method for the tip station differs noticeably from measured data. The experimental data have a large peak near 15% chord and are noticeably lower than predicted values from 30% - 90% chord. These differences are reflected into the computed oscillatory data presented in Figure 8-3. The real part is not affected by cross flow. The cross flow corrections have significantly improved agreement of calculated data with experimental data for the imaginary part.

The authors believe they have overcome the major difficulties. More work to test the reformulated method with cross flow needs to be done. This method will be used to calculate generalized forces used in flutter analyses.

9. W. J. McCROSKEY, P. KUTLER, AND J. O. BRIDGEMAN: "Status and Prospects of Computational Fluid Dynamics for Unsteady Transonic Viscous Flows"

In the review of the past progress, the authors point out a 10-year lag for developing unsteady codes after basic steady aerodynamic contributions are made. These lags are due to difficulties and complexities of performing time-accurate calculations at low frequency and the fewer scientists working in the area.

The improved paneling possible for steady subsonic flows has now been extended to steady supersonic flow and aircraft. TSP methods have been replaced by full potential and Euler methods for more complex geometries. An algebraic mixing length viscous model has been extended by Mansour to compute streamlines on a highly swept, low aspect ratio wing at 5 degrees incidence. Shock waves, tip vortex, separation, and reattachment zones were shown for the wing thereby indicating the great progress in steady 3-D Navier-Stokes methods. MacCormack's prediction is quoted that a Reynolds-averaged Navier-Stokes solution for a complete airplane will be obtained in 1985. In the viscous unsteady area, the

last ten years produced few engineering results of direct interest to the practicing aeroelastician. However, application of the 2-D Euler method and of the 3-D inviscid TSP method had been made. Progress can be judged by present achievements in unsteady 3-D full potential methods and 2-D Reynolds-averaged Navier-Stokes methods. Recently (1984), Horiuti et al. presented results shown in Figure 9-1 for an oscillating flap using Reynolds-averaged Navier-Stokes methods with simple eddy-viscosity modeling. Tunnel walls significantly affect the phase angles on the rear of the airfoil. The present authors stress the marginal capability in predicting the effects from ventilated-wall wind tunnels.

The paper discusses in detail the projections of capabilities in grid generation (including component-adaptive and solution-adaptive grids for bluff parachutes), grid spacing versus accuracy and stability, computer memory and speed, and also algorithm and solution methodology. The latter are more important in time-dependent problems where numerical instabilities arise.

Figure 9-2 gives estimates of CPU time for a wing with flap, simple body or store. As method complexity increases, maturity and confidence would decrease. TSP and full potential unsteady methods may be the most popular for the next few years. With advanced algorithms and computers, time-linearized methods seem practical for wide industrial use while thin layer (streamwise diffusion neglected) and Reynolds-averaged Navier-Stokes methods would likely be used for research, physical insight, or very critical problems. Dr. McCroskey expressed hope for the full potential method with integral formulation and also the Euler method with differential formulation for boundary layer effects. Figure 9-3 gives their overview of turbulence modeling. The authors point out that only viscous wedge, velocity profile (integral boundary layer), and zero-equation eddy-viscosity models have been used for unsteady flows up to now. It was expected that the two-equation eddy-viscosity model would be applied to aeroelastic problems in the near future and to flows with separation. (In Figure 9-3, W sub GT is the operations per grid point per time step.) The authors state that turbulence modeling is the weakest link, greatest challange, and primary pacing item for both steady and unsteady flows. "Flutter calculations will only be as good as the viscous model," said Dr. McCroskey!

Vortical flow modeling was discussed, including that of Caradonna et al. who used concentrated vorticies in potential flow methods. Srinivasan and McCroskey prescribed a vortex but allowed it to develop its path in space. It has been used successfully for potential, Euler, and thin-layer Navier-Stokes analyses of unsteady airfoil-vortex interactions. [It will be recalled that V. J. E. Stark showed a 17% drop in flutter speed when leading edge vorticies were taken into consideration in a crude way (AGARD CP-226)].

Pre-, intermediate-, and post-processing of data will require improved graphic display technology and increased access time.

The last item touched upon research for, and use of, artificial intelligence or heuristic, knowledge-based, expert systems to proceed through a maze of possible paths and to interpret a large amount of data.

Final conclusions and recommendations made in the paper and presentation included exploitations of codes including user training and management indoctrination, code validation through selected experiments and calculation-test combinations, vortical flow modeling, nonlinear aerodynamic-structural coupling methods wherein finite difference methods are used for the flow and finite element methods are used for the structure, and turbulence modeling. Research on wind tunnel wall effects could be added to this list.

10. P. MULAK AND J. J. ANGELINI: "Amelioration et Extension d'une Methode de Calcul D'Ecoulements Transsoniques Tridimensionnels"

A variational principle of Bateman and the optimization of the pressure functional lead to the correct approximation for the small disturbance equation with consistent boundary conditions. The alternating direction implicit procedure is extended to wings of general planiform and provides jump conditions for swept shocks. Time linearization is used.

The method is applied to two 3-D wings. The first is a 30-degree swept, semispan wing with supercritical profiles and considerable twist. Calculations are made for the case of inboard oscillating (15%) flaperon. Calculated steady pressures for the wing with 1.44 degrees incidence and for the midflaperon station underpredict the height and width of the leading edge shock on the upper side. Near the mid semispan and outboard of the flaperon, the steady pressure peak height is correctly predicted, but the experimental peak is wider and the shock strength is higher. The nose peak pressure predicted for the 72% semispan station is higher than the experimental peak which is also wider. The predicted shock locations are slightly forward of the experimental ones. The predicted lower surface pressure distributions are consistently higher than the experimental ones across the span. The authors discuss boundary layer, circulation, turbulent vortex sheet, and shock-circulation effects as possible explanations for deviations. Figure 10-1 and Figure 10-2 show experimental and calculated unsteady pressure distributions at spanwise stations. Test data show the leading edge shock effects due to flap oscillations. Disturbances are amplified outboard. The calculated unsteady peaks are less pronounced and reflect the statements made for the steady case.

The second application was made to a highly swept, low aspect ratio F-1 model which was oscillated in pitch about a swept axis. Steady chordwise pressure distributions for various spanwise stations show reasonable agreement with test data. The latter indicate

separation near the trailing edge by the lower levels of pressure. Measured and calculated unsteady pressures for pitch oscillations are shown in Figures 10-3 and 10-4. The test data show fluctuations and several peaks. Theses are thought to be caused by effects from the rough wood leading edge and a tip restraint cable.

The authors conclude that the results are satisfactory for the extreme wing designs. They are investigating ways to improve predictions of shock location, strength, and movement. In addition, the method will be extended to flexible modes and will be applied to a supercritical wing.

A CPU time of 7 minutes was mentioned for each steady or unsteady case for the calculations reported without program restructuring. Vectorial programming could reduce CPU time to 2.5 minutes.

11. M. H. L. HOUNJET AND J. J. MEIJER: "Application of Time-Linearized Methods to Oscillating Wings in Transonic Flow and Flutter"

Results from field panel, time-linearized, modest cost methods are presented. FTRAN2 is a 2-D code using small perturbation theory and small disturbance boundary conditions. FTRANF solves the time-linearized full potential equation with complete boundary conditions and is applicable to thicker airfoils. FTRAN3 solves the time-linearized full potential equation with small disturbance boundary conditions. To relieve the small shock displacement restriction, for some calculations, the authors average steady flow fields for several angles to approximate shock trajectories with amplitude. Furthermore, a warning is given against direct comparison of measured shock peak shapes with calculated values since calculated characteristics are artificially related to shock trajectories by mesh width, etc. Peaks based on mean (averaged) steady flow field are thought "to be related to physical shock displacements plus additional artificial mesh related shock displacements." While further results might be needed for final judgements, this use of averaged steady flow fields gave more favorable results.

Application of FTRANF to a pitching airfoil (NACA 64A010) showed very good agreement with experiment for the chordwise pressure distribution at a subsonic Mach number (0.5). Mean (steady) flow averaging for M = 0.796 moves loading a little aft just downstream of the shock. Unsteady pressure distributions calculated by TSP FTRAN2, full potential FTRANF, and averaged-flow-field FTRANF, showed reasonable agreement with NASA Ames test data except near shocks. Figure 11-1 shows analytical and experimental trends of unsteady pressure distributions with frequency. Best agreement occurs at intermediate frequencies. Lift coefficient variation with frequency was reasonably well predicted. Quarter chord moment coefficients showed differences due to variations in measured and calculated unsteady pressure near the shock.

Applications of FTRAN3 to the LANN wing are shown in Figure 11-2 for various frequencies. Agreement with experiment is stated as acceptable. Difficulties were encountered with pressure pickups so caution was advised in interpreting integrated and some local loads. Calculated imaginary parts tend to agree with experiment. The subsonic lower surface should show better agreement. A model resonance is evident at a reduced frequency of 0.2. Frequency trends are predicted correctly. Spanwise distributions of the real oscillatory lift were overpredicted more on the lower side but seemed acceptable. Deficiencies decreased with increasing frequency. Computed spanwise distributions of unsteady moments showed poor agreement with experimental data throughout the frequency range.

Quasisteady calculations were made by FTRAN3 and steady-state XFL022 for the LANN wing. Calculated quasisteady chordwise pressures at three spanwise stations show reasonable agreement between the two prediction methods and with measured data at M = 0.82. Amplitude (incidence) effects are noticed in the data from tests from leading edge to the shock. Two shock peaks occur at the inboard station with a single bigger peak at the middle station. XFL022 predicts the two peaks at the inboard station better. These effects are seen in the low frequency unsteady pressure distributions shown in Figure 11-3 which also gives FTRAN3 results. Experimental and calculated results show some agreements. Peaks are underpredicted on the upper side but the initial warning about peaks should be remembered. The lower surface is subcritical.

To demonstrate industrial capability, flutter analyses are made for a fighter with tip missiles or inboard stores. FTRAN3 is used for unsteady transonic airloads on the wing only. The doublet lattice method provides unsteady airloads for other aircraft parts. With transonic effects on the wing, the predicted instability is less severe than that predicted by linear doublet lattice methods. Experimental data show a lightly damped mode. Calculations for other store cases also showed a more stabilized flutter boundary using transonic unsteady airloads on the wing.

12. J. B. MALONE, S. Y. RUO AND N. L. SANKAR: "Computation of Unsteady Transonic Flows About Two-Dimensional and Three-Dimensional AGARD Standard Configurations"

The XTRAN3, 3-D small perturbation code was applied to the LANN wing in pitch. The steady flow suction at the leading edge was underpredicted and caused differences between theory and experiment downstream to the shock. Calculated unsteady first harmonic pressures are shown in Figure 12-1. (k is based on mean aerodynamic chord.) Agreement with experiment is reasonable and better away from the shock.

The SUNTANS finite difference method for the 2-D full potential equation was used for airfoil applications. Boundary conditions were applied exactly on the instantaneous surface. The method is applicable to thick, blunt airfoils in inviscid flow from M = 0.1 to 1.2. Calculations were made for the NACA 64A010 airfoil at minus 0.10 degrees while the test angle was minus 0.21 degrees. Predicted steady pressures are in quite good agreement with experiment at M = 0.82, although the suction in front of the shock is overpredicted. Calculated lift coefficient magnitude, and phase and moment coefficient magnitude variations with frequency are in excellent agreement with test data except at very low frequencies. Calculated moment coefficient phases versus frequency are about 10 degrees too high compared to test data. The 2-D SUNTANS was also applied to the oscillating flap on a NACA 64A006 airfoil. Steady pressure predictions at M = 0.875 are in reasonable agreement with test data. Suction levels forward of the shock are overpredicted while pressures are overpredicted aft of the shock. Theory predicted the irregular B-type shock behavior at k = 0.234, as shown in the tests. The shock disappears during part of the flap oscillation cycle. Unsteady chordwise pressure distributions at the same reduced frequency are quantitatively reproduced reasonably well, but the calculated unsteady shock pulses are 10% chord further upstream. Otherwise, agreement would be much better. The predicted steady shock was 2% - 5% chord more downstream than the experimental shock. Inclusion of viscous effects in theory could improve agreement with test data.

The SUNTANS 2-D code was also applied to the blunt, thick NLR-7301 airfoil. Steady inviscid theory provided a strong shock which was too far aft, thus viscous steady theory was used. Lower surface pressure predictions agree quite well with experiment, and upper surface predictions agree reasonably well with test data. The predicted shock position is reasonably close to the test location. Unsteady viscous approximations used the same transpiration velocities found in the steady viscous solutions and were held fixed during the unsteady calculations. Figure 12-2 shows the calculated, first harmonic unsteady pressure distribution which noticeably underpredicts the measured shock pulses. Predicted shock pulse locations and phase angles seem satisfactory.

The 3-D full potential code UPSIPWING was applied to the low aspect ratio, clean F-5 wing which has high leading edge sweep. For unsteady calculations, the flow tangency is "calculated at the instantaneous wing surface position, but applied along the original, or mean wing surface shape." The predicted steady pressure distribution for M = 0.8 (subcritical flow) agrees very well with test data. Agreement was also good for steady data at M = 0.90 except near the tip. For M = 0.95, theory predicted the shocks shown by the experiment on both upper and lower surfaces as well as the slightly more aft upper surface shock. For M = 0.8, the unsteady pressure distributions for sections along the span are quite well predicted. The real components of the first harmonic unsteady pressure show the drooped nose effects. Calculated data also correlate with test data reasonably well for M = 0.90 where linear theory would not apply. First harmonic unsteady pressure components for M = 0.95 are shown in Figure 12-3. The authors stated that the phase angles between real and imaginary parts are also predicted qualitatively for both upper and lower surfaces at M = 0.8 and M = 0.9. Inclusion of viscous effects into theory could decrease discrepancies with test data.

While F-5 steady and unsteady test data for the clean wing and wing-with-stores are not included in the SMP test selection cases, they present a valuable standard for evaluating and improving theories.

Recommendations were made for additional correlations to provide proven codes for the flutter engineer and for development of methods and grids to model complex surface-body combinations.

13. A. LAURENT: "*Calcul D'Ecoulement Transsonique Instationnaire Autour D'Aile a Forte Fleche*"

Variational principles are employed to define the transonic small perturbation equation and compatible limits. The local direction of flow and its sonic type are determined so calculations may be made in the physical plane without space transformations. The method is an extension of 2-D Murman-Cole ideas to 3-D and is fully conservative. It uses an alternate direction implicit approach. It applies to highly swept, low aspect ratio wings with lateral flows. Calculations are reported for wings in pitch.

Mesh size investigations were applied to the F-1 tail. Differences are noticed near the shock and t'.e leading edge, and they increase towards the tip.

Calculated steady chordwise pressures for several spanwise stations for an extremely low aspect ratio rectangular wing at M = 0.85 show good agreement with those from the Jameson, nonconservative, full potential method for regions forward of the shock. The nonconservative method gives shocks and compressions which are upstream of those from the conservative small perturbation method.

Steady pressure distributions computed for a rectangular wing with 30 degrees sweepback and NACA 0012 profiles show a sharp, thin, high supersonic zone near the wing tip. The shock is strong and located near the quarter chord point. For wing mid semispan, the supersonic zone is lower and broader. The shock is located at mid chord and is weaker. For the root, the supersonic zone is even lower and also more broad. The shock

is located near three-quarters chord and has a higher rate of compression than at mid semispan. The sonic line is near the leading edge. Instantaneous pressure distributions were calculated throughout a pitch cycle and show, most interestingly, the three kinds of shock motion found experimentally by Tijdeman. The stronger shock near the tip leads to a nondisappearing shock during pitch motion with smaller chordwise motion (Type A shock). The shock disappears during a large portion of the pitch cycle at the mid semispan station (Type C shock). At the root, the shock appears to move upstream during part of the cycle, disappears, and later reappears at the rear of the airfoil (Type B shock). The calculations show a 17% contribution from the second harmonics in the unsteady pitch moment coefficients.

Applications are made to the highly swept, low aspect ratio F-1 model. It had deficiencies such as leading edge roughness and a joint step, and sometimes a tip cable. Steady pressure distributions calculated for M = 0.9 (slightly transonic) show generally good agreement with test data for most spanwise stations except those near the tip. For strong transonic flow at M = 0.95, comparisons are debatable due to model deficiencies and trailing edge separation. However, calculated pressures agree reasonably well with test data in front of the shocks and for shocks near the leading edge. Unsteady pressures were calculated for M = 0.95, and results show more shock movement for 10 Hz than for 20 Hz. Unsteady first harmonic pressure coefficients for M = 0.95 are shown in Figures 13-1 and 13-2 for two spanwise stations (near 57% and 76% semispan). The general behavior of unsteady test and calculated results seemed more similar when test and calculated steady data agreed.

Calculated and test steady pressure distributions for several spanwise stations show very good agreement for a slightly supersonic Mach number of 1.02. The cable affects data at the tip. Agreement in calculated test data could be improved for the trailing edge regions by including viscous effects in calculations. Unsteady data were not shown. Flow field calculations were made for the NORA (F-1 tail) model at M = 0.95 and compared to test data having a slightly different tip. Figure 13-3 shows the local Mach number for the steady case. Calculations agree with test data rather well for shock locations and strength. Some of the differences between test and calculated values at the root and middle of the wing may be due to wall effects. The undulating peaks in front of the shock seem to be predicted generally.

14. P. M. GOORJIAN AND G. P. GURUSWAMY: "Unsteady Transonic Aerodynamic and Aeroelastic Calculations About Airfoils and Wings"

Development and applications of the NASA Ames 2-D ATRAN2 and 3-D ATRAN3S (XTRAN3S) are discussed. Both are for the small disturbance formulation. Many of the applications include viscous effects by the ramp and lag entrainment methods.

For the NACA 64A010 airfoil at M = 0.796, the viscous methods predict the steady shock location, the magnitude of the lift coefficient versus frequency, and the magnitude of the moment coefficient versus frequency better. Both inviscid and viscous methods overpredict lift and moment phase angles due to pitch at low reduced frequencies. The shock pulse peaks in the unsteady pressure loadings at various reduced frequencies are lowered, are moved upstream, and are in better agreement with measured data when viscous corrections are included.

Viscous corrections significantly improve agreements with measured upper surface steady pressures over an MBB-A3 airfoil. Calculations show very significant reductions in the heights and upstream displacements of real and imaginary unsteady shock pulses especially for the lag entrainment method at k = 0.1 and M = 0.756 for airfoil pitch.

Viscous wedge corrections were also applied to the NACA 64A006 airfoil with oscillating flap. The lag entrainment calculations required time steps that were too small. Correlations with measured unsteady pressure data were qualitatively improved at M = 0.853. Improvements were more noticeable at M = 0.877 and M = 0.879, and for higher reduced frequency. Calculations showed that the lift coefficient could be predicted using the first harmonic of unsteady pressures. Shock strength contained higher harmonics.

Applications to the NACA 0012 airfoil in pitch with large (2.5 degrees) amplitude were made using viscous corrections. The chordwise unsteady pressure loads which were predicted for eight time spots around the cycle showed rather good agreement with experimental data. Differences between inviscid and wedge calculations were small except near the shock. The formation of a strong shock and also the shock disappearance over part of the cycle were predicted.

No data for the blunt, thick NLR-7301 airfoil were presented since the calculations showed poor agreement with experiment. This airfoil was considered to have been outside the small disturbance limits.

A modified shear transformation for the grid was recently developed for application to highly swept wings of low aspect ratio. Applications were made to the F-5 wing in pitch. Calculated lower and upper surface pressures now showed major improvements in agreement with test data at M = 0.9, except near the nose, for four spanwise stations. Figure 14-1 shows the rather good agreement between calculated and measured unsteady pressures.

Unsteady aerodynamic loads were used in flutter analyses with various levels of success. Viscous ramp and lag entrainment methods were applied to a plunging-pitching NACA 64A010 airfoil. The lag entrainment correction produced the closest agreement with the trend of flutter speed versus mass ratio obtained using measured unsteady aerodynamic coefficients. However, the former gave flutter speeds which were 25% - 12% unconservative compared to the latter, which used measured coefficients, over the range of mass ratios from 50-250. Viscous corrections lowered the computed flutter speeds for high mass ratios.

LTRAN3 flutter calculations (inviscid) for a circular arc, AR = 5 wing at M = 0.715, show good agreement with experiment in both flutter speed and frequency for a mass ratio near 37. Linear methods show trends similar to LTRAN3 calculations as mass ratio is increased, but the linear methods show lower flutter speeds.

Flutter calculations were also conducted for a model of a Japanese transport with NACA 65A012 section. Results are shown in Figure 14-2. The lower Mach number side of and most of the transonic flutter speed dip are well predicted. No flutter was predicted for M = 0.85. Later verbal comments stated that linear theory and XTRAN3S flutter speeds agreed at lower Mach numbers and that viscous effects in calculations did not change the calculated boundary. Comparisons with flutter frequencies, amplitude ratios, and phases were not given.

Applications were made to a rectangular AR = 4 wing with NACA 64A010 section and for a high wing-air mass ratio. Flutter speed results are shown in Figure 14-3. Inclusion of viscous effects lowers lift coefficients and causes significant changes in the phase angle. A 10% increase in flutter speed results. The flutter frequency is near the first bending mode. Flutter characteristics could be predicted using first bending and first torsion modes.

Two bending modes and two torsion modes were used in the flutter analyses of a swept wing with MBB-A3 profiles. The incorporation of the second torsion mode caused a 5% drop in flutter speed.

The authors conclude that ATRAN2 and ATRAN3S are ready for practical applications where transonic small perturbation limits apply.

15. H. ZIMMERMAN: "The Application of Transonic Unsteady Methods for Calculations of Flutter Airloads"

Applications of the Angelini-Couston transonic small perturbation technique, the linear TSP method of Voss, Deslandes' Euler method, and the doublet lattice method, with and without corrections for aerodynamic center and lift curve slope, are made to an airfoil with pitch or plunge oscillations.

Steady pressure distributions for an MBB-A3 supercritical airfoil predicted by various methods show differences upstream of the shock, but the agreement between methods for M = 0.765 and M = 0.8 is generally satisfactory. Unsteady real and imaginary pressure distributions from TSP show higher peaks than linear TSP near the shocks for pitch. TSP shocks are more downstream at lower frequencies. The differences decrease with increasing frequency. The unsteady peaks for TSP methods and plunge motions are much higher than those from linear TSP and increase with frequency, perhaps unrealistically said the author, for M = 0.765.

Figure 15-1 shows pitch and plunge aerodynamic coefficients versus frequency. Results for the three methods converge at higher frequency except for moment due to plunge. Noticeable differences between TSP and linear TSP methods occur for the real part of moment due to pitch, real part of lift due to plunge, and especially for the imaginary part of lift due to pitch. Variations of numeric parameters can cause 10% changes in TSP results. Some unsteady Euler calculations were also made for M = 0.80 and an angle of minus 0.4 degrees, and show the same general trend for pitch and plunge coefficients with frequency as other methods do. TSP results agree better with Euler data.

Unsteady pressure distributions were calculated for linear TSP using steady velocity potentials from TSP or the full potential method. The differences between the two linear TSP unsteady pressure distributions were small.

Flutter calculations were conducted for a 2-D airfoil with two modes. The lower frequency mode was mostly plunge with a nodal point well in front of the leading edge. The second mode was essentially pitch. The modes were selected to grossly simulate wing bending and engine pitch modes of a transport wing. Two frequency combinations were used. One combination had lower frequencies for mode 1 (10 Hz) and mode 2 (30 Hz). The second combination had higher frequencies for mode 1 (40 Hz) and mode 2 (60 Hz), and a higher frequency ratio. Flutter calculations are shown in Figure 15-2 for M = 0.76 and an angle of 0.85 degrees and M = 0.80 for an angle of minus 0.4 degrees. Tunnel stagnation pressure at the flutter point is greater for TSP, corrected doublet lattice, linear TSP, and uncorrected doublet lattice methods respectively, for M = 0.76. The differences are noticeable. As tunnel stagnation pressure increases, the airfoil-air mass ratio decreases.

The more negative the imaginary part of lift due to pitch is, the more likely is the possibility of a "single degree of freedom flutter" with nearly the first bending mode and frequency. This occurs for the TSP results at the higher Mach number of 0.80. Euler-type calculations for this Mach number show flutter involving both mode 1 and mode 2. For both Mach numbers, the corrected doublet lattice method results give a neutral point stagnation pressure almost equal to that from linear TSP.

Flutter calculations for the higher combination of modal frequencies, 40 Hz and 60 Hz, show that the stagnation pressure for flutter is essentially equal for linear TSP and TSP results. The uncorrected doublet lattice method gives the same critical stagnation pressure, but the corrected doublet lattice method gives a much lower stagnation pressure. The author states that these behaviors could be due to variations of lift due to pitch at low frequencies.

The effect of incidence was investigated for the flutter case with lower modal frequencies (10 Hz and 30 Hz). Critical flutter stagnation pressures versus incidence are shown in Figure 15-3. The TSP method shows the largest drop with incidence. Single degree of freedom flutter in the first bending mode occurs for the higher angles at both Mach numbers.

In the later discussion period, Mr. J. Edwards pointed out an unusual bending type instability that occurred during transonic wind tunnel testing of an aeroelastic model of the DAST-ARW-2 wing. Mr. Edwards also discussed possibilities of predicting this phenomenon.

Flutter analyses for other cases are obviously needed since this particular model may be oversensitive.

The author concludes by recommending that static aeroelastic deflections due to steady loadings be considered in predicting unsteady loadings. Also, the various angles possible in high speed flight should be investigated. He stated that time-linearized flow equations do offer advantages.

A comment was made to the author that viscous corrections could cause effects equal to the differences between the various inviscid methods presented. The author agreed and stated that investigations including viscous effects were planned.

16. K. ISOGAI: "The Development of Unsteady Transonic Three-Dimensional Full Potential Code and Its Aeroelastic Applications"

A two-step, semiimplicit, time-marching, finite difference method for solving the 3-D full potential equation in quasilinear form has been developed at the Japanese National Aerospace Laboratory. It employs the quasiconservative form of Jameson's rotated difference scheme to capture shock waves. Flow tangency conditions are satisfied on mean contours.

Applications to the highly swept, low AR NORA wing, with nose-up twist and NACA 63006 section, were made and are shown in Figure 16-1. The agreement between theory and experiment is reasonable.

Flutter calculations were made for a high aspect ratio, clean transport wing with nose-down tip twist using time integration of structural and flow equations. Six modes were used for structural responses which only consumed 1% of the total computing time. The flow equation computations required almost all of the time.

Computed steady-state pressures used a 2-D strip boundary layer correction which significantly improved the agreement with test steady pressure distributions for M = 0.8 as shown in Figure 16-2. The bottom of the transonic flutter dip occurs near this Mach number. The modified airfoil shapes and slopes found were then applied in unsteady calculations without inner-outer flow unsteady interactions.

The calculated and experimental flutter characteristics are shown in Figure 16-3. The stagnation pressure at flutter increases with angle of attack (possibly due to aeroelastic untwisting for swept wings as recently discussed by Gravelle, Honlinger, and Vogel at the September, 1984, ICAS meeting). Flutter stagnation pressures and the dip are well predicted. Frequency is reasonably well predicted, but the large disagreement with experimental frequency at the lower Mach numbers could not be explained. Unsteady aerodynamic calculations were performed for a twisted wing simulating elastic and geometric twist angles at flutter statically. This modified rigid wing was oscillated in pitch at M = 0.8. Steady pressures show a shock on the lower surface at 15% chord and at 85% semispan. This is reflected in sharp peaks of real and imaginary unsteady pressures and is thought to be the cause of minimum dynamic pressure. A rapid rise in flutter dynamic pressure occurs with the expansion of the supersonic region with increasing Mach number.

(Japanese report NAL TR-726T mentioned success in predicting the flutter characteristics of the supercritical wing model tested by Farmer-Hanson of NASA.)

The authors discussed a clever method for calculating static aeroelastic phenomena at a given Mach number and a given dynamic pressure using their time marching code. Velocity is decreased and air density is increased at constant dynamic pressure to produce low wing-air mass ratios. At high reduced frequencies, oscillatory wing responses damp rapidly with time to give converged static aeroelastic deformations. An example demonstrated the method.

Flutter calculations were also made for a transport wing with engines. The full potential code shows a large transonic flutter dip for Mach numbers just above 0.8 in the inboard wing torsion mode. Doublet lattice methods predict significantly higher speeds at the dip and are quite unconservative.

The author applies the full potential method to predict (a) steady-state pressures for the ONERA M-6 wing at M = 0.84, (b) unsteady lift and moments for a swept rectangular wing (flat plate) at M = 0.8, and (c) unsteady pressures for an inboard flap on an RAE swept tapered wing. The latter case is shown in Figure 16-4. The various data for the above cases are in reasonable to good agreement with other methods or test data.

The time domain calculations were also applied to simulate flutter suppression systems using active controls to eliminate the instability.

The author states that gust response, gust alleviation, and aileron reversal applications are straightforward.

Thus, the state of the art in Japan is quite high and appears ready for industrial flutter applications.

THE ROUND TABLE DISCUSSION

Five questions were proposed as listed next. A discussion of each question follows.

1. How is transonic flutter clearance done today in the aircraft industry?

The unsteady airloads used for safety-against-flutter evaluations are now computed from modified linear theories such as strip theory, kernel function, and doublet lattice methods for the subsonic region and supersonic kernel, harmonic gradient, supersonic parallelogram integration, and the conventional Mach box method for the supersonic regime. Transonic trends are estimated from correlations between flutter model test data and the linear theories. Final flutter calculations are made with quasisteady corrections for lift curve slope and aerodynamic center and other modifications to the theory.

In Europe, measured unsteady pressures are sometimes used to guide estimates of oscillatory airloads. Messieurs Boer and Houwink of NLR used measured 2-D transonic unsteady airloads together with quasisteady 3-D corrections from steady tests (EQS method) to predict the two transonic flutter speed dips shown by experiments.

The Japanese National Aerospace Laboratory has had success in predicting the flutter speed of the Farmer-Hanson model and a model of a preliminary design of a Japanese transport. Their 3-D full potential code requires considerable computer times. Practical methods for clean surfaces now exist, even if long.

2. Will the emerging transonic CFD methods change the procedures?

The consensus was that these new methods will have a great impact on the flutter calculation process, but not in the near-term future.

Additional validations to establish the improved reliability by comparisons with test data are required for realistic industrial cases before the methods will be accepted by managers and, especially, by civilian and military approval agencies. Also, the total costs of increased computer times and engineering support must be minimized. Efficient engineering and preliminary design methods are required. Thus, the contribution of milestone developments and their acceptances are likely to be evolutionary.

The same general process consisting of flutter calculations at various design stages, ground vibration tests, stiffness tests, model tests, flight flutter tests, etc., will still be used. The flutter analyses will improve in accuracy and will increase with the intent of minimizing flutter model and flight tests.

A crisis could accelerate the acceptance and use of the new unsteady CFD methods.

3. How will transonic flutter clearance be done in five years?

Few significant changes are likely in the next five years. However, the new methods with quicker turnaround times are likely to be used for intermediate design particularly if margins of safety are small or inadequate. TSP and full potential methods may receive main attention.

4. How will transonic flutter clearance be done in ten years?

The consensus of both scientific and industrial representatives was that, beyond five years, the new unsteady CFD methods would be used extensively. The methods would have matured, been evaluated and validated, and gained acceptance.

No definite conclusions could be drawn about the impact of the new technology on flutter model tests. The selection of the number and kind of models will certainly be improved. Trade-off studies to evaluate free-flying versus cantilevered models could be conducted as well as studies to minimize wing-store cases in model and flight tests. However, development of new grids and methods to handle wing-stores, T-tails, etc., is required before a sharp reduction in model and flight tests is possible.

Theory shows marked effects on flutter characteristics due to surface angles, and these results are supported by some tests. However, other tests of wings up to 6 degrees show that the transonic flutter speed dip extends over a very narrow Mach number range and is not influenced strongly by the angle of attack.

Separation effects have strongly influenced the results of flutter model tests.

Flutter model construction (surface smoothness) and testing certainly has to be improved as emphasized by several papers.

No definitive and quantitative statements were made about reductions in flight flutter testing although hopes were expressed. Any reductions would be significant in view of the very high costs per hour of flight time. However, the added complications of the angle of attack effects for both attached and separated flow as well as the increase in potentially critical cases, due to improved accuracy of prediction methods, make estimates difficult.

5. What are the research needs for the next five years?

Several opinions were expressed about the adequate state of the art for airfoils and available unsteady test data. Suggestions were made to conduct future tests on small 3-D models to decrease wind tunnel interference and to investigate realistic configurations.

Some research needs in the model area are:

1. Two-dimensional plunge-pitch flutter tests at various angles or lift coefficients.
2. Unsteady airload measurements over flexible models.
3. Prediction of flutter characteristics corresponding to Reynolds numbers at flutter model conditions and also for full-scale flight Reynolds numbers.
4. Comparison of flutter model data obtained at low Reynolds numbers and those obtained in new high Reynolds number facilities. Perhaps this can be accomplished through a cooperative program.
5. Wall and tunnel resonance effects on unsteady aerodynamics and flutter measurements.
6. Improved flutter model construction techniques and more careful test conditions.

Analytical research needs include:

1. Grids and methods for surface-bodies, T-tails, etc.
2. Viscosity.
    a. Improved turbulence modeling.
    b. Continued development of semiempirical viscous methods for 3-D wings and extension of separated flow methods to 3-D.
    c. Extension of Navier-Stokes methods to buffet phenomena.
    d. Investigation of problems of fighter aircraft during high angle, maneuvering, transonic combat.
    e. Further studies of self-induced flow instabilities over rigid, nonmoving airfoils.
    f. Methods to predict wing torsional buzz and swept-wing bending buzz at higher angles.
    g. Methods to predict vortical flow effects on flutter.
3. Nonlinearities.

Methods for the simultaneous time integration of strongly nonlinear structural, unsteady aerodynamic and electrohydraulic elements (stability analyzed in the time domain as compared to the frequency domain).

4. Application needs:
    a. Selection of standard AGARD SMP industrial-type flutter cases and model test results.
    b. Investigations of simplicity versus utility versus computer times in various transonic unsteady airload methods by application to realistic cases.
    c. Training of flutter engineers.
    d. Indoctrination of civilian and military approval agencies in the new techniques.

CONCLUSIONS AND RECOMMENDATIONS

1. The new unsteady transonic CFD methods with their more realistic simulation of transonic physical phenomena are vital for improving accuracy in flutter predictions.
2. The AGARD cooperative program on transonic unsteady aerodynamics and aeroelastic applications has certainly stimulated excellent contributions and advanced the state of the art.
3. General conclusions on the state of the art seem to be:

   a. The various methods predict subsonic unsteady pressure distributions equally well.
   b. Unsteady pressure distributions for conventional airfoils are quite well predicted by inviscid methods at lower transonic Mach numbers and for attached flow. The agreement with test data deteriorates with increased angle and shock strength. Viscous corrections improve agreements as do increased frequencies.
   c. Agreement of predicted unsteady data with test data is better when steady pressure data agree.
   d. Supercritical airfoils are very sensitive to flow conditions and require viscous corrections to improve agreement with test data. Some of the simpler TSP methods fail to adequately predict unsteady loads for blunt, thick surfaces.
   e. Viscous corrections are essential to even qualitatively predict unsteady aerodynamic pressure trends due to oscillating trailing edge flaps. The state of the art is fair, at best, and further improvements are needed for active control applications.
   f. Separated flow drastically changes the variations of unsteady pressures and phases with frequency. Flutter characteristics are altered significantly. Applications of new strong coupling-viscous methods predict the correct trends for 2-D airfoils. No 3-D methods for separated unsteady flow are available.
   g. Research on unsteady turbulence modeling and on wall effects requires high priority attention.
   h. Three-dimensional methods for predicting unsteady airloads for transonic flutter analyses of clean wings are now available even if lengthy and tentative. Methods for interfering surfaces-bodies are needed.
   i. Economic methods for preliminary design are needed.

4. Liaison between unsteady CFD scientists and flutter engineers must increase as well as training for the latter.
5. The tremendously useful data produced by the SMP cooperative program certainly requires continuous collation.
6. Application of the new methods by industrial flutter engineers should be presented at AGARD meetings and also national group meetings to accelerate transition of this more accurate and vital technology.

ACKNOWLEDGMENTS

Special thanks are due to:

1. Messieurs H. C. Garner (U.K.) and N. C. Lambourne (U.K.) for their most helpful input to this summary report.
2. Messieurs H. C. Garner (U.K.), N. C. Lambourne (U.K.), J. J. Angelini (France), J. Becker (Germany), and R. F. O'Connell (U.S.A) for their stimulating comments and lively participation in the Round Table Discussion.
3. Messieurs R. J. Zwaan (Netherlands) and J. W. Edwards (U.S.A) for their additional presentations during the Round Table Discussion.
4. Dr. Edward S. Wright, Director, Army Materials and Mechanics Research Center, Watertown, Mass., U.S.A., for arranging for typing and artwork, and to Ione Haines, Diane Valeri, Nancy Fleming, Marion Gould, and Sharon Ross for expedient and skillful preparation of this report.

1. "Transonic Unsteady Aerodynamics and Its Aeroelastic Applications," AGARD SMP CP-374.

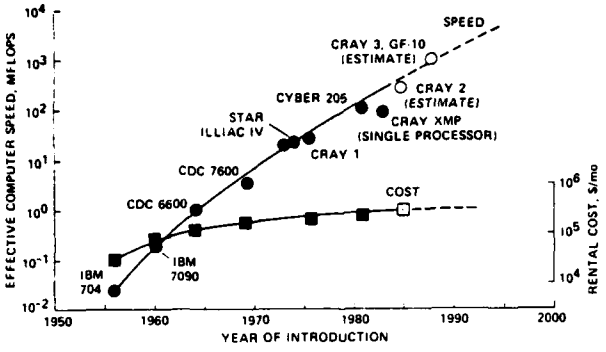

Figure 1-1. Growth with time of computer speed and cost.

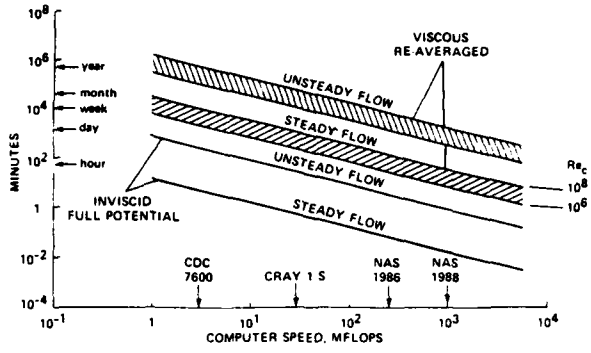

Figure 1-2. Times required to compute steady and unsteady flows about wings - 1984 algorithms.

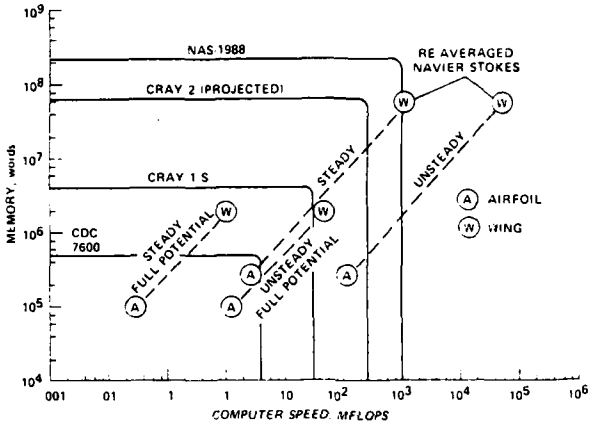

Figure 1-3. Computer speed and memory requirements for aerodynamic calculations - 15-minute runs using 1984 algorithms.

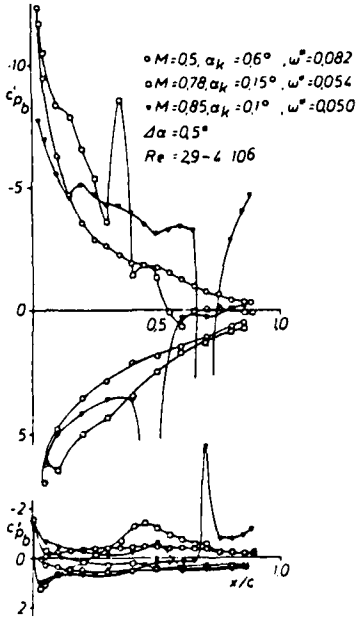

Figure 2-1. Effects of Mach number. Pitch oscillation about the c/4 axis.

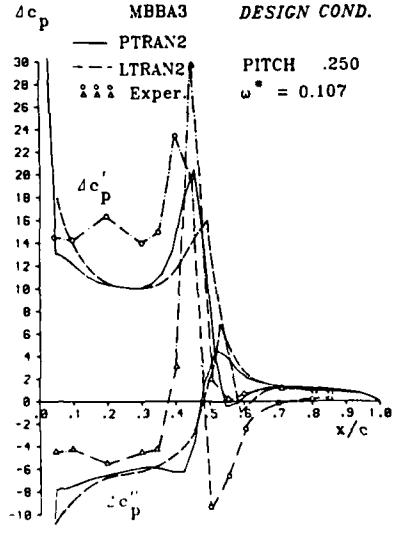

Figure 2-2. Two-dimensional unsteady load distributions - (CT3).

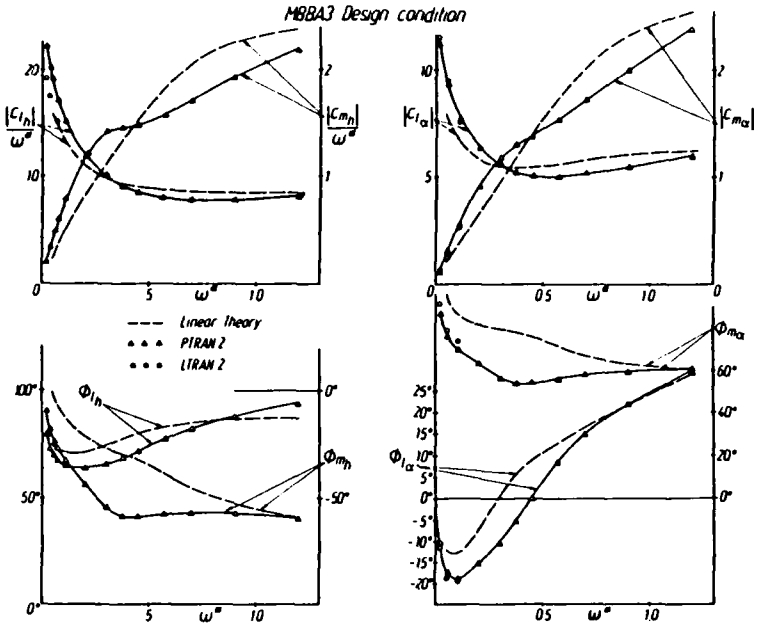

Figure 2-3. Frequency dependence of unsteady lift- and moment- (about c/4) coefficients due to pitching and heave motion.

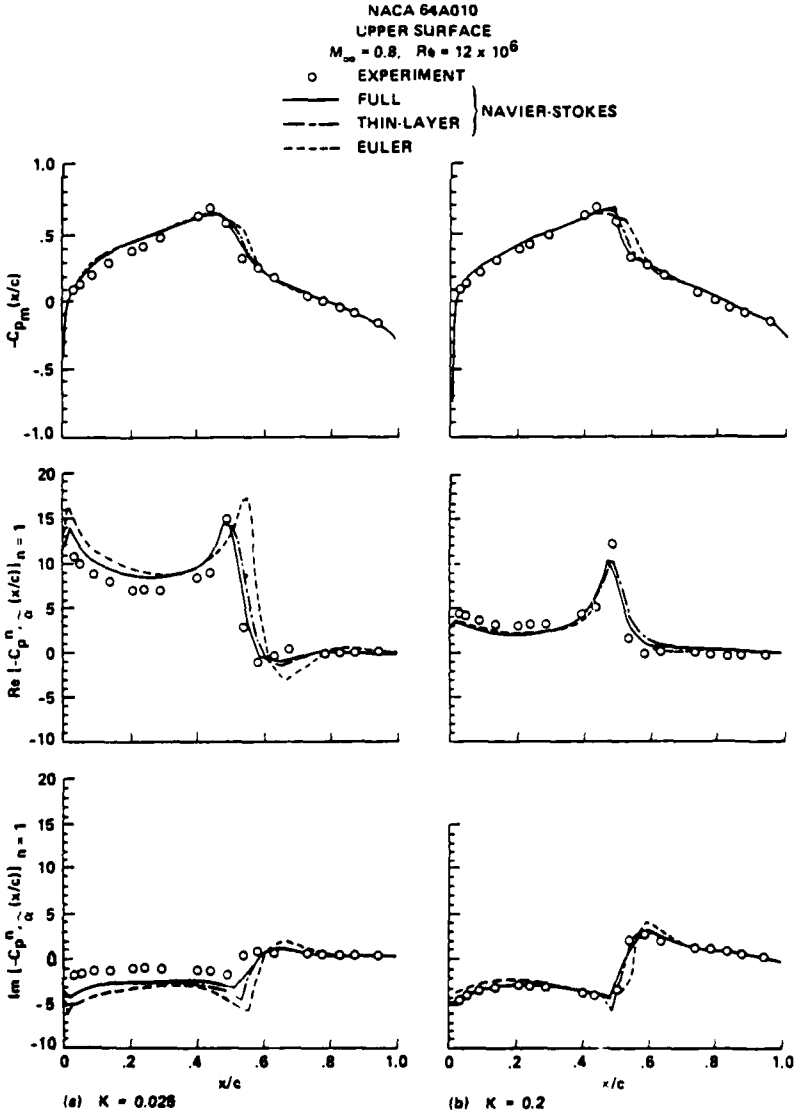

Figure 3-1. Mean and first harmonic complex components of pressure coefficients: $\alpha = 0^0 + 1^0 \cos \omega t$.

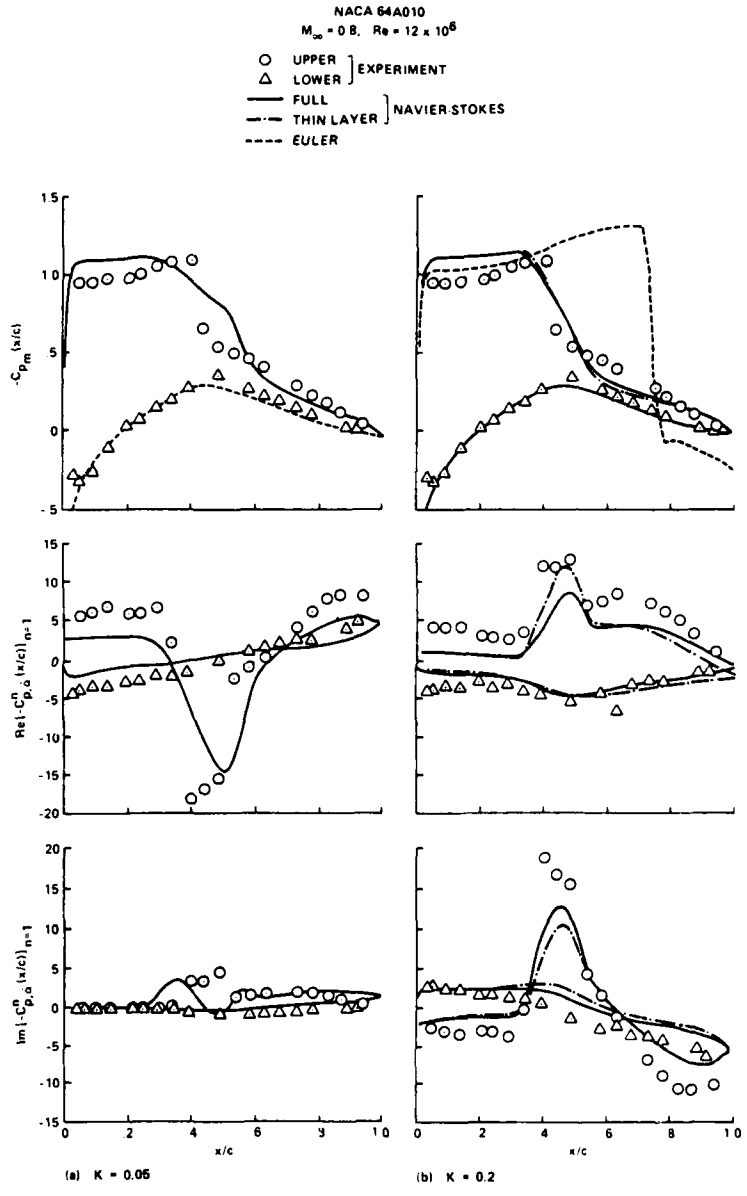

Figure 3-2. Mean and first harmonic complex components of pressure coefficients: $\alpha = 4^o + 1^o \cos \omega t$.

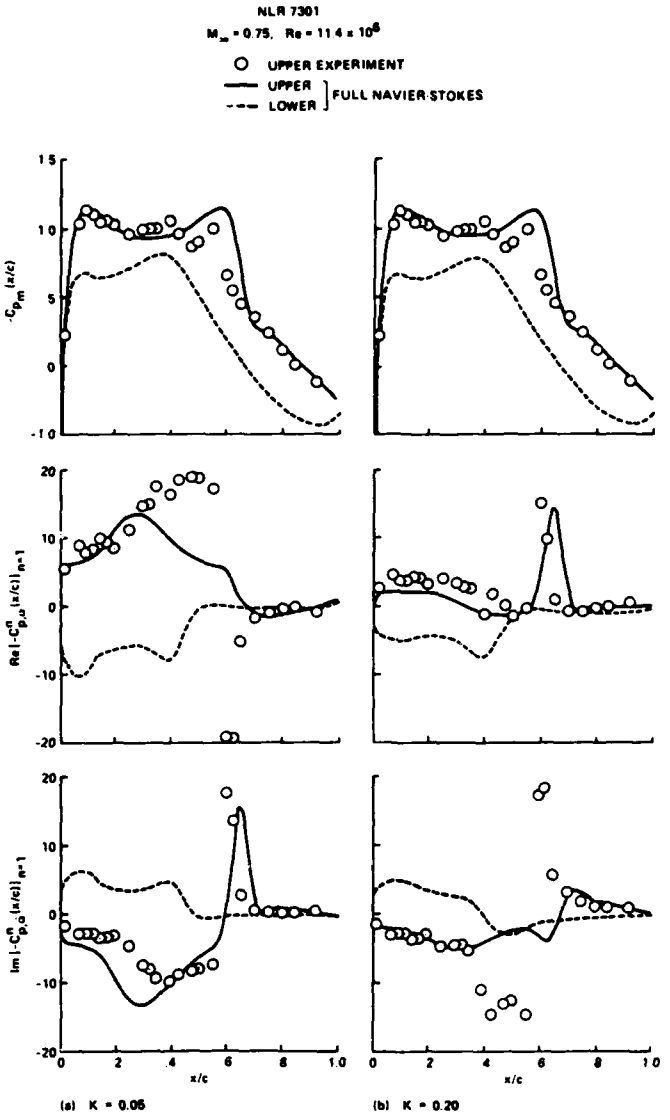

Figure 3-3. Mean and first harmonic complex components of pressure coefficients: $\alpha = 0.37^\circ + 0.5^\circ \cos \omega t$.

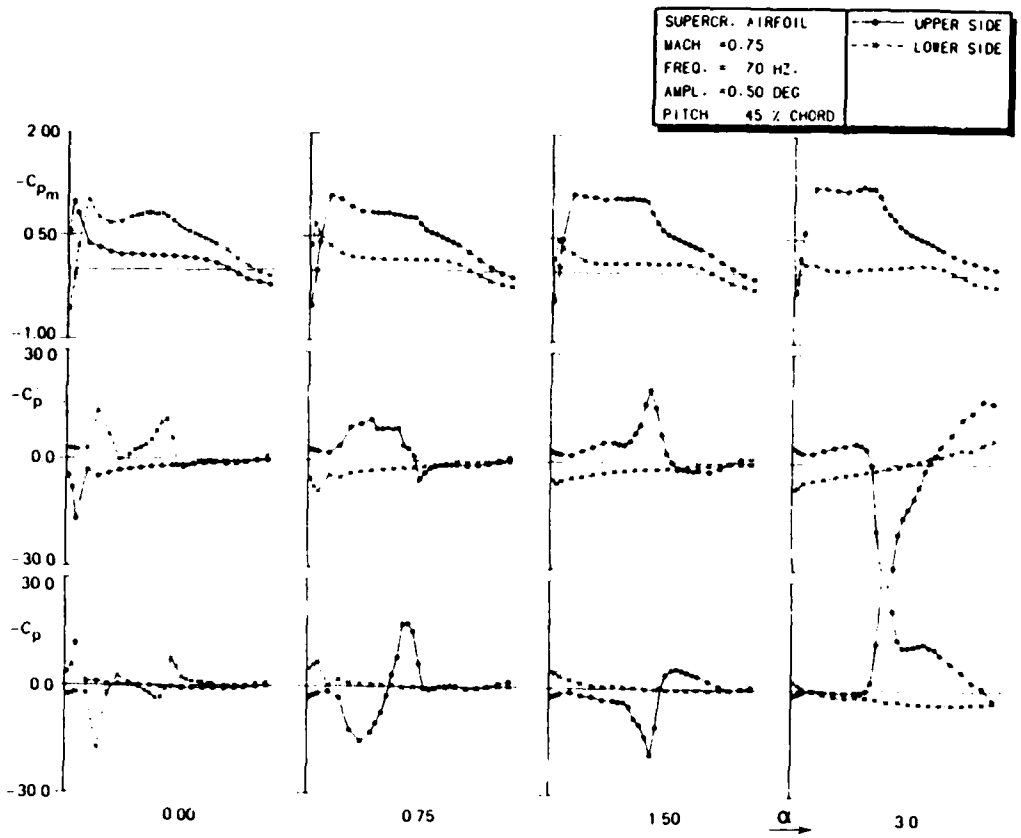

Figure 4-1. Mean and unsteady pressure distribution at four incidences.

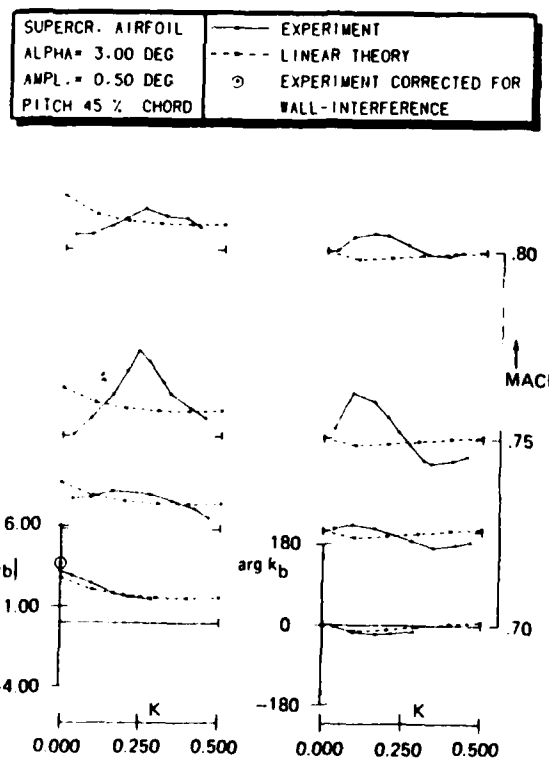

Figure 4-2. Influence of reduced frequency on unsteady lift coefficient, at various Mach numbers.

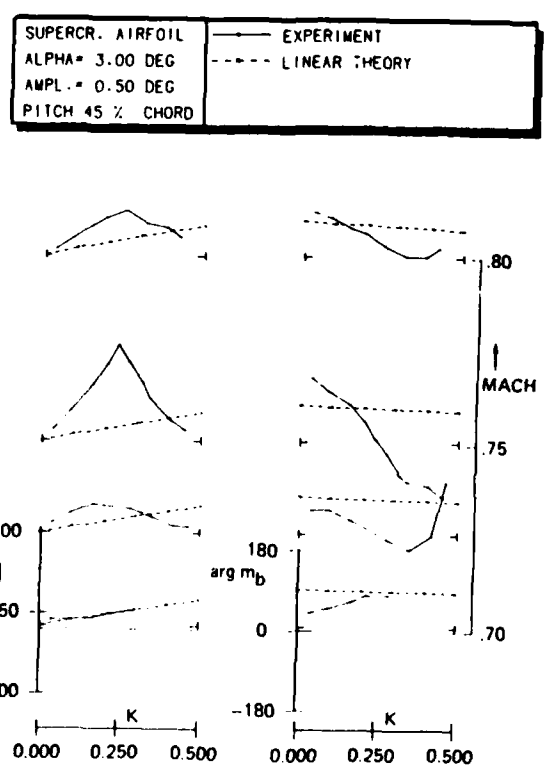

Figure 4-3. Influence of reduced frequency on unsteady moment coefficient, at various Mach numbers.

SUPERCR. AIRFOIL	+ EXPT.
ALPHA = 0.75 DEG	— SUBSONIC THEORY
AMPL = 0.5 DEG	TRANSONIC THEORY (LTRAN2-NLR)
F = 40 HZ	⊙ INVISCID
K ≈ 0.1	⊡ WEAK INTERACTION
PITCH 0.45 CHORD	■ STRONG INTERACTION

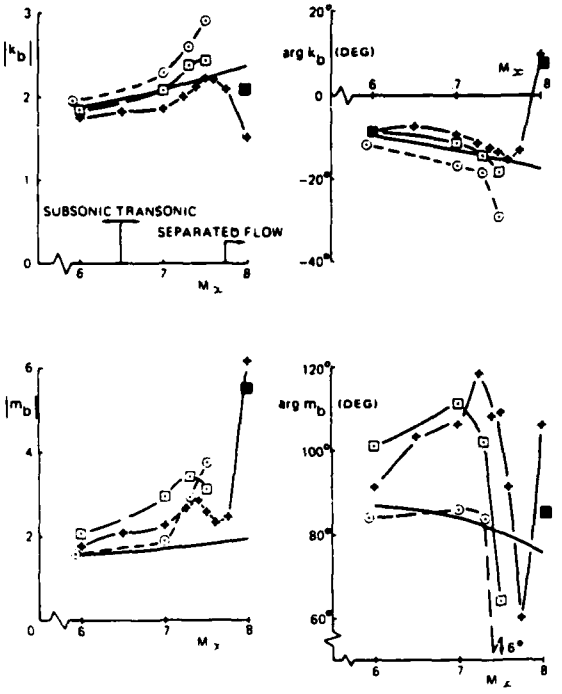

Figure 4-4. Unsteady lift and moment coefficients on an oscillating supercritical airfoil.

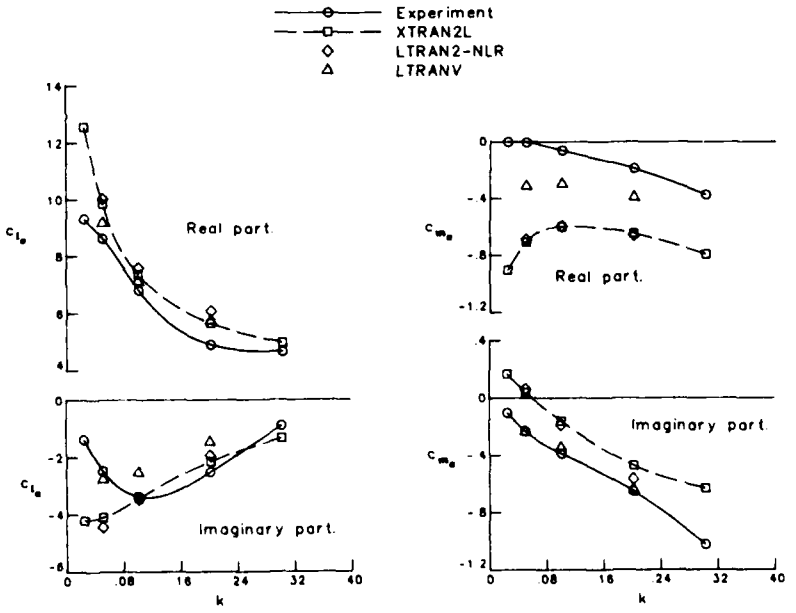

Figure 5-1. Comparison of unsteady forces for the NACA 64A010A airfoil at M = 0.796, $\alpha_0 = 1^0$ (CT 3-7).

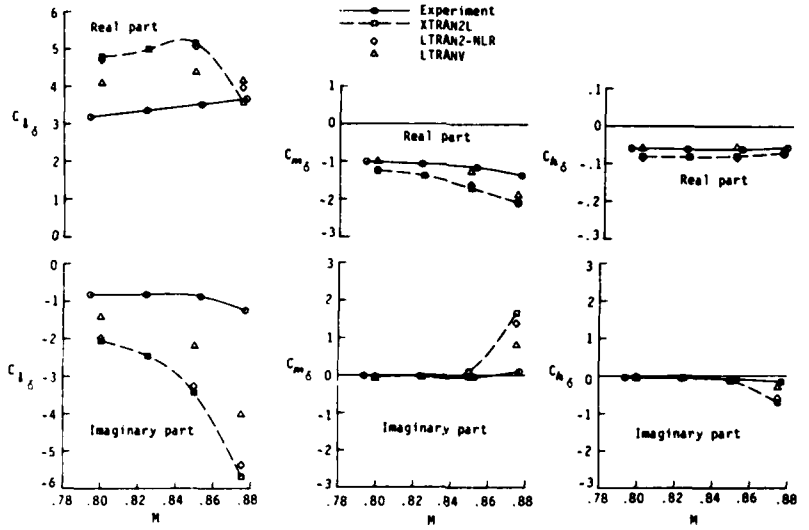

Figure 5-2. Comparison of unsteady forces for the NACA 64A006 airfoil at $\delta_0 = 1^o$, k = 0.06 (CT 1, 3, 6, 8).

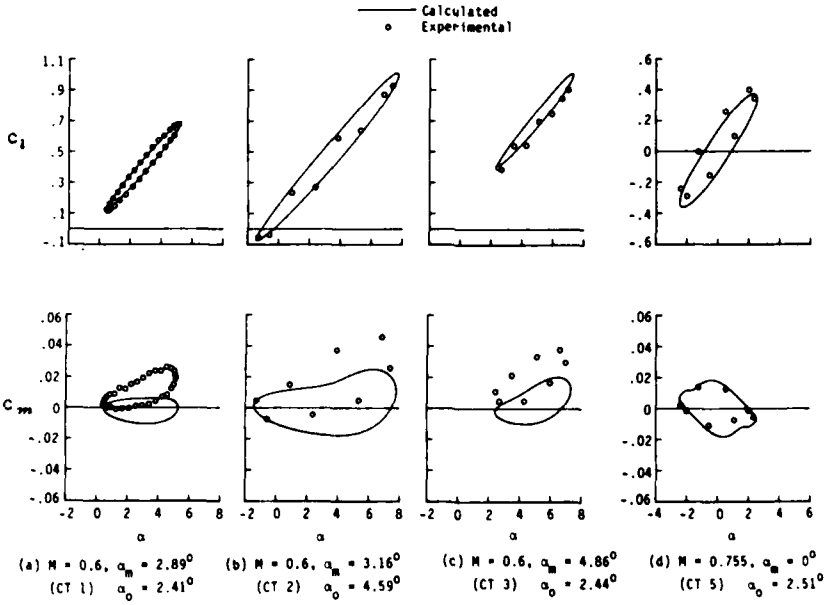

Figure 5-3. Comparison of unsteady forces for the NACA 0012 at k = 0.081 (CT 1-3, 5).

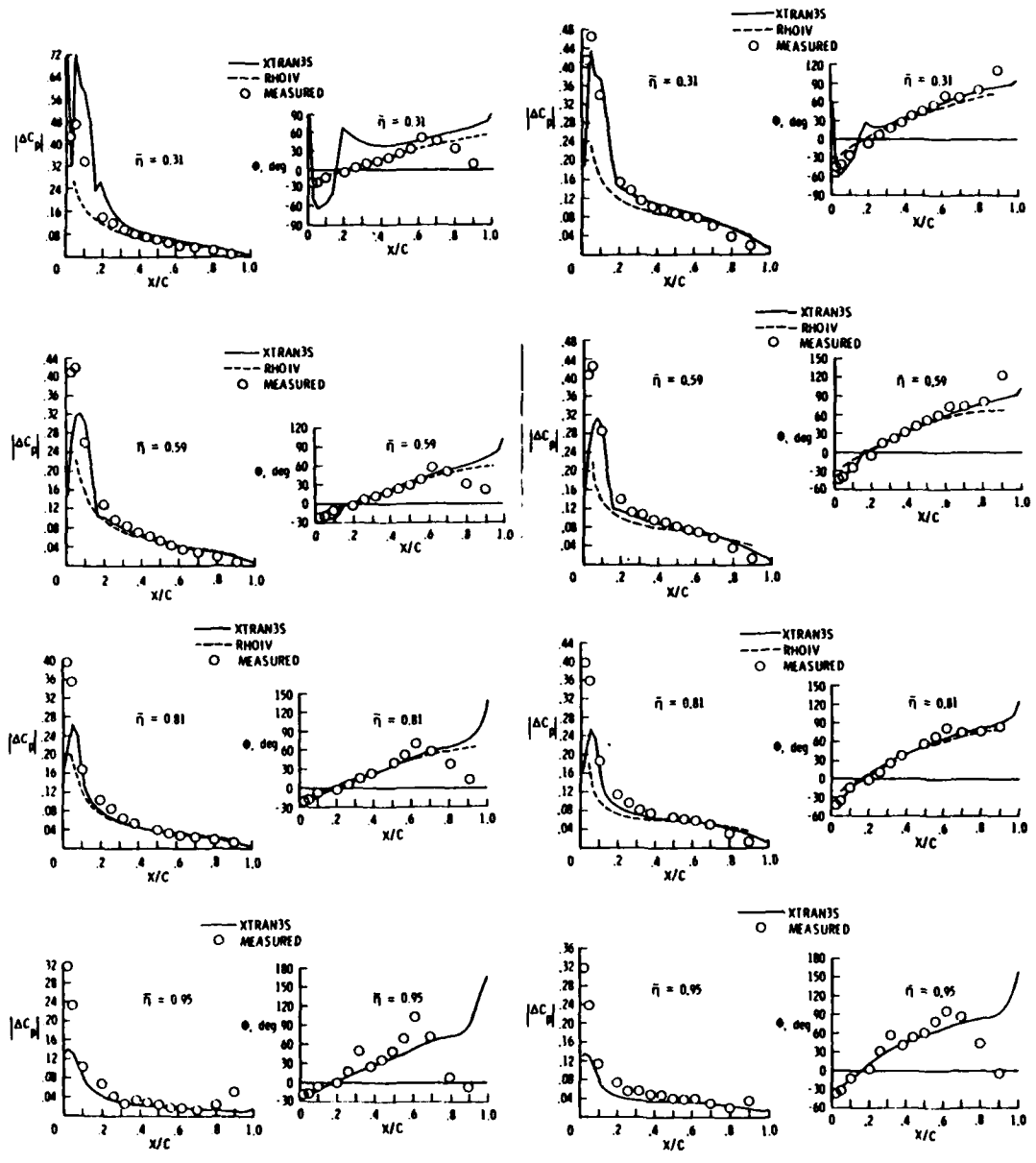

Figure 5-4. Comparison of measured and calculated unsteady pressure distributions for rectangular supercritical wing at M = 0.7, $\alpha_m = 2^o$, $\alpha_o = 1^o$.

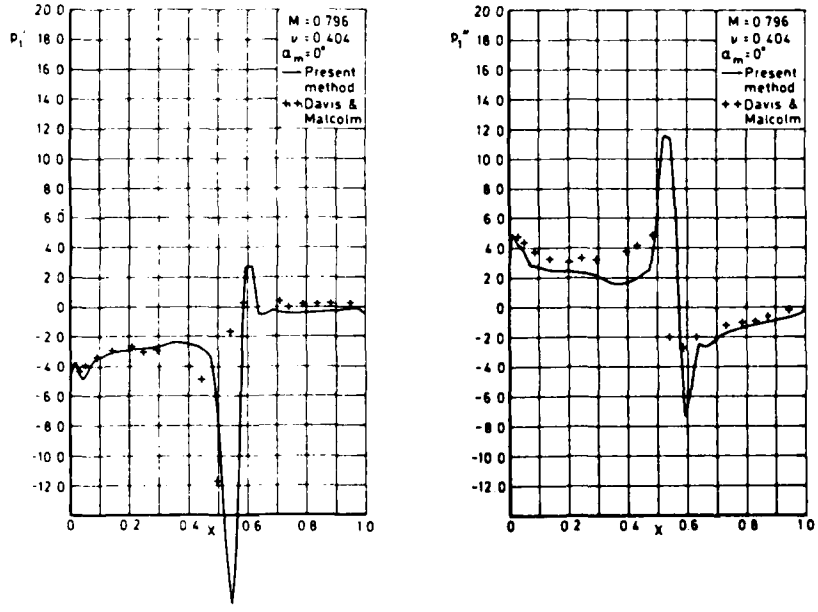

Figure 6-1. In-phase and in-quadrature parts of first harmonic pressure distribution for oscillation in pitch about the quarter chord of NACA 64A010 (Ames model).

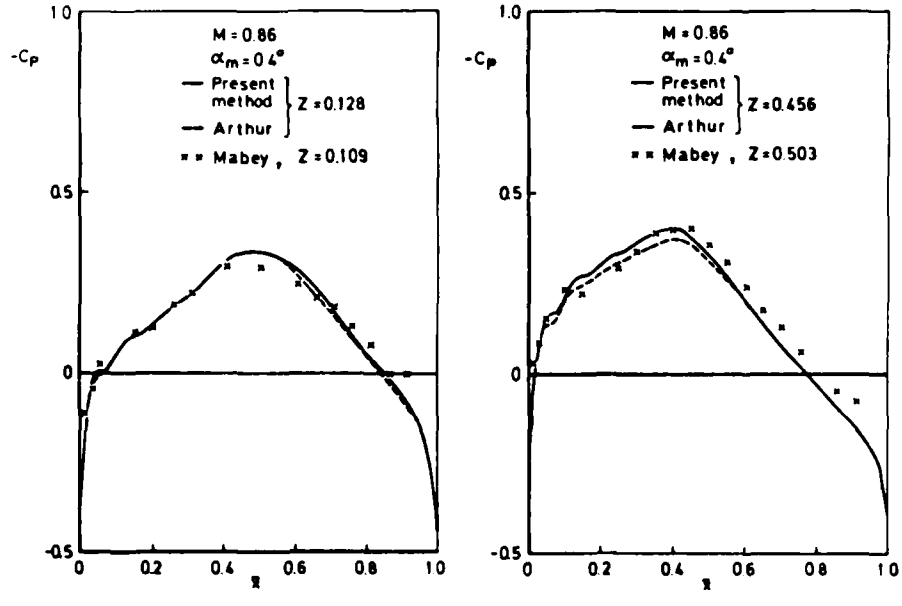

Figure 6-2. Steady pressure distribution for AGARD tailplane

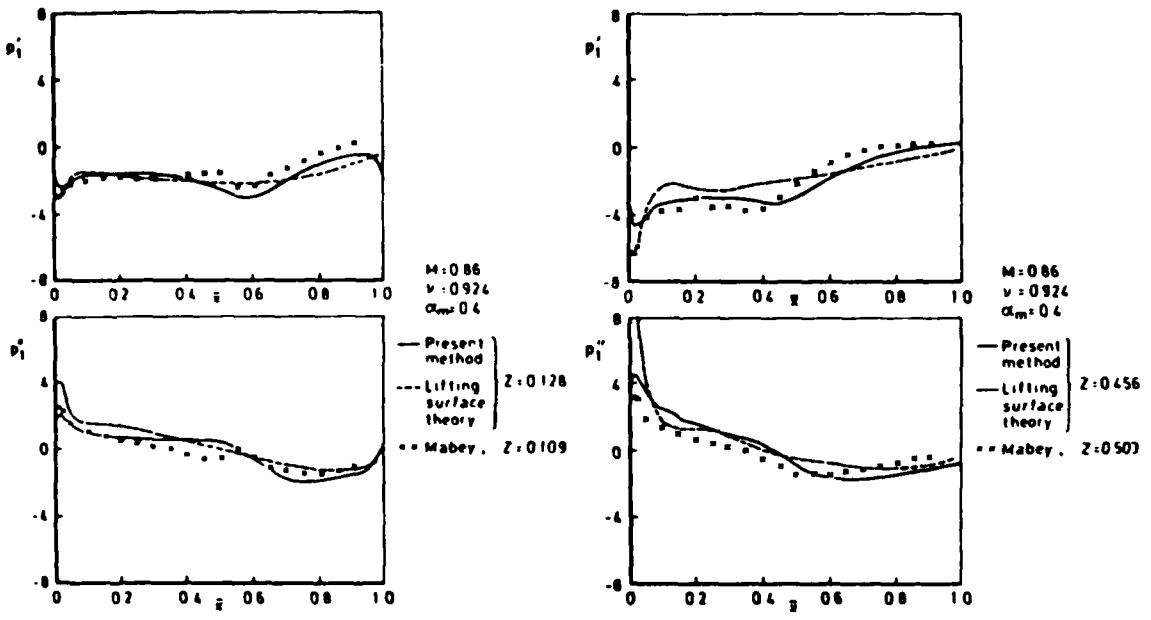

Figure 6-3. In-phase and in-quadrature parts of first harmonic pressure distribution for oscillation in pitch of AGARD tailplane.

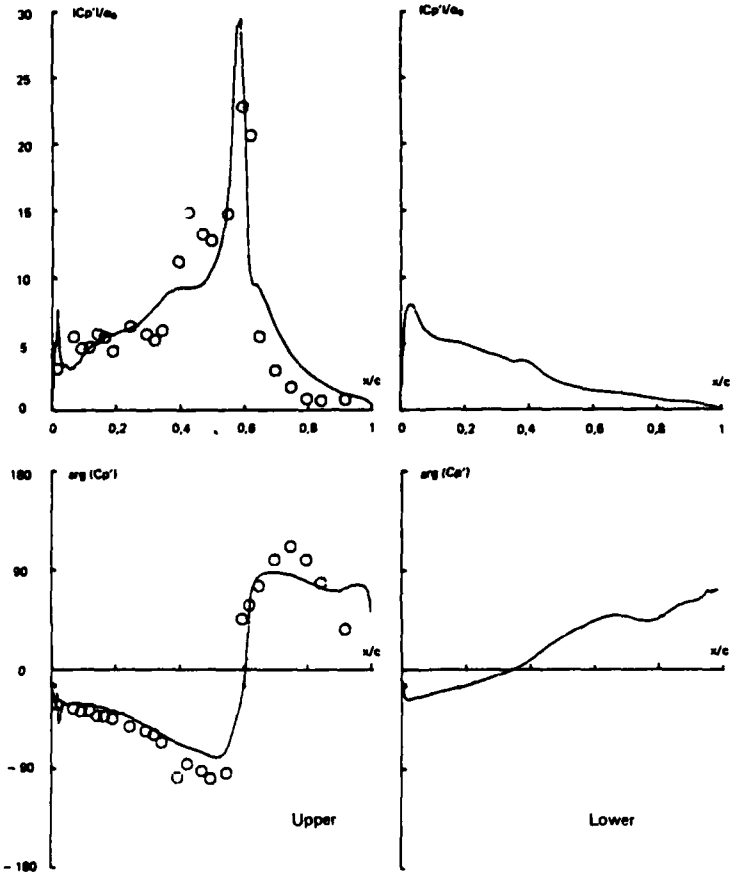

Figure 7-1. Profile NLR 7301. M = 0.75; $\alpha = 0.37^{o} - 0.5^{o} \sin \omega t$; Re = 11 x 10^{6}; k = 0.40.
First harmonic of pressure coefficient. (Calculated---, test NASA Ames o o o o).

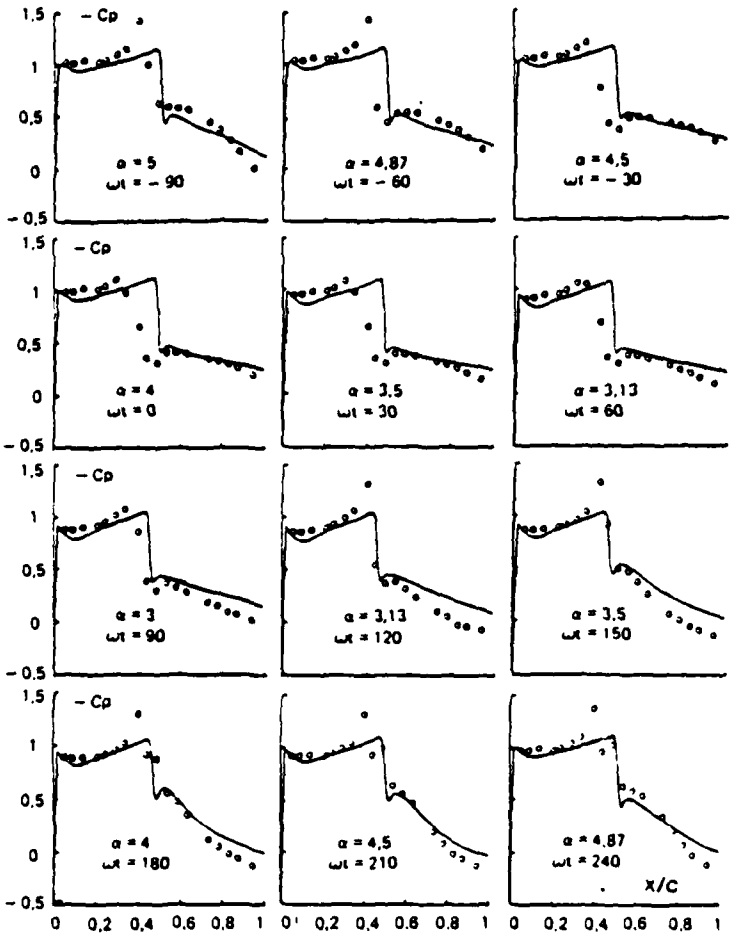

Figure 7-2. Profile NACA 64A010. M = 0.789; $\alpha = 4^{o} - 1^{o} \sin \omega t$; Re = 12 x 10^{6}; k = 0.40.
Instantaneous pressure coefficient. Upper surface. (Calculated---, test NASA Ames o o o o).

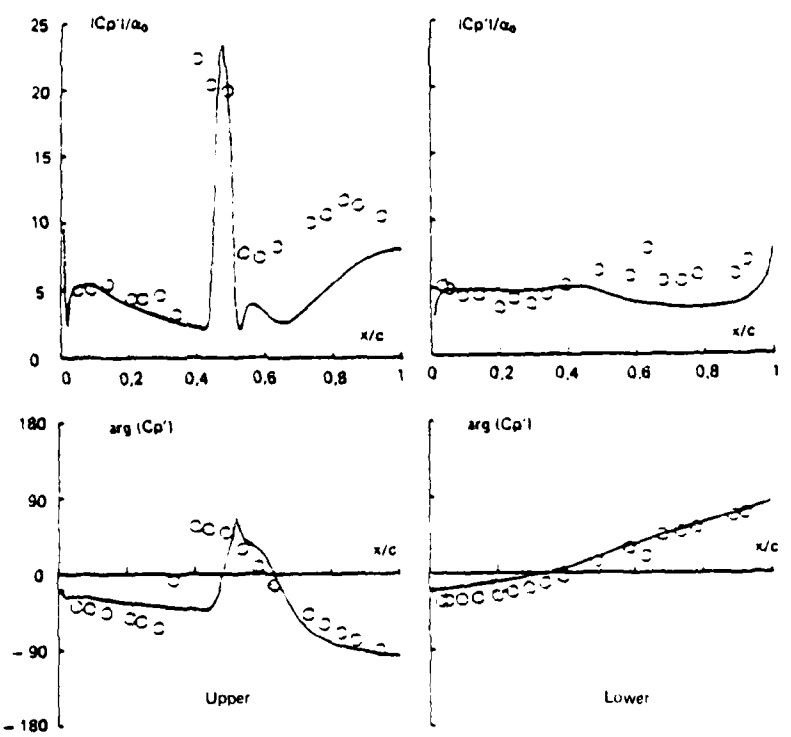

Figure 7-3. Profile NACA 64A010. M = 0.789; $\alpha = 4^{o} - 1^{o} \sin \omega t$. Re = 12 x 10^{6} k = 0.40
First harmonic pressure coefficient. (Calculated---, test NASA Ames o o o o).

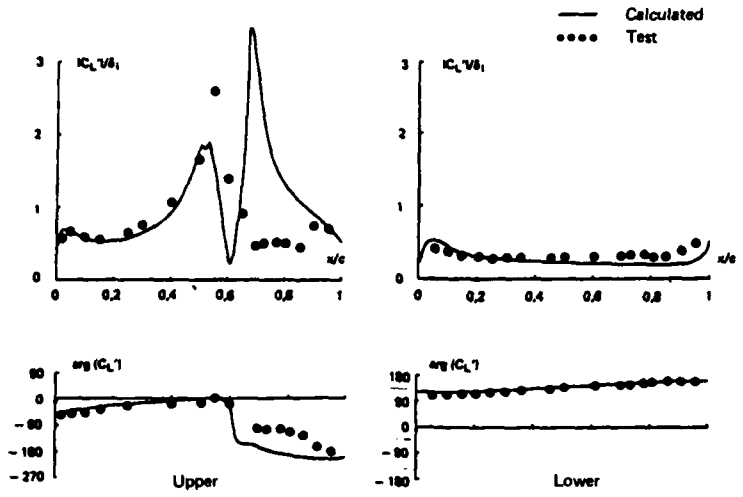

Figure 7-4. Profile RA 16SC1 with oscillating spoiler. First harmonic of pressure coefficient. ($M = 0.06$; $\alpha_m = 0^o$; $Re = 4 \times 10^6$; $\delta_{sp} = 10^o \cdot 1^o \sin \omega t$; $k = 0.30$).

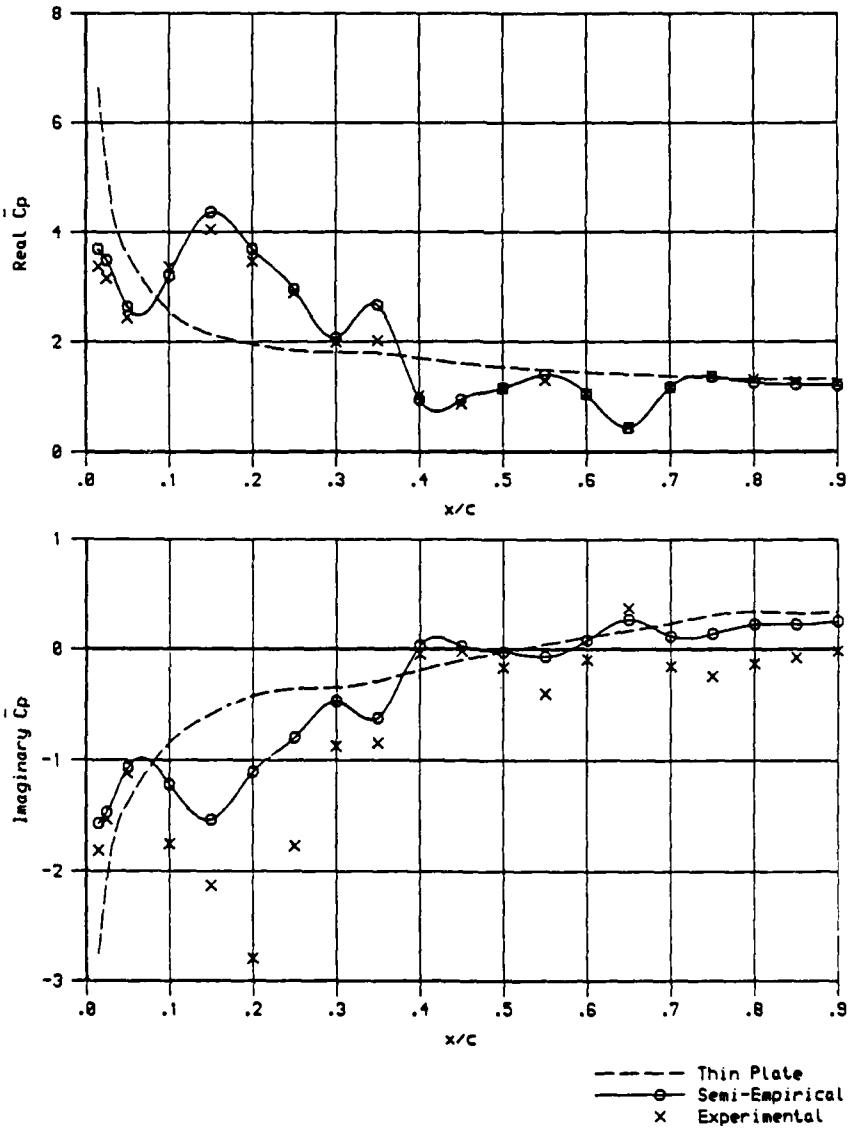

Figure 8-1. Oscillatory lower surface pressures, Section 3, M = 1.32, Frequency (Hz) = 70.0, Incidence = -5.0.

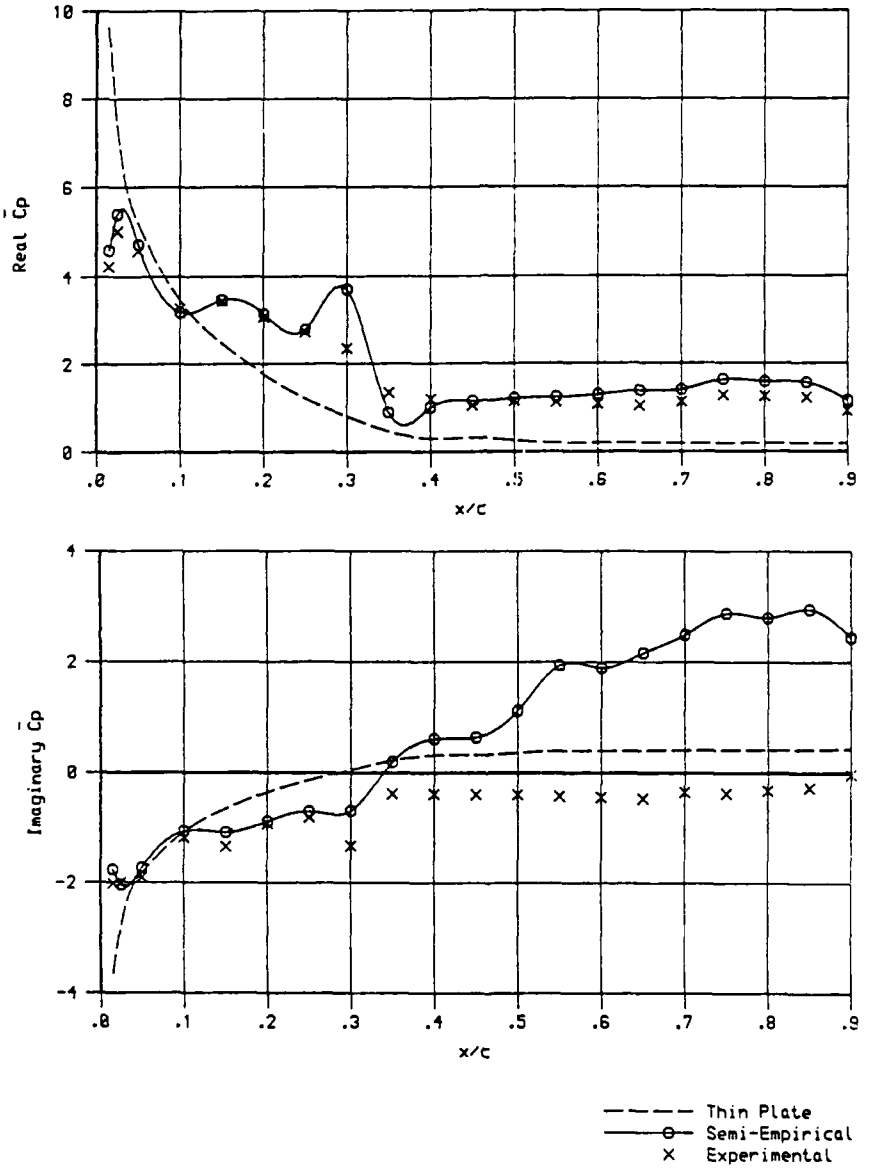

Figure 8-2. Oscillatory lower surface pressures, Section 5, M = 1.32, Frequency (Hz) = 70.0, Incidence = -2.0.

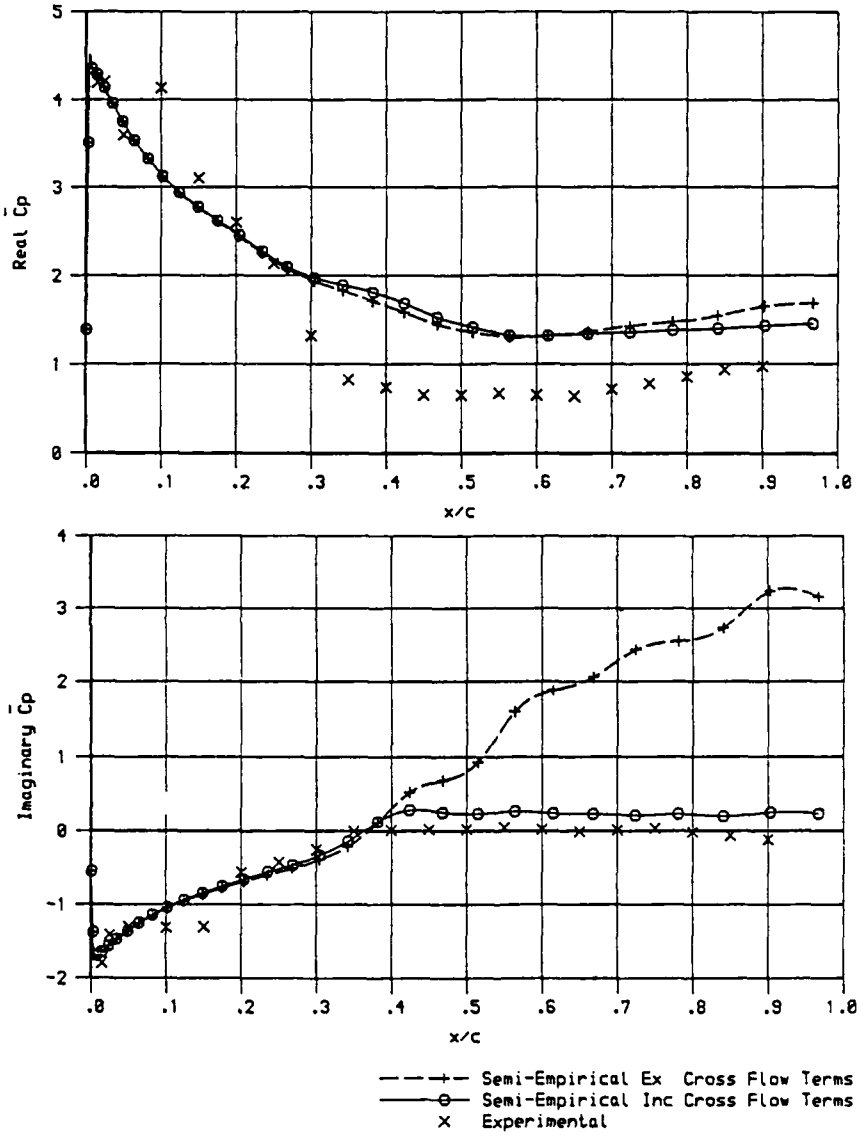

Figure 8-3. Oscillatory lower surface pressures, Section 5, M = 1.32, Frequency (Hz) = 70.0, Incidence = 0.0.

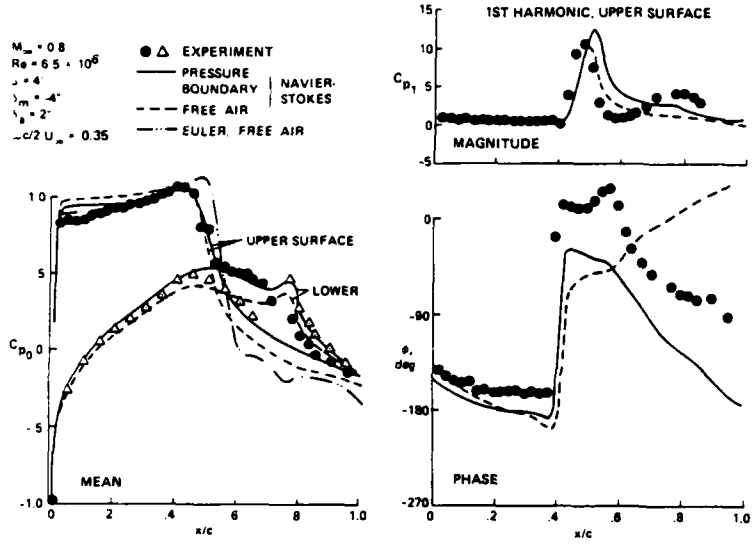

Figure 9-1. Transonic viscous flow over an airfoil with an oscillating flap.

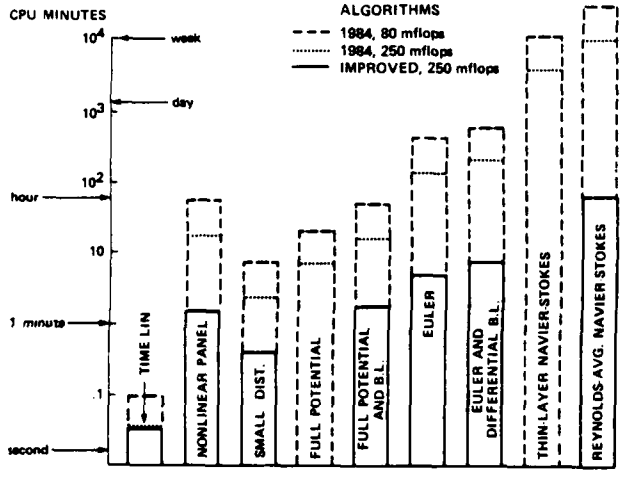

Figure 9-2. Solution times for a wing of moderate complexity; 75 chords travel/case, improved algorithms, 250 mflops.

Model	Physical Generality	Numerical Compatibility	Remarks
Viscous wedge	Very low	Very high	Shock-B.L. interaction
Integral B.L.	Low	High	Very good when highly tuned
Eddy viscosity			
Zero eqn	Low	High	Needs more tuning
.			
.			
.			
2-eqn	Medium	Low to high	ΔW_{GT} = 20%, $\Delta\tau$ = ?
Reynolds stress equations	High	Low	3-D separation?
Large eddy	Very high	Low (?)	Guidelines for above
Complete simulation	Complete	nth generation supercomputers	

Figure 9-3. Turbulence models.

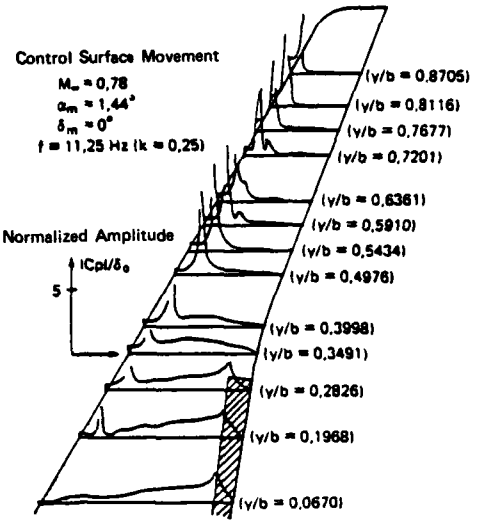

Figure 10-1. Distribution of unsteady experimental pressures (upper) at spanwise stations.

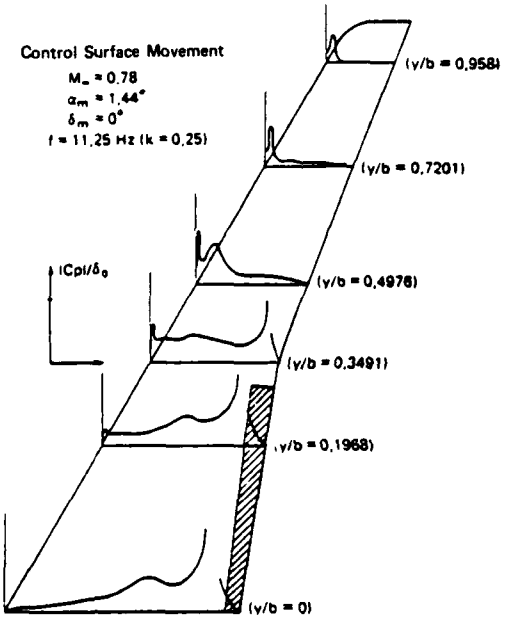

Figure 10-2. Distribution of calculated unsteady pressures (upper) at spanwise stations.

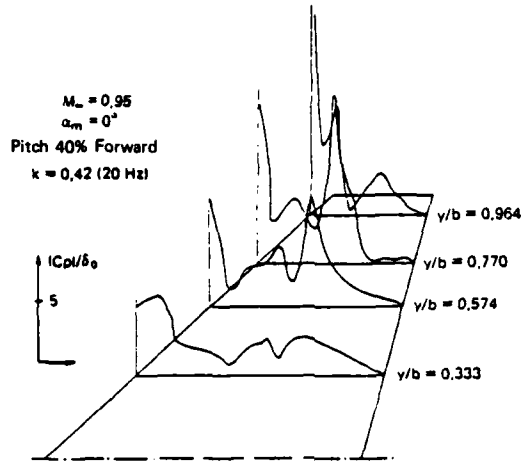

Figure 10-3. Distribution of experimental unsteady pressures at spanwise stations. Normalized amplitude/Cpl/α_0.

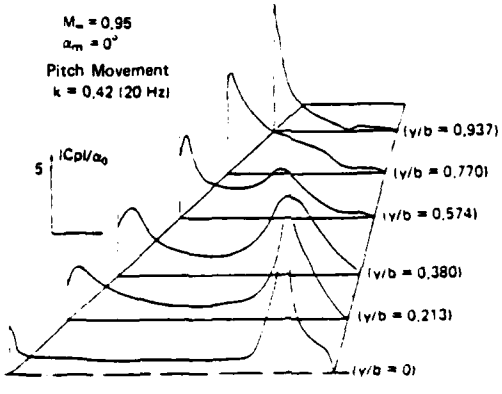

Figure 10-4. Distribution of calculated unsteady pressures at spanwise stations. Normalized amplitude/Cpl/α_0.

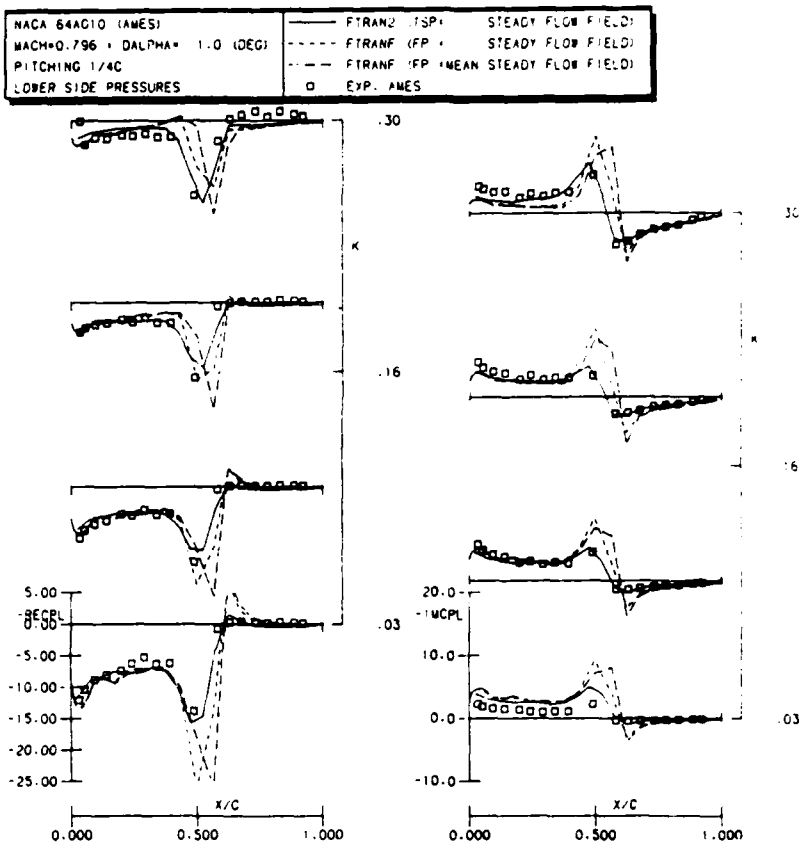

Figure 11-1. Experimental and calculated frequency-wise distributions of unsteady pressure coefficients.

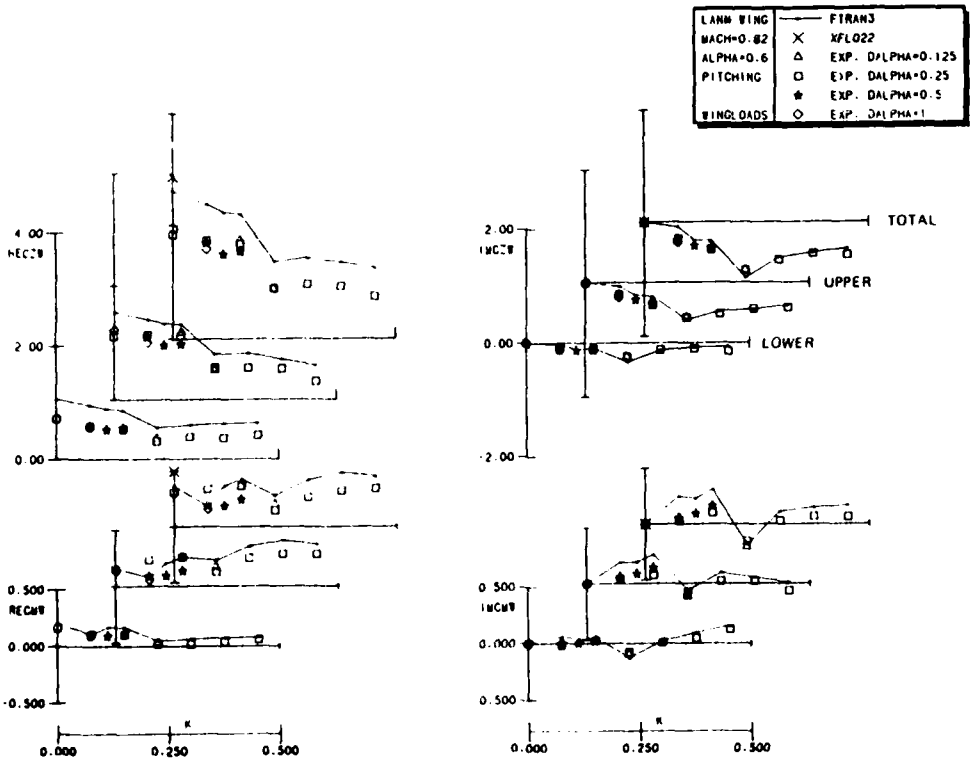

Figure 11-2. Comparison of experimental and calculated unsteady lift and moment coefficients on LANN wing.

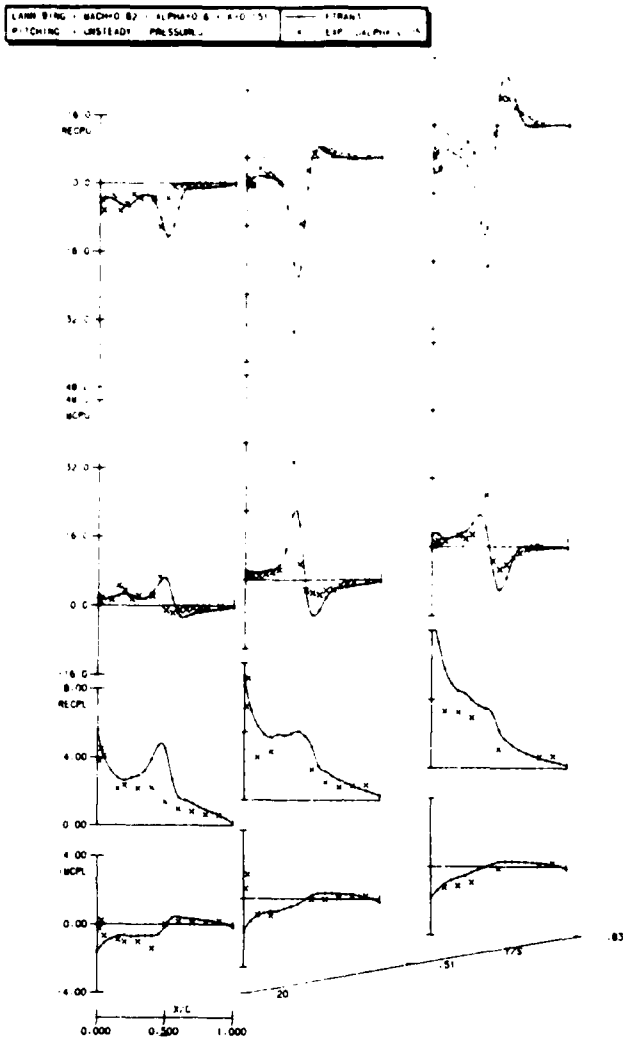

Figure 11-3. Comparison of experimental and calculated distributions of unsteady pressure coefficients at low reduced frequency.

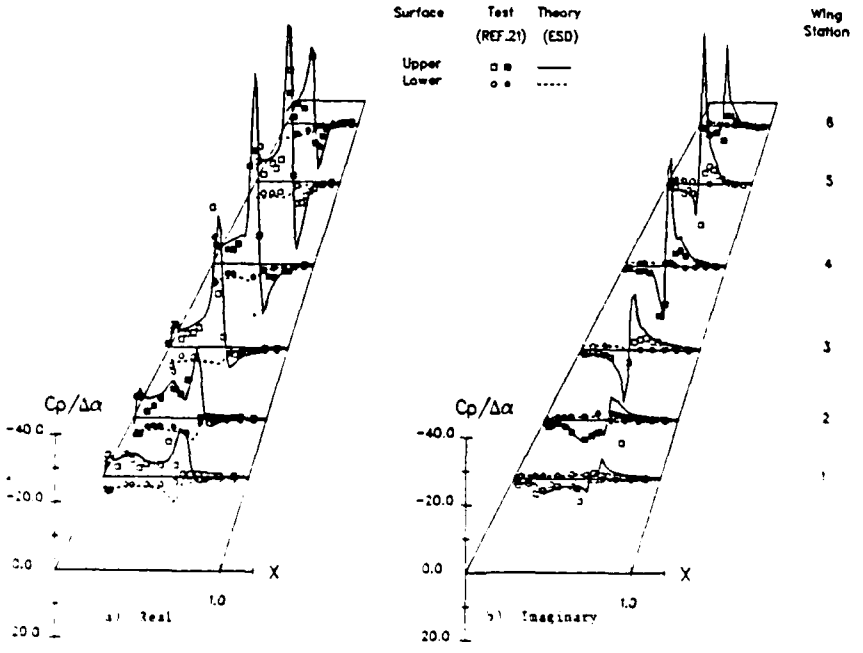

Figure 12 1. Unsteady pressures on the LANN wing, M_∞ = 0.82, k = 0.076, α_0 = 0.62 degrees.

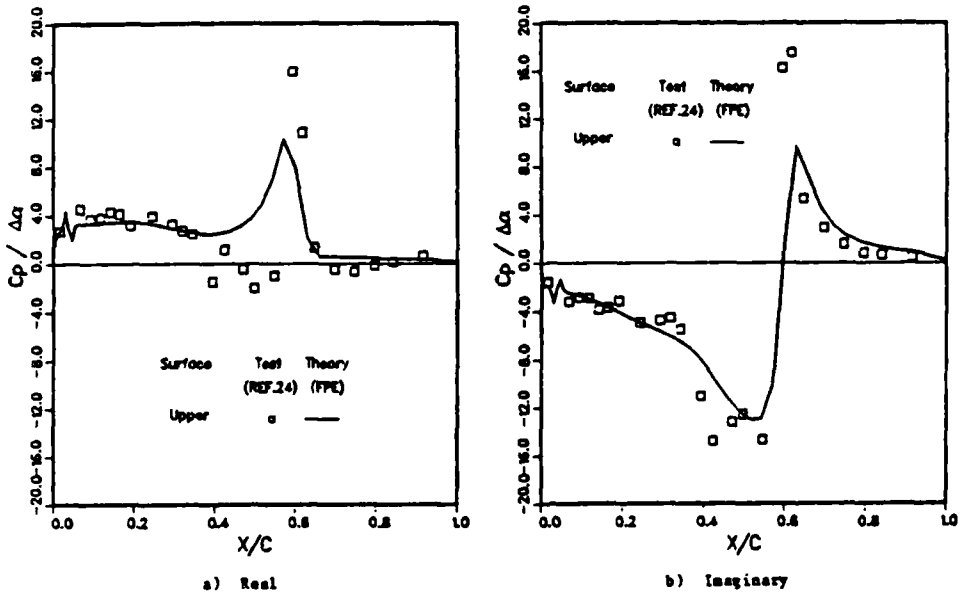

Figure 12-2. Unsteady pressures on a NLR 7301 airfoil, M_∞ = 0.751, k = 0.201, α_0 = 0.37 degrees.

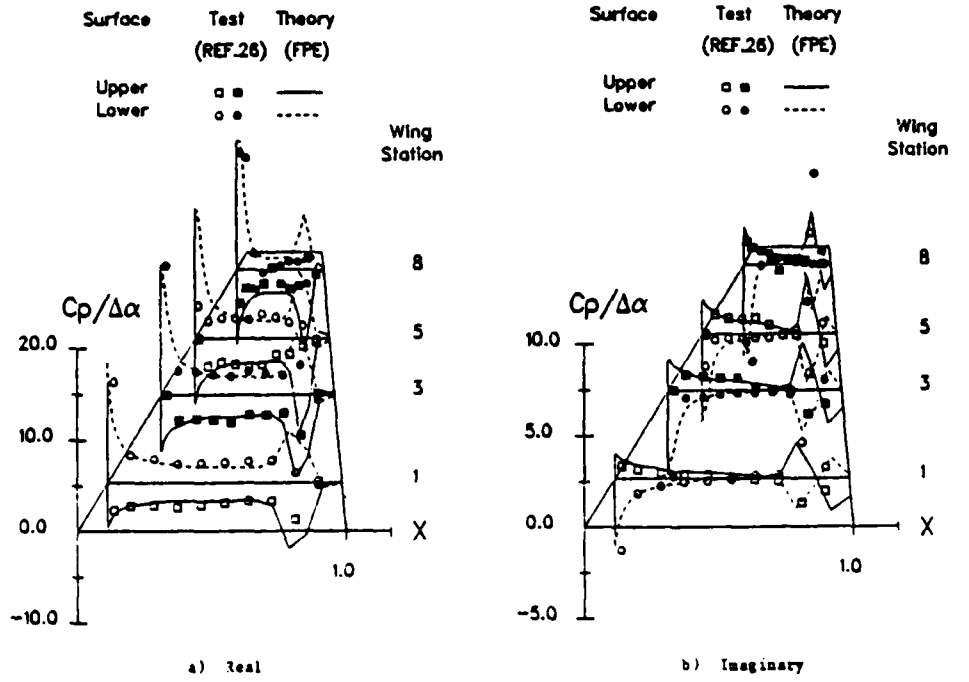

Figure 12-3. Unsteady pressures on the F-5 wing, M_∞ = 0.95, k = 0.132, α_0 = 0.0 degrees.

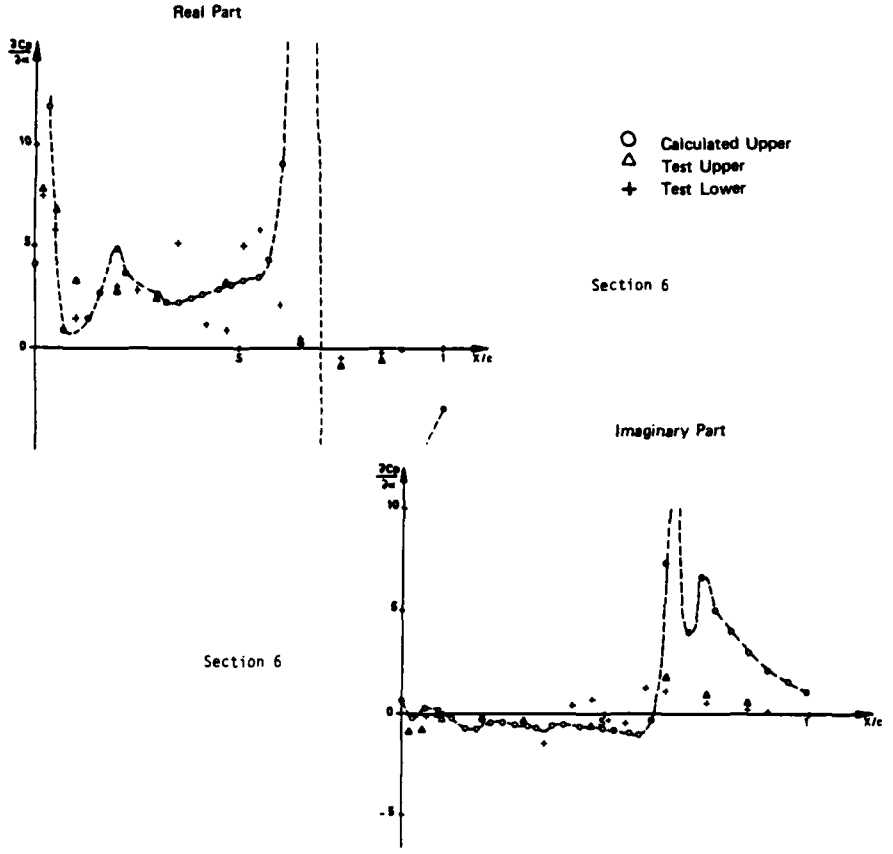

Wing F1 M = 0.95 f = 10 Hz Pitch 0.25° Zero Incidence

Figure 13-1. Comparison between theory and test of unsteady Cp.

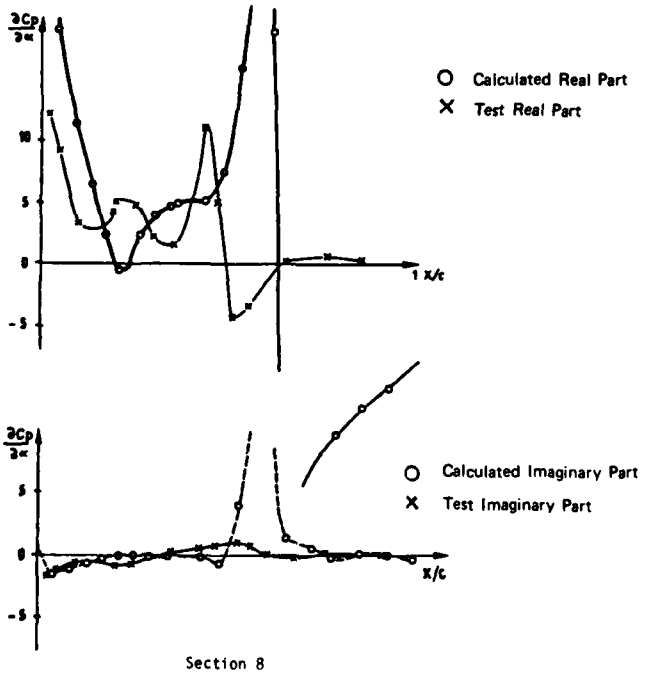

Wing F1 M = 0.95 f = 10 Hz Pitch 0.25° Zero Incidence

Figure 13-2. Comparison between theory and test of unsteady Cp.

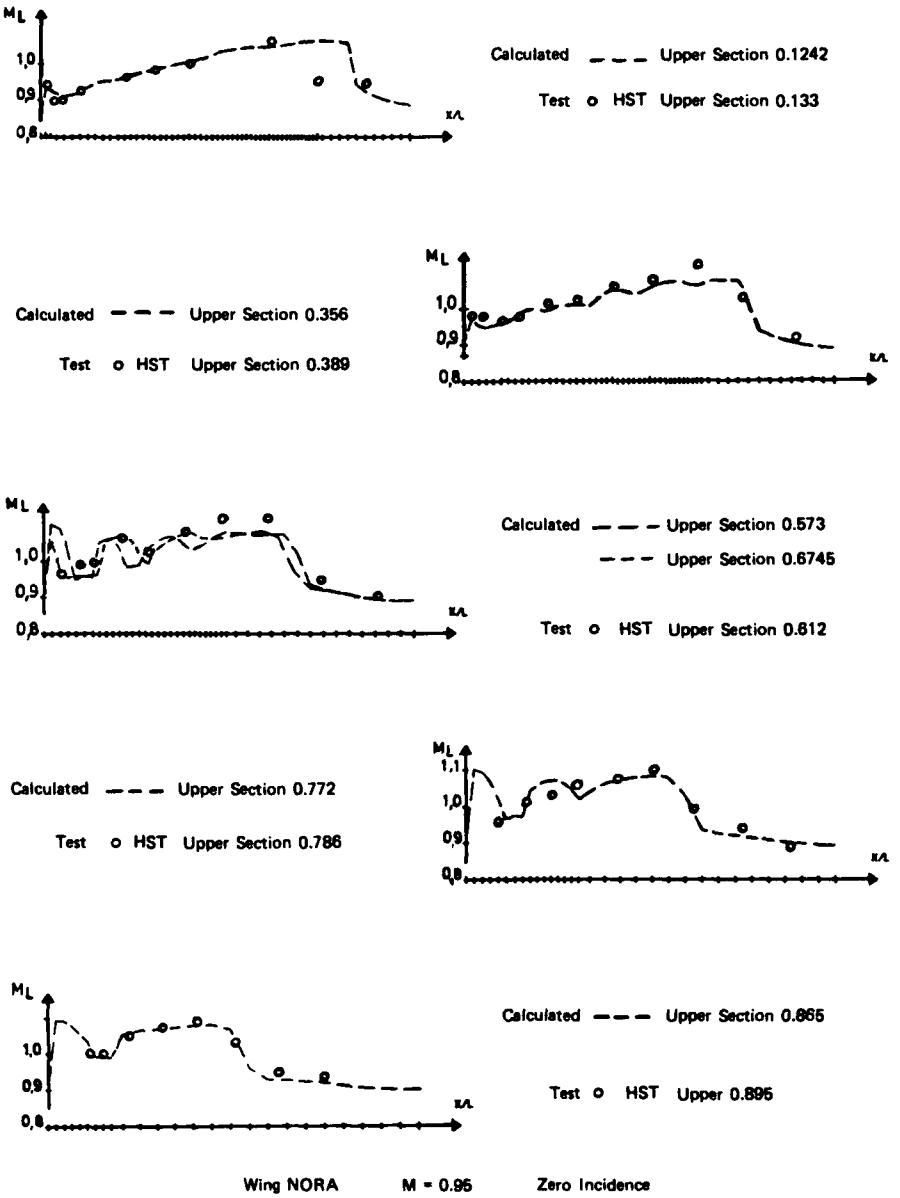

Figure 13-3. Comparison between theory and experiment steady flow.

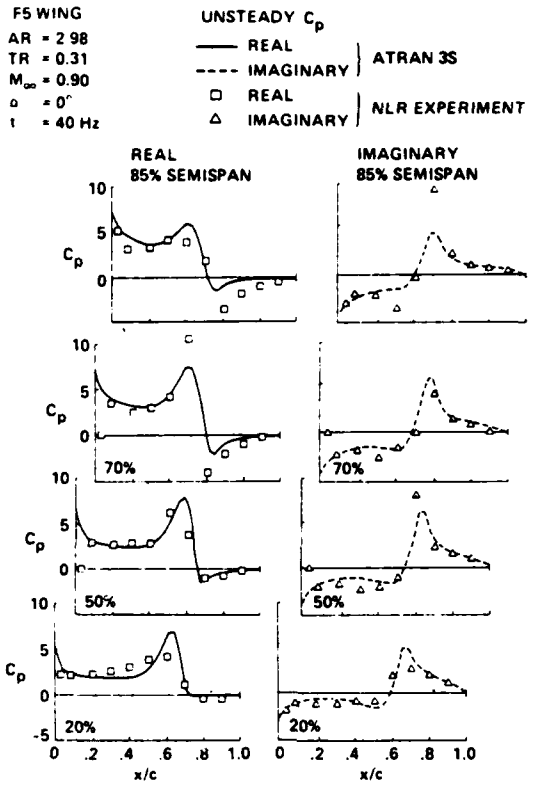

Figure 14-1. Comparison of unsteady pressures, theory and experiment: M = 0.90.

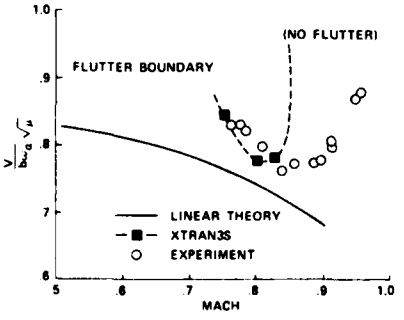

Figure 14-2. XTRAN3S flutter boundary for the Japanese transport wing.

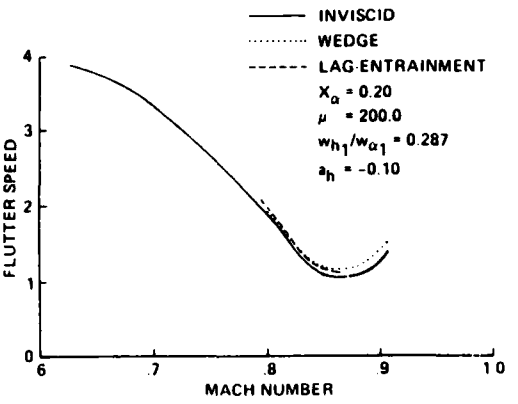

Figure 14-3. Effect of Mach number and viscosity on flutter speed of the rectangular wing.

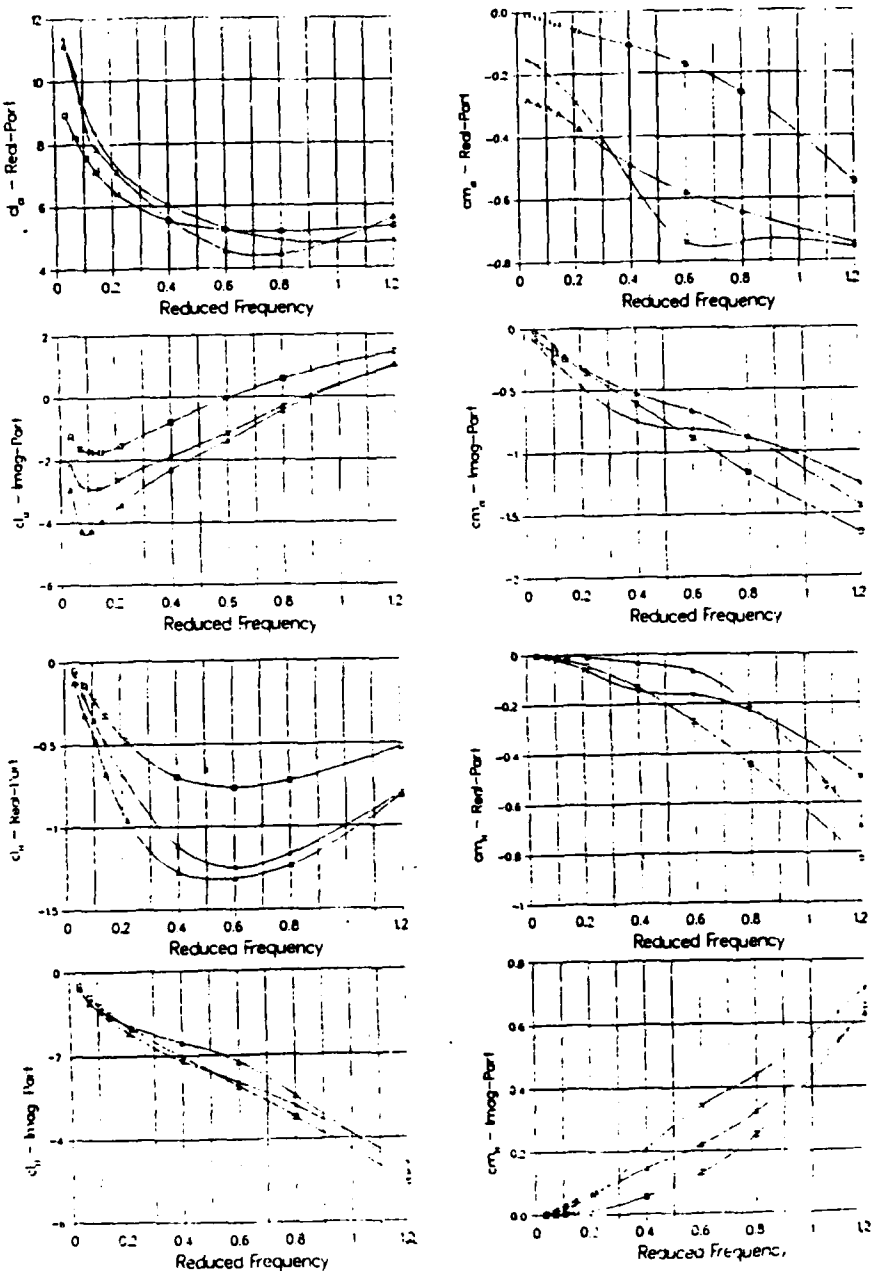

Δ TSP

× Lin. TSP

□ Doublet-Lattice

Figure 15-1. Unsteady aerodynamic coefficients: M = 0.765, $\alpha = 0.850^{o}$.

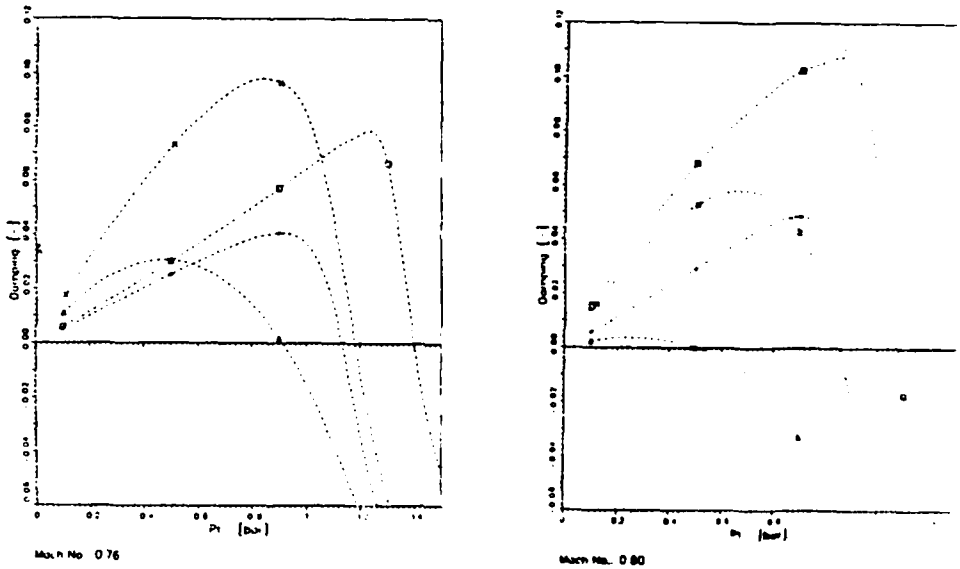

Figure 15-2. Flutter calculation results for low frequencies (f = 10 and 30 Hz)

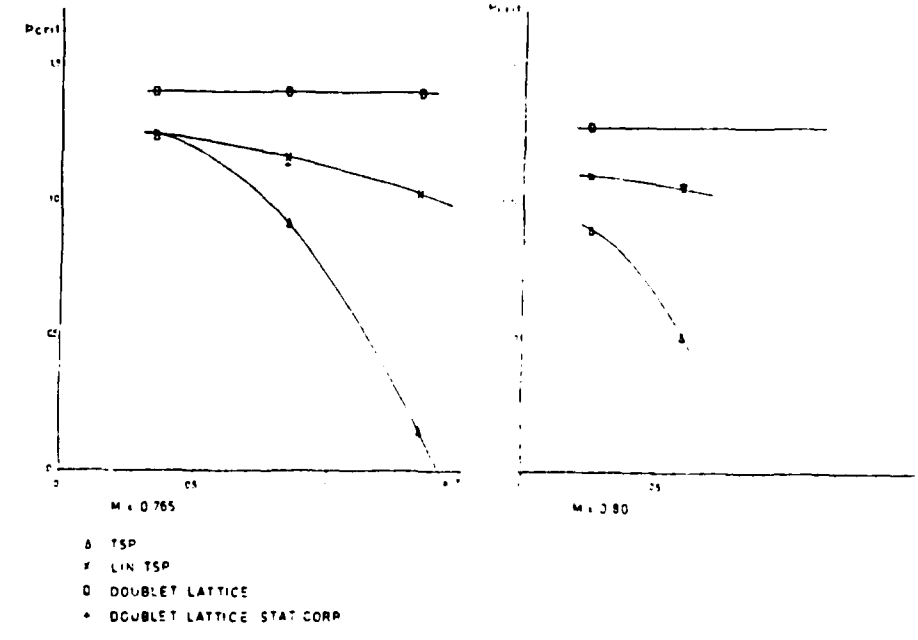

Figure 15-3. Influence of incidence on flutter for low frequencies.

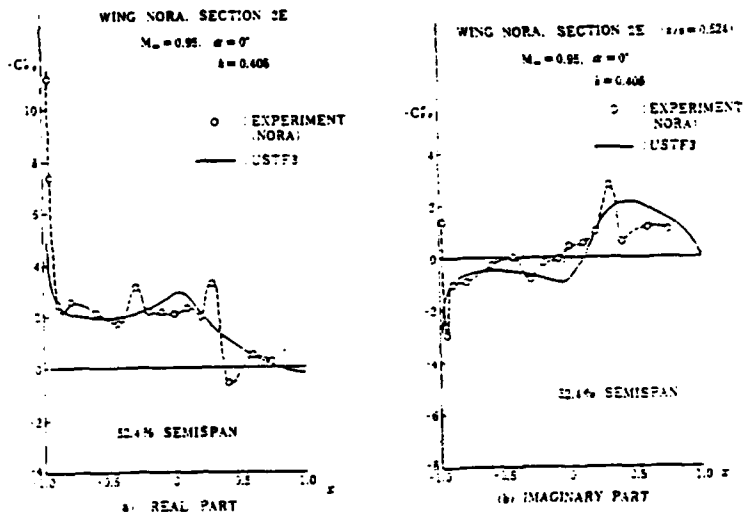

Figure 16-1. Unsteady pressure distributions (first harmonics) on upper surface of oscillating NORA Wing.

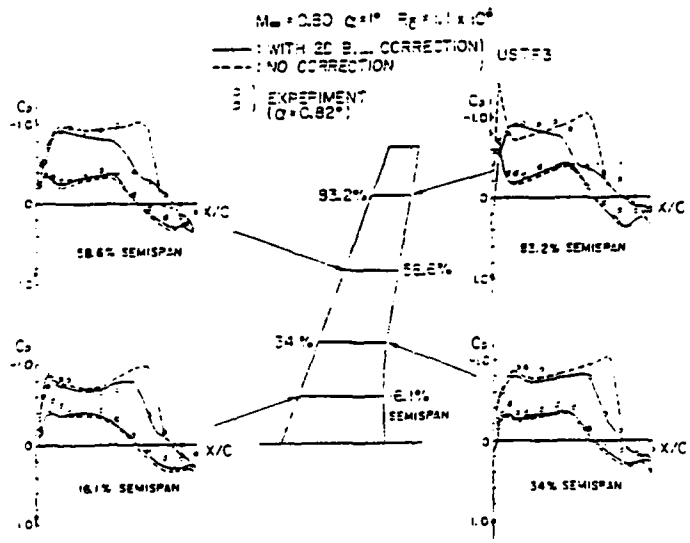

Figure 16-2. Calculated and experimental steady-state pressure distributions on high-aspect-ratio transport wing. Experimental data courtesy of JADC.

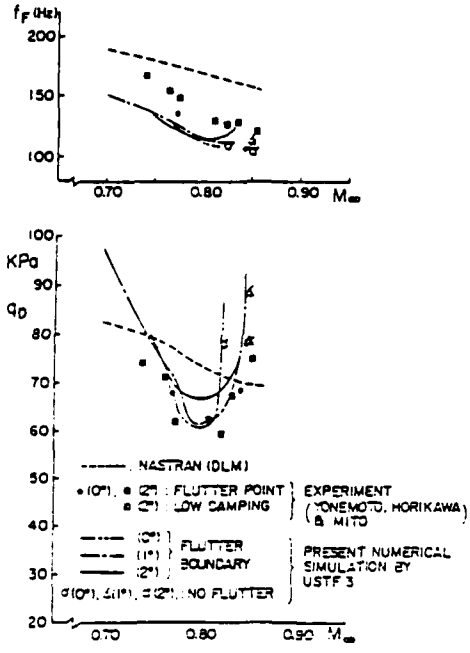

Figure 16-3. Comparison of calculated and experimental flutter boundary for high-aspect-ratio transport wing.

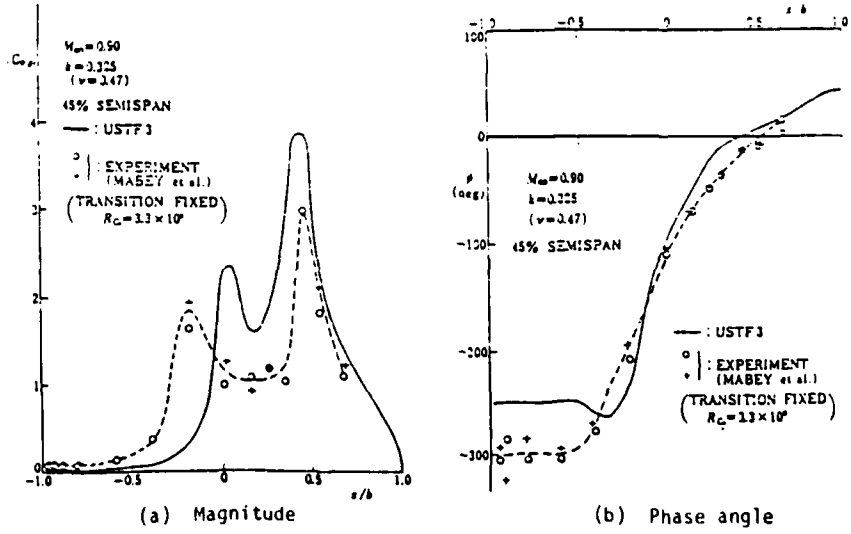

Figure 16-4. Calculated and experimental unsteady pressure distributions (first harmonics) on upper surface of RAE Swept Tapered Wing with oscillating part-span control surface.

TRANSONIC AERODYNAMIC AND AEROELASTIC CHARACTERISTICS OF A VARIABLE SWEEP WING

P. M. Goorjian
NASA Ames Research Center, Moffett Field, California 94035, USA

G. P. Guruswamy
Informatics General Corporation, Palo Alto, California 94035, USA

H. Ide
Rockwell International, Los Angeles, California 90009, USA

and

G. Miller
Rockwell International, Los Angeles, California 90009, USA

SUMMARY

The flow over the B-1 wing is studied computationally, including the aeroelastic response of the wing. Computed results are compared with results from wind tunnel and flight tests for both low-sweep and high-sweep cases, at 25.0° and 67.5°, respectively, for selected transonic Mach numbers. The aerodynamic and aeroelastic computations are made by using the transonic unsteady code ATRAN3S. Steady aerodynamic computations compare well with wind tunnel results for the 25.0° sweep case and also for small angles of attack at the 67.5° sweep case. The aeroelastic response results show that the wing is stable at the low sweep angle for the calculation at the Mach number at which there is a shock wave. In the higher sweep case, for the higher angle of attack at which oscillations were observed in the flight and wind tunnel tests, the calculations do not show any shock waves. Their absence lends support to the hypothesis that the observed oscillations are due to the presence of leading edge separation vortices and are not due to shock wave motion as was previously proposed.

1. INTRODUCTION

The variable sweep B-1 wing has been observed to undergo aeroelastic oscillations at certain angles of attack in both flight and wind tunnel tests (Refs. 1 and 2). These oscillations occurred in the transonic regime at both low- and high-sweep angles. Motivated by these observations, in this paper the flow over the B-1 wing is studied computationally, including the aeroelastic response of the wing. Computed results are compared with results from the wind tunnel and flight tests for both the low- and high-sweep cases. In the low-sweep case, the comparisons demonstrate the capability of the computational methods to properly stimulate the flow in the presence of shock waves. In the high-sweep case, where the sweep angle is equal to 67.5°, the comparisons at a low-angle of attack demonstrate the capability of the computational methods to properly simulate the flow at an extreme sweep angle. Finally, a comparison is presented in the high-sweep case for a higher angle of attack at which oscillations were observed. The calculations do not show any shock waves. Their absence lends support to the hypothesis (private communication, Yoshihara, 1984) that the observed oscillations at the high-sweep angle are separation-induced oscillations (SIO). These oscillations are due to the presence of leading-edge separation vortices, and not due to shock-induced oscillations as previously proposed (Ref. 1).

To study the transonic aeroelastic characteristics of wings, efficient computational tools are required to compute unsteady flows over wings. There is an extensive effort in the area of computational fluid dynamics (CFD) (Ref. 3) to develop methods for transonic unsteady aerodynamics. To date methods based on the small disturbance potential theory (Ref. 4) are being routinely used in two-dimensional aeroelastic analysis (Ref. 5). The use of three dimensional methods for practical wings has begun.

An unsteady, small-disturbance transonic code called XTRAN3S that is based on a time-integration method was developed by Borland and Rizzetta (Ref. 6) as an extension to three dimensions. Also this code has the capability of conducting static and dynamic aeroelastic computations by simultaneously integrating the aerodynamic and structural equations of motion. The authors illustrated the capability of XTRAN3S by computing flutter boundaries for a rectangular wing with a 6% thick parabolic-arc airfoil section at transonic Mach numbers. Guruswamy and Goorjian (Ref. 7), and Seidel et al. (Ref. 8) have illustrated the applications to other rectangular wings and Myers et al. (Ref. 9) have illustrated the applications to a transport wing with an aspect ratio of 8, a taper ratio of 0.4, and a leading-edge angle of 20°.

The use of the original version of XTRAN3S was limited to wings with high-aspect ratios, large taper ratios and small sweep angles because of the nature of the coordinate transformation employed. Guruswamy and Goorjian (Ref. 10) developed an alternate efficient coordinate transformation which is incorporated in ATRAN3S. ATRAN3S is a modified version of XTRAN3S with many other new features. As a result, ATRAN3S makes computations faster, more accurate, and more stable than XTRAN3S as is illustrated in Ref. 10 for the F-5 wing, which is a low-aspect, small-taper ratio, high-sweep, fighter wing. An improved version of the viscous corrections that were originally implemented in XTRAN3S by Rizzetta and Borland (Ref. 11) are presently in

ATRAN3S. The viscous computing capability of ATRAN3S was illustrated by Marstiller et al. (Ref. 12) for a rectangular wing and for a typical transport wing.

In this work, a transonic aeroelastic analysis is conducted for the B-1 wing, which is a variable sweep wing. The sweep angle of the wing varies from 15° to 67.5°, and the aircraft cruises in the transonic regime. Flight tests on the wing and wind tunnel tests (Ref. 2) on the 1/10 scale model of the wing showed angle of attack dependent zero damped aeroelastic oscillations. In a recent aeroelastic model experiment conducted in the NASA Ames 11- by 11-Foot Transonic Wind Tunnel (Ref. 2), significant aeroelastic limited oscillations in the wing-first bending mode were observed in the higher transonic regime over a narrow band of angles of attack. Those oscillations occurred at high-sweep angles of approximately 65°. At the sweep angle of 25°, some small aeroelastic oscillations were also observed, which were attributed to aerodynamic buffeting.

Motivated by these observations, the flow over the B-1 wing is studied computationally, including the aeroelastic response of the wing. The NASA Ames Research Center, transonic, unsteady, code ATRAN3S is used for this purpose. Aerodynamic and aeroelastic analyses are conducted at two sweep angles, 25.0° and 67.5° for selected Mach numbers, and the results are compared with wind tunnel and flight results.

2. AERODYNAMIC EQUATIONS OF MOTION

In this analysis the modified unsteady three-dimensional transonic small-disturbance equation is employed:

$$A\phi_{tt} + B\phi_{xt} = (E\phi_x + F\phi_x^2 + G\phi_y^2)_x + (\phi_y + H\phi_x\phi_y)_y + (\phi_z)_z \qquad (1)$$

where ϕ is disturbance velocity potential; $A = M_\infty^2$; $B = 2M_\infty^2$; $E = (1 - M_\infty^2)$; $F = -1/2(\gamma + 1)M_\infty^2$; $G = (1/2)(\gamma - 3)M_\infty^2$; and $H = -(\gamma - 1)M_\infty^2$.

This equation is solved in the computer code ATRAN3S by a time accurate finite-difference scheme that employs an alternating direction implicit (ADI) algorithm (Ref. 4). Whereas ATRAN3S employs the modified coordinate transformation technique (Ref. 10), it is noted here that the conventional transformation originally employed in XTRAN3S (Ref. 6) is not adequate for the high-sweep case of the B-1 wing. During the course of this work, ATRAN3S was further improved by modifying the code to implicitly treat some additional terms in the finite-difference form of Eq. (1) in order to improve the stability of the algorithm. This speeded up the code by a factor of two.

For all cases considered in this study, a grid with 64 points in the streamwise direction, 40 points in the vertical direction and 20 points in the spanwise direction were employed. The wing surface was defined by 39 points in the streamwise direction and by 13 points in the spanwise direction. Computational boundaries were located as follows: the upstream boundary was at 15 chords, the downstream boundary was at 25 chords, the far span boundary was at 1.6 semispans, the region above the wing boundary was at 25 chords, and the boundary below the wing was at 25 chords.

3. AEROELASTIC EQUATIONS OF MOTION

The governing aeroelastic equations of motion of a flexible wing are obtained by the Rayleigh-Ritz method (Chapter 3, Ref. 13). In this method the resulting aeroelastic displacements are expressed at any time as functions of a finite set of assumed modes. The contribution of each assumed mode to the total motion is derived by using Lagrange's equation. Further, it is assumed that the deformation of the continuous wing structure can be represented by deflections at a number of discrete points. This assumption facilitates the use of discrete structural data such as the modal vector, the stiffness matrix and the mass matrix generated that is by a finite element analysis or by experimental influence coefficient measurements.

The final matrix form of the aeroelastic equations of motion is

$$[M]\{\ddot{q}(t)\} + [C]\{\dot{q}(t)\} + [K]\{q(t)\} = \{F(t)\} \qquad (2)$$

where

[M] = the generalized mass matrix
[C] = the generalized damping matrix
[K] = the generalized stiffness matrix
{F(t)} = the generalized aerodynamic force vector
q(t) = the generalized displacement vector
• denotes the time derivative

These equations of motion are solved numerically by integrating Eq. (2) in time by the linear acceleration method which is the same as the explicit finite difference Euler method. This procedure was successfully employed previously to solve the aeroelastic equations of motion of a two-degrees-of-freedom aeroelastic system (Ref. 5).

The step-by-step integration procedure for obtaining the aeroelastic response was carried out as follows. Free-stream conditions are assumed and wing surface boundary conditions are obtained from a set of selected starting values of the generalized displacement, velocity and acceleration vectors. Then the generalized aerodynamic force vector $\{F(t)\}$ at time $t + \Delta t$ is computed by solving Eq. (1). Using this aerodynamic vector, the generalized displacement, velocity, and acceleration vectors for the time level $t + \Delta t$ are calculated by numerically integrating Eq. (2). From the generalized coordinates computed at the time level $t + \Delta t$, the new boundary conditions on the surface of the wing are computed. With these new boundary conditions the aerodynamic vector $\{F(t)\}$ is computed at the next time level by using Eq. (1). This process is repeated at every time step to solve the aerodynamic and structural equations of motion forward in time until the required response is obtained.

4. MODELING THE WING FOR THE ANALYSIS

A schematic diagram of the B-1 aircraft is given in Fig. 1. From this configuration, isolated wing planforms are modeled to represent the aerodynamic and structural characteristics of the wing as closely as possible. The two planforms modeled for sweep angles of 25.0° and 67.5° are shown in Fig. 2. For both cases, the wing root is located at the pivot point of the wing. The resulting aspect ratio and taper ratio for the 25.0° sweep case are 8.26 and 0.41, and the corresponding values for the 67.5° sweep case are 1.85 and 0.38, respectively.

5. VIBRATIONAL ANALYSIS

In this analysis the assumed modes used in Eq. (2) were taken from the natural modes of the wing as determined from a vibrational analysis. The data for the vibrational analysis was prepared from the measured structural stiffnesses and from the mass distributions of the wing. The first six natural modes were selected to represent the wing for the aeroelastic analysis. The modes and their associated frequencies that were determined by the vibrational analysis in addition to the frequencies of the actual wing from ground vibration tests of the B-1 aircraft are given in Fig. 3. The frequencies from the vibration analysis on the model planform of the wing that are prepared for the code are close to those measured for the actual wing in the ground vibration test as shown in Fig. 3. Thus the model in the code closely represents the structural characteristics of the actual wing.

6. STEADY AERODYNAMIC ANALYSIS

Steady aerodynamic computations were made in order to verify that the modeling of the wing was adequate for representation of the actual aerodynamic characteristics of the wing. This verification was made by comparing the results from ATRAN3S with the wind tunnel results measured at the NASA Ames 11- by 11-Foot Tunnel on a 1/10-scale model of the wing (Ref. 2).

Steady aerodynamic pressures were computed by integrating Eq. (1) in time and by setting the steady boundary conditions on the wing. The time-step size required for the computation depended mainly upon the sweep angle. The time-step sizes required for the 25.0° and the 67.5° sweep cases were 0.01 and 0.002, respectively.

Steady-state computations were made for subsonic and transonic Mach numbers equal to 0.65 and 0.75, respectively, at the sweep angle of 25°. Steady pressure distributions are compared with experiment at four semispan stations along the sections perpendicular to the elastic axis at 46, 61, 72, and 83% locations. Figure 4 shows the steady pressure distribution at $M = 0.65$ and $\alpha = 0.0°$ where the flow is subsonic. As expected the ATRAN3S results compare well with experiment. Figure 5 shows the comparison of steady pressure distributions at $M = 0.75$ and $\alpha = 4.11°$. Results compare well between the code and the experiment for all span stations. These close comparisons between the code and the experiment show that the planform modeled in Fig. 2 for the sweep of 25° is adequate to aerodynamically represent the wing.

Steady-state computations were then made for several Mach numbers ranging from 0.80 to 0.873 at various angles of attack for the sweep angle of 67.5°. The physical grid required to make computations is shown in Fig. 6. Note the scale in the span direction was stretched by a factor of ten in Fig. 6a in order to show the details of the grid. In the actual grid, the wing appears swept back by 67.5° as shown in Fig. 6b. It is noted here that the physical grid generated by the original XTRAN3S (Ref. 7) is not adequate (Ref. 10) for this high-sweep case. Because of the high sweep and the associated low Mach numbers normal to the leading edge, the flow remained subsonic for all the cases considered. The code compared fairly well with the experiment at small angles of attack. For example, Fig. 7 shows steady pressure comparisons between the code and the experiment at four semispan stations along sections perpendicular to the elastic axis at 46, 61, 72, and 83% locations at $M = 0.873$ and $\alpha = 2.06°$. Comparisons are favorable for all span stations except the 46% semispan station. The disagreement at the 46% semispan is due to the presence of the glove close to that span station in the wind tunnel tests and the glove is not modeled in the code.

For the high-sweep angle of 67.5°, at higher angles of attack, both in flight tests and in wind tunnel tests, the wings were observed to undergo oscillations (Refs. 1 and 2). For the flight tests, the oscillations occurred in the range of 8.1-8.4° in angle of attack, and for the wind tunnel tests the oscillations occurred at 7.44°. It had been proposed in Ref. 1 that the oscillations were due to the motion of shock

waves. However, upon examination of the wind tunnel detail (Refs. 1 and 2), which included pressure coefficient plots, oil flow charts, and lift curve slopes, H. Yoshihara (private communication, 1984) suggested that the oscillations were due to "the presence of leading-edge separation vortices modified by secondary separation effects." Furthermore, the oscillations could be explained by the following mechanism: "Here wing bending (primary mode) leads to outboard washout changes that cause vortex-flow loading changes (180° out of phase) that reinforce the bending oscillations."

To determine whether shock waves were contributing to the oscillation, calculations were performed at $M = 0.80$ and at $\alpha = 6.0°$ and $11.0°$ angles of attack. At these angles of attack, the wind tunnel data showed no oscillations, and the calculations should indicate the presence of shock waves if they are there. However, the code ATRAN3S models the flow by a velocity potential as shown in Eq. (1), and hence cannot account for the presence of vortices in the flow. Figure 8 shows the comparison at $\alpha = 6.0°$ between wind tunnel test results and calculations. The calculations show no sign of the presence of shock waves and differ significantly from the experimental results. Note that the experimental data falls below C_p^*. Figure 9 shows the computed results at $\alpha = 11.0°$. Again there is no sign of the presence of shock waves and the results differ significantly from the experimental results shown in Fig. 9. Hence there are probably no shock waves present at the intermediate angle of attack of 7.44° at which the oscillations were observed. To properly model the flow in these cases, where leading edge vortices are apparently present and the effects of separation are important in understanding the oscillations, a Navier-Stokes code must be used.

7. AEROELASTIC RESPONSES

In this section several calculations will be presented that simulate the aeroelastic response of the wing by simultaneously integrating Eqs. (1) and (2). The first case will examine the response of the wing at low sweep under the subsonic flow conditions given in Fig. 4. A transonic case will then be computed at the low-sweep angle to determine the presence of shock waves. Finally a subsonic case will be computed at the high-sweep angle, under the flow conditions given in Fig. 7, to examine the change in the response of the wing as the sweep angle is increased.

For the first case, an aeroelastic analysis is conducted at the subsonic Mach number of 0.65 and $\alpha = 0.0°$ in order to study the nature of subsonic response of the wing. In this case the steady pressures from the code compared well with the experiment as shown in Fig. 4. Flow parameters are taken for an altitude of 33,000 ft. The response computations were initiated by giving an arbitrary unit displacement to the first generalized coordinate $q(1)$. The aerodynamic and structural equations of motion were simultaneously integrated forward in time until a steady aeroelastic equilibrium state was approached. This required about 10,000 time-steps of size 0.02, which corresponds to approximately 6 sec of physical time at the altitude of 33,000 ft.

In order to simulate an external disturbance to initiate oscillations, an instantaneous change of 2.0° to the mean angle of attack was given to the wing and the response computations were further continued. After initial oscillations the wing again approached a steady aeroelastic equilibrium position. This required approximately 5,000 time-steps. Similar responses were repeated for 4.0° of instantaneous change in the angle of attack. These responses for the first normal mode are shown in Fig. 10. The responses for the other 5 modes were of smaller amplitude in comparison to the first mode. For all the three instantaneous angles of attack, the wing reached a steady aeroelastic equilibrium position within approximately 3.5 sec.

For the next case, the response analysis was conducted for the transonic flow at $M = 0.72$ and $\alpha = 4.0°$ and an altitude of 33,000 ft. At these conditions some oscillations were observed in the flight test of the B-1 aircraft (Refs. 1 and 2). Response computations were initiated by giving an arbitrary unit displacement to the first generalized coordinate $q(1)$. Then aerodynamic and structural equations of motion were simultaneously integrated in time until a steady aeroelastic equilibrium state was approached. This required about 10,000 time-steps of size 0.02, which corresponds to 6 sec of physical time at the altitude of 33,000 ft. The response time was similar to the subsonic case. The deformed shape of the wing at its steady aeroelastic equilibrium position is shown in Fig. 11. This deformed shape of the wing is close to the first bending mode shape of the wing. The corresponding upper- and lower-surface pressure distributions are shown in Fig. 12. A shock wave is evident on the outboard portion of the upper surface of the wing.

To simulate an external disturbance to initiate oscillations, an instantaneous change in the mean angle of attack was given to the wing and response computations were further continued. After some initial oscillations, the wing again approached a steady aeroelastic equilibrium position within 3.0 sec. This required approximately 5,000 time-steps. Such responses were conducted for two instantaneous changes in angle of attack of 2.0° and 4.0°. These responses are shown for the first normal mode in Fig. 13. For the two cases, the wing reaches a steady aeroelastic equilibrium position within approximately 3.0 sec.

In spite of the presence of shock waves on the wing, the nature of response is similar to that observed for the subsonic case at $M = 0.65$. It is noted that the wing does not pick up oscillations caused by the external disturbance even when shock waves are present on the wing. However, these calculations did not simulate the effects of the shock wave interaction with the boundary layer. Hence they could not simulate buffet, which was the cause of the oscillations that were observed in wind tunnel and flight tests (Refs. 1 and 2) at these flow conditions.

For the final computation, a case at $M = 0.873$ and $\alpha = 2.06°$ was selected for response analysis at the altitude of 33,000 ft. For this case steady pressures from ATRAN3S compared favorably with the experiment as shown in Fig. 7.

Because of the low aspect ratio of 1.8 of the wing at the 67.5° sweep-case, the time-step size required was 0.002, which is ten times smaller than the time step size required for the 25.0° sweep case. Because of the large computational time required for the aeroelastic analysis, only a limited response analysis was conducted. The aeroelastic response of the first normal mode is shown in Fig. 14 for approximately two cycles of oscillation starting from the free-stream conditions with an initial unit value for the first generalized displacement $q(1)$. The response computations which corresponds to 1.35 sec of physical time required about 15,000 time-steps of computation. The response showed damping but at a very small rate. The rate of damping for this case is much smaller than those observed for the case of 25.0° sweep. This small damping, in addition to the proposed formation of leading-edge vortices at higher angles of attack might have caused the aeroelastic oscillations that were observed on the B-1 wing at the high-sweep angle.

8. CONCLUSION

The transonic code ATRAN3S was used to study the aerodynamic flow and the aeroelastic response of the B-1 wing at low- and high-sweep angles of 25.0° and 67.5°, respectively. Steady pressures from the code compared well with experimental results in the low-sweep case for both subsonic and transonic flows. At high sweep, the comparisons were good at low angles of attack. But at higher angles of attack, the calculations did not show shock waves as had been previously proposed. An alternative source for the oscillations that were observed at the higher angles of attack is proposed to be leading-edge separation vortices. A Navier-Stokes code is required to properly simulate such flows. Aeroelastic response studies showed that the damping of the wing response significantly decreased when the sweep angle was increased. The calculations using ATRAN3S were performed on a CRAY X-MP computer and they required 0.46 sec of CPU time to calculate one time step for a total of 1.9 hr of CPU time for one complete aeroelastic response analysis for a low-sweep case.

REFERENCES

1. Stevenson, J. R., "Shock Induced Wing Oscillation Wind Tunnel Test Results," Aerospace Flutter and Dynamics Council Conference, Williamsburg, Va., April 4-6, 1984.

2. Dobbs, S. K. and Miller, G. D., "Self Induced Oscillation Wind Tunnel Test of a Variable Sweep Wing," (to be presented at the AIAA 26th Structural Dynamics Conference, Orlando, Fla., April 1985).

3. Goorjian, P. M., "Computations of Unsteady Transonic Flows." In Recent Advances in Numerical Methods in Fluids, Vol. IV. Advances in Computational Transonic, ed. W. G. Habashi, Pineridge Press Ltd., U.K., 1984.

4. Ballhaus, W. F. and Goorjian, P. M., "Implicit Finite Difference Computations of Unsteady Transonic Flows About Airfoils," AIAA J., Vol. 15, Dec. 1977, pp. 1728-1735.

5. Guruswamy, P. and Yang, T. Y., "Aeroelastic Time Response Analysis of Thin Airfoils by Transonic Code LTRAN2," Computers and Fluids, Vol. 9, No. 3, Dec. 1980, pp. 409-425.

6. Borland, C. J. and Rizzetta, D. P., "Transonic Unsteady Aerodynamics for Aeroelastic Applications, Volume I--Technical Development Summary for XTRAN3S," AFWAL-TR-80-3107, June 1982.

7. Guruswamy, P. and Goorjian, P. M., "Comparison Between Computational and Experimental Data in Unsteady Three Dimensional Transonic Aerodynamics Including Aeroelastic Applications," AIAA Paper 82-0690-CP, May 1982.

8. Seidel, D. A., Bennett, R. M., and Ricketts, R. H., "Some Recent Applications of XTRAN3S," NASA TM 85641, May 1983.

9. Myers, M. R., Guruswamy, P., and Goorjian, P. M., "Flutter Analysis of a Transport Wing Using XTRAN3S," AIAA Paper 83-0922, May 1983.

10. Guruswamy, P. and Goorjian, P. M., "An Efficient Coordinate Transformation Technique for Unsteady Transonic Aerodynamic Analysis of Low Aspect Ratio Wings," AIAA Paper 84-0972-CP, 25th AIAA Structural Dynamics Conference, Palm Springs, May 1984.

11. Rizzetta, D. P. and Borland, C. J., "Numerical Solution of Three-Dimensional Unsteady Transonic Flow Over Wings, Including Inviscid/Viscous Interaction," AIAA Paper 82-0352, Jan. 1982.

12. Marstiller, J. W., Guruswamy, P., Yang, T. Y., and Goorjian, P. M., "Effects of Viscosity and Modes on Transonic Flutter Boundaries of Wings," AIAA Paper 84-0870-CP, 25th AIAA Structural Dynamics Conference, Palm Springs, Calif., May 1984.

13. Bisplinghoff, R. L., Ashley, H., and Halfman, R. L., "Aeroelasticity." Addison Wesley, Menlo Park, Calif., Nov. 1957.

ACKNOWLEDGMENT

We would like to thank Dr. H. Yoshihara for his helpful comments on interpreting the experimental data and acknowledge his introduction of the concept of separation-induced oscillations (SIO), i.e., the presence of leading edge separation vortices modified by secondary separation effects as being the source of the oscillations that were observed to occur on the wing in the high sweep case.

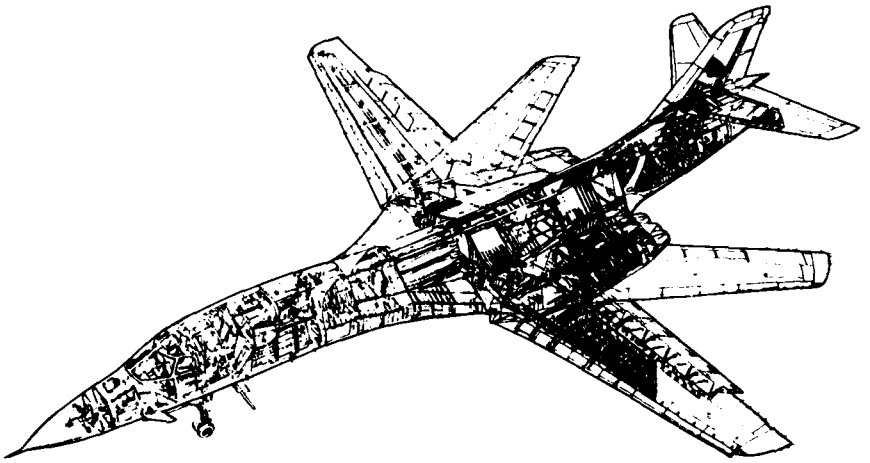

Fig. 1. The B-1 aircraft.

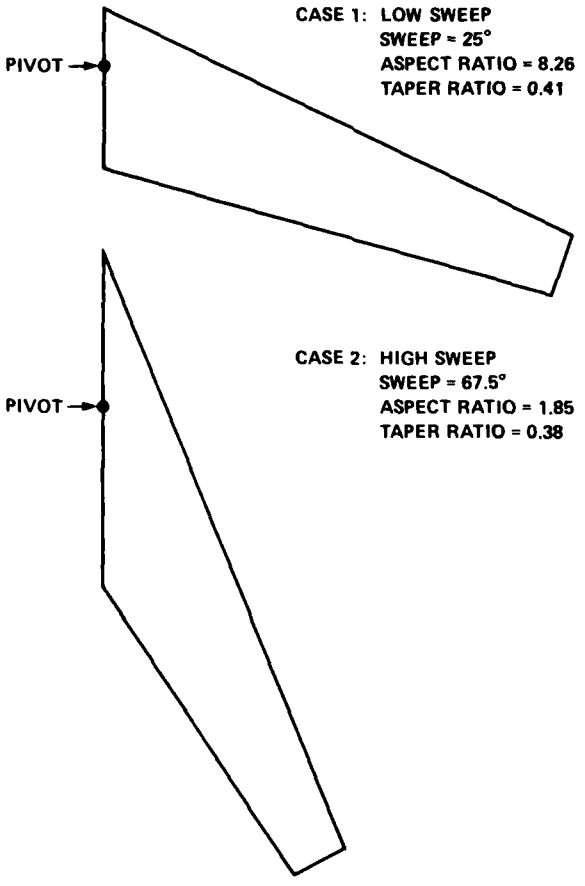

Fig. 2. Wing planforms for analysis.

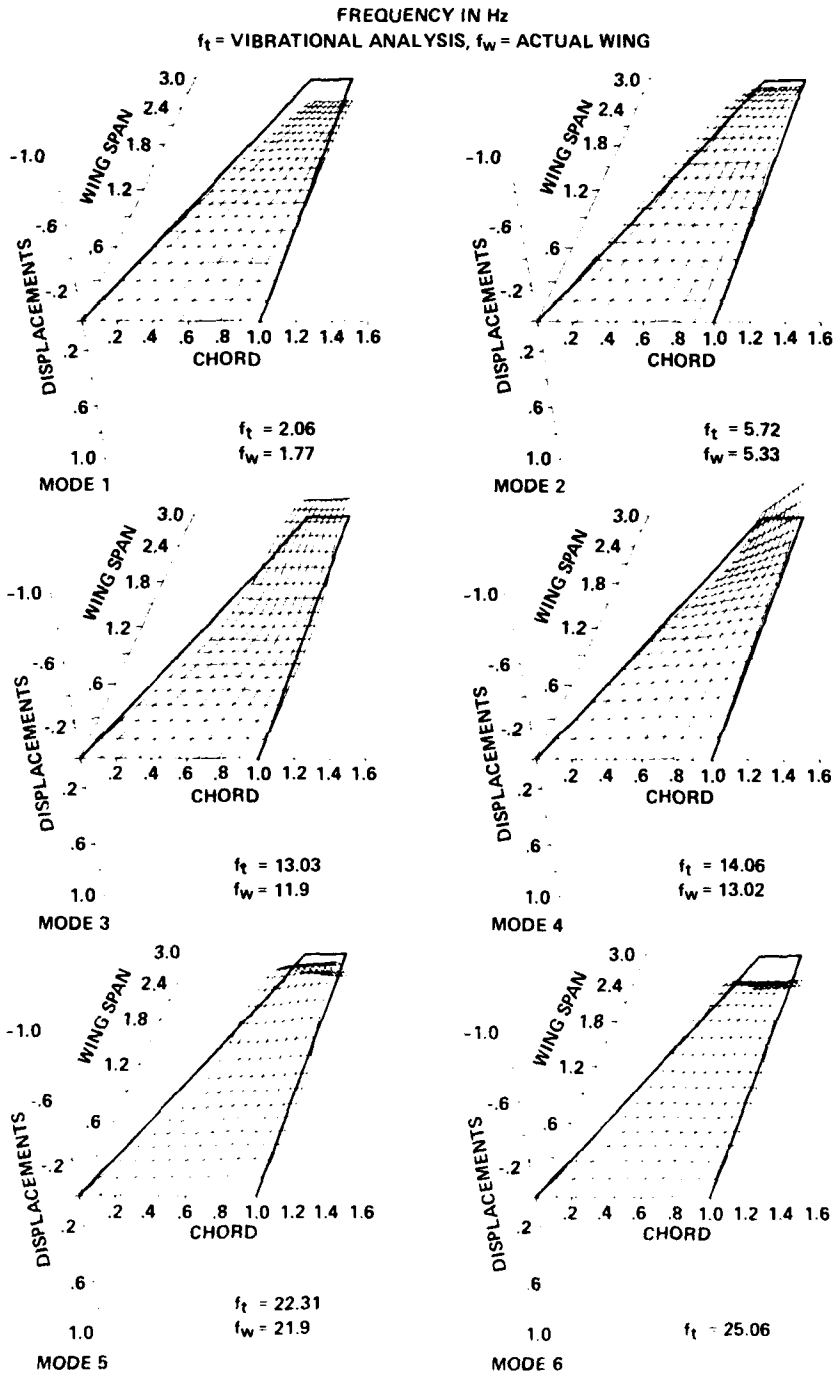

Fig. 3. Six natural vibration modes.

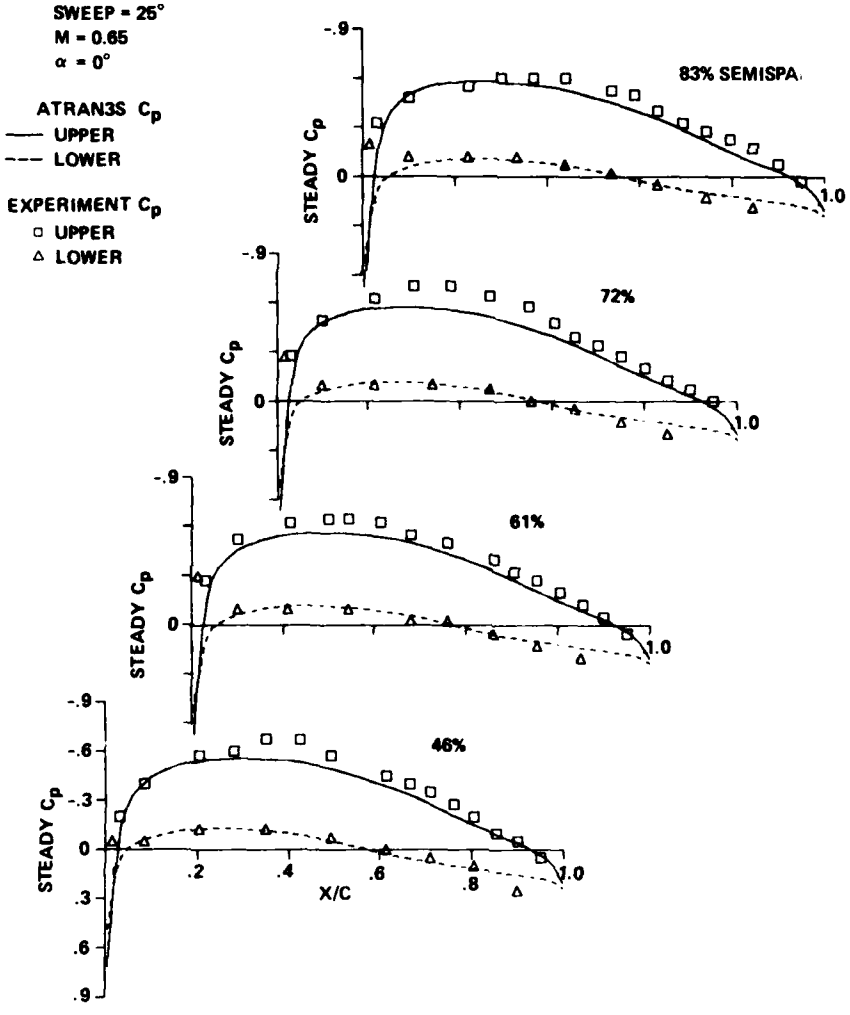

Fig. 4. Steady pressure distributions for the 25° sweep case at M_∞ = 0.65.

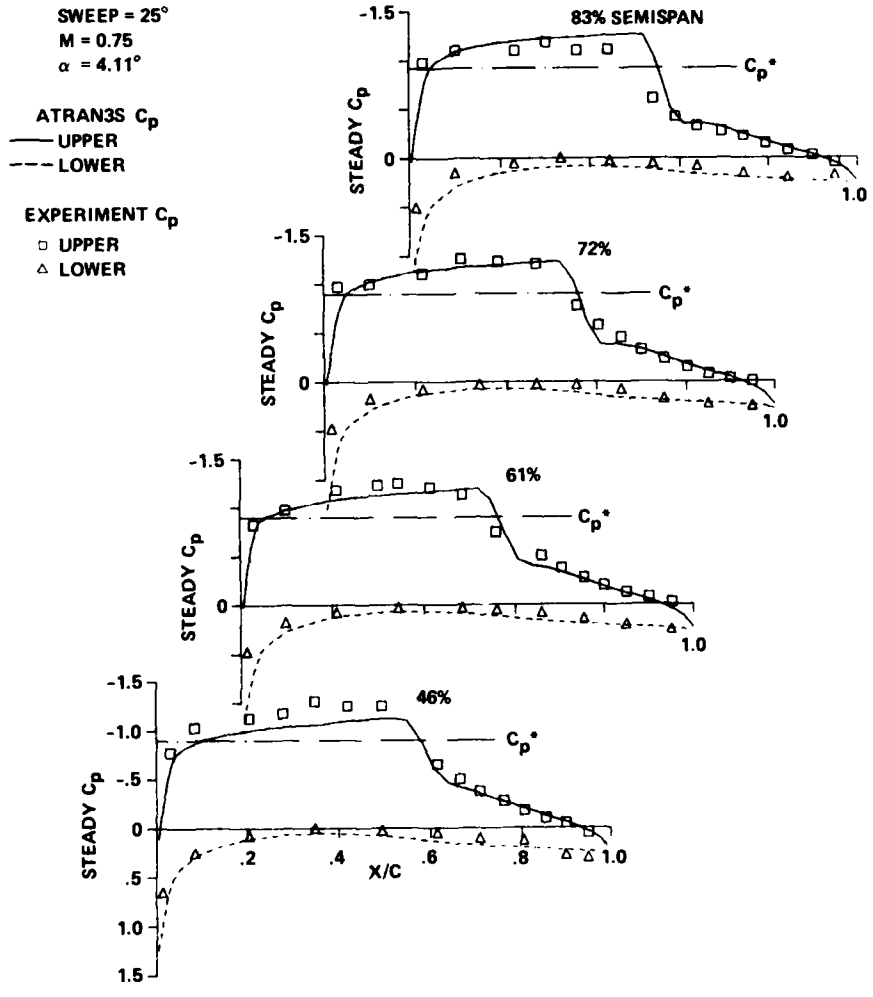

Fig. 5. Steady pressure distributions for the 25° sweep case at M_∞ = 0.75.

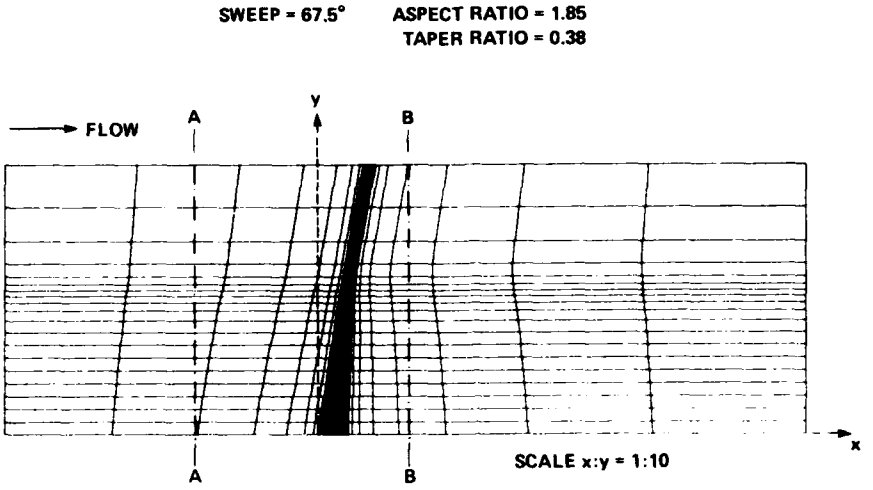

(a) Full grid.

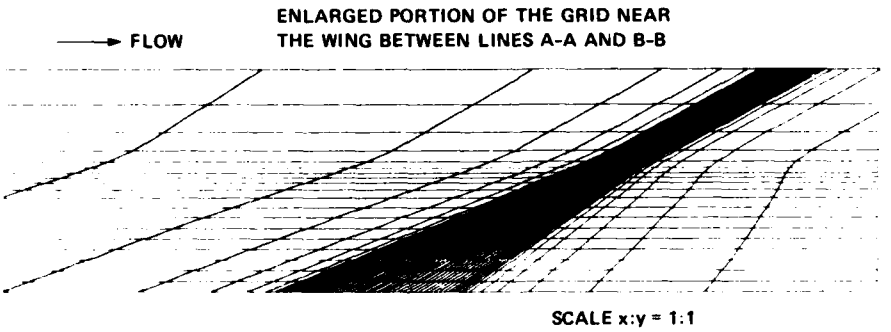

(b) Blow up near wing.

Fig. 6. Physical grid for the 67.5° sweep case.

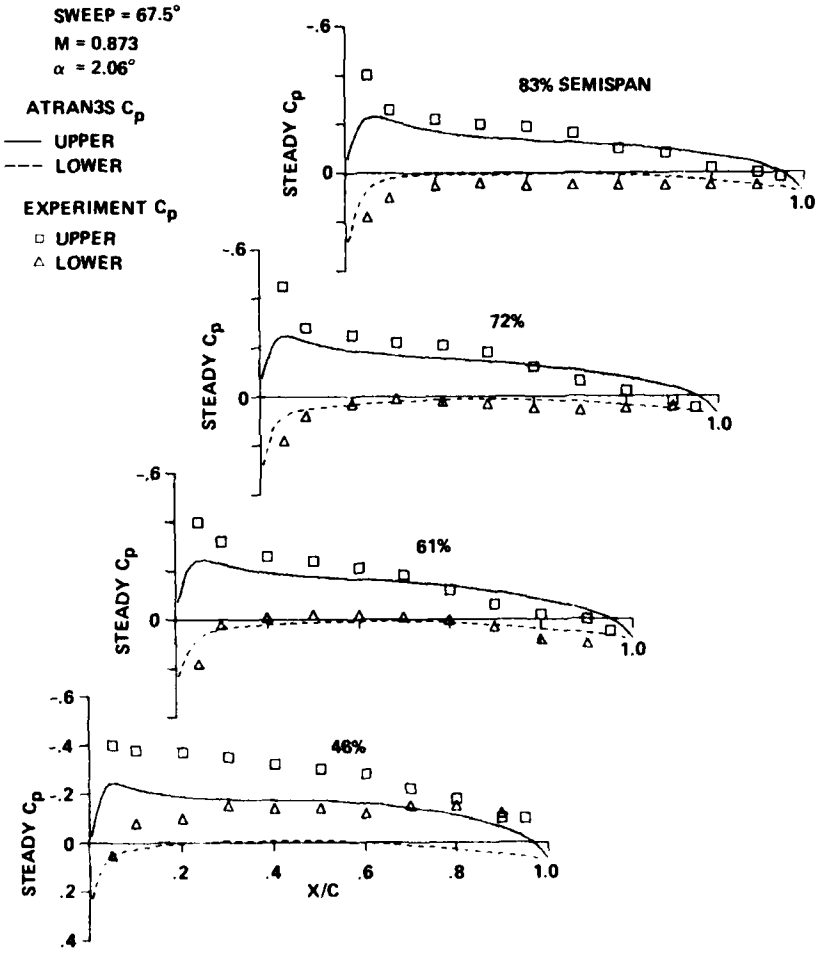

Fig. 7. Steady pressure distributions for the 67.5° sweep case at M_∞ = 0.873 and α = 2.06°.

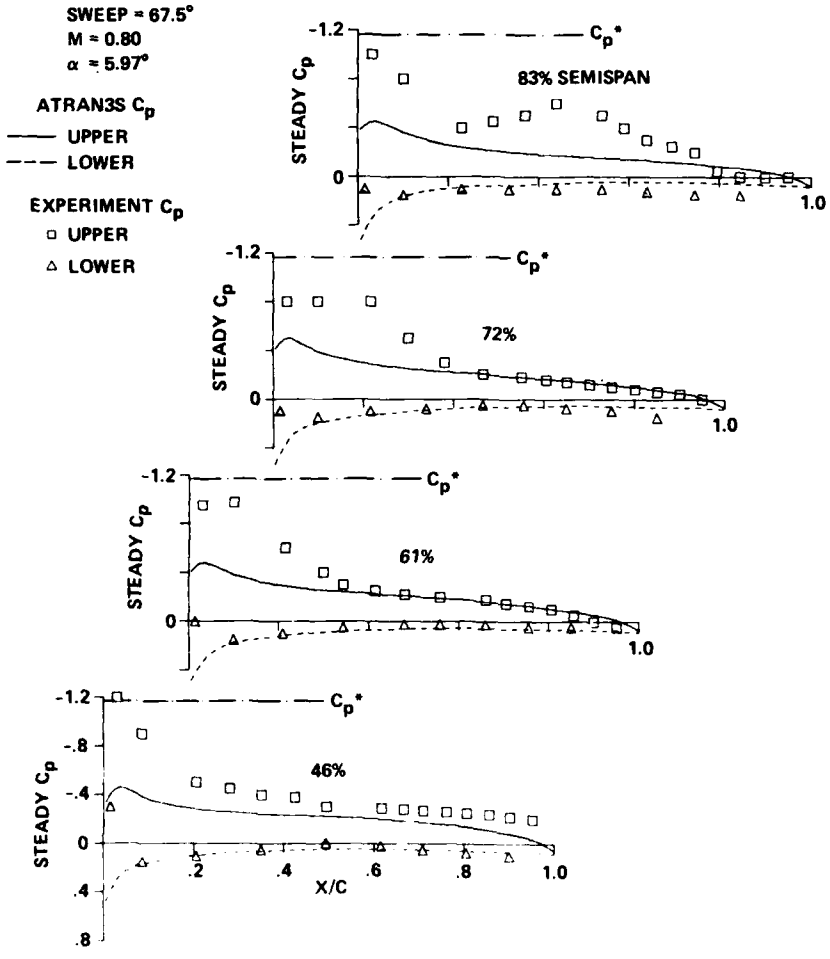

Fig. 8. Steady pressure distributions for the 67.5° sweep case at $M_\infty = 0.80$ and $\alpha = 5.97°$.

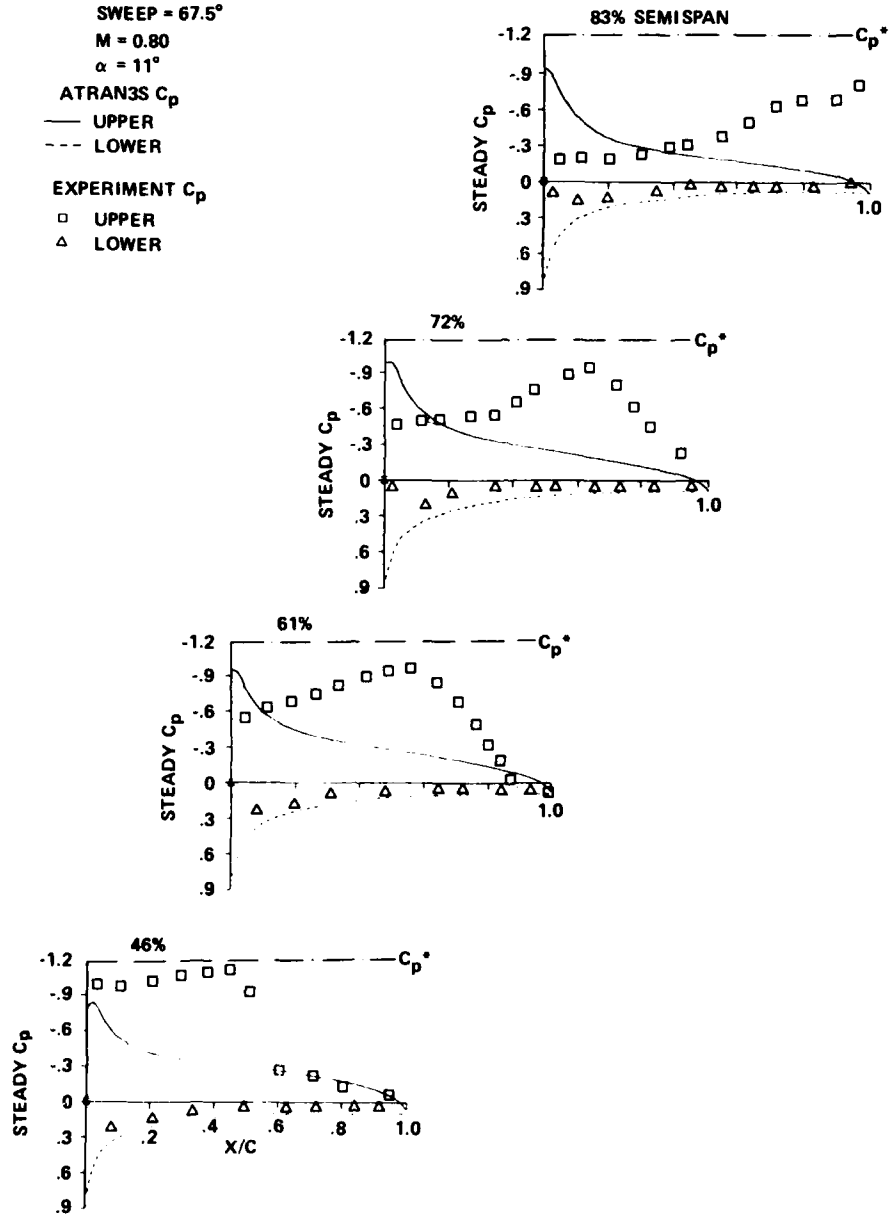

Fig. 9. Steady pressure distributions for the 67.5° sweep case at $M_\infty = 0.80$ and $\alpha = 11.0°$.

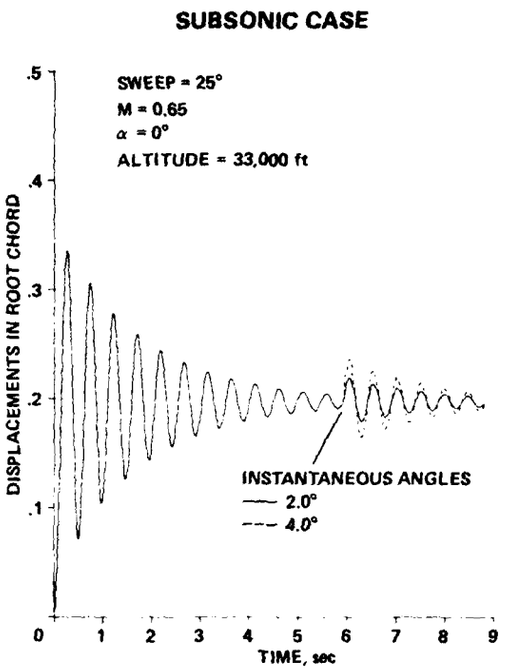

Fig. 10. Dynamic aeroelastic responses of the first normal mode for the 25° sweep case at M = 0.65.

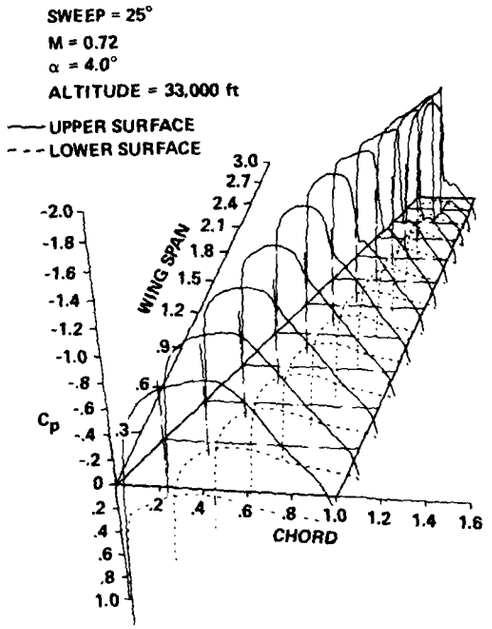

Fig. 12. Pressure distributions at the static aeroelastic equilibrium position.

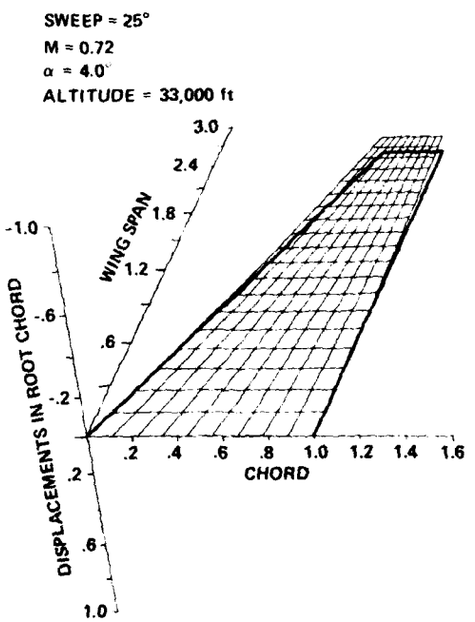

Fig. 11. The deformed shape at the static aeroelastic equilibrium position.

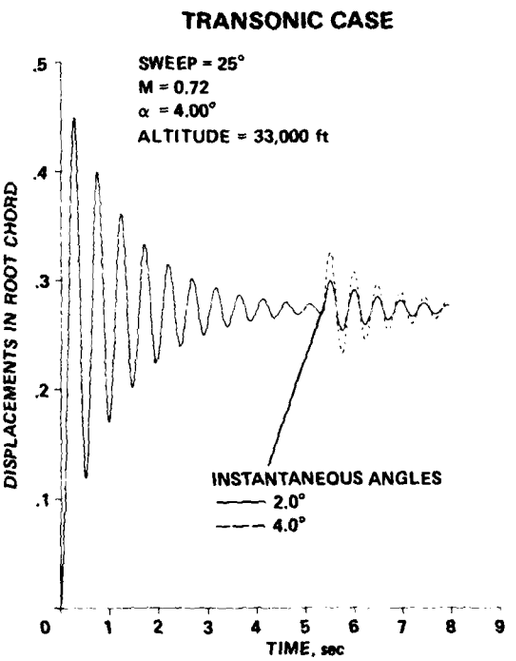

Fig. 13. Dynamic aeroelastic responses of the first normal mode for the 25° sweep at M_∞ = 0.72.

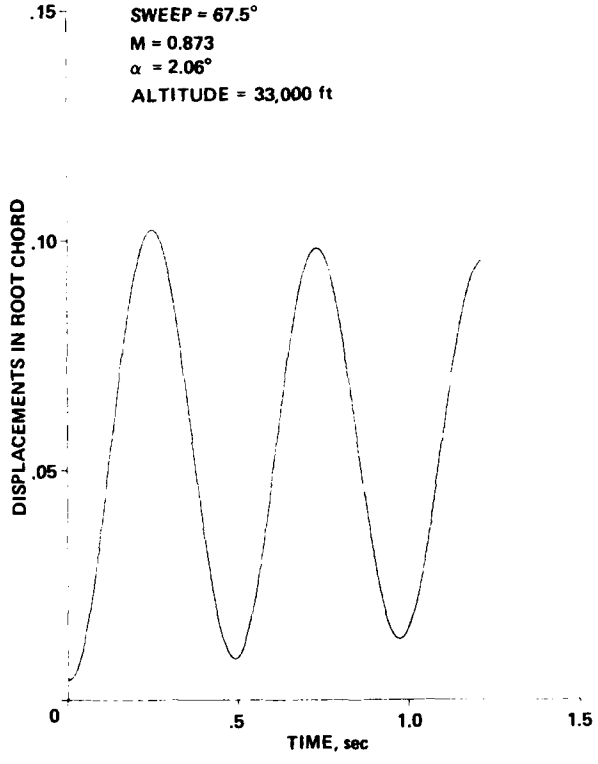

Fig. 14. Dynamic aeroelastic response of the first normal mode for the 67.5° sweep at $M_\infty = 0.873$.

UNSTEADY AIRLOAD COMPUTATIONS FOR AIRFOILS OSCILLATING IN ATTACHED AND SEPARATED COMPRESSIBLE FLOW*

by
R. Houwink**
National Aerospace Laboratory (NLR)
Anthony Fokkerweg 2
1059 CM Amsterdam
THE NETHERLANDS

SUMMARY

Recent developments in coupled inviscid flow-boundary layer computations are discussed for airfoils in unsteady motion in attached and separated subsonic and transonic flow. The applicability of quasi-simultaneous strong interaction coupling procedures for transonic small perturbation theory and boundary layer integral methods is illustrated for oscillating airfoils with shock-induced separation. The relevance of the predicted airloads for aeroelastic applications is illustrated using the analysis of an aeroelastic instability of a supercritical wing wind-tunnel model.

LIST OF SYMBOLS

a, b	coefficients of boundary layer equations (1) and (5)
c	airfoil chord
c, d	coefficients of inviscid flow equation (4)
C_ℓ, CL	lift coefficient
C_f	skin friction coefficient
C_m	moment coefficient relative to ¼ c (positive nose down)
CM	leading edge moment coefficient (Figs. 6, 8)
Cp	pressure coefficient
f	frequency (Hz)
j	index of x-coordinate of grid point
k	reduced frequency based on semi-chord, $k = \pi fc/U_\infty$
k_α	unsteady lift coefficient (Eq. 6)
m_α	unsteady moment coefficient (Eq. 7)
M_∞	free stream Mach number
n	index of time level
Po	total pressure (kPa) (Fig. 13)
R	residual in relaxation equation (2)
Re	Reynolds number based on chord
t	time
u	x-component of local velocity relative to free stream velocity, $u = 1 + \phi_x$
U_∞	free stream velocity
x	location of transition point
z	coordinate normal to free stream direction, relative to chord
α	angle of attack (deg)
α_v	viscous correction to inviscid flow boundary conditions on airfoil (Fig. 1)
δ^*	displacement thickness, relative to chord
ϕ	perturbation potential, relative to $U_\infty c$
$\tilde{\phi}$	preliminary ϕ at new time level, computed in x-sweep of ADI method (Fig. 2)
ρ	local density (Fig. 1)
ω	angular frequency, $\omega = 2\pi f$
ω	relaxation factor (Eq. 2)

Subscripts

F	at flutter stability boundary (Fig. 13)
m	mean steady state
0	mean steady state
1	first harmonic component

Superscripts

-	unconverged result, computed in z-sweep (Fig. 3, 4)

1. INTRODUCTION

In various stages of design, development and certification of an aircraft or helicopter and its propulsion system it is necessary to predict unsteady airloads on the lifting surfaces. Knowledge of these airloads is needed, for instance, for the prediction of dynamic stability and flutter, active control effectivity, noise and structural vibrations.

With the fast growth of computational resources the role of computational methods for such predictions has been increased significantly. On the one hand unsteady airload computations based on linearized subsonic and supersonic theory for three-dimensional configurations are widely used in aircraft design and development. On the other hand, more accurate methods have been developed or are in development in which transonic and viscous effects on unsteady airloads are taken into account. This improvement has been stimulated by the increasing pursuit of optimized aircraft design in the past decade, and is relevant for unsteady airload computations for in particular supercritical airfoils, control surfaces, rotating blades of helicopters, (advanced) propellers, and turbofans. In these cases the presence of shock waves and the interaction of the inviscid outer flow with viscous layers on the lifting surface are known to have a significant and

* This investigation has been carried out under contract with the Netherlands Agency for Aerospace Research NIVR

** Senior Research Engineer

sometimes dominating influence on the unsteady airloads, in particular when flow separation occurs. In addition, the development of supercritical airfoils, natural laminar flow airfoils and of cryogenic wind-tunnel testing requires attention for the effect of unsteady displacement of transition points on unsteady airloads.

Following similar developments in steady flow computations, various approaches are made to account for the above inviscid and viscous effects. They can be classified roughly in methods for solving the unsteady Navier-Stokes equations and coupled inviscid flow-boundary layer methods. From the former methods the capability to resolve complex unsteady viscous flow problems has been demonstrated convincingly for both attached and separated unsteady compressible flows (Refs. 1,2). However, because of the large computational effort required in particular for the time-accurate solution of the Navier-Stokes equations, these methods are not yet attractive for engineering applications. Also the accuracy of these methods is not yet fully satisfactory, in spite of the sophisticated mathematical modelling of the flow. This is associated in particular with uncertainty about the proper modelling of transition and turbulence, and with the interaction of physical and numerical viscosity.

The second approach, in which unsteady inviscid transonic flow methods are coupled with boundary layer approximations to the Navier-Stokes equations, is more attractive due to the considerably lower computational effort required. The advantages of this approach are even more relevant for unsteady than for steady flow problems. The required accuracy of unsteady airload computations is generally lower than of steady flow computations. Usually the unsteady airloads are only one element of a more complex aeroelastic analysis, sharing limited accuracy with the modal characteristics of the vibrating structure like generalized mass, structural damping, etc. The unsteady flow computations, however, require significantly larger effort compared to steady flow computations.

The above considerations and the need for a better prediction of unsteady airloads than attainable with inviscid flow computations has led to the development of various methods, based on unsteady non-linear potential theory and boundary layer integral methods (Refs. 3 to 14). Initially the applicability of all these methods was limited to attached flows due to the direct (velocity prescribed) computation of the boundary layer involved in the coupling procedures (Refs. 3-12). Recently, however, this limitation has been eliminated in two methods, developed simultaneously and independently at ONERA (Ref. 13) and NLR (Ref. 14). These methods are based on two-dimensional unsteady transonic small perturbation theory and integral boundary layer methods. Inviscid flow and boundary layer are solved partly simultaneously in order to avoid the singularity which inevitably is encountered in a direct computation of a separating boundary layer. These quasi-simultaneous coupling procedures are partly based on similar methods for the computation of steady flows with separation (Refs. 15-17) and unsteady attached flows (Ref. 7). The effectivity of the present coupling procedures has been demonstrated convincingly in various preliminary computations of unsteady flows about airfoils with shock- and spoiler-induced separation (Refs. 18,19). The accuracy of the results and the cost-effectiveness of the methods is very promising for engineering applications to predict unsteady airloads for the analysis of shock induced flutter, buzz, dynamic stall and control surface effectivity.

In the present paper the methods with quasi-simultaneous coupling procedures are summarized. The applicability of these methods is illustrated for oscillating airfoils with shock-induced separation. The relevance of the predicted airloads for aeroelastic applications is illustrated using the analysis of an aeroelastic instability of a supercritical wing wind-tunnel model.

2. SUMMARY OF THE METHODS

In the following the main features of the methods are summarized with emphasis on the coupling procedures at the airfoil surface. For a more detailed description one is referred to references 13 and 14.

In both methods the inviscid outer flow is modelled by an unsteady transonic perturbation potential equation, and the viscous flow by boundary layer integral methods. The flow regions are coupled using various relations between viscous and inviscid flow quantities. One relation is the boundary condition for the inviscid flow computation, describing flow or mass flow tangency to the inviscid unsteady airfoil contour corrected by a viscous flow angle α_v (Fig. 1). The other relations are the expression of the flow quantities at the edge of the boundary layer, occurring in the boundary layer equations, as functions of the inviscid flow potential distribution ϕ.

Consistent with the small perturbation assumptions underlying the modelling of the inviscid region, the flow is computed on a rectangular grid with airfoil and wake boundary conditions applied on the x-axis. The development of the flow with time is computed in a number of time steps using the Alternating Direction Implicit (ADI) finite difference procedure of the NASA-Ames code LTRAN2 (Ref. 20). The ADI method is summarized in figure 2. Essential for the strong-interaction coupling procedures is the z-sweep, in which the potential distributions $\phi(z)_x$ on the new time level t^{n+1} are computed for the new viscous boundary conditions $f(\phi^{n+1}) = \alpha_v^{n+1}$, using a downstream marching procedure. Figure 2 also shows the classical weak-interaction coupling (direct method) which breaks down at separation.

Figures 3 and 4 give a global comparison of the two methods considered here, which have the above features in common. The method developed at ONERA (Fig. 3) employs the fully unsteady TSP equation and unsteady boundary layer defect equations. In order to be able to compute a quasi-simultaneous solution for α_v and ϕ in the z-sweep, a relaxation relation between these quantities has been derived from the boundary layer equations and difference relations:

$$\alpha_v + a\,\phi + b = R = 0 \tag{1}$$

In this relation the coefficients a and b are highly non-linear functions of the inviscid flow and boundary layer quantities. Eq. (1) is comparable to the relation between displacement thickness $\delta_x^* \approx \alpha_v$ and velocity gradient ϕ_{xx} derived by East, Smith and Merryman for a steady boundary layer (Ref. 21). The latter relation is used as basis for the quasi-simultaneous coupling procedures in Rizzetta's method (Ref. 7) and in the NLR method discussed later (Eq. 5). Near separation the coefficients a and b become very large and change sign, causing the well-known singular behaviour of α_v if ϕ is prescribed. In order to avoid this problem, Eq. (1) is used as basis for a relaxation relation between α_v and ϕ which is added as a boundary condition to the z-sweep:

$$\alpha_v - \bar{\alpha}_v + a\,(\phi - \bar{\phi}) = -\omega R \tag{2}$$

In Eq. (2) ω is a relaxation factor which can be taken $\omega = 1$, and R is a residual. This residual is obtained by substituting in Eq. (1) the result of $\hat{\alpha}_v(\bar{\phi})$ of a direct boundary layer computation or $\hat{\phi}(\bar{\alpha}_v)$ of an inverse computation, depending on the local state of the boundary layer (Fig. 3). By simultaneous solution of Eq. (1) with the inviscid flow equations in the z-sweep, the singular behaviour of the solution for ϕ and α at separation is in general avoided. In order to approach a converged and time accurate solution at each time step ($R = 0$) the downstream marching z-sweep is repeated until the residual has become sufficiently small in all x-stations. The combination of this procedure with the unsteady TSP and boundary layer method and a fine grid appears to yield very encouraging predictions of various types of shock-induced separation, including aerodynamic resonance phenomena on fixed and oscillating airfoils (Ref. 18).

The method developed at NLR is shown schematically in figure 4. This method is based on the NASA-Ames code LTRAN2, and has been modified at NLR in various stages to improve the accuracy and applicability for unsteady viscous flow computations (Refs. 5, 6, 14, 22). Compared to the ONERA method, low frequency approximations underly the TSP equation, and Green's lag-entrainment method for the steady turbulent boundary layer and wake (Ref. 23) is used. The viscous correction α_v to the inviscid flow angle is approximated by the displacement thickness gradient:

$$\alpha_v = \delta^*_x \tag{3}$$

Further differences are the matching of velocities instead of mass flow ($\rho = 1$ in figure 1), which leads to somewhat different small perturbation approximations of the boundary conditions, and the details of the coupling procedure. In the downstream marching z-sweep at each station x_j a quasi-simultaneous solution of inviscid flow and boundary layer is computed before proceeding to the next station x_{j+1}. This is possible because at each station the set of linear differential equations solved in the z-sweep can be reduced to one linear relation between ϕ and δ^*_x:

$$\phi + c\,\delta^*_x + d = 0 \tag{4}$$

The coefficient c is a constant depending on the TSP equation used, on the difference equations and on mesh width and time step. The coefficient d depends on the time history of the flow computed. Simultaneously a similar relation is derived from the steady boundary layer equations:

$$\phi + \frac{1}{a}\,\delta^*_x + \frac{b}{a} = 0 \tag{5}$$

This equation is derived from the relation of East, Smith and Merryman (Ref. 21) and is comparable to Eq. (1) used in the ONERA method. The advantage of the form of Eq. (5) compared to Eq. (1) is, that Eq. (5) does not become singular at separation ($\frac{1}{a} \to 0$). In an iteration process, Eqs. (4) and (5) are solved simultaneously and the coefficients a and b are updated using direct computation of the (non-singular) boundary layer equations, until convergence. In the present version of the method, the z-sweep is carried out only once, using old downstream values of the velocity $U = 1 + \phi_x$ in the difference relation for the velocity gradient underlying Eq. (5). This leads to a very cost-effective computation of attached and separated unsteady flows. However, because the z-sweep is carried out only once each time step, the procedure is not fully time accurate. Essentially the upstream influence on the boundary layer of a downstream change of the flow is retarded by one time step. This may lead to less accurate results in particular at shock- induced separation. The problem can be cured easily by iteration of the z-sweep at each time step.

Besides a cost effective computation, the use of Eqs. (4) and (5) also gives insight in the essential of the strong viscous-inviscid interaction. In attached flows, $\frac{1}{a}$ in Eq. (5) is large, indicating a weak interaction of the displacement thickness with the inviscid flow Eq. (4). In separated flow, $\frac{1}{a}$ is small and changes sign at separation or reattachment. In that case, the interaction with the inviscid flow is strong, and the inviscid outer flow solution is largely prescribed by the boundary layer equation (5). Both weak and strong interaction are properly accounted to by simultaneous solution of Eqs. (4) and (5).

3. UNSTEADY AIRLOADS ON OSCILLATING AIRFOILS WITH SHOCK-INDUCED SEPARATION

One of the challenging computational test cases for unsteady transonic flow computations proposed by AGARD (Ref. 24) is the NACA 64 A010 airfoil at a mean angle of attack $\alpha_m = 4$ deg, Mach number $M_\infty = 0.8$, oscillating about ¼ chord at an amplitude of 1 deg. Experimental data for these conditions at various Reynolds numbers and frequencies were obtained by Davis and Malcolm (Ref. 25). In figures 5 to 8 experimental data at a Reynolds number $Re = 12 \times 10^6$ are compared with results of the full Navier-Stokes equations and more approximate methods obtained by Chyu and Kuwahara (Ref. 2) and of the coupled TSP-boundary layer method developed at ONERA (Ref. 18).

In the following only the first harmonic components of unsteady airloads are considered (index 1). In some cases the first harmonic components of lift and moment coefficients are scaled as follows:

$$k_\alpha = \frac{1}{\pi}\, C_{\ell_1} / \alpha_1 \tag{6}$$

$$m_\alpha = \frac{2}{\pi}\, C_{m_1} / \alpha_1 \tag{7}$$

This representation is acceptable in the present analysis for low amplitudes. Of course for a more detailed analysis of unsteady flows with separation also non-harmonic representations should be used, in particular at higher amplitudes where non-linear effects dominate.

The mean steady pressure distributions shown in figures 5 and 7, exhibit shock-induced separation. The steady result of the coupled method is rather satisfactory (Fig. 7) and at least of equal accuracy as compared to the mean steady solution of the full Navier-Stokes equations (Fig. 5). Both methods also give a satisfactory prediction of the unsteady airloads (Figs. 6, 8), indicating that the essential phenomena of the flow are properly modelled. The good results of the coupled method for all frequencies considered is very encouraging for applications in aeroelastic analysis, as will be illustrated later. It should be noted that the measured behaviour of the unsteady airloads, which differs completely from inviscid subsonic theory (Fig. 6), indicates the existence of an aerodynamic natural frequency near $k = 0.2$ associated with

unsteady shock induced separation. This phenomenon has been observed also for supercritical airfoils (Refs. 26, 27) and has been analyzed in more detail in reference 28.

In figures 9 and 10 similar experimental results for a supercritical airfoil are shown in comparison with results computed using the LTRAN2-NLR code. The results were obtained for a lower incidence (α = 0.75 deg) and Reynolds number (Re = 2×10^6). The pitch axis was located at 45 % chord and the amplitude was 0.5 deg. The mean steady pressure distribution (Fig. 9) exhibits shock-induced separation, and is well predicted. The experimental unsteady airloads shown in figure 10 exhibit a similar, slightly weaker aerodynamic resonance phenomenon compared to the NACA 64 A010 airfoil. The effect of frequency on the unsteady airloads, however, is not well predicted due to a low accuracy at the higher frequency. This is probably associated with the low frequency approximations, and the semi-time-accurate coupling procedure as compared to the method developed at ONERA. Also the relatively crude grid may have led to less accurate results. These sources of inaccuracy can be removed rather easily, which will be part of further development of the LTRAN2-NLR code.

Another useful verification of this code is presented in figure 11, which compares the development of the measured unsteady lift with Mach number at $k \approx 0.1$ with results of viscous and inviscid flow computations. The decreasing magnitude and the large positive phase shift of k_α due to flow separation ($M_\infty > 0.76$) are predicted satisfactorily. These results also show the improved accuracy of the viscous flow computation compared to the inviscid subsonic and transonic results.

The encouraging results of the two coupled inviscid flow-boundary layer methods demonstrate that they provide a cost-effective alternative to time-accurate solution of the Navier-Stokes equations. Their applicability may be demonstrated by the prediction and explanation of transonic dips in the flutter stability boundary of a supercritical wing model in the wind tunnel.

4. ANALYSIS OF AEROELASTIC INSTABILITY AT SHOCK-INDUCED SEPARATION

In references 29 and 27 experimental and theoretical analyses are presented of the flutter boundaries of a supercritical wing wind-tunnel model. The vibration modes (Fig. 12) and frequencies of this study model were designed to yield flutter at subsonic and transonic conditions, as a basis for analysis and for verification of computational methods. Because during the tests pressure measurements were taken at 70 % of the semi-span and a large amount of pressure data were available for a similar model, the mean steady flow conditions were known quite accurately. At an incidence of α = 2 deg an interesting behaviour of the flutter boundary was measured, shown in figure 13. In addition to the rather conventional transonic dip near M_∞ = 0.7 a second dip was encountered at separated transonic flow conditions around M_∞ = 0.75. This instability could be correlated with the measured behaviour of unsteady airloads on a two-dimensional wing section at similar flow conditions (Ref. 28). The correlation was made by flutter calculations with these airloads as aerodynamic input (EQS method, Ref. 27). As an example, figure 14 shows the measured 2-D unsteady lift coefficient k_α at attached and separated flow conditions for various reduced frequencies, including $k_\alpha \approx 0.1$ encountered in the flutter investigation. The Reynolds number at these conditions was Re $\approx 2 \times 10^6$. The results at M_∞ = 0.7 show the conventional behaviour for attached flow conditions. At M_∞ = 0.75, however, the behaviour is completely different and indicates the presence of an aerodynamic resonance frequency at k = 0.25. This behaviour is quite similar to that shown in figures 8, 10 and 11. The flutter computations with these airloads on the outer wing as input give a correct prediction of the second dip. The presence of this dip and the change of the flutter mode of the wind-tunnel model (Fig. 13) can be correlated with the change of the imaginary part of k_α at $k \approx 0.1$ from a negative value at M_∞ = 0.7 to a positive value at M_∞ = 0.75.

In view of the capability of the coupled methods to predict correctly the effect of Mach number on the unsteady airloads on the 2-D wing section, also the observed instability appears to be within the range of applicability of these methods.

5. CONCLUDING REMARKS

For the computation of unsteady airloads on airfoils, oscillating in attached and separated compressible flows including shock-induced separation, the quasi-simultaneous coupling of TSP methods and boundary layer integral methods yields a cost-effective alternative to methods based on the Navier-Stokes equations. A satisfactory prediction of the influence of the frequency is obtained when such a coupled method involves fully unsteady modelling of inviscid flow and boundary layer, time accurate coupling and a fine computational grid at the shock-boundary layer interaction region. Low frequency approximations and a relatively crude grid, which still allow cost-effective computations at attached flow conditions with satisfactory accuracy, lead to less accurate results for shock-induced separation.

The two coupled methods considered here are shown to be applicable in predictions of aeroelastic instability of a high aspect ratio wing, associated with shock-induced separation. Considering also the promising preliminary results for oscillating spoilers and dynamic stall, further investigation of accuracy and applicability are necessary for a wider range of conditions. For cases where the modelling of the flow is inadequate, quasi-simultaneous coupling of more accurate methods can be considered, for instance for the prediction of three-dimensional flows and of vortex separation at leading edge stall. These investigations need to be supported by experimental information, both for the modelling of 3-D effects, unsteady transition and separation, and for verification of the computed results.

6. REFERENCES

1. Deiwert, G.S. and Bailey, H.E.: Time-Dependent Finite-Difference Simulation of Unsteady Interactive Flows. Numerical and Physical Aspects of Aerodynamic Flows II, Chapter 1, Ed. T. Cebeci, Springer, New York, 1984.
2. Chyu, W.J. and Kuwahara, K.: Computations of Transonic Flow over an Oscillating Airfoil with Shock-induced Separation. AIAA paper 82-0350, 1982.
3. Couston, M., Angelini, J.C., Le Balleur, J.C. and Girodroux-Lavigne, P.: Prise en compte d'effets de couche limite instationnaire dans un calcul bidimensionnel transsonique. AGARD-CP-296, paper 6, 1981.
4. Desopper, A., and Grenon, R.: Couplage fluide parfait fluide visquex en écoulement instationnaire bidimensionnel incompressible et transsonique, AGARD-CP-291, paper 5, 1981.

5. Houwink, R.: Results of a new version of the LTRAN2-NLR code (LTRANV) for unsteady viscous transonic flow computations. NLR TR 81078 U (July 1981).
6. Houwink, R.: Unsteady viscous transonic flow computations using the LTRAN2-NLR code coupled with Green's lag-entrainment method. Numerical and Physical Aspects of Aerodynamic Flows II, Chapter 15, Ed. T. Cebeci, Springer, New York, 1984.
7. Rizzetta, D.P.: Procedures for the computation of unsteady transonic flows including viscous effects. NASA-CR-166249, August 1981.
8. Guruswamy, P. and Goorjian, P.M.: Effects of Viscosity on Transonic-Aerodynamic and Aeroelastic Characteristics of Oscillating Airfoils. AIAA paper 83-0888, 1983.
9. Rizzetta, D.P. and Borland, C.J.: Numerical Solution of Three-Dimensional Unsteady Transonic Flow over Wings Including Inviscid/Viscous Interaction. AIAA paper 82-0352, 1982.
10. Lee, S.C.: A Fast Viscous Correction Method for Unsteady Transonic Flow about Airfoils. AIAA paper 83-0264, 1983.
11. Malone, J.B. and Sankar, N.L.: Numerical solutions of 2-D Unsteady Transonic Flows Using Coupled Potential Flow/Boundary-Layer Methods. AIAA paper 84-0268, 1984.
12. Howlett, J.T.: Efficient Self-Consistent Viscous-Inviscid Solutions for Unsteady Transonic Flow. AIAA paper 85-0482, 1985.
13. Le Balleur, J.C. and Girodroux-Lavigne, P.: Méthode numérique semi-implicite et instationnaire d'interaction fluide visqueux-fluide parfait pour les écoulements décollés transsoniques. La Recherche Aérospatiale, no. 1984-1, pp. 15-37, 1984.
14. Houwink, R. and Veldman, A.E.P.: Steady and unsteady separated flow computations for transonic airfoils. AIAA paper 84-1618, 1984. Also: NLR MP 84028 U.
15. Wai, J.C. and Yoshihara, J.: Planar transonic airfoil computations with viscous interactions, AGARD-CP-291, paper 9, 1980.
16. Le Balleur, J.C.: Strong matching method for computing transonic viscous flow including wakes and separations. Lifting airfoils. La Recherche Aérospatiale (English Edition) No. 1981-3, 1981.
17. Veldman, A.E.P., Lindhout, J.P.F.: Quasi-simultaneous calculations of strongly interacting viscous flow. NLR MP 84095 U (1984).
18. Le Balleur, J.C., Girodroux-Lavigne, P.: A viscous-inviscid interaction method for computing unsteady transonic separation. Paper presented at the 3rd Symposium on Numerical and Physical Aspects of Aerodynamic Flows, Long Beach, USA, January 1985.
19. Houwink, R.: Computations of separated subsonic and transonic flows about airfoils in unsteady motion. NLR MP 84094 U, 1984.
20. Ballhaus, W.F. and Goorjian, P.M.: Implicit finite difference computations of unsteady transonic flows about airfoils, including the treatment of irregular shock wave motion. AIAA paper 77-205, 1977.
21. East, L.F., Smith, P.D. and Merryman, P.J.: Prediction of the development of separated turbulent boundary layers by the lag-entrainment method. RAE Technical Report 77046, 1977.
22. Houwink, R. and Van der Vooren, J.: Improved version of LTRAN2 for unsteady transonic flow computations. AIAA Journal, Vol. 18, no. 8, pp. 1008-1010, 1980.
23. Green, J.E., Weeks, D.J. and Brooman, J.W.P.: Prediction of turbulent boundary layers and wakes in compressible flow by a lag-entrainment method. ARC R and M No. 3791, 1973.
24. AGARD: Compendium of Unsteady Aerodynamic Measurements. AGARD R-702, data set 3, 1982.
25. Davis, S.S. and Malcolm, G.N.: Unsteady Aerodynamics of Conventional and Supercritical Airfoils. AIAA paper 80-0734, 1980.
26. Houwink, R.: Some remarks on boundary layer effects on unsteady airloads, AGARD-CP-296, paper 5, 1980.
27. Zwaan, R.J.: Verification of calculation methods for unsteady airloads in the prediction of transonic flutter, AIAA 84-0871-CP. Also: NLR MP 84016 U.
28. Den Boer, R. and Houwink, R.: Analysis of transonic aerodynamic characteristics for a supercritical airfoil oscillating in heave, pitch and flap rotation. Paper 4, AGARD-CP-374 (1984). Also: NLR MP 84076 U.
29. Persoon, A.J., Horsten, J.J., Meijer, J.J.: On measuring transonic dips in the flutter boundaries of a supercritical wing in the wind tunnel. Journal of Aircraft, Vol. 21, no. 11, pp. 906-912, 1984.

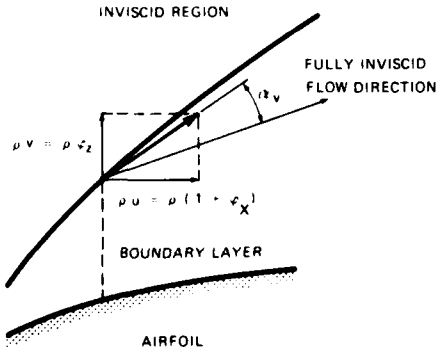

Fig. 1 (Mass) flow tangency in coupled inviscid perturbation potential flow/boundary layer modelling

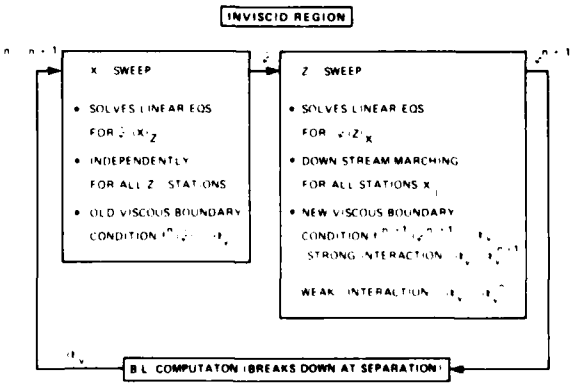

Fig. 2 Scheme of ADI method for unsteady inviscid outer flow computation, coupled in weak interaction with boundary layer (direct method)

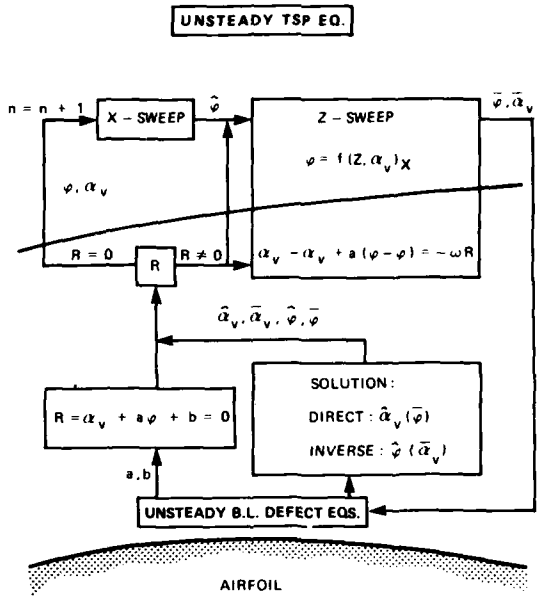

Fig. 3 Organisation of time-accurate quasi-simultaneous coupling procedure (Le Balleur/Girodroux-Lavigne)

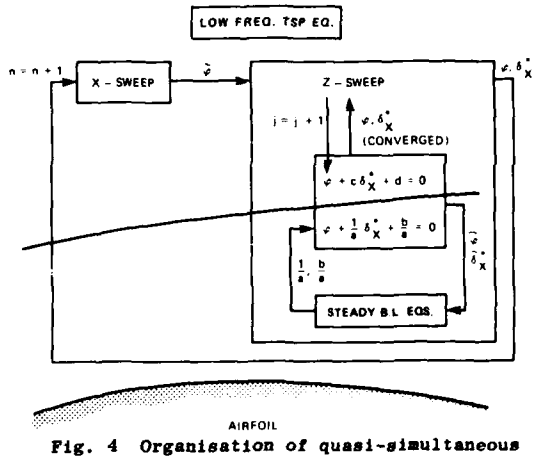

Fig. 4 Organisation of quasi-simultaneous coupling procedure (Houwink/Veldman)

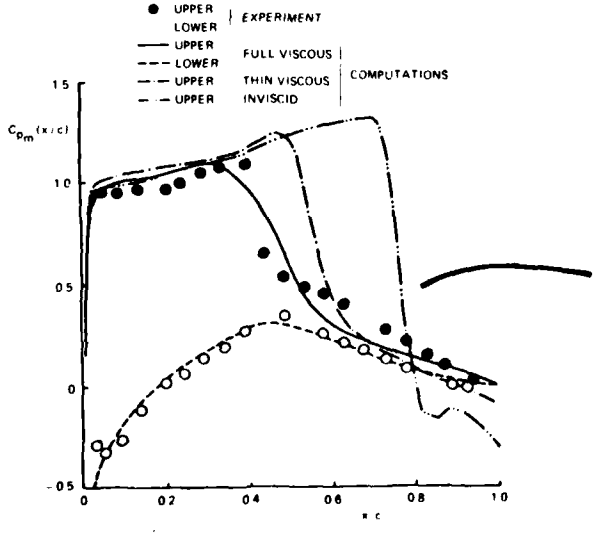

Fig. 5 Mean steady pressure distribution on NACA 64 A010 airfoil (M_∞ = 0.8, α_m = 4 deg, Re = 12x10^6) (Ref. 2)

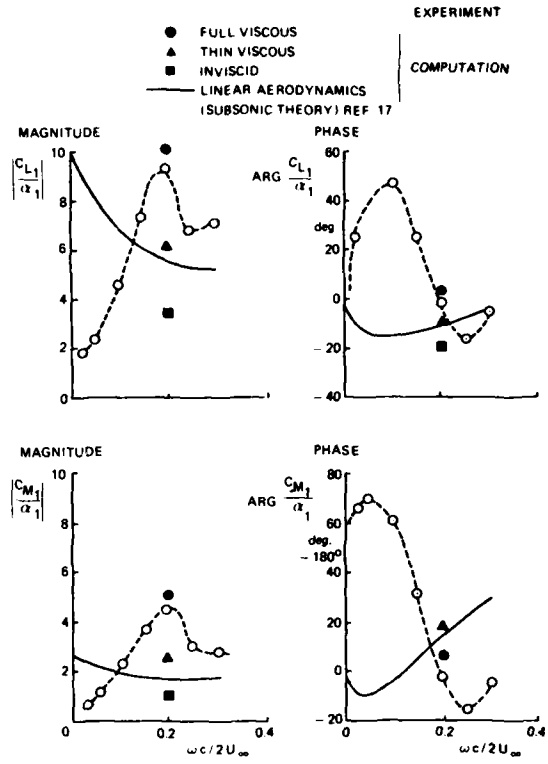

Fig. 6 Unsteady lift and moment coefficients on oscillating NACA 64 A010 airfoil (Ref. 2)

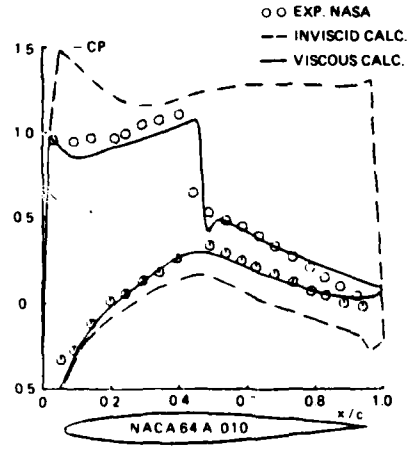

Fig. 7 Steady pressure distributions (M_∞ = 0.789, α_m = 4 deg, Re = 12x10^6)(Ref. 18)

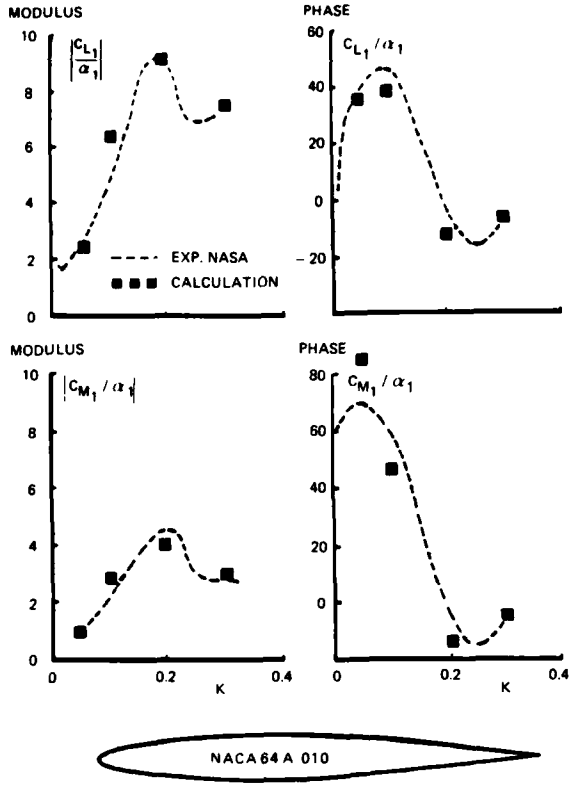

Fig. 8 Unsteady lift and moment coefficients on oscillating NACA 64 A010 airfoil (Ref. 18)

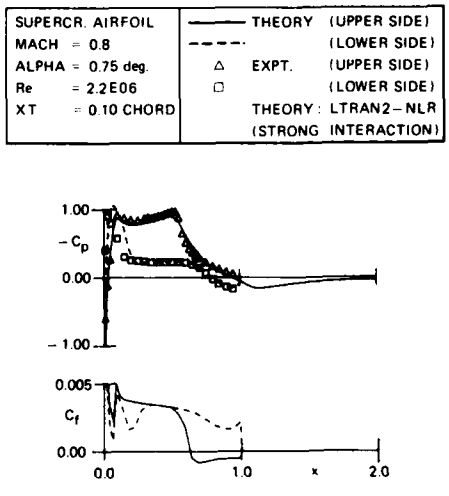

Fig. 9 Mean steady pressure and skin friction distributions at shock-induced separation

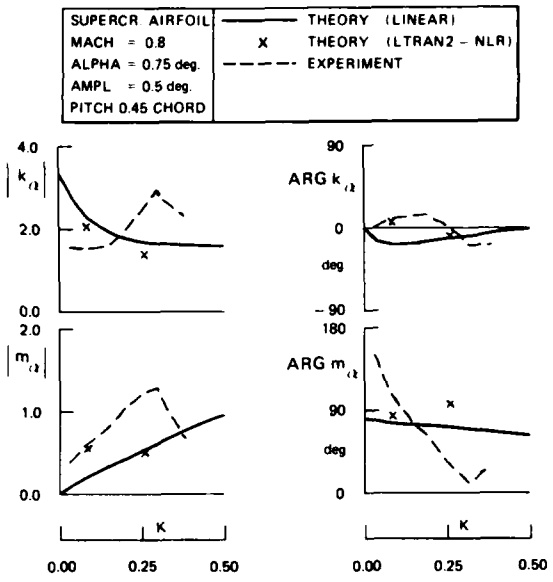

Fig. 10 Unsteady lift and moment coefficients on oscillating supercritical airfoil showing effect of frequency (separated flow)

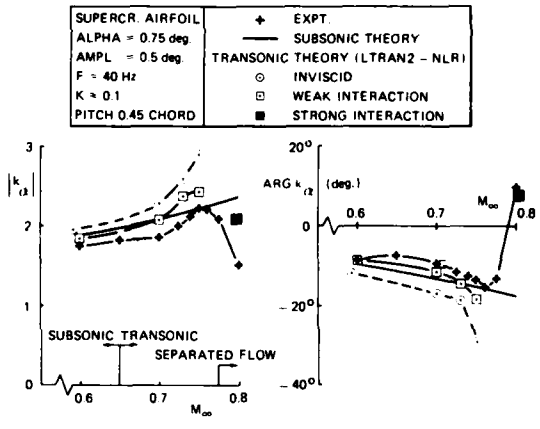

Fig. 11 Unsteady lift coefficients for oscillating supercritical airfoil showing effect of Mach number

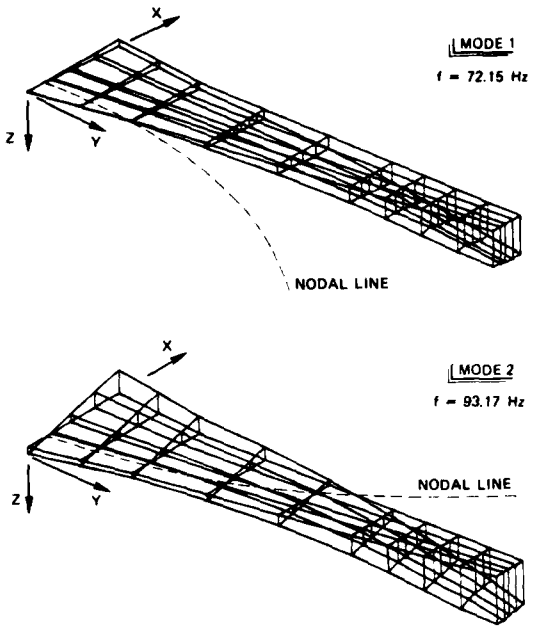

Fig. 12 Vibration modes of the wing model

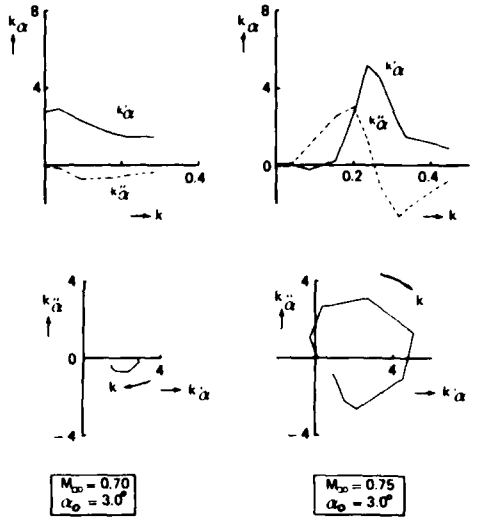

Fig. 14 Measured 2-D unsteady lift coefficients for pitching about 0.45 chord

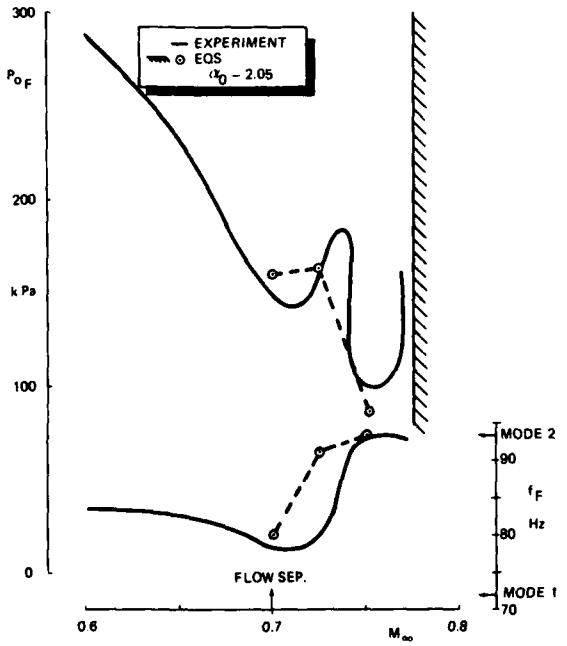

Fig. 13 Flutter results according to experiment and EQS prediction method

Wind Tunnel and Flight Test Analysis and Evaluation of the Buffet Phenomena for the Alpha Jet Transonic Wing

by

H. Buers

Dornier GmbH
Postfach 1420
D-7990 Friedrichshafen, FRG

V. Schmitt

O N E R A
B.P. No. 72
F-92322 Chatillon, France

Summary

In addition to previous presentations of wind tunnel and flight test data of the Dornier TST-program, results of local flow surveys on the wing in the buffeting region are presented. The vibration levels on the wing and at the pilot's seat are also shown. The paper presents the separated effects of the slats in use both with and without trailing edge flaps as manoeuvre flaps up to the transonic flight regime.

1. INTRODUCTION

Though there was remarkable progress in the improvement of aerodynamic design tools, there is still uncertainty in predicting the aerodynamic flow behaviour in the flight region with more or less extended flow separation.

The usability of calculation methods is limited to the simplification of flow physics and aircraft geometry. Wind tunnel tests at high speed are conducted at much lower Reynoldsnumbers than in flight test, which results in different boundary layer conditions with falsified high angle of attack and shock wave/-boundary layer interaction. Additional handicaps are wall interferences, effects of model installation and different elastical behaviour of the model in the wind tunnel and the aircraft in flight.

Thus the available correlation between calculation, wind tunnel and flight test results give useful informations for future projects.

The Dornier TST-program (Transsonischer Tragflügel = Transonic Wing) sponsored by the BMVg (Ministry of Defense) and conducted in cooperation with the DFVLR, the former VFW-Fokker Company, the ONERA and the German Air Force Flight Test Center E 61, as a main purpose incorporated the examination of the theoretical and experimental design tools by correlation with flight test results, demonstrated by the wing design of a fighter aircraft for the transonic flight region.

Background information on the TST program is given in ref (1). The total aircraft performances obtained from flight tests in comparison with wind tunnel results and with the conventional wing were discussed at previous presentations (2,3,4,5). Fig. 1 shows the transonic wing at the Alpha Jet testbed aircraft.

The character of the transonic airfoils much depends on shock boundary layer interaction. Compared with a large transport aircraft the fighter wing has lower aspect ratio and is more affected by three dimensional flow effects. Both the theoretical treatment of transonic flow and the wind tunnel tests at Reynolds numbers less than that in flight embody the uncertainty, if the aircraft in flight can meet the design goals.

The risk in the TST wing design was higher than for a conventional one. This was the reason why the 1:10 Highspeed-Model as well as the wing in flight were equipped with an extensive test set up, to get as much information as possible on the correlation of wind tunnel and flight tests.

2. INVESTIGATIONS OF THE BUFFET BOUNDARY

As mentioned above, the improvement in total aircraft performances by the TST-wing was already demonstrated in previous publications (Ref. 2 - 5).

Especially it was shown, that the buffet limits of the TST were improved inspite of the 20 % higher thickness of the transonic wing, compared with the conventional wing.

The previous buffet investigations were completed with regard to the total aircraft behaviour, neglecting local flow effects on the wing, which will be discussed in this paper by the interpretation of steady and unsteady pressure gage results. This presentation further informs about the relation between wing vibration level and the vibration level at the pilot's seat. Additional information is given about the effect of manoeuvre flaps on the buffet behaviour.

Since the data reduction and evaluation of the unsteady pressure measurements for local flow analysis is very expensive in time and money, only a few test points could be evaluated. Therefore the results presented allow no deduction of general statement, but together with informations from other projects they are one piece in the puzzle of better understanding unsteady aerodynamics.

2.1 The Test Equipment of the Wing

In order to get informations about local flow conditions the 1:10 high speed model and the TST wing on the Alpha Jet were equipped with (Fig. 2):

- static pressure tubes in four wing sections to document the steady pressure distribution
- kulites in 4 wing sections to record unsteady pressure variations
- accelerometers and strain gages for buffet and structural analysis at the wing and at pilot's seat

At the wind tunnel model holes were installed to eject coloured fluid on the wing surface for flow visualization.

2.2 Test Procedure

Wind Tunnel

The wind tunnel tests with the 1:10 model combined with tests for local flow survey exclusively took place in the S 2 tunnel of the ONERA. The tests mostly were conducted with free transition at Reynolds numbers (Re based on aerodynamic chord length 1μ) of $2{,}5 \times 10^6$.
Several runs demonstrated the effects of fixed transition (0,1 mm ballotini at x/c = 0,1) and of Reynoldsnumber ($1 \times 10^6 < Re < 4 \times 10^6$). The tests with fixed transition were not optimized with regard to best agreement in boundary layer thickness at the shock location between wind tunnel and flight test.

Before the flight tests started, the original wing was tested with the flight test equipment in the S 1 wind tunnel at Modane. For these tests the Reynoldsnumbers achieved were as high as 20×10^6 and the runs were conducted with free transition. An overview of all conducted tests is given in [2]. For frequency-analysis the test runs were stabilised in Machnumber and angle of atack (AOA). The signals from the gages were frequency modulated (FM) and recorded on a magnetic tape. The tests for RMS-data recording took place with continuous increase in AOA ($\dot{V}_\alpha \approx 0{,}2°$/sec.) up to heavy buffet conditions.
The S1 tests with the original wing were not suitable for buffet investigations, because there was a limitation for tolerable loadings of the wind tunnel balance. But as later demonstrated, interesting results in the correlation between wind tunnel and flight tests were obtained from these tests at flow conditions just before buffet onset.

Flight

During the flight tests, discussed in Ref. 2-5, the wind up turn (WUT) manoeuvre was usually chosen to check out the buffet boundary. This procedure has the inherent problem of exact calculation of lift and drag polars, for the classic methods of polar determination require stable engine conditions, which are not given for WUT manoeuvres. In order to reduce the thrust influence on lift, the buffeting evaluation took place at higher altitude, and thus the error derived from unstable engine conditions could be reduced to about 2 %. Fig. 3 demonstrates aircraft behaviour during a WUT manoeuvre by means of some recorded test parameters, given as a function of time.

2.3 Data Reduction

This paper only informs about the data reduction of the unsteady flow conditions in flight and wind tunnel; the data reduction of the steady pressure measurements is described in ref 2 to 4.

Wind Tunnel

As to the wind tunnel tests the analogue signals from the unsteady pressure and accelerometer gages were handled in two ways

1. analogue integrated and digital converted to RMS-Values
2. recorded on tape for frequency analysis

The following table shows the frequency range recorded for the different gages:

gage	RMS-Value Hz	frequency spectrum Hz	RMS-Value Hz	frequency spectrum Hz
accelerometers	0,3 to 2000	3,0 to 2.000	0,5 to 100	0,5 to 100
strain gages	3,3 to 10000	3,5 to 10.000	0,5 to 200	0,5 to 200
kulites	3,0 to 15000		0,5 to 3000	0,5 to 500
	S 2 tests, 1:10 model		S 1 tests, original half wing	

Flight

In flight test the signals from the accelerometers and the strain gages were digitally converted and inserted into the PCM-frame, the remaining tracks of the tape on bord were used to record analogue signals of selected kulites.

The frequency range for flight test data reduction was:

gage	RMS (Hz)	frequency spectrum (Hz)
accelerometers	0,5 to 100	0,5 to 100
strain gages	0,5 to 200	0,5 to 100
kulites	0,5 to 3000	0,5 to 500

3.0 TEST RESULTS FROM WIND TUNNEL AND FLIGHT

3.1 Summary of previous buffeting investigations

The previous buffeting analysis [2] led to the buffet limits for the clean configuration summarized in Fig. 4. The curves are based on the criteria presented in Fig. 5, which are in good correlation with the criteria from [6]. The agreement between wind tunnel and flight tests was good for the buffet onset boundary [2]; but for higher buffeting levels no correlation between wind tunnel and flight was found.

3.2 Correlation of Wingtip Accelerometer in Wind Tunnel and Flight

Fig. 6 correlates the RMS-Values of the wingtip accelerometer from wind tunnel and flight test. The value of Δg = 0,2 g from flight test occurs at the angle of attack, where the wind tunnel signal shows the first kink.

According to pilot's comments moderate buffet in flight corresponds very well with the strong increase in vibration level. The wind tunnel curves show no remarkable change at that AOA. No relation between wind tunnel and flight tests for higher buffeting levels was found.

3.3 Vibration at Wingtip and Pilot's Seat

Fig. 7a demonstrates the correlation between wing tip vibration level and vibration at pilot's seat at Mach 0,75; pilot's comment for the different buffet levels is indicated. These relations are suitable if flow separation is assumed to be due to compression shocks; for stall induced buffeting at lower Machnumbers the vibration levels are shown in Fig. 7b.

3.4 Local State of Flow on the Wing - Analysis of RMS-values

As shown in Fig. 2 unsteady pressure gages were installed in four sections of the TST wing as well on the wind tunnel model as on the original wing in flight. One point of interest was, of course, the state of the flow at the design Machnumber Ma = 0,84. In section 1 only the kulite at 87 % chord had been wired to the tape recorder. Due to the limited available tracks on the magnetic tape only the kulites of the most interesting wing areas were used for data collecting.
In Fig. 8 the RMS-values from the kulite 4 signal, analog-digitally converted to technical pressure units are plotted versus angle of attack (AOA). In flight there is no increase in the RMS-value up to moderate buffeting (AOA ≈ 4,5°), whereas in the wind tunnel there is a light increase, starting at about 1,5° AOA. Moderate buffet from flight tests coincides with a change in the slope of the wind tunnel curves.

The kulite RMS-values from the gages of section 2 are plotted in Fig. 9. For AOA higher than zero degrees kulite 6, at x/c = 0,37 is situated upstream of the compression shock as indicated by Fig. 10. At pilot's top for buffet onset neither flight- nor wind tunnel free transition curve show any change in RMS-value. The fixed transition curve seems to break at buffet onset. In Flight kulite 6 gives a distinct increase in pressure variation ΔP, - termed moderate buffet by the pilot -, which is also seen in the wind tunnel free transition curve with a light shift in AOA. Kulite 7, placed at x/c = 0,63, is, for this Machnumber, situated close to the shock (Fig. 10). At flow condition "moderate buffet" the three curves show changes in slope.
Kulite 8 failed in flight, that's why only wind tunnel results are plotted. The light increase in RMS seems to represent the growing of shock strength. At buffet onset a quasisteady state level is indicated, probably based on a local separation bubble behind the shock.

The RMS-values of the unsteady pressure gages of section 3 are shown in fig. 11. For this section, which is situated more at the outer part of the wing, the differences in kulite signals between wind tunnel and flight test grow in the region upstream of the shock (Kulite 10). When pilot gives top for "moderate buffet", kulite 11 indicates a strong increase in pressure variation. Heavy buffet from pilot correlates with the sharp kink in the RMS-value of kulite 12.

Kulite RMS-values from section 4 are given in Fig. 12. At flight angle of attack for buffet onset kulite 14 shows a remarkable change in RMS in the wind tunnel tests. Kulite 15, in this case downstream of the shock, reveals a light increase in RMS after buffet onset. In flight test only kulite 16 was recorded on the tape. This kulite is located at 87 % local chord of the wing and lies on the upper surface of the aileron. In the wind tunnel kulite 16 at free transition correlates with pilot's comment "buffet onset". For the state of flow at "moderate buffet" all three curves indicate a change of slope.

Fig. 13 compares the wing areas affected by flow separation in flight and in wind tunnel tests at AOA for buffet onset and moderate buffet (AOA from flight test, pilot's comment). The shaded regions indicate kulites with increased RMS-level at the given AOA for the different buffet levels.

At buffet onset there are greater differences between wind tunnel and flight test than at moderate buffet. The wind tunnel tests with fixed transition (ballotini strip at x/c = 0,1) lead to bigger boundary layer thickness in the rear part of the wing and thus the flow is more sensitive to shock effects and pressure rise.

3.5 Interpretation of Kulite Signals

For better understanding and interpretation of kulite signals it is useful to look at the pressure distributions, measured at wing sections close to the kulite gages.
For example in Fig. 14 the first increase in RMS-value of kulite 10 is the answer to the compression shock crossing this kulite. When the trailing edge pressure decreases to about c_p = 0,05 (indicated by pressure distribution for $\alpha = 5°$) the pressure variation at kulite 12 increases. For AOA > 4 degrees the compression shock moves upstream; kulite 10 shows a strong rise in RMS.

In Fig. 15 the pressure distribution of section 3 from flight test is plotted in combination with the RMS-values of pressure variation of kulite 10 and 12. The shock passing kulite 10 also in flight is reflected by the RMS-values of kulite 10. The pressure distribution from flight at AOA = 4,9 indicates separated flow behind the shock. As demonstrated in Fig. 14, the wind tunnel pressure distribution at $\alpha = 5°$ has a shock position more upstream than in flight. Therefore the RMS-values from kulite 10 in the wind tunnel increase at lower AOA than in flight. In flight kulite 12 shows a continuous increase in turbulence, whereas the wind tunnel result exhibits a step-like increase in the RMS-signals with steady conditions for about one degree in AOA.

As told above the wing for the testbed aircraft with complete flight test equipment was measured in the ONERA S 1 wind tunnel as half model. In Fig. 16 kulite signals of section 3 from the S 1 test are compared with flight test results and those from the S 2 tests with the 1:10 model. The RMS-levels of the three kulites measured in the S 1 wind tunnel are closer to the flight level than the S 2 results. It's interesting, that the two wind tunnel signals differ so much in RMS-level. To answer this question it is necessary to look at the frequency spectra.

3.6 Investigations by means of Frequency Analysis

As shown in the previous section the curves of various rms-values exhibit a rather different behaviour. In order to provide a better insight in the physical relationships it is helpful to use spectrum analysis allowing a representation of the signal as a function of frequency.

From the point of view of interpretation of the results it is very important to know what are the wing eigenfrequencies on both the 1/10-Model and the experimental aircraft. These eigenfrequencies were provided by special structure tests. Particular structure tests were made on the actual wing using the experimental set-up of the S 1 investigations (wing mounted on the wind tunnel balance). The results of these tests are given in the following table:

	right hand wing	
1/10 - model - S2MA	S1MA	experimental aircraft
111 Hz flex. 1 kn A		
133 Hz flex. 2 kn S	9 Hz flex. 2 kn S	10,1 Hz flex. 2 kn S
205 Hz flex. 3 kn A		15,0 Hz flex. 3 kn A
	36,5 Hz flex. 4 kn S	37,0 Hz flex. 4 kn S
		34,0 Hz flex. 5 kn A
456 Kz flex. 6 kn S		
564 Hz tors.	44,0 Hz tors.	44,8 Hz tors.

The high eigenfrequencies on the 1/10 - model confirm the idea that his wing can be considered as a rigid wing. On the other hand, the differences in the eigenfrequencies of the actual wing when mounted for the S1-test and on the experimental aircraft may be explained by the different fixing conditions.

These eigenfrequencies of the model and of the actual wing may be easily detected in the wind tunnel and flight tests, if signals of accelerometers are submitted to spectrum analysis. A first example is given in Figure 17 which shows results of the 1/10 model at M = 0.84 in the S2-tunnel provided by the wing tip accelerometer A3. In this figure the Fourier transform modulus (FTM) is depicted as a function of the frequency. One has to note, that the eigenfrequencies appear not only for angles of attack beyond buffet onset ($\alpha = 4°$) or at higher buffeting levels ($\alpha = 6°$) but also for angles of attack lower than the buffet onset limit ($\alpha = 2°$). The response to the torsion mode should be influenced by the location of the transducer near by the neutral axis of the wing. Further frequency peaks correspond to higher wing modes. Furthermore, it appears that these acceleration spectra lead to rather high rms-values even if buffet onset is not reached. This may be explained on the one side by the large bandwidth considered (the acceleration is proportional to the square of frequency) and on the other side by the strong excitation of the model due to wind tunnel noise as it will be shown later.

In the same manner the accelerometer BT3, which has a similar location at the actual wing, reveals (Fig. 18) the eigenfrequencies of the wing in both wind tunnel and flight tests. In this figure the power spectral density (PSD) of each signal is represented as a function of frequency. The selected test points correspond to angles of attack below the buffet onset limit. A significant difference is noticeable in the total level of the wing response which is much stronger in the S1-test than in the flight. The figure allows another comparison between the informations delivered by the accelerometers BT3 at the wing tip and BRSZ under the pilot seat. The comparison gives some indications about the transfer function between the corresponding measurement points. On the other hand, it becomes obvious that the BRSZ spectrum includes frequency peaks which come from the fuselage and other aircraft components. Compared to the accelerometer BT3 the total response (rms-value) is significantly lower.

The next figures concern the analysis of local flow behaviour by means of Kulite transducers. Due to the remarkable increase of the pressure fluctuations they reveal in particular shockwaves and flow separations

as already shown by the rms-values. The figures 19 and 20 depict spectra from the transducers K11 and K12 of the 1/10 model in a bandwidth up to 5 KHz at Mach number M = 0.84 and several angles of attack. At $\alpha = 2°$, that is to say below the buffet onset limit, the spectra are quite similar. It becomes clear that these spectra exhibit not only effects of the local boundary layer, but -as shown by other inivestigations in the S2-tunnel [8]- are mainly the result of wind tunnel noise created by the wall perforation which leads to so-called edge tones. The corresponding effects are noted 1, 2, 3 in the spectra. In addition, a frequency peak 2fc appears which corresponds to the double compressor frequency. On the other hand, the eigenfrequencies of the model motion cannot be identified in general, except the torsion mode noted T at K12 and this angle of attack. Increasing the angle of attack the results of K11 and K12 become fairly different. For K11 (Fig. 19) located at 62 % of the wing chord a main modification of the spectrum is observed only at $\alpha = 8°$, whereas for K12 (fig. 20) located at 87 % of the chord in the same wing section the spectrum is already modified at $\alpha = 4°$. In both cases the transformation of the spectrum corresponds to the appearance of the flow separation at the location of each transducer. Then the perturbations due to the wind tunnel walls as well as the eigenfrequencies of the wing, even if buffeting occurs, can no longer be recognized.

Similar observations -as far as low angles of attack are concerned- may also be made on the actual wing in the S1-tunnel (Fig. 21). The spectra of the Kulites K11 and K12 at M = 0.84 and $\alpha = 2°$ are characterized by frequency peaks issued from the two stage ventilator. This noise is mainly transmitted by the diffusor of the tunnel, because spectra deduced from Kulites located in a supercritical flow field do not show such peaks. This may also explain particular evolutions of the rms-value with α depending mainly on the location of each Kulite-transducer, as demonstrated in the previous section.

The same figure shows in similar flight conditions, i.e. below the buffet onset limit, for the same Kulites typical turbulence spectra corresponding to the local boundary layer state. Furthermore, it is noticeable again that the total excitation level is much lower than in the wind tunnel.

As previously mentioned the buffeting investigations in flight were conducted by wind up turn manoeuvres which do not allow any frequency analysis. For this, sufficient stabilisations are needed which were realized only in a few number of stationary turns. An example is given in Figure 22. First of all, it shows a comparison of the K12 response at load factors n=1 of the previous case and n=2.2 corresponding at M = 0.83 to a light buffeting situation. The transformation of the spectrum occurs again mainly in the low frequency range (0-50 Hz), where the excitation level due to the flow separation strongly increases. By comparison of the K12 and BT3 spectra (same figure) it becomes obvious that the wing motion cannot be identified in the Kulite spectrum. On the other hand, the comparison of the BT3 spectra without buffeting at n=1 (Fig. 18) and at n =2.2 reveals the significant rise of the wing response when buffeting occurs.

4. EFFECT OF MANOEUVRE FLAPS ON BUFFETING BEHAVIOUR

The TST wing was equipped with leading and trailing edge devices, consisting of 15 % slats and 25 % single-slotted fowler flaps. The flap positions for different configurations are given in Fig. 23 for wing section 3. The extension of the buffet free range in Machnumber Ma and lift coefficient C_L and the general improvement of the aircraft performances due to manoeuvre flaps were already presented in (2).

Additional flight tests were conducted to evaluate the separated effects of the slat on buffeting for the following trailing edge flap configurations:

- trailing edge flap retracted
- trailing edge flap $\eta_k = 5°$
- trailing edge flap $\eta_k = 15°$

Fig. 24 gives an impression of the slat efficiency on buffet onset. It can be seen that for the case of retracted flaps the slat brings no improvement in the Machnumber range $0{,}68 < 0{,}74$. But it must be remembered that the flights took place with fixed slat and flap positions. There will be an improvement if slat position varies with Machnumber.

For Machnumbers between 0,5 and 0,68 the slat shows a remarkable extension of the buffet free flight region. For higher Machnumbers the TST wing with either extended slats or trailing edge position 5° had nearly the same buffet onset limit.

Fig. 25 shows that the vibration levels at the wingtip and at the pilot's seat vary for different manoeuvre flap configurations. With extended slats the 15 degree flap configuration shows less vibration than the clean wing.

5. CONCLUSIONS

The Dornier TST program included extensive buffeting investigations. Besides total aircraft behaviour also the local state of flow over the wing was regarded by means of steady and unsteady pressure transducers. The kulites give informations about shock movement and flow separation. With regard to RMS-values from unsteady pressure transducer and accelerometers differences between wind tunnel and flight were found in the level. As spectra analysis demonstrated, the wind tunnel level is higher due to the noise from wall perforation and from the compressor. The spectra of the signals of unsteady accelerometers on the wing show the wing eigenfrequencies, whereas the kulites scarely reflect these typical frequencies.

Manoeuvre flaps are a useful mean to reduce buffeting vibration level and thus the structural straining will be reduced and the aircraft buffet free flight envelope can be extended.

6. REFERENCES

[1] Lotz, M.; Monnerie, B.:
The Franco-German Experimental Program for the Evaluation of a Supercritical Wing for a Combat Aircraft Application
ICAS paper 76-26, Oct. 1976

[2] Jacob, D.; Welte, D.; Wünnenberg, H.:
Ground/Flight Correlation on the Alpha Jet Experimental Aircraft with a Transonic Wing.
AGARD CP-339 Paper 4A; Oct. 1982, Çeşme

[3] Buers, H.; Schmitt, V.; Lerat, A.:
Ground/Flight Correlation on the Alpha Jet Experimental Aircraft with a Transonic Wing.
AGARD CP-339, Paper 4B, Oct. 1982, Çeşme

[4] Thomas, D.; Jacob, D.:
The Dornier Transonic Wing-Design and Flight Test Results
CA81 Flight Test Symposium, March 1982

[5] Schmidt, W.; Welte, D.; and Moeken, B.:
Evaluation of the Design Criteria and Flight Testing Results of a Transonic Wing for a Subsonic Combat Aircraft
ICAS, Toulouse, Oct. 1984

[6] Hamilton, W.T., et. al.:
Manoeuvre Limitations of Combat Aircraft.
AGARD Advisory Report AR-155A, 1979

[7] X. Vaucheret:
Fluctuations acoustiques engendrées par les parois perméables d'une soufflerie transsonique.
AGARD-CP n° 174-London (1975)

ABBREVIATIONS

AOA	angle of attack
A3, BT3	wing tip accelerometer
BRSZ	accelerometer at pilot's seat
BRZ1	total aircraft vertical accelerometer
Hz	Hertz
K	kulite
K11	kulite number 11
Ma	Machnumber
PSD	power spectral density
Re	Reynoldsnumber
RMS	root mean square
S 1, S 2	ONERA wind tunnel at Modane
TST	Transonic wing at the Alpha Jet
WUT	wind up turn (flight manoeuvre)

Fig. 1

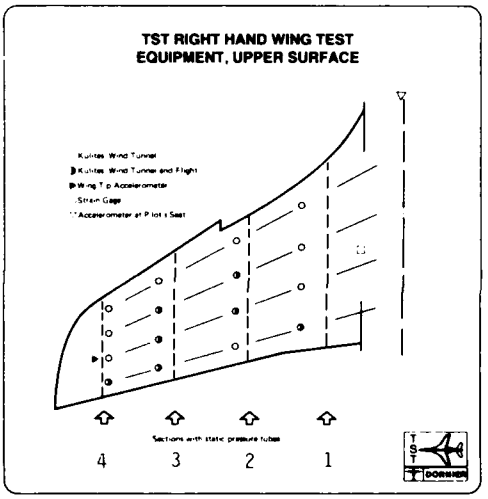

Fig. 2

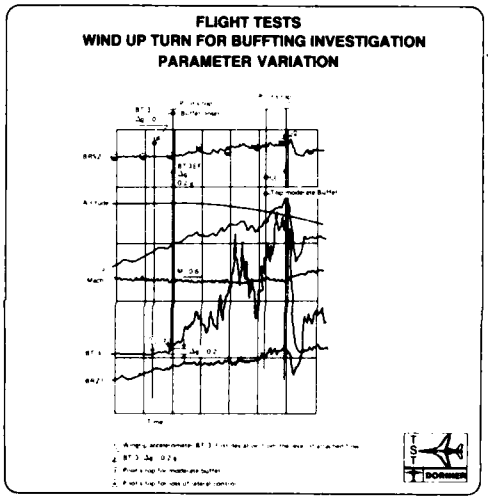

Fig. 3

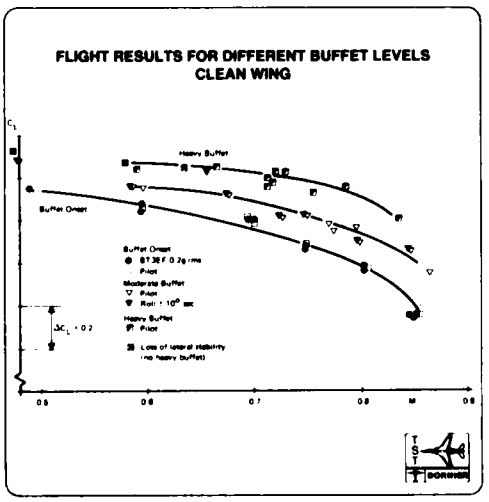

Fig. 4

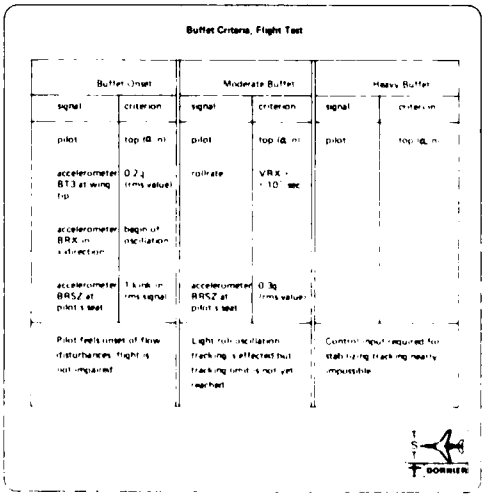

Fig. 5

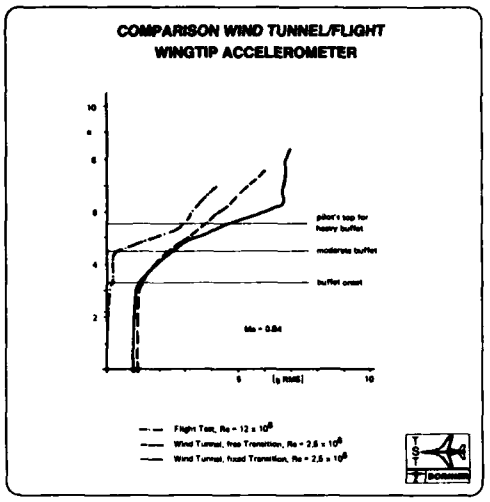

Fig. 6

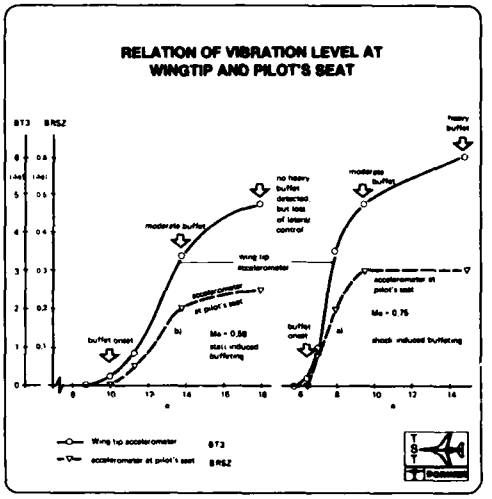

Fig. 7

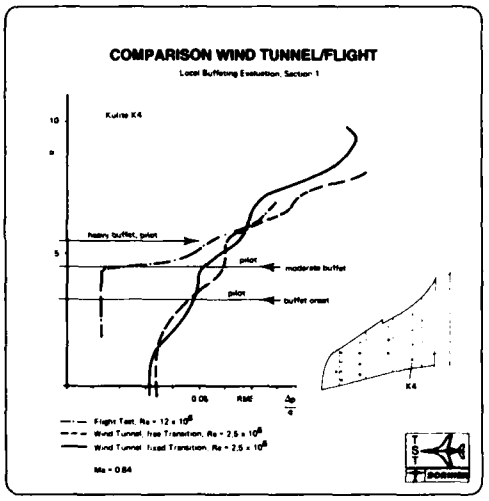

Fig. 8

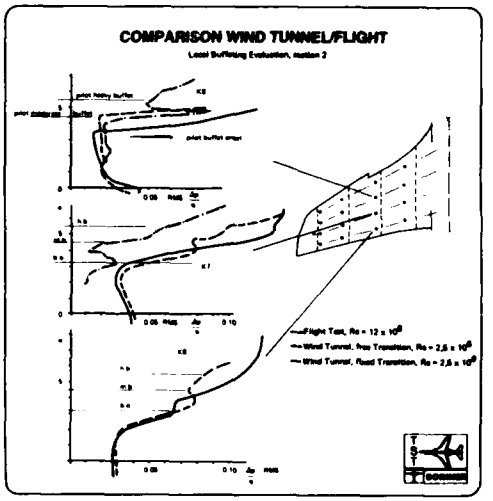

Fig. 9

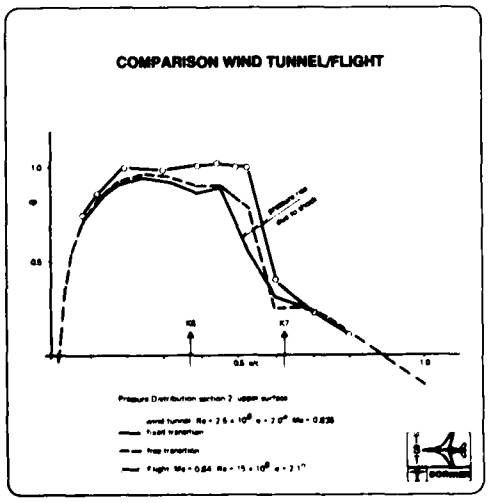

Fig. 10

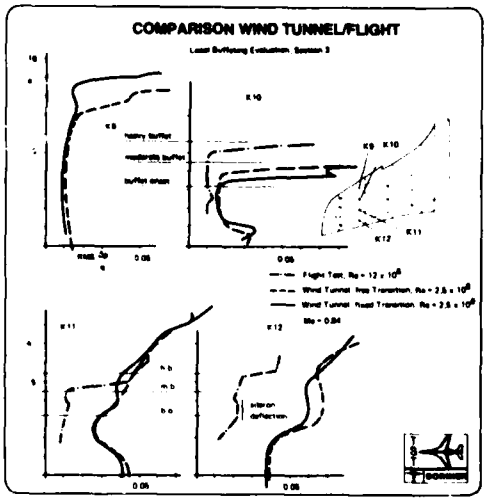

Fig. 11

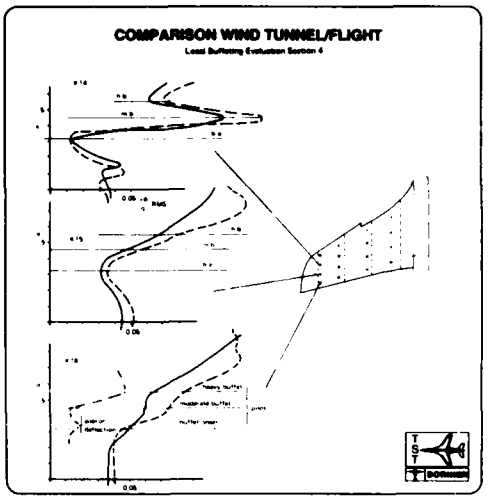

Fig. 12

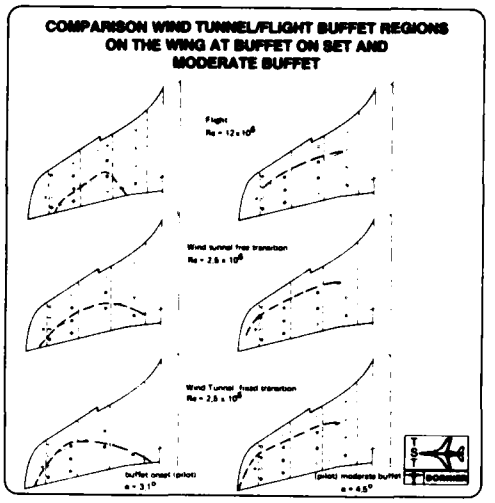

Fig. 13

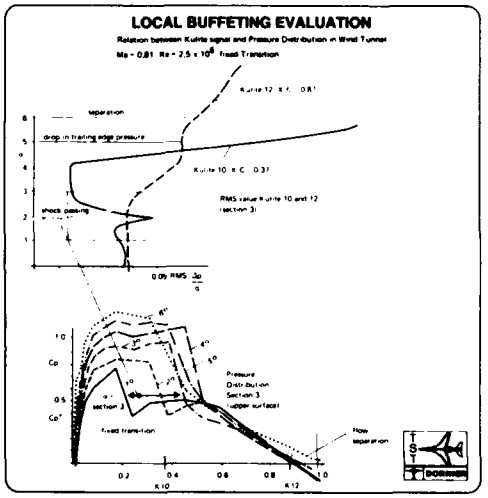

Fig. 14

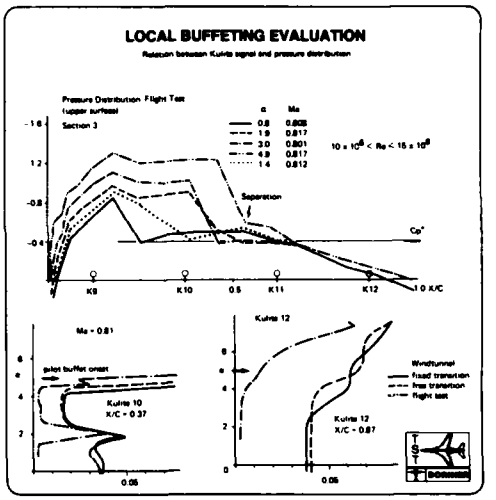

Fig. 15

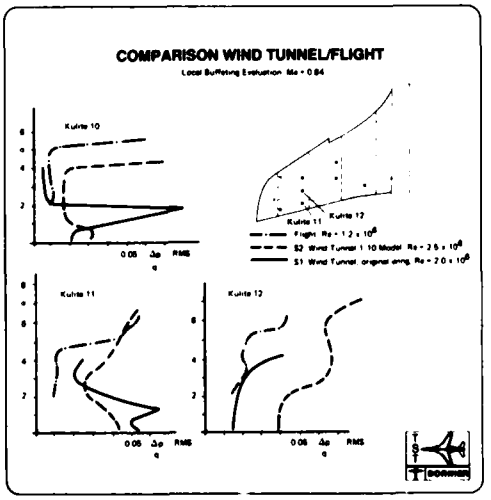

Fig. 16

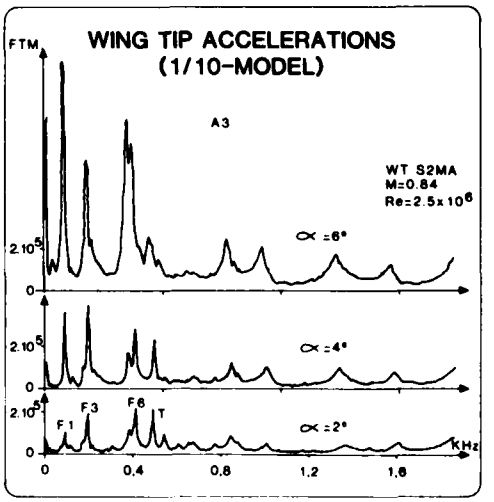

Fig. 17

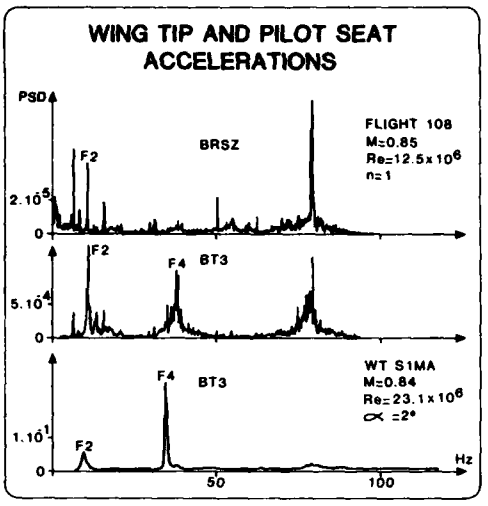

Fig. 18

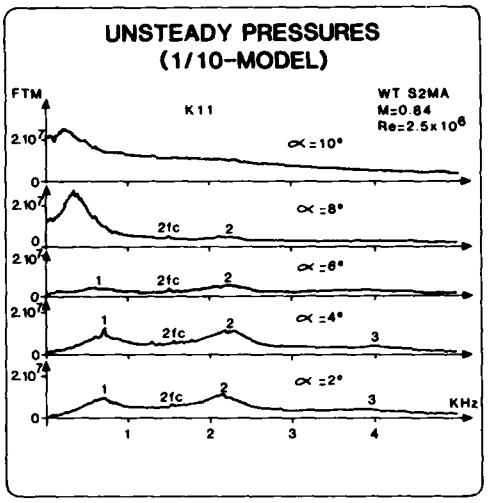

Fig. 19

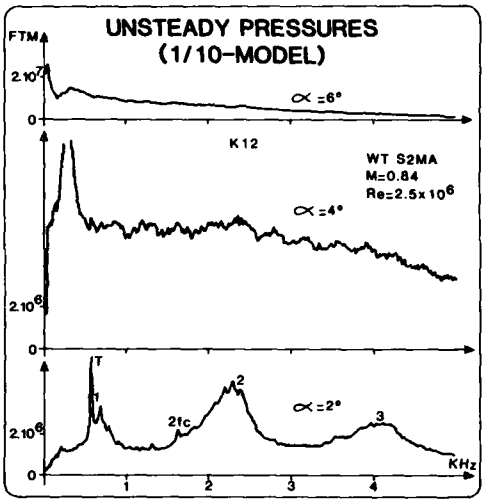

Fig. 20

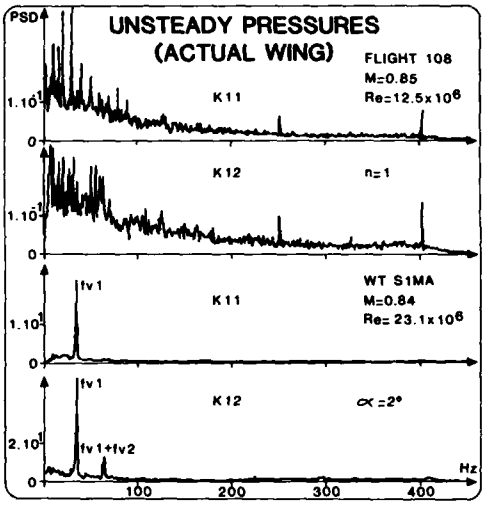

Fig. 21

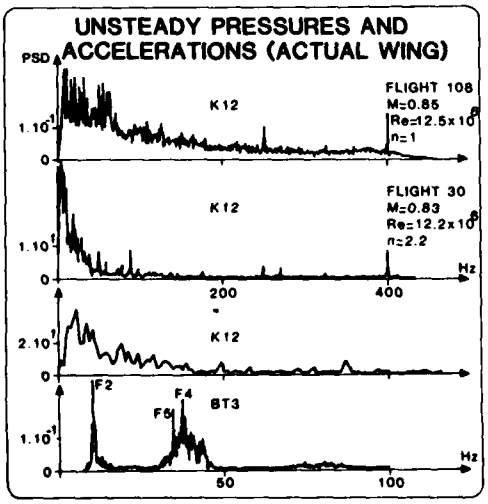

Fig. 22

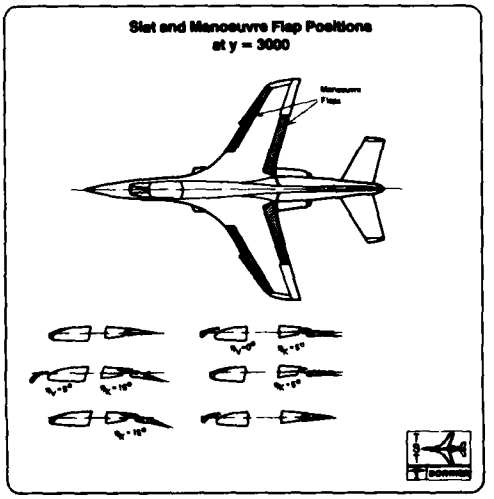

Fig. 23

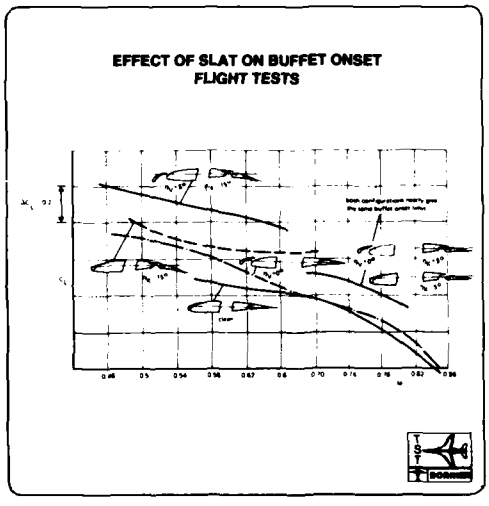
EFFECT OF SLAT ON BUFFET ONSET
FLIGHT TESTS

Fig. 24

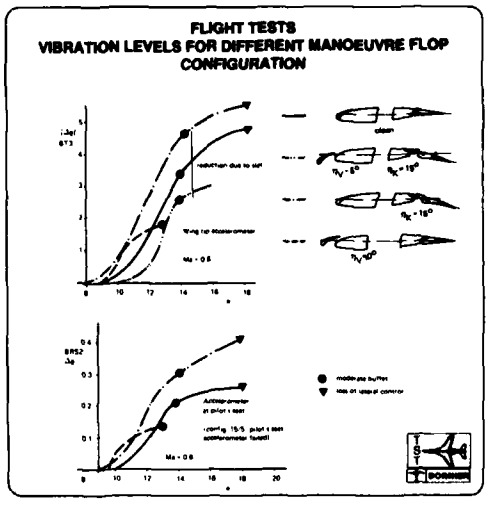
FLIGHT TESTS
VIBRATION LEVELS FOR DIFFERENT MANOEUVRE FLOP CONFIGURATION

Fig. 25

Unsteady Vortex Airfoil Interaction

by

G.E.A. Meier and R. Timm

Max-Planck-Institut für Strömungsforschung
Böttingerstr. 4-8
D-3400 Göttingen
Federal Republic of Germany

SUMMARY

The unsteady flow in the vicinity of an airfoil in a subsonic flow with strong vortices is investigated for a two-dimensional problem. The investigation is concentrated on the interaction of the passing vortex flow field with the steady flow field of the airfoil. Unsteady flow separation and generation of new vortices of the airfoil occurs depending on vortex strength and core path. Inviscid calculations of vortex pathes and sound generation are compared with the experimental results. The associated pressure waves have a strong directivity. The vortices used for the interaction experiments are generated by different vortex shedding cylinders in a stationary duct flow or by airfoils in the starting flow of a shock-tube. High speed interferometric flow recording and wall pressure measurement are the main experimental techniques.

INDRODUCTION

The interaction of vortices with solid boundaries is one of the main reasons for airoacoustic noise and unsteady load. This is found as well for the microscopic scale of a turbulent boundary layer as for the macroscopic scale of vortex airfoil interaction in wakes. Examples for the latter type of interaction are found especially in helicopter rotor noise, where the tip vortex may interact with the blade, and in the unsteady load on the blades of turbo machinery, which often operate in the wake of an upstream stage.

Because of the present lack of knowledge about the unsteady, viscid near field flow, which includes the vortex boundary layer interaction, at the surface of an airfoil experiments must be carried out to establish reasonable boundary conditions for theoretical considerations and also some ideas about the relevant physical phenomena. As a model case for a viscid vortex boundary interaction we have used a two-dimensional flowfield with a vortex interacting with an airfoil. In a duct of a width of 100 mm an airfoil (NACA 0012) of equal span was used for two different experiments. First the interaction of a Karman vortex street and the airfoil was investigated. Additionally in the same duct a shock tube experiment was performed. Single starting vortices of an additional upstream airfoil were generated for interaction experi-

ments. In this latter case the boundary layers are very thin and the vortices have more similarity to potential vortices. These experiments allow quantitativ comparisons to the idealized conditions of inviscid model calculations. Therefore this paper refers more to the shock tube experiments. The Karman vortex street with vortices of more distributed vorticity is used to demonstrate the similarity of the interaction phenomena in this case.

1. An inviscid two-dimensional model for vortex trajectories around an airfoil

The trajectory of a two-dimensional vortex around a Joukowsky airfoil is calculated by potential theory without taking into account a Kutta condition [1] .
This is justified because up to now there is no method known which has no similiar restrictions. Additionally it is not clear if the Kutta-condition is a reasonable condition in case of a high frequency distortion of the flow field of an airfoil.

A simple approach to the problem is achieved by potential theory. By conformal mapping of a vortex and its mirror vortex counterpart one can get a vortex in a flow over a Joukowsky airfoil. The procedure is well established and not discussed in detail here (1, 2, 3, 4, 5). The formula for the complex potential is given by:

$$\Phi = \frac{\gamma}{2\pi} \cdot ($$

vortex component: $\log\,(A(z) - A(z_o))$

mirror vortex " : $-\log\,(A(z) + A(\bar{z}_o))$

circulation " : $+\log\,C(z)\,)$

stationary flow " : $+\frac{1}{cZ}\,(C(z) + \frac{1}{C(z)})$

The capitals A and C are given by:

$$B(z) = z + z \cdot \sqrt{1 - \frac{1}{z^2}} \quad , \qquad \mathrm{Re}\,(\sqrt{1-\frac{1}{z^2}}) \geq 0$$

$$A(z) = \frac{B(z) + 2a + b - 1}{B(z) - b - 1} \quad , \qquad C(z) = \frac{B(z) + a - 1}{a + b}$$

The small letters a and b are parameters for the airfoil shape, c is given by:

$$C = 1 + \frac{1}{(b+1) \cdot (2a + b - 1)}$$

The circulation coefficient Z gives the strength of the vortex circulation:

$$Z = \frac{2\ \Gamma_{vortex}}{U_\infty \cdot \text{airfoil length}}$$

The circulation of the airfoil is the sum of the mirror vortex and the circulation component. The circulation is set to be zero, so the Kutta condition is fulfilled, when the vortex is far away from the airfoil. When the vortex gets closer to the airfoil there is a flow around the trailing edge in this theory. This does not seem to be very realistic, although we know that the Kutta condition is not always fulfilled for high frequencies.

Another approach is to fulfill Kutta condition by the generation of starting vortices (6). But this is also not realistic, because starting vortices are generated only under special conditions in the experiment.

Figure 1 and 2 show two sets of six vortex trajectories calculated with the first mentioned method. The flow comes from the left hand side and the sense of direction

of the vortices is counterclockwise. Figure 1 is an airfoil case (a=1.075, b=0.038) with a circulation coefficient of 1.0. Figure 2 is a flat plate case (a=1.0, b=0.) with a high circulation coefficient of 10. Below the flat plate we see the trajectory of a trapped vortex.

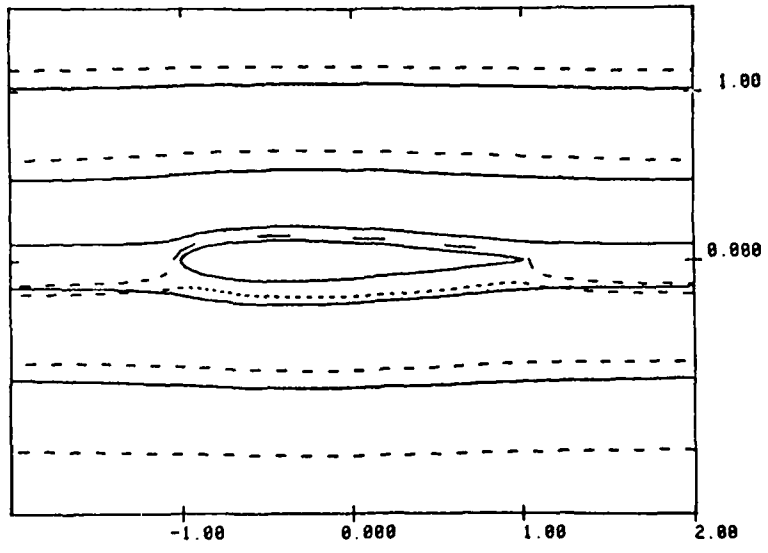

figure 1: 6 vortex trajectories around a Joukouwsky airfoil (dashed lines), the circulation coefficient is 1. The solid lines are streamlines of stationary flow.
(sense of direction of the vortex is counterclockwise)

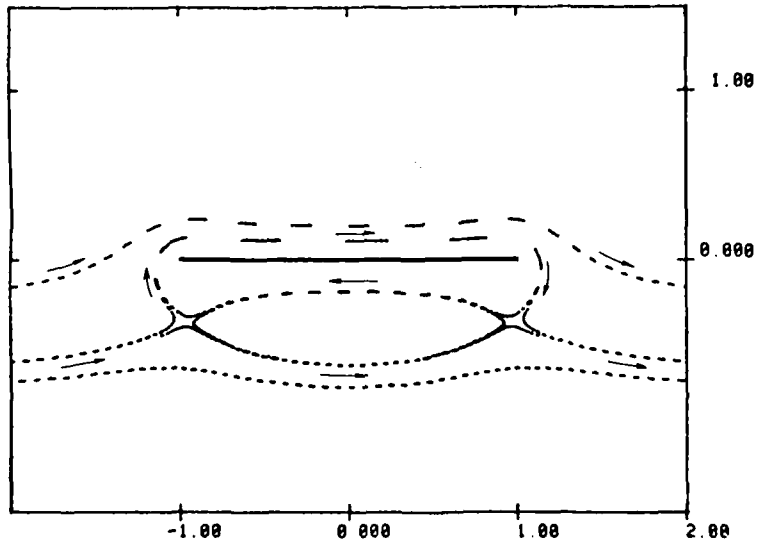

figure 2: 6 vortex trajectories around a flat plate, the circulation coefficient is 10. The flow is from left to right, the sense of direction of the vortex is counterclockwise.

To investigate viscid vortex-airfoil-interaction two experiments are carried out. In the shock tube experiment a shock wave passes an airfoil and generates a starting vortex. Downstream of this vortex generator is another airfoil. The flow generated by the shock carries the vortex to this airfoil, with which the vortex-airfoil-interaction takes place (see figure 3 and 4). The velocity of the flow was varied from Machnumber 0.2 to 0.8, the circulation coefficient from 0.3 to 2.0.

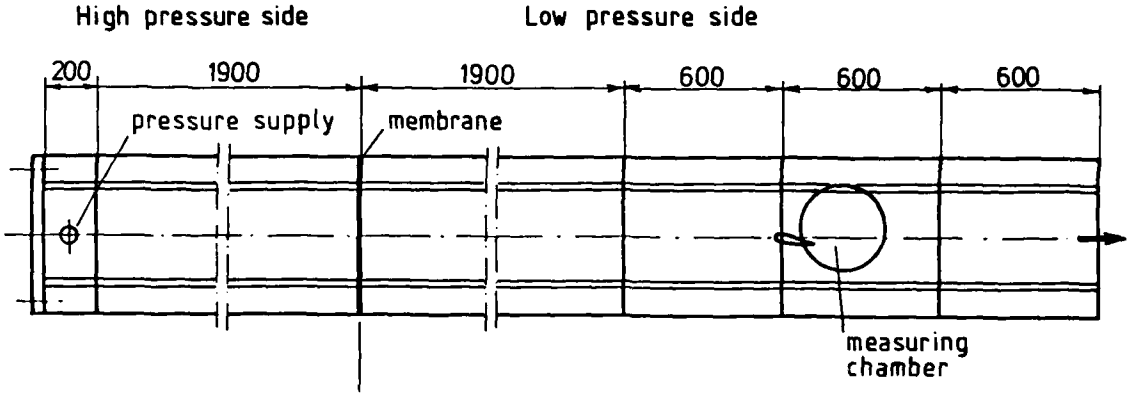

figure 3: Side view of shock tube.

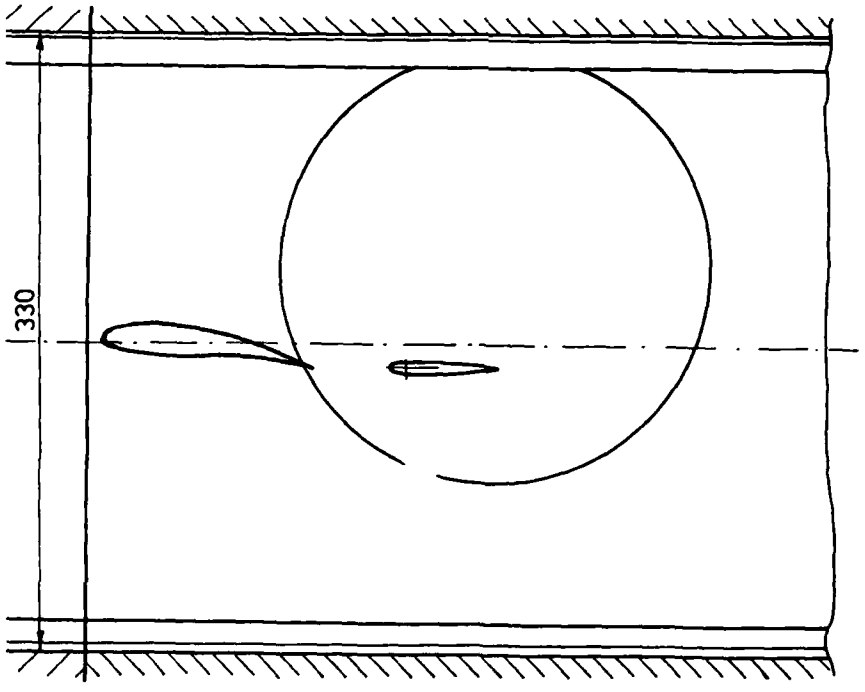

figure 4: Measuring chamber of shock tube vortex generating airfoil and test airfoil.

The second experiment is done with vortices of a Karman vortex street in a stationary windtunnel flow. A symmetric airfoil is placed in the vortex street of a square cylinder (see figure 5). Vortices of alternating sense of direction interact with the profile flow. The flow Machnumber is from 0.25 to 0.35 and the circulation coefficient is from 0.9 to 4.0.

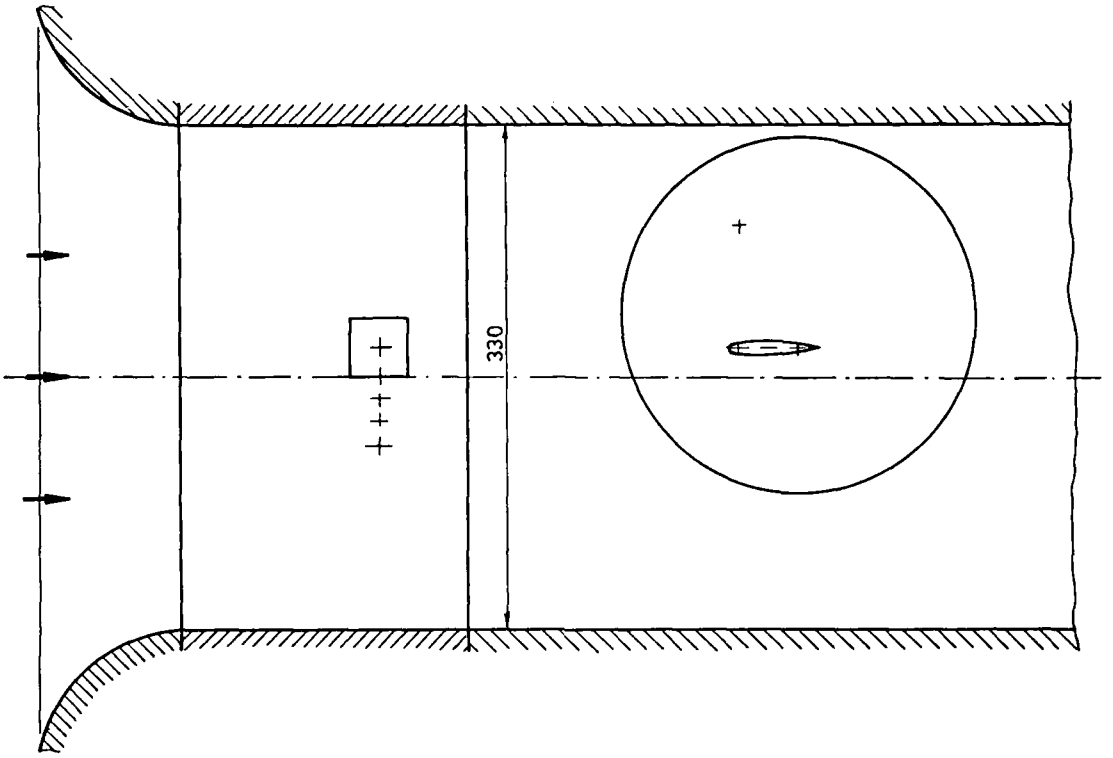

figure 5: Stationary windtunnel with square cylinder and test airfoil.

In both experiments the main measurement device is a Mach-Zehnder interferometer.

The shock tube experiment generates vortices with very small core radii. The velocity distribution of these vortices is close to a potential vortex and the low turbulence level allows reproducible results. Thus this experiment is well suited to test the predictions of the theory on the vortex trajectory. In figure 6 there is a comparison of measured and calculated vortex trajectories. The measured trajectories show a stronger deviation from the horizontal near the airfoil. As already discussed in the theoretical part the vortex seems to change the circulation of the airfoil, which is not included in our calculation.

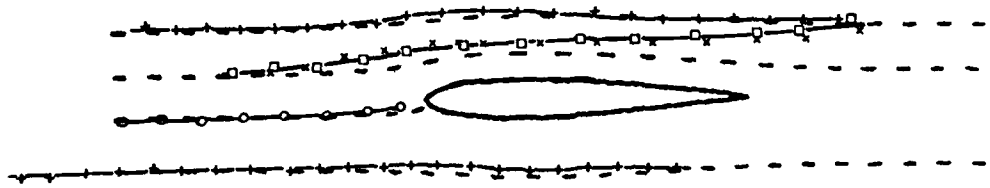

figure 6: Comparison of measured vortex trajectories (solid line) and calculated trajectory (dashed line).
Circulation coefficient Z = 0.5

An interesting detail in the measured vortex trajectories is the difference of the two upper trajectories in the tail region of the airfoil. The upper trajectory stays quite close to the calculated line while the lower trajectory gets very close to the upper one and finally crosses it. The different behavior of the vortex close to the airfoil is due to boundary layer effects. The interaction with boundary layer causes a loss of circulation of the vortex and the generation of a secondary vortex. The secondary vortex induces an upward velocity.

One of the trajectories ends in front of the leading edge of the airfoil. Vortices which hit directly the leading edge disappear totally in the following interferograms. At high Machnumbers this leads to the generation of a strong sound wave.

Parthasarathy (6) included in his theory the generation of potential vortices and fulfilled the Kutta condition. In his calculation he uses a very high circulation coefficient of 3.14. The highest value in the shock tube experiment has been 2.0. Figure 7 is a qualitative comparison of the measured (Z=2.0) and the calculated (Z=3.14) trajectories. Parthasarathy uses in his calculations a Joukowsky airfoil shape with trailing edge angle zero and 13 per cent thickness while the experiment airfoil shape is in this case NACA 0018. Although there are differences of this kind in the parameters there should be a qualitative similarity of the results. But the trajectories look entirely different, in the trailing edge region the measured trajectory is directed downwards while the calculated one is directed upwards.

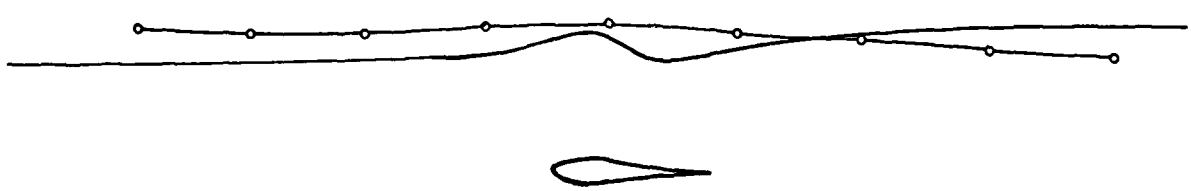

figure 7: Comparison of measured vortex trajectory (open symbols) and a calculation of Parthasarathy).
Circulation coefficient Z = 2.0 (Measurement)
Z = 3.14 (Parthasarathy)

The boundary layer plays an important role in vortex airfoil interaction. The closer the vortex gets to the airfoil the stronger is the effect on boundary layer. Figure 8 is an overview on the different interaction phenomena. (The flow comes from the left side, the sense of direction of the vortex is counterclockwise). The interaction is shown in 4 timesteps. Depending on the distance to the airfoil axis we can find eight (a-h) principally different cases. The phenomena are very much alike for Machnumbers from 0.2 to 0.8 and circulation coefficients from 0.3 to 1.5. The case f happens only at circulation coefficients above 2.0. Case c needs a circulation coefficient above 0.5 or a high Machnumber.

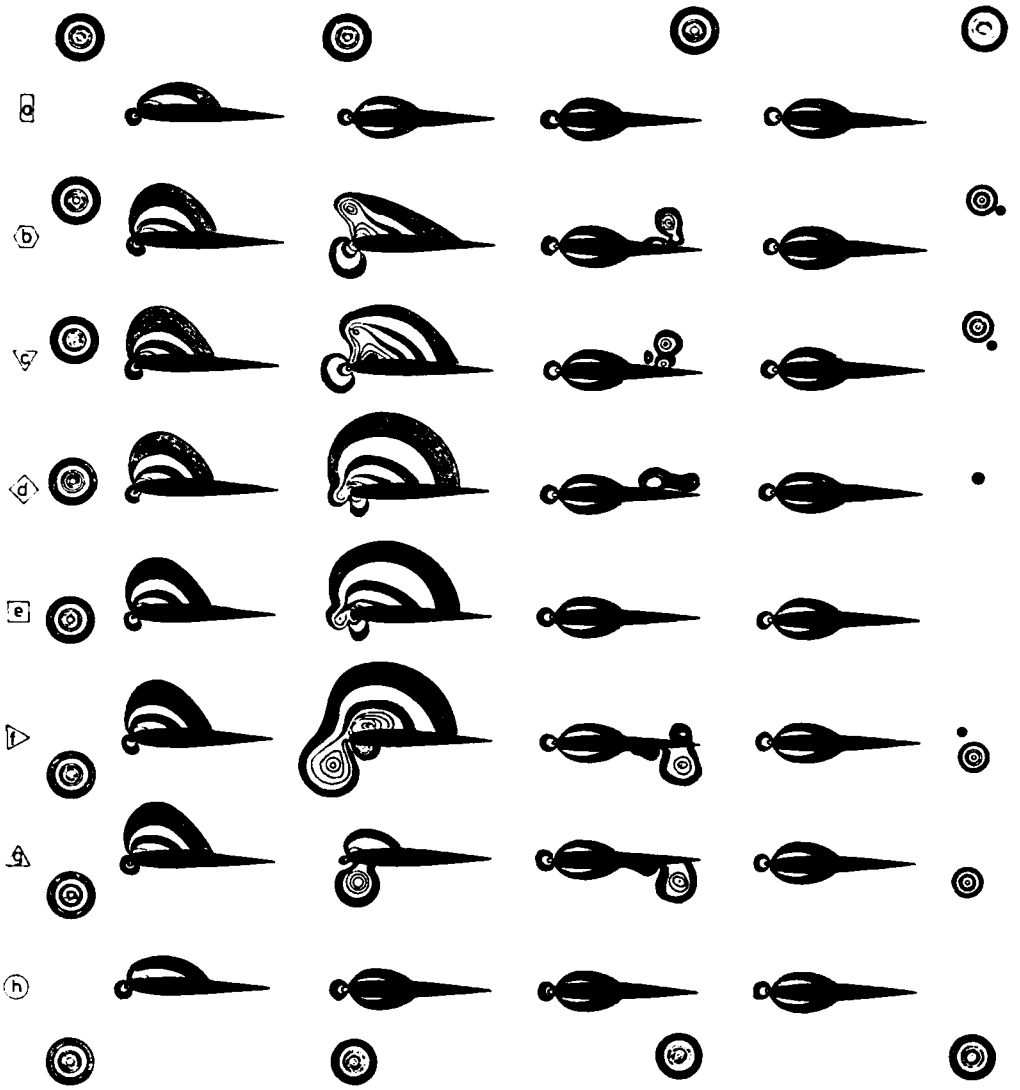

figure 8: 8 cases of vortex-airfoil interaction depending on flight height of the vortex.

Cases a and h: At a greater distance from the airfoil axis, that is more than one third of airfoil length at a circulation coefficient of 0.5, there is nearly no interaction with airfoil boundary layer. Only the stagnation point is moving downwards and a tiny suction region is generated on the upper side of the airfoil. After the vortex has passed the leading edge there are no strong deviations from the stationary flow around the airfoil.

Cases b and g: When the vortex comes closer to the airfoil the interferogram shows a small thickening in boundary layer between vortex and airfoil boundary. The thickening is generated at about one quarter of airfoil cordlength. It is travelling with the vortex and it is slowly growing. This thickening can be the source of a secondary vortex, when the interaction is strong enough. This secondary vortex is generated downstream of the primary vortex if the vortex is above the airfoil and upstream if the vortex is below the airfoil.

Cases c and f: If the vortex is stronger there is a separation in the suction peak which becomes a secondary vortex. Case f, where the vortex passes under the airfoil occurs only at circulation coefficients above 2.0. At very high circulation coefficients of about 4.0 there is separation at the suction peak if the vortex is still more than half an airfoil length away from the leading edge.

Cases d and e: If the vortex hits directly the leading edge, it vanishes totally (Case e). If the vortex passes very close to the profile the vortex looses a lot of its circulation and only a very small turbulent spot is left (Case d).

The figures 9, 10, 11 and 12 are examples for the cases b, c, e and f. The figures 9, 10 and 11 are related to the shock tube experiment while Fig. 12 comes from the stationary windtunnel experiment. Figure 9 contains ten frames. A vortex is coming from the left side and while passing the airfoil it generates a secondary vortex. Figure 10 and 11 are experiments at the high Machnumber of 0.8. In the first of the 5 frames the shock wave and the vortex are at a close distance. Before the vortex gets into contact with the airfoil it passes the leading edge reflection of the shock. When the vortex gets close to the leading edge there is a strong interaction. In both cases the vortex nearly vanishes. But this strong interaction generates a strong acoustic wave. Figure 12 shows an interaction of the airfoil with a vortex of the high circulation coefficient of 4. There appears a strong secondary vortex generated in the suction region of the airfoil.

Literature:

1 Betz, A., Konforme Abbildung. Springer-Verlag Berlin/Göttingen/Heidelberg (1964)

2 Obermeier, F., On a New Representation of Aeroacoustic Source Distribution. II. Two-dimensional Model Flows, Acustica (1979) 42(1), 62-71

3 Routh, E.J., Some Application of Conjugate Functions. Proceedings of the London London Mathematical Society (1881)

4 Lin, C.C., On the Motion of Vortices in Two Dimensions. Applied Mathematics Series No.5. University of Toronto Studies.

5 Obermeier, F., Effects of Solid Boundaries on Aerodynamic Sound Generation. Max-Planck-Institut für Strömungsforschung (1979) Bericht 114/1979

6 Parthasarathy, R., Aerodynamic Sound Generation due to Vortex-Airfoil Interaction. Dissertation Stanford University (1972).

figure 9a/b: Mach 0.2, Z = 0.5, Re = 290 000

figure 10: Ma = 0.8, Z = 0.7, Re 280 000

figure 11: Ma = 0.8, Z = 0.7, Re = 280 000

figure 12: M 0.25, Z = 4.0, Re = 340 000

UNSTEADY AERODYNAMICS APPLICATION TO HELICOPTER NOISE AND VIBRATION SOURCES

by

T.S.Beddoes
Westland Helicopters Ltd
Yeovil, Somerset BA20 2YB
UK

Abstract.

A study has been conducted into the feasibility of producing aerodynamic loads of sufficient fidelity to enable a realistic acoustic signal to be derived. The need arises from the excessive blade/slap noise which results from blade/vortex interaction. A tool is required to investigate the influence of design and operational parameters as a routine procedure. For this purpose a simplified two dimensional model is developed and validated against a more sophisticated analysis. The model is extended to the rotor application where the complex wake geometry is the determining factor in the character of the loading. From the distributed transient loading an acoustic signal has been derived which has been compared with experimental data. A comprehensive correlation has not yet been performed but the preliminary results are encouraging.

Introduction.

There are many sources of helicopter noise, however, under appropriate conditions the ones that become most obtrusive can be attributed to thickness effects and to blade/vortex interaction. Thickness noise, due to the displacement effect of the blade may become severe at high advancing blade Mach number where strong shocks are generated and propagated into the atmosphere; a problem which becomes more apparent as forward speed is increased. For single rotor helicopters blade/vortex interaction does not normally occur in steady level flight. It is promoted by manoeuvring and descending flight when the rotor and wake are forced into closer proximity, in particular, during prolonged approach conditions the maximum nuisance value may be experienced.

The work presented here constitutes a feasibility study. The objective is to determine whether it is possible to produce meaningful noise signatures from the calculated time dependent aerodynamic loading generated in a practical computer rotor/wake program. It is intended to produce a program which is suitable for extensive parametric studies, routine use in rotor design and the evaluation of tests and operating procedures. To produce a loading time history which can be processed into a noise signal, the timewise sampling requirement is much more severe than in the conventional rotor loads analysis. Typically, the significant portion of the blade/vortex interaction may encompass only 3 millisec and azimuth sampling of, at most, 1/2 degree is necessary. Rotor loads programs conventionally consider only one control point on the chord at each radial station but when a vortex with a core radius of about 5% chord is in close proximity to the blade it is necessary to consider at least 20 points on the chord. To construct the noise signature requires interpolation of the loads radially and in time which means that at least 20 radial stations are required. All these requirements make it difficult to construct a program with moderate memory and c.p.u. demands.

2 Dimensional Model.

Procedures have been developed (reference 1) for calculating the lift response to arbitrary forcing using indicial response functions. The total lift is obtained by superposition of responses to a sequence of step inputs which in aggregate represent the time history of the forcing function. By suitable choice of indicial functions the numerical algorithms used to implement the superposition integral may be kept extremely simple though still accurate. The formulation, which will accomodate mixed modes of forcing and varying freestream Mach number, utilises a control point at the three quarter chord location and although the effect of pitch rate is included, further nonuniformity of forcing within the chordal dimension is ignored. Any extension of the above approach to the blade/vortex interaction problem is obliged to take into account the large variation in boundary conditions within the scale of the chord and it is not immediately obvious that such an extension would be realistic. However the enormous computational implications of any alternative approach and the attractive simplicity of the indicial method provide the justification for an attempt at such an extension.

Firstly, a review of the indicial lift model presented in reference 1. The lift response to an instantaneous change in incidence is split into two components, a circulatory term which is initially zero and exponentiates towards the appropriate steady state value and an impulsive term which initially corresponds to the value given by piston theory and subsequently decays exponentially to zero. The form of the circulatory indicial lift function $\phi c(s')$ corresponds to the Kussner function but the coefficients have been modified in the light of experimental and theoretical studies (ref.1); i.e.

$$\Delta C_{Lc}(s') = C_{L_\alpha} \cdot \Delta\alpha \, \phi c(s')$$

$$\text{where} \quad \phi c(s') = 1 - 0.3\, e^{-.14\, s'} - 0.7\, e^{-.53 s'}$$

$$s' = s\,(1 - M^2), \quad s = t * 2V / c$$

From piston theory the initial value of lift is $C_{L_i}(0) = 4\,\Delta\alpha / M$ and in reference 1 the decay time constant was rationalised from considerations of the initial slope. Subsequent correlation studies have substantiated that a much simpler and physically more meaningful time constant equal to c/a produces improved results throughout the subsonic Mach number range for frequency response comparisons. Thus the

impulsive lift term is given by :

$$\Delta C_{L_I} = \Delta\alpha \frac{4}{M} e^{-ta/c} \quad \text{or} \quad \Delta\alpha \frac{4}{M} e^{-s/2M}$$

The resultant behaviour is illustrated by figure 1 which shows the lift response of a moderately thin airfoil at a Mach number of 0.72 to a step change in angle of 2 degrees. This case was the subject of a theoretical calculation using a finite difference solution of the Euler equations (reference 4), the result of which is included in figure 1 for comparison.

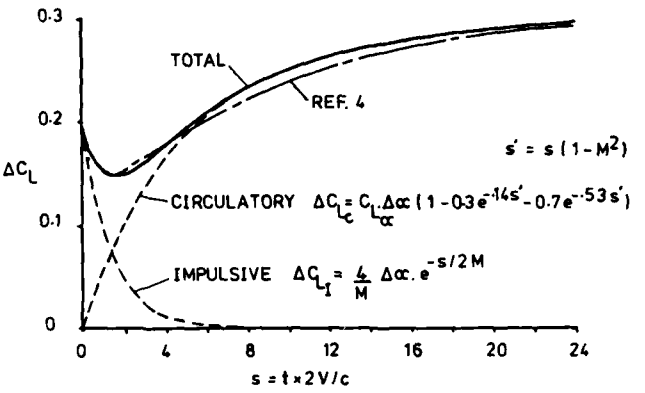

Fig.1 Lift response to step change in incidence.

The tip vortices generated by a full scale rotor have a core radius of the order of 5% chord in the moderately short term. Thus, for close proximity of a vortex to a rotor blade, it is necessary to define the boundary conditions on the chord at a minimum of 20 points. To extend the indicial model to accomodate blade/vortex interaction the following approach has been taken.

Dividing the blade chord into a number of segments, a control point is positioned in the middle of each. Boundary conditions in terms of the velocity component normal to the surface are evaluated at each point and the impulsive force is calculated for each segment independently using the decay time constant c/a . The circulatory lift is evaluated by integrating the influence of the boundary conditions along the chord in a manner analogous to steady state thin airfoil theory and then applying the circulatory lift function $\phi_c(s')$ to the resultant change in the lift forcing function. The appropriate equations and numerical procedures for implementation are presented in the appendix.

It is quite obvious that the above approach lacks rigour and in order to justify its use it is necessary to substantiate it by comparison with more rigorous theory and experimental data. Two theoretical sources are available. In reference 2 Caradonna et al. utilise a finite difference solution of the transonic small disturbance equations to simulate the passage of a vortex line parallel to a 2 dimensional NACA 0012 airfoil at M=0.8. The same calculation has been repeated by McCroskey and Goorjian (reference 3) using the LTRAN2 code modified to incorporate further high frequency terms. McCroskey has extended the study to the NACA 64A006 airfoil at M=0.82 and 0.85 and has investigated the sensitivity of the solution to various simplifying assumptions. Figure 2 compares the results of the various calculations for the NACA 0012 at M=0.8 and $\alpha = 0.5^0$ subject to the passage of a vortex , strength equivalent to a $C_L = 0.4$ at a distance z = 0.26 chords below the airfoil. No influence of the airfoil on the the vortex is assumed. In reference 2 the results are presented in the form of surface pressure distributions from which the C_L values have been deduced with some loss of accuracy. The early differences between the results of the indicial solution and those of reference 3 may be attributed in part, at least, to the process of initialisation. Relative importance of the impulsive and circulatory terms are shown in figure 3 where it can be seen that the impulsive term has a significant effect on the phasing of the lift response.

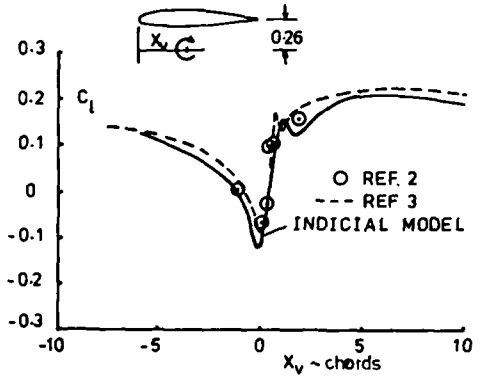

Fig.2 Lift response to vortex passage.

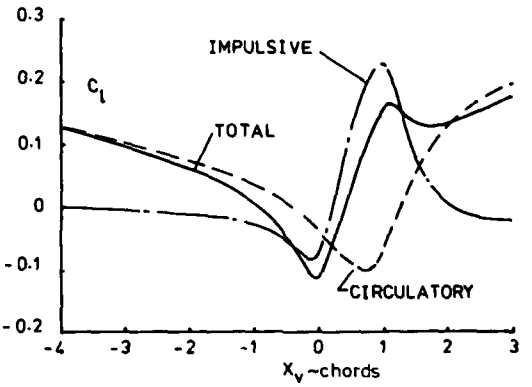

Fig.3 Impulsive and circulatory lift components.

A similar case involving the Naca 64A006 at M=0.85 is shown in figure 4a. For this case the calculation was repeated in reference 3 allowing the vortex path to be influenced by the airfoil. To simulate this variation using the indicial model the vortex path was prescribed appropriately, the results were quite comparable and are shown in figure 4b. It can be seen that the effect of the airfoil in displacing the vortex is small though not negligible. In the rotor application the interaction involves a vortex curved in three dimensions for which the induced displacement is likely to be much smaller.

From the above comparisons it can be concluded that the indicial model is capable of producing, somewhat fortuitously perhaps, results which compare favourably to a first order with those produced by

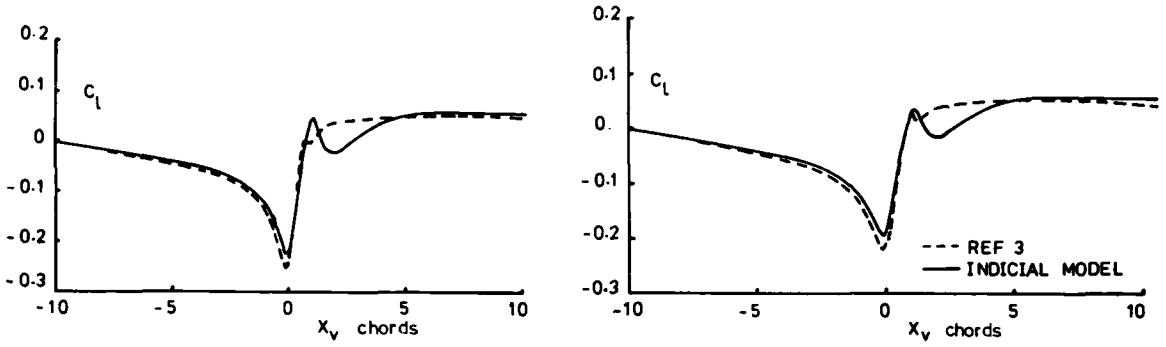

a) No interaction.

b) Vortex displaced by airfoil.

Fig.4 Effect of vortex displacement.

more rigorous and infinitely more lengthy methods. The only obvious inconsistency, at present, comprises an accentuation of the impulsive lift decay as the vortex leaves the region of the trailing edge. Reference 3 also assesses the significance of ignoring the inplane velocity perturbation and concludes that it does not have much effect on the integrated load; in fact, the indicial calculation (which ignores the inplane term) matches the corresponding calculation of reference 3 very closely indeed. To determine the sensitivity of the solution to the timewise sampling interval, various values were tried; the minimum sampling to avoid degraded response amounted to Δt V/c of 0.10.

3 Dimensional Model.

For the rotor model, the boundary conditions vary considerably across the blade. They are determined by the blade motion and the contribution of the trailing vortex wake as outlined elsewhere. Implementation of the lift calculation is by means of strip theory and in the tip region the boundary conditions are dominated for most of the time by the influence of the tip vortex, the strength of which is determined by the integrated lift from the prior sampling. In addition, for the impulsive loading, the characteristics are determined by the decay time constant which equals c/a for the 2D case. The blade tip provides another path for the impulsive pressure signal to equalise and thus it may be anticipated that the time constant will be reduced as the tip is approached. It is assumed that the governing parameter is the distance from the tip, expressed in chordlengths (y/c) and that the time constant T is given by ϵ.c/a where $\epsilon = (1-e^{-y/c})$.

A blade /vortex interaction experiment was performed by McCormick and Surendraiah (reference 6) in 1970 in which local pressures at 95% radius were measured. Qualitative agreement has been obtained with the results of this experiment but in view of the subsequent significant advances in instrumentation since it was performed, the experiment is being repeated to provide better resolution and more extensive coverage of the blade. The results will form a basis for comparison with the 3D model and for its improvement.

The Rotor Wake.

In forward flight the rotor wake is characterised by a cycloidal pattern of the rolled up tip vortices from each of the blades. In the absence of mutual distortion effects the vortices would appear to be positioned on the surface of a skewed cylinder originating in the tip path plane and projecting downward and to the rear. There is, however, significant distortion of the vortex loci, primarily in the vertical plane, which is strongly time dependent. Methods exist, which are fairly rigorous mathematically, to calculate the time varying vortex wake. However, for the present task, the rigorous approach is out of the question in view of the excessive computing requirements. An alternative wake model has been developed for application to the blade vortex interaction problem and is documented in reference 7.

For the purpose of illustrating the procedures and results of the rotor calculation a specific flight condition is utilised, namely, a 4 bladed rotor (W30) at a forward speed of 70 kts and descent rate of 670 ft/min. Under these conditions the advancing blade encounters some of the trailing vortices and the phenomenon is used to demonstrate the nature of the induced loading and its potential consequences.

Some general views of the rotor wake are shown in figure 5, the level flight condition is used since the basic geometry is shown more clearly. In descent the wake is pushed upwards relatively and figure 6 illustrates the degree of vertical distortion encountered by the vortex originating from a blade at 90° azimuth; the undistorted locus is determined by the momentum downwash and shown for comparison. As discussed later, the major blade/vortex interaction occurs at around 50° azimuth and figure 7 is used to illustrate the relative geometry of the blade and a succession of vortices which are in immediate proximity. Changing the rate of descent will modify the vertical separation. When the vortices are very close the vortex core structure becomes important and must be taken into account in determining the boundary conditions on the airfoil. A generalised form of core structure is used which expresses the radial variation of effective circulation with the equation $\Gamma' = \Gamma \cdot \rho^2/(1+\rho^2)$ where ρ is the radial co-ordinate non-dimensionalised with respect to the core radius.

The results of the rotor downwash calculation are shown in figure 8 for the four quadrants of the rotor revolution. In the first quadrant a regular procession of ridges mark the passage of trailing vortices, the alignment of the ridges has a strong radial component which means that the local timewise variation of downwash is large. The two major interactions occur at about 35° and 50° azimuth and involve vortices from the following blade shed 1.75 revolutions earlier and from the opposite blade at 1.5 revolutions earlier. For the second and third quadrants the wake vortices are not so close to the

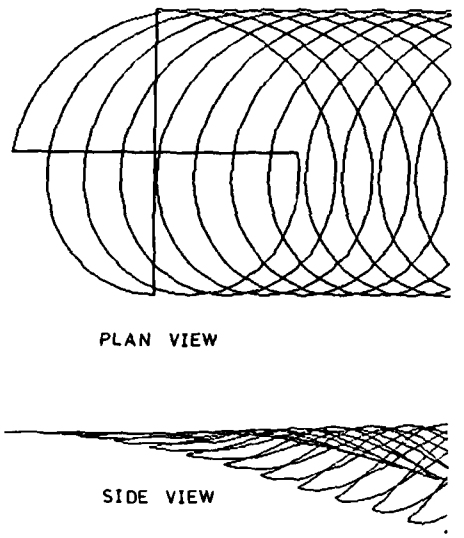

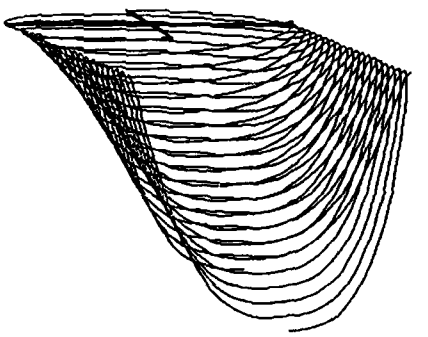

REAR (3/4) VIEW, FROM ABOVE DISC PLANE

Fig.5 Rotor wake - general view.

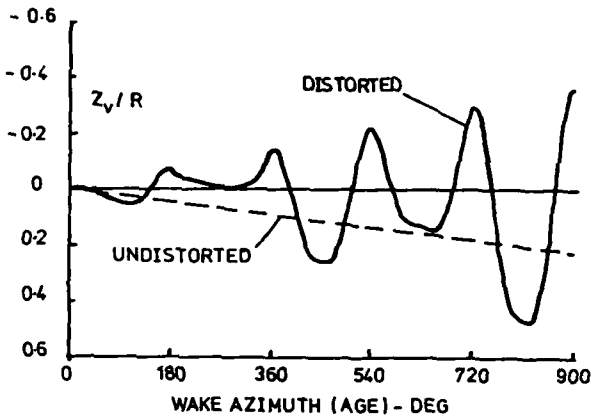

Fig.6 Vertical distortion of vortex trail.

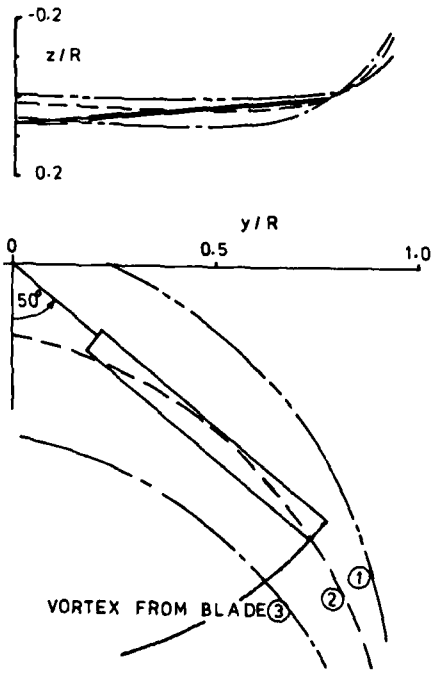

Fig.7 Relative geometry of blade and vortices.

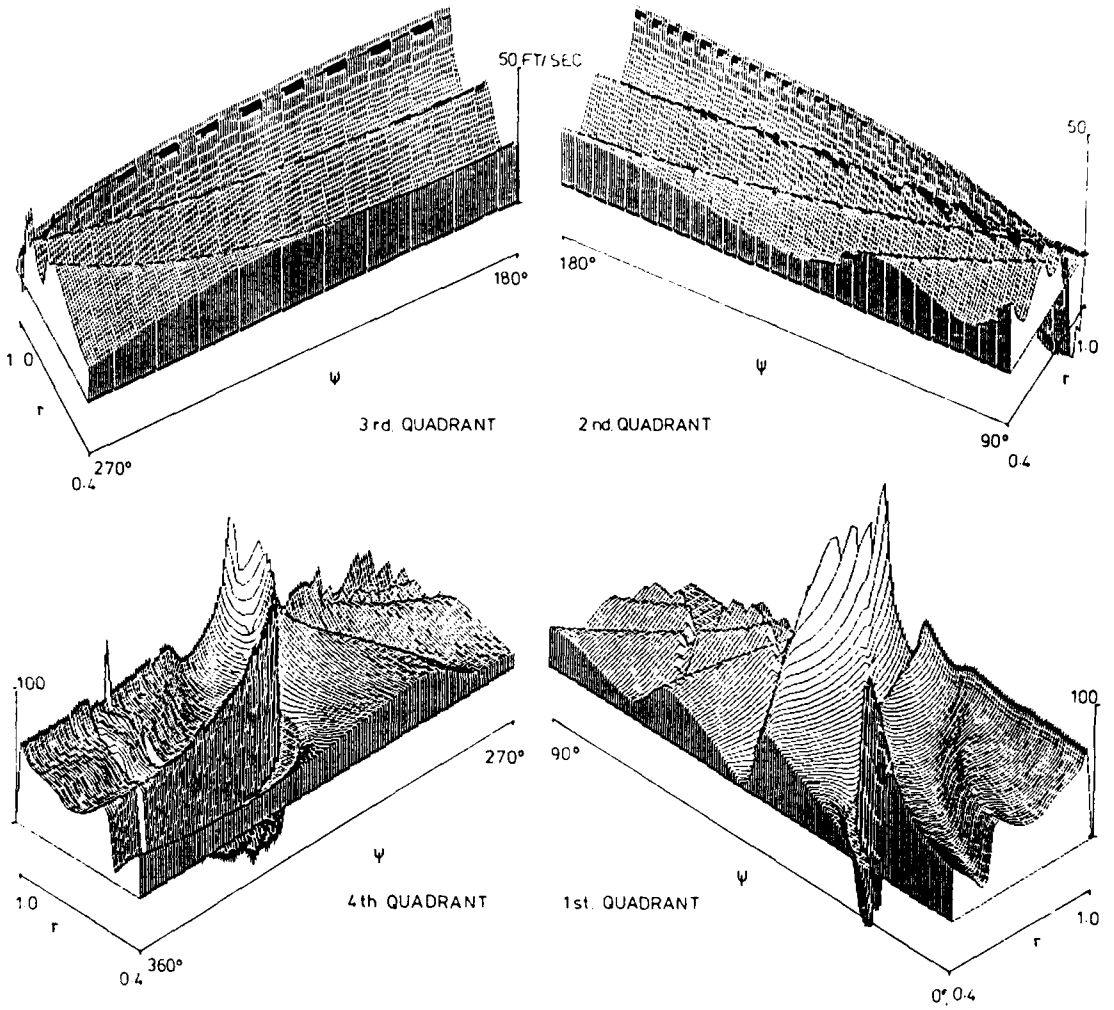

Fig.8 Downwash encountered by the rotating blade.

blade but their influence is nevertheless apparent; the vortices are now aligned more at right angles to the blade, moving slowly inboard at first and then outboard. The timewise variation in downwash for a point on the blade is, in general, not large. In the fourth quadrant the picture is more similar to the first, in that a strong interaction with a large timewise variation occurs at an azimuth of about 310°, the vortex has been trailed from the same blade about 1.2 revolutions earlier.

The Rotor Model.

For the purpose of this study the rotor blade response formulation has been kept simple since the objective is to determine whether the time history of the airloads will yield a realistic acoustic signal. The trim of the rotor is determined firstly by a balance of the thrust vector against weight and drag, taking into account the flight path. This determines the orientation of the tip path plane and subsequently, using a linear analysis, the required rotor collective and cyclic pitch requirements are determined. The airloads are calculated in detail for one rotor revolution only which is sufficient for the present purpose but the whole procedure will need to be refined considerably for calculation of blade modal response and transmitted steady and vibratory forcing.

A blade azimuthal time stepping procedure is adopted to calculate the airloads. The blade is divided into 24 radial segments extending from 0.4 radius to the tip. At each radial station 20 control points are positioned along the chord and after obtaining the local boundary conditions which include the downwash component the lift solution follows the form described for the 2 dimensional analysis.

The blade lift, which results from a spanwise integration, is used to update the strength of the vortex trailing from the blade tip which in turn figures in determining the boundary conditions for the the next calculation. Compressibility effects are accounted for via the appropriate instantaneous value of lift curve slope and the spatial transformation implied in the form of the indicial lift functions. Stall effects are not included at present but, for the conditions studied here, the lift coefficient values are sufficiently low that stall would not be encountered.

Blade Loading Time History.

It is apparent from study of the wake geometry that for a wide range of descent rates there will be several close encounters between the advancing blade and the vortex trails within the wake. At no time will there be perfect alignment such as may be studied in an idealised form and thus there will be considerable variation in the magnitude and phasing of the peak loads and the reinforcing effect of multiple encounters. The complexity and implications of this problem have yet to be studied. The purpose here is to look at a particular case in order that the resultant noise signatures may be evaluated.

A noise survey has been conducted on the W30 to determine the flight conditions which exhibit the maximum noise signature and to define the operating procedures for which the noise levels are relatively innocuous. An appropriate test for the theoretical evaluation is provided by the configuration producing the maximum interaction and, presumably, noise signature; this comprises descent at a nominal 6° angle, 670 ft/min at 70 kts. Discussion of the wake model has described the relevant geometry and nature of the downwash encountered. The resultant integrated blade load time history is presented in figure 9. A double peak transient of a magnitude which is one third of the mean lift is observed in the azimuth range 35° to 60°, this corresponds to an elapsed time of 13 millisecs or blade travel of 6 chordlengths relative to the local stream at 70% radius.

Fig.9 Integrated blade lift time history.

A more detailed look at the loads distribution around the azimuth is given in figure 10. These reflect the forcing of the downwash field, the freestream components, cyclic pitch and first harmonic flapping. Relative to the downwash, some smoothing effect and re-phasing can be noted. In the first quadrant, at around 35° the load peaks first in the inboard region and the large gradients shift outboard as the blade rotation continues. At around 50° the gradients are in phase for a greater radial extent. This relative phasing will be seen to be important when the acoustic effects are evaluated at the location of a remote observer. Output from the loads program is stored on disc in a form suitable for access by the program which performs the acoustic analysis.

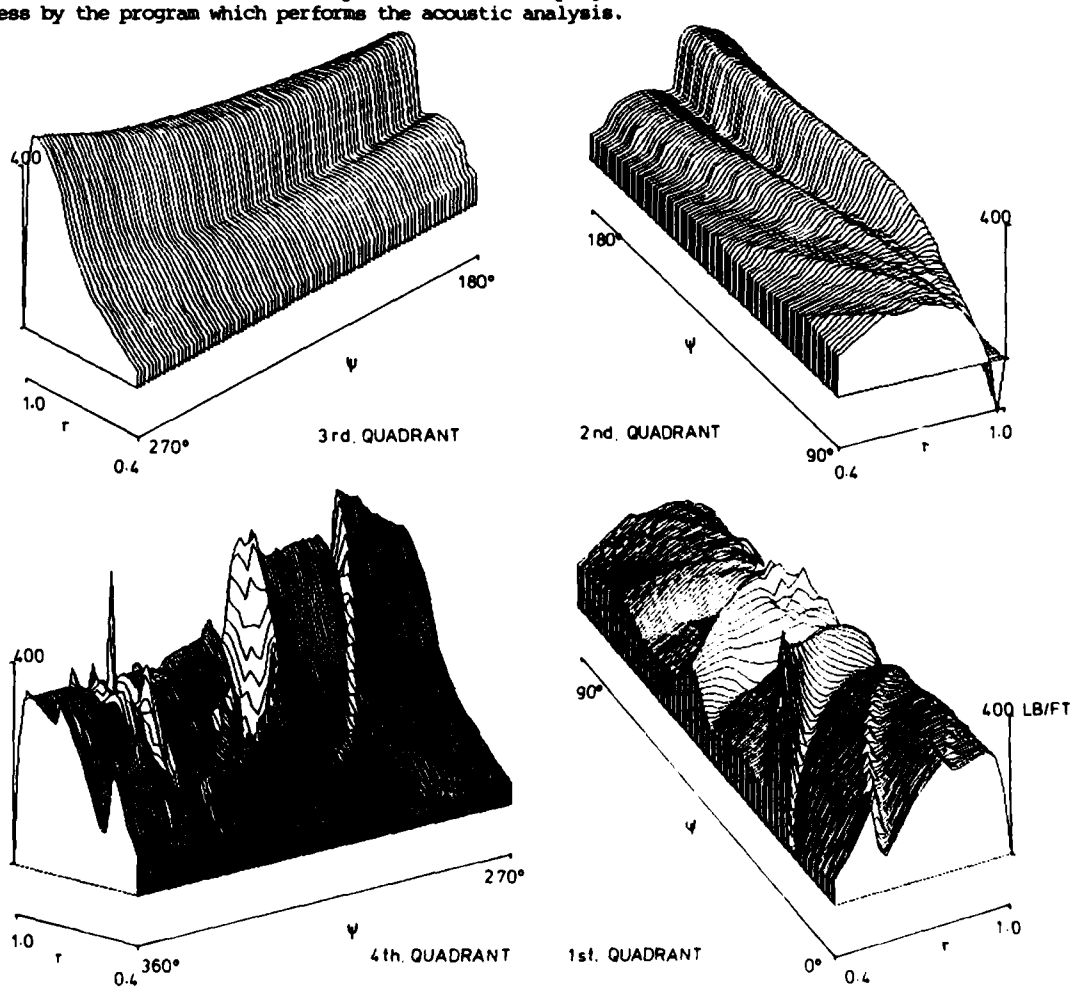

Fig.10 Blade load distribution.

The acoustic signal.

The original objective of the study was to determine whether a realistic acoustic signal could be obtained from the calculated blade/vortex loading time history. Numerous tests have documented the character and intensity of the blade slap impulse and in principle the appropriate acoustic theory has existed for many years. The acoustic theory used for this evaluation has been formulated by D. Hawkings (reference 8) and the particular application incorporates simplifying assumptions appropriate to the 'far field' solution, the inclusion of lift terms only and the replacement of the chordwise integral by a point load.

For the purpose of discussion the fundamental equation for the acoustic pressure at an observer location, at some distance from the rotor, may be further debased to the form:-

$$p(t) = K \frac{\partial}{\partial t} \int \frac{L\,(R,\tau)}{1 - M(\tau)}\, dR$$

That is, the acoustic pressure is a function of the time rate of change of the integrated blade loading. For assessment at the observer location and timebase the evaluation of the loading integral must take into account the relative motion of the blade and for a numerical solution the components must be phased appropriately. This is accomplished by substitution, in the rotor frame of reference, of the observer 'retarded' time $\tau = t - r/a_o$ which relates the radial position and azimuth of source points which are in phase at the observer position. Numerical integration is then performed along lines of constant τ , as illustrated in figure 11, which involves interpolation in space and time within the calculated time history of the radial load distribution.

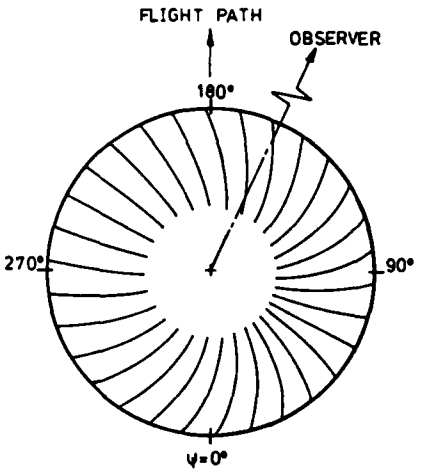

Fig.11 Integration paths related to observer time.

To enable comparison with measured data, the calculated noise signal has been obtained for an observer location 492 ft. to the advancing side of the W30 rotor at a horizontal distance of 1056 ft. and altitude of 515 ft. The flight conditions comprise a weight of 12000 lb., speed of 70 kts. and rate of descent of 670 ft/min. Measurements were made with a microphone positioned at the standard height of 1.2 metres above the ground and thus are influenced by ground reflections.

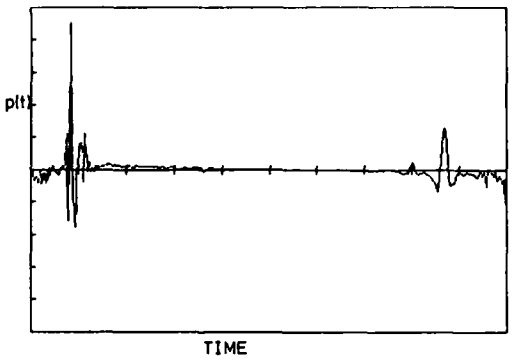

a) Unreflected signal, complete revolution.

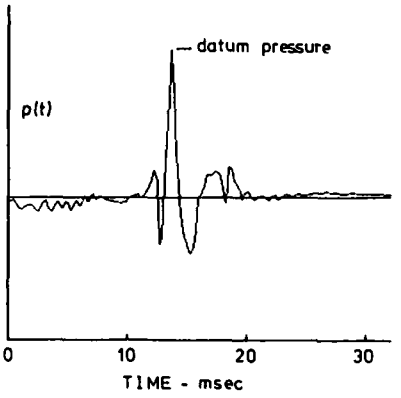

b) Unreflected signal, advancing blade.

Fig.12 Predicted acoustic signal for a singe blade.

Build up of a signal for comparison with test starts with the free air (unreflected) signal derived from the single blade analysis through the azimuth range, figure 12a. This shows two events, a high amplitude short duration signal which is generated by the advancing blade/vortex interaction and a smaller amplitude wider pulse generated by a retreating blade interaction. Primary interest centres on the advancing blade waveform which is shown in figure 12b on an expanded timescale. A significant modification to the signal is contributed by the ground reflection which introduces an additional pulse, figure 13.

When the free air signal from the four blades is synthesised by superposition, the waveform for each of the four separate impulses is modified slightly but the primary pulse is relatively unaffected, figure 14a. Finally, the reflected signal for all four blades, figure 14b, may be compared with the measured data ,figure 15. The measured data include the contributions from several other sources the most important of which comprise blade thickness effects and the tail rotor. A certain amount of variability in amplitude and

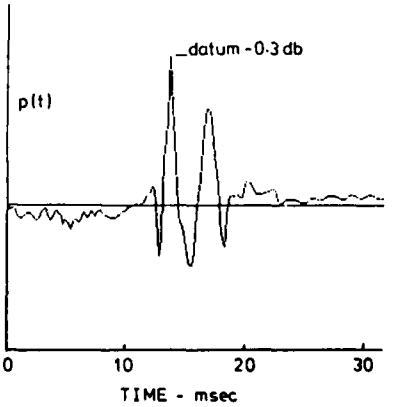

Fig.13 Predicted reflected signal, advancing blade.

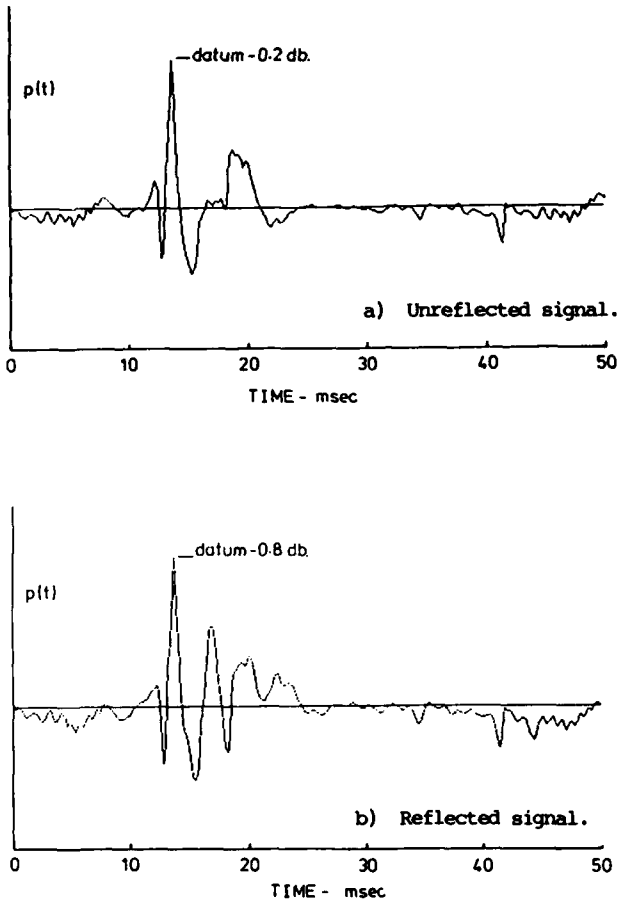

Fig.14 Predicted acoustic signal, advancing blade.

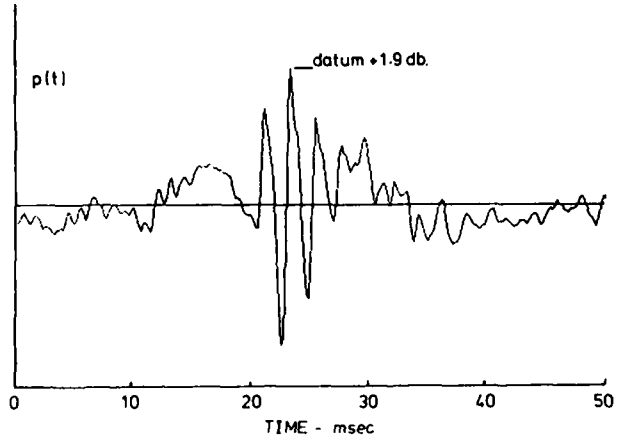

Fig.15 Acoustic signal, measured data.

waveform is discernable in the time scale which corresponds to successive rotor revolutions but, additionally, variations in the nominal rate of descent contribute to more significant variability in the measured signal. No attempt, at this time, has been made to average the measured signal. Notably, the pulse width of the major event is about 1.3 msec, at the zero crossing, in both estimated and measured data. The estimated peak amplitude is within 2.7 db. of the measurement, though this may eventually prove to be fortuitous. Considering the preliminary state of the theoretical analysis the comparison with measured data, both in amplitude and waveform, is better than was anticipated at the initiation of the study.

Conclusions.

An analysis has been developed which will predict the transient blade loading resulting from direct encounter with the vortices present in the rotor wake. In developing the analysis and the associated computer program priority has been given to the need for a practical tool with which to examine the acoustic problem associated with blade/vortex interaction. Consequently, the computational requirements are relatively modest. The objective thus far has been to determine whether it is possible to calculate the aerodynamic loads with sufficient accuracy and resolution so that a realistic acoustic signal may be derived. From the work done to date it would appear that the objective has been realised. Although the results are preliminary it appears that both the waveform and amplitude of the derived acoustic signal are capable of reproducing the characteristics observed in measured data though it is obviously necessary to substantiate this conclusion by further correlation studies.

The methodology provides the basis for studying the consequences of varying the important parameters involved in the blade/vortex interaction problem; namely:-

1. Vortex strength and core size.
2. Blade geometry, including swept tips etc.
3. Blade loading parameters.
4. Vehicle trim and operating procedures.

It may be anticipated that the results of the correlation and parametric studies will make apparent aspects of the model which will require revision or improvement. At the same time, use of the model should aid in the analysis and interpretation of the acoustic measurements. A developed model should be capable of predicting at the design stage of a new helicopter the acoustic implications of blade/vortex interaction for the chosen rotor and operational parameters.

The aerodynamic model which has been developed is capable of producing transient rotor loads of much greater accuracy and detail than has been possible previously. For the purpose of this study the loads have not been coupled to the elastic response of the blade and it may be anticipated that extension of the model to a coupled analysis will provide a significant improvement in the ability to predict vibratory loads and response for higher modes and frequencies.

In due course the aerodynamic model may be extended to include the influence of separated flow.

References.

1. Beddoes, T.S. Practical computation of unsteady lift. Eighth European Rotorcraft Forum, 1982. (Reprinted in Vertica Vol. 8, No. 1, 1984).
2. Caradonna, F.X., Desopper, A., Tung, C. Finite difference modelling of rotor flows including wake effects. Eighth European Rotorcraft Forum, 1982.
3. McCroskey, W.J., Goorjian, P.M. Interaction of airfoils with gusts and concentrated vortices in unsteady transonic flow. A.I.A.A. Paper 83-1691, 1983.
4. Ballhaus, W.F., Magnus, R., Yoshihara, H. Some examples of unsteady transonic flows over airfoils. Proc. Symp. University of Arizona, March 1975.
5. Glauert, H. The elements of aerofoil and airscrew theory. Cambridge University Press, 1948.
6. McCormick, B.W., Surendraiah, M. A study of blade-vortex interaction. American Helicopter Society, Annual Forum, 1970.
7. Beddoes, T. S. A wake model for high resolution airloads. U.S. Army/ AHS. International Conference on Rotorcraft Basic Research. Feb. 1985.
8. Hawkings, D.L. Theoretical analysis of blade/vortex interaction noise. Westland Helicopters Ltd. A.A. Note 1417, 1984.

Acknowledgement.

The author wishes to acknowledge the contributions of M.A.Reed and A.C.Pike who have developed the acoustic analysis and produced the corresponding data for this presentation.

APPENDIX

Impulsive Lift.

From piston theory, for a step change (w) in the velocity normal to the surface.

$$L_I(0) = 2\varrho\, acw$$

The subsequent timewise variation of impulsive lift is assumed to comprise an exponential decay to zero value; i.e.

$$L_I(t) / w = 2\varrho\, ace^{-t / T_I}$$

In operational form $\frac{L_I(p)}{w(p)} = 2\varrho\, ac \frac{T_I\, p}{1 + T_I\, p}$

In reference 1 numerical methods for implementing $L_I(t)$ for arbitrary forcing are discussed and it is concluded that for practical purposes it is preferable to consider the sampled time history of w(t) as a series of ramp rather than step inputs. Re-deriving the response to ramp input $\dot{w}(t) = K_w$, then in operational form $w(p) = K_w / p^2$.

$$\text{Thus } L_I(p) = 2\varrho\, acK_w \frac{T_I}{p\,(1 + T_I p)}$$

$$\text{and } L_I(t) = 2\varrho\, acK_w.T_I\,(1 - e^{-t/T_I})$$

$$\text{i.e if } T_I = c/a \text{ then } L_I(t) = 2\varrho\, c^2 K_w (1 - e^{-ta/c})$$

In general, to accomodate 3D effects, $T_I = \epsilon \cdot c/a$
Following ref.1 for the numerical implementation a half step lead is introduced so that:-

$$L_I(n) = 2\rho c^2 \epsilon \left(K_w(n) - K_I(n) \right), \qquad \text{where } K_w(n) = \left(w(n) - w(n-1) \right)/\Delta t$$

$$\text{and } K_I(n) = K_I(n-1)\, e^{-\Delta t/T_I} + \left(K_w(n) - K_w(n-1) \right) e^{-\Delta t/2T_I}$$

Circulatory Lift.

Following the procedure of Glauert (ref.5, p87) for thin airfoils, the velocity induced at a point x' on the airfoil by the distributed vorticity is given by :

$$v(x') = \int_o^c \frac{k\, dx}{2\pi(x - x')} \quad \text{and the total circulation } \Gamma = \int_o^c k\, dx$$

For a flat plate $w/V + v/V = 0$, where w is the component of free stream velocity normal to the surface.

Substituting $x = c(1 - \cos\theta)/2$ and $k = 2V\left[A_o \cot(\theta/2) + \sum_1^\infty A_n \sin n\theta \right]$ leads to the solution for the lift:-

$$L = \pi c \rho V^2 \left(A_o + A_1/2 \right) \text{ or } C_L = 2\pi\left(A_o + A_1/2 \right)$$

i.e. only A_o and A_1 need to be determined.

Now $v/V = -A_o + \sum_1^\infty A_n \cos n\theta = -w/V$, to satisfy the boundary conditions.

Thus $A_o = 1/\pi \int_o^\pi (w/V)\, d\theta$ and $A_n = -2/\pi \int_o^\pi (w/V) \cos n\theta \; d\theta$

Returning to x co-ordinates :- $d\theta = \frac{2}{c \sin\theta} dx$, $\cos\theta = \left(1 - \frac{2x}{c} \right)$, $\sin\theta = \left[1 - \left(1 - \frac{2x}{c} \right) \right]^{1/2}$

Thus $A_o = \frac{2}{\pi V} \int_o^1 \frac{w}{[1-(1-2x/c)^2]^{1/2}} d(x/c)$ and $A_1 = -\frac{4}{\pi V} \int_o^1 \frac{w\,(1-2x/c)}{[1-(1-2x/c)^2]^{1/2}} d(x/c)$

The term $\left(A_o + A_1/2 \right)$ represents the forcing for the time dependent circulatory lift. It is equivalent to the angle of attack and is used in the same manner for the implementation of the indicial lift response. Representing $\left(A_o + A_1/2 \right)$ by α , the numerical procedure is, as presented in ref.1, where

$$C_L(n) = C_{L\alpha} \cdot \alpha_E(n)$$

$$\text{and } \alpha_E(n) = \alpha(n) - X(n) - Y(n)$$

$$X(n) = X(n-1)\, e^{-\Delta t/T_1} + 0.3\left(\alpha(n) - \alpha(n-1) \right) e^{-\Delta t/2T_1}$$

$$Y(n) = Y(n-1)\, e^{-\Delta t/T_2} + 0.7\left(\alpha(n) - \alpha(n-1) \right) e^{-\Delta t/2T_2}$$

where $T_1 = 0.14\,(1-M^2).\,2V/c$, $T_2 = 0.53\,(1-M^2).\,2V/c$

RECENT DEVELOPMENTS IN ROTARY-BALANCE TESTING OF FIGHTER AIRCRAFT CONFIGURATIONS AT NASA AMES RESEARCH CENTER

Gerald N. Malcolm and Lewis B. Schiff
NASA Ames Research Center, Moffett Field, California

SUMMARY

NASA Ames Research Center has an ongoing research program to investigate high-angle-of-attack aerodynamic phenomena associated with high-performance aircraft. As part of this research effort, two rotary-balance apparatuses have recently been developed for testing airplane models in a coning motion. A new large-scale apparatus, developed for use in the 12-Foot Pressure Wind Tunnel primarily to permit testing at high Reynolds numbers, was recently used to investigate the aerodynamics of a 0.05-scale model of the F-15 fighter aircraft. Effects of Reynolds number, spin-rate parameter, model attitude, presence of a nose boom, and model/sting mounting angle were investigated.

A smaller apparatus, which is a modernized version of a coning rig developed several years ago to investigate the aerodynamics of bodies of revolution in a coning motion, has been used in the 6- by 6-foot Supersonic Wind Tunnel to investigate the aerodynamic behavior of a simple representation of a modern fighter, the Standard Dynamics Model (SDM). Effects of spin-rate parameter and model attitude were investigated. This paper presents a description of the two rigs and a discussion of some of the results obtained in the respective tests.

SYMBOLS

A	reference area, F-15 (0.1472 m^2, 1.52 ft^2), SDM (0.0174 m^2, 0.187 ft^2)
b	wingspan, F-15 (0.652 m, 2.14 ft), SDM (0.2286 m, 0.75 ft)
$\bar{c}$	wing mean aerodynamic chord, F-15 (0.243 m, 0.797 ft), SDM (0.0862 m, 0.283 ft)
C_A	axial force/qA
C_ℓ	rolling moment/qAb
C_{ℓ_ω}	$dC\ell/d(\omega b/2V)$, slope of rolling moment coefficient versus $\omega b/2V$ at $\omega = 0$
C_m	pitching moment/qA$\bar{c}$ (center of moment at 0.25 $\bar{c}$)
C_n	yawing moment/qAb (center of moment at 0.25 $\bar{c}$)
C_{n_ω}	$dCn/d(\omega b/2V)$, slope of yawing moment coefficient versus $\omega b/2V$ at $\omega = 0$
C_N	normal force/qA
C_Y	side force/qA
M	free-stream Mach number
q	free-stream dynamic pressure
R	Reynolds number based on $\bar{c}$
V	free-stream velocity
α	angle of attack
α_s	sting angle (Fig. 4)
β	angle of sideslip
$\phi_{1,2,3}$	rotational position axes (Fig. 3)
ω	angular velocity of rotary apparatus about the wind axis

Note that force and moment coefficients are with respect to body-fixed axes.

1. INTRODUCTION

NASA Ames Research Center sponsors a research program to understand and exploit the aerodynamic phenomena which occur on high-performance fighter aircraft, particularly at high angles of attack. A number of facets comprise this research program, including fundamental fluid-mechanics studies, derivation and verification of aerodynamic mathematical models, assessment of the aerodynamics effects on flight dynamics, and the development of new test apparatuses for performing the necessary wind-tunnel experiments.

One of the required experiments is to measure the aerodynamic properties of a vehicle in a continuous spin motion about the velocity vector, sometimes referred to as a coning motion. This experiment can be performed with a rotary-balance apparatus or, simply, a rotary rig. Rotary rigs have been developed in the United States and a number of other countries in the past few years. Some of these rigs have been described in a recent AGARD lecture series (Ref. 1).

Two rotary rigs have been developed at NASA Ames Research Center. The first rig to be discussed is a large-scale apparatus for testing airplane configurations in the Ames 12-Foot Pressure Wind Tunnel. This rig was developed to provide a capability for high-Reynolds-number rotary-balance tests. A preliminary report on the development of this rig is given in Ref. 2. The first wind-tunnel test using this rig was recently completed on a 0.05-scale model of the F-15 fighter aircraft. Availability of flight-test data from NASA Dryden Research Facility was the main reason for choosing the F-15 configuration. The flight tests were conducted on a 0.375-scale F-15 Spin Research Vehicle (SRV) and provided extensive data on steady and nearly steady spins. Although this paper addresses only the wind-tunnel test apparatus and data, a long-term objective of the research program is to compare wind-tunnel and flight-test data for steady spin cases.

The second rig is a small-scale rotary rig that was originally constructed for tests on bodies of revolution in the Ames 6- by 6-Foot Supersonic Wind Tunnel (Ref. 3), and later was modified for exploratory tests in the 12-foot tunnel (Refs. 4 and 5) on simple airplane configurations. This rig has recently been refurbished with a new hydraulic drive system and associated hardware and a modern control system. The first test of this apparatus was recently completed in the Ames 6- by 6-foot tunnel using a simplified version of a modern fighter aircraft, referred to as the Standard Dynamics Model (SDM).

This paper is a report of recent progress in the development and use of rotary rigs at NASA Ames. Some examples of data recently obtained on both apparatuses are presented. The details of each apparatus are addressed in Section 2. Similarly, the results of the individual wind-tunnel experiments are discussed in Section 5. Both rigs use a common data-acquisition system and share a common data-reduction technique, and they are discussed in Sections 3 and 4.

2. DESCRIPTION OF WIND-TUNNEL FACILITIES AND APPARATUSES

2.1 12-Foot Pressure Wind Tunnel Apparatus

The objectives for the first test of this apparatus in the tunnel were three-fold. The first was to install and check the apparatus and all associated equipment and instrumentation in the wind-tunnel environment. The second was to acquire aerodynamic data on a fighter aircraft model in a spin motion at various attitudes (α = -5° to 90°, β = -15° to +15°) at Reynolds numbers ranging from 1 to 5.5 milllon based on wing mean aerodynamic chord. The third was to acquire wind-tunnel data that could be used for comparison with the Dryden SRV flight-test data. Since the SRV had a rather large nose boom to measure model attitude and speed in flight, the wind-tunnel model was tested both with and without a nose boom.

2.1.1 12-Foot Pressure Wind Tunnel

The 12-Foot Pressure Wind Tunnel is a variable-pressure, low-turbulence facility with a total pressure capability range of 5.0 atm. Mach number can be varied from 0.1 to 0.98; however, because of the solid-wall test section and limited power, operation of the tunnel beyond a Mach number of 0.5 yields questionable results. A unit Reynolds number up to approximately 25 million/m can be obtained at M = 0.28.

2.1.2 Apparatus and Model

The rotary apparatus and the model with the nose boom attached are shown installed on a laboratory test stand in Fig. 1. A protective enclosure surrounds the apparatus for safety purposes while it is rotating. The rig and model (minus the nose boom) installed in the 12-foot tunnel test section are shown in Fig. 2. A sketch of the apparatus is shown in Fig. 3. For efficient operation in a pressure tunnel, it is essential to minimize the number of tunnel startups and shutdowns necessary to change model attitude. To accomplish this, the rig was designed with electrically driven movable arms which permit remote change of the angles of attack and sideslip. The desired angles are obtained by rotating two arms on the rig (while it is stationary) about the axes ϕ_1 and ϕ_2 as shown in Fig. 3. These axes intersect the spin axis at the designated longitudinal location on the model representing the center of gravity of a full-scale, free-flying vehicle. By using a straight, base-mounted sting, the angle of incidence of the model with respect to the flow can be varied from 0 to±30°. By top-mounting the model on bent stings (α_s = 45° and 70°), the angles of attack and sideslip can be varied over the envelope shown in Fig. 4 (α from -30° to +100° with β between ±30°). Figure 5 shows a photograph of the model mounted on each of the three stings. A remotely

driven counterweight (Figs. 1-3) was positioned to statically balance the mass distribution of the system about the spin axis prior to rotating the rig. Potentiometers mounted on the arms gave remote indications of the positions of the arms and of the counterweight position.

The apparatus is rotated about an axis parallel to the wind-tunnel airstream at speeds ranging from 0 to 37 rad/sec (0-350 rpm) in either a clockwise or counterclockwise direction using a servo-controlled hydraulic drive system. No attempt was made to dynamically balance the system. The magnitude of the centrifugally induced dynamic moment was, in the worst case, as much as 45,200 N·m (400,000 in.-lb). Because of the large dynamic loads experienced by the fixed part of the rotary rig and the tunnel support system, special provisions were made to secure the system as rigidly as possible. The center body of the support system is normally traversed and pitched on the vertical blade strut to vary the model attitude. For this test, the center body was rigidly fastened to the strut with threaded pins to prevent any motion between the rig/centerbody and the tunnel strut. To eliminate possible resonance of the rotary-apparatus/tunnel support system, it was designed to have a natural frequency at least three times the maximum rotational frequency of 37 rad/sec.

The model is a 0.05-scale version of an F-15 fighter configuration with two nose configurations available, one with a nose boom and one without. The center of moments is at 0.25 of the mean aerodynamic chord of the wing. This location is also the center of rotation of the model about the spin axis. Control deflections can be changed manually. The horizontal tails can be varied at any desired angle in 5° increments. The aileron and rudder surfaces can be set at 0° or at the maximum angles of ±20° for the ailerons and ±30° for the rudders.

The forces and moments are measured using a 5.08-cm (2 in.) diameter, six-component, strain gage balance mounted in the model. Since the spin axis of the rig is parallel to the wind stream, constant angles of attack and sideslip are maintained during a rotation cycle. Thus, the resulting balance output is constant at any given rotational speed, except for cyclical variations due to model weight and aerodynamically induced unsteadiness. The one-piece balance, constructed especially for use with this apparatus and model, can be attached to the sting through the rear or the top of the model. Electrical power and signal paths from the balance are provided by a slip-ring assembly mounted in the circular housing near the strut mount. The slip-ring assembly also carries the power leads to the electrically driven movable arms and the signals from the arm-position potentiometers. A resolver is mounted on the rear of the slip-ring unit to measure the angular position of the rig about the spin axis. A tachometer to determine spin rate is mounted on the hydraulic drive motor shaft.

Because of the extremely large centrifugally induced oscillatory loads on the apparatus and the tunnel support system (caused by the large dynamic imbalance of the rig), an extensive amount of data was collected continuously during the test to monitor the structural integrity of the apparatus and support. Numerous locations on the apparatus and the tunnel support system were instrumented with strain gages to monitor stresses, eddy-current proximity probes to measure deflections, and accelerometers to measure the vibration amplitudes and frequencies. In addition, pressure instrumentation was used to monitor the important pressures within the hydraulic drive system. Although essential to safe operation of the apparatus, the monitoring instrumentation is not discussed further in this paper.

2.2 6- by 6-Foot Supersonic Wind Tunnel Apparatus

2.2.1 6- by 6-Foot Supersonic Wind Tunnel

The 6- by 6-Foot Supersonic Wind Tunnel is a variable-pressure tunnel with a total pressure range of 0.3 to 1.0 atm. The Mach number can be varied from 0.25 to 2.2 continuously. Reynolds numbers to 15×10^6/m can be achieved. The tunnel has an asymmetric sliding-block nozzle for changing Mach number and a test section with perforated floor and ceiling to permit testing at transonic Mach numbers.

2.2.2 Apparatus and Model

Figure 6 is a diagram of the small-scale rotary-balance apparatus. A hydraulic motor is used to turn a shaft aligned nominally parallel to the wind-tunnel airstream. Any one of a series of interchangeable bent stings can be attached to the rotating shaft to vary the angle of incidence with respect to the airstream. The stings are designed to support a model on a strain-gage balance at pitch angles ranging from 0 to 30° while keeping the same axial model station on the axis of rotation. The rig follows the same basic concept, and uses the same bent stings, as an earlier rotary-balance apparatus (described in Ref. 3), but it is considerably more sophisticated in that it uses speed and position sensors and the corresponding feedback control loops (similar to those of the 12-ft tunnel apparatus) to give the operator close control of either the speed or angular position of the rotating shaft.

The balance used was a standard six-component Task Corporation 3.81 cm (1.5 in.) diameter MK XIXA balance, with all power and signal lines routed through the bent sting and the shaft of the hydraulic motor. A set of gold slip rings and brushes was used to transfer the signals to the nonrotating portion of the rig. Model attitude was set by adjustment of the pitch and roll angles of the model. Pitch angles were determined by the choice of bent sting, and roll angles by choice of a fixture located between the balance and the model which maintained a set roll angle. A set of such roll fixtures was available, including one for use with all bent stings giving zero sideslip angle, and one for each of the bent stings to obtain sideslip angles of either -5° or +5°.

The rig is capable of being driven at rotation rates from 0 to 63 rad/sec (600 rpm) in either direction. Since the rotating parts are neither statically nor dynamically balanced, the centrifugally induced oscillatory loads generated on the nonrotating structures at maximum rotation rate are quite large. The rig is designed to withstand these loads, but some additional measures were necessary to prevent excessive deflection of the rig support structure in the tunnel. The tunnel's body of revolution, which is vertically supported by lead screws and laterally restrained by rollers, was clamped rigidly to the vertical strut in this case. Brass pads were installed between the body of revolution and the vertical strut to distribute the load and prevent damage to the strut surface. In addition, a pair of diagonal braces, extending from the leading edge of the vertical strut to the tunnel floor, was installed to restrain lateral movement of the rig support. Vibration amplitudes, in both vertical and lateral planes, were monitored by accelerometers mounted on the body of revolution, and these confirmed that no excessive vibration levels occurred while the rig was running.

An additional feature of the rotary rig is the camera enclosure shown in Fig. 6. This is capable of holding a miniature video or movie camera, with power and signal lines routed through the previously mentioned slip ring set. The camera views the upper surface of the model, and since the camera and model rotate together the model image remains steady regardless of the motion of the rig. This feature was included to enable vapor-screen investigations of the behavior of the vortex wake of the model in response to coning motion.

Figure 7 is a photograph of the model (designated the Standard Dynamics Model, SDM) used in this investigation. The basic planform is that of a current high-performance aircraft configuration. It was deliberately designed for manufacture by simple machining techniques to encourage its widespread use as a standard model for testing in different wind tunnels and on different dynamic test rigs. The model was designed and manufactured by the National Aeronautical Establishment (NAE), Canada. A more complete description of its geometry and characteristics is contained in Refs. 6 and 7. The center of moments was located at 0.35 of the wing mean aerodynamic chord, which was coincident with the center of rotation of the model about the spin axis.

3. DATA ACQUISITION AND REDUCTION SYSTEM

The data for both rotary-balance apparatuses were taken and reduced with a common stand-alone microcomputer system. Conventional analog signal-conditioning equipment was used to process and filter the balance and tachometer signals. Low-pass filtering of the balance signals eliminated the oscillatory signals due to model weight. A special data-acquisition unit processed the signals from the balance, shaft tachometer, rig angular position encoder, and (in the case of the 12-ft tunnel apparatus) the arm-position potentiometers. Tunnel conditions, including tunnel temperature and pressures, were routed to the system by paralleling the conventional tunnel sensors.

In addition to the data-acquisition unit and the main central processing unit, the data system included a dual floppy disk drive, external printer, and a multicolor on-line plotter. The data system provided complete on-line listings and plots of the six force and moment coefficients as a function of the apparatus spin rate.

4. ROTARY AND STATIONARY TARE MEASUREMENTS

There are three types of forces and moments acting on the balance when the apparatus and model are rotated in the wind tunnel. The first are the inertial forces and moments due to the moments of inertia of the rotating model. These vary with model attitude and rotation speed, and may be compensated for by measuring wind-off rotating tares and subtracting them from the wind-on data. The second are oscillatory forces caused by the change in orientation of the model mass relative to gravity. Although it is possible to account for these forces analytically, they were eliminated in a more straightforward manner by low-pass filtering the balance signals. The remaining forces and moments are the aerodynamic loads of interest.

The magnitude of the inertial loads can be calculated in a straightforward manner if the moments of inertia about the principal axes of the model and the location of the model center of mass with respect to the rotation axis are known and do not vary with rotation rate. However, the model/sting combination deflects during rotation, and will cause the actual inertial loads to vary from the analytically determined values. Therefore, it is necessary to measure wind-off tare loads at the model attitude and rotation rates planned for the wind-on tests. These measurements are stored in the data-acquisition system and later subtracted from the wind-on measurements.

For accuracy, the inertial tare loads should be measured with the model either in a complete vacuum or surrounded by an enclosure that rotates with it. This will prevent any interaction of the surrounding still air with the model as it rotates. However, in some cases, depending on such factors as model size, rotation rates, and expected wind-on loads, the contribution from this effect can be ignored. In these tests, the tare values measured in the clockwise and counterclockwise directions were averaged. For the case where the sideslip angle is set to zero, the effects of the surrounding air on side force, yawing moment, and rolling moment should be equal and opposite in sign. In this case, averaging the measured values is nearly the same as measuring the tares in a vacuum. However, the effects on normal force, pitching moment, and axial force are not eliminated by averaging the measurements from both rotational directions. It is felt that the

still-air loads are small enough to ignore, particularly for these experiments where the inertial loads and the air loads are very large in comparison.

Typically, wind-off forces and moments were determined at several fixed rotation rates ranging from 0 to the maximum for each rotary rig. The respective forces and moments were fit with a five-term polynomial of the form

$$F = A_0 + A_1\omega + A_2\omega^2 + A_3\omega^3 + A_4\omega^4$$

where F is the force or moment and ω is the rotation rate. The coefficients A_0 through A_4 were then stored. The same procedure was used for rotation in the opposite direction. The two sets of coefficients were then averaged to create a combined tare file of one set of coefficients that was applicable to all rotation rates for that particular angle of attack and sideslip.

The original intent was to measure all the rotating tare loads in the laboratory prior to installing the apparatus in the tunnel, and store them for later use during the tunnel test. The purpose was to eliminate the expenditure of valuable tunnel occupancy time to perform the tare measurements. Tares were, in fact, measured prior to tunnel installation, but it was soon recognized, after repeating some tare measurements in the tunnel, that there was enough variation in the measurements (when compared to those previously acquired in the laboratory) that new tares would have to be measured in the tunnel. The discrepancy was caused by a small difference between the stiffness of the support systems in the tunnel and the laboratory which resulted in a difference in the deflection of the model center of mass relative to the rotation axis for the two support systems.

An additional effect of deflection is the change in position of the model with respect to the rotation axis caused by the wind-on load as compared to the wind-off condition. This effect cannot easily be accounted for and, since it was felt to be small, no attempt was made to correct the wind-on data.

When data are taken with the model stationary ($\omega = 0$) in the wind tunnel with the wind on, the weight of the model must be accounted for. (For the case where the model is rotating, the weight is averaged to zero over a cycle by using low-pass analog filters.) Model weight is accounted for by performing a series of wind-off static tare measurements at various known angular positions around the rotation axis and determining the weight effect on the balance. The weight component on the balance with the wind on is then calculated, using the angular position of the rig with respect to the tunnel and the attitude of the model with respect to the rig.

5. EXPERIMENTAL RESULTS

5.1 12-Foot Tunnel Experiments

The effects of a number of variables on the aerodynamics were examined during this experiment. Included are variations in Reynolds number, angles of attack and sideslip, sting angle, and the presence of a nose boom. A Mach number of 0.28 was selected for the majority of the tests, since this maximizes the Reynolds number capability of the tunnel. Later in the test program, in order to obtain larger values of the spin-rate parameter $\omega b/2V$ (where b is the span and V the tunnel free-stream velocity), some runs were conducted at a decreased velocity, resulting in a decrease of the Mach number to 0.2. Comparisons between the results measured at Mach 0.2 and 0.28 indicated that effects due to the change in Mach number were negligible. The aerodynamic coefficients determined included: normal force, pitching moment, side force, yawing moment, and rolling moments. Axial force was also measured, but it was not determined with accuracy comparable to the other components, nor was it felt to be particularly important for these tests. The following discussion will introduce some examples of the data obtained during this test and will highlight some of the more interesting results.

5.1.1 Static Aerodynamic Data

The variations of the normal-force and pitching-moment coefficients with angle of attack are shown for the configuration without the nose boom in Fig. 8. Results are shown for Reynolds numbers of 1.5 million and for 4.0 or 5.5 million. Also shown for comparison are the data obtained at much lower Reynolds numbers (0.2 million) on a rotary rig in the NASA Langley Research Center spin tunnel (Ref. 8). As explained earlier in the description of the apparatus, data were acquired with three different stings but at some angles of attack there is an overlap of the data. For example, data were obtained at $\alpha = 30°$ on both the straight base-mounted sting and the top-mounted 45° sting. Between α of 50° and 70° data were obtained on both the 45° and 70° stings. The overlapping sets of data are shown in Fig. 8. As can be seen from Fig. 8, the normal-force coefficient peaks between α of 35° and 40° and remains almost constant for $40° \leq \alpha \leq 90°$, except for a slight decrease between α of 50° and 60°. There is some variation with Reynolds number and, interestingly, the trend in direction with Reynolds number is consistent with the data from the Langley rotary rig. There are noticeable differences, as well, due to the different sting angles. The moment center for the pitching-moment coefficient data is the 0.25 position of the wing mean aerodynamic chord. The variation with Reynolds number is primarily caused by the behavior of the flow over the forebody and fuselage and not by variations of the flow over the wing and tail surfaces. This is particularly true at the higher angles of attack since the flow almost assuredly separates at the wing leading edge regardless of the Reynolds number. Conversely, the flow separation around the forebody and the rounded

corners of the inlets, and the resulting variation of the forces and moments, are known to be sensitive to Reynolds number.

The variation of the yawing- and rolling-moment coefficients with angle of attack, for a range of Reynolds numbers, is shown in Fig. 9 for the configuration without the nose boom. There is little effect of Reynolds number variation on the yawing-moment coefficient for $\alpha \leq 40°$, and very little effect on the rolling-moment coefficient at all angles of attack. At angles of attack where significant crossflow separation exists, Reynolds number variation mainly affects the flow over the forebody and the fuselage. The resulting differences in the forces and moments would be expected primarily in the yawing moment. In addition, the effects of different sting angles are also sizable, particularly at R = 1.5 million. The primary effect of changing the sting angle is to influence the leeward flow field and the resulting interaction of the leeside vortices over the fuselage and vertical and horizontal tail surfaces. Many of the studies that have been done to investigate the asymmetric vortex phenomena on ogive-cylinder bodies at high angles of attack have shown that the maximum asymmetry and resulting values of side force and yawing moment occur between α of 50° and 70°. The results of this experiment are consistent with that observation. There appears to be a slight bias in the direction of the rolling-moment coefficient at all angles of attack although the sideslip is supposedly zero. It is possible that there is a slight asymmetry in the model or perhaps a very small sideslip angle caused by misalignment of the model in the airstream.

A similar presentation of the yawing- and rolling-moment data is shown in Fig. 10 for the model with the nose boom installed. Again, the variation with Reynolds number is fairly significant for angles of attack greater than 40°. Even more interesting, however, is the change in the coefficients, particularly the yawing-moment coefficient, when compared to the boom-off case shown in Fig. 9. At higher angles of attack, the presence of the nose boom can significantly alter the vortex flow field on the forebody and noticeably influence the resulting moments. For example, at $\alpha = 60°$ with a sting angle of 45°, the yawing moment shown in Fig. 10 at R = 4.0 million has the opposite sign to that shown in Fig. 9. However, it is also apparent that the sting angle has a major influence on the result. This can be seen by comparing the data at $\alpha = 60°$ and R = 4.0 million for sting angles of 45° and 70° (Fig. 10).

The implication of the results shown are certainly of some concern for determining the aerodynamics of configurations at high angles of attack. The differences caused by the presence of a nose boom illustrate the sensitivity of the aerodynamics to the forebody configuration. Since many flight-test aircraft employ a nose boom to acquire air data, there can be significant differences between the aerodynamics of the flight-test aircraft and the operational aircraft which, typically, do not have a nose boom. The differences observed due to the sting angle also illustrate the problems of supporting a model in a wind tunnel at large incidences without altering the leeward-side flow field.

5.1.2 Rotary Aerodynamic Data

The data in this section are shown as variations of yawing-moment and rolling-moment coefficients with the nondimensional rotation rate or spin-rate parameter, $\omega b/2V$. Figure 11 shows results for angles of attack from 0° to 90° and a Reynolds number of 1.5 million for the configuration without the nose boom. For angles of attack ranging from 0° to 40°, the variation of C_n with spin rate is reasonably linear. Above $\alpha = 40°$ the behavior is fairly nonlinear, and for the case of $\alpha = 60°$, there is a sizable offset in the yawing-moment at zero rotation rate. In all cases the overall slopes of the Cn curves exhibit an anti-spin behavior. Despite this, the offset in the nonrotating value of the yawing-moment coefficient at $\alpha = 60°$ causes a significant pro-spin tendency for all values of $\omega b/2V$ less than zero. The behavior of the rolling-moment coefficient with increasing angle of attack is worth examining. The rolling moment is anti-spin for angles of attack up to 20°, but for α from 25° to 40° and for α of 80° to 90°, the rolling moment is generally pro-spin. Figure 12 shows similar results for Reynolds numbers of 4.0 and 5.6 million. Comparing the results to those shown in Fig. 11, some differences are observed due to Reynolds number variation, particularly at angles of attack above 30°.

Figures 13-15 show the yawing-moment coefficient for angles of attack of 30°, 50°, and 70°, respectively, for the model with and without the nose boom. The different curves compare results obtained at high and low Reynolds numbers for a given sting angle, and for results obtained with different sting angles at the same Reynolds number. Figure 13, for $\alpha = 30°$, shows linear behavior of the moment with the spin-rate parameter for both the boom-off and boom-on configurations. Some differences due to Reynolds number can be observed at the higher rotation rates, especially for the case with the boom on. There is a slight effect of sting angle on the data as well, primarily at the higher rotation rates. Similar data obtained for $\alpha = 50°$ are shown in Fig. 14. The results, in general, show a higher degree of nonlinearity than for $\alpha = 30°$.

The most interesting case is shown in Fig. 15 for $\alpha = 70°$. Looking first at the configuration without the nose boom in Fig. 15a, there is very little effect of the sting angle at the higher Reynolds number. However, at the lower Reynolds number, a significant effect of the sting angle is observed at the higher rotation rates. There is also a considerable difference between the results obtained for the two Reynolds numbers using the same sting.

The effects of adding the nose boom at this angle of attack are rather dramatic, as seen in Fig. 15b. The first characteristic to note is that the data obtained with the 70° sting at R = 1.5 million (circles) show a yawing-moment coefficient that is multivalued over a wide range of values of the spin-rate parameter. This multivalued variation and the accompanying hysteresis loop indicate that two flow field states

can exist around the model for a given spin rate. Which of the two possible states that can exist depends on the past history of the flow, that is, whether that spin rate is approached from a rate that is higher or lower. (A description of the hysteresis loop and details of the dependence of its characteristics on Reynolds number are discussed later in this section in connection with Fig. 16.) The hysteresis effect is quite sensitive to model support interference. Although two flow states are also evident for the results obtained using the 45° sting at R = 1.5 million, the hysteresis is almost negligible. This difference in hysteresis effect and the large difference between yawing-moment coefficient values at negative spin rates demonstrate the sensitivity of the aerodynamics to sting angle differences and resulting support interference effects. It is apparent from these results that there is a sizable influence of the two stings on the leeward flow field which, in turn, affects the yawing moment. For the measurements made at $\alpha = 70°$, the 70° sting is parallel to the tunnel airstream. Conversely, for $\alpha = 70°$, the 45° sting is inclined with respect to the airstream and probably creates more of a disturbance in its wake, thus influencing the flow field more severely. At the higher Reynolds number, 4.0 million, no hysteresis was observed in the measurements made with either sting, and the results obtained with both stings are in reasonably close agreement.

Figure 16 illustrates, in more detail than Fig. 15b, the effect of Reynolds number variation on the yawing-moment coefficient versus the spin-rate parameter. The case shown is for $\alpha = 70°$, $\alpha_s = 70°$, and Reynolds numbers ranging from 1.0 million to 4.0 million. The most obvious effect of Reynolds number variation is the change in the value of the spin-rate parameter at which a "jump" in the yawing-moment coefficient occurs, caused by switching from one flow state to another. At R = 1.0 million there is no jump or significant hysteresis except for a small hysteresis loop at the larger positive values of the spin-rate parameter. At a slightly larger Reynolds number, 1.2 million, the jump occurs at a value of $\omega b/2V$ near -0.08. With further increase in Reynolds number, to 1.3 million, the jump point is observed at a value of spin-rate parameter near -0.04. A small hysteresis loop is observed in both these cases surrounding the jump condition. For R = 1.3 million it is interesting to note that the first jump (indicated by a (1) on the curves) occurs at $\omega b/2V = -0.01$. The flow was relatively unstable and soon returned to the original state (2) until the spin-rate parameter reached -0.04, where the moment jumped again (3). With an increase in Reynolds number to 1.5 million, the yawing-moment coefficient becomes multivalued, as described previously in Fig. 15b, and significant hysteresis loops are observed. The following describes the sequence of acquiring the data in the hysteresis loop.

For the case shown at R = 1.5 million, the initial value of the yawing-moment coefficient was negative. The initial rotation direction was in the negative direction, and the yawing-moment coefficient remained negative until $\omega b/2V = -0.036$, then it jumped to a positive value (1). The moment remained positive as the rotation rate was slowly increased in the negative direction to $\omega b/2V = -0.12$. The rotation rate was then slowly decreased to zero and increased in the opposite or positive direction. The corresponding yawing-moment coefficient response remained positive until the model reached a value of spin-rate parameter of 0.09 then jumped (2) to a negative value. As the spin-rate parameter was slowly increased to its maximum value and then decreased through zero, the yawing-moment coefficient again jumped to a positive value as $\omega b/2V$ decreased through -0.03 (3). However, as the spin-rate parameter was decreased to its maximum negative value and then increased through zero for the second time, the jump in the yawing-moment coefficient to a negative value occurred at $\omega b/2V = 0.01$ (4) rather than at $\omega b/2V = 0.09$ as before. It is apparent, following this path as shown, that there is hysteresis in the value of the yawing-moment coefficient with variation of the spin-rate parameter. This type of variation indicates the dependency of the flow field asymmetry, not only on the direction of rotation, but on the history of the rotation direction. It is interesting that this characteristic of a multivalued yawing-moment coefficient was observed only at this angle of attack and a small range of Reynolds numbers on the configuration with the nose boom. Repeated runs at these same conditions produced essentially the same results with only a small variation in the value of $\omega b/2V$ where the jumps occurred. The repeatability of the jump condition is very sensitive to the Reynolds number.

Data obtained for R = 2.4 million and R = 4.0 million do not indicate two flow states and are essentially single-valued. The only exception is observed at the extreme negative values of $\omega b/2V$. The variation is relatively linear and, for the highest Reynolds number, R = 4.0 million, there is little offset in the yawing-moment coefficient at zero spin rate. At the higher Reynolds numbers the flow on the forebody and inlet surfaces is likely to be turbulent, and the flow separation is not as sensitive to the rotation-induced local flow angularity.

The effect of variation of sideslip angle on the hysteresis is illustrated in Fig. 17. Data are shown for R = 1.5 million at $\alpha = 70°$ for the boom-on configuration, with β ranging from -5° to +10°. At $\beta = 5°$ and $\beta = -5°$ the jumps in the yawing-moment coefficient occur at values of spin-rate parameter on either side of the value at which the jump was observed at $\beta = 0°$. For $\beta = 10°$, the flow angularity on the model resulting from the combination of sideslip and rotation angles is apparently not sufficient to cause a jump in the flow orientation as seen in the other cases. For comparison, the data are shown for the model without a nose boom at $\beta = 0°$ at the same conditions. As seen in Fig. 15a, there is little indication of asymmetry, which is a significant contrast to the data obtained with nose boom on.

5.2 6- by 6-Foot Tunnel Experiments

The tests conducted on the SDM in the 6- by 6-ft tunnel were all performed at Mach 0.6 and a Reynolds number of 0.88 million based on the wing mean aerodynamic chord. These test conditions were chosen to match those of complementary forced-oscillation tests performed at the NAE (Refs. 6 and 7). The aerodynamic coefficients measured in the 6- by 6-ft tunnel and reported in Ref. 9 included normal force, pitching

moment, side force, yawing moment, rolling moment and axial force. The model center of rotation was located at 0.35 of the wing mean aerodynamic chord. This point was also chosen as the moment reference center. Some of the results obtained will be presented in the following sections.

5.2.1 Rotary Aerodynamic Data

Some results will be shown in this section to illustrate the variation of the aerodynamic coefficients with the spin-rate parameter, $\omega b/2V$. Figure 18a shows the force and moment coefficients measured at $\beta = 0°$, $\alpha = 10°$. Similar results obtained at $\beta = 0°$ and $\alpha = 30°$ are shown in Fig. 18b. Note that although data were taken at zero spin rate, they have not been included in Fig. 18 because a small misalignment between the rotary rig spin axis and the local free-stream direction made these static data dependent on the angular position of the rig. However, with the rig rotating, low-pass filtering of the data signals effectively averaged out the effect of flow angularity.

At zero angle of sideslip, symmetry conditions dictate that the lateral aerodynamic coefficients (C_Y, C_n, and C_ℓ) should be odd functions of the spin-rate parameter, while the longitudinal aerodynamic coefficients (C_N, C_A, and C_m) should be even functions of the spin rate. This is demonstrated by the data presented in Fig. 18. For all angles of attack tested, the lateral aerodynamic coefficients were observed to be nearly linear with respect to spin-rate parameter over the range of spin rates achieved in the test. The longitudinal aerodynamic coefficients were seen to be even functions of the spin-rate parameter. At the lower angles of attack, characterized by the results shown for $\alpha = 10°$ in Fig. 18a, the longitudinal aerodynamic coefficients are almost independent of spin rate. At the higher angles of attack, typified by the results shown for $\alpha = 30°$ in Fig. 18b, the axial-force and pitching-moment coefficients show a parabolic variation in spin-rate parameter rate. Some of this parabolic variation is undoubtedly real, and is probably caused by increased velocities and dynamic pressure on the tail resulting from the coning motion, which produces increased tail lift. However, limitations of data resolution at these low levels of C_A and C_m, and in particular the choice of the moment center position, may also be responsible for exaggerating the scale of the variation.

The effects of variation of sideslip angle are shown in Fig. 19, which presents data obtained at $\beta = -5°$ and $\beta = +5°$. Figure 19a shows data obtained at $\alpha = 9°$, while corresponding data measured with $\alpha = 30°$ are shown in Fig. 19b. Once again, the linear variation of the lateral aerodynamic coefficients with spin-rate parameter is apparent. The nonlinear variation of the longitudinal aerodynamic coefficients with spin rate is also apparent. The longitudinal aerodynamics also show an effect due to sideslip, which, as expected, introduces a reasonably symmetric and linear component with spin-rate parameter. In general, the results show a reasonable symmetry with direction of sideslip, but with some offsets possibly introduced by small asymmetries in the model and/or the effects of combined centrifugal and aerodynamic loading.

5.2.2 Static Aerodynamic Data

Static aerodynamic data are presented in Figs. 20 and 21. These data were obtained from the intercepts, at $\omega = 0$, of the low-spin-rate data analogous to that presented in Figs. 18 and 19. The actual static data taken at $\omega = 0$ were not used because of the scatter caused by flow angularity relative to the rotary rig's axis of rotation.

The effects of variations in the angle of attack and sideslip on the normal-force and pitching-moment coefficients are shown in Fig. 20, while the corresponding effects on the yawing-moment and rolling-moment coefficients are presented in Fig. 21. Also shown are the static data given in Ref. 6, obtained at the NAE using the same model on a similarly sized sting support. In most respects the two sets of data are well-matched, with the exception of the normal-force and pitching-moment coefficients measured at the larger angles of attack. It is suggested that this discrepancy is probably attributable to wall- and strut-interference effects in the small 0.75 m × 0.38 m solid-wall tunnel used for the NAE tests. Such effects should be negligible for the measurements made in the 6- by 6-ft tunnel, where the blockage based on total planform area of the model and test section cross-sectional area was approximately 1%, and the ratio of wing chord to tunnel test section height was approximately 0.05.

5.2.3 Dynamic Rotary Derivatives

The rotary derivatives presented in Fig. 22 were obtained by least-squares fitting of straight lines through the data presenting the aerodynamic forces and moments as functions of the spin-rate parameter (e.g., Figs. 18 and 19). The derivatives presented in Fig. 22 are the slopes of these lines. The results show a gradual change with angle of attack from 0 to 15°, then a more rapid change as angle of attack reaches and exceeds 20°. In particular, the rolling-moment derivative changes from anti-spin to pro-spin, indicating a significant change in flow characteristics within the angle of attack range from 15° to 20°. This is in agreement with the static aerodynamic data which also show a major change in lateral aerodynamics within the 15° to 20° angle of attack range. In addition, vapor-screen flow visualization studies indicated a major change in the vortices shed from the wing leading-edge strake. At a 15° angle of attack, these vortices passed over the wing surface and remained intact well downstream of the wing trailing edge, but at 20° angle of attack, they burst while still above the wing surface.

6. CONCLUDING REMARKS

As part of an ongoing research program at the NASA Ames Research Center to investigate the aerodynamic phenomena affecting high-incidence flight, two rotary-balance apparatuses have been developed for testing models of airplane configurations in coning motion. The rigs were recently utilized for inaugural tests conducted using a model of the F-15 aircraft in the 12-Foot Pressure Wind Tunnel, and for tests conducted using the Standard Dynamics Model in the 6- by 6-Foot Supersonic Wind Tunnel. Results obtained using both rigs have demonstrated their capabilities as tools for investigating the high-incidence aerodynamics of aircraft at a variety of test conditions.

Tests were conducted in the 12-ft tunnel on a 0.05-scale model of the F-15 airplane, at Mach numbers ranging from 0.2 to 0.28, and at Reynolds numbers, based on wing mean aerodynamic chord, ranging between 1.0 million and 5.5 million. The angles of attack considered ranged from 0 to 90°, with sideslip angles ranging between -15° and +15°. In addition, the effects on the aerodynamics due to the presence or absence of a fuselage nose boom were investigated. Aerodynamic force and moment coefficients were measured at spin rates of up to 350 rpm (nondimensional spin-rate parameter values up to 0.125) in both the clockwise and counterclockwise directions. Some of the main observations from these tests are:

1. Effects of Reynolds number variation generally become significant at angles of attack above 40° and Reynolds numbers below 2.4 million.

2. Variations of the aerodynamic coefficients with spin-rate parameter are nearly linear up to $\alpha = 20°$.

3. Effects of the nose boom are significant at angles of attack above 40°. At $\alpha = 70°$ and $R = 1.5 \times 10^6$, the presence of the nose boom caused major effects on the yawing-moment coefficient. These included the occurrence of multivalued aerodynamic responses, and accompanying aerodynamic hysteresis, over a range of the spin-rate parameter.

4. The effects of sting-support interference can be significant with a top-mounted model, even at large incidence. The angle that the top-mounted sting makes with respect to the model was seen to have a significant effect, particularly at Reynolds number values below 1.5×10^6.

Tests were also conducted in the 6- by 6-ft wind tunnel on the SDM (a simplified generic fighter-aircraft shape) in coning motion at $M = 0.6$, at a Reynolds number, based on wing mean aerodynamic chord, of 0.88 million. The angles of attack considered ranged from 0 to 30°, with sideslip angles ranging between -5° and +5°. These conditions matched those of complementary forced-oscillation tests conducted at the NAE in Canada.

Aerodynamic force and moment coefficients were measured on the SDM at spin rates ranging up to 600 rpm (nondimensional spin-rate parameter values up to 0.04) in both directions. Over the angle-of-attack range investigated, the lateral aerodynamic characteristics show a linear variation over the full range of spin-rate parameters achieved in the tests. Although no discontinuous changes in the aerodynamic characteristics of the SDM were observed with changes in attitude or spin rate, evidence exists of a significant change in flow characteristics between 15° and 20° angles of attack. This is believed to be associated with forward movement of the burst point of the wing strake vortices with increasing incidence; from behind the wing at $\alpha < 15°$, to above the wing at $\alpha > 20°$.

REFERENCES

1. Malcolm, G. N., "Rotary and Magnus Balances," AGARD Lecture Series No. 114, Dynamic Stability Parameters, Paper 6, May 1981, pp. 1-26.

2. Malcolm, G. N., "New Rotation-Balance Apparatus for Measuring Airplane Spin Aerodynamics in the Wind Tunnel," AIAA J. of Aircraft, Vol. 16, No. 4, April 1979, pp. 264-268.

3. Schiff, L. B. and Tobak, M., "Results from a New Wind-Tunnel Apparatus for Studying Coning and Spinning Motions of Bodies of Revolution," AIAA Journal, Vol. 8, No. 11, November 1970, pp. 1953-1957.

4. Clarkson, M. H., Malcolm, G. N., and Chapman, G. T., "Experimental Post-Stall Rotary Aerodynamic Coefficients for Airplane-Like Configurations," AIAA Journal, Vol. 13, No. 8, August 1976, pp. 565-570.

5. Malcolm, G. N. and Clarkson, M. H., "Wind-Tunnel Testing with a Rotary-Balance Apparatus to Simulate Aircraft Spin Motions," Proceedings of AIAA 9th Aerodynamic Testing Conference, Arlington, Texas, June 1976, pp. 143-156.

6. Beyers, M. E. and Moulton, B. E., "Stability Derivatives Due to Oscillations in Roll for the Standard Dynamics Model at Mach 0.6," Report LTR-UA-64, National Aeronautical Establishment, NRC, Canada, January 1983.

7. Beyers, M. E., Kapoor, K. B., and Moulton, B. E., "Pitch- and Yaw-Oscillation Experiments on the Standard Dynamics Model at Mach 0.6," Report LTR-UA-76, National Aeronautical Establishment, NRC, Canada, June 1984.

8. Barnhart, B., "F-15 Rotary Balance Data for an Angle-of-Attack Range of 8 Deg to 90 Deg," NASA Contractor Report 3478, May 1982, Prepared for NASA Langley Research Center by Bihrle Applied Research, Inc.

9. Jermey, C. and Schiff L. B., "Aerodynamic Characteristics of Standard Model in Coning Motion at Mach 0.6," proposed NASA TM-86717.

Fig. 1. Model and apparatus on laboratory test stand.

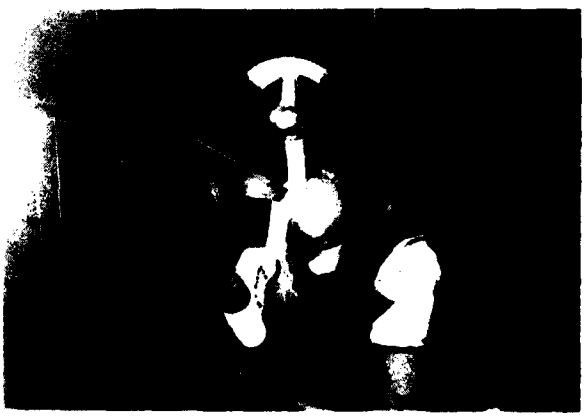

Fig. 2. Model and apparatus in 12-Foot Pressure Wind Tunnel.

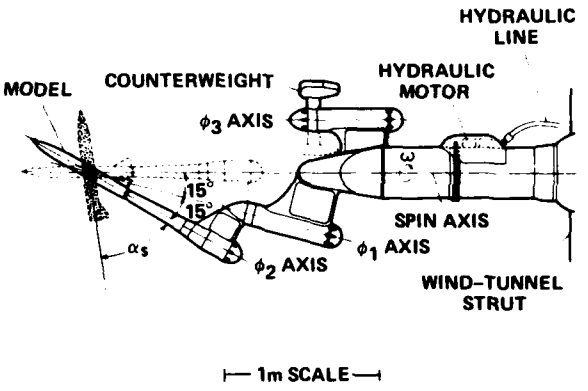

Fig. 3. Large-scale rotary-balance apparatus.

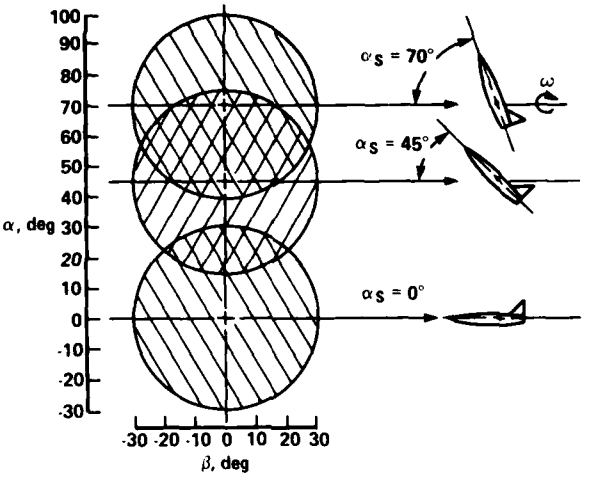

Fig. 4. Attitude envelope for large-scale rotary-balance apparatus.

Fig. 5. F-15 model mounted on various stings. (a) $\alpha_s = 0°$. (b) $\alpha_s = 45°$. (c) $\alpha_s = 70°$.

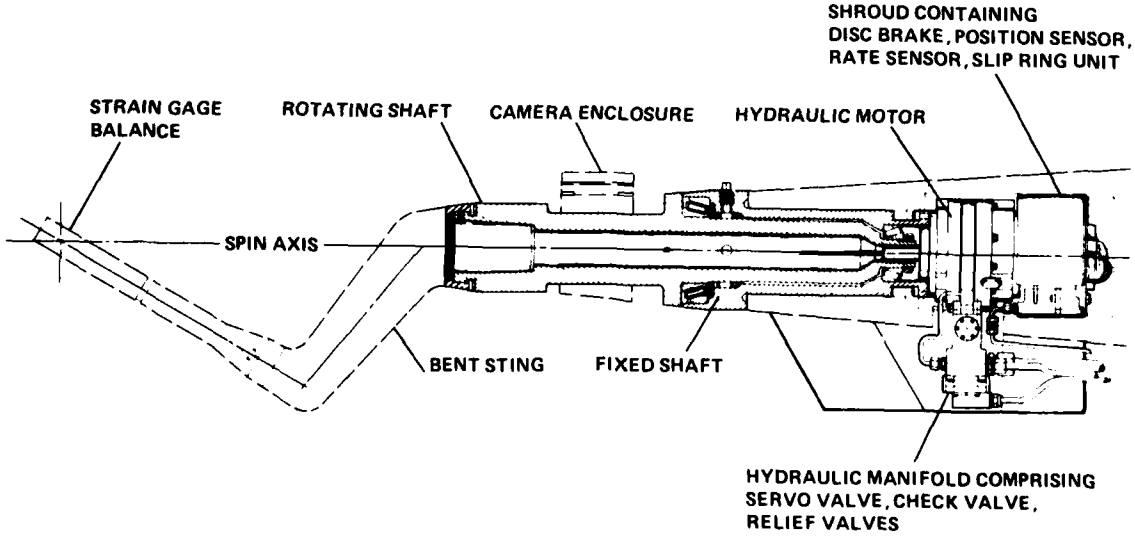

Fig. 6. Small-scale rotary-balance apparatus.

Fig. 7. Standard Dynamics Model on 30° bent sting in 6- by 6-Foot Supersonic Wind Tunnel.

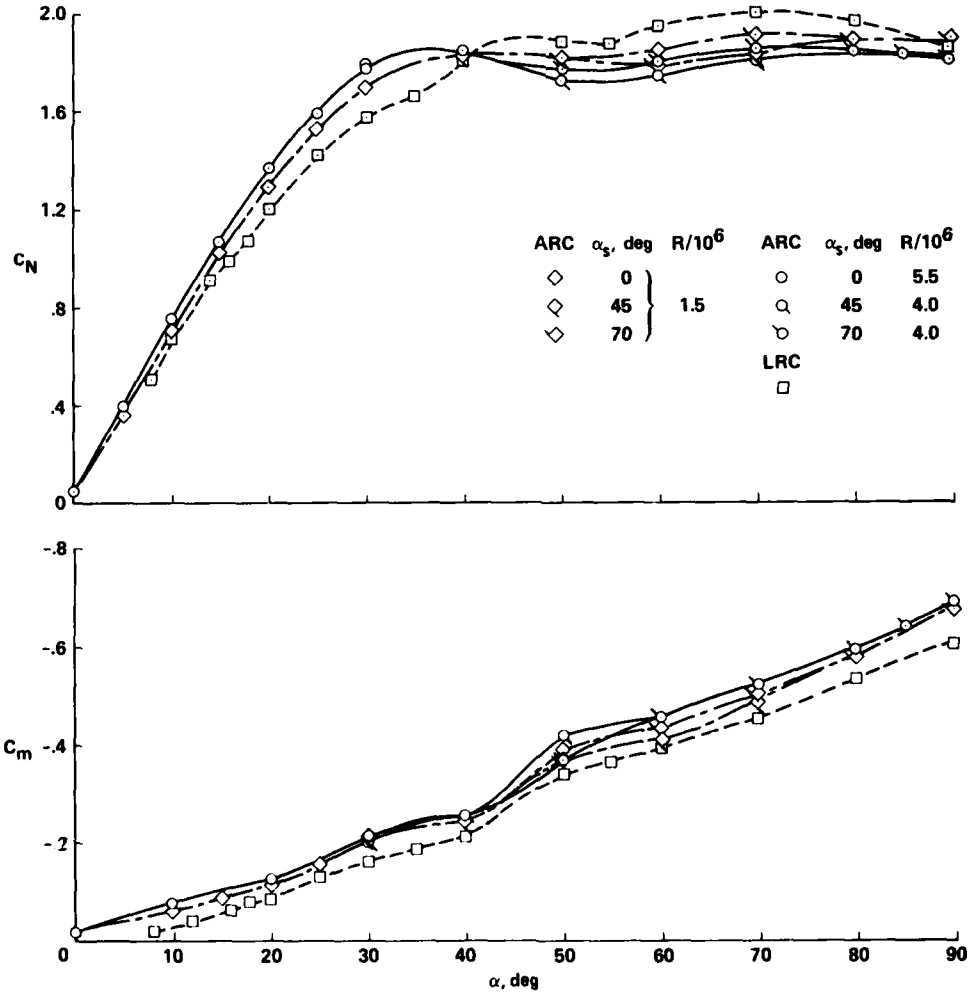

Fig. 8. Effect of Reynolds number on the longitudinal aerodynamic coefficients for the F-15, nose boom off. (a) Normal-force coefficient. (b) Pitching-moment coefficient.

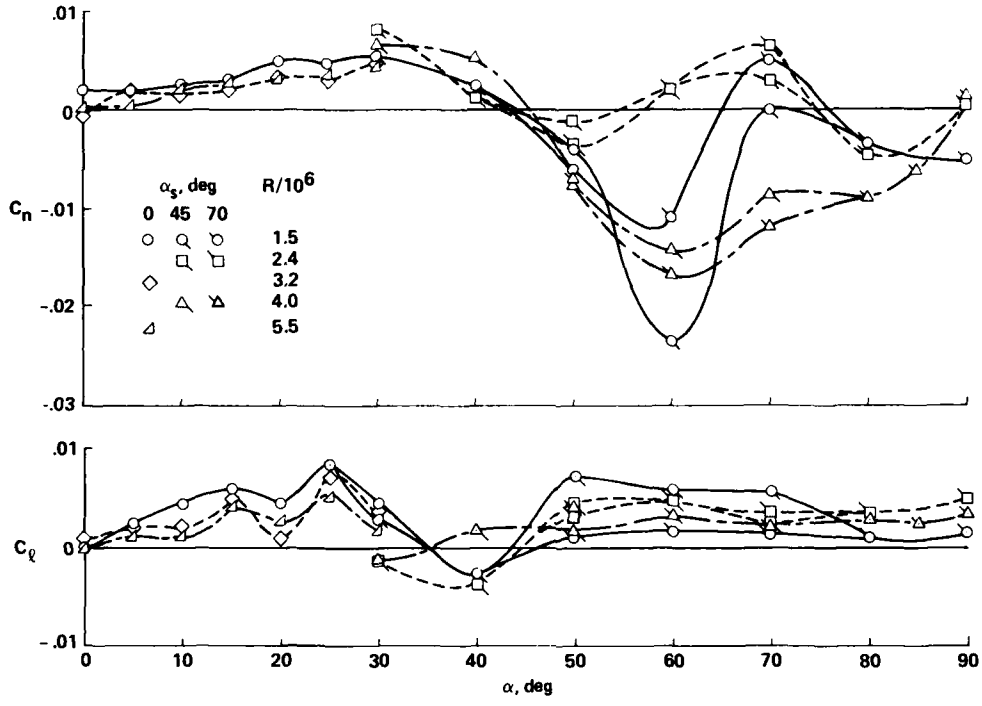

Fig. 9. Effect of Reynolds number on the lateral-directional aerodynamic coefficients for the F-15, nose boom off. (a) Yawing-moment coefficient. (b) Rolling-moment coefficient.

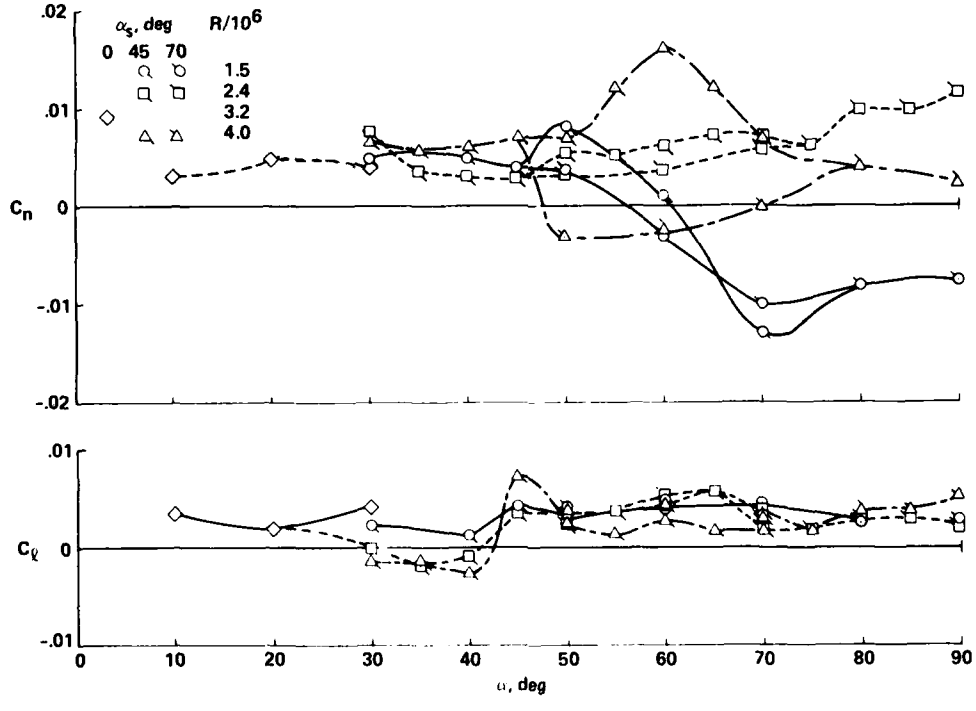

Fig. 10. Effects of Reynolds number on the lateral-directional aerodynamic coefficients for the F-15, nose boom on. (a) Yawing-moment coefficient. (b) Rolling-moment coefficient.

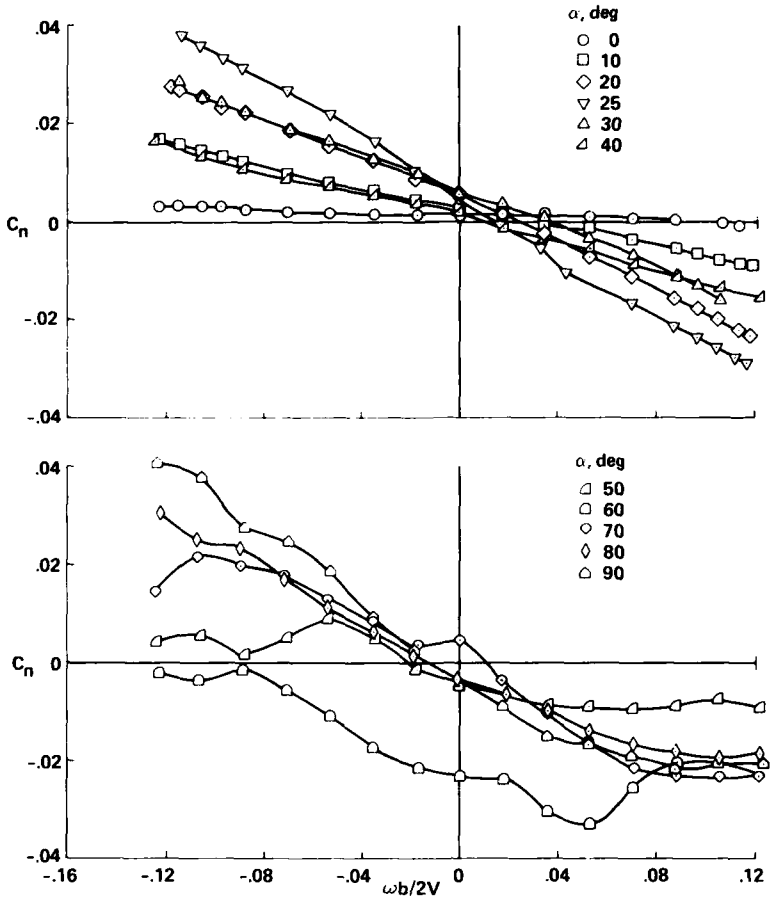

(a) Yawing-moment coefficient.

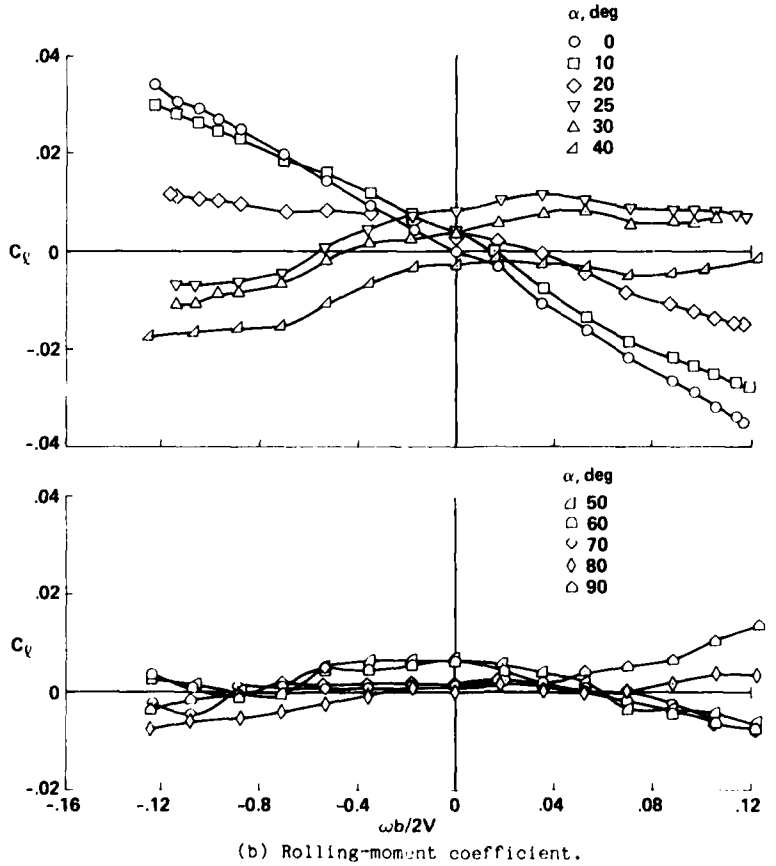

(b) Rolling-moment coefficient.

Fig. 11. Effects of rotation rate and angle of attack on the lateral-directional aerodynamic coefficients for the F-15, nose boom off, R = 1.5 million.

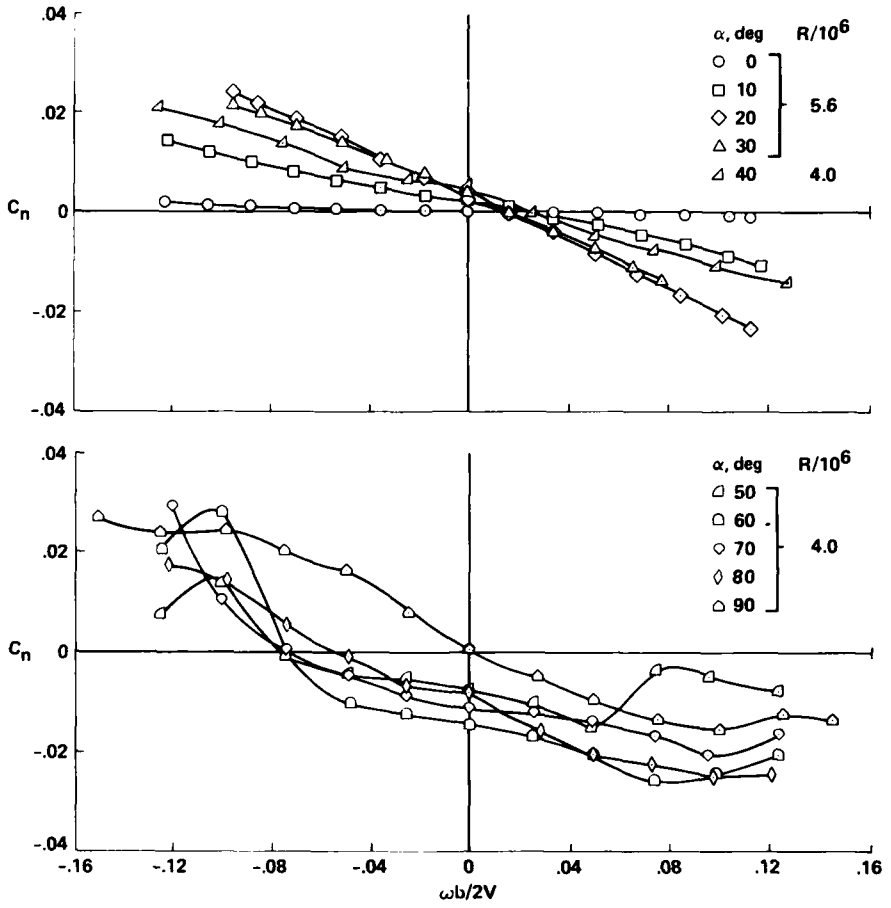

(a) Yawing-moment coefficient.

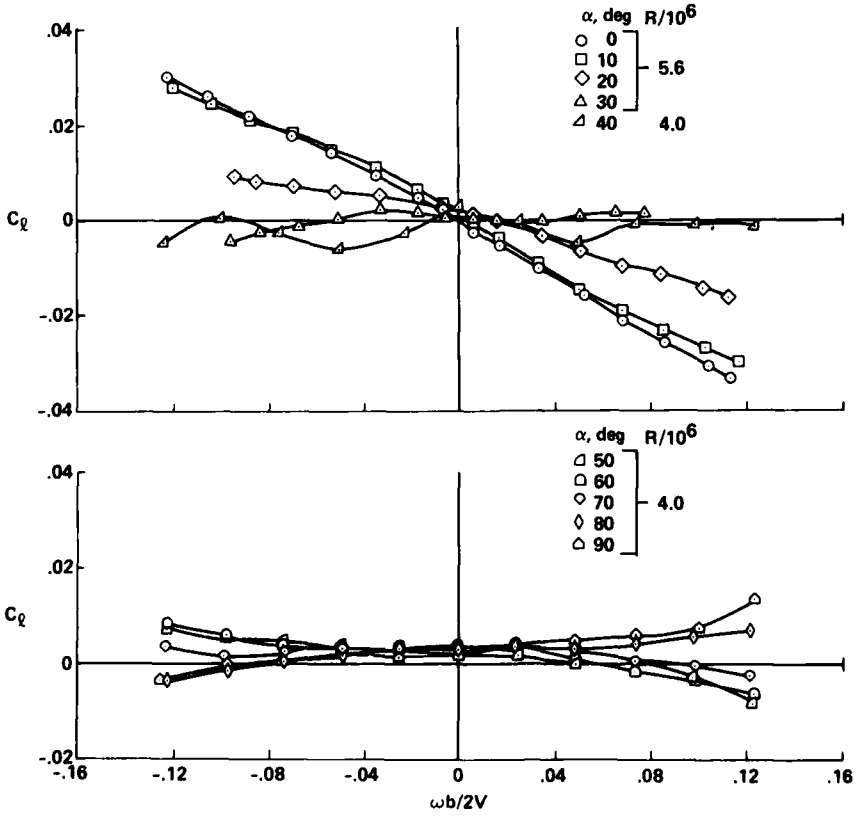

(b) Rolling-moment coefficient.

Fig. 12. Effects of rotation rate and angle of attack on the lateral-directional aerodynamic coefficients for the F-15, nose boom off, R = 4.0 and 5.6 million.

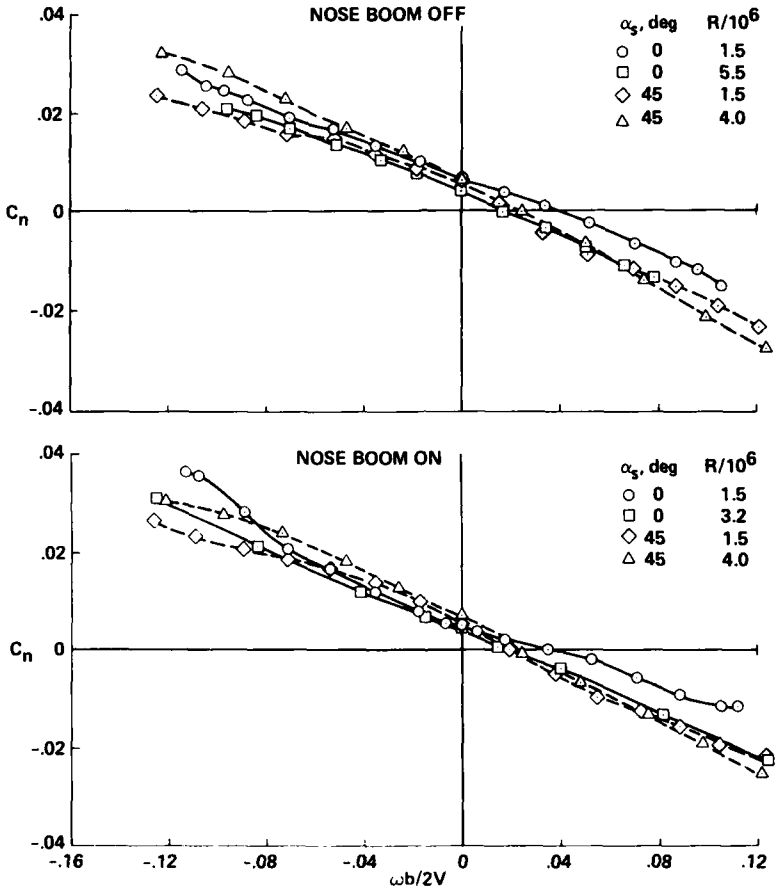

Fig. 13. Effects of rotation rate and sting angle on the yawing-moment coefficient for the F-15 at α = 30°. (a) Nose boom off. (b) Nose boom on.

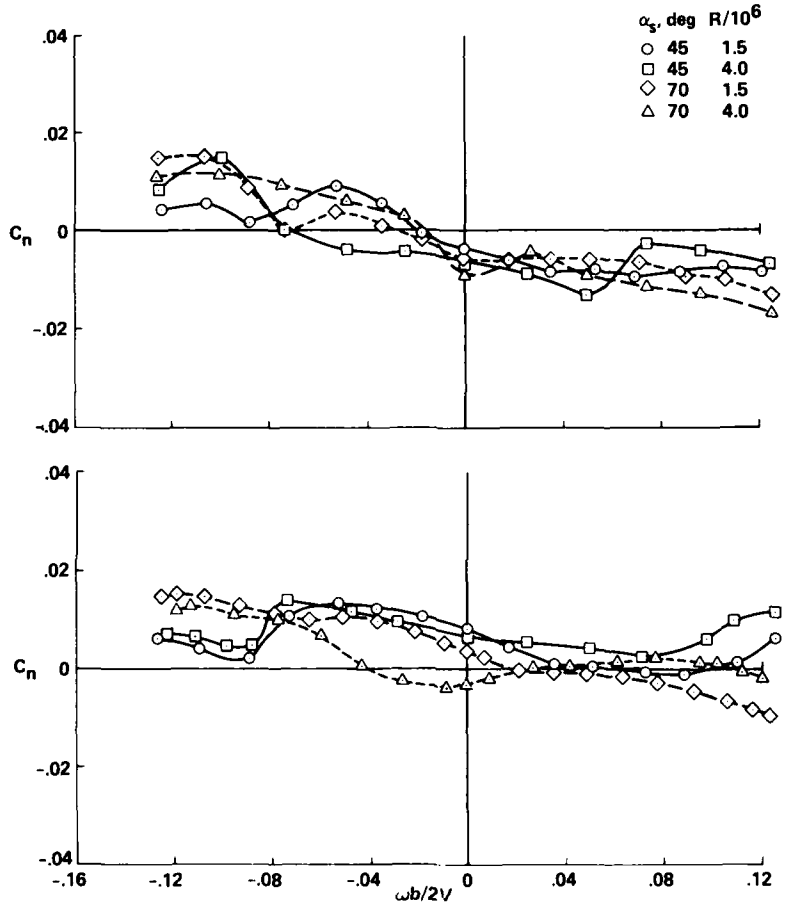

Fig. 14. Effects of rotation rate and sting angle on the yawing-moment coefficient for the F-15 at α = 50°. (a) Nose boom off. (b) Nose boom on.

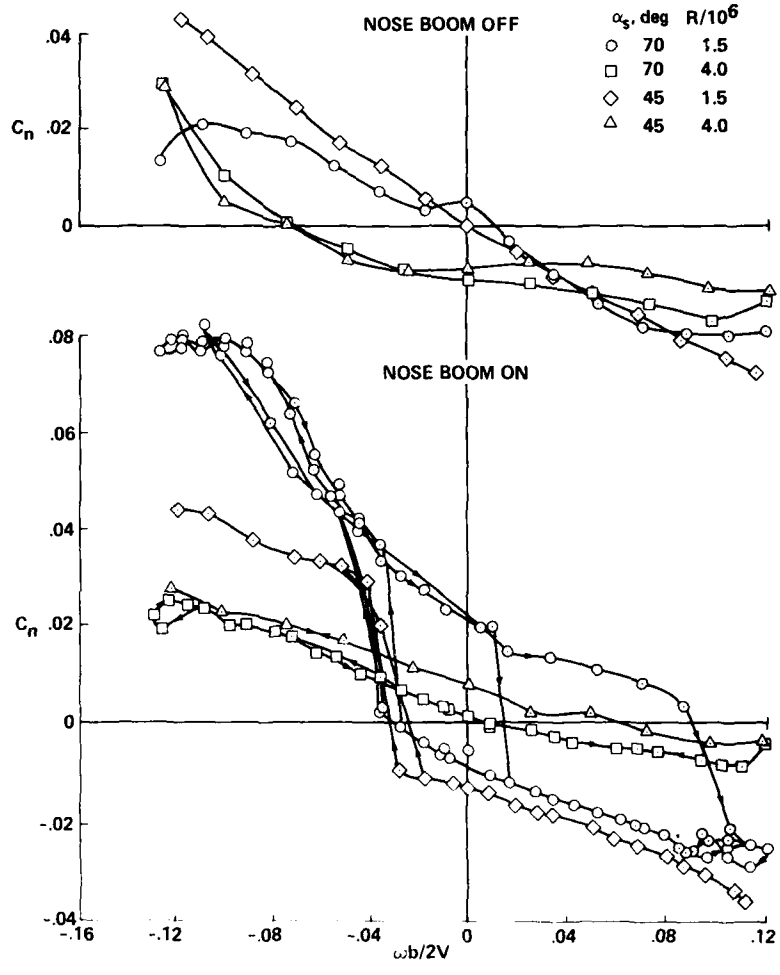

Fig. 15. Effects of rotation rate and sting angle on the yawing-moment coefficient for the F-15 at $\alpha = 70°$. (a) Nose boom off. (b) Nose boom on.

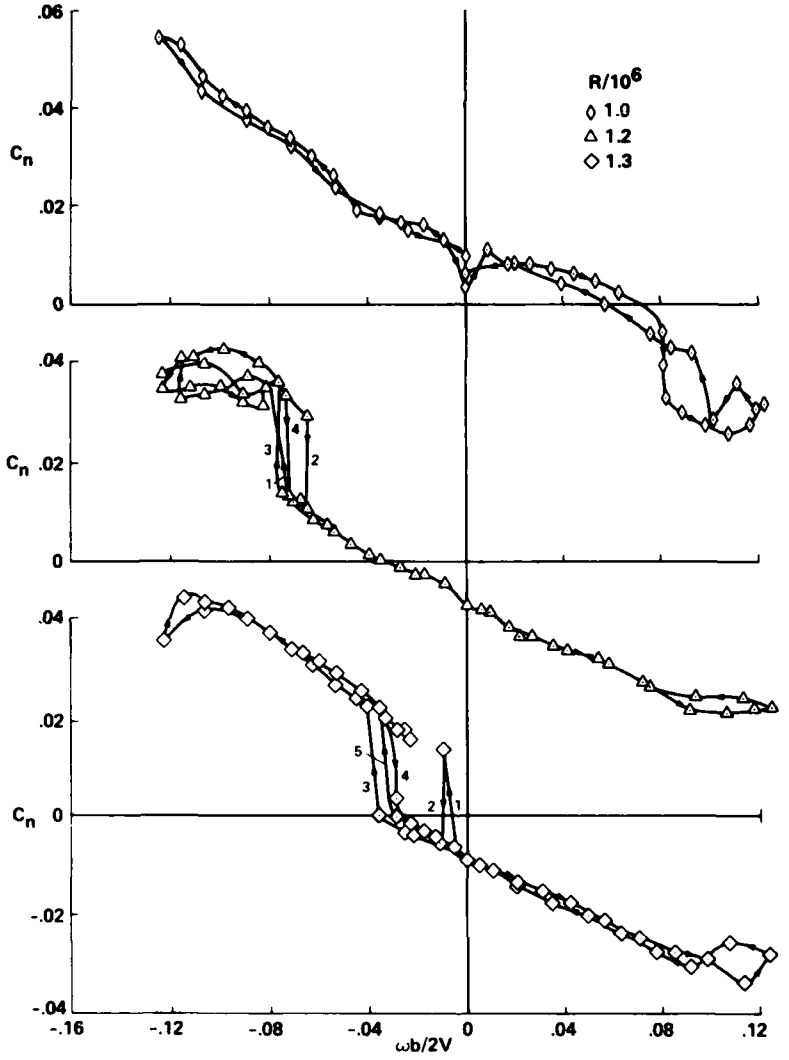

(a) $\alpha = 70°$.

Fig. 16. Effects of rotation rate and Reynolds number on the yawing-moment coefficient for the F-15, nose boom on.

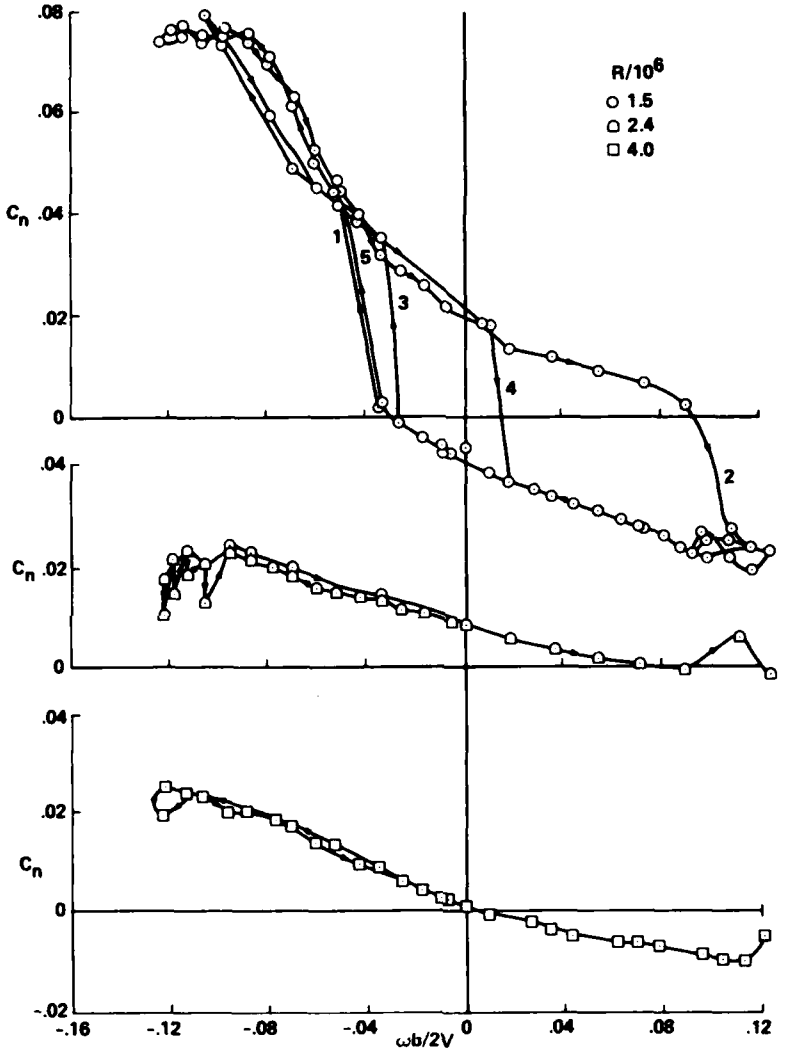

(b) α_s = 70°.

Fig. 16. Concluded.

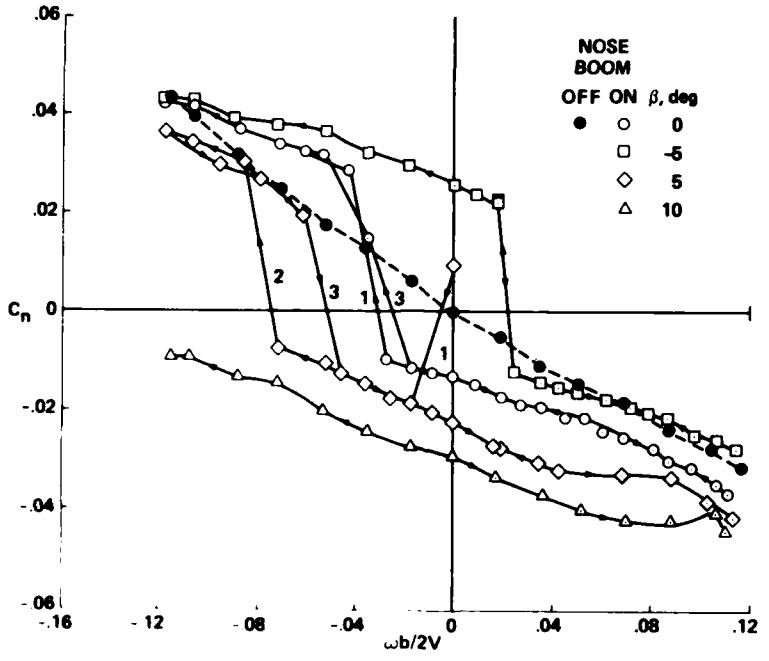

Fig. 17. Effects of rotation rate and sideslip angle on the yawing-moment coefficient for the F-15, $\alpha = 70°$, $\alpha_s = 45°$, R = 1.5 million.

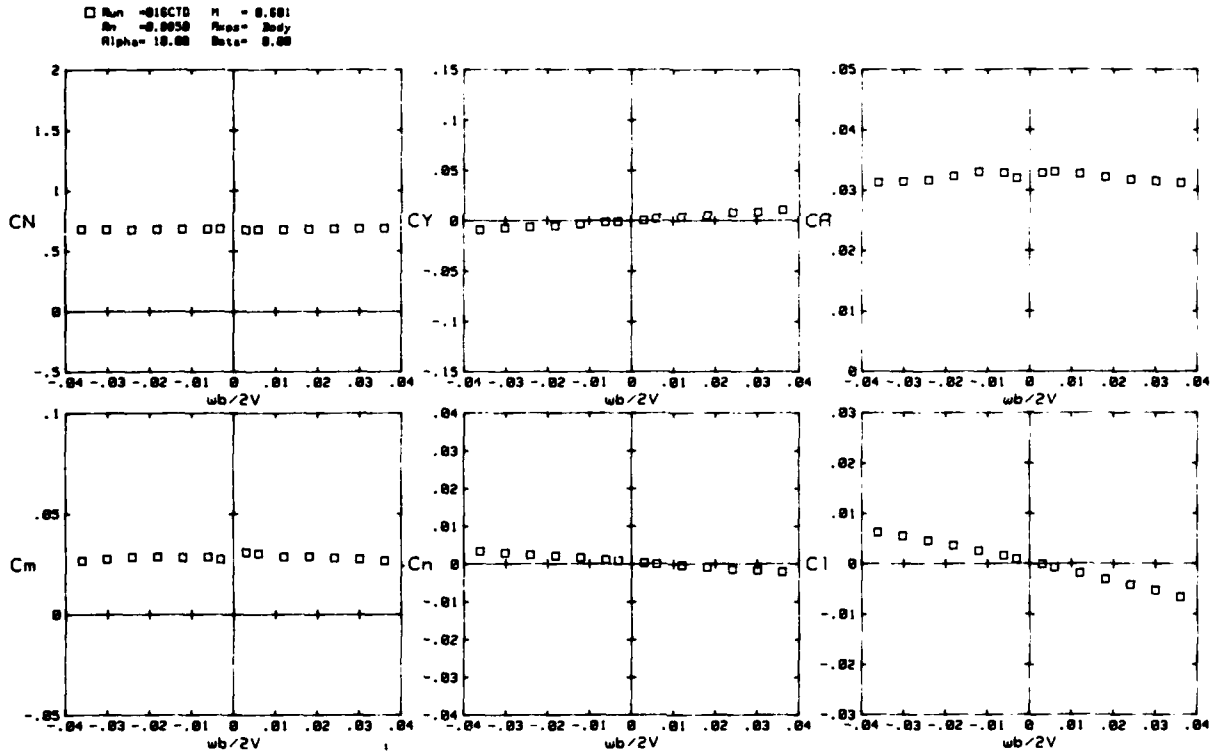

(a) $\alpha = 10°$.

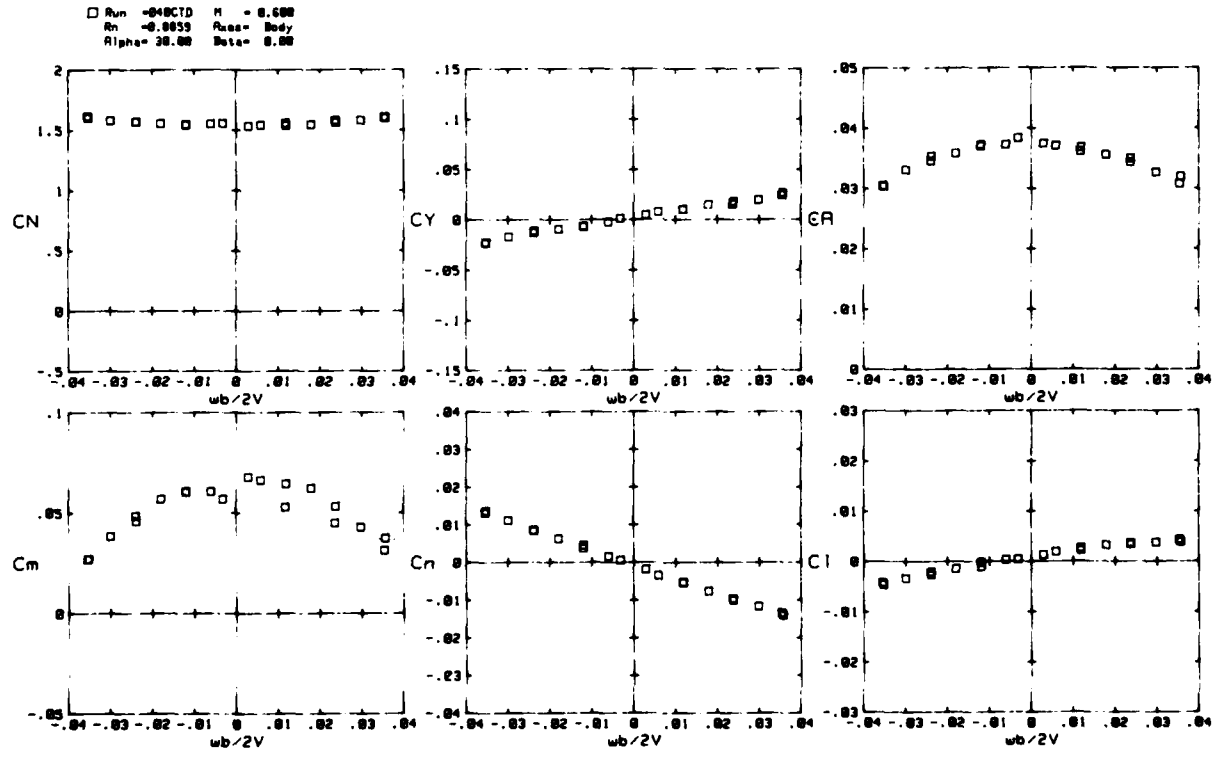

(b) $\alpha = 30°$.

Fig. 18. Effect of rotation rate on aerodynamic coefficients for Standard Dynamics Model at $\beta = 0°$.

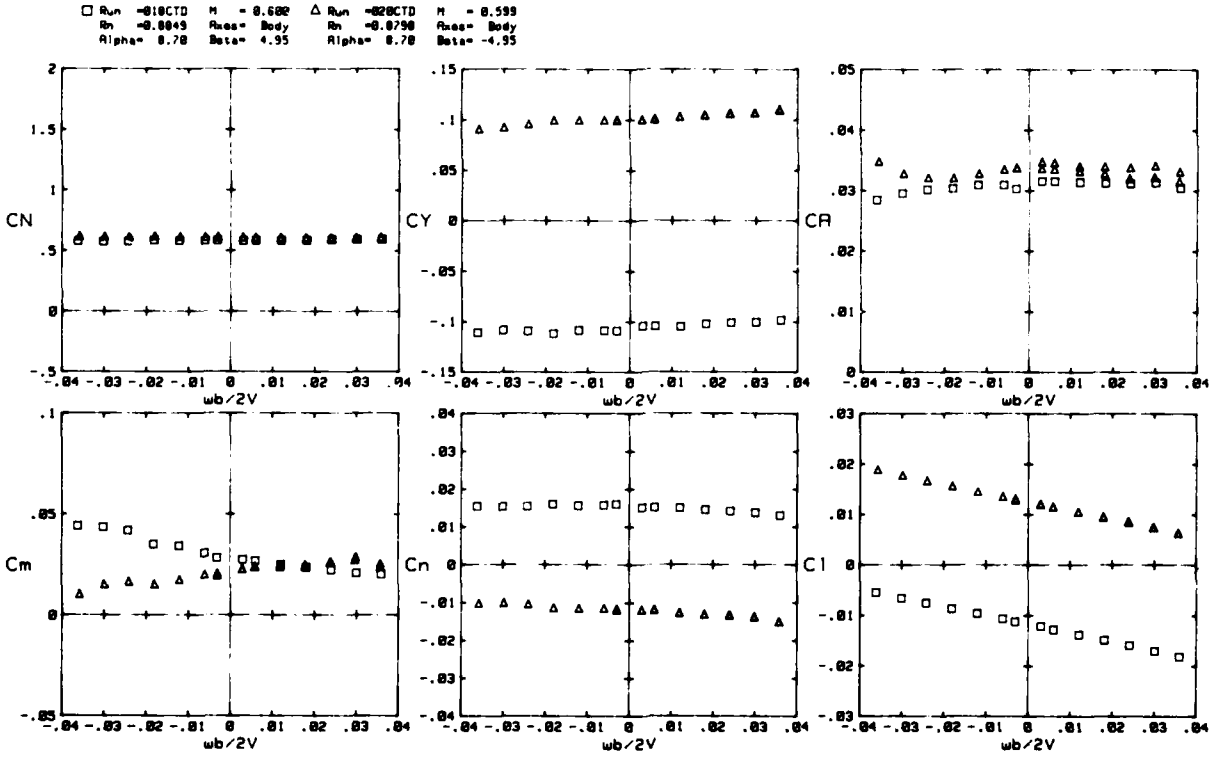

(a) $\alpha = 10°$.

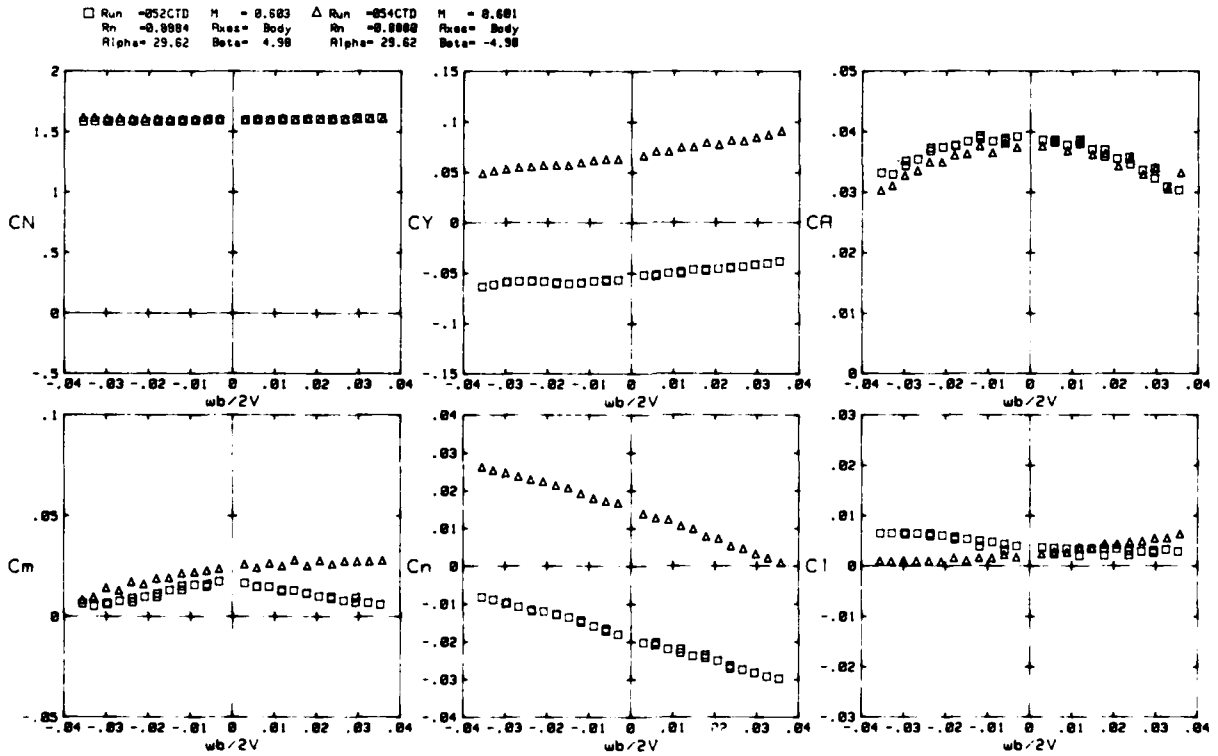

(b) $\alpha = 30°$.

Fig. 19. Effect of rotation rate on aerodynamic coefficients for Standard Dynamics Model at $\beta = +5°$ and $-5°$.

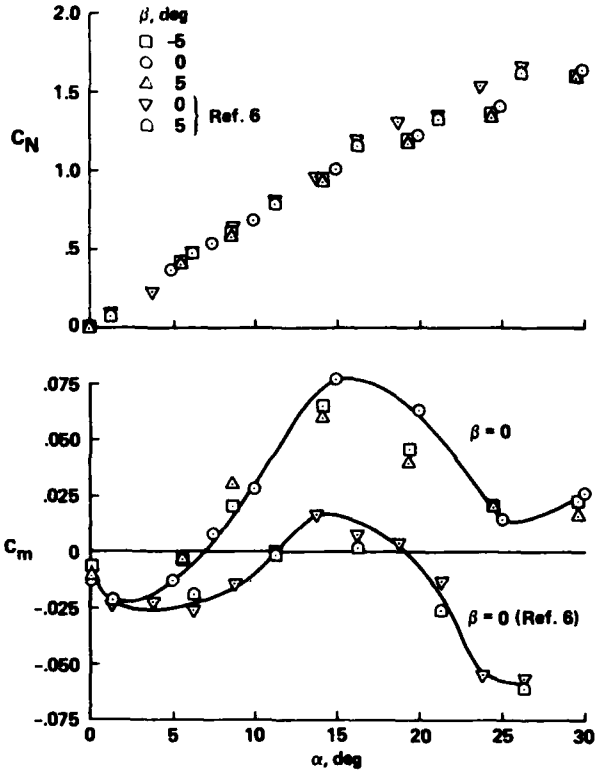

Fig. 20. Longitudinal aerodynamic coefficients for Standard Dynamics Model. (a) Normal-force coefficient. (b) Pitching-moment coefficient.

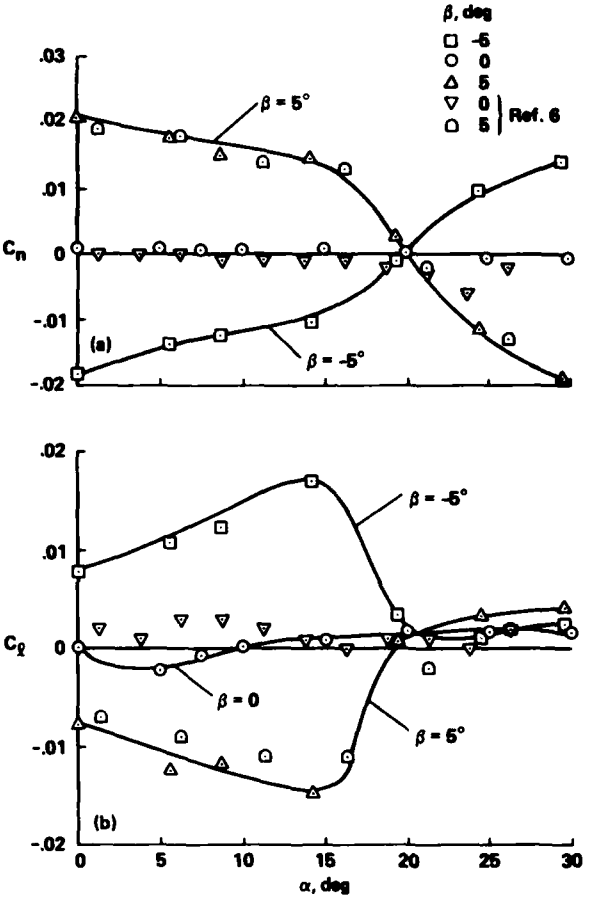

Fig. 21. Lateral-directional aerodynamic coefficients for Standard Dynamics Model. (a) Yawing-moment coefficient. (b) Rolling-moment coefficient.

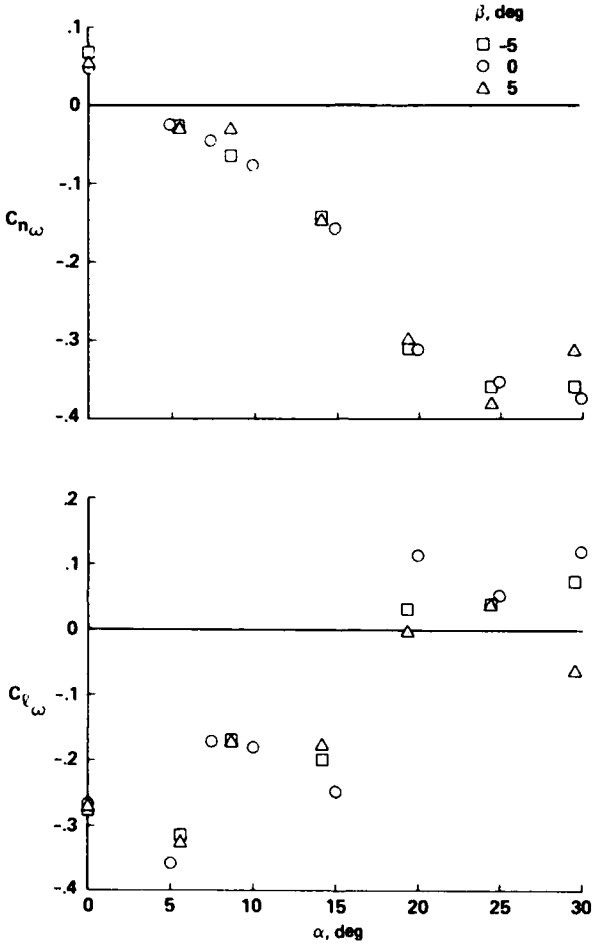

Fig. 22. Variation of lateral-directional rotary derivatives with angle of attack for Standard Dynamics Model. (a) Yawing-moment derivative. (b) Rolling-moment derivative.

NEW ROTARY RIG AT RAE AND EXPERIMENTS ON HIRM

by

C.O. O'Leary
E.N. Rowthorn

Royal Aircraft Establishment, Aerodynamics Department,
Bedford MK41 6AE, ENGLAND

SUMMARY

A rig for measurement of forces and moments due to continuous rate of roll has been commissioned at RAE Bedford. Tests have been made on a High Incidence Research Model (HIRM) in two wind tunnels at M = 0.2, 0.4 and 0.7. At present models can be tested up to 40° angle of attack at rotational speeds up to 350 rpm.

Tests on HIRM included an investigation of configuration and Reynolds number effects. Results are compared with similar data from tests with another rolling rig and from small amplitude oscillatory tests.

1 INTRODUCTION

For adequate mathematical modelling of combat aircraft flight characteristics at high angle of attack there is a requirement for data from dynamic as well as static wind tunnel tests. At RAE, small amplitude oscillatory rigs have provided valuable data on the longitudinal and lateral derivatives of combat aircraft over the past fifteen years. Recently dynamic test capability has been extended by the commissioning of a continuous rotary or rolling rig for use in both low speed and high speed wind-tunnels. This rig allows measurement of forces and moments due to continuous rate of roll; such data are more appropriate to the modelling of high amplitude lateral motions and spinning of combat aircraft.

A three surface configuration known as HIRM (High Incidence Research Model) has been the subject of an RAE programme of work[1] to gain knowledge of advanced combat aircraft aerodynamics and especially to formulate a mathematical model to predict flight characteristics at high angle of attack. Extensive static and dynamic wind-tunnel tests have been made and free flight glide models have been used to validate the mathematical model. An important feature of the wind-tunnel tests has been the continuous rolling tests on the new rig at RAE and on a large low speed rig[2] at BAe Warton. Results from these tests are compared with results from small amplitude oscillatory tests also made at RAE.

2 DESCRIPTION OF RIG AND LABORATORY TESTS

A diagram of the rig plus supporting structure in the 4m × 2.7m Low Speed Wind-Tunnel is shown in Fig 1. The non-rotating components, comprising shaft housing, motor, valve and transducers, are duplicates of those specified by BAe Warton for the 'Multi Facility Rolling Derivative Rig'[3] built under MOD contract. The rotating assembly has been designed, to an RAE specification, with the aim of providing a relatively unsophisticated facility which could be used in both low speed and high speed wind-tunnels. Since high utilisation was not envisaged, angle of attack and balance weights are manually adjusted. The rotor can be statically balanced but facilities for dynamic balancing were not included.

Details of the rotating assembly are shown in Fig 2. A five-component strain-gauge balance (axial force is excluded) is machined on to the end of the sting which can be axially rotated by means of a worm-and-wheel mechanism in the sting carrier. The root end of the sting fits into a socket in the carrier and clamped with pinch bolts. Facilities for axial adjustment and fixing of the sting are provided. The carrier is traversed along the machined steel rotor to vary angle of attack in increments of one degree. Maximum angle of attack is 40° with the straight sting shown but a sting with a 50° crank is being manufactured to allow tests up to 90° angle of attack. When angle of attack is set the carrier is secured to the rotor with clamping bolts normal to the plane of the rotor and screwed wedges in the plane of the rotor. Weight carriers are bolted to the ends of the rotor and a selection of weights can be fixed to either carrier to maintain static balance. At the higher angles of attack the weight carrier nearer the sting carrier is removed so that a smaller balance weight is required at the other end of the rotor. A channel in the rotor accommodates any slack in the cable from the strain gauge balance as angle of attack is varied. The rotor is bolted to the rotor holder which is fixed to the drive shaft with a tapered joint. The shaft runs in bearings in a cast steel housing and is driven by a hydraulic rolling vane motor mounted on the end of the housing. A variable displacement pump supplies the motor with fluid at 1500 psi pressure. Rotational speed is controlled by a servo valve with feedback from a tacho generator geared to the drive shaft. Strain gauge balance signals are brought out by a cable through a bore hole in the drive shaft and a slip ring unit at the motor end of the shaft. Vibration level on the rig is continuously monitored using an accelerometer on the forward shaft bearing housing. A visual and audible alarm is triggered if vibration increases beyond a preset level. The rotor can be brought to rest from maximum rotation speed in eight seconds.

The rig was first operated in the laboratory to demonstrate integrity of the rotating assembly, eliminate speed control problems and establish maximum rotation speed. For these tests the rig was mounted on a 4ft x 3ft engineering surface table bolted to the floor. A specially designed safety cage was placed around the rotating assembly. Vibration monitoring on the forward shaft bearing revealed a dramatic increase in vibration at approximately 420 rpm and vibration of the housing was visible. This speed gave 7 Hz excitation, which proved to be half the frequency of a rig oscillatory mode. With the rotor arm in the vertical plane a frequency of approximately 14 Hz was measured after a lateral 'bonk' of the model. This is believed to be the lowest natural frequency of the rig. During development testing several small peaks in vibration were observed at various rotation speeds and it was considered that these corresponded to submultiples of frequencies of the various modes of oscillation of the rig. It is possible that speeds higher than 420 rpm could have been achieved by quickly passing through this peak vibration speed but safety considerations determined otherwise! After speed control had been established to ±1 rpm the rig was considered safe for wind-tunnel testing up to a maximum rotation speed of 400 rpm.

3 DESCRIPTION OF MODEL

A general arrangement of HIRM is shown in Fig 3 and dimensional details are given in Table 1. The model tested on the Rolling Rig (M2131) was 2/9 scale relative to the free flight model.

The fuselage of the model is made of aluminium alloy with a steel balance adaptor. Wings and fin are also made of aluminium alloy but the foreplanes and tailplanes are steel. Range of travel of the control surfaces is +10° to -40° and all surfaces are removable. For rolling tests it is highly desirable that the cg of the model should remain on the balance centre so heavy-metal compensating weights are fitted in the model to replace the masses of the control surfaces removed. It is also necessary to fit heavy-metal weights in the fuselage below the centre line to balance the fin and wings. Some of these weights are replaced by aluminium alloy when the model is tested fin-off. Prior to testing, model balance is checked using knife edges in x, y and z axes.

4 SIGNAL PROCESSING

4.1 Physical system

A block diagram of the system is shown in Fig 4.

Signals from the five-component strain gauge balance are processed in a unit containing signal conditioning amplifiers and an analogue computing network which eliminates first order interactions of the balance. The corrected signals are then fed to the computer input system consisting of an Analogue to Digital Converter and Direct Memory Interface.

A digital encoder segment provides a square wave at the model rotational frequency 'f' which, together with the number of samples/rev. 'K' from the computer, is fed to a pulse multiplier to generate 'Kf' pulse/second which determine the sampling times. When a 'Kf' pulse arrives at the Analogue to Digital Converter External Scan Control, signals are sampled in parallel, serially digitised with a resolution of 15 bits and passed via a Direct Memory Access controller into one of two computer memory buffers. When a buffer is full the processor is interrupted and the other buffer used. The buffers are used alternately until 'K' samples of all channels have been taken. At the same time an interlocking program accesses the buffers and performs an averaging process on each signal. As this is a real-time process these signals may be averaged over as many cycles as required.

The pulse multiplier is fundamental to correct results and hence an additional board is attached permitting a computer controlled diagnostic check to be performed automatically before each measurement.

The rate of revolution of the model is obtained from the digital encoder segment and recorded for each run.

4.2 Computer operations

The strain gauge signals consist of a steady component due to inertia and aerodynamics, and a sinusoidal component due to gravity, oscillating at a frequency equal to the rate of revolution of the model. This gravity component is eliminated by averaging over one complete cycle.

The computer algorithm is: $\frac{1}{K} \sum_{k=1}^{k=K} F(k) . C$

Where:

K is the number of samples per revolution,
C is a scaling constant,
F(k) represents any of the measured signals.

Other signal components which might give rise to errors are harmonics of the gravitational components and 'noise' generated by either electrical interference or mechanical

imperfections in the system. Aliasing errors, which could arise from the correspondence of harmonic frequencies with sampling frequency, are constant for each measurement and may be eliminated by selectively changing, under computer control, the number of samples/cycle 'K' and hence the sampling frequency. Aliasing errors due to 'noise' (ie oscillatory signals not phase-locked to the rotational frequency) vary with each measurement and are eliminated by averaging over more cycles of revolution.

5 WIND-TUNNEL TESTS

5.1 Low speed tests

Tests were made in the 4m × 2.7m Atmospheric Wind Tunnel at RAE Bedford and in the 2.4m × 1.8m Variable Density Wind Tunnel at RAE Farnborough. Model configurations tested are given in Table 2. Tests on configuration C1 were repeated in the 2.4m × 1.8m at atmospheric pressure to assess repeatability of results and at two atmospheres to check for Reynolds number effects.

Before tests began it was necessary to statically balance the rotor (including sting and model) for each angle of attack to be set in the tests using a special shaft mounted on needle roller bearings. A set of fifteen weights was used to balance the rotor for all angles of attack required up to 40°.

Rig and supporting structures in the two wind tunnels are shown in Figs 1 and 5. Initial wind-off tests indicated that the vibration level at 400 rpm was bordering on the unacceptable so the limit was lowered to 350 rpm. Test procedure was to set angle of attack and take data for each configuration at rotation speeds between ±30 and ±350 rpm wind-off and wind-on (70 m/s). The rig was observed on a video display and vibration level monitored by means of an accelerometer on the housing of the drive shaft bearing, as for laboratory tests.

5.2 High subsonic speed tests

These tests were made in the 2.4m × 1.8m Wind Tunnel. One model configuration (C5, Table 2) was tested at M = 0.4 and M = 0.7 for angles of attack up to 20°. Reynolds number, based on aerodynamic mean chord $\bar{c}$, was 1.2×10^6 except that for M = 0.7, $\alpha > 8°$ it was limited to 0.6×10^6 because of lateral deflection of the support frame caused by rotation of the increasing normal force vector on the model. Another limitation in these high speed tests was that the desired rotation speed of 350 rpm could not always be achieved due to inadequate torque from the hydraulic motor. With weight carriers on both ends of the rotor and the larger balance weights fitted, air damping forces on the rotor and model limited rotation speed to approximately 250 rpm. Consideration is being given to increasing the rigidity of the support frame and installation of a more powerful hydraulic motor for high speed testing at up to 400 rpm.

Test procedure was similar to that adopted for low speed tests except that it was necessary to zero the balance after a preliminary 'warm up' run immediately before the wind-on tests. In this way zero drifts on the balance signals due to large temperature changes on running up the tunnel were minimised. In addition, zero error corrections were made to the data by interpolation using errors noted at the end of the test.

6 TEST RESULTS

6.1 Analysis and presentation

When the model is rolling at constant speed, each channel of the strain gauge balance measures components due to gravity, inertia and aerodynamics. The component due to gravitational force is a cyclic, equal and opposite variation about zero whereas the inertial force is a function of model mass distribution and proportional to rotational speed. The aerodynamic damping force is proportional to wind speed and also to rotational speed. The gravity component is eliminated from both wind-on and wind-off data by integrating and averaging the signal. The inertial component is assumed to be constant wind-on and wind-off so the aerodynamic component is the difference between wind-on and wind-off measurements at the same rotational speed, provided the wind-off tests are made in a vacuum. However if wind-off tests are made at atmospheric pressure, as in the present tests, the wind-off damping is also subtracted from the wind-on measurement. To reduce the wind-off measurement to the inertial component alone it is necessary to take the mean of the balance output for positive and negative rotations at the same speed where wind-off damping should be equal and opposite but inertial forces will be constant. This mean is then subtracted from the wind-on reading at the same rpm to give the total aerodynamic damping.

For these tests, rolling motion was about an aerodynamic body axis or 'wind axis' whereas the balance measured forces and moments are about geometric body axes. The coefficients were therefore converted to aerodynamic body axes before plotting against reduced roll rate, pb/2V for each configuration and angle of attack. It was not possible to convert for rolling about a geometric body axis without corresponding data on parameters due to yaw. Results for the three lateral coefficients C_n, C_y and C_ℓ only are presented.

The rate of change of C_n, C_y and C_ℓ with pb/2V was calculated using linear regression over the range pb/2V = ±0.05 to give C_{n_p}, C_{y_p} and C_{ℓ_p} for comparison with small amplitude oscillatory measurements.

6.2 Results from low speed tests

6.2.1 Variation of force coefficients with pb/2V

The variations of C_n, C_y and C_ℓ with pb/2V are considered for configuration C1 at three angles of attack, α = 16°, 24° and 40° in Figs 6, 7 and 8 respectively. These results are from 4m × 2.7m Wind Tunnel tests. At α = 16° there is some non-linearity in the characteristics, especially in C_n and C_ℓ at high values of pb/2V, but at α = 24° non-linearities are very marked in C_y and C_ℓ. The gradient of the C_ℓ characteristics is slightly positive at low pb/2V but negative for pb/2V > 0.05. There is some scatter in C_y at low pb/2V, α = 24°, owing to the low aerodynamic force and the unsteady flow conditions on the model at this angle of attack. At α = 40° (Fig 8) the coefficients have large non-zero values at zero roll rate, indicating asymmetric forces and moments larger than those measured in static tests on a 4/9 scale HIRM model[4]. It was established in these static tests that the side forces and yawing moments were generated by asymmetric vortices shed by the nose of the model, whereas the rolling moments were due to asymmetric flow separations from the wings. The asymmetry is also apparent in the local slopes $\partial C_n/\partial(pb/2V)$ and $\partial C_\ell/\partial(pb/2V)$ which are different for large positive and large negative rates of roll.

The effect of wind-off damping on rolling moment is shown in Fig 9, where C_ℓ is plotted as measured in geometric body axes for α = 16°. As explained in section 4.3 the wind-off damping is included by subtracting the mean of the wind-off measurement for equal but opposite rotations from the wind-on measurement. Although there is no significant difference apparent in the two characteristics at low pb/2V there is a 10-15% difference in C_ℓ for pb/2V = 0.15.

Measurements of C_ℓ at three Reynolds numbers are shown in Fig 10 for configuration C1, α = 24°. At $R_e = 0.9 \times 10^6$ results are shown from both 4m × 2.7m and 2.4m × 1.8m tests. There is some variation between the characteristics but this may be partly due to effects other than Reynolds number as is evidenced by the two sets of data at $R_e = 0.9 \times 10^6$. However, at α = 36°, Fig 11 shows that there is a substantial Reynolds number effect, mainly on the static rolling moment. Measurements of C_ℓ are shown from four runs at $R_e = 0.9 \times 10^6$ and two runs at $R_e = 1.8 \times 10^6$. Although there is some scatter in the repeated measurements it is clear that a significant positive displacement of rolling moment occurs at the higher R_e. At high values of pb/2V the two sets of measurements tend to converge.

Fin contribution to C_y, C_n and C_ℓ at α = 24° are shown in Figs 12 and 13 respectively. In general, sideforce generated by a fin is the sum of contributions due to sidewash over the fin arising from differential lift on the wings and to fin incidence due to rolling. For a positive rate of roll, air flows from port to starboard giving a positive sidewash contribution. At low angle of attack the contribution from fin incidence is negative, resulting in a small net sideforce contribution. However, at high angle of attack, when most of the fin area is below the rotation axis, the contribution from fin incidence is positive and, as shown in Fig 12, the total fin contribution is large and positive. As might be expected, Fig 13 shows that a positive fin contribution to C_y results in a negative increment in C_n and a small negative increment in C_ℓ due to fin displacement below the rotation axis. At α = 36°, Fig 14 shows that the positive increment in sideforce due to fin is maintained, as are the negative increments in C_n and C_ℓ (Fig 15). The fin-off roll damping has recovered to some extent compared to the low level at α = 24°. Scatter in the measurements of C_y and C_n at low pb/2V is due to unsteady flow conditions and the small aerodynamic loads to be measured by the balance.

The effect of foreplanes on C_ℓ is shown in Fig 16 for α = 18°, 20°, 24° and 26°. At α = 18° the variation of C_ℓ with roll rate is linear at low roll rate with some reduction in gradient as pb/2V approaches 0.1. The foreplanes give about 20% increase in roll damping. At α = 20° the gradient is virtually zero at low roll rate without foreplanes and there are marked non-linearities at higher roll rates. With foreplanes on, there is a substantial gradient through the origin with some fall-off in gradient at higher roll rate. It is probable that the foreplane contribution arises mainly from beneficial effects on wing lift rather than the increment due to damping forces on the actual foreplanes. When angle of attack is increased to 24° non-linearities in roll damping increase to the extent that the gradient appears to change sign between pb/2V = 0 and ±0.05. This effect is less severe with foreplanes on. At α = 26° the gradient is small for low roll rates but rolling moments increase suddenly at pb/2V = 0.1.

6.2.2 Derivatives due to rate of roll

Gradients of C_n, C_y and C_ℓ vs pb/2V for low values of pb/2V are plotted against angle of attack for configuration C1 in Fig 17. Three sets of data are compared: from tests at $R_e = 0.9 \times 10^6$ in the 4m × 2.7m Wind Tunnel and the 2.4m × 1.8m Wind Tunnel and at $R_e = 1.8 \times 10^6$ in the 2.4m × 1.8m Wind Tunnel. There is good agreement between the results and no significant Reynolds number effects are evident.

Plots of C_{n_p}, C_{y_p} and C_{ℓ_p} vs α are shown in Figs 18, 19 and 20 for the four configurations tested in the 4m × 2.7m Wind Tunnel. The measurements are appropriate to low

values of pb/2V (≈ 0.02) so that comparisons could be made with results from HIRM tests on the Small Amplitude Oscillatory Rig. At angles of attack where the variation of C_n, C_y and C_ℓ was strongly non-linear near the origin, gradients could only be approximated by eye.

Measurements of C_{n_p} and C_{ℓ_p} (Figs 18 and 20) on configuration C1 are also compared with data from tests on a 4/9 scale HIRM in a 5.5m Wind Tunnel[2] at BAe Warton. There is good agreement between results from the two rolling tests except at the highest angles of attack. There is also fair agreement with SAOR data at low angles of attack but for $\alpha > 20°$ the rolling rig measurements indicate more variation of C_{ℓ_p} with angle of attack (Fig 20). It is conceivable that separated flow areas are not so readily established on an oscillating model, alleviating the effect on roll damping. At some angles of attack closer correlation could have been obtained by measuring gradients at higher values of pb/2V where non-linearities were less severe. There is considerable scatter on SAOR data for C_{y_p} but they show a broadly similar trend to the RAE Rolling Rig measurements (Fig 19).

Figs 18a&b show the effect of the fin on C_{n_p}, which is a significant negative contribution at high angle of attack and Figs 19a&b show a positive increment to C_{y_p}. These effects are consistent with the explanation given in the previous section. The fin effect on C_{ℓ_p} is small but can be detected in Fig 20.

Foreplanes have an insignificant effect on C_{n_p} and C_{y_p} but a comparison of Figs 20a&c shows foreplanes increase roll damping C_{ℓ_p} at $\alpha = 18°$ and delay the loss in C_{ℓ_p} to a higher angle of attack. As discussed in the previous section, wing lift is enhanced by the foreplanes which delay separation on the down-going wing and maintain differential lift due to rate of roll.

The tailplanes have no significant effect on C_{n_p} and C_{y_p} but Figs 20a&c shows that loss of roll damping at $\alpha = 24°$ is, apparently, more severe without tails. However the gradient of C_ℓ vs pb/2V was very non-linear for low roll rate so gradient measurement at this angle of attack is very approximate.

6.3 Results from high speed tests

The coefficients C_n, C_y and C_ℓ are plotted against reduced roll rate for $M = 0.4$, $\alpha = 20°$ in Fig 21. Results from tests at two Reynolds numbers are shown but there is no significant difference in the gradients of the two sets of characteristics which are fairly linear. Some scatter is evident in C_n and C_y at low roll rates. It is probable that, in spite of attempts to eliminate zero errors due to temperature changes, small errors remained and may explain the vertical displacements between the two sets of data.

Fig 22 shows how C_n, C_y and C_ℓ vary with reduced roll rate at $M = 0.7$ for $\alpha = 0°$, 12° and 20°. Rolling moment varies linearly with roll rate for all angles of attack but there are some non-linearities in C_n and C_y, especially at low roll rates.

Derivatives C_{n_p}, C_{y_p} and C_{ℓ_p} appropriate to pb/2V = 0.05 are shown in Fig 23 for $M = 0.4$ and $M = 0.7$. Both the cross damping C_{n_p} and the damping in roll derivative C_{ℓ_p} are substantially negative up to $\alpha = 20°$. There is little difference in any of the derivatives between $M = 0.4$ and $M = 0.7$, but at $M = 0.7$ there appears to be a loss of roll damping at an earlier angle of attack than at $M = 0.4$.

7 CONCLUSIONS

(i) A rig for the measurement of forces and moments due to continuous rate of roll has been commissioned at RAE Bedford. Tests have been made on a High Incidence Research Model in two wind tunnels at $M = 0.2$, 0.4 and 0.7. Data quality from the tests was generally good although there was some scatter in the measurement of yawing moment and sideforce at low roll rate.

(ii) There is good agreement between results from tests with the RAE rig and from tests with a larger, lower speed rig at BAe Warton.

(iii) Results from tests on HIRM show that damping in roll is adequate up to $\alpha = 20°$. Foreplanes improve the linearity of rolling moment variation with roll rate and delay the loss in roll damping to a higher angle of attack. The tests indicate a more severe loss of roll damping for $20° < \alpha < 28°$ than was measured in tests with the Small Amplitude Oscillatory Rig.

(iv) Wind-off damping can be a significant proportion of the total damping at high rates of roll.

REFERENCES

1 G.F. Moss, A.Jean Ross, G.F. Butler. A programme of work on the flight dynamics of departure using a high incidence research model (HIRM). RAE Technical Memorandum Aero 1950 (1982).

2 P.J.P. Allen. Large scale rolling rig tests on the RAE Model 2130 (HIRM 2) in the BAe Warton 5.5m Low Speed Wind Tunnel. BAe Report AXR 103 (1983).

3 A.W. Mathews. The feasibility study, design, manufacture, commissioning and technique development of a rolling rig for the measurement of dynamic derivatives. Part 1 Design and manufacture of the rig, drive system, data acquisition and control system and calibration equipment. BAe Report AXR 60, Pt 1, (1978).

4 A.Jean Ross, G.E.A. Reid. The development of mathematical models for a high incidence research model. Part 1 Analysis of static aerodynamic data. RAE Technical Report 83037.

TABLE 1 LEADING DIMENSIONS OF HIRM (2/9 SCALE)

	mm or mm^2
Wing area, S	101825
Aerodynamic mean chord, $\bar{c}$	192.9
Wing span, b	578.6
Foreplane area (each surface)	6700
Foreplane exposed semi-span	76.1
Tailplane area (each surface	8150
Tailplane exposed semi-span	115.7
Fin area	11650
Fin exposed height	138.9

TABLE 2 DETAILS OF CONFIGURATIONS TESTED

Configuration number	Foreplane	Tailplane	Fin	LE droop
C1	-10°	-20°	on	20°
C2	-10°	-20°	off	20°
C3	off	-20°	on	20°
C4	off	off	on	20°
C5	0°	0°	on	0°

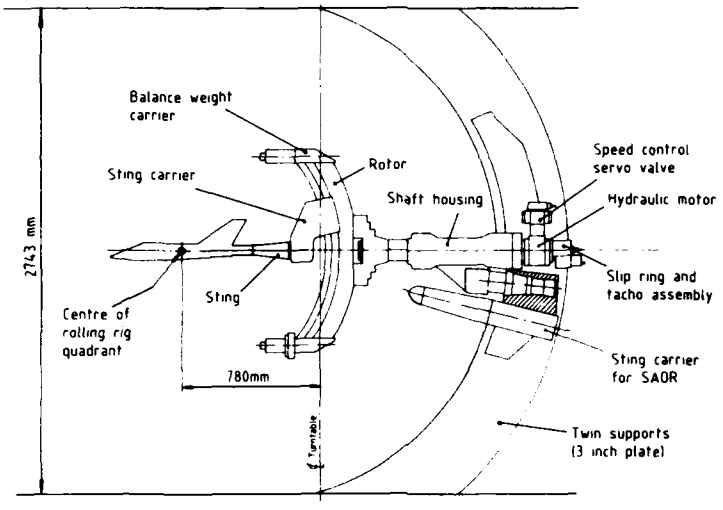

Fig. 1 RAE Rolling Rig in 4m x 2.7m Wind Tunnel

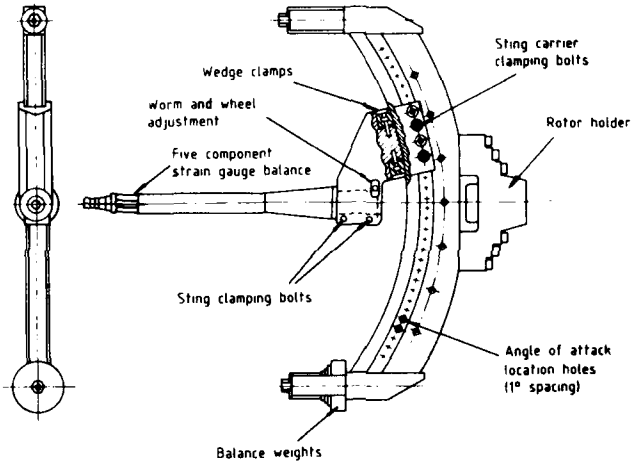

Fig. 2 Rotor and sting

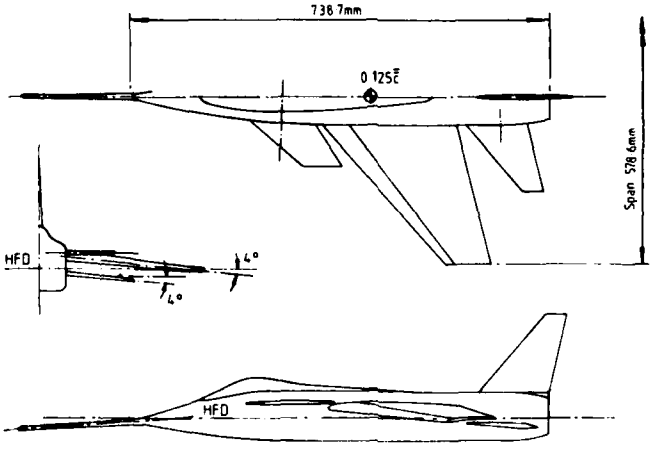

Fig.3 General arrangement of HIRM (M 2131)

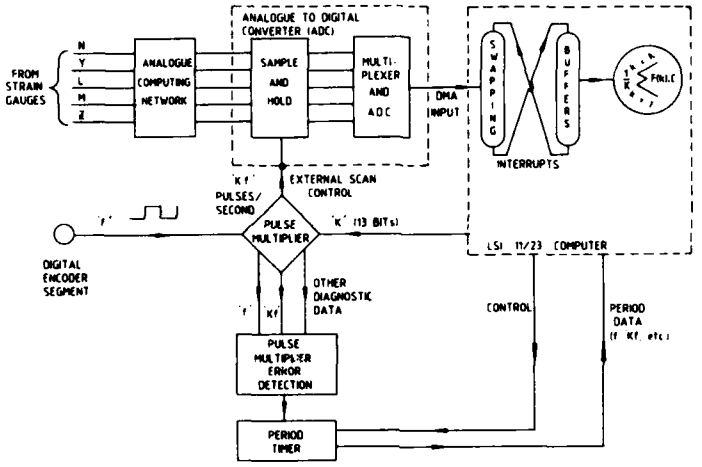

Fig. 4 Schematic of Signal Processing

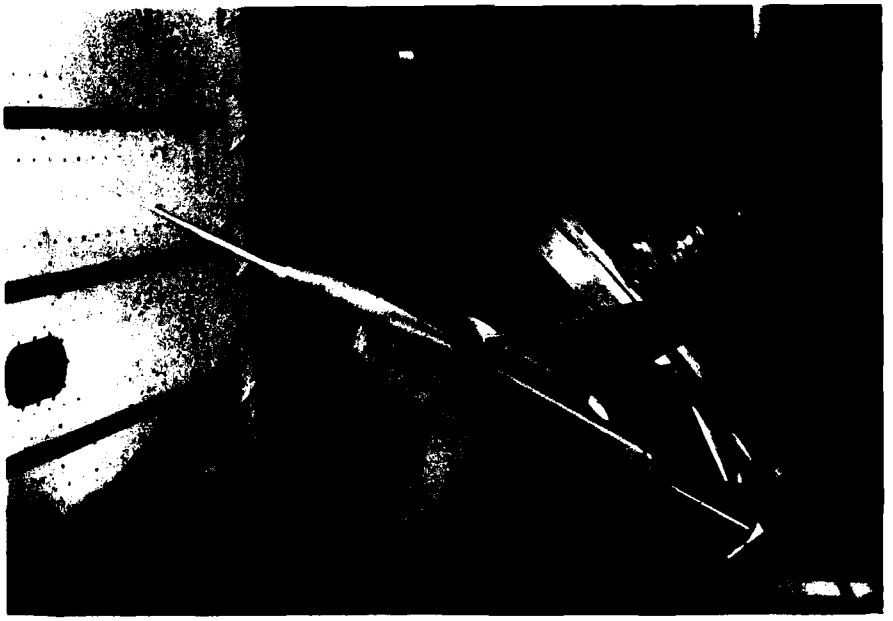

Fig. 5 Rolling rig in 2.4m × 1.8m wind tunnel

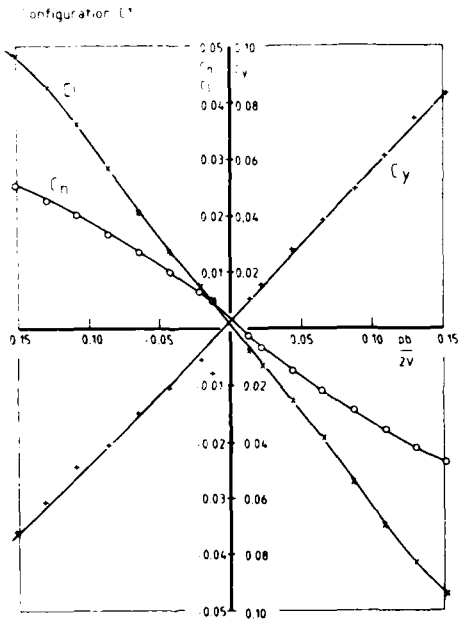

Fig 6 Variation of force coefficients with rate of roll. M = 0.2, α = 16°

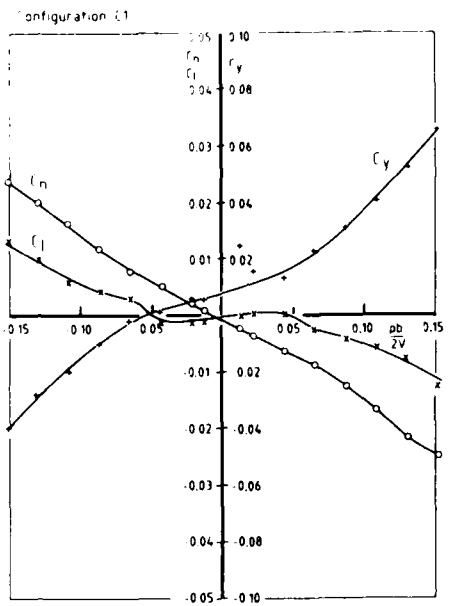

Fig 7 Variation of force coefficients with rate of roll. M = 0.2, α = 24°

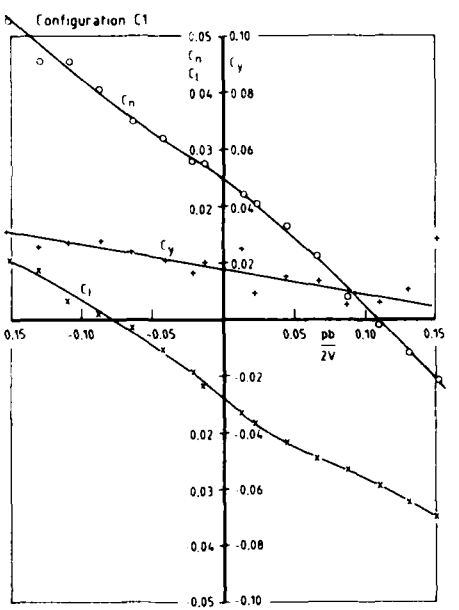

Fig 8 Variation of force coefficients with rate of roll. M = 0.2, α = 40°

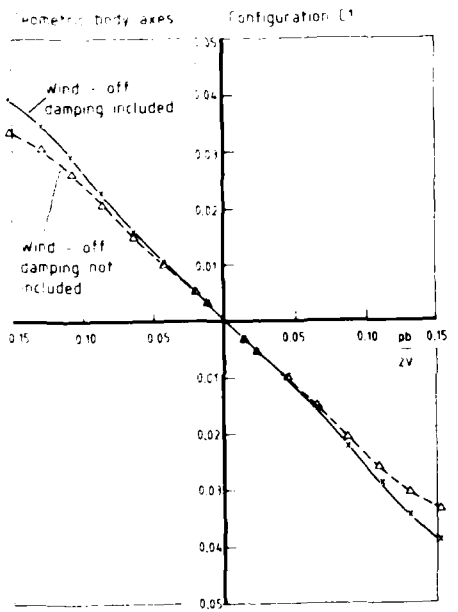

Fig 9 Wind - off damping M = 0.2, α = 16°

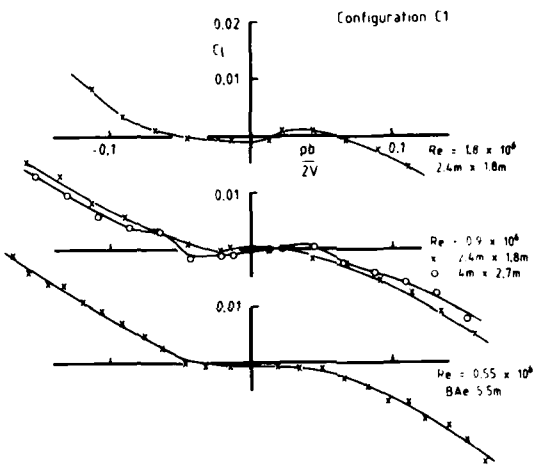

Fig 10 Effect of Reynolds number on Cl
M = 0.2, α = 24°

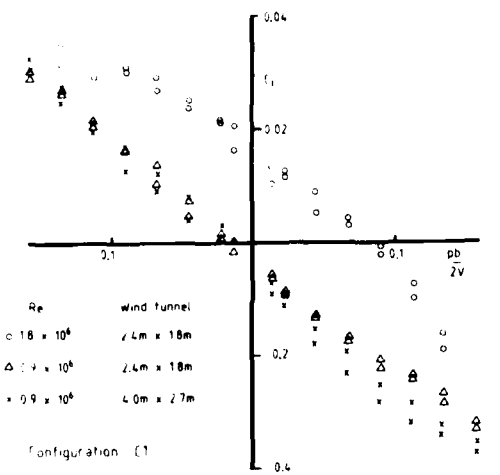

Fig 11 Effect of Reynolds number on Cl
M = 0.2, α = 36°

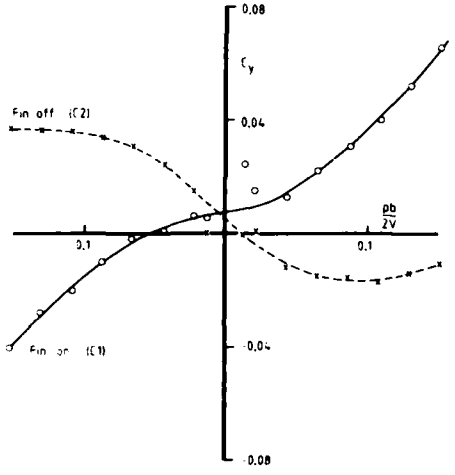

Fig 12 Effect of fin on C_y. M = 0.2, α = 24°

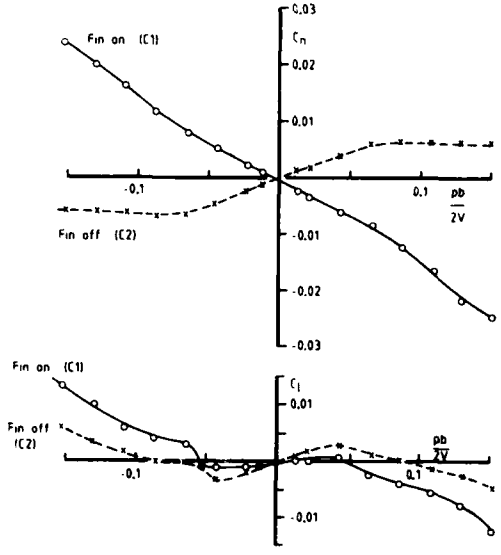

Fig 13 Effect of fin on C_n and C_l. M = 0.2, α = 24°

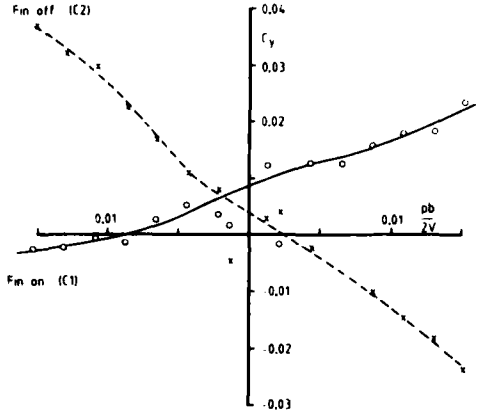

Fig 14 Effect of fin on C_y. M = 0.2, α = 36°

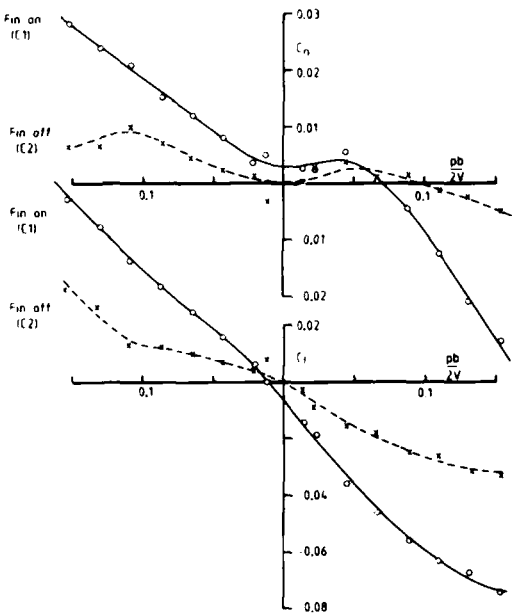

Fig 15 Effect of fin on C_n and C_l M = 0.2, α = 36°

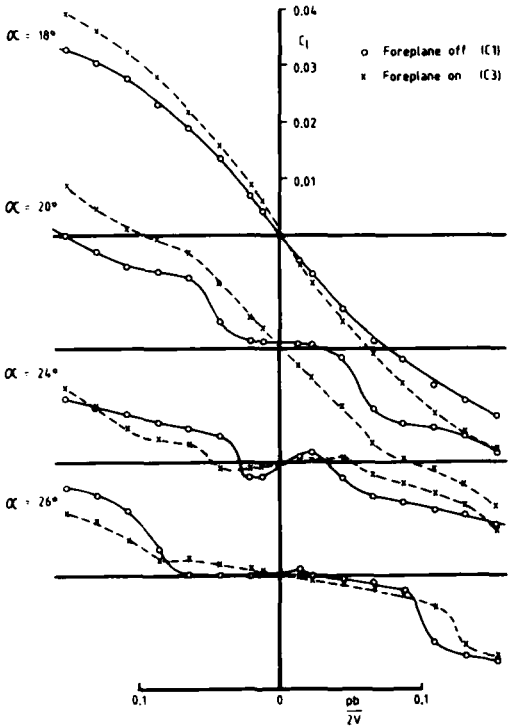

Fig. 16 Effect of foreplane on C_l M = 0.2

-AD356 p 19.12 40%

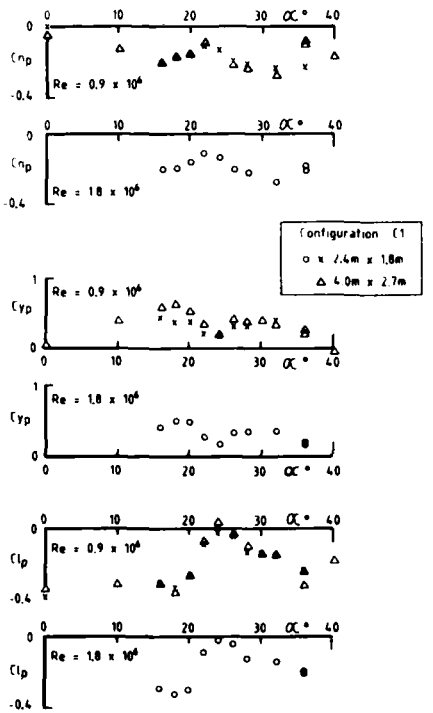

Fig. 17 Effect of Reynolds number on derivatives M = 0.2

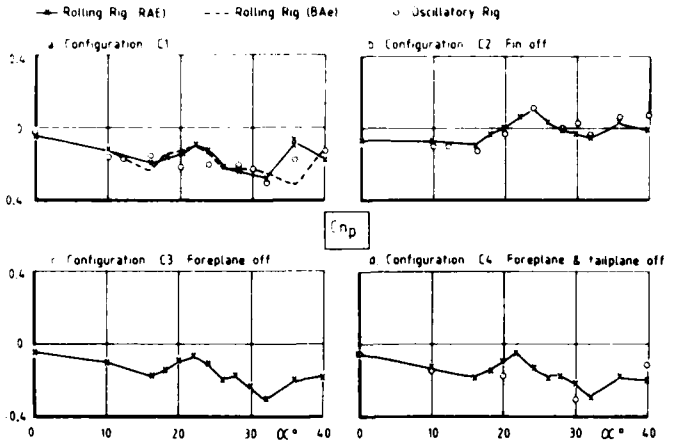

Fig 18 Effects of configuration on yawing moment due to rate of roll

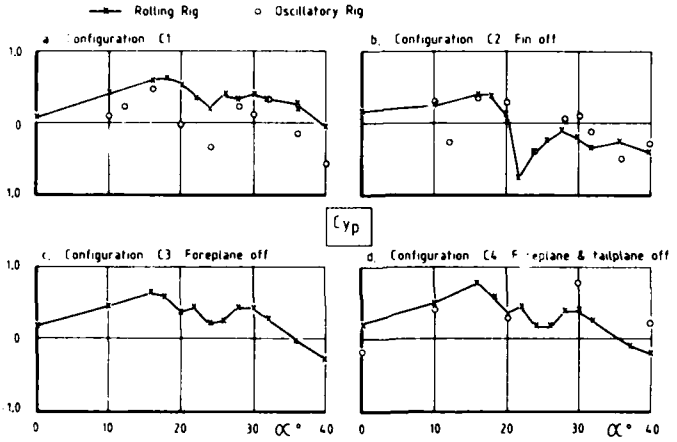

Fig 19 Effects of configuration on sideforce due to rate of roll

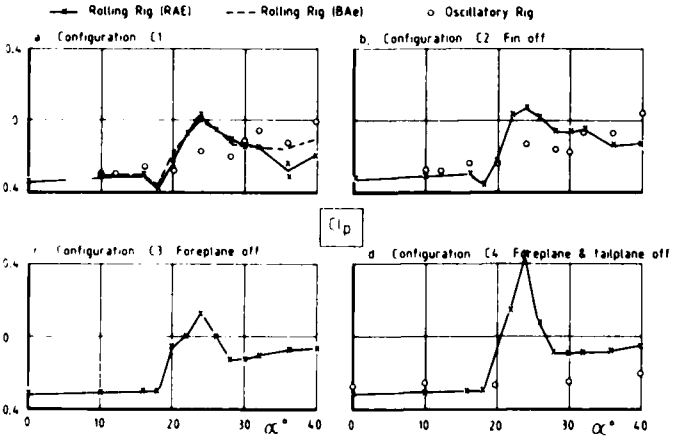

Fig 20 Effects of configuration on rolling moment due to rate of roll

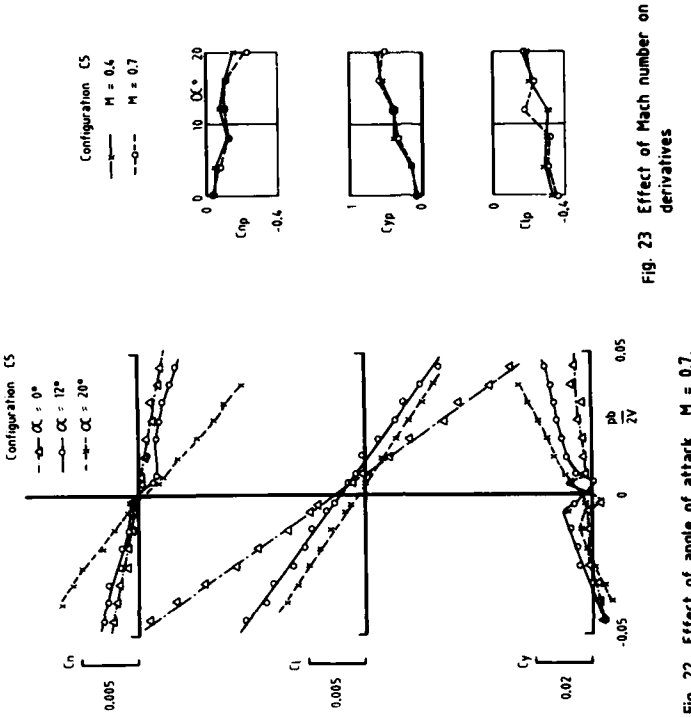

Fig. 23 Effect of Mach number on derivatives

Fig. 22 Effect of angle of attack. M = 0.7, Re = 0.6 x 10^6

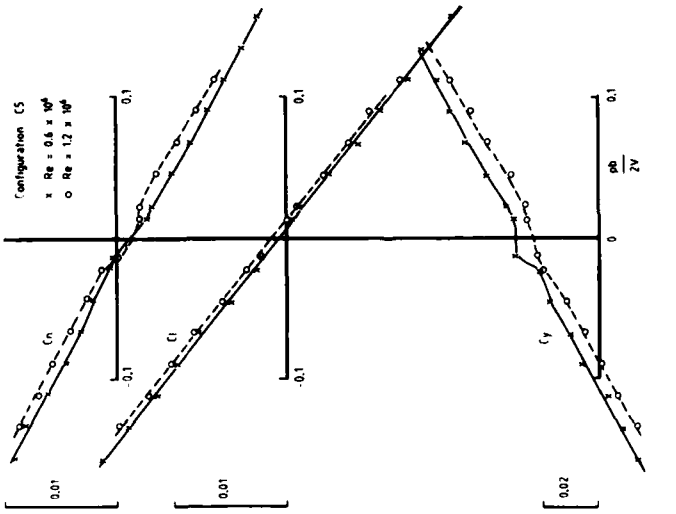

Fig 21 Effect of Reynolds number. M = 0.4, α = 20°

NEW DYNAMIC TESTING TECHNIQUES AND RELATED RESULTS AT FFA

by

Torulf Jansson and Lars Torngren
The Aeronautical Research Institute of Sweden (FFA),
S-161 11 BROMMA, Sweden

Summary

With the advent of the JAS fighter project, a need for improved dynamic testing of wind tunnel models arose at FFA both in the subsonic and transonic speed range. Some old rigs have been refurbished and some new ones have been developed. These will all be briefly described and in some cases results from tests with different models including the Standard Dynamics Model will be shown.

1 INTRODUCTION

Dynamic derivative testing has only been sparsely conducted at FFA in the past. Derivatives due to pitch, yaw and roll oscillations were calculated from data obtained from free oscillation tests. In order to get more accurate results the method of forced oscillation has been adopted. With the free oscillation apparatuses only direct static and dynamic derivatives could be measured but with the newly developed forced oscillation apparatuses both cross- and crosscoupling derivatives could also be measured as well as static coefficients. Mini-computers are now used for data aquisition and handling together with modern correlation techniques. The old way of calculating dynamic derivatives was done by measuring the time for the free oscillation amplitude to diminish to a half.

2 TESTING AT SUBSONIC SPEEDS

Dynamic derivative testing at subsonic speeds has been done in the low speed wind tunnel L2 at the FFA Aeronautics Lab., situated at the Royal Institute of Technology (KTH), Fig. 1. The tunnel has an octagonal closed test section of 2 × 2 m and the maximum speed is 65 m/s.

Two test rigs have been used. One rig for measurement of derivatives due to forced yaw and pitch oscillations and one for measurement of rotary derivatives.

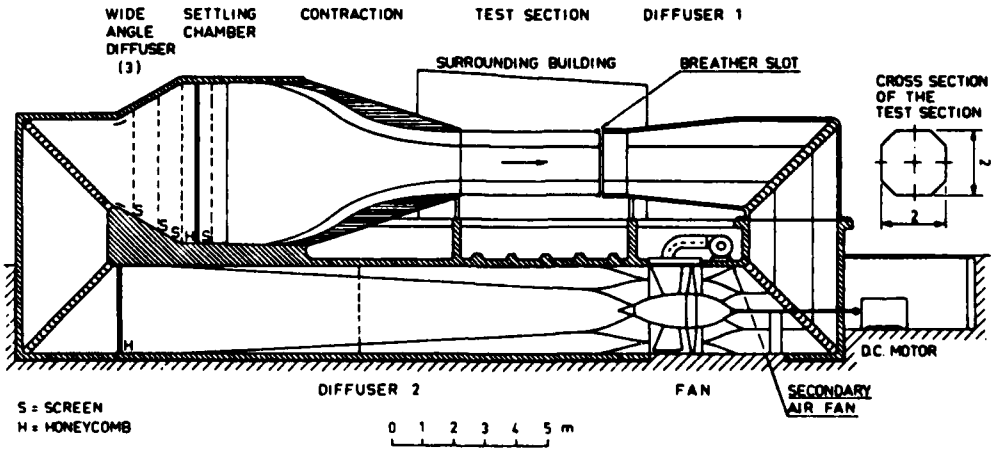

Fig. 1 The low-speed wind tunnel L2

2.1 Forced oscillation testing in pitch or yaw

2.1.1 Pitch/yaw apparatus

The pitch-yaw apparatus, Fig. 2, is built on a vertical strut model support. The angle of attack range is from -5° to 37°. Possible angles of sideslip are $\beta = -5^{\circ}, 0^{\circ}, 5^{\circ}, 10^{\circ}, 15^{\circ}, 20^{\circ}$. Four different oscillation amplitudes can be used $2^{\circ}, 4^{\circ}, 6^{\circ}, 8^{\circ}$. The highest frequency is 5 Hz.

The apparatus is driven by a tachometer equipped electric motor connected to a gearbox, a flywheel, a crankshaft and a long connecting rod attached to pivoting arms (one for yaw-

ing oscillation and one for pitching oscillation). It is possible to get either pitching oscillations or yawing oscillations by the apparatus. There are two different pivoting arms on the apparatus one for yawing and one for pitching. The type of oscillation obtained depend on which arm the long connecting rod is attached to, it drives either of them. The crankshaft can be mounted on different radii on the flywheel to give the desired oscillation amplitude. The flywheel permits a smooth motion and the use of a long connecting rod makes it almost harmonic.

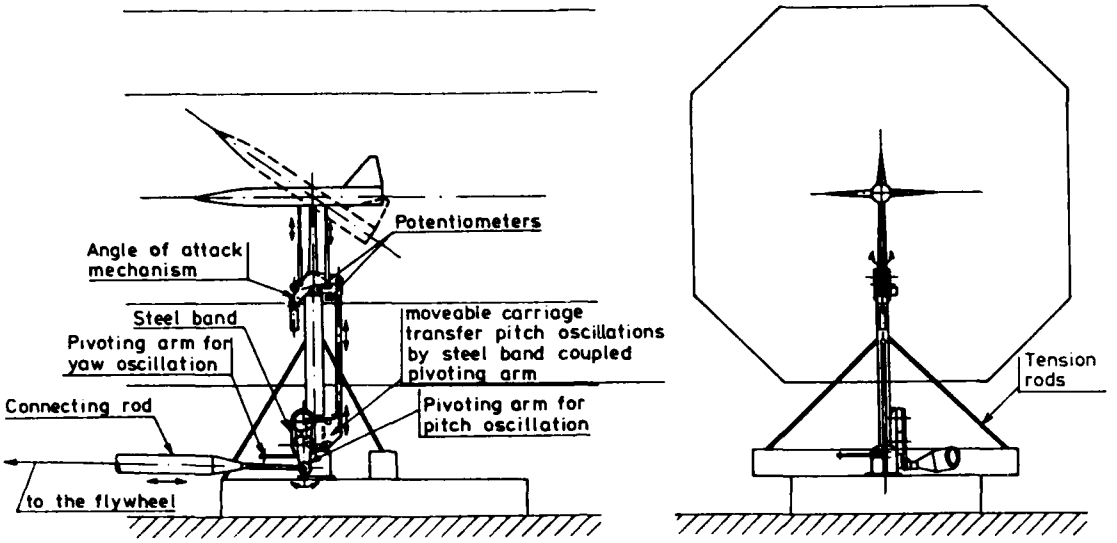

Fig. 2 The pitch-yaw apparatus.

The angle of attack can be changed continuously by a screw mechanism driven by an electric servomotor and is remotely controlled from the outside of the wind tunnel. The angle of sideslip can be set only to the fixed values mentioned earlier.

The angle of attack, angle of sideslip and oscillation amplitudes are measured by potentiometers, which are very accurately calibrated with laser equipment when mounted in the tunnel. The model forces and moments are measured with a 5-component balance (no tangential force measuring capability). The balance is symmetrical with respect to the pitch, roll and yaw axes and stiff enough to keep any natural frequencies well above the oscillation frequencies.

2.1.2 Instrumentation and data acquisition

The data acquisition was done primarily on an analogue computer, where signals from the wind tunnel, the strain gauge balance and the potentiometers were amplified and scaled. These signals were filtered with a cut off frequency of 20 Hz. The filters were very carefully selected to give the same phase lag across each filter. The filtered signals are connected to an AD-converter which is part of a SEL 32/77 computer. The data from the AD-converter are stored in a data buffer in the computer with a sample speed of 100 Hz.

The signal processing technique for evaluation of the dynamic derivatives is of the single sine type. It consists of an integration over one period after multiplying by either a sine or a cosine factor. This gives an in-phase (sine) or out-of-phase (cosine) result.

The out-of-phase result is the dynamic derivatives after normalizing with reference area and reference length. The in phase results are mainly a sum of inertia loads and static derivatives. To find the static derivatives at a certain oscillation frequency, inertia forces must be known. These are measured with the model oscillating in the tunnel and at zero wind speed.

The desired static force is the mean value over one period. Several periods are stored in the computer data buffer (the number of periods depends on the test frequency and the oscillation and sampling speeds). Each period in the data buffer is first treated separately then the mean value and standard deviation over several periods are determined.

Two different procedures are used in these tests depending on whether the static derivatives should be measured at a certain, frequency or not.

1) No static derivative will be measured, just dynamic derivatives. One measurement at the specified frequency is enough.

2) Both static and dynamic derivatives are required. One measurement is taken at a given frequensy with zero wind speed to obtain the inertial forces and one measurement at the same frequency with the tunnel running. Subtracting the inertial forces from the in-phase integral will give the static derivative and to a smaller extent acceleration derivatives. The out-of-phase analysis will give the dynamic damping derivative.

2.1.3 Results

Depending on the design of the pitch and yaw rig it is possible to evaluate either wind-refered derivatives or body-fixed derivatives. Pitching oscillations are body fixed oscillations. Therefore it is possible to estimate body fixed dynamic pitching derivatives for both forces and moments.

At non-zero sideslip angles it is possible to combine results from rotary test with the results from the pitching oscillations. Unfortunately there are only five components in the strain gauge balance the tangential force is lacking. For that reason it is not possible to convert the forces and moment completely. Only the moment can be transformed into the wind axis system. Therefore it is possible to measure the dynamic moment derivatives refered to the wind axes.

Dynamic derivatives due to pitching oscillations are presented for a simple delta wing in Fig. 3.

Yawing oscillations were performed about the wind fixed yaw axis and during this test only dynamic moment derivatives refered to the wind fixed coordinate system were calculated. An example of dynamic derivatives due to yaw oscillations is presented as an exemple in Fig. 4.

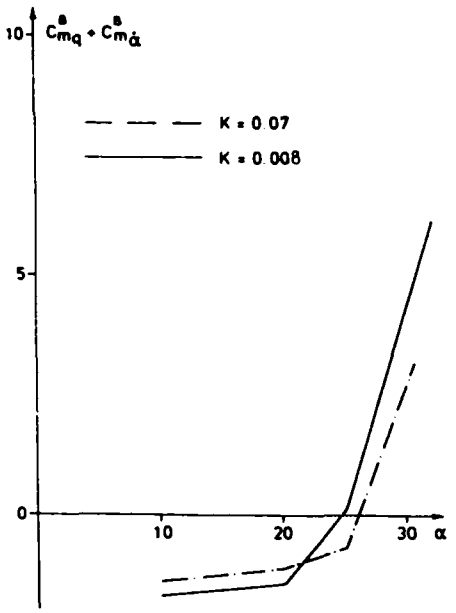

Fig. 3 Body-fixed pitching moment derivatives due to pitching oscillation.

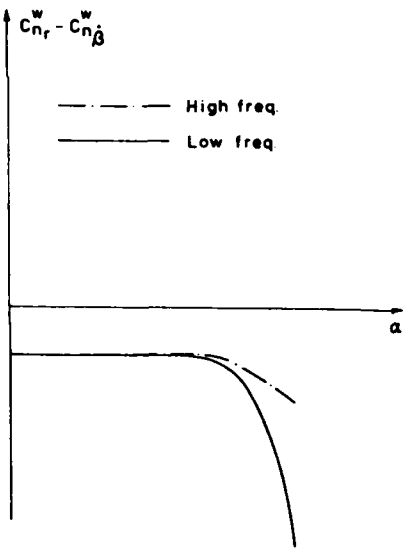

Fig. 4 Wind-refered yawing moment derivatives due to yawing oscillation.

2.2 Rotary derivative rig

The rotary rig has been used at KTH since the early sixties. In the last few years some modifications have been carried out including the installation of a new digital data acquisition system. The rig is shown in Fig. 5 installed in the wind tunnel.

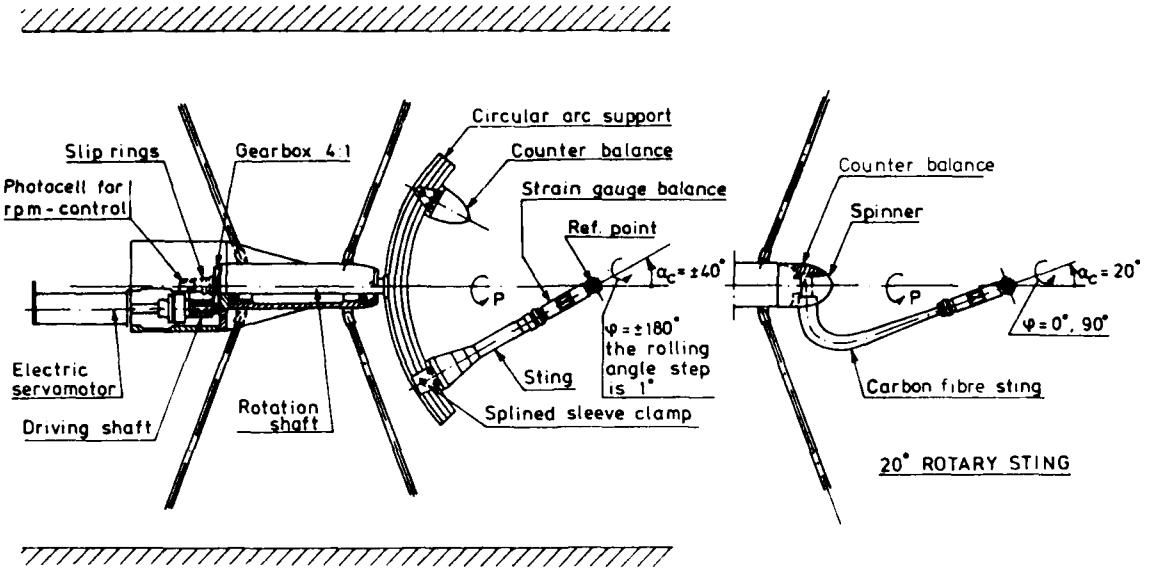

Fig. 5 Rotary apparatus.

2.2.1 Description of the apparatus

The rig is mounted in the tunnel with tension rods, with the rotating shaft aligned with the tunnel centre line. In the rear part of the rig is an electric servomotor installed. The highest rotation rate is about 300 rpm. A set of goldplated slip rings conduct the rotary balance signals from the moving part of the rig to its static part. The rotary balance is a 6-component strain gauge balance mounted on a sting. The sting can be rolled in increments of 1^0 along its centre line. A combination of body roll angle and the angle between body and rotation axes can be transferred to a set of α and β angles. The sting is designed in such a way that the centre of the balance is situated on the axis of rotation, where the model reference point is also located. The angle between the tunnel centerline and the sting can vary from 0^0 to $\pm 40^0$. During tare runs the model is put in a container to let the surrounding air close to the model rotate together with the model and thus not interfere with the inertia measurements.

2.2.2 Data acquisition and data reduction

The data acquisition technique is the same as for the pitch/yaw rig and the sample speed is also the same, 100 Hz.

The evaluation of the rotary derivatives is carried out as if it were a static test. Because of the rotation around the wind vector the rotary damping forces and moments are evaluated in a wind fixed coordinate system. The forces and moments from the 6-component balande are converted from the body fixed coordinate system to the wind system.

To evaluate the forces and moments a mean value calculation is performed by integration over a single revolution of the model. For each revolution data are stored and mean value and standard deviation of all revolutions are calculated.

The moments and forces depending on rotary damping are evaluated in several steps.

1) Measurement of inertia forces and moments during a fast tare run, at the same rotational speed as during the wind-on run. The model is enclosed in the container.

2) The model is slowly rotated (10 rpm) during a tare run to record the gravitational forces and moments at the wind off condition.

3) Measurement of forces and moments at a slow rotational speed (10 rpm) with wind on.

4) Measurements of forces and moment at the desired high rpm with the wind tunnel running.

Calculation of static forces and moments is done by subtracting 2) from 3) and the rotary damping forces by subtracting tare forces and static forces from the wind on high rpm data. The computation of the rotary roll derivatives for a fixed angle of attack is then carried out by dividing the rotary damping force and moment coefficients by the rotating reduced frequency. This procedure is valid as long as the derivatives are independent of roll rate.

2.2.3 Results

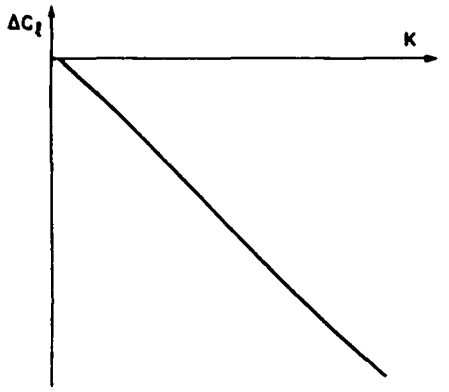

Most of the results are presented as rotary damping forces and moments as a functions of the rotational reduced frequency, Fig. 6. To investigate the interference effects from the counter balance weight at the angle of attack 20°, a special sting made of carbon fibre has been manufactured. This sting design is intended to minimize the sting support interference effects and is also shown in Fig. 5. Only small differences between the two stings can be seen mainly on the side force and yawing moment, Fig. 7.

Fig. 6 Wind-refered rotary damping rolling moment.

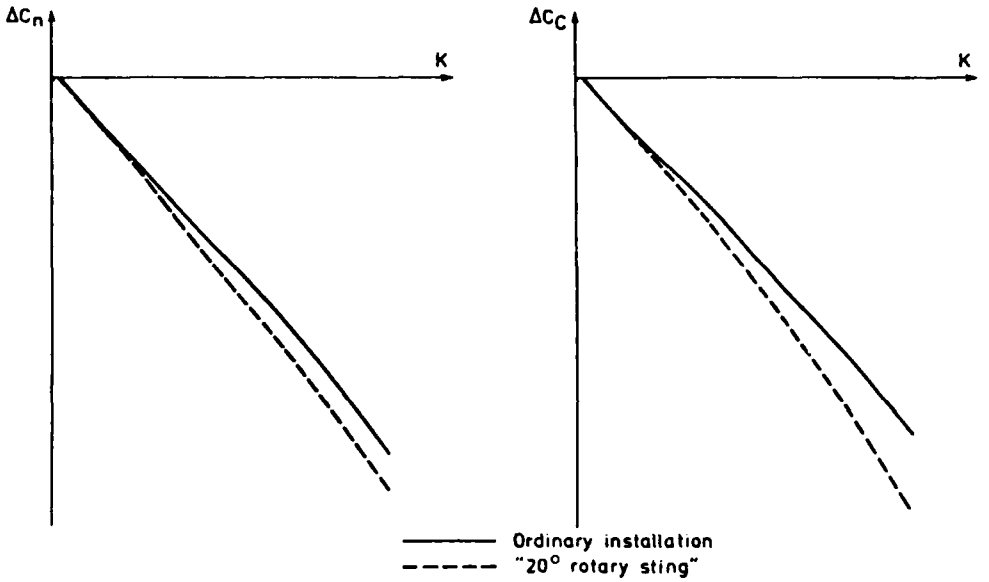

Fig. 7 Interference effect on wind-refered rotary damping side force and yawing moment.

3 TESTING AT TRANSONIC/SUPERSONIC SPEEDS

In this section three different apparatuses will be described, a forced oscillation pitch-yaw apparatus, a rotary derivative apparatus and a control surface oscillation apparatus.

FFA has two high speed wind tunnels suitable for dynamic derivative testing: the transonic/supersonic S4 intermittent suction wind tunnel and the continuous HT transonic wind tunnel. S4 has a test section cross area of 0.8 m^2 and a stagnation pressure slightly less than ambient pressure while the HT wind tunnel is 0.7 m^2 and has a variable stagnation pressure which at transonic speeds is lower than ambient pressure. The S4 has a rectangular cross section with slotted walls in the floor and the ceiling while the side walls are solid. In HT the cross section is octagonal with a slot in each corner. The pitch-yaw apparatus is designed for both tunnels while the other two apparatuses only can be mounted in the S4 wind tunnel.

3.1 Forced oscillation testing in pitch or yaw

3.1.1 Pitch/yaw apparatus

The pitch-yaw apparatus, figure 8, is mounted on a 10° cranked angle support, which can be rotated to give any choosen combination of angle of attack and angle of sideslip. The angle of sideslip is however limited to 10° but the model is always situated in a horizontal plane when the angle of attack is zero. The apparatus consists mainly of a sting, a rocker arm, a cross flexure and a 5-component balance.

The sting is mounted to the 10° cranked angle support to the rear and to the cross flexure in front. The sting cross section at the model base is elliptical to get as large oscillation amplitude as possible. Inside the sting is a rotating drive shaft which

gives the rocker arm an up and down movement. The rocker arm is mounted in the front part of the cross flexure with the same bolts as the 5-component balance. The cross flexure is made of a single piece of Armco 17-4 PH stainless steel by the spark erosion technique. The flexure elements are wider at the ends to increase the loadcarrying capability during yaw oscillation tests. Inside the rocker arm is a cantilever spring, which together with the cross flexure, gives the apparatus a spring constant suitable for oscillation at resonance. The displacement strain gauges are glued to the cantilever spring. Thus no normal loads will affect the displacement signal.

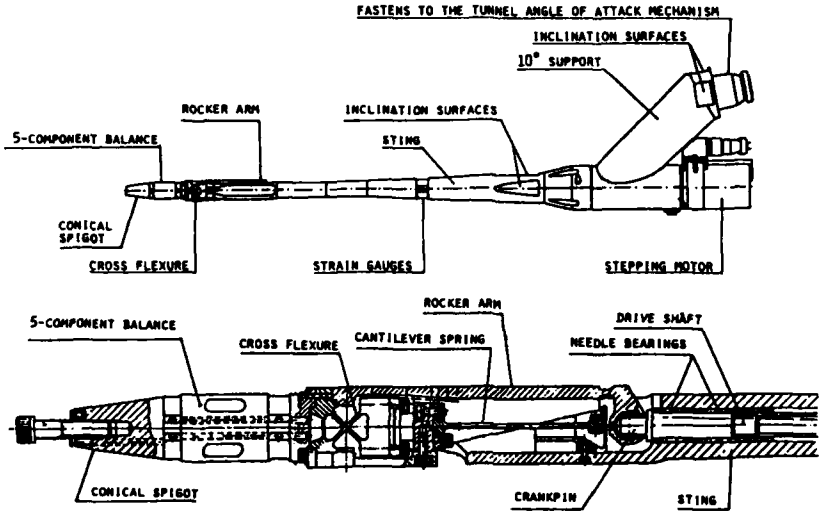

Fig. 8 The pitch/yaw apparatus and details of its forward part.

The 5-component balance (no axial measuring capability) is symmetrical with respect to the pitch and yaw axes and very stiff to keep any natural frequencies well above the oscillation frequencies. Because of its stiff design it is equipped with semiconductor strain gauges. Semiconductor strain gauges are also used on the rocker arm, to measure the moment needed to keep the oscillation stationary, and on the sting. The model is oscillated by means of a stepping motor placed at the back of the sting and the 10° cranked sting support. Although the least energy required is when oscillating at resonance, the motor is powerful enough to run at frequencies off resonance. The highest frequency is 20 Hz and the oscillation amplitude is 1.2 deg.

3.1.2 Instrumentation and data acquisition

All data acquisition and handling was done on the wind tunnel minicomputer, the General Automation SPC 16/65. The standard peripherals include two 12-channel bridge amplifiers of FFA design and a 13 bit AD-converter with multiplexer. Some additional instrumentation was also designed and built: a stepping motor control unit with cycle timer, a 12-channel signal generator and a 12-channel filter unit.

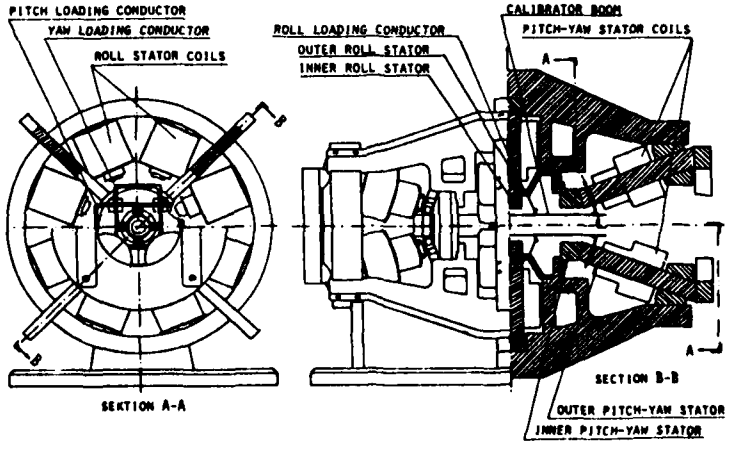

Fig. 9 The dynamic calibrator.

The measured signals were first fed to the bridge amplifiers in the usual way but instead of directing them to the AD converter, they were directed to the filter unit. In the filter unit each signal was split into a DC and AC part by means of filters. It was then possible to amplify the AC part up to an additional 100 times. The filter unit also housed a sample and hold circuit where some different sampling frequencies could be selected. The DC and AC signals were then redirected to the AD converter and there were thus twice as many channels recorded as there were channels from the apparatus.

With the signal generator known DC and AC voltages were input to the data acquisition system. The DC and AC gains were then calibrated as well as the phase shift for each AC channel with respect to the displacement channel. In spite of the sample and hold capability there were small differences in phase shift due to individual differences in the filters.

From the stepping motor control unit, start and stop of the motor and its frequency was controlled. The cycle timer recorded the average of all cycles during a run and stored it for later access by the computer. The computer was also recording and checking the settings of the signal generator voltages and the sample and hold speed.

The balance was first statically calibrated and then, to check the whole data acquisition and data reduction process and to calibrate for magnification, the apparatus was put in a dynamic calibrator, Fig. 9. This calibrator works on the same principles as for example the calibrator mentioned in reference 1. Dynamic loads which are known to their amplitude and phase with respect to the primary motion were applied in the pitch, yaw and roll plane. They were applied independant of each other in the different planes of motion. The result from the data reduction programme was divided with the known load in the same plane of motion and plotted against the ratio of oscillation frequency to sting natural frequency. After tests at some different oscillation frequencies had been concluded a function for correction due to magnification was incorporated in the data reduction program.

The semiconductor strain gauges used on the apparatus are quite temperature sensitive. Most of the zero shift was taken care of by temperature compensating resistances placed in the tunnel. The gain factor of the strain gauges was also quite temperature sensitive but this was taken care of by statically loading the apparatus at two different temperatures and making shunt calibration at the same temperatures. By making shunt calibrations before and after each run the correct gain factor could be calculated.

A typical wind tunnel run consists of three parts: an amplifier calibration run, when known voltages from the signal generator are fed into the system, a tare run when the model is oscillated but with the tunnel not running and finally a wind on run. Data were sampled for 15-20 seconds at 100-150 Hz depending on oscillating frequency. If only the angle of attack was changed between two runs and no gain settings were changed the amplifier calibration and tare run could be omitted.

The signal processing was done with a cross-correlation technique according to Ref. 2. For all AC signals an amplitude and phase angle with respect to the primary motion was calculated and for the DC signals an average was calculated.

3.1.1 Wind tunnel model

To familiarize with the apparatus and its equipment a Standard Dynamics Model (SDM) was built, figure 10. This model was originally designed at NAE, Canada and later built to different scales at various wind tunnel institutions. There are also quite a lot of results published, Refs. 3, 4 and 5, with which comparisons can be made. The scale of the FFA SDM model was choosen so as to give the model a blockage ratio of 0.6 % in the HT wind tunnel. The size of the model then resulted in a span of 290 mm and a length of 450 mm. All following results are refered to the 35 % mean aerodynamic chord point and the model configuration designations are the same as the ones used by AEDC, Ref. 3.

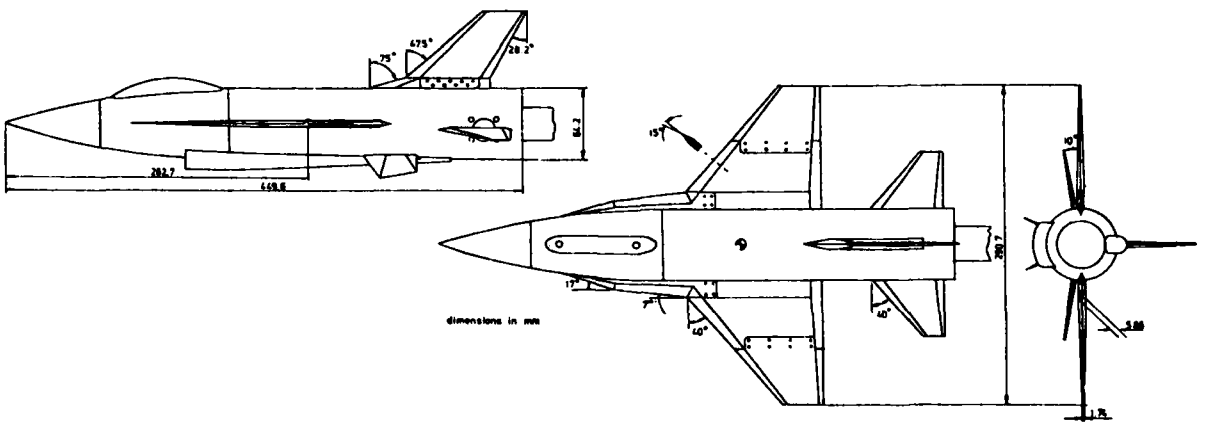

Fig. 10 The Standard Dynamics Model.

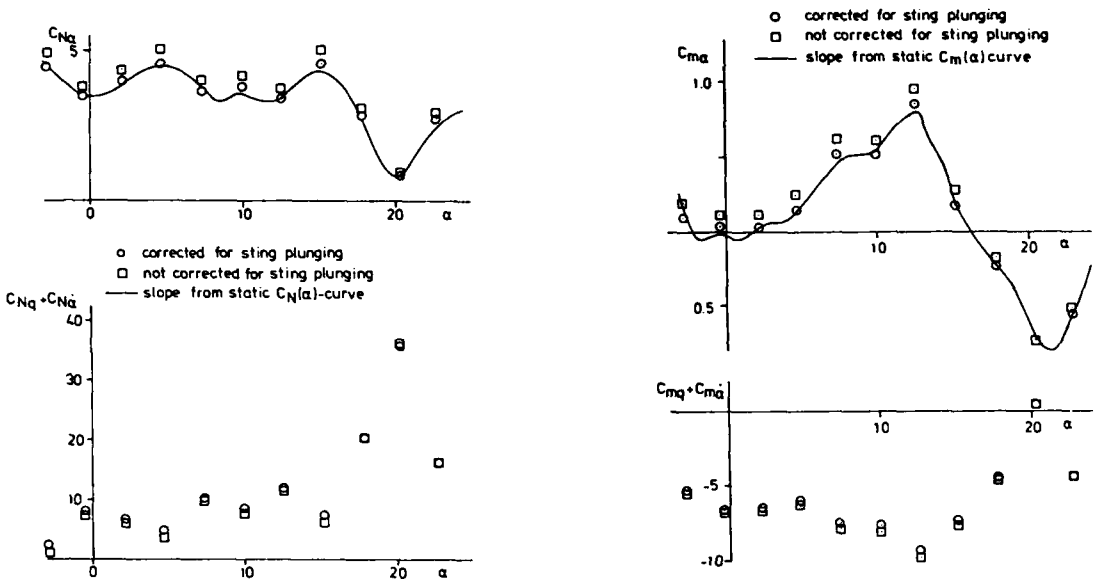

Fig. 11 Effect of correction for sting plunging on C_{m_α}, $C_{m_q}+C_{m_{\dot\alpha}}$, C_{N_α} and $C_{N_q}+C_{N_{\dot\alpha}}$ derivatives, M = 0.60.

3.1.4 Results

The SDM tests in the HT wind tunnel were done in the Mach number range 0.60 - 1.05. The stagnation pressure was below ambient and decreased with increasing Mach number which gave an almost constant Reynolds' number of 1 million based on the mean aerodynamic chord.

The effect of sting plunging has been taken care of in the data reduction programme according to Ref. 6. In Fig. 11 C_{m_α}, $C_{m_q}+C_{m_{\dot\alpha}}$, C_{N_α} and $C_{N_q}+C_{N_{\dot\alpha}}$ have been plotted both with and without correction for sting plunging. The static derivatives are also compared with data from a static test run with a conventional six component balance. The slopes of this static test agree fairly well with the dynamic data corrected for sting plunging. The correction also agrees with Ref. 6 i.e. if the data are not corrected the pitch static stability decreases and the dynamic stability increases compared with a rigid sting.

The effect of oscillation frequency has been investigated at M = 0.80 on both pitch and yaw oscillations, Figs. 12 and 13. In pitch oscillation the model has been oscillated at four different frequencies. One was at resonance and in this case the model moment of inertia was increased with weights. The static pitching moment derivative is obviously unaffected by oscillation frequency when oscillating off resonance but at resonance a slightly more statically stable model is indicated although these data are measured with the five-component balance which is within the oscillating system. These data are also compared with data from a static test which show that the dynamic data from the off resonance tests seem to be the best. The dynamic stability is unaffected by oscillation frequency at small angles of attack but at angles above 12° the stability decreases with increasing oscillation frequency.

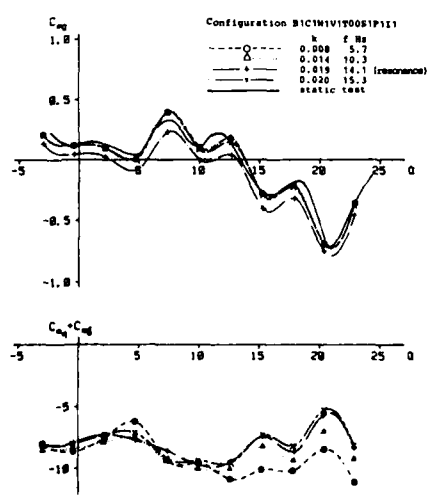

Fig. 12 Effect of pitch oscillation frequency, M = 0.80.

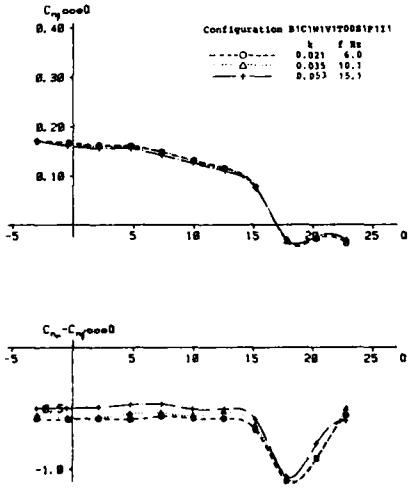

Fig. 13 Effect of yaw oscillation frequency, M = 0.80.

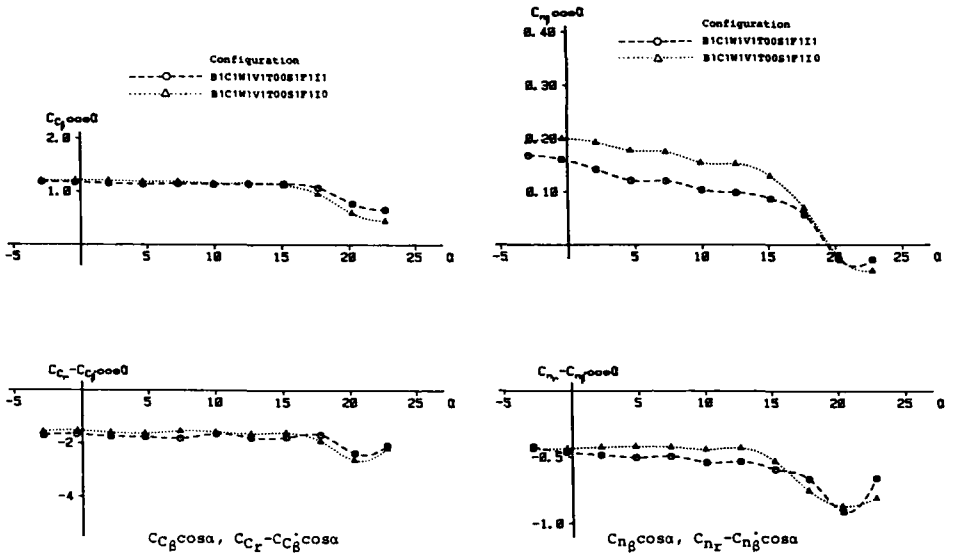

Fig. 14 Effect of air intake, yaw oscillation data, k = 0.035, M = 0.60.

During yaw oscillation no test was done at resonance. The static yaw derivative is unaffected by a change in oscillation frequency but the dynamic derivative shows a slightly decreasing stability with increasing oscillation frequency. This effect is valid over the whole angle of attack range investigated except perhaps at the highest angle.

The effect of the "air intake" has been studied during both pitch and yaw oscillation tests at M = 0.60 . There is no air going through the intake and with its flat front surface with sharp edges a separated flow is created on the lower surface of the fuselage. There is however no significant change in the pitch oscillation data (not shown here) and the same comment is valid for the side force derivatives due to yaw oscillation, Fig. 14. The biggest effect is found in the static yawing moment derivative where the static stability increases when the intake is removed. The dynamic stability in yaw is slightly less with no intake at angles of attack up to 15°.

One way of creating an asymmetrical flow field on the model at moderate angles of attack is to remove one strake, in this case the port strake was removed. At pitch oscillation, M = 0.60, there is a neglible effect at angles of attack below 10 , but at higher angles both the direct derivatives and the cross-coupling derivatives are influenced, Fig. 15. During yaw oscillation at the same Mach number there is almost no effect on the direct derivatives and also very small effect on the rolling moment cross derivative, Fig. 16.

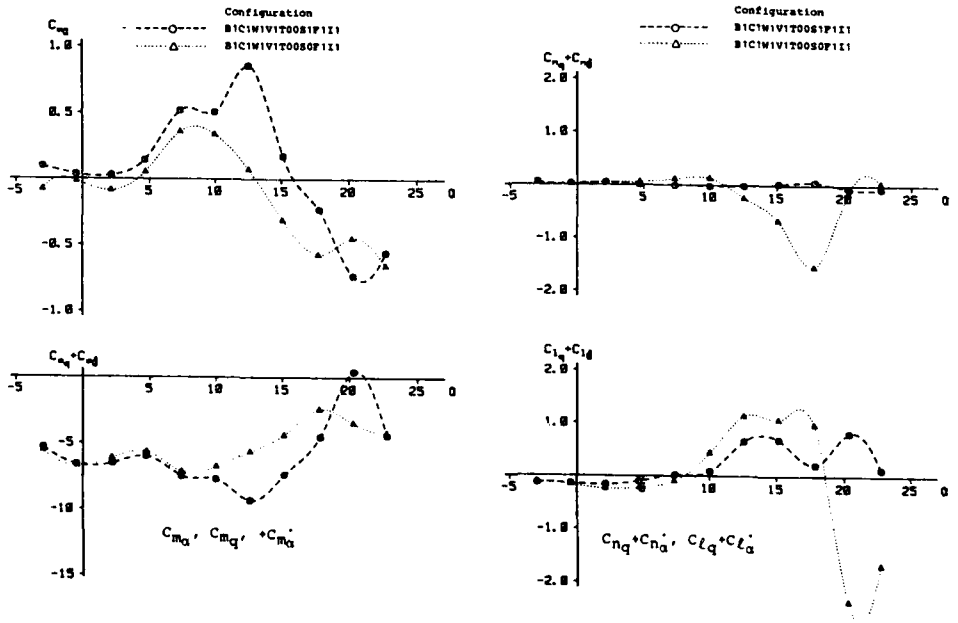

Fig. 15 Effect of asymmetrical aircraft, pitch oscillation data, k = 0.022, M = 0.60

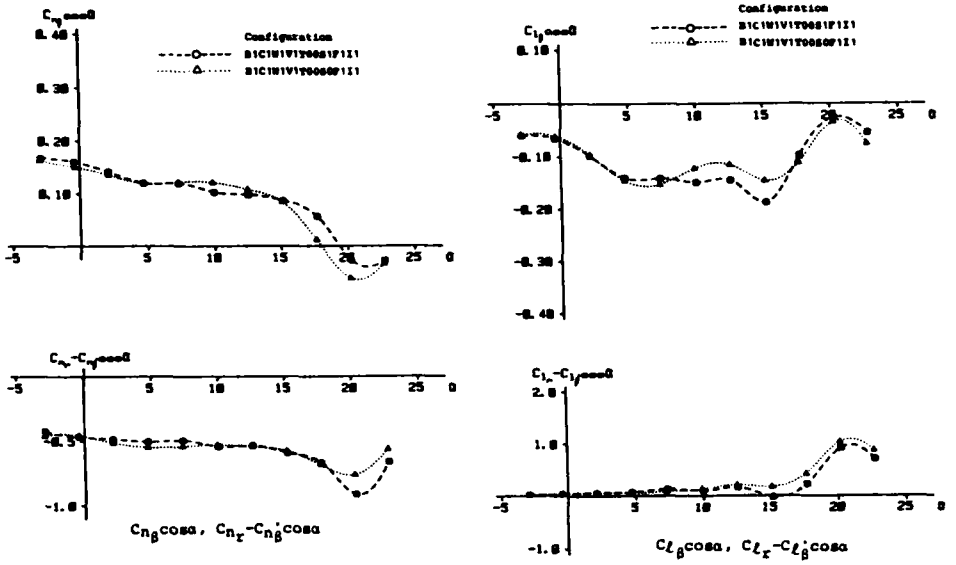

Fig. 16 Effect of asymmetrical aircraft, yaw oscillation data, k = 0.035, M = 0.60.

3.2 Rotary derivative rig

FFA's rotary rig used in tests at transonic speeds is quite old and was used for the first time in 1965. Results obtained with this rig has earlier been reported, Refs. 7 and 8. However during the recent years some modifications have been done including a new digital data acquisition and data reduction process.

3.2.1 Description of the apparatus

The rotary rig can only be operated in the S4 wind tunnel and in Fig. 17 the rig is shown installed in that tunnel. Because of the rather large volume the rig occupies in the tunnel the slotted walls have been shortened to maintain a good velocity distribution within the test section.

The rig is mounted on the tunnel strut with its axis along the tunnel centre line. In the lower part of the rig a hydraulic motor is installed. It is fed from outside the tunnel by an electric driven hydraulic pump. On an extension of the hydraulic motor drive shaft is a tachometer mounted. The highest rotation rate is 700 rpm but 600 rpm is the most common rotation rate used. The motive torque is transmitted from the hydraulic motor to the main drive shaft by a set of gears. The drive shaft is also connected to a set of goldplated slip rings where the signals from the rotating balance are fed to the static part of the rig. Different cranked stings can be attached, each sting gives a fixed angle of attack. The stings are designed in such a way that the centre of balance is situated on the axis of rotation. The model is then mounted with its moment reference point as close to the centre of the balance as possible.

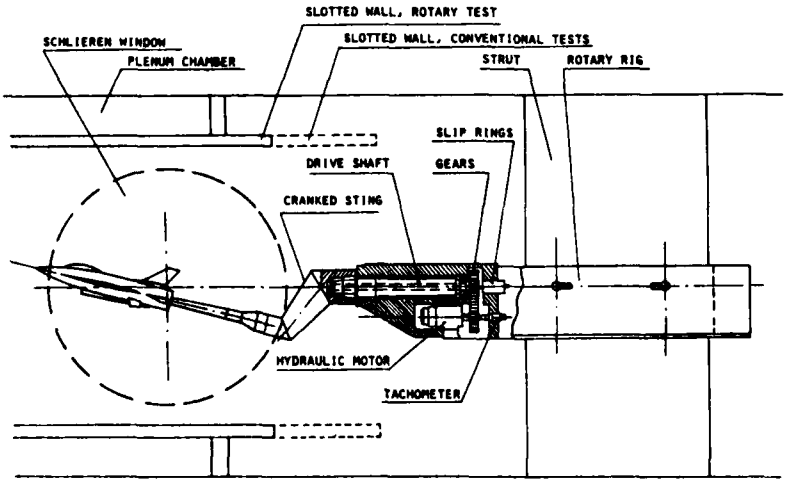

Fig. 17 The FFA rotary rig in the S4 wind tunnel.

3.2.2 Data acquisition and data reduction

All data handling now takes place on the General Automation computer at the wind tunnel. A typical wind tunnel run consists of:

a) with the tunnel at rest and the sting slowly rotating data sampling during one complete revolution

b) the tunnel is started the sting is brought to a high rotational speed and data are sampled during a number of complete revolutions

c) the sting is slowed down to the same speed as in a) and data are once again sampled during one complete revolution

d) the sting is rotated with the same high speed as in b) but in the other direction and data are sampled during the same number of complete revolutions

By subtracting b) from d) the asymmetrical derivatives in the body axes system due to rotation around the wind axis can be found. Subtracting a) from c) and with proper correction for the roll dependant aerodynamic part and the centrifugal part (the centrifugal effects have earlier been investigated by high speed rotation in an ambient pressure close to vacuum) the static coefficients can be calculated. By sampling data during complete revolutions there will be no net effect by the gravitational forces.

3.2.3 Results

Because of the solid side walls in S4 it was important to investigate if disturbances from the model reflecting in the side walls and back on the model would alter the results. Instead of sampling data during the complete revolution data were sampled between the roll angles -30° to 30° and 150° to 210°. These results were compared with results from data sampled between the roll angles 30° to 150° and 210° to 330°. The wing is thus turned against either a slotted wall or a solid wall during data acquisition. The result was however that the differences observed were of the same order as in repetition tests ($\Delta C_{\ell_p} \sim 0.004$).

It was also felt that interference from the bulky rotary rig could affect the results. To find out if there were any effects a schematic canard fighter model was run in three different axial positions, by means of different lengthening pieces between the balance and the sting. The Mach number range was 0.5 - 1.0 but only the effects at zero angle of attack were investigated, Fig. 18. The three different positions were with the model moment reference point at 32 mm behind, 168 mm infront of and 268 mm infront of the centre of the schlieren window. According to figure 18 it is beneficial to move the model as fast as possible from the rotary rig, at least in the transonic speed regime. This result could also be interpreted as a sting interference effect as the length/diameter ratio of the sting increases as the model is moved ahead.

The SDM model has also been run on the rotary rig, though only at $\alpha = -1^{\circ}$ and 4°. The rolling moment derivative is shown as a function of Mach number for these two angles of attack in Fig. 19. The damping moment increases slightly with increasing Mach number and is higher at $\alpha = 4^{\circ}$ than at $\alpha = -1^{\circ}$ except close to $M = 1.0$. Data points from roll oscillation tests at AEDC, Ref. 3, and NAE, Ref. 9, are compared with the FFA data at $M = 0.6$. At roll oscillation tests with oscillations around the body axis the damping derivative has the form $C_{\ell_p} + C_{\ell_{\dot{\beta}}} \sin\alpha$. However close to $\alpha = 0$ this derivative reduces to C_{ℓ_p}. The agreement between AEDC data at $\alpha = 0^{\circ}$, NAE data at $\alpha = -1^{\circ}$ and FFA data at $\alpha = -1^{\circ}$ is also quite good despite the two different testing methods.

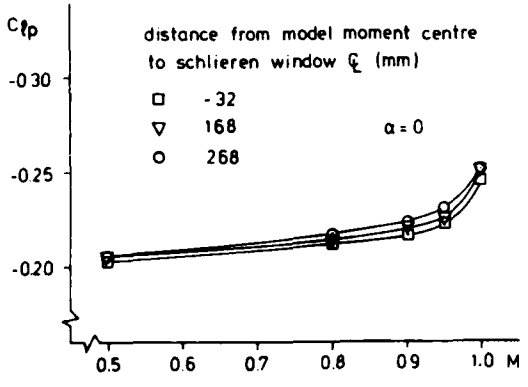

Fig. 18 Effect of different axial model position on C_{ℓ_p}, $\alpha = 0^{\circ}$.

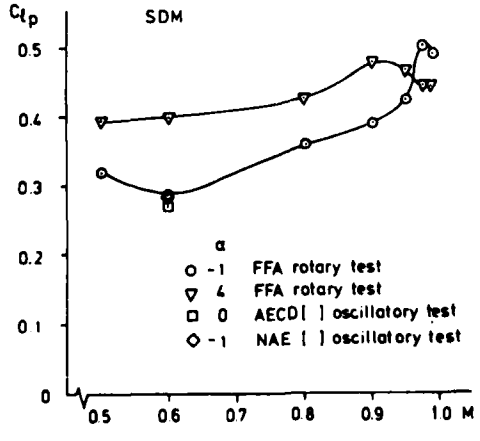

Fig. 19 C_{ℓ_p} (M) for the SDM model, $\alpha = -1^{\circ}$ and 4°.

3.3 Control surface oscillation testing

It is a trend today to design aircraft to be more or less statically unstable in certain flight regimes. That increases the need for good control authority throughout the whole flight envelope. In order to measure not only the static but also the dynamic reactions to control deflections, a control surface oscillation apparatus was designed and built at FFA. The main purpose of the apparatus is not to measure hinge moment derivatives but to measure pitching moment derivatives due to control deflections and especially look for any dynamic derivatives, which can be of detrimental effect.

3.3.1 Description of the apparatus

The FFA wind tunnels are quite small and consequently it was quite clear that a full-span model with oscillating controls could not be made. Instead a semi-span model was designed and an oscillating apparatus was integrated with the model, Fig. 20. The apparatus is designed for the S4 wind tunnel, where one of the large schlieren windows is removed and a traverse mechanism is installed. On the traverse mechanism is a new four-component balance mounted. The balance is welded of thin rectangular steel tubes and has four measuring elements equally spaced around its perimeter. The balance is able to measure normal force, pitching moment, axial force and root moment. There are two sets of pitching moment strain gauges, one of conventional type and one of semiconductor type. The axial force is also measured with semiconductor strain gauges.

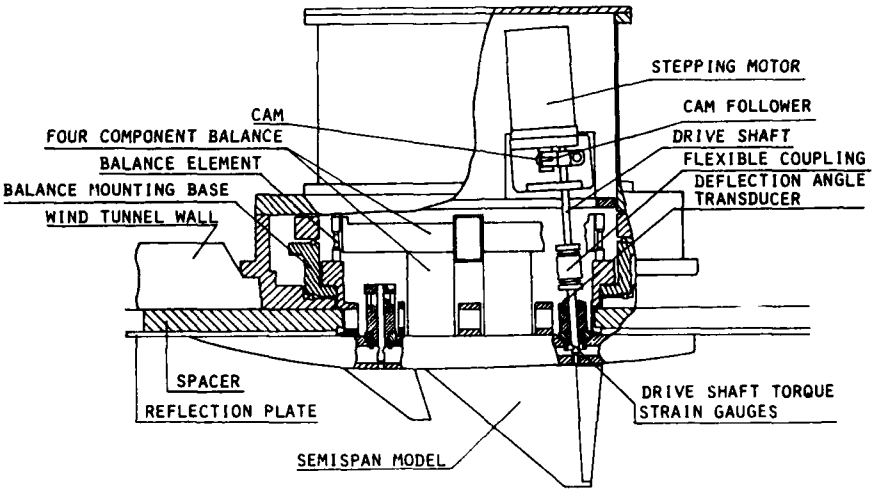

Fig. 20 Control surface oscillation apparatus.

The model is designed to have either an oscillating canard or an oscillating elevator. The oscillatory motion is achieved with a stepping motor with a cam and a cam follower. The highest oscillatory frequency is 54 Hz and since the torque of a stepping motor rapidly falls with increasing frequency, the cam is designed to give two oscillations for one revolution of the stepping motor.

A few cams had to be fabricated before a satisfactory harmonic motion had been obtained. The stepping motor is mounted on the traverse mechanism and its weight i consequently not felt by the balance. To minimize the risk of feeding the aerodynamic loads to anything but the balance elements a coupling is inserted on the drive shaft. This coupling is torsional stiff but flexible in bending. The oscillation amplitude is ± 3 degrees and the control can be preset to any desired angle. Strain gauges on the drive shaft outside the shaft bearings give information of drive shaft torque and a resistance transducer is calibrated to measure control deflection angle. The control surface that is not oscillated is locked into a predetermined position.

Because of the holed that have to be accommodated for the control drive shafts in the reflection plate, the angle of attack range is limited to -5 to +10 degrees. The gap between model and reflection plate is sealed with a lightly springloaded PTFE strip. The whole apparatus is tightly enclosed from the outside so that no air will enter the test section through the apparatus.

3.3.2 Data acquisition and data reduction

The instrumentation and data acquisition process is the same as for the forced oscillation pitch-yaw apparatus. The control oscillation frequency is however higher than the forced pitch-yaw frequency which necessitates a higher cut-off frequency in the filter unit and a faster sample rate.

Data reduction is done with a linear 4×4 matrix, which contrary to the balance matrix in Ref. 10, is obtained through a static calibration. The measured pitching moment and, in cases where the control drive shaft is not at right angles to the reflection plate, the root moment is corrected with the drive shaft torque because the stepping motor is not within the balance system. No attempt has been done to dynamically calibrate the balance, but with its very stiff and light weight design and high resonance frequency (~ 700 Hz) the statically obtained matrix must also be good dynamically.

3.3.3 Results

So far only tests with oscillating canard have been performed. In Fig. 21 the effect of Mach number and angle of attack on $C_{m_{\dot{\delta}_C}}(\partial C_m/\partial(\dot{\delta}\bar{c}/2V))$ is shown. The reduced frequency based on the wing reference chord is 0.256 at M = 0.5 and 0.131 at M = 0.975. At low Mach numbers an oscillating canard gives a sligtly undamping contribution to the pitching moment but at $M \geq 0.95$ the oscillating canard is stabilizing. The effect of angle of attack is however a little more inconsistent. A change from $\alpha = 0^o$ to $\alpha = 5^o$ is stabilizing but a further increase to 10^o is destabilizing. It is even less stable at $\alpha = 10^o$ than at $\alpha = 0^o$.

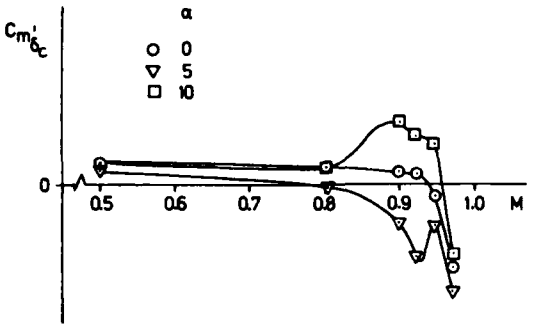

Fig. 21 Pitching moment damping derivative due to oscillating canard.

4 CONCLUSIONS

Wind tunnel testing with the main objective to extract dynamic derivatives has been of large interest in recent years at FFA. This is shown by the number of different rigs developed and in use, both in the subsonic and transonic wind tunnels. Brief descriptions of the different rigs, testing procedures and data handling have been given in this paper. The intention has also been to publish at least some results from each rig. This paper thus gives a wide survey of the different rigs used for dynamic derivative testing and the corresponding testing capabilities at FFA.

ACKNOWLEDGEMENT

The rigs and the tests have been sponsored by the Swedish Defence Materiel Administration, Air Materiel Department and SAAB-SCANIA AB. SAAB-SCANIA AB have also, to a large extent, contributed with ideas during the tests.

5 REFERENCES

[1] Hanff, E.S.
A Dynamic Calibrating Apparatus for Cross Derivative Experiments
ICIASF, Shrivenham, England, 1977

[2] Forster, L.R., Hanff, E.S.
A Second Generation Instrumentation System for Measuring Cross Coupling Derivatives.
ICIASF, Monterey, California, 1979

[3] Coulter, S.M., Marquart, E.J.
Dynamic stability Tests of the Standard Dynamics Model Utilizing the New 1500 lb Balance Machanisms.
AEDC-TSR-81-P11, 1981

[4] Beyers, M.E., Kapoor, K.B., Moulton, B.E.
Pitch- and Yaw-Oscillation Experiments on the Standard Dynamics Model at Mach 0.60.
NRD NAE LTR-UA-76, 1984

[5] Schmidt, E., Stange, H.
Derivativawaage für den Transkanal Göttingen (TRAD), Teil 5: Windkanal-messungen am "Standards Dynamics Model" bei Nickschwingung.
DFVLR-AVA Bericht Nr IB 232-83 J 05, 1983

[6] Burt, G.E., Uselton, J.C.
Effect of Sting Oscillations on the Measurement of Dynamic Stability Derivatives.
Journal of Aircraft,Vol. 13, No. 3, March 1976, pp. 210-216

[7] Hedman, S.G.
Measurements of Derivatives due to Roll on AGARD B and C Models at Transonic Speed.
FFA Memorandum 46, 1966

[8] Ehn, G., Landén, T.
Measurements of Dynamic Stability Derivatives of an Ogive Delta Wing Model at Transonic and Supersonic Speeds.
FFA Technical Note AU-925, 1974

[9] Beyers, M.E., Moulton, B.E.
Stability Derivatives due to Oscillations in Roll for the Standard Dynamics Model at Mach 0.60.
NRC NAE LTR-UA-64, 1983

[10] Lambourne, N.C., Wight, K.C., Welch, B.L.
measurements of Control-Surface Oscillatory Derivatives on a Sweptback, Tapared Model Wing in Two Transonic Tunnels.
ARC R & M, No. 3806, 1977

[11] Torngren, L.
Dynamic Pitch and Yaw Derivatives of the Standard Dynamics Model.
FFA TN 1985-5. 1985

STANDARD DYNAMICS MODEL EXPERIMENTS WITH THE DFVLR/AVA TRANSONIC DERIVATIVE BALANCE

by

Dr.-Ing. E. Schmidt, Institut fuer Aeroelastik, DFVLR-AVA Goettingen,
Bunsenstr. 10, D-3400 Goettingen, West Germany

SUMMARY

A slender high-load forced-oscillation measuring system for dynamic derivatives of aircraft and missile models in a transonic wind tunnel is presented together with typical test results of the significant aerodynamic coefficients and stability derivatives of the Standard Dynamics Model, a simplified fighter aircraft model with a wing span of 0.345 m. The measurements in the rotational modes pitch, yaw and roll encompass Mach numbers from 0.6 to 1.2, angles of attack from 0 to 30 degrees and excitation frequencies from 2 to 20 Hz at a constant Reynolds number of 7.8 Mio/m. Most of the stiffness and damping derivatives gathered show substantial nonlinear dependence on Mach number and angle of attack, whereas the influence of reduced frequency is less prominent. The results are closely related to published measurements on Standard Dynamic models performed in other NATO countries.

NOTATION

referred to German DIN definitions [1]

x,y,z		body-fixed Cartesian reference axes with origin at 35% MAC
ALFA, α	[°]	angle of attack
CL=L/(q*S*s)		rolling moment coefficient
CLBC=LR/(q*S*s*DPSI)		roll cross stiffness in yaw times cos(α)
CLBS=LR/(q*S*s*DPHI)		roll stiffness times sin(α)
CLP=LI/(q*S*s*DPHI*OMS)		damping in roll
CLR=LI/(q*S*s*DPSI*OMS)		roll cross damping in yaw
CM=M/(q*S*MAC)		pitching moment coefficient
CMQ=MI/(q*S*MAC*DTETA*OMS)		damping in pitch
CMT=MR/(q*S*MAC*DTETA)		pitch stiffness
CN=N/(q*S*s)		yawing moment coefficient
CNBC=NR/(q*S*s*DPSI)		yaw stiffness times cos(α)
CNBS=NR/(q*S*s*DPHI)		yaw cross stiffness in roll times sin(α)
CNP=NI/(q*S*s*DPHI*OMS)		yaw cross damping in roll
CNR=NI/(q*S*s*DPSI*OMS)		damping in yaw
COSA		trigonometric function cos(α)
CY=Y/(q*S)		side force coefficient
CYBC=YR/(q*S*DPSI)		side force stiffness times cos(α)
CYBS=YR/(q*S*DPHI)		side force cross stiffness times sin(α)
CYP=YI/(q*S*DPHI*OMS)		side force cross damping
CYR=YI/(q*S*DPSI*OMS)		side force damping
CZ=Z/(q*S)		normal force coefficient
CZQ=ZI/(q*S*DTETA*OMS)		normal force damping
CZT=ZR/(q*S*DTETA)		normal force stiffness
dL=LR+j*LI	[Nm]	dynamic rolling moment
dM=MR+j*MI	[Nm]	dynamic pitching moment
dN=NR+j*NI	[Nm]	dynamic yawing moment
dY=YR+j*YI	[N]	dynamic side force
dZ=ZR+j*ZI	[N]	dynamic normal force
DPHI	[rad]	amplitude in roll (1.0° or 1.5°)
DPSI	[rad]	amplitude in yaw (0.96°)
DTETA	[rad]	amplitude in pitch (0.96°)
f	[Hz]	oscillation frequency
j		imaginary unit
L	[Nm]	static rolling moment
M	[Nm]	static pitching moment
MA		free stream Mach number
MAC	[m]	mean aerodynamic chord (0.1301 m)
N	[Nm]	static yawing moment
OMS=2*PI*f*s/V		reduced frequency (s replaced by MAC in pitch)
PI		transcendental number 3.1416
q	[N/m²]	dynamic pressure
RE=V*s/ν	[Mio]	Reynolds number (s replaced by MAC in pitch)
s	[m]	wing semispan (0.1724 m)
S	[m²]	wing area (0.03962 m²)
SINA		trigonometric function sin(α)
V	[m/s]	free stream velocity
Y	[N]	static side force
Z	[N]	static normal force
ν	[M²/s]	kinematic viscosity

1. INTRODUCTION

The flight envelopes of present-day fighter aircraft and tactical missiles encompass maneuvers at high angles of attack in the transonic speed range. These flight conditions are characterized by flow phenomena such as shock-induced boundary layer separation, reversed flow regimes, vortex shedding and burst etc., and their mutual interference on fuselage, wing and control surfaces. The resultant aerodynamic reactions to the vehicle are expressed by highly nonlinear static and dynamic loads [2]. Furthermore, hysteresis effects are included, which cause ambiguous values of certain parameters observed at a fixed flight condition, depending on the time history of the pertinent state variables of the vehicle [3, 4]. This dynamic behavior was one of the main reasons for establishing new nonlinear concepts for mathematical modelling of the aircraft flight mechanics [5,6], leaving the classical linear approach to normal flight conditions.

In parallel, the lack of information on dynamic stability characteristics in the transonic high angle of attack regime was recognized [7], which led to the development of some excellent experimental methods to gather the dynamic stability derivatives from model tests in wind tunnels. These new techniques are well documented in the proceedings of the AGARD-FDP lecture series on "Dynamic Stability Parameters" at Ames/Brussels in 1981 [8 to 12] and the AGARD-FMP symposium at CESME in 1982 [13]. They include small-amplitude forced-oscillation rigs with secondary degrees of freedom to measure cross-coupling derivatives of lateral and longitudinal motions, rotary rigs to study yaw and roll departure and spin in the extreme angle of attack range up to 90 degrees, and special arrangements to directly measure the alpha-dot and beta-dot derivatives. Even hysteresis effects can be recorded with the large-amplitude roll balance of NAE Canada, using higher harmonics data reduction in the frequency domain [14].

In West Germany the construction of stability derivative measuring equipment has been restricted to reliable standard techniques suited to the existing wind tunnels. A forced-oscillation pitch/yaw/roll balance and a rotary balance are available in the 3m low-speed wind tunnel of DFVLR Brunswick for the low to medium angle of attack range [15,16]. With the forced-oscillation balance, a dynamic data base has been gathered from a basic fighter aircraft model with three different wing planforms, removable strakes and horizontal and vertical stabilizer variations [17]. The high speed range is covered with a small-amplitude forced-oscillation rig for missile model tests at extreme angles of attack in the trisonic blow-down tunnel at DFVLR Cologne. Similar design principles were used on a more versatile pitch/yaw apparatus for the 1m transonic wind tunnel at DFVLR Goettingen (its abbreviation TRAD stands for "Transonic AVA Derivative Rig"). Initial tests with this rig have been performed successfully on two slender tactical missile configurations up to 30 degrees angle of attack [18].

In the following presentation the main features of the TRAD mechanism, including a new roll component, will be described in conjunction with remarks on the data reduction to aerodynamic coefficients and static and dynamic derivatives. Furthermore, some typical results from extensive measurements on the Standard Dynamics Model [19] in pitch, yaw and roll oscillation will be discussed in comparison with equivalent wind tunnel results obtained at AEDC Tullahoma [20], NAE Ottawa [21] and FFA Bromma [22].

2. TEST DESCRIPTION

2.1 Wind tunnel

The closed-loop transonic wind tunnel of DFVLR/AVA Goettingen [23] is furnished with a 1 x 1 meter working section. Its four walls have inclined 6% perforations enabling suction at transonic speeds. Mach numbers from 0.5 to 2.2 can be sustained at a constant static temperature of 310 K and variable total pressure from 0.2 to 1.6 bar. Maximum power consumption is 16 MW, including 4 MW of the suction compressor.

2.2 TRAD mechanical arrangement

According to Orlik-Rueckemann's classification [8], the TRAD apparatus is a sting support mechanism for inexorable small-amplitude angular oscillation of wind tunnel models of slender aircraft and missile configurations. Special design features are high stiffness in regard to aerodynamic loads at large angles of attack, small diameter comparable to internal static strain-gauge balances and ease of installation in the wind tunnel.

The mechanical setup for oscillation in pitch is sketched in Figure 1a. An angle adapter of 15° is clamped to the α-traverse of the wind tunnel, thus enabling remote setting of the angle of attack from -2° to 32°. Attached to the angle adapter is the slender conical model sting with a bifurcated front end. This carries a pair of cross flexures, forming the pitch axis about which the attached movable head with the enclosing model can be rotated.

Oscillation is generated by the rearward mounted five-phase stepping motor (Quinstep motor) fastened to the continuously rotating shaft within the model sting. The eccentric roller bearing at the tip of the shaft has gliding contact to the rearward end of the movable head. The amplitude of oscillation is forced from the fixed eccentricity of the roller bearing, whereas the frequency can be controlled according to a pulse stream fed to the motor control.

Figure 2 is a photograph of the DFVLR Standard Dynamics Model on the TRAD pitch mechanism installed in the AVA wind tunnel.

The total forces and moments acting on the model are measured with the five-component balance situated between movable sting head and model. A tangential force element was omitted in order to gain bending stiffness.

For oscillation in yaw the model sting with the drive mechanism must be turned in the angle adaptor by 90° around its longitudinal axis, whereas the five-component balance with the model is kept in the previous position. Thus the oscillation amplitude and the balance sensitivities are retained.

For oscillation in roll a second model sting with a simpler oscillation mechanism has been constructed as shown in Figure 1b. In this case the Quinstep motor shaft itself rotates in a sinusoidal manner to avoid the wear and tear of kinematic transformation from shaft rotation into oscillatory model motion. A steel hoop with a transmission gear of ratio 1:3.6 connects the motor with the driving shaft within the model sting. Thus, a model roll amplitude of 1.0° is resolved into 200 motor steps. The movable head of the driving shaft is supported by removable roll flexures to withstand the prevailing high normal forces. Further details of the TRAD construction may be found in the internal reports [24,25,33].

2.3 Measuring system

A block diagram of the measuring system, shown in Figure 3, illustrates the data acquisition process.

As previously mentioned, the global model loads are measured with a five-component strain-gauge balance located between movable head and model. The components comprise the pitching moment and indirectly the normal force taken as bending stresses on two bending elements in pitch direction, as well as the yawing moment and the side force from the two bending elements in yaw direction and the rolling moment taken as torsional stress on the rear pitch bending element. In addition, both the pitch/yaw and the roll mechanism have an extra strain-gauge bridge on one of the support springs of its movable head, in order to provide a synchronous analog motion signal of the model.

The six unfiltered strain-gauge signals are preamplified in parallel and monitored on a multi-channel storage oscilloscope. The signals are fed directly into integrating digital voltmeters (IDVM, accuracy 0.02%) to obtain time-averaged values (static loads). The dynamic signal parts are analyzed by vector component resolvers (VCR, accuracy 0.5%) serving as active band-pass filters. They are tuned with an appropriate low-frequency generator, which supplies two sinusoidal voltages of 0° and 90° phase shift to the model oscillation. Thus, real (i.e. in-phase) components and imaginary components (which lead the model movement by 90 degrees) are generated and their values are measured by subsequent IDVMs.

The pulse rate for controlling the Quinstep motor is generated by a crystal oscillator, which represents the time basis of the measuring system. The excitation frequency is read from an optical pulse generator on the motor shaft, used to synchronize the low-frequency generator to produce a pure real deflection amplitude, and then registered by a six-digit period counter. The motor control for the roll component contains a microprocessor, which selects the proper pulses and the motion direction signal from the pulse rate generated by the crystal oscillator.

The displayed values of all IDVMs, the counter as well as the wind tunnel data (pressure, temperature, angle of attack, model identifier, run number, etc.) are stored in the display memory until the subsequent measuring cycle has ended. Concurrently, the entire data is stored on a magnetic cassette by serial data transmission (party line) for security purposes, before a transfer to the central computer is initiated. Experience has shown that a measuring cycle duration or IDVM integration time of 20 seconds is sufficient for wind-on tests, while 6 seconds are adequate under wind-off conditions.

2.4 Data reduction

The online data reduction is performed by an IBM central computer. It stores data on disc and magnetic tape, provides preliminary data evaluation of each test point and prints the initial results on a line-printer in the wind tunnel control room (see [25] for details).

The independent offline evaluation of the disc data is executed after conclusion of a test run. The evaluation process is simplified due to the fact that the dynamic signals have been previously reduced into their real and imaginary amplitude components by the vector component resolvers; in pure angular oscillation the real component is directly proportional to the stiffness or static derivative and the imaginary component to the damping derivative. The data of a test run is processed as follows:

1. Validity control of the values,
2. Sorting of data sets into four groups:
   a) Dynamic wind-on measurements,
   b) Dynamic wind-off measurements (mechanical loads),
   c) Static wind-on measurements (blocked excitation),
   d) Zero-points (wind-off, blocked excitation),
3. Determination of free-stream values,
4. Calculation of absolute loads (using the static calibration matrix of the five-component balance),
5. Subtraction of mechanical loads,
6. Calculation of model motions,

7. Calculation of nondimensional aerodynamic coefficients and derivatives,
8. Conversion from balance-fixed to model-fixed coordinate system,
9. Output of tabulated results,
10. Plots.

The method used to evaluate the actual model motion includes sting deflection corrections as discussed in [25]. This approach is simpler than the methods published in the past [26 to 28], because the acquired bending signals of the five-component balance are interpreted as a measure of the secondary motion, based on previous static load tests.

Wind tunnel interference was corrected neither in the static coefficients nor in the dynamic derivatives (see Refs.[29,30]).

2.5 Model

Significant dimensions of the DFVLR Standard Dynamics (DSD) model are presented in Figure 4. The positions of the pitch (or yaw) axis and the axis of reference for moments in pitch and yaw (35% MAC) are indicated. Geometrical details of wing, strakes, tail, fins and fuselage with cockpit dome and engine inlet are recorded in the internal report on pitch oscillation tests [31].

The DSD model has a fuselage diameter of 3.000 inches, whereas the corresponding AEDC model is 4.375 inches wide [19]. The geometry is identical except for a minor difference in the strake surface; its maximum width at the wing leading edge is reduced from 19.0 to 18.3 mm, whilst position, sweep angle and chamfer of leading edges are retained.

The mixed construction of the model was fabricated in the DFVLR workshops. The body suspension tube as well as the wing halves, strakes, tail surfaces and fins are constructed of aluminum alloy, while the horizontally divided body shell with cockpit dome, engine inlet and detachable ogival tip is of laminated carbon fiber. All the metal parts can be replaced. The horizonal tail may be trimmed in steps of 8°; during the tests it was kept in neutral zero position.

The model mass is 1.53 kg excluding the balance. Dynamic wind-off measurements on the balance yielded the following torsional moments of inertia:

in pitch	0.020 m^2kg,
in yaw	0.028 m^2kg,
in roll	0.009 m^2kg,

referred to the oscillation axis.

A turbulence strip was attached to the ogival nose in order to maintain a turbulent boundary layer on the fuselage at all flow conditions. The Tu-strip is made of corundum powder with a maximum grain of 0.15 mm and located 50 to 60 mm from the tip.

2.6 Test program

The test program performed on the DSD model in pitch, yaw and roll oscillation is presented in Table 1. The three-digit numbers indicate test runs at up to ten angles of attack α. For each α, two to four data sets were taken in order to obtain information on data scatter.

The tunnel pressure was adjusted between 0.5 and 1.1 bar corresponding to the given Mach and Reynolds numbers. The majority of the measurements was taken at Re = 1.03 Mio (referred to MAC). The projected value of 1.42 Mio could not be attained due to unexpectedly high normal forces (C_{Zmax} = 2.1 at Ma = 1.2 with α = 31°); during run 332 at α = 30° the cross flexures of the pitch unit broke. Subsonic tests at Re = 1.54 Mio and comparative runs without Tu-strip supplement the program with respect to Reynolds number effects.

A standard test run with ten α-values lasted approximately 40 minutes. So-called long runs including static wind-on measurements took nearly one hour (e.g. runs 343 to 347).

3. PRESENTATION OF RESULTS

The complete results of the DSD model tests are collected in the DFVLR reports [31 to 33] in the form of tables and plots. The following figures show an extract of typical examples from the abundance of plots. The angle of attack α corrected for static system deflections serves as abscissa, whereas the measured aerodynamic coefficients and stability derivatives are plotted in vertical direction. Spline functions connect the mean values of up to four test points at identical test conditions (OMS, MA, RE, α = const.) to emphasize the trends and to keep the scattering of the values visible.

The DSD model has been chosen for verification tests on the new TRAD mechanisms because test results from other research centers were available for comparisons. However, each establishment used a model of different scale according to the wind tunnel size. Taking the largest model from AEDC Tullahoma as reference, one finds the following geometric data:

Establishment	Wt cross section	Model scale
AEDC [20]	1.22m x 1.22m	1.000
DFVLR	1.00m x 1.00m	0.686
FFA [22]	0.90m x 0.90m	0.56
NAE [21]	0.75m x 0.40m	0.455 .

Only the global aerodynamic loads acting on the model were measured at DFVLR Goettingen. Visualization techniques of the flow field around the model have not been applied to identify the interactions of vortex formations from fuselage, strakes and wing or their influence on the tail controls.

3.1 Aerodynamic coefficients

The aerodynamic coefficients displayed have been extracted from the time averages of dynamic measurements in lateral motions to keep the reference length of Reynolds number and reduced frequency unchanged (the mean aerodynamic chord MAC is the reference length in pitch oscillation, whereas the semispan s is used for yaw and roll oscillation).

Figure 5 shows typical curves of the longitudinal coefficients CZ and CM compared to corresponding FFA results. The scattering of the DFVLR values is hardly greater than is typically found in static wind tunnel tests even for large angle of attack α. The Ma-dependent kink in the CZ-curve for α between 14° and 21° is conspicuous. Beyond this region the pitching moment becomes stable even at subsonic speed. The CZ-values are somewhat lower than the FFA results, probably because the AVA wind tunnel with 6% perforation is "relatively open" as opposed to the Swedish slotted-wall wind tunnel (see [29]). The shift of the CM-curve may be caused by wind tunnel interference as well.

Typical plots of the lateral aerodynamic coefficients CY, CN and CL are presented in Figure 6. Since these plots are functions of α and not of the yaw angle, the very small values reflect only asymmetries of the model finish, which are evidently greatest at the vertical tail of the DSD model (CY-deviation) and on the FFA wing (CL deviation). The larger AEDC model features somewhat smaller asymmetries. It might be noticed that the scattering of DFVLR values is only visible in the CY-curve, reinforcing the confidence in the aerodynamic coefficients obtained as a by-product of the dynamic measurements, with the advantage that they are produced concurrently with the stability derivatives.

The influence of the turbulence strip attached to the fuselage tip is striking only in CM, as illustrated in Figure 7. The CM-curve with Tu-strip remains practically unchanged at Re = 2.0 Mio (not pictured). The influence of the Tu-strip and Re on the stability derivatives will be discussed in Section 3.4.

3.2 Derivatives due to pitch

The stiffness and damping derivatives of normal force and pitching moment due to pitch at reduced frequency OMS = 0.027 (referred to MAC) are shown in Figures 8 and 9 for the three Mach numbers 0.60, 0.88 and 1.05. The marked undulation of all four derivatives, which is more pronounced at higher angles of attack, is strongly dependent on the Mach number. The α values should have been placed more closely in order to register every peak. The scattering margin is very small in the entire range covered.

The available FFA results, taken up to α = 22° at the same Re-number of 1.0 Mio (referred to MAC) are also plotted. The discrepancies are larger than the scattering of DFVLR results. But the stiffness derivative curves are well matched. The damping derivatives show differences at Ma = 0.88 beyond 15°; the damping kink at 7.5° has not been detected by the DFVLR points.

The frequency effects on the pitch derivatives, shown in Figures 10 and 11 at Ma = 0.95 for three OMS values from 0.015 to 0.040 is insignificant. The damping derivative curves are nearly identical and their discrepancies remain within the scattering margin. Deviations of the stiffness derivatives become noticeable above Ma = 0.8.

Reynolds number effects (not shown here) were also investigated on the DSD model with attached turbulence strip for Re = 1.0 and 1.5 Mio at Ma = 0.80 and 1.20. The deviations in damping remain negligible within the α-range up to 25°. The stiffness deviations are very small up to α = 30°.

3.3 Derivatives due to yaw

The measured derivatives of side force, and yaw and rolling moment due to yaw oscillation are plotted in Figures 12 to 14 at reduced frequency OMS = 0.035 (referred to semispan; absolute frequencies are the same as in pitch oscillation) with the Mach numbers 0.60, 0.88 and 1.05. The nonlinear effects of the angle of attack are evident for all six derivatives. Beyond α = 15° these effects lead to strongly Ma-dependent undulations.

Directional stability of the model (CNB positive) is not maintained in the entire α-range; at low speed the limit is at 18°, it shifts to 26° in the transonic region and declines again to 20° at Ma = 1.05. Sufficient lateral stability (CLB negative) is maintained at higher Mach numbers also at large incidence, whereas the low-speed curve shows two unstable kinks near 19° and 27°. A small amount of yaw damping (CNR negative) is sustained at all Mach numbers up to α = 28°. The only exception is for Ma = 0.95 in the vicinity of α = 22.5° (see Figure 16 below). The cross damping CLR is very small up to 15°. It remains positive in the Ma-α-range tested, except for Ma = 1.20 at α = 22° to 27°.

The scattering margin of the stiffness derivatives is nearly as small as that in pitch oscillation. But beyond 15° incidence the damping scatter is unusually large, i.e. up to 18% of the measured yaw damping CNR. That the scattering margin increases with incidence, although the TRAD measuring technique was unchanged in the α-range tested, might indicate unsteady aerodynamic effects, which are not fully covered with the chosen integration time

of 20 sec.

Again, corresponding FFA results at the same Re = 1.3 Mio (referred to semispan) were entered in the plots. As in the case of pitch derivatives the agreement is quite good up to α = 10°, and for subsonic speed even up to 17°. Beyond 10° at transonic speed the discrepancies of the side force and rolling moment are larger, whereas the yawing moment is a better match; this is possibly due to the greater roll asymmetry of the Swedish model (see Fig.6). The DFVLR curves of the yaw damping derivatives are further supported by AEDC results at Ma = 0.95, the good agreement of which up to α = 21° is evident in the subsequent figures.

Frequency effects on the yaw derivatives are shown in Figures 15 to 17 for OMS = 0.021 to 0.052 at Ma = 0.95. The deviations of the damping curves practically vanish in the scatter spread, as in the pitching case. The trend of the stiffness curves is likewise unaffected, but with a slight shift towards higher values as OMS increases.

Reynolds number effects were tested with Tu-strip attached only at Re = 1.3 and 1.9 Mio for OMS = 0.035 and Ma = 0.80 (not pictured). The influence is negligible in the stiffness derivatives, but becomes significant in the damping derivatives beyond 22° angle of attack, which leads to instability at 28° for the larger Reynolds number.

3.4 Derivatives due to roll

The derivatives of the aerodynamic lateral loads due to roll oscillation could only be measured up to Ma = 0.88 (see Table 1), because a defect occurred in the deflection strain gauge bridge fixed to the roll flexure bearing; this defect was unrepairable within the available wind tunnel time schedule. Therefore the roll amplitude as additional test parameter was not altered at every test condition; the amplitude was set at 1.5° unless stated otherwise. The minor amplitude effects on the roll derivatives are illustrated in Figures 18 to 20 for OMS = 0.021 and Ma = 0.88; the deviations found for the two amplitudes are covered by the spread of the measured derivatives, which is smaller at larger amplitude.

The standard plots of the derivatives due to roll are shown in Figures 21 to 23 for the same reduced frequency and Reynolds number as in the yaw case using only two Mach numbers 0.60 and 0.88 for clarity. All the stiffness derivatives (β-derivatives times $\sin\alpha$) have strong nonlinear trends in angle of attack and Mach number, and exhibit small scattering even at high α. The stiffness curves are in accordance with the trends evaluated from the yaw oscillation tests. CYBS and CLBS are negative in the covered range, with the exception of the positive low-speed kink of CLBS. CNBS changes to negative values at larger α. The cross damping derivatives CYP and CNP are very small below α = 15°, but they are still measurable. Also, the roll damping CLP values show sufficiently small scattering; nonlinear trends with α and Mach number are obvious.

In the roll case NAE results for Ma = 0.60 were only available for comparison at the lower Reynolds number of 1.2 Mio. Unfortunately, the agreement with DFVLR results of the cross stiffness derivatives CYBS and CNBS is quite poor, whereas the much more decisive rolling moment derivatives show close correspondence of the undulations with angle of attack.

Since DFVLR results for Ma = 0.95 were not available, the frequency effects on the roll derivatives at Ma = 0.88 are demonstrated in Figures 24 to 26 for OMS 0.021 to 0.052. Again, the damping values fall almost completely within the scattering margin, and the stiffness deviations of the moments CNBS and CLBS remain small, whereas those of the side force CYBS are conspicuous.

In the roll case at OMS = 0.035 and Ma = 0.80 Reynolds number effects were measured without turbulence strip as well. Figures 27 to 29 illustrate that the damping derivatives up to α = 27° are practically independent of whether the Tu-strip was used or whether the Re number was raised 50%. Correspondingly, the more sensitive stiffness derivatives remain unchanged up to 10°; deviations are small beyond that limit and increase only between 18° and 24°. All Re-effects are an order of magnitude smaller than the differences between NAE and DFVLR measurements (Figs.21 and 22).

3.5 Repeatability

The scattering of redundant test points taken under the same test conditions during a test run has already been discussed with the derivative plots. Additionally, some entire test runs were repeated another day to obtain further information on the repeatability of the measured values. Plots of these checks were used to extract the scattering margin of each derivative from the three motions tested. The margins are presented in Table 2 as absolute values and as a percentage of the entire range of the corresponding derivative.

The spread of scattering is a good means of judging test results from different measuring techniques. For example, the new NAE roll balance [21] exhibits approximately the same scattering margin in roll damping as the TRAD mechanism, although the former was tested only at subsonic speed. Because the relative scattering is referred to the measured magnitude, it must be smaller for the stiffness derivatives than for the damping derivatives and largest for the extremely small cross damping values due to roll. It is obvious that, in changing the reference from the dynamic loads to the design loads of the derivative balance, including the high static loads, one would obtain relative errors in the usual order of less than 1 percent. The widely used standard deviations have the disadvantage of being directly related to the number of values taken.

4. CONCLUSION

The new derivative balance TRAD for the transonic wind tunnel of DFVLR/AVA Goettingen has been constructed to measure aerodynamic coefficients and stability derivatives on slender aircraft and missile models in applying a small-amplitude forced-oscillation technique. The verification tests of the pitch/yaw and the roll mechanism have been made using the Standard Dynamics Model, a simplified model of the F16 fighter aircraft, because comparable results of this configuration are available from other research establishments.

Some typical examples of the comprehensive data measured at DFVLR have been presented in comparison with FFA results from the newly developed pitch/yaw mechanism described in the foregoing paper [34] and also in comparison with suitable results published by AEDC and NAE. In general, the nonlinear trends in the derivatives as a function of angle of attack (including static and dynamic cross derivatives) are repeated with sufficiently small discrepancies. But it should be mentioned that, the Standard Dynamics Model is not the most suitable model for verification tests of new derivative balances, because it is very sensitive to small changes in angle of attack and Mach number with strong nonlinear behavior even at small α. Furthermore the model construction is complicated.

5. REFERENCES

[1] DIN-Luftfahrtnorm Flugmechanik, LN 9300, Bl.1, 1970.

[2] W.E. Hall, Identification of Aircraft Stability Derivatives for the High Angle-of-Attack Regime, System Control Inc., Palo Alto/Calif., Techn.Rep.No.1, 1972.

[3] G.N. Malcolm, Impact of High-Alpha Aerodynamics on Dynamic Stability Parameters of Aircraft and Missiles, AGARD LS-114, 1981, pp.2-1 to 2-18.

[4] K.J. Orlik-Rueckemann, Aerodynamic Aspects of Aircraft Dynamics at High Angles of Attack, J. Aircraft, Vol.20, 1983, pp.737 to 752.

[5] M. Tobak, L.B. Schiff, Aerodynamic Mathematical Modeling - Basic Concepts, AGARD LS-114, 1981, pp.1-1 to 1-32.

[6] H.H.B.M. Thomas, G. Edwards, Mathematical Models of Aircraft Dynamics for Extreme Flight Conditions, AGARD CP-235, 1978, pp.27-1 to 27-52.

[7] K.J. Orlik-Rueckemann, Dynamic Stability Testing of Aircraft - Needs versus Capabilities, Prog. Aerosp. Scie., Vol.16, 1975, pp.431 to 447.

[8] K.J. Orlik-Rueckemann, Review of Techniques for Determination of Dynamic Stability Parameters in Wind Tunnels, AGARD LS-114, 1981, pp.3-1 to 3-28.

[9] E.S. Hanff, Direct Forced-Oscillation Techniques for the Determination of Stability Derivatives in Wind Tunnels, AGARD LS-114, 1981, pp.4-1 to 4-23.

[10] C.O. O'Leary, Wind-Tunnel Measurement of Aerodynamic Derivatives Using Flexible-Sting Rigs, AGARD LS-114, 1981, pp.5-1 to 5-15.

[11] G.N. Malcolm, Rotary and Magnus Balances, AGARD LS-114, 1981, pp.6-1 to 6-26.

[12] J.R. Chambers, S.B. Grafton, Curved-Flow, Rolling-Flow and Oscillatory Pure-Yawing Wind-Tunnel Test Methods for Determination of Dynamic Stability Derivatives, AGARD LS-114, 1981, pp.7-1 to 7-13.

[13] J. Williams, Technical Evaluation Report on the FMP Symposium at CESME, Oct. 82, on 'Ground/Flight Test Techniques and Correlation,' AGARD AR-191, 1983.

[14] E.S. Hanff, Determination of Non-Linear Loads on Oscillating Models in Wind Tunnels, ICIASF '83 Record, 1983, pp.145 to 151.

[15] X. Hafer, Wind Tunnel Testing of Dynamic Derivatives in W-Germany, AGARD CP-235, 1978, pp.5-1 to 5-12.

[16] J.v.d. Decken, E. Schmidt, B. Schulze, On the Test Procedures of the Derivative Balances Used in West-Germany, AGARD CP-235, 1978, pp.6-1 to 6-17.

[17] D. Altenkirch, Flugmechanische Analyse der dynamischen Derivative des Dornier-Variationsmodells, DFVLR-FB 83-38, 1983.

[18] H. Fuchs, E. Schmidt, F.-J. Niezgodka, Experimental and Theoretical Prediction of Dynamic Derivatives of Missiles, AGARD CP-336, 1983, pp.25-1 to 25-13.

[19] B.L. Uselton, A Description of the Standard Dynamics Model (SDM), Paper of 56th STA Meeting at MIT Cambridge/Mass., 1981.

[20] S.M. Coulter, E.J. Marquart, Cross and Cross-Coupling Derivative Measurements on the Standard Dynamics Model at AEDC, AIAA Paper 82-0596, 12th Aerodynamic Testing Conf., 1982.

[21] M.E. Beyers, Subsonic Roll Oscillation Experiments on the Standard Dynamics Model, AIAA Paper 83-2134, 10th Atmosph. Flight Mech. Conf., 1983.

[22] L. Torngren, FFA Results for Dynamic Derivatives of the Standard Dynamics Model in Pitch and Yaw Oscillation. Private communication, 1984.

[23] T.H. Hottner, W. Lorenz-Meyer, Der Transsonische Windkanal der Aerodynamischen Versuchsanstalt Göttingen (Zweite Ausbaustufe), DGLR-Jahrbuch 1968, pp. 1 to 10.

[24] E. Schmidt, K.-H. Sauerland, Derivativawaage fuer den Transkanal Goettingen (TRAD), Teil 1: Beschreibung der Messeinrichtung, DFVLR-IB 232-81 J 10, 1982.

[25] E. Schmidt, Derivativawaage fuer den Transkanal Goettingen (TRAD), Teil 2: Mess- und Auswerteverfahren bei Nickschwingung, DFVLR-IB 232-82 J 09, 1983.

[26] M. Canu, Mesure en soufflerie de l'amortissement aérodynamique en tangage d'une maquette d'avion oscillant suivant deux degrés de liberté, Rech. Aérospatiale, 1971, pp.257 to 267.

[27] G.E. Burt, J.C. Uselton, Effect of Sting Oscillations on the Measurement of Dynamic Stability Derivatives, J. Aircraft, Vol.13, 1976, pp.210 to 216.

[28] M.E. Beyers, Measurement of Direct Moment Derivatives in the Presence of Sting Plunging, NRC Canada No.20935, NAE-AN-1, 1983.

[29] N.C. Lambourne, Wind Tunnel Wall Interference in Unsteady Transonic Testing, AGARD VKI-LS-1981-4, 1981.

[30] L.E. Ericsson, J.P. Reding, Practical Solutions to Simulation Difficulties in Subscale Wind Tunnel Tests, AGARD CP-348, 1984, pp.16-1 to 16-12.

[31] E. Schmidt, H. Stange, Derivativawaage fuer den Transkanal Goettingen (TRAD), Teil 5: WK-Messungen am SD-Modell bei Nickschwingung, DFVLR-IB 232-83 J 05, 1983.

[32] E. Schmidt, H. Stange, Derivativawaage fuer den Transkanal Goettingen (TRAD), Teil 7: WK-Messungen am SD-Modell bei Gierschwingung, DFVLR-IB 232-85 J 03, 1985.

[33] E. Schmidt, D. Moehle, Derivativawaage fuer den Transkanal Goettingen (TRAD), Teil 8: WK-Messungen am SD-Modell bei Rollschwingung, DFVLR-IB 232-85 J 04, 1985.

[34] L. Torngren, New Dynamic Testing Techniques and Related Results at FFA, AGARD FDP Symposium 'Unsteady Aerodynamics', Goettingen, May 1985, Paper 20.

ACKNOWLEDGEMENTS

The test technicians of the Institute of Aeroelasticity contributed decisively to the successful performance of the difficult experimental phases of the TRAD test facility, which was brought to the limit of its capacity and beyond. Considerable assistance was also given by the "Measurement Electronics" Task Group of the Institute. Ms. Schlosser is thanked for helping to translate and prepare the manuscript.

Table 1 Test program of DSD model

a) Pitch oscillation

OMS[1]	Re[1] [Mio]	MA = 0.60	0.80	0.88	0.95	1.05	1.20
0.015	1.03		335				334
	1.42		314	317	321	325/329	332
	1.54	300/301	311				
0.027	1.02	345[2]	336	344[2]	346[2]		347[2]
	1.42		315	318	322	326/330	
	1.53	304/305	312				
0.040	1.03		343[2]				
	1.41		316	319	323	327/331	
	1.54	306/310	313				

b) Yaw oscillation

OMS[3]	Re[3] [Mio]	MA = 0.60	0.80	0.88	0.95	1.05	1.20
0.021	1.36	349	352	362	365	368	371
0.035	1.36	350	353/379	363	366/378	369	372[2]
	1.88		380				
0.052	1.36	351	354[2]	364[2]	367[2]	370[2]	377

c) Roll oscillation

OMS[3]	Re[3] [Mio]	Ma = 0.60	0.80	0.88	Remarks
0.021	1.36	401	406	417	DPHI = 1°
		402/403	428	430	1.5°
0.035	1.36		408	418	1°
		404	429[2]		1.5°
		431	432		1.5°, Tu-strip off
0.052	1.36	427	409	419[2]	1°
		405			1.5°

[1] referred to mean aerodynamic chord (MAC = 130.1 mm)
[2] long run (static tests included)
[3] referred to halfspan (s = 172.4 mm)

Table 2 Margin of derivative scattering

a) Pitch oscillation

derivative	CZT	CMT	CZQ	CMQ
extreme values	-6.8/-1.1	-1.0/0.6	-19/5	-13/-1
scattering margin	0.05	0.025	1.1	0.6
percentage	1	2	4	5

b) Yaw oscillation

derivative	CYBC	CNBC	CLBC	CYR	CNR	CLR
extreme values	-1.9/-0.4	-0.5/0.8	-0.45/0.3	-1./4.3	-2.7/1.1	-0.3/5.6
scattering margin	0.020	0.030	0.030	0.80	0.55	0.48
percentage	1	2	4	15	14	8

c) Roll oscillation

derivative	CYBS	CNBS	CLBS	CYP	CNP	CLP
extreme values	-0.43/0	-.15/.08	-0.13/.12	-.64/.66	-.79/.61	-1.7/0.6
scattering margin	0.012	0.011	0.018	0.34	0.62	0.40
percentage	3	5	7	26	44	18

Figure 1 Transonic derivative balance (TRAD) for AVA wind tunnel

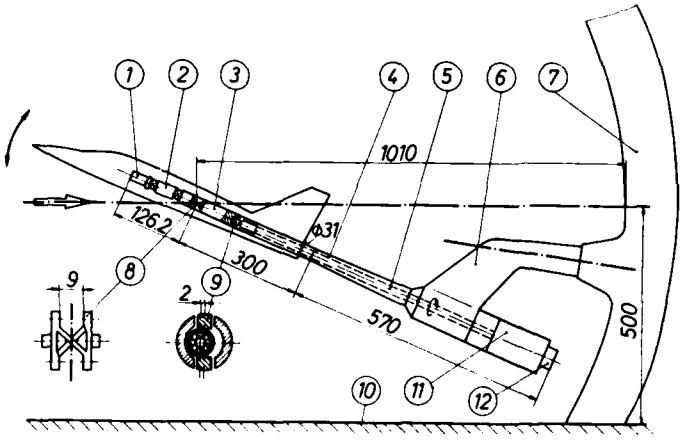

a) TRAD Assembly for Pitch Oscillation

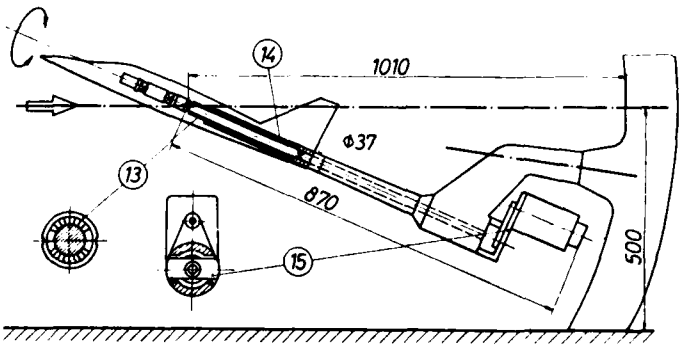

b) TRAD Assembly for Roll Oscillation

(1) Model Joint
(2) Five-Comp. Balance
(3) Movable Head
(4) Model Sting
(5) Rotating Shaft
(6) 15° Angle Adaptor
(7) WT α Traverse
(8) Cross Flexures (Pitch Axis)
(9) Eccentric Drive
(10) Tunnel Floor
(11) Quinstep Motor
(12) Pulse Generator
(13) Forward Roll Flexure
(14) Rearward Roll Flexure
(15) Drive Transmission 10 36

Figure 2 TRAD mechanism for pitch oscillation with DSD model in the AVA wind tunnel test section

Figure 3 Block diagram of TRAD measuring system

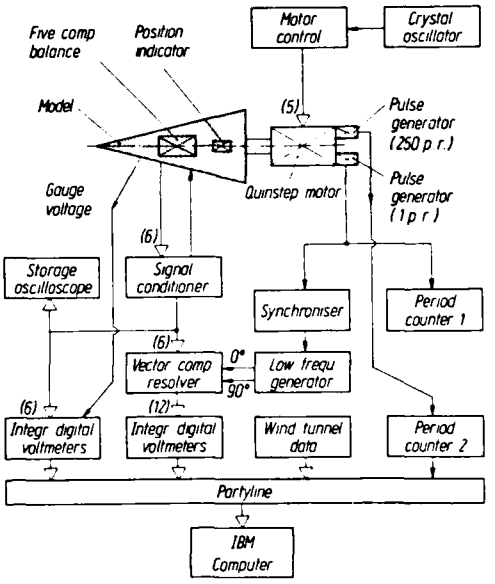

Figure 4 Dimensions of DFVLR Standard Dynamics (DSD) model

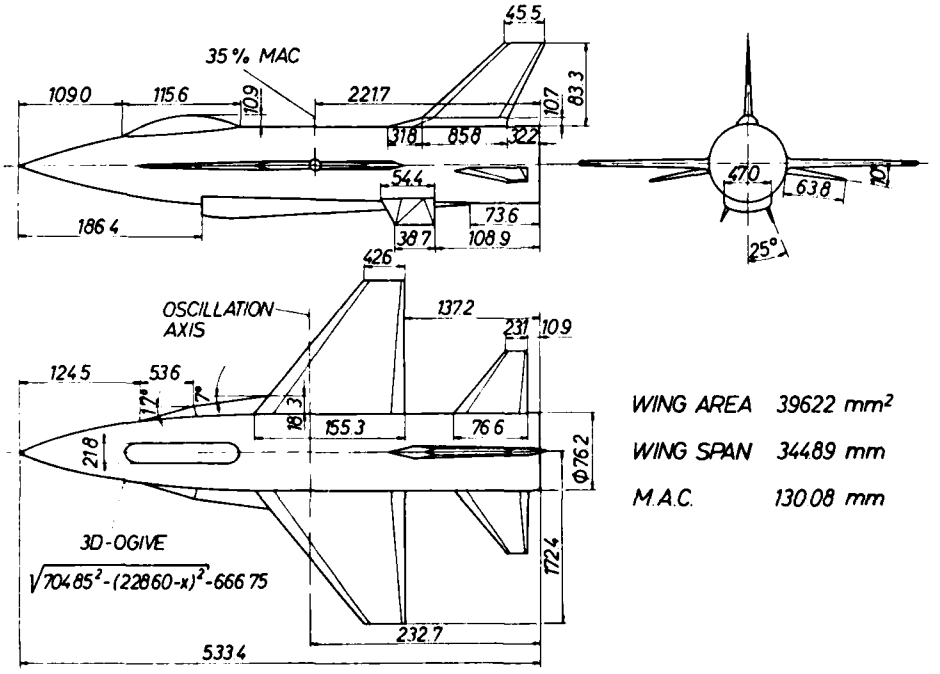

Figure 5 Coefficients CZ, CM(α); Mach number effects

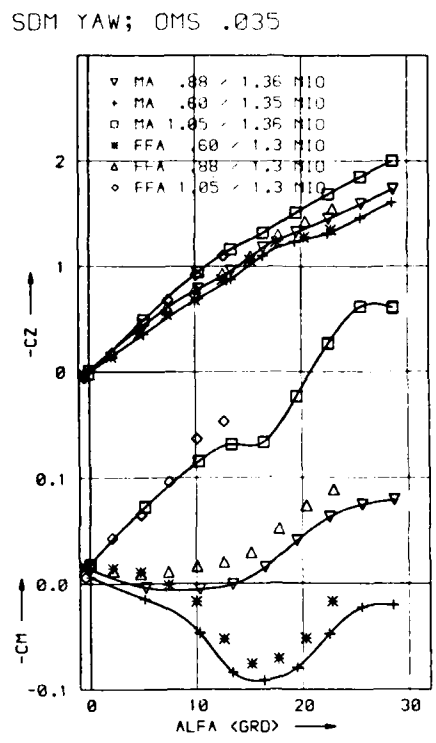

Figure 6 Coefficients CY, CN, CL(α); Mach number effects

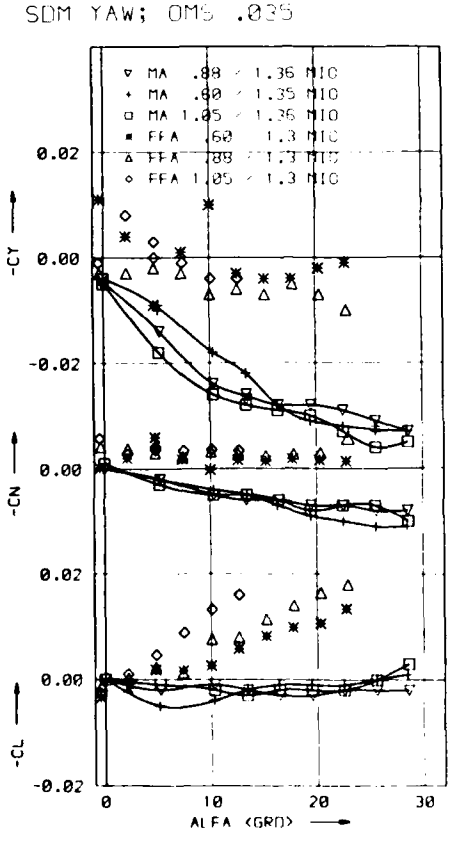

Figure 7 Coefficients CZ, CM(α); Reynolds number effects

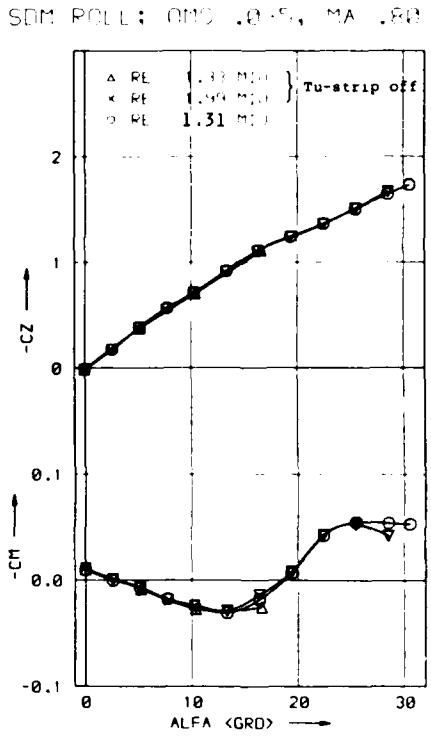

Figure 8 Pitch derivatives CZQ, CZT(α); Mach number effects

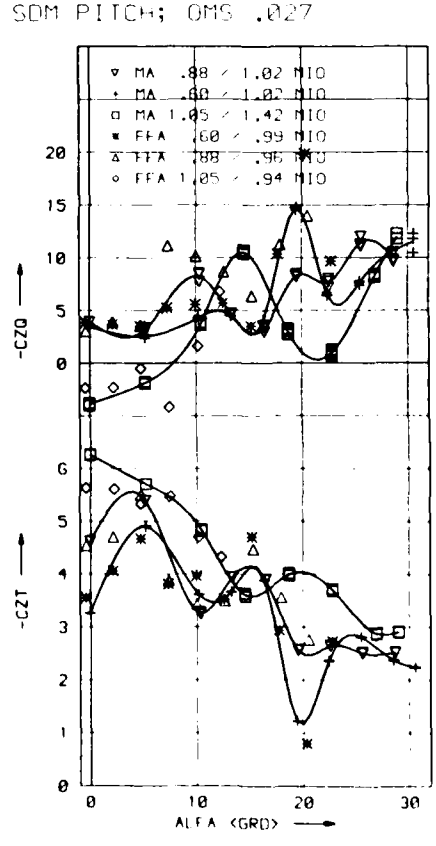

Figure 9 Pitch derivatives CMQ, CMT(α); Mach number effects

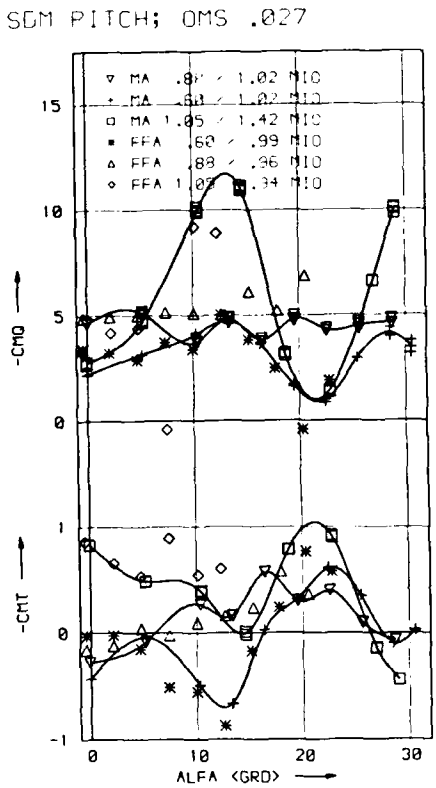

Figure 10 Pitch derivatives CZQ, CZT(α); effects of reduced frequency

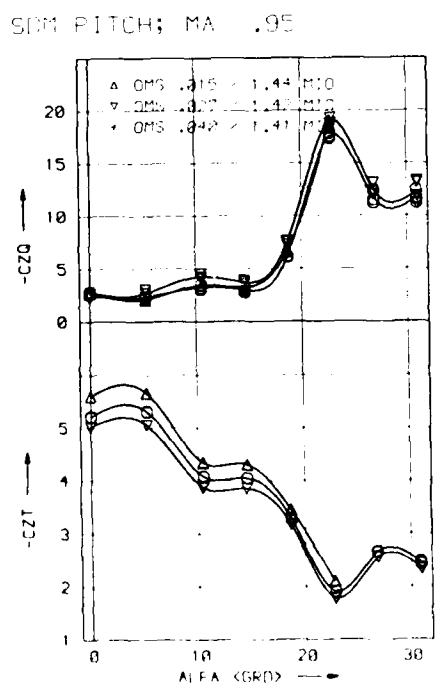

Figure 11 Pitch derivatives CMQ, CMT(α); effects of reduced frequency

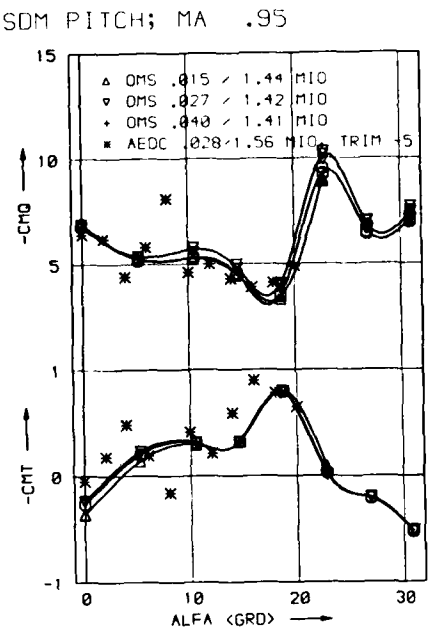

Figure 12 Yaw derivatives CYBC, CYR(α); Mach number effects

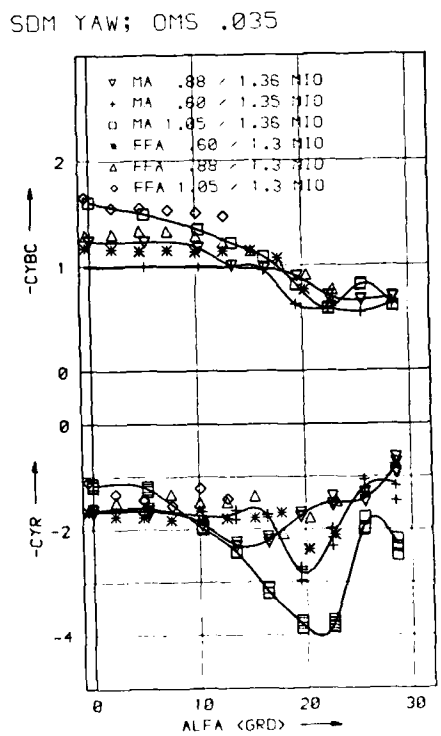

Figure 13 Yaw derivatives CNBC, CNR(α); Mach number effects

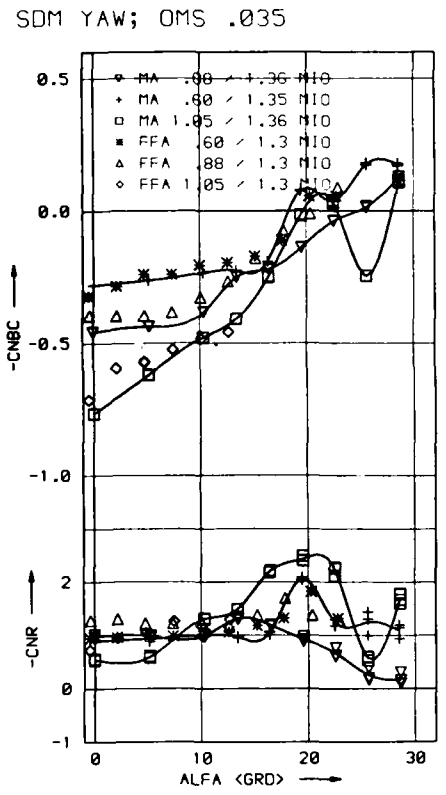

Figure 14 Yaw derivatives CLBC, CLR(α); Mach number effects

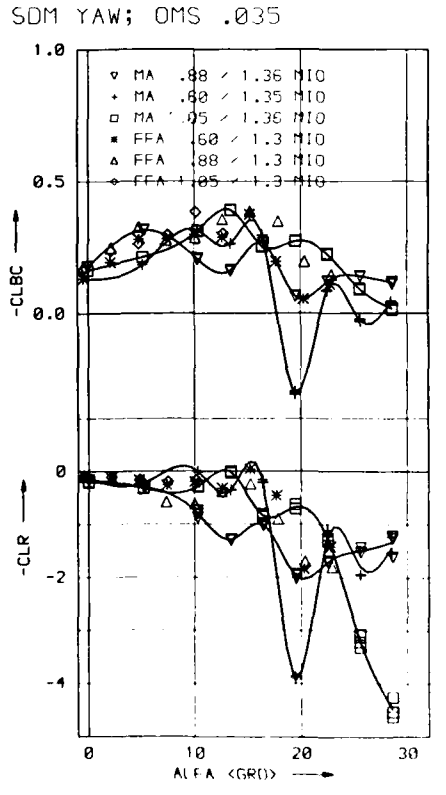

Figure 15 Yaw derivatives CYBC, CYR(α); effects of reduced frequency

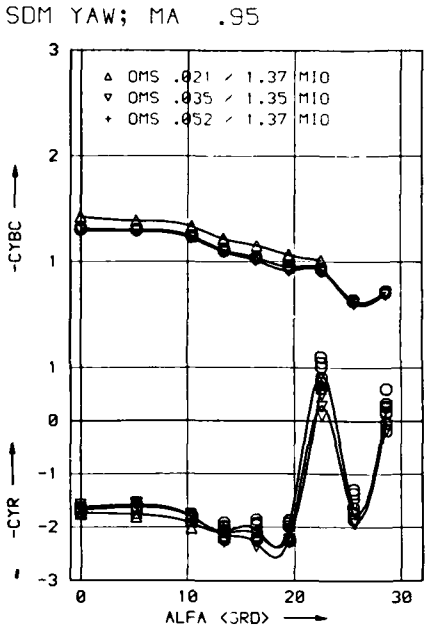

Figure 16 Yaw derivatives CNBC, CNR(α); effects of reduced frequency

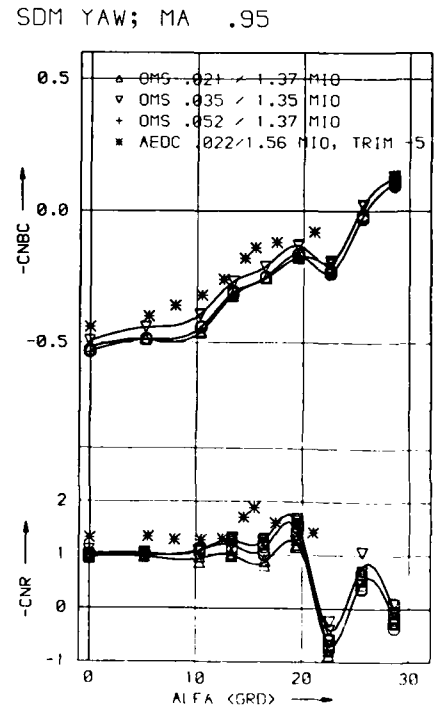

Figure 17 Yaw derivatives CLBC, CLR(α); effects of reduced frequency

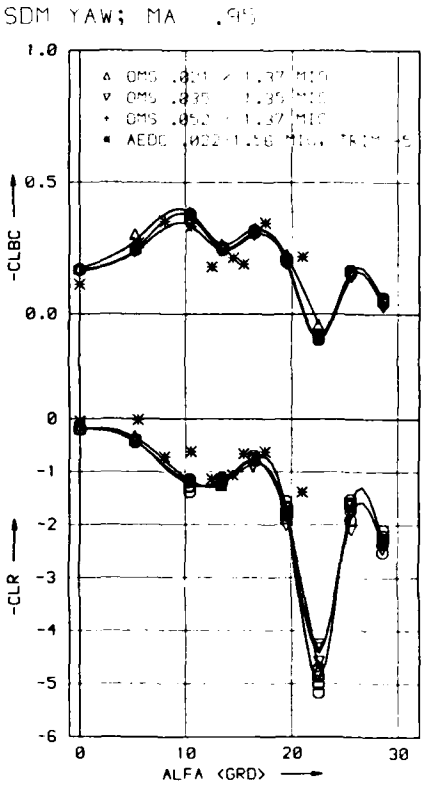

Figure 18 Roll derivatives CYBS, CYP(α); amplitude effects

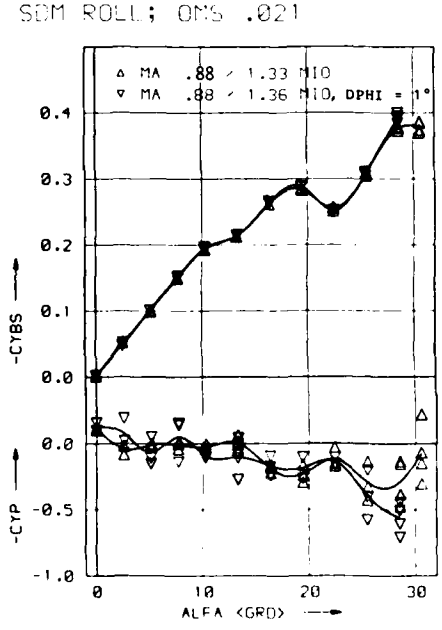

Figure 19 Roll derivatives CNBS, CNP(α); amplitude effects

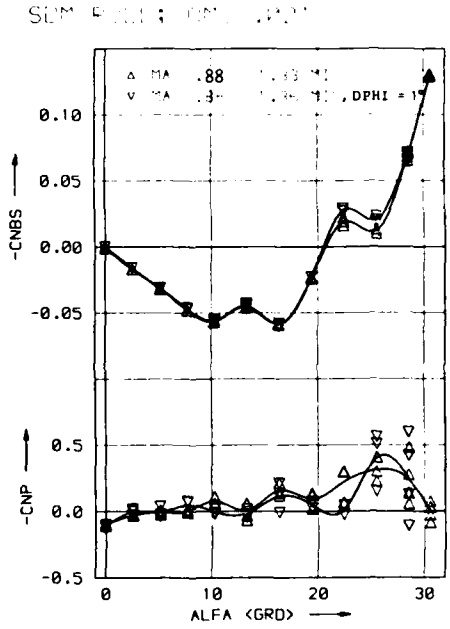

Figure 20 Roll derivatives CLBS, CLP(α); amplitude effects

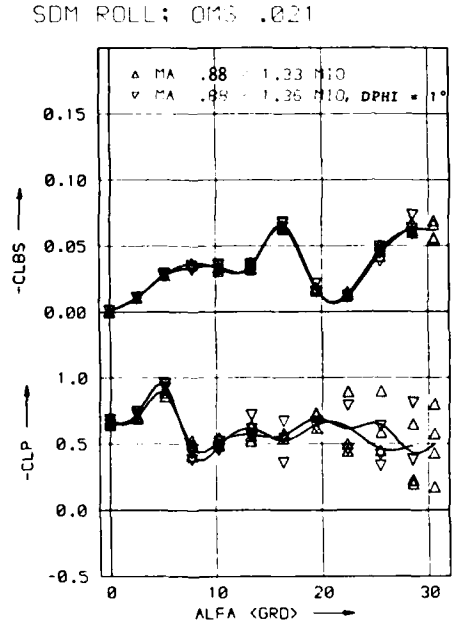

Figure 21 Roll derivatives CYBS, CYP(α); Mach number effects

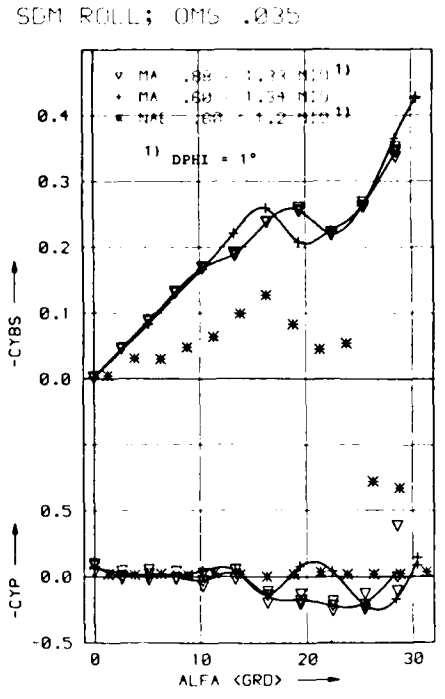

Figure 22 Roll derivatives CNBS, CNP(α); Mach number effects

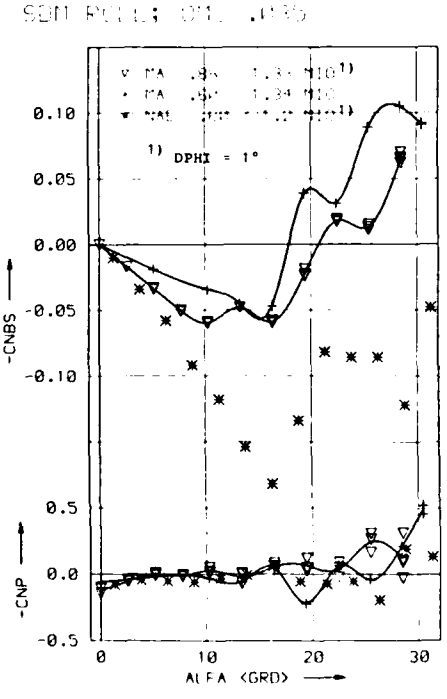

Figure 23 Roll derivatives CLBS, CLP(α); Mach number effects

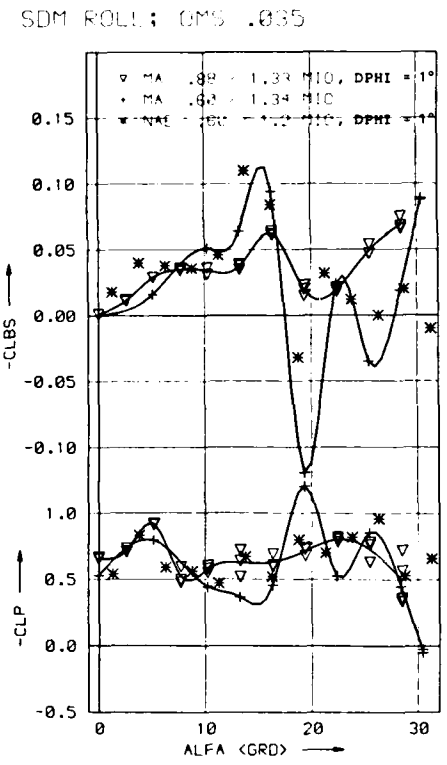

Figure 24 Roll derivatives CYBS, CYP(α); effects of reduced frequency

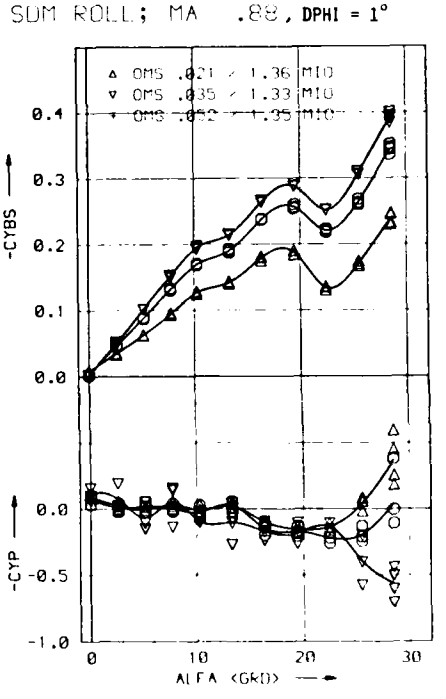

Figure 25 Roll derivatives CNBS, CNP(α); effects of reduced frequency

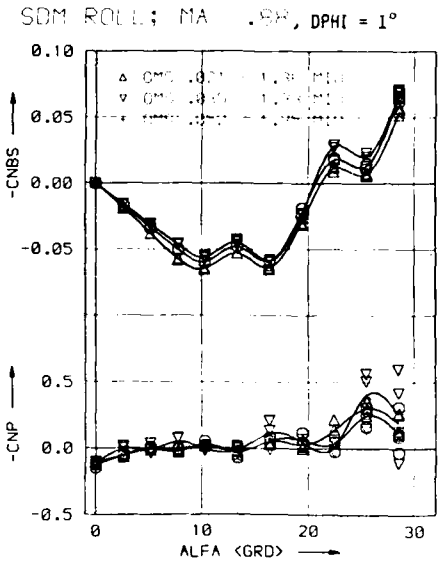

Figure 26 Roll derivatives CLBS, CLP(α); effects of reduced frequency

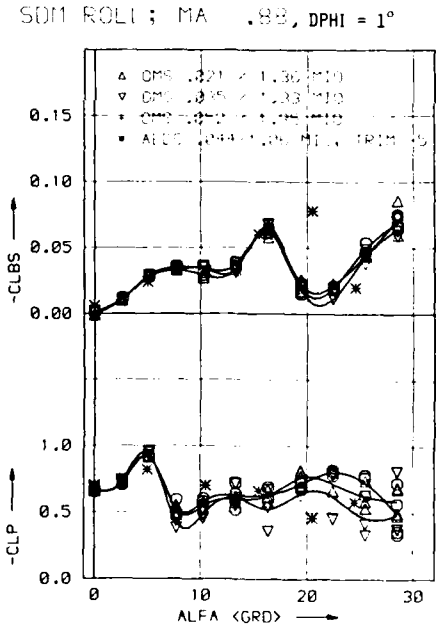

Figure 27 Roll derivatives CYBS, CYP(α); Reynolds number effects

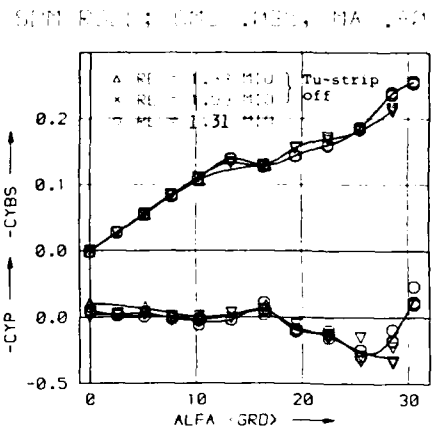

Figure 28 Roll derivatives CNBS, CNP(α); Reynolds number effects

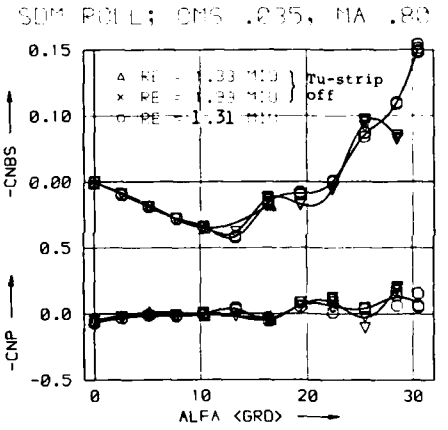

Figure 29 Roll derivatives CLBS, CLP(α); Reynolds number effects

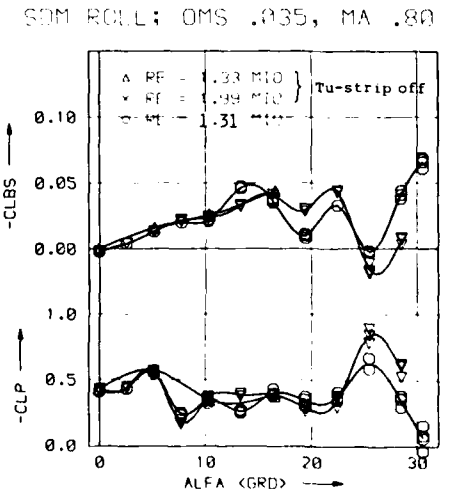

RECENTS DEVELOPPEMENTS DES TECHNIQUES DE SIMULATION DYNAMIQUE APPLIQUEES A L'IDENTIFICATION DES PARAMETRES DE STABILITE

D. Tristrant - O. Renier
Ingénieurs
ONERA-IMFL
5, boulevard Paul Painlevé
59000 LILLE - FRANCE

RESUME

Dans le cadre de la prédiction du comportement dynamique d'un avion, ce papier présente des méthodes expérimentales et d'analyse qui, au travers d'un modèle linéaire, permettent d'identifier les paramètres de stabilité dynamique à l'aide d'un unique moyen d'essais, installé à l'IMFL. Nous décrirons les caractéristiques du montage, la procédure expérimentale, la méthode d'identification ainsi que quelques résultats obtenus sur différentes maquettes. Un accent particulier est mis sur l'intérêt apporté dans la méthode par un certain degré de liberté du montage, celui dénommé λ, qui est l'angle entre le vecteur vitesse et le vecteur rotation. On montre en effet que la réalisation d'essais en rotation à λ non nul offre des possibilités intéressantes en identification et permet en particulier d'évaluer les paramètres d'un modèle linéaire autour d'une trajectoire quasi rectiligne.

Il est également présenté un dispositif récemment développé et utilisé sur ce moyen d'essais, introduisant un degré de liberté supplémentaire dénommé rayon de giration qui, au travers d'un choix judicieux d'essais, permet d'accéder à l'ensemble des paramètres intervenant dans un modèle linéaire assez général. Enfin, les mesures dynamiques obtenues sur maquette lorsque l'angle λ est non nul mettent en relief à grande incidence des phénomènes aérodynamiques instationnaires de forte amplitude qui ne peuvent être ignorés si l'on veut prédire des évolutions décrochées (comme le départ en vrille, la récupération, les auto-tonneaux) où les vecteurs vitesse et rotation ne sont plus colinéaires.

SUMMARY

In the aircraft dynamic behaviour prediction context this paper presents the experimental methods and the analytical procedures allowing the mathematical linear modeling parameters to be identified, using a unique test apparatus located at IMFL. The rig characteristics, the experimental procedures, the identification methods and results about different aircraft models will be described. Emphasis is put on the interest of a specific λ D.O.F.(*), angle formed by the rotational vector and the velocity vector. Effectively, it is shown that rotational tests with a non zero value of λ (oscillatory coning) offer interesting possibilities for identification and allow the estimation of linear model parameters in the case of a quasi linear path.

It is also presented how an other D.O.F. called "giration radius" was obtained by fixing a special mechanism onto the test apparatus. By carrying out a carefully selected tests program, this D.O.F. allows the whole set of stability parameters to be identified, given the structure of the linear mathematical model. Finally, dynamic measures obtained during oscillatory coning using a complete aircraft model put in evidence the large amplitude of unsteady aerodynamic phenomena at high angles of attack, that one could not ignore if we aim prediction of post stall evolutions (spin departure, spin recovery, autoroll...) during which the velocity and rotational vectors lines of action are no more parallel.

1. INTRODUCTION

Le but de ce papier est de présenter quelques méthodes expérimentales et d'analyse qui, utilisant le moyen d'essai "tournebroche" de l'IMFL dont nous verrons les particularités, contribuent à la prédiction du comportement dynamique des avions dans un domaine de vol pouvant être très large en incidence. L'identification des paramètres de stabilité dynamique à partir d'essais en soufflerie a bien progressé ces dernières années. Des efforts importants ont en effet été réalisés de par le monde sur cette question, car beaucoup plus de coefficients dérivés sont maintenant requis sur les avions de combat modernes. Pour pouvoir accéder à ces divers coefficients : les dérivées d'amortissement, les dérivées croisées ou couplées-croisées, les termes d'accélération, de nombreux montages dynamiques ont été développés récemment [1].

Les techniques et méthodes expérimentales employées, la définition des programmes d'essais dépendent étroitement des buts visés, c'est-à-dire du modèle aérodynamique de l'avion défini a priori et dont on cherche à identifier les paramètres. Aussi les hypothèses de départ quant à la structure du modèle aérodynamique sont elles fondamentales car elles conditionnent les types de sollicitations à exercer en soufflerie sur la maquette et à partir desquelles l'analyse de la réponse aérodynamique de la maquette fournit les paramètres du modèle.

Il a été montré [2] qu'à partir d'une formulation intégrale chaque composante du torseur aérodynamique exprimée en axes avion, sous les hypothèses de linéarité, pouvait être approximée par une expression polynomiale du premier degré vis-à-vis des variables dynamiques p, q, r, $\dot{\alpha}$ et $\dot{\beta}$.

$$(1)\quad C_i = C_i(\alpha,\beta) + C_{ip}^{(\alpha,\beta)}\frac{pl}{V} + C_{iq}^{(\alpha,\beta)}\frac{ql}{V} + C_{ir}^{(\alpha,\beta)}\frac{rl}{V} + C_{i\dot{\alpha}}^{(\alpha,\beta)}\frac{\dot{\alpha}l}{V} + C_{i\dot{\beta}}^{(\alpha,\beta)}\frac{\dot{\beta}l}{V}$$

où les divers paramètres sont dépendants de l'incidence et du dérapage. Si de plus, l'hypothèse de vol quasi rectiligne est justifiée, cette expression peut encore se ramener sous une forme plus simple :

$$(2)\quad C_i = C_i(\alpha,\beta) + C'_{ip}^{(\alpha,\beta)}\frac{pl}{V} + C'_{i\dot{\alpha}}^{(\alpha,\beta)}\frac{\dot{\alpha}l}{V} + C'_{i\dot{\beta}}^{(\alpha,\beta)}\frac{\dot{\beta}l}{V}$$

Dans cette expression chaque nouveau paramètre C'_{ij} est une combinaison des précédentes appartenant à l'expression plus générale (1) et chacun de ces termes peut être associé à un mouvement particulier au cours duquel il peut être déterminé.

(*) D.O.F. = Degree of Freedom

Les 4 essais caractéristiques correspondant à ce modèle sont alors les suivants :

- l'essai statique à incidence et dérapage fixés,
- la rotation continue (coning motion) à incidence et dérapage constants,
- les oscillations en tangage et lacet autour d'une incidence et/ou d'un dérapage donnés.

Alors que la réalisation de ces mouvements nécessitera le plus souvent de disposer de plusieurs installations ou montages, nous montrerons qu'à partir d'une formulation bien définie du modèle aérodynamique il est possible, avec la seule balance rotative de l'IMFL, d'identifier les différents paramètres du système (2), et ceci grâce, en particulier, à la possibilité existant sur ce montage de paramétrer l'angle λ entre le vecteur vitesse et le vecteur rotation instantanée de la maquette. Nous décrirons la méthode expérimentale et de restitution, la procédure utilisée dans le choix sélectif des essais, la méthode employée en identification, et nous illustrerons ceci par des résultats concrets.

Ensuite, moyennant l'utilisation du paramètre dénommé rayon de vrille (ou plutôt rayon de giration), nous verrons qu'il est également possible sur ce même montage d'accéder à l'ensemble des paramètres du système (1).

Enfin, pour terminer, nous présenterons des résultats de mesure à grande incidence réalisés en dynamique et qui illustrent parfaitement sur maquette des phénomènes aérodynamiques instationnaires importants (en particulier le décrochage dynamique), ceci grâce à l'existence sur cette balance rotative du degré de liberté λ qui permet de caractériser, d'un point de vue mécanique du vol, ce phénomène.

2. LE MOYEN D'ESSAIS "TOURNEBROCHE"

Le montage tournant dit "tournebroche" est situé dans la soufflerie verticale de l'IMFL dont le diamètre est de 4 m et dont la vitesse maximale est de 45 m/s. Un schéma de ce montage avec la description de ces principaux degrés de liberté est présenté planche 1.

Ce montage a été conçu pour pouvoir effectuer des simulations dynamiques à grandes incidences, plus particulièrement dans le domaine de la vrille ; aussi certains des degrés de liberté de ce montage comme le rayon de vrille ou le cap relatif existent-ils afin de pouvoir simuler différents types de mouvements à grande incidence, apparentés à la vrille.

Les degrés de liberté du montage qui nous intéresseront en premier lieu sont :

Θ_2 : angle de pivotement en assiette de la maquette autour du centre de résolution balance

ϕ_2 : angle de rotation propre de la maquette

Ω : vitesse angulaire de la rotation continue

λ : angle de basculement de tout le montage par rapport au vent ascendant et qui est l'angle entre le vecteur vitesse soufflerie et le vecteur rotation

Toutes ces valeurs sont constantes au cours d'un essai.

Il est évident que les possibilités de la méthode d'identification et le type de dérivées susceptibles d'être identifiées dépendent étroitement des possibilités cinématiques du montage et de son aptitude à pouvoir simuler chaque variable du modèle indépendamment de toutes les autres.

Pour cette raison, nous rappellerons ici les relations mathématiques liant, d'une part, les degrés de liberté du montage et, d'autre part, les variables utilisées habituellement en modélisation, à savoir : α, β, p, q, r, $\dot{\alpha}$ et $\dot{\beta}$. Pour cela, nous devons avant tout distinguer les différents types d'essais susceptibles d'être réalisés actuellement avec le montage tournebroche. Ceux-ci se divisent en 3 catégories :

a) les essais statiques

Les variables λ, Θ_2 et ϕ_2 permettent de positionner la maquette en un point quelconque du plan (α, β).

L'identification en statique ne pose a priori aucun problème particulier. Les formules cinématiques sont les suivantes :

$$\begin{aligned} \beta &= \text{Arc sin } (\sin \phi_2 \sin (\Theta_2 + \lambda)) \\ \alpha &= \text{Arctg } (\cos \phi_2 \text{ tg } (\Theta_2 + \lambda)) \end{aligned} \qquad (I)$$

L'accessibilité en incidence dérapage est donc très large et ne pose aucune contrainte dans le cadre de notre propos.

b) les rotations stationnaires

Ce sont des rotations continues où incidence et dérapage sont constants au cours d'une période ; elles se produisent lorsque le degré de liberté λ est identiquement nul. Incidence et dérapage se déduisent alors des formules (I) et les composantes p, q, r du vecteur rotation instantanée sont données par :

$$\begin{aligned} p &= \Omega \cos \Theta_2 \\ q &= \Omega \sin \Theta_2 \sin \phi_2 \\ r &= \Omega \sin \Theta_2 \cos \phi_2 \end{aligned} \qquad (II)$$

Puisque λ est nul, nous ne disposons pour ces essais que de 3 degrés de liberté du montage, à savoir : Θ_2, ϕ_2 et Ω. Or, nous avons 5 relations ; il existe donc 2 relations cinématiques liant entre elles les variables de la mécanique du vol.

En éliminant les variables propres au montage, on a :

$$p = \Omega\cos\alpha\cos\beta \qquad r = p\ tg\ \alpha$$
$$q = \Omega\sin\beta \quad \text{soit encore} \quad \text{et} \qquad (III)$$
$$r = \Omega\sin\alpha\cos\beta \qquad q = p\ tg\ \beta/\cos\alpha$$

Il convient, lorsque l'on définit un programme d'essais comportant des rotations stationnaires, d'avoir à l'esprit ces relations, et nous verrons par la suite leur incidence sur l'identification des coefficients d'amortissement. Ces relations sont d'ailleurs celles qui existent sur tous les montages "balance rotative" traditionnels et qui limitent leurs possibilités propres en identification.

c) les rotations dynamiques

Cette fois, l'angle λ entre le vecteur vitesse et le vecteur rotation instantanée n'est pas nul, et l'incidence et le dérapage varient de façon périodique au cours d'un tour. Le calcul de α, β dépend donc également de Ψ_2, position angulaire de la maquette au cours d'un tour. Puisque le pivotement d'angle λ est un pivotement de l'ensemble du montage (et donc à la fois de la maquette et de l'axe de rotation en Ω), les composantes p, q et r sont indépendantes de λ, et les formules (II) sont encore valables. Puisque α, β varient au cours de la rotation, on voit que ce type d'essai fait intervenir la contribution cinématique des variables $\dot{\alpha}$ et $\dot{\beta}$ qui varient au cours d'un cycle et dont l'amplitude de variation est proportionnelle à $\sin\lambda$. Les variables α et β sont périodiques oscillatoires et évoluent de façon quasi sinusoïdale au cours d'un cycle (voir planche 2-b). L'introduction du paramètre λ permet de transformer les relations (III) de contraintes entre les variables aérodynamiques en les suivantes :

$$\dot{\alpha} = q - tg\ \beta(p\cos\alpha + r\sin\alpha)$$
$$\dot{\beta} = p\sin\alpha - r\cos\alpha \qquad (IV)$$

Celles-ci englobent les précédentes et traduisent les nouvelles contraintes entre α, β, p, q, r, $\dot{\alpha}$ et $\dot{\beta}$.

Ces relations entre variables du modèle aérodynamique permettent de caractériser les limitations du montage tant du point de vue accessibilité que du point de vue observabilité. En effet, ces relations fournissent les évolutions possibles pour les différentes variables ainsi que les dépendances mathématiques entre ces variables. Les relations sont également d'un grand intérêt dans le choix d'un programme d'essais.

3. PROCEDURE D'IDENTIFICATION

La procédure générale comporte différentes phases qui se succèdent suivant une démarche chronologique comportant : le postulat d'une structure de modèle, laquelle conditionne le choix des essais, la restitution à partir de ces essais des valeurs des coefficents aérodynamiques globaux et des variables du modèle, puis l'identification mathématique des paramètres du modèle.

3.1 Modèle aérodynamique

Le modèle mathématique que nous utiliserons correspond à la formulation simplifiée en axes avion (1) ou (2) dans le cas d'une trajectoire quasi rectiligne. Dans ces formulations les coefficients dépendent de l'incidence et du dérapage suivant des lois inconnues ou plutôt suivant des lois qu'il convient de déterminer. On recherche donc le comportement de ces fonctions dans le plan (incidence-dérapage). Pour cela, on peut effectuer un découpage du plan (α, β) en zones adjacentes. Ce découpage peut être choisi de façon suffisamment fine pour qu'à l'intérieur de chaque domaine les coefficients dérivés puissent être considérés constants. On effectue ainsi en quelque sorte une discrétisation du plan (α, β) permettant d'obtenir une discrétisation des lois inconnues.

En pratique nous avons effectué un découpage beaucoup plus fin en incidence qu'en dérapage. Partant de l'idée que, vu les hypothèses de linéarité, l'effet du dérapage sur les dérivées dynamiques pouvait être supposé constant tant que celui-ci restait toutefois dans des limites raisonnables (8 à 10 degrés par exemple). L'incidence, par contre, qui détermine le régime d'écoulement, est considérée comme la variable caractéristique sur les coefficients dérivés. En restant entre des valeurs bornées du dérapage, on effectuera donc un découpage en tranches d'incidence (de largeur deux degrés) de façon à restituer tant que possible tout type d'évolution des paramètres en fonction de l'incidence. A l'intérieur de chaque tranche on effectuera des essais, on les restituera et on effectuera des identifications séparées et indépendantes d'une tranche à l'autre.

3.2 Méthode mathématique d'identification

Position du problème

On dispose d'un ensemble de n points de mesure et l'on cherche la meilleure approximation linéaire liant d'une part (y_i) i = 1,n qui représente les valeurs prises par un coefficient aérodynamique mesuré et, d'autre part (x_{ij}), i = 1,n et j = 1,m qui représente le tableau des valeurs prises par les m variables du modèle au cours des essais.

Méthode envisagée

Celle-ci est inspirée de résultats d'algèbre linéaire lesquels sont notamment employés en analyse des composantes principales qui est une méthode d'analyse des données multidimensionnelles [3].

On se place dans l'espace de dimension p = m + 1 où m désigne le nombre des variables envisagées dans le modèle ; la variable x_p représentant alors les valeurs du coefficient y.

Dans cet espace, on dispose d'un nuage de points N défini comme suit :

$$N = \left\{ x_i \in \mathbb{R}^p \ , \ p_i > 0 \ \ , \ \ i \in \{1,..,n\} \ \ , \ \ \Sigma p_i = 1 \right\}$$

où P_i représente le poids du point i,

n est le nombre de points de mesure disponibles.

Dans cet espace de dimension p = m + 1, on recherche la combinaison linéaire de m variables, approximant le mieux possible le nuage de points expérimentaux. Ceci revient à chercher l'hyperplan de l'espace par rapport auquel le nuage N a une inertie minimale. Il est évident (d'après le théorème d'Huygens) que cet hyperplan doit passer par le centre d'inertie du nuage. Supposons donc que nous ayons centré nos variables (x_j) pour j = 1... p, c'est-à-dire que $\Sigma p_i \ x_{ji} = 0$
Supposons de plus que $\mathbb{R}^p$ soit muni du produit scalaire associé à une matrice symétrique définie positive donnée a priori Q.

Soit V la matrice d'inertie de terme général $v_{jk} = \Sigma p_i \ x_{ji} \ x_{ki}$

On peut écrire $V = X^T D X$ en désignant par $X = (x_{ji})$ la matrice des données (i = 1... n et j = 1... p), D la matrice diagonale des poids P_i.

La matrice V est encore appelée matrice de variance-covariance empirique des variables $x_1, x_j \ldots x_p$ lorsque celles-ci sont centrées.

On démontre [3] que l'hyperplan d'inertie minimale est orthogonal au vecteur propre u associé à la plus petite valeur propre μ de la matrice VQ.

Application à l'identification en mécanique du vol

Soit C un coefficient aérodynamique quelconque que l'on souhaite modéliser en fonction de m variables (X_j), j = 1... M. Pour cela, on dispose d'un ensemble de n mesures $(C_i)_{i = 1 \ldots n}$ et d'un tableau $(x_{ji})_{\substack{j = 1 \ldots n \\ i = 1 \ldots n}}$ caractérisant l'ensemble des valeurs prises corrélativement par les différentes variables du modèle choisi.

En tout point i, le modèle s'écrit :

$$C_i = C_{x_1} X_{1_i} + C_{x_2} X_{2_i} + \ldots + C_{x_m} X_{m_i}$$

Cette expression peut se ramener sous la forme :

$$(3) \quad 0 = C_{x_1} x_{1_i} + C_{x_2} x_{2_i} + \ldots + C_{x_m} x_{m_i} - x_{p_i}$$

où x_{ji} désigne la valeur au point de mesure i de la variable j centrée : $x_{ji} = X_{ji} - \overline{X}_j$, et où x_{ip} désigne la valeur centrée prise par le coefficient aérodynamique mesuré. L'objectif est donc, dans cette expression, d'identifier les paramètres $C_{x1}, C_{x2} \ldots C_{xm}$ de façon que les mesures soient approximées au mieux par un hyperplan de $\mathbb{R}^p$.

On calcule donc les valeurs et vecteurs propres associés à VQ. Ces valeurs propres sont toutes réelles et positives puisque la matrice VQ est symétrique et définie positive.

Soit μ la plus petite valeur propre, et soit u, de composantes (u_j), le vecteur propre associé à μ. Vu que l'hyperplan approximant au mieux les points de mesure est orthogonal au vecteur u, son équation s'écrit :

$$u_1 \ x_1 + u_2 \ x_2 + u_j \ x_j + u_p \ x_p = 0$$

On retrouve ainsi nos coefficients aérodynamiques dérivés par :

$$C_{x_1} = - \frac{u_1}{u_p} \ , \ \ldots \ C_{x_j} = - \frac{u_j}{u_p}$$

Vu que μ représente l'inertie de N par rapport à l'hyperplan, plus la valeur de μ sera faible, plus l'inertie du nuage de points expérimentaux par rapport à l'hyperplan identifié sera faible, et donc plus la modélisation du nuage par l'hyperplan sera proche de l'ensemble des résultats expérimentaux.

Commentaire sur la méthode

Cette méthode permet d'évaluer simultanément tous les paramètres, et de plus ceci peut être réalisé globalement sur l'ensemble des résultats.

Cette méthode d'identification se rapproche assez de celle dite des moindres carrés, mais la fonctionnelle minimisée n'est pas tout à fait la même.

Pour observer la différence entre ces 2 méthodes, plaçons nous dans un cas simple à 2 dimensions, la solution correspond dans ce cas à une droite D du plan x, y.

On peut voir sur la planche 3 que les 2 méthodes diffèrent sur le type de fonctionnelle concernée.

La méthode exposée ici revient géométriquement à trouver la droite D qui minimise la somme des carrés des distances réelles entre les points et la droite (droite d'inertie minimale).

La méthode de régression de y par rapport à x revient à trouver la droite qui minimise la somme des carrés des écarts entre les valeurs de y mesurées et celles estimées.

Les deux fonctionnelles sont donc différentes, les solutions seront également différentes. Ces différences seront d'autant plus fortes que le gradient sera fort et que la mesure sera bruitée. Les moindres carrés ne procurent pas une solution satisfaisante lorsque la pente est importante. Par contre, la méthode présentée ici fournit une solution indépendante du gradient puisque la droite d'inertie minimale existe toujours, quelle que soit la répartition des points de mesure.

3.3 Contraintes expérimentales

D'un point de vue purement physique, une bonne identification des coefficients de stabilité dynamique nécessite que certaines conditions soient réunies. Hormis les problèmes inhérents à la réalisation d'essais dynamiques en soufflerie (vibrations, couplages, déformées, champ aéro...), il est certaines conditions sur lesquelles il nous semble intéressant d'insister. De plus, souligner plus particulièrement ces conditions permettra à la fois d'entrevoir les possibilités offertes par la méthode et dégagera les principales limitations dans la définition du programme d'essais.

Nous en citerons 3, en particulier :

a) La nécessité d'avoir un bon niveau de sensibilité de chaîne de mesure de façon à pouvoir estimer correctement la contribution de la variable concernée sur le coefficient aérodynamique mesuré.

En effet, la contribution sur l'aérodynamique des variables dynamiques est parfois faible devant celle de l'incidence, par exemple, ou du dérapage en statique. Pour évaluer des effets dynamiques, il convient souvent de posséder un haut niveau de sensibilité dans la mesure. Or cela nécessite évidemment que la balance soit sensible et que cet outil soit utilisé avec une maquette à une échelle adaptée, et avec une vitesse du vent suffisante de façon à pouvoir conserver un bon rapport signal-bruit dans la mesure. Mais ceci n'est pas encore suffisant. Modifier la vitesse du vent ou choisir une autre taille de maquette ne revient qu'à modifier l'intensité des efforts mesurés dans leur globalité. Ces différents paramètres permettent d'adapter globalement l'outil de mesure à son champ d'utilisation. Mais cette adaptation peut être plus ou moins bien réalisée suivant le coefficient que l'on considère.

Le poids de tel ou tel coefficient d'amortissement ou instationnaire peut être plus ou moins élevé en fonction des caractéristiques propres à l'avion testé, à sa géométrie. Et donc, indépendamment du moyen d'essai proprement dit, l'identification d'un coefficient dérivé nécessite que celui-ci ne soit pas trop faible vis-à-vis des autres et que les signaux correspondants à son effet soient supérieurs au seuil de sensibilité de la chaîne de mesure afin qu'ils ne soient pas noyés dans le bruit de mesure.

b) La nécessité d'avoir un moyen d'essai permettant d'effectuer des simulations dynamiques d'intensité suffisante pour sensibiliser le modèle aérodynamique à identifier. En d'autres termes, si l'on veut identifier par exemple le C_{lp}, il est évident qu'il convient d'effectuer des mouvements où la vitesse de roulis $\left(\frac{pl}{V}\right)$ est de module suffisamment élevé.

Dans le cas contraire, la composante induite $\frac{1}{2}\rho\, S\, l\, V^2\, C_{lp}\, \frac{pl}{V}$ ne serait pas détectable par la balance et en conséquence le coefficient ne serait pas identifiable. Un même moyen d'essai n'a donc pas pour chaque variable d'un modèle des possibilités en identification dynamique identiques, ceci d'autant plus que les valeurs de p, q, r, $\dot{\alpha}$, $\dot{\beta}$ réalisables dépendent du point statique considéré (valeurs de α, β). Les formules (III) montrent en l'occurrence que sur le montage on ne peut faire de rotations stationnaires à vitesse de tangage non nulle sans imposer un dérapage. Globalement, on peut dire que la vitesse de roulis est privilégiée devant celle de lacet et de tangage tant que l'on reste aux incidences faibles ou modérées.

De plus, il convient de prendre en compte les limitations relatives au domaine de linéarité aérodynamique des caractéristiques de l'avion considéré.

La méthode développée ici fait l'hypothèse d'un modèle et d'un comportement aérodynamique linéaires. Il importe donc d'entreprendre des essais en soufflerie qui respectent cette condition, sinon l'identification correspondante perd son sens. Sur ce point, deux types de caractéristiques aérodynamiques nous semblent devoir être prises en compte. La première concerne le domaine de linéarité de l'avion en statique (incidence et dérapage maxi). Ces deux limites en incidence et dérapage entraîneront des premières limitations quant aux valeurs de p, q, r (à travers les formules III) lors des rotations stationnaires.

En particulier, si le domaine de linéarité de l'avion en dérapage est faible, les vitesses de tangage réalisables le seront tout autant.

De plus, lors de simulations dynamiques, les incidences locales, notamment en extrémité d'aile, peuvent être élevées.

Le programme d'essais doit donc être réalisé de façon à éviter les éventuels décrochages locaux et conserver un comportement linéaire en dynamique.

c) La nécessité de pouvoir définir un programme d'essais dans lequel il n'existe pas de corrélation trop forte entre les différentes valeurs prises par les variables du modèle. Si, dans la définition du programme d'essais, 2 variables (p et r par exemple) étaient fortement liées, il serait alors impossible d'identifier l'effet de chacune d'elles, on ne pourrait estimer que les coefficients dérivés relatifs à une combinaison linéaire de ces 2 variables. C'est d'ailleurs ce qui se produit en règle générale sur d'autres montages où, pour des raisons purement cinématiques, on ne peut distinguer l'effet de la vitesse de tangage de celui de $\dot{\alpha}$, ou encore l'effet de la vitesse de lacet de celui de $\dot{\beta}$. Ceci est le cas général des oscillations forcées.

Parallèlement on peut noter sur les montages en balance rotative classiques des relations de même type ($r = p \operatorname{tg} \alpha$) qui empêchent mathématiquement une observabilité séparée des effets des vitesses de roulis et de lacet pour une incidence donnée. Ceci conduit alors à utiliser les mesures provenant de plusieurs installations pour identifier complètement les effets aérodynamiques.

Plusieurs caractéristiques dans la définition générale d'un programme d'essais, qui est lié, rappelons le, à un modèle aérodynamique, sont déterminées par ces 3 conditions. En particulier les bornes maximales et minimales du dérapage limitant le domaine identifié linéairement conditionnent le programme d'essai et les possibilités en observabilité.

3.4 Définition du programme

Nous cherchons donc, pour toute incidence $\alpha = \alpha_0$, et sous l'hypothèse que $\beta \in [\beta_{min}, \beta_{max}]$, à identifier les coefficients de l'expression :

$$C_i = C_i(\alpha, \beta) + C_{ip}(\alpha_0)\frac{pl}{V} + C_{iq}(\alpha_0)\frac{ql}{V} + C_{ir}(\alpha_0)\frac{rl}{V} + C_{i\dot{\alpha}}(\alpha_0)\frac{\dot{\alpha}l}{V} + C_{i\dot{\beta}}(\alpha_0)\frac{\dot{\beta}l}{V}$$

Alors, vu les contraintes cinématiques du montage (IV), la relation $\dot{\beta} = p\sin\alpha_0 - r\cos\alpha_0$ fait office de relation linéaire entre les variables $\dot{\beta}$, p et r, et on ne peut identifier C_{ip}, C_{ir} et $C_{i\dot{\beta}}$ séparément mais 2 combinaisons linéaires parmi les 3, par exemple : $C_{ip} + C_{i\dot{\beta}}\sin\alpha_0$ et $C_{ir} - C_{i\dot{\beta}}\cos\alpha_0$.

Si les valeurs maximales et minimales du dérapage ne sont pas trop faibles, alors en effectuant des essais à différents dérapages, il est possible d'éviter l'existence d'une liaison linéaire entre les variables $\dot{\alpha}$ et q, et il est alors possible d'identifier séparément les effets de $\dot{\alpha}$ et q sur ce montage.

Mais cela nécessite l'existence du degré de liberté λ sans lequel les essais en rotation continue seraient limités à une simple identification aérodynamique vis-à-vis de la seule variable Ω à incidence donnée. Pour chaque valeur de l'incidence, on peut définir un programme d'essai optimal pour l'identification. Celui-ci comprend :

- les essais statiques nécessaires pour identifier $C_i(\alpha_0, \beta)$
- au minimum deux rotations stationnaires ($\lambda = \dot{\alpha} = \dot{\beta} = 0$) pour deux valeurs différentes du dérapage, par exemple : l'une à dérapage nul (q = 0), l'autre à dérapage maximal.

Nous aurons alors les sollicitations à $\dot{\alpha} = \dot{\beta} = 0$ et $(p_{max}, 0, r_{max})$ et (p, q_{max}, r) avec $\dot{\alpha} = \dot{\beta} = 0$ pour l'incidence considérée.

- au minimum 2 essais en rotation dynamique ($\lambda \neq 0$). Le premier ($\phi_2 = 0, \Theta_{2max}, \lambda_{max}$) permet d'effectuer un essai à $\dot{\alpha} = q = 0$ et où $\dot{\beta}$ est maximal à l'incidence de passage qui nous intéresse. Le second, inversement, ($\phi_2 \simeq 90°, \Theta_{2max}, \lambda_{max}$) permet d'effectuer $\dot{\beta} = r = 0$ et $\dot{\alpha} = q$ à cette même incidence et pour $\beta \simeq 0$ (voir planche 4).

Si l'incidence α_0 n'est pas trop faible, un essai complémentaire ($\phi_2 = 0, \Theta_2 = 0, \lambda = \alpha_0$) permet d'obtenir des points de mesure à $p = \Omega$, $q = r = \dot{\alpha} = 0$, $\beta = \beta_{max} = \Omega.\alpha$.

Cas	Sollicitation	$\dot{\alpha}$	$\dot{\beta}$	p	q	r
1	stationnaire 1	0	0	X	0	X
2	stationnaire 2	0	0	X	X	X
3	dynamique 1	0	X	X	0	X
4	dynamique 2	X	0	X	X	X
5	complémentaire	X	X	X	0	0

Tableau 1

Vu les hypothèses d'additivité, on voit que les cas 2 et 4 du tableau 1 contribuent à dissocier les effets de q et $\dot{\alpha}$, tandis que les cas 1 et 3 contribuent à évaluer 2 coefficients sur les 3 variables p, r et $\dot{\beta}$, et ceci est possible, rappelons le, pour chaque valeur de l'incidence pour le système (1).

De toutes façons les coefficients du système (2) (en p, $\dot{\alpha}$ et $\dot{\beta}$ uniquement) peuvent en théorie être tous identifiés grâce aux essais dynamiques.

Lorsque l'on définit a priori un programme d'essais sur un montage complexe, il est important d'observer la valeur des coefficients de corrélation entre les variables d'un modèle de façon à favoriser l'observabilité séparée des paramètres qui leur correspondent. Dans ce but, on calcule donc en règle générale les coefficients de corrélation entre les couples de variables du modèle (termes de la matrice V). Cependant, ces coefficients de corrélation ne traduisent que des dépendances sur 2 variables. Aussi suggère-t-on de calculer les valeurs propres de la matrice de variance-covariance des variables (centrées réduites) qui peut être obtenue à partir de la matrice V en y supprimant la dernière ligne et la dernière colonne, lesquelles correspondent au coefficient aérodynamique. Ces valeurs propres traduisent "l'importance" de chaque direction principale du nuage des points expérimentaux dans l'espace des variables du modèle. Si la distribution de ces variables à travers le programme d'essais est isotrope, les valeurs propres seront toutes voisines de 1, c'est alors le cas idéal de la distribution sphérique d'un programme d'essais. Par contre, s'il existe une valeur propre bien plus petite que les autres, cela traduira une faiblesse dans la définition du programme d'essais, donc un risque de forte corrélation intervariables, c'est-à-dire un risque de non observabilité des coefficients dérivés correspondants.

Ayant défini a priori un programme, on calculera donc cette matrice et les valeurs propres, de façon à éventuellement le modifier pour en améliorer l'efficacité vis-à-vis du but visé. Ceci peut être réalisé facilement pour chaque valeur de l'incidence où l'on désire effectuer des identifications dynamiques.

4. RESULTATS ET PROBLEMES RENCONTRES

Le moyen d'essais tournebroche est opérationnel depuis 1979, mais son utilisation à des fins d'identification de paramètres de stabilité n'a vraiment commencé qu'en 1983. A ce jour, trois configurations d'avion ont pu être testées. Celles-ci étaient avec des voilures de type :

- aile delta,
- aile en flèche,
- aile trapézoïdale à grand allongement.

Les essais portant sur une géométrie d'avion à aile delta n'ont pas soulevé de problèmes sur l'estimation des paramètres de stabilité et ont pu être comparés avec des données issues d'autres souffleries et d'essais en vol. Ont ainsi pu être identifiés de manière satisfaisante, et en fonction de l'incidence, les valeurs des coefficients d'amortissement (C_{mq}, C_{lp}...), les termes croisés (C_{lr}, C_{np}) et les termes d'accélération ($C_{m\dot{\alpha}}$, $C_{z\dot{\alpha}}$...).

Pour la configuration aile en flèche l'identification fut un peu plus difficile. Des phénomènes d'origine aérodynamique peuvent aller à l'encontre de l'hypothèse de linéarité du modèle et rendre en effet plus délicate l'identification des paramètres de stabilité. Ils ont nécessité de prendre un certain nombre de précautions dans l'établissement du programme d'essais. Ce cas présente en effet une incidence de décrochage plus faible que l' aile delta. Or, au cours d'essais en rotation à λ important - donc à larges incursions dans le plan incidence-dérapage - des phénomènes liés au décrochage dynamique peuvent apparaître. Cela se traduit par un cycle d'hystérésis sur la mesure qui, même à faible incidence, est d'amplitude d'autant moins négligeable que l'incidence de décrochage (statique) est faible. Ces phénomènes sont évoqués et illustrés plus loin dans ce papier, dans le cadre des grandes incidences. Ils imposent des limitations sur les essais vis-à-vis de l'amplitude des mouvements en incidence-dérapage, afin que l'identification soit réalisée sur des essais où la dynamique a toujours un comportement linéaire et où le modèle postulé est toujours valable.

Enfin, des difficultés plus sérieuses ont été rencontrées en ce qui concerne l'avion à aile de grand allongement. La première est que, sur ce type de voilure, la rotation peut induire d'importantes variations d'incidence locale d'un bout de l'aile à l'autre. Dès lors une partie de la voilure peut décrocher, et l'hypothèse de linéarité du comportement aérodynamique vis-à-vis des taux de rotation est remise en cause. Cela impose des limitations sur le module du taux de rotation Ω lors de tels essais, d'où, par voie de conséquence, une perte sur la sensibilité de la mesure. La seconde difficulté soulevée est que ces voilures ont généralement un profil "laminaire" qui présente une très grande sensibilité à l'effet Reynolds. Cette caractéristique a pour conséquence de poser le problème de la similitude de l'écoulement sur l'avion grandeur et sur la maquette. Par ailleurs, cet effet Reynolds tend à réduire l'incidence de décrochage relevée sur maquette en statique, ce qui conduit encore à amplifier les difficultés évoquées pour le cas de l'aile en flèche.

En effectuant l'identification des termes de stabilité, nous avons pu obtenir des valeurs des coefficients d'amortissement en roulis tout à fait satisfaisants et conformes aux prévisions obtenues par le calcul et aux résultats d'essais en vol. Par contre, les valeurs calculées pour les termes d'amortissement de lacet s'écartent sensiblement des autres données. Les deux difficultés citées précédemment contribuent certainement à expliquer cet écart, mais à ceux-ci vient s'ajouter une autre raison pouvant être cause d'erreur. Elle tient dans le fait qu'au cours des essais en rotation, la vitesse de lacet n'apparaît jamais de façon pure. Elle n'existe qu'en présence d'une vitesse de roulis relativement importante en module. Comme l'envergure est importante, il s'ensuit vraisemblablement un écoulement à forte nature hélicoïdale sur les parties arrière de la maquette, ce qui nous écarte des hypothèses du modèle. L'identification des effets du roulis n'en est pas affectée , mais celle relative à la vitesse de lacet ne correspond pas alors à des coefficients dérivés provenant d'un point de vol équilibré faiblement perturbé, mais à ceux provenant d'un vol à fort taux de roulis (du type tonneau) faiblement perturbé en lacet.

5. EXTENSION DE LA CINEMATIQUE

5.1 Le montage "TETA 3"

Les contraintes inhérentes au montage décrit précédemment - relations linéaires entre p et r (resp. p, r et $\dot{\beta}$) pour les rotations stationnaires (resp. instationnaires) à incidence donnée - peuvent être levées en introduisant le rayon de giration R et nous ont conduits à créer dans la cinématique tournebroche un degré de liberté supplémentaire par une articulation nommée "TETA 3", permettant de faire pivoter la maquette autour d'un axe horizontal. Une combinaison adaptée des angles Θ_2 et Θ_3 permet d'amener la maquette aux faibles incidences tout en affichant un rayon de giration R important, bien supérieur à celui permis initialement par le montage (planche 1). Le tournebroche n'autorisait auparavant qu'un rayon de vrille faible (R = 0.2 m) par coulissement du chariot supportant le secteur angulaire, le dard et la maquette. Ce rayon peut être porté jusqu'à 0.9 m (Θ_2 = 45, Θ_3 = -45), ce qui correspond par ailleurs à la limite admissible d'utilisation, étant donné le diamètre de la veine (4 m) et l'envergure des maquettes (planche 5).

L'introduction de cette nouvelle variable cinématique va évidemment modifier l'expression des variables aérodynamiques. En posant $\Theta = \Theta_2 + \Theta_3$, l'expression des taux de rotation reste néanmoins inchangée :

$$p = \Omega \cos \Theta$$

$$q = \Omega \cos \Phi \sin \Theta$$

$$r = \Omega \sin \Phi \sin \Theta$$

Les liaisons cinématiques peuvent être mises en évidence en exprimant la vitesse du centre de gravité maquette par rapport à l'air :

$$\vec{V_c} = \vec{V_0} + \vec{\Omega} \wedge \vec{OC}$$

$\vec{V_0}$ vitesse du vent dans la soufflerie
$\vec{\Omega}$ vecteur rotation instantanée
$\vec{OC}$ vecteur excentrement

La dérivation de cette expression dans le repère maquette permet d'aboutir à trois expressions scalaires dont la deuxième s'exprime ainsi :

$$\dot{V} \sin \beta + V \cos \beta \left[\dot{\beta} + r \cos \alpha - p \sin \alpha \right] = q\,(p\,a + r\,c) - b\,(p^2 + r^2)$$

(a, b, c composantes de $\vec{OC}$ dans le repère maquette)

Si le rayon de vrille est nul, a, b et c sont nuls. La vitesse V soufflerie est constante, donc $\dot{V}$ est nul : on retrouve alors l'équation de liaison entre $\dot{\beta}$, p et r

$$\dot{\beta} + r \cos \alpha - p \sin \alpha = 0$$

Avec un rayon de vrille non nul et un choix adéquat d'essais, il est possible d'obtenir différentes valeurs du second membre de l'équation de liaison. On obtient ainsi une meilleure distribution des variables $\dot{\beta}$, p et r, ce qui contribue à "casser" la liaison linéaire qui existait auparavant.

L'intérêt de ce nouveau degré de liberté de la cinématique du montage peut déjà être bien mis en relief au travers des essais en rotation à $\lambda = 0$. Auparavant nous avions $r = p \operatorname{tg} \alpha$, l'incidence étant imposée, r et p étaient toujours proportionnels quelle que soit la valeur du taux de rotation Ω. En particulier à incidence nulle la vitesse de lacet (pour un essai stationnaire $\dot{\alpha} = \dot{\beta} = 0$) était donc obligatoirement nulle.

Mais à présent l'existence d'un rayon de giration modifie la valeur de l'incidence réelle. Une variation de l'incidence est due à la vitesse induite par le mouvement circulaire uniforme. Et en particulier il est donc possible de réaliser un essai stationnaire à vitesse de lacet non nulle et à incidence réelle nulle.

La réalisation d'essais en rotation avec un rayon de giration paramétrable permet donc de réaliser, à incidence donnée, un ensemble de sollicitations en roulis-lacet tel que les 2 vitesses angulaires correspondantes p et r ne soient plus constamment proportionnelles.

Aussi peut-on alors entrevoir la possibilité de décorréler $\dot{\beta}$, p et r et d'effectuer des identifications séparées pour les paramètres de stabilité concernés et pour chaque valeur de l'incidence.

5.2 Choix d'un programme d'essais

La complication des formules donnant incidence et dérapage, induite par ce degré de liberté supplémentaire nous a conduits à établir la construction géométrique de la planche 6 qui, si elle ne constitue qu'une approximation, est bien suffisante pour permettre de dresser un programme.

On peut illustrer l'utilisation de cet abaque dans les cas particuliers d'essais à $\lambda = 0$ pour mettre en évidence d'une part son utilité pour guider le choix d'un programme d'essais, et d'autre part le rôle du rayon de giration R.

Supposons que l'on s'intéresse à une tranche d'incidence de valeur moyenne α_0 et que l'on se fixe une limite β_{max} en dérapage.

- En prenant $\Theta = \alpha_0$, $\Phi = 0$, pour différentes valeurs de Ω/V, on décrit dans le plan (α, β) la droite $\alpha = \alpha_0$; alors $\beta \simeq \Omega R/V$. Les taux de roulis et de lacet sont liés par la relation $r = p \operatorname{tg} \alpha_0$.

- En prenant $\Theta = \alpha_0$, $\Phi = 90$, on décrit dans le plan (α, β) la droite $\beta = \Theta$. En particulier, en choisissant Ω et V tels que $\alpha_0 = \frac{\Omega_0 R}{V}$, on atteint le point d'incidence α_0. Le taux de lacet est nul et le taux de roulis est donné par $p = \Omega \cos \Theta$.

- Pour des valeurs de Φ quelconques, en choisissant judicieusement les valeurs de Θ et Ω, on peut obtenir dans la limite du dérapage admissible des points de mesure à l'incidence $\alpha = \alpha_0$, avec la relation entre les taux de roulis et de lacet $r/p = \cos \Phi \operatorname{tg} \Theta$. En particulier, des valeurs de Φ comprises entre 180 et 360° permettent d'atteindre des rapports r/p négatifs (planche 7).

On voit donc que l'intérêt du rayon de giration R est de pouvoir "piloter" l'incidence et/ou le dérapage, à l'aide de Ω et de V, et ce dans des plages de variations importantes. On obtient par exemple pour $\Phi = 90°$ $\Omega = 400$ d°/s et V = 30 m/s, pour un rayon R = .7 m, une variation d'incidence supérieure à 9 degrés.

Par ailleurs, les trois cas d'essais précédemment décrits permettent d'obtenir une dispersion des valeurs (p, r) qui, dans le cas d'un rapport signal/bruit satisfaisant, rendra possible l'identification des termes d'amortissement à l'aide des seuls essais stationnaires.

Au cours d'un essai en rotation avec $\lambda \neq 0$, le point courant dans le plan (α, β) décrit une trajectoire pouvant être assimilée à un cercle de rayon λ, de centre le point courant correspondant à $\lambda = 0$ (rotation stationnaire).

On peut donc choisir des essais de ce type en fixant les paramètres cinématiques de manière que la trajectoire dans le plan (α, β) passe par une incidence α_0 fixée, pour un dérapage admissible, et avec une valeur de $\dot{\beta}$ suffisamment importante pour sensibiliser les mesures.

5.3 Procédures d'essais et acquisition des données

L'existence d'un rayon de vrille non négligeable remet en question la procédure traditionnelle des essais qui consiste à faire la différence entre le torseur mesuré au cours d'un essai avec vent, et celui mesuré pour un essai sans vent, à configurations cinématiques identiques. En effet, ceci suppose que les efforts aérodynamiques supportés par la maquette au cours de la séquence à vitesse de soufflerie nulle sont eux aussi nuls. Ce qui est certainement vrai pour les balayages en λ (quasi statiques) l'est peut-être moins pour les rotations (amortissement de l'air ambiant sur la maquette) mais l'est certainement encore moins pour

les essais en rotation comportant un rayon de giration de la maquette, car il existe alors, au cours de tels essais, une vitesse relative de la maquette par rapport à l'air au repos qui, même si elle est faible (max : 7 à 8 m/s) peut induire au niveau balance un signal non négligeable et mesurable. Il convient alors d'envisager une méthode appropriée qui permette de prendre en compte ces efforts.

Au cours d'un essai la balance 6 composantes fournit un signal électrique provenant de la superposition de différents effets :

- les "zéros électriques", tensions qu'on mesurerait si aucun effort n'était appliqué sur la balance,
- les tensions induites par les efforts de gravité,
- les tensions induites par les efforts d'inertie,
- les tensions induites par les efforts aérodynamiques : c'est ce que l'on cherche.

Si on connaît la masse, le centrage et les inerties des parties pesées par la balance (maquette, pièces de liaison, partie pesée balance) on pourra soustraire à la mesure globale les efforts d'inertie et de gravité.

Or, la masse, le centrage et les termes d'inertie du système pesé peuvent être identifiés avec la balance rotative par une série d'essais appropriés. En effet, des essais statiques sans vent réalisés pour différentes attitudes de la maquette permettent de retrouver la masse et le centrage.

L'identification des termes inertiels nécessite des essais en rotation sans vent pour différentes configurations cinématiques. Pour chacune de ces dernières, on effectue 2 rotations à taux de rotation opposés ($\pm \Omega$). On fait en effet l'hypothèse simple que les moments aérodynamiques pouvant être mesurés sont des termes d'amortissement et antisymétriques vis-à-vis de Ω. Ils pourront donc être éliminés en considérant des couples d'essais en rotation (Ω^+, Ω^-). Connaissant masse et centrage, on en déduit par moindres carrés les termes inertiels intervenant dans les équations d'équilibre, à savoir : $I_{zz} - I_{yy}$, $I_{yy} - I_{xx}$, $I_{xx} - I_{zz}$ et I_{zx}. Cette procédure a le double avantage suivant :

- elle permet d'identifier et d'extraire les efforts aérodynamiques réels rencontrés au cours des essais en rotation,

- elle évite de réaliser des essais en rotation sans vent et diminue le volume et la durée des essais. La procédure est en effet alors limitée à la réalisation d'une séquence statique sans vent (pour identifier les zéros électriques) et de la séquence dynamique avec vent.

Ce dispositif "Θ_3" a été monté récemment à l'IMFL, et des essais ont été effectués sur une maquette ayant déjà fait l'objet d'une campagne "classique" d'identification des termes dérivés sur le montage tournant de l'Institut. La comparaison entre les résultats peut être faite en considérant la relation linéaire liant auparavant les variables p, r et β.

En effet, les essais sans rayon fournissent, comme nous l'avons vu, les coefficients $C_{ip} + C_{i\dot{\beta}} \sin\alpha$ et $C_{ir} - C_{i\dot{\beta}} \cos\alpha$. Or, ces valeurs peuvent être recalculées à partir des identifications de C_{ip}, C_{ir} et $C_{i\dot{\beta}}$ réalisées avec la même maquette sur des essais disposant du degré de liberté R rayon de giration.

Les résultats ont montré un très bon accord entre les 2 bases de coefficients identifiés.

Par ailleurs, une estimation des efforts aérodynamiques rencontrés lors des essais "sans vent" a montré que :

- ceux-ci étaient faibles, voire négligeables, pour les essais sans rayon. Mais cette conclusion n'est certainement pas générale, elle dépend beaucoup des tailles maquette (envergure) et des taux de rotation appliqués,

- par contre, il convenait de les prendre en compte pour les essais avec rayon avant d'effectuer des identifications sur les mesures.

6. DECROCHAGE DYNAMIQUE SUR BALANCE ROTATIVE

Jusqu'ici nous avons parlé d'identification de paramètres de stabilité dynamique et de modèle aérodynamique linéaire. Nous avons à ce propos assez insisté sur l'intérêt cinématique de la rotation oscillatoire (rotation continue mais avec α, β pulsés) et du degré de liberté λ.

A présent, nous allons également signaler un autre intérêt du degré de liberté λ au travers cette fois d'effets dynamiques instationnaires non linéaires à grande incidence.

L'un des phénomènes aérodynamiques grande incidence qui a peut-être suscité le plus d'intérêt ces dernières années dans la communauté aéronautique est le décrochage dynamique. De nombreux travaux ont été réalisés sur cette question et il existe des publications variées sur ce sujet. L'essentiel de la connaissance provient de recherches expérimentales.

Mac Croskey [4] décrit les principales caractéristiques physiques de ce phénomène relevé sur un profil oscillant en tangage. Celui-ci se caractérise principalement par une augmentation très sensible de l'incidence de décrochage en dynamique ainsi que par un effet d'hystérésis important (planche 8) sur les coefficients longitudinaux. Celui-ci est attribué physiquement au développement et au déplacement sur l'extrados d'un vortex qui induit des fluctuations du champ de pression non linéaires.

Le même type de phénomène a pu être mis en évidence lors de mouvements de type "pilonnement" (plunging motion) [5], et les différences entre ces deux sollicitations, qui apparaissent dans certains cas, ont été attribuées à un effet de bord d'attaque. Pareillement, des fluctuations de vitesse et d'incidence sur un profil effectuant des mouvements de type "tamis" ont également révélé l'existence de très forts effets

instationnaires [6] en particulier lorsque l'incidence dépasse l'incidence du décrochage stationnaire.

Ici nous n'avons l'ambition que d'apporter quelques informations expérimentales sur ce sujet, obtenues sur le montage tournebroche, c'est-à-dire au cours d'essais sur une maquette effectuant un mouvement de rotation continue autour d'un axe incliné par rapport au vecteur vitesse : la vitesse est constante en module alors que l'incidence et le dérapage évoluent sinusoïdalement et en quadrature au cours d'un cycle.

Les résultats de mesure obtenus avec ce type de sollicitation montrent le même type de phénomène caractérisé par un effet hystérésis important et par un effet dynamique important en module et directement lié aux variations d'incidence. En effet, celui-ci se révèle indépendant des vitesses angulaires p, q, r qui sont constantes (planche 9).

On peut noter une bonne répétitivité du phénomène et une quasi indépendance de celui-ci vis-à-vis du sens de rotation. Les courbes obtenues à Ω^+ et à Ω^- sont tout à fait similaires et superposables. De plus, les mesures obtenues en chaque point d'un essai à Ω^+ sont sensiblement identiques pour les points de l'essai à Ω^- ayant la même loi $\alpha(t)$. Comme corrélativement les lois $\beta(t)$ sont opposées, ceci renforce l'idée de l'indépendance de l'effet de dérapage sur les coefficients longitudinaux même en dynamique décroché.

Cet effet apparaît plus important aux grandes incidences, à ce titre la comparaison des planches 9 et 10 est assez révélatrice.

La zone d'incidence "moyenne" joue un grand rôle sur le phénomène. Le comportement du coefficent de portance en particulier dépend de cette valeur. C'est lorsque l'évolution de l'incidence recouvre à la fois la zone linéaire et la zone décrochée que l'on retrouve un effet de "prolongement " de la zone linéaire qui se traduit par une augmentation sensible de l'incidence de décrochage (planche 11).

Les résultats présentés ici illustrent le fait que sur avion on peut rencontrer des phénomènes aérodynamiques instationnaires importants en module. Ceci est surtout vrai dans la région des grandes incidences comme nous venons de le voir. Par ailleurs, il y a toute raison de penser que des phénomènes de cette intensité se rencontrent, ou peuvent se produire, sur des phases transitoires dynamiques du type entrée en vrille, sortie de vrille, autotonneaux... où l'incidence évolue rapidement. Cette évolution de l'incidence est d'ailleurs en général liée à l'apparition d'un mouvement de rotation de l'avion de grande amplitude, où les vecteurs vitesse et rotation instantanée ne sont plus colinéaires. Or nous venons de voir que l'existence d'un angle λ entre ces deux vecteurs modifie très sensiblement les efforts aérodynamiques sur l'avion, et ceci pour des taux de rotation tout à fait réalistes, les vitesses angulaires réduites ($\Omega b/V$) rencontrées sur avion sont très comparables à celles simulées sur le montage. Ceci nous laisse à penser que pour pouvoir simuler ou prédire ces différentes phases et évolutions à grande incidence il sera nécessaire d'effectuer des mesures dynamiques au cours d'essais en rotation continue où les vecteurs vitesse et rotation ne sont pas colinéaires.

7. CONCLUSION

L'utilisation du moyen d'essais "tournebroche" pour l'étude du comportement aérodynamique d'un avion et la recherche de paramètres de stabilité dynamique nous ont permis de mettre en évidence les points suivants :

- l'intérêt des simulations dynamiques de mouvements pour lesquels les vecteurs vitesse et rotation ne sont pas colinéaires,

- la possibilité offerte par les essais en rotation à λ non nul (λ = angle entre les vecteurs vitesse et rotation) pour identifier les coefficients du modèle linéaire autour d'une trajectoire quasi rectiligne,

- l'intérêt de l'utilisation des méthodes d'analyse multidimensionnelle pour l'optimisation d'un programme d'essais et pour l'identification des paramètres de stabilité,

- les précautions à prendre dans un programme d'essais vis-à-vis de la géométrie de l'avion, et des caractéristiques aérodynamiques qui en découlent, pour conserver les hypothèses de linéarité du modèle mathématique,

- l'intérêt des essais en rotation avec excentrement de la maquette, permettant d'atteindre l'ensemble des coefficients du modèle polynômial linéaire avec un unique moyen d'essais,

- la possibilité de mise en évidence de phénomènes liés au décrochage dynamique au cours de rotations continues, pouvant s'apparenter à certaines phases transitoires du vol à grande incidence.

CONCLUSION

Studying aircraft dynamic behaviour and identifying stability parameters using the "tournebroche" test apparatus has allowed to outline the following points of interest :

- dynamic simulations of aircraft movements for the case where the lines of action of the velocity and rotational vectors are not parallel,

- the possibility provided by rotational tests with a non zero value of λ (angle formed by the velocity and rotational vectors) in identifying the linear mathematical model coefficients in the case of a quasi linear path,

- multidimensional analysis methods used in optimizing test programs and in identifying stability parameters,

- the tests program precautionary measures concerning the aircraft geometrical layout, and consequently the aerodynamic characteristics, to be taken in order to keep the mathematical model linearity assumption valid,

- rotational tests with a giration radius, allowing the whole set of linear polynomial model to be identified with the unique test apparatus,

- the possibility to show phenomena related with the dynamic stall during continuous rotations, similar (in certain cases) to transcient motions.

BIBLIOGRAPHIE

[1] K. ORLIK-RUCKEMANN
"Review of Techniques for Determination of Dynamic Stability Parameters in Wind Tunnels"
AGARD LS 114

[2] M. TOBAK, L.B. SCHIFF
"Aerodynamic mathematical Modeling. Basic Concepts"
AGARD LS 114

[3] P. BERTIER, J.M. BOUROCHE
"Analyse des données multidimensionnelles"
P.U.F.

[4] W.J. Mc CROSKEY
"The Phenomena of dynamic Stall"
VKI LS 1981-4

[5] L.E. ERICSSON, J.P. REDING
"Unsteady Flow Concepts for dynamic Stall Analysis"
J. of Aircraft - Août 1984 - p 601

[6] D. FAVIER, L. MARESCA, J. REBOUT
"Dynamic Stall due to Fluctuations of Velocity and Incidence"
AIAA Journal - Juillet 1982

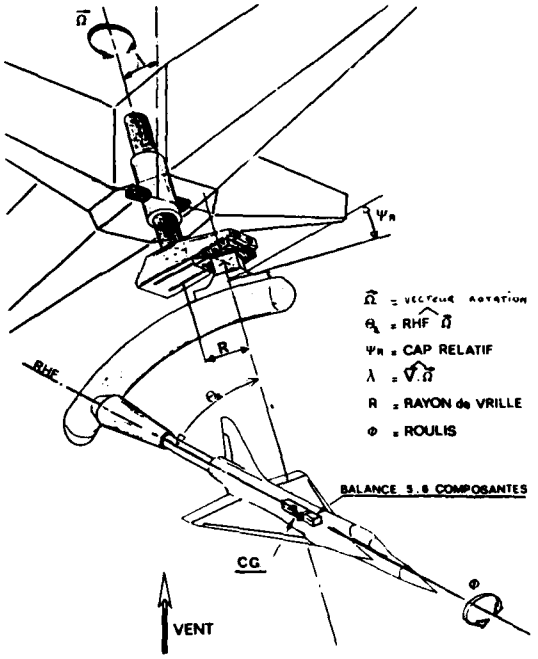

Planche 1 - Cinématique du moyen d'essais "Tournebroche"

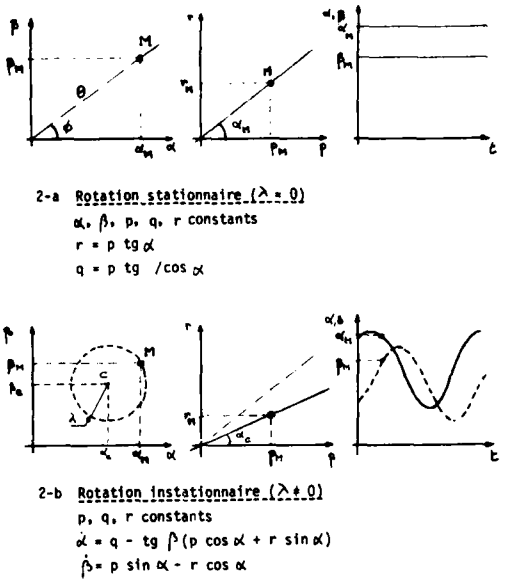

Planche 2 - Essais dynamiques sur tournebroche

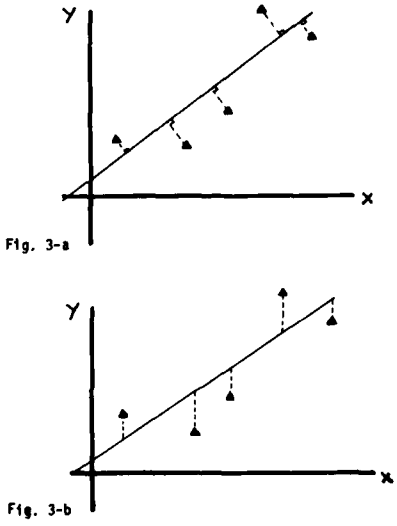

Planche 3 - Illustration dans $\mathbb{R}^2$ des méthodes d'identification par moindres carrés (3-b) et moindre inertie (3-a)

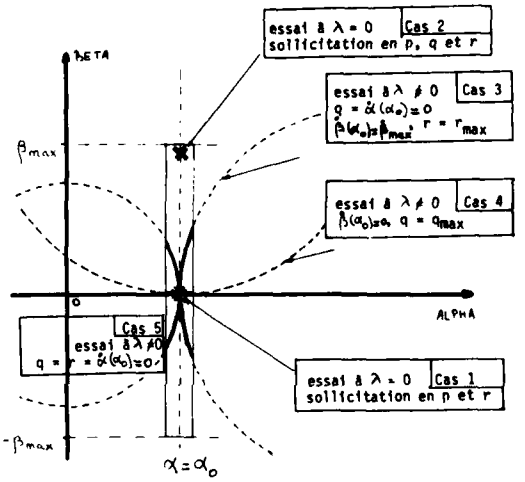

Planche 4 - Programme minimum d'essais pour l'identification des coefficients dérivés à une incidence donnée

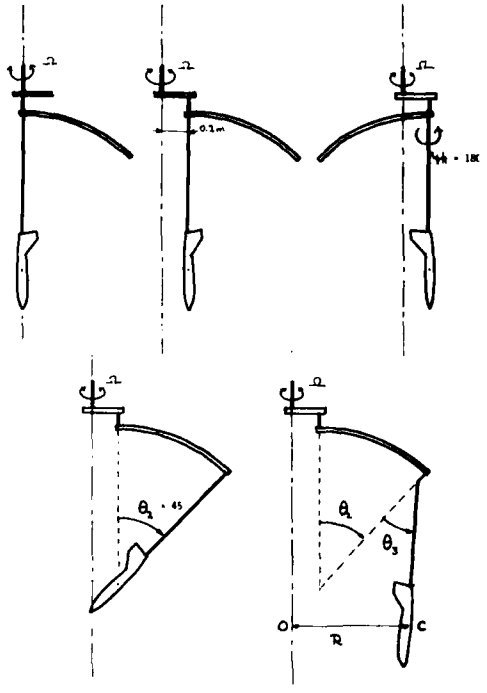

Planche 5 - Principe du dispositif "TETA 3"

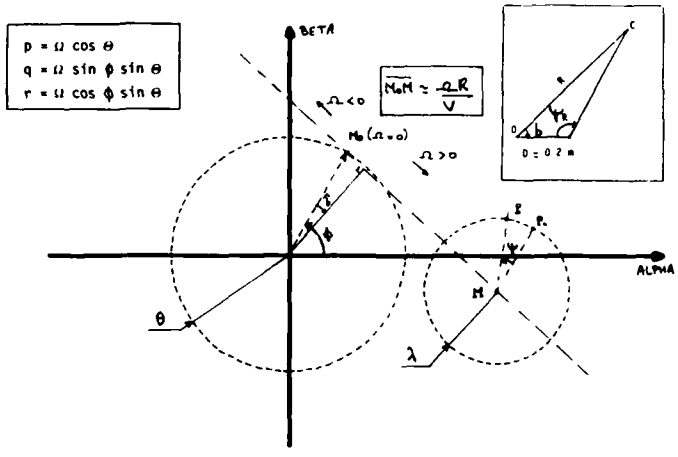

Planche 6-a - Construction géométrique dans le plan (α,β) relative au dispositif "TETA 3"
Cas général

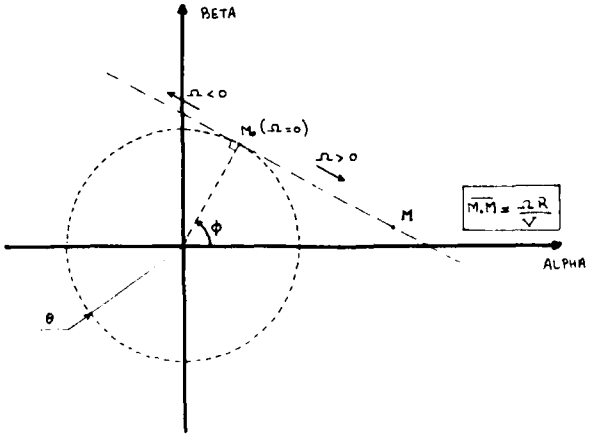

Planche 6-b - Construction géométrique relative au dispositif "TETA 3"
Cas particulier $\Psi_R = 180°$, $\lambda = 0$

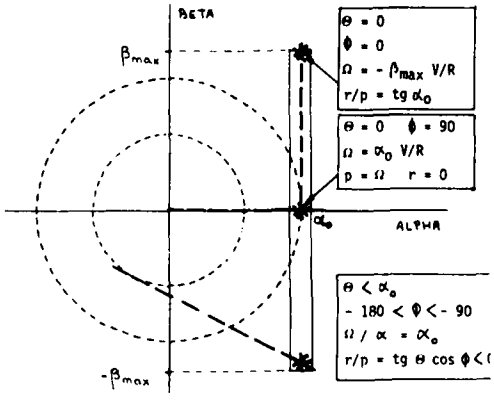

Planche 7 - Programme minimum d'essais en rotations stationnaires pour l'identification des termes d'amortissement

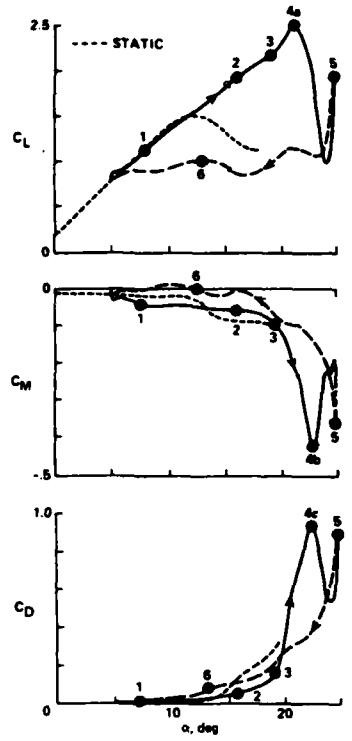

Fig. 2. Dynamic stall events on the Vertol VR-7 airfoil at $M_\infty = 0.25$, $\alpha = 15° + 10° \sin \omega t$, and $k = 0.10$.

Planche 8 - Extrait de [4]

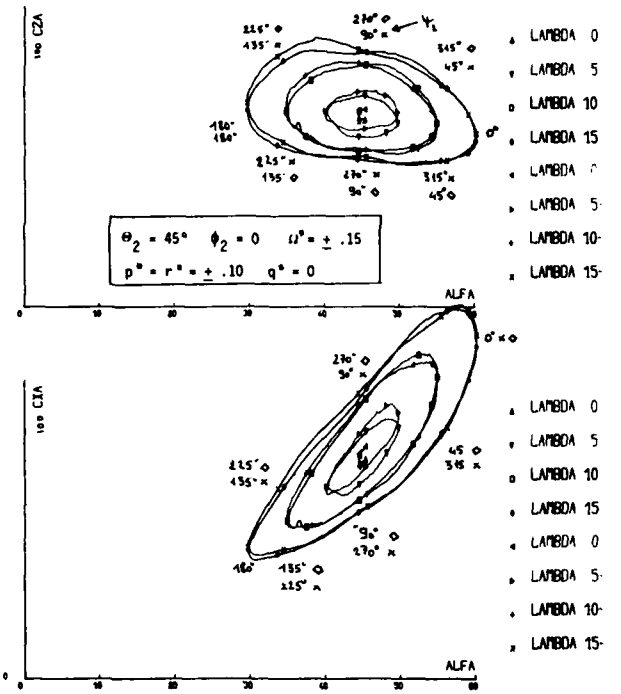

Planche 9 - Rotations instationnaires
Incidence centrale 45°

$\alpha \simeq \alpha_0 + \lambda \sin \omega t$
$\beta \simeq \lambda \sin \omega t - \pi/2$

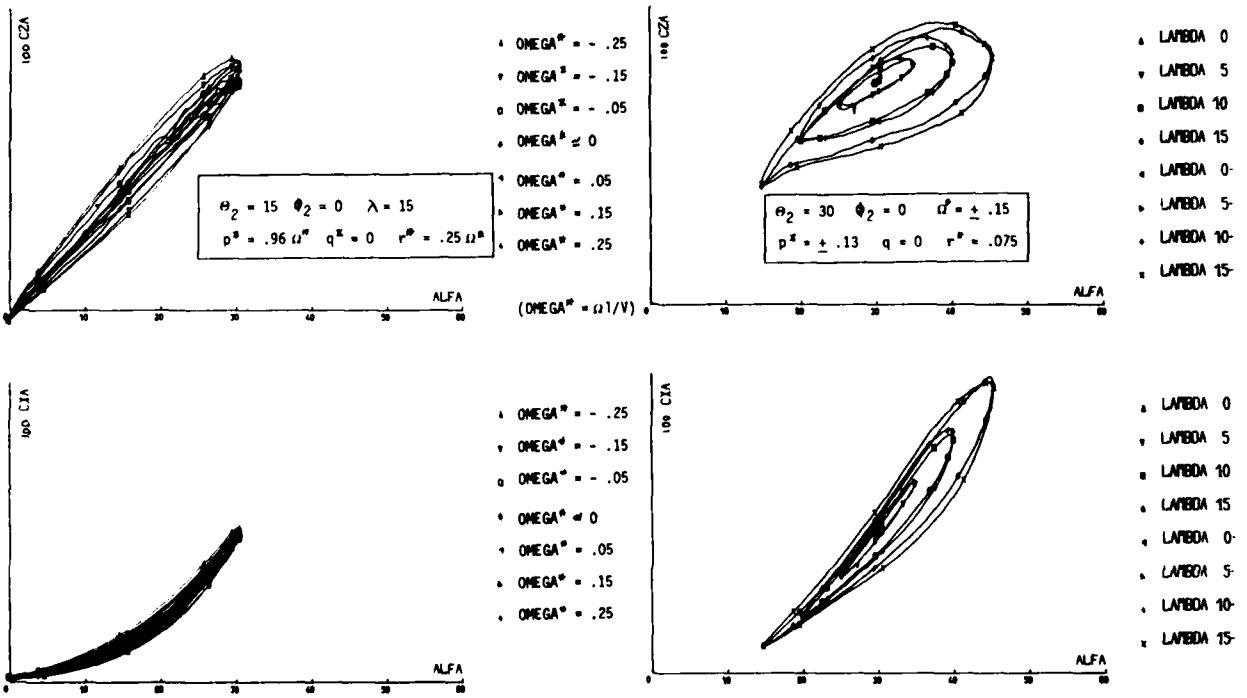

Planche 10 - Rotations instationnaires
Incidence centrale 15°

Planche 11 - Rotations instationnaires
Incidence centrale 30°

GENERATION OF TWO-DIMENSIONAL GUST FIELDS IN SUBSONIC WIND-TUNNELS

by

B. Krag
Institut für Flugmechanik
Deutsche Forschungs- und Versuchsanstalt
für Luft- und Raumfahrt e.V. (DFVLR)
D 3300 Braunschweig-Flughafen, West Germany

and

W. Wegner
Institut für Strömungsmechanik der TU Braunschweig
D 3300 Braunschweig, West Germany

SUMMARY

For a variety of flight-vehicles, problems during flight in turbulence at subsonic speeds are expected. This concerns mainly slow flying helicopters, tilt rotorcraft, aircraft manoeuvring at high angles of attack, wing in ground effect vehicles and aircraft with active controlled wings. The investigation of these problems still poses large difficulties and the analyst very rapidly enters domains where computational methods fail and where wind-tunnel experiments are necessary. This raises the problem of simulating atmospheric turbulence in a wind-tunnel. Until now, no fundamental investigations of the problem of gust generation in wind-tunnels have been undertaken. On behalf of considerations by the Deutsch-Niederländischer Windkanal (DNW) to install a gust generator, principal investigations of gust generation were started in a model subsonic wind-tunnel of the DFVLR in Braunschweig. In order to recognize the influence of the main parameters, like number of lift generating wings, chord length, trailing edge-flap or jet-flap, constant chord wing or side-wall mounted winglets, four different types of gust generators were investigated. The gust field was harmonically oscillating. Frequency response measurements of the gust angle of attack were made, covering the complete volume of the test section. Additionally the flow field in the wind-tunnel behind harmonically oscillating gust generator-flaps was calculated. The results were compared with the measurements.

1. INTRODUCTION

The extreme demands on modern airplanes and the introduction of active control techniques have led to a greater emphasis on dynamic wind-tunnel testing techniques. In measuring non-stationary aerodynamic forces wind-tunnel model balances are employed which allow several motion degrees of freedom for the model, whilst the wind-tunnel airflow remains uniform and steady.

In many active control applications, however, a more exact knowledge of the influence of gusts on the aircraft aerodynamics is required. Whilst a reproduction of the detailed aerodynamic load distribution on an aircraft can be obtained from an appropriately constructed model, a detailed reproduction of atmospheric disturbances is not generally available in the wind-tunnel. Turbulence or gusts can be generated, however, through the use of an appropriately designed gust generator.

2. THE APPLICATION OF GUST GENERATORS

The application of gust generating devices is conceivable in subsonic, transonic and supersonic flow. Gust generators have either been built or planned for all these flow regimes. In all three regimes there are applications for which gust generators would be of benefit. In subsonic flow these are:

- the development of active control systems for the low speed regime,
- the interaction of rotary wing systems with gusts,
- the effects of gusts on ground effect vehicles,
- the treatment of gust response and gust penetration problems.

In transonic flow:

- the development of active control systems,
- the treatment of gust response and gust penetration problems,
- engine intake flow investigations.

Gust generators have been developed over a number of years, in various forms, and applied to specific problems:

- Development and testing of flutter damping systems for large aircraft (Refs.1,2,3).
- Evaluation of gust loads on flexible aircraft (Ref. 4).
- Investigation of the gust sensitivity of tilt rotors (Refs. 5, 6).
- Testing of gust alleviation systems (Refs. 7, 7a, 8).
- Determination of Küssner functions for delta wings in unsteady flows (Refs. 9, 10).

The majority of current applications in industry and the research institutions reflect a trend towards the use of gust generators in transonic flow. At low speeds a considerable requirement for gust generators in connection with helicopter flight is expected. Here the study of the interference of gusts on rotors in low speed flight is emphasized, for which a computational method is not available at present. The current interest in gust generators for low speed wind-tunnels is indicated in publications relating to already built or newly planned equipment of this type.

Considerations leading to a recommendation to install gust generators in transonic and subsonic facilities are at present concentrated on the S1-Modane tunnel, on the one hand, and the DNW on the other. The following possible applications relate to a gust generator in the DNW:

- gust interference on a helicopter rotor,
- gust interference with a tilt rotor at low speeds,
- the affect of helicopter rotor Higher Harmonic Control (HHC) systems in turbulence,
- testing of AC systems for low speeds (effects on flight control systems during approach flight conditions, gust alleviation systems ... etc.),
- testing and calibration of sensors,
- behaviour of Mini RPV's in turbulent air,
- investigation of gust penetration effects on complex aircraft geometries,
- gust penetration of combat aircraft at high angles of attack,
- engine intake flow disturbances at high angles of attack,
- effects of gusts on ground effect vehicles,
- effects of gusts on VTOL aircraft (stabilisation systems, recirculation ... etc.).

Various other applications could be named for gust generators in subsonic flight conditions. Not all of the applications listed are currently a subject of investigation in German industry and research institutions; but their urgent realization might become, however, somedays necessary.

3. REQUIREMENTS FOR A GUST GENERATOR

The requirements for a gust generator for the operation in subsonic wind-tunnels result from the topics already listed. From these the maximum gust frequency, gust amplitude, desired gust profiles and distributions can be specified. In addition to these specific requirements, others of a qualitative nature and requirements simply in terms of cost and usefulness must be determined.

These requirements involve the quality and geometric properties of the gust patterns, which themselves depend on the design of the gust generator and the particular conditions within a given tunnel.

A gust generator should simulate the conditions of the atmospheric turbulence in the wind-tunnel. The atmospheric turbulence is generally considered as stationary and isotropic (Ref. 11). In isotropic turbulence the characteristic properties of the gust field in terms of variance, autocovariance and power-spectral-density, remain constant in all spatial directions. In a stationary gust field these characteristic properties are independent of time. The gust frequency, which an aircraft feels during flight in turbulence therefore depends solely on the gust wavelength and the velocity of the aircraft.

The main requirements for the quality of a gust field therefore are its isotropic and stationary properties. There are other requirements which are either of little importance, or which must be disregarded with respect to the enormous cost of their realization. The qualitative requirements of a gust generator are summarized in Table 1. This implies that the typical form of the gusts is not changed as they traverse the tunnel test section, otherwise the interpretation of the test results is beset with considerable difficulty. Similar importance attaches to the problem of matching the velocity of propagation of the gusts to the wind-tunnel speed. If these velocities are not matched then model and full scale conditions will not correspond. In addition, correspondence between the gust profile and the form of the gust generator input signal would have to be achieved. This would permit the representation of various gust profiles (sine, impulse, ramp, stochastic gusts). The gust field should also exhibit a constant behaviour in terms of vertical distribution, so that vertical movement of the model will not entail passage through zones of varying gust intensity. Also the dependence of the gust field on the gust generator amplitude and tunnel velocity should display a linear relationship in order also to generate complicated gust profiles in the tunnel, corresponding to natural atmospheric turbulence.

Another requirement is a constant gust amplitude in lateral direction, which is desirable. But experience with gust generators indicate that the tunnel walls influence the gust field in their vicinity. Accurate knowledge of the lateral distribution of the gust amplitude does, however, eliminate restrictions which otherwise would be imposed. The task of providing an arbitrarily adjustable lateral distribution of gusts certainly adds considerably to the cost involved in the construction of a gust generator.

Most applications are, however, covered by the provision of a two-dimensional gust field. Undesirable characteristics result from the frequency dependency of the gust field and the superimposed longitudinal turbulence. Experience shows that neither of these effects can be avoided, but investigations are required to devise means of keeping

them as small as possible.

4. POSSIBLE LAYOUTS FOR GUST GENERATING EQUIPMENT

A gust generating facility should be capable of producing a two-dimensional, isotropic and stationary gust field. It should be possible to generate different gust forms with various amplitudes. The latter requirement demands the facility to be built as a servo system. A gust is the superposition of a time variable velocity component on the steady wind-tunnel flow. The gust produced in this way is transported with the tunnel flow and reproduces the same effect on the model as in the natural turbulence in full scale conditions when an aircraft penetrates a gust front. The gust generator therefore must always be upstream of the model in the test section. Other conceivable forms of gust generation, possibly by lateral injection of air into the tunnel, or by a variable deformation of the tunnel walls are very costly and are excluded for this reason. A review of gust generators already constructed can be found in Ref. 12. Most of these are of the first named type: a vertical flow component is superimposed on the tunnel flow upstream of the model. This vertical flow component subsequently traverses the test section, where possible in an unmodified condition. A common method of generating the vertical velocity components is through the use of adjustable lifting surfaces whose fixed and wake vortex systems generate these cross flow components.

The application of this principle leads to the development of relatively simple and hence cost effective gust generators. Because the generation of cross components in the flow is necessarily coupled with the generation of lift by the lifting surfaces, they are subject to the principles of unsteady aerodynamics. This implies a dependency on frequency for the gust field and therefore the requirement for a stationary ("frozen") gust field is hurt.

A characteristic parameter for the influence of unsteady effects is given by the non-dimensional frequency $\omega^* = \omega\, l_\mu / V_o$ where l_μ is the chord of the lifting surface and V_o is the tunnel velocity. The correct choice of l_μ and V_o, however, enables some influence on the frequency dependency of the gust field to be obtained, which can be used to advantage. Various layouts are conceivable for the gust generating wings:

- completely movable wings,
- wings with moving trailing edge flaps,
- wings with jet flaps,
- separate, movable vanes.

All these possibilities have their advantages and disadvantages, which must be weighed against a particular application. In planning a gust generator care must be taken to ensure that undesirable effects which could adversely effect the quality of the gust field are avoided. These effects include, in particular:

- turbulence behind jet flaps, caused by the injection of a jet with a relatively high velocity,
- turbulence which can arise due to flow separations in the boundary layers in corners and at edges,
- elastic vibrations of the wing, which also lead to variations in lift.

Another source for undesired disturbances of the air flow are slotted tunnel walls. These allow an exchange with the surrounding air outside of the test section. The investigations have shown, that air is sucked in and blown out through the slots, when the gust generator is operating. This causes much turbulence near the tunnel walls, with increasing intensity downstream of the gust generator. Therefore the following points are of importance with the design of a gust generator:

- profiles of good aerodynamic efficiency should be employed,
- the manufacture of these profiles must be to an appropriately high standard,
- the construction must be rigid enough to avoid elastic vibrations in the relevant frequency range,
- corners, edges and other potential sources of turbulence due to flow separation should be avoided,
- the gust generator should be installed at a position in front of the model so that the latter is not affected by the flaps wake,
- excitation of wind-tunnel pumping oscillations should be avoided,
- the air exchange between tunnel and external atmosphere through perforated or slotted tunnel walls should be minimized in order to avoid the superposition of longitudinal gusts,
- blockage effects, due to the use of too many wings or wings which are too voluminous, should also be avoided.

Special mention should be made of the gust generator with separate, opposed winglets. This type of gust generator system causes very little blockage and can even be used to generate rolling gusts, by antimetric deflection of the winglets. The wing tip vortices are responsible for the generation of vertical flow components in this case.

However, a uniform, homogeneous gust field is only established at some relatively large distance downstream of the generator and then only over a small part of the tunnel width.

5. DFVLR INVESTIGATIONS WITH GUST GENERATORS IN THE MODEL SUBSONIC TUNNEL (MUB)

The intention of installing a gust generator in the DNW tunnel led to the requirement to further investigate the problem of gust generation in wind-tunnels. Although some gust generators have been built, worldwide, available documentation on them remains inadequate to make scientific comparisons. The tests involved were a principal investigation in which the types of gust generators presented in the previous section were tested under similar conditions and compared with each other. The tests were undertaken in 1981 in the DFVLR model subsonic tunnel (MUB) at Braunschweig. This particular tunnel was selected because it has a slotted test section like the DNW (12 % ratio) [12a].

The experimental layout is shown in Fig. 1, together with gust generator 1. The test section is of square cross section (1.3 m x 1.3 m) and 2.4 m long, with the gust generators sited aft of the nozzle. The wings are arranged symmetrically and positioned at 25 % and 75 % of the test section height. Electro-hydraulic actuators are used to deflect the gust generators, to provide a maximum value $\beta = \pm 40^{\circ}$. The maximum achievable gust frequency is 16 Hz. The 16 Hz bandwidth is initially adequate for the principle investigations, allowing a relatively large range of reduced frequencies ($0 < \omega^* < 2.0$) to be covered. The available actuator power limited the frequency of operation to a maximum of 16 Hz.

Gust generator 1 consists of two wings of constant chord fitted with 25 % chord trailing edge flaps. The wing chord is 0.4 m, with a NACA 64_1-012 symmetrical laminar profile section. The fixed portions of the wings are machined from aluminium and the flaps from CFK reinforced rigid foam. Operation of the flaps is by a rod and lever mechanism driven by an electro-hydraulic actuator.

Gust generator 2 is a jet flap (Fig. 2). The fixed portion of gust generator 1 is retained and the trailing edge flaps are replaced by tubes 15 mm in diameter. Each tube has 351 0.5 mm diameter orifices and can be rotated through the full $\pm 40^{\circ}$ range of deflection angles. Compressed air supply is passed through a pressure reducing valve to provide an 8 bar working pressure. The mass flow is measured by a metal cone flow meter. At a mass flow of 134 gr/s and a tunnel speed of 20 m/s an impulse coefficient $C_{\mu} = 0.42$ is obtained.

Gust generator 3 (Fig. 2) consists of 4 flapped wings of constant chord, equidistributed over the working section height. The wing chords measure 0.2 m, but otherwise the construction is as for gust generator 1.

Gust generator 4 consists of 4 separate wings of aspect ratio 1,2 arranged as vanes, adjacent to the curved walls of the tunnel nozzle (Fig. 2). A NACA 64_1-013 section is employed and the wings have a rigid foam core and outer surface of GFK.

The propagation of the gust field is of prime interest to the user. Frequency response measurement of the gust angle of attack in relation to generator flap position is the most effective method of analysis for this purpose; the investigations being restricted to sinusoidal gusts of variable frequency and amplitude. This leads to simpler test arrangements and procedures and permits the automatic control of test runs. Fig. 3 shows the equipment used in the experiments. The core of the installation is the frequency response measuring equipment (FRM), which is controlled by a processor. The FRM provides a sinusoidal input signal to the actuators and special software converts measured data to physical values and displays the results on the screen of the processor. All computed data are stored on tape in digital form and all measured signals are registered on analogue tape. An additional option is provided by the facility to measure power spectra, if required.

The flow field is measured using five flow direction orobes. In addition a total pressure probe is used to provide a measurement of horizontal velocity fluctuation. The probe rake can be traversed along the test section to any required position to provide a complete record of the gust field pattern along the tunnel. The flow direction probes have a conical head with miniature pressure transducers inset in the holes (Kulite XCS-093 $\pm$ 5 PSI-D). In order to obtain phase free pressure measurements the differential pressure is calculated. It was assured that all the pressure transducer reference pressure tappings are connected to the ambient pressure and that pressure fluctuations in the tunnel are not transmitted to the reference pressure tubes of the transducers. The latter effect would lead to an undesirable slowing down in the pressure measurement process leading to phase errors. The pressure transducers are attached to temperature compensating amplifiers in order to inhibit temperature drifting. In addition, the measured signals are freed of bias and high frequency noise in a band pass filter. This band pass filter does not produce an amplitude decrease within the investigated frequency range. The phase characteristic of the filter was taken into account in determining the time delays. All the probes were statically and dynamically calibrated in a calibration tunnel.

6. CALCULATION OF THE GUST FIELD

The experimental investigation of different gust generators arose interest also to

give a theoretical description of the flow field behind oscillating wings. This facilitates the physical interpretation of the measured results and allows the variation of parameters. These calculations were performed at the institute for fluid dynamics of the Technical University of Braunschweig.

The flow field was calculated for vertically arranged wings, performing harmonically pitching and heaving oscillations (Fig. 4). Both motions were superimposed to produce the same lift like wing with oscillating trailing edge flap. A two-dimensional incompressible potential airflow was assumed. The pressure distribution of the wing was calculated using H.G. Küssner's (Ref. 13) concept of an acceleration potential. The singularities had to be carefully considered. The resulting integral equation was numerically solved using a collocation technique which was first given by B. Laschka (Ref. 14). The integral relations for the calculation of the induced velocities for arbitrary collocation points were taken from Ref. 15.

The interference between the vertically staggered wings can be treated using a linear interference model (Ref. 16). This interference model covers the stationary case as well as the instationary case, introducing the corresponding complex quantities for the induced velocities and pressure distribution. The presence of the tunnel wall was considered only for the case of two gust generator wings. The walls were considered by introducing mirror images of the singularities.

The calculations are valid only for a completely closed test section. So the measured results taken from a slotted test section will differ more or less from the calculated results.

7. EVALUATION OF THE TEST RESULTS

The sequence given in Table 1 is followed in evaluating the test results. Where possible, the results are compared with results obtained from calculations. In addition a comparison was made with data obtained from gust generator measurements made in a tunnel with an open test section (Refs. 17, 18). Measurements were also made with the test section slots sealed, in order to investigate the effect of these. In these tests first the floor- and roof-slots were sealed, and subsequently the remaining slots were sealed, in order to obtain a completely closed test section. In the case of the jet flaps all the measurements were made at the same impulse coefficient.

7.1 THE STATIONARY GUST PROPAGATION

A stationary gust field propagates with the same speed as the tunnel speed. This does not apply to gusts, generated by lifting surfaces in wind-tunnels. The generation of the gust field is determined by the formation and distribution of the wake vortices behind the gust generator. This vorticity on the other hand is governed by the laws of instationary aerodynamics. This results in a strong dependence of the gust amplitude on the reduced frequency ω^*.

Fig. 5 shows the dependence of the gust amplitude on reduced frequency. For the purpose of comparison a gust amplitude distribution is given, taken from measurements in an open test section. The other measurements show the influence of the slots in the walls of the test section, which becomes more prominent with decreasing ω^*. Fig. 5 shows another three important features:

- The stationary deflection of the airflow ($\omega^* = 0$) ist stronger if the air is allowed to escape through slots. This effect is of course most evident for the open test section.
- For increasing reduced frequencies the effect of slots becomes less important.
- A slot ratio of 12 % just produces least dependency on frequency.

Fig. 6 gives a comparison of the measurements in a closed test section with calculations. The calculations strongly confirm the measurements, that the consideration of the wall interferences in the domain of lower reduced frequencies is important. For higher reduced frequencies the measured gust angles are smaller than the calculated values, because the gust generator produces less lift than the calculation using potential flow theory.

Fig. 7 gives a comparison of the four different gust generators in the slotted test section. The efficiency of the jet flap is comparable small. This can be improved when larger deflections of the jet are allowed. The influence of reduced frequency on the jet flap is very small, which seems to be advantageous. On the other hand, the injection of a high velocity jet produces an intolerable amount of turbulence. No surprise are the very low amplitudes for the gust generator 4. Two wings and four wings with trailing edge flaps deliver nearly equivalent gust amplitudes.

Fig. 8 compares the calculated and the measured gust propagation speed with the tunnel speed. This figure gives the strongest evidence of the non-stationary character of the flow field. The assumption of a "frozen gust field" is valid only for low reduced frequencies ($\omega^* < 0.2$). The gust tends to lag behind the wind-tunnel speed. The calculations show more lag than the measurements, which again is explained by the different lift.

Fig. 9 gives a comparison of the four gust generators. The figure shows similar phase characteristics for gust generators 1 and 3. This characteristic is shifted to lower reduced frequencies for the gust generator 3 because it has only half the chord of gust generator 1. Gust generator 4 shows no significant deviation from the tunnel speed below $\omega^* = 1$. But the measurements showed big scatter and therefore are less trustworthy. For this gust generator phase measurements near the tunnel wall show a 180^o phase shift relative to the measurements on the centerline. This indicates no constant phase in lateral (y-) direction. The phase measurements of the jet flap are incorrect due to direct impact of the jet on the probes.

7.2 THE HOMOGENEOUS GUST FIELD

In a homogeneous gust field the amplitude must not change in downstream direction. Fig. 10 shows that this requirement cannot be satisfied in the wind-tunnel. Depending on the reduced frequency, the gust amplitude varies in the downstream direction. The effect is less meaningful for positions greater than two chord lengths behind the gust generator.

Fig. 11 again demonstrates a general similarity between gust generators 1 and 3. Due to the different chord lengths the distance x behind the gust generator is twice as large for gust generator 1 as for gust generator 3. Gust generator 4 shows least variations of the gust amplitude.

7.3 THE LATERAL DISTRIBUTION OF THE GUST FIELD

The gust generators 1, 2 and 3 are designed to produce an one-dimensional gust field. Therefore the lateral distribution of the gust amplitude should be constant. Fig. 12 shows a measured lateral distribution of the gust amplitude. As expected all the gust amplitude distributions disappear near the tunnel side walls. All gust generators produce a region of nearly even gust amplitude distribution around the centerline. Depending of the span of a model, the gust amplitude distribution can be considered as constant or non-uniform. The jet flap produces the flattest distribution. This is an effect of the strong jet, which is constant along the span of the gust generator. The winglets produce only a very small region of constant gust amplitude around the centerline. An attempt was made to produce "rolling gusts" by antimetrically deflected winglets. The amplitude distribution is also presented in Fig. 12 by the dotted line. The poor results indicate, that winglets of this type cannot generate rolling gusts in the vicinity of the centerline. Results obtained at ONERA (Ref. 19) with winglets of greater span, weren't much better. The rolling gust problem is closely coupled to the problem of giving the wind-tunnel flow a rotary momentum. This cannot be achieved by such simple devices as described here. Moreover a wind-tunnel of circular cross section would be more suited to this type of gusts.

7.4 THE VERTICAL DISTRIBUTION OF THE GUST FIELD

The vertical distribution of the gust amplitude is important if models which either have a large vertical extension or which are moving in vertical direction are investigated. The models must remain in a region of uniform gust amplitude.

Fig. 13 shows the calculated vertical distributions of the gust amplitude for two and four wings. The calculations show a rather flat gust amplitude distribution between the wings for low reduced frequencies. The peaks behind the trailing edges of the wings become more prominent with increasing reduced frequency. Four wings produce less prominent peaks but the region of indisturbed flow between the wings is much smaller. For the purpose of comparison measurements for the slotted testsection are presented additionally in Fig. 13. They agree in general to the calculations. two of the measurements points lie in the wake of the wing. This causes a less peaky appearence of the measured distribution.

Figure 14 gives a comparison of the four gust generators. The position of the flow direction probes didn't allow a measurement at the position of the wings. So the peaks behind the trailing edges, which are shown in the calculations, do not appear in the measurements. The measurements show however, that the jet-flap produces the largest differences of the gust amplitude in the vertical direction.

7.5 SUPERIMPOSED LONGITUDINAL GUSTS

The wake vorticity behind the gust generator wings also generates horizontal flow components. From Fig. 4 we can deduce that a step of the horizontal flow components occurs behind each wing. This is clearly demonstrated by the calculations shown in Fig. 15. Besides, there must be no horizontal flow component on the centerline. While the last fact is clearly verified by the measurements, the horizontal velocity steps do not come out (see Fig. 16). More measurement points in the vertical direction are necessary in order to show these steps. Fig. 16 gives distinct evidence that the jet-flap produces the largest horizontal flow components.

8. CONCLUSIONS

In 1981 experiments with gust generators have been carried out in the MUB wind-tunnel of the DFVLR Braunschweig. It was the aim of these investigations to find a gust generator which is best suited for an application in a subsonic wind-tunnel. Four different types of gust generators were investigated. These investigations realized some insight into the behaviour of the airflow behind oscillating wings. Some important conclusions can be made:

- The conditions of a homogeneous and stationary gust field can be realized in the wind-tunnel only to a limited scale ($\omega^* < 0{,}5$).
- For gust generators, which extend across the complete width of the test section, the spanwise distribution of the gust amplitude is nearly constant within a broad domain around the centerline.
- The vertical extension of the region with nearly constant gust amplitude is large enough for values of the reduced frequency $\omega^* < 0{,}5$.
- Gust generators with two wings are advantageous. They are more efficient and offer the largest area of undisturbed air flow between the wings.
- For low reduced frequencies, slots are beneficial. They are responsible for larger gust amplitudes.
- Jet-flaps produce more turbulence and disturbances than other gust generators. Low thrust coefficients and larger deflection angles of the jet however will improve the situation.
- The generation of horizontal flow components is an intrinsic characteristic of the system. Fortunately, the effects are very small near the centerline.
- The position of the model should not be too far behind the wings. Positions of one or two chord lengths behind the gust generator are recommended.

REFERENCES

[1] Redd, L.T.; Gilman, J.; Cooley, D.E.; Sevart, F.D.; Wind-Tunnel Investigaton of a B-52 Model Flutter Suppression System. J. Aircraft, Vol. 11, No. 11, November 1974.

[2] Grosser, W.F.; Hollenbeck; W.W.; Eckholt, D.C.; The C-5A Active Lift Distribution Control System; AGARD-CP-157, 1974.

[3] Thompson, G.O.; Sevart, F.D.; Wind-Tunnel Investigation of Control Configured Vehicle Systems; Presented at AGARD-SMD-Specialists Meeting on "Flutter Suppression and Structural Load Alleviation", Brussels, Belgium, April 15; 1975.

[4] Gilman, J.; Bennett, R.M.; A Wind-Tunnel Technique for Measuring Frequency Response Functions for Gust-Load Analysis; J. Aircraft Vol. 3, No. 6, November-December 1966.

[5] Lafon, P,; Courmelin, J.; Essais d'un Generateur de Rafales periodiques. Procès-Verbal d' Essais No. 79/2751 GNA. 1973.

[6] Bicknell, J.; Parker, A.G.; A Wind-Tunnel Stream Oscillation Apparatus. J. Aircraft 9 (1972), No. 6.

[7] Krag, B.; Rohlf, D.; Wünnenberg, H.; OLGA, A Gust Alleviation System for Improvement of Passenger Comfort of General Aviation Aircraft. ICAS Proceedings 5.4, 1980.

[7a] Subke, H.; Krag, B.; Dynamic Simulation in Windtunnels, Part II. AGARD-CP-187, 1975.

[8] Stewart, E.C.; Doggett, R.V.; Dynamic Wind-Tunnel Tests of an Aeromechanical Gust Alleviation System Using several different Combinations of Control Surfaces. NASA Techn. Memorandum 78638, 1978.

[9] Patel, M.H.; The Delta Wing in Oscillatory Gusts, AIAA Journal, Vol. 18, No. 5, May 1980.

[10] Garby, L.C.; Kuethe, A.M.; Schetzer, J.D.; The Generation of Gusts in a Wind-Tunnel and Measurement of unsteady Lift on an Airfoil.; Wright Air Development Center technical Report 57 - 401, 1957.

[11] Military Specification MIL-F-8785C. Flying Qualities of Piloted Airplanes, Nov.1980

[12] Krag, B.; Untersuchung über den Einsatz von Böenerzeugungsanlagen in Windkanälen. DFVLR IB 154-80/17, 1980.

[12a] Krag, B.; Vermessung des Böenfeldes hinter harmonisch schwingenden Böenerzeugern im Modell-Unterschall-Kanal (MUK). DFVLR-FB 82-26.

[13] Küssner, H.G.; Allgemeine Tragflächentheorie. Luftfahrtforschung, Vol. 13, 1936.

[14] Laschka, B.; Zur Theorie der harmonisch schwingenden tragenden Fläche. Doctor's Thesis, Technical University Munich,1961.

[15] Laschka, B.; Neue Ergebisse der ebenen instationären Tragflügeltheorie. Sonderdruck MBB, Ottobrunn, 1977.

[16] Laschka, B.; Interfering Lifting Surface in Subsonic Flow. ZFW, Vol. 18, Nr. 9/10, 1970.

[17] Christ, D.; Böenerzeugung im Niedergeschwindigkeits-Windkanal der DFVLR-Braunschweig DFVLR-IB 157-76 A21 (1976).

[18] Freymann, R.; Die Böensimulationsanlage des 3 m x 3 m - Niedergeschwindigkeits-Windkanals der DFVLR in Göttingen. DFVLR-FB 85-04.

[19] Böenerzeugung im ONERA S3CH-Résultats provisoires; PV 2/0854 GNA (1982).

Table 1
Requirements for the Quality of the Flow Field.

Requirements for the Quality of the Flow Field	necessary	desirable	undesirable
Homogeneous in downstream Direction	Δ		
Stationary (Gust Propagation=Tunnel Speed)	Δ		
Conform with Input Signal	Δ		
Uniform in lateral Direction		Δ	
Uniform in vertical Direction		Δ	
Superimposed longitudinal Gusts			Δ

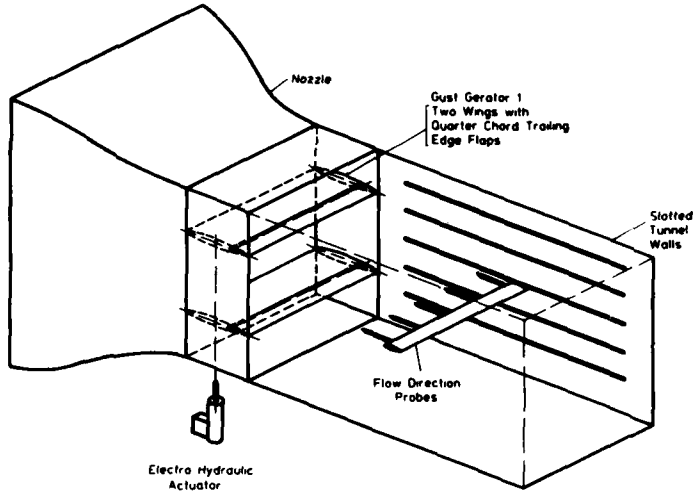

Fig. 1
Arrangement of the Gust Generator 1 in the DFVLR Model Subsonic Wind-Tunnel.

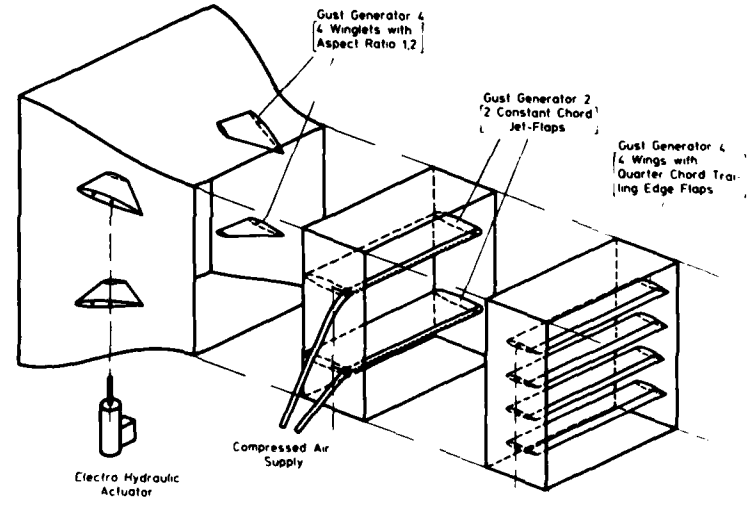

Fig. 2
Arrangements of the Gust Generators 2, 3 and 4.

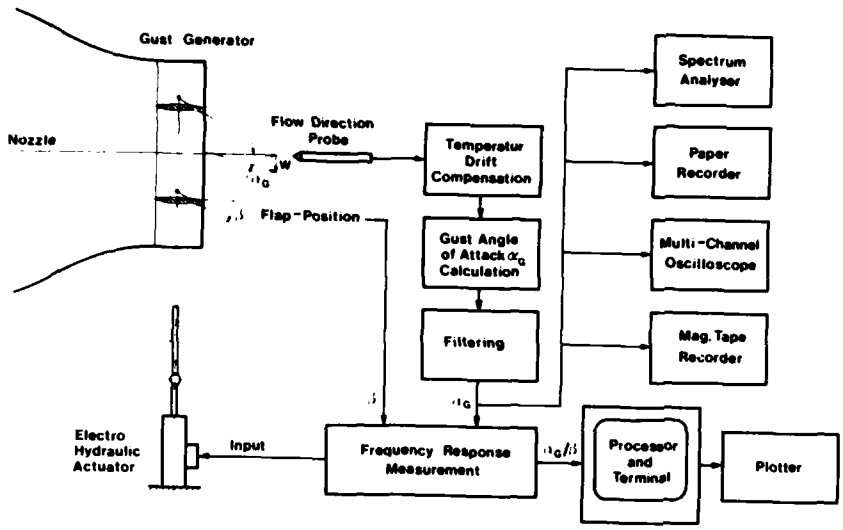

Fig. 3
Equipment for dynamic Flow Direction Measurements.

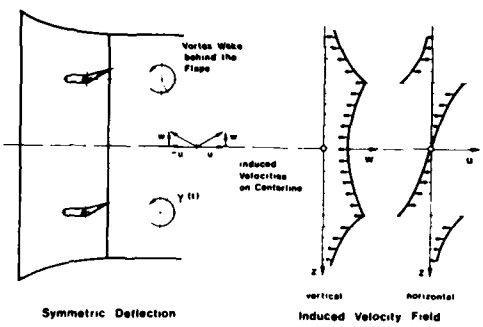

Fig. 4 Model for the Calculation of the Flow Field.

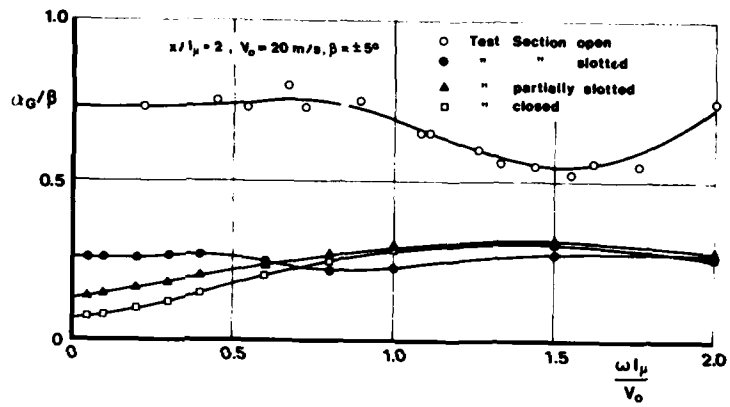

Fig. 5 Measured Frequency Response of the Gust Angle of Attack (Modulus). Influence of Test Section.

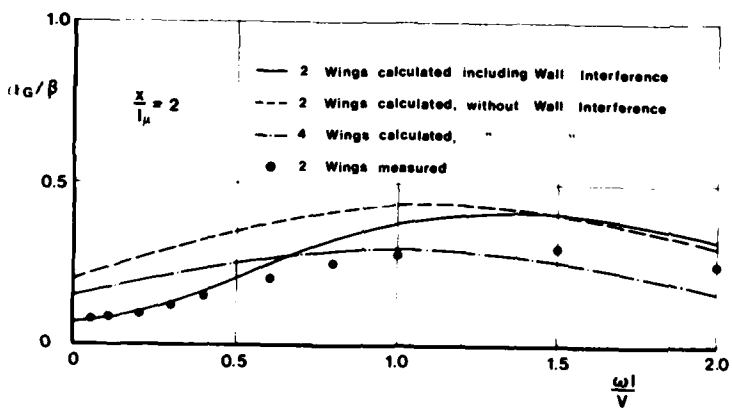

Fig. 6
Calculated Frequency Response of the Gust Angle of Attack (Modulus).

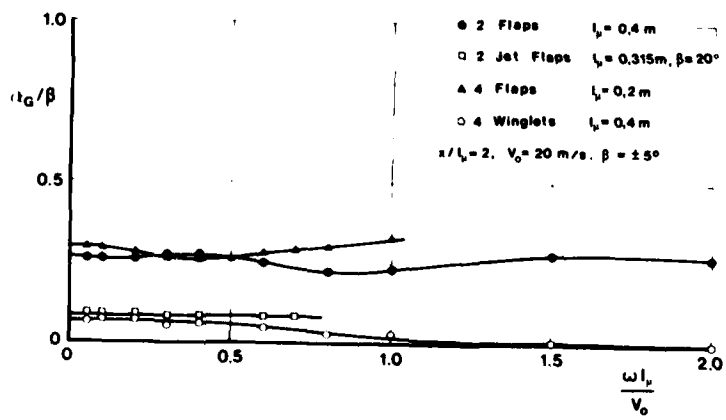

Fig. 7
Measured Frequency Response of Gust Angle of Attack (Modulus). Comparison of the Gust Generators.

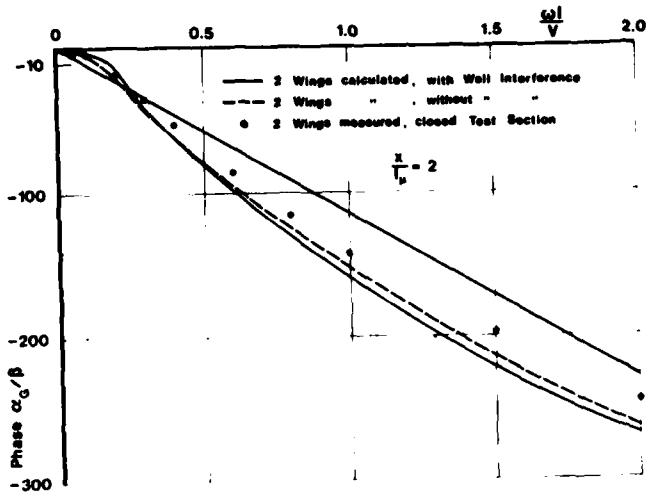

Fig. 8
Calculated Frequency Response of the Gust Angle of Attack (Phase).

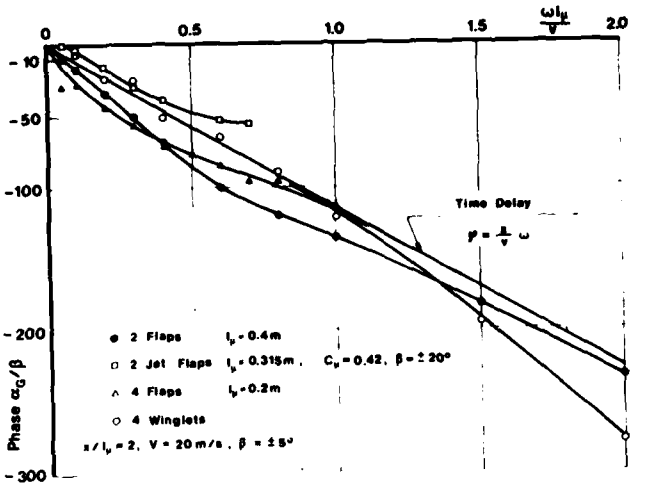

Fig. 9
Measured Frequency Response of Gust Angle of Attack (Phase). Comparison of Gust Generators.

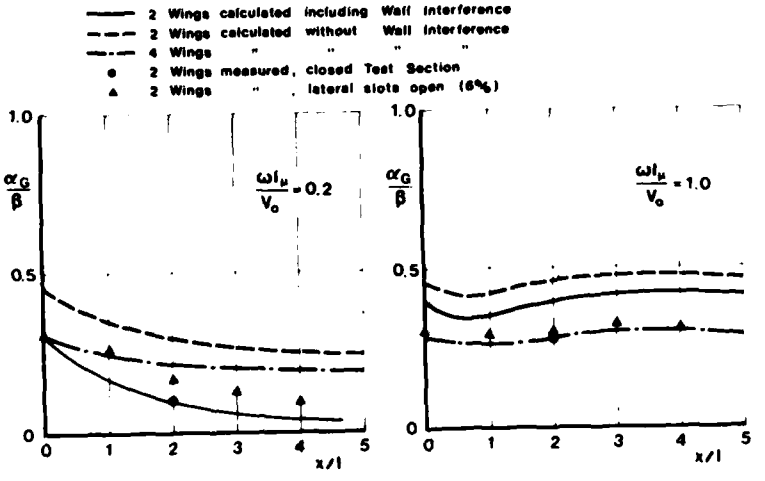

Fig. 10 Calculated downstream Variation of the Gust Amplitude.

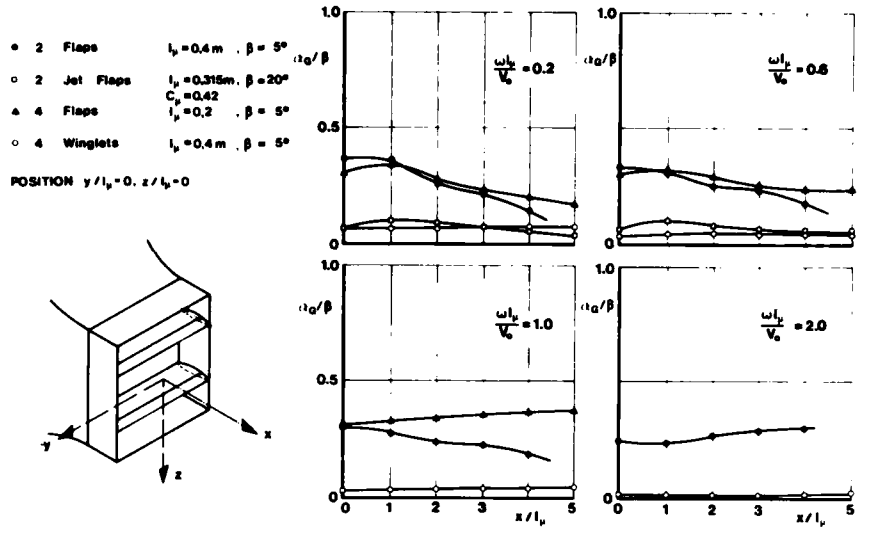

Fig. 11
Measured downstream Variation of the Gust Amplitude. Comparison of Gust Generators.

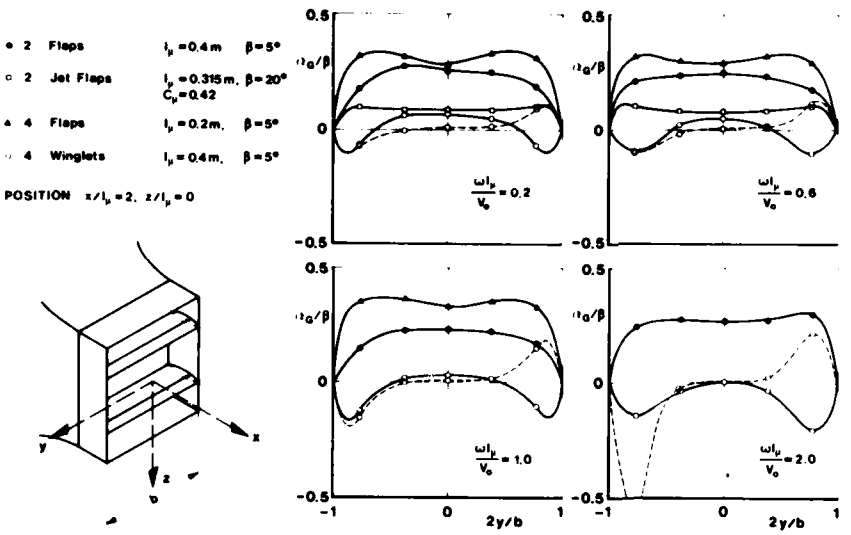

Fig. 12
Lateral Distribution of the Gust Amplitude. Comparison of Gust Generators.

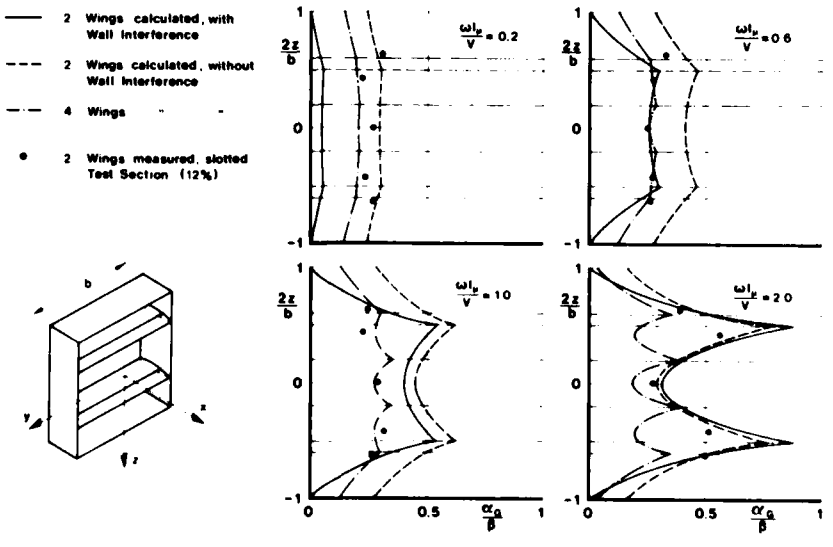

Fig. 13
Calculated vertical Distribution of Gust Amplitude.

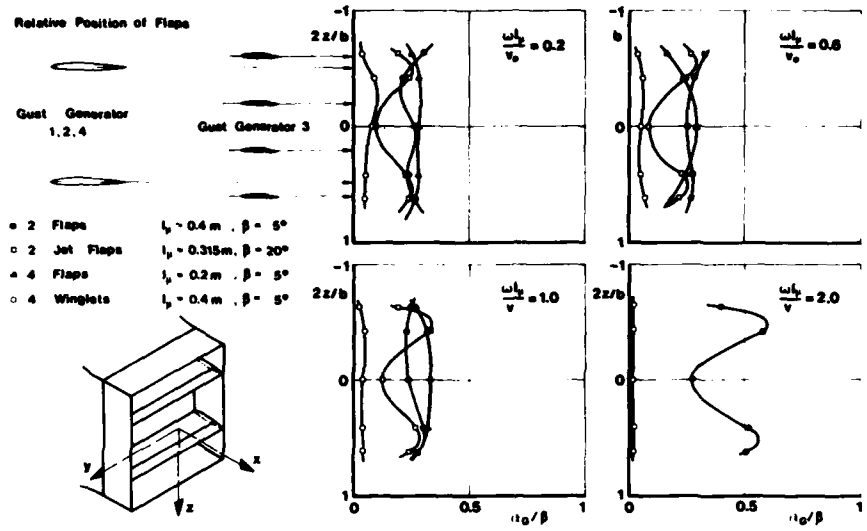

Fig. 14 Measured vertical Distribution of Gust Amplitude. Comparison of Gust Generators.

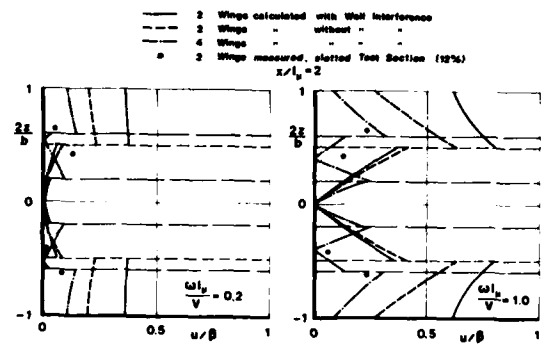

Fig. 15 Calculated vertical Distribution of horizontal Gusts.

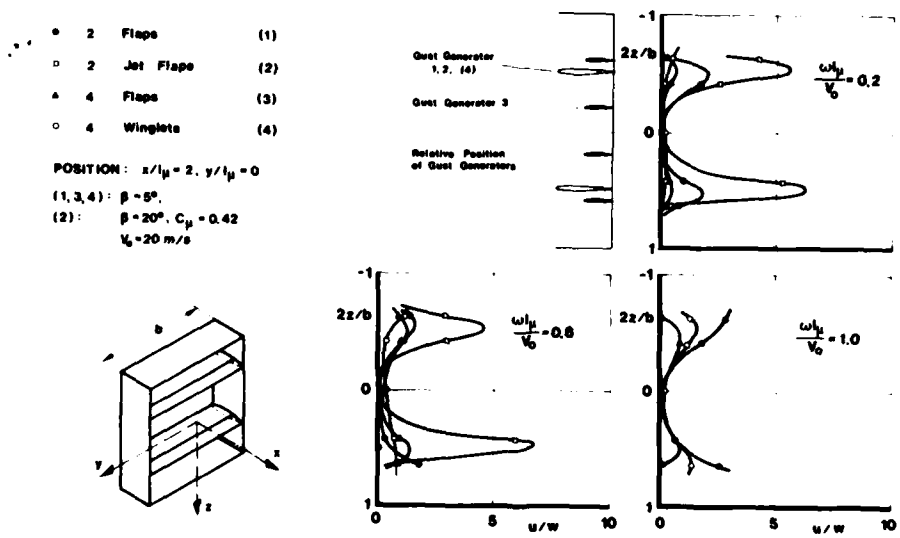

Fig. 16 Measured vertical Distribution of horizontal Gusts. Comparison of Gust Generators.

EXTRACTION OF AERODYNAMIC PARAMETERS FOR AIRCRAFT AT EXTREME FLIGHT CONDITIONS

Kenneth W. Iliff
Senior Staff Scientist
NASA Ames Research Center
Dryden Flight Research Facility
Edwards, California 93523
U.S.A.

SUMMARY

The maximum likelihood estimator has been used to extract stability and control derivatives from flight data for many years. Most of the literature on aircraft estimation concentrates on new developments and applications, assuming familiarity with basic concepts. This paper briefly discusses the maximum likelihood estimator and the aircraft equations of motion that the estimator uses. The current strength and limitations associated with obtaining flight-determined aerodynamic coefficients in extreme flight conditions is assessed. The importance of the careful combining of wind tunnel results (or calculations) and flight results and the thorough evaluation of the mathematical model is emphasized. The basic concepts of minimization and estimation are examined for a simple computed aircraft example, and the cost functions that are to be minimized during estimation are defined and discussed. Graphic representations of the cost functions are given to help illustrate the minimization process. Finally, the basic concepts are generalized, and estimation of stability and control derivatives from flight data is discussed.

1. INTRODUCTION

Currently, an important thrust in the aerodynamic community is to specify completely the aerodynamic mathematical model for an aircraft. The ultimate goal of this thrust is to obtain a complete understanding of the physical laws (phenomenology) governing all aspects affecting the behavior of the aircraft. Presently we fall short of this goal in all flight regimes, but we have a particularly long way to go in extreme flight regimes, such as transonic or high-angle-of-attack flight, which are typically dominated by separated flow. As much as possible, we rely on experience and analogies that can be drawn from better understood regimes, such as subsonic flight with attached flow. But even with this wealth of experience, we still progress very slowly to the complete understanding of aircraft being flown at extreme flight conditions in complex flow fields.

In traditional regimes of less complex flow fields, certain aspects of understanding a particular phenomenon can sometimes proceed in a simple fashion, more or less ignoring the results of those working in different but related disciplines. This is not the case for understanding the physical laws that determine the characteristics of flight dominated by complex separated flows. We must begin by postulating candidate mathematical models, then test these models with all the techniques available. In addition, new testing techniques must be developed when existing techniques are not capable of testing portions of the mathematical model. Currently, the techniques that can contribute to validating the mathematical model can be divided into three categories: wind tunnel testing, computational fluid dynamic analysis, and flight testing.

Wind tunnel testing, computational fluid dynamic analysis, and flight testing serve complementary roles (with some overlap) to the overall validation of the mathematical model. Each category can contribute in a unique way to the overall validation. Quite probably, validation will not be possible without contributions from each category. System identification and parameter estimation techniques are needed to analyze flight test data because forces and moments cannot be measured directly. These techniques are used to extract force and moment coefficients from the motions measured in flight.

This paper discusses ways in which analysis of flight data can contribute to the formulation and testing of the mathematical model. To date, no comprehensive flight results are available for extreme flight conditions. This paper is intended to inform nonflight specialists of the current state of flight data coefficient estimation. The references cited in the paper reflect a representative sampling of current flight results. The paper first points out some of the differences between the approaches used for the less complicated, traditional flow regimes, and the approaches used for extreme flight conditions in the separated flow regime. It discusses the interrelationship of the mathematical model, the wind tunnel, and computational fluid dynamic results, and how they can be used with flight results. Parameter estimation, which is the primary method of extracting estimated coefficients from flight data so that results can be used to assess the mathematical model, is described in detail. The description is intended to emphasize the characteristics (both strengths and weaknesses) of system identification and parameter estimation. The mathematics involved are avoided wherever possible.

2. SYMBOLS

A,B,C,D,G	system matrices	C_n	coefficient of yawing moment
b	reference span, ft	c	reference chord, ft
C_ℓ	coefficient of rolling moment	$f(\cdot)$, $g(\cdot)$	general functions
C_m	coefficient of pitching moment	GG*	measurement noise covariance matrix

I_x, I_{xz}, I_y, I_z	moment of inertia about subscripted axis, slug-ft^2
i	general index
J	cost function
L	rolling moment divided by I_x, deg/sec^2
L	rolling moment, ft/lb
m	mass, slug
N	number of time points or cases
n	state noise vector or number of unknowns
p	roll rate, deg/sec
q	pitch rate, deg/sec
$\bar{q}$	dynamic pressure, lb/ft^2
r	yaw rate, deg/sec
s	reference area, ft^2
T	time increment, sec
t	time, sec
u	control input vector
V	forward velocity, ft/sec
x	state vector
z	observation vector
$\tilde{z}_\xi$	predicted Kalman-filtered estimate
α	angle of attack, deg
β	angle of sideslip, deg
Δ	time sample interval, sec
δ	control deflection, deg
δ_a	aileron deflection, deg
η	measurement noise vector
μ	mean
ξ	vector of unknowns
σ	standard deviation
τ	time, sec
ϕ	bank angle, deg
ψ	heading angle, deg
∇_ξ	gradient with respect to ξ

Subscripts:

e	engine
m	measured quantity
$p,r,\alpha,\beta,\dot{\beta},\delta,\delta_a$	partial derivative with respect to subscripted quantity
0	bias or at time zero

Other nomenclature:

~	predicted estimate
^	estimate
*	transpose
'	moment, ft-lb

3. PARAMETER ESTIMATION AT EXTREME FLIGHT CONDITIONS

General overviews of the problems of understanding aerodynamics and flight characteristics are given in Refs. 1 and 2. The issues affecting parameter estimation of flight characteristics and some of the results are given in Refs. 3 to 5. References 3 and 4 concentrate on estimation of characteristics obtained in traditional flight regimes not dominated by unsteady aerodynamics.

To appreciate the complexities of validating the mathematical model for flight data obtained at extreme flight conditions (such as high-angle-of-attack flight, transonic flight, or flight dominated by separated flow), it is useful to compare it to validation in traditional flight regimes, such as low angle of attack, subsonic, well established supersonic, or regimes with all flow essentially attached. The flow chart in Fig. 1 depicts the general elements required to validate the mathematical model in traditional flight regimes. Wind tunnel test and computational fluid dynamic calculations are used to design an aircraft with characteristics that meet the design criteria for a specific aircraft. These data are used along with information from other disciplines (such as control, structural, thermal, or propulsion characteristics) to define an aircraft. Once the aircraft is built, it will be flight tested. The data acquisition system must be specified based on the type of aircraft and the flight regimes to be flown. The mathematical model expressed by equations of motion, which is representative of the aircraft dynamic characteristics (usually including stability and control derivatives), is then specified. Representative forms of the equations of motion are given in Refs. 6 to 8. Then, knowing the mathematical model and the flight conditions of interest, the pertinent mass characteristics are estimated. At this point, the maneuvers that are needed for model validation are defined and flown. A parameter estimation technique, such as a maximum likelihood estimator, is then used to determine the stability and control derivative estimates from the flight data (Refs. 9 to 11). (Parameter estimation is discussed in detail in a later section.) These parameter estimates are assessed, summarized, and compared to the best predicted set of computational and wind tunnel estimates. These predicted estimates may be the data set that was used to design the aircraft, or they may be that data supplemented with subsequent computational and wind tunnel results produced after the aircraft design was frozen. The comparison of flight estimates with other estimates may generate additional flight, computational, or wind tunnel tests. These estimates can then

be assessed in the same way, as depicted by the flow chart. When all tests are complete and their results compared, a composite representation of these tests is put in a data base. This data base may be used to aid in future design or may be put into a real-time simulator to be used for pilot training, control system redesign, or mission analysis.

In contrast to Fig. 1, Fig. 2 shows the additional complexity involved in the mathematical model validation for data obtained at extreme flight conditions. Figure 2 represents only the crosshatched area from Fig. 1. The two figures are to about the same level of detail. Figure 2 is representative of the process and is not necessarily an exact representation of the procedure followed by any given analyst. The flow chart of figure 2 not only has more elements, but also is significantly more complex in that the "flow" between the various elements may need to be iterated more times. In the following sections, each of the various elements is discussed in detail.

3.1 MATHEMATICAL MODEL SELECTION

Since the primary outcome of the flow chart is the validation of the mathematical model, it is appropriate to specify the mathematical model first. Initially, a mathematical model or a set of candidate mathematical models must be specified. It should be kept in mind that each element of the chart is subject to change as the entire flow chart is iterated. The form of the model may be specified by wind tunnel tests, as shown in Fig. 2. Probably the most promising set of mathematical models based on strong phenomenological consideration is given in Ref. 12. The models are derived under the assumptions that (1) response to a steady motion is itself steady, (2) the response is a single-valued function of the orientation of the body (although it may be nonlinear), and (3) the responses are linear in the motion rates. The authors of Ref. 12 showed how a nonlinear variation of the responses with coning rate could be accommodated. The models as given do not include the effects of control deflection. Control terms can be added to the model in a fashion analogous to the way that the flow angle (α and β) terms are included, and probably would initially be functions of angle of sideslip and angle of attack. Reference 12 also discusses the inclusion of terms that involve aerodynamic hysteresis. For the mathematical model to have much generality, it would probably need to account for hysteresis as it is highly probable that hysteresis occurs at extreme flight conditions. However, regardless of the initial model chosen, if the subsequent analysis shows a need for hysteresis terms, they can be added during a future iteration. It is highly probable that for the gyrations observed at extreme flight conditions, terms involving nonlinear coning effects and aerodynamic hysteresis would need to be included in the general mathematical model. Reference 13 discusses how phenomena that violate the restrictions of Ref. 12 can be accommodated within the mathematical model.

3.2 MASS CHARACTERISTICS

The next element of Fig. 2 is the specification of the mass characteristics. These characteristics have, in the past, been given very little consideration in the analysis of data obtained at extreme flight conditions, because experience gained in the analysis of data obtained in traditional flight regimes has shown that the data only need to be known to an accuracy of about 10 percent. If an error of 10 percent in mass characteristics is present in the analysis of traditional flight data, it will probably be noted when comparing flight results to wind tunnel estimates, and, if necessary, can be compensated for at that point. However, data obtained at an extreme flight condition is usually highly oscillatory in all axes, and the kinematic cross-coupling effects are highly dependent on the mass characteristics. The mass is usually easily determined, but the moments of inertia are difficult to determine accurately. Any error in accounting for the kinematic coupling terms becomes an error that is added to the remaining terms or the aerodynamic terms.

The following equations (also given in Refs. 6 to 8) demonstrate this difficulty:

$$\dot{p}I_x - \dot{r}I_{xz} - qr(I_y - I_z) - pqI_{xz} = \bar{q}sbC_\ell \tag{1}$$

$$\dot{q}I_y - rp(I_z - I_x) - (r^2 - p^2)I_{xz} - NrI_{x_e} = \bar{q}scC_m \tag{2}$$

$$\dot{r}I_z - \dot{p}I_{xz} - pq(I_x - I_y) + qrI_{xz} + NqI_{x_e} = \bar{q}sbC_n \tag{3}$$

Equations (1) to (3) assume that I_{xy} and I_{yz} are zero. The individual kinematic terms (left side of the equations) are frequently larger than the aerodynamic terms during wild gyrations and spins. Even C_m is affected by I_x, I_y, I_z, I_{xz}, and I_{x_e} in a nonlinear fashion. This is still true when the rates are known exactly. I_x, I_y, and I_z are always significant terms, and I_{xz} usually is. I_{x_e} would affect any aircraft with a rotating engine. A current challenge is to obtain an accurate set of these moments of inertia to within less than 1 percent, which may not be within the current state of the art.

It should also be noted that these numbers vary significantly with the amount and location of the fuel during the maneuver. Since many of the maneuvers of interest result in wild gyrations, an additional source of error is fuel sloshing. The issues involving fuel quantity and fuel location (sloshing or otherwise) and the rotating engine mass make unpowered aircraft more attractive as initial candidates for assessing mathematical models.

Current experience shows that if very detailed calculations are made for the weight, location, and inertias of each component (no matter how small) of an aircraft, then fairly consistent values of the mass characteristics are obtained. The other method of obtaining moments of inertia is by swinging the vehicle,

as discussed in Ref. 14. The author's experience has shown that moments of inertia obtained by swinging a vehicle are adequate for the traditional regimes if done with extreme care. These experimentally obtained numbers are in good agreement with calculated numbers when both are done with extreme care. In general, it seems doubtful that swinging the vehicle will provide adequate accuracy for analysis of an aircraft during wild gyrations.

3.3 MANEUVER DEFINITION

Definition of the maneuvers to be flown is the next element of the flow chart. Certain characteristic motions are necessary to assess any given mathematical model. Reference 12 discusses the characteristic motions required to assess the models it proposes. These characteristic motions can be generated, at least in theory, in a wind tunnel by using a specific rig, such as the rotary rig (Ref. 15). Unfortunately, an aircraft always flies close to the trimmed condition, even when undergoing violent gyrations. The time required for a vehicle to complete a wild gyration, including a spin, is very short; therefore, these motions provide very little information because all the state variables are changing rapidly. Figure 3 shows an example of this for an aircraft entering a spin. In addition, oscillations tend to repeat a set of state variable values each oscillation. All these problems result in trajectories that repeat, are highly transient, and contain only a small amount of information about the desired characteristic motion. Therefore, no matter how carefully a maneuver to be flown is specified, one has very little control over how much of the characteristic motion is obtained. This is not to say that one cannot obtain useful information from careful specification of maneuvers; it simply means that the "matrix" of test conditions is limited compared to those that can be obtained in the wind tunnel. Although this is an obvious contribution of wind tunnel testing (a highly controlled experiment), flight test data do have the advantage of giving exactly the correct motions throughout the flight envelope, regardless of what the assumed mathematical model is. Even though the aircraft cannot give specific characteristic motions, it does give a great deal of highly dynamic motion that can result in invaluable information when analyzed with modern parameter estimation techniques. This information describes the aircraft motion along the flight trajectory, but it does not completely define the global mathematical model.

One would assume that aerodynamic characteristics (information about the "true" mathematical model) can be obtained from the combined applicaton of computational, wind tunnel, and flight data analysis techniques that cannot be determined from any single technique.

3.4 INSTRUMENTATION REASSESSMENT

The next element in the flow chart of Fig. 2 is the reassessment of instrumentation. When an aircraft is flying at an extreme flight condition, the accurate measurement of the flow (flow angles, and dynamic and static pressure) can be greatly compromised because of separated or vortical flows, or shock waves in the vicinity of the instrument or sensor. The sensor will normally measure only the local flow, which may or may not be representative of the free-stream flow. In a highly dynamic gyration, the flow measurement is likely to be better at one time than it is at another. This suggests that flow measurements should be made at several locations so that the true free-stream flow can be inferred from the combination of measurements. If a fixed pitot head is used when flying at a high angle of attack, the pitot head should be canted to obtain accurate pressures at high angle of attack. Flow angles can be measured with either vanes or pressure sensors. Problems can occur with either of these techniques because of the dynamic characteristics of the vane or the time lags in the pressure sensors. A detailed discussion of flow measurements is beyond the scope of this paper, but it is nonetheless extremely important to obtain accurate measurements of the flow. It may seem that the free-stream flow conditions could be obtained from inertial measurements. This would be true if one could fly in an airmass that does not move with respect to the inertial frame of reference. One might occasionally encounter a portion of the airmass that is at rest, but the rule is that the airmass is constantly in motion. The motion exhibited by winds and turbulence not only varies spatially but also varies as a function of time. This makes it imperative to obtain external flow measurements if one is to make sense of flight data obtained at extreme conditions. Perfect flow measurements cannot be made by any intrusive sensor; therefore, one must be able to improve the raw flow measurements by some means. The next section treats this problem.

3.5 DATA AND TRAJECTORY RECONSTRUCTION

The next element in the flow chart of Fig. 2 is data and trajectory reconstruction, which is sometimes referred to as consistency checking. This is the generic procedure that is intended to improve the raw flow measurements. Reconstruction can improve all the measurements in that reconstruction procedures force the data to conform to the physical laws of a rigid aircraft. They also reduce the sensor modelling errors and the sensor measurement noise. Most of these procedures use the extended Kalman filter as the basic algorithm. The extended Kalman filter provides a very powerful and consistent technique to improve the aircraft data measurements, but the procedure can be very time consuming because weighting factors must be determined for each of the measurements. The relative weighting of one measurement to another is representative of the confidence one has in a given measurement. This confidence can be a function of vehicle attitude or flow condition, so in most cases it will vary over time and from maneuver to maneuver. Another difficulty encountered in using the extended Kalman filter is that the filter implementation may become unstable, forcing the analyst to use *ad hoc* procedures to stabilize the filter. A complete discussion of data and trajectory reconstruction techniques is beyond the scope of this paper, but a representative sample of these techniques is given in Refs. 11, 16, and 17.

During the data and trajectory reconstruction phase, measurements obtained from the ground can be used in conjunction with those obtained on board the aircraft. Figure 2 shows these ground sources as radar and optical measurements. The primary source of optical data is phototheodolite. In the near future, data from the Global Positioning System (GPS) will also be available. Radar, optical, and GPS sources are independent, inertially based data sources that can be used to improve the accuracy of the reconstructed trajectory. It should be pointed out that data and trajectory reconstruction techniques are also used for

data obtained in the traditional flight regimes. These techniques are used to improve onboard measurements and reduce the measurement noise so that noise-sensitive regression or equation error techniques can be used. These techniques are discussed thoroughly in Ref. 11.

3.6 MODEL STRUCTURE DETERMINATION

The key element of Fig. 2 is the model structure determination (MSD) element. As shown, it is strongly coupled with other major elements of the flow chart. The model structure referred to here is simply another way of stating the form of the mathematical model. The proposed mathematical models of Ref. 12 are model structures. The concept of this block is slightly more restrictive in that there may be a large collection of candidate elements in the mathematical model or model structure. Model structure determination is the procedure that, by some criterion, selects for the model structure only those terms that can be accurately estimated from the available flight data. Of course, the model structure can also be specified by information from computation, wind tunnel, or previous flights. However, the intent of the MSD element is to further define the model structure based on the information content of the flight data. That is, the candidate elements of the model structure could be some of those proposed in Ref. 12. Some elements could be eliminated, or their values fixed, on the basis of wind tunnel tests, such as rotary balance tests. The candidate elements can be based purely on phenomenological considerations or they can be based purely on *ad hoc* considerations.

Most of the MSD algorithms use stepwise regression to assess the effect of individual elements on the motion observed from a flight maneuver. Some of the proposed MSD algorithms are described in Refs. 7, 18, and 19. The details of the algorithm are not described here, but a heuristic description is given. The algorithm is a regression technique in which the individual candidate elements of the proposed mathematical model are evaluated one by one. The elements are rejected if they have a low correlation with acceleration terms or a high correlation based on a given set of flight data to one of the other more significant elements. Being rejected indicates that the element makes no significant contribution to explaining the behavior of the flight data. The stepwise regression technique can be automated to select the best set of elements from a given maneuver. Independent testing on other data is needed to determine the final set of elements of the mathematical model. The models that stepwise regression algorithms evaluate frequently use spline formulations with variable knot partitions (break points). This means that the data are partitioned as a function of the more important aircraft variables, such as angle of attack or elevator deflection. The stepwise regression algorithm can select the types of candidate elements, including the spline, as well as the partitions for the flight data.

3.7 RESULT EVALUATION

The next step of Fig. 2 compares the output of the MSD algorithm for several maneuvers and looks for consistency or *inconsistency* in the elements being selected. The types of errors that are consistent for several maneuvers are also examined. The outcome of this step is either (1) that the proposed mathematical model is in all likelihood a good model and we should proceed to the final analysis of the flight data, or (2) that the model is found lacking and additional elements are required. At this point, the flight results are compared with the computational and special apparatus wind tunnel results. Inconsistencies in this comparison may indicate that further modifications to the mathematical model or additional computational or wind tunnel results are required.

This concludes the discussion of Fig. 2 and how it iterates to converge on a promising mathematical model before final maximum likelihood estimation analysis is performed. The details of the maximum likelihood estimation are given in the next section. Some of the more encouraging results for analysis of flight data at extreme flight conditions are given in Refs. 5 to 7, and 20 to 25.

In summary, the simplest mathematical model is selected based on physical laws. The types of wind tunnel apparatuses and tests required are determined based on this model. The results of the tests may indicate the need for changes in the mathematical model (to make it either less or more complex). Accurate values of the mass characteristics must be obtained as a function of fuel loading. Aircraft maneuvers must be defined to stimulate the characteristic motions defined by the mathematical model. The best instrumentation possible for obtaining data at extreme flight conditions must be defined and installed. Data and trajectory reconstruction must be performed to improve the flow measurements, to reduce the sensor noise and modelling errors, and to include radar and optical data if available. The simplest model structure for a given set of data must be determined. This can be done with stepwise regression techniques since the "measurement" noise was reduced in the preceeding step. Elements and coefficient values from the wind tunnel tests may be used in this step. The consistency between the mathematical model and data for several maneuvers must be evaluated at this point. If the model is found lacking, the mathematical model may need to be reevaluated and additional computations or wind tunnel tests may need to be performed. If either of these is necessary, the steps in the flow chart are iterated again to reevaluate the flight data. If the model is found adequate, we proceed to the final analysis with the maximum likelihood estimator. The model may still be found inadequate at this point, indicating the need for a refinement in the mathematical model. Once the model is refined, the flowchart steps are interated again.

4. SIMPLE EXAMPLE OF PARAMETER ESTIMATION

In the previous section the overall procedures were discussed for extracting aerodynamic information from flight data. That discussion contrasted the relative complexities for analyzing data obtained at traditional flight conditions with the analysis of data obtained at extreme flight conditions. A parameter estimation phase is required for either of these regimes. Parameter estimation techniques are necessary because direct force and moment measurement is not possible for an aircraft in flight. These techniques extract aerodynamic coefficents from aircraft flight motions. The parameter estimation phase is essentially the same for data obtained in either of these flight regimes. The differences are in (1) the complexity of the underlying mathematical model that has been assumed, (2) the difficulty in getting the

parameter estimation algorithm to converge, and (3) the interpretation of the results. All of these differences pertain to the degree to which the concepts of parameter estimation are involved and not whether or not the concept is fundamental to the estimation. Therefore, the remainder of the paper illustrates the concepts involved in applying the parameter estimation algorithms to flight data. The parameter estimation concepts are illustrated with simple models, but the concepts generalize to include the most complex analysis of data from extreme flight regimes.

The parameter estimation algorithm discussed here is the maximum likelihood estimation algorithm, or output error method. The theory and formulation of the method are given in Ref. 26, and an example of the computer code used for this type of analysis is given in Refs. 9 and 10. The mathematical models used in these examples are the same as those used for analysis in the traditional linear flight regimes for estimating stability and control coefficients. The same estimation algorithm is used whether the mathematical model formulation is linear or nonlinear.

The models of Ref. 12, including the one that accounts for aerodynamic hysteresis, can be implemented and the algorithm will remain essentially unchanged. In essence, the model must be written in some functional form. The functional form can be in a piecewise linear or spline form. Increasing the complexity of the model does not change the essential estimation algorithm, it just increases the complexity of the implementation and the time required to execute the computer codes. In general, models that are highly nonlinear, include a very complicated structure, or have a large number of states will require larger and more complex flight maneuvers to provide satisfactory estimates from any estimation algorithm. Computer roundoff errors are the only real limitations on how complex the model (written in functional form) can be or how many unknown aerodynamic coefficients can be determined from high-quality flight maneuvers.

4.1 DESCRIPTION OF A PARAMETER ESTIMATION PROGRAM

The Iliff-Maine code (MMLE3 program) described in Ref. 9 is used throughout the remainder of this paper to obtain estimates of the coefficients of the differential equations of motion.

Figure 4 illustrates the maximum likelihood estimation concept for aircraft data as used by MMLE3. The measured response of the aircraft is compared with the estimated response, and the difference between these responses is called the response error. The Gauss-Newton computational algorithm (Ref. 26, section (2.5.2)) is used to find the coefficient values that maximize the likelihood functional. Each iteration of this algorithm provides new estimates of the unknown coefficients on the basis of the response error. These new estimates of the coefficients are then used to update the mathematical model of the aircraft, providing a new estimated response and, therefore, a new response error. The updating of the mathematical model continues iteratively until a convergence criterion is satisfied. The estimates resulting from this procedure are the maximum likelihood estimates.

The maximum likelihood estimator also provides a measure of the reliability of each estimate based on the information obtained from each dynamic maneuver. This measure of the reliability, analogous to the standard deviation, is called the Cramèr-Rao bound (Ref. 25) or the uncertainty level. The Cramèr-Rao bound as computed by current programs should generally be used as a measure of relative accuracy rather than absolute accuracy. The bound is obtained from the approximation of the information matrix (Ref. 26).

4.2 EQUATIONS FOR SIMPLE EXAMPLE

The basic concepts involved in a parameter estimation problem can be illustrated by using a simple example representative of a realistic aircraft problem. The example chosen here is representative of an aircraft that exhibits pure rolling motion from an aileron input. This example, although simplified, typifies the motion exhibited by many aircraft in particular flight regimes, such as the F-14 aircraft flying at high dynamic pressure, the F-111 aircraft at moderate speeds with the wing in the forward position, and the T-37 aircraft at low speed. The model of this example is linear, but the results from a more complex example would lead to the same conclusions. A more complex example only makes the basic concepts more difficult to illustrate.

Derivation of an equation describing this motion is straightforward. Figure 5 shows a sketch of an aircraft with the x-axis perpendicular to the plane of the figure (positive forward on the aircraft). The rolling moment (L'), roll rate (p), and aileron deflection (δ_a) are positive as shown. For this example, the only state is p and the only control is δ_a. The result of summing moments is

$$I_x\dot{p} = L'(p,\delta_a) \tag{4}$$

The first-order Taylor expansion then becomes

$$\dot{p} = L_p p + L_{\delta_a}\delta_a \tag{5}$$

where

$$L' = I_x L$$

Since the aileron is the only control, it is notationally simpler to use δ instead of δ_a for the discussion of this example. Equation 5 can then be written as

$$\dot{p} = L_p p + L_\delta \delta \tag{6}$$

In the nondimensional form this becomes

$$\dot{p}I_x = \bar{q}sb\left(C_{\ell_p}\frac{pb}{2V} + C_{\ell_\delta}\delta\right) \tag{7}$$

The dimensional form of Eq. (6) is used hereafter since it is simpler notationally.

Equation (6) is a simple aircraft equation where the forcing function is provided by the aileron and the damping by the damping-in-roll term, L_p. Equation (7) can be written and solved in the same form as Eq. (65) of Ref. 12, but the addition of the hysteresis term in Eq. (65) would only complicate the essential character of the estimation. In subsequent sections we examine in detail the parameter estimation problem where Eq. (6) describes the system. For this single-degree-of-freedom problem, the maximum likelihood estimator is used to estimate either L_p or L_δ or both for a given computed time history.

Now that we have specified the equations describing our simple model, we can examine the characteristics of the maximum likelihood estimation in this simple case. Chapters 2, 7, and 8 of Ref. 26 describe maximum likelihood estimation in detail for the general case. Our simple example requires only a few of the results from that reference, so those results are repeated briefly below.

Where, as in our example, there is no state noise and the equations of motion are linear, the equations are

$$x(t_0) = x_0 \tag{8}$$

$$\dot{x}(t) = Ax(t) + Bu(t) \tag{9}$$

$$z(t_i) = Cx(t_i) + Du(t_i) + Gn_i \tag{10}$$

where x is the state vector, z is the observation vector, and u is the control vector.

The maximum likelihood estimator minimizes the cost function

$$J(\xi) = \frac{1}{2}\sum_{i=1}^{N}[z(t_i) - \tilde{z}_\xi(t_i)]^*(GG^*)^{-1}[z(t_i) - \tilde{z}_\xi(t_i)] \tag{11}$$

where GG* is the measurement noise covariance, and $\tilde{z}_\xi(t_i)$ is the computed response estimate of z at t_i for a given value of the unknown parameter vector ξ. The cost function is a function of the difference between the measured and computed time histories.

To minimize the cost function $J(\xi)$, we can apply the Newton-Raphson algorithm which chooses successive estimates of the vector of unknown coefficients, $\hat{\xi}$. Let L be the iteration number. The L + 1 estimate of $\hat{\xi}$ is then obtained from the L estimate as follows:

$$\hat{\xi}_{L+1} = \hat{\xi}_L - \left[\nabla^2_\xi J(\hat{\xi}_L)\right]^{-1}\left[\nabla^*_\xi J(\hat{\xi}_L)\right] \tag{12}$$

The first gradient is defined as

$$\nabla_\xi J(\xi) = -\sum_{i=1}^{N}[z(t_i) - \tilde{z}_\xi(t_i)]^*(GG^*)^{-1}[\nabla_\xi \tilde{z}_\xi(t_i)] \tag{13}$$

The Gauss-Newton approximation to the second gradient is

$$\nabla^2_\xi J(\xi) \cong \sum_{i=1}^{N}[\nabla_\xi \tilde{z}_\xi(t_i)]^*(GG^*)^{-1}[\nabla_\xi \tilde{z}_\xi(t_i)] \tag{14}$$

The Gauss-Newton approximation, which is sometimes referred to as modified Newton-Raphson, is computationally much easier than Newton's method because the second gradient of the innovation never needs to be calculated. In addition, it can have the advantage of speeding the convergence of the algorithm.

Equation (11) then gives the cost function for maximum likelihood estimation. The weighting GG* is unimportant for this problem, so let it equal 1. For our example, Eqs. (9) and (10) become $x_i = p_i$ and $z_i = x_i$. Therefore, Eq. (11) becomes

$$J(L_p, L_\delta) = \frac{1}{2}\sum_{i=1}^{N}[p_i - \tilde{p}_i(L_p, L_\delta)]^2 \tag{15}$$

where p_i is the value of the measured response p at time t_i and $\tilde{p}_i(L_p, L_\delta)$ is the computed time history of $\tilde{p}$ at time t_i for $L_p = \hat{L}_p$ and $L_\delta = \hat{L}_\delta$. Throughout the rest of the paper, where simulated data are used, the measured time history (simulated) refers to p_i, and the computed time history refers to $\tilde{p}_i(L_p, L_\delta)$.

The computed time history is a function of the current estimates of L_p and L_δ, but the measured time history is not. The expression for obtaining $\tilde{p}_i(L_p,L_\delta)$ is given in Ref. 9.

The maximum likelihood estimate is obtained by minimizing Eq. (11). The Gauss-Newton method described earlier is used for this minimization. Equation (12) is used to determine successive values of the estimates of the unknowns during the minimization. The first and second gradients are defined by Eqs. (13) and (14). For this simple problem, $\hat{\xi} = [\hat{L}_p \; \hat{L}_\delta]^*$ and successive estimates of L_p and L_δ are determined by updating Eq. (12).

The entire procedure can now be written for obtaining the maximum likelihood estimates for this simple example. To start the algorithm, initial estimates of L_p and L_δ are needed. This is the value selected for $\hat{\xi}_0$. With Eq. (12), $\hat{\xi}_1$ and subsequently $\hat{\xi}_L$ are defined by using the first and second gradients of $J(L_p,L_\delta)$ from Eq. (15). The gradients for this particular example from Eqs. (13) and (14) are

$$\nabla_\xi J(\hat{\xi}_L) = -\sum_{i=1}^{N} (p_i - \tilde{p}_i)\nabla_\xi \tilde{p}_i \tag{16}$$

$$\nabla_\xi^2 J(\hat{\xi}_L) \cong \sum_{i=1}^{N} (\nabla_\xi \tilde{p}_i)^* \; (\nabla_\xi \tilde{p}_i) \tag{17}$$

With the specific equations defined in this section for this simple example, we can now proceed in the next section to the computational details of a specific example.

4.3 COMPUTATIONAL DETAILS OF MINIMIZATION

In the previous section we specified the equations for a simple example and described the procedure for obtaining estimates of the unknowns from a dynamic maneuver. In this section we give the computational details for obtaining the estimates. Some of the basic concepts of parameter estimation are best shown with computed data where the correct answers are known. Therefore, in this section we study two examples involving simulated time histories. The first example is based on data that have no measurement noise, which results in estimates that are the same as the correct value. The second example contains significant measurement noise similar to the noise that occurs in data obtained at extreme flight conditions; consequently, the estimates differ from the correct values. Throughout the rest of the paper, where simulated data are used, the term "no-noise case" is used for the case with no noise added and "noisy case" for the case where noise has been added.

For this simulated example, 10 time sample points are used. The simulated data, which we refer to as the measured data, are based on Eq. (6). We use the same correct values of L_p and L_δ (-0.2500 and 10.0, respectively) for both examples. In addition, the same input (δ) is used for both examples, the sample interval (Δ) is 0.2 sec, and the initial conditions are zero. Tables of all the significant intermediate values are given for each example. These values are given to four significant digits, although to obtain exactly the same values with a computer requires the use of 13 significant digits, as in the computation of these tables. In both examples, the initial values of L_p and L_δ (or $\hat{\xi}_0$) are -0.5 and 15.0, respectively. More complete detailed calculations are given in Ref. 8.

4.3.1 Example With No Measurement Noise

The measurement time history for no measurement noise (no-noise case) is shown in Fig. 6. The aileron input starts at zero, goes to a fixed value, and then returns to zero. The resulting roll-rate time history is also shown.

For each value of L (number of iterations), we can get ξ_L by using Eq. (12). Table 1 shows the values for $\hat{L}_p$, $\hat{L}_\delta$, and J for each iteration. In three iterations the algorithm converges to the correct values to four significant digits for both L_p and L_δ. $\hat{L}_\delta$ overshoots slightly on the first iteration and then comes quickly to the correct answer. $\hat{L}_p$ overshoots slightly on the second iteration.

Figure 7 shows the match between the measured data and the computed data for each of the first three iterations. The match is very good after two iterations. The match is nearly exact after three iterations.

Although the algorithm has converged to four-digit accuracy in L_p and L_δ, the value of the cost function, J, continues to decrease rapidly between iterations 3 and 4. This is a consequence of using the maximum likelihood estimator on data with no measurement noise. Theoretically, using infinite accuracy, the value of J at the minimum should be zero. However, with finite accuracy, the value of J becomes small but never quite zero. This value is a function of the number of significant digits being used. For the 13-digit accuracy used here, the cost eventually decreases to approximately 0.3×10^{-28}.

4.3.2 Example With Measurement Noise

The data used in the example with measurement noise (noisy case) are the same as those used in the previous section, except that pseudo-Gaussian noise has been added to the roll rate. The time history is shown in Fig. 8. The signal-to-noise ratio is quite low in this example, as one would expect in data obtained at extreme flight conditions. This is readily apparent when Figs. 6 and 8 are compared. Table 2

shows the values of $\hat{L}_p$, $\hat{L}_\delta$, and J for each iteration. The algorithm converges in four iterations. The behavior of the coefficients as they approach convergence is much like the no-noise case. The most notable result of this case is the converged values of $\hat{L}_p$ and $\hat{L}_\delta$, which are somewhat different from the correct values. The difference in converged values is caused by the measurement noise. As stated in Section 3.5, DATA AND TRAJECTORY RECONSTRUCTION, the parameter estimates can be improved by reducing the measurement noise. The match between the measured and computed time history is shown in Fig. 9 for each iteration. No change in the match is apparent for the last two iterations. The match is very good considering the low signal-to-noise ratio of this example.

In Fig. 10, the computed time history for the no-noise estimates of L_p and L_δ is compared to that for the noisy-case estimates of L_p and L_δ. Because the algorithm converged to values somewhat different than the correct values, the two computed time histories are similar but not identical.

4.4 COST FUNCTIONS

In the previous section, we obtained the maximum likelihood estimates for computed time histories by minimizing the values of the cost function. To fully understand what occurs in this minimization, we must study in more detail the form of the cost functions and some of their more important characteristics. In this section, the cost function for the no-noise case is discussed briefly. The cost function of the noisy case is then discussed in more detail. The same two time histories studied in the previous section are examined here. The noisy case is more interesting because it has a meaningful Cramèr-Rao bound and is more representative of aircraft flight data.

First we will look at the one-dimensional case, where L_δ is fixed at the correct value, because it is easier to grasp some of the characteristics of the cost function in one dimension. Then we will look at the two-dimensional case, where both L_p and L_δ are varying. It is important to remember that everything shown in this paper on cost functions is based on simulated time histories that are defined by Eq. (5). For every time history we might choose (computed or flight data), a complete cost function is defined. For the case of n variables, the cost function defines a hypersurface of n + 1 dimensions. It might occur to us that we could just construct this surface and look for the minimum, avoiding the need to bother with the minimization algorithm. However, this is not a reasonable approach because, in general, the number of variables is greater than two. Therefore, the cost function can be described mathematically but not pictured graphically.

4.4.1 One-Dimensional Case

To understand the many interesting aspects of cost functions, it is easiest to first look at cost functions having one variable. In an earlier section, the cost function of L_p and L_δ was minimized. That cost function is most interesting in the L_p direction. Therefore, the one-variable cost function studied here is $J(L_p)$. All discussions in this section are for $J(L_p)$ with L_δ equal to the correct value, 10. Figure 11 shows the cost function plotted as a function of L_p for the case where there is no measurement noise (no-noise case). As expected for this case, the minimum cost is zero and occurs at the correct value of L_p = -0.2500. It is apparent that the cost increases much more slowly for a more negative L_p than for a positive L_p. Physically this makes sense since the more negative values of L_p represent cases of high damping, and the positive L_p represents an unstable system. Therefore, the p_i for positive L_p becomes increasingly different from the measured time history for small positive increments in L_p.

In Fig. 12, the cost function based on the time history with measurement noise (noisy case) is plotted as a function of L_p. The correct value of L_p (-0.2500) and the value of L_p (-0.3218) at the minimum of the cost (3.335) are both indicated on the figure. The general shape of the cost function in Fig. 12 is similar to that shown in Fig. 11. Figure 13 shows the comparison between the cost functions based on the noisy and no-noise cases. The comments relating to the cost functions' dependence on L_p error in the no-noise case also apply to the cost function based on the noisy case. Figure 13 shows clearly that the two cost functions are shifted by the difference in the value of L_p at the minimum and increased by the difference in the minimum cost. The difference shown here illustrates the penalty if one does not pay close attention to reducing the measurement noise. A similar shift would occur if an incorrect model were used. This was discussed earlier in reference to data reconstruction.

Figure 14 shows the gradient of $J(L_p)$ plotted as a function of L_p for the noisy case. This is the function for which we were trying to find the zero (or equivalently, the minimum of the cost function) using the Gauss-Newton method that is discussed in a previous section. The gradient is zero at L_p = -0.3218, which corresponds to the value of the minimum of $J(L_p)$.

The usefulness of the Cramèr-Rao bound was discussed earlier. At this point it is useful to digress briefly to discuss some of the ramifications of the Cramèr-Rao bound for the one-dimensional case. The Cramèr-Rao bound has meaning only for the noisy case. In the noisy example, the estimate of L_p is -0.3218 and the Cramèr-Rao bound is 0.0579. This relatively large value of the Cramèr-Rao bound is caused by the low signal-to-noise ratio (data from extreme flight conditions) for this case. The Cramèr-Rao bound indicates that we are getting a poor estimate of the rate-dependent coefficient L_p. The Cramèr-Rao bound is an estimate of the standard deviation of the estimate. One would expect the scatter in the estimates of L_p to be of about the same magnitude as the estimate of the standard deviation. For the one-dimensional case discussed here, the range of L_p (-0.3218) plus or minus the Cramèr-Rao bound (0.0579) nearly includes the correct value of L_p (-0.2500). If noisy cases are generated for many time histories (adding different measurement noise to each time history), then the sample mean and sample standard

deviation of the estimates for these cases can be calculated. Table 3 gives the sample mean, sample standard deviation, and the standard deviation of the sample mean (standard deviation divided by the square root of the number of cases) for 5, 10, and 20 cases. The sample mean, as expected, gets closer to the correct value of -0.2500 as the number of cases increases. This is also reflected by the decreasing values column of Table 3, which are estimates of the error in the sample mean. The next to last column of Table 3 shows the sample standard deviations, which indicate the approximate accuracy of the individual estimates. This standard deviation, which stays more or less constant, is approximately equal to the Cramèr-Rao bound for the noisy case being studied here. In fact, the Cramèr-Rao bounds for each of the 20 noisy cases used here (not shown in the table) do not vary significantly from the values found for the noisy case being studied. Both of these results are in good agreement with the theoretical characteristics (Ref. 27) of the Cramèr-Rao bounds and maximum likelihood estimators in general.

The examples shown here indicate the value of obtaining more sample time histories (maneuvers). More samples improve confidence in the estimate of the unknowns. The same result holds true in analyzing actual flight time histories (maneuvers); thus it is always advisable to obtain several maneuvers at a given flight condition to improve the best estimate of each derivative. This is especially true when analyzing data obtained at extreme flight conditions.

The size of the Cramèr-Rao bounds and of the error between the correct value and the estimated value of L_p is determined to a large extent by the length of the time history and the amount of noise added to (or modeling error present in) the correct time history. For the example being studied here, it is apparent from Fig. 8 that the amount of noise being added to the time history is large. The effect of the power of the measurement noise (GG*, Eqs. (9) and (10)) on the estimate of L_p for the time history is given in Table 4. The estimate of L_p is much improved by decreasing the measurement noise power. A reduction in the value of G to one-tenth of the value in the noisy example being studied yields an acceptable estimate of L_p. For flight data, the measurement noise is reduced by improving the accuracy of the output of the measurement sensors or through data and trajectory reconstruction, as discussed in an earlier section.

4.4.2 Two-Dimensional Case

In this section, the cost function (dependent on both L_p and L_δ) is studied. The no-noise case is examined first, followed by the noisy case.

Even though the cost function is a function of only two unknowns, it becomes much more difficult to visualize than the one-unknown case. The cost function over a reasonable range of L_p and L_δ is shown in Fig. 15. The cost increases rapidly in the region of positive L_p and large values of L_δ. The reason is just an extension of the argument for positive L_p given in the previous section. The shape of the surface can be depicted in greater detail if we examine only the values of the cost function less than 200 for L_p less than 1.0. Figure 16 shows a view of this restricted surface from the upper end of the surface. The minimum must lie in the curving valley that gets broader as we go to the far side of the surface. Now that we have a picture of the surface, we can look at the isoclines of constant cost on the L_p-versus-L_δ plane. These isoclines are shown in Fig. 17. The minimum of the cost function is inside the closed isocline. The steepness of the cost function in the positive-L_p direction is once again apparent. Inside the closed isocline the shape is more nearly elliptical, indicating that the cost is nearly quadratic here, so fairly rapid convergence in this region would be expected. The L_p axis becomes an asymptote in cost as L_δ approaches zero. The cost is constant for $L_\delta = 0$ because no response would result from any aileron input. The estimated response is zero for all values of L_p, resulting in constant cost.

Figure 17 includes the minimum value of the cost function, which, as seen in the earlier example (Table 1), occurs at the correct values for L_p and L_δ of -0.2500 and 10.0, respectively. This is also evident from the cost function surface shown in Fig. 18. The surface has its minimum at the correct value. As expected, the value of the cost function at the minimum is zero.

Sometimes nonestimation specialists get the impression that the final estimate of a parameter (stability and control coefficient) is dependent on the starting value, but this is not the case for the maximum likelihood estimator. If the maximum likelihood estimator is used to obtain the maximum likelihood estimates, the estimate will be the minimum of the cost function, as shown in Figs. 13, 16, and 18. These minima are independent of the starting values. If the estimation technique includes *a priori* information in the cost function (such as a maximum *a posteriori* estimator), the minimum value is affected by *a priori* estimates of the coefficient. Usually the *a priori* value is used as the starting value for maximum likelihood estimators, leading some to the conclusion that the estimate is a function of the starting values for all estimators. For all cases that are discussed in this paper the minimum of the cost function is independent of the starting value. Of course, the further one starts the algorithm from the minimum value, the longer it takes the algorithm to converge. Therefore, especially for data obtained at extreme flight conditions, it is important to have good wind tunnel and computational fluid dynamic estimates. These other estimates also can prove useful for fixing values of coefficients of the estimates as we did L_δ in the one-dimensional case. This information can also be used in the maximum *a posteriori* estimators.

As shown before in the one-dimensional case, the primary difference between the cost functions for the no-noise and noisy cases was a shift in the cost function. In that instance, the noisy case was shifted so that the minimum was at a higher cost and a more negative value of L_p. In the two-dimensional case, the no-noise and noisy cost functions exhibit a similar shift. For two dimensions, the shift is in both the L_p and L_δ directions. The shift is small enough that the difference between the two cost functions is not visible at the scale shown in Fig. 15 or from the perspective of Fig. 16. Figure 19 shows the

isoclines of constant cost for the noisy case. The figure looks much like the isoclines for the no-noise case shown in Fig. 17. The difference between Figs. 17 and 19 is a shift in L_p of about 0.1. This is the difference in the value of L_p at the minimum for the no-noise and noisy cases. Heuristically, one can see that the same would be true for cases with more than two unknowns. The primary difference between the two cost functions is near the minimum.

The next logical part of the cost function to examine is near the minimum. Figure 20 shows the same view of the cost function for the noisy case as was shown in Fig. 10 for the no-noise case. The shape is roughly the same as that shown in Fig. 18, but the surface is shifted such that its minimum lies over $L_p = -0.3540$ and $L_\delta = 10.24$, and is shifted upward to a cost function value of approximately 3.3.

To get a more precise idea of the cost of the noisy case near the minimum, we once again need to examine the isoclines. The isoclines (Fig. 21) in this region are much more like ellipses than they are in Figs. 17 and 19. We can follow the path of the minimization example used before by including the results from Table 2 on Fig. 2. The first iteration (L = 1) brought the values of L_p and L_δ very close to the values at the minimum. The next iteration essentially selected the values at the minimum when viewed at this scale. One of the reasons the convergence is so rapid in this region is that the isoclines are nearly elliptical, indicating that the cost is very nearly quadratic in this region. Had we started the Gauss-Newton algorithm at a point where the isoclines are much less elliptical (as in some of the border regions in Fig. 19), the convergence would have been much slower initially, but much the same as it entered the nearly quadratic region of the cost function. The process, of course, results in the same minimum regardless of the starting values.

A final point to be made in examining cost functions deals with the relative shape of the cost function. Although these shapes are somewhat apparent in Figs. 15, 16, and 17, they are most readily studied for constant-cost isoclines as in Figs. 19 and 21. The result we want here is related to the steepness of the cost near the minimum. The minimum shown in Fig. 21 occurs at a cost of 3.3. If we project the isocline for the cost of J = 5 onto the L_p axis, we intersect values for L_p of approximately 0 and -0.7. This is a small increase in cost (about 50 percent), yet the values spanned for L_p are ±100 percent of the noise-contaminated estimate. If we project the same isocline onto the L_δ axis, we intersect values for L_δ of approximately 9 and 11. This is only a change of about 10 percent for the same increase in cost. This shows that the rate-dependent coefficient L_p has a much flatter shape near the minimum than does the control derivative L_δ, which means that relative accuracy in estimating L_p is much poorer than for L_δ. This result can be generalized for all the rate-dependent coefficients as compared with the primary stability and control coefficients, such as L_β, N_β, and L_δ. Going one step further, the cross and cross-coupling coefficients (such as L_r or $L_{\dot{\beta}}$) are even flatter near the minimum than are the rotary coefficients (such as L_p and N_r). This fact points out the necessity of obtaining the best possible estimates from other predictive techniques for rate-dependent coefficients. These coefficients can be estimated from rotary balance or forced oscillation tests. It remains to be seen if these wind tunnel estimates will be more accurate than the flight-determined estimates. Currently the thought is that each source of these coefficients will have deficiencies, but with information from both sources we may be able to determine the relative importance of accurate values of the coefficients in defining a good model. One final item on the relative flatness of the cost functions is that the flatness can be reduced by (1) increasing the length of the flight maneuver, (2) reducing the number of unknown coefficients (fixing the values at computed or wind tunnel values), (3) reducing the noise in the instrumentation system through better instruments or through data reconstruction, (4) reducing equation errors with better estimates of the mass characteristics, and (5) increasing the information content of the maneuver by defining and flying specifically designed maneuvers at extreme flight conditions.

Before concluding our examination of the two-dimensional case, we need to examine the Cramèr-Rao bound. Figure 22 shows the uncertainty ellipsoid, which is based on the Cramèr-Rao bounds defined in an earlier section. The relationships between the Cramèr-Rao bound and the uncertainty ellipsoid are discussed in Ref. 27. The uncertainty ellipsoid almost includes the correct value of L_p and L_δ. The Cramèr-Rao bound for L_p and L_δ can be determined from the projection of the uncertainty ellipsoid onto the L_p and L_δ axes, and compared with the values of the Cramér-Rao bound, which are 0.1593 and 1.116 for L_p and L_δ, respectively.

5. CONCLUDING REMARKS

This paper discusses the increased complexity and effort required in comparing parameter estimation in the traditional and extreme flight regimes. The analysis in the extreme flight regimes requires more care and understanding in selecting the mathematical model, the mass characteristics, the maneuvers flown, and the type and location of instrumentation sensors. Additional analytical techniques, such as data and trajectory reconstruction and model structure determination, are needed. The evaluation of results is also more complex, and several iterations may be required to evaluate the mathematical model. The essential characteristics of the maximum likelihood estimation technique are studied with the help of a simple, but representative, simulated aircraft flight example. The basics of minimization and the general concepts of cost functions are discussed. The example showed the value of low measurement noise, multiple estimates at a given flight condition, and the Cramèr-Rao bounds. The relative flatness of the cost functions in the direction of the rate-dependent coefficients is demonstrated. This flatness is shown to result in poor estimation of these coefficients. The need for a close interplay between computation, wind tunnel, and flight analysis is also discussed.

6. REFERENCES

1. Dynamic Stability Parameters. AGARD-CP-235, 1978.

2. Dynamic Stability Parameters. AGARD-LS-114, 1981.

3. Methods for Aircraft State and Parameter Identification. AGARD-CP-172, 1975.

4. Parameter Identification. AGARD-LS-104, 1979.

5. AIAA Atmospheric Flight Mechanics Conference Proceedings. AIAA CP849, Aug. 1984.

6. Iliff, Kenneth W.: Aircraft Identification Experience. AGARD-LS-104, paper 6, 1979.

7. Klein, Vladislav; Batterson, James G.; and Murphy, Patrick C.: Determination of Airplane Model Structure From Flight Data by Using Modified Stepwise Regression. NASA TP-1916, 1981.

8. Iliff, Kenneth W.; and Maine, Richard E.: Maximum Likelihood Estimation with Emphasis on Aircraft Flight Data. Proceedings of Workshop on Identification and Control of Flexible Space Structures, June 1984.

9. Maine, Richard E.; and Iliff, Kenneth W.: User's Manual for MMLE3, a General FORTRAN Program for Maximum Likelihood Parameter Estimation. NASA TP-1563, 1980.

10. Foster, G.W.: A Description of the Weighted Least Squares Output-Error Method of Parameter Identification. RAE TM FS 215, 1978.

11. Mulder, J.A.; Jonkers, H.L.; Horsten, J.J.; Breeman, J.H.; and Simons, J.L.: Analysis of Aircraft Performance, Stability and Control Measurements. Parameter Identification, AGARD-LS-104, paper 5, 1979.

12. Tobak, Murray; and Schiff, Lewis B.: Aerodynamic Mathematical Modeling — Basic Concepts. Dynamic Stability Parameters, AGARD-LS-114, paper 1, 1981.

13. Tobak, Murray; and Chapman, Gary T.: Nonlinear Problems in Flight Dynamics Involving Aerodynamic Bifurcations. Unsteady Aerodynamics — Fundamentals and Application of Aircraft Dynamics, AGARD paper 25, May 1985.

14. Wolowicz, Chester H.; and Yancy, Roxannah B.: Experimental Determination of Airplane Mass and Inertial Characteristics. NASA TR R-433, 1974.

15. Malcolm, Gerald N.; and Schiff, Lewis B.: Recent Developments in Rotary-Balance Testing of Fighter Aircraft Configurations at NASA Ames Research Center. Unsteady Aerodynamics — Fundamentals and Applications of Aircraft Dynamics, AGARD paper 18, May 1985.

16. Klein, V.; and Schies, J.R.: Compatability Check of Measured Aircraft Responses Using Kinematic Equations and Extended Kalman Filter. NASA TN D-8514, 1977.

17. Bach, R.E., Jr.; and Wingrove, R.C.: Applications of State Estimation in Aircraft Flight Data Analysis. AIAA-83-2087, 1983.

18. Gupta, N.K.; Hall, W.E., Jr.; and Trankle, T.L.: Advanced Methods of Model Structure Determination from Test Data. AIAA J. Guidance & Control, vol. 1, no. 3, 1978, pp. 197-204.

19. Trankle, T.L.; Vincent, J.H.; and Franklin, S.N.: System Identification of Nonlinear Aerodynamic Models. The Techniques and Technology of Nonlinear Filtering and Kalman Filtering, AGARD-AG-256 paper 7, 1982

20. Iliff, Kenneth W.; Maine, Richard E.; and Shafer, Mary F.: Subsonic Stability and Control Derivatives for an Unpowered, Remotely Piloted 3/8-Scale F-15 Airplane Model Obtained From Flight Test. NASA TN D-8136, 1976.

21. Klein, V; and Batterson, J.G.: Estimated Low-Speed Aerodynamic Parameters of an Advanced Fighter from Flight and Wind Tunnel Data. 14th ICAS Congress, Sept. 1984.

22. Anderson, L.C.; Vincent, J.H.; and Hildreth, B.L.: AV-8B System Identification Results from Full Scale Development Flight Test Program. AIAA-83-2746, AIAA/AHS/IES/SETP/SFTE/DGLR 2nd Flight Testing Conference, Las Vegas, Nev., U.S.A, Nov. 1983.

23. Iliff, K.W.: Stall/Spin Flight Results for the Remotely Piloted Spin Research Vehicle. AIAA Atmospheric Flight Mechanics Conference, AIAA-80-1563, Aug. 1980.

24. Gupta, Naren K.; and Iliff, Kenneth W.: Identification of Aerodynamic Indicial Functions Using Flight Data. AIAA Atmospheric Flight Mechanics Conference, AIAA-82-1375, Aug. 1982.

25. Ross, A.J.; and Edwards, G.F.: Correlation of Predicted and Free-Flight Responses Near Departure Conditions of a High Incidence Research Model. Unsteady Aerodynamics — Fundamentals and Applications to Aircraft Dynamics, AGARD paper 31, May 1985.

26. Maine, Richard E.; and Iliff, Kenneth W.: Identification of Dynamic Systems. AGARD Flight Test Techniques Series, AGARD-AG-300-vol.2, 1985.

27. Maine, Richard E.; and Iliff, Kenneth W.: The Theory and Practice of Estimating the Accuracy of Dynamic Flight-Determined Coefficients. NASA RP-1077, 1981.

Table 1 Pertinent values for no-noise case as a function of iteration

L	$\hat{L}_p(L)$	$\hat{L}_\delta(L)$	J_L
0	-0.5000	15.00	21.21
1	-0.3005	9.888	0.5191
2	-0.2475	9.996	5.083×10^{-4}
3	-0.2500	10.00	1.540×10^{-9}
4	-0.2500	10.00	1.060×10^{-14}

Table 2 Pertinent values for noisy case as a function of iteration

L	$\hat{L}_p(L)$	$\hat{L}_\delta(L)$	J_L
0	-0.5000	15.00	30.22
1	-0.3842	10.16	3.497
2	-0.3518	10.23	3.316
3	-0.3543	10.25	3.316
4	-0.3542	10.24	3.316
5	-0.3542	10.24	3.316

Table 3 Mean and standard deviations for estimates of L_p

Number of cases, N	Sample mean, $\mu(\hat{L}_p)$	Sample standard deviation, $\sigma(\hat{L}_p)$	Sample standard deviation of the mean, $\sigma(\hat{L}_p)/\sqrt{N}$
5	-0.2668	0.0739	0.0336
10	-0.2511	0.0620	0.0196
20	-0.2452	0.0578	0.0129

Table 4 Estimate of L_p and Cramèr-Rao bound as a function of the square root of noise power

Square root of noise power, G	Estimate of $\hat{L}$	Cramèr-Rao bound
0.0	-0.2500	-------
0.01	-0.2507	0.00054
0.05	-0.2535	0.00271
0.10	-0.2570	0.00543
0.2	-0.2641	0.0109
0.4	-0.2783	0.0220
0.8	-0.3071	0.0457
1.0	-0.3218	0.0579
2.0	-0.3975	0.1248
5.0	-0.6519	0.3980
10.0	-1.195	1.279

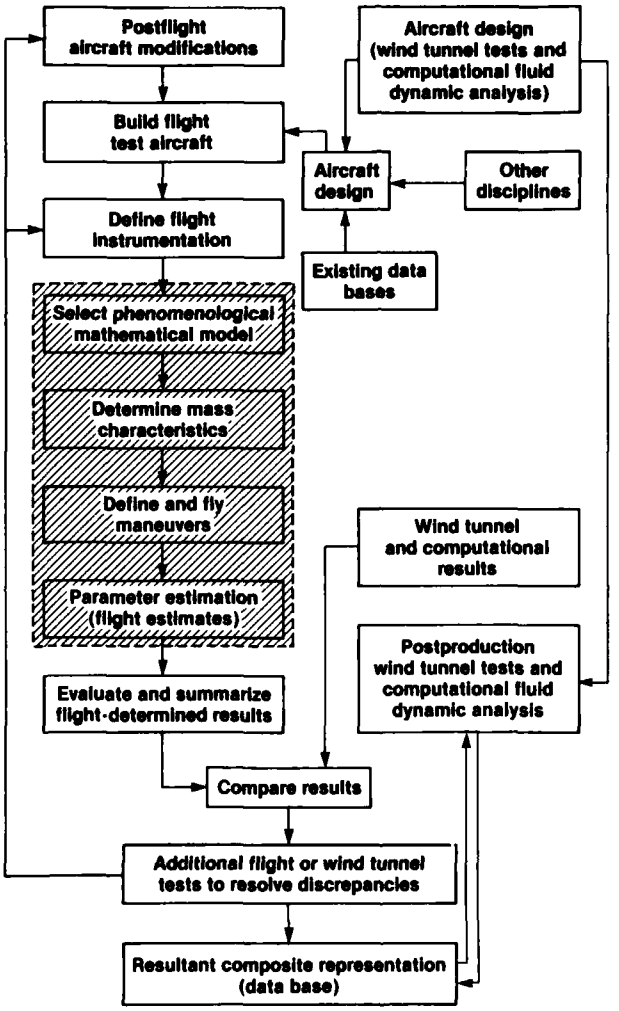

Fig. 1 Approach to validating mathematical model in traditional flight regimes.

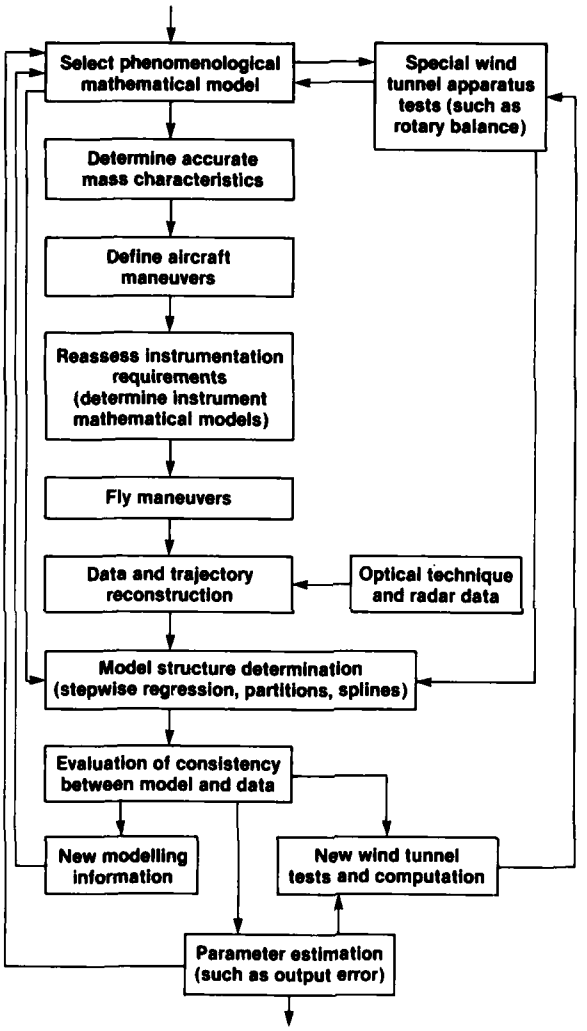

Fig. 2 Approach to validating mathematical model at extreme flight conditions.

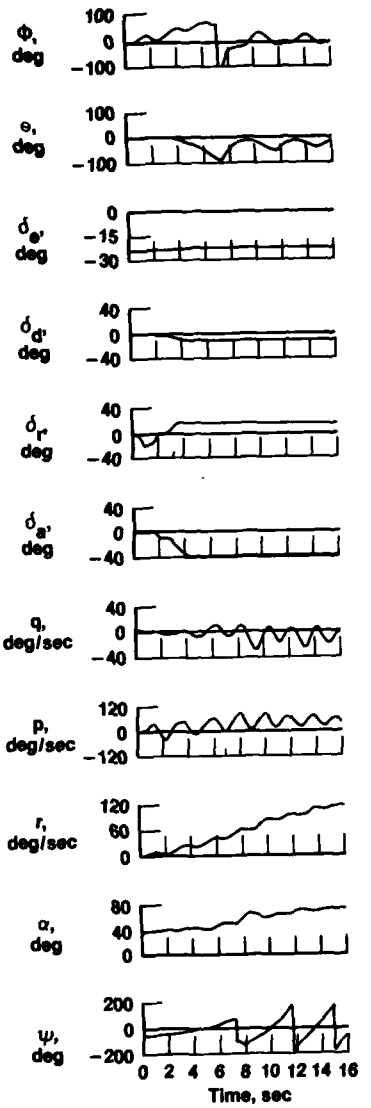

Fig. 3 Typical time history of spin entry.

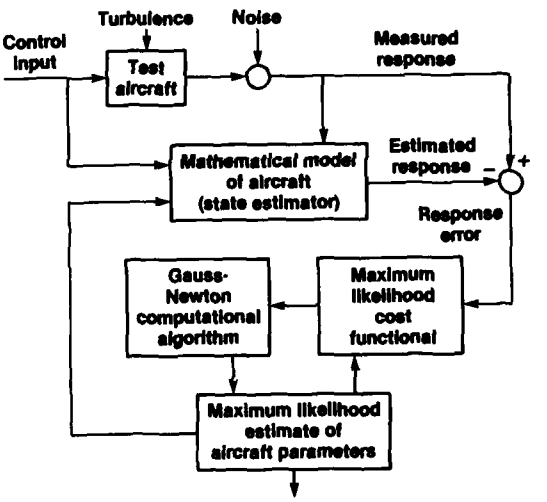

Fig. 4 Maximum likelihood estimation concept.

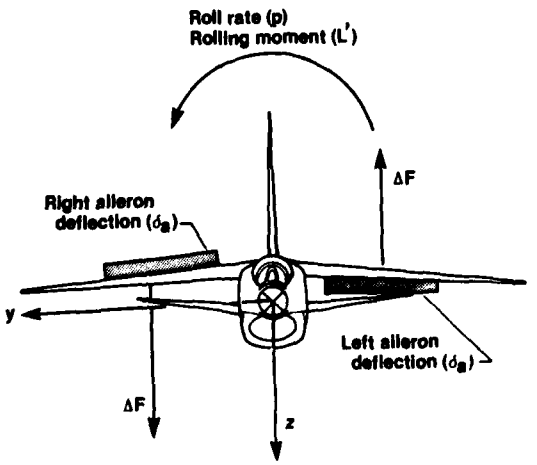

Fig. 5 Simplified aircraft nomenclature.

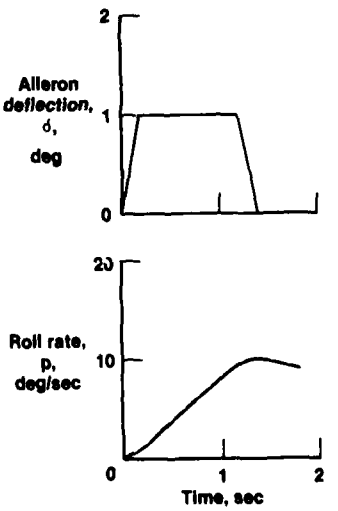

Fig. 6 Time history with no measurement noise.

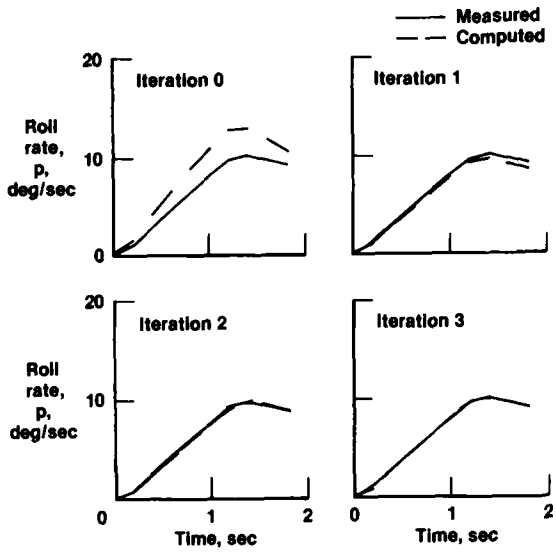

Fig. 7 Comparison of measured and computed data for each of the first three iterations.

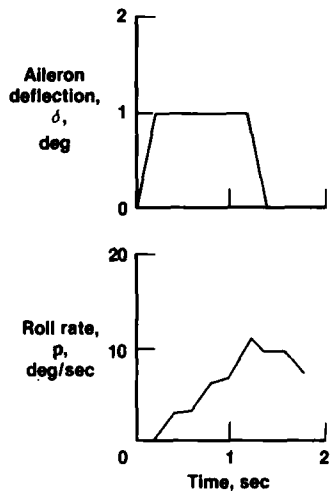

Fig. 8 Time history with measurement noise.

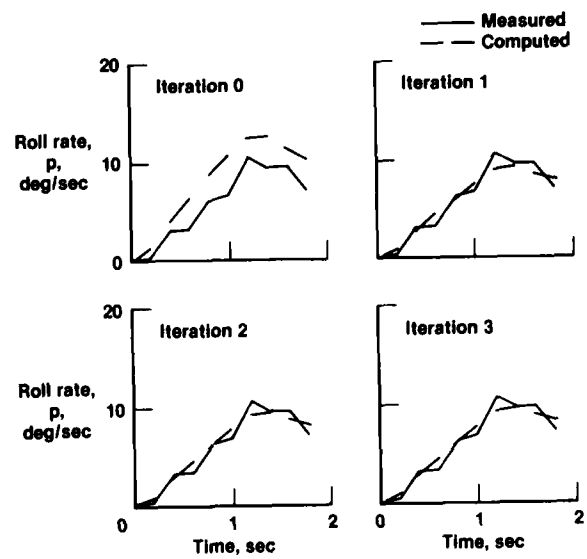

Fig. 9 Comparison of measured and computed data for each iteration.

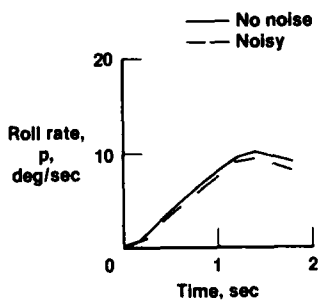

Fig. 10 Comparison of estimated roll rate from no-noise and noisy cases.

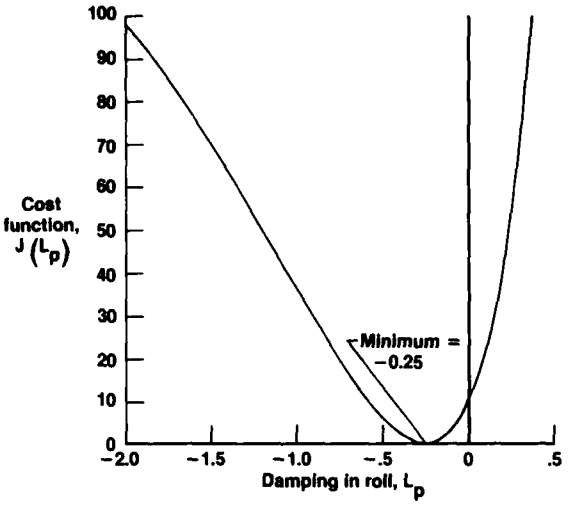

Fig. 11 Cost function ($J(L_p)$) as a function of L_p for no-noise case.

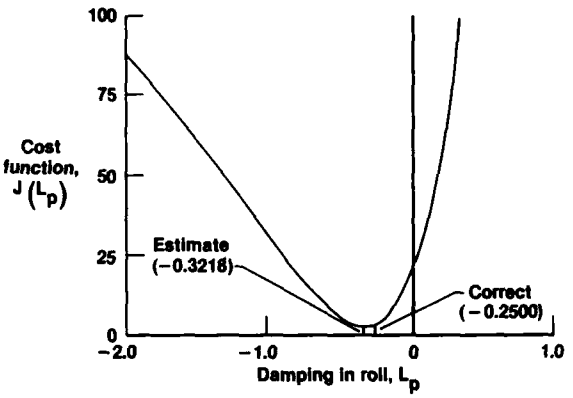

Fig. 12 Cost function as a function of L_p for noisy case.

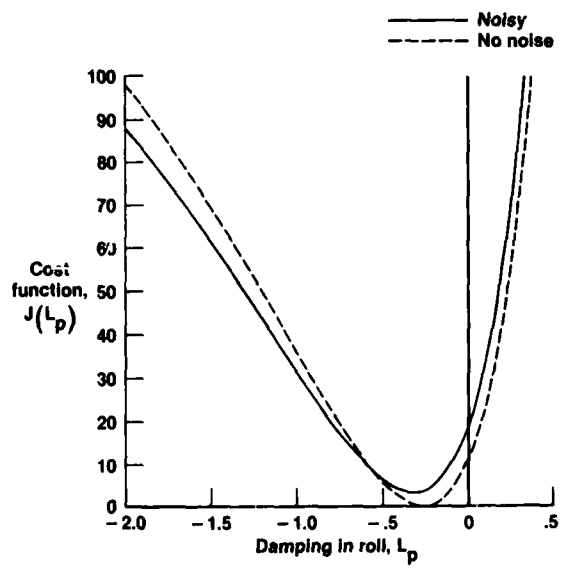

Fig. 13 Comparison of the cost functions for the no-noise and noisy cases.

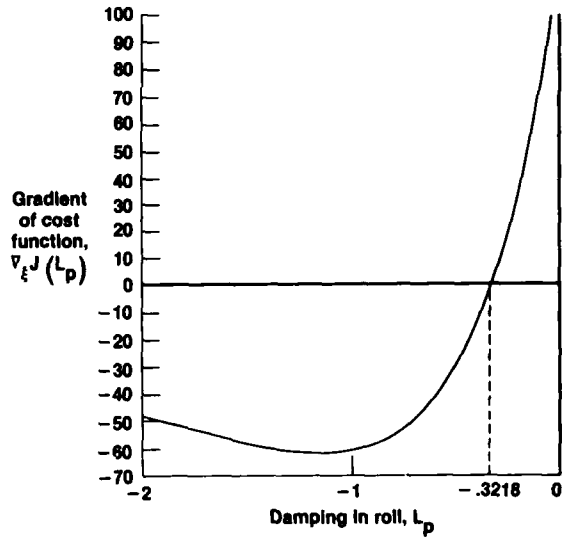

Fig. 14 Gradient of $J(L_p)$ as a function of L_p for noisy case.

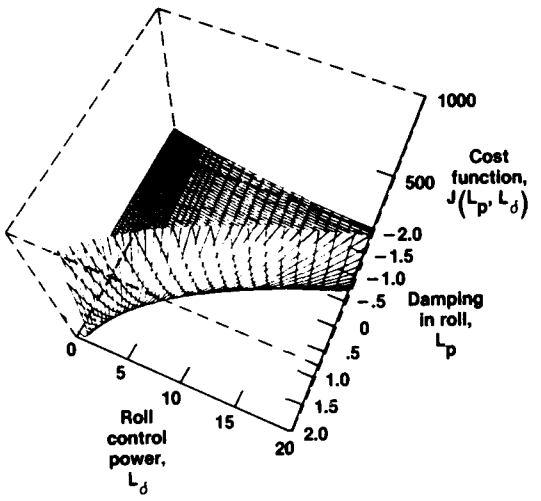

Fig. 15 Large-scale view of cost function surface.

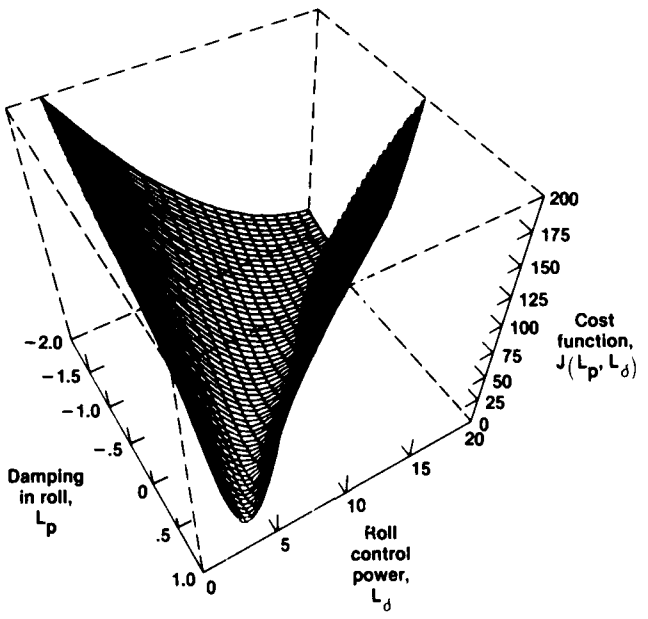

Fig. 16 Restricted view of cost function surface.

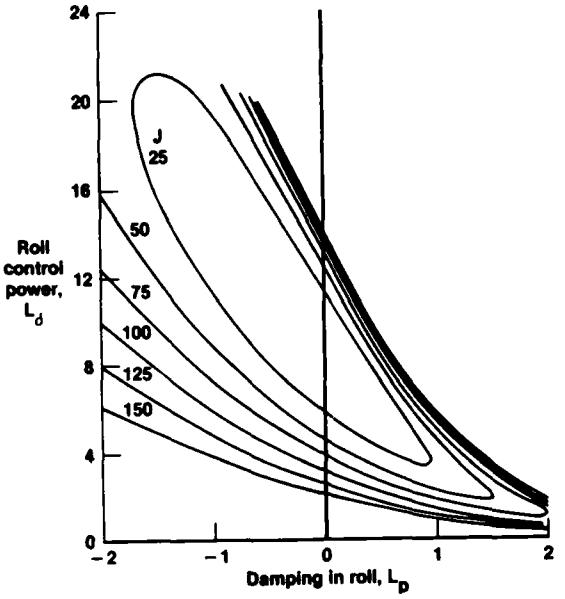

Fig. 17 Isoclines of constant cost of L_p and L_δ for the no-noise case.

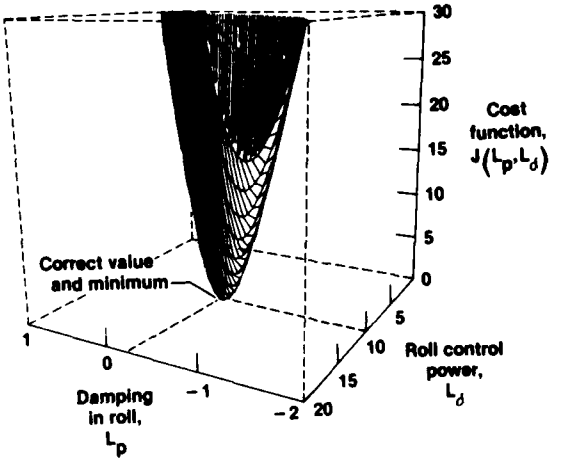

Fig. 18 Detailed view of cost function surface for no-noise case.

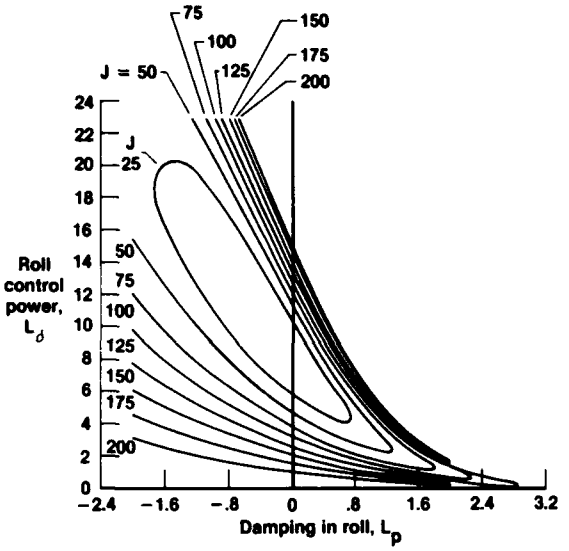

Fig. 19 Isoclines of constant cost in L_p and L_δ for the noisy case.

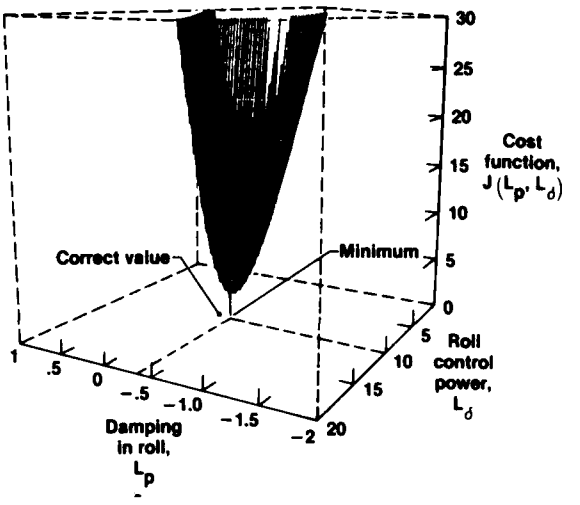

Fig. 20 Detailed view of cost function surface for noisy case.10

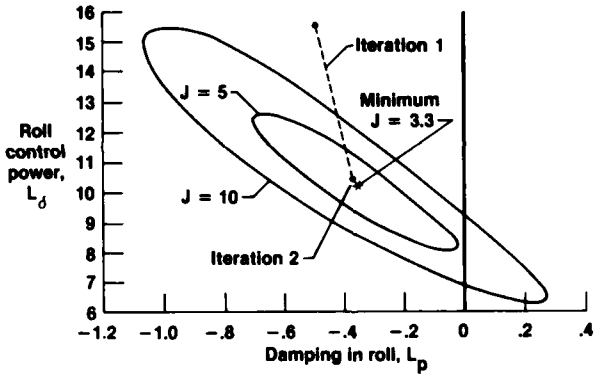

Fig. 21 Isoclines of constant cost for region near minimum for noisy case.

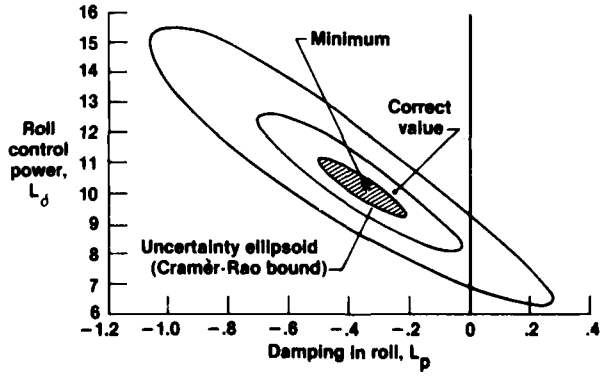

Fig. 22 Isoclines and uncertainty ellipsoid of the cost function for the noisy case.

NONLINEAR PROBLEMS IN FLIGHT DYNAMICS INVOLVING AERODYNAMIC BIFURCATIONS

Murray Tobak and Gary T. Chapman
Research Scientists
NASA Ames Research Center, Moffett Field, California 94035, U.S.A.

SUMMARY

Aerodynamic bifurcation is defined as the replacement of an unstable equilibrium flow by a new stable equilibrium flow at a critical value of a parameter. A mathematical model of the aerodynamic contribution to the aircraft's equations of motion is amended to accommodate aerodynamic bifurcations. Important bifurcations such as, for example, the onset of large-scale vortex-shedding are defined. The amended mathematical model is capable of incorporating various forms of aerodynamic responses, including those associated with dynamic stall of airfoils.

1. INTRODUCTION

In recent years we have become increasingly aware of the connections which link our approach to nonlinear problems in flight dynamics to the body of theory underlying the rapidly growing field known as "nonlinear dynamical systems." In Ref. 1, we attempted to identify the connections explicitly within a framework designed to facilitate study of the aerodynamic contribution to the flight-dynamics system. The framework is composed of parallel observational and mathematical components. A study of observations of fluid flows singled out four important elements for the observational component. First, flow patterns have definite structure (e.g., three-dimensional vortical structures). Second, structures undergo systematic changes with variations in parameters such as angle of attack or Reynolds number. Third, under some conditions the changes lead to chaos (e.g., turbulence). Fourth, the structures have definite spatial and temporal scales. Parallel elements of the mathematical component feature the language of topology and concepts drawn from dynamical-systems theory. The premises of the theoretical framework are: (1) Structures are describable in topological terms. (2) Changes in structure are describable by bifurcation theory. (3) Chaos is describable by the theory of strange attractors and fractals. (4) Scales are describable by group theory ideas. Recently (Ref. 2), we proposed that the framework may be useful as well for the understanding and the potential modeling of turbulent flows.

Here, we shall focus on one element of the framework, namely, change, and its representation by means of bifurcation theory. Bifurcation theory has two principal realms of application in flight-dynamics studies. First, when the form of the aerodynamic contribution to the aircraft's equations of motion is known, and the equations of motion are of the appropriate form, bifurcation theory provides a useful means of analyzing the aircraft's motion, particularly in the vicinity of stability boundaries. This first realm was the subject of study in Ref. 3, and the study is pursued further in Ref. 4 at this conference. The second realm, which will be the subject of this paper, is concerned with the mathematical modeling of the aerodynamic contribution itself.

Reference 5, a companion paper of Ref. 1, was a reconsideration of an approach to mathematical modeling of the aerodynamic characteristics, in which nonlinear indicial responses are used as a basis for arriving at the form of the aerodynamic response to arbitrary motions. Without modification, validity of the approach rests on a fundamental assumption that the indicial response exists and is unique in every incremental step of the motion. The question, "When does the fundamental assumption fail?" led to the recognition that the assumption may be invalidated through the mechanism of flow instability. On exceeding a critical value of a parameter (e.g., angle of attack), the flow field corresponding to the equilibrium state of an aerodynamic response may become unstable to small disturbances. The replacement of the unstable state by a new stable equilibrium state satisfying the same boundary conditions implies failure of the uniqueness condition, and may imply failure of the existence condition as well. Thus, the equilibrium state undergoes a bifurcation, and the circumstances are precisely those that bifurcation theory is designed to address. Although the requisite amendments were not carried out in Ref. 5, it was concluded that bifurcation theory would provide the means to extend the mathematical model so as to acknowledge the occurrence of aerodynamic bifurcation phenomena. As a consequence, the model would have the potential of accounting for those critical points in maneuvers where sudden and dramatic changes in flow structure may occur.

In this paper, we shall try to validate the conclusion of Ref. 5, and demonstrate how the mathematical model can be amended to accommodate the occurrence of aerodynamic bifurcations. A number of important aerodynamic bifurcations will be defined and some of their potential effects on dynamical systems illustrated. Following the analysis presented in Ref. 5, we shall show how the approach to the modeling involving nonlinear indicial responses can be made compatible with an approach based on the use of nonlinear algebraic functional expansions. The latter approach, which has the virtue of concreteness, was formulated originally (Ref. 6) to address nonlinear problems in the field of electrical circuits and systems. Its adaptation here exemplifies the community of interests developing across various disciplines through the unifying medium of research in nonlinear dynamical systems.

2. MODELING INFLUENCE OF PAST MOTION BY PULSES

The following is a slightly modified version of the analysis originally presented in Ref. 5. Again, for clarity, the two-dimensional wing is adopted as illustration, although the results will have more general bearing.

Let the wing move away from a coordinate system whose origin is fixed in space at the center of gravity at a time $\xi = 0$. The distance traveled by the center of gravity along the flightpath is measured by a coordinate s. Let the center of gravity move at constant velocity V_o, so that the trace of its path, plotted against time ξ, is a straight line. This is shown on Fig. 1. The wing is allowed to undergo changes only in the angle of attack α, where α is the angle between the velocity vector and the wing chord line. Projections of the leading and trailing edges of the wing onto the plane containing the velocity vector are maximum when $\alpha = 0$. These maximum projections also trace out straight lines on Fig. 1, parallel to the trace of the center of gravity.

As illustrated in Fig. 1, let the angle of attack α be zero for all time ξ except at $\xi = \xi_1$, where a pulse occurs of amplitude $\alpha(\xi_1)$ and of infinitesimal duration $\Delta\xi_1$. Consider the response to the pulse at ξ_1 of the lift coefficient C_L at a measuring time t subsequent to ξ_1. The lift response at t will be a function of the elapsed time $t - \xi_1$ and the amplitude of the pulse $\alpha(\xi_1)$. If we assume that there will be a range of α $(0 < \alpha < \alpha_1)$ in which the dependence of C_L on $\alpha(\xi_1)$ is <u>analytic</u>, then we can write the response in C_L as a Taylor-series expansion in $\alpha(\xi_1)$ of the form

$$C_L(t) = C_L(t - \xi_1, \alpha(\xi_1))_{dir} = \sum_n a_n(t - \xi_1)[\alpha(\xi_1)]^n \Delta\xi_1 \tag{1}$$

The first of the forms in Eq. (1) will be used in the subsequent analysis to distinguish between direct (subscript dir) and interference (subscript int) effects.

Now let us consider the response in C_L at the measuring time t to a pair of pulses located at ξ_1 and ξ_2 with $\xi_1, \xi_2 < t$. Here, in addition to the direct influence of each of the pulses acting as if in isolation, the interference between the pulses also will influence the lift. The interference effect can be written in a form resembling a product of responses to single pulses

$$C_{L_{int,2}} = \sum_{m,n} b_{mn}(t - \xi_1, t - \xi_2)[\alpha(\xi_1)]^m[\alpha(\xi_2)]^n \Delta\xi_1 \Delta\xi_2 \tag{2}$$

where the subscript (int,2) means "interference between a pair of pulses." The form vanishes properly with the vanishing of either of the pulses and retains the analytic dependence on angle of attack. With the addition of the direct influence of the two pulses, the lift coefficient at time t takes the form

$$C_L(t) = C_L(t - \xi_1, \alpha(\xi_1))_{dir} + C_L(t - \xi_2, \alpha(\xi_2))_{dir} + C_L(t)_{int,2} \tag{3}$$

The process of adding pulses can be continued indefinitely in the same way. At the next stage, the interference between triplets of pulses must be considered as well as that between pairs. Going to the limit of a continuous distribution of pulses starting at time $\xi = 0$ yields a summation of multiple integrals having the form

$$C_L(t) = C_{L_{dir}} + C_{L_{int,2}} + C_{L_{int,3}} + \cdots \tag{4}$$

with

$$C_{L_{dir}} = \sum_n \int_o^t a_n(t - \xi_1)[\alpha(\xi_1)]^n \, d\xi_1 \tag{5}$$

$$C_{L_{int,2}} = \sum_{m,n} \int_o^t [\alpha(\xi_2)]^m \, d\xi_2 \int_o^{\xi_2} b_{mn}(t - \xi_1, t - \xi_2)[\alpha(\xi_1)]^n \, d\xi_1 \tag{6}$$

$$C_{L_{int,3}} = \sum_{m,n,p} \int_o^t [\alpha(\xi_3)]^m \, d\xi_3 \int_o^{\xi_3} [\alpha(\xi_2)]^n \, d\xi_2 \times \int_o^{\xi_2} c_{mnp}(t - \xi_1, t - \xi_2, t - \xi_3)[\alpha(\xi_1)]^p \, d\xi_1 \tag{7}$$

. . .

Written as a nonlinear functional expansion, Eq. (4) represents the lift coefficient at time t in response to an arbitrary variation of α over the time interval zero to t. The form of Eq. (4) confirms an important point made in Ref. 6. It will be noted that a partial summation consisting of the leading term from each of Eqs. (5), (6), . . . forms a Volterra series (Refs. 6,7). The fact that there are terms left over confirms that the a priori adoption of a Volterra series to represent the lift coefficient would have been insufficiently general to accommodate the Taylor series form of the dependence on angle of attack.

3. FORMATION OF INDICIAL RESPONSE

Given Eq. (4), one can now use it to form the indicial response in accordance with the definition in Ref. 8. To indicate the form of the result, it will suffice to consider terms in Eq. (4) only through the series representing $C_{L_{int,2}}$. Two motions need to be considered. In the first, the wing undergoes the motion under study $\alpha(\xi)$ from time zero up to a time $\xi = \tau$, where $\tau < t$. Subsequent to τ, α is held constant at $\alpha(\tau)$. Thus, in Eqs. (4), (5), and (6),

$$\left.\begin{aligned} \alpha_1(\xi) &= \alpha(\xi) \ ; \quad 0 < \xi < \tau \\ &= \alpha(\tau) \ ; \quad \xi \geq \tau \end{aligned}\right\} \tag{8}$$

The direct and interference contributions to $C_L(t)$ take the form

$$\left.\begin{aligned} C_{L_{dir}} &= \sum_n \int_o^\tau a_n(t-\xi_1)[\alpha(\xi_1)]^n \, d\xi_1 + \sum_n [\alpha(\tau)]^n \int_\tau^t a_n(t-\xi_1)d\xi_1 \\ C_{L_{int,2}} &= \sum_{m,n} \int_o^\tau [\alpha(\xi_2)]^m \, d\xi_2 \int_o^{\xi_2} b_{mn}(t-\xi_1, t-\xi_2)[\alpha(\xi_1)]^n \, d\xi_1 \\ &\quad + \sum_{m,n} [\alpha(\tau)]^m \int_\tau^t d\xi_2 \int_o^\tau b_{mn}(t-\xi_1, t-\xi_2)[\alpha(\xi_1)]^n \, d\xi_1 \\ &\quad + \sum_{m,n} [\alpha(\tau)^{m+n}] \int_\tau^t d\xi_2 \int_\tau^{\xi_2} b_{mn}(t-\xi_1, t-\xi_2)d\xi_1 \end{aligned}\right\} \tag{9}$$

In functional notation (Ref. 7), the lift response to the same motion is

$$C_L(t) = C_L[\alpha_1(\xi)] = C_L[\alpha(\xi); t, \tau] \tag{10}$$

where the notation in the first form should be understood to mean that $C_L(t)$ is a functional of the variation $\alpha_1(\xi)$ over the interval $0 < \xi < t$. The second form, which is defined in Ref. 8, is designed to make more explicit that $\alpha_1(\xi)$ represents the motion under study $\alpha(\xi)$ over the interval $0 < \xi < \tau$, but is constrained to remain constant at $\alpha(\tau)$ for $\tau \leq \xi \leq t$. Thus, $C_L(t)$ is both a functional of $\alpha(\xi)$ and a function of t and τ.

In the second motion, the wing undergoes the same angle-of-attack history $\alpha(\xi)$ up to time τ. Subsequent to τ, the angle of attack is again held constant, but is given an incremental step change $\Delta\alpha$ over its previous value of $\alpha(\tau)$. Thus, in the second motion,

$$\left.\begin{aligned} \alpha_2(\xi) &= \alpha(\xi) \qquad ; \quad 0 < \xi < \tau \\ &= \alpha(\tau) + \Delta\alpha \ ; \quad \xi \geq \tau \end{aligned}\right\} \tag{11}$$

The direct and interference contributions to $C_L(t)$ become

$$\left.\begin{aligned} C_{L_{dir}} &= \sum_n \int_o^\tau a_n(t-\xi_1)[\alpha(\xi_1)]^n \, d\xi_1 + \sum_n [\alpha(\tau)+\Delta\alpha]^n \int_\tau^t a_n(t-\xi_1)d\xi_1 \\ C_{L_{int,2}} &= \sum_{m,n} \int_o^\tau [\alpha(\xi_2)]^m \, d\xi_2 \int_o^{\xi_2} b_{mn}(t-\xi_1, t-\xi_2)[\alpha(\xi_1)]^n \, d\xi_1 \\ &\quad + \sum_{m,n} [\alpha(\tau)+\Delta\alpha]^m \int_\tau^t d\xi_2 \int_o^\tau b_{mn}(t-\xi_1, t-\xi_2)[\alpha(\xi_1)]^n \, d\xi_1 \\ &\quad + \sum_{m,n} [\alpha(\tau)+\Delta\alpha]^{m+n} \int_\tau^t d\xi_2 \int_\tau^{\xi_2} b_{mn}(t-\xi_1, t-\xi_2)d\xi_1 \end{aligned}\right\} \tag{12}$$

Again, written as a functional, the lift response to the motion $\alpha_2(\xi)$ is

$$C_L(t) = C_L[\alpha_2(\xi)] \tag{13}$$

The indicial lift response is formed by taking the difference between Eqs. (9) and (12) (or between Eqs. (10) and (13)), dividing by the incremental step $\Delta\alpha$, and going to the limit as $\Delta\alpha \to 0$. Existence of the limit is ensured by the analyticity of the functional dependence on $\alpha(\xi)$. The result is

$$\lim_{\Delta\alpha\to 0} \frac{\Delta C_L(t)}{\Delta\alpha} = \lim_{\Delta\alpha\to 0} \left(\frac{C_L[\alpha_2(\xi)] - C_L[\alpha_1(\xi)]}{\Delta\alpha} \right)$$

$$= \sum_n n[\alpha(\tau)]^{n-1} \int_\tau^t a_n(t - \xi_1) d\xi_1$$

$$+ \sum_{m,n} m[\alpha(\tau)]^{m-1} \int_\tau^t d\xi_2 \int_0^\tau b_{mn}(t - \xi_1, t - \xi_2)[\alpha(\xi_1)]^n \, d\xi_1$$

$$+ \sum_{m,n} (m + n)[\alpha(\tau)]^{m+n-1} \int_\tau^t d\xi_2 \int_\tau^{\xi_2} b_{mn}(t - \xi_1, t - \xi_2) d\xi_1 \qquad (14)$$

Eq. (14) reveals the form of the indicial lift response to a step change in angle of attack in terms of functional expansions. The first and third terms on the right-hand side of Eq. (14) do not depend on the past motion, but only on the level of the angle of attack at which the step was made. The second term depends on the past motion, since $\alpha(\xi_1)$ with $0 < \xi_1 < \tau$ appears within the integral. The leading term of this past dependence has the form

$$\int_\tau^t d\xi_2 \int_0^\tau b_{11}(t - \xi_1, t - \xi_2)\alpha(\xi_1) d\xi_1$$

Dependence on the past thus arises from interference effects between pulses prior to τ, the origin of the step, and perturbation pulses of $O(\Delta\alpha)$ originating subsequent to τ. In the general case, and just as before (Ref. 8), the indicial response is itself a functional.

In fact, in formal terms (see Ref. 9 for a useful account of the essentials) the operations involved in forming the indicial response amount to taking a Fréchet derivative of the functional $C_L[\alpha_1(\xi)]$. To see this, we adopt the notation of Ref. 9, letting

$$h = \varepsilon\eta \qquad (15)$$

where we set

$$\left.\begin{aligned} \varepsilon &= \Delta\alpha \\ \eta &= 0 \; ; \quad 0 < \xi < \tau \\ &= 1 \; ; \quad \xi \geq \tau \end{aligned}\right\} \qquad (16)$$

so that

$$\alpha_2(\xi) = \alpha_1(\xi) + \varepsilon\eta \qquad (17)$$

Then, following Ref. 9, we have

$$\lim_{\Delta\alpha\to 0} \frac{\Delta C_L(t)}{\Delta\alpha} = \lim_{\varepsilon\to 0} \left(\frac{C_L[\alpha_1(\xi) + \varepsilon\eta] - C_L[\alpha_1(\xi)]}{\varepsilon} \right)$$

$$= \frac{d}{d\varepsilon} C_L[\alpha_1(\xi) + \varepsilon\eta]\Big|_{\varepsilon=0}$$

$$= C_L'[\alpha_1(\xi)]\eta \qquad (18)$$

The equivalence of the operations yielding Eqs. (14) and (18) should be evident. Finally, to conform with the notation of Ref. 8, we set

$$\lim_{\Delta\alpha\to 0} \frac{\Delta C_L(t)}{\Delta\alpha} = C_L'[\alpha_1(\xi)]\eta = C_{L_\alpha}[\alpha(\xi); t, \tau] \qquad (19)$$

where the indication of a separate dependence on t and τ rather than on elapsed time $t - \tau$ alone should be noted. It can be easily verified that the first and third terms in Eq. (14), which depend only on $\alpha(\tau)$, indicate a dependence on $t - \tau$ alone; however, as a consequence of its dependence on the past motion, the second term cannot be cast as a function of $t - \tau$ alone.

4. GENERALIZED SUPERPOSITION INTEGRAL

Just as before, Eq. (19) can be used to form a generalized superposition integral for the response in C_L to an arbitrary angle-of-attack variation. The result is

$$C_L(t) = C_L(t; \alpha(0)) + \int_0^t C_{L_\alpha}[\alpha(\xi); t, \tau] \frac{d\alpha}{d\tau} d\tau \qquad (20)$$

with

$$C_L(t;\alpha(0)) = C_L[\alpha(\xi);t,0] \tag{21}$$

It is important to understand the meaning of the first term in Eq. (20). It is the contribution to the lift at time t caused by the flow field existent at the initial instant $\xi = 0$. It would be the only contribution if the angle-of-attack variation subsequent to $\xi = 0$ had remained constant at $\alpha(0)$. A reading of the notation of the second form for this term in Eq. (21) (cf. the definitions following Eq. (10)) provides a more complete interpretation: The first term in Eq. (20) is the lift at time t due to an angle-of-attack variation $\alpha(\xi)$ which is equal to the motion history prior to $\xi = 0$, and which is constrained at $\xi = \tau = 0$ to remain constant at $\alpha(0)$ for all $\xi \geq \tau = 0$. by substituting Eq. (14) for $C_{L_\alpha}[\alpha(\xi);t,\tau]$ in the integral term in Eq. (20) and carrying out the integration, one will verify that the form of Eq. (4) is restored through terms of the series representing $C_{L_{int,2}}$ (i.e., through Eqs. (5) and (6)). We conclude first that an approach to modeling based on nonlinear indicial responses and generalized superposition integrals is compatible with one based on nonlinear functional expansions. Second, validity of the approach rests on the assumption of Fréchet differentiability of the lift response $C_L[\alpha(\xi);t,\tau]$ over the interval $0 < \tau < t$. Invalidation of this assumption may signal the occurrence of an aerodynamic bifurcation.

5. CONNECTION WITH BIFURCATION THEORY

Consider the first of the two maneuvers involved in the formation of the indicial response, that is, the maneuver (cf. Eqs. (8) and (10)) to which the lift response $C_L[\alpha(\xi);t,\tau]$ corresponds. The angle of attack attains a constant value $\alpha(\tau)$ subsequent to τ, and it is reasonable to expect that the flow field at the subsequent time t will approach an equilibrium state that corresponds to this fixed boundary condition as the elapsed time $t - \tau \to \infty$. Heretofore (Ref. 8), the analysis has contained an implicit assumption that as the flow field approached the equilibrium state it became time-invariant, which meant that the corresponding lift coefficient C_L approached a unique constant value $C_L(\infty;\alpha(\tau))$ as $t - \tau \to \infty$. As long as this was true, it was reasonable to expect that an incremental change in $\alpha(\tau)$ of $O(\Delta\alpha)$ would result in an incremental change in $C_L(\infty;\alpha(\tau))$, likewise of $O(\Delta\alpha)$. We now recognize that at least two conditions must be satisfied in order that this be true: (1) The change of $O(\Delta\alpha)$ must not result in a loss of analyticity in the dependence of $C_L[\alpha(\xi);t,\tau]$ on $\alpha(\xi)$. (2) The time-invariant equilibrium flow represented by $C_L(\infty;\alpha(\tau))$ must be asymptotically stable to small perturbations. We deal with the second condition here, assuming for the moment that the first condition has been satisfied. Although exceptions to sufficiency can be envisioned, we shall restrict our study to the class of flows for which asymptotic stability of the equilibrium state is not only necessary, but also sufficient, to ensure that $C_L[\alpha(\xi);t,\tau]$ will be Fréchet differentiable.

It can happen, however, that as $\alpha(\tau)$ is increased in small increments, a critical value of $\alpha(\tau)$ can be reached at which the stationary equilibrium flow represented by $C_L(\infty;\alpha(\tau))$ will no longer be stable to small perturbations. Loss of asymptotic stability signals loss of Fréchet differentiability at the critical value of $\alpha(\tau)$. With the stationary equilibrium state asymptotically unstable, the system will seek a new equilibrium state, and of those that are possible will select one that can remain stable to small perturbations. This is precisely the situation that bifurcation theory is designed to address. Bifurcation theory provides a means of classifying and characterizing the properties of the new equilibrium states that can arise when the given equilibrium state becomes unstable. We call the replacement of an unstable equilibrium state by a new stable equilibrium state an aerodynamic bifurcation. We will now show how the mathematical model Eq. (20) can be amended to acknowledge its occurrence.

Referring to Fig. 2, let us assume that the angle-of-attack variation under study $\alpha(\tau)$ passes through a critical value α_c at a value of $\tau = \tau_c$ within the interval of interest $0 < \tau < t$. If the angle-of-attack variation $\alpha(\tau)$ were constrained to remain constant at α_c for all $\tau > \tau_c$, the corresponding lift response $C_L[\alpha(\xi);t,\tau_c]$ would begin to depart from an initially infinitesimally close neighboring response, such that $C_L[\alpha(\xi);t,\tau_c]$ would not be Fréchet differentiable. Thus, we cannot allow the integration in Eq. (20) to proceed beyond τ_c without acknowledging the loss of Fréchet differentiability. Let us assume that for all other angles of attack within the range $\alpha(0) < \alpha < \alpha(t)$ the lift responses represent asymptotically stable flows permitting Fréchet differentiation. Then we can isolate the critical state by stopping the integration in Eq. (20) just short of τ_c and starting again just beyond τ_c. Within the isolated interval $\tau_c - \varepsilon < \tau < \tau_c + \varepsilon$, we acknowledge the aerodynamic bifurcation by allowing the solution to change discretely to a new equilibrium state. Thus,

$$C_L(t) = C_L(t;\alpha(0)) + \int_0^{\tau_c-\varepsilon} C_{L_\alpha}[\alpha(\xi);t,\tau]\,\frac{d\alpha}{d\tau}\,d\tau + \int_{\tau_c+\varepsilon}^{t} C_{L_\alpha}[\alpha(\xi);t,\tau]\,\frac{d\alpha}{d\tau}\,d\tau + \Delta C_L(t;\alpha_c) \tag{22}$$

where

$$\Delta C_L(t;\alpha_c) = C_L[\alpha(\xi);t,\tau_c + \varepsilon] - C_L[\alpha(\xi);t,\tau_c - \varepsilon] \tag{23}$$

This procedure was introduced earlier (Ref. 8) to acknowledge the occurrence of mean or constant values of the lift coefficient in the equilibrium state $C_L(\infty;\alpha(\tau))$ which could exhibit the discontinuous

and double-valued behavior characteristic of hysteresis. This was a case in which the first of the two conditions just stipulated, namely, analytic dependence of $C_L[\alpha(\xi);t,\tau]$ on α, was violated. The particular way in which this occurred is common in aerodynamics: The variation with α of the lift coefficient in the equilibrium state $C_L(\infty;\alpha(\tau))$ develops a fold at a critical value of α, α_c, so that the slope of $C_L(\infty;\alpha(\tau))$ versus α becomes infinite there. A jump in $C_L(\infty;\alpha(\tau))$ necessarily ensues to the upper branch of the folded curve with an infinitesimal increase in α beyond α_c, and hysteresis follows on the return route. We show this as sketch (a) in Fig. 3 along with, for comparison, sketches (b) and (c) of the two most common forms of aerodynamic bifurcation. These sketches represent bifurcation to another time-invariant equilibrium state. The distinction between the class represented by sketch (a) (the class studied in Ref. 8) and the examples of aerodynamic bifurcations should be noted. In sketch (a) there is only one solution curve; no new branches resulting from instability appear. Discontinuous and double-valued behavior result merely from the fold that develops in the solution curve. In the case of supercritical bifurcation, sketch (b), a new branch of stable solutions appears which is connected to the old branch at the critical point α_c. Beyond α_c, two branches of solutions exist satisfying the same boundary conditions, of which one is stable and the other is unstable. Supercritical bifurcation solutions start from zero and are initially infinitesimal as α increases beyond α_c, so that Eq. (23) would be zero. Supercritical bifurcation is not an important mechanism by which time-invariant equilibrium states exchange stability. The bifurcation can be easily superseded by smooth alternative solution curves through a variety of means (cf. Refs. 10-12). In subcritical bifurcation, sketch (c), the bifurcation solution curve that branches away from the now unstable branch is itself unstable. If it turns back, as indicated in sketch (c), the upper branch will be stable. A discontinuous jump in $C_L(\infty;\alpha(\tau))$ results as α increases beyond α_c, and hysteresis follows on the return route, just as in sketch (a). Here, of course, Eq. (23) will have a value.

Figure 3 has had the important function of reminding us that there are at least two mechanisms which can invalidate the conditions permitting Fréchet differentiation of the lift response $C_L[\alpha(\xi);t,\tau]$. There may be others. Joseph (Refs. 11,12) notes, for example, that isolated solution branches of flows in the equilibrium state can exist which are not connected to other solution branches through bifurcation. Later, we shall entertain the possibility that the initial flow as well as the stability of flow in the equilibrium state may influence Fréchet differentiability. A theory of the means of invalidating Fréchet differentiability of the lift response offers the possibility of an alternative to bifurcation theory. Inasmuch as it would incorporate the latter, it would be a potentially more inclusive way of classifying aerodynamic phenomena that are important in flight-dynamics applications.

6. QUALIFICATIONS

Before proceeding with the study of aerodynamic bifurcations, we must introduce some important qualifications. Our current understanding of fluid-dynamic bifurcations stems almost entirely from results of analytical and computational studies of laminar flows governed by the incompressible Navier-Stokes equations. Within these confines, studies have been further limited to flows in bounded domains. Boundary conditions have been simple enough to permit reduction of the linear stability problem (the necessary first step in the study of bifurcations) to the form of ordinary differential equations (e.g., the Orr-Sommerfeld equations). The principal findings on which our current understanding is based are summarized in Refs. 10-13. Qualifications are necessary when we attempt to extrapolate this body of knowledge to the study of the aerodynamic bifurcations that occur under full-scale flight conditions. These involve turbulent compressible flows which, if averaging and modeling are introduced, will be governed not by the compressible Navier-Stokes equations but by evolution equations of unknown forms. Further, the domains of the flows are typically unbounded, rather than bounded. Finally, the boundary conditions, reflecting the geometries typical of modern aircraft, ordinarily will not allow reduction of the linear stability problem to the level of ordinary differential equations.

The situation requires us to stipulate a list of presuppositions which will be the basis for the extrapolations we make. The list is inspired by one that Lanford compiled to justify the study of turbulence within a framework based on the incompressible Navier-Stokes equations (Ref. 14). Our list will merely supplement Lanford's, taking additional account of turbulence modeling, compressibility, and the necessity to consider flows in unbounded domains. The issue of boundary conditions is not addressed on the assumption that their increased complexity does no more than increase the role of numerical computations.

6.1 Turbulence Modeling

Let us consider the flow field to which a typical lift response $C_L[\alpha(\xi);t,\tau]$ corresponds. We assume that the flow field at time $\xi = \tau$ is given (to within a certain accuracy), and we must determine the subsequent flow at time t. Inasmuch as $\alpha(\xi)$ remains constant at $\alpha(\tau)$ for all $\xi = t > \tau$, we have fixed boundary conditions. This form of the fluid-dynamics problem is known as an initial boundary value problem (IBVP; cf. Ref. 11). We assume that any given realization of the IBVP is governed with sufficient accuracy by the compressible Navier-Stokes equations. Paralleling Ref. 14, in the absence of proof we simply postulate that a solution of the IBVP would exist for all $\xi = t \geq \tau$ and would be unique. However, the Reynolds number is sufficiently high so that a solution would exhibit chaotic behavior, implying a sensitive dependence on the initial conditions. Thus, small perturbations of the initial conditions would cause repetitions of the given motion to result in a set of motions having stochastic properties.

The situation calls for the application of some form of averaging of the compressible Navier-Stokes equations to suppress the appearance of the small-scale chaotic structures. After averaging, the repertory of solutions of the resulting equations must remain faithful to that of the unaveraged equations, neither allowing uncharacteristic solution forms nor losing essential ones. The necessity of closing the averaged equations in conformity with this requirement introduces the turbulence modeling problem. The convergence of interests this situation represents for the fields of research concerned with turbulence modeling and with the modeling of aerodynamic responses has been noted in Ref. 5. In Ref. 2, we have tried to show how the theoretical framework underlying the deterministic approach to the study of turbulence might assist the modeling effort, particularly at this juncture, where it is important to give adequate representation of bifurcation phenomena. We cannot go further here in specifying modeling requirements except to postulate the one feature that must be retained in common with the original Navier-Stokes equations: Whatever the form of modeling adopted, it must remain possible to cast the modeled equations in the form of autonomous evolution equations, namely,

$$\vec{u}_t = H(\vec{u},\lambda) \tag{24}$$

where $\vec{u}$ is the velocity vector and λ is a parameter (e.g., angle of attack, Reynolds number, Mach number). We believe that the premise is a reasonable one, involving no more in principle than the use of orthogonal projections (Refs. 15,16) to eliminate gradient terms (e.g., the pressure term) from the modeled equations.

6.2 Compressibility

We shall assume that modeled equations of turbulent flows resulting from averaging the compressible Navier-Stokes equations remain at least as well-behaved as the original equations and their incompressible counterparts. Of course, the new parameters introduced by compressibility (e.g., Mach number) will themselves have critical values at which additional bifurcations should be expected.

6.3 Unbounded Domains

Let us return to the IBVP represented by $C_L[\alpha(\xi);t,\tau]$ and assume that the premises of the previous sections are now in force. Henceforth, the equations governing the flow field are assumed to be modeled equations of turbulent flow, of known form, and satisfying the form of Eq. (24) by suitable projections.

The issue concerning the absence of bounds on the flow domain arises in evaluating the stability of the flow field in the equilibrium state. We say that the equilibrium state is reached in the limit as $t - \tau \to \infty$, so that transient effects associated with the initial conditions have vanished. A study of the stability of the equilibrium flow must be undertaken first, since bifurcation of the equilibrium state will not occur unless a critical value of the parameter in question (here, α) exists at which the flow field in the equilibrium state becomes unstable. Stability is evaluated by determining whether an infinitesimal perturbation of the equilibrium flow decays or grows with time. The perturbation's fate can be determined from a linear spectral problem, the governing equations being obtained from a linearized perturbation of the equations governing the equilibrium flow. Typically, with a bounded domain, it can be shown that solution of the spectral problem yields a countably infinite set of isolated eigenvalues in a complex plane. Stability is indicated if all of the eigenvalues lie in the left-hand plane. On the other hand, little is known about the spectrum of eigenvalues for unbounded domains. In the case of flows in unbounded domains governed by the incompressible Navier-Stokes equations, it is believed (Refs. 17,18) that an incomplete set of discrete eigenvalues exists which again controls stability, and that there is additionally a continuous spectrum having negative real part (i.e., lying in the left half of the complex plane). We postulate that what is believed to be the case for flows in unbounded domains governed by the incompressible Navier-Stokes equations is in fact the case for our problem.

6.4 Conclusions

Accepting the last premise (which implies accepting all of the previous ones) leads to several conclusions concerning the role of bifurcation theory in the modeling of aerodynamic responses. First, since we have postulated that stability of the equilibrium state continues to be controlled by the discrete part of the eigenvalue spectrum alone, entailing no change from the rules governing bounded domains, we conclude that the role of bifurcation theory regarding the equilibrium state should carry over intact to flows in unbounded domains. That is, all of the instability mechanisms that have been uncovered by studies of flows in bounded domains governed by the incompressible Navier-Stokes equations should have counterparts in flows in unbounded domains governed by modeled turbulent flow equations. With the onset of instability of the equilibrium state, bifurcation theory again should be capable of classifying and characterizing the properties of the new stable equilibrium states that can arise to replace the unstable one.

On the other hand, concerned as it is only with the equilibrium state, bifurcation theory does not suffice to completely resolve the IBVP from which the indicial lift response is derived. We note that when the eigenvalue spectrum lies in the left-half plane, indicating stability of the equilibrium state, the IBVP for an infinitesimal step perturbation of the boundary condition $\alpha(\xi)$; $\xi \geq \tau$ is a <u>linear</u> problem. In fact, the transient flow field from which the indicial response $C_L[\alpha(\xi);t,\tau]$ is derived can be obtained from a suitable superposition of the eigensolutions (including both the discrete and continuous parts) of the linear spectral problem. The superposition is made determinate by the necessity of matching a prescribed flow field at the initial instant $\xi = \tau$. This is how the dependence on the past

motion is expressed, which makes $C_L[\alpha(\xi);t,\tau]$ a nonlinear functional even though derivable from linearized perturbation equations. Thus, recalling the derivation by means of functional expansions, we affirm that so long as stability of the equilibrium state ensures that $C_L[\alpha(\xi);t,\tau]$ will be Fréchet differentiable, the differential $\Delta_\alpha C_L[\alpha(\xi);t,\tau]$ can be determined from a linear problem. With the onset of instability, however, the perturbation flow no longer can be obtained from the solution of the linear spectral problem, since at least one of the discrete eigensolutions would grow without bounds. Thus, the incremental change in lift coefficient given by Eq. (23) must be determined from the fully nonlinear perturbation flow equations.

7. AERODYNAMIC BIFURCATIONS

In Ref. 1, we postulated six major subdivisions in the form of aerodynamic force and moment responses by means of a set of sketches, and these are reproduced in Fig. 4. Although the ordinate f_a in each of the sketches can be made to represent a variety of characteristics, it will be convenient here to let f_a represent the lift coefficient in the equilibrium state. We now briefly outline how modeling of the aerodynamic responses incorporating the six forms of lift coefficient may be effected by means of the amendment we have introduced to accommodate aerodynamic bifurcations.

7.1 Major Subdivisions

First, it should be clear that aerodynamic systems represented by sketches (a) and (b) in Fig. 4, involving linear or nonlinear single-valued lift variations, do not require modification of the treatment contained in, for example, Ref. 8. In formal terms, these systems can be characterized as having aerodynamic responses $C_L[\alpha(\xi);t,\tau]$ that are Fréchet differentiable over the entire angle-of-attack range of interest.

Sketch (c) in Fig. 4 introduces a class of multivalued solutions of the flow in the equilibrium state. Mean or constant values of the lift coefficient in the equilibrium state exhibit the discontinuous and double-valued behavior characteristic of hysteresis. As we have already noted, such cases were treated in Ref. 8 by a procedure similar to the one described here. The class includes both solution curves having folds, and subcritical exchanges of stability between time-invariant equilibrium states.

Sketches (d) and (e) in Fig. 4 introduce bifurcations that result in time-dependent equilibrium states. Accommodating these phenomena within the mathematical model will require the use of Eqs. (22) and (23). Hopf bifurcation is indicated in sketch (d), wherein a formerly stable time-invariant equilibrium state is replaced by a time-varying periodic equilibrium state. The difference in lift responses resulting from these two forms of equilibrium states is reflected in Eq. (23). Hopf bifurcations are common in aerodynamics. Physically, the usual origin of such a large-scale oscillatory state is the onset of vortex-shedding. Of the many examples, we cite here stall on airfoils when the angle of attack exceeds a critical value (Refs. 19,20) and the wake of the flow past a cylinder when the Reynolds number exceeds 50 (Ref. 21). The equilibrium state resulting from a Hopf bifurcation is often succeeded by bifurcation to a quasi-periodic equilibrium state with further increase of the parameter. To accommodate this and subsequent bifurcations, the integration regime in Eq. (22) must be interrupted at each such occurrence, and an interval of $O(\varepsilon)$ inserted in which a discrete change, such as Eq. (23), to a new equilibrium state is allowed. The quasi-periodic state may be succeeded by an aperiodic (chaotic) equilibrium state. As noted in sketch (e) in Fig. 4, appearance of the latter state signals the presence of a "strange attractor." The slender body of revolution may undergo such a sequence of bifurcations as angle of attack is increased incrementally toward 90°. This example, among others, is discussed at length in Ref. 1. Several additional examples of bifurcation sequences relevant to aerodynamic applications are contained in Refs. 2 and 22.

The last subdivision in Fig. 4, sketch (f), representative of aerodynamic systems having strong rate dependence, goes beyond the previous ones in that more is at issue in the modeling than accommodating bifurcations of the equilibrium state. An adequate representation of the aerodynamic system in this category of problem represents a severe test for any mathematical model. We believe that the oscillating airfoil in what is referred to as dynamic stall is exemplary in characterizing the nature of the problem in this category. Fortunately, a comprehensive set of experimental results exists for the problem, reported in a series of papers by McAlister, Carr, and McCroskey (Refs. 19,20). Included are excellent flow-visualization pictures which reveal many features of the physical mechanisms involved. In the following section we refer to these results and briefly demonstrate the extent to which our amended model, Eqs. (22) and (23), is capable of capturing their essentials.

7.2 Dynamic Stall

Figure 5, reproduced from Ref. 1, is representative of some of the principal results of Refs. 19 and 20. Here, angle of attack α is defined geometrically rather than kinematically as before. Flow-visualization pictures (obtained by means of the hydrogen-bubble technique, Ref. 19) of the airfoil oscillating about the quarter-chord clearly show that as the airfoil passes through a given angle of attack ($\alpha = 15°$) with α increasing ($\dot{\alpha} > 0$), the flow has a very different character than it has as the airfoil passes through the same angle of attack with α decreasing ($\dot{\alpha} < 0$). The plots of C_L versus α at the bottom of Fig. 5 (Ref. 20) reveal that the lift variations likewise are very different, depending on whether α is increasing or decreasing. With α increasing, the instantaneous value of the lift

coefficient can significantly exceed its static value (more precisely, in our terms, the mean value of the lift response in the equilibrium state), while the opposite is true with α decreasing. Finally, the differences between lift coefficient with α increasing and decreasing are dramatically enhanced as the reduced frequency k is increased incrementally. Increasing k may be interpreted as increasing the magnitude of $\dot{\alpha}$, since with $\alpha = \alpha_m + \alpha_o \sin \omega t$ (Fig. 5) and $k = \omega c/2V_o$, we have $|\dot{\alpha}c/2V_o|_{max} = \alpha_o k$. Thus, both sign and magnitude of $\dot{\alpha}$ significantly influence the experimental results. These are important new features that a mathematical model ought to be capable of capturing.

Let us first take up the issue of aerodynamic bifurcation in the equilibrium state for the airfoil under study. As the angle of attack is increased incrementally, a critical value of α is reached ($\alpha < 10°$) at which separation of the flow begins, signaled by the appearance of a singular point in skin friction on the upper surface near the leading edge. With an infinitesimal increase in α, the singular point splits to form a half-saddle point of separation followed by a half-saddle point of reattachment, creating the familiar leading-edge separation bubble. The onset of separation is designated a structural bifurcation, inasmuch as it signals a change in the topological structure of the flow (Refs. 1,22). The change occurs uniquely (the original flow structure no longer represents a possible solution of the flow equations) and the flow remains steady. At an angle of attack of about 12°, an inflexional flow profile within the bubble becomes unstable, and periodic vortex-shedding begins. This is a Hopf bifurcation and available evidence suggests that it is supercritical. Figure 6 is a bifurcation diagram of the event with amplitude of the periodic lift fluctuation, designated $C_{L_o}(\infty;\alpha(\tau))$, as ordinate. The mean value of the lift coefficient in the equilibrium state is shown in the same figure. To conform with the notation of Ref. 5, we designate it by $\overline{C_L(\infty;\alpha(\tau))}$. Beyond $\alpha = \alpha_c = 12°$, the diversion of some of the available energy to maintain the fluctuation causes $\overline{C_L(\infty;\alpha(\tau))}$ to begin to drop away from the values it would have taken (dashed curve) if the original stationary flow had remained stable. Its variation with α is that of the measurements for the curves labeled "static" in the plots of C_L versus α in Fig. 5. In the absence of contrary evidence, we assume that no further aerodynamic bifurcations occur over the remaining range of angle of attack. Thus, Eqs. (22) and (23) should apply to the oscillatory motion illustrated in Fig. 5, with Eq. (23) required at $\alpha = \alpha_c = 12°$.

Now let us examine the behavior of a typical lift response $C_L[\alpha(\xi);t,\tau]$ for the part of a cycle in which α is increasing ($\dot{\alpha} > 0$), and let us choose $\alpha(\tau)$ to be somewhat larger than $\alpha_c = 12°$. During the portion of the motion ($0 < \xi < \tau$) before $\alpha(\xi)$ is constrained to remain constant at $\alpha(\tau)$, the conditions correspond to those depicted via flow visualization in the left-hand photograph of Fig. 5. Let us focus attention on the flow component parallel to the airfoil surface at a station near the leading edge at time ξ just prior to $\xi = \tau$. We choose to observe the flow in the same reference frame as the one in which the camera photographing the flow was situated. The origin of coordinates is fixed to the airfoil's axis of rotation, but, rather than rotating with the airfoil, the coordinates remain stationary relative to the oncoming wind. Within this reference frame, the instantaneous velocity profile at the fixed station may be viewed as having two components, as shown in Fig. 7(a). The first profile is the time-invariant mean profile which would exist alone were the airfoil to remain stationary at the instantaneous position $\alpha(\xi) = \alpha(\tau)$. It has a region of reversed flow typical of the velocity profiles within the separation bubble in the equilibrium state. The second profile represents velocity induced by the motion of the airfoil. Its magnitude at the airfoil surface is directly proportional to the angular velocity $\dot{\alpha}(\xi)$, and in particular, since $\xi = \tau$, it is proportional to $\dot{\alpha}(\tau)$. It is clear that with $\dot{\alpha}(\tau) > 0$, this contribution tends to diminish the region of separated flow, and more so as $\dot{\alpha}(\tau)$ is increased.* The situation begins to change as soon as ξ exceeds τ, for then α is constrained to remain constant at $\alpha(\tau)$. As shown in Fig. 7(b), while the first profile remains the same, the second profile immediately changes, since the velocity at the wall must go to zero as soon as the airfoil stops moving. With increasing values of ξ this profile decays progressively, so that the zone of separated flow associated with the first profile gradually begins to appear. After a lapse of time, a separation profile emerges that is unstable to small perturbations. In response, the periodic fluctuation characteristic of vortex-shedding begins, and its amplitude grows toward the constant value corresponding to the amplitude of fluctuations in the equilibrium state at the chosen value of $\alpha(\tau) > \alpha_c$. We show this schematically in Fig. 8. The interval of ξ during which the onset of fluctuations is delayed is denoted by T; clearly, the duration of T is directly proportional to the magnitude of $\dot{\alpha}(\tau)$. During the interval T, in which the flow over the upper surface of the airfoil remains more or less attached, the mean value of the lift coefficient tends toward a value representative of the attached-flow condition. A conservative estimate for it would be the value obtained from a computation based on inviscid flow theory; we indicate it on Fig. 8 as an upper bound (dashed line). After the fluctuation begins, the mean value of the lift coefficient begins to decline toward the value it reaches in the equilibrium state. Thus, with $\dot{\alpha}(\tau) > 0$, the instantaneous mean value of the lift coefficient can overshoot its "static" value; the extent depends directly on the length of the interval T, which in turn depends directly on the magnitude of $\dot{\alpha}(\tau)$.

The behavior of the analogous lift response $C_L[\alpha(\xi);t,\tau]$ for the part of a cycle in which α is decreasing ($\dot{\alpha} < 0$) is very much the reverse of the behavior just described. Let $\alpha(\tau)$ have the same value as before ($\alpha(\tau) > \alpha_c$), so that over the portion of the motion $0 < \xi < \tau$, conditions correspond to those depicted in the right-hand photograph of Fig. 5. In sharp contrast to the previous case with $\dot{\alpha} > 0$, the velocity profile induced by the airfoil's motion drastically extends the separated flow regime, particularly while the airfoil is moving, and the more so as $\dot{\alpha}(\tau)$ is increased negatively. After ξ exceeds τ, whereupon α is constrained to remain constant at $\alpha(\tau)$, the violent fluctuations begin to die down as the second profile dies away. In contrast to the previous case, there is no interval in which the airfoil is free of fluctuations. The time it takes for the violent fluctuations to die down to the level

* The reader will recognize this as an instance of what Ericsson and Reding have termed the "moving-wall effect" (Ref. 25)

representative of the equilibrium state is directly proportional to the magnitude of $|\dot{\alpha}(\tau)|$. During this interval, the mean value of the lift coefficient must be less than its "static" value; the extent of the difference again depends directly on the magnitude of $|\dot{\alpha}(\tau)|$. (We note in passing that large values of $|\dot{\alpha}(\tau)|$ may represent a class where Fréchet differentiability could depend on more than stability of flow in the equilibrium state. It may depend as well on the nature of the initial flow. The possibility will require further study.)

This explanation of events suggested by the form of modeling we have adopted would appear to be in full accord with experimental observations. With one potential reservation, we conclude that a mathematical model at the level of Eqs. (22) and (23) will be capable of incorporating the events we have described.

7.3 Applications to Dynamical Systems

We have seen that the amended mathematical model should be capable of describing the aerodynamic characteristics in all six forms of aerodynamic force (or moment) responses illustrated in Fig. 4. The forms involving aerodynamic bifurcations that result in time-dependent equilibrium states (sketches (d)-(f), Fig. 4) are of particular interest. Applied to problems involving dynamical maneuvers of aircraft, these forms will require extensive and novel experimentation. Problems in this category can be divided into two subclasses.

The first subclass of problems involves oscillatory motions about an equilibrium state at which a bifurcation occurs. This was the case in the dynamic stall experiment studied in the last section. Similar cases need to be studied in which the oscillatory motions are free, rather than forced, to determine how vortex-shedding frequencies may be modulated by the system's natural frequencies, causing, for example, "frequency lock-in." Another potentially important question is whether vortex-shedding (from, e.g., three-dimensional analogs of the airfoil's leading-edge separation bubble) may be a source of wing rock. Here, the phase relations between vortex-shedding on the two wing panels would appear to be a controlling factor.

The second subclass of problems involves oscillatory motions that remain within a space free of critical values of parameters. Here, simplifications in the modeling can be effected as previously (Ref. 8) in connection with time-invariant equilibrium states. Dynamical systems within this subclass of problems involving vortex-shedding from obstacles have inspired a large collection of literature under the category of "vortex-induced oscillations." Excellent surveys of the field have been published by Sarpkaya (Ref. 23) and very recently by Bearman (Ref. 24). The archetypal problem is the flexibly mounted cylinder immersed in a uniform oncoming stream. Applied to this problem, our approach to modeling yields a differential equation of the form

$$\ddot{h} + 2\mu\dot{h} + \kappa^2 h = B(\dot{h})\sin(\omega(\dot{h})t) \tag{25}$$

where the quantities h,μ,κ characterizing the spring-mass system are illustrated in Fig. 9(a). The forcing term, which expresses the contribution of the fluctuating lift due to vortex-shedding, is novel in that the amplitude B and frequency ω are coupled to the velocity $\dot{h}$ on the left-hand side. Our modeling approach provides an explanation as follows: Amplitude B is a function of instantaneous Reynolds number (Fig. 9(b)), which makes it a function of total velocity $\sqrt{U_\infty^2 + \dot{h}^2}$. Strouhal number k, the dimensionless frequency of the fluctuating lift in the equilibrium state, is a constant, independent of Reynolds number in the range of velocities of interest (Fig. 9(b)). This makes ω, the actual frequency, a function of $\dot{h}$ through

$$k = \frac{\omega d}{U_{tot}} = \frac{\omega d}{\sqrt{U_\infty^2 + \dot{h}^2}} = \text{const.} \tag{26}$$

We have found that Eq. (25) has a rich repertory of solutions, and appears to be capable of capturing distinctive features of the system's behavior (frequency lock-in, amplitude jumps, hysteresis) that careful experiments have revealed (Refs. 23,24). The equation's richness is easier to understand if we transform it into a set of autonomous first-order equations. There are three such equations, a number which suffices to permit solutions having "chaotic" behavior. We believe that study of simple systems such as this one can teach us how to perceive what otherwise might seem bizarre or even random behavior on the part of more complicated dynamical systems such as maneuvering aircraft.

8. CONCLUDING REMARKS

This paper is a continuation of our effort to provide a consistent formulation and theoretical method for studying nonlinear problems in flight dynamics. We have proposed a framework having parallel observational and mathematical components to facilitate study of the aerodynamic contribution to the flight-dynamics system. The observational component consists of the elements structure, change, chaos, and scale. These are complemented by elements of a mathematical framework featuring the language of topology and concepts drawn from the theory of nonlinear dynamical systems. Here, particular emphasis has been placed on the element of change and its mathematical representation by means of bifurcation theory.

Of the two principal realms of application of bifurcation theory to flight-dynamics studies, we have concentrated attention on its role in the mathematical modeling of the aerodynamic contribution to the

aircraft's equations of motion. Our study stressed a number of themes which led to the following conclusions:

1. Studies in nonlinear flight dynamics can be enhanced by linking them to the common features of parallel studies in various allied fields. The unifying medium is the rapidly growing body of theory underlying research in nonlinear dynamical systems. Exemplifying this, our approach to modeling, involving nonlinear indicial responses and generalized superposition integrals, was made compatible with one originating in the field of electrical circuits and systems, based on the use of nonlinear functional expansions. Operations involved in forming the indicial response were found to be equivalent to Fréchet differentiation. Invalidation of Fréchet differentiability proved to be the common element signaling the necessity of amending the mathematical model to accommodate potential discontinuous aerodynamic behavior. Aerodynamic bifurcation is one means of invalidating Fréchet differentiability.

2. Aerodynamic bifurcation can be defined as the replacement of an unstable equilibrium flow by a new stable equilibrium flow at a critical value of a parameter. Acceptance of a list of presuppositions permitted extrapolating our understanding of aerodynamic bifurcations from a framework involving bounded laminar flows governed by the incompressible Navier-Stokes equations to one involving unbounded turbulent flows governed by modeled evolution equations based on the compressible Navier-Stokes equations. The issue of aerodynamic bifurcations represents a convergence of interests for the fields of turbulence modeling and the modeling of aerodynamic responses. Amended to accommodate aerodynamic bifurcations, with one potential reservation the mathematical model should be capable of describing the aerodynamic characteristics of all six major subdivisions that we have postulated for the aerodynamic response.

3. Aerodynamic bifurcation is one of at least two means of invalidating Fréchet differentiability of the aerodynamic response. A theory for enumerating these means offers a possible alternative to bifurcation theory. Inasmuch as it would incorporate the latter, it would be a potentially more inclusive way of classifying aerodynamic phenomena that are important in flight-dynamics applications.

REFERENCES

1. Chapman, G. T. and Tobak, M., "Nonlinear Problems in Flight Dynamics." NASA TM-85940, May 1984. To appear in Proc. Berkeley-Ames Conference on Nonlinear Problems in Control and Fluid Dynamics, Math Sci. Press, 1985.

2. Chapman, G. T. and Tobak, M., "Observations, Theoretical Ideas, and Modeling of Turbulent Flows--Past, Present and Future." To appear in Proc. ICASE/NASA Workshop on Theoretical Approaches to Turbulence, Springer-Verlag, New York, 1985.

3. Hui, W. H. and Tobak, M., "Bifurcation Theory Applied to Aircraft Motions Near the Stability Boundary." NASA TM-85881, Jan. 1984. To appear in Proc. Berkeley-Ames Conference on Nonlinear Problems in Control and Fluid Dynamics, Math Sci. Press, 1985.

4. Hui, W. H. and Tobak, M., "Bifurcation Theory Applied to Aircraft Motions." To appear in AGARD Symposium on Unsteady Aerodynamics--Fundamentals and Applications to Aircraft Dynamics," Gottingen, W. Germany, May 1985.

5. Tobak, M., Chapman, G. T., and Schiff, L. B., "Mathematical Modeling of the Aerodynamic Characteristics in Flight Dynamics." NASA TM-85880, Jan. 1984. To appear in Proc. Berkeley-Ames Conference on Nonlinear Problems in Control and Fluid Dynamics, Math Sci. Press, 1985.

6. Fliess, M., Lamnabhi, M., and Lamnabhi-Lagarrigue, F., "An Algebraic Approach to Nonlinear Functional Expansions." IEEE Transactions on Circuits and Systems, Vol. 30, No. 8, Aug. 1983, pp. 554-570.

7. Volterra, V., "Theory of Functionals and of Integral and Integro-Differential Equations," New York, Dover Pub., Inc., 1959.

8. Tobak, M. and Schiff, L. B., "Aerodynamic Mathematical Modeling-Basic Concepts," AGARD Lecture Series No. 114, Paper 1, March 1981.

9. Nowinski, J. L., "Note on the Applications of the Fréchet Derivative." Int. J. Non-Linear Mech., Vol. 18, No. 4, 1983, pp. 297-306.

10. Benjamin, T. B., "Bifurcation Phenomena in Steady Flows of a Viscous Fluid. I, Theory. II, Experiments." Proc. Roy. Soc. London, Ser. A, Vol. 359, 1978, pp. 1-43.

11. Joseph, D. D., "Stability of Fluid Motions I." New York, Springer-Verlag, 1976.

12. Joseph, D. D., "Hydrodynamic Stability and Bifurcation." Hydrodynamic Instabilities and the Transition to Turbulence: Topics in Applied Physics, Vol. 45, H. L. Swinney and J. P. Gollub, eds., New York, Springer-Verlag, 1981, pp. 27-76.

13. Sattinger, D. H., "Bifurcation and Symmetry Breaking in Applied Mathematics." Bull. (New Series) Amer. Math. Soc., Vol. 3, No. 2, 1980, pp. 779-819.

14. Lanford, O. E., "Strange Attractors and Turbulence." Hydrodynamic Instabilities and the Transition to Turbulence: Topics in Applied Physics, Vol. 45, H. L. Swinney and J. P. Gollub, eds., New York, Springer-Verlag, 1981, pp. 7-26.

15. Ladyzhenskaya, O. A., "The Mathematical Theory of Viscous Incompressible Flow." New York, Gordon and Breach, 1969.

16. Iooss, G., "Bifurcation and Transition to Turbulence in Hydrodynamics." Bifurcation Theory and Applications: Lecture Notes in Mathematics 1057, L. Salvadori, ed., New York, Springer-Verlag, 1984, pp. 152-201.

17. Grosch, C. E. and Salwen, H., "The Continuous Spectrum of the Orr-Sommerfeld Equation, Part 1: The Spectrum and the Eigenfunctions." J. Fluid Mech., Vol. 87, Part 1, 1978, pp. 33-54.

18. Herron, I. H., "A Diffusion Equation Illustrating Spectral Theory for Boundary Layer Stability." Stud. Appl. Math., Vol. 67, No. 3, Dec. 1982, pp. 231-241.

19. McAlister, K. W. and Carr, L. W., "Water-Tunnel Experiments on an Oscillating Airfoil at Re = 21,000." NASA TM-78446, Mar. 1978.

20. McAlister, K. W., Carr, L. W., and McCroskey, W. J., "Dynamic Stall Experiments on the NACA 0012 Airfoil." NASA TP-1100, Jan. 1978.

21. Nishioka, M. and Sato, H., "Mechanism of Determination of the Shedding Frequency of Vortices Behind a Cylinder at Low Reynolds numbers." J. Fluid Mech., Vol. 89, Part 1, 1978, pp. 49-60.

22. Tobak, M. and Peake, D. J., "Topology of Three-Dimensional Separated Flows." Ann. Rev. Fluid Mech., Vol. 14, 1982, pp. 61-85.

23. Sarpkaya, T., "Vortex-Induced Oscillations." J. App. Mech., Vol. 46, No. 2, June 1979, pp. 241-258.

24. Bearman, P. W., "Vortex Shedding from Oscillating Bluff Bodies." Ann. Rev. Fluid Mech., Vol. 16, 1984, pp. 195-222.

25. Ericsson,L.E. and Reding,J.P., "Analytical Prediction of Dynamic Stall Characteristics". AIAA Paper 72-682, 1972.

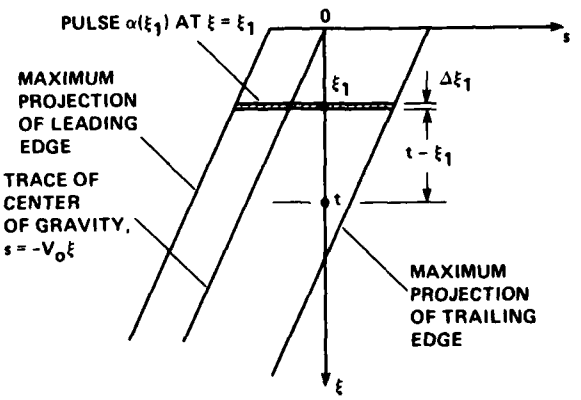

Fig. 1 Boundary conditions for lift at time t due to pulse in angle of attack at time ξ_1.

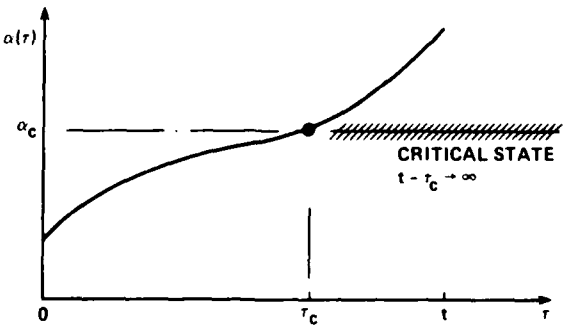

Fig. 2 Passage of angle of attack through a critical value α_c at which equilibrium flow becomes unstable.

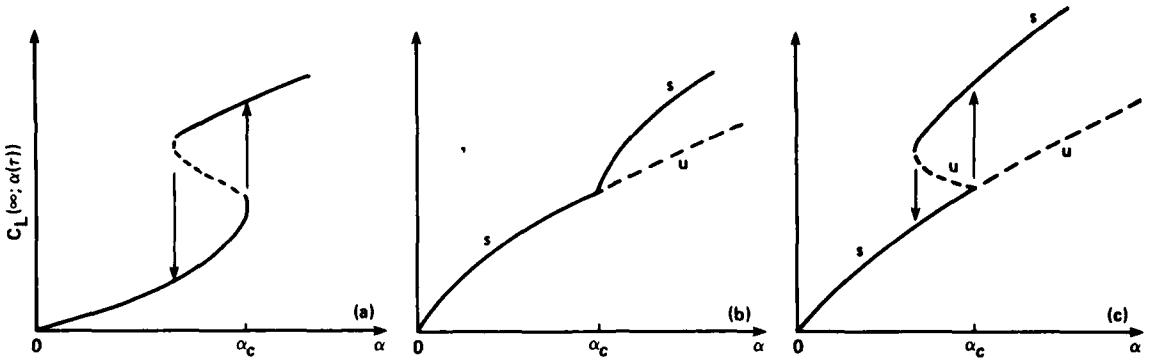

Fig. 3 Comparison of forms of time-invariant lift coefficients in the equilibrium state. (a) Fold; no bifurcation. (b) Supercritical bifurcation. (c) Subcritical bifurcation.

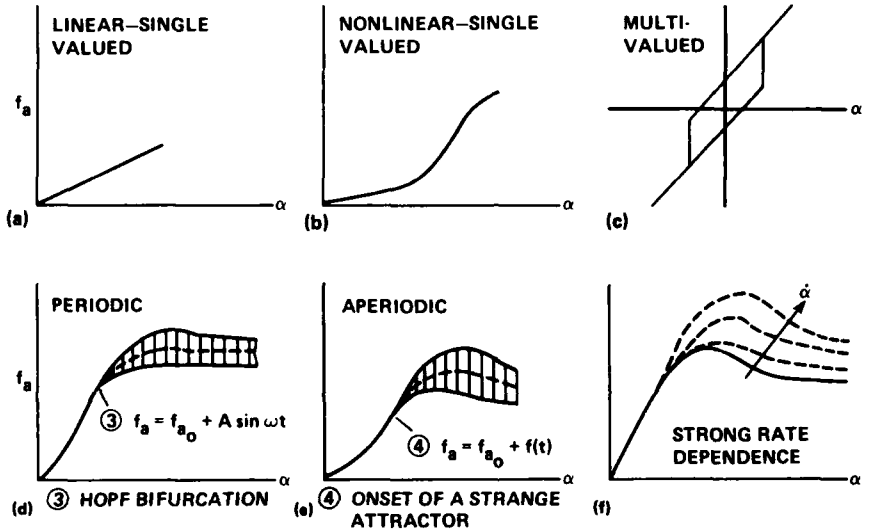

Fig. 4 Major subdivisions of aerodynamic forces and moments.

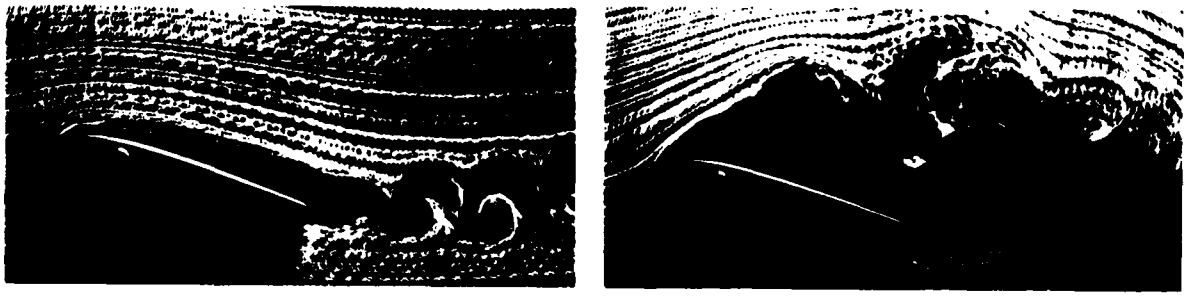

$\alpha = 15, \dot{\alpha} > 0, k = 0.25$

$\alpha = 10 + 10 \sin \omega t$
(McALISTER AND CARR)

$\alpha = 15, \dot{\alpha} < 0, k = 0.25$

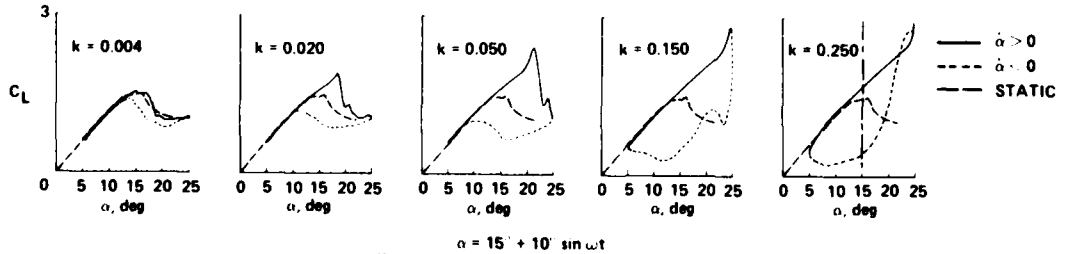

$\alpha = 15 + 10 \sin \omega t$
(McALISTER, CARR AND McCROSKEY)

Fig. 5 Aerodynamics of an oscillating airfoil: dynamic stall.

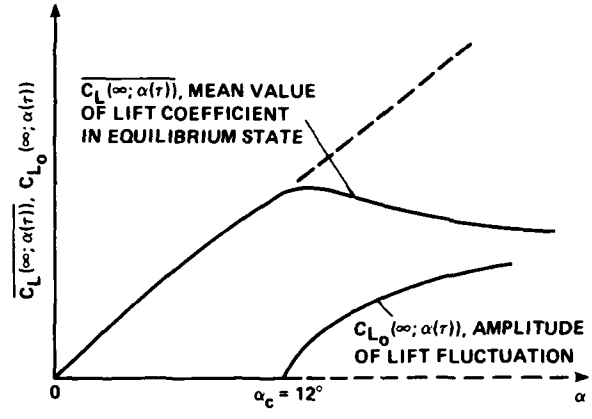

Fig. 6 Bifurcation diagram for amplitude of lift fluctuation.

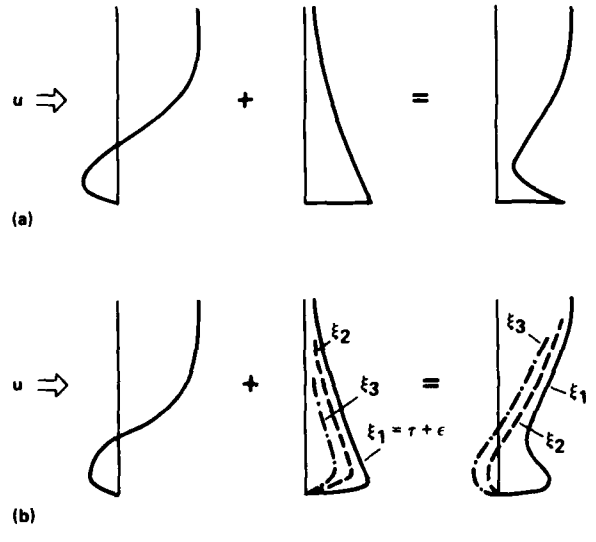

Fig. 7 Velocity profiles near leading edge. (a) $\xi < \tau$. (b) $\xi > \tau$.

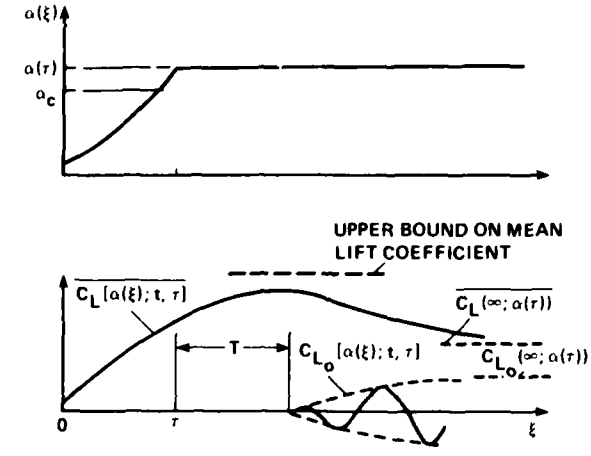

Fig. 8 Mean and fluctuating lift responses.

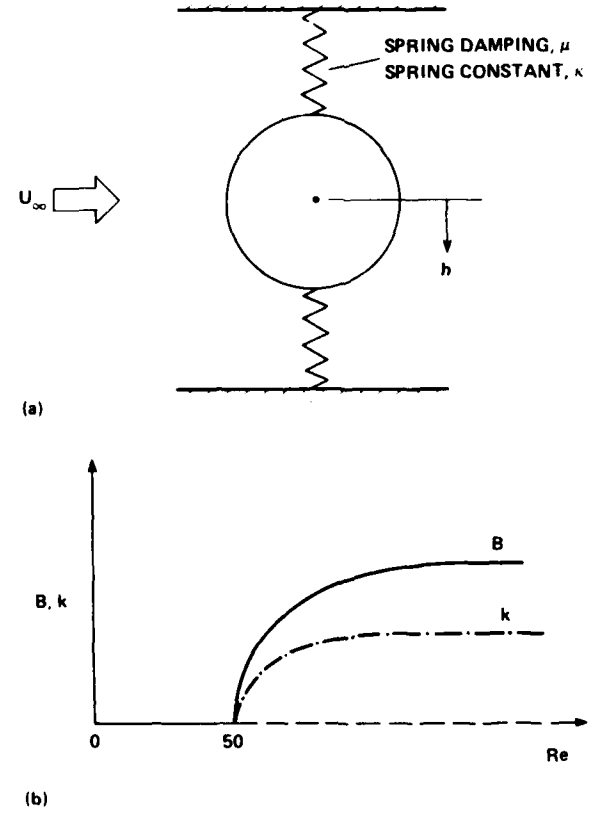

Fig. 9 Flexibly mounted cylinder. (a) Spring-mass system. (b) Bifurcation diagram for cylinder in uniform stream.

BIFURCATION THEORY APPLIED TO AIRCRAFT MOTIONS

W. H. Hui
Professor of Applied Mathematics and Mechanical Engineering
University of Waterloo, Waterloo, Ontario, Canada N2L 3G1

Murray Tobak
Staff Scientist
NASA Ames Research Center, Moffett Field, California 94035, U.S.A.

SUMMARY

Bifurcation theory is used to analyze the nonlinear dynamic stability characteristics of single-degree-of-freedom motions of an aircraft or a flap about a trim position. The bifurcation theory analysis reveals that when the bifurcation parameter, e.g., the angle of attack, is increased beyond a critical value at which the aerodynamic damping vanishes, a new solution representing finite-amplitude periodic motion bifurcates from the previously stable steady motion. The sign of a simple criterion, cast in terms of aerodynamic properties, determines whether the bifurcating solution is stable (supercritical) or unstable (subcritical). For the pitching motion of a flat-plate airfoil flying at supersonic/hypersonic speed, and for oscillation of a flap at transonic speed, the bifurcation is subcritical, implying either that exchanges of stability between steady and periodic motion are accompanied by hysteresis phenomena, or that potentially large aperiodic departures from steady motion may develop. On the other hand, for the rolling oscillation of a slender delta wing in subsonic flight (wing rock), the bifurcation is found to be supercritical. This and the predicted amplitude of the bifurcation periodic motion are in good agreement with experiments.

1. INTRODUCTION

Problems of aerodynamic stability of aircraft flying at small angles of attack have been studied extensively. With increasing angles of attack the problems become more complicated and typically involve nonlinear phenomena such as coupling between modes, amplitude and frequency effects, and hysteresis. The need for investigating stability characteristics at high angles of attack was clearly demonstrated by Orlik-Rückemann (Ref. 1) in his survey paper which deals largely with experiments.

On the theoretical side, much of an extensive body of work is based on the linear theory, in which the unsteady flow is regarded as a small perturbation of some known steady flow (possibly nonlinear in, e.g., the angle of attack) that prevails under certain flight conditions. The question of the validity and limitations of such a linearized perturbation theory is of fundamental importance. Yet, it has rarely been investigated. One may argue that, in principle, it should be possible to advance to higher and higher angles of attack α by a series of linear perturbations since the solution at each step should include a steady-state part which, when added to the previous steady-state solution, would provide the starting point for the next perturbation. This may well be true provided that at each step the steady motion is both statically and dynamically stable, and that the actual disturbances, e.g., the amplitude of oscillation, remain small. However, when the angle of attack exceeds a certain critical value α_{cr} at which the steady motion is no longer stable, the linear theory predicts an exponential growth of the perturbation with time and, therefore, must cease to be valid after finite time. The motion of the aircraft under these conditions can only be studied by means of a nonlinear theory.

In this paper we investigate three types of problems in which a steady motion becomes unstable. Padfield (Ref. 2) studied a similar class of problems using the method of multiple scales, which is valid only for weakly nonlinear oscillations. We shall study the problem using bifurcation theory. This allows us to draw on recent mathematical developments (see Ref. 3) that are particularly well-suited to investigating fundamental questions in linear and nonlinear stability theory. A numerical scheme based on bifurcation theory was proposed earlier (Ref. 4) for analyzing aircraft dynamic stability in a general framework. More recent work by Guicheteau (Ref. 5) demonstrates the considerable potential of bifurcation theory in flight dynamics studies, particularly toward establishing a method for the design of flight control systems to ensure protection against loss of control. While acknowledging the importance of the aerodynamic model in determining aircraft stability characteristics, neither study contains an adequate assessment of the model requirements. The treatment of unsteady flow effects receives no attention. In contrast, we shall focus on just this aspect of the motion analysis.

We shall restrict this study to the single-degree-of-freedom motions, e.g., pitching or rolling, of an aircraft about its trimmed flight condition. This enables us to analyze motions for which complete aerodynamic information (exact analytical or numerical solutions) is available for certain shapes. The information is obtained from solutions of the unsteady inviscid flow equations (Refs. 6-12) or from results of experiments (Ref. 13). In this way it is possible to establish a form revealing a precise analytical relationship between the basic aerodynamic coefficients and the characteristics of the motion.

Specifically we shall consider the following three examples:

A. Pitching supersonic/hypersonic airfoil in rectilinear flow (Fig. 1);

B. Flap oscillations in transonic flow (Fig. 2);

C. Wing rock of a slender delta wing in subsonic flow (Fig. 3).

2. MATHEMATICAL FORMULATION

Let the aircraft or flap be in level, trimmed flight until time $t = 0$ when it is perturbed from its trim position. During the subsequent motion the center of gravity continues to follow a rectilinear path at constant velocity V_∞. For a single-degree-of-freedom oscillatory motion, the equation of motion is

$$I \frac{d^2\xi}{dt^2} = G(t;\lambda) \tag{1}$$

where $\xi(t)$ is the instantaneous angle-of-attack perturbation in example A, flap-angle perturbation in example B, and roll angle in example C; I is the appropriate moment of inertia; and $G(t)$ is the corresponding instantaneous perturbation moment of the aerodynamic forces.

In Eq. (1), λ represents a set of parameters defining steady flight at the trim condition. Flight Mach number M_∞, ratio of specific heats γ, and trim angle of attack α_m are included in these parameters. We shall consider λ to be the trim angle of attack α_m in examples A and C, and the mean flap deflection angle δ_m in example B. In other words, all other defining parameters will be held fixed when considering the consequence of varying λ on aircraft motion characteristics. We assume that the moment required to trim the aircraft or flap at λ has been accounted for, so that $G(t;\lambda)$ is a measure of the perturbation moment only.

The instantaneous motion state, $\xi(t)$ and $\dot{\xi}(t)$, and the instantaneous moment $G(t)$ are a result of the interaction of aircraft or flap motion and the unsteady aerodynamic forces from time zero to time t. Consequently, the instantaneous moment $G(t)$ depends not only on the instantaneous motion state, $\xi(t)$ and $\dot{\xi}(t)$, but also on the past motion history from time zero to t. This is to say that $G(t)$ is a functional of $\xi(t_1)$, $(0 \le t_1 \le t)$ as described in Ref. 14. Thus

$$G(t) = G\left[\xi(t_1)\right]_0^t \tag{2}$$

For motions for which $\xi(t_1)$ is analytic, the functional is equivalent to a function of an infinite set of variables,

$$G(t) = G\left[\xi(t_1)\right]_0^t$$

$$= G\left(\xi(t), \dot{\xi}(t), \ddot{\xi}(t), \ldots, \frac{d^n\xi(t)}{dt^n}, \ldots\right) \tag{3}$$

For most problems encountered in the study of dynamic stability, the motion is slow although its amplitude may be finite or large. Under these conditions $\ddot{\xi}(t)$, $\dddot{\xi}(t)$, ... in Eq. (3) may be neglected and, as a first approximation

$$G(t) = G(\xi(t), \dot{\xi}(t)) \tag{4}$$

We further assume that G is an analytic function of ξ and $\dot{\xi}$. Expanding Eq. (4) as a Taylor series, we neglect terms of $O(\dot{\xi}^2)$ and higher for slow motions, and after reintroducing the parameter λ,

$$G(t;\lambda) = G_0(\xi(t);\lambda) + \frac{\dot{\xi}(t)\ell}{V_\infty} G_1(\xi(t);\lambda) \tag{5}$$

where ℓ is a characteristic length and

$$G_0(0;\lambda) = 0 \tag{6}$$

as required at the trim condition. The form of the instantaneous moment $G(t;\lambda)$ in Eq. (5) is consistent with the exact analytic solution for the pitching moment in example A (Ref. 10), the numerical solution for the hinge moment in example B (Ref. 12), and the experimentally derived empirical formula for the rolling moment in example C (Ref. 13).

In summary, the single-degree-of-freedom motions considered in this paper will be based on the following mathematical problem

$$I \frac{d^2\xi}{dt^2} = G_0(\xi;\lambda) + \frac{\dot{\xi}\ell}{V_\infty} G_1(\xi;\lambda) = G(\xi,\dot{\xi};\lambda) \tag{7a}$$

$$\xi(0) = \hat{\xi}_0 \tag{7b}$$

$$\dot{\xi}(0) = \hat{\xi}_1 \tag{7c}$$

The functions $G_0(\xi;\lambda)$ and $G_1(\xi;\lambda)$ are generally nonlinear in ξ and have to be determined from the study of unsteady aerodynamics, either theoretically or experimentally. Evidently G_0 is related to the restoring moment and G_1 is related to the damping moment.

In many situations, it is known that when the parameter λ reaches some critical value λ_{cr}, the aerodynamic damping G_1 vanishes and steady flight at the trim condition λ_{cr} loses its stability. We use bifurcation theory to determine the motion characteristics of an aircraft or flap whose trim condition is near or beyond λ_{cr}.

3. BIFURCATION THEORY

We introduce the dimensionless time $\tau = V_\infty t/\ell$, where ℓ is a characteristic length, equal to the chord length of the airfoil in example A, the chord length of the forebody plus flap in example B, and the chord length of the wing in example C. Hereafter we use $(')$ to denote $d/d\tau$. We further let

$$\begin{aligned} F(\xi,\dot{\xi};\lambda) &= G(\xi,\dot{\xi};\lambda)/(I\, V_\infty^2/\ell^2) \\ &= F_0(\xi;\lambda) + \dot{\xi} F_1(\xi;\lambda) \end{aligned} \tag{8}$$

Then Eq. (7a) may be written

$$\frac{d\xi}{d\tau} = \dot{\xi} \tag{9a}$$

$$\frac{d\dot{\xi}}{d\tau} = F(\xi,\dot{\xi};\lambda) \tag{9b}$$

An expansion of $F(\xi,\dot{\xi};\lambda)$ in a Taylor series in ξ and $\dot{\xi}$ and a change of notation $u_1 = \xi$, $u_2 = \dot{\xi}$ yield for Eqs. (9)

$$\dot{u}_i = A_{ij}(\lambda)u_j + B_{ijk}(\lambda)u_j u_k + C_{ijk\ell}(\lambda)u_j u_k u_\ell + O(|\vec{u}|^4), \quad (i = 1,2) \tag{10}$$

where

$$A = \begin{bmatrix} 0 & 1 \\ -S(\lambda) & -D(\lambda) \end{bmatrix} \tag{11a}$$

$$S(\lambda) = -F_0'(0;\lambda), \quad D(\lambda) = -F_1(0;\lambda) \tag{11b}$$

$$B_{1jk} = 0, \quad B_{2jk} = \frac{1}{2!} \left.\frac{\partial^2 F}{\partial u_j \partial u_k}\right|_{\vec{u}=0} \tag{11c}$$

and

$$C_{1jk\ell} = 0, \quad C_{2jk\ell} = \frac{1}{3!} \left.\frac{\partial^3 F}{\partial u_j \partial u_k \partial u_\ell}\right|_{\vec{u}=0} \tag{11d}$$

(Although Eqs. (9) have been derived on the assumption of slow oscillations, subsequent bifurcation analysis of Eq. (9) will hold for general $F(\xi,\dot{\xi};\lambda)$, i.e., as if no restriction had been placed on the magnitude of $\dot{\xi}$.)

In Eqs. (11), the tensors B and C represent the effects of finite amplitude to the second and third order. The following symmetry properties hold:

$$B_{2jk} = B_{2kj} \tag{12a}$$

$$C_{2jk\ell} = C_{2j\ell k} = C_{2k\ell j} = C_{2\ell jk} = C_{2\ell kj} \tag{12b}$$

On the basis of Eq. (10), we discuss the linear and nonlinear stability of the motion.

3.1 Linear Stability Theory

The stability of steady motion at the trim condition λ to infinitesimal disturbances is determined by the nature of the eigenvalues of the matrix A. They are

$$\eta_{1,2}(\lambda) = \frac{1}{2}\left[-D(\lambda) \pm \sqrt{D^2(\lambda) - 4S(\lambda)}\right] \tag{13}$$

Case I: $S(\lambda) < 0$. In this case, $\eta_1 > 0$, $\eta_2 < 0$. The steady motion at this condition λ is always unstable.

Case II: $S(\lambda) > 0$.

IIa: $D(\lambda) < 0$. In this case, $\mathrm{Re}(\eta_{1,2}) > 0$ and the steady motion at λ is unstable.

IIb: $D(\lambda) > 0$. In this case, $\mathrm{Re}(\eta_{1,2}) < 0$ and the steady motion at λ is stable.

Only in Case IIb, when both stiffness derivative $S(\lambda)$ and damping derivative $D(\lambda)$ are positive, is the steady motion at the trim condition λ stable to infinitesimal disturbances. In fact, stability theory (Ref. 3) can be used to show that stability of the steady motion in this case is assured if and only if the disturbance is sufficiently small.

When linear theory predicts growth of the disturbance amplitude, growth is exponential and the linear theory is no longer valid when the amplitude becomes large after a finite time. What happens to a motion with growth of disturbances predicted from linear theory cannot be predicted by using only the linear theory. To determine the ultimate state of motion, the full nonlinear inertial equation (or a suitable approximation of it, such as Eq. 10) must be used. Of particular interest is the dynamic stability boundary $\lambda = \lambda_{cr}$, where $S(\lambda_{cr}) > 0$ and $D(\lambda_{cr}) = 0$. The stability characteristics near this boundary will be studied presently.

3.2 Hopf Bifurcation Theory

At the dynamic stability boundary $\lambda = \lambda_{cr}$, we have $S(\lambda_{cr}) > 0$; hence,

$$\eta_{1,2}(\lambda_{cr}) = \pm i\sqrt{S(\lambda_{cr})} = \pm i\omega_0 \tag{14}$$

The existence of purely imaginary eigenvalues of the matrix A at $\lambda = \lambda_{cr}$ is the characteristic sign of a Hopf bifurcation (Refs. 3 and 15), signaling a changeover from stable steady motion to periodic motion. On crossing $\lambda = \lambda_{cr}$, the steady motion that had been stable for $\lambda < \lambda_{cr}$ becomes unstable to disturbances, resulting (after a transient motion has died away) in the existence of a new motion, which (if it is stable) is periodic. In the vicinity of $\lambda = \lambda_{cr}$, the circular frequency of the periodic motion is nearly equal to ω_0. We call the new solution of the equation of motion a bifurcation solution. In this section we shall determine its character and a criterion for its stability.

For λ slightly larger than λ_{cr}, the eigenvalues of the matrix A are

$$\eta_{1,2} = -\frac{1}{2} D(\lambda) \pm i\Omega(\lambda) \tag{15}$$

where

$$\Omega(\lambda) = \sqrt{S(\lambda) - D^2(\lambda)/4} \tag{16}$$

We shall assume that

$$D'(\lambda_{cr}) < 0 \tag{17}$$

which is the usual case in applications. (The case $D'(\lambda_{cr}) > 0$ can be treated in exactly the same way.) The normalized eigenvector $\hat{\zeta}(\lambda)$ associated with the eigenvalue $\eta(\lambda)$ is

$$\vec{\zeta}(\lambda) = \begin{bmatrix} \zeta_1(\lambda) \\ \zeta_2(\lambda) \end{bmatrix} = \frac{1 - i}{2\sqrt{\Omega(\lambda)}} \begin{bmatrix} 1 \\ \eta(\lambda) \end{bmatrix} \tag{18}$$

whereas the adjoint eigenvector $\vec{\zeta}^*(\lambda)$ with eigenvalue $\bar{\eta}(\lambda)$, which is the complex conjugate of $\eta(\lambda)$, is

$$\vec{\zeta}^*(\lambda) = \begin{bmatrix} \zeta_1^*(\lambda) \\ \zeta_2^*(\lambda) \end{bmatrix} = \frac{1 + i}{2\sqrt{\Omega(\lambda)}} \begin{bmatrix} \bar{\eta}(\lambda) + D(\lambda) \\ 1 \end{bmatrix} \tag{19}$$

A. Hopf Bifurcation. The bifurcation solution $\vec{u}(\tau,\lambda)$ may be written as

$$\vec{u} = a(\tau)\vec{\zeta} + \bar{a}(\tau)\bar{\vec{\zeta}} \tag{20}$$

Following Iooss and Joseph (Ref. 3, p. 125), we get

$$\left.\begin{aligned} a &= \varepsilon b_1(s) + \varepsilon^2 b_2(s) + \varepsilon^3 b_3(s) + O(\varepsilon^4) \\ s &= [\omega_0 + \varepsilon^2\omega_2 + O(\varepsilon^4)]\tau \\ \lambda &= \lambda_{cr} + \varepsilon^2\lambda_2 + O(\varepsilon^4) \end{aligned}\right\} \tag{21}$$

where, for brevity, we omit the lengthy solutions for ε, b_n, ω_2, and λ_2 (Ref. 11). The solution is periodic in τ with circular frequency equal to $\omega_0 + \varepsilon^2\omega_2 + O(\varepsilon^4)$.

B. Stability of the Bifurcation Periodic Solution. According to Floquet theory (Ref. 3), the stability of the bifurcation periodic solution Eq. (21) is determined by the sign of an index μ. To $O(\varepsilon^4)$, μ has the form

$$\mu = D'(\lambda_{cr})\lambda_2\varepsilon^2 + O(\varepsilon^4) \tag{22}$$

The bifurcation periodic solution is stable if $\mu < 0$ and unstable if $\mu > 0$. Since we have assumed $D'(\lambda_{cr}) < 0$, stability depends on the sign of λ_2, with $\lambda_2 > 0$ denoting stability and $\lambda_2 < 0$ instability. It remains to cast λ_2 in more recognizable terms. Considerable manipulation yields

$$\mu = \frac{\varepsilon^2}{4\omega_0^3}\left[\left(\frac{\partial^2 F}{\partial u_1^2} + \omega_0^2\frac{\partial^2 F}{\partial u_2^2}\right)\frac{\partial^2 F}{\partial u_1 \partial u_2} + \omega_0^2\left(\frac{\partial^3 F}{\partial u_1^2 \partial u_2} + \omega_0^2\frac{\partial^3 F}{\partial u_2^3}\right)\right]_{\substack{\vec{u}=0 \\ \lambda=\lambda_{cr}}} \tag{23}$$

in terms of $F(u_1,u_2;\lambda)$. From Eq. (8) we see that the function F is directly related to the moment $G(\xi,\dot{\xi};\lambda)$ acting on the aircraft or flap which is performing a finite-amplitude oscillation ξ around the trim position λ. Equation (23) demonstrates that the stability of periodic motion near the dynamic stability boundary λ_{cr} is determined by the behavior of the aerodynamic response $G(\xi,\dot{\xi};\lambda)$ in that vicinity.

With the assumption of slow oscillations under which the form of Eq. (5) was derived (terms of $O(\dot{\xi}^2,\ddot{\xi})$ neglected), we may substitute Eq. (5) with Eq. (8) into Eq. (23) to get

$$\mu = \frac{\varepsilon^2}{4\omega_0^3}\left(F_0''F_1' + \omega_0^2F_1''\right)_{\substack{\xi=0 \\ \lambda=\lambda_{cr}}} \tag{24}$$

Since from Eqs. (14) and (11b)

$$\omega_0 = \sqrt{S(\lambda_{cr})} = \sqrt{-F_0'(0;\lambda_{cr})} \tag{25}$$

Eq. (24) becomes, after using Eq. (8),

$$\mu = -\frac{\varepsilon^2\omega_0}{4}\left[\frac{d}{d\xi}\left(\frac{F_1'(\xi;\lambda_{cr})}{F_0'(\xi;\lambda_{cr})}\right)\right]_{\xi=0} \tag{26a}$$

or

$$\mu = -\frac{\varepsilon^2\omega_0}{4}\left[\frac{d}{d\xi}\left(\frac{G_1'(\xi;\lambda_{cr})}{G_0'(\xi;\lambda_{cr})}\right)\right]_{\xi=0} \tag{26b}$$

Using Eq. (10) we get

$$\mu = \frac{\varepsilon^2 \omega_0}{2} \frac{C_{2112}(\lambda_{cr})}{S(\lambda_{cr})} \tag{26c}$$

We have thus established the following criterion: bifurcation periodic motion is stable or unstable according to

$$\mu < 0 \quad \text{or} \quad \mu > 0 \tag{27a}$$

or alternatively, since $S(\lambda_{cr}) > 0$, according to

$$C_{2112}(\lambda_{cr}) < 0 \quad \text{or} \quad C_{2112}(\lambda_{cr}) > 0 \tag{27b}$$

The two possibilities are well illustrated in the form of bifurcation diagrams as shown in Figs. 4a and 4b.

In a bifurcation diagram, the abscissa represents the bifurcation parameter λ, while the ordinate is a parameter characteristic of the bifurcation solution alone. In this case it is ε, a measure of the amplitude of the bifurcation periodic solution. Stable solutions are indicated by solid lines and unstable solutions are indicated by dashed lines. Thus over the range of the bifurcation parameter $\lambda < \lambda_{cr}$ where the steady-state motion is stable, ε is zero, and the stable steady motion is represented along the abscissa by a solid line. The steady motion becomes unstable for all values of $\lambda > \lambda_{cr}$ as the dashed line along the abscissa indicates. Periodic solutions bifurcate from $\lambda = \lambda_{cr}$, either supercritically or subcritically.

When $C_{2112}(\lambda_{cr}) < 0$, hence $\mu < 0$ (implying $\lambda_2 > 0$), the bifurcation is called supercritical and its characteristic form is shown in Fig. 4a. In this case, stable periodic solutions (solid curves in Fig. 4a) exist for values of $\lambda > \lambda_{cr}$. The amplitude of the periodic solution at a given value of $\lambda - \lambda_{cr}$ is proportional to ε, hence is vanishingly small when $\lambda - \lambda_{cr}$ is small, varying essentially as $(\lambda - \lambda_{cr})^{1/2}$.

When $C_{2112}(\lambda_{cr}) > 0$ hence $\mu > 0$ (implying $\lambda_2 < 0$), the bifurcation is called subcritical and its characteristic form is shown in Fig. 4b. In this case, periodic solutions exist for values of $\lambda < \lambda_{cr}$, but they are unstable (dashed curve in Fig. 4b). The existence of stable periodic solutions for $\lambda > \lambda_{cr}$ depends predominantly on the behavior of the damping $G_1(\xi;\lambda)$ for $\lambda > \lambda_{cr}$. If no stable periodic solutions exist for $\lambda > \lambda_{cr}$, then when λ is increased beyond λ_{cr} the aircraft or flap may undergo an aperiodic motion whose departure from the steady motion at $\lambda = \lambda_{cr}$ is potentially large.

In the more likely event that stable periodic solutions do exist for $\lambda > \lambda_{cr}$, their amplitudes must be finite, and not infinitesimally small, even for small positive values of $\lambda - \lambda_{cr}$. It is likely that this branch of stable periodic solutions will join that of the unstable branch as illustrated in Fig. 4b. In this event, the form of the bifurcation curve for values of $\lambda < \lambda_{cr}$ helps explain the situation where the steady-state motion could be stable to sufficiently small disturbances but become unstable to larger disturbances. For $\lambda < \lambda_{cr}$, Fig. 4b suggests disturbances with small enough amplitudes (lying below curve OB) will die out and the steady motion will remain stable. However, disturbances with amplitudes sufficiently larger than those of the unstable branch may actually grow up to the ultimate motion as $\tau \to \infty$, which will be that of the stable branch of periodic solutions (curve BA in Fig. 4b). Finally, we note that if the motion does attain the stable branch of periodic solutions (say, for $\lambda < \lambda_{cr}$), then hysteresis effects will manifest themselves with further changes in λ. When λ is increased beyond λ_{cr}, motion will continue to be periodic with finite amplitude (point A in Fig. 4b). If λ is now decreased below λ_{cr}, periodic motion will persist, even at values of λ where previously there had been steady motion when λ was being increased. Not until λ is diminished beyond a certain point (point B in Fig. 4b) will the motion return to the steady-state condition (point C in Fig. 4b) that had been experienced when λ was increasing.

4. APPLICATIONS TO AIRCRAFT MOTIONS

In this section we shall apply the theory developed in Secs. 2 and 3 to three different single-degree-of-freedom motions.

4.1 Pitching Motion of Supersonic/Hypersonic Airfoil

We retain the symbol ξ in all three cases to designate the perturbation variable. The other symbols will be replaced as necessary by the parameters relevant to the particular motion.

In the case of pitching oscillation (Fig. 1) of a supersonic/hypersonic airfoil in rectilinear flight, the parameter λ is the trim angle of attack, designated α_m in Fig. 1, measured relative to the horizontal velocity vector. The instantaneous angle of attack is $\alpha(t)$, also measured relative to the horizontal velocity vector, so that the perturbation variable $\xi(t)$ is the inclination $\alpha(t) - \alpha_m$ from the fixed trim angle of attack. The perturbation moment G in this case is the perturbation pitching moment about the center of gravity. Thus,

$$G(t;\lambda) = qS\ell C_m(t;\alpha_m,M_\infty,\gamma,h) \tag{28}$$

where q is the dynamic pressure, and S and ℓ are the reference area and length. The instantaneous pitching-moment coefficient C_m is also a function of the trim angle of attack α_m, the flight Mach number M_∞, the ratio of specific heat γ, and the (dimensionless) pivot axis position h.

For large-amplitude slow oscillations, exact solutions for C_m exist for simple shapes (Refs. 10 and 11), and their form is consistent with Eq. (5), i.e.,

$$C_m(\tau;\alpha_m) = C_{m_0}(\xi(\tau);\alpha_m) + \dot{\xi}C_{m_1}(\xi(\tau);\alpha_m) - C_{m_0}(0;\alpha_m) \tag{29}$$

Moreover, it is shown that (Refs. 10 and 11)

$$C_{m_i}(\xi;\alpha_m) = C_{m_i}(\xi + \alpha_m) , \quad (i = 0, 1) \tag{30}$$

Accordingly

$$\frac{\partial C_{m_i}}{\partial \xi} = \frac{\partial C_{m_i}}{\partial \alpha_m} \qquad (i = 0, 1) \tag{31}$$

and Eq. (26b) reduces to

$$\mu = -\frac{\varepsilon^2\omega_0}{4}\frac{d}{d\alpha_m}\left[\frac{D'(\alpha_m)}{S(\alpha_m)}\right]_{\alpha_m=\alpha_{cr}} \tag{32}$$

where the stiffness derivative $S(\alpha_m)$ and the damping-in-pitch derivative $D(\alpha_m)$ are related to the pitching-moment coefficient C_m by

$$S(\alpha_m) = -C'_{m_0}(\alpha_m) , \qquad D(\alpha_m) = -C_{m_1}(\alpha_m) \tag{33}$$

and

$$D(\alpha_{cr}) = 0 \tag{34}$$

A typical example of the variation of damping derivative $D(\alpha_m)$ versus α_m is shown in Fig. 5 (Ref. 16).

We conclude that when the trim angle of attack α_m is increased beyond a critical value α_{cr} at which the aerodynamic damping vanishes, i.e., $D(\alpha_{cr}) = 0$, the steady motion at α_{cr} loses its stability. A new finite-amplitude periodic motion, called the bifurcation solution, will replace it for values of $\alpha_m \geq \alpha_{cr}$ if it is stable. Stability of the bifurcation solution depends on whether $D'(\alpha_m)/S(\alpha_m)$ is increasing or decreasing on crossing the stability boundary α_{cr}.

By utilizing an approximate relation (Ref. 17)

$$D(\alpha_m) = b[S(\alpha_{cr}) - S(\alpha_m)] , \qquad b > 0$$

in Eq. (32), we get

$$\mu = \frac{\varepsilon^2\omega_0 b}{4}\left[\frac{d^2}{d\alpha_m^2}\ln S(\alpha_m)\right]_{\alpha_m=\alpha_{cr}}$$

For the case of a flat-plate airfoil in supersonic/hypersonic flow, the stiffness and damping-in-pitch derivatives $S(\alpha_m)$ and $D(\alpha_m)$ are known exactly in analytical form (Ref. 7) for values of α_m up to the shock detachment angle. It is shown in Table 1 that $\mu > 0$ for all combinations of M_∞ and h. Thus, the bifurcation is subcritical. The bifurcation periodic solution is therefore unstable, which implies one of two alternatives. The steady motion is either replaced by a finite-amplitude periodic motion accompanied by hysteresis phenomena, or by a potentially large aperiodic motion. In either case the loss of stability of the steady-state motion must be accompanied by a discrete change to a new stable state.

4.2 Flap Oscillation in Transonic Flow

The case of a flap oscillating about a hinge is conceptually similar to that of an airfoil pitching about a pivot axis. In effect, the oscillating flap may be regarded as an airfoil pitching in the nonuniform oncoming stream that results from a uniform free stream passing over the fixed forebody (Fig. 2).

In this case (Fig. 2), $\delta(t)$ is the instantaneous flap deflection angle, measured relative to the undeflected position. The parameter λ here is the fixed mean deflection angle δ_m, also measured from the undeflected position. Thus, $\xi(t)$, the perturbation variable, is the inclination $\delta(t) - \delta_m$ from the fixed mean deflection angle δ_m. The perturbation moment G is the perturbation hinge moment about the hinge line. Thus

$$G(t;\lambda) = qS\ell C_h(t;\delta_m,M_\infty,\gamma) \tag{35}$$

where C_h is the instantaneous hinge-moment coefficient. In direct parallel with the oscillating airfoil case of Eq. (29), we assign C_h the form

$$C_h(\tau;\delta_m) = C_{h_0}(\xi(\tau);\delta_m) + \dot{\xi}C_{h_1}(\xi(\tau);\delta_m) - C_{h_0}(0;\delta_m) \tag{36}$$

Equation (36) is consistent with Eq. (5). A similar form was validated in Ref. 12 by comparison with results of large-scale numerical integrations of the coupled inertial/flow field equations.

Equation (5) or Eq. (36) for the hinge-moment coefficient allows calculation of $C_{h_1}(\xi(\tau);\delta_m)$ by linearizing the flow field equations about the steady flow corresponding to fixing the instantaneous deflection angle, $\xi(\tau) + \delta_m$ (see Eq. (39)). Calculation of $C_{h_1}(\xi(\tau);\delta_m)$ from the linearized equations may require less computing time than the nonlinear method used in Ref. 12, yet it is consistent with the level of approximation leading to Eq. (5) or Eq. (36). This simplification of the calculation of $C_{h_1}(\xi(\tau);\delta_m)$ reinforces the main conclusion of Ref. 12 that the cost of computations to determine the flap's motion will be very small if the aerodynamic contribution to the equations of motion is modeled, as compared to the computational cost required to solve the coupled inertial/flow field equations.

It was further established (Ref. 11) that

$$C_{h_i}(\xi;\delta_m) = C_{h_i}(\xi + \delta_m) , \qquad (i = 0, 1) \tag{37}$$

which in turn reduces Eq. (26b) to

$$\mu = -\frac{\epsilon^2\omega_0}{4}\left[\frac{d}{d\delta_m}\frac{D'(\delta_m)}{S(\delta_m)}\right]_{\delta_m=\delta_{cr}} \tag{38}$$

where

$$S(\delta_m) = -C'_{h_0}(\delta_m) , \quad D(\delta_m) = -C_{h_1}(\delta_m) , \quad D(\delta_{cr}) = 0 \tag{39}$$

We therefore reach a conclusion regarding the characteristics of the flap oscillation near the mean flap deflection angle δ_{cr} which is directly analogous to that of Sec. 4.1 regarding the characteristics of the airfoil pitching motion in the neighborhood of α_{cr}.

Numerical results from Ref. 12 for $S(\delta_m)$ and $D(\delta_m)$ are reproduced (by means of spline fitting) in Fig. 6. These are results for an NACA 64A010 airfoil at zero mean angle of attack in a transonic stream with $M_\infty = 0.8$ and $\gamma = 1.4$. It is found that

$$\left[\frac{d}{d\delta_m}\frac{D'(\delta_m)}{S(\delta_m)}\right]_{\delta_m=\delta_{cr}} = -59.20 \quad \text{at} \quad \delta_{cr} = 2.7°$$

Hence, the bifurcation is subcritical and the bifurcation periodic solution is unstable. Just as we found for the flat-plate airfoil in supersonic/hypersonic flow, loss of stability of the steady-state transonic flow about the flap at $\delta_m = \delta_{cr}$ implies a <u>discrete</u> change to a new stable state. The new state may be either a finite-amplitude periodic oscillation about δ_m accompanied by hysteresis phenomena, or it may be a potentially large aperiodic departure from the steady state. The fact that $D(\delta_m)$ becomes positive again at $|\delta_m| = 17°$ (Fig. 6(b)) implies that the first of these alternatives will be the preferred one (Ref. 11).

4.3. Wing Rock of Slender Delta Wing in Subsonic Flow

The phenomenon known as "wing rock" of a slender delta wing in subsonic flow has been the subject of intensive investigation by many researchers (Refs. 13, 18-21). It is now well-documented (Refs. 13 and 18) that as the trim angle of attack α_m is raised incrementally, a critical value α_{cr} is reached where roll-damping moment changes from stabilizing to destabilizing. Ericsson (Ref. 21) has shown how the leeside vortices, which appear and grow stronger as α_m is raised, may lag behind a rolling motion of the wing. The pressures they induce may contribute a rolling-moment component proportional to rolling velocity that is destabilizing and eventually becomes large enough to surpass the stabilizing component that had existed

alone at smaller α_m. Consequently, at $\alpha_m \geq \alpha_{cr}$, small disturbances in the flow field excite a growing roll oscillation. Bifurcation theory again can be applied to help determine the ultimate state of the oscillation.

For this case, we take the parameter λ to be the fixed trim angle of attack α_m, while the perturbation variable $\xi(t)$ is the roll deflection angle $\phi(t)$ (Fig. 3), measured from the position of zero roll angle. The perturbation moment G is the rolling moment about the wing longitudinal axis. Thus

$$G(t;\lambda) = qS\ell C_\ell(t;\alpha_m,\Lambda) \tag{40}$$

where, for incompressible flow, the instantaneous rolling-moment coefficient C_ℓ depends on the trim angle of attack α_m and the sweepback angle Λ of the delta wing. Results of experiments (Refs. 13 and 18) and numerical computations (Ref. 19) have shown that, for a given Λ, it is a good approximation to the instantaneous rolling-moment coefficient to take

$$C_\ell = C_{\ell_0}(\xi(\tau);\alpha_m) + \dot{\xi}C_{\ell_1}(\xi(\tau);\alpha_m) \tag{41}$$

which is consistent with Eq. (5).

As an example, for the 80° sweep-back flat delta wing studied in Ref. 18, C_ℓ is approximated by a power series (Ref. 19) which leads to the following equation for the rolling motion

$$\begin{aligned}\ddot{\xi} &= F(\xi,\dot{\xi};\alpha_m)\\ &= [b_1(\alpha_m)\xi + b_3(\alpha_m)\xi^3] + \dot{\xi}[b_0 + b_2(\alpha_m) + b_4(\alpha_m)\xi^2]\\ &= F_0(\xi;\alpha_m) + \dot{\xi}F_1(\xi;\alpha_m)\end{aligned} \tag{42}$$

Taking account of the scaling factors adopted in Ref. 19,

$$b_i(\alpha_m) = \kappa^2 C_1 a_i(\alpha_m), \qquad (i = 1, 3) \tag{43a}$$

$$b_j(\alpha_m) = \kappa C_1 a_j(\alpha_m), \qquad (j = 2, 4) \tag{43b}$$

In Eqs. (43), κ is a factor accounting for the difference between scalings adopted for the time variable in Ref. 19 and this study. From Ref. 19, $\kappa = 2c/\ell = 2 \times 0.429/0.107 = 8$, $C_1 = 0.088$. The $a_i(\alpha_m)$ are tabulated in Table 5 of Ref. 19, which yields the following table for the $b_i(\alpha_m)$:

α_m	10°	15°	20°	25°
b_1	-0.0265	-0.0721	-0.1977	-0.3320
b_2	-0.0101	0.0090	0.0596	0.0959
b_3	-0.1222	-0.2214	-0.0501	0.2894
b_4	+0.1491	0.1159	-0.1799	-0.9977

From Eq. (11b), the linear contribution to the damping in roll is

$$D(\alpha_m) = -F_1(0;\alpha_m) = -b_0 - b_2(\alpha_m) \tag{44}$$

where $-b_0 > 0$ is proportional to the wind-off roll-damping moment due to bearing friction in the experimental setup used in Ref. 18. In order to compare our theoretical prediction with the experimental results of Ref. 18, we choose a value of $-b_0$ such that Eq. (44) yields zero damping in roll at the same angle of attack, $\alpha_{cr} = 18.6°$, as that reported in Ref. 18. The function $D(\alpha_m)$ is then plotted in Fig. 7 by means of spline fitting.

From Eq. (26c), the index for stability of the bifurcation periodic rolling oscillation is

$$\mu = -\frac{b_4(\alpha_{cr})}{b_2'(\alpha_{cr})} \tag{45}$$

At $\alpha_{cr} = 18.6°$, we find from the table above that $b_2(\alpha_{cr}) = -0.0$[illegible]. From the spline-fit curve for $b_4(\alpha_{cr})$ (Fig. 8), we find that $b_4(\alpha_{cr}) = -0.0$[illegible]. Hence $\mu > 0$, and the bifurcation is supercritical, implying that the bifurcation periodic roll oscillation is stable. This is in agreement with the experimental finding in Ref. 18.

We now further compare the supercritical bifurcation diagram predicted by the present theory with experimental results from Ref. 18. Combining Eq. (21c) with Eq. (22) to eliminate λ_2 and then using Eq. (45), we get

$$\alpha_m - \alpha_{cr} = -\varepsilon^2 \left[\frac{\omega_o}{2}\frac{b_4}{D'b_1}\right]_{\alpha_m=\alpha_{cr}}$$

$$= \varepsilon^2 \left[\frac{b_4}{2D'\sqrt{-b_1}}\right]_{\alpha_m=\alpha_{cr}} \tag{46}$$

The last equation was obtained by using Eqs. (25) and (42). From Fig. 7 (noting that $1° = \pi/180$), we get $D'(\alpha_{cr}) = -0.6131$. Hence Eq. (46) reduces to

$$\alpha_m - \alpha_{cr} = 0.1120\ \varepsilon^2 \tag{47}$$

where ε is the amplitude of the bifurcation periodic solution (Ref. 11). Equation (47) is plotted in Fig. 9 for the 80° sweep-back delta wing and compared with the experimental results of Levin and Katz (Ref. 18). The agreement is excellent near α_{cr}, where the bifurcation theory is particularly applicable.

It should be noted that although $\mu < 0$ and the bifurcation is supercritical, the magnitude of $|\mu|$ is small in the example. This implies that the bifurcation is close to the boundary between subcritical and supercritical. Consequently, on increasing the angle of attack α_m by a small amount, the amplitude of the resulting periodic motion will be quite large. This is confirmed by the experimental results shown in Fig. 9. For example, increasing α_m by 1° past α_{cr} (=18.6°) results in a stable periodic roll oscillation with an amplitude of 22.6°.

5. CONCLUDING REMARKS

We have shown how bifurcation theory can be used to study the nonlinear dynamic stability characteristics of an aircraft or flap subject to single-degree-of-freedom motion about its trim position. When the bifurcation parameter λ (e.g., the angle of attack) is increased past the stability boundary λ_{cr}, where the aerodynamic damping vanishes, the steady motion loses its stability. This results in a finite-amplitude periodic motion after the transient motion has died away. We have also established a simple criterion for the stability of the bifurcation periodic motion in terms of the aerodynamic coefficients. The theory predicts that bifurcation solutions are unstable (subcritical) for the pitching airfoil in supersonic/hypersonic flow and for flap oscillations in transonic flow. Bifurcation solutions are stable (supercritical) for roll oscillations of the slender delta wing in subsonic flow. The latter prediction is in good agreement with available experimental results.

When the theory predicts subcritical bifurcation, the abrupt change in the motion that results when λ is increased past λ_{cr} may cause an abrupt structural change of the flow field. This in turn may render invalid the form of the perturbation moment of the aerodynamic forces that was used. Under these conditions, aerodynamic information in a different form may be required. However, the theory as developed in this paper is valid up to λ_{cr} and can be used to predict the onset of subcritical bifurcation.

When the theory predicts supercritical bifurcation, the bifurcation periodic solution is stable to small disturbances for a range of λ beyond λ_{cr}. With further increase in λ, however, the periodic motion may lose its stability. This in turn may result in another bifurcation at $\lambda = \lambda_2 > \lambda_{cr}$, which could be either subcritical or supercritical. The resulting bifurcation solution may be quasi-periodic, and the sequence of bifurcations may continue.

Finally, the theory may be generalized to apply to aircraft motions involving more than a single degree of freedom. For motions involving two degrees of freedom or more, one should be aware of the possibility of chaotic behavior occurring after a finite number of successive bifurcations.

REFERENCES

1. Orlik-Rückemann, K. J., "Dynamic Stability Testing of Aircraft--Needs Versus Capabilities." Progress in Aerospace Sciences, Vol. 16, No. 4, Pergamon Press, New York, pp. 431-447, 1975.

2. Padfield, G. D., "Nonlinear Oscillations at High Incidence." AGARD CP-235, Dynamic Stability Parameters, Paper No. 31, May 1978.

3. Iooss, G. and Joseph, D. D., "Elementary Stability and Bifurcation Theory," Springer-Verlag, New York, 1980.

4. Mehra, R. K. and Carroll, J. V., "Bifurcation Analysis of Aircraft High Angle of Attack Flight Dynamics," New Approaches to Nonlinear Problems in Dynamics, Ed. P. J. Holmes, SIAM, Philadelphia, 1980, pp. 127-146.

5. Guicheteau, P., "Bifurcation Theory Applied to the Study of Control Losses on Combat Aircraft," La Recherche Aerospatiale, 1982-83, pp. 1-14.

6. Hui, W. H., "Stability of Oscillating Wedges and Caret Wings in Hypersonic and Supersonic Flows," AIAA J., Vol. 7, No. 8, Aug. 1969, pp. 1524-1530.

7. Hui, W. H., "Supersonic/Hypersonic Flow Past an Oscillating Flat-Plate at High Angles of Attack," ZAMP, Vol. 29, Fasc. 3, 1978, pp. 414-427.

8. Hui, W. H., "An Analytic Theory of Supersonic/Hypersonic Stability at High Angles of Attack," AGARD CP-235, Dynamic Stability Parameters, Paper No. 22, May 1978.

9. Hui, W. H. and Tobak, M., "Unsteady Newton-Busemann Flow Theory. Part I: Airfoils," AIAA J., Vol. 19, No. 3, Mar. 1981, pp. 311-318.

10. Hui, W. H., "Large-Amplitude Slow Oscillation of Wedges in Inviscid Hypersonic and Supersonic Flows," AIAA J., Vol. 8, No. 8, Aug. 1970, pp. 1530-1532.

11. Hui, W. H. and Tobak, M., "Bifurcation Analysis of Aircraft Pitching Motions About Large Mean Angles of Attack," J. Guidance, Control, and Dynamics, Vol. 7, 1984, pp. 113-122.

12. Chyu, W. J. and Schiff, L. B., "Nonlinear Aerodynamic Modeling of Flap Oscillations in Transonic Flow: A Numerical Validation," AIAA J., Vol. 21, No. 1, Jan. 1983, pp. 106-113.

13. Nguyen, L. T., Yip, L., and Chambers, J. R., "Self-Induced Wing Rock of Slender Delta Wings," AIAA Paper 81-1883, Atmospheric Flight Mechanics Conference, Albuquerque, NM, Aug. 1981.

14. Tobak, M. and Schiff, L. B., "Aerodynamic Mathematical Modeling--Basic Concepts," AGARD Lecture Series No. 114 on Dynamic Stability Parameters, Lecture No. 1, March 1981.

15. Hopf, E., "Abzweigung einer periodischen Lösung von einer Stationären Lösung einer Differentialsystems," Berichten der Mathematisch-Physischen Klasse der Sächsischen Akademie der Wissenschaften zu Leipzig, Vol. XCIV, 1942, pp. 1-22.

16. Hui, W. H., "Unified Unsteady Supersonic/Hypersonic Theory of Flow Past Double Wedge Aerofoils," ZAMP, Vol. 34, 1983, pp. 458-488.

17. Tobak, M. and Schiff, L. B., "On the Formulation of the Aerodynamic Characteristics in Aircraft Dynamics," NASA TR R-456, Jan. 1976.

18. Levin, D. and Katz, J., "Dynamic Load Measurements with Delta Wings Undergoing Self-Induced Roll-Oscillations," J. Aircraft, Vol. 21, 1984, pp. 30-36.

19. Konstadinopoulos, K., Mook, D. T., and Nayfeh, A. H., "Subsonic Wing Rock of Slender Delta Wing," AIAA Paper 85-0198, Jan. 1985.

20. Hsu, C. H. and Lan, C. E., "Theory of Wing Rock," AIAA Paper 85-0199, Jan. 1985.

21. Ericsson, L. E., "The Fluid Mechanics of Slender Wing Rock," J. Aircraft, Vol. 21, 1984, pp. 322-328.

ACKNOWLEDGMENT

Professor Hui's contributions to this study were funded by NASA Grant NAGW-575.

TABLE 1. VALUES OF STABILITY CRITERION $\mu(M_\infty, h)$ FOR FLAT-PLATE AIRFOIL; $\varepsilon = 1$, $\gamma = 1.4$; $\mu > 0$ SUBCRITICAL BIFURCATION, $\mu < 0$ SUPERCRITICAL BIFURCATION

M_∞ \ h	0	0.1	0.2	0.3	0.4	M_∞ \ h	0	0.1	0.2	0.3	0.4
1.5	36.5	19.0	---	---	---	2	39.5	25.8	17.2	13.0	14.7
1.6	39.6	23.4	13.6	8.8	10.7	3	57.2	38.6	26.8	20.9	23.3
1.7	40.0	24.8	15.5	11.0	12.8	4	84.7	58.4	41.4	32.8	36.4
1.8	39.7	25.3	16.3	12.0	13.7	5	107.3	74.8	53.7	42.9	47.5
1.9	39.4	25.5	16.8	12.6	14.3	6	123.6	86.7	62.6	50.3	55.6
2.0	39.5	25.8	17.2	13.0	14.7						

M_∞ \ h	0.25	0.26	0.27	0.28	0.29	0.30	0.31	0.32	0.33	0.34	0.35
1.6	10.6	10.1	9.7	9.3	9.0	8.8	8.6	8.5	8.4	8.4	8.5
1.7	12.6	12.2	11.8	11.5	11.2	11.0	10.8	10.7	10.6	10.6	10.7
1.8	13.6	13.2	12.8	12.5	12.2	12.0	11.8	11.7	11.6	11.7	11.7
1.9	14.1	13.7	13.4	13.0	12.8	12.5	12.4	12.3	12.2	12.2	12.3
2.0	14.5	14.1	13.8	13.5	13.2	13.0	12.8	12.7	12.6	12.7	12.7

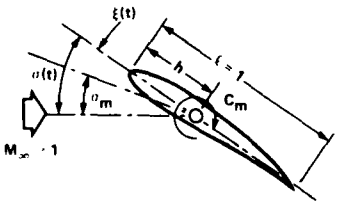

Fig. 1. Pitching airfoil in supersonic/hypersonic flow.

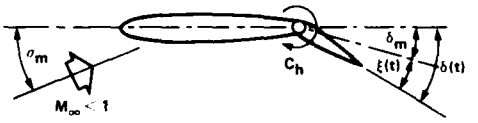

Fig. 2. Flap oscillation in transonic flow.

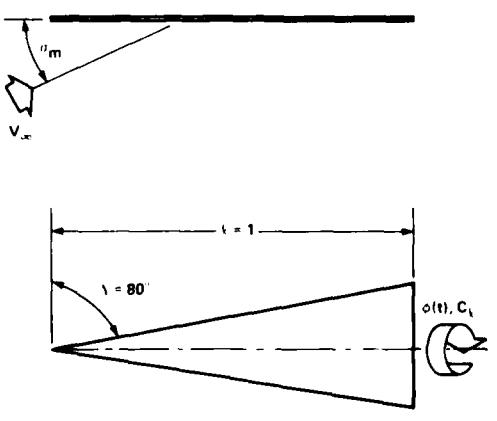

Fig. 3. Wing rock of slender delta wing in subsonic flow.

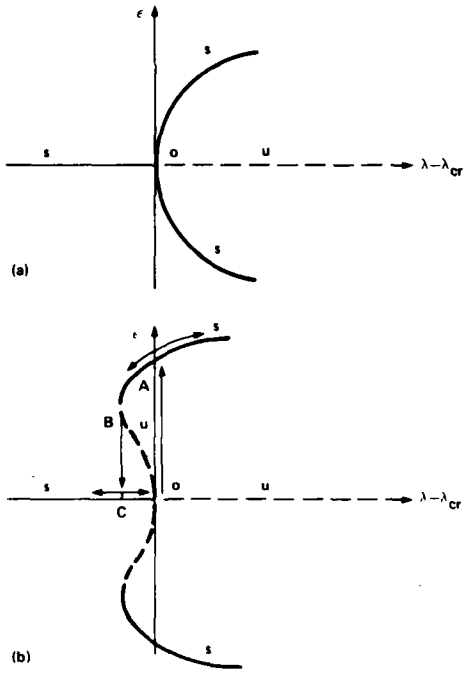

Fig. 4. Typical forms of bifurcation diagrams near the dynamic stability boundary λ_{cr} where $D(\lambda_{cr}) = 0$. (a) Supercritical, $\mu < 0$. (b) Subcritical, $\mu > 0$.

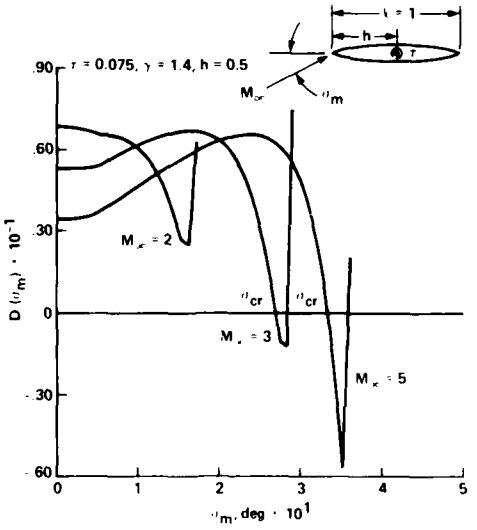

Fig. 5. Damping-in-pitch derivative D versus angle of attack σ_m for a biconvex circular arc airfoil (Ref. 16), h = 0.5, γ = 1.4, τ = 0.075.

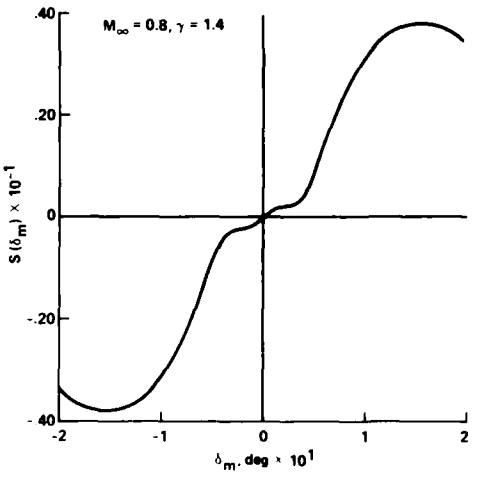

Fig. 6a. Stiffness derivative S versus mean deflection angle δ_m of a transonic flap on NASA 64A010 airfoil (Ref. 12). M_∞ = 0.8, γ = 1.4, σ_m = 0.

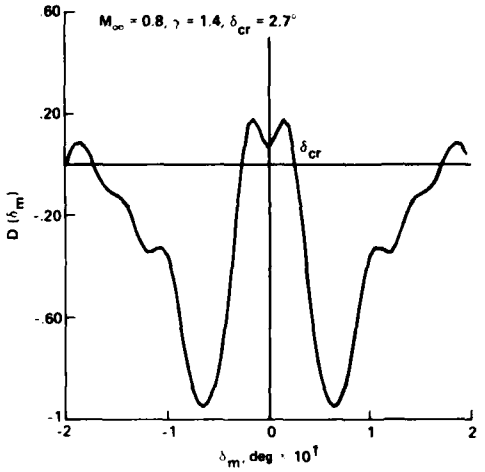

Fig. 6b. Damping derivative D versus mean deflection angle δ_m of a transonic flap on NASA 64A010 airfoil (Ref. 12). M_∞ = 0.8, γ = 1.4, σ_m = 0, δ_{cr} = 2.7°.

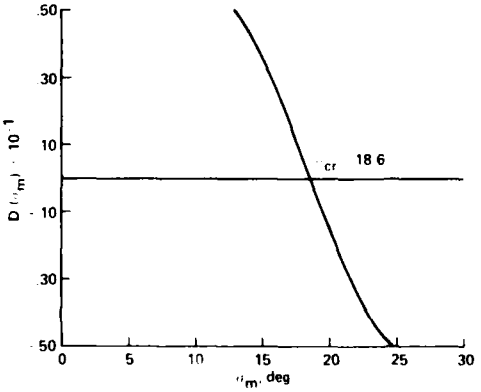

Fig. 7. Damping in roll D of an 80° sweep-back flat delta wing versus angle of attack σ_m in incompressible flow (Refs. 18, 19), Eq. (44). σ_{cr} = 18.6°.

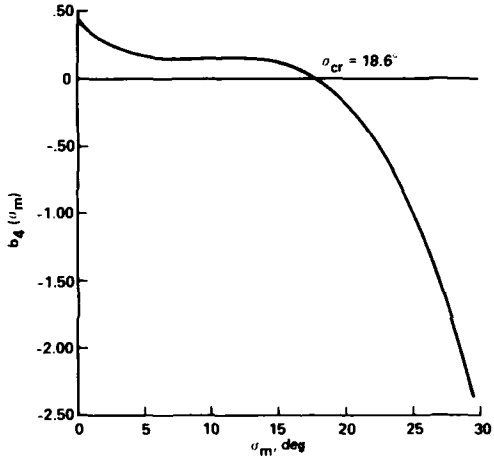

Fig. 8. Rolling aerodynamic coefficient $b_4(\alpha_m)$ of an 80° sweep-back flat delta wing versus angle of attack α_m in incompressible flow (Refs. 18, 19). Observe $b_4(\alpha_{cr}) = -0.05473 < 0$.

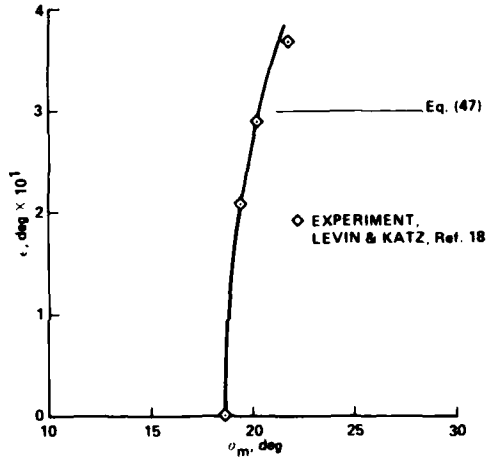

Fig. 9. Amplitude ϵ of bifurcation periodic motion of an 80° sweep-back delta wing versus angle of attack α_m; Eq. (47); ◇ experiments (Ref. 18). $\alpha_{cr} = 18.6°$.

DYNAMIC NONLINEAR AIRLOADS - REPRESENTATION AND MEASUREMENT

E.S. Hanff,
National Aeronautical Establishment,
National Research Council of Canada,
Ottawa, Ontario, Canada

SUMMARY

A new representation of aerodynamic reactions in terms of the motion variables, which does not rely on assumptions of linearity, is proposed. This representation is therefore indicated for extreme flight conditions where a locally linearized model is usually of questionable value. The significance within the present context of stability derivatives is discussed with the intention of pointing out their range of applicability.

A wind-tunnel technique, capable of efficiently obtaining the bulk of the data required for the effective use of the above representation, is briefly described.

SYMBOLS

b : span

C_ℓ : rolling moment coefficient

$\bar{C}_\ell$: static (mean) rolling moment coefficient

C_{ℓ_ϕ} : $\partial C_\ell / \partial \phi$

C_{ℓ_p} : $\partial C_\ell / \partial \frac{bp}{2V}$

I_x : rolling moment of inertia

$\hat{L},\hat{M},\hat{N}$: direction numbers of normal to plane (with respect to ϕ, p, C_ℓ)

$\hat{l},\hat{m},\hat{n}$: direction cosines of normal to plane (with respect to ϕ, p, C_ℓ)

p : roll rate

$P = \frac{bp}{2V}$: reduced roll rate

$\bar{q}$: free stream dynamic pressure

S : reference area

V : free stream velocity

ϕ : roll angle

ω : circular frequency (rad/sec)

1. INTRODUCTION

Over the past several years a consensus has been developing that the locally linear analysis technique for the determination of aerodynamic reactions acting on an aircraft in terms of its motion variables is inadequate under extreme flight conditions where highly "non linear" aerodynamics prevails. Such conditions are encountered mainly at high angles of attack where severe flow separation and possibly asymmetry (even at zero angle of sideslip) are present (Refs. 1,2).

In recognition of this situation substantial work is currently underway to develop techniques that can provide a better understanding and more accurate prediction of aircraft behaviour in this regime. Most of the work appears to be of a rather theoretical nature, essentially consisting of an attempt to identify and implement a mathematical formalism capable of handling the various types of non-linearities present under the above conditions. An approach considered particularly promising, based on bifurcation analysis and catastrophe theory, has been described by various authors over the last several years (Refs. 3-7).

In this paper, on the other hand, a more empirical formulation to treat aerodynamic non-linearities is proposed, which is based on a knowledge of the instantaneous values of airloads as a function of the corresponding instantaneous values of the pertinent motion variables. The formulation is based on the assumption that there is a well defined (although not necessarily single valued) relationship between any given aerodynamic reaction and the motion variables, which, in a topological sense, corresponds to the existence of a unique "reaction hypersurface" that defines the reaction in terms of n motion variables.

If the hypersurface could be experimentally obtained in its entirety, it could then be used to carry out simulations without resorting to mathematical models with their inherent limitations. Practical considerations, however, limit the number of

experiments that can be performed to obtain the very large data base required to suitably define the hypersurface, therefore necessitating some level of mathematical modelling to supplement the empirically obtained data.

Clearly the value of the proposed formulation depends critically on the availability of experimental techniques that can efficiently yield the necessary data. A wind-tunnel technique and data reduction system that meets these requirements has been recently developed (Ref. 8). Its purpose is to determine the instantaneous value of the airloads acting on a model as a function of the corresponding values of the motion variables, the latter being defined by the arbitrary motion imposed on the model. A brief description of the wind-tunnel technique is presented here for completeness.

2. CHARACTERISTICS OF THE REPRESENTATION

The postulated existence of a well defined relationship between the airloads and the motion variables implies that the values of the loads - for a given set of motion variables - are independent of the past history of the motion. This is not necessarily so, nevertheless the assumption of history independence is initially made for the sake of simplicity. The case of history dependence is briefly considered in Section 2.3.

Rather than discussing the proposed formulation with its fairly wide-ranging implications in general terms, a specific application to a simple case will be considered first, as it affords a better visualization of various concepts of interest. To this effect the case of a motion in a single DOF is examined below. The more general case where a reaction depends on more motion variables will be discussed in Section 2.2.

2.1 Motion in One Degree of Freedom

For the sake of clarity, a rolling motion is assumed, although the approach is completely general and can be applied to any 1 DOF motion. The rolling moment, the reaction under study in this case, is assumed to depend only on the instantaneous value of the roll angle (ϕ) and of the roll rate (p) The reaction hypersurface is thus reduced to a three-dimensional surface that defines C_ℓ in terms of ϕ and p (such as the very schematic hysteretical one shown in Fig. 1) that can, in principle, be experimentally determined by performing wind-tunnel tests involving combinations of these two quantities.

At this stage a short digression regarding 1 DOF hysteretical reaction surfaces is in order. The one shown in Fig. 1 is characterized by the independence of the threshold values in terms of the rate, corresponding to a "static" hysteresis case. Furthermore, the surface is single-valued except along the line defining the step which in conjunction with the presence of the step at p = 0 implies the existence of minor loops for motions between the threshold values. If the minor loops do not exist, that is, the transition between levels can only occur at the thresholds, the surface becomes partially double valued, as shown in Fig. 2. Another interesting situation arises when convective time lags have an impact on the threshold values, in which case a more or less linear relationship between the latter and the rate is present. Such a "dynamic" hysteretical relationship is depicted in Fig. 3.

Clearly the resolution of the surface depends on the number and distribution of the ϕ-p combinations used to define it, and although it may appear that an inordinately large number of tests might be required to obtain sufficient resolution, the availability of suitable testing techniques such as the one described in Section 3 renders this number quite reasonable.

Specifically, the reaction surface can be readily defined by carrying out a series of oscillatory tests using sinusoidal motions of different amplitudes and/or frequencies which are represented by a family of ellipses in the phase plane (ϕ,p) used here to describe the motion. Fig. 4 shows the same reaction surface as Fig. 1 but defined by the trajectory of the "load point", i.e. instantaneous value of C_ℓ as a function of ϕ and p as the model describes a sinusoidal motion at different amplitudes. Each closed line represents the result of a single wind-tunnel test indicating that only a few tests are required to define a surface that does not exhibit severe "radial" discontinuities.

2.1.1 Linear Case

Assuming a linear relationship between the instantaneous reaction, position and rate, we have that for a sinusoidal motion

$$\phi = \phi_o \sin \omega t \tag{1}$$

$$\dot{\phi} = \phi_o \omega \cos \omega t \tag{2}$$

and

$$C_\ell = C_{\ell_o} \sin(\omega t + \eta)$$

$$C_\ell = C_{\ell_o} (\sin \omega t \cos \eta + \sin \eta \cos \omega t) \tag{3}$$

substituting from (1) and (2) and including a static term $\bar{C}_\ell$ we obtain

$$C_\ell = \frac{C_{\ell o} \cos \eta}{\phi_o} \phi + \frac{C_{\ell o} \sin \eta}{\phi_o \omega} \dot{\phi} + \bar{C}_\ell$$

which in the ϕ, p, C_ℓ space corresponds to a plane whose normal has the following direction numbers:

$$\hat{L} = \frac{C_{\ell o} \cos \eta}{\phi_o}, \quad \hat{M} = \frac{C_{\ell o} \sin \eta}{\phi_o \omega}, \quad \hat{N} = -1$$

with the corresponding direction cosines:

$$\hat{l} = \frac{\hat{L}}{\sqrt{\hat{L}^2 + \hat{M}^2 + \hat{N}^2}}, \quad \hat{m} = \frac{\hat{M}}{\sqrt{\hat{L}^2 + \hat{M}^2 + \hat{N}^2}}, \quad \hat{n} = \frac{\hat{N}}{\sqrt{\hat{L}^2 + \hat{M}^2 + \hat{N}^2}}$$

Therefore the load point travels within a <u>plane</u> oriented in a way such that its normal has the above direction cosines.

In general, however, the reaction surfaces are not planar due to aerodynamic non-linearities, in which case the reaction contains both the same frequency as that of the primary motion as well as some harmonics, implying that a process of linearization is applied when the harmonic content of the reaction is ignored.

2.1.2 Non-linear Case - Interpretation of Stability Derivatives

The validity of such linearized results is obviously dependent on the local curvature of the reaction surface in the area under study. This raises the issue of the extent to which stability derivatives are useful as a modelling tool for aircraft behaviour. As is well known, stability derivatives were originally conceived to be used in the modelling of aircraft subject to very small perturbations about its steady flight. Under such conditions the local linearization implicit in the derivative formulation is generally correct; however, subsequent attempts to utilize derivatives to model aircraft performance without regard to the perturbation magnitude have largely not been very successful (Ref. 9). It is therefore appropriate to examine the meaning of stability derivatives within the context of the present formulation and then assess their value as a means of describing aerodynamic reactions in terms of aircraft motion.

Again, resorting to the example of motion in roll, we have that in the linear formulation the rolling moment coefficient is given by

$$C_\ell = \bar{C}_\ell[\bar{\phi}] + C_{\ell\phi}[\bar{\phi}] \ (\phi - \bar{\phi}) + \frac{b}{2V} C_{\ell p}[\bar{\phi}] p \qquad (4)$$

where $\bar{C}_\ell$, $C_{\ell\phi}$ and $C_{\ell p}$ may be determined by means of static and/or dynamic tests in which the model is oscillated with a small amplitude about the mean roll angle $\bar{\phi}$. As the square brackets indicate, all three quantities are assumed to be functions - not necessarily linear - of $\bar{\phi}$ only, implying that for a given value of $\bar{\phi}$ the reaction is linearly related to p, corresponding to a reaction surface defined by straight generators parallel to the C_ℓ, p plane.

Rearranging (4) and using the reduced rate $P = \frac{b}{2V} p$ we obtain

$$C_\ell = C_{\ell\phi}[\bar{\phi}]\phi + C_{\ell p}[\bar{\phi}]P + \bar{C}_\ell[\bar{\phi}] - C_{\ell\phi}[\bar{\phi}]\bar{\phi}$$

indicating that the direction numbers of a normal to the planar approximation of the reaction surface -when the reduced rate P rather than p is used in the corresponding axis - are

$$\hat{L} = C_{\ell\phi}[\bar{\phi}], \quad \hat{M} = C_{\ell p}[\bar{\phi}], \quad \hat{N} = -1$$

In other words, the static and dynamic derivatives are related to the orientation of the reaction plane defined by the linear analysis of the aerodynamic reactions resulting from the small amplitude oscillatory tests used to establish the derivatives. For the sake of clarity it should be pointed out that in the presence of aerodynamic stiffness only ($\hat{M} = 0$), the reaction plane is parallel to the P axis and inclined with respect to the ϕ and C_ℓ axes, whereas in the case of aerodynamic damping only ($\hat{L} = 0$), the plane is parallel to the ϕ axis and inclined with respect to the P and C_ℓ axes. Generally, however, when both quantities are present and the plane is arbitrarily oriented, it is useful to keep in mind that its slope with respect to ϕ and P is related to aerodynamic

stiffness and damping, respectively ($C_{\ell\phi} = \partial C_\ell/\partial\phi$; $C_{\ell p} = \partial C_\ell/\partial P$).

The trajectories of the load point corresponding to tests at various values of ϕ to determine the local derivatives on a reaction surface are shown in Fig. C1 in red, whereas the planar approximation is shown in green. In most cases the reaction surface can be expected to be curved and therefore its exact coincidence with the plane defined by the local derivatives is only possible at the test point where the derivatives were obtained provided the test amplitude and frequency approach zero. Depending on the local curvature of the reaction surface, a significant error may be introduced by obtaining the derivatives using a larger amplitude and/or frequency, and a further error can be expected when extrapolating the local reaction plane to other regions of the surface. A case in point is the observed amplitude and frequency dependence of some derivatives under certain conditions (Refs. 10,11). Such effects can be easily visualized using the present formulation, as shown in Figs. C2 and C3 where the linearized (green) and actual (red) trajectories of the load point are shown for tests carried out at different amplitudes and frequencies, respectively, for the case of a schematic reaction surface that describes a rather narrow-loop static hysteretical process. The relative magnitudes of the static and dynamic derivatives are plotted in Figs. 5 and 6 where the solid symbols indicate the values corresponding to the trajectories shown. Conversely, the shape of the reaction surface can be roughly reconstructed if sufficient values for the derivatives in terms of attitude, amplitude and frequency are available. Such an exercise has been carried out recently for the case of the rolling moment coefficient of a slender delta wing subject to motion in roll (Ref. 12). The results, obtained on the basis of experimental data from Ref. 13 are very encouraging.

2.1.3 Simulation

Assuming that the reaction surface has been determined, e.g. by means of a family of experimentally obtained closed loops (Fig. 4), the value of C_ℓ for any combination of ϕ and p can be established by suitable interpolations. A simulation can then be carried out by using such values as the aerodynamic forcing function in the appropriate equation of motion. For the case of the 1 DOF rolling motion under consideration, the simulation merely involves solving

$$\ddot{\phi} = \frac{\bar{q}Sb\ C_\ell}{I_x}$$

Such a simulation has been carried out, using arbitrary values for the above constants for the surface depicted in Fig. 7 where the trajectory of the load point on the surface is also shown. The surface is the same as that in Fig. 1 but with a reduced "step" size, to avoid the excessively large limit cycle amplitude that would result from the original high undamping. The corresponding time domain representation of the roll angle is shown in Fig. 8. The growth of the oscillation is due to the energy added to the system by the flow, as indicated by the counterclockwise motion of the load point when projected on the C_ℓ, ϕ plane (Fig. 9). When the amplitude of the oscillation reaches the hysteretical threshold levels, energy begins to be lost during the part of the cycle where the load point travels in a clockwise direction. Equilibrium is reached when the area enclosed by the clockwise and counterclockwise motions are equal, resulting in a limit cycle oscillation. As expected, the damping derivative obtained for this surface with a sinusoidal oscillation of an amplitude equal to that of the limit cycle is approximately zero.

An interesting simulation case arises when the reaction surface includes undesired attractors, namely unwanted stable solutions to the simulation equation. In the case of a 1 DOF motion like the one under consideration, attractors exist at intersections of the ϕ axis with the reaction surface, provided the latter exhibits static and dynamic stability at these locations. An example of a reaction surface containing two attractors - symmetrically located about the origin - is shown, together with a simulation, in Fig. 10. The values for the static and dynamic derivatives as a function of ϕ are shown in Fig. 11 where the solid symbols correspond to the values at the ϕ grid lines in Fig. 10.

2.2 Extension to More Degrees of Freedom

In the previous section it was assumed that the instantaneous value of the load coefficient was a function of one position and its corresponding rate (ϕ & p) only. Although this assumption is useful to clarify some concepts and valid for the simulation of fixed axis motions such as encountered in typical dynamic wind-tunnel tests, it may represent an unacceptable simplification in a more realistic situation. It thus becomes necessary to expand the above concept to include the effect of more than one position-rate pair on the instantaneous value of a reaction. The relevant parameters may be associated with the motion in the plane of the reaction, e.g. C_m, α, $\dot{\alpha}$, q, leading to the concept of "direct reactions" (to supersede direct derivatives) or with motion parameters in a plane other than that of the reaction ("cross reactions").

It should be pointed out that this separation is arbitrary and, in fact, likely of limited use within the context of the non-linear formulation under consideration, since superposition - the original justification for the separation -is not generally applicable. The concept of direct and cross reactions may therefore be useful only in single plane motions or in situations where the pertinent non-linearities

can be neglected.

In general, however, the reaction surfaces must be viewed in an (m + 1) dimensional space where m corresponds to the total number of motion parameters with an impact on the reaction under study. Although this is, in principle, a rigorous approach, the experimental determination of the hypersurfaces poses a serious practical problem, in that a very large number of tests must be carried out to fill in the sufficiently dense multidimensional grid required to obtain an acceptable definition of the hypersurfaces. Clearly, in order to obtain the required combinations of motion variables, some tests must involve more complex motions than those present in fixed-axis oscillation and coning experiments, thus necessitating the development of new wind-tunnel rigs capable of producing the desired motions. For example, the orbital apparatus concept proposed in Ref. 14 appears to provide a feasible means for generating a substantial range of important motion variable combinations with a single rig.

In any case, regardless of the complexity of the test program, some modelling is likely still required to supplement the experimentally-obtained data in order to define the complete hypersurfaces. Fortunately, however, the better understanding of the underlying aerodynamics that can be derived from the detailed information obtained from this type of testing should considerably facilitate the modelling process. A good deal of judgement is required to establish a reasonable balance between the experimental and theoretical contributions to the hypersurface generation, while retaining an acceptable accuracy for the overall aerodynamic force model.

Since the formulation presented here is intended to extend the simulation domain beyond the linear regime, currently covered by the derivative formulation, into the non-linear regime, it is important to avoid ignoring discontinuities and generally the fine structure features of the reaction surface by oversimplifying the modelling,as this may result in an unacceptable loss of accuracy. Once the hypersurfaces are defined, simulations can be performed using existing main frame computers and software, and, if required, specialized simulation computers can also be used. Inasmuch as the present formulation can be viewed as a rather general form of an aerodynamic force model, it follows that in addition to being used as a simulation instrument, it can also serve to identify and verify more specific and restrictive models, which in itself can be of substantial value in non-linear flight regime applications.

2.3 History Dependent Reactions

The discussion has so far been based on the assumption that the reactions are only a function of the instantaneous position and rates. It is known that this is not always the case as, for example, in dynamic stall where motion past history also has an effect on the aerodynamic reactions. This effect can be visualized as leading to a "thickness" in the reaction surface which then would not uniquely define the reaction in terms of the instantaneous motion parameters. The thickness is, of course, a function of the severity of the history effects and can, in principle, be reduced by resolving the motion into additional components, specifically, higher order time derivatives such as $\dot{p}$, $\dot{q}$, $\dot{r}$ which would implicitly account for more of the motion immediate past history. Unfortunately, the benefits of such an approach have to be weighed against the concomitant increase in the required number of tests and data points referred to in the previous section, plus the inherent loss in the accuracy with which the higher derivatives can be obtained and the well-known diminishing return accrued by adding higher order terms in a Taylor's expansion. Therefore, no claim can be made that in practice this approach could account for "longer" past history effects.

3. WIND-TUNNEL TECHNIQUE

The previous sections described a proposed method for the topological representation of aerodynamic reactions in terms of the pertinent motion variables, based on the assumption that such a relationship can be largely experimentally determined. A wind-tunnel technique developed with this purpose in mind has been described in some detail (Ref. 8) and is thus only briefly summarized here for the sake of completeness.

3.1 Description

A well-defined, periodic motion is imparted to the model by means of a suitable drive mechanism. Although typically a sinusoidal motion in one degree of freedom (primary DOF) is used, the technique is quite general, permitting the application of an arbitrary periodic motion in any number of degrees of freedom. Moreover, as no assumption of aerodynamic linearity is implicit in the technique, the allowable amplitude of the motion is usually only limited by the mechanical hardware.

In the presence of aerodynamic non linearities, the airloads caused by the model motion contain a number of frequency components harmonically related to the fundamental frequency of the motion. Keeping in mind that the desired reaction hypersurface must be defined for the complete range of realistic deflections and reduced rates, the oscillatory tests must be performed at frequencies where a direct conversion from balance outputs (deflections) to their causative aerodynamic loads cannot generally be carried out. Rather, the loads must be determined from the balance outputs by accounting for the dynamic response of the model-balance subsystem, namely, by dividing the relevant frequency components of the balance outputs by the corresponding mechanical deflection-to-load transfer functions. This is, of course, only possible if the above

mechanical subsystem is linear, a reasonable assumption if proper care is exercised in the design and construction of the wind-tunnel apparatus.

Inertial effects are removed by means of tare measurements and the relationships between the instantaneous model position and balance outputs are obtained by taking the inverse Fourier transform of the spectra of these quantities. Even though a very large number of harmonics may be required to accurately describe any arbitrary reaction, a practical limitation on the number of meaningful harmonics is imposed by the model aeroelastic effects, sting vibration modes, etc. This frequency truncation results in a smoothing out of discontinuities and sharp contour changes in the reaction hypersurface. Although the smoothing may complicate somewhat the aerodynamic interpretation of the hypersurface, as it tends to mask the physical phenomena leading to discontinuities, its effect in a flight mechanics sense is considerably less pronounced by virtue of the inherent inertia-caused filtering characteristics of an aircraft. It is, in any case, desirable to maximize the number of usable frequencies by taking the above effects into account in the design of the equipment.

3.2 Data Handling

As mentioned in the previous section, the frequency components of the balance outputs harmonically related to the fundamental frequency of the primary motion are required to determine the desired airloads. Under typical wind-tunnel testing conditions, however, the balance outputs are significantly contaminated by noise caused by the flow unsteadiness, which must be largely eliminated in order to obtain acceptably accurate results. This is accomplished by computing the Fourier transform of the balance outputs - using an FFT algorithm - on records containing an exact number of periods of the primary oscillation, thereby ensuring that the components of interest coincide with some of the FFT spectral lines as required for this type of harmonic analysis (Ref. 15).

Although in each record the sampling is done synchronously with the primary motion, no attempt is made to ensure that the records always start at a given phase angle of this motion. Instead, upon completion of the FFT computation for a given record, all components are shifted by the time corresponding to the phase of the well-defined fundamental component of the primary motion, which thus automatically becomes the desired reference vector. The effect of noise is then reduced to an acceptable level by ensemble averaging the components so obtained from a number of records. The required number is obviously a function of the signal-to-noise ratio present, and must therefore be empirically assessed by the operator on the basis of the emerging results. These are presented in the form of cross plots between the primary position and each of the balance outputs obtained after taking the inverse Fourier transform of the corresponding spectra using an appropriate number of harmonics. This type of representation has been selected because it best provides an early indication of aerodynamic non linearities. The CRT display used by the operator is shown in Fig. 12 where six channels are presented in this format. The reactions can also be individually displayed in the time domain if desired.

The instrumentation system and signal processing software have been extensively tested, yielding very satisfactory results. An example of the signal extraction capability of the technique is shown in Figs. 13 to 16. A sinusoidal primary signal of 25 Hz (not shown) and a synchronous complex secondary signal (Fig. 13) were applied to the system. Records of 256 samples were taken with a sampling frequency of 1600 Hz. The signals, cross-plotted in Fig. 14, were obtained by taking the inverse Fourier transform of their fundamental and first nine harmonic components. Due to the absence of noise, only one record of data is required to obtain the cross plot. By contrast, when the secondary signal is contaminated with noise - as in the case shown in Fig. 15, where a post antialiasing filter S/N = -10 dB is present - more averaging time is required to obtain valid results.

Fig. (16a) to (16h) shows a sequence of the cross plots at the times indicated, for the noise contaminated signal. Since the plots are updated in real time they cannot be easily photographed. The sequence is therefore not a single one but rather one of the final ensemble averages for a series of independent sequences with an increasing number of records as shown. Clearly, if the random processes causing the noise are stationary, the two approaches are equivalent. The results indicate that for the signal-to-noise ratio under consideration -deemed to be representative of the rather severe conditions encountered in some wind-tunnel tests - the duration of a test must be approximately one minute in order to sufficiently reduce the effect of noise (compare, Fig. 16h with Fig. 14), which is satisfactory, especially in view of the substantial amount of data yielded by such a test.

The reader is reminded that the above cross plots represent the relationship between the primary position and a balance output, rather than the latter's causative airload, which must be obtained by following the procedure described in Section 3.1. Once this is done in the case of a motion in one DOF, however, a closed curve is defined on the reaction surface, corresponding to the trajectory of the motion in the phase plane. Fig. C4 shows one such trajectory as determined using both the linear data analysis (green), and the non-linear one with 10 frequency components (blue), the latter clearly yielding results that correspond much more closely to the correct trajectory (red).

The reaction surface shown in Figs. 1 and 4, but obtained by means of the non-

linear analysis - again on the basis of ten frequency components -is depicted in Fig. 17 where the edges of the actual surface have been outlined. The main features of the surface are readily discernible, although the smoothing effect imposed by the frequency truncation has the expected noticeable results for a surface with such marked discontinuities. In general, if the determination of a multi-dimensional hypersurface is required, the well-known model motion can be kinematically resolved into a suitable set of motion variables.

3.3 Wind-Tunnel Apparatus

The prototype of a hydraulically-driven oscillatory roll apparatus (Ref. 8) was built to verify the validity of the experimental technique described herein. Preliminary tests were carried out on a delta-wing conical-body model (Fig. 18) at α = 30° and M = 0.7. A sinusoidal oscillation with an amplitude of 15° - corresponding to the maximum allowed by the apparatus - and a frequency of 15 Hz was imparted to the model. Since at the time of the testing the instrumentation system and software were not yet available, a laboratory spectrum analyzer was used to establish whether the rolling moment did exhibit some harmonic content as expected.

Table I shows the relevant frequency components of the balance roll output. The figures correspond to the difference between wind-on and tare conditions and are obtained from the power spectral density functions determined by the analyzer, and thus do not include the phase information needed to reconstruct the waveform. No corrections were made to account for inertial effects due to possible changes in the primary waveform between tare and wind-on conditions, which are likely quite small due to the inexorable nature of the drive mechanism. Moreover, no corrections were made for the dynamic response of the system that could, indeed, have had a large impact on the results. In any case, the results clearly indicate the presence of harmonics in the rolling moment, thus confirming the expectation of non-linear effects under the above test conditions.

Unfortunately, mechanical problems with the prototype rig arose during testing, which resulted in the need for considerable redesign. At the same time it became apparent that a larger oscillation amplitude capability would be desirable, leading to a completely new design that incorporates all the needed specifications including a maximum oscillation amplitude of $\pm$40°. The construction of this apparatus is expected to commence soon, together with the implementation of some modifications on the existing dynamic calibrator (Ref. 16), to enable it to apply the non-linear loads needed to calibrate the new equipment.

4. CONCLUSIONS

In recognition to the limitations in the applicability of the locally linearized aerodynamic force models to high angle-of-attack and to non-linear flight regimes generally, a new representation for the aerodynamic reactions in terms of the motion variables has been proposed. This representation relies on the availability of experimental data relating the instantaneous value of the reactions to the corresponding values of the pertinent motion variables. A wind-tunnel technique specifically developed to obtain these data has also been briefly described.

Some of the more salient features of the new representation are:

- no assumptions on linearity are required, thereby rendering the representation applicable to non-linear flight regimes,
- flight mechanics simulation can, in principle, be performed once the aerodynamic data base is available,
- a large number of dynamic wind tunnel tests are needed to obtain the data base, however, the efficiency of the proposed wind-tunnel technique reduces this number considerably,
- the "fine-structure" information yielded by this representation can be very useful for the interpretation of aerodynamic phenomena,
- the representation can be used to identify and verify specific aerodynamic force models,
- although capable of handling "recent" motion history effects, the formulation cannot be used to account for "long past" effects.

ACKNOWLEDGEMENTS

The author is most grateful to S. Jenkins for developing the extensive software required for this work.

REFERENCES

1. M. Tobak, L. Schiff "Aerodynamic mathematical modeling-basic concepts" AGARD LS-114, 1981.

2. K.J. Orlik-Rückemann "Aerodynamic aspects of aircraft dynamics at high angles of attack" J. of Aircraft, 20, 9, September 1983.

3. P. Guicheteau "Application de la theorie des bifurcations a l'etude des pertes de controle sur avion de combat" AGARD FMP Symposium on Combat Aircraft Manoeuvrability, AGARD CP 319, October 1981.

4. J.V. Carroll, R.K. Mehta "Bifurcation analysis of nonlinear aircraft dynamics" J. of Guidance, Control and Dynamics, 5, 5, September-October 1982.

5. W.H. Hui, M. Tobak "Bifurcation analysis of aircraft pitching motions about large mean angles of attack" J. of Guidance, Control and Dynamics, 7, 1, January-February 1984.

6. M. Tobak, G.T. Chapman, L. Schiff "Mathematical modelling of the aerodynamic characteristics in flight dynamics" NASA TM85880, 1984.

7. G.T. Chapman, M. Tobak "Nonlinear problems in flight dynamics" NASA TM85940, May 1984.

8. E.S. Hanff "Determination of non-linear loads on oscillating models in wind tunnels" IEEE 10th International Congress on Instrumentation in Aerospace Simulation Facilities, September 1983.

9. J. Kalviste "Use of rotary balance and forced oscillation test data in a six degree of freedom simulation" AIAA 9th Atmospheric Flight Mechanics Conference, AIAA 82-1364, August 1982.

10. S.B. Grafton, E.L. Anglin "Dynamic stability derivatives at angles of attack from -5° to 90° for a variable sweep fighter configuration with twin vertical tails" NASA TN D-6909, October 1972.

11. J.R. Chambers, W.P. Gilbert, L.T. Nguyen "Results of piloted simulator studies of fighter aircraft at high angles of attack" AGARD FDP Symposium on Dynamic Stability Parameters, AGARD CP-235, May 1978.

12. E.S. Hanff "Non-linear representation of aerodynamics of wing rock of slender delta wing" Submitted for presentation at the AIAA 12th Atmospheric Flight Mechanics Conference, August 1985.

13. L.T. Nguyen, L. Yip, J.R. Chambers "Self-induced wing rock of slender delta wings" AIAA Atmospheric Flight Mechanics Conferece, AIAA-81-1883, August 1981.

14. M.E. Beyers "Characteristic motions for simulation of post-stall manoeuvres and flight instabilities" AeSSA/SAIAeE Journal, Aeronautical Society of South Africa, 5, 1, 1984.

15. E.O. Brigham "The Fast Fourier Transform" Prentice Hall, 1974.

16. E.S. Hanff "Direct forced oscillation techniques for the determination of stability derivatives in wind tunnels" AGARD FDP LS-114, 1981.

TABLE I. Harmonic content of the rolling moment balance output. (f_{osc} = 15 Hz)

Freq (Hz)	Volts
15	-3.1
30	2.3
45	0.6
60	0.9
75	0.4
90	0

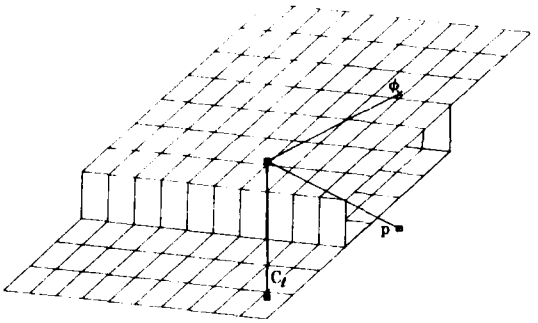

FIG. 2 Schematic "static" hysteretical reaction surface (minor loops not permitted).

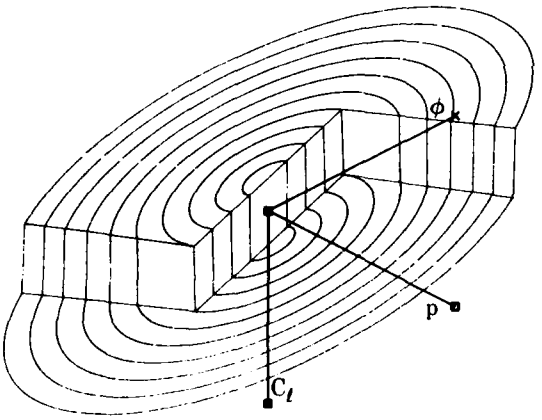

FIG. 4 Definition of reaction surface by means of oscillatory tests.

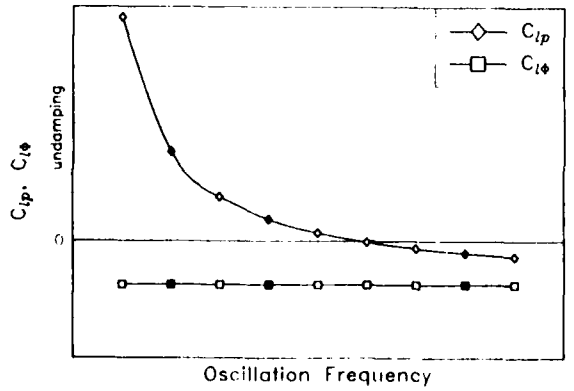

FIG. 6 Frequency effect on stability derivatives (see Fig. C3).

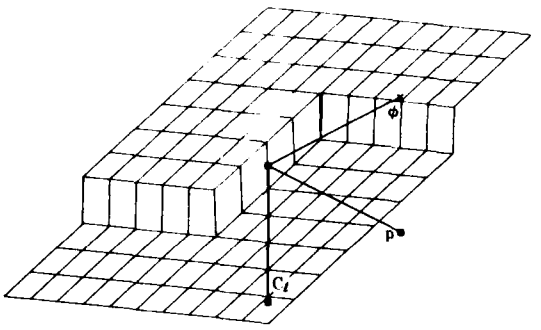

FIG. 1 Schematic "static" hysteretical reaction surface (minor loops permitted)

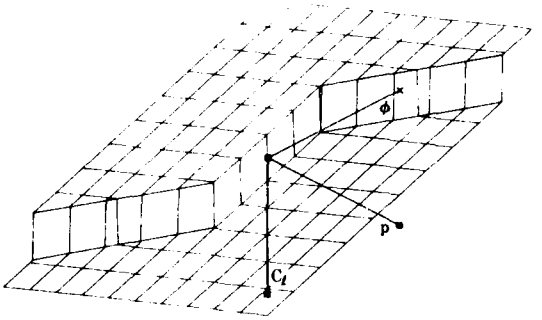

FIG. 3 Schematic "dynamic" hysteretical reaction surface.

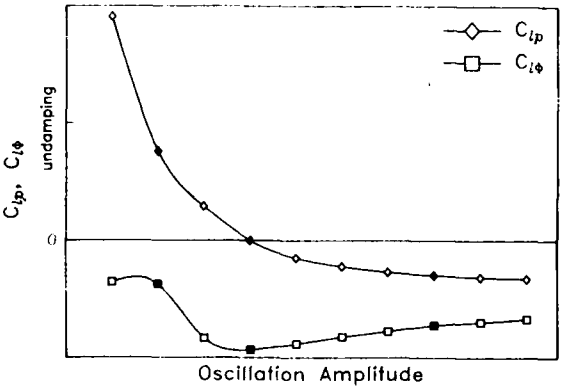

FIG. 5 Amplitude effect on stability derivatives (see Fig. C2).

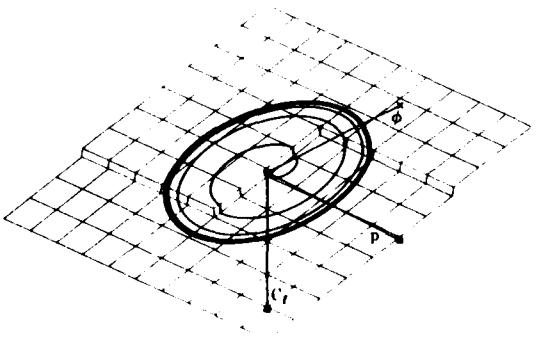

FIG. 7 Trajectory of "load point" in simulation.

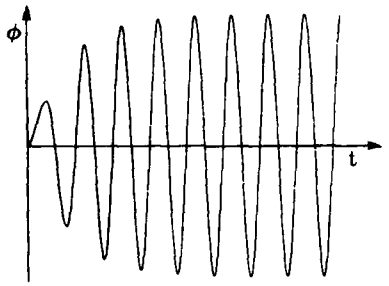

FIG. 8. Roll angle history

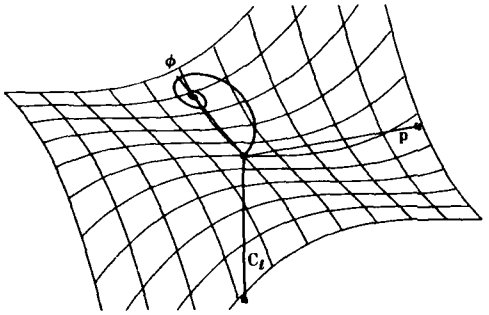

FIG. 10 *Simulation in the presence of* attractor

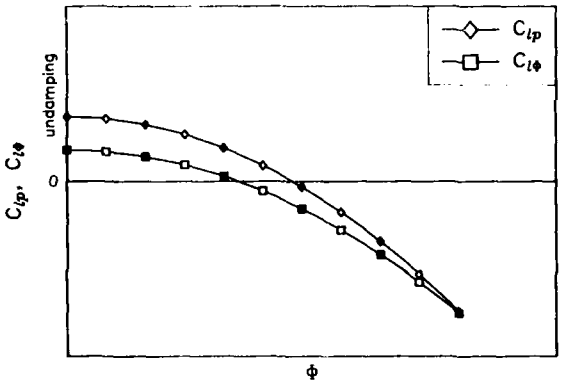

FIG. 11 Stability derivatives vs. roll angle.

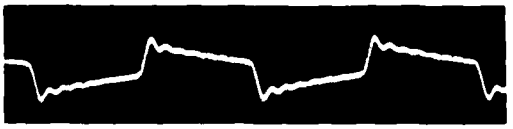

FIG. 13 Complex secondary waveform (no noise).

FIG. 14 Cross plot of primary and secondary signals.

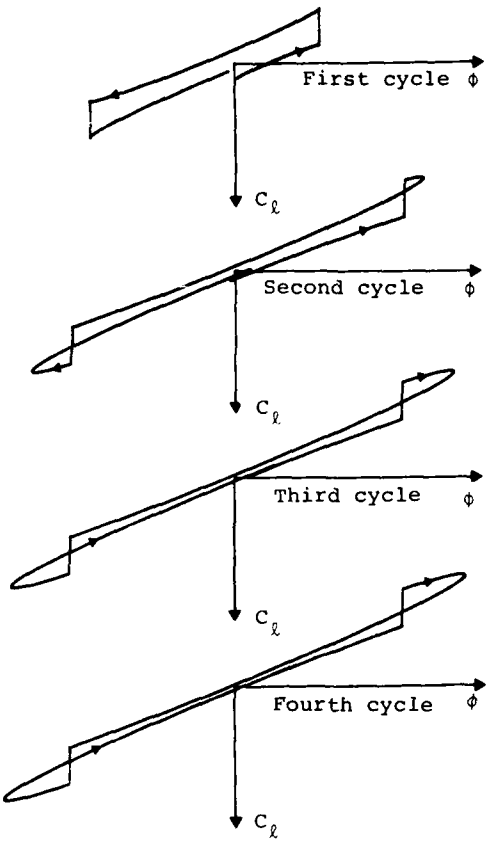

FIG. 9 Energy exchange in simulation

FIG. 12 View of operator's display.

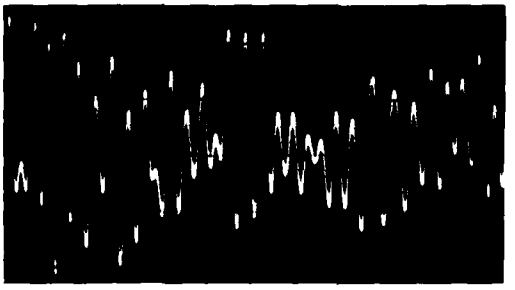

FIG. 15 Noise-contaminated secondary signal.

a) 2 records, .32 sec.

e) 32 records, 5.12 sec.

b) 4 records, .64 sec.

f) 64 records, 10.24 sec.

c) 8 records, 1.28 sec.

g) 128 records, 20.48 sec.

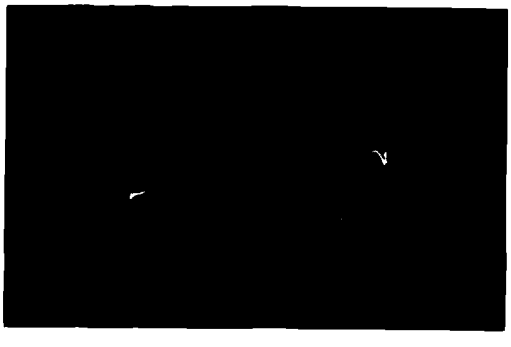

d) 16 records, 2.56 sec.

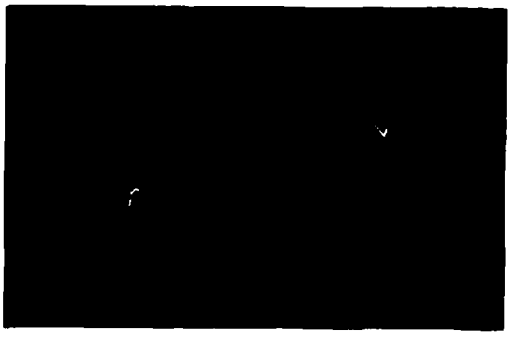

h) 256 records, 40.96 sec.

FIG. 16 Primary vs. secondary signal plots in the presence of noise. Ensemble averages at number of records and times indicated

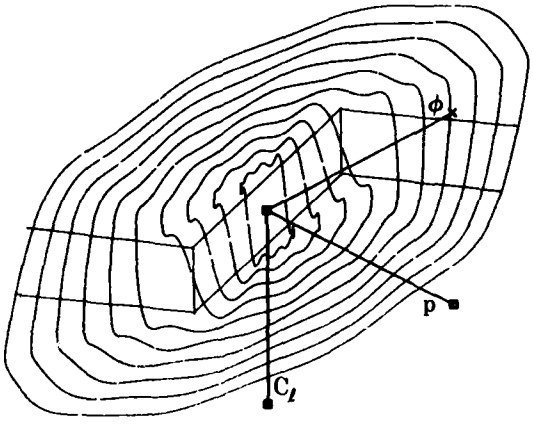

FIG. 17 Reaction surface as defined by non-linear analysis.

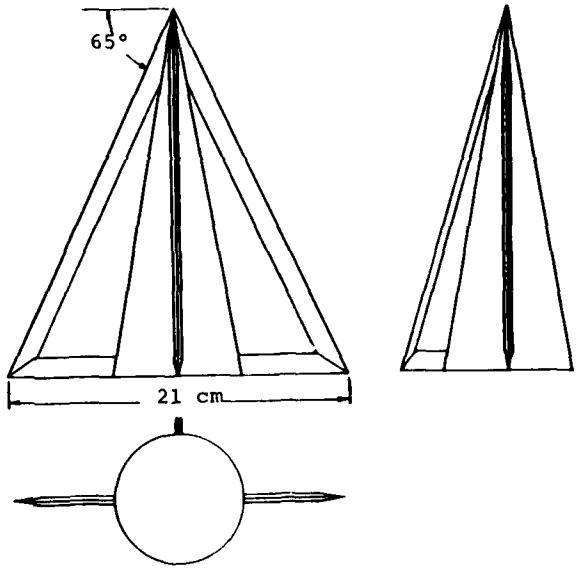

FIG. 18 Schematic of cone-wing-fin model.

Figs. C1-C4 are shown on the following pages.

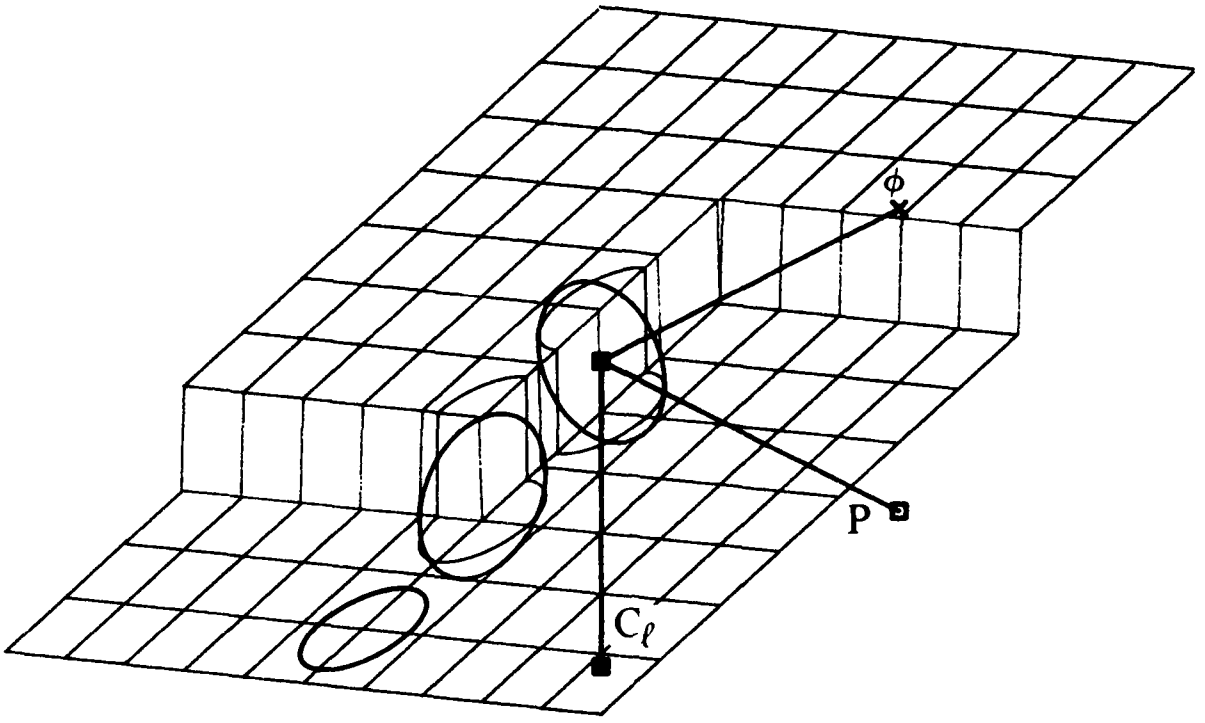

FIG. C1 Load point trajectories for small amplitude tests
(red: actual, green: linear approximation)

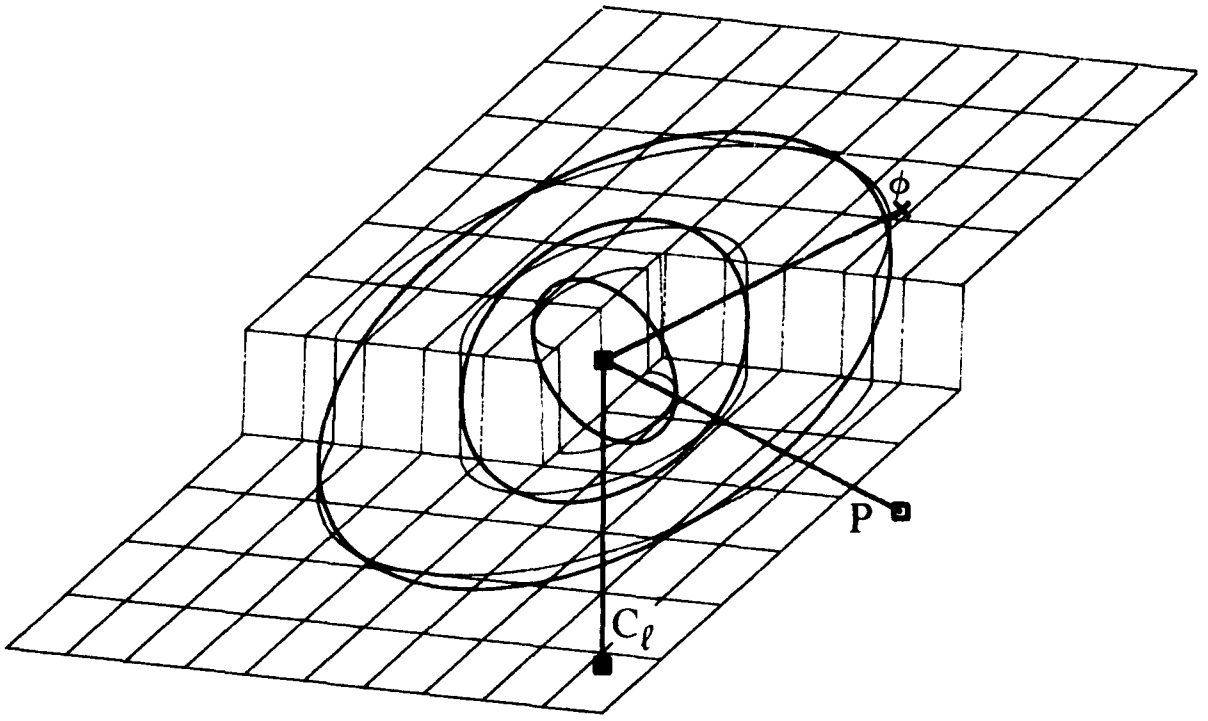

FIG. C2 Load point trajectories for different oscillation amplitudes
(red: actual, green: linear approximation)

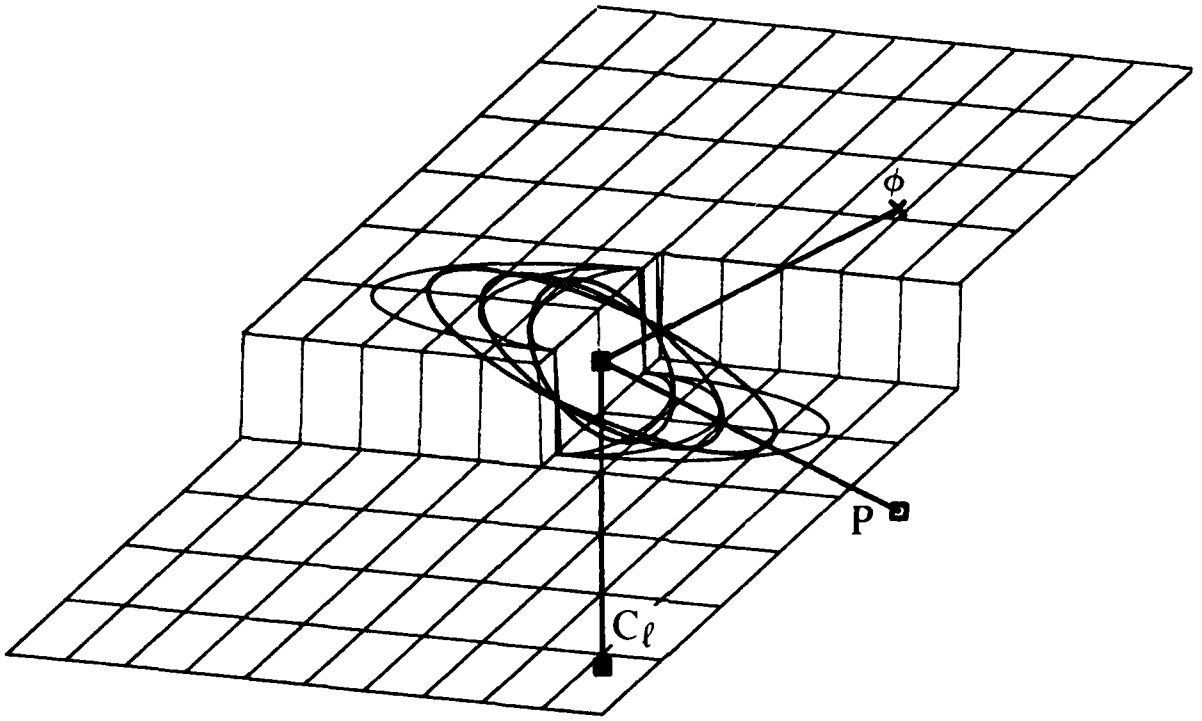

FIG. C3 Load point trajectories for different oscillation frequencies (red: actual, green: linear approximation)

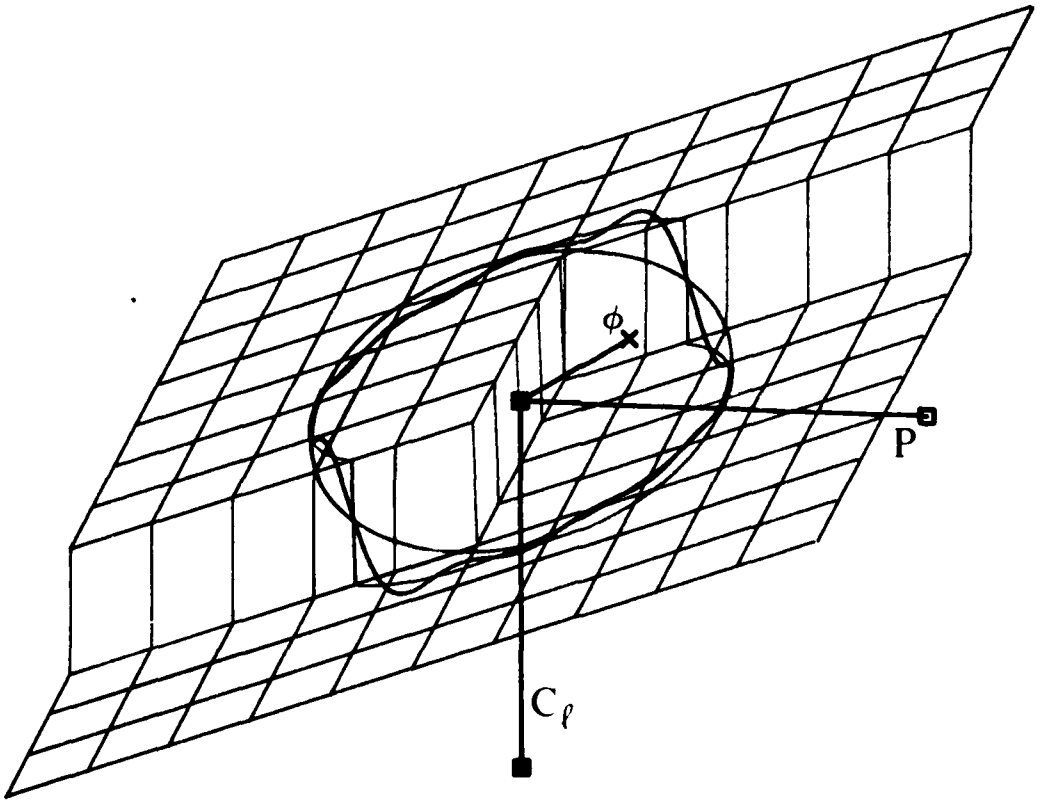

FIG. C4 Load point trajectories for sinusoidal oscillation (red: actual, blue: non linear (10 freqs.), green: linear)

RECENT EXPERIENCES OF UNSTEADY AERODYNAMIC EFFECTS ON AIRCRAFT FLIGHT DYNAMICS AT HIGH ANGLE OF ATTACK

by
Luat T. Nguyen, Raymond D. Whipple, and Jay M. Brandon
NASA Langley Research Center
Mail Stop 355
Hampton, Virginia 23665

SUMMARY

This paper highlights recent research conducted at the NASA Langley Research Center on two high angle-of-attack flight dynamic phenomena which are dominated by unsteady aerodynamic effects: wing rock and tumbling. Studies of wing rock induced by strong vortical flows and tumbling characteristics observed on an advanced configuration are reviewed. Results of wind tunnel experiments are summarized and the aerodynamic mechanisms involved in the phenomena are discussed.

SYMBOLS

b	wing span, ft
$\bar{c}$	mean aerodynamic chord, ft
C_L	lift coefficient
C_ℓ	rolling-moment coefficient
C_{ℓ_p}	$\frac{\partial C_\ell}{\partial \frac{pb}{2V}}$
$\bar{C}_{\ell_p} = C_{\ell_p} + C_{\ell_{\dot\beta}} \sin\alpha$	roll damping parameter obtained in forced oscillation tests
C_{ℓ_β}	$\frac{\partial C_\ell}{\partial \beta}$
C_m	pitching-moment coefficient
C_{m_α}	$\frac{\partial C_m}{\partial \alpha}$
C_{m_q}	$\frac{\partial C_m}{\partial \frac{q\bar{c}}{2V}}$
$\bar{C}_{m_q} = C_{m_q} + C_{m_{\dot\alpha}}$	pitch damping parameter obtained in forced oscillation tests
G_x	longitudinal acceleration, g
G_z	normal acceleration, g
I_x	roll moment of inertia, slug-ft^2
I_y	pitch moment of inertia, slug-ft^2
k	reduced frequency
P	period, sec
p	roll rate, rad/sec or deg/sec
q	pitch rate, rad/sec or deg/sec
$\bar{q}$	free stream dynamic pressure, lb/ft^2
S	reference area, ft^2
V	free stream velocity, ft/sec
α	angle of attack, deg
α_o	angle of attack at zero roll angle, deg
β	angle of sideslip, deg
β_o	angle of sideslip at zero roll angle, deg
δ_c	canard deflection, deg
δ_s	strake flap deflection, deg
ϕ	roll angle, deg

INTRODUCTION

Modern air combat requires the ability to maneuver effectively at high angle of attack flight conditions. To exploit this flight regime, today's fighters incorporate numerous high angle of attack design features including slender forebodies, wing-body strakes, optimized empennage configurations, and control systems which not only prevent departures and spins, but also enhance maneuvering throughout the angle-of-attack range. Recent advances in air-to-air missile capabilities have not decreased the fighter airplane's requirements for maneuverability. In fact, all-aspect "point and shoot" missiles dictate the need for rapid, transient maneuvers at high angles of attack, including brief excursions into post stall conditions. As a result of this shift in emphasis towards transient maneuvering and agility, unsteady aerodynamics will play an increasingly important role in aircraft high-α flight dynamics. Whereas today's fighters were designed primarily on static aerodynamics considerations (C_{n_β}, C_{ℓ_β}, $C_{n_{\beta_{dyn}}}$, etc), tomorrow's fighters will also require design technology that addresses unsteady aerodynamic effects at high angles of attack. Understanding, controlling, and exploiting these unsteady effects will enable achievement of the goal of aggressive use of high angle of attack maneuvering for maximum air combat effectiveness.

This paper will summarize recent research conducted at the NASA Langley Research Center on two high angle of attack flight dynamic phenomena which are dominated by unsteady aerodynamic effects: wing rock and tumbling. Wing rock is an undamped oscillation primarily in the roll axis that is exhibited by many modern combat aircraft.[1] Wing rock causes maneuver limitations ranging in severity from degradation in tracking effectiveness to loss of control. Currently, development of aerodynamic and control system techniques to alleviate this problem is constrained by the limited understanding of the basic aerodynamic mechanisms which cause the phenomenon. To address this problem, NASA Langley is conducting a research investigation aimed at providing fundamental information on the aerodynamics associated with wing rock at subsonic speeds. A number of different aircraft configurations and isolated wings known to exhibit wing rock in flight are being subjected to a series of unique wind-tunnel tests particularly suited for exploring the phenomenon. The present paper will review the results of investigations of wing rock caused by strong vortex flows: wing rock of highly-swept configurations, and slender forebody induced wing rock.

The second topic to be discussed is tumbling, which is a sustained autorotative pitching motion. Although most current fighters are not susceptible to this dangerous phenomenon, present design trends emphasizing high levels of relaxed stability, and incorporating features such as tailless configurations and canard controls, may lead to more tumble-prone designs. In addition, the desire for very high pitch rate capability for transient maneuvering will further increase the likelihood that tumbling will become a flight mechanics concern for future fighters. An advanced configuration that has exhibited tumbling in sub-scale dynamic model tests is the X-29A Forward-Swept Wing Demonstrator airplane. The present paper will highlight some preliminary experimental and analytical results from the studies conducted at Langley on this configuration.

WING ROCK

Slender Delta Wings: The wing rock susceptibility of delta wings with leading-edge sweep greater than 76° is well known. One of the earliest observations of this characteristic was made by McKinney and Drake during free-flight model tests conducted in 1947.[2] since then, numerous other investigations of the delta wing wing-rock phenomenon have been made and reported in the literature (references 3 to 5, for example). However, only recently has a clearer understanding of the fundamental flow mechanisms that cause wing rock for this class of configurations been established. Systematic low-speed wind tunnel experiments were conducted at Langley on a flat-plate delta wing of 80° leading-edge sweep.[6] The wing was constructed of wood and had a beveled sharp leading-edge (figure 1). The wing was subjected to conventional static-force tests and dynamic wind-tunnel experiments which included forced-oscillation, rotary, and free-to-roll tests. In addition, visualization of the flow phenomena involved was obtained by observing tuft patterns and using a helium-bubble technique.

The primary wind-tunnel test technique used to study the wing rock phenomenon of the subject configuration was the free-to-roll tests. In these tests, the model was sting-mounted on an apparatus (figure 2) consisting of two concentric cylindrical barrels attached by ball bearing assemblies which allowed the model to rotate freely about its roll axis with no angular limitation. A potentiometer provided continuous information of model roll angle, ϕ, which was then digitized and stored in a mini computer at 136 samples per second. From this data, estimates of roll rate, $\dot{\phi}(t_1)$, and roll acceleration, $\ddot{\phi}(t_1)$, were derived by fitting a smoothing cubic spline to the $\phi_{(t_1)}$ data points. An estimate of the total aerodynamic rolling moment coefficient acting on the model during the motions was then obtained from the relationship:

$$C_{\ell_{aero}}(t_1) = \frac{I_x \ddot{\phi}(t_1)}{\bar{q}Sb}$$

The free-to-roll tests were conducted in the Langley 12-Foot Low-Speed Wind tunnel at a dynamic pressure of 1.1 lb/ft^2.

During these tests, the model did not begin to wing rock until angle of attack was increased above 25°. For $\alpha > 25°$, the model began to wing rock even without any external disturbance beyond the inherent turbulence of the tunnel flow. This characteristic is illustrated in figure 3 which presents a time history of the roll angle of the model showing a buildup of the wing rock to the limit-cycle condition. The data were obtained by increasing angle of attack from 20°, where the model did not wing rock, to 27° and holding at that incidence to allow the wing rock to establish itself. It is seen that the wing rock buildup was not an abrupt phenomenon; on the contrary, the buildup to the limit-cycle condition ($-33° < \phi < 36°$) occurred fairly gradually over about 10 to 15 oscillation cycles. It was also found that the model always reached this same limit-cycle condition independent of initial disturbance or roll angle. Shown in figure 4 is a phase plane plot ($\dot{\phi}$ versus ϕ) of a buildup to and a number of cycles of the equilibrium wing rock condition. The steady, gradual buildup of the oscillation is reflected in the smooth outward spiral of the plot. Note also the repeatability of the steady state motions from one cycle to the next. These characteristics are very typical of a classic limit cycle. Table I summarizes the wing-rock characteristics in terms of the limit-cycle amplitude $(\Delta\phi)_{WR}$, period, P_{WR}, and averaged reduced frequency, k_{WR}. The data show that once the limit cycle appeared above $\alpha = 25°$, it persisted to much higher angles of attack.

The variations of the measured lift and pitching-moment coefficients with angle of attack are presented in figure 5. The data show that maximum lift occurred at $\alpha = 36°$

and that the configuration exhibited pitch up in this region. Flow visualization using a helium-bubble technique verified that vortex breakdown reached the wing trailing edge at $\alpha = 36°$ and was the cause of these characteristics. Since the model was observed to exhibit wing rock for angles of attack as low as $\alpha = 25°$, vortex breakdown was apparently not a factor in inducing the wing rock.

The effect of sideslip on vortex flow patterns at $\alpha = 28°$ and 40° are shown in figures 6 to 8. Two basic flow characteristics were observed with the wing sideslipped at high angles of attack: (1) vortex bursting on the windward side that progressed toward the wing leading edge as the angle of sideslip was increased (shown in figure 7); and (2) the leeward vortex core being displaced above the wing (shown in figure 8). With regard to the first effect, it is interesting to note that the photographs in figure 6 show that at $\alpha = 28°$, which is above the angle of attack for wing rock onset, breakdown of the windward vortex does not appear to have reached the wing trailing edge even at the large sideslip angles shown. Thus, vortex bursting over the wing is not a wing-rock inducing mechanism in this case. On the other hand, the displacement of the leeward vortex with sideslip is certainly occurring even at the lowest angles of attack where wing rock was observed.

Figure 9 shows a summary plot of the lateral stability derivative, C_{ℓ_β}, versus α obtained by sloping the rolling-moment data measured at $\beta = \pm 4°$. The very high levels of lateral stability for $\alpha > 20°$ are due in large part to the displacement of the leeward vortex under sideslip as discussed above. This high level of C_{ℓ_β} in the wing rock angle-of-attack range provides a stiff "restoring spring" effect during the limit cycle wing rock oscillations observed in the free-to-roll tests.

As discussed earlier, analysis of the motions obtained in the free-to-roll tests were made by operating on the measured roll angle data to obtain estimates of α, β, $\dot{\phi}$, and the total aerodynamic rolling moment coefficient, $C_{\ell_{aero}}$. Having $C_{\ell_{aero}}$ was particularly valuable in that it permitted examination of the aerodynamics during actual wing-rock conditions. Plotted in figure 10 are time histories of ϕ, α, β, $\dot{\phi}$, and $C_{\ell_{aero}}$ for one cycle of the limit-cycle wing rock at $\alpha = 27°$ presented in figure 3. The data show that angle of attack varied between 23° and 27° while sideslip peaked at about ±15°. Cross plots of $C_{\ell_{aero}}$ versus ϕ and β with the arrows indicating increasing time are shown in figure 11. Based on energy exchange considerations, it can be shown that aerodynamic energy is added to the model ($\Delta E>0$, destabilizing) for clockwise loops in the $C_{\ell_{aero}}$ versus ϕ cross plot, whereas energy is extracted from the model ($\Delta E<0$, stabilizing) for counter-clockwise loops[6]. Figure 11 shows that a large clockwise or destabilizing loop exists for roll angle magnitudes less than about 18° whereas smaller counter clockwise or stabilizing loops exist at larger roll angles. Because sideslip is directly related to roll angle, it is possible to apply the same energy exchange concepts to the $C_{\ell_{aero}}$ versus β cross plot. Thus, figure 11 shows that negative damping ($\Delta E>0$) is exhibited for sideslip magnitudes less than about 8° while positive damping ($\Delta E<0$) occurs at larger sideslips. These results suggest that the wing rock exhibited by the test configuration is caused by the variation of roll damping with sideslip magnitude such that unstable damping exists at lower $|\beta|$'s whereas stable damping exists at larger $|\beta|$'s with the crossover occurring near $|\beta| = 8°$. If this hypothesis is true, then the model should not exhibit wing rock in the free-to-roll tests if they are conducted at sufficiently large sideslip angles. Tests at sideslip were conducted by introducing a lateral c.g. offset by adding mass to the windward side of the wing. The gravity-induced rolling moment negated the aerodynamic rolling moment thus providing a "statically balanced" condition at the particular sideslip angle. The results of these tests were that when the model was sideslipped to angles greater than about 8°, it did not wing rock. Figure 12 illustrates the results obtained at $\beta = 10°$. At $t = 0$, the model was set at $\phi = 20°$ and released, and as shown by the time history, the motion damped out after a number of cycles.

Further evidence of the roll damping variation with sideslip was obtained in the forced-oscillation tests conducted in the Langley 30- by 60-Foot Wind Tunnel in the manner described in reference 7. Data were obtained at reduced frequencies of $k = .09$, and .16 for an oscillation amplitude of ±5° at a dynamic pressure of 2 lb/ft^2. Measurements at various sideslips were obtained by oscillating the model about mean roll angles of $\bar{\phi} = 0$, 10°, 20°, and 30°. The results for $k = .16$ which is close to the wing rock frequencies of the free-to-roll tests are shown in figure 13. The zero sideslip data ($\bar{\phi} = 0$) indicate stable roll damping at low angles of attack followed by loss in roll damping beginning at moderate angles of attack such that unstable values of $\bar{C}_{\ell_p}$ are exhibited for $\alpha > 19°$. The results of figure 13 also show a significant effect of mean roll angle, $\bar{\phi}$, for angles of attack above 15°. Between 15° and 35°, the measured roll damping values become significantly more stable with increasing $\bar{\phi}$. For example, at $\alpha_o = 27°$, the data show that $\bar{C}_{\ell_p}$ transitions between unstable and stable characteristics somewhere between 10° and 20° of roll angle. This result is in good agreement with the free-to-roll data discussed earlier which indicated crossover at about 18° of roll angle. Converting $\bar{\phi}$ to β allows plotting of the roll damping results versus sideslip magnitude as presented in figure 14 for $\alpha_o = 25°$ and 30°. The data show that at the angles of attack observed for wing rock onset ($\alpha_o > 25°$), the roll damping does in fact vary significantly with sideslip magnitude. The damping is highly unstable for small sideslips and highly stable for large sideslip with the crossover occurring near 6.4°. Again, the results correlate well with the free-to-roll analysis which indicated crossover at about 8° of sideslip.

rock exhibited by the missile at $\alpha = 27°$. Analysis of one of the cycles in the form of a cross plot of $C_{\ell_{aero}}$ vs β is shown in figure 20. As in the case of the delta wing discussed earlier, the results indicate unstable roll damping at lower sideslip and stable damping at higher sideslips with the crossover occurring near $|\beta| = 7°$.

Flow visualization using a helium bubble technique was used to observe the vortices during actual wing rock conditions. Again, the primary mechanism noted was the alternating "lifting-off" and reattachment of the leading-edge vortices during each oscillation cycle. Thus, it is concluded that the same fundamental vortex interaction mechanisms which cause wing rock on slender delta wings are also responsible for the phenomenon exhibited by the missile. It is interesting to note that the blunt sides of the missile body (as contrasted with the sharp leading edge of the delta wing) did not apparently have a significant effect on the wing rock inducing mechanisms.

The effect of the wings and tails were investigated by conducting body alone tests. The free-to-roll results for this configuration are summarized in Table III. Comparison of these results to those for the complete configuration (Table II) indicates that the wing and tails provide a positive damping component through most of the angle-of-attack range. At any given angle of attack above 20°, the body alone wing rock amplitude is significantly larger than that for the complete configuration. In fact, in the $32° < \alpha < 42°$ range, the wing rock diverged beyond 90° amplitude into a continuous 360° rotation in one direction.

Slender forebody induced wing rock.- Numerous studies have been conducted on the vortices shed from slender fuselage forebodies at high angles of attack and their effect on static stability characteristics of fighter aircraft (references 11-13, for example). Researchers have shown that the forebody flow separation and vortex flow field can become asymmetric and produce significant side force. Furthermore it has been noted that this vortex asymmetry is similar to that exhibited by slender wings such as the 80° delta discussed earlier.[14] In addition to the forces directly induced by the vortices on the forebody, studies have also indicated significant interaction of these vortices with other components of the airplane such as the wing and empennage. This interaction is illustrated by the water-tunnel flow visualization photograph shown in figure 21.

In view of the potentially large effect of slender forebody flow on static aerodynamics of fighter aircraft at high angles of attack, it would be expected that there may be a significant effect on airplane aerodynamic characteristics under oscillatory conditions as well. In particular, intuitive extensions of the wing rock results for the delta wing and missile discussed earlier suggest that the vortex shed by slender forebodies could also strongly influence overall roll damping of an airplane at high angles of attack. This phenomenon was first observed some years ago in low-speed wind-tunnel tests of a fighter model based on the F-5 configuration.[11] In order to examine wing planform effects on these characteristics, the model was tested with three wings: the basic F-5 wing, a swept wing, and a delta wing (figure 22). Comparison of static data for the three configurations showed that the wing had a secondary effect on the departure/spin resistance of the configuration and that it was the slender forebody with a flat elliptical cross-section that provided the very high levels of static directional stability exhibited by the configuration at high angles of attack. Roll damping data were also obtained from low-speed forced-oscillation tests and the results are summarized in figure 23. Plotted are the variations of the roll damping parameter, $\bar{C}_{\ell_p}$, versus angle of attack for the three configurations tested. The data for the basic configuration show highly unstable roll damping characteristics for $30° < \alpha < 42°$ indicating susceptibility to wing rock. It is interesting to note that the full-scale F-5 airplane exhibits large amplitude wing rock in this angle-of-attack range. The results for the other two configurations, the swept wing and the delta wing, also show highly unstable roll damping in the same angle-of-attack range. Because of the markedly different wing planforms, these results suggest that the wing is not responsible for the unstable roll damping above $\alpha = 30°$. Further evidence was recently obtained during tests of a model of the X-29A Forward Swept Wing Demonstrator airplane.[15] This configuration incorporates the exact fuselage forebody of the F-5 but is radically different from it in almost every other aspect. Forced oscillation data measured for the X-29A showed the same high level of unstable roll damping in the 30° to 45° angle-of-attack range. The fact that all four configurations exhibit this highly unstable roll damping characteristic, combined with the fact that the only common configuration feature between the four is the forebody strongly suggests that the forebody is the basic cause of the unstable damping.

Roll forced oscillation data were measured on the basic F-5 model at three oscillation frequencies, $k = .08, .12$, and $.16$ at three oscillation amplitudes, $\Delta\phi = \pm5°$, $\pm10°$, $\pm20°$. The effects of oscillation frequency and amplitude on the roll damping of the configuration are illustrated in figure 24. The first plot presents data measured at the three frequencies with $\Delta\phi = \pm10°$. Up to $\alpha = 25°$, the results show essentially no frequency effect. However, in the angle-of-attack range of the instability, a significant and consistent frequency effect is apparent in which increasing frequency reduces the instability level. The second plot presents data measured at the three oscillation amplitudes with $k = .12$. As with the frequency results, the data indicate no amplitude effect up to $\alpha = 25°$. Again, however, in the 30° to 40° angle-of-attack range the data show a very strong dependence of roll damping on oscillation amplitude such that increasing the amplitude significantly improves the roll damping. For example, at $\alpha = 35°$, the roll damping transitions between unstable and stable damping at an oscillation amplitude somewhere between 10° and 20°. It is easy to imagine how this variation of damping from highly unstable values at small amplitudes to highly stable values at large

amplitudes could result in a susceptibility to limit cycle wing rock which the airplane is known to exhibit in this angle-of-attack range.

Further investigations of the wing rock of the F-5 model were conducted using the free-to-roll test technique described earlier. It was found that the basic configuration exhibits large amplitude wing rock ($\Delta\phi > \pm 20°$) in the 30° to 40° angle-of-attack range, as predicted by the forced oscillation results. In an attempt to isolate the component responsible for the wing rock, tests were also conducted with the wing and vertical tail removed from the model. With just the wing removed, the model still exhibited the wing rock, thus verifying that the wing does not provide the driving mechanism for this phenomenon. Removal of the vertical tail alone also did not significantly alter the wing rock characteristics which further supports the hypothesis that the forebody is responsible for the wing rock inducing mechanism. With both the wing and vertical tail removed, no roll oscillations were observed. This result indicates that the interaction of the forebody flow with the wing and empennage may also play an important role in causing the wing rock. Currently, however, understanding of the very complex flow mechanisms involved in the forebody-induced wing rock phenomenon remains very limited.

To provide a systematic data base for further analysis of the phenomenon static and dynamic wind-tunnel experiments are currently being conducted at Langley on a generic fighter model with variable geometry flexibility. The model consists of a very simple cylindrical fuselage on which can be mounted a number of different wings, forebodies, and tails. Figure 25 and 26 show photographs of the wings and forebodies that can be fitted to the model.

A preliminary series of tests utilizing this model is underway to investigate the effect of forebody cross-sectional shape on high angle of attack static and dynamic stability characteristics. For these experiments, the model is configured with the trapezoidal wing with 26° leading-edge sweep and conventional horizontal and vertical tail arrangements. Four forebodies with the same fineness ratio (3.9) but different cross-sectional shapes (circular, vertical ellipse, horizontal ellipse, and triangular) are being tested. A drawing of the model is shown in figure 27 and a photograph of the model incorporating the horizontal ellipse forebody is shown in figure 28. Static, forced-oscillation, free-to-roll, and flow-visualization tests are being conducted in several low-speed wind-tunnel facilities and analysis of the data is just getting underway. This paper will, therefore, only highlight some of the preliminary results obtained to date.

Static directional stability, C_{n_β}, for the four configurations is summarized in figure 29. At high angles of attack, C_{n_β} varies considerably with cross sectional shape, with values ranging from highly unstable for the vertical ellipse nose to highly stable for the horizontal ellipse and triangular noses. These results are consistent with data obtained in numerous earlier investigations.

Static lateral stability, C_{ℓ_β}, for the four configurations is summarized in figure 30. The data show that forebody cross-sectional shape also has a dramatic influence on C_{ℓ_β} at high angles of attack. Again, the vertical ellipse nose has the least favorable effect while the horizontal ellipse and the triangular noses have the most favorable effects. The large impact of nose geometry on lateral stability indicates a strong interaction of the vortices shed from the slender forebody with the wing and horizontal tail flow fields. Note that this interaction is largest in the 20° to 40° angle-of-attack range. Above 40°, C_{ℓ_β} does not vary significantly with nose shape which suggests that the forebody/wing/tail flow fields are no longer strongly coupled.

Free-to-roll results for the four configurations are summarized in figure 31 in terms of observed wing rock amplitude versus angle of attack. The data show a significant effect of forebody geometry on wing rock susceptibility in the 25° to 42° angle-of-attack range. The configuration incorporating the vertical ellipse nose was the most resistant to wing rock, exhibiting only irregular, small amplitude oscillations. The circular nose configuration was a little more prone to wing rock, particularly in the 30° to 35° angle-of-attack range where the oscillation amplitude reached about 10°. The configurations with the horizontal ellipse and triangular forebodies, on the other hand, were found to be highly susceptible to wing rock particularly in the 30° to 35° angle-of-attack range where oscillation amplitudes as high as 30° were observed. It is interesting to note the geometric similarity of the horizontal ellipse nose to that of the F-5 model discussed earlier and the corresponding similarity in the wing rock characteristics of the two configurations. Furthermore, the importance of flow interaction between the forebody, wing, and tail as a wing rock causing mechanism indicated by the F-5 tests, is also suggested in these results in that the wing rock occurs in the angle-of-attack range in which the static lateral stability data show strong coupling between the forebody/wing/tail flow fields.

Review of the forebody cross-sectional shape effect on static stability and wing rock susceptibility reveals an interesting trend. The nose shapes that provide the highest levels of static stability also cause the highest susceptibility to wing rock and vice versa. This trend is illustrated in figures 32 and 33 which show plots of C_{n_β}, C_{ℓ_β}, and $(\Delta\phi)_{WR}$ for the four nose configurations at an angle of attack of 30°. Much additional testing and analysis is required, however, before it can be determined if this is a general trend.

Figure 34 presents a time history of a buildup to "steady state" wing rock con-

ditions exhibited by the configuration incorporating the horizontal ellipse nose at α = 35°. The corresponding phase plane plot is shown in figure 35. Comparison of these figures to the corresponding ones for the 80° delta wing (figures 3 and 4) indicates that the forebody-induced wing rock is far less regular and repeatable than the wing rock of the slender wing. This difference may be due largely to the fact that interaction of the forebody vortices with other components such as the wing and tail is an important mechanism in addition to direct action of the vortices on the component from which they emanate which is the only factor involved in the slender wing rock.

As stated earlier, fundamental understanding of the complex flow mechanisms involved in the forebody-induced wing rock phenomenon is at present very limited. The available data suggest that some of these mechanisms are similar to those involved in the slender wing rock. For example, dynamic interaction of the primary vortices due to their being so close together is certainly occurring in both cases. The effect of sideslip and roll rate on this vortex interaction is also likely to be very similar. There are, of course, some very important differences between the two wing rock situations. A primary one is the component flow interaction which is important in the forebody-induced wing rock but which is not a factor in the slender wing rock. Another difference is the so-called moving wall effects as discussed in reference 16. Extensive wind-tunnel tests of the generic fighter model will continue at Langley. Data to be obtained include the effects of forebody fineness ratio, nose strakes, wing planform, and empennage geometry. Analysis of this systematic data base will hopefully advance understanding of the basic aerodynamic mechanisms involved in this complex phenomenon. It should be noted, however, that this set of data is being generated in wind-tunnel tests conducted at very low Reynolds number and that viscous effects may be very significant in this case. High Reynolds number data will also have to be obtained in order to assess these effects and to allow confident application of the results to full-scale conditions.

TUMBLING

Historical background.- Dynamic model free-tumbling tests were performed in the Langley Vertical Spin Tunnel during World War II and continued through the early 1950's. Reference 17 mentions the phenomenon of tumbling reported in 1942 for "a conventional fighter airplane" (no further identification) and cites a fatal crash of a tailless airplane which might have been tumble related. Spin tunnel investigations established the existence of the phenomenon in model tests and tumble tests were often included in the normal spin tunnel program, especially for tailless configurations.

Reference 17 is a summary of the tumbling results for 14 model configurations, including considerations of emergency recovery parachutes, accelerations on the pilot, and pilot escape. These 14 designs represented a wide diversity of aerodynamic approaches including conventional fighters, a tail-first configuration, an extremely close-coupled model, a forward-swept wing, flying wings, a "flying saucer", a tailless type, and a simple delta wing. From the observations of these free-tumbling tests, the authors drew a number of conclusions, quoted here directly.

1. Conventional airplanes will not tumble, whereas tailless and tail-first airplanes may tumble.

2. Increasing the static longitudinal stability tends towards the prevention of tumbling.

3. Tailless airplanes having low aspect ratio and a large pitching inertia parameter (I_y/mb^2) are less likely to tumble than those having high aspect ratio and a small pitching inertia parameter.

4. Ailerons and rudder have little or no effect on tumbling.

5. Movement of the elevators to oppose the tumbling rotation will generally be effective in producing recovery from a tumble when the static longitudinal stability is marginal.

6. Two parachutes, one attached to each wing tip, will generally be effective in producing recovery from a tumble.

7. Accelerations in a tumble may be exceptionally dangerous.

The first two conclusions suggest the reason for the rapid decline in tumbling interest after this period. Most new designs were conventional and statically stable. This general design trend has continued up to the current generation of fighter aircraft. However, certain "pro-tumbling" features identified in this early research have reappeared in the X-29A configuration and these features are seen in proposed future high performance aircraft: tail-first (X-29A canard) and tailless designs; significant levels of relaxed static stability (X-29A static margin = -.35); low pitch inertia and high aspect ratio of tailless aircraft, e.g. flying wings. A research effort has been initiated at NASA Langley to address this phenomenon for contemporary designs. The X-29A is the first configuration to be investigated in this program. A three-view drawing of the airplane is shown in figure 36.

Experimental investigation.- The experimental investigation was conducted in the Langley 20-Foot Vertical Spin Tunnel. Tests were performed using a 1/25-scale model of the X-29A dynamically scaled in weight and inertia to an equivalent full-scale altitude of 25,000 feet.

Free tumbling tests were conducted by launching the model into the vertically rising airstream from any desired attitude, with or without an initial pitch rate. Initial tests for the X-29A were conducted in the high angle-of-attack configuration: wing flaps full down, strake flaps 30° down and canard 60° trailing edge up, i.e., the flight control system commanding maximum nose down moments. When released from a nose-high altitude (α = 180°) in this configuration, the model underwent an irregular, but clearly autorotative pitching motion in the nose-down sense. There was a horizontal translational component to the trajectory and the model impacted the tunnel safety net after a few tumble cycles.

The observed motion was complex with cyclic variations in linear as well as angular rates. After release, the model would accelerate in pitch and forward velocity, passing rapidly through 0° angle of attack. As the motion progressed beyond -90° angle of attack, the pitch rate slowed very noticeably until the nose-highpoint (α = -180°) was reached when the model would once again accelerate into the next cycle. The model tumble motion, converted to full-scale values for the airplane, correspond to pitch rates varying from 20° per second to over 200° per second (averaging 120° per second) at a sink rate on the order of 250 feet per second.

The complexity of the model motions and the extremely limited run time for each free-tumbling test made analysis difficult. In an effort to simplify the motion and expand test duration, the free-to-pitch test was implemented, essentially reducing the problem to a single degree of freedom. In this technique the same dynamically scaled model was mounted at its center of gravity on bearings so that it was free to rotate in pitch only (figure 37).

In the free-to-pitch tests, autorotation was obtained by either imparting an initial rotation to the model in the proper direction, or by releasing the model from a proper attitude with zero rate. Once initiated, the autorotation persisted indefinitely. Autorotation was obtained for speeds equivalent to 150 to 300 feet per second and was very similar to the tumbling motions observed in the free-tumbling experiments. The effect of control surface position on this motion was studied by setting the controls to the maximum positive, negative, and neutral positions. The canard and wing flap positions had little effect on the motion. The strake flaps, on the other hand, demonstrated a very strong effect on the motion. With the strake flaps deflected full down, only nose-down autorotation could be induced. Attempts to force a nose-up rotation either damped out or reversed to the nose-down motion. Reversing the strake flaps to full up permitted a nose-up autorotation.

Analytical investigation.- An important objective of the current effort is to develop a valid mathematical model of the tumbling aerodynamics so that the phenomenon can ultimately be studied in piloted simulation. This objective represents a particularly formidable challenge because of the highly unsteady flow conditions resulting from a number of factors including angle of attack sweeping through 360° during each tumble cycle at a rapid non-constant rate. The validity of a conventional model in which the aerodynamic forces and moments are represented by a static term and damping term is questionable. Using such a model, the aerodynamic pitching moment is expressed as:

$$C_{m_{TOTAL}} = C_{m_s} + C_{m_q} \frac{q\bar{c}}{2V}$$

The validity of this model was tested by studying its ability to predict the single-degree-of-freedom autorotation observed in the free-to-pitch tests. To obtain the static and damping data through ±180° angle-of-attack range required in the mathematical model, tests were conducted in the Langley Spin Tunnel and 30- by 60-Foot Wind Tunnel. A 1/8-scale X-29A model used for rotary-balance testing (figure 38) was tested in the spin tunnel to obtain the necessary static data because the model mounting system was most amenable to the requirements. The 0° to 90° and -90° angle-of-attack data were obtained with the sting entering the top and bottom of the fuselage, respectively, as is conventionally done during rotary tests. By essentially reversing the model on the sting of each position, the 90° to 180° and -90° to -180° quadrants were obtained. Forced-oscillation tests were conducted on a 0.16-scale model in the 30- by 60-foot wind tunnel to determine $\bar{C}_{m_q}$ through the ±180° angle-of-attack range. Data were measured at an oscillation amplitude of ±5° at a reduced frequency of 0.25.

Figure 39 shows the static pitching-moment data measured for neutral, full nose-up, and full nose-down strake flap deflections with neutral canard and flap settings. The data between ±45° angle of attack exhibit the highly unstable characteristics inherent to this configuration. In the ±45° to ±140° ranges, the data show very stable characteristics such that very large values of pitching moment are generated in the ±140° angle-of-attack regions. Beyond ±140°, the characteristics again break highly unstable.

Plotted in figure 40 are the values of the damping in pitch parameter $\bar{C}_{m_q}$ obtained in the forced oscillation tests. It is seen that the damping is stable (negative) through most of the angle-of-attack range except in fairly narrow regions centered about α = 130° and α = -120°.

Returning to the static pitching-moment data of figure 39, qualitative correlation with the experimental results can be obtained by "walking through" one cycle of the tumbling as would be predicted by the static data, ignoring damping effects. Starting at α = 180°, representative of the nose-high launch technique used in the free-tumbling tests, the static pitching-moment data would cause the model to accelerate rapidly in the nose-down direction due to the highly unstable C_{m_α} driving the model into the angle

of attack region of very large negative values of C_m. By the time C_m becomes positive below $\alpha = 70°$, the model has built up sufficient kinetic energy to drive it over the positive C_m "hump" between 70° and 10°. From 10° to -80°, the model again accelerates in pitch due to the negative values of C_m. Below $\alpha = -70°$, the nose-down rate begins to slow significantly because of the very large positive C_m "hump" centered around -140°. At $\alpha = -175°$, the pitch rate has decelerated to its slowest point as C_m crosses the zero value and the model once again begins to accelerate in the nose down direction at the start of the next cycle. These qualitative motion predictions based on the measured static data agree very well with the experimental results from the free-tumbling and free-to-pitch tests described earlier.

A more exact evaluation of the analytically predicted motions was obtained by inputting the static and dynamic wind-tunnel data into a simulation program to obtain time histories of the motions. The results obtained for the case described above are shown in figure 41. The calculations were done for a full-scale airplane at V = 200 ft/sec. The computations were started with zero pitch rate and $\alpha = 180°$ with controls fixed at $\delta_c = 0$ and $\delta_s = 30°$. The time histories show a nose down tumbling motion rapidly developing such that steady-state conditions are achieved after about 5 cycles. The average pitch rate is about -130°/sec with the minimum rate of -95°/sec occurring at $\alpha = -180°$ as was observed in the tunnel experiments. Also shown are calculated values of normal and axial accelerations at the pilot station. The results indicate that during tumbling, the pilot will be subjected to a very severe g environment which may be incapacitating and may make ejection impossible.[18]

Quantitative comparison of the computed and experimental tumbling motions over one cycle for the case discussed above is shown in figure 42. The experimental data were obtained by frame-by-frame reading of movies taken of the model during the free-to-pitch tests and then scaling the time up to full scale. The results show generally good agreement between the two sets of attitude data. However, more detailed examination of the comparisons indicate that the match of velocity and acceleration is not nearly as close. It is clear that improved mathematical models of the tumbling aerodynamics are needed and methods for obtaining the data for use in these models must be developed.

Susceptibility to tumbling.- Based on the preliminary experimental and analytical results obtained to date, it appears that the subject configuration may be susceptible to tumbling with the controls fixed. However, for a highly augmented airplane such as the X-29A, the controls are not likely to remain fixed through a large amplitude maneuver such as tumbling. Thus at this point in time, it is unknown whether it will be possible for the fully augmented airplane to enter a tumbling condition. Of greater concern, perhaps, are the off-nominal situations involving serious failures in the airplane control system which can lead to conditions which may facilitate entry into a tumble.

The eventual goal of the analytical study is to provide an aerodynamic and mathematical model which will permit piloted simulation of the transition from normal flight to the tumbling conditions. Susceptibility is the key issue for a given configuration and will drive the form of control laws used to provide desired levels of tumble resistance. Based on the limited results obtained to date, it appears that control laws that limit the pitch agility of the airplane will inherently enhance resistance to tumbling. Hard limiters on angle of attack and control laws that limit the attainable pitch rate to "controllable" values would fall into this category. Unfortunately, careful trade-offs versus the desire for high pitch rate capability for nose-pointing agility must be made in designing such systems. Research is currently underway at Langley to develop control laws for highly relaxed stability fighters which combine the desired features of maximum agility and good resistance to pitch departures.

CONCLUDING REMARKS

Current fighter aircraft design trends combined with developing air combat requirements stressing transient maneuvering indicates that unsteady aerodynamic effects will play an increasingly important role in the high angle of attack flight dynamics of combat aircraft. Researchers are faced with the challenges of advancing understanding of the highly complex flow mechanisms involved, formulating valid mathematical models of the aerodynamics, developing wind-tunnel and analytical techniques for generating the inputs to these models, and providing readily usable design guides to the aircraft designer.

This paper has summarized recent research at the NASA Langley Research Center on two high angle-of-attack flight dynamic phenomena which are dominated by unsteady aerodynamic effects: wing rock and tumbling. The wing rock investigations are focused on the phenomena exhibited by slender wings and aircraft configurations incorporating slender forebodies. Some understanding of the cause of the slender wing rock and the flow mechanisms involved have been established. The slender forebody-induced wing rock, on the other hand, is not well understood at the present time although similarities with slender wing rock have been noted. The tumbling phenomenon has not received much attention for many years. Recent design trends, however, have reestablished tumbling as a concern for future combat aircraft.

Much additional research is needed in both the wing rock and tumbling areas. Only by developing technology to control phenomena such as these can the goal of aggressive exploitation of high angle of attack maneuvering for maximum air combat effectiveness be achieved.

REFERENCES

1. Manoeuvre Limitations of Combat Aircraft. AGARD-AR-1545A, August 1979.

2. McKinney, M. O., Jr.; and Drake, H. M.: Flight Characteristics at Low Speed of Delta-Wing Models. NACA RM No. L7R07, January 1948.

3. Paulson, J. S.; and Shanks, R. E.: Investigation of Low-Subsonic Flight Characteristics of a Model of a Flat-Bottom Hypersonic Boost-Glide Configuration Having a 78° Delta Wing. NASA TN D-894, 1961.

4. Shanks, R. E.: Low-Subsonic Measurements of Static and Dynamic Stability Derivatives of Six Flat-Plate Wings Having Leading-Edge Sweep Angles of 70° to 84°. NASA TN D-1822, 1963.

5. Boisseau, P. C.: Investigation of the Low-Subsonic Flight Characteristics of a Model of a Reentry Vehicle With a Thick Flat 78° Swept Delta Wing and a Half-Cone Fuselage. NASA TN D-1007, 1962.

6. Nguyen, L. T.; Yip, L. P.; and Chambers, J. R.: Self-Induced Wind Rock of Slender Delta Wings. AIAA-81-1883, August 1981.

7. Chambers, J. R.; and Grafton, S. B.: Investigation of Lateral-Directional Stability of a Tilt-Wing V/STOL Transport. NASA TN D-5673, 1970.

8. Bihrle, W., Jr.; Hultberg, R. S.; and Mulcay, W.: Rotary-Balance Data for a Typical Single-Engine Low-Wing General Aviation Design for an Angle-of-Attack Range of 30° to 90°. NASA CR-2972, 1978.

9. Sawyer, W. C.; Jackson, C. M., Jr.; Blair, A. B., Jr.: Aerodynamic Technologies for the Next Generation of Missiles. Paper presented at AIAA/ADPA Tactical Missile Conference, Gaithersburg, MD, April 1977.

10. King, H. A.; and Wedan, B. W.: Topside Weapons Release An Analytical Study. AIAA 81-1655, August 1981.

11. Grafton, S. B.; Chambers, J. R.; and Coe, P. L., Jr.: Wind Tunnel Free-Flight Investigation of a Model of a Spin-Resistant Fighter Configuration. NASA TN D-7716, June 1974.

12. Carr, P. C.; and Gilbert, W. P.: Effects of Fuselage Forebody Geometry on Low-Speed Lateral-Directional Characteristics of Twin-Tail Fighter Model at High Angles of Attack. NASA TP-1592, December 1979.

13. Erickson, G. E.; and Gilbert, W. P.: Experimental Investigation of Forebody and Wing Leading Edge Vortex Interactions at High Angles of Attack. AGARD CP-342, April 1983.

14. Keener, E. R.; and Chapman, G. T.: Similarity in Vortex Asymmetries Over Slender Bodies and Wings. AIAA Journal, Vol. 15, No. 9, September 1977.

15. Murri, D. G.; Nguyen, L. T.; and Grafton, S. B.: Wind-Tunnel Free-Flight Investigation of a Model of a Forward-Swept-Wing Fighter Configuration. NASA TP-2230, February 1984.

16. Ericsson, L. E.: Flow Phenomena Causing Wing and Body Rock. AIAA 84-2177, August 1984.

17. Stone, R. W., Jr.; and Bryant, R. L.: Summary of Results of Tumbling Investigations Made in the Langley 20-Foot Free-Spinning Tunnel on 14 Dynamic Models. NACA RM L8J28, December 1948.

18. Whipple, R. D.; Croom, M. A.; and Fears, S. P.: Preliminary Results of Experimental and Analytical Investigations of the Tumbling Phenomenon for an Advanced Configuration. AIAA 84-2108, August 1984.

TABLE I.- Wing Rock Characteristics of 80° Delta Wing

α, deg	$(\Delta\phi)_{WR}$, deg	P_{WR}, sec	k_{WR}
<25°		NO WING ROCK	
27°	34°	.98	.21
32°	40°	.96	.22
37°	40°	1.0	.21
42°	32°	.98	.22

TABLE II.- Wing Rock Characteristics of Monoplanar Missile - Complete Configuration

α, deg	$(\Delta\phi)_{WR}$, deg	P_{WR}, sec	k_{WR}
<20°		NO WING ROCK	
22°	25°	1.62	.12
27°	34°	1.54	.13
32°	41°	1.5	.13
37°	43°	1.46	.14
42°	33°	1.4	.15
47°	20°	1.24	.17
>50°		NO WING ROCK	

TABLE III.- Wing Rock Characteristics of Monoplanar Missile - Body Alone

α, deg	$(\Delta\phi)_{WR}$, deg	P_{WR}, sec	k_{WR}
<20°		NO WING ROCK	
22°	23°	2	.10
27°	63°	2.5	.08
32°	DIVERGENT WING ROCK		
37°	TO CONTINUOUS ROTATION		
42°			
47°	25°	1.32	.16
52°	7°	1.10	.19

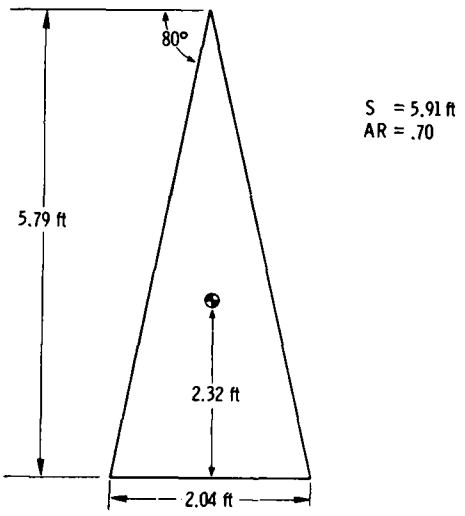

Figure 1.- Drawing of 80° delta wing.

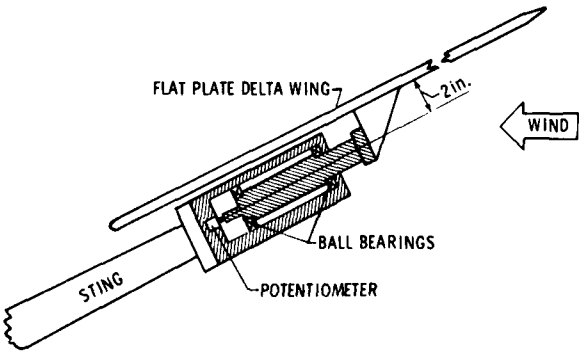

Figure 2.- Free-to-roll test apparatus.

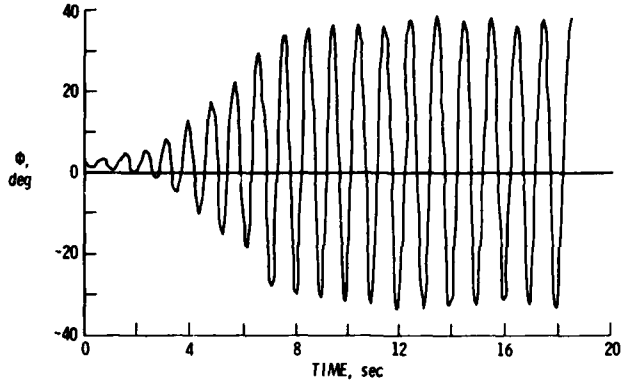

Figure 3.- Time history of wing rock buildup in 80° delta wing free-to-roll tests. α_o = 27°.

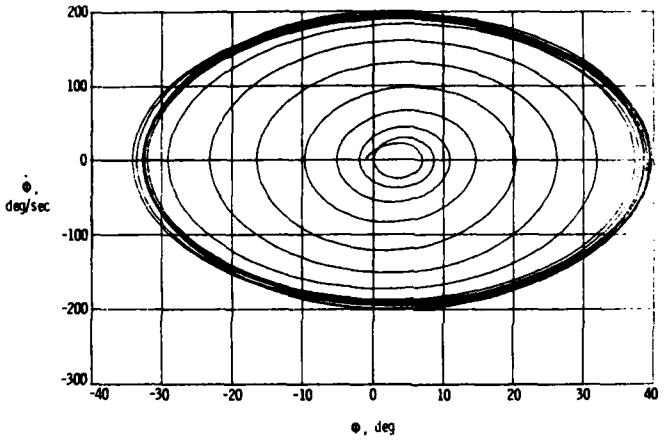

Figure 4.- Phase plane plot of 80° delta wing rock buildup.

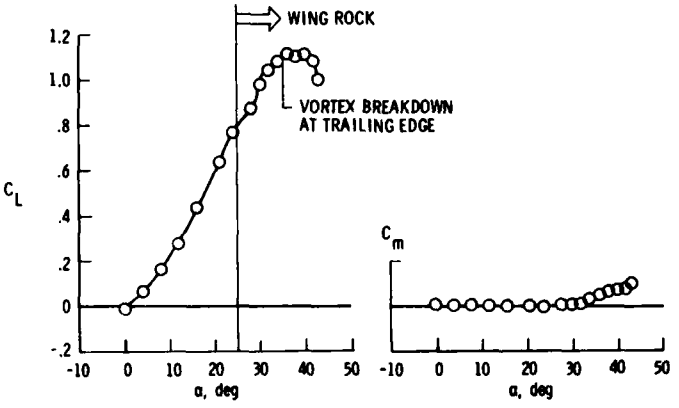

Figure 5.- Longitudinal aerodynamic characteristics of 80° delta wing.

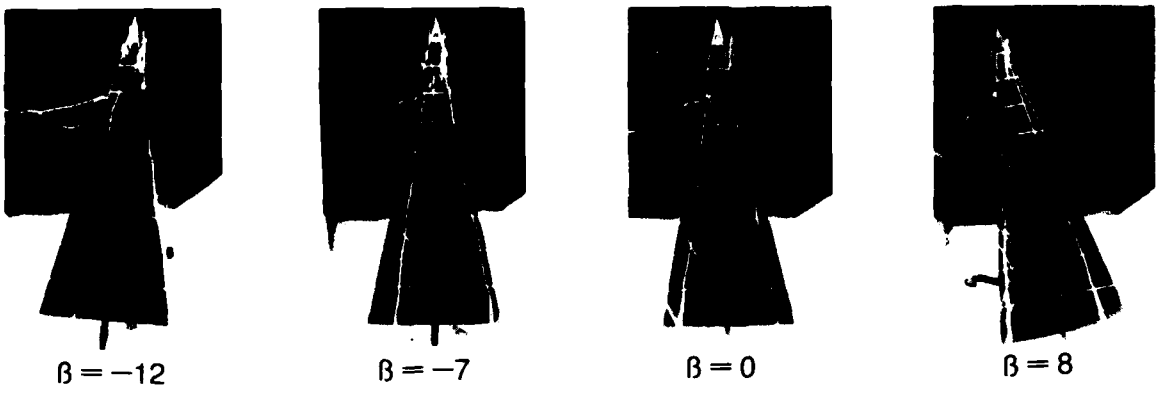

Figure 6.- Effect of angle of sideslip on vortex bursting. α = 28°, 80° delta wing.

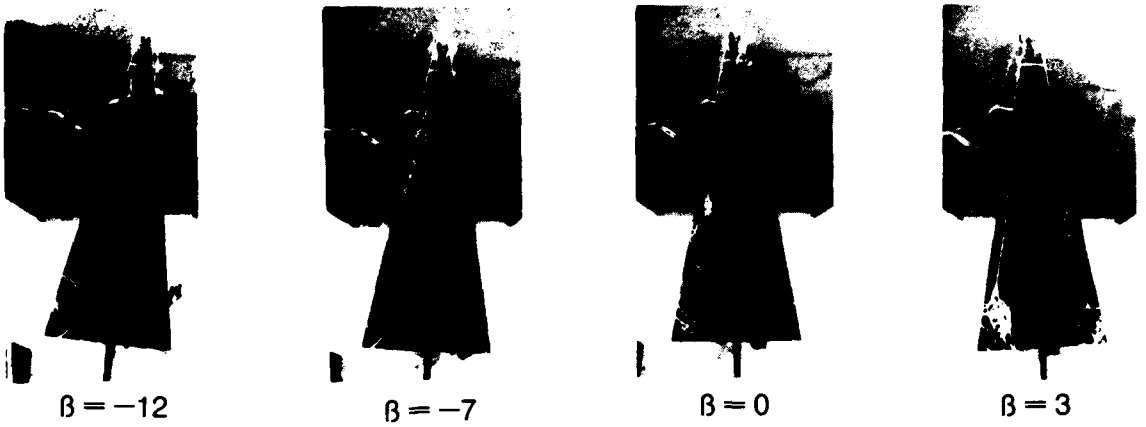

Figure 7.- Effect of angle of sideslip on vortex bursting. α = 40°, 80° delta wing.

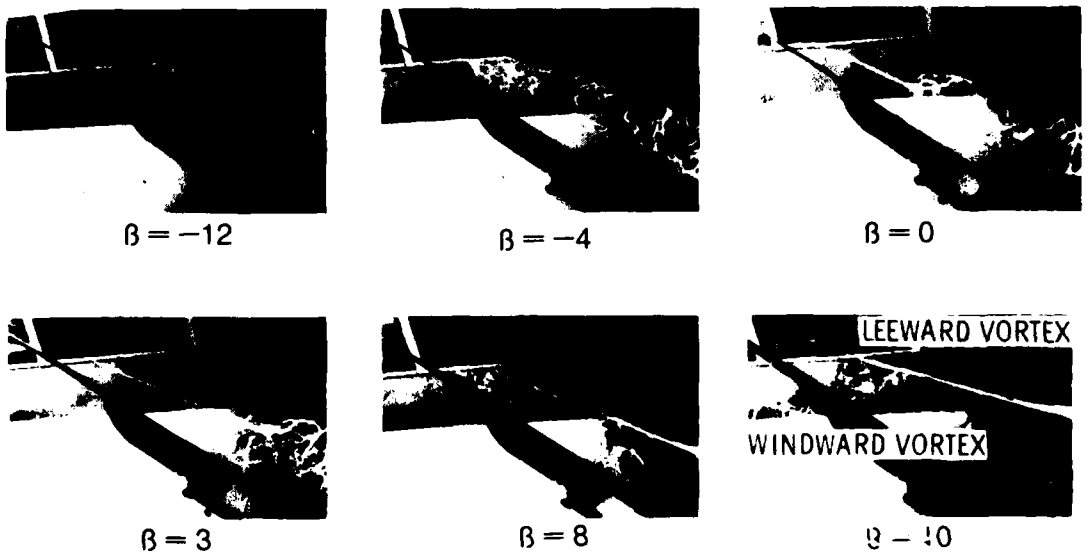

Figure 8.- Effect of angle of sideslip on vortex bursting. α = 40°, 80° delta wing, side view.

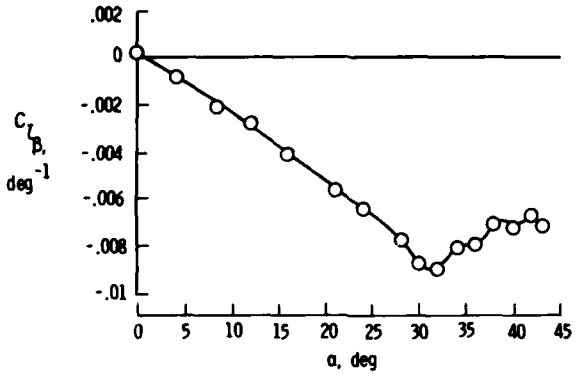

Figure 9.- Variation of lateral-stability derivative with angle of attack, 80° delta wing.

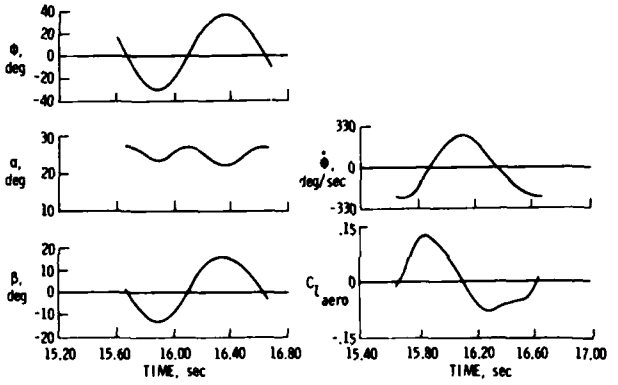

Figure 10.- Time histories of one cycle of steady state wing rock. α_o = 27°, 80° delta wing.

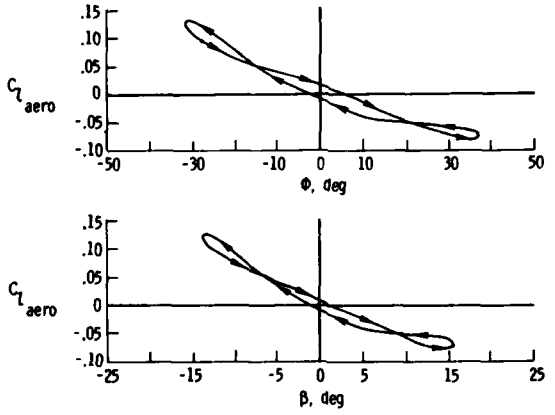

Figure 11.- $C\ell_{aero}$ versus Φ and β crossplots for one cycle of wing rock. α_o = 27°, 80° delta wing.

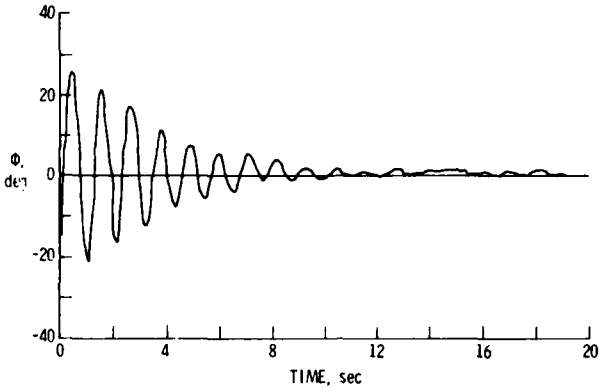

Figure 12.- Response to -20° initial roll angle. α_o = 27°, β_o = 10°, 80° delta wing.

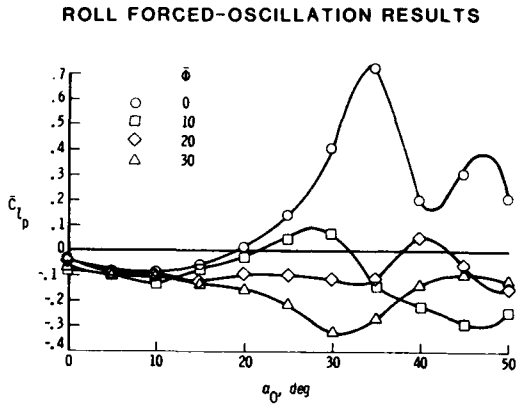

Figure 13.- Effect of mean roll angle on forced oscillation data. k = 0.16, 80° delta wing.

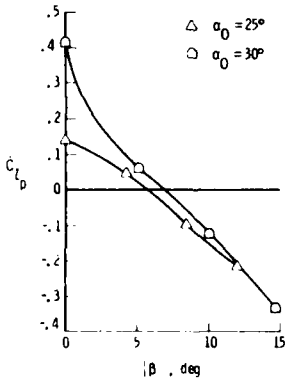

Figure 14.- Effect of sideslip on roll damping. 80° delta wing.

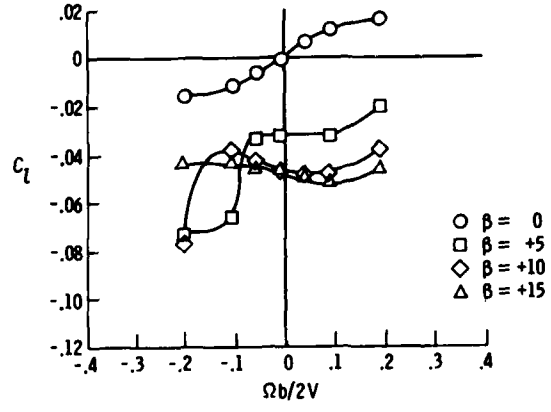

Figure 15.- Effect of sideslip on rotary data, α = 30°, 80° delta wing.

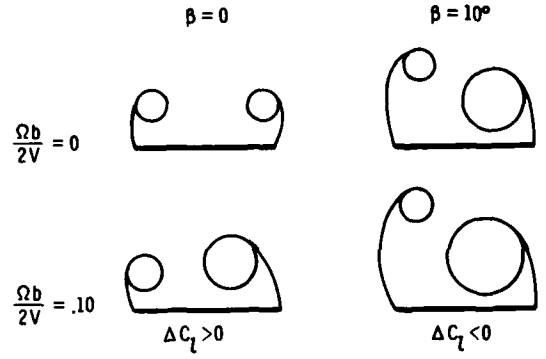

Figure 16.- Schematic representation of effects of sideslip and rotation rate on vortex patterns. α_o = 30°, rear view. 80° delta wing.

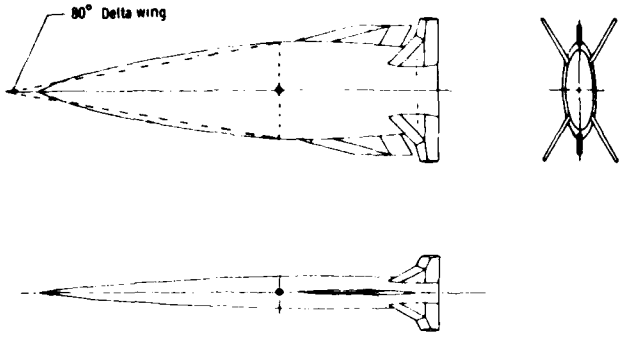

Figure 17.- Drawing of monoplaner missile and comparison with 80° delta wing.

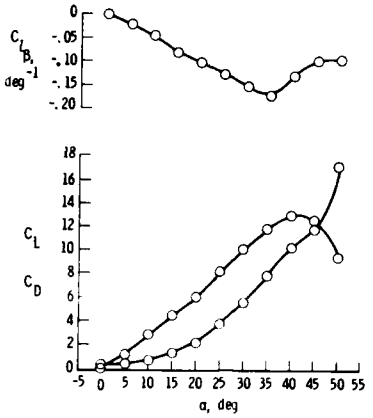

Figure 18.- Aerodynamic characteristics of monoplanar missile.

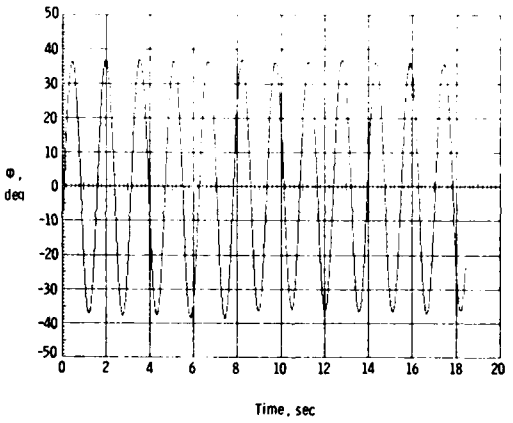

Figure 19.- Time history of steady state wing rock. α_o = 27°, monoplanar missile.

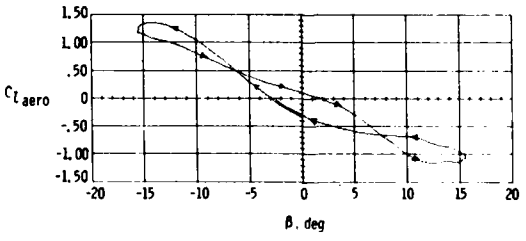

Figure 20.- $C\ell_{aero}$ versus β crossplot for one cycle of wing rock. α_o = 27°, monoplanar missile.

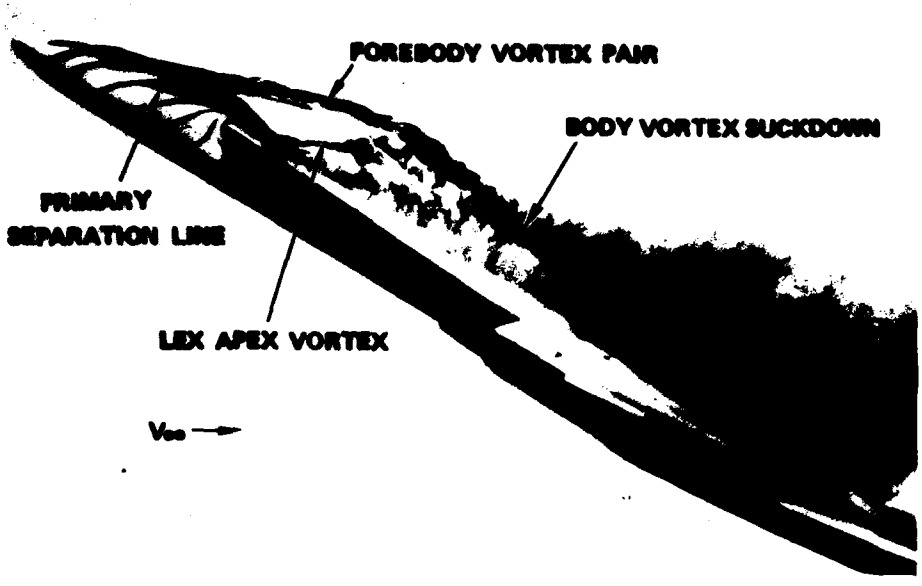

Figure 21.- Water tunnel flow visualization showing vortex interaction.

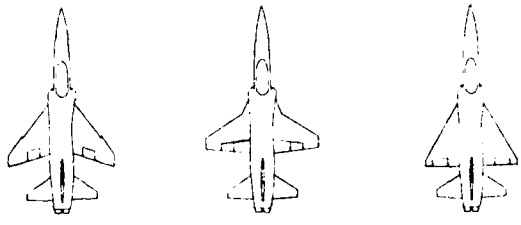

Figure 22.- Wing planforms tested with model based on F-5 configuration.

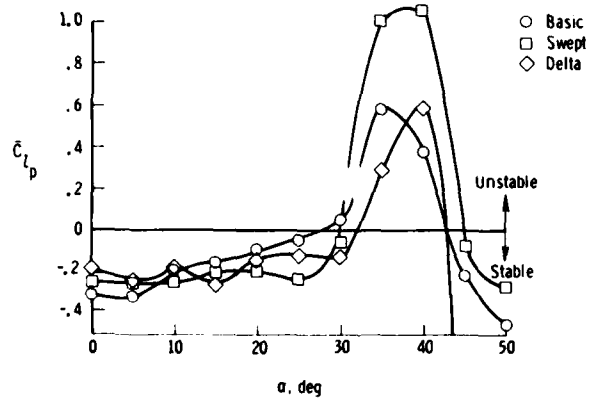

Figure 23.- Forced oscillation roll damping results for three wing planforms using F-5 model.

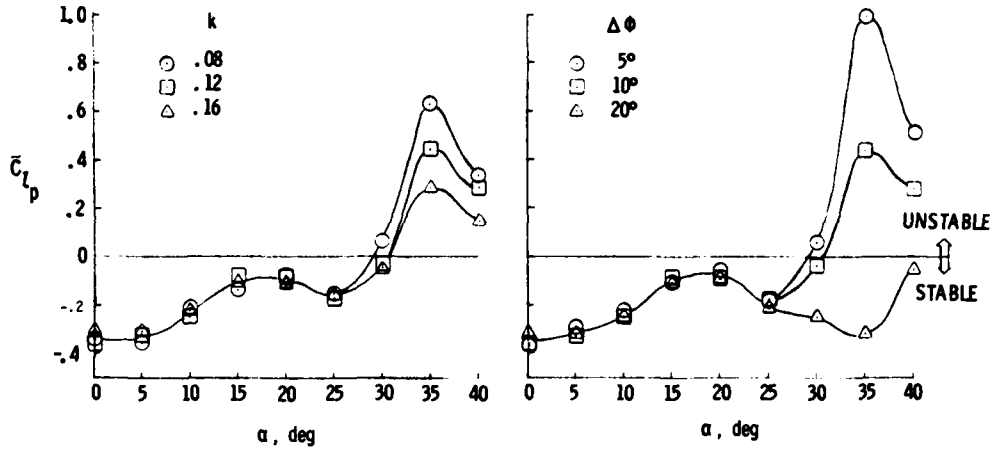

Figure 24.- Effect of frequency and amplitude on forced oscillation data for basic F-5 configuration.

Figure 25.- Wing shapes for generic fighter model.

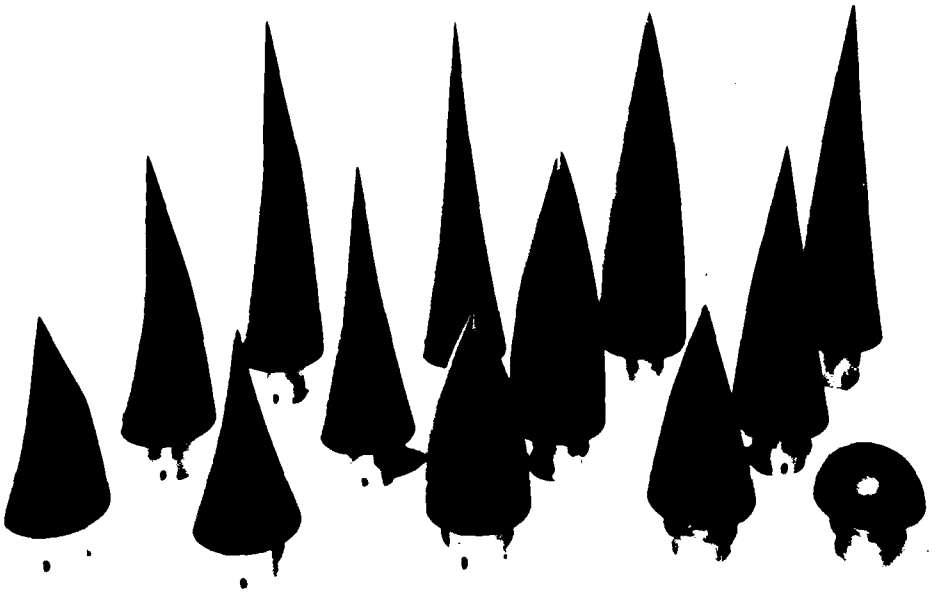

Figure 26.- Forebodies available for generic fighter model.

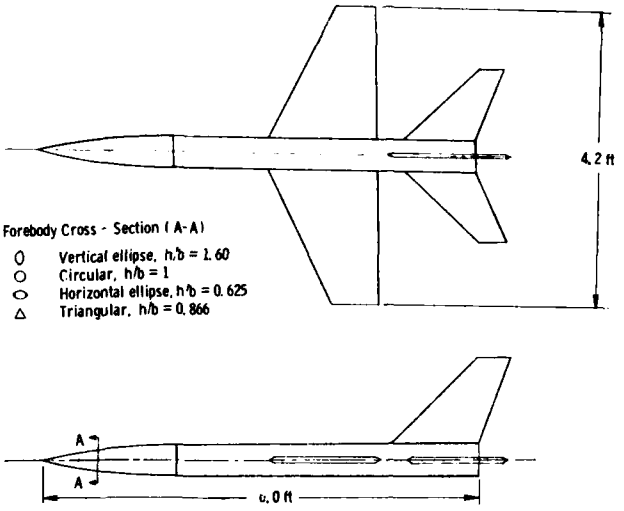

Figure 27.- Drawing of generic fighter model.

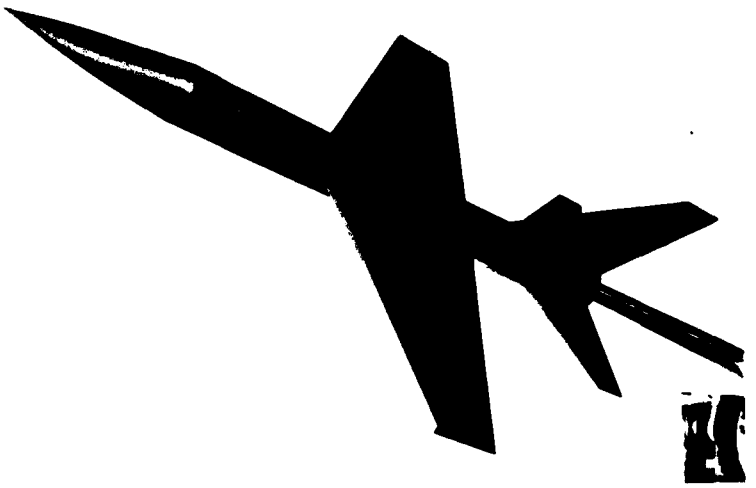

Figure 28.- Photograph of generic model with horizontal ellipse forebody.

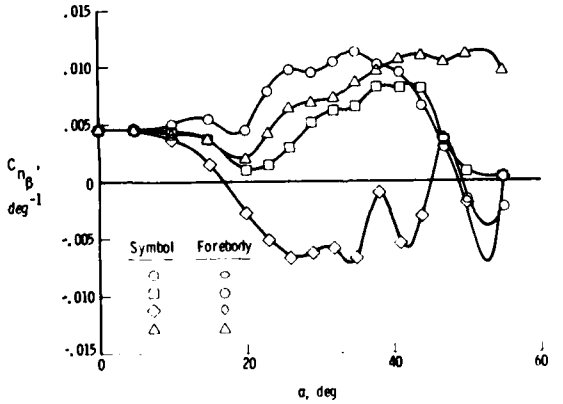

Figure 29.- Effect of forebody cross-sectional shape on static directional stability. Generic fighter model.

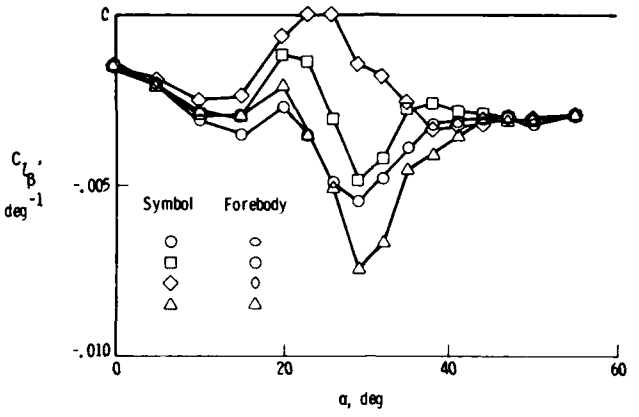

Figure 30.- Effect of forebody cross-sectional shape on static lateral stability. Generic fighter model.

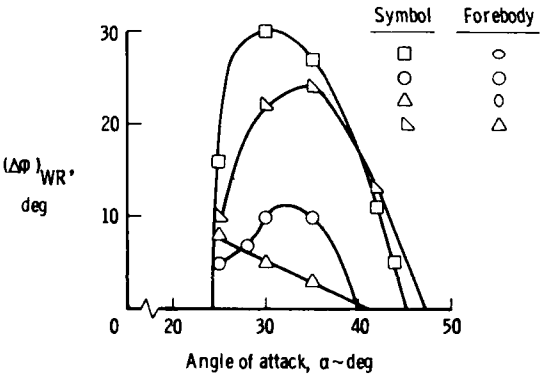

Figure 31.- Effect of forebody cross-sectional shape on wing rock amplitude. Generic fighter model.

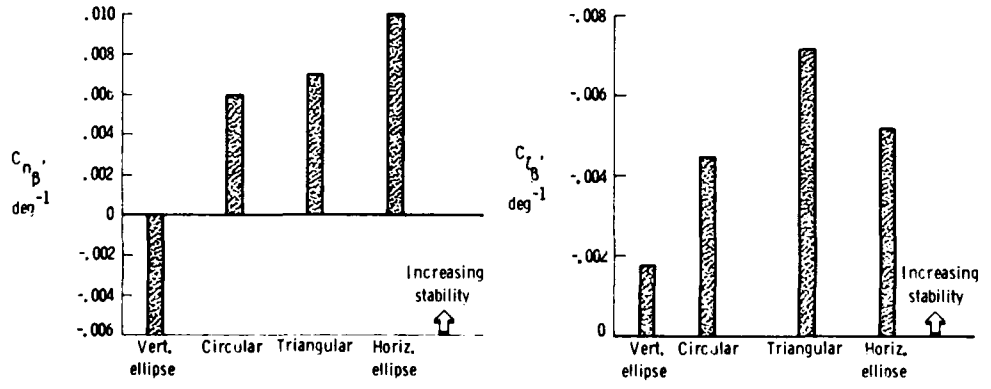

Figure 32.- Static lateral-directional characteristics of generic fighter model with four forebody cross-sectional shapes. $\alpha = 30°$.

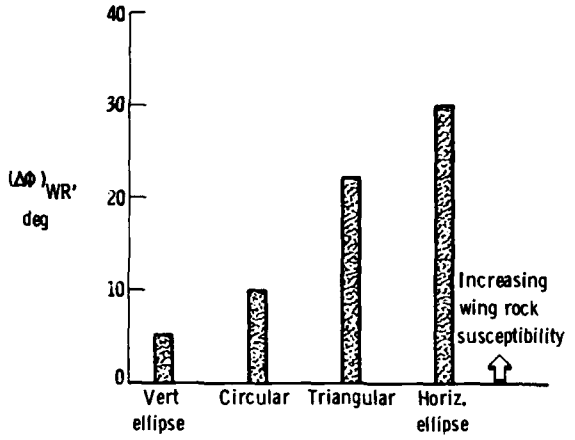

Figure 33.- Wing-rock amplitude of generic fighter model with four forebody cross-sectional shapes. α_o = 30°.

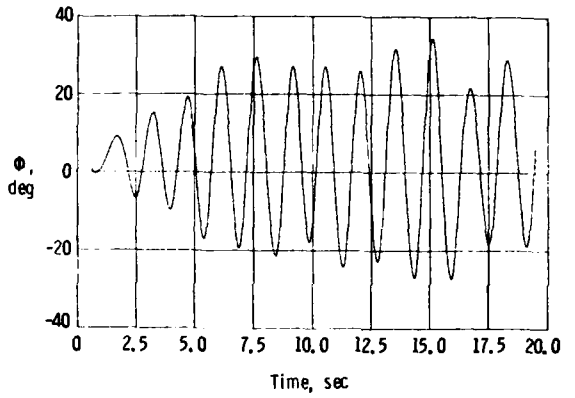

Figure 34.- Time history of generic fighter model wing rock buildup. α_o = 35°.

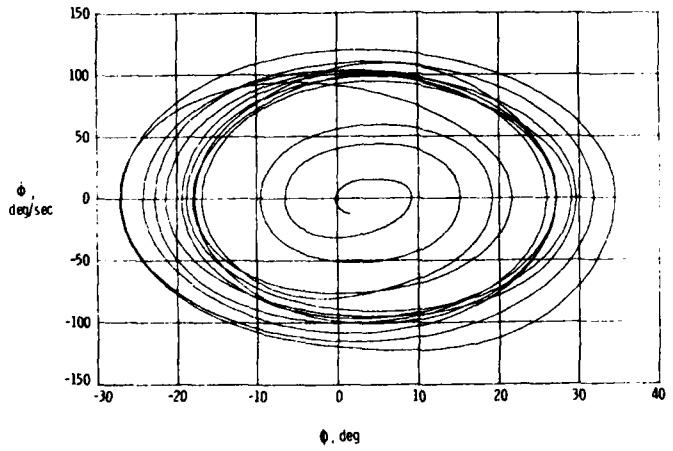

Figure 35.- Phase plane plot of generic fighter model wing-rock buildup. α_o = 35°.

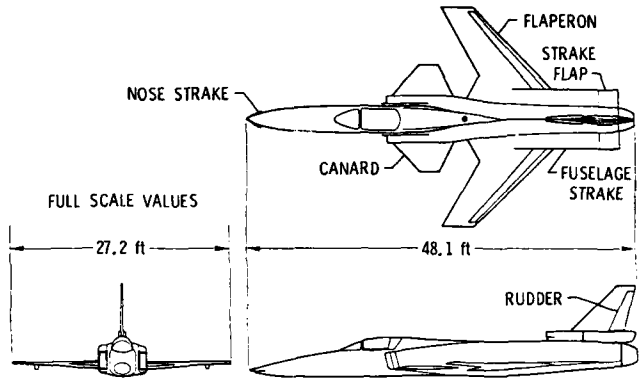

Figure 36.- Drawing of X-29A aircraft.

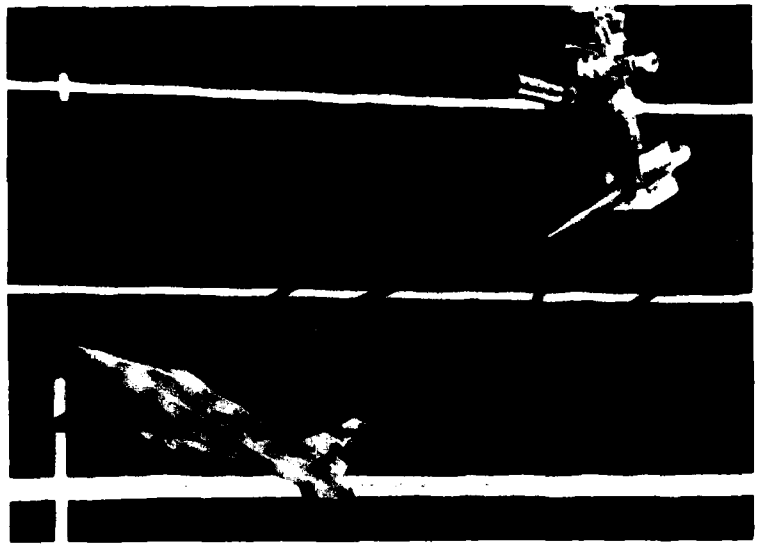

Figure 37.- X-29A model mounted on free-to-pitch rig.

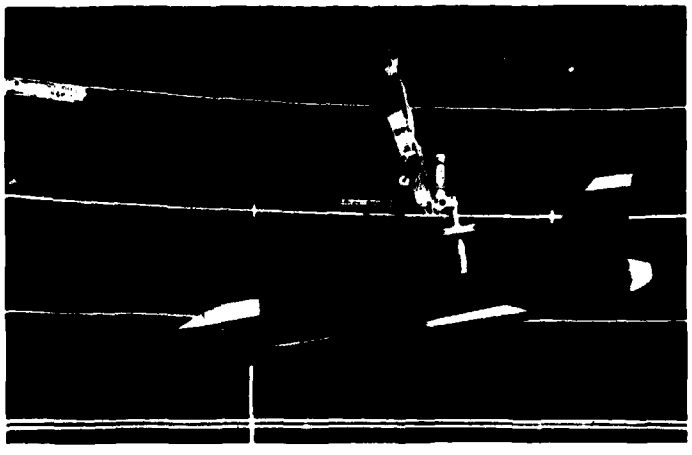

Figure 38.- 1/8-scale model of X-29A on rotary balance apparatus.

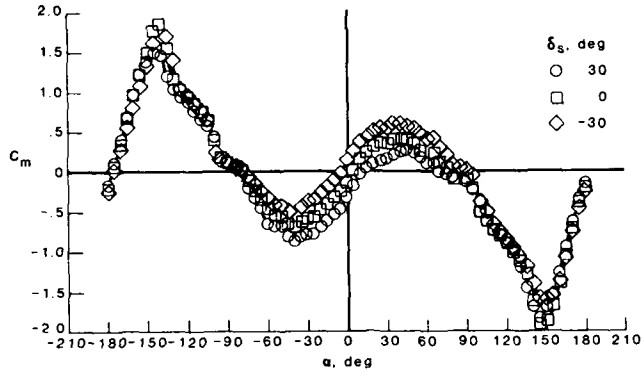

Figure 39.- Pitching moment variation with angle of attack, X-29A model.

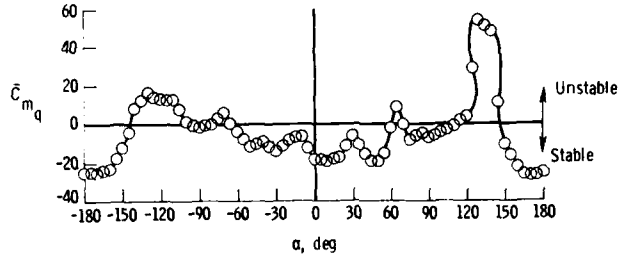

Figure 40.- Pitch damping parameter variation with angle of attack, X-29A model.

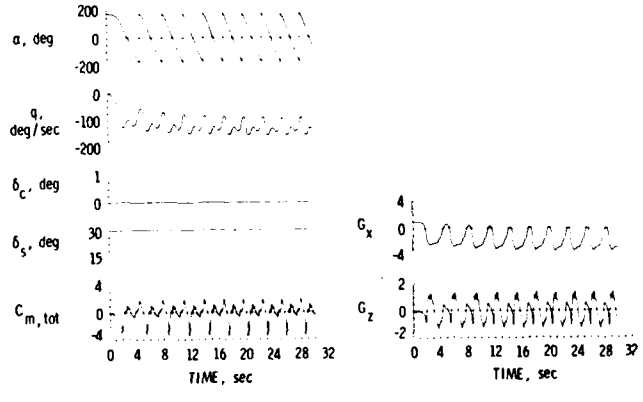

Figure 41.- Time history of a computed tumbling motion, X-29A configuration.

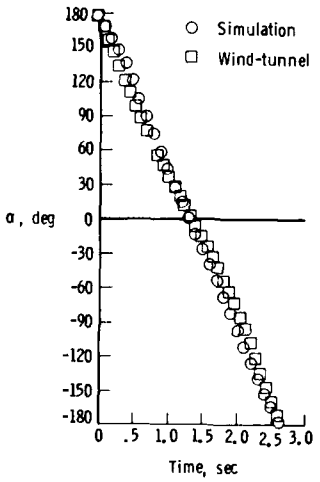

Figure 42.- Comparison of computed and experimental tumbling data, X-29A configuration.

UNSTEADY AERODYNAMICS AND DYNAMIC AIRCRAFT MANEUVERABILITY

James D. Lang, Colonel, USAF
Director, Avionics Laboratory
AFWAL/AA
Wright-Patterson AFB OH 45433
USA

Michael S. Francis, Major, USAF
Chief, SSTS Systems Development Branch
SD/YNCS
P O Box 92960
Worldway Postal Center
Los Angeles CA 90009
USA

. INTRODUCTION

Air combat of the future can be expected to differ greatly from that of the past--a result attributable to advances in enabling aircraft technologies and paced by a new generation of air-to-air weapons capabilities. Anticipated developments in the areas of structures and structural materials, control systems and the vehicle-pilot interface may be coupled with an emerging new understanding of unsteady aerodynamic behavior to provide a new level of dynamic maneuverability heretofore not thought possible. This paper is focused on a vision of that capability as suggested by a base of available supporting evidence.

The case for the development of a "supermaneuverable" flight capability is built on both anticipated operational need and perceived technological opportunity. While both are addressed in ensuing sections, the primary objectives herein are to describe the potential of this unique flight environment and discuss its underlying unsteady aerodynamic characteristics. The result, we hope, provides a significant basis for advocacy of future research and development necessary to achieve this valuable combat capability.

II. OPERATIONAL NEED AND TECHNOLOGICAL OPPORTUNITY

Future combat scenarios are expected to initially involve beyond-visual-range (BVR) encounters which are characterized by the need to detect, categorize, and assign targets at long range and in which high speed maneuvering is exploited to gain first firing opportunities. This scenario incorporates a need for coordination with other friendly aircraft, optimized delivery of long range missiles, and selective disengagement while BVR.

There will also be a need to selectively close and engage targets within-visual-range (WVR) as the air combat encounter develops. In this situation, "all aspect" short range missiles combined with guns in an integrated flight/fire control system offers the potential for rapid delivery of weapons on target in a highly dynamic maneuvering combat environment. The need to selectively disengage, and perhaps to re-enter combat during the same sortie at BVR conditions, adds another element of dynamic maneuvering to the future combat environment.

II.1 Weapons of the Future

The scenario outlined above relies heavily on the successful integration of technologies associated with target identification, classification, and control of the friendly elements of an air combat force. The need to coordinate and manage separate combat vehicles while providing for decentralized, single ship weapons delivery is an essential and complex ingredient of BVR and WVR phases of combat. The need for "situation awareness" and coordination of combat crews is paramount. But of equal importance is the need for a very high level of dynamic maneuvering performance from each combat vehicle.

These performance needs will include capabilities:

- to rapidly accelerate or decelerate
- to turn tightly and quickly
- to change maneuver conditions rapidly (i.e., the ability to quickly alter the turning and longitudinal accelerating forces, through rolling, pitching, aerodynamic flow management, and thrust vector control)
- to obtain rapid fire control solutions and weapons delivery

- to rapidly disengage and move on to the next target

It is in this context of increased combat performance that the word "supermaneuverability" is used to connote "very high levels of agility and maneuverability available throughout an extended flight envelope for future fighter aircraft." In effect, it describes an expansion of the air vehicle performance envelope in the broadest sense, including high-speed and low-speed cruise, sustained turning, and instantaneous turning coupled with longitudinal acceleration/deceleration capability. Further, the term "agility" is here defined as "the ability of an aircraft to move from one maneuver condition to another at a rapid rate." It relates to expanded ability to change roll, pitch, and yaw orientation and to quickly change the magnitude and direction of lift, drag, and thrust vectors.

The highly dynamic nature of future air combat will reward those combatants who can maneuver selectively, deliver weapons on target effectively, and move to the next target rapidly.

II.2 Technology Opportunities

In order to achieve unprecedented levels of supermaneuverability and agility, several new and developing technologies must be successfully integrated. They form the core of enabling technologies which are key interactive elements of the highly capable future fighter weapons system. Among them are:

- "all aspect" short range missiles
- advanced sensors (e.g., navigation and threat)
- high speed electronic data processing devices and techniques
- digital, fault-tolerant control systems for integrated, automatic control of interactive elements, including:
    - engines, nozzles, inlets
    - structural shape and aeroelastic response
    - aerodynamic flowfield behavior
    - "all aspect" flight and weapon control
- pilot/vehicle interface technologies such as:
    - helmet mounted sights and displays
    - cockpit information displays and control devices
    - environmental protection devices (e.g., rapid response "g" suits, escape systems)
    - workload reduction through tailored degrees of automation
    - optimized system dynamics to achieve a high level of flying qualities

Each of these technology areas requires continuing development on its own merit, but the greatest payoff will be realized when they are blended properly into an overall system design.

The remainder of this paper will concentrate on the key areas of active and interactive flowfield control and, to a lesser extent, interactive thrust vector control. The successful development of these fledgling technology areas is crucially dependable on the synergistic interaction of the aerodynamics and controls communities.

II.3 Envelope Expansion

From a flight vehicle perspective, the ability to achieve supermaneuverability can best be illustrated by reference to an aircraft load factor versus Mach number diagram as shown in Figure 1. This representation identifies the maximum lift region where attainable combinations of lift and Mach number constrained by buffet, stall, or control limits define the useful flight envelope. Enhanced transonic and subsonic maneuvering performance, usually associated with WVR combat, is sought throughout the region of moderate-to-high angles-of-attack. Figure 1 also identifies areas for high-speed maneuver enhancement which are often restricted by control or aeroelastic limits.

Another dimension of supermaneuverability is the potential for rapid transition (energy gain and loss ability) between the BVR and WVR "combat arenas" which are shown highlighted on an altitude versus Mach number plot in Figure 2.

Supermaneuverability can thus be viewed as a natural and need-driven extension to the performance and maneuvering capabilities which have traditionally been associated with fighter aircraft. It is a direct result of projected operational considerations and will be attainable in the near future due to technology opportunities on the immediate horizon.

III. VEHICLE DYNAMICS OF "SUPERMANEUVERS" - A GENERALIZED VIEW

The evaluation of air-to-air combat capability is currently accomplished by restricting the combat arena to prescribed, fixed specific altitude and airspeed conditions as well as specific power settings. Furthermore, comparisons between fighter aircraft are made assuming that these conditions are equal for all combatants, even though this is rarely the case except in lengthy, sustained turning engagements where flight conditions may stabilize.

Conventional wisdom has emphasized the specific excess power, P_s, as an especially relevant "measure of merit" in analyzing combat capability. This parameter is related to aircraft climb and acceleration (energy rate) capabilities and to aircraft forces and speed through the well-known relation:

$$P_s = \frac{(T\cos\alpha_t - D)V}{W} = \frac{dH}{dt} + \frac{V}{g}\frac{dV}{dt} \qquad \ldots(1)$$

where: T is thrust, α_t is the angle between the thrust vector and the aircraft velocity vector, V is aircraft true airspeed, and H is altitude.

Plots of P_s are used to determine single aircraft capabilities or to compare energy maneuverability capabilities between two aircraft.

Point performance comparisons often have involved sustained and instantaneous turn rate capabilities as shown in Figure 3 or have been portrayed as in Figure 4 where P_s is plotted versus turn rate. These familiar methods fall short of characterizing the "dynamic" maneuver states which may occur between two aircraft as they both attempt to gain advantage in minimum time. All-aspect weapons and the technology potential for supermaneuverable flight will force the aerial engagement away from sustained maneuvers characterized by constant airspeed, load factor, and energy conditions, and towards maneuvers in which energy is readily traded to gain first firing opportunities.

To this end, more comprehensive measures of merit are currently sought. Research is currently underway to define and compare maneuvers in which dynamically changing flight conditions enable pilots to turn and/or point the nose quickly, track the target, and shoot or launch first.[1]

To illustrate, Figure 5 depicts a hypothetical combat engagement sequence where an aircraft starting at point 1 moves quickly through a series of maneuver conditions, and recovers to its initial state. The pilot in this example attempted to sequentially minimize turn radius, maximize turn rate, keep constant altitude, and turn via a loaded roll. Note that transient events included: (1-2) "pitch up" and engine deceleration, (2-3) rapid deceleration, (3-4) rapid turn at $C_{L_{max}}$, (4-5) "pitch down" and engine spool-up, and (5-6) level acceleration.

The time history of turn rate during these events might appear as shown in Figure 6. The area under the curve (1-5) in Figure 6, gives the total turning angle change in this level turn example. The effects of engine spool-down and spool-up time may be very significant in rapid maneuvering, which leads to the conclusion that measures of merit which more completely define maneuvering should evaluate and quantify the following performance traits: (1) deceleration control, (2) roll performance while maneuvering (onset rate and maximum rate), and (3) engine spool time.

III.1 Post-Stall Maneuvers

Herbst[2] has reported on a series of air combat simulations where thrust vectoring was used to augment aerodynamic pitch and yaw control and to provide a large component of thrust perpendicular to the flight path to augment lift for turning. His simulation results show a greatly improved turned performance which was decisive in increasing combat exchange ratios even in multiple target engagements. The term, "supermaneuverability", was originally coined by Herbst as a descriptive term for the ability to perform the types of maneuvers discovered during those simulations. An example of such a maneuver, shown in Figure 7, involves a low speed, low radius portion of the maneuver at a very high turn rates through post-stall angles-of-attack (up to 90°). Herbst has hypothesized that this portion of the maneuver will require use of thrust vectoring fully integrated into the flight control system in order to achieve controlled flight "beyond the stall". In simulations employing the "Herbst vehicle",

pilots employed that capability very selectively and infrequently, but with decisive results in simulated combat situations. Herbst's results have provided the impetus for a new look at the potential for increased maneuverability by expanding the envelope through use of thrust vectoring at post-stall angles-of-attack.

The concept of a post-stall maneuver accomplished at low speeds is believed to be just one example of a class of dynamic maneuvers which could exploit the post-stall regime and which extends from very low to very high speeds. All may offer greatly enhanced combat capability. It has recently been shown that post stall maneuvering is optimum to achieve short duration, quick, tight turns.[3]

Until recently, most of the aerodynamic analysis applied to those rapid, pitch-up maneuvers has embraced quasi-steady or steady flow aerodynamic models. The deficiencies in this characterization as applied to supermaneuverable flight will be discussed at length below.

III.2 Point-Shoot Ability

The ability to control an aircraft in a dynamic pitch-up maneuver through the stall angle-of-attack has another potential combat benefit, perhaps of greater importance than improved turn performance. Controlled pointing of the nose also leads to a vastly improved point/shoot capability. Coupled with a fast response flight/fire control ability, the ability to point the nose results in a system capability to shoot or launch a short-range missile very rapidly and to recover and maneuver to the next target. This, however may require an extension to current missile launch envelope limits.

The ability to point and shoot as well as to turn quickly and tightly relies on achieving control of aircraft attitude and flight path beyond the stall. Flight envelope expansion can then be represented by additional turn performance, which can be depicted on either a load factor versus Mach number diagram or on a turn rate versus Mach number diagram as shown in Figures 8a and b.

The ability to achieve control at orientations extending to very high angles-of-attack provides the added benefit of "departure free" flight. This additional combat capability will allow a pilot to aggressively maneuver his aircraft with confidence to exploit the full range of performance and maneuver capabilities.

IV. UNSTEADY AERODYNAMICS OF SUPERMANEUVER

The attainment of supermaneuverable flight will pose significant engineering and technological challenges including those brought about by the need to cope with continuously varying, complex aerodynamic conditions. The prospect of rapid changes in vehicle orientation and velocity, including large amplitude excursions to very high angles-of-attack, suggests that the traditional concept of flight be reconsidered. The aerodynamic perspective which characterizes maneuver as a succession of steady flow, equilibrium states may no longer be valid. The concept of supermaneuverable flight requires that the definition be expanded to include unsteady, non-equilibrium flow conditions in which the aerodynamic time history might have a significant effect. In this regard, the classical dependence on Reynolds and Mach numbers to characterize the aerodynamic environment is augmented by a need for a more extensive parameter set which captures significant time dependent effects in all relevant degrees of freedom.

The evolving flight vehicle flowfield cannot be expected to possess the classical attributes, i.e., domination by attached turbulent boundary layers with small regions of separation bounded by a large region of irrotational, inviscid flow. Instead, massive regions of flow separation can be anticipated to evolve which will be significantly influenced by the time dependent variations of the boundary conditions. Depending on the severity of these unsteady effects, many of the traditional methods for describing aerodynamic characteristics and relating them to the vehicle dynamics, e.g., the classical stability derivatives, may have little utility.

IV.1 Rapid Pitch-Up to High-α , An Example

To account for the myriad complex flow phenomena and interactions which might occur during the course of a complicated supermaneuver would be difficult, if not impossible, given their dependence on the vehicle configuration and the current level of understanding of unsteady aerodynamics. As an illustration, however, it is useful to consider the relatively simple example of an aircraft undergoing a rapid increase in angle-of-attack to a large terminal angle (approximately 70°-90°) from an initially high subsonic cruise condition. For additional simplicity, we consider the entire "maneuver" to take place in the vehicle's plane of symmetry. Some of the qualitative flow features which may be present are visually depicted in three different states of development in Figure 9.

The initiation of the maneuver may involve large amplitude control surface deflections which, in turn, generate unsteady vortex structures capable of affecting the performance of neighboring and downstream-located lifting surfaces (Figure 9a). Although of relatively short duration, these interactions are potentially significant due to the high dynamic pressures which exist during the initial stages of the maneuver.

As the vehicle reaches higher angles-of-attack (Figure 9b), unsteady effects caused by the rapid, pitch-up motion can be expected to significantly influence flowfield development. For example, instead of experiencing massive, chaotic flow separation and concomitant loss of lift, wings and other lifting surfaces may witness the development of energetic, dynamic stall vortices which temporarily "reorganize" the flowfield and result in lift and drag increases, as the vehicle decelerates along its flight path. The development of methods to control and manage these unsteady flow structures could lead to their eventual exploitation for maneuver control enhancement. Alternatively, the unchecked evolution of these vortices may lead to undesirable asymmetric forces (and, possibly, departure) if sensitive instabilities result in premature vortex breakdown on either side of the aircraft. In this sense, the unsteady effects can be thought of as a "two-edged sword". Simulations of post-stall maneuvers up to now have been based on quasi-steady aerodynamics with limited modeling of body rate effects on the flowfield. In the authors' opinion, this represents a serious weakness in the fidelity of those simulations, since the phenomena associated with dynamic stall have not been adequately modeled.

Unsteady vortices generated from other sources including the forebody region and other sharp edges may also play an important role in the overall vehicle dynamics. Similar phenomena can be expected to occur in the engine inlet region where they may affect the overall aerodynamic performance of the inlet and possibly alter engine behavior.

The potential influence of compressibility on these unsteady flow features is another factor which must be considered. Little is known about this Mach number dependence and any attempt to characterize these effects in a situation where the Mach number itself is varying with time is purely speculative.

As the aircraft reaches its maximum incidence angle and greatly reduced forward flight speeds (Figure 9c), motion-induced aerodynamic effects are no longer dominant. Instead, natural instabilities are the driver for an unsteady wake region dominated by three-dimensional vortices which are shed around the planform periphery. This flow can be expected to create a more chaotic load distribution which may make vehicle orientation control difficult.

Perhaps the greatest obstacle to attaining supermaneuverable flight can be appreciated by recalling that the entire sequence of events just described transpires in a few seconds, or less. This compressed time frame with all of its potentially significant dynamic events poses a considerable challenge to vehicle controlability that may only be met with some form of automated real-time, flow management system.

IV.2 The Unsteady Separation Process

The hypothesized description of supermaneuver aerodynamics just provided is not purely fictional, but based upon a considerable body of knowledge available in the literature. Research directed at gaining insight into the physical processes which initiate and govern unsteady separated flow behavior is receiving renewed attention. Key to this understanding is the role of time dependent boundary and initial conditions and the influence of their history on flowfield development.

Many recent studies have focused on generic, or at least simplified, flow geometries in an attempt to logically separate the various physical effects and parametric dependencies while simultaneously minimizing configuration unique issues.[4-11] As an example, the intracacies and complexity of the unsteady separation process have recently been captured in flow visualizations by Freymuth and his colleagues[10-11] for the case of an airfoil at incidence subjected to a constant freestream acceleration from rest, as shown in Figure 10. Although these results were obtained over a very low Reynolds numbers range, they illustrate a time developing sequence of near surface and free vortex interactions which may serve as the elemental building blocks of more complex high Reynolds number flows.

Especially relevant to the supermaneuverability question are studies which involve airfoils and wings in unsteady motion. Evidence of significant unsteady effects arising from large amplitude, lifting surface motions can be traced back to the 1930s.[12] More recent efforts in this area which are germane to the supermaneuver application have been motivated by problems of torsional blade oscillations prevalent in helicopter applications. Much of this work has focused on two-dimensional analyses of oscillating airfoil motions which emulate the helicopter rotor environment. In the course of these studies, the dynamic stall phenomenon has received considerable attention.

Significant insight into the development of the airfoil dynamic stall flowfield has been provided by McCroskey and his coworkers[13-17], and their contemporaries.[18-22] In the course of these efforts, the unique effects of imposed unsteadiness including time (phase) lags in flowfield development, hysteretic force time histories and the vortical character of the developing unsteady separated region have been discovered, described, and quantified. Parametric studies have been conducted over a broad range of reduced frequencies and chord Reynolds numbers with only limited attention given to the influence of Mach number.

Although these sources have collectively provided a useful conceptual foundation, only recently have research efforts been directed at the unique aerodynamic aspects of the supermaneuver flight environment. Among the many issues now receiving attention are the influence of very large motion amplitudes on dynamic stall development, the effects of different motion "types" (e.g., oscillatory versus ramp) to characterize the overall importance of motion time history, and the subject of three-dimensional effects, to name a few.

IV.3 Airfoil Studies Continued

Considerable recent effort has been expended on studies of airfoil motions but emphasizing non-oscillatory behavior. Francis and Keesee[23] have conducted an experimental survey of constant rate airfoil pitching motions extending to large termination angles-of-attack (approximately 60°). Measurements of unsteady surface pressure distributions on two different symmetrical airfoil shapes have been used to reconstruct the flow events which shape the dynamic stall process. These results have captured the footprint of the energetic separation vortex which originates at the leading edge and exerts a substantial influence on the loading as it convects downstream (see Figure 11). This same evolutionary pattern was found to occur over the entire range of pitch rates and amplitudes studied ($0.001 < k_\alpha < 0.21$; $20° < \alpha_{max} < 60°$, where $k_\alpha \equiv \dot{\alpha}c/2U_\infty$), although event timing and suction pressure magnitudes varied from case to case. In all cases, motion was initiated from a steady flow, zero lift condition.

Visual verification of the separation vortex has been obtained by Walker, et. al.[24], for similar flow and motion conditions (see Figure 12). The extent of vortex entrapment in the near wake region is observed to correlate closely with the prolonged suction peak presence on the leeward airfoil surface. Similar visual records of the induced unsteady separation process obtained by other investigators in several different experimental geometries have confirmed that many qualitative similarities exist in these flows despite the configurational differences.[5-6]

The delay in boundary layer breakdown to separated flow conditions induced by airfoil pitching motion has been the subject of recent studies by Schreck[25] and Daley.[26] The strong dependence of stall onset angle on the dimensionless pitch rate has been documented in both investigations (see Figure 13). The monotonic increase in this relationship suggests that the rate of unsteady motion plays an important role in "controlling" the occurrence of the separation events.

Unsteady forces and moments have also been inferred from pressure distribution data for numerous airfoil motion histories.[23] Several examples of these results are provided in Figures 14 and 15. The influence of both pitch rate and amplitude on the character of force and moment histories is apparent from an examination of these results. The evolution of the lift coefficient as the motion progresses is significant. The magnitude of the overshoot beyond the static maximum lift value is especially dramatic, as is the persistence of these high lift levels to very large incidence angles. These results appear to be largely independent of airfoil shape. In some situations, near maximum lift levels were observed to sustain to nearly the maximum incidence condition. It is not clear whether this behavior would have continued to even higher angles had larger motion amplitudes been employed. Lift values were observed to decrease once the pitch-up motion was terminated. The slopes of the lift curves at low incidence are also seen to be somewhat affected by the extent of the unsteady pitch rate.

The pressure drag coefficient curves are also profoundly influenced by the magnitude of the pitch rate. However, the airfoil shape appears to play a more significant role in the determination of drag.

The pitching moment histories displayed in Figures 14 and 15 behave in a manner consistent with the model of a convecting spanwise-oriented vortex dominating the unsteady separated flowfield. An initial lag in pitching moment variation is followed by a pronounced nose down moment whose amplitude well exceeds the steady flow equivalent. The moment stall characteristics have been observed to exhibit some dependence on airfoil shape.

Francis, et. al.[23], have also examined the lift force history as a function of the dimensionless pitch rate, k_α. The variations of both the maximum lift incidence angle and the maximum lift coefficient with this parameter are depicted in Figure 16. These results incorporate data for several values of the maximum (or termination) angle, α_{max}. The overall shape of the curves and dependence on k_α are remarkably similar. Both variables increase rapidly and monotonically at low pitch rates followed by a decrease in the rate of rise when k_α exceeds 0.05. For any given dimensionless pitch rate, the magnitude of either variable can be affected by the maximum incidence angle. The above results suggest that unsteady vortex generation is influenced more profoundly at lower values of the dimensionless pitch rate and that a point of diminishing returns is soon reached if one attempts to delay separation and increase lift by increasing the airfoil pitch rate.

In the supermaneuver application, an overshoot of $C_{L_{max}}$ poses both a problem and a potential benefit. In an aerodynamic environment dominated by dynamic stall, the problem of achieving control of aircraft attitude and flight path is complicated by the

need for more control authority and responsiveness in order to offset the upsetting forces and moments due to asymmetric stall once it occurs. However, a benefit in terms of improved turn performance due to additional aerodynamic lift (and drag) may be achieved if control is retained.

Although the peak values of the parameters just described are good indications of airfoil performance, they are incapable of capturing the overall aerodynamic effects which are specific to variations in the airfoil motion history. To compensate for this deficiency, a parameter has been introduced which at least partly accounts for these temporal effects and is, itself, independent of motion type. This parameter is defined as the effective lift impulse function, and is formally described by the relation:

$$I_C \equiv \int_0^{T^*} \Delta C_\ell \, d\left(\frac{t}{\tau}\right) \qquad \ldots(2)$$

for all $\Delta C_\ell \equiv C_\ell - C_{\ell_{max_s}} \geq 0$

and $\tau = {}^{c}/_{U_\infty}$

and $T^* = \frac{TU_\infty}{c}$

where T is the total time that the lift coefficient exceeds the maximum static value. A similar definition can be created for other force or moment parameters. This parameter can be described as the area bounded by the lift-time curve from above and the static maximum lift value from below. It is a versatile measure of performance since it incorporates both lift magnitude and duration in a single variable. Note also that the freestream time constant is accounted for implicitly in the normalization.

The variation of the impulse parameter with dimensionless pitch rate for several cases is provided in Figure 17.

A rapid increase in the impulse parameter at low pitch rates is observed to be followed by a more gradual increase at the higher rates of motion. Significantly, the results suggest that maximum performance does not monotonically increase with maximum incidence of motion. In fact, results suggest that best performance for a given pitch rate can be obtained by terminating the unsteady motion at some maximum incidence angle which is, itself, a function of the pitch rate. A speculation is that the optimum termination angle is related to a particular stage in separation vortex development which is, of course, rate dependent. Termination at very large angles-of-attack is undesirable for maximizing lift generation since it results in an unfavorable geometric orientation with respect to the freestream.

V. CONTROL OF SUPERMANEUVERING FLIGHT

V.1 Vehicle Flight Mechanics and Control

The key to attaining supermaneuvering flight lies in the ability to control aircraft attitude and flight path while rapidly maneuvering into and out of the post-stall regime. Such control must also be blended with other capabilities of the weapons system in order to optimize total system performance and effectiveness. The role of the pilot in overall control of the system must be well thought out since his contribution is vital in the dynamic environment envisioned for future air combat.

One way to examine the potential vehicle control benefits expected from supermaneuverability is to compare the expected increased turn performance to that of a baseline modern aircraft which is limited in control to an angle-of-attack regime below stall. Consider a simplified representation of turn performance where gravity and thrust vector components are neglected. This simplification can be shown to yield good results for load factors, n, which exceed a value of about three, where $n = \frac{L}{W}$. In our approximation, turning rate (i.e., rate of change of velocity vector angular orientation with respect to the earth) is:

$$\dot{\gamma} \approx n \frac{g}{V} = \left(\frac{L}{W}\right)\frac{g}{V} = \frac{C_L \, \rho V S g}{2W} \qquad \ldots(3)$$

Total angle change during a maneuver can then be expressed:

$$\Delta\gamma = \int_0^T \dot{\gamma} \, dt \approx \frac{g}{W} \int_0^T \left(\frac{L}{V}\right) dt$$

or, equivalently:

$$\Delta\gamma \propto \frac{g\rho S}{2W} \int_0^T (C_L V) \, dt \qquad \ldots(4)$$

From an aerodynamic standpoint, this result relates the integrated effect of circulation to vehicle turn performance during the maneuver. It should be noted that, in this simplified analysis, lateral forces in the body-fixed coordinate system

have been neglected. However, the significance of increased additional lift on vehicle turn performance is readily apparent.

To amplify on this notion further, consider an aircraft whose lifting capabilities can be defined by the graph in Figure 18a. In this figure, C_{L_s} is a representative lift coefficient for a typical sustained maneuver condition. At a somewhat higher value, C_{L_1} represents a typical limit determined by design constraints, such as control authority. $C_{L_{max}}$ is the steady-flow maximum lift limit usually associated with cataclysmic stall, while C_{L_2} is a transient dynamic stall overshoot value which is determined by the non-dimensional pitch rate and amplitude.

Four maneuvers are plotted and compared in Figures 18 and 19. Figure 18b depicts the load-factor versus Mach number and $P_s = 0$ characteristics of the aircraft where the initial condition for each maneuver is shown at point A. Figure 19 shows the corresponding turn rate time histories. Maneuver (1) involves a rapid pitch-up (i.e., $\dot{\alpha} \geq$ 30°/sec) to the angle-of-attack for sustained performance. Note that a moderate, constant value of turn rate is achieved for this steady, level turn. Maneuver (2) also involves a rapid pitch-up, only to a high value of C_L. In this case, higher values of turn rate are achieved while speed decreases initially but stabilizes once drag equals thrust. Maneuver (3) involves faster turn rates, but more rapid deceleration to a sustained turn rate condition. Maneuver (4) is assumed to involve the transient dynamic stall effect which provides even better initial turning performance. The possibility of a large departure from the steady flow envelope is evident here.

In these examples, the advantages of high-angle-of-attack capability are shown to result in faster turning especially during the initial portion of dynamic maneuvers. It should be noted that other means of initiating the dynamic maneuver (i.e., different lift-time histories) and penetrating the stall regime may lead to similarly favorable performance improvements.

Turn radius is another important parameter. In the assumed approximation which neglects gravity, lateral body forces, and the thrust turning component, an expression for turn radius may be written:

$$R \approx \frac{V^2}{ng} = \frac{2W}{\rho S g}\left(\frac{1}{C_L}\right) \qquad \ldots(5)$$

This relation shows the advantage of high values of lift coefficient for achieving a reduced turn radius.

Mere recognition of the importance of enhanced dynamic forces is not enough. Ultimately, they can be exploited and optimized only if a means can be found to control them. The possible use of new aerodynamic techniques to achieve this capability is discussed in the next section. However, it is important to consider the potential of thrust vectoring as another possible means to this end.

Thrust vectoring can be used along with gravity to affect both turn rate and radius. Analysis, simulation, and flight experience have shown that use of thrust vectoring and management of flight path to take advantage of gravity are important in further control of acceleration, deceleration, and turning of the velocity vector during combat. The additional ability to "point and shoot", as discussed previously, is of perhaps equal importance in determining combat effectiveness.

The overriding requirement, however, is to achieve control of aircraft attitude and flight path in a way that involves the pilot functioning in an optimum sense as the system manager. The direct control of the flowfield and thrust vector necessary to achieve a high degree of supermaneuverability will require a high level of automation. The need for interactive (active feedback) control of the flowfield and thrust vector presents a technical challenge which involves extensive integration of complex functions and technologies.

V.2 Flow Control

The ability to manage and control the time dependent, separated flows which earmark the aerodynamic environment is of paramount importance if true supermaneuverable flight is to be achieved. Any successful scheme for controlling flight vehicle attitude and flight path must have some provision for manipulating the aerodynamic forces which will be encountered. The exercise of that control may involve both global and local separation phenomena and any of a variety of potential techniques. Both enhancement and suppression of those phenomena offer possible control strategies.

The topic of flow separation control is receiving a great deal of attention, as evidenced by the results of the recent AIAA Shear Flow Control Conference.* This interest is due, in part, to the availability and degree of capability of several enabling technologies including structures, actuator mechanisms and, most

* AIAA Shear Flow Control Conference was held in Boulder, Colorado (USA), from 12-14 March 1984.

significantly, digital real-time control methodologies. Although man has only recently reached the threshold of success in controlling separated flows, nature has incorporated these techniques in the flying and propulsion capabilities of several organisms, albeit at much lower Reynolds and Mach numbers.[27-28]

V.2.1 Control Techniques Under Investigation

Past attempts to "control" separated flows have focused primarily on reducing or eliminating regions of separation and promoting attached flow behavior to the maximal extent. The classical vortex generator found on many contemporary aircraft is an example of a control device designed for just this purpose. Although the consequences of this approach can often result in a reduction in efficiency (i.e., increased surface friction drag), the potential benefits have been found to outweigh this negative aspect in many conventional applications.

Based on the previous discussion, however, the supermaneuver aerodynamic environment can be expected to be anything but conventional. It can be expected to be dominated by separated flow to a degree that defies the use of conventional control methodologies. The prospect of controlling an unsteady, motion driven flow environment offers new challenges and new opportunities. The energetic, unsteady leading edge separation vortex may be one of these. A virtual fact of life in dynamic, high angle-of-attack applications, this type of flow structure must be reckoned with in any case, but may prove to be highly beneficial if appropriately manipulated. If energy can be added to the stall vortex, or if its residence time near the lifting surface can be increased, enhanced transient lift (and drag) could provide improvements in turning and pointing performance. In a sense, all investigations of dynamic stall phenomena are studies of open loop control as effected by prescribed time-dependent boundary conditions.

Several efforts have focused on these types of flows with an orientation toward the control aspect. Lang[29] examined the unsteady loading induced by a harmonically oscillating fence-type spoiler located on one surface of an airfoil and its effect on both a fixed and moving trailing edge flap. A follow-on investigation of the spoiler-generated flowfield by Francis, et. al.[4] revealed the developing vortical character of the separation zone and correlated the behavior of the suction peak on the airfoil surface.

The influence of oscillating spoiler motion on the flowfield of an airfoil at high incidence has recently been investigated by Luttges, et. al.[30] In their experiments, a spoiler located at the 20% chord location on the suction surface was found to induce small spanwise vortices which profoundly effected flowfield curvature in manner suggestive of increased lifting performance. More recent measurements of unsteady load enhancements of 60 - 110% above the maximum steady flow value have confirmed this hypothesis.[31] These results and the overall flow phenomenology have been verified for cases of combined airfoil pitching and spoiler oscillations as well. Furthermore, separate experiments employing a pulsed air jet in place of the spoiler have revealed a similar flow structure in those cases.

The advantages of a generic flow geometry for studying control issues have best been exploited in several recent experimental investigations by Koga, et. al.[5] and Reisenthal.[6] Their efforts have focused on a variety of motions produced by a computer controlled hinge-type spoiler in concert with various boundary conditions including a flat surface, an upstream-located two-dimensional wedge and an upstream-located backward facing step. Koga's studies[5] of the unsteady separated region produced by different duty cycles (motion time histories) have indicated a profound influence on the character of separation by the time-dependent boundary conditions (Figure 20). Given identical amplitude and period conditions, the triangular waveform, 90% duty cycle case at the right side of the Figure is observed to result in a more well organized, energetic, and persistent vortex than the other cases having the same amplitude and period.

The effect of the oscillating spoiler located downstream of the wedge (illustrated in Figure 21) is equally profound. With the spoiler retracted, the wedge generates a separated free shear layer emanating from the surface at the wedge angle, emulating the flowfield of a classical separation bubble. Although blanketed completely by the wedge, the spoiler has demonstrated its effectiveness in altering the separated flowfield for a variety of amplitude and frequency conditions. The energized flow can greatly shorten the mean reattachment distance (factor of 2) under some conditions.

Reisenthal's results[6] show similar behavior and effects on the otherwise separated flow downstream of a backward facing step. The additional advantage of this flow geometry is the degree of control provided on the initial, separating boundary layer. The effect on an initially turbulent boundary layer is shown in Figure 22 which illustrates an instantaneous visualization, isovorticity contours, and the surface pressure distribution for two phase points in a triangular motion cycle. These results strongly suggest that the control imparted by the active oscillation is independent of the character of the incoming boundary layer; i.e., transitional versus turbulent.

Reisenthal has also documented the effect of spoiler frequency on reattachment length and provided an explanation for the peculiar behavior of this function (see Figure 23). Local minima found at several low frequencies are attributed to different physical mechanisms. At the lowest reduced frequencies, the unsteady modulation of the separated shear layer by the oscillating spoiler determines the flow reattachment history and mean location. This mechanism has been termed "induced shear-layer control". For $k \geq 0.03$, the formation of a large scale vortical structure of significant energy plays a significant role in the control process. The influence of this second mechanism, referred to as "formed vortex control", increases as the reduced frequency is increased. The combination of both phenomena at $k \approx 0.06$ leads to an optimum reattachment condition. At larger values of k, the control optimization curve bifurcates into an intermediate pressure recovery branch characterized by multiple formed vortices and an asymmetric pressure recovery branch which reflects a deterioration of control at very high frequencies. The scaling laws which govern the above behavior have recently been postulated by Nagib, et. al.[32]

Finally, it is appropriate to mention several recent investigations of acoustically-induced separation control. Ahuja[33] has demonstrated a reduction in size of the separated region on an airfoil at incidence when the separated shear layer is actively stimulated with sound at selected frequencies. This result is a reaffirmation of the findings of Quinn[34] and others.[35-36] The potential utility of acoustically driven control in supermaneuver applications is speculative at best given the demands of the changing, dynamic environment expected.

V.2.2 Prospects for Interactive Control

Attempts to implement real-time, interactive control of attached viscous shear flows have met with limited success under some conditions. These experiments have involved transitioning boundary layers and included nonlinear but periodic time dependent wave shapes with two-dimensional mean and unsteady flow spatial characteristics achieved in a laboratory setting.[37]

Despite the more complex, rotational character of motion-induced, unsteady separation, there are signs that true interactive control may be possible in these circumstances as well. The relatively large time constants associated with the slow convection speeds of these vortical structures (typically 15-50% of freestream velocity) coupled with the low speeds expected in portions of the supermaneuver envelope, provide optimism from the standpoint of practical control utility. The degree of flow reorganization resulting from the induced effects of the energetic separation vortex is also considered to be a promising positive factor.

The key to the successful demonstration of interactive control of unsteady separated flows is a more complete understanding of the role of the continually changing boundary conditions. The ability to sense change in the flowfield character even at real-time speeds is secondary to the need for a practical means of altering the boundary conditions to influence flow developments in a known and positive manner. For example, little is known of the influence of continuous boundary shaping as means of achieving vortex entrapment (e.g., changing airfoil camber in real time in response to the instantaneous position of the vortex centroid). The development of interactive control methodologies hinges on a continued research program focused on fundamental concepts as well as assessing and extending practical limitations of control implementation.

VI. THE IMPORTANCE OF INTEGRATION

Effectiveness of a fighter aircraft with supermaneuver capabilities requires that the pilot be involved at a very high level of decision-making and control. He must have access to data on the threat, the external (combat) situation, and on the state of his vehicle. Such data must be blended from appropriate sensors and presented to him in a format which allows for rapid interpretation and action. The data must illustrate the "big picture" of the combat situation so that his actions can be quickly determined. Once initiated, the aircraft and weapons must respond quickly to implement the intended tactic.

Detailed control functions must be automated to a very high degree. Time constants associated with complex sequences of dynamical events are too short for direct pilot inputs and interaction. Our concept is that an "automation core" which involves integration of propulsion (thrust vector -- inlet, engine, and nozzle), flowfield, structural shape and dynamics (aeroelastic effects), navigation, fire, and weapons control functions, should be aggressively developed to relieve the pilot of high workload demands during combat.

The ultimate basis to be used to design the next generation, supermaneuverable aircraft would be a radical extension of current flying qualities criteria. The flight path, vehicle, and man/machine dynamics of such a weapons system will undoubtedly force us to define new pilot-centered design criteria.

The integration of the many advanced technologies necessary to achieve true supermaneuverable flight possess significant technical and management challenges. To meet and overcome them will require dedicated teams of advanced technology specialists

led by a new breed of multi-disciplinary, system-level design engineers willing to experiment with new integration methodologies. The potential operational payoff justifies the investment in time, people, and development costs.

VII. FUTURE RESEARCH REQUIREMENTS

VII.1 Vehicle Control

Further studies are needed in the areas of:

a. operational effectiveness of supermaneuvers

b. definition of "supermaneuvers"

c. determination of flowfield and propulsion control requirements

d. design criteria for control systems -- flow, propulsion, and flight control

e. new control methodologies

f. pilot/vehicle dynamic interactions

g. aircraft/weapons capability tradeoffs

h. new flying qualities criteria

i. multidiscipline design methodology

The recommended approach is to aggressively pursue concurrent and coordinated basic research, exploratory, and advanced development programs. Experiments, including those involving extensive integration and piloted simulations, should be used to provide understanding of the payoffs and technical needs.

Control of aircraft attitude and flight path in a highly dynamic post-stall maneuvering environment is expected to require development of interactive flow control and the use of integrated thrust vectoring. The path to achieve success is not exactly clear, but the objective of controlled flight beyond traditional aircraft limits is fairly well defined.

VII.2 Aerodynamics and Flow Control Research

An improved understanding of the aerodynamic environment anticipated in supermaneuvering flight and the pursuit of methods to control it are continuing objectives of both basic and applied research activities. The current state of knowledge in unsteady aerodynamics in which large amplitude, time-dependent changes in the boundary conditions may play a significant role is in its infancy. Much less is known of how to control and exploit resulting flow phenomena.

Continuing emphasis should be devoted to studies of flow separation mechanisms as they apply on both a global and local scale. These efforts should explore a variety of flow geometries including all forms of lifting and nonlifting surfaces and bodies, as well as "generic" configurations which might be capable of isolating specific physical mechanisms of importance. A way to characterize and categorize the effects resulting from the complex time-dependent boundary conditions should be pursued in this regard.

More attention should be directed toward the potential significance of three-dimensional effects in these flows. As indicated in a previous section, most research on lifting surfaces, to date, has focused on airfoil flows and performance. It should be recognized that three-dimensional flow behavior can result from several possible sources, including:

a. naturally induced effects initiated by inherent flow mechanisms such as shear layer instability

b. shape-induced effects which result from the three-dimensional character of the boundary shape or planform (e.g., wing tip geometry effects); or

c. motion-induced effects which may be caused by complex time-dependent behavior of boundaries in multiple degrees of freedom.

The important role of vortex behavior is evident from much of the preceding discussion. The fundamental understanding of vortex surface and vortex-vortex interactions must also be pursued intensely.

The development of new and efficient (from a flight vehicle point of view) flow control strategies represents another major arena destined to receive increased attention. The effects of motion history and three-dimensionality must be understood irrespective of the method of control. Active and interactive control methodologies to be explored include those involving mechanical techniques (e.g., actuated surfaces),

control jets and shear layers, and possibly, methods which exploit acoustic interactions.

The optimization of vortex energization and subsequent entrapment poses a significant control challenge. Can the dynamic stall vortex (or any unsteady separation vortex) be thought of as a short duration "aerodynamic battery"? If so, what is the ultimate potential for exploitation? If the answers to these questions are positive, the potential advantage of a robotic wing capable of real time aerodynamic interaction using deformable surfaces, control jets, etc., may well be worth the development costs.

Finally, the control of highly coherent, high intensity turbulent flow structures at low and high velocities will improve handling and ride qualities and may improve overall aerodynamic efficiency.

VIII. CONCLUSIONS

A forecast of future aerial combat predicated on anticipated technological advances and weapons developments suggests a need for supermaneuverable aircraft possessing greatly enhanced turning and virtually instantaneous point-and-shoot capabilities. The potential advantages of exploiting this unique flight environment have been discussed along with a detailed description of expected vehicle dynamic behavior. An emerging picture of the unsteady aerodynamic behavior which will be experienced during these violent maneuvers dictates a need for greater vehicle and flowfield control capabilities far in excess of any previously employed in application. However, the successful implementation of advanced control techniques may well beneficially exploit the unusual flow phenomena associated with this nonclassical method of flight. The research discoveries and developmental ideas generated during the next decade will likely alter the concept of maneuvering flight as we know it and lead to a new generation of aircraft with vastly improved combat capabilities.

REFERENCES

1. Skow, A. and Hamilton, W., "Advanced Measures of Merit for Fighter Aircraft Performance and Maneuverability", draft report prepared under contract F33615-83-C-3000, Task 84-17, AFWAL/FIG, Wright-Patterson AFB OH, September 1984.

2. Herbst, W.B., "Supermaneuverability", DGLR Paper No. 83-106, Munich, Germany, 7 October 1983.

3. Miller, L.E., "Post Stall Maneuvers and Thrust Vectoring Performance Analysis", AFWAL Technical Report 84-3109, AFWAL/FIM, Wright-Patterson AFB OH, (to be published).

4. Francis, M.S., Keesee, J.E., Lang, J.D., Sparks G.W., and Sisson, G.E., "Aerodynamic Characteristics of an Unsteady Separated Flow", AIAA Journal, Vol 17, 1979, pp 1332-1339.

5. Koga, D.J., Reisenthal, P., and Nagib, H.M., "Control of Separated Flowfields Using Forced Unsteadiness", Illinois Institute of Technology, Fluids and Heat Transfer Report R84-1, January 1984.

6. Reisenthal, P.H., "Reattachment Control Behind a Rearward Facing Step Using Forced Unsteadiness", M.S. Thesis, Illinois Institute of Technology, December 1984.

7. Sears, W.R. and Telionis, D.P., "Unsteady Boundary-Layer Separation", Internal Report, Cornell University, 1970.

8. Simpson, R.L., Shivaprasad, B.G., and Chew, Y.T., "Some Features of Unsteady Separating Turbulent Boundary Layers", Proceedings of the 7th Biannual Symposium on Turbulence, University of Missouri-Rolla, 1981.

9. Viets, H., Piatt, M. and Ball, M., "Forced Vortices Near a Wall", AIAA 19th Aerospace Sciences Meeting, St Louis Mo, 12-15 January 1981.

10. Palmer, M. and Freymuth, P., "Analysis of Vortex Development from Visualizations of Accelerating Flow Around on Airfoil, Starting from Rest", AIAA-84-1568, June 1984.

11. Finaish, F., Palmer, M., and Freymuth, P., "A Parametric Analysis of Vortex Patterns Visualized Behind Airfoils in Accelerating Flow", Proceedings of the 9th Biannual Symposium on Turbulence, October 1984 (also to appear in Experiments in Fluids).

12. Kramer, M., "Die Zunahme des Maximalauftriebes von Tragflugeln bei plotzlicher Anstellwinkel-vergroszerung (Boeneffekt)", Zeitschrift fur Flugtechnik und Motorluftschiffahrt, Vol 23, No. 7, 14 April 1932, pp. 185-189.

13. Carr, L.W., McAlister, K.W., and McCroskey, W.J., "Analysis of the Development of Dynamic Stall Based on Oscillating Airfoil Experiments", NASA TN D-8382, January 1977.

14. McCroskey, W.J., Carr, L.W., and McAlister, K.W., "Dynamic Stall Experiments on Oscillating Airfoils", AIAA Journal, Vol 14, No. 1, January 1976, pp. 57-63.

15. McAlister, K.W., Carr, L.W., and McCroskey, W.J., "Dynamic Stall Experiments on the NACA 0012 Airfoil", NASA Technical Paper 1100, January 1978.

16. McCroskey, W.J., "Some Current Research in Unsteady Fluid Dynamics - The 1976 Freeman Scholar Lecture", Journal of Fluids Engineering, March 1977, pp. 8-39.

17. McCroskey, W.J., McAlister, K.W., Carr, L.W., Pucci, S.L., Lambert, O. and Indergand, R.F., "Dynamic Stall on Advanced Airfoil Sections", Journal of the American Helicopter Society, July 1981, pp. 40-50.

18. Ham, Norman D., "Aerodynamic Loading on a Two-Dimensional Airfoil During Dynamic Stall," AIAA Journal, Vol. 6, No. 10, October 1968, pp. 1927-1934.

19. Ham, N.D., and Garelick, M.S., "Dynamic Stall Considerations in Helicopter Rotors," Journal of the American Helicopter Society, Vol. 13, April 1968, pp. 49-55.

20. Hsieh, B.J., "Dynamic Stall on Oscillating Airfoils in Oscillating Free Streams," Ph.D. Dissertation, Illinois Institute of Technology, Chicago IL, May 1979.

21. Saxena, L.S., Fejer, A.A., and Morkovin, M.V., "Effects of Periodic Changes in Free Stream Velocity on Flows Over Airfoils Near Static Stall," Nonsteady Fluid Dynamics, Proceedings of the Winter Annual Meeting ASME, San Francisco CA, 10-15 December 1978, pp. 111-116.

22. Carta, F.O. and Ham, N.D., "An Analysis of the Stall Flutter Instability of Helicopters Rotor Blades", American Helicopter Society, 23rd Annual National Forum Proceedings, No. 130, May 1967.

23. Francis, M.S. and Keesee, J.E., "Airfoil Dynamic Stall Performance with Large Amplitude Motions", to appear in AIAA Journal.

24. Walker, J.M., Helin, H.E., and Strickland, J.H., "An Experimental Investigation of an Airfoil Undergoing Large Amplitude Pitching Motions", AIAA-85-0039, January 1985.

25. Schreck, S. J., "Continued Experimental Investigation of Dynamic Stall", M. S. Thesis, Air Force Institute of Technology, AFIT/GAE/AA/83D-21, 1983.

26. Daley, Daniel C., "Experimental Investigation of Dynamic Stall," M. S. Thesis, Air Force Institute of Technology, AFIT/GAE/AA/82D-6, 1983.

27. Maxworthy, T., "The Fluid Dynamics of Insect Flight", Annual Review of Fluid Mechanics, Vol. 13, 1981, pp. 329-350.

28. Luttges, M.W., Somps, C.J., Kliss, M., and Robinson, M.C., "Unsteady Separated Flows: Generation and Use by Insects", Workshop on Unsteady Separated Flow, Proceedings, U.S. Air Force Academy, August 1983, pp. 127-136.

29. Lang, J.D., "The Interaction of an Oscillating Airfoil and/or Flap with a Separating Flow", Ph.D. Thesis, Cranfield Institute of Technology, Cranfield, England, January 1975.

30. Luttges, M.W., Robinson, M.C., and Kennedy, D.A., "Control of Unsteady Separated Flow Structures on Airfoils", AIAA-85-0531, AIAA Shear Flow Control Conference, Boulder CO, March 1984.

31. Luttges, M.W., Private Communication, January 1985.

32. Nagib, H.M., Reisenthal, P.H., and Koga, D.J., "On the Dynamical Scaling of Forced Unsteady Separated Flows", AIAA-85-0553, AIAA Shear Flow Control Conference, Boulder CO, March 1984.

33. Ahuja, K.K., "Basic Experimental Study of the Coupling Between Flow Instabilities and Incident Sound", NASA CR 3789, March 1984.

34. Quinn, B., "The effect of sound on the tail of several bodies", First-Award Student Papers, Institute of Aerospace Sciences, 1961.

35. Mueller, T.J. and Batill, S.M., "Experimental Studies of the Laminar Separation Bubbles on a Two-Dimensional Airfoil at Low Reynolds Numbers", AIAA Journal, Vol 20, 1982, pp 457-463.

36. Rockwell D. and Toda, K., "Effects of application of acoustic fields on attached jet flows", ASME Transactions, Journal of Basic Engineering, Vol 93, 1971, pp 63-73.

37. Nosenchuck, D.M. and Lynch, M.K., "Active Control of Low-Speed Streak Bursting in Turbulent Spots", AIAA-85-0535, AIAA Shear Flow Control Conference, Boulder CO, March 1984.

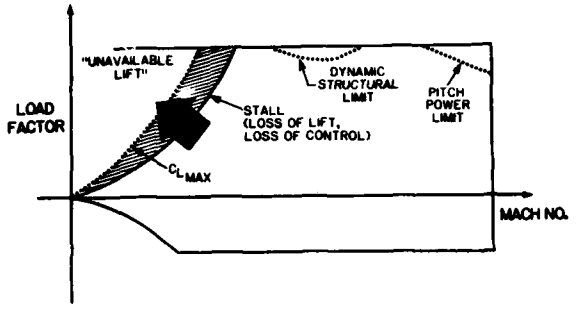

Figure 1. FLIGHT ENVELOPE LIMITS

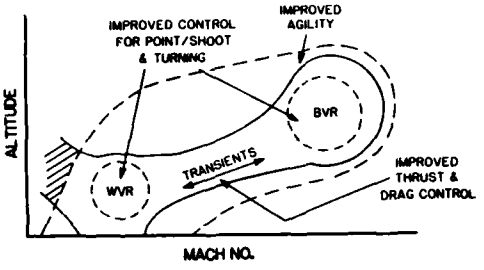

Figure 2. COMBAT ARENAS

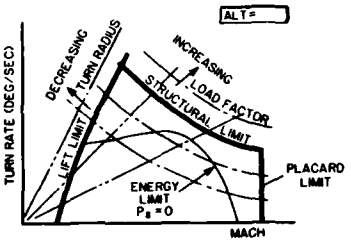

Figure 3. STATIC MANEUVERABILITY

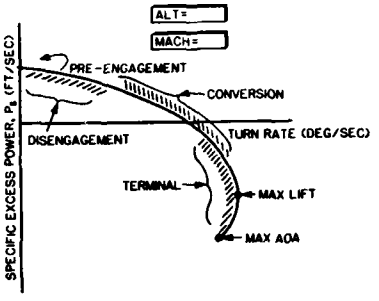

Figure 4. CLASSIC ENERGY-MANEUVERABILITY

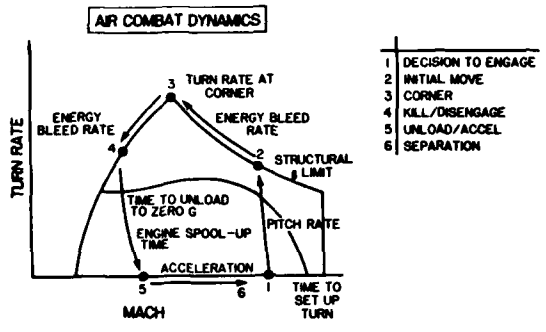

Figure 5. ENGAGEMENT SEQUENCE

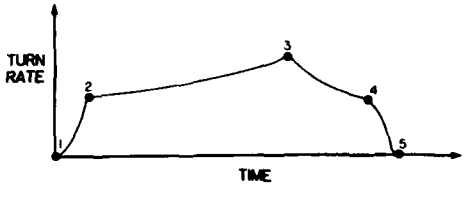

Figure 6. ENGAGEMENT TURN-RATE HISTORY

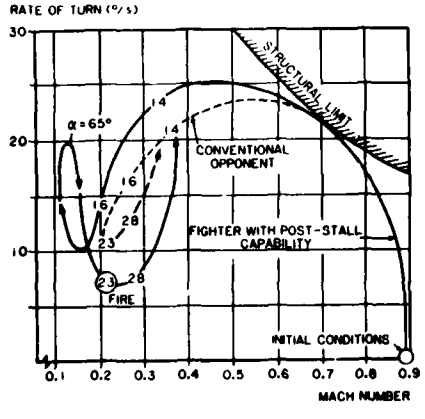

Figure 7. POST-STALL & CONVENTIONAL MANEUVERING

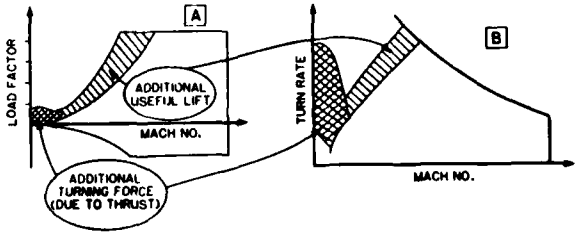

Figure 8. EFFECT OF IMPROVED CONTROL

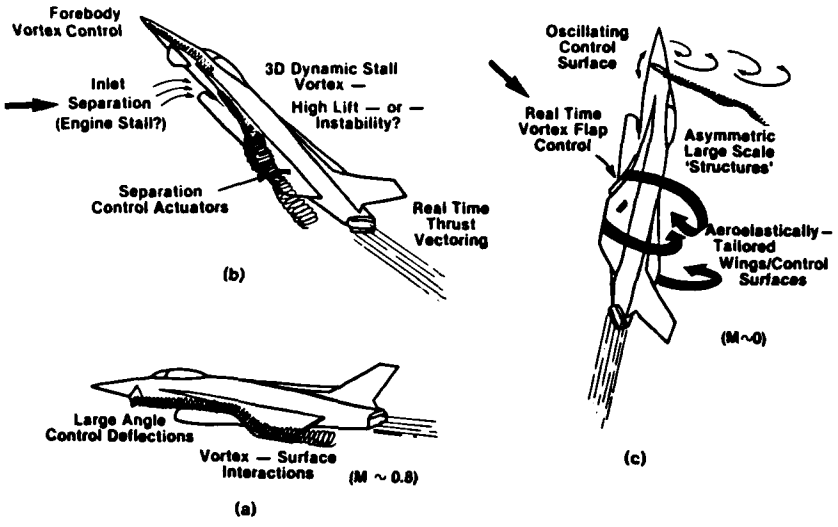

Figure 9. POST STALL MANEUVER - ENTRY PHASE

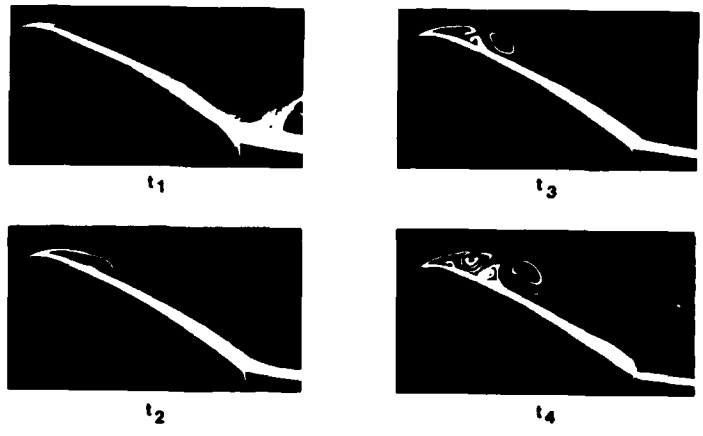

FIGURE 10. VISUALIZED EVOLUTION OF AIRFOIL LEADING EDGE FLOW SEPARATION, NACA 0015, FLOW ACCELERATED FROM REST.

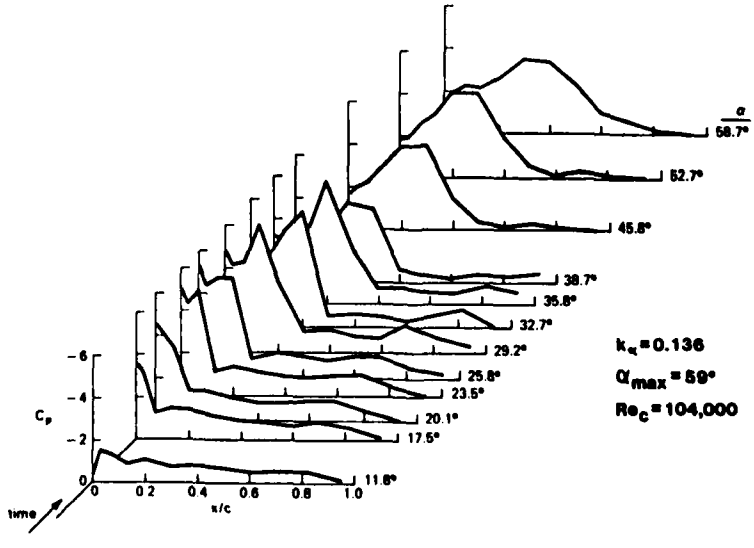

Figure 11. SUCTION SURFACE PRESSURE DISTRIBUTIONS - EVOLUTION WITH INCREASING ANGLE-OF-ATTACK (TIME), NACA 64_1 A012(13).

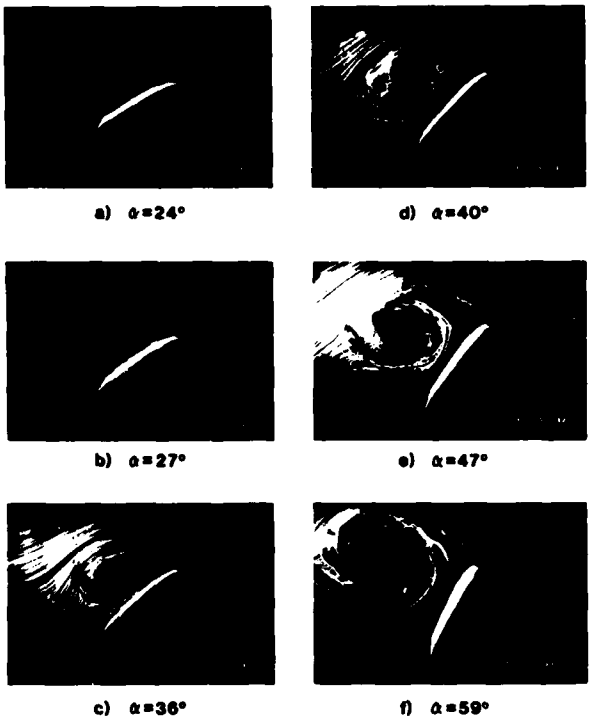

FIGURE 12. DEVELOPMENT OF DYNAMIC STALL VORTEX, CONSTANT $\dot{\alpha}$ MOTION; K_α = 0.1, REYNOLDS NUMBER = 45,000.

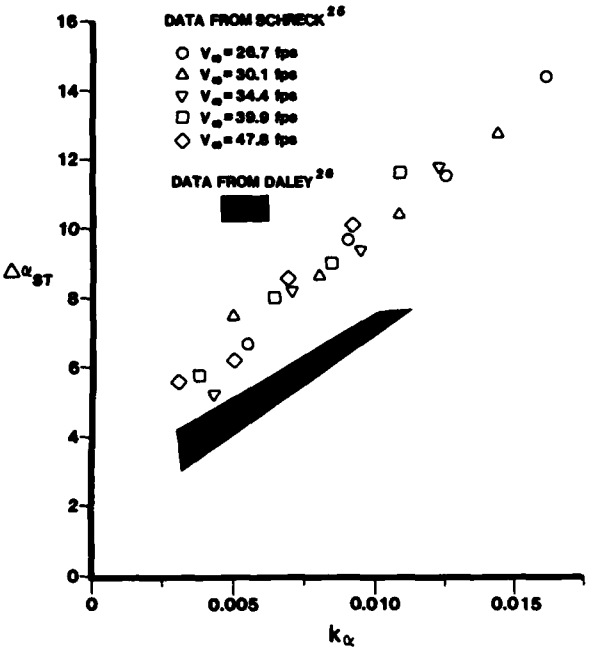

Figure 13. VARIATION OF DYNAMIC STALL ANGLE INCREMENT $[\Delta\alpha_{ST} = \alpha_{STALL} - \alpha_{STALL(STEADY)}]$ WITH NONDIMENSIONAL PITCH RATE.

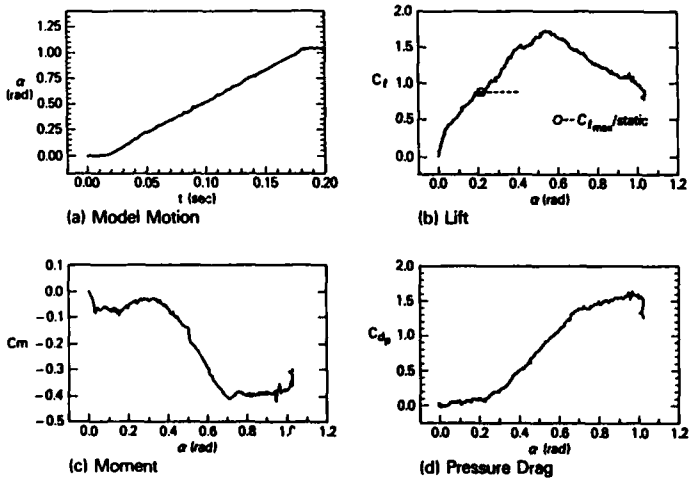

Figure 14. FORCE AND MOMENT CHARACTERISTICS, NACA 0012; k_α=0.047, α_{max}=60°, REYNOLDS NUMBER=80,000.

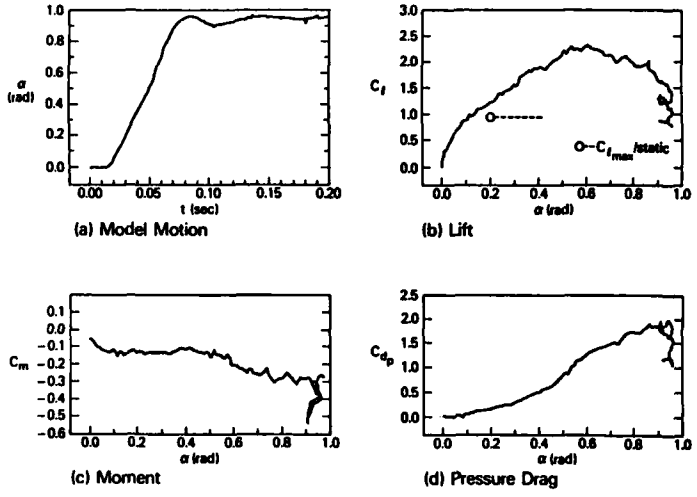

Figure 15. FORCE AND MOMENT CHARACTERISTICS, NACA 0012; $k_\alpha = 0.130$, $\alpha_{max} = 55°$, REYNOLDS NUMBER = 81,500.

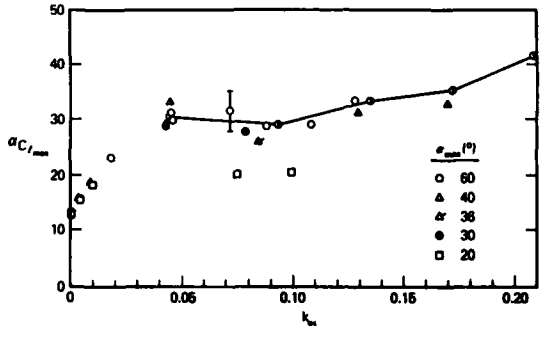

(a) MAXIMUM LIFT ANGLE

Figure 16. VARIATION OF AIRFOIL MAXIMUM LIFT PARAMETERS WITH DIMENSIONLESS PITCH RATE [OPEN SYMBOLS - NACA 0012, *HALF-SOLID* SYMBOLS-NACA 64, A012(13)].

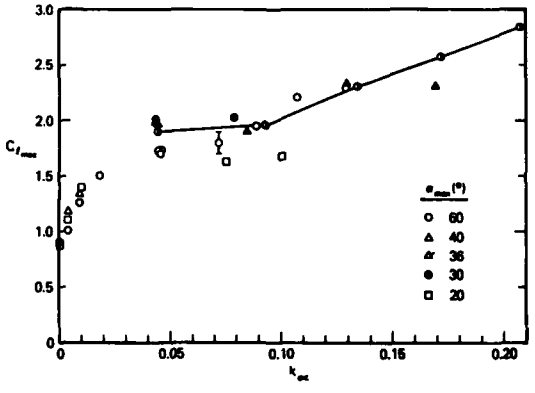

(b) MAXIMUM LIFT COEFFICIENT

Figure 16 (CONT.)

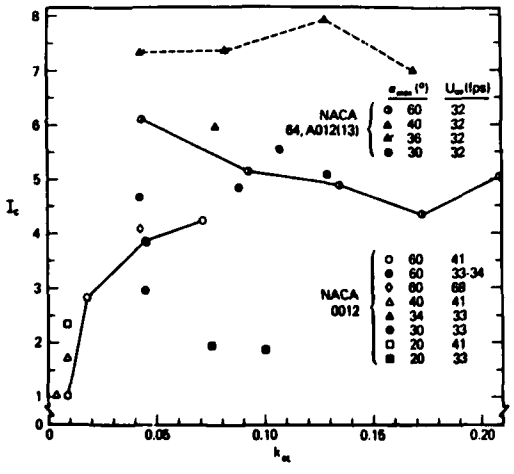

Figure 17. DIMENSIONLESS IMPULSE VARIATION WITH PITCH RATE.

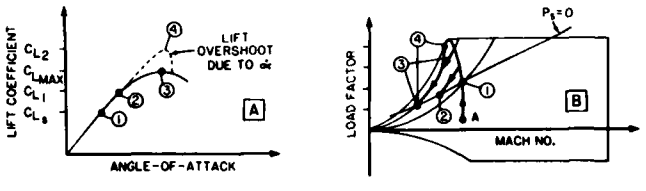

Figure 18. MANEUVER SEQUENCES

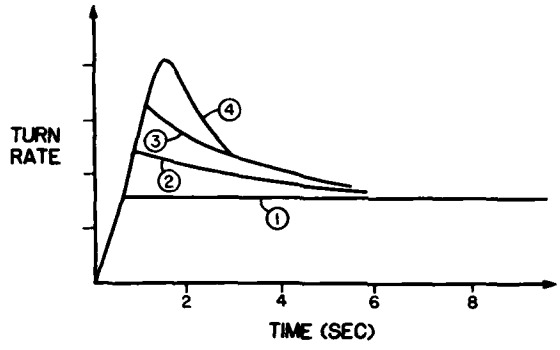

Figure 19. TURN RATE TIME HISTORIES

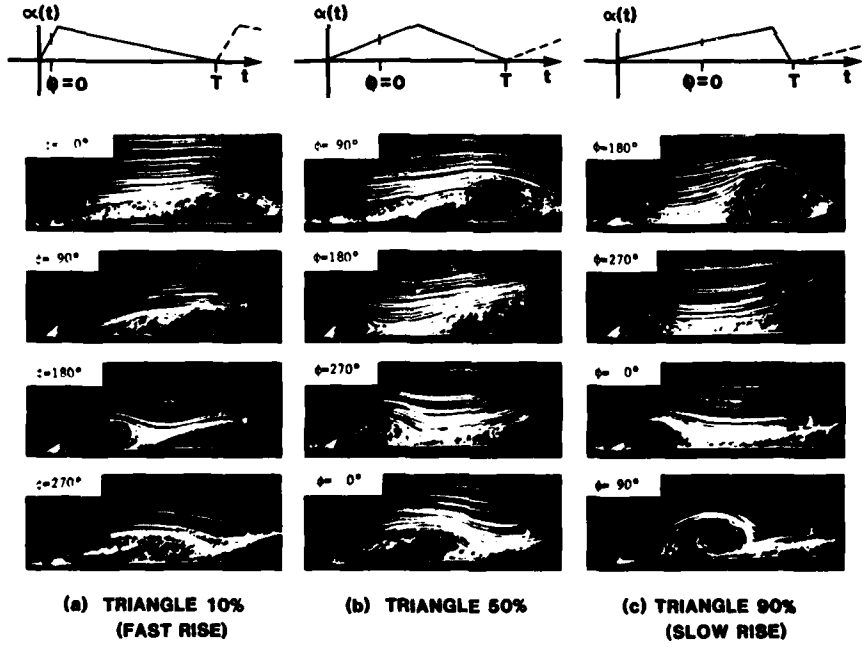

(a) TRIANGLE 10% (FAST RISE)

(b) TRIANGLE 50%

(c) TRIANGLE 90% (SLOW RISE)

FIGURE 20. FLOW VISUALIZATION - EFFECT OF OSCILLATING FLAP WAVEFORM AT EQUIVALENT REDUCED FREQUENCY, $K_{FLAP} = 0.04$

FIGURE 21. FLOW VISUALIZATION-SEPARATED FLOW CONTROL COMPARISON OF PASSIVE AND ACTIVE CONTROL FLAPS

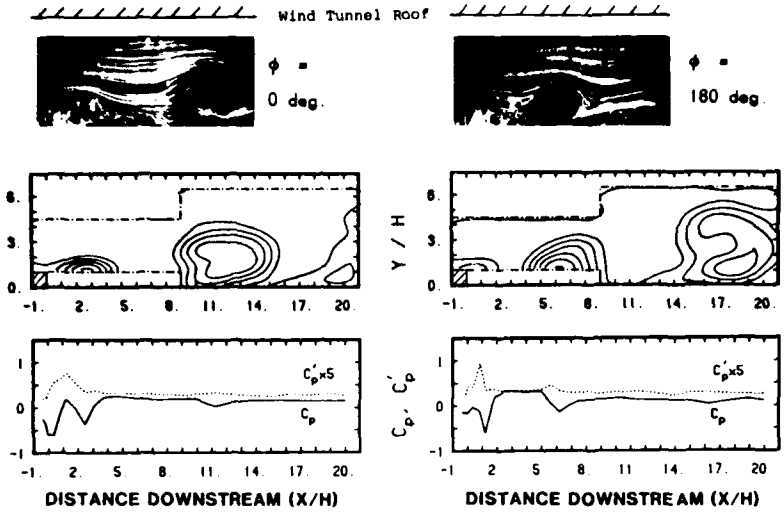

FIGURE 22. COMPOSITE FLOWFIELD DESCRIPTION FOR TRIANGULAR WAVE FORM AT HIGH FREQUENCY (90% TRIANGLE, 10 Hz, 0 TO 90 DEG., 5M/S, TURBULENT, κ'=0.08, x'/H = 0)

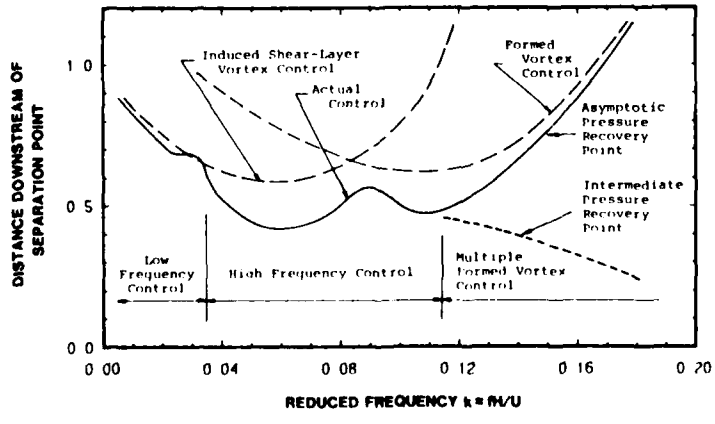

Figure 23. SCHEMATIC SUMMARIZING THE DIFFERENT MECHANISMS INVOLVED IN UNSTEADY SEPARATED FLOW CONTROL - VARIATION OF REATTACHMENT LOCATION WITH CONTROL FREQUENCY

ON THE INTERFACE BETWEEN UNSTEADY AERODYNAMICS, DYNAMICS AND CONTROL

by

G.J.Hancock and R.Vepa
Department of Aeronautical Engineering
Queen Mary College
(University of London)
Mile End Road
London E1 4NS
England

SUMMARY

This Paper explains the problems of interfacing the mathematical representation of linearised unsteady aerodynamics with dynamic response such that the eigenvalues of the dynamic response are correctly obtained. These eigenvalues are then used in control synthesis.

Particular attention is paid to $C_{M_{\dot{\alpha}}}$ in the context of aircraft dynamics, the concept of quasi-steady aerodynamics is clarified.

NOTATION

c	mean chord
$C_{M_H}(\hat{t})$	moment coefficient, about pitch axis, of response to step input
$C_{M_\delta}(\hat{t})$	moment coefficient, about pitch axis, of response to impulse input
$\tilde{C}_M(\nu)$, $\tilde{C}_{M_\theta}(\nu)$, $\tilde{C}_{M_{\dot{\theta}}}(\nu)$	oscillatory moment coefficients
$\bar{C}_{M_H}(s)$, $\bar{C}_{M_\delta}(s)$	Laplace Transforms
C_{M_θ}, $C_{M_{\dot{\theta}}}$	constant coefficients
$C_{M_H}(\hat{t})$, $C_{M_\delta}(\hat{t})$	functions within $C_{M_H}(\hat{t})$ and $C_{M_\delta}(\hat{t})$
k_0, k_1, k_2	constants
M_∞	free stream Mach number
$s(=\mu+i\omega)$	Laplace Transform
S_W	wing area
t	time
$\hat{t}=tV/c$	non-dimensional time
V	forward speed
θ	pitch angle
$\nu(=\omega c/V)$	frequency parameter
ω	frequency (rad/s)
μ	real part of s

1. INTRODUCTION

The title of this Conference is Unsteady Aerodynamics - Its Fundamentals and Applications to Aircraft Dynamics. It is right and proper that fundamentals and applications should be discussed together. Unsteady aerodynamics, unlike steady aerodynamics, is not a discipline or subject area which can be isolated from the context(s) in which it is to be used. In fact it is more relevant and constructive to concentrate on the applications first, so a more appropriate title might be 'Unsteady Aerodynamics - Its Applications and Appropriate Fundamentals'. It is only by studying applications that the specification for unsteady aerodynamics can be understood and requirements for research in unsteady aerodynamics can be formulated.

Unsteady aerodynamics affect all aerospace vehicles; fixed wing aeroplanes, helicopters and missiles. But for brevity, this presentation is limited to fixed wing aeroplanes.

To indicate the range of applications of unsteady aerodynamics, the various technical areas in the design and operation of aircraft and which incorporate unsteady aerodynamics in varying degrees are:

Overall Controllability

Flutter

Structural Strength of Transport Aircraft

Control System Design

Flight Simulation (Research and Training)

Fatigue Monitoring in Operation

Overall controllability, or alternatively 'aircraft dynamics', involves the integrated inertia characteristics, quasi-steady structural stiffness and very low frequency aerodynamics.

Flutter, the primary topic in the domain of aeroelasticity, involves inertial distributions, normal structural modes and medium frequency aerodynamics.

Static structural strength is concerned with the load bearing structure to ensure that it supports the extremes of load expected in operation. For transport aircraft the design condition for wings comes from extreme gust loads. The description of the gust behaviour, its discrete character and its spectral features, and the corresponding aircraft and structural response involves unsteady aerodynamics.

Control system design for stability augmentation, manoeuvre demand, spin preventation, and active control technology (reduced static stability, manoeuvre load, gust alleviation, flutter suppression, ride quality), involves a full knowledge of inertial characteristics, structural stiffness characteristics, unsteady aerodynamics, sensor characteristics, hydraulic power and actuator systems and on-board microprocessors and mini computers, all depending on the type and level of control theory and optimisation used.

Flight simulation embraces aircraft dynamics control and real time computation with an interface with the human pilot.

Fatigue monitoring comes in at the operation phase. The requirement here is for a mathematical model which gives the response and hence fatigue life of the vulnerable parts of an aircraft structure with a minimum number of operational recorders.

These various areas have evolved with distinctive procedures. Aircraft stability and control uses axes fixed in the aircraft, essentially with velocities as the independent variables. Aeroelasticians use simple translational axes; overall and flexibility motions are derived relative to this axis system using displacements as the independent variables. The stressman who is interested in structural strength, only analyses the load bearing part of the structure whereas the aeroelastician needs to incorporate those non-load bearing components which contribute significantly to the structural stiffness characteristics, but not to strength. The control specialist has to translate and convert information from structures, aerodynamics, hydraulics, etc., into forms which are compatible with control analysis and design procedures, these design procedures operate in the time domain, the frequency domain, the (Laplace) s plane, and for sampled data, the Z plane; because of the growing application of active control technology and configured vehicles the control field is becoming increasingly important. Flight simulation depends for its effectiveness on the realism of aircraft behaviour to human perception and input. Monitoring of operational fatigue in the past was done with just one vg recorder, nowadays it is somewhat more sophisticated nevertheless the technique remains rather gross.

Because of the individual practices within each of the above technical areas there are problems of communication at the interfaces which introduce difficulties of transferring know-how from one area to another. Perhaps there should be a debate on

whether or not it is desirable and feasible to formulate a philosophy for an overall comprehensive mathematical model which embraces the whole subset of mathematical models for the above technical areas in a compatible manner; and if so, perhaps such a venture could be sponsored by AGARD.

2. BASIC CONSIDERATIONS

There are essentially three stages to the interface between unsteady aerodynamics and their applications,

i) unsteady aerodynamics,

ii) coupling of unsteady aerodynamics with dynamics (i.e. dynamic response),

iii) dynamic response, including unsteady aerodynamics, with feedback, (i.e. control analysis and synthesis).

Each of these three stages has its own set of requirements and approximations; it is necessary to understand the sequence of approximations introduced at each stage and the interrelationship of these approximations. There is also a need to relate the level of the mathematical analysis and detail to the practical scenario.

For simplicity in this presentation only linearised subsonic aerodynamics are discussed. It is important that the linearised situation is well understood before introducing the complexities of real non-linear aerodynamics.

3. UNSTEADY AERODYNAMICS

In unsteady aerodynamics conceptual understanding differs from the way in which unsteady aerodynamic effects are calculated.

Conceptually unsteady aerodynamics are associated with lag effects arising from vorticity shed continuously into a wake, and the radiation of pressure waves from the surface of the unsteady wing (or aircraft) and the unsteady wake. If a finite isolated wing is given a sudden step change in 'pitch' about an axis of rotation, as shown in Fig. 1,

$$\theta(t) = \theta_0 H(t) \tag{1}$$

where $H(t)$ is the unit step function

$$H(t) = 0 \quad t<0$$
$$= 1 \quad t>0.$$

Note that 'pitch' as defined here has the 'incidence angle' equal to the pitch angle. The step moment response about the pitch axis, can be written in the form

$$M_H(\hat{t})\Big|_{\substack{\text{pitch}\\ \text{axis}}} = \tfrac{1}{2}\rho V^2 S_W c\, C_{M_H}(\hat{t})\,\theta_0 \tag{2}$$

where

S_W = wing area

c = mean chord

$$C_{M_H}(\hat{t}) = k_2\dot{\delta}(\hat{t}) + k_1\delta(t) + k_0 H(\hat{t}) + \zeta_H(\hat{t}) \tag{3}$$

where the dot denotes differentiation with respect to $\hat{t}$, the non-dimensional time defined as

$$\hat{t} = t/(c/V) \tag{4}$$

where the unit of time (c/V) is the time the free stream moves one chord length, and

$$\zeta_H(0) = 0. \tag{5}$$

A typical curve for $C_{M_H}(\hat{t})$ is shown in Fig. 2.

At $M_\infty = 0$, k_2 and k_1 are associated with the so called 'apparent mass'. For $M_\infty > 0$, k_2 is zero and k_1 is given by the piston theory solution of the step motion.

As $\hat{t} \to \infty$,

$$C_{M_H}(\hat{t}) \rightarrow k_0 + C_{J_H}(\infty) \equiv \frac{dC_M}{d\alpha}_{steady} \qquad (6)$$

For a finite wing as $\hat{t} \rightarrow \infty$

$$C_{M_H}(\hat{t}) \rightarrow \frac{dC_M}{d\alpha}_{steady} \quad \text{as} \quad \frac{1}{\hat{t}^2} \qquad (7)$$

whereas for a two dimensional aerofoil

$$C_{M_H}(\hat{t}) \rightarrow \frac{dC_M}{d\alpha}_{steady} \quad \text{as} \quad \frac{1}{\hat{t}} \qquad (8)$$

For a general 'pitching' motion $\theta(\hat{t})$ defined for $\hat{t} > 0$ (assuming $\theta(\hat{t})$ is zero for $\hat{t} < 0$) the aerodynamic moment about the pitch axis is, assuming linearised aerodynamics, obtained by convolution, so

$$M(\hat{t}) = \tfrac{1}{2}\rho V^2 S_W c\, C_M(\hat{t})$$

where

$$\begin{aligned} C_M(\hat{t}) &= k_2\ddot{\theta}(\hat{t}) + k_1\dot{\theta}(\hat{t}) + k_0\theta(\hat{t}) + \int_0^{\hat{t}} C_{J_H}(\hat{t}-\hat{\tau})\frac{d\theta(\hat{\tau})}{d\hat{\tau}}\,d\hat{\tau} \\ &= k_2\ddot{\theta}(\hat{t}) + k_1\dot{\theta}(\hat{t}) + k_0\theta(\hat{t}) + \int_0^{\hat{t}} C_{J_\delta}(\hat{t}-\hat{\tau})\theta(\hat{\tau})\,d\hat{\tau} \end{aligned} \qquad (9)$$

where the dots again denote differentiation with respect to $\hat{t}$; $C_{M_\delta}(\hat{t})$ is the non-dimensional impulsive moment response where

$$C_{M_\delta}(\hat{t}) = \dot{C}_{M_H}(\hat{t})$$

so

$$C_{J_\delta}(\hat{t}) = \dot{C}_{J_H}(\hat{t}). \qquad (10)$$

Eqn.(9) is essentially the starting point of all applications of unsteady aerodynamics.

Traditionally, the step response function $C_{M_H}(\hat{t})$ is not calculated directly. Because oscillatory aerodynamics are required for flutter, the calculation of unsteady aerodynamics has concentrated on the prediction of oscillatory derivatives. The step response function is calculated subsequently once the oscillatory derivatives are known.

When a wing is oscillating in 'pitch' in simple harmonic motion,

$$\theta(t) = \theta_0 e^{i\omega t} \qquad (11)$$

the oscillatory moment $\tilde{M}(t)$ about the pitch axis can be expressed in the form

$$\tilde{M}(t) = \tfrac{1}{2}\rho V^2 S_W c\, \tilde{C}_M(\nu)\,\theta_0 e^{i\omega t} \qquad (12)$$

where

$$\tilde{C}_M(\nu) = \tilde{C}_{M_\theta}(\nu) + i\nu\, C_{M_{\dot\theta}}(\nu)$$

$$\nu = \text{frequency parameter} = \omega c / V. \qquad (13)$$

Here $\tilde{C}_{M_\theta}(\nu)$ represents the in-phase component and $\tilde{C}_{M_{\dot\theta}}(\nu)$ represents the quadrature, or out-of-phase, component.

As $\nu \rightarrow 0$, then

$$\tilde{C}_{M_\theta}(\nu) \rightarrow \frac{dC_M}{d\alpha}_{steady} + O(\nu^2 \ln \nu) \qquad (14)$$

$$\tilde{C}_{M_{\dot\theta}}(\nu) \rightarrow \begin{cases} O(\ln \nu) & \text{in 2 dimensions} \\ \text{constant} + O(\nu, \nu^2 \ln \nu) & \text{in 3 dimensions} \end{cases} \qquad (15)$$

As $\nu \rightarrow \infty$, then

$$\left.\begin{aligned} \tilde{C}_{M_\theta}(\nu) &\rightarrow -k_2\nu^2 + k_0 \\ \tilde{C}_{M_{\dot\theta}}(\nu) &\rightarrow k_1 \end{aligned}\right\} \qquad (16)$$

where k_0, k_1, k_2 are the same constants as those in eqn.(3) for the step response function. The manner in which $\tilde{C}_M(\nu)$ approaches its asymptotic state as $\nu \rightarrow \infty$ is discussed later.

In general because of numerical limitations $\tilde{C}_M(\nu)$ can only be calculated for a limited frequency range

$$0 < \nu < \nu_{max} \qquad (17)$$

For 2 dimensional aerofoils ν_{max} has been taken up to about 30, while for finite wings ν_{max} is about 6. For the purposes of flutter calculations $0<\nu<\nu_{max}$ covers all practical cases.

Now oscillatory loads are related to the step (or impulsive) response functions through the Fourier Transform

$$\tilde{C}_M(\nu) = \tilde{C}_{M_\theta}(\nu) + i\nu\,\tilde{C}_{M_{\dot\theta}}(\nu)$$
$$= -k_2\nu^2 + k_1\nu + k_0 + \int_0^\infty e^{-i\nu\hat{t}}\,C_\delta(\hat{t})\,d\hat{t} \qquad (18)$$

where $C_\delta(\hat{t})$ is defined in eqn.(10). Eqn.(18) can be inverted to give

$$C_\delta(\hat{t}) = \frac{2}{\pi}\int_0^\infty (\tilde{C}_{M_\theta}(\nu) + k_2\nu^2 - k_0)\cos\nu\hat{t}\,d\nu \qquad (19)$$

$$= -\frac{2}{\pi}\int_0^\infty \nu\,(\tilde{C}_{M_{\dot\theta}}(\nu) - k_1)\sin\nu\hat{t}\,d\nu. \qquad (20)$$

The double form for $C_\delta(\hat{t})$ arises from the fact that $C_\delta(\hat{t})$ is real, and zero for $\hat{t}<0$.

Thus $C_\delta(\hat{t})$ depends on the whole frequency range $0<\nu<\infty$; it is therefore necessary to extrapolate $\tilde{C}_{M_\theta}(\nu)$ and/or $\tilde{C}_{M_{\dot\theta}}(\nu)$ from

$$\nu = \nu_{max} \longrightarrow \infty.$$

Now k_1 is known from piston theory and k_2 is zero for $M_\infty>0$, but k_0 is not known *a priori*, however

$$k_0 = \frac{dC_M}{d\alpha}_{steady} + \frac{2}{\pi}\int_0^\infty (C_{M_{\dot\theta}}(\nu) - k_1)\,d\nu \qquad (21)$$

The asymptotic behaviour of $\tilde{C}_M(\nu)$ in two dimensions for large ν is strange; $C_{M_{\dot\theta}}(\nu)$ approaches k_1 as expected with increasing ν but then wanders about k_1, although not significantly; the actual convergence to k_1 is rather obscure. Nevertheless a simple extrapolation for $C_{M_{\dot\theta}}(\nu)$ from ν equal to ν_{max} to infinity seems to suffice for practical purposes. The function $C_\delta(\hat{t})$ can then be obtained from eqn.(20). In general it is not possible to extrapolate $\tilde{C}_{M_\theta}(\nu)$ from ν_{max} to infinity because of the odd behaviour of this function; calculations in 2 dimensions suggest that convergence of $\tilde{C}_{M_\theta}(\nu)$ to its asymptotic state takes place about ν equal to 60; the equivalent value in 3 dimensions is not known.

To generalise from oscillatory aerodynamics to unsteady aerodynamics, the key issue concerns the extrapolation of the oscillatory derivatives of ν from ν_{max} to infinity.

4. COUPLING OF DYNAMICS WITH UNSTEADY AERODYNAMICS

Unsteady aerodynamics is always used in the context of aircraft response.

Consider an isolated wing with the single degree of 'pitch' rotation, $\theta(t)$, about an axis of rotation. In still air the equation of the pitching motion, following an impulsive moment at $t=0$, is

$$I\ddot\theta + D\dot\theta + K\theta = M_0\,\delta(t) \qquad (22)$$

where

I = moment of inertia,

D = damping coefficient,

K = stiffness.

The solution of this second order equation is given in terms of

$$\theta(t) = \theta_1 e^{\lambda_1 t} + \theta_2 e^{\lambda_2 t} \qquad (23)$$

where λ_n satisfies the characteristic equation

$$I\lambda^2 + D\lambda + K = 0, \qquad (24)$$

which has the two roots λ_n (or eigenvalues or poles; these terms are synonomous) where

$$\left.\begin{aligned} \lambda_1 &= \mu_1 + i\omega_1, \qquad \lambda_2 = \mu_1 - i\omega_1, \\ \mu_1 &= -\frac{D}{2I}, \quad \omega_1 = \left(\frac{K}{I} - \left(\frac{D}{2I}\right)^2\right)^{1/2} \end{aligned}\right\} \qquad (25)$$

The two poles of eqn.(24) determine the motion, which from eqns.(23,25), is obviously damped.

In moving air the equation of pitching motion is

$$I\ddot{\theta} + D\dot{\theta} + K\theta = M_0\delta(\hat{t}) + \tfrac{1}{2}\rho V^2 S_W c \int_0^{\hat{t}} C_{M_H}(\hat{t}-\hat{\tau})\frac{d\theta(\hat{\tau})}{d\hat{\tau}}d\hat{\tau}$$
$$= M_0\delta(\hat{t}) + \tfrac{1}{2}\rho V^2 S_W c \int_0^{\hat{t}} C_{M_\delta}(\hat{t}-\hat{\tau})\,\theta(\hat{\tau})d\hat{\tau}\,, \qquad (26)$$

where $C_{M_H}(\hat{t})$ is the non-dimensional step response function, and $C_{M_\delta}(\hat{t})$ is the non-dimensional impulse response function (related by eqn.(10)).

Before discussing the solution to eqn.(26) it is useful to consider the type of solution expected.

The first question is whether the solution can be expressed purely in terms of simple poles in the form

$$\theta(\hat{t}) = \sum_{n=1}^{N} \theta_n e^{\lambda_n \hat{t}} \qquad (27)$$

The answer is no. Because $C_{M_H}(\hat{t})$ behaves at large time like $1/\hat{t}^2$ in 3 dimensions (or as $1/\hat{t}$ in 2 dimensions) then the motion $\theta(\hat{t})$ cannot be expressed purely in terms of exponential terms. But it is expected that the solution can be expressed primarily in terms of some poles, but there will be additional, or residual, behaviour.

The second question concerns the number of poles. The rigorous answer is not known but on the basis of calculations as reported in the literature, it is thought that in this exercise of a single degree of freedom system there are only two poles (i.e. the same number as in still air).

However in numerical terms the solution to eqn.(26) can be computed once $C_{M_\delta}(\hat{t})$ has been computed. This numerical solution of $\theta(\hat{t})$, obtained in the time domain, does not identify the poles which dominate the response.

Equation (26) can also be solved directly numerically in the frequency domain. Applying the Fourier Transform to eqn.(26) the equation becomes

$$\left\{-\nu^2\left(\frac{IV^2}{c^2}\right) + i\nu\left(\frac{DV}{c}\right) + K - \tfrac{1}{2}\rho V^2 S_W c\,\tilde{C}_M(\nu)\right\}\hat{\theta}(\nu) = M_0 \qquad (28)$$

Hence by inversion

$$\theta(\hat{t}) = \frac{1}{2\pi}\int_{-\infty}^{+\infty} \frac{e^{i\nu\hat{t}}\,d\nu}{\left[-\nu^2\left(IV^2/c^2\right) + i\nu\left(DV/c\right) + K - \tfrac{1}{2}\rho V^2 S_W c\,\tilde{C}_M(\nu)\right]} \qquad (29)$$

The numerical inversion depends on knowledge of the oscillatory derivatives $\tilde{C}_{M_\theta}(\nu)$ and $\tilde{C}_{M_{\dot\theta}}(\nu)$ over the full frequency range. The numerical inversion of eqn.(29) also does not identify the dominant poles. Computationally it might be faster to compute $\theta(\hat{t})$ from eqn.(29) than from eqn.(26) because for eqn.(26) it is necessary to undertake the lengthy computation of $C_{M_\delta}(\hat{t})$ first. However, once $C_{M_\delta}(\hat{t})$ is known the computation of $\theta(\hat{t})$ for a range of parameters is obtained relatively quickly.

A third way of approaching the solution of eqn.(26) is via the Laplace Transform. Define the Laplace Transform

$$\bar{f}(s) = \int_0^\infty e^{-s\hat{t}} f(\hat{t})\,d\hat{t} \qquad (30)$$

where

$$s = \mu + i\omega$$

The function $\bar{f}(s)$ only exists over part of the s plane where

$$\mu > \mu_1 \qquad (31)$$

and μ_1 depends on the form of $f(\hat{t})$. The inverse of eqn.(30) is

$$f(\hat{t}) = \frac{1}{2\pi i}\int_{\sigma-i\infty}^{\sigma+i\infty} e^{s\hat{t}}\bar{f}(s)\,ds \qquad (32)$$

where

$$\sigma > \mu_1 \,. \qquad (33)$$

The value of μ_1 is the same in eqns.(31,33). In the region $\sigma > \mu_1$, the function $\bar{f}(s)$ is defined, according to eqn.(30), so eqn.(32) is well defined.

The interesting part of the inversion process is that although $\bar{f}(s)$ can only be defined for μ (real part of s) $> \mu_1$, a well behaved function $\bar{f}(s)$, can be continued analytically into the other part of the s plane, namely $\mu < \mu_1$; poles can then be

identified in the region $\mu < \mu_1$ and the inversion can be derived in terms of residues at the poles. Analytic continuation is at the heart of the Laplace Transform method.

Applying the Laplace Transform, eqn.(26) becomes

$$\left\{ I s^2 + D s + K - \tfrac{1}{2}\rho V^2 S_w c\, \bar{C}_M(s) \right\} \bar{\theta}(s) = M_0 \tag{34}$$

where

$$\bar{C}_M(s) = k_2 s^2 + k_1 s + k_0 + \int_0^\infty e^{-s\hat{t}}\, C_\delta(\hat{t})\, d\hat{t} \tag{35}$$

Note, comparing eqns.(18,35)

$$\bar{C}_M(i\nu) = \tilde{C}_M(\nu) \tag{36}$$

Although $\tilde{C}_M(\nu)$ can be obtained from $\bar{C}_M(s)$; $\bar{C}_M(s)$ cannot be obtained from $\tilde{C}_M(\nu)$.

Suppose that in principle $\bar{C}_M(s)$ can be continued analytically throughout the entire s plane. Then two poles (at least) can be obtained from

$$I s^2 + D s + K - \tfrac{1}{2}\rho V^2 S_w c\, \bar{C}_M(s) = 0 \tag{37}$$

To invert $\bar{\theta}(s)$, to obtain $\theta(t)$, a contour must be drawn enclosing the poles. But because $\bar{C}_M(s)$ involves a term like $\ln s$ it is necessary to introduce a cut along the negative real axis as shown in Fig. 3. Thus the form of $\theta(t)$ in principle is

$$\theta(t) = \theta_1 e^{s_1 t} + \theta_2 e^{s_2 t} + \text{residual term}(t), \tag{38}$$

where s_1, s_2 are the two poles (i.e. solutions of eqn.(37)) and the residual term arises from integrating $\bar{\theta}(s)$ along the cut.

It is seen that there is a problem for an overdamped system if a pole lies on the negative real axis.

But from a practical point of view $\bar{C}_M(s)$ can only be evaluated numerically from eqn.(35) for

$$\mu \ (\equiv \text{real part of } s) > 0$$

To proceed with the method it is necessary to analytically continue $\bar{C}_M(s)$ into the negative real part of the s plane. This can be done at M_∞ equal to zero because $\bar{C}_M(s)$ can be expressed in analytic form. However for $M_\infty > 0$ eqn.(35) has to be solved numerically so in this approach analytic continuation is not possible. Since, as explained later, for control purposes there is a need to know where the poles in eqn.(34) lie; there is considerable interest in knowing whether or not an exact analytic continuation can be achieved (by other means than implied above); some say yes, some say no.

In an alternative approach $C_\delta(\hat{t})$ can be approximated by an analytic function, eqn.(35) can then be determined in analytic form. This approximate analytic form can be continued analytically over the entire s plane. But there are dangers, simple analytic approximations to $C_\delta(\hat{t})$ can actually produce spurious poles. To illustrate this point suppose that $C_\delta(\hat{t})$ is approximated by

$$C_\delta(\hat{t}) = a_1 e^{\lambda_1 \hat{t}} + a_2 e^{\lambda_2 \hat{t}} \tag{39}$$

where the constants $a_1, a_2, \lambda_1, \lambda_2$ are chosen such that the approximated $C_\delta(\hat{t})$ is close to the exact $C_\delta(\hat{t})$. The Laplace Transform of eqn.(39) is

$$\bar{C}_\delta(s) = a_1/(s-\lambda_1) + a_2/(s-\lambda_2) \tag{40}$$

Thus the characteristic equation (37) becomes of the form

$$I s^2 + D s + K - \tfrac{1}{2}\rho V^2 S_w c \left(k_2 s^2 + k_1 s + k_0 + \frac{a_1}{s-\lambda_1} + \frac{a_2}{s-\lambda_2} \right) = 0 \tag{41}$$

The characteristic equation now becomes a fourth order polynomial with four poles. Thus two spurious poles have been introduced.

Although it is usually thought that such spurious poles do not play a significant role in the actual dynamic response, the introduction of spurious poles in a feedback loop could cause uncertainties.

A better approximate form assumes

$$C_{l_\delta}(\hat{t}) = \sum_{n=1}^{N} b^n \left(\frac{a}{a+\hat{t}}\right)^n \qquad (42)$$

which satisfies the correct asymptotic behaviour as $\hat{t} \to \infty$. The Laplace Transform of eqn.(42) comes out in terms of exponential functions, which have the correct $1/s$ behaviour.

Summarising the main problem in unsteady aerodynamics/dynamic response coupling is how $\bar{C}_M(s)$ can be obtained in the negative half of the s plane in order to obtain the poles of the system response.

5. CONTROL DESIGN

Control design is concerned with dynamic response, involving unsteady aerodynamics, and the modification of that response through a feedback system.

Standard control design is based on the assumption that the system behaviour can be expressed in terms of simple poles only. There is then a query whether the residual aerodynamic response mentioned in the previous section (eqn.(38)) plays a part in the response of the closed loop feedback system.

But for standard control purposes it is assumed that the motion of the example used in this note can be represented in the form

$$I\ddot{\theta} + D\dot{\theta} + K\theta = M_0 \delta(t) + \tfrac{1}{2}\rho V^2 S_W c \left(C_{M_\theta}\theta + C_{M_{\dot\theta}}\dot{\theta}\right) \qquad (43)$$

where C_{M_θ} and $C_{M_{\dot\theta}}$ are constants. But the values of these constants are not given from purely aerodynamic considerations, their values depend on the totality of the motion, not only on the aerodynamics but also on I, D and K. It should be emphasised that constant C_{M_θ} and $C_{M_{\dot\theta}}$ is not equivalent to implying steady or quasi-steady aerodynamics. In effect C_{M_θ} and $C_{M_{\dot\theta}}$ are chosen so that the poles of eqn.(37) are identical with the poles s_1 and s_2 as defined in eqn.(38). And essentially the residual term in eqn.(38) for the full response is neglected in eqn.(43).

This situation is already well known in flutter calculations where the equivalent equation would be

$$\left(-I\omega^2 + Di\omega + K\right)\theta_0 e^{i\omega t} = \tfrac{1}{2}\rho V^2 S_W c \left\{\tilde{C}_{M_\theta}(\nu) + i\nu\, C_{M_{\dot\theta}}(\nu)\right\}\theta_0 e^{i\omega t} \qquad (44)$$

where the derivatives $\tilde{C}_{M_\theta}(\nu)$ and $\tilde{C}_{M_{\dot\theta}}(\nu)$ depend on the frequency parameter of the system response.

As already stated for general motions the values of C_{M_θ} and $C_{M_{\dot\theta}}$ in eqn.(43) have to be chosen such that the poles of the motion in eqn.(37) are the correct poles. This is why eqn.(34), the response equation in the s plane, is important because that equation is the one where the poles are identified.

Thus the aim in control design is to determine for a particular response the appropriate constant values of C_{M_θ} and $C_{M_{\dot\theta}}$ which give the correct 'pole' behaviour. Unfortunately if they are chosen from the open loop characteristics then the closed loop characteristics will be incorrect.

6. AIRCRAFT DYNAMICS

The technical area of main interest to this Conference is aircraft dynamics, which is broadly concerned with the prediction of overall aircraft motion following a pilot input (either human or automatic). Inherent in these predictions are studies of stability, incorporating the characteristics of the augmented or active control systems. For transport aircraft static structural deformation effects are significant but less so for combat type aircraft.

Because the rate of change in aircraft dynamics $O(Vt/c\mu)$, where μ, the relative mass parameter is small compared with the rate of change of aerodynamic characteristics $O(Vt/c)$, so-called quasi-steady aerodynamics are used via 'aerodynamic derivatives'.

Restricting the initial discussion to attached flows, the genius of Bryan in his

classic formulation of the equations of motion of an aircraft was the introduction of the concept of aerodynamic derivatives where aerodynamic forces and moments are formulated independently of the dynamic motion in such a way that the dynamic equations could be easily solved. Such methodology has stood the test of time, it is now an established and permanent part of the techniques of aircraft dynamics. Nevertheless there are a number of fundamental issues which need to be recognised.

Before introducing unsteadiness it is important to recognise what is steady aerodynamics. Steady aerodynamics are said to exist when the aerodynamic loads do not change with time. Obviously steady incidence and sideslip give rise to steady conditions, thus $C_{L_\alpha}, C_{M_\alpha}, C_{N_\beta}$ are steady state (static) derivatives. But steady conditions also arise for steady pitch rate, roll rate and yaw rate, thus $C_{M_q}, C_{l_p}, C_{N_r}$ are also steady state (rotary) derivatives. But it is known that it is necessary to incorporate a term like $C_{M_{\dot\alpha}}$ into the equations, where $C_{M_{\dot\alpha}}$ is normally regarded conceptually in terms of a lag effect between main wing and tailplane. Thus $C_{M_{\dot\alpha}}$ is one derivative ($C_{N_{\dot\beta}}$ is another) which depends on an understanding of unsteady aerodynamics.

In text books it is suggested that following an arbitrary motion $\alpha(t)$ of an isolated aerofoil the pitching moment coefficient can be expanded in the form

$$C_M(t) = C_{M_0} + C_{M_\alpha}\alpha(t) + C_{M_{\dot\alpha}}\dot\alpha(t) + C_{M_{\ddot\alpha}}\ddot\alpha(t) + \cdots \tag{45}$$

where $C_{M_0}, C_{M_\alpha}, C_{M_{\dot\alpha}}$ etc. are all constants. It is often suggested that the series has a mathematical basis (e.g. a Taylor series). Such a suggestion is completely fallacious, the series does not exist. For a two dimensional aerofoil at subsonic Mach numbers, mathematically constant values of C_{M_0} and C_{M_α} can be identified but $C_{M_{\dot\alpha}}, C_{M_{\ddot\alpha}}$ etc. are all infinite. For a three dimensional finite wing at subsonic Mach numbers, then mathematically constant values of C_{M_0}, C_{M_α} and $C_{M_{\dot\alpha}}$ can be identified but $C_{M_{\ddot\alpha}}$ etc. are again infinite.

To be precise all that can be written is

$$\text{in 2D} \quad C_M(t) = C_{M_0} + C_{M_\alpha}\alpha(t) + \text{residual term}, \tag{46}$$

$$\text{in 3D} \quad C_M(t) = C_{M_0} + C_{M_\alpha}\alpha(t) + C_{M_{\dot\alpha}}\dot\alpha(t) + \text{residual term}. \tag{47}$$

The two dimensional result is given parity here with the three dimensional result because strip theory is often applied to finite wings. Eqn.(46,47) should not be interpreted as implying that the residual terms are necessarily small and negligible.

It can be shown that

$$C_{M_{\dot\alpha}} = k_0 + \int_0^\infty \left(\varphi_H(\infty) - \varphi_H(\hat\xi)\right) d\hat\xi \tag{48}$$

where $k_0, \varphi_H(\hat\xi)$ are defined in the step response function (see shaded area in Fig. 2). It is now seen that in two dimensions since $\varphi_H(\hat\xi)$ approaches $\varphi_H(\infty)$ as $1/\hat\xi$, $C_{M_{\dot\alpha}}$ is infinite; in three dimensions since $\varphi_H(\hat\xi)$ approaches $\varphi_H(\infty)$ as $1/\hat\xi^2$, $C_{M_{\dot\alpha}}$ is finite. This behaviour is reflected in the oscillatory derivatives where

$$C_{M_{\dot\alpha}} = \tilde C_{M_{\dot\alpha}}(\nu)\big|_{\nu\to 0} = O(\ln\nu) \text{ in 2D} \tag{49}$$

$$= \text{constant} + O(\nu) \text{ in 3D} \tag{50}$$

Thus $C_{M_{\dot\alpha}}$ for a finite wing on the basis of two dimensional strip theory does not exist but with a full three dimensional analysis $C_{M_{\dot\alpha}}$ is finite.

The function $(C_{M_{\dot\alpha}} + C_{M_q})(\nu)$ is shown in Fig. 4 for a rectangular wing of aspect ratio 6 oscillating about an axis at mid chord at M_∞ equal to 0.7. As seen in Fig. 4(i) even at the low frequencies associated with the short period mode $C_{M_{\dot\alpha}}$ is not strictly constant (C_{M_q} is constant); taking the value of $C_{M_{\dot\alpha}}(0)$ could give an error of about 5%. But for ν greater than 0.03 the value of $C_{M_{\dot\alpha}}(\nu)$ begins to change significantly; this point becomes important when feedback tends to increase the frequency of the motion.

However in aircraft dynamics a major contribution to $C_{M_{\dot\alpha}}$ is from the 'lag' effect of the downwash on the tailplane. It is usually argued that the downwash lag is represented by

$$\epsilon(t) = \frac{\partial \epsilon}{\partial \alpha}\left(\alpha(t) - \frac{l_c}{V}\dot{\alpha}(t)\right) \tag{51}$$

where l_c/V is the time taken for the free stream to travel from the main wing to the tailplane. This concept is not correct or useful because it neglects the effects of the shed bound vorticity (i.e. the sequence of starting vortices with axes in the spanwise direction which are shed from the main wing trailing and convected with the stream). In fact when the main wing changes its incidence, l_c/V is the time taken for a starting vortex to reach the tailplane. The time variation of the downwash about the tailplane is a compound of the effects of a sequence of starting vortices shed from the wing trailing edge and time dependent trailing vortices.

A self consistent, but not accurate, set of time dependent calculations by the authors are, at low speeds:

non-swept aircraft configuration:

$$\frac{\partial \epsilon}{\partial \alpha} = 0.44$$

$$C_{M_q}|_{wing} \sim 0.0 \qquad C_{M_q}|_{tailplane} = -8.8$$

$$C_{M_{\dot{\alpha}}}|_{wing} \sim -0.75 \qquad C_{M_{\dot{\alpha}}}|_{tailplane} = -6.0$$

swept aircraft configuration:

$$\frac{\partial \epsilon}{\partial \alpha} = 0.54$$

$$C_{M_q}|_{wing} = -0.39 \qquad C_{M_q}|_{tailplane} = -3.0$$

$$C_{M_{\dot{\alpha}}}|_{wing} = -0.48 \qquad C_{M_{\dot{\alpha}}}|_{tailplane} = -2.15$$

It is seen that the customary formula

$$C_{M_{\dot{\alpha}}}|_{tailplane} = \frac{\partial \epsilon}{\partial \alpha} C_{M_q}|_{tailplane}$$

is not accurate. Furthermore the contribution of $C_{M_{\dot{\alpha}}}$ from the wing is not negligible; and this wing contribution increases with M_∞.

7. CONCLUSIONS

The aim of this presentation has been to illustrate some of the elementary ideas underlying the interactions between unsteady aerodynamics, dynamics, and control analysis and design.

These ideas can be carried over to multi-degree of freedom systems but now, in addition to determining and matching the poles, eigenvectors must also be evaluated and matched.

There are also other developments, for example working in the domain of differential delay models where the unsteady aerodynamic effects are approximated in the Z plane. Open and closed loop stability of the residual response can be ensured on the basis of robustness relations as developed for multivariable control systems.

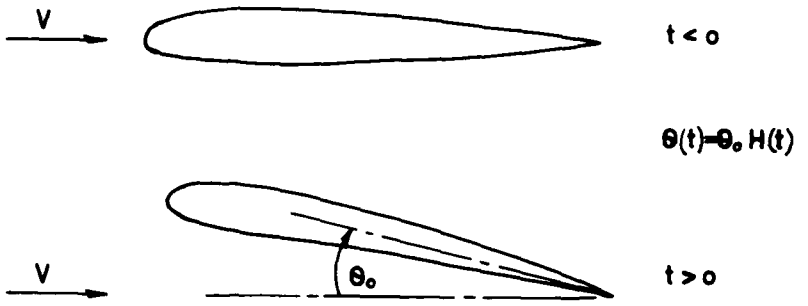

Fig. 1 STEP CHANGE IN 'PITCH' ANGLE

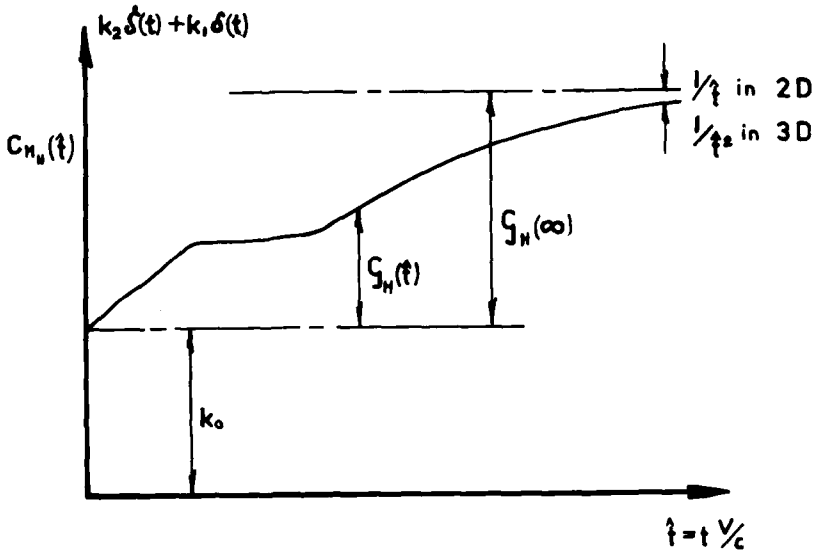

Fig. 2 STEP MOMENT PESPONSE

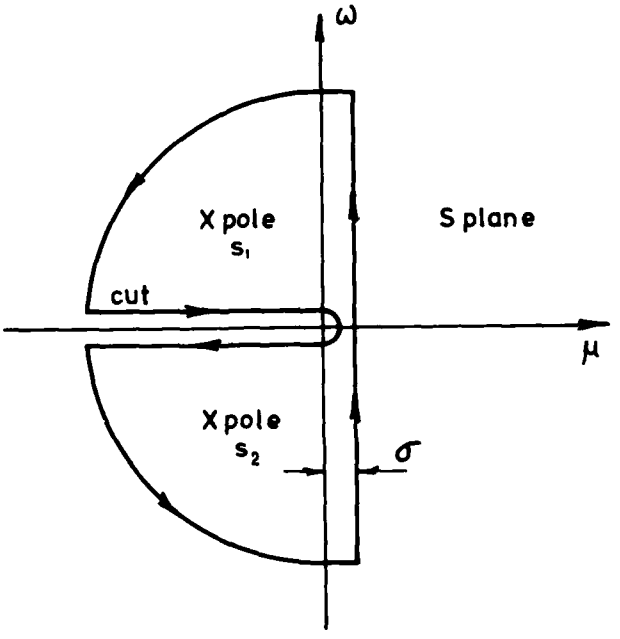

Fig. 3 CONTOUR OF INTEGRATION

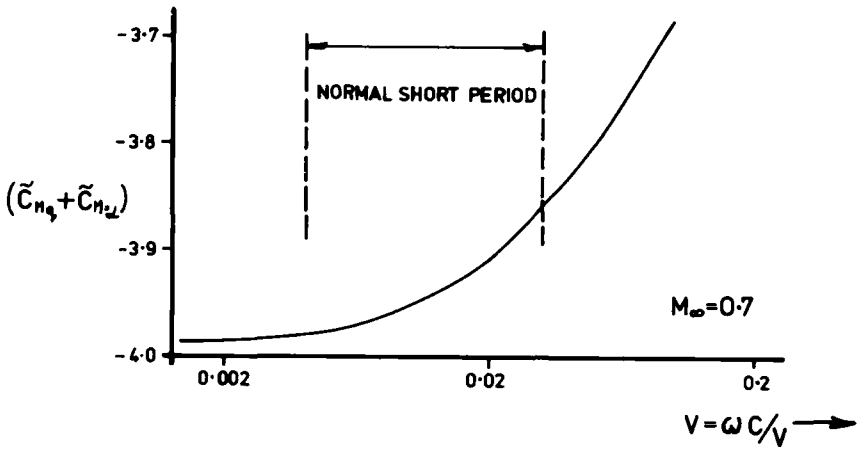

Fig. 4(i) VARIATION OF $(C_{H_q}+C_{H_{\dot{\alpha}}})$ AT LOW FPEQUENCIES

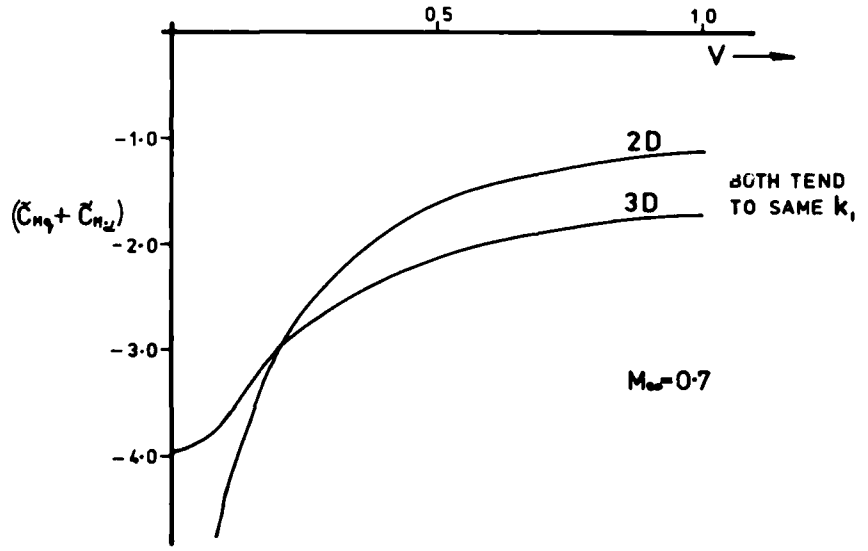

Fig. 4(ii) VARIATION OF $(C_{H_q}+C_{H_{\dot{\alpha}}})$ WITH FREQUENCY PARAMETED

CORRELATION OF PREDICTED AND FREE-FLIGHT RESPONSES NEAR DEPARTURE CONDITIONS OF A HIGH INCIDENCE RESEARCH MODEL

A. Jean Ross, Geraldine F. Edwards
Royal Aircraft Establishment
Farnborough, Hampshire, GU14 6TD, UK

SUMMARY

The mathematical model of aerodynamic forces and moments is described, based on results from various wind-tunnel experiments with the RAE High Incidence Research Model (HIRM). Simulations of the responses due to longitudinal and lateral control inputs at high angles of attack are compared with the responses measured on free-flight models of the configuration. It is shown that the main features of the flight behaviour are reproduced, in particular such phenomena as roll-off, wing rock and nose slice.

1 INTRODUCTION

The declared objective of the RAE research programme[1] using the High Incidence Research Model (HIRM) is "the widening of understanding of the flight-dynamics phenomena of combat aircraft at high angles of attack. Central to this is the development of mathematical modelling techniques to predict such phenomena at or near departure at low speeds, and to provide data from free-flight and wind-tunnel experiments for this purpose". The extensive wind-tunnel tests are nearing completion and results have been published describing data from static, oscillatory, steady-rolling and large-amplitude pitching experiments[2-5]. The results have been used to define mathematical models of the aerodynamic forces and moments for the whole angle of attack range, 0° to 90°, and models of varying complexity and based on different data sets have been compared. The first series of free-flight experiments were conducted in Autumn 1983, and a selection of the results is discussed in this paper, the aim being to show that it is possible to simulate the main characteristics of the response using a mathematical model with inputs from wind-tunnel data.

Since the flights cover an angle of attack range beyond the stall, the static lift, drag and pitching moment results are best represented as data arrays derived directly from the wind-tunnel results, and the derivatives due to pitch rate are also represented in this way. However, there are choices to be made between lateral data sets measured using different techniques, *eg* sideslip derivatives may be obtained from either static tests or the oscillatory rig tests, and the derivatives due to roll rate may be derived from either the oscillatory or steady rolling tests. The types of wind-tunnel results available are described briefly in this paper, and the form of the mathematical model chosen is indicated, being based on the classical derivative representation. Three of the free-flight trials have been chosen to illustrate the various phenomena encountered in flight, and in particular to indicate the degree of correlation between the overall characteristics of simulated and experimental responses.

2 CHOICE OF MATHEMATICAL MODEL

2.1 Wind-tunnel data available

A variety of wind-tunnel experiments have been conducted on the HIRM configuration (shown in Fig 1) and most of the results pertinent to the free-flight experiments have been described in Refs 2 and 3. The static tests[2] on a preliminary model covered a wide range of angles of attack (0° to 40° mostly, with some 0° to 90°), over a matrix of symmetric canard (η_c) and tailplane (η_t) settings appropriate to trim conditions between α = 0° and 30°. Some of these configurations were tested at sideslips up to 6°, and with differential canard (ξ_c) and differential tailplane (ξ_t) settings, and one rudder (ζ) setting of 10°. A selection of these configurations were repeated with the definitive 4/9-scale model, and the results gave different trim conditions and differences in sideslip data for $\alpha > 20°$. These changes could only be partly accounted for from estimated increments due to the different rear fuselage shape of the models. However, the incremental effects due to control deflections were the same for the two models, and so the two sets of data could be amalgamated, to give forces and moments due to (α,β,η_c,η_t), with control powers due to ξ_c,ξ_t and ζ. Most of these results were obtained with tunnel speeds of 70 m/s, *ie* at similar Reynolds' number to the free-flight experiments, but above angles of attack of 25° the speed had to be reduced to 40 m/s, due to model vibration.

The trim conditions are crucial for designing free-flight experiments, and so a further series of static tests were undertaken using a full-scale free-flight model in the RAE 5-metre tunnel. These tests also gave data at larger angles of sideslip, up to 18°, and calibrations for the two sets of incidence vanes (one set for α and β on the probe, and one set of three vanes on the fuselage) and for the pitot - static pressure

measurements (pitots on the probe, with static pressures on the probe and near the angle of attack vanes on the fuselage sides). It was possible to use a tunnel speed of 50 m/s, above the mean trim speed for the free-flight experiments, at just above atmospheric pressure, so the Reynolds' number is greater than that in flight. The pitching moments were found to be slightly different again* at the stall (Fig 2), but it was possible to design a short free-flight test on the RAE Larkhill range to check the trim conditions for one canard/tailplane setting. This first flight confirmed that the tunnel results from the 4/9-scale model in the RAE 13ft by 9ft tunnel give reasonable values of trimmed angle of attack, for $\eta_c = -10°$. The flight value of α_{trim} for $\eta_t = -17°$ is 21°, compared to the predicted 23°, whereas the wind-tunnel results from the preliminary model indicated about 29°.

Special attention was also paid to the magnitudes of the asymmetric sideforce, rolling and yawing moments due to vortices shed from the nose at zero sideslip, and it appeared that the long nose probe effectively suppressed them for $\alpha < 30°$. The relatively small asymmetric sideforce and moments occurring between $20° < \alpha < 30°$ were included in the mathematical model, together with the larger asymmetries for $\alpha > 30°$, as shown in Fig 3.

The 4/9-scale model has been tested on an oscillatory rig at RAE Bedford, over an α-range of 0° to 85° for rolling and yawing motions at various control settings, and for $0° < \alpha < 60°$ in pitch for $\eta_c = -10°$, 0° and 10°, with η_t to trim about the balance centre. The wind-tunnel speeds in the RAE 13ft by 9ft tunnel were again 70 m/s for $\alpha < 25°$ and 40 m/s for $\alpha > 25°$. Tests on a large-amplitude pitch rig showed that the damping-in-pitch derivative is not highly dependent on amplitude for angles of attack up to 30°, and so the oscillatory rig results have been used in the mathematical model.

Steady rolling tests have been conducted on both the 4/9-scale model on the BAe (Warton) rig[4], and the 2/9-scale model at RAE[5], and the agreement is very good. However, there is marked difference in roll-damping characteristics between the linear derivative obtained from the steady rolling tests (aerodynamic body axes) and the oscillatory data obtained by converting the oscillatory rig results from geometric body axes. For $\alpha > 20°$, the rolling and yawing moments are also nonlinear functions of roll rate.

The oscillatory rig has also been used to measure cross-derivatives, and non-zero values of pitching moment due to roll rate, M_p, and rolling moment due to pitch rate, L_q, were measured for $\beta = -6°$, and $\beta = 0°$.

2.2 Form of mathematical model

For the design of the free-flight experiments, it was decided to represent the results from the static wind-tunnel tests in the form of data look-up tables, with implied linear interpolations over small intervals in the variables whose effects could not be adequately represented by linear derivatives. Analysis of the available results indicated that normal force, axial force and pitching moment could be represented* by, eg

$$C_m = C_{m_0}(\alpha,\eta_t) + M_{\eta_c}(\alpha,\eta_t)\eta_c + M_q(\alpha,\eta_c)\frac{q\bar{c}}{V}$$

The detail of mathematical model for the first two terms is indicated in Fig 2. No attempt has been made as yet to separate the oscillatory derivatives into the contributions from q and $\dot{\alpha}$, and the small values of the derivative M_p have been neglected in these simulations.

The sideforce, rolling and yawing moments were also represented by linear derivatives, dependent on α, η_c and η_t. Three-dimensional arrays of data were avoided by analysing the data to determine significant variations with η_c and/or η_t. There are choices in data sets, either static or oscillatory derivatives for sideslip, and either oscillatory or rotary derivatives for rolling, but all the linearised derivatives could be expressed as, eg

$$L_v = L_{v_{Ref}}(\alpha) + L_{v_{\eta_c}}(\alpha)\,\Delta\eta_c + L_{v_{\eta_t}}(\alpha)\Delta\eta_t$$

where $\Delta\eta_c$ and $\Delta\eta_t$ are increments in control setting from the chosen reference settings.

---

* The current British notation is used in the text, but both American and British equivalents are shown on Figs 6,7, and 8.

Thus an extension of the classical linear derivative representation of lateral aerodynamic forces and moments has been used, and the purpose of this paper is to show that this seems adequate for simulating the main characteristics of the dynamic responses. However, nonlinear effects have been included for the non-zero C_y, C_ℓ and C_n at $\beta = 0°$, and it is possible to include variation of moments with angle of sideslip and roll rate.

The dependence of rolling moment due to pitch rate on angle of sideslip seems to be open to debate. Experimental results[4,5] for HIRM indicate near-zero values at $\alpha = 0°$, with a significant peak near $\alpha = 20°$ for $\beta = -6°$ (ie near wing stall), and NAE experiments[6] on a simplified model indicate that L_q takes the sign of β, for $\beta = \pm 5°$. The current simulations reported here use the second-order derivative $L_{q\beta}$, assuming that $dC_\ell/(\frac{q\bar{c}}{V})$ is linearly dependent on β. In contrast, the simulations of responses of aircraft[7] at high angles of attack have used $C_{\ell q} = +2$ or -2, independent of β, and these show a very significant effect on the damping of the responses. This was also observed in simulations of HIRM responses, using $C_{\ell q} = 2$ near $\alpha = 35°$, (ie near onset of large asymmetric sideforce and yawing and rolling moments), but the results are not shown here.

3 PREDICTED STABILITY AND CONTROL CHARACTERISTICS

3.1 Trim conditions

As mentioned in section 2, the different wind-tunnel models indicate different trim conditions, as illustrated in Fig 4. Small differences in C_{m_0}, combined with low values of $dC_m/d\alpha$ corresponding to the 5% static margin chosen for the first series of free-flight tests, and slightly different stall characteristics, mean that the trim condition $C_m(\alpha, n_c, n_t) = 0$ is very sensitive to test conditions. For trimmed angles of attack between 16° and 30°, the tailplane angle to trim varies between -10° and -17° for $n_c = 0°$, and between -15° and -22° for $n_c = -10°$, based on 4/9-scale model tests, (Fig 4).

3.2 Longitudinal stability and control

The static stability (local $-dC_m/d\alpha$) remains positive at trimmed conditions (except for extreme control settings of $n_c = -40°$, $n_t = -40°$) and the pitch damping is high, so the longitudinal short period mode should be well-behaved. However, since the phugoid mode is lightly damped at the high angles of attack, and there is unavoidable mis-match between model trim speed and angle of attack (near zero) when the model is released from the helicopter, large variations in airspeed occur eg $V_{trim} \approx 45$ m/s, $\Delta V \approx 15$ m/s. The model flight has to be terminated if $V > 70$ m/s, which is the limiting speed for deploying the recovery parachutes.

The tailplane remains an effective pitch control until at least $\alpha = 40°$, with some effectiveness up to $\alpha = 90°$ for negative mean tailplane setting. The lift and pitching moment due to canard deflection are highly dependent on angle of attack and mean canard setting, but also maintain control power in pitch to $\alpha = 40°$, becoming zero near $\alpha = 60°$.

3.3 Lateral stability and control

The characteristics of the lateral motion are the major concern at high angles of attack, since the departures from controlled flight are usually due to adverse characteristics of the Dutch roll mode, either loss in damping or loss in frequency. The latter possibility is indicated by zero value of the parameter

$$C_{n_{\beta\ \text{dynamic}}} = N_v - \frac{ix}{iz} L_v \sin\alpha$$

, which is approximately proportional to ω_D^2, where ω_D is the frequency of the Dutch roll oscillation. Results[2] for sideslip derivatives obtained on the preliminary HIRM model (which had different rear fuselage shape) indicated that the frequency should remain positive for trimmed flight conditions, but could become zero at angles of attack above 30° for untrimmed n_c and n_t settings. The linear stability characteristics evaluated[3] using results from the definitive 4/9-scale model confirmed that the frequency remains positive up to $\alpha = 36°$, except for $n_c = 0°$, $n_t = -20°$, where zero frequency occurs at $\alpha = 35°$. However, if the values of the sideslip derivatives obtained from the oscillatory tests are used in the calculations, the frequency remains significantly higher at the higher angles of attack, because of the rolling moments due to sideslip remaining more negative than the results from the static tests. These calculations also showed that the damping of the Dutch roll mode can become zero above about $\alpha = 23°$, although this critical α is dependent

on control configuration, and which sets of sideslip and roll rate derivatives are used. It was decided to use the static wind-tunnel data for sideslip, and oscillatory rig data for the dynamic derivatives as the basis for the mathematical model to design the free-flight experiments, since these indicated undamped Dutch roll at $\alpha = 25°$, and divergence for $\alpha = 35°$. The other lateral modes, ie the roll subsidence and spiral modes, are damped, but can combine to form a second lateral oscillation (usually known as the lateral phugoid), which also remains damped, for $\alpha < 40°$.

The differential tailplane remains effective as a roll control up to $\alpha = 40°$, but the associated yawing moment is large and negative, becoming zero and positive for $\alpha > 36°$. Zero values of the Lateral Control Departure Parameter, $N_v - N_{\xi t} L_v / L_{\xi t}$ also indicate when use of roll control is likely to cause large responses, and perhaps departures. Although $N_{\xi t}$ remains healthily negative for $\alpha < 35°$, the large negative values of N_v cause LCDP to become zero near $\alpha = 25°$. The usual method of improving LCDP is to incorporate an aileron-rudder interconnect in the control system, to counteract the adverse (positive) aileron yaw, but this does not alleviate the problem for differential roll control if N_v is negative.

The effects of the nonlinearities in roll rate and sideslip have been simulated[3,6], and show that the increasing local damping and stiffness with increasing amplitude are sufficient to contain the linear undamped Dutch roll oscillation within a limit cycle, ie a wing rock type of motion.

3.4 Coupled responses

Some calculations have been made[8] of the characteristics of coupled longitudinal/lateral modes for flight at non-zero sideslip or roll rate conditions. The results indicate possibilities of divergence at the higher angles of attack, due to aerodynamic coupling such as rolling moment due to angle of attack at constant sideslip.

The predictions used to design the free-flight experiments are also based on coupled equations of motion, and the results are discussed in the following section.

4 FREE-FLIGHT TESTS, AND CORRELATION WITH SIMULATIONS

4.1 Design of experiments

The aim of the first flight of the model at the RAE Larkhill range was to establish a trim condition, for a static margin of about 5%, between $\alpha = 20°$ and $\alpha = 25°$, and then to increase angle of attack slightly to see if the model departed from controlled flight. The limits imposed by the range size at Larkhill meant that control settings had to be chosen so that the glide path was steep enough for the model to keep within the safety trace, but at an angle of attack where the model would not depart before a trim state was reached. The aim was achieved, and the main series of experiments to be conducted at NASA Dryden were then planned, primarily to obtain data over the range $15° < \alpha < 30°$. The two Dryden flights discussed here were designed to give responses due to differential tailplane doublet, differential canard doublet and rudder pulse at each of three different trim conditions. For the trial designated HD1 the fixed mean canard setting η_c was $-10°$, and HD2 was flown with $\eta_c = 0°$. The amplitudes and timings of the lateral control inputs were chosen to give acceptable magnitudes of response, and inputs predicted to give possible departures were placed towards the end of each trial. Four more similar trials were achieved at Dryden during September/October 1983, with actual flight times of between 20 and 110 seconds; it is possible to plan for flights of about 160 seconds duration for the Dryden Spin Area range, if there are no departures to cause increased height loss.

4.2 Larkhill trial, HL1

The experiment was designed using static test data for the sideslip derivatives, lateral dynamic derivatives from the oscillatory rig, and the asymmetric sideforce, rolling and yawing moments, which excite lateral motion, as measured in the 5-metre tunnel. With the canard set at $-10°$, the model was released with $\eta_t = -17°$, and allowed to stabilise at the trim angle of attack before moving the tailplane to $-21°$ after 10 seconds (Fig 5a). The flight was terminated after 20 seconds to ensure a landing, with recovery parachutes, within the range area. The predicted responses are fairly close to those actually experienced in flight, as shown in Fig 5. The model trims at an angle of attack of about 21°, and then departs with a nose slice between t = 12 and 13 seconds when the angle of attack is increased to a theoretical trim angle of about 28°. The predicted departure occurs about 2 seconds after the actual departure, but the character is the same; it should be noted the lateral asymmetries cause the predicted response to depart, as neglecting them gives a steady trim $\alpha = 27.5°$, with zero lateral responses.

The correlation was sufficiently close for the same mathematical model to be used for designing the trials at NASA Dryden; the revised mathematical model discussed in the following paragraph does simulate the responses more closely (also shown in Fig 5), although the departure is more violent.

4.3 Dryden trials, HD1 and HD2

The responses of the first trial at Dryden were much more lively in roll than had been predicted, due partly to the trimmed angles being higher (tailplane settings were slightly more negative than specified) and partly to the mathematical model. Simulations using flight values of tailplane settings did not reproduce the flight characteristics, and so changes were progressively made to the mathematical model. The current model is based on wind-tunnel results, but the most adverse lateral data have had to be used, ie (i) an envelope of amplitudes of asymmetric sideforce, rolling and yawing moments from all the wind-tunnel tests, instead of results from one test configuration which gave an oscillatory variation with angle of attack for $\alpha < 55°$, (ii) damping-in-roll derivative (and other dynamic lateral derivatives) derived* from rotary rig and oscillatory rig experiments, instead of only oscillatory results, to give lower damping of the Dutch roll mode for $\alpha > 20°$, (iii) derivatives due to sideslip from a combination of static wind-tunnel tests to give maximum effects of flow breakdown and vortex flows, taking the most positive values of rolling moment (L_v) and most negative values of yawing moment (N_v) for $\alpha > 20°$.

The original and current values of these lateral parameters with angle of attack used in the mathematical models are compared with the wind-tunnel data in Figs 6,7 and 8 for three test configurations, $n_c = -10°$, $n_t = -20°$ being close to control settings used in HD1, and $n_c = 0°$, $n_t = -10°$ and $-20°$ being close to the control settings used in HD2, $(n_c = 0°, n_t = -15°)$. The variation of the damping of the Dutch roll mode is shown in Fig 9, for both sets of derivatives and the mass and inertias of the free-flight model. The revised set of derivative values gives zero damping at $\alpha = 23.5°$, for the canard setting of $-10°$, compared with $\alpha = 27.5°$ obtained using the original static sideslip and oscillatory dynamic derivatives. The divergence is also much greater. For $n_c = 0°$, the Dutch roll is damped for most of the angle of attack range below 32°, except between $\alpha = 25°$ and $26.5°$, where the divergence is small. The original values of the derivatives again indicated better damping.

The final comparisons of flight and simulated response are shown in Figs 10 and 11 for the first 100 seconds of HD1 and HD2, for the responses in angle of attack and roll rate. The other response variables measured show similar characteristics, and so are not reproduced here. The overall behaviour is simulated quite well, and various features are discussed in the following paragraphs.

4.3.1 Response after release from tow, t = 0 to 20 seconds

For HD1, the initial response in angle of attack trims to a mean angle of about 26°, but oscillates irregularly about this mean with an amplitude up to 3°, after the release disturbance has damped out (Fig 10a). The simulated trim angle of attack is also about 26°, and the oscillatory component is about the same amplitude, but the frequency appears higher than in flight. This oscillation is due mainly to the kinematic coupling term, $p\beta$, and so the lateral responses have to be in reasonable agreement before the α-response correlates. There is a large positive peak in roll rate soon after release, which is due to the asymmetric rolling and yawing moments (simulations with zero asymmetries shown in Fig 10b do not have such a peak), and then diverges to a large amplitude oscillation, usually termed wing rock. In order to simulate the frequency and amplitude of the divergent Dutch roll measured in flight at this angle of attack, it was necessary to change the rolling moments due to sideslip and roll rate from their original values, as discussed above.

The derivative $L_{q\beta}$ was found to be sufficient to limit the growth of this divergent oscillation, although it would also be possible to introduce nonlinear variation of the lateral moments with sideslip and roll rate to produce the same effect. Further analysis, including parameter identification, will continue, to study these alternatives.

The trimmed angles of attack for zero canard setting appear to be higher than predicted using the results of the 4/9-scale model tests, and so the simulated responses give an initial trim state of $\alpha \approx 26°$, with the tailplane setting of $-14.6°$ (Fig 11a). At this angle of attack, the Dutch roll is predicted to have near-zero damping, and so the simulated lateral oscillations shown in Fig 11b are larger in amplitude, and more sustained, than those measured in flight (Fig 11c). If the tailplane setting is changed to $-15.7°$ in the simulation, to give the flight angle of attack of 28°, then the lateral response is more damped (Fig 11d) and similar to the flight record. This flight also shows the typical 'roll-off' after release. The magnitude of the first peak in roll rate is calculated reasonably well, and the resulting peak in bank angle is between 30° and 40°.

---

* The assumptions made in transforming the rotary rig results from aerodynamic to geometric body axes are described in Ref 3.

4.3.2 Step change in tailplane setting, t = 57 to 66 seconds

Since the lateral responses depend on the mean angle of attack, it is convenient to discuss the changes in trim states before describing the effects of lateral control inputs.

The first change in tailplane setting in HD1 is from -18.6° to -17.1° at t = 57 seconds (the latter setting being close to the -17° of the first trial, HL1). The angle of attack trims to a mean of approximately 21° in flight, similar to HL1, before the differential tail input causes a change in mean level to 24°. However, the simulated response trims to the expected theoretical value of 24°, which is very sensitive to n_t, the slope of the trim curve $d\alpha_{trim}/dn_t$ being about -5°. The second change to a tailplane setting of -16.3° (not shown) gave a mean trim angle of 18°, after which the flight was terminated, having reached the height at which the recovery parachutes deploy. The simulated response trims to $\alpha = 19°$, where the lateral responses are well damped.

The marked influence of trimmed angle of attack on the lateral response is shown again in HD2 after the tailplane setting is changed from -14.6° to -13.8°. At the trimmed angle of attack of about 26° observed in flight, the Dutch roll appears to be undamped, and the small lateral disturbances grow immediately to a wing rock type response (Fig 11c). The simulated responses can be made to correlate by using a change in tailplane setting (as discussed in the previous section) from -15.7° to -14.6°, so that the simulated angle of attack agrees with the flight value (Figs 11a&d). Thus it appears that the pitching moment in the mathematical model needs to be modified, perhaps using the results from the full-scale model in the 5m wind-tunnel, in order to give better correlation for zero canard settings. The results discussed in the following sections have been simulated using the tailplane settings needed to obtain the observed angle of attack, shown in Fig 11a&d.

4.3.3 Differential tailplane doublet, t = 20 to 32.5, and 66 to 79 seconds

The first differential tailplane input at 20 seconds in the HD1 trial (Fig 10) occurs during the limit cycle motion and so does not cause significant changes in the character of the responses. The simulated response gives a larger amplitude in angle of attack than observed in flight, so the roll rate response is initially also of larger amplitude, but when the angle of attack settles to a smaller amplitude, so does the roll rate. The second differential tailplane input causes a significant increase in the mean angle of attack from about 19° to 25° in flight, whereas the simulated response occurs for angle of attack varying about $\alpha = 23.5°$, where the Dutch roll oscillation has near-zero damping, and is well-damped for $\alpha < 23°$. Thus the simulated response with the current mathematical model is not the same as the flight record for this input, due to the slightly different variation in angle of attack. However, it may be noted that the simulation with zero aerodynamic coupling does agree quite well.

The lateral response to the first differential tailplane input in HD2 (Fig 11) is initially damped in flight, at mean $\alpha = 27.5°$, but an increase in mean α to 28.3° at 24 seconds appears to cause a continuation of the lateral oscillation of increasing and decreasing amplitude, which is not reproduced in the simulation. Such coupling has been observed in responses of other free-flight models, and an attempt is being made to identify the coupling terms by using stepwise regression techniques. The second differential-tail input occurs during the wing rock oscillation in flight, and causes a change in phase, but in the simulation the input occurs when the lateral disturbances are very small, and the oscillation then diverges to a limit cycle. The amplitude and frequency of this oscillation are reproduced remarkably well.

4.3.4 Rudder pulse, t = 32.5 to 47, and 79 to 94 seconds

The significant effect of the rudder pulse on the angle of attack is overestimated in the simulation of HD1 at t = 32.5 seconds, and underestimated at t = 79 seconds (as shown in Fig 10). These changes in angle of attack are due mainly to the coupling term '$p\beta$' in the equation of motion for $\dot{\alpha}$, and so are sensitive to the other aerodynamic coupling terms *ie* the asymmetric sideforce and moments, and $L_{q\beta}$, which alter the phase between p and β. However, the resulting lateral response agrees reasonably well, being divergent to a limit cycle for the first rudder pulse, and convergent at the second. The first rudder pulse also caused a large excursion in bank angle, to more than 90°, which is reproduced in the simulation.

For HD2, the magnitude of the rudder pulse was reduced, and so the angle of attack does not change so rapidly after the first rudder input, but the lateral response in flight is of greater magnitude than simulated (Fig 11a&d). The second rudder input does cause a large reduction in mean angle of attack, so that the Dutch roll is damped in flight. The simulated reduction in angle of attack is smaller, resulting in a near-constant amplitude of the Dutch roll mode, which does not decay until the tailplane setting is changed at t = 79 seconds.

4.3.5 Differential canard doublet, t = 47 to 57, and 94 to 104 seconds

The frequency of the roll oscillation in flight appears to decrease after the first differential-canard input in HD1, possibly due to the increase in mean angle of attack. The simulated response in angle of attack is rather different, but the responses are similar for both α and p after the differential canard returns to zero. The correlation for the second input of differential canard is good. The variation in angle of attack after the first differential canard input in HD2 is simulated quite well, but it appears that the canard effectiveness is underestimated in the mathematical model, since the calculated roll response is of smaller magnitude. The second differential canard input occurs in flight when the lateral responses are small, and causes a divergent oscillation, similar to that already present in the simulated response.

4.4 Summary of observed phenomena at high angle of attack

The most obvious feature of the free-flight records is the wing rock type of oscillation in roll over certain ranges of angle of attack, the range depending mainly on canard setting. It is possible to simulate these oscillations using a mathematical model based on results from wind tunnel experiments, although the values of some of the derivatives probably need to be updated, using Parameter Identification techniques on the flight records to get detailed agreement. For example, interference from the model support in a wind tunnel on vortex breakdown is known to have significant effects on the sideslip characteristics, and can be expected to have some effects on results from dynamic experiments at high angles of attack.

The damping of the Dutch roll oscillation is the major parameter governing the onset and decay of the wing rock oscillations in the simulations. It may be noted that the two sets of simulated responses for HD2 with $n_t = -14.6°$, ie t = 0 to 57 seconds with flight values of n_t (Fig 11b), and t = 57 to 104 seconds with the adjusted value of $n_t = -14.6°$ (Fig 11d), give different amplitude oscillations in roll rate, even though the mean angle of attack is the same. This indicates that these responses are more like linear oscillations with near-zero damping, with amplitude dependent on initial conditions, rather than the classic nonlinear limit cycles, where the amplitude is independent of the initial conditions. It is possible to introduce nonlinear variation of the lateral moments with sideslip and roll rate[3,8], based on wind tunnel experiments, to produce limit cycles in the simulated responses.

Some of the lateral control inputs, particularly rudder, caused large excursions in bank angle (which are usually corrected by a pilot, but can lead to a type of departure resulting in a steep spiral dive for the free-flight models), and these are also simulated reasonably well.

The onset of the post-stall gyration encountered on the first flight at Larkhill is simulated quite well, (Fig 5, t = 11 to 13 seconds) and is due to a nose slice with roll rate and sideslip of opposite sign, leading to increase in angle of attack. The lateral stability roots indicate that this is initially a rapidly diverging oscillation, and the resulting responses are large enough for the kinematic cross-coupling terms in the equations of motion to become dominant. The fact that the simulated nose slice is to starboard, while the actual departure is to port, is immaterial, since the sign depends only on the small lateral disturbances prior to change in tailplane setting.

5 CONCLUDING REMARKS

The values of some of the derivatives used in the mathematical model have had to be changed slightly from those originally derived from wind tunnel tests, in order to obtain acceptable correlation between flight and simulated responses. The crucial parameter appears to be the damping of the Dutch roll oscillation at given angle of attack, and it seems that the most adverse values of the lateral data have to be chosen in order to simulate the flight responses following various lateral control inputs, for angles of attack between 20° and 40°. Addition of cross-coupling effects such as asymmetric sideforce, rolling and yawing moments, and rolling moment due to pitch rate appears to improve the correlation between flight and simulated responses. The results described here serve as a basis for the analysis being done to extract the aerodynamic data from the flight records, using Stepwise Regression and Maximum Likelihood techniques. They are also being used to design a departure prevention system, which is to be tested in future trials, and to guide the wind tunnel and free-flight experiments being planned for a new tail-less, highly-swept High Incidence Research Model.

REFERENCES

1 G.F. Moss, A.Jean Ross, G.F. Butler. A programme of work on the flight dynamics of departure using a High Incidence Research Model (HIRM). RAE unpublished.

2 A.Jean Ross, G.E.A. Reid. The development of mathematical models for a High Incidence Research Model (HIRM) Part 1. Analysis of static aerodynamic data. RAE Technical Report 83037 (1983)

3 A.Jean Ross, G.E.A. Reid. The development of mathematical models for a High Incidence Research Model (HIRM) Part 2. Analysis of dynamic test data. RAE Technical Report 84072 (1984)

4 P.J. Allen, D. Booker. Large-scale rolling rig tests on the RAE Model 2130 (HIRM 2) in the BAe Warton 5.5m low-speed wind tunnel. BAe Report AXR 103 (1982)

5 C.O. O'Leary. Dynamic tests on a high incidence research model (HIRM) in a low-speed wind tunnel. RAE Technical Report 84111 (1984)

6 K.J. Orlik-Ruckemann, E.S. Hanff. Experiments on cross-coupling and translational acceleration derivatives. Paper 8 of AGARD CP 235 (1978)

7 W.H. Curry, K.J. Orlik-Ruckemann. Sensitivity of aircraft motion to aerodynamic cross-coupling at high angles of attack. Paper 34 of AGARD CP 235 (1978)

8 R. Thorne. Some experimental and theoretical studies in aircraft stability at high angles of attack. Ph.D.Thesis, College of Aeronautics, Cranfield Institute of Technology (1983)

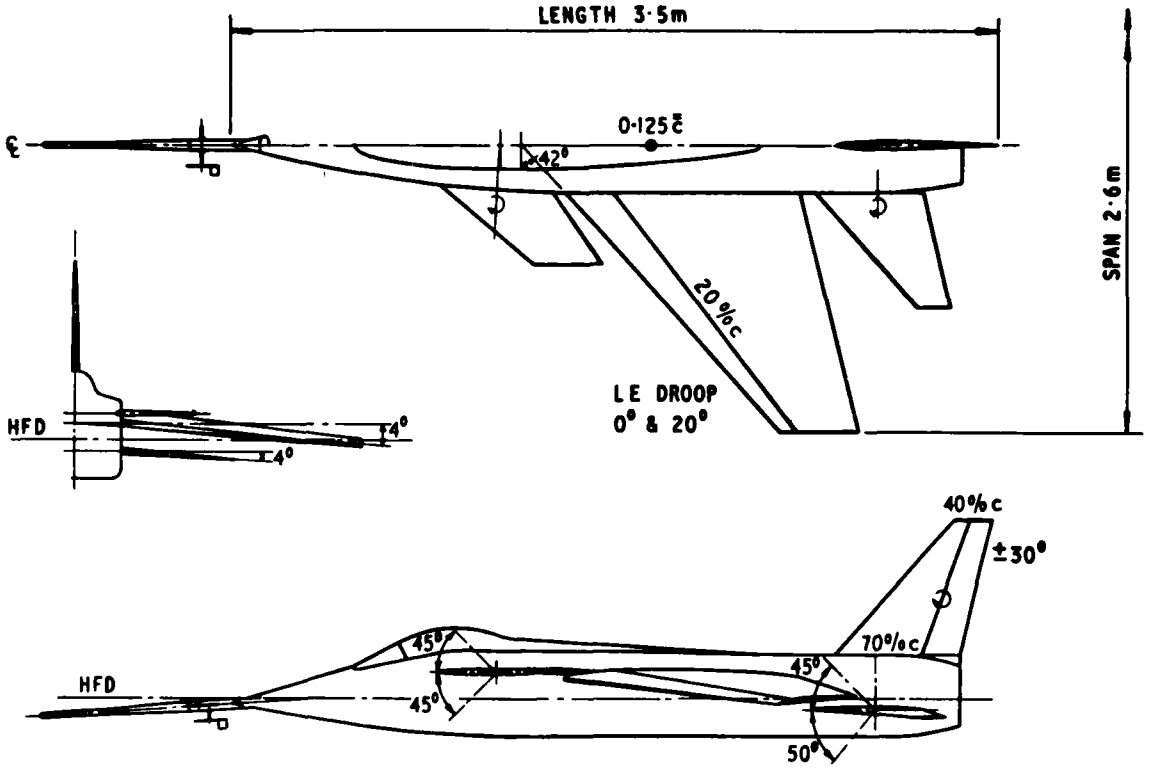

Fig 1 General arrangement of RAE 'HIRM' (free flight)

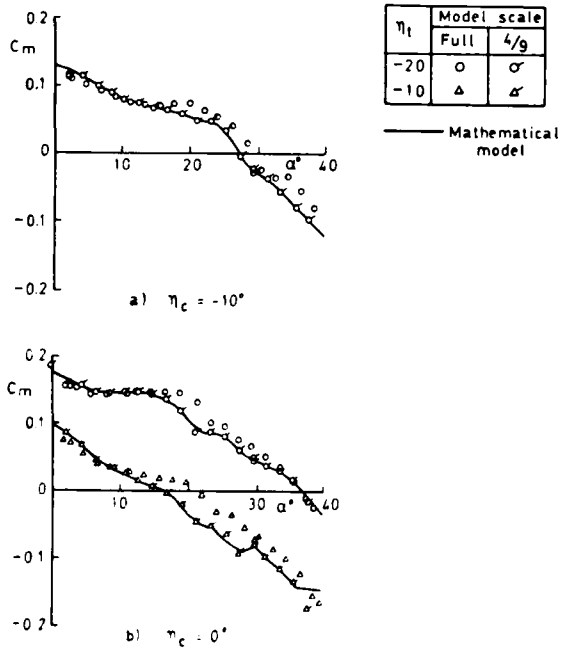

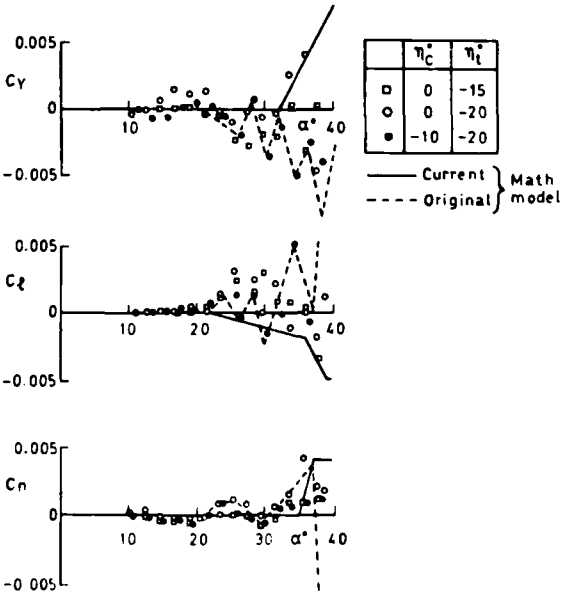

Fig 2 Pitching moment due to angle of attack

Fig 3 Sideforce and moments at zero sideslip

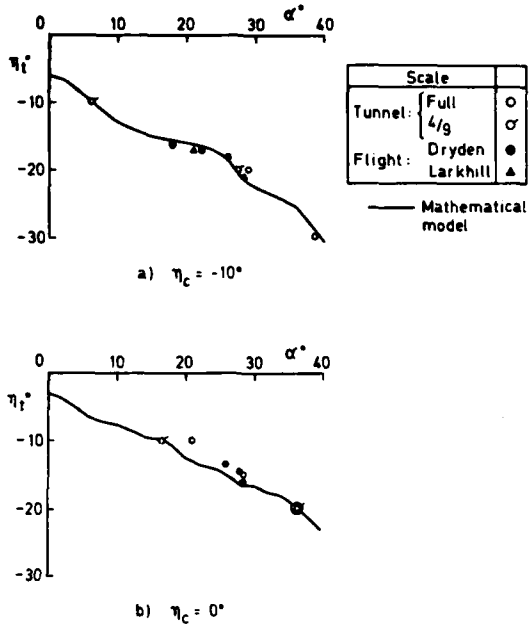

Fig 4 Tailplane angle to trim, cg at 0.125 $\bar{\bar{c}}$

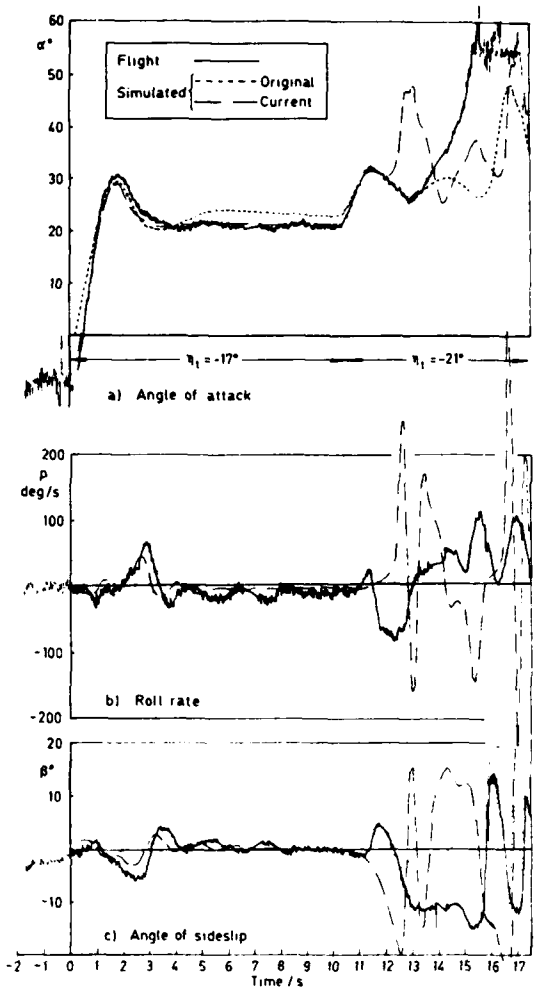

Fig 5 Comparison of flight and simulated responses, Trial HL1, η_c = -10°
(a) Angle of attack
(b) Roll rate
(c) Angle of sideslip

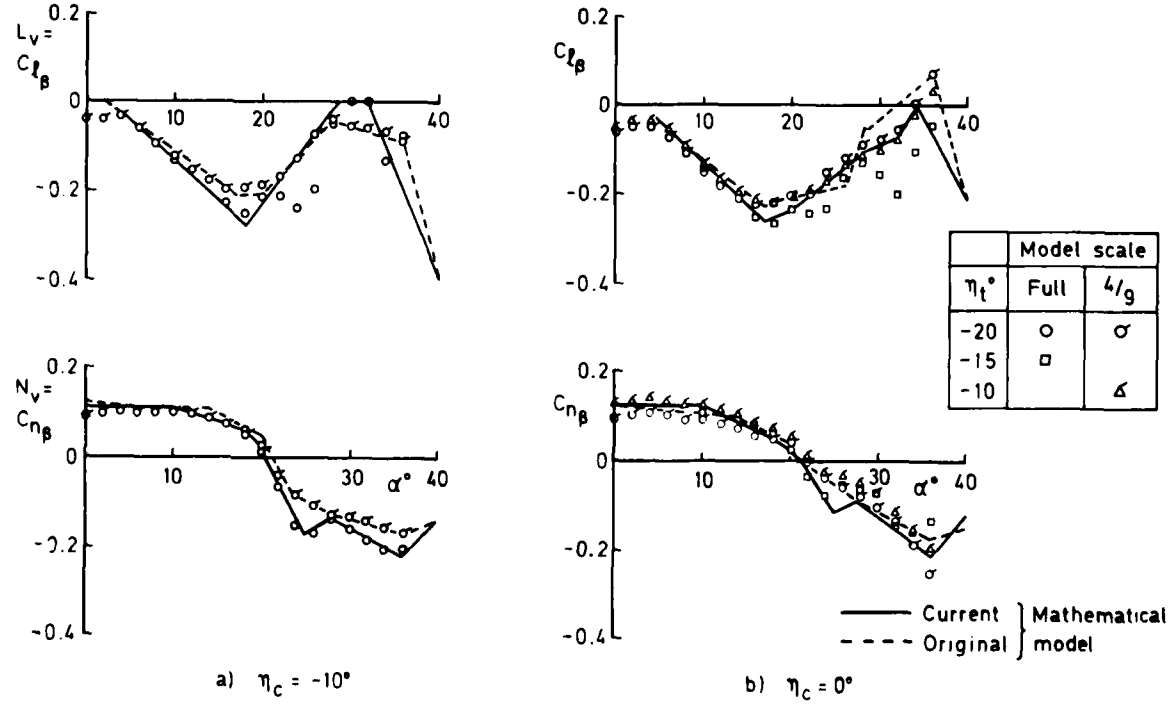

Fig 6 Rolling and yawing moment derivatives due to sideslip

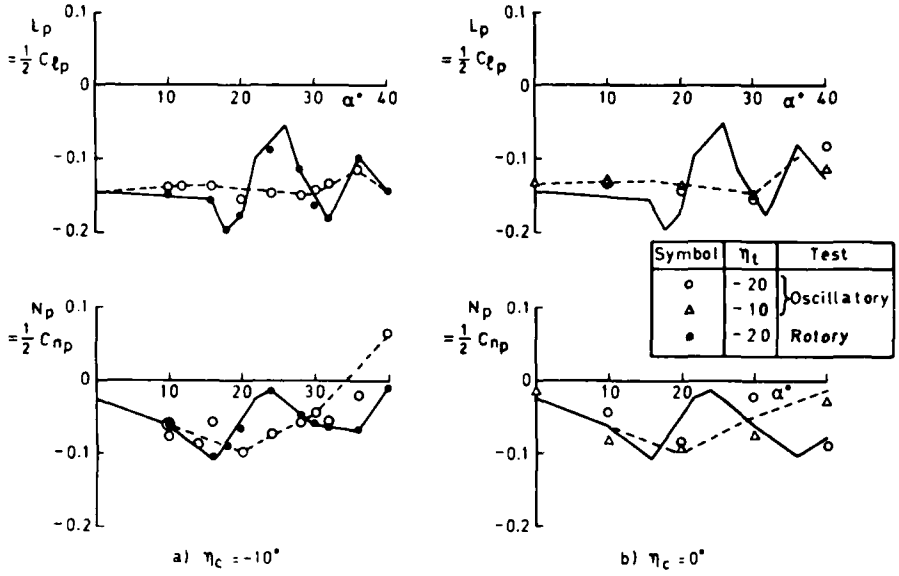

Fig 7 Rolling and yawing moment derivatives due to roll rate

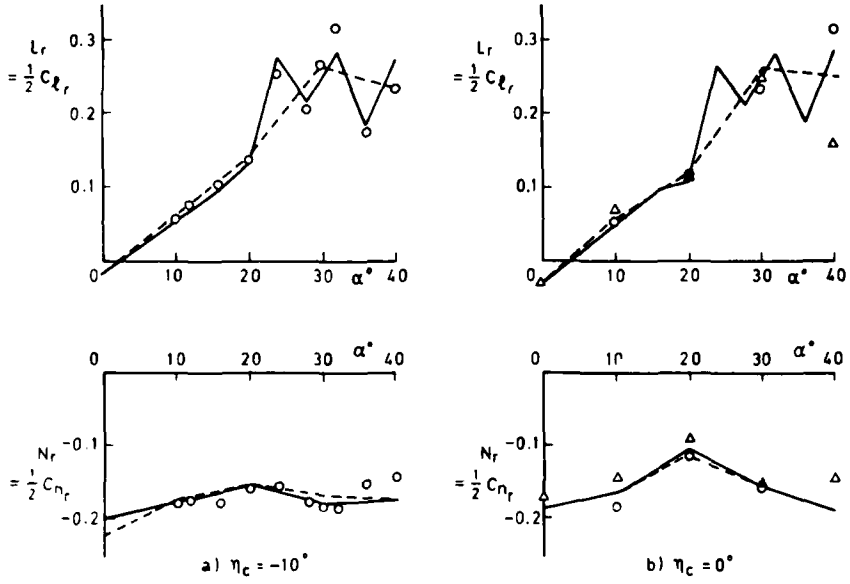

Fig 8 Rolling and yawing moment derivatives due to yaw rate

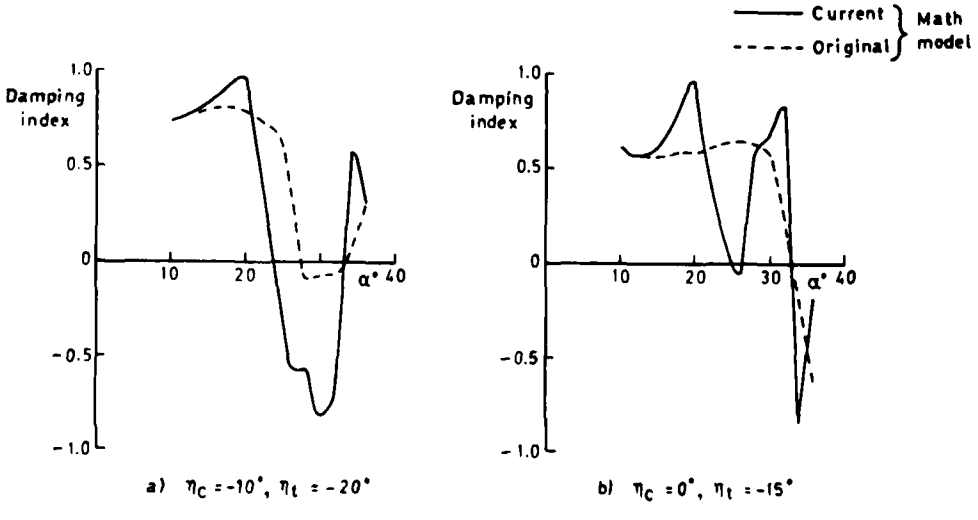

Fig 9 Damping of Dutch roll mode

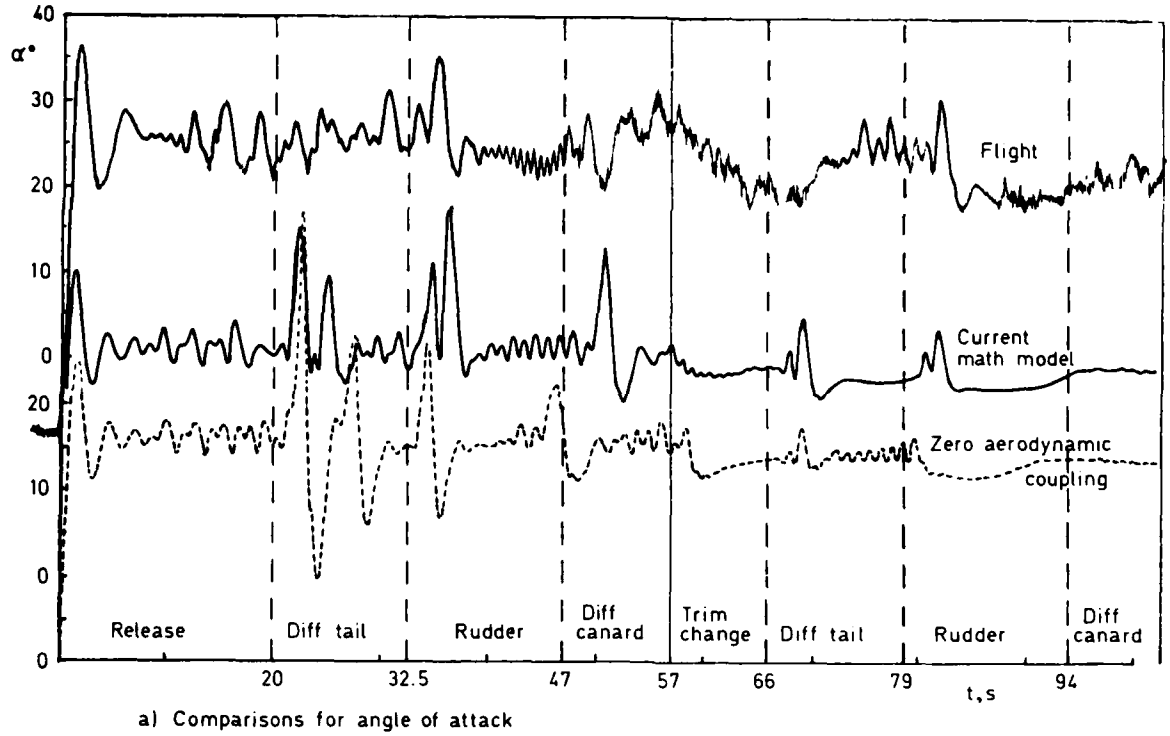

a) Comparisons for angle of attack

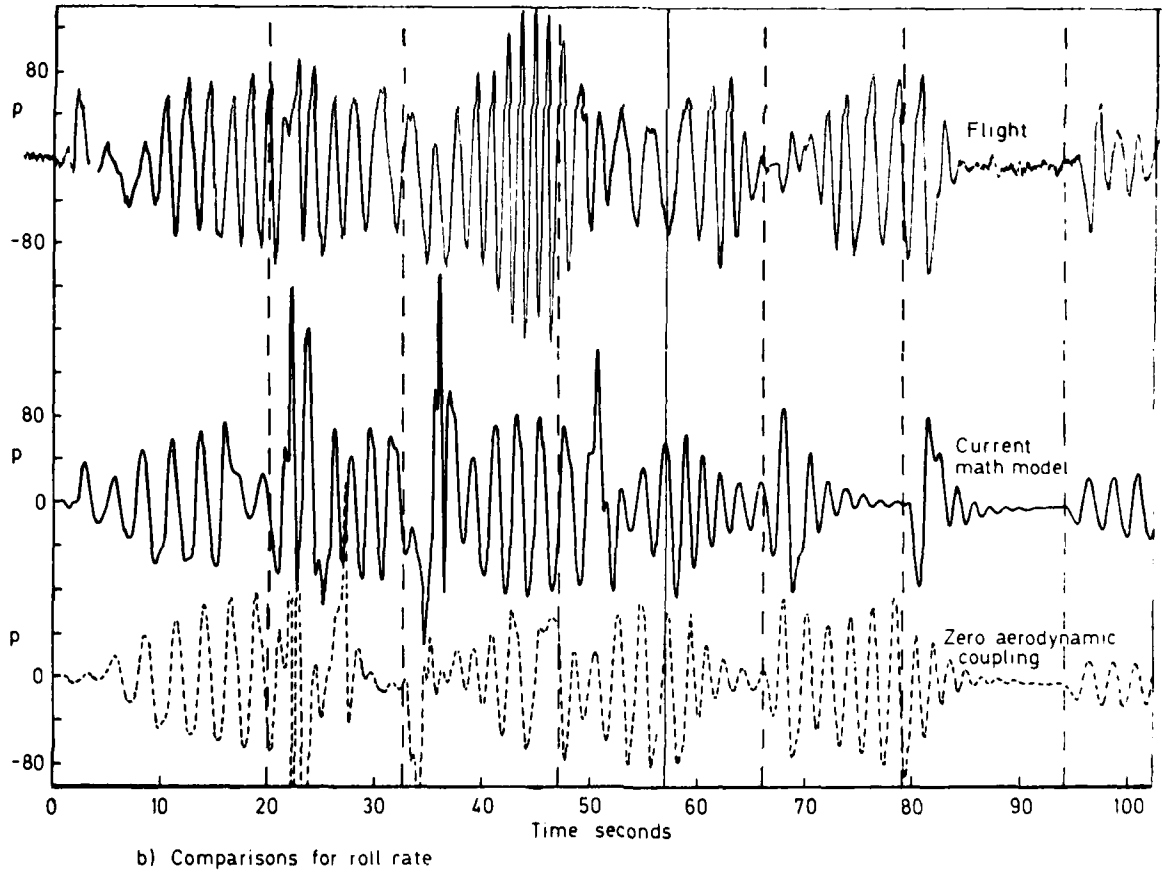

b) Comparisons for roll rate

Fig 10 Comparison of flight and simulated responses, Trial HD1, $\eta_c = -10^0$

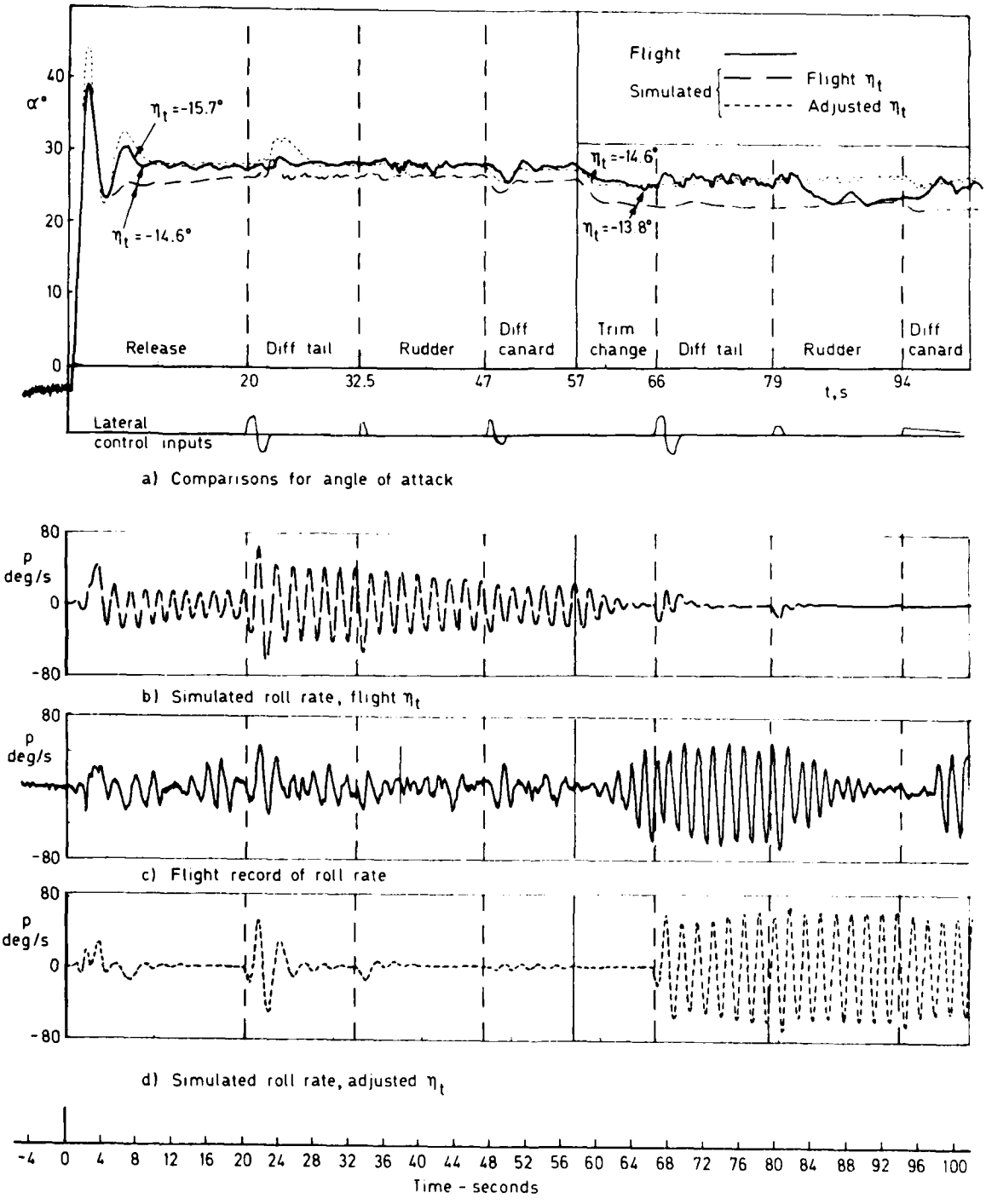

Fig 11 Comparison of flight and simulated responses, Trial HD2, $\eta_c = 0^0$

Theoretical Prediction of Wing Rocking

C. Edward Lan
Professor of Aerospace Engineering
University of Kansas
Lawrence, Kansas 66045
U.S.A.

SUMMARY

Wing rock is primarily a rolling oscillation about the longitudinal body axis at high angles of attack. It involves nonlinear interaction between flight dynamics and aerodynamics. A nonlinear aerodynamic model was proposed earlier to predict the wing rock frequency and amplitude of low aspect-ratio configurations with good accuracy. In this paper, the theory is applied to a twin-jet fighter airplane of moderate aspect ratio and to a low-speed configuration of high aspect ratio. For the purpose of predicting necessary aerodynamic derivatives, a lifting surface method coupled with nonlinear airfoil section data is developed. The results show that wing rock can be predicted with the present wing-rock and aerodynamic theories. It is also found that for configurations of high aspect ratio, the one degree-of-freedom dynamic model in the present wing-rock theory should be used. For other configurations, the three degree-of-freedom model is more appropriate.

LIST OF SYMBOLS

A	amplitude of wing rock
AR	aspect ratio
a	amplitude of roll oscillations
b	wing span
C_L	lift coefficient
C_ℓ	rolling moment coefficient
C_{ℓ_o}	rolling moment coefficient at zero sideslip
C_{ℓ_p}	roll damping coefficient
$C_{\ell_{pp}}$	$= \partial C_{\ell_p}/\partial \bar{p}$
$C_{\ell_{p\beta}}$	$= \partial C_{\ell_p}/\partial \beta$
$C_{\ell_{pt}}$	total roll damping coefficient
C_{ℓ_r}	variation of rolling moment coefficient with yaw rate
C_{ℓ_β}	variation of rolling moment coefficient with sideslip
C_n	yawing moment coefficient
C_{n_o}	yawing moment coefficient at zero sideslip
C_{n_p}	variation of yawing moment coefficient with roll rate
$C_{n_{pp}}$	$= \partial C_{n_p}/\partial \bar{p}$
$C_{n_{p\beta}}$	$= \partial C_{n_p}/\partial \beta$
C_{n_r}	variation of yawing moment coefficient with yaw rate
C_{n_β}	variation of yawing moment coefficient with sideslip
C_Y	side force coefficient
C_{Y_o}	side force coefficient at zero sideslip
C_{Y_p}	variation of side force coefficient with roll rate
C_{Y_r}	variation of side force coefficient with yaw rate
C_{Y_β}	variation of side force coefficient with sideslip
G	amplitude ratio of the β-mode to the ϕ-mode at wing-rock
g	acceleration of gravity
H	amplitude ratio of the ψ-mode to the ϕ-mode at wing-rock limit-cycle conditions
$\bar{I}$	$= (1 - I_{xz}^2/I_{xx}I_{zz})^{-1}$
I_{xx}, I_{zz}	moments of inertia about the X-axis and Z-axis
I_{xz}	product of inertia
L_o	$= \bar{q}SbC_{\ell_o}/I_{xx}$

$L_{po} = \bar{q}Sb^2C_{\ell_{po}}/2I_{xx}V$

$L_{pp} = \bar{q}Sb^3C_{\ell_{pp}}/4I_{xx}V^2$

$L_{p\beta} = \bar{q}Sb^2C_{\ell_{p\beta}}/2I_{xx}V$

$L_{\beta} = \bar{q}SbC_{\ell_{\beta}}/I_{xx}$

$L_r = (\bar{q}Sb^2C_{\ell_r}/2I_{xx}V)\cos\alpha_s$

$\bar{L}_o = \bar{I}(L_o + (I_{xz}/I_{xx})N_o)$

$\bar{L}_{po} = \bar{I}(L_{po} + (I_{xz}/I_{xx})N_{po})$

$\bar{L}_{pp} = \bar{I}(L_{pp} + (I_{xz}/I_{xx})N_{pp})$

$\bar{L}_{\beta} = \bar{I}(L_{\beta} + (I_{xz}/I_{xx})N_{\beta})$

$\bar{L}_{p\beta} = \bar{I}(L_{p\beta} + (I_{xz}/I_{xx})N_{p\beta})$

$\bar{L}_r = \bar{I}(L_r + (I_{xz}/I_{xx})N_r)$

M Mach number

m airplane mass

$N_o = \bar{q}Sb\ C_{no}/I_{zz}$

$N_{po} = \bar{q}Sb^2C_{n_{po}}/2I_{zz}V$

$N_{pp} = \bar{q}Sb^3C_{n_{pp}}/4I_{zz}V^2$

$N_{p\beta} = \bar{q}Sb^2C_{n_{p\beta}}/2I_{zz}V$

$N_r = (\bar{q}Sb^2C_{n_r}/2I_{zz}V)\cos\alpha_s$

$N_{\beta} = \bar{q}SbC_{n_{\beta}}/I_{zz}$

$\bar{N}_o = \bar{I}(I_{xz}/I_{zz})L_o + N_o)/\cos\alpha_s$

$\bar{N}_{po} = \bar{I}(I_{xz}/I_{zz})L_{po} + N_{po})/\cos\alpha_s$

$\bar{N}_{pp} = \bar{I}((I_{xz}/I_{zz})L_{pp} + N_{pp})/\cos\alpha_s$

$\bar{N}_{\beta} = \bar{I}((I_{xz}/I_{zz})L_{\beta} + N_{\beta})/\cos\alpha_s$

$\bar{N}_{p\beta} = \bar{I}((I_{xz}/I_{zz})L_{p\beta} + N_{p\beta})/\cos\alpha_s$

$\bar{N}_r = \bar{I}((I_{xz}/I_{zz})L_r + N_r)/\cos\alpha_s$

$\bar{p}$ dimensionless reduced roll rate, pb/2V

$\bar{q}$ freestream dynamic pressure

R_N Reynolds number

r yaw rate

S wing area

V flight velocity

$Y_o = \bar{q}SbC_{Y_o}/mV$

$Y_p = \bar{q}SbC_{Y_p}/2mV^2$

$Y_r = \bar{q}SbC_{Y_r}/2mV^2$

$Y_{\beta} = \bar{q}SC_{Y_{\beta}}/mV$

α angle of attack

α_s steady-state angle of attack

β sideslip angle

δ phase angle of the ψ mode

ϵ phase angle of the β mode

η amplitude ratio of the ψ mode to the ϕ mode
θ pitch attitude angle
$\nu = \Omega t$
ξ amplitude ratio of the β mode to the ϕ mode
ϕ bank angle
ψ heading angle
Ω frequency of the limit cycle in roll oscillations

1. INTRODUCTION

Wing rock is one type of lateral-directional instabilities for airplanes flying at high angles of attack. It involves nonlinear interaction between aerodynamics and flight dynamics. Several theoretical models have been proposed in the past to describe the phenomenon. These models include cubic terms in the roll damping derivatives or static yawing moment derivatives (Refs. 1 and 2), aerodynamic hysteresis (Refs. 3 and 4), vortex lift asymmetry (Ref. 5) and numerical solution of coupled unsteady vortex lift aerodynamics and the one-dimensional equation of motion (Refs. 6 and 7). As they stand at the present time, the last two methods are applicable only to those configurations exhibiting strong vortex lift effect.

Experimental results indicate that not only low aspect-ratio configurations are susceptible to wing rock (Ref. 8), but also moderate aspect-ratio ones, such as F-5 (Refs. 3 and 9) and a twin-jet fighter (Ref. 10), and high aspect-ratio configurations as well (Refs. 11 and 12). In an effort to develop a unified theory applicable to all configurations, a new nonlinear aerodynamic model based on experimental evidence was proposed in Ref. 13. Closed-form solutions to the one degree-of-freedom (DOF) and three DOF flight dynamics equations were obtained for the limit-cycle amplitude and frequency of wing rocking by applying the Beecham-Titchener method (Ref. 14). Applications of the theory to low aspect-ratio configurations have been summarized in Ref. 15.

In this paper, applications of the theory of Ref. 15 to a low-speed configuration of aspect ratio 9.18 and a twin-jet fighter of aspect ratio 2.82 will be presented.

2. THEORETICAL FORMULATION

Experimental data (Ref. 8) indicate that roll damping derivatives depend not only on roll rates but also on sideslip angles. Based on this observation, the total rolling moment coefficient can be written as

$$C_\ell(t) = C_{\ell_o} + C_{\ell_\beta}\,\beta + C_{\ell_{pt}}\,\bar{p} \tag{1}$$

where the total roll damping derivative ($C_{\ell_{pt}}$) is defined as

$$C_{\ell_{pt}} = C_{\ell_{po}} + C_{\ell_{p\beta}}\,|\beta| + C_{\ell_{pp}}\,|\bar{p}| \tag{2}$$

A similar expression for the yawing moment derivative ($C_{n_{pt}}$) can also be defined. This aerodynamic model, Eqs. (1) and (2), will produce hysteresis for the rolling moment coefficient (C_ℓ) as shown in Ref. 15. Using these aerodynamic expressions, the three DOF lateral-directional equations of motion based on body axes can be written as

$$\dot{\beta} = \bar{Y}_o + \bar{Y}_\beta\,\beta + \bar{Y}_p\,p + \bar{Y}_r\,r + \bar{Y}_\phi\,\phi \tag{3}$$

$$\dot{p} = \bar{L}_o + \bar{L}_\beta\,\beta + (\bar{L}_{po} + \bar{L}_{p\beta}\,|\beta| + \bar{L}_{pp}\,|p|)\,p + \bar{L}_r\,r \tag{4}$$

$$\dot{r} = \bar{N}_o + \bar{N}_\beta\,\beta + (\bar{N}_{po} + \bar{N}_{p\beta}\,|\beta| + \bar{N}_{pp}\,|p|)\,p + \bar{N}_r\,r \tag{5}$$

where the dimensional stability derivatives are defined in the List of Symbols. Assuming $\dot{\psi}$ is small compared with $\dot{\phi}$ in the roll rate equation and $\dot{\theta}$ is negligible in the yaw rate equation, the following kinematic equations (Ref. 16) can be used:

$$p = \dot{\phi}\ , \quad r = \dot{\psi}\cos\alpha_s \tag{6}$$

The solutions to Eqs. (3)-(5) are assumed to be

$$\beta(t) = a(t)\,\xi(t)\cos[\nu(t) + \epsilon(t)] \tag{7}$$

$$\phi(t) = a(t)\cos\nu(t) \tag{8}$$

$$\psi(t) = a(t)\,\eta(t)\cos[\nu(t) + \delta(t)] \tag{9}$$

where ξ and η are the instantaneous amplitude ratios of β and ψ modes to the ϕ mode.

and ε and δ are the corresponding phase angles. To apply the Beecham-Titchener method, it is assumed that both the frequency and amplitude of wing rock do not vary greatly during one cycle of oscillation. They will be evaluated at some average conditions to be discussed later. After lengthy derivation, the following first-order approximate solutions for the limit-cycle amplitude and frequency can be obtained (Ref. 13).

Amplitude

$$A = -\frac{3\pi}{4}\frac{\bar{L}_{p0} + H\bar{L}_r}{G\bar{L}_{p\beta} + 2\Omega\bar{L}_{pp}}$$

$$= -\frac{3\pi}{4}\frac{gC_{\ell_{p0}} + fC_{n_{p0}}}{G(gC_{\ell_{p\beta}} + fC_{n_{p\beta}}) + \frac{\Omega b}{V}(gC_{\ell_{pp}} + fC_{n_{pp}})} \tag{10}$$

Where

$$h = \frac{I_{zz}C_{\ell_r} + I_{xz}C_{n_r}}{I_{xz}C_{\ell_r} + I_{xx}C_{n_r}} \tag{11}$$

$$g = 1 - h\frac{I_{xz}}{I_{zz}} \tag{12}$$

$$f = \frac{I_{xx}}{I_{zz}}\left(\frac{I_{xz}}{I_{xx}} - h\right) \tag{13}$$

Frequency

$$\Omega^2 = -G\bar{L}_\beta$$

$$= -G\bar{q}Sb\frac{I_{zz}C_{\ell_\beta} + I_{xz}C_{n_\beta}}{I_{xx}I_{zz} - I_{xz}^2} \tag{14}$$

Where

$$G = \bar{Y}_p + H\bar{Y}_r$$

$$= \sin\alpha_s - H\cos\alpha_s + \frac{\bar{q}Sb}{2mV^2}C_{Y_p} + H\frac{\bar{q}Sb}{2mV^2}C_{Y_r}\cos\alpha_s \tag{15}$$

$$H = -\frac{1}{\bar{N}_r}\left[\bar{N}_{p0} + \frac{4}{3\pi}A\left(G\bar{N}_{p\beta} + 2\Omega\bar{N}_{pp}\right)\right.$$

$$= -\frac{I_{xz}C_{\ell_{p0}} + I_{xx}C_{n_{p0}} + \frac{4}{3\pi}A\left[G\left(I_{xz}C_{\ell_{p\beta}} + I_{xx}C_{n_{p\beta}}\right) + \frac{b\Omega}{V}\left(I_{xz}C_{\ell_{pp}} + I_{xx}C_{n_{pp}}\right)\right]}{I_{xz}C_{\ell_r} + I_{xx}C_{n_r}} \tag{16}$$

It should be noted that Eqs. (7)-(9) imply that the β and ψ modes appear in the oscillation at the wing-rock frequency. This assumption seems to be a good approximation for low aspect-ratio configurations investigated previously. For moderate to high aspect-ratio configurations, it is possible that a one DOF solution is more appropriate than those given by Eqs. (10) and (14) by setting H and I_{xz} to zero. The solution can be shown to be

$$A = -\frac{3\pi}{4}\frac{C_{\ell_{p0}}}{\sin\alpha_s C_{\ell_{p\beta}} + \frac{\Omega b}{V}C_{\ell_{pp}}} \tag{17}$$

$$\Omega^2 = -\frac{\bar{q}Sb}{I_{xx}}\sin\alpha_s C_{\ell_\beta} \tag{18}$$

To evaluate Eqs. (10) and (14) or Eqs. (17) and (18), various aerodynamic derivatives are needed. Unfortunately, data for some of these derivatives, such as $C_{\ell_{p\dot{\beta}}}$, $C_{\ell_{pp}}$ etc. are almost non-existent. Therefore, it is necessary to resort to theoretical estimation. For a configuration with strong vortex lift effect, the method of Ref. 17 with an empirical factor accounting for vortex breakdown effect may be used. However, for configurations of moderate to high aspect ratios with weak or no vortex lift effect, viscous separation effect must be properly included. However, no existing aerodynamic methods appear to be capable of predicting lateral-directional stability derivatives at high angles of attack with viscous flow separation accounted for. For the present purpose, the lifting-surface code of Ref. 17 is modified to incorporate nonlinear airfoil section data in the calculation. This is based on the nonlinear lifting-line concept, but is expected to provide more accurate results than the lifting-line theory itself. Recent applications of nonlinear lifting-line theory have been reported in Ref. 18. The present method is summarized in Appendix A.

3. NUMERICAL RESULTS

The wing-rock amplitude (A) and frequency (Ω), Eqs. (10) and (14) or Eqs. (17) and (18), depend on various aerodynamic derivatives which in turn depend on the sideslip angle, and hence A, and the roll rate, and hence Ω. Therefore, the problem must be solved iteratively. According to the Beecham-Titchener method, these aerodynamic derivatives should be evaluated at some average dynamic condition. The latter is taken to be one satisfying the following phase-plane relation (Ref. 13):

$$\phi^2 + \frac{\dot{\phi}^2}{\Omega^2} = A^2/4 \tag{19}$$

From Eq. (19), the average bank angle ϕ_{ave}, the roll rates $\bar{p}_{ave}$, $\bar{p}_{max}$ and sideslip angle β_{ave} can be obtained as

$$\phi_{ave} = 1/2\ A \tag{20}$$

$$\bar{p}_{ave} = \dot{\phi}_{ave} \frac{b}{2V} = (1/2\ \Omega\ A) \frac{b}{2V} \tag{21}$$

$$\bar{p}_{max} = 2\ \bar{p}_{ave} \tag{22}$$

$$\beta_{ave} = \phi_{ave} \sin\alpha_s = \frac{A}{2} \sin\alpha_s \tag{23}$$

The derivative $C_{\ell_{p\beta}}$ is calculated by a simple finite difference between the following two dynamic conditions: ($\beta = \beta_{ave}$, $\bar{p} = 0$) and ($\beta = 0$, $\bar{p} = \bar{p}_{ave}$). Note that both conditions satisfy Eq. (19). The derivative $C_{\ell_{pp}}$ is calculated from the following dynamic conditions: ($\beta = \beta_{ave}$, $\bar{p} = \bar{p}_{max}$) and ($\beta = \beta_{ave}$, $\bar{p} = 0$).

The iterative process is started by choosing a proper value of β_{ave} and $\bar{p}_{ave}$. Aerodynamic derivatives are then calculated under the appropriate dynamic conditions noted above. These aerodynamic derivatives are then used to calculate A, and hence β_{ave} (Eq. 23), and Ω, and hence $\bar{p}_{ave}$ (Eq. 21). The next β_{ave} and $\bar{p}_{ave}$ to be used are taken to be the average values of the new and old ones. The process is repeated until convergence is achieved.

Applications of this method to low aspect-ratio configurations have been reported earlier (Refs. (13) and (15)). In the following, applications to one configuration with AR = 9.18 and the other one with AR = 2.82 will be presented.

A High Aspect-Ratio Configuration

The configuration to be analyzed is shown in Fig. 1 (Ref. 19). It is equipped with high canards, strakes and winglets. The wing airfoil is that of NASA LS(1)-0417 (Mod). Since no airfoil data at the test condition of $R_N = 0.50 \times 10^6$ and high α are available, Eppler's code (Ref. 20) is used to calculate the airfoil lift curve up to $c_{\ell_{max}}$. The trend after $c_{\ell_{max}}$ is assumed to be that of LS(1)-0417 reported in Ref. 21. The resulting airfoil lift curve is shown in Fig. 2. The airfoil drag curve is assumed to be that of LS(1)-0417 as shown in Fig. 3. The canard airfoil lift and drag curves are based on data with linear extrapolation to high angles of attack. The predicted lift and drag curves for the complete configuration are presented in Fig. 4. It is seen that the prediction is reasonably good despite the fact that the viscous separated flow field is highly three-dimensional (Ref. 22). The calculated roll rate derivatives are presented in Fig. 5. The calculated results are referred to the stability axes to avoid the unknown $\dot{\beta}$ derivatives, while the data were obtained in

forced oscillation test and based on the body axes. Although the instability (i.e. positive C_{ℓ_p}) is predicted at the correct angle of attack ($\approx 17^o$), the trend at higher angles of attack is not well predicted, perhaps because of uncertainty in the assumed airfoil lift and drag curves at high α. The sideslip derivatives are presented in Fig. 6. The lower predicted values of C_{ℓ_β} at low α are due to negative dihedral of 4 deg on the wing. However, the data do not show this effect. Note that C_{ℓ_β} at α = 17 deg is correctly predicted.

Since calculation shows dynamic instability in roll at α = 17 deg, the wing rock condition will be calculated at this angle of attack. The calculation is based on the one DOF expressions, Eqs. (17) and (18). In fact, when the three DOF expressions, Eqs. (10) and (14), are used, the results show that the yaw amplitude (i.e. H) dominates and the wing rock amplitude becomes negative. This obviously violates the assumptions made in deriving the equations in that roll oscillation dominates the motion. It should be noted that for this configuration I_{xx}/I_{zz} = 0.32.

The iterative process is started by assuming $\bar{p}_{ave}$ = 0.01 and $\bar{\beta}_{ave}$ = 0.0872 (=5 deg). The convergence characteristics are shown in Fig. 7. The free flight test was made at a wing $R_N \approx$ 300,000 (Ref. 12), while the calculation is based on a wing R_N = 500,000 to compare with different sets of data shown in Figs. 5 and 6. The predicted amplitude and frequency are 8.3 deg and 0.45 cycle/sec (hertz), respectively, as compared with 10 deg and 0.35 ~ 0.5 hertz in free flight at a lower R_N.

A Twin-Jet Fighter Configuration

The flight record of a twin-jet fighter airplane as shown in Fig. 8 at M = 0.4 and 25,000 ft (7620 m) altitude was analyzed in Ref. 10 about its lateral-directional characteristics. The same configuration was also tested in the wind tunnel (Ref. 23), using forced oscillation test for roll rate derivatives.

To analyze this configuration, Eppler's code is again applied to predict the airfoil characteristics as shown in Fig. 9. Based on the comparison shown in the top figure of Fig. 9, the airfoil lift curve at the test Reynolds number of Ref. 23, shown in the bottom of Fig. 9, is modified. The predicted lift and drag characteristics for the complete configuration are presented in Fig. 10. Note that the effect of vortex breakdown has been included in both viscous and inviscid calculations. It is seen that the prediction is reasonably good. At high angles of attack, the results are again affected by the accuracy of assumed airfoil lift curve.

The roll rate derivatives with $\bar{p}$ = 0.01 are presented in Fig. 11. The calculated results predict roll instability at an angle of attack of 20 deg with good agreement with data.The predicted sideslip derivatives (not shown) also show good agreement with data.Therefore, the predicted results are reasonably good except at high angles of attack above that of roll instability.

To predict the wing rock characteristics at flight conditions of the full-scale vehicle, the airfoil characteristics are re-calculated at a Reynolds number of 22×10^6 corresponding to the flight conditions to be analyzed. The calculated results of airfoil characteristics (not shown) are quite reasonable so that no modification of the lift curve is made. By calculating C_{ℓ_p} at $\bar{p}$ = 0.01 for different angles of attack, it is found that C_{ℓ_p} becomes most positive at α = 26 deg. Therefore, the wing-rock characteristics will be calculated at this angle of attack.

Application of three DOF expressions, Eqs. (10) and (14), indicates that the yaw amplitude ratio (H) is moderately large ($\approx$ - 0.388). This is mainly caused by a negative but significant C_{n_p} ($\approx$ - 0.14). However, the three DOF equations do produce converged solutions for wing-rock conditions. In the real situation as analyzed in Ref. 10, a directional divergence follows the wing-rock condition almost immediately under the maneuvering condition with increasing angle of attack. Therefore, the limit-cycle condition of wing rock did not have a chance to develop. However, as noted in Ref. 10, a severe wing rock appeared at $\alpha \approx$ 22 deg.

Now assume that a limit-cycle wing rock is developed. The calculated frequency and amplitude at α = 26 deg. are presented in Fig. 12 based on both three DOF and one DOF expressions. The iteration is started by taking $\bar{p}_{ave}$ = 0.01 and ϕ_{ave} = 10 deg for the one DOF calculation. The three DOF calculation is started by using the converged conditions for the one DOF equations. The converged results based on the three DOF equations show that the frequency is 0.26 hertz and the amplitude is 13.9 deg. On the other hand, the one DOF expressions produce a frequency of 0.26 hertz and an amplitude of 18.6 deg. Based on the time history of maneuver presented in Ref. 10, the amplitude of wing rock is estimated to be 13 deg and the frequency to be about 0.18 cycle/sec. Calculation also indicates that $C_{\ell_{pp}}$ derivative becomes dominant over $C_{\ell_{p\beta}}$ for this

configuration, contrary to the situation for the high aspect-ratio configuration and low aspect-ratio configurations analyzed earlier.

4. CONCLUSIONS

A theory of wing rock developed earlier has been applied to a high aspect-ratio configuration and a twin-jet fighter airplane. For the purpose of estimating the necessary aerodynamic forces and moments at high angles of attack involving viscous flow separation, a lifting-surface method coupled with nonlinear airfoil section data is developed. The calculated results indicate that the present wing-rock theory together with the present aerodynamic method can be successfully employed to predict wing rock characteristics of low to high aspect-ratio configurations. For high aspect-ratio configurations, a one degree-of-freedom dynamic model should be used. On the other hand, for low to moderate aspect-ratio configurations, the three degree-of-freedom model is more suitable.

5. REFERENCES

1. Ross, A.J., "Lateral Stability at High Angles of Attack, Particularly Wing Rock," Paper 10, AGARD-CP-260, Sept. 1978.

2. Ross, A.J., "Investigation of Nonlinear Motion Experienced on a Slender-Wing Research Aircraft," Journal of Aircraft, Vol. 9, Sept. 1972, pp. 625-631.

3. Cord, T., "Hysteresis - Induced Wing Rock," AFFDL-TM-75-76-FGC, The US Air Force, June 1975.

4. Schmidt, L.V., "Wing Rock due to Aerodynamic Hysteresis," Journal of Aircraft, Vol. 16, March 1979, pp. 129-133.

5. Ericsson, L.E., "The Fluid Mechanics of Slender Wing Rock," Journal of Aircraft, Vol. 21, May 1984, pp. 322-328.

6. Konstadinopoulos, P., Mook, D.T., and Nayfeh, A.H., "Numerical Simulation of the Subsonic Wing-Rock Phenomenon," AIAA Paper 83-2115, Aug. 1983.

7. Konstadinopoulos, P., Mook, D.T. and Nayfeh, A.H., "Subsonic Wing Rock of Slender Delta Wings," AIAA Paper 85-0198. Jan. 1985.

8. Nguyen, L.T., Yip, L.P. and Chambers, J.R., "Self-Induced Wing Rock of Slender Delta Wings," AIAA Paper 81-1883, Aug. 1981.

9. Hwang, C. and Pi, W.S., "Some Observations on the Mechanism of Aircraft Wing Rock," Journal of Aircraft, Vol. 16, June 1979, pp. 366-373.

10. Chambers, J.R. and Anglin, E.I., "Analysis of Lateral-Directional Stability Characteristics of a Twin-Jet Fighter Airplane at High Angles of Attack," NASA TN D-5361, Aug. 1969.

11. NASA 1981 Annual Report of Langley Research Center R & T, NASA TM-83-221, pp. 24-25.

12. Satran, D.R., "Exploratory Low-Speed, Wind-Tunnel Investigation of the Flight Characteristics of an Advanced Canard General Aviation Airplane Configuration," a proposed NASA Technical Paper.

13. Hsu, C.H., "Theory of Wing Rock," Ph.D. Dissertation, University of Kansas, Feb. 1984.

14. Beecham, L.J. and Titchener, I.M., "Some Notes on an Approximate Solution for the Free Oscillation Characteristics of Non-Linear Systems Typified by $\ddot{x} + F(x,\dot{x}) = 0$," British ARC R & M No. 3651, Aug. 1969.

15. Hsu, C.H. and Lan, C.E., "Theory of Wing Rock," AIAA Paper 85-0199, Jan. 1985.

16. Roskam, J., "Airplane Flight Dynamics and Automatic Flight Controls," Roskam Aviation and Engineering Corporation, RR 4, Box 274, Ottawa, Kansas 66067.

17. Lan, C.E. and Hsu, C.H., "Effects of Vortex Breakdown on Longitudinal and Lateral-Directional Aerodynamics of Slender Wings by the Suction Analogy," AIAA Paper 82-1385, Aug. 1982.

18. Anderson, J.D. Jr., Corda, S. and VanWie, D.M., "Numerical Lifting Line Theory Applied to Drooped Leading-Edge Wings Below and Above Stall," Journal of Aircraft, Vol. 17, Dec. 1980, pp. 898-904.

19. Holmes, B.J., Obara, C.J. and Yip, L.P., "Natural Laminar Flow Experiments on Modern Airplane Surfaces," NASA TP-2256, June 1984.

20. Eppler, R. and Somers, D.M., "A Computer Program for the Design and Analysis of Low-Speed Airfoils," NASA TM-80210, Aug. 1980.

21. Satran, D. and Snyder, M.H.," Two-Dimensional Tests of GA(W)-1 and GA(W)-2 Airfoils at Angles-of-Attack From 0 to 360 Degrees," WER-1, Wind Energy Laboratory, Wichita State University, Wichita, Kansas, Jan. 1977.

22. Winkelmann, A.E., "On the Occurrence of Mushroom Shaped Stall Cells in Separated Flow," AIAA Paper 83-1734, June 1983.

23. Grafton, S.B. and Libbey, C.E., "Dynamic Stability Derivatives of a Twin-Jet Fighter Model for Angles of Attack from -10^{o} to 110^{o}," NASA TN D-6091, Jan. 1971.

24. Loftin, L.K. Jr. and Cohen, K.S., "Aerodynamic Characteristics of a Number of Modified NACA Four-Digit-Series Airfoil Sections," NACA TN-1591, June 1948.

6. ACKNOWLEDGEMENTS

This work was supported by NASA Grant NAG 1-134 through Langley Research Center. Mr. William P. Gilbert was the technical monitor.

The author wishes to express his appreciation to Mr. Dale Satran of Langley Research Center for providing data on the high aspect-ratio configuration analyzed in this paper.

APPENDIX A

A Lifting-Surface Method Using Nonlinear Section Data

Based on the lifting-line concept, the three-dimensional (3-D) sectional lift ($c_{\ell(3\text{-}D)}$) is given by the two-dimensional (2-D) value evaluated at an effective angle of attack. For the present purpose, the effective angle of attack is defined as

$$\alpha_e = \alpha_n - \alpha_i - \alpha_o - \Delta\alpha \tag{A.1}$$

where α_n is the geometric α normal to the section which may have dihedral, α_i is the induced angle of attack, α_o is the angle of zero lift, and $\Delta\alpha$ represents a reduction in α to be calculated due to viscous effect. It follows that

$$c_{\ell(3\text{-}D)} = c_{\ell_\alpha} \sin(\alpha_n - \alpha_i - \alpha_o - \Delta\alpha) \tag{A.2}$$

Assuming $c_{\ell_\alpha} = 2\pi/(1-M^2)^{1/2}$, Eq. (A.2) can be solved for α_i:

$$\alpha_i = \alpha_n - \sin^{-1}\left[\frac{c_{\ell(3\text{-}D)}}{c_{\ell_\alpha}}\right] - \alpha_o - \Delta\alpha \tag{A.3}$$

Let the 2-D section lift coefficient evaluated at $\alpha_n - \alpha_i$ be $c_{\ell(2\text{-}D)}$ and let

$$f = c_{\ell(2\text{-}D)} / c_{\ell(3\text{-}D)} \tag{A.4}$$

Since f is usually less than 1.0, a geometric angle of attack (α') which produces the reduced lift can be found. That is

$$\sin\alpha' = f \sin\alpha_n ,$$

or

$$\alpha' = \sin^{-1}(f \sin\alpha_n) \tag{A.5}$$

It follows that $\Delta\alpha$ in Eq. (A.1) can be found to be

$$\Delta\alpha = \alpha_n - \alpha' \tag{A.6}$$

The solution is obtained iteratively as follows:

(1) Assume $\Delta\alpha = 0$.
(2) Find α_i from Eq. (A.3).
(3) Calculate f from Eq. (A.4).
(4) Determine $\Delta\alpha$ from Eqs. (A.5) and A.6).
(5) Use $\Delta\alpha$ to reduce α in the 3-D boundary condition to determine $c_{\ell(3\text{-}D)}$.

(6) Repeat steps (2)-(5).

Based on experience, in the first three iterations an over-relaxation parameter of 1.75 for $\Delta\alpha$ worked quite well. After that, under-relaxation should be used. In the present computer program, convergence is assumed to be achieved if successive calculated lift coefficients(C_L) differ by less than 0.5%.

Once the longitudinal loading is calculated, the lateral-directional loading is added at each spanwise station to determine the final antisymmetrical loading. The antisymmetrical loading can have its sign reversed if the combined loading happens to be on the back side (i.e. with negative slope) of the curve for the normal force coefficient (c_N). The normal force coefficient is defined to be

$$c_N = c_{\ell(2\text{-}D)} \cos(\alpha_n - \alpha_i) + c_{d(2\text{-}D)} \sin(\alpha_n - \alpha_i) \qquad (A.7)$$

There are exceptions to the concept described above:

(1) On a strake, the flow is assumed to be attached until the strake vortex breakdown is predicted.
(2) For a configuration of moderate aspect ratio with some vortex lift, the iterative procedures described above are not started until the predicted vortex breakdown occurs. This means that at low α after the inviscid loading is obtained, the viscous effect is calculated in one pass only without iteration.
(3) When the flow is separated near the tip under symmetrical loading, it will separate further on one side under rolling condition. However, on the other side, if the leading-edge vortex does not burst, potential lift will be recovered. This is similar to the "vortex lift recovery" discussed in Ref. 17 and may make the roll damping derivative positive.

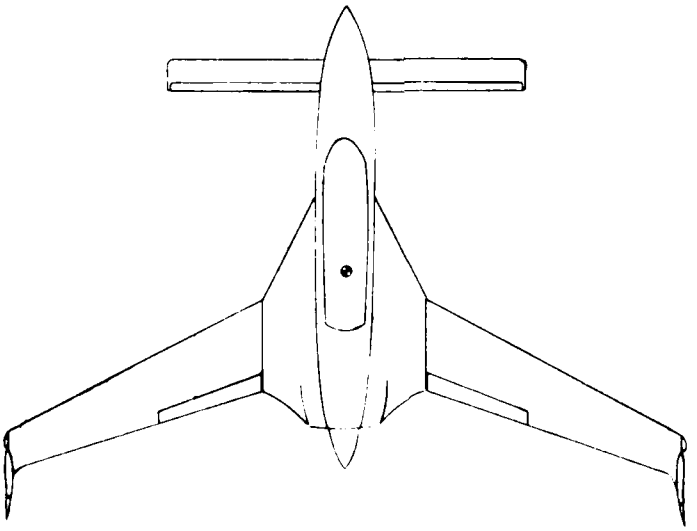

Figure 1 A High Aspect-Ratio Configuration with Canards, Strakes and Winglets.

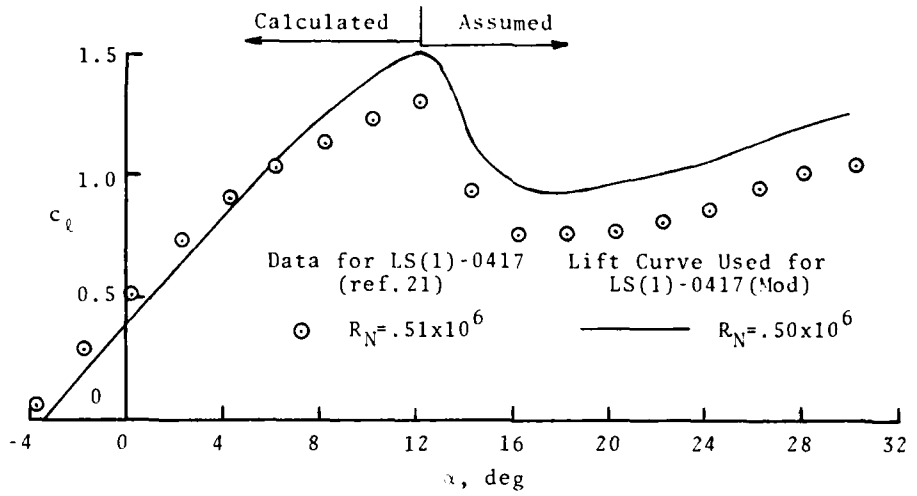

Figure 2 Lift Curves for Two NASA Low-Speed Airfoils. M = 0.

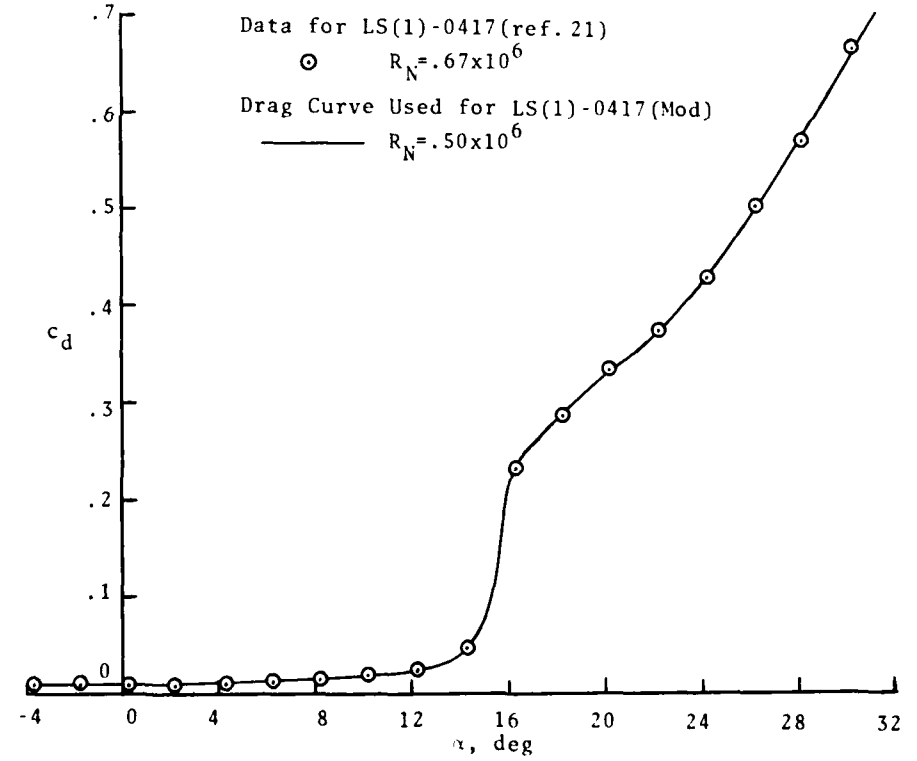

Figure 3 Drag Curves for Two NASA Low-Speed Airfoils. M = 0.

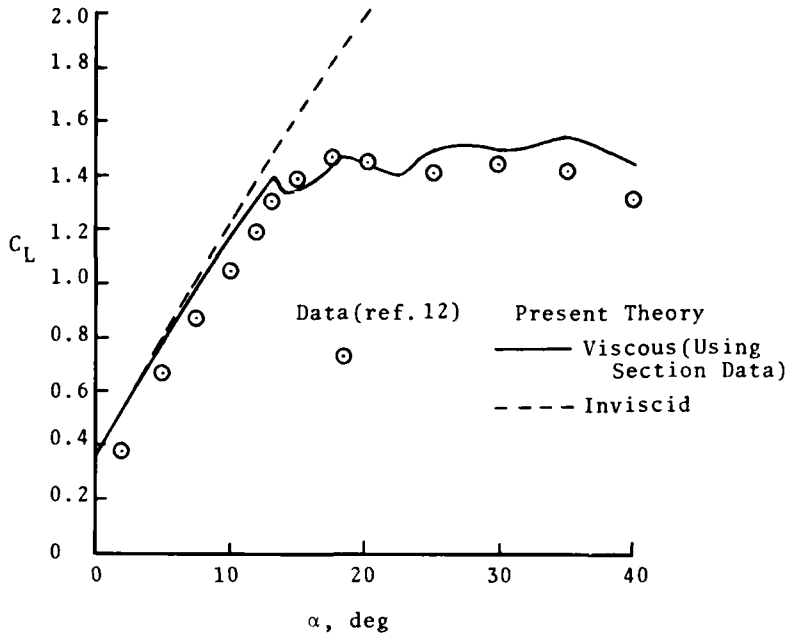

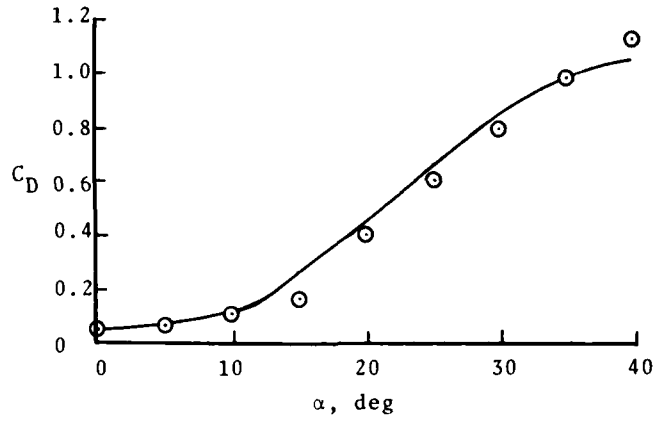

Figure 4 Aerodynamic Characteristics of the High Aspect-Ratio Configuration Shown in Fig. 1. R_N = 500,000 , M = 0.

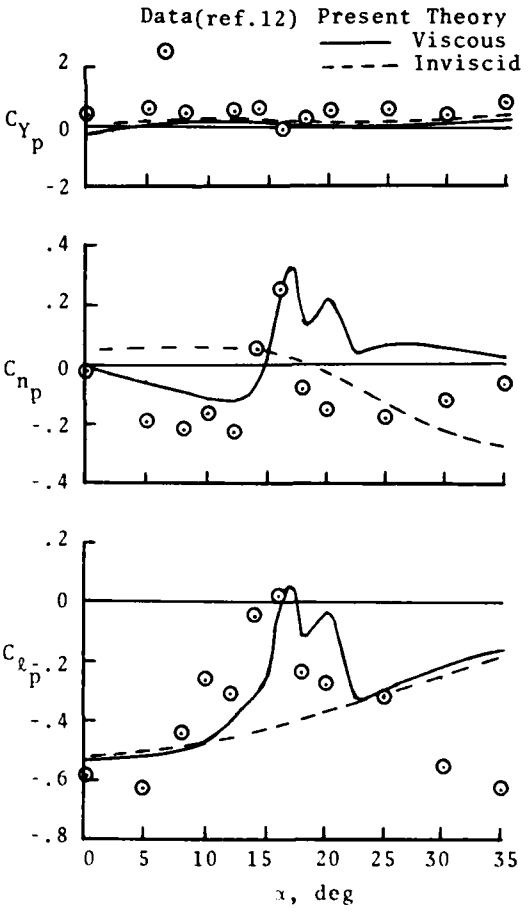

Figure 5 Roll Rate Derivatives Calculated at $\bar{p}$ = 0.01 (Stability Axes) for the High Aspect-Ratio Configuration (Fig. 1). Data from Forced Oscillation Tests. R_N = 500,000 , M = 0.

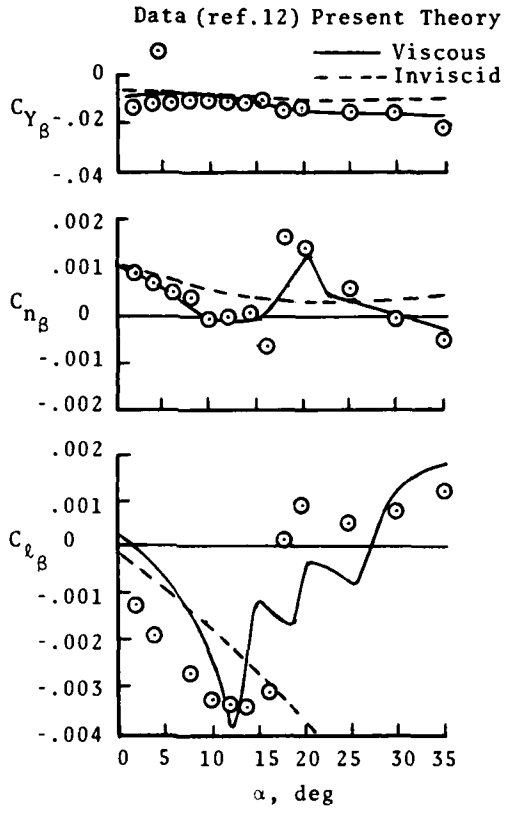

Figure 6 Sideslip Derivatives in per deg Calculated at β = 5 deg for the High Aspect-Ratio Airplane of Fig. 1. M=0, R_N=500,000.Referred to Body Axes.

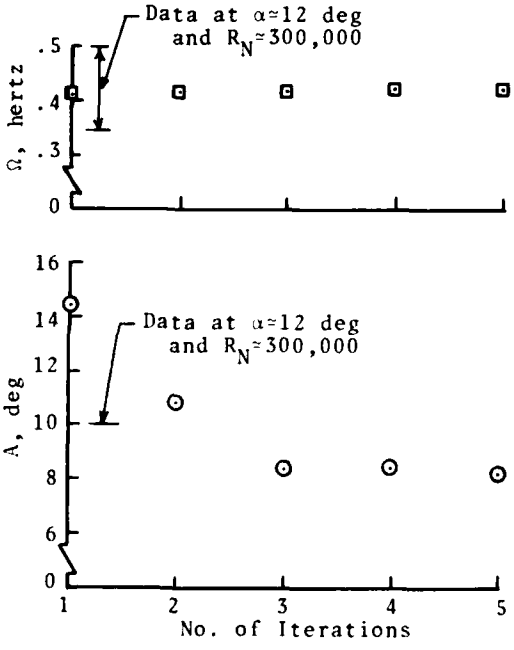

Figure 7 Convergence Characteristics of Wing Rock Frequency(Ω) and Amplitude(A) at α=17 deg and M=0 for the Configuration of Fig. 1. R_N=500,000.

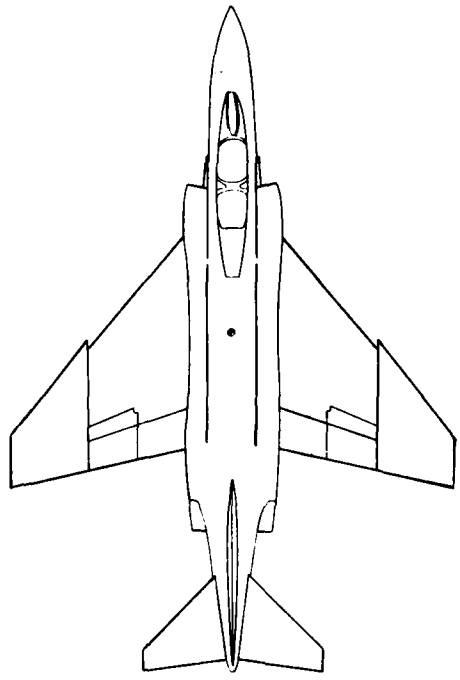

Figure 8 A Twin-Jet Fighter Configuration.

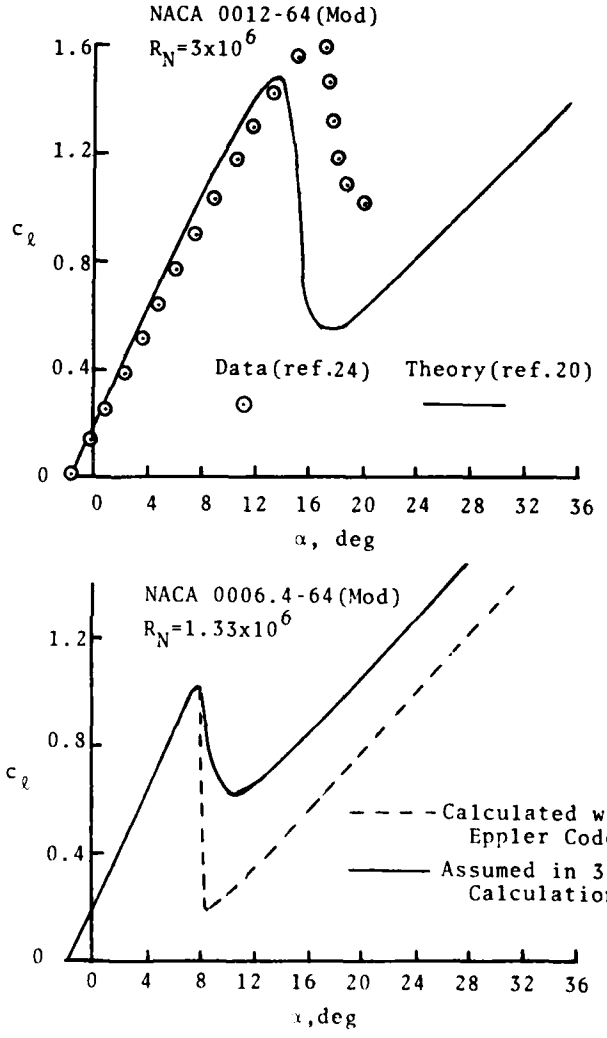

Figure 9 Airfoil Lift Curves for the Twin-Jet Fighter Configuration of Fig. 8.

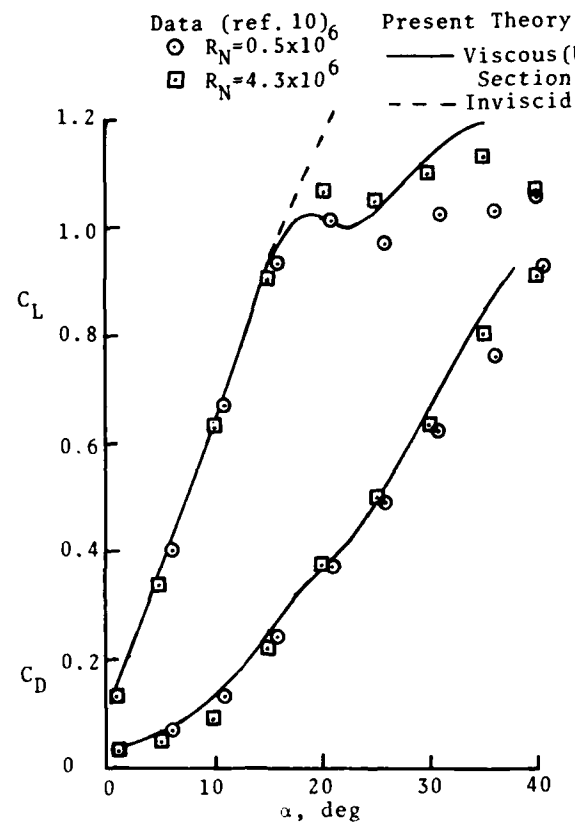

Figure 10 Longitudinal Aerodynamic Characteristics for the Twin-Jet Fighter of Fig. 8 with Vortex Breakdown Effect at M = 0.

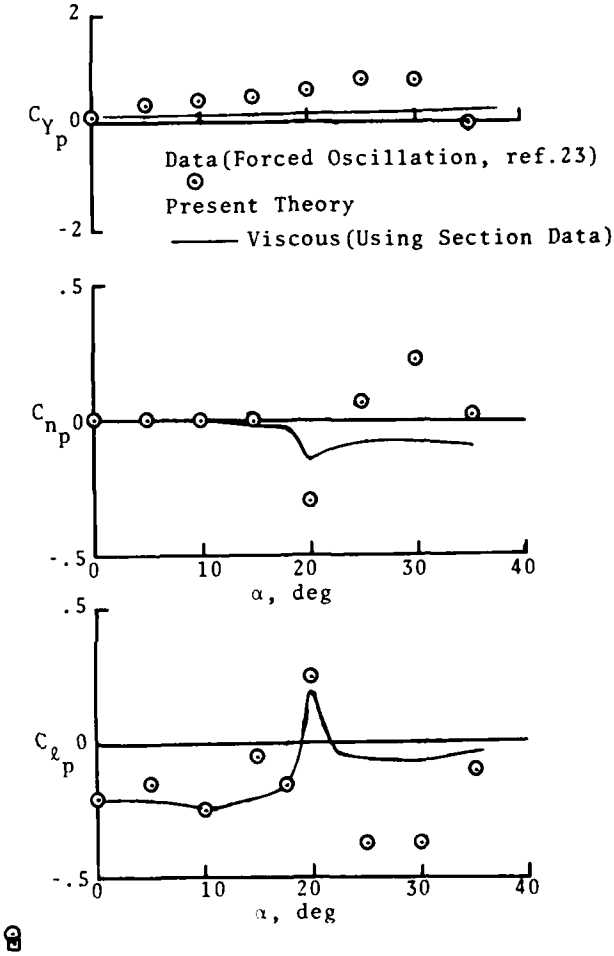

Figure 11 Roll Rate Derivatives Calculated at $\bar{p}$ = 0.01 (Stability Axes) for the Twin-Jet Fighter of Fig. 8 at M = 0.

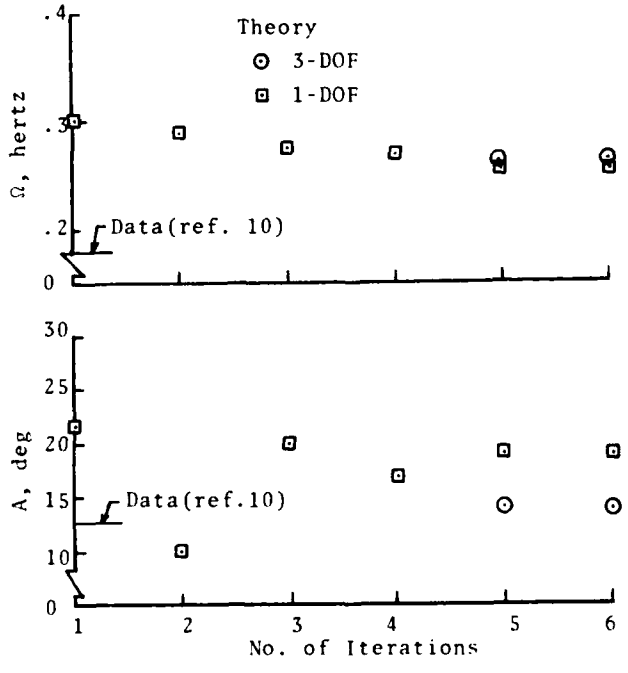

Figure 12 Convergence Characteristics of Wing Rock Frequency (Ω) and Amplitude (A) at α = 26 deg and M = 0.4 for the Twin-Jet Fighter of Fig. 8. R_N = 22x10^6.

Effects of aerodynamic lags on aircraft responses

by

J.C. van der Vaart

Delft University of Technology
Department of Aerospace Engineering
Kluyverweg 1
2629 HS Delft

Summary

Results of a theoretical study on the effects of unsteady aerodynamics on symmetric aircraft responses due to elevator and vertical turbulence inputs, are presented.
Several linear models were developed to describe unsteady lift and downwash and delays due to horizontal tail length. Results for three example aircraft types show that calculated normal acceleration levels due to turbulence are very little affected by including unsteady wing lift and downwash. However, there appears to be a noticable influence on plunging acceleration and pitch rate response to elevator or vertical turbulence inputs.

Introduction

From the literature, it is evident that there are quite a number of sophisticated ways to mathematically model the aerodynamic forces and moments in unsteady flight conditions, see Ref. 1.
In the field of handling qualities research, stability and control, flight simulation, controller design and model identification, the influence of unsteady aerodynamic forces and moments is usually modelled in a much more simple way, although some publications in this area do feature more elaborate modelling of non-stationarity (see Refs. 2 and 3, for instance).
For practical reasons very elaborate models may not be desirable and it is usually tacitly assumed that more refined models are not necessary in order to obtain acceptably accurate mathematical formulations of aircraft dynamics. The present Paper attempts to verify whether this is justified for aircraft responses due to control deflections and atmospheric turbulence.
The main symmetric unsteady aerodynamic phenomena are reviewed here and their possible influence on aircraft responses are assessed. In addition to the well-known aerodynamic delays caused by the horizontal tail length, the gust response delay due to wing sweep and the unsteady wing lift and pitching moment due to plunging motion and vertical turbulence are taken into account and modelled by way of low order linear filters. Unsteady effects can thus be formulated by adding a linear set of ordinary differential equation to the classical linear equations of motion.
Results of calculations on some representative airplane types, restricted to responses of pitching velocity q and normal acceleration factor n are presented and compared.
This is done under the assumption of constant flight-speed, frozen field type gaussian vertical turbulence (Dryden spectrum), uniformly distributed over the wing span.
The main part of the Paper is on rigid aeroplanes, but some results are shown for a simple, non-rigid case, illustrating the possible influence of wing flexibility on gust response.

Aircraft responses to elevator inputs

Modelling of delays and lags

The block diagram of Fig. 1 shows the seperate contributions of the wing and the tail to the total Z-force and to the pitching moment due to angle of attack (plunging motion) alone.
Two categories of unsteady effects are distinguished. The first, denoted here by "delays", is caused by the fact that the change in downwash of the wing due to a change in angle of attack, (plunging motion) reaches the horizontal tail delayed by ℓ_h/V secs. In the frequency domain, or in real-time simulations, a pure delay may be retained, but for other applications, it is necessary to introduce a linear approximation, of which the first order Taylor series approximation yields the well known derivatives $C_{Z_{\dot{\alpha}}}$ and $C_{m_{\dot{\alpha}}}$, see Ref. 4.

Another possibility is to use a first (or higher) order Padé approximation, which is, in principle, more accurate, see the Appendix and Refs. 5 and 7.
The second class of unsteady effects, denoted in this Paper by "lags" is related to unsteady wing lift and wing pitching moment. These are approximated here by a second order linear filter, see the Appendix.

The following models were considered.

1) Aerodynamic delay due to horizontal tail length, modelled by derivatives $C_{Z_{\dot{\alpha}}}$ and $C_{m_{\dot{\alpha}}}$. (First order Taylor series approximation).
2) Aerodynamic delay due to horizontal tail length, modelled by first order Padé approximation.
3) Horizontal tail length delay according to 2. Unsteady wing lift, downwash and pitching moment modelled by second order linear filter (Approximating, linearized Theodorson function).

In the linear equations of motion, the Z-force and the pitching moment due to pitch rate q and due to elevator deflection δ_e were computed in the usual fashion by using the stability derivatives C_{z_q}, C_{m_q}, $C_{z_{\delta_e}}$ and $C_{m_{\delta_e}}$, effects due to "apperent additional mass" were neglected (Ref. 4).

Horizontal tailplane lift was assumed to change instanteneously with tailplane angle of attack in all models and flight speed was assumed to be constant. Each of the three above models can readily be included in the classical equations of motion, resulting in a modified set of linear, ordinary differential equations of, for models 2) and 3), increased order. For details, the reader is referred to Ref. 5. Characteristic roots (eigenvalues), and elevator step input responses were calculated for three representative aircraft types:

A) DeHavilland DHC-2 "Beaver"
B) Fokker F27 "Friendship"
C) Boeing 747

Main characteristics have been summarized in Table 1.

Results

From Fig. 2 it appears that models 1) and 2) give almost equal root locations. However, addition of unsteady wing lift and pitching moment (model 3) causes, for aircraft C for instance, a change in root location well in the order of magnitude of a change due to a c.g. shift from the most forward to the most aft position. The influence of nonsteady wing lift and wing pitching moment alone is illustrated by a model denoted by 3a, in which the effect of nonsteady wing lift on downwash was neglected.
Physically, the change in root location, especially for aircraft types A and C, can be explained by a delayed destabilizing effect of both the wing pitching moment (3a) and the downwash at the tail (3).
These effects of modelling can also be seen from the elevator step input responses (Figs. 3 and 4).
It is tempting to try and manipulate a single lumped parameter, for instance the tail length ℓ_h in the delay of model 2) or the derivates $C_{Z_{\dot{\alpha}}}$ and $C_{m_{\dot{\alpha}}}$ of model 1), in order to match the roots of model 3). For aircraft type C it is shown in Fig. 2 that such a lumped parameter description is not appropriate here. The root location of model 3 could be matched by models 1) or 2) by independently manupulating the tail length in the delay modelling and in the pitching moment equation, thereby effectively increasing the static stability. (Not shown in Fig. 2.) This possibility is to be rejected on physical grounds, since it would violate the steady state conditions.

So far, it may be concluded that, firstly, for elevator response calculations, a first order Taylor series approximation of horizontal tail lenght delay (model 1) is just as good as using a first order Padé approximation (model 2).
Secondly, if the present second order Theodorson function approximation does not grossly overestimate the influence of non-stationarity of wing lift and pitching moment and its subsequent influence on downwash, then it may be worthwhile to include model 3) for more accurate calculations.
In future work it is intended to check model 3) against results of more elaborate models of unsteady lift and pitching moment.

Aircraft responses to vertical turbulence

The block diagram of Fig. 5 shows the additional contributions, due to vertical turbulence only, of the wing and the tail to the Z-force and the pitching moment.
Again two categories of unsteady effects are distinguished, those due to pure time-delay and those due to unsteady wing lift and pitching moment.
The first category, sometimes referred to as "gust penetration effect", stems from the fact that different parts of the aeroplane are being hit by the same gust at different instants in time.
For aircraft with little or no wing sweep, the most imporant contribution is due to the horizontal tail and is characterised by the same time delay as in the case of plunging motion. In principle, this time delay can again be modelled either by a first order Taylor series approximation or by a Padé approximation.
Also in the category of penetration effects are the delays caused by wing sweep. For a swept wing, it will take a finite time to penetrate, for instance, a straight, sharp-edged gust. For wing leading edge sweep angles of around 35 to 40°, the distance in X-direction between root and tip chord leading edge may well be in the order of magnitude of the tail length. In order to assess its influence on aircraft gust response, this effect was accounted for by taking, in the case of a straight sharp-edged gust, a ramp function rather than a step input as the gust input to the wing. In the Appendix, a simple approximating linear filter is derived for mathematically modelling the wing sweep gust penetration effect for arbitrary gust inputs.
In principle, the point where the additional lift is acting, would not be constant during wing gust penetration. This phenomenon was not included in the calculation of the pitching moment, since it would lead to a non-linear operation.
The second category of unsteady effects, due to vertical turbulence, (Küssner or Sears functions) are approximated by a second order linear filter.
It should be remarked, that the wing penetration effect is accounted for by a Sears function for a three dimensional swept wing.
By combining the forces and moments according to Fig. 1 with those according to Fig 5, together with those due to pitch rate q, the linear equations governing the motions due to verrtical turbulence, under the assumption of constant flight speed, were obtained. For a detailed description of the relevant equations of motion, the reader is referred to Ref. 5.

Modelling the tail gust penetration effect

Just as for plunging motion, the time-delay of the tail length penetration effect is most easily modelled by a first order Taylor approximation. In that case, simple expressions for additional ' gust derivates' $C_{Z_{\dot{\alpha}_g}}$ and $C_{m_{\dot{\alpha}_g}}$ can be obtained, see Ref. 6. Gust response transfer functions and Power Spectral Density functions (P.S.D.'s, for short) were derived in Ref. 7 by using these derivatives. This first order Taylor approximation appeared, for the motion variables α and q, to yield reasonable approximations of transfer functions and P.S.D's when compared to those obtained by including pure time-delays (which

poses no problem in the frequency domain). When, however, the P.S.D. of the normal acceleration factor n is considered, it appears that the power spectrum remains constant for high frequencies, implying an infinite variance of n, which is of course physically impossible (see Fig. 6, taken from Ref. 7). This discrepancy, which has been elaborated in some detail in Ref. 8, can easily be circumvented by using the first order Padé approximation, which is also readily applied in the time-domain. Due to the problem of infinite variance of n, the Taylor approximation of the tail length gust penetration effect is rejected for the gust response calculations described below.

Mathematical models for airplane response to vertical turbulence

After rejecting the first order Taylor series approximation for the case of gust response calculations, the following models were compared.

1) Aerodynamic delay for plunging motion due to horizontal tail length modelled by derivates $C_{Z_{\dot{\alpha}}}$ and $C_{m_{\dot{\alpha}}}$. No gust penetration effect (single point approximation of the aeroplane, see Ref. 4).
2) Aerodynamic delays for plunging motion and gust penetration effect due to horizontal tail length only, modelled by first order Padé approximation.
3) Horizontal tail length delays modelled according to 2). Unsteady wing lift, downwash and wing pitching moment modelled by second order linear filters (approximating, linearized Theodorson and Sears functions).

For aircraft type C, the wing sweep penetration effect was considered seperately in versions denoted by the subscript w.p.

Results

Figs. 7 and 8 compare airplane responses of pitch rate and normal acceleration due to a unit step (sharp edged) gust. Firstly, it can be seen that the single point approximation is not permissable, not even for the rather small aircraft type A. These cases of gust response very well illustrate the influence of tail length penetration effect and unsteady wing lift and pitching moment.
For models 2) and 3), responses are initially a backward pitching velocity, accompanied by an initially positive (upward) normal acceleration. The reaction opposed to the initial response due to the tail penetration effect is more pronounced for aircraft types B and C. Lags due to the unsteady wing lift and pitching moments tend to alleviate the initial gust response and the opposed, subsequent reaction. Including the wing sweep penetration effect for aircraft type C, also has an alleviating effect on the initial response.

Fig. 9 shows the gains of the transfer functions for normal acceleration due to vertical turbulence. Marked differences, especially for high frequencies are apparent due to the different ways of modelling. However, these differences are of relatively little practical importance since they appear at frequencies at which the power spectrum of vertical atmospheric turbulence decreases rapidly, see the dotted lines in Fig. 9.
A practical measure for the level of normal accelerations due to turbulence, both for applications to ride comfort and gust load calculations is the (steady state) variance δ_n^2 of the normal acceleration factor. This was calculated for the different models, using the Dryden spectrum for vertical turbulence. Computed values are summarized in Table 2, which also shows results for a special case (model 3a), where, the influence of unsteady wing lift on downwash was neglected.
In order to facilitate a comparison, the variances, normalized with respect to the variance obtained by using model 1) are plotted in Fig. 10.

In the first place it can be remarked that the variance of n for airplane type C is relatively insensitive to the modelling of the unsteady aerodynamics, as long as the wing sweep penetration effect (C w.p. model 2) is left out of consideration.
Further it can be seen that aircraft types A and B follow a similar trend, the tail penetration effect increases normal acceleration variance (model 2) unsteady lift and pitching moment (model 3a) have an alleviating effect but delayed downwash due to unsteady wing lift tends to increase the variance (model 3). For an interpretation it should be borne in mind firstly that the normal acceleration factor n (at the centre of gravity) is a linear combination of plunging acceleration $\dot{\alpha}$ and pitch rate q:

$$n = \frac{V}{g}(q - \dot{\alpha})$$

and hence the variance of n follows from

$$\sigma_n^2 = \left(\frac{V}{g}\right)^2 \left(\sigma_q^2 + \sigma_{\dot{\alpha}}^2 - 2\sigma_{q\dot{\alpha}}\right)$$

where σ_q^2 and $\sigma_{\dot{\alpha}}^2$ denote the variances and $\sigma_{q\dot{\alpha}}$ the covariance of q and $\dot{\alpha}$.
As a consequence, a certain value of σ_n^2 may well be caused by quite different values of the variances of $\dot{\alpha}$ and q and the covariance of $\dot{\alpha}$ and q. This is clearly demonstrated by the computed variances and covariances for the different models, see Table 2 and Figure 11. Next, it is evident that, due to the much larger inertia in pitch of aircraft type C relative to types A and B (as expressed by the dimensionless radius of inertia K_Y^2, see Table 1), the pitch rate q will, for aircraft type C, yield a much smaller contribution to the normal acceleration relative to the contribution caused by the plunging acceleration $\dot{\alpha}$.
Since the Z-forces due to the tail are relatively small if compared to those due to the wing, the effects of delayed downwash (either due to tail length or unsteady wing lift), will mainly influence the pitching

moment. As downwash has an alleviating effect on the pitching moment contribution of the tail due to a vertical gust, a delay in downwash postpones this alleviating effect. The large inertia in pitch of aircraft type C explains the much smaller effect of unsteady phenomena on the calculated values of σ_n^2.

Finally, in Table 2, calculated values have been given for a very simplified case, formerly used in classical calculations of gust loads (Ref. 11). This case, where only vertical translations of the aircraft are considered, yields very reasonable estimates of the levels of normal acceleration (denoted by 2* in Table 2). Closer condideration of the numerical values will reveal, however, that this only holds for the net levels of the normal accelaration variance and not for the contributions due to $\dot{\alpha}$ in case the pitching motion is included in the equations of motion.

Effect of wing flexibility on vertical turbulence response

Since the unsteady aerodynamic effects considered in this Paper are of relatively high frequency, the question arises of course what the influence of other high frequency phenomena i.e. those related to aircraft flexibility will be on response to turbulence.
Again, the question was raised whether this influence could be modelled in a simple and straightforward manner, such that a reliable mathematical model for aircraft stability and control analysis is obtained.
As a first attempt, a numerical example was taken from Ref. 9, featuring an aeroplane with wing sweep back, including the dynamics of the first wing bending mode and (coupled) wing torsion. In Ref. 9, the equations of motion including wing-flexibility are derived by using Langrange's method, (semi-rigid, three degrees of freedom equations of motion). In this way, seperate groups of equations of motions for the rigid airplane and the oscillating wing are obtained with additional coupling terms accounting for the interaction.
For the response to vertical turbulence of the rigid aeroplane, the model no 2) was used (horizontal tail length delay modelled by first order Padé approximation). For the additional, generalized force due to vertical turbulence, the appropriate derivative (of the flexible wing) with respect to the angle of attack was taken.
For a comparison, a so called quasi-static mathematical model (flexible inertia and damping terms assumed to be zero, see Ref. 9) was also included. For details of the mathematical model, the reader is referred to Ref. 10.

Step responses for pitch rate q, normal acceleration and wing-tip displacement due to vertical turbulence are shown in Fig. 12. It can be seen that in particular the subsequent reaction is being alleviated by the wing flexibility, an effect that is also very well reflected in the plot for the quasi-static case.

References

1. Roos, R.: The use of panel methods for stability derivatives AGARD C.P. no 235, Paper no 21, 1978.
2. Kočka, V.: Parameter estimation of an unsteady aerodynamics model for longitudinal motion of an aeroplane from flight measurements. ICAS-Paper 84-2.2.2., 1984.
3. Queijo, M.J. Wells, W.R. and Keskar, D.A.: Influence of unsteady aerodynamics on extracted aircraft parameters.
   J. Aircraft Vol. 16, no. 10, Oct. 1979, 708-713.
4. Etkin, B.: Dynamics of atmospheric flight. John Wiley and Sons. inc. New York, London, Sydney, Toronto, 1971.
5. Van der Vaart, J.C. and Roost, J.J.M.: Linear equations of aircraft motions including tailplane delays and unsteady wing lift and pitching moment. Delft University of Technology, Department of Aerospace Engineering, Report LR. 464 (To be published).
6. Gerlach, O.H.: Calculation of the response of an aircraft to ramdom atmosperhic turbulence. Part. I: Symmetric motions. Technological University Delft, Department of Aeronautical Engineering Report VTH-138, 1966.
7. Van der Vaart, J.C.: the calculations of the R.M.S. values of an aircraft's normal acceleration due to Gaussian atmospheric turbulence. Delft University of Technology, Department of Aerospace Engineering, Report VTGH-213, 1976.
8. Van der Vaart, J.C.: The cross-covariance of gust velocities and their time-derivates. Delft University of Technology, Department of Aerospace Engineering, Report VTH-207, 1975.
9. Mc Laughlin, M.D.: A theoretical investigation of the short-period dynamic longitudinal stability of airplane configurations having elastic wings of 0° to 60° sweepback. NACA T.N. 3251, 1954.
10. Van der Vaart, J.C. and Roost, J.J.M.: Linear equations for aircraft gust response including the effect of wing flexibility. Delft University of Technology, Department of Aerospace Engineering, Report, LR- (to be published).
11. Bisplinghoff, R.L., Ashley, H and Halfman, R.L. Aeroelasticity. Addison-Wesley Publ. Cy, Cambridge Mass, 1955.

Acknowledgement

The author wishes to acknowledge the contribution of J.J.M. Roost, student of Aerospace Engineering, who did most of the calculations.

Table 1 Main characteristics of example aircraft types.

	Type A DeHavilland DHC-2 "Beaver	Type B Fokker F27 "Friendship	Type C Boeing 747
h (m)	0	6100	0
W(N)	22447.	158922	2449066
$S(m^2)$	23.23	70.0	511
$W/S\ (N/m^2)$	966,3	2270.3	4792.7
L_g(m)	150	300	150
V (m/sec)	45,0	125,5	66,14
$\bar{c}$ (m)	1,59	2,58	8,32
ℓ_h(m)	6,23	10,50	31,10
μ_c	50,65	137,5	48,40
K_Y^2	1,20	2,72	3,77
C_{Z_α}	-5,44	-5,90	-5,34
$C_{Z_{\dot\alpha}}$	-0,49	-1,29	-2,00
C_{Z_q}	-2,44	-3,48	-2,84
$C_{Z_{\delta_e}}$	-0,48	-0,41	-0,36
C_{m_α}	-0,97	-0,80	-1,54
$C_{m_{\dot\alpha}}$	-1,91	-5,24	-1,70
C_{m_q}	-9,56	-14,20	-10,75
$C_{m_{\delta_e}}$	-1,91	-1,67	-1,41

Table 2 Calculated variance σ_n^2 and contributions of $\dot\alpha$ and q to σ_n^2. Dryden spectrum, σ_{w_g} = 1 m/sec.

Aircraft	model	$(\frac{V}{g})^2 \cdot \sigma_{\dot\alpha}^2$	$(\frac{V}{g})^2 \cdot \sigma_q^2$	$(\frac{V}{g})^2 \cdot \sigma_{q\dot\alpha}$	σ_n^2
A L_g = 150m	1	10.86×10^{-3}	$2,19\times10^{-3}$	$4,83\times10^{-3}$	$3,40\times10^{-3}$
	2	$6,97\times10^{-3}$	$1,86\times10^{-3}$	$1,54\times10^{-3}$	$5,76\times10^{-3}$
	2*	$5,35\times10^{-3}$	-	-	$5,35\times10^{-3}$
	3a	$8,94\times10^{-3}$	$1,80\times10^{-3}$	$3,02\times10^{-3}$	$4,70\times10^{-3}$
	3	$6,62\times10^{-3}$	$1,08\times10^{-3}$	$1,06\times10^{-3}$	$5,57\times10^{-3}$
B L_g = 300 m	1	$11,52\times10^{-3}$	$2,87\times10^{-3}$	$5,64\times10^{-3}$	$3,12\times10^{-3}$
	2	$8,02\times10^{-3}$	$9,02\times10^{-3}$	$6,56\times10^{-3}$	$3,93\times10^{-3}$
	2*	$4,46\times10^{-3}$	-	-	$4,46\times10^{-3}$
	3a	$10,25\times10^{-3}$	$3,51\times10^{-3}$	$5,14\times10^{-3}$	$3,48\times10^{-3}$
	3	$8,39\times10^{-3}$	$2,24\times10^{-3}$	$3,47\times10^{-3}$	$3,70\times10^{-3}$
C L_g = 150 m	1	$15,34\times10^{-4}$	1.83×10^{-4}	$3,04\times10^{-4}$	$1,11\times10^{-3}$
	2	$10,34\times10^{-4}$	$1,13\times10^{-4}$	$0,55\times10^{-4}$	$1,04\times10^{-3}$
	2*	$9,80\times10^{-4}$	-	-	$0,98\times10^{-3}$
	3a	$16,69\times10^{-4}$	$2,66\times10^{-4}$	$4,24\times10^{-4}$	$1,09\times10^{-3}$
	3	$12,90\times10^{-4}$	$1,25\times10^{-4}$	$1,90\times10^{-4}$	$1,04\times10^{-3}$
$C_{w.p.}$ L_g = 150m	1				$1,11\times10^{-3}$
	2				$0,53\times10^{-3}$
	3a				$0,97\times10^{-3}$
	3				$0,93\times10^{-3}$

C : no wing sweep penetration effect
$C_{w.p.}$: wing sweep penetration effect included
2*: plunging (α) motion only

Appendix

Linear filter transferfunctions for tail length time-delays and unsteady wing lift.

Tail length time delay

The pure time-delay transfer function is

$$H(s) = e^{-\tau_d s} \tag{1}$$

where $\tau_d = \ell_h/V$ (secs) (ℓ_h = tail length, V = flight speed).

Approximating eq (1) by a truncated Taylor series yields

$$H_1(s) = 1-\tau_d s \tag{2}$$

After transformation to the time-domain, and distinguishing contributions due to α and $\dot{\alpha}$, the well-known stability derivatives C_{Z_α} and C_{m_α} and the additional derivates $C_{Z_{\dot{\alpha}}}$ and $C_{m_{\dot{\alpha}}}$ are obtained, see Ref. 4. No additional equations are needed here.

A different way is to approximate Eq. (1) by a first order Padé filter with transfer function

$$H_2(s) = \frac{1 - \tau_{d/2} \cdot s}{1 + \tau_{d/2} \cdot s} \tag{3}$$

Transformation of Eq. (3) into the time domain results in one additional (first order) equation in the airplane equations of motion, see Ref. 5.
Where a pure time-delay, Eq (1), features a unit gain and a phase angle of $-\omega\tau_d$, Eq (2) yields an increasing gain and a maximum phase lag of 90°. Equation (3) gives unit gain and a maximum phase lag of 180°.

Unsteady wing lift

The linear filter for unsteady wing lift due to plunging motion was obtained by using the following linear approximation of the well-known Wagner function (see Ref. 11.)

$$\Phi(\hat{t}) = 1 - 0{,}165e^{-0{,}0415\,\hat{t}} - 0{,}335e^{-0{,}3\,\hat{t}} \tag{4}$$

where $\hat{t} = t\frac{2V}{\bar{c}}$

Taking Eq. (4) as the lift growth due to a unit stepwise change of angle of attack (plunging motion), the relevant transfer function for arbitrary changes of α can be derivied as:

$$H_w(s) = \frac{C_{Z_w}(s)}{\alpha(s)} = C_{Z_{w_\alpha}} \cdot \frac{(1+\tau_1 s)(1+\tau_2 s)}{(1+\tau_3 s)(1+\tau_4 s)} \tag{5}$$

where $\tau_1 = 18{,}6\,\frac{\bar{c}}{2V}$ (secs), $\tau_2 = 1{,}96\,\frac{\bar{c}}{2V}$ (secs)

$\tau_3 = 21{,}98\,\frac{\bar{c}}{2V}$ (secs), $\tau_3 = 3{,}33\,\frac{\bar{c}}{2V}$ (secs)

A similar filter for unsteady lift due to vertical turbulence was derived by taking the following linear approximation of the Küssner function for wing lift response to a sharp-edged, unit step gust input (see Ref. 11).

$$\Phi(s) = 1-0{,}5\,e^{-0{,}13\hat{t}} - 0{,}5\,e^{-\hat{t}} \tag{6}$$

where, again, $\hat{t} = t\frac{2V}{\bar{c}}$

The linear filter transfer function for arbitrary turbulence inputs is,

$$H_K(s) = \frac{C_{Z_w(s)}}{\alpha_g(s)} = C_{Z_{w_\alpha}} \cdot \frac{1 + \tau_5 s}{(1+\tau_6 s)(1+\tau_7 s)} \tag{7}$$

where $\tau_5 = 4{,}35\,\frac{\bar{c}}{2V}$ (secs), $\tau_6 = 7{,}69\,\frac{\bar{c}}{2V}$ (secs), $\tau_7 = \frac{\bar{c}}{2V}$ (secs).

The linear filters characterized by Eqs (5) and (7) both yield two additional first order equations in the airplane equations of motion.

Wing sweep penetration effect

A straight, sharp edged gust takes a certain time to travel along the leading edge of a swept wing. For a constant sweep angle Λ, the relevant time-constant is

$$\tau_\Lambda = \frac{b}{2V}\tan\Lambda \text{ (secs)}$$

Instead of a unit step gust input, it is supposed that an equivalent onswept wing experiences a ramp input

$$u(t) = at - a(t-\tau_\Lambda) \tag{8}$$

where $u(t) = 0$, for $t<0$,

and $a(t-\tau_\Lambda) = 0$, for $t<\tau_\Lambda$, and $a\tau_\Lambda = 1$

Transforming Eq. (9) into the complex domain, yields

$$U(s) = \frac{a}{s^2} - \frac{a}{s^2} e^{-\tau_\Lambda s} \tag{9}$$

Next the time-delay in eq (9) is approximated by a first order Padé filter:

$$U(s) = \frac{a}{s^2} \left(1 - \frac{1 - \tau_\Lambda/2\, s}{1 + \tau_\Lambda/2\, s}\right) = a\tau_\Lambda \cdot \frac{1}{s} \cdot \frac{1}{1 + \tau_\Lambda/2\, s} \tag{10}$$

If, finally, Eq (10) is considered as the Laplace transform of the response of an additional filter to a wing step input, the following additional filter transfer function for the modelling of the wing sweep penetration effect is obtained:

$$H_p(s) = \frac{1}{1 + \tau_\Lambda/2\, s} \tag{11}$$

In the computations of unsteady lift response of a swept back wing to vertical turbulence, the filters according to eq (11) and eq (7) were cascaded.

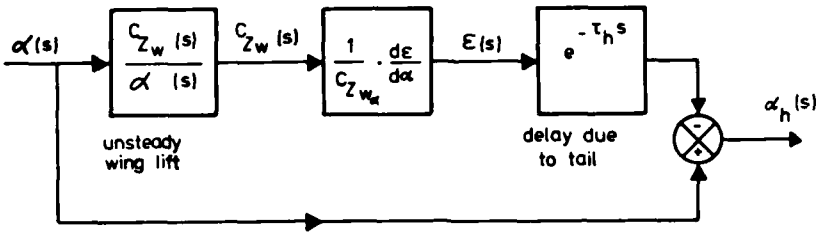

Fig. 1 Block diagram for the calculation of unsteady wing lift and delay due to the tail length (plunging motion)

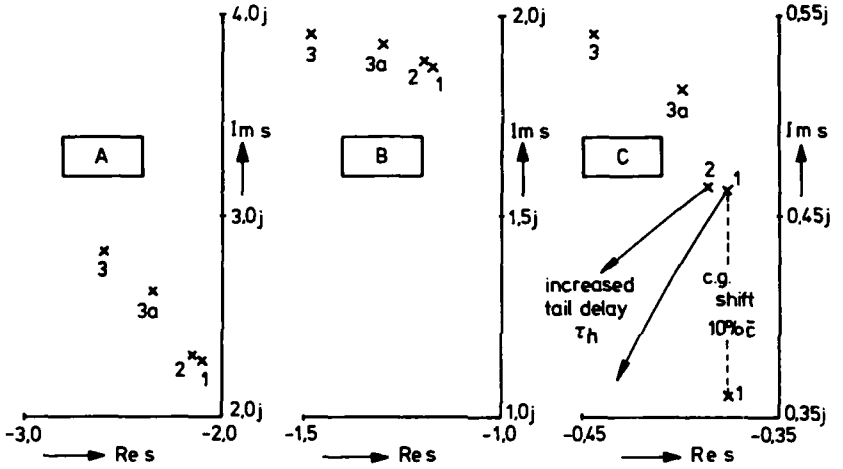

Fig. 2 Influence of modelling of unsteady aerodynamics on short period root locations for the three example aircraft (3a: unsteady wing lift neglected for downwash)

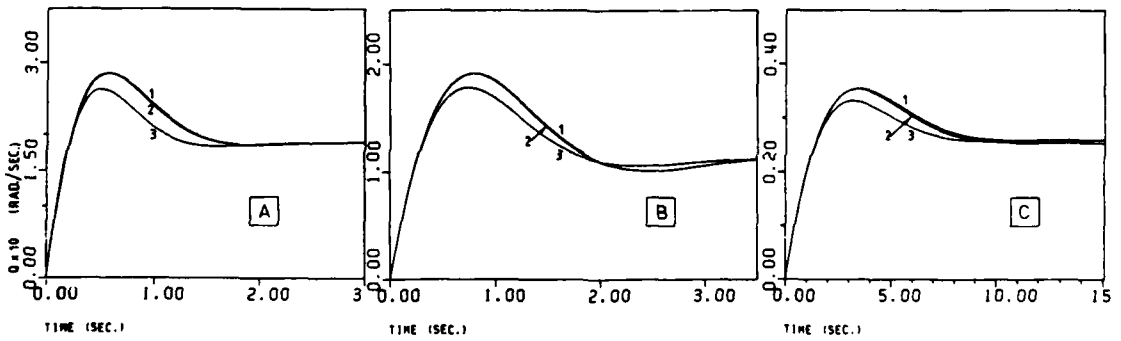

Fig. 3 Responses of pitch rate q on elevator step inputs ($\Delta\delta_e$ = - 0,1 rad)

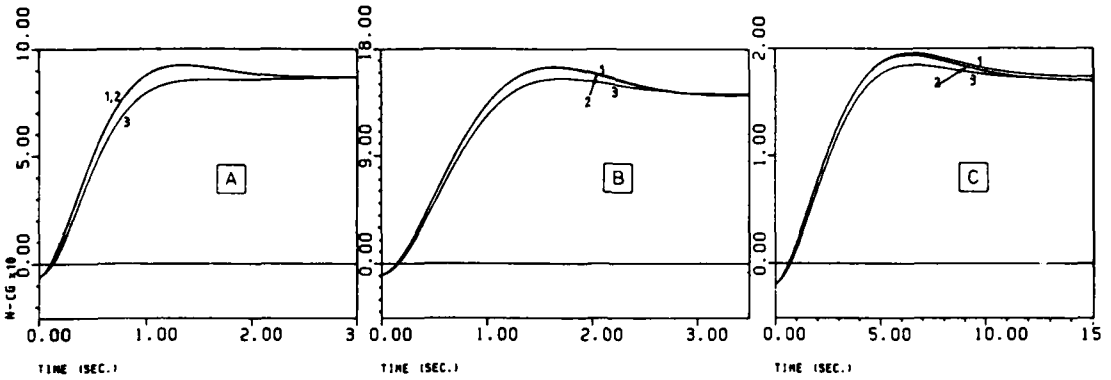

Fig. 4 Responses of normal acceleration n on elevator step inputs ($\Delta\delta_e$ = - 0,1 rad)

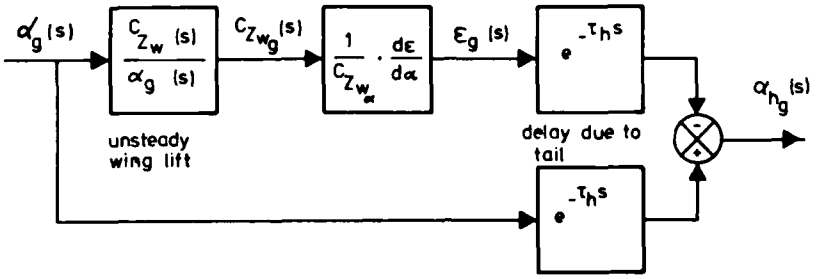

Fig. 5 Block diagram for the calculation of unsteady wing lift and delay due to the tail length for vertical turbulence α_g

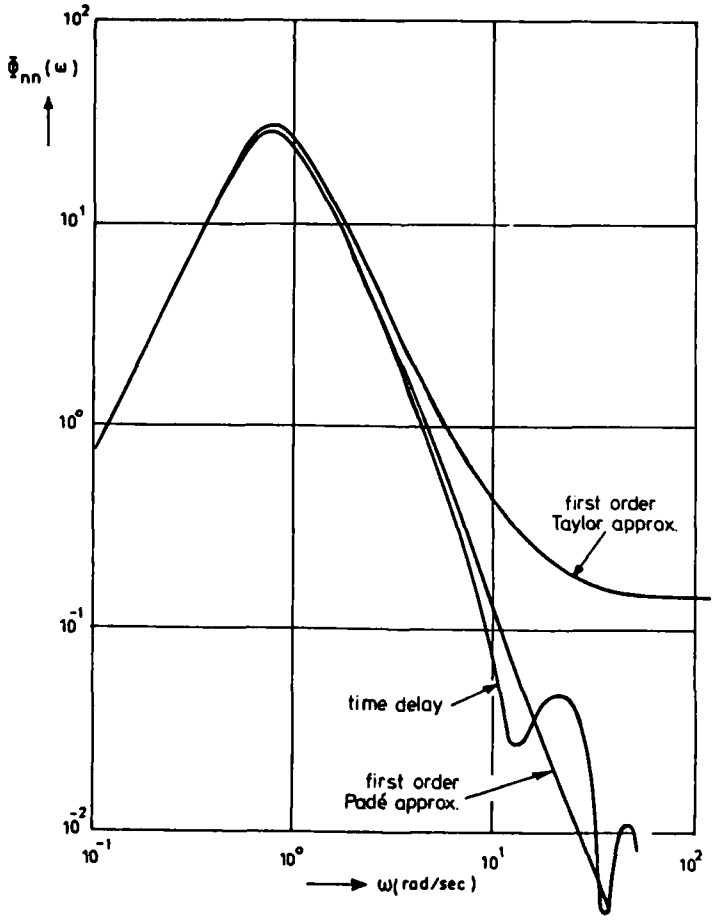

Fig. 6 Example of power spectral density functions of the normal acceleration factor n due to vertical turbulence, taken from Ref. 7

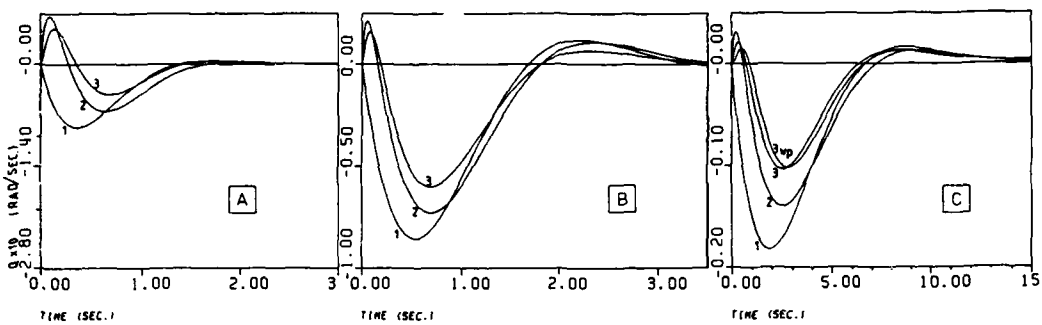

Fig. 7 Responses of pitch rate q on vertical step gust inputs ($\Delta\alpha_g$ = 0,1 rad)

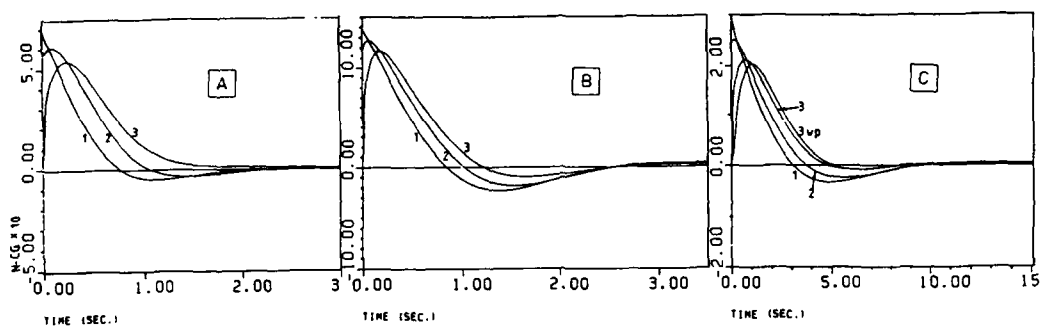

Fig. 8 Responses of normal acceleration n on vertical step gust inputs ($\Delta\alpha_g$ = 0,1 rad)

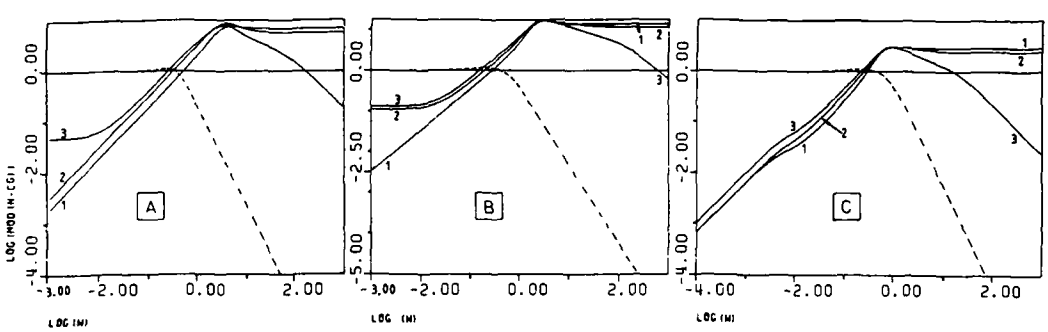

Fig. 9 Gain of transfer functions of normal acceleration due to vertical turbulence.
Dotted lines: power spectral densities of vertical turbulence.

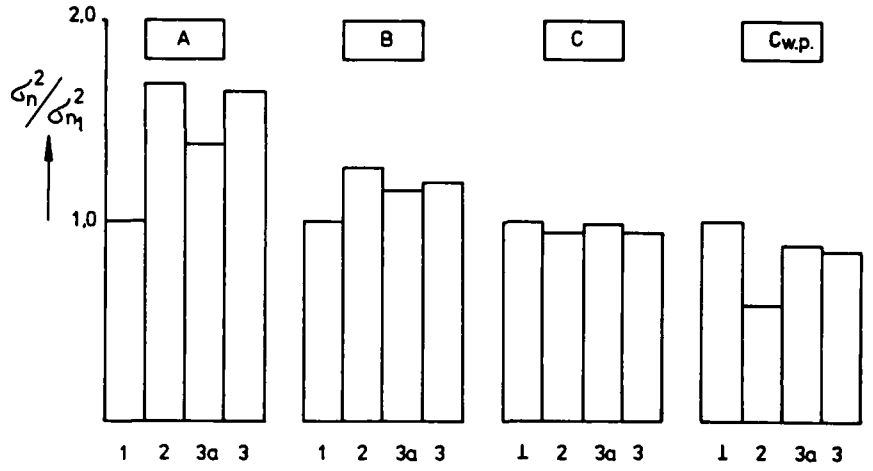

Fig. 10 Influence of modelling of unsteady aerodynamics on the normal acceleration variance σ_n^2, normalized relative to model 1

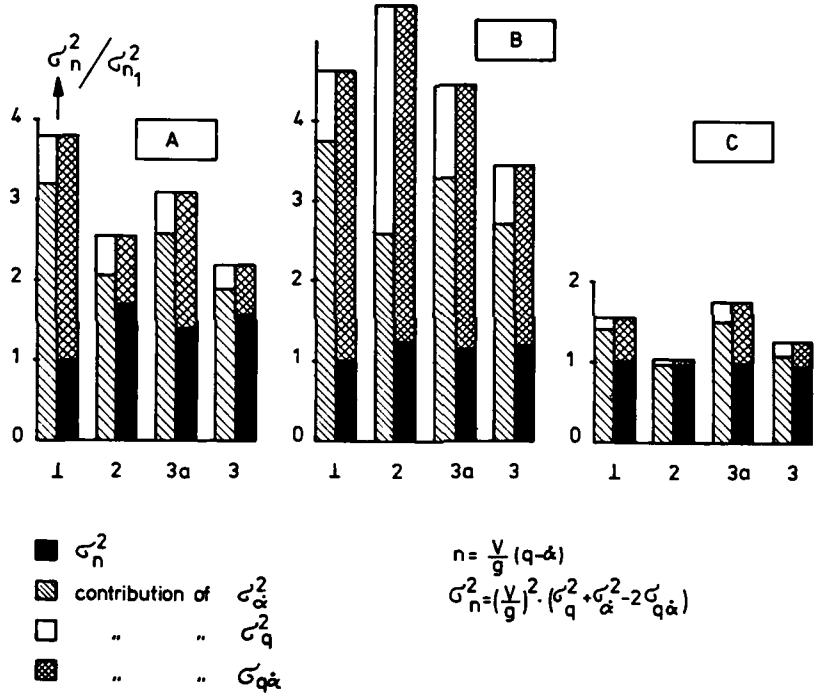

Fig. 11 Contributions of plunging acceleration $\dot\alpha$, pitch rate q and covariance of $\dot\alpha$ and q to the variance of the normal acceleration n, normalized relative to model 1

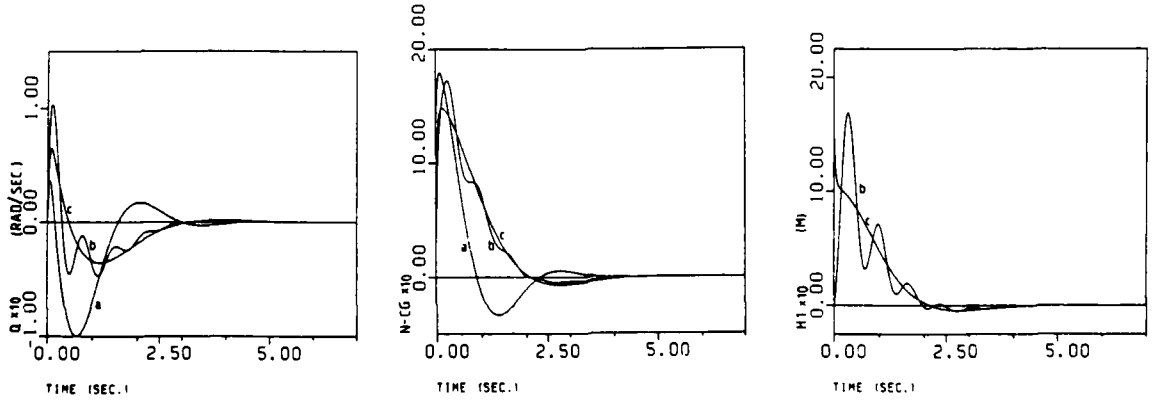

Fig. 12 Response of pitch rate q, normal acceleration n and wing tip deflexion h on vertical step gust inputs ($\Delta\alpha_g$ = 0,1 rad).
a: rigid aeroplane. b: semi-rigid aeroplane. c: quasi-static case

A SELF-ORGANISING CONTROL SYSTEM FOR NON-LINEAR AIRCRAFT DYNAMICS

by

C. Evans
Smith Associates Consulting
System Engineers Limited,
45-47 High Street,
Cobham,
Surrey,
England. KT11 3DP

SUMMARY

At high angles-of-attack (AOA) flow separations can produce non-linear and time varying aerodynamic loads, which cannot be predicted with great certainty. Such loads make control system development extremely difficult. A control system has thus been developed which can can accomplish on-line reduction of the a-priori uncertainties pertaining to the effective control of the aircraft. The self-organising control system was developed to suppress unacceptable pitch-up tendencies of an aircraft at high AOA, without the use of AOA measurement. The final control system demonstrated good performance for a variety of inputs although performance was not as good in turbulence.

INTRODUCTION

At high angles-of-attack (AOA) flow separations can produce non-linear and time-varying aerodynamic loads which cannot be predicted with great certainty. The problems associated with such loads have manifested themselves on a number of current combat aircraft as undemanded aircraft motions which the pilot cannot control, i.e. departures. Current control system technology will enable next-generation combat aircraft to achieve high AOA much more readily whilst, at the same time, offering the capability of actively controlling undesirable aircraft motions. To develop such a control system both a mathematical model of the aircraft's dynamics as well as suitable sensors to measure its motion are required. The afforementioned uncertainties present in the aerodynamic loads at high AOA produce significant uncertainties in both the mathematical model and the sensor readings, with the result that control system development is extremely difficult.

The conventional approach to dealing with such uncertainties is to develop robust feedback control laws and incorporate manoeuvre limiting sub-systems to prevent the aircraft entering flight regimes in which the aircraft's motion cannot be predicted with confidence. An alternative approach is to develop a control system which can accomplish on-line reduction of the a-priori uncertainties pertaining to the effective control of the aircraft as the manoeuvre evolves. Such a control system is termed self-organising, although the descriptors adaptive and parameter adaptive have also been used.

Self-organising control systems have been investigated on numerous occasions for aircraft. However, it is only in the last few years, with the growth of digital computers that the implementation of complex adaptive algorithms has become feasible. The F-8c programme considered a number of such systems [2,3,4,5] and one was implemented for flight test [2]. Self-organising control systems have also been presented for an F-4[6] and a missile [7]. These studies only dealt with flight at low AOA and thus only considered the aircraft as a time varying linear system. A high AOA application of a self-organising control system was presented by Asher [8] but only a linear simulation of the aircraft dynamics was used.

This paper concerns the design of a self-organising control system to suppress unacceptable trends in the longitudinal aerodynamic loads of a ground attack aircraft. The work was carried out using a comprehensive digital simulation previously developed as part of an investigation into high AOA handling characteristics [1]. The final control system developed produced encouraging results, although much work would be required before a practical implementation of such a system could be achieved.

SELF-ORGANISING CONTROL

Many self-organising control algorithms attempt to produce convergence to an optimal control. At high AOA the requirement is primarily for adequate control in a short time. A self-organising control algorithm is thus required which allows some choice in the selection of feedback signals and the strategy for their use. The partioning algorithm of Lainiotis provides such a choice and was thus used in this work.

Partioned adaptive control (PAC) utilises a multiple-model approach such that a finite number of models are used to represent the parameter space, each model being defined by a parameter vector $\underline{\theta}_i$. For each model a corresponding gain matrix $\underline{k}(\underline{\theta}_i)$ and control vector, $\underline{u}(\underline{\theta}_i)$ can then be calculated. The algorithm operates by calculating the probability that each model is the best model and uses these probabilities to weight the control input vectors, $\underline{u}(\underline{\theta}_i)$. The probabilities are estimated by using the error between the actual measurements of the system and the corresponding values predicted by each model of the dynamics. The error vectors are generated by Kalman filters, which

also supply state estimates for the calculation of each model conditional control. The control system (Fig. 1) thus consists of a number of computational channels, each representing a given parameter vector, which are processed in parallel to produce model conditional error vectors and control demands. The non-linear equations for the calculation of the probabilities are separated from the linear estimation procedure, carried out by the Kalman filters.

The model conditional control, at time t_k, is given by:

$$\underset{\sim}{u}_k\ (\theta_i) = \underset{\sim}{K}_k\ (\theta_i)\ \underset{\sim}{\hat{x}}_k\ (\theta_i) \tag{1}$$

The imposed control is then given by

$$\underset{\sim}{u}_k{}^* = \sum_{i=1}^{n} pr_k\ (\theta_i)\ \underset{\sim}{u}_k\ (\theta_i) \tag{2}$$

where

n = number of models

$pr_k\ (\theta_i)$ = model conditional probability.

To obtain the probabilities, the error vector, $\underset{\sim}{z}_k$, and its convariance matrix, B_k, are required from each Kalman filter. The model conditional probabilities are given by the recursive Bayes rule;

$$pr_k\ (\theta_i) = \frac{L_k(\theta_i)\ pr_{k-1}(\theta_i)}{\sum_{j=1}^{n} L_k(\theta_j)\ pr_{k-1}(\theta_j)} \tag{3}$$

where

$$L_k(\theta_i) = |\underset{\sim}{B}_k|^{-\frac{1}{2}}\ \exp\ \{-\tfrac{1}{2}\underset{\sim}{z}_k{}^T \underset{\sim}{B}_k{}^{-1} \underset{\sim}{z}_k\} \tag{4}$$

Additionally, the best estimate of the state vector is given by:

$$\underset{\sim}{\hat{x}}^* = \sum_{j=1}^{n} pr_k(\theta_i)\ \underset{\sim}{\hat{x}}_k(\theta_i) \tag{5}$$

To apply this algorithm to the non-linear dynamics of an aircraft at high AOA a segmentwise stationary approach was used. In this method the non-linear dynamics are approximated by linear perturbation models which remain valid for a fixed length of time. The Kalman filters are thus reset after a set time interval, Δt_o. During each time interval the sensor measurements at the start of the interval are subtracted from each subsequent measurement to obtain perturbation values. This method has the advantage that linear models of the dynamics can be used and similarly linear time-invariant Kalman filters.

AIRCRAFT MODEL

The specific problem considered was a loss of pitch stiffness at high AOA. A number of different pitching moment curves were used (Fig. 2) to ensure that the system was responding to the correct parameter. Measurements of pitch rate, normal acceleration, dynamic pressure, airspeed and tailplane deflection were assumed available with the noise characteristics shown in Table 1. The effects of turbulence were modelled using digitised records of moderate to severe turbulence [10].

The simulation modelled both the continuous aircraft dynamics and the digital operation of the control system. A sample rate of 50Hz was used for the digital control system and the compute delay was taken to be 90% of the sampling interval. Analogue anti-alias filters with a break frequency of 12.5 Hz and damping ratio 0.5 were also incorporated (Fig. 3). The tailplane servo was modelled as a first order lag with a time constant of 0.04s and a rate limit of $60^o/s$.

IMPLEMENTATION CONSIDERATIONS

In order to minimise the computational requirement and ensure a rapid decision making capability the simplest models of the dynamics were used. Within each reset period the dynamics were considered to be linear and time-invariant. Only the aircraft's short period dynamics were thus considered with the effects of changes in airspeed and height being allowed for at each reset. The non-stationary behaviour of the aircraft at each reset point also had to be allowed for. The perturbation equations of motion were thus represented by:

$$\underset{\sim}{\hat{x}}' = \underset{\sim}{A}\ \underset{\sim}{x}' + \underset{\sim}{B}\underset{\sim}{u}' + \underset{\sim}{\hat{x}}_o + \underset{\sim}{G}\alpha_g \tag{7}$$

where α_g is the turbulence input. An approximation for the rate term $\dot{\underline{x}}_o$ was obtained viz:

$$\hat{\underline{x}}\ (t_o) = (\underline{x}^*(t_o) - \underline{x}^*(t_o - \Delta t))/\Delta t \qquad (8)$$

where Δt is the sampling interval. The equations of motion and the resultant Kalman filter equations are shown in App. A.

Two channels only were used as follows:

a) Channel 1 represented stable acceptable dynamics;

b) Channel 2 represented unacceptable dynamics.

The gain matrix, K, for Channel 2 was calculated such that the closed loop dynamics produced the same short-period characteristics as the open loop dynamics of Channel 1. The simple equations of motion used (App. A) enabled this condition to be solved algebraically. This gain matrix was updated at each reset. For Channel 1 the gain matrix, $\underset{\sim}{K}$, was set to zero. The use of perturbation values for the feedback loops meant that a summing procedure had to be invoked to maintain continuity of demand. Writing:

$$t_{o_j} = \text{time at j'th reset}$$

and if t_k is the time such that

$$t_{o_j} < t_k \leq t_{o_{j+1}}$$

then the perturbation feedback is expressed as:

$$u_c(t_k) = \sum_{i=1}^{n} pr_k(\theta_i)\ \underset{\sim}{K}(\theta_i)\ \underline{x}_k(\theta_i) \qquad (9)$$

the sum of the perturbation feedbacks at the end of each linearisation period is given by:

$$u_{c_o}(t_{o_j}) = \sum_{i=1}^{j} u_c(t_{o_i}) \qquad (10)$$

and the total control demand, including pilot demand δ_p is thus expressed as:

$$\eta_c = \delta_p + u_c + u_{c_o} \qquad (11)$$

Initial work indicated a need to compensate for the effects of high levels of atmospheric turbulence. A common scale factor on the noise statistics [2] was incorporated in the probability calculation along with a minimum value on the likelihood [3] function to prevent oversensitivity in the absence of turbulence. The common scale factor, $\hat{\sigma}$, is given by:

$$\hat{\sigma}_k^2 = J/rk \qquad (12)$$

where r is the number of measurements and:

$$J(\theta_i) = \sum_{1=1}^{k} \underline{z}_1^T \underset{\sim}{B}_1^{-1} \underline{z}_1 \qquad (13)$$

this to be evaluated for the candidate model which produces the maximum probability. Eqn.s 4 and 5 were thus replaced as follows:

$$\text{let, } d_k(\theta_i) = \tfrac{1}{2}\underline{z}_k^T(\theta_i)\ (\hat{\sigma}_k^2 \underset{\sim}{B}_k(\theta_i))^{-1} \underline{z}_k(\theta_i) \qquad (14)$$

$$d_k(\theta^*) = \min(d_k(\theta_i)) \qquad (15)$$

and

$$L_k''(\theta_i) = |B_k(\theta_i)|^{-\frac{1}{2}} \exp\{d_k(\theta^*) - d_k(\theta_i)\} \quad (16)$$

where

$$d_k(\theta_i) - d_k(\theta^*) < 88.0, \quad (17)$$

then

$$pr_k(\theta_i) = \frac{L_k''(\theta_i) pr_{k-1}(\theta_i)}{\sum_{j=1}^{n} L_k''(\theta_j) pr_{k-1}(\theta_j)} \quad (18)$$

This ensured that at least one of the channels had an exponential term within the computational limits of the computer. The minimum value on the likelihood function prevented updating of the probabilities at each time step (Eqn. 18) unless at least one channel satisfied the following condition:

$$\underset{\sim}{z}_k^T \underset{\sim}{B}_k^{-1} \underset{\sim}{z}_k > \hat{\sigma}_k^2 E, \quad (19)$$

where E was a pre-set constant.

DEVELOPMENT

Developing the system to obtain the optimum combination of parameters proved extremely difficult due to the lack of analytical methods which could be applied. As a result, numerous simulations had to be run to evaluate the effects of parameter variations. The choice of the parameters for the models of each channel proved especially difficult due to the approximate nature of the models. Utilising only 2 channels made the problem manageable allowing 2 extreme parameter sets to be chosen. The use of the white noise approximation, in the Kalman filter equations, to the non-white instrumentation noise and turbulence meant that the choice of values for the Q and R matrices was not straight forward. Additionally, tests indicated that the Kalman filters were also compensating for modelling errors so that the covariance matrices Q and R were acting as weighting matrices for all of the errors present.

The reset length, Δt_o, was easier to define as too short a reset length resulted in modelling errors which were too small for recognition. Conversely, too long a reset length resulted in loss of the local linear approximation. The reset length had also to be balanced against the error level E (Eqn. 19). Large values of E increased the time required for a decision whilst small values of E had no effect. A suitable value of E resulted in a single decision once the unacceptable aircraft dynamics had been encountered.

The final values of the system parameters obtained are shown in Table 2.

The other problem that emerged during the development work was the behaviour of the stored feedback control (Eqn. 10). Due to the lags within the system it was found that subsequent to a pitching manoeuvre the stored feedback could have a finite value when the aircraft returned to low AOA, which was unacceptable. To prevent this a digital washout filter was applied to the stored feedback to guarantee that the stored feedback would always return to zero at low AOA. Due to the possibility of short spurious decisions at high AOA it was found necessary to include a complex system of logic to ensure that the washout was only applied at the desired time (Fig. 4). The final control system configuration is shown in Fig. 5

PERFORMANCE OF THE CONTROL SYSTEM

Many different manoeuvres were simulated to assess the performance of the control system. Fig. 6 shows a typical pitching manoeuvre for aircraft models using schedules 1 and 3 from Fig. 1 for the pitching moment characteristic. It can be seen that the control system produced good model following behaviour with only a small AOA overshoot when channel 2 was engaged. Some variation in performance of the closed-loop system occured depending on the position of the reset points relative to the manoeuvre. Turbulence became more of a problem during slow pitching manoeuvres due to the lower signal to noise ratio (Fig. 7) with channel 2 being engaged when both schedule 3 and schedule 1 of Fig. 2 were used in the model. Sharp tailplane demands caused positive recognition of channel 2 but due to the inherent lag of the control system the AOA overshoot increased (Fig. 8).

In the absence of the control system schedule 1 from Fig. 2 produced a sharp pitch departure when pitching manoeuvres such as those shown in Fig. 6, 7 and 8 were attempted. In all cases the self-organising control system prevented such pitch departure and allowed sustained manoeuvring at high AOA. The system also prevented pitch-up caused by inertia coupling during rapid rolls at high AOA.

One of the most difficult cases for such a control-system is a sustained high AOA manoeuvre with small changes in tailplane demand and rapid rolls. Fig. 9 shows such a manoeuvre of the model using schedule 3 to represent the "ideal" behaviour.Fig. 10 shows the same manoeuvre using schedule 1. The self-organising control system produced reasonable model-following behaviour although with a marked loss of damping.Fig. 11 shows the same case as Fig. 10 but in the presence of turbulence. This was the worst case recorded for the system as although pitch departure was prevented the latter part of the manoeuvre was suppressed by inputs from the control system.

In general the system worked well preventing pitch departure in all cases and producing good model following behaviour in most cases. Performance did, however, deteriorate, in the presence of turbulence, with significant variation in performance becoming evident. Nevertheless the system does offer considerable scope for both theoretical and practical development, although much work would be required before an implementable system could be derived. The complexity of such a system also means that it would have to form part of a full authority manoeuvre demand system. Thus, before making a judgement on the acceptibility of the self-organising control system which has been developed, it would be necessary to consider its performance when integrated with such a full authority manoeuvre demand system. This is the direction which further work should take to derive a practical self-organising control system from the one herein developed.

CONCLUSIONS

A self-organising control system has been developed to suppress unacceptable pitch-up tendencies at high AOA in an aircraft, without the use of AOA measurement. The system used a stationary approach to analyse the aircraft motion in time segments so that the controller could use linear models of the dynamics. The system, in its final form, demonstrated good performance for a wide variety of inputs. Performance was not as good in the presence of turbulence, but in all cases pitch departure was prevented. The system , as presented, offers considerable scope for development. The main question remaining to be answered is how the self-organising control system would perform when integrated with a more comprehensive manoeuvre demand system.

APPENDIX A KALMAN FILTER EQUATIONS

The aircraft equations of motion used for the control system were:

$$\dot{\underset{\sim}{x}}' = \underset{\sim}{A}\underset{\sim}{x}' + \underset{\sim}{B}\underset{\sim}{u}' + \dot{\underset{\sim}{x}}_o + \underset{\sim}{G}\alpha_g$$

where,

$$\underset{\sim}{x}' = \underset{\sim}{x}(t') = \begin{bmatrix} q' \\ \alpha' \end{bmatrix} = \begin{bmatrix} q(t) \\ \alpha(t) \end{bmatrix} - \begin{bmatrix} q(t_o) \\ \alpha(t_o) \end{bmatrix}$$

$$t' = t - t_o$$

t_o = reset time

$$\underset{\sim}{A} = \begin{bmatrix} M_q + M_{\dot{\alpha}} & M_\alpha + M_{\dot{\alpha}} Z_\alpha \\ 1 & Z_\alpha \end{bmatrix}$$

$$\underset{\sim}{B} = \begin{bmatrix} M_\eta + M_{\dot{\alpha}} Z_\alpha \\ Z_\eta \end{bmatrix}$$

$$\underset{\sim}{u}' = \underset{\sim}{u}(t') = \underset{\sim}{u}(t\ ) - \underset{\sim}{u}(t_o)$$

$$\underset{\sim}{G} = \begin{bmatrix} M_\alpha + M_{\dot{\alpha}} Z_\alpha \\ Z_\alpha \end{bmatrix}$$

The measurements were represented by:

$$\underset{\sim}{y}' = \underset{\sim}{H}\underset{\sim}{x}' + \underset{\sim}{D}\underset{\sim}{u}' + \underset{\sim}{v}$$

where

$$\underset{\sim}{Y}' = \underset{\sim}{y}(t') = \underset{\sim}{y}(t) - \underset{\sim}{y}(t_o)$$

$\underset{\sim}{v}$ = noise

$$\underset{\sim}{y} = \begin{bmatrix} q \\ a_n \end{bmatrix}$$

then,

$$\underset{\sim}{H} = \begin{bmatrix} 1 & 0 \\ (M_q + M_{\dot{\alpha}})x_a g & ((M_\alpha + M_{\dot{\alpha}} Z_\alpha)x_a - Z_\alpha V_o)/g \end{bmatrix}$$

and,

$$\underset{\sim}{D} = \begin{bmatrix} 0 \\ ((M_\eta + M_{\dot{\alpha}} Z_\eta) x_a - Z_\eta V_o)/g \end{bmatrix}$$

The digital implementation of these equations of motion was expressed as:

$$\underset{\sim}{x}_k = \underset{\sim}{\phi}\underset{\sim}{x}_{k-1} + \underset{\sim}{\Gamma}\underset{\sim}{u}_{k-1} + \underset{\sim}{\psi}\underset{\sim}{\dot{x}}_o + \underset{\sim}{w}_{k-1}$$

$$\underset{\sim}{Y}_k = \underset{\sim}{H}\underset{\sim}{x}_k + \underset{\sim}{D}\underset{\sim}{u}_k + \underset{\sim}{v}_k$$

where $\underset{\sim}{\phi}$, $\underset{\sim}{\Gamma}$ and $\underset{\sim}{\psi}$ are the appropriate transition matrices.

The Kalman filter equations used were:

$$\underset{\sim}{\hat{x}}'_k = \underset{\sim}{\phi}\underset{\sim}{\hat{x}}_{k-1} + \underset{\sim}{\Gamma}(\underset{\sim}{u}_{k-1} + \underset{\sim}{u}_k)/2 + \underset{\sim}{\psi}\underset{\sim}{\hat{x}}_o$$

$$\underset{\sim}{P}'_k = \underset{\sim}{\phi}\underset{\sim}{P}_{k-1}\underset{\sim}{\phi}^T + \underset{\sim}{Q}$$

$$\underset{\sim}{B}_k = \underset{\sim}{H}\ \underset{\sim}{P}'_k\underset{\sim}{H}^T + \underset{\sim}{R}$$

$$\underset{\sim}{z}_k = \underset{\sim}{Y}_k - \underset{\sim}{H}\underset{\sim}{\hat{x}}'_k - \underset{\sim}{D}\underset{\sim}{u}_k$$

$$\underset{\sim}{K}_k = \underset{\sim}{P}'_k\ \underset{\sim}{H}^T\ \underset{\sim}{B}_k^{-1}$$

$$\underset{\sim}{\hat{x}}_k = \underset{\sim}{\hat{x}}'_k + \underset{\sim}{K}_k\underset{\sim}{z}_k$$

$$\underset{\sim}{P}_k = \underset{\sim}{P}'_k - \underset{\sim}{K}_k\underset{\sim}{H}\ \underset{\sim}{P}'_k$$

The noise covariance matrices were taken as:

$$\underset{\sim}{Q} = \underset{\sim}{T}\ \sigma_T^2\ \underset{\sim}{T}^T$$

where

σ_T = r.m.s. of turbulence

$\underset{\sim}{T}$ = transition matrix for turbulence inputs.

$$\underset{\sim}{R} = \begin{bmatrix} \sigma_q^2 & 0 \\ 0 & (\underset{\sim}{H}(2,2))^2\ \sigma_T^2 + \sigma_{a_n}^2) \end{bmatrix}$$

The transition matrices were taken as:

$$\underset{\sim}{\phi} = \underset{\sim}{I} + \underset{\sim}{A}\Delta t + \underset{\sim}{A}^2\frac{\Delta t^2}{2}$$

$$\underset{\sim}{\Gamma} = \underset{\sim}{B}\Delta t + \underset{\sim}{A}\underset{\sim}{B}\frac{\Delta t^2}{2}$$

$$\underset{\sim}{\psi} = \underset{\sim}{I}\Delta t + \underset{\sim}{A}\frac{\Delta t^2}{2}$$

$$\underset{\sim}{T} = \underset{\sim}{G}\Delta t$$

REFERENCES

1. Evans, C. "The Control of Aircraft Dynamics at High Angles of Attack". PH.D. Thesis, University of Bristol, 1984.

2. Hartmann, G.L. et al. "F-8c Adaptive Flight Control Laws", NASA CR-2880, 1977.

3. Athans, M., Castanon, D., Dunn, K. "The Stochastic Control of the F-8c Aircraft Using a Multiple Model Adaptive Control Method - Part 1; Equilibrium Flight". IEEE, AC-22 No. 5, 1977.

4. Alag, G., Kanfman, H. "An Implementable Digital Adaptive Flight Controller Designed Using Stablised Single-Stage Algorithms". IEEE, AC-22, No. 5, 1977.

5. Dunn, H.J., Montgomery, R.C. "A Moving Window Parameter Adaptive Control System for the F-8 DFBW Aircraft". IEEE, AC-22, No. 5, 1977.

6. Hartmann, U., Krebs, V. "Command and Stability Systems for Aircraft: A New Digital Adaptive Approach". Automatica, Vol. 16, 1980.

7. Young, D. "A Second Generation Adaptive Autostabilisation System for Airborne Vehicles". Automatica, Vol. 17, No. 3, 1981.

8. Asher, R.B., Goebel, D. "High Angle-of-Attack Flight Control Using Stochastic Model Reference Adaptive Control". IEEE, AC-16, pp 1203-1210, 1977.

9. Lainiotis, D.G. "Partitioning: A Unifying Framework for Adaptive Systems, II: Control", Proc. IEEE, Vol. 64, No. 8, pp 1182-1198, August 1976.

10. Anthony, M.G. "Pilot Control of a Large Transport Aircraft in Atmospheric Turbulence". Ph.D. Bristol University, 1977.

ACKNOWLIDGEMENTS

This work was funded by British Aerospace in association with the Science and Engineering Research Council.

Table 1 Instrumentation noise characteristics

Sensor	T(sec)	1σ
Pitch rate gyro	0.08	0.5 deg.sec
Normal acceleration	0.008	0.06 g
Airspeed	0.16	2.0 ft/sec
Servo position	0.01	0.1 deg

T - first order low pass filter time constant

Table 2 Final control system parameters

Channel 1, acceptable dynamics

$C_{m_\alpha} = -0.75$ $C_{m_\eta} = -1.7$

$C_{m_q} + C_{m_{\dot\alpha}} = -15.0$ $C_{z_\eta} = -0.77$

$C_{z_\alpha} = -3.8$

Channel 2, unacceptable dynamics

$C_{m_\alpha} = 0.0$ $C_{m_\eta} = -1.3$

$C_{m_q} + C_{m_{\dot\alpha}} = -12.0$ $C_{z_\eta} = -0.60$

$C_{z_\alpha} = 0.0$

Common parameters

$\sigma_T = 1.8 m/s$

$Q(\theta_2) = Q(\theta_1)$

$0.1 < \theta < 5.0$

$E = 5$

$R(1,1) \triangleq 0.5°/s$

$R(2,2) \triangleq 0.25'g'$

$\Delta t_o = 0.4s$

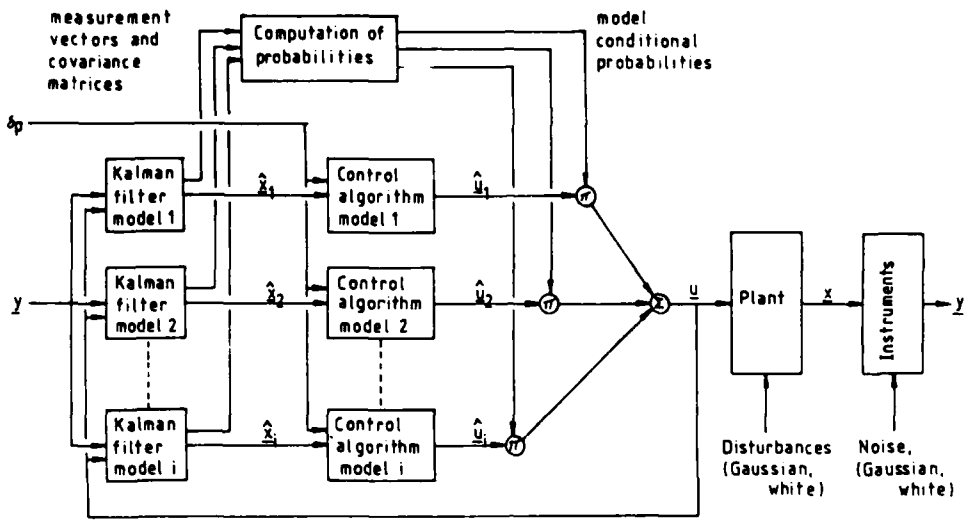

Figure 1 Structure of Partioned Adaptive Control

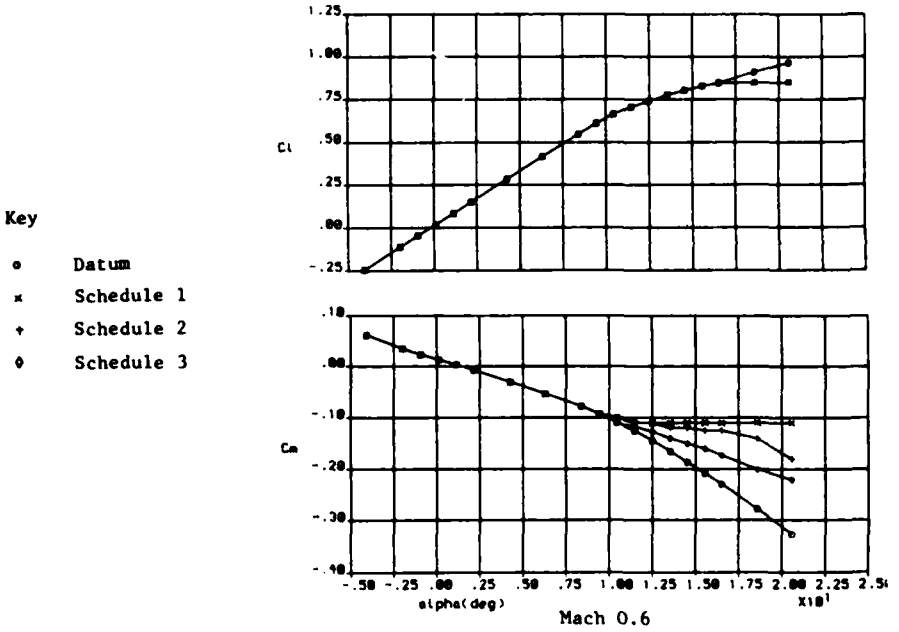

Figure 2 Longitudinal aerodynamic data

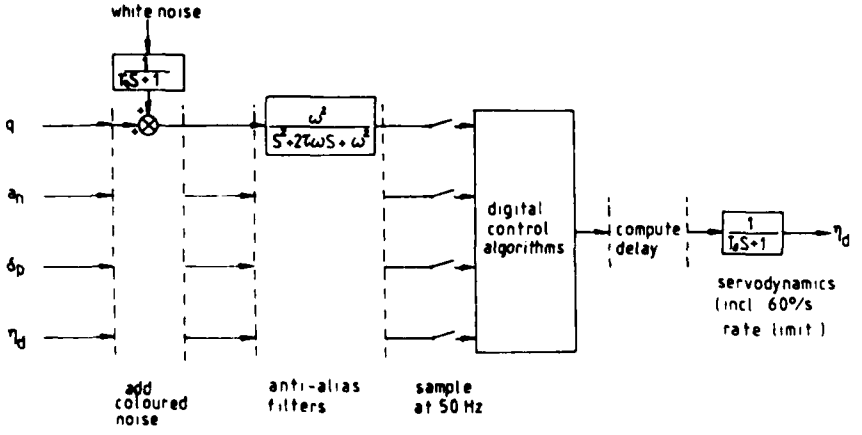

Figure 3 Features of aircraft control system simulation

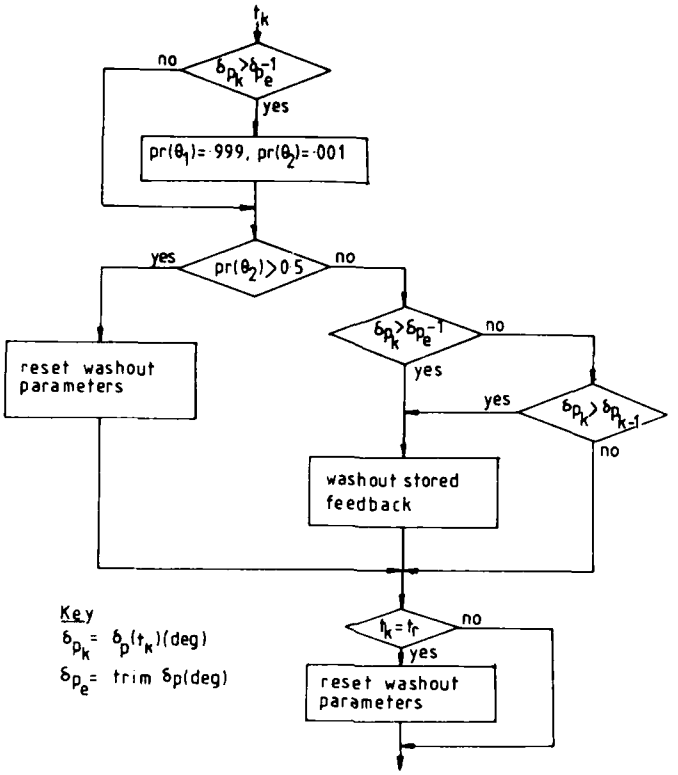

Figure 4 Logic for washout of stored feedback

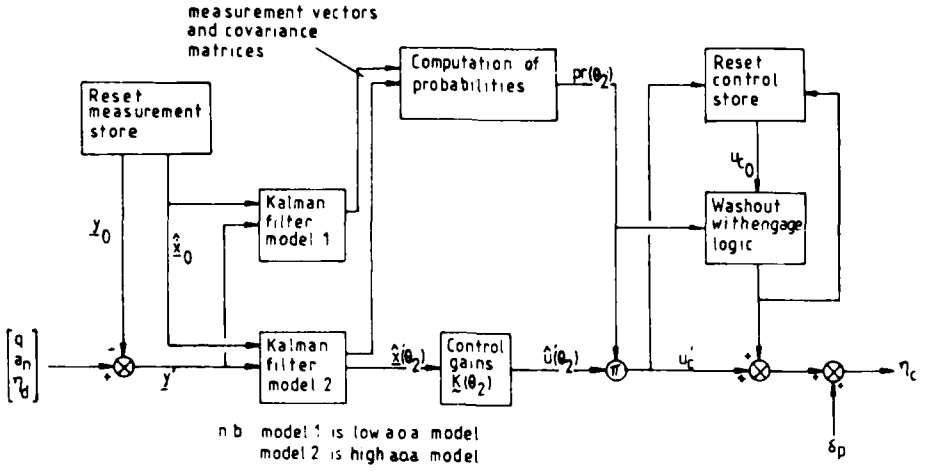

Figure 5 Structure of self-organising control system

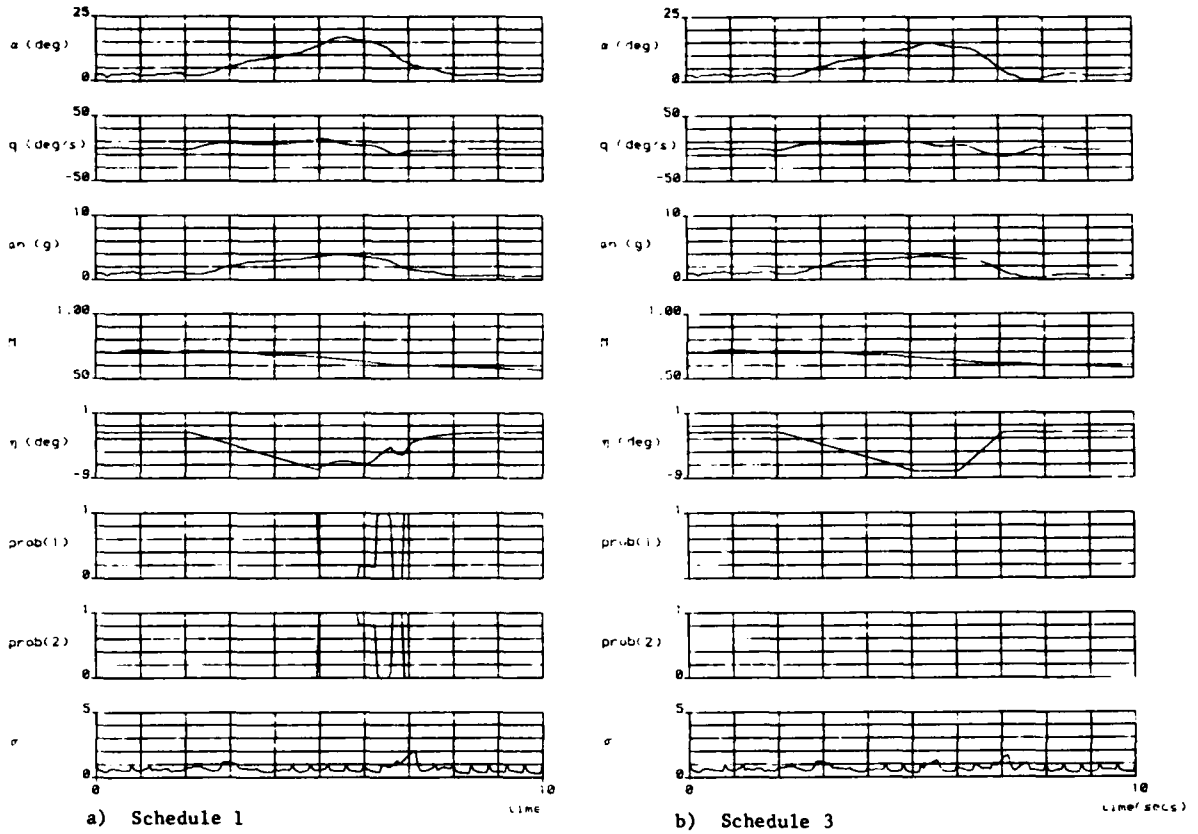

a) Schedule 1 b) Schedule 3

Figure 6 Pitching manoeuvre in turbulence

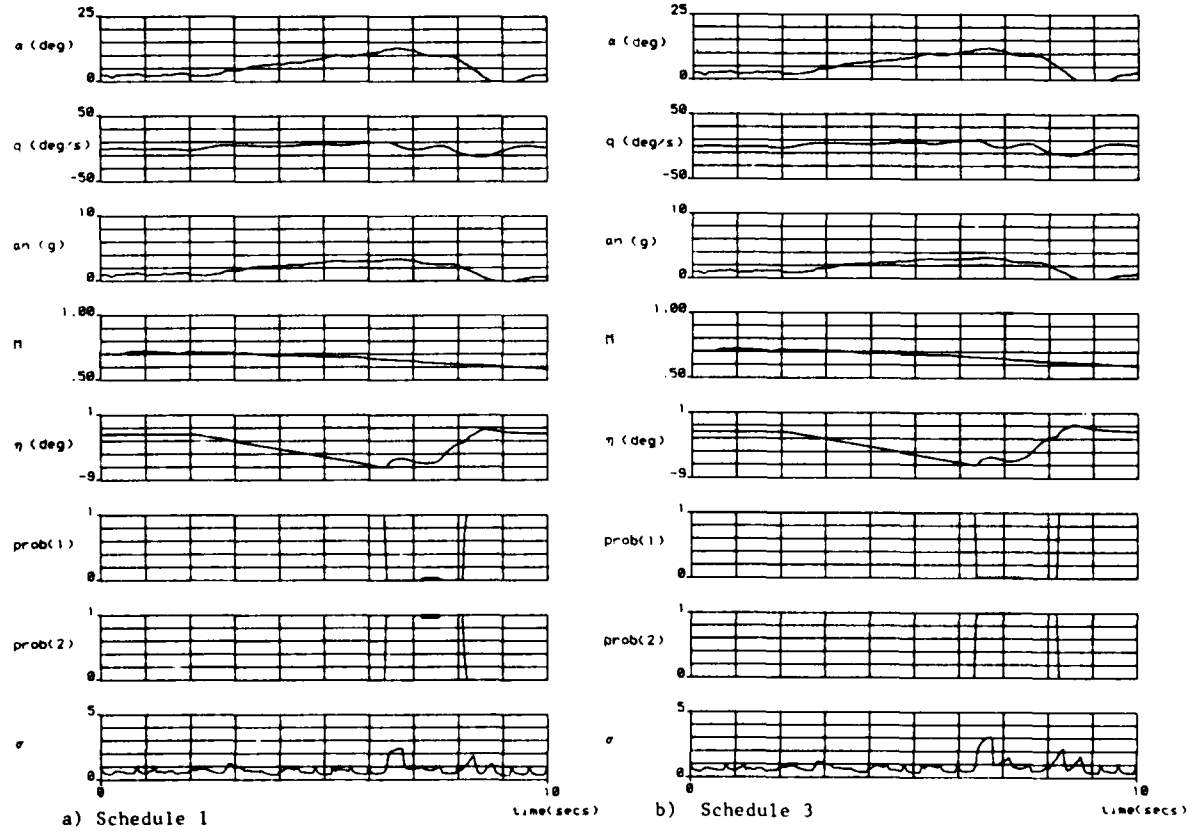

a) Schedule 1 b) Schedule 3

Figure 7 Slow pitching manoeuvre in turbulence

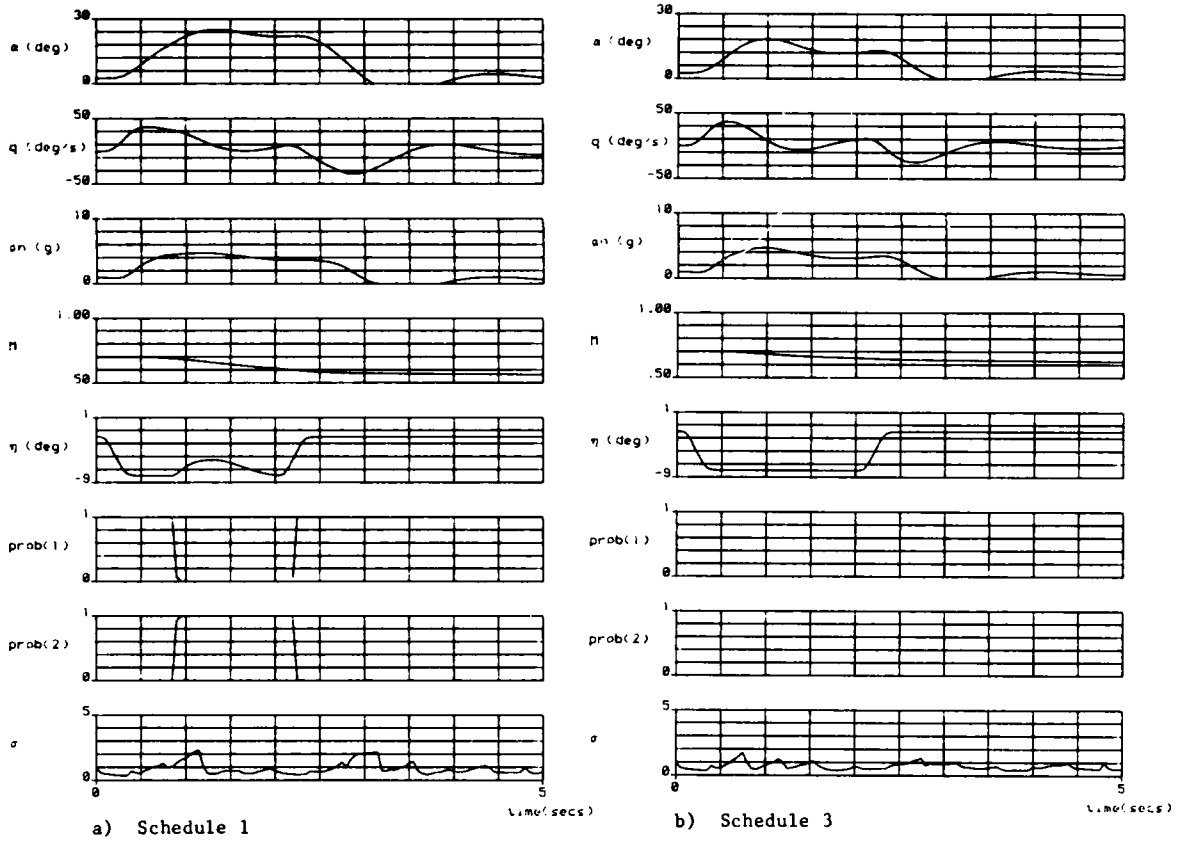

a) Schedule 1 b) Schedule 3

Figure 8 Sharp pitching manoeuvre

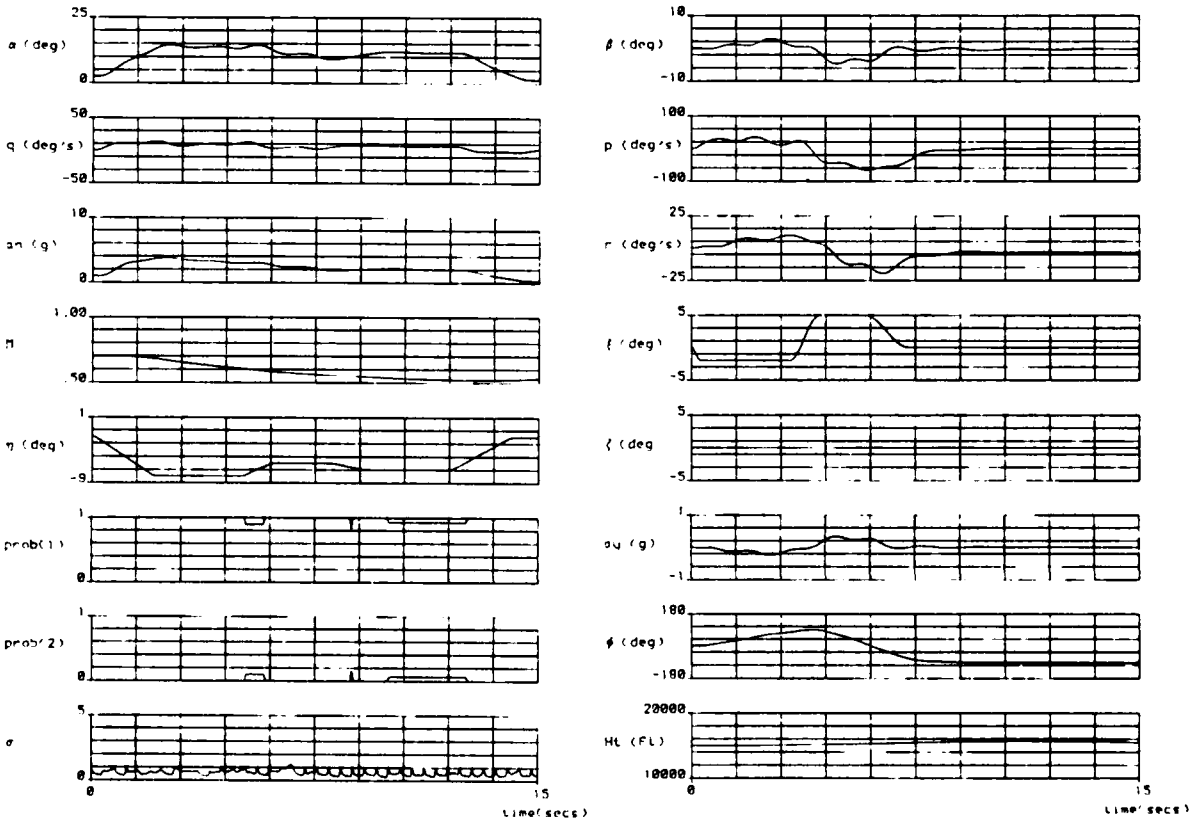

Figure 9 High AOA manoeuvre of "ideal" aircraft model

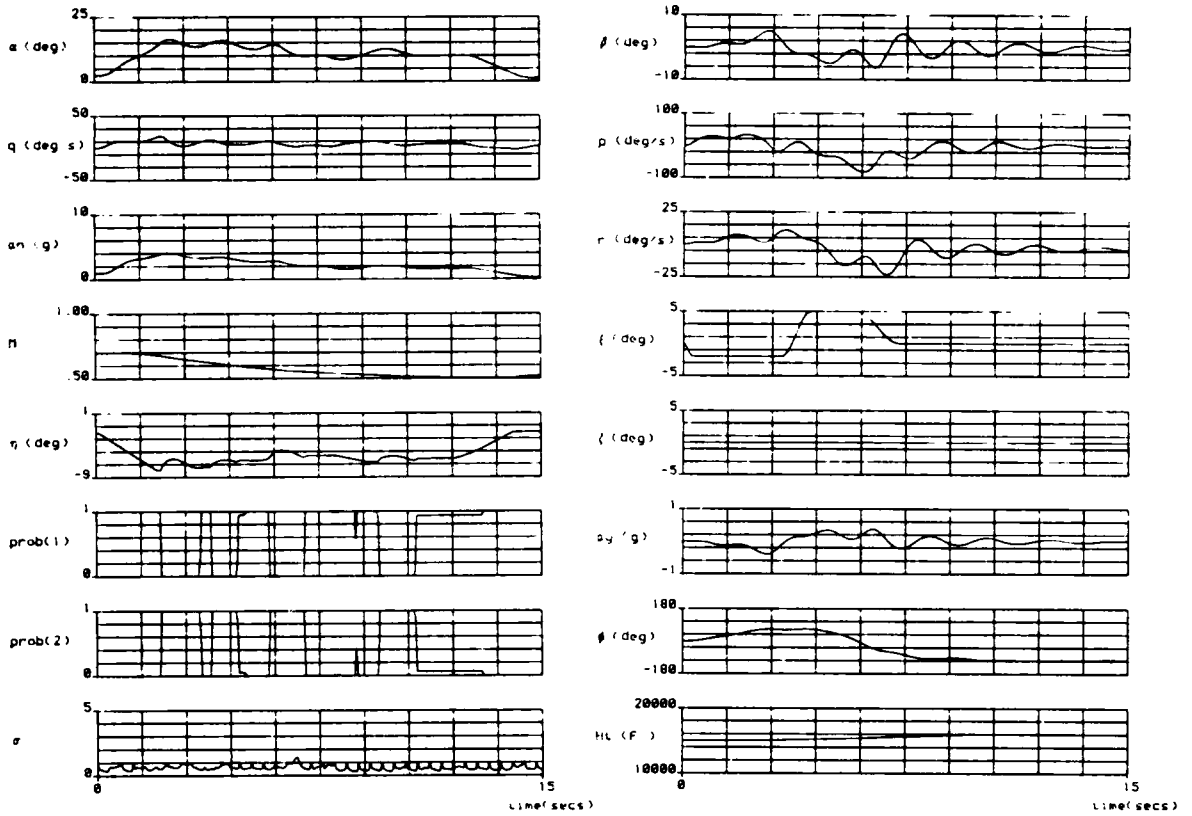

Figure 10 High AOA manoeuvre of aircraft model using schedule 1

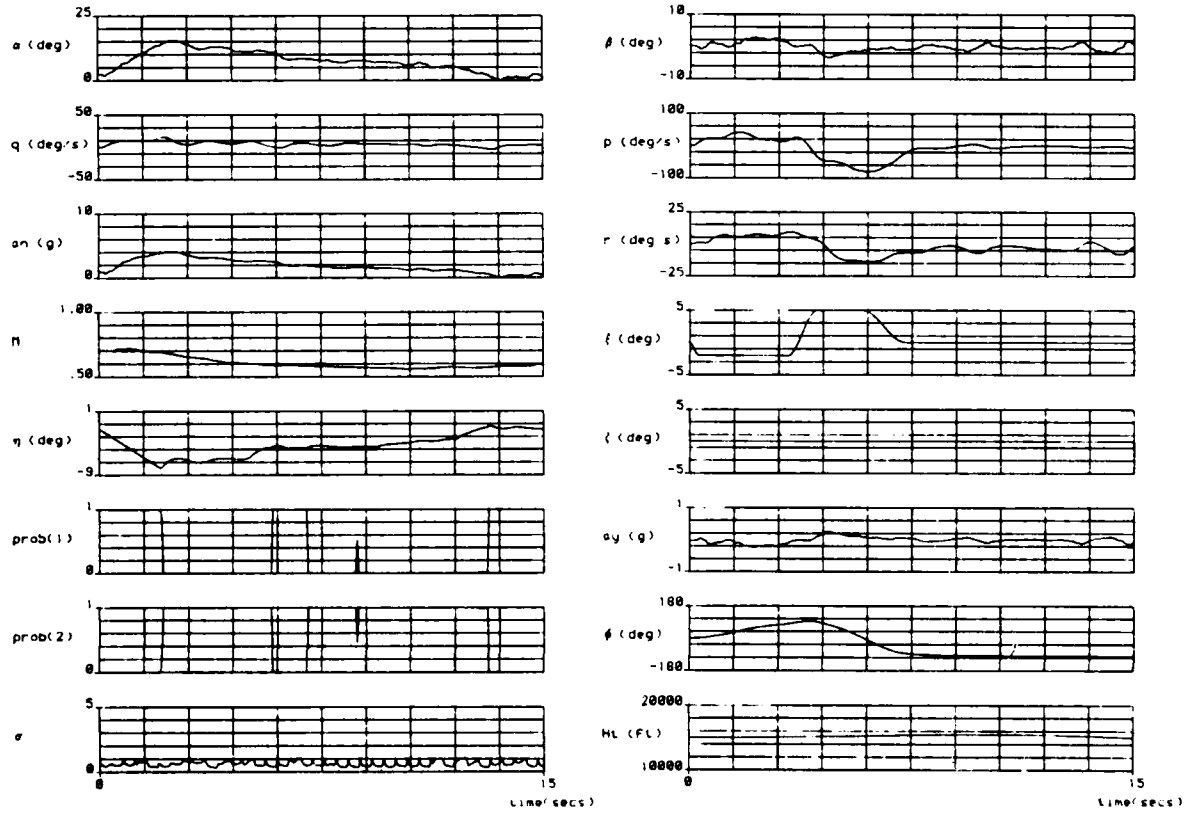

Figure 11 High AOA manoeuvre of aircraft model using schedule 1, in turbulence

GUST ALLEVIATION ON A TRANSPORT AIRPLANE

by

J. Becker, F. Weiss

MESSERSCHMITT-BÖLKOW-BLOHM GmbH.
Hubschrauber und Flugzeuge
P.O. Box 801160, 8000 Munich 80
W.-Germany

and

E. Cavatorta, C. Caldarelli

AERITALIA
80038 Pomigliano D'Arco (Napoli) Italy

SUMMARY

An analytical study was performed at Aeritalia and at MBB to define a Gust Alleviation System on a preliminary configuration of a commuter airplane. The analysis takes into account the influence of elasticity of the airplane, unsteady aerodynamic effects, mechanical nonlinearities such as backlash-deadzone and control surface rate and deflection limitations. A relatively simple model shows that ride comfort can be improved by at least 50 %.

DESCRIPTION

1. Mathematical Model of Turbulence

The investigation is based on the definition of turbulence as described in MIL-F-8785 where the power spectral densities are presented for the three velocity components of the turbulence in the von Karman form, which is applied in the frequency domain analysis, and the more simple form of Dryden used to determine the dynamic response in the time domain (Fig. 1).

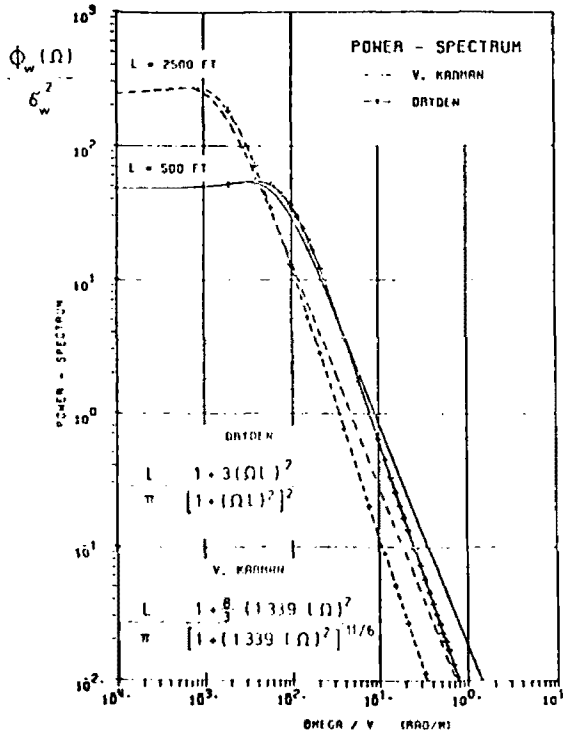

$$D_i = \left[\int_{0.1}^{f_t} |W(f)|^2 |T_{cs}(f)|^2 \Phi_u(f) df \right]^{1/2}$$

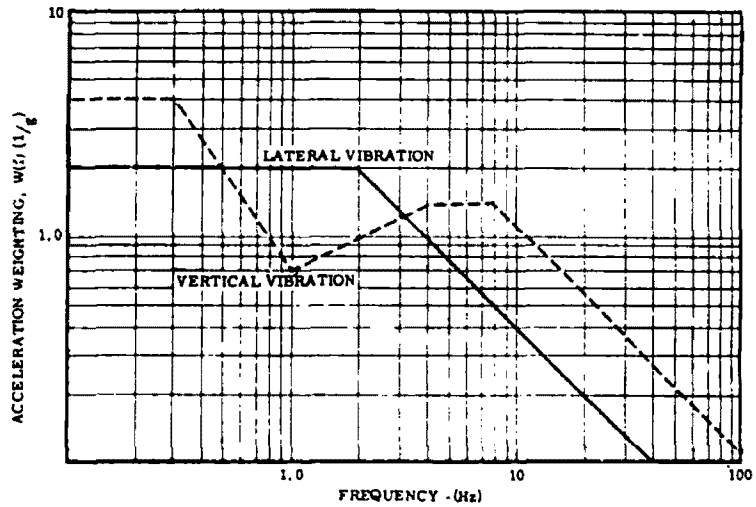

RIDE DISCOMFORT INDEX LIMITS

	Ride Discomfort Index, D_i	Flight Phase Duration (Exposure Time)	Probability of Exceeding RMS Turbulence Intensity
Long Term Requirement	0.10	Over 3 Hours	0.20
	0.13	From 1.5 to 3 Hours	0.20
	0.20	From 0.5 to 1.5 Hours	0.20
Short Term Requirement	0.28	Less than 0.5 Hour	0.01

FIG.1 DEFINITION OF RIDE COMFORT

2. Definition of the Passengers Ride Comfort

The aim is to quantisize the comfort. Therefore the most promising criterium, the "Ride Discomfort Index D_i" as reported in MIL-F-9490 D is applied. The criterium utilises the weighted turbulence induced acceleration, where the weighting function includes human receptance to define the index D_j, which for example reaches a limiting number of 0.2 at the exposure time of 0.5 to 1.5 hours (Fig. 1).

3. Mathematical Model of the Airplane

A mathematical model of the airplane flying in turbulence has been established to investigate the problems related to the definition of a gust alleviation system. By the application of a dynamic response analysis in time and frequency domain the different acceleration levels at each station along the fuselage may then be calculated. The complete dynamic representations consists of the flight dynamic and the structural dynamic description. The structural dynamic representation of the airplane is obtained in modal form after a finite element idealisation and a vibration calculation for the determination of the normal modes. Generalised masses, stiffnesses and structural dampings are utilised. In the dynamic system used for the investigation, rigid flight dynamic state variables together with aileron and elevator rotations and 10 elastic normal modes are taken into account. In addition the model also includes generalized aerodynamic forces in order to introduce unsteady aerodynamics to account for delay effects in the development of forces and moments especially when rapid variations of the aircraft and control surfaces are occuring. Also the Küssner effect due to the penetration of the gust is introduced. The calculation of the unsteady aerodynamic forces is performed using the lifting surface theory method /1/ and in parallel for comparison the doublet lattice method /2/ including the interference effects between wing and horizontal tail.

Fig. 2 demonstrates the scheme of the global aircraft mathematical model in matrix formulation, which is used for dynamic response calculations. Here the coupled classical flight mechanical and structural dynamic equations together with the equations representing the control laws of the gust alleviation system are shown. The coupling of the flight mechanical equations of motion for small perturbations in a body fixed system and the structural dynamic modal equations is achieved by the introduction of unsteady aerodynamic coupling terms, $Z_j(i\omega)$, $M_j(i\omega)$ and $L_j(i\omega)$. The first two terms represent the normal force and pitch moment contributions in the lift and moment equations due to the normal mode deflections or vibrations. These two terms "elastify" dynamically the rigid airplane aerodynamics. The third term is representative of the rigid airplane effects on the structural dynamics.

$$(A' + iA'')\ X = P' + iP''$$

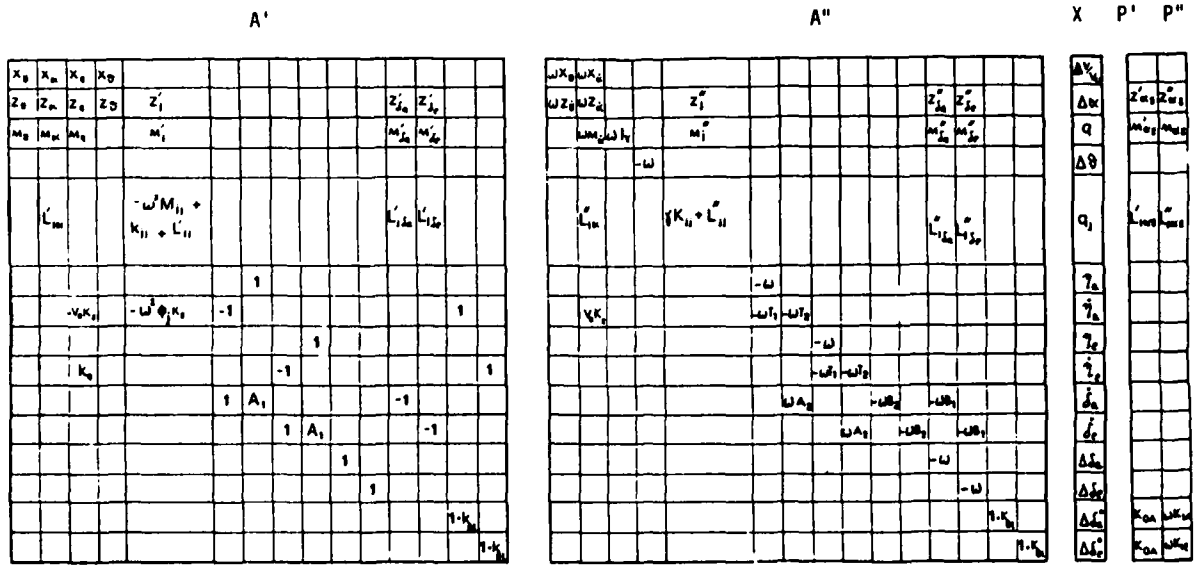

FIG.2 GLOBAL DYNAMIC SYSTEM MATRIX

Because the controls are in the dynamic loop, the unsteady aerodynamic normal force $Z_{\delta}(i\omega)$ and pitch moment $M_{j\delta}(i\omega)$ of the control surfaces are introduced. The $L_{j\delta}(i\omega)$ coupling terms explain the influence of the control surface rotations on the structural dynamics.

The excitation of the dynamic system is achieved by the disturbance vector of the right hand side $P'(\omega) + iP''(\omega)$ which describes the normal force and pitch moment $Z_{\alpha_g}, M_{\alpha_g}(i\omega)$ and the generalised forces $L_{j\alpha_g}(i\omega)$ induced by the gust.

Solving the system of linear equations

$$\left[A'(\omega) + i\,A''(\omega) \right] x(i\omega) = \left[P'(\omega) + iP''(\omega) \right]$$

the admittance function of the system is known

$$H(i\omega) = \left[A'(\omega) + i\,A''(\omega) \right]^{-1} \left[P'(\omega) + iP''(\omega) \right]$$

and then the transfer functions $Y(i\omega)$ of the state variables and the power spectral densities $S_y(\omega)$

$$Y(i\omega) = H(i\omega)\ \alpha_g(i\omega)$$

$$S_y(\omega) = |H(i\omega)|^2 S_g(\omega)$$

and the total (rigid + elastic) acceleration - transfer functions $n_z(i\omega)$ and corresponding power spectral densities

$$S_{n_z}(\omega) = |n_z(i\omega)|^2 S_g(\omega)$$

and the Ride Discomfort Index

$$D_i = \left[\int_{\omega_1}^{\omega_2} |W(f)|^2 S_{n_z}(f)\,df \right]^{\frac{1}{2}}$$

are derived.

W(f) being the physiological weighing function of the acceleration /3/.

4. Discomfort Index of Basic Aircraft

The Ride Discomfort Index of the transport airplane has been evaluated for the flight condition cruise using the intensity of turbulence given by

$$w_g = 6.6 \text{ ft/s}$$

according to Ref. 3.

The distribution of the index D_i along the fuselage axis is presented in Fig. 3 (curve a). Near the center of gravity the index reaches a value slightly above the considered limit value of 0.2 for the exposure time 0.5 to 1.5 hours.

In cruise condition the passenger comfort is therefore practically neutral. It should be concluded that the introduction of a gust alleviation system to get a reduction of the index D_i could be interesting.

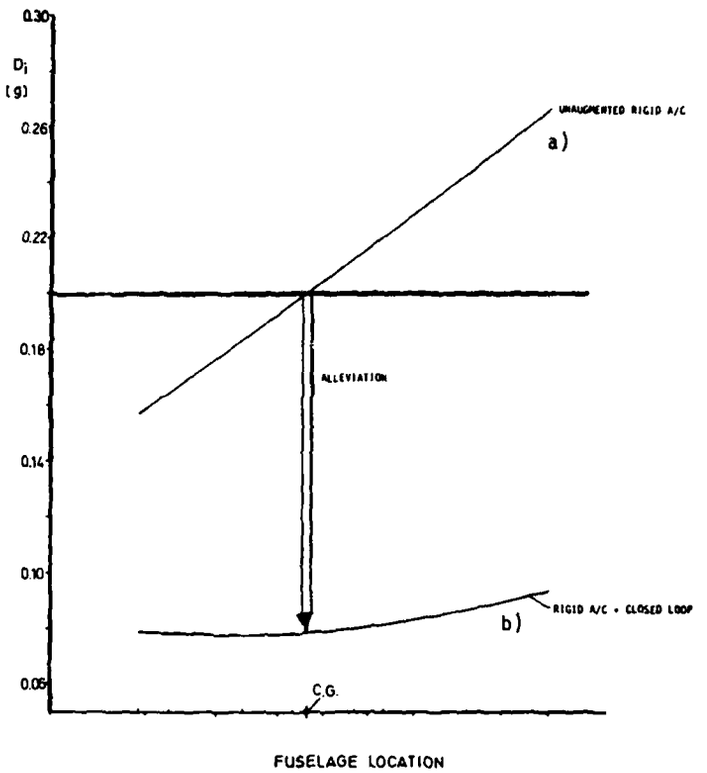

FIG.3 RIDE DISCOMFORT INDEX

COMPARISON RIGID A/C

UNAUGMENTED AND CLOSED LOOP SYSTEM

5. Control Laws

5.1 Closed Loop Control

The gust alleviation "closed loop" system is based upon the concept of measuring dynamic response signals of the aircraft to actuate the control surfaces generally ailerons and elevators.

Since the vertical acceleration mainly influences the passenger comfort, it is convenient to use this signal to command the ailerons symmetrically in order to counteract the effects of the gusts on the aircraft. In addition the pitch rate signal could be used as feedback to the elevator for stability augmentation. A first order low pass filter is generally introduced in order to limit the high frequency control surface activities which result from high frequency acceleration due to elastic fuselage modes, and a notch filter is included to avoid structural coupling effects with the first symmetrical wing bending mode with dominant fuselage bending contribution at 6 Hz. An additional notch filter to eliminate the second fuselage bending mode at 16 Hz is not considered.

Some results of the rigid aircraft analysis with this control loop are presented in Fig. 4. It is demonstrated that different control feedback gains lead to variations of the stability of the airplane in terms of short period roots and of the Ride Discomfort Index due to the increasing symmetrical aileron and elevator deflections and the resulting increase in damping.

By using for example the gains $K_{nz} = 0.3$ rad/ms^{-2} for the acceleration feedback and no pitch rate feedback the short period root is $\sigma_1 = -1.94, \sigma_2 = -0.44$ as shown in Fig. 4a, where as the additional pitch rate feedback $K_{\omega y} = 0.2$ will lead to a coupling of the short period with the actuator as shown in Fig. 4b.

The effect of elevator (pitch rate feedback) on the ride discomfort index is found to be disadvantageous, the system may therefore be simplified by cancelling the feedback to the elevator, with a higher reduction of the PDI. The effects are illustrated in Fig. 4c. The simplification will allow to maintain the elevator command completely unaffected (manual control).

The acceleration feedback system needs an interconnect filter to decouple pilots commands from active control commands. This filter may be derived theoretically from the transfer function of the vertical acceleration due to elevator input. In this way the gust alleviation system can operate in turbulence even if pilot stick commands are present. The interconnect filter will influence to some extent the handling characteristics and therefore possible PIO tendencies should be investigated in advance.

The interconnect filter $F_{INT}(i\omega)$ which is derived for cruise condition is shown in Fig. 5, which illustrates also the low pass filter and the actuator transfer function. A phase advance filter will be introduced in order to cancell low frequency phase lays caused by the notch filter. These effects are not shown in the report.

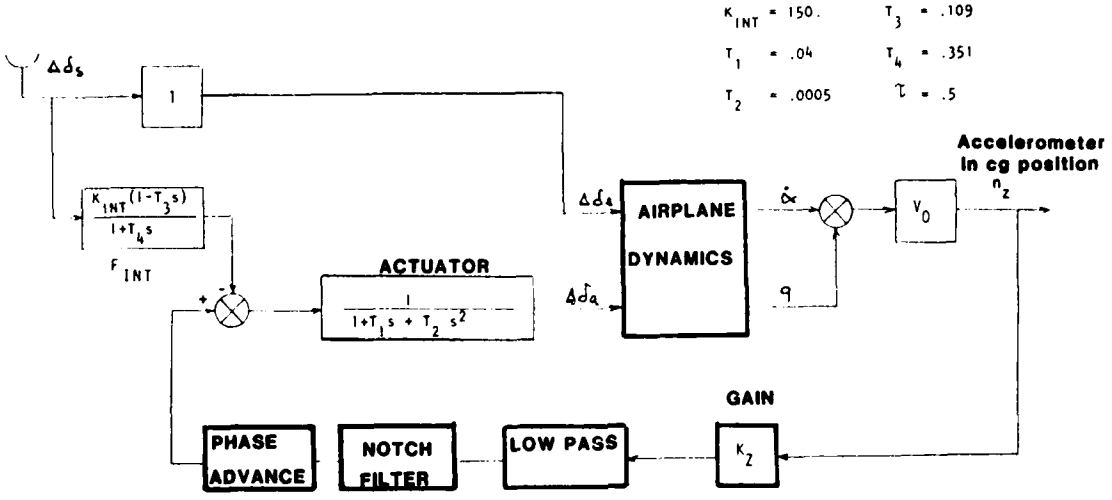

FIG.5 BLOCKDIAGRAM

5.2 Closed Loop Versus Open Loop Comparison

There are some aspects of the open loop system which are believed to be of importance. The basic assumption of the open loop alleviation system is the possibility to measure precisely the gust induced angle of attack. A fundamental limitation of this system is in general that the gust induced lift increment cannot be compensated totally by the control surfaces activated by the gust sensors due to limited control surface effectiveness rate. In addition the open loop system necessitates the elevator feedback for pitch moment compensation.

An investigation has been performed for the open loop system which consisted mainly in a variation of the percentage of ideal compensation to get a comparison with closed loop results. The study demonstrated in Fig. 6, indicates, that the closed loop system, in case of equivalent aileron rms deflection is more efficient.

GAINS			DYNAMIC RESPONSE(rms) σ_g=2.01 m/sec					
rad/m/sec²	rad/rad/sec	sec	rad	rad	rad/sec	rad/sec	m/sec²	RDI
Kz	Kq	τ	Δδa	Δδe	δ̇a	δ̇e	nz	DI
0	0	0	0	0	0	0	0.97	0.202
.2	.5	.5	.063	.0017	.2	.0055	.63	140
.35	.5	.5	.098	.0013	.31	.0046	.58	120
.5	.5	.5	.129	.0012	.39	.0041	.52	.105
.5	0	.5	.115	0	.31	0	.56	.08

FIG.6 RIGID AND ELASTIC AIRPLANE RESPONSE

RIGID A/C

	WITHOUT ELEVATOR	CLOSED LOOP	OPEN LOOP	
			WITH LOW PASS	WITHOUT LOW PASS
Δδa (rms)	0	5.8 °	6.06 °	6.42 °
Δδe (rms)	0	0	0.069 °	0.072 °
DI (RDI)	.217	.105	.181	.145

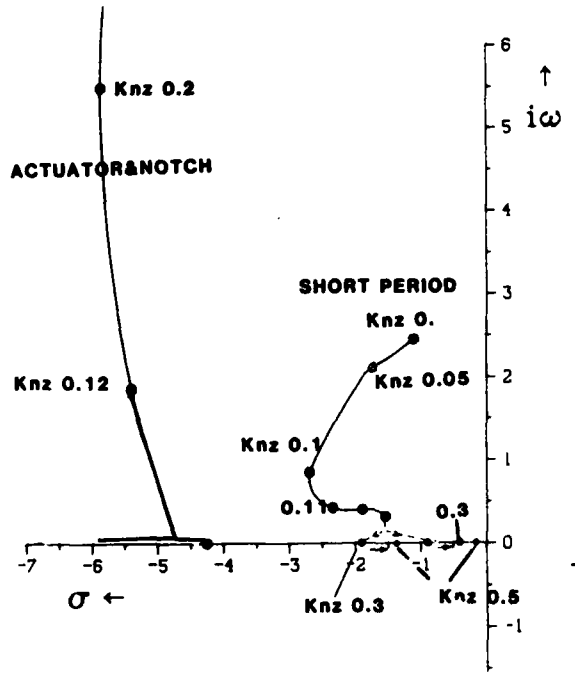

FIG.4a GAIN ROOT LOCUS OF AILERON CONTROL

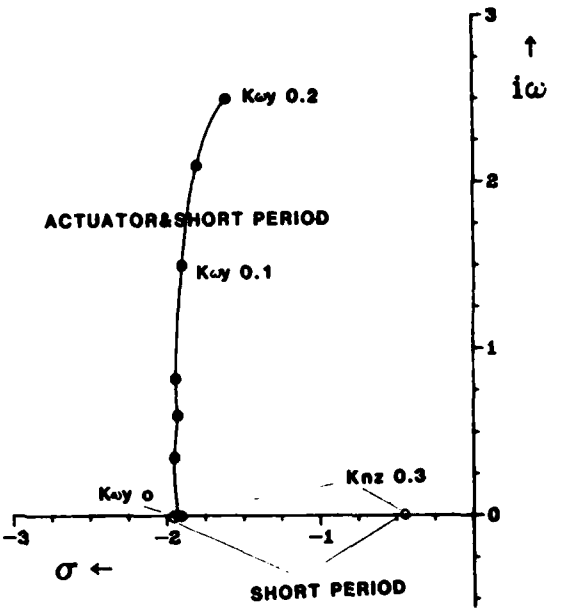

FIG.4b GAIN ROOT LOCUS OF AILERON &ELEVATOR CONTROL

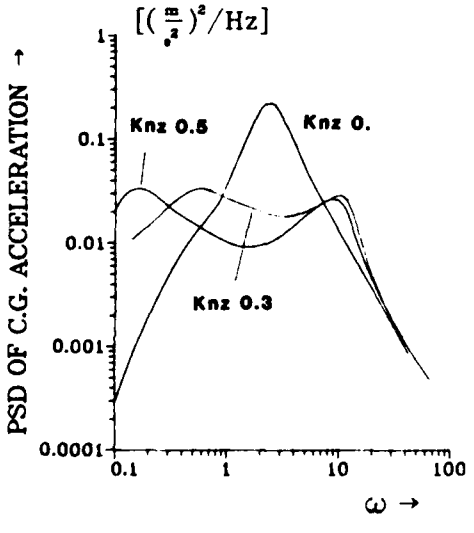

FIG.4d POWER SPECTRAL DENSITY OF C.G. ACCELERATION FOR Knz 0.3 and Knz 0.5

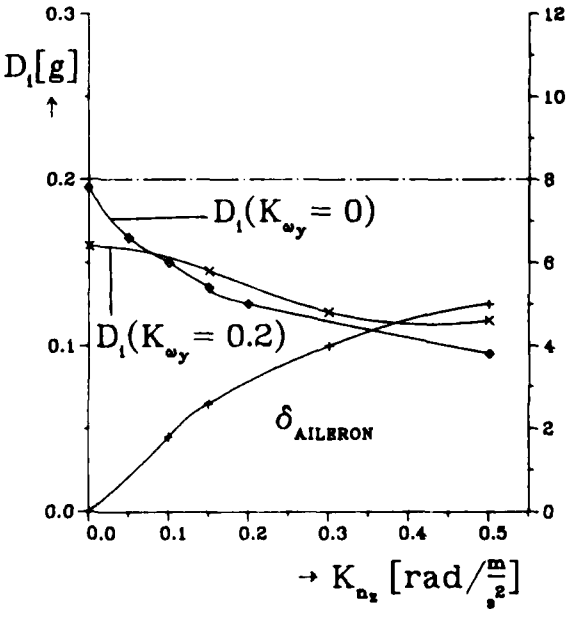

FIG.4c RIDE DISCOMFORT INDEX AS FUNCTION OF GAIN

6. Influence of Nonlinearities

The investigation of nonlinearities has been carried out in time domain using the model of the Dryden spectrum and the dynamic description of the rigid airplane.

In Fig. 7 the reduction of rms vertical acceleration at the c.g. position is presented. 40 percent of alleviation of the control without nonlinearities is used as reference value. A decrease to 30 percent in alleviation is obtained for an assumed, very pessimistic deadzone of 0.013 sec and backlash of $\pm$ 0.1 deg.

In addition the influence of aileron deflection- and rate limitation were investigated. The reduction of the maximum deflection from 7 to 6 degs and rate limitation from 26 to 20 degs gives an alleviation of 20%. Increasing the limitations to 8 degs of deflection and 30 deg/s of rate in the closed loop system the alleviation reaches again 30%.

The effects of nonlinearities are also shwon in Fig. 7 for open loop system, which demonstrates more severe effects.

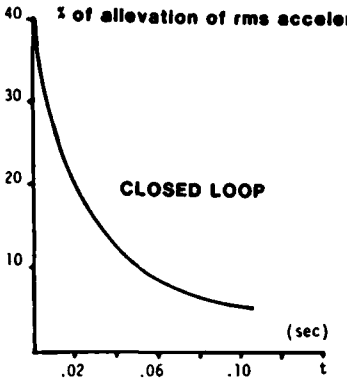

OPEN LOOP

Dead-zone sec.	Limiter	Filter Low Pass	Alleviation
0	NO	NO	51 %
0.0187	NO	NO	38 %
0.0375	NO	NO	22 %
0.0375	$\pm$ 60°/sec $\pm$ 15°	NO	22 %
0.0187	$\pm$ 30°/sec $\pm$ 8°	NO	24 %
0	NO	$\frac{1}{1+.5s}$	12 %
0.0187	NO	$\frac{1}{1+.5s}$	2 %

FIG.7 EFFECT OF DEADZONE ON ALLEVIATION OF ACCELERATION

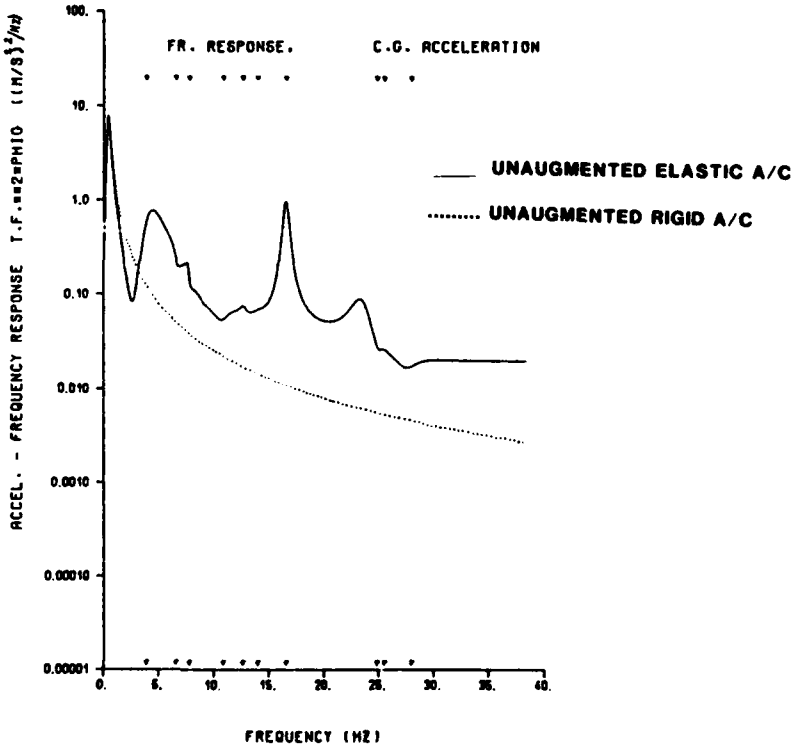

FIG.8 EFFECT OF AEROELASTICITY
ON PSD OF VERTICAL C.G. ACCELERATION
CRUISE CONDITION Ma 0.44 6000m

7. Influence of Aeroelasticity

The unsteady aerodynamics and the structural dynamic effects produce increments in the total acceleration as depicted in Fig. 8 for the airplane without control. The figure shows a comparison of the C.G. acceleration power spectral density for the rigid and elastic case. The peaks in the total PSD correspond to the dynamic response in the frequencies of the short period and the structural models. The magnitude of the elastic mode contributions especially in the frequency of the first wing bending at 5 Hz, the first fuselage bending at 7.8 Hz and of the second fuselage bending at 16 Hz is significant.

Concerning the airplane with control system, aeroelastic effects are in general of high concern because of structural coupling. The structural coupling is caused by the elastic mode contributions in the acceleration feedback signal. For instance the vertical C.G. acceleration leads to a aileron PSD shown in Fig. 9, which reflects all properties of the acceleration signal itself. Therefore the aileron could excite the airplane in the frequency around 3 - 8 Hz and at 16 Hz. In order to avoid the excitation the feedback signal should be filtered at the interesting frequencies (especially at frequencies of the fuselage) using different notch filters. In our example a notch filter was introduced which works in the region of first wing and fuselage bending. The notch influence on the aileron signal is also demonstrated in Fig. 9.

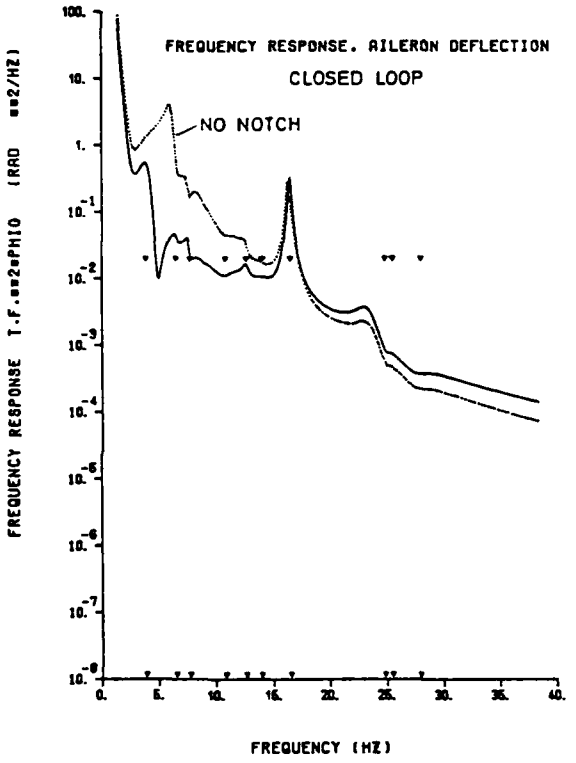

FIG.9 EFFECT OF NOTCH FILTER ON THE PSD OF AILERON DEFLECTION

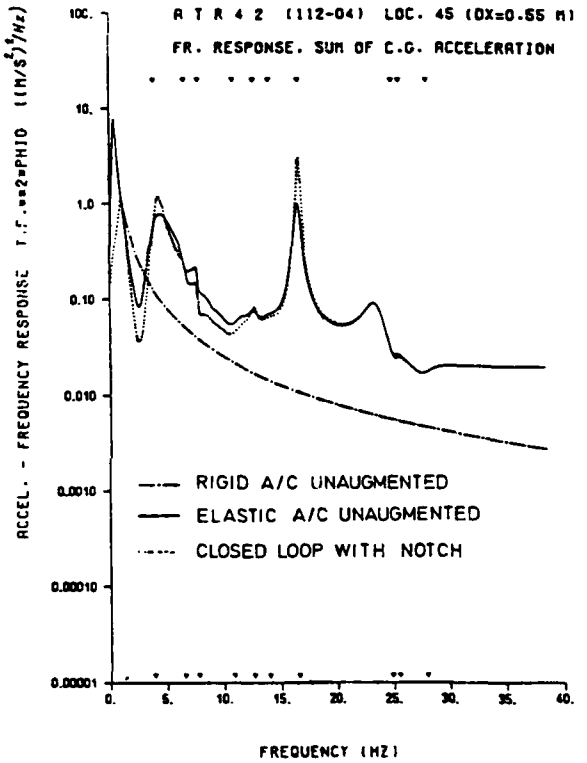

FIG.10 EFFECT OF NOTCH FILTER ON THE PSD OF C.G.ACCELERATION

The influence of aeroservoelasticity is shown in Fig. 10 comparing the PSD of C.G. acceleration with and without control (with notch filter). As expected the excitation of the C.G. acceleration in the 5 - 8 Hz region is small due to the notch filter effects. Fig. 11 shows the final result in terms of Ride Discomfort Index at different fuselage locations. The figure demonstrates the effect of the notch filter especially at the forward fuselage positions. Without notch filter an excitation is observed. The results shown were derived for a system without phase advance filter. Such a filter will be necessary in order to cancel out the phase introduced in low frequency range by the notch filter improving further the alleviation. Fig. 11 shows at the C.G. position an alleviation of RDI of almost 50%.

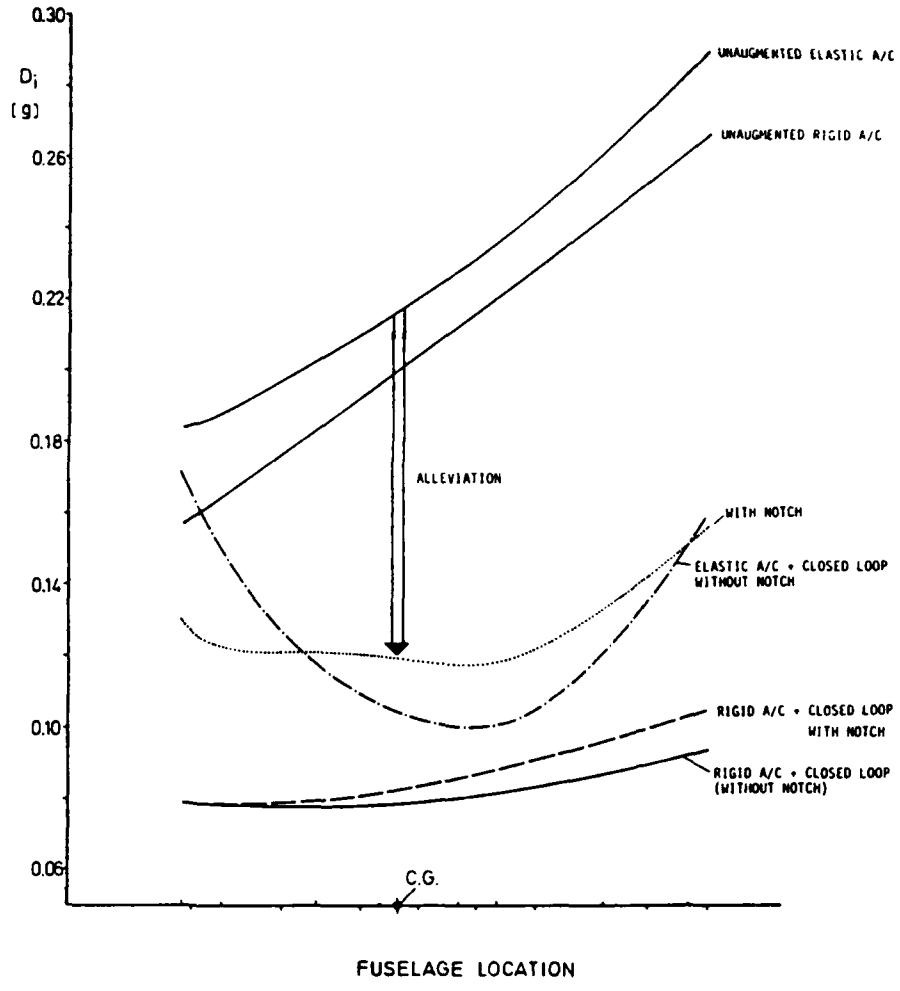

FIG.11 RIDE DISCOMFORT INDEX ALONG FUSELAGE

EFFECT OF CLOSED LOOP AILERON CONTROL

EFFECT OF AEROELASTICITY

o. CONCLUSIONS

The unaugmented airplane, according to the analytical results of the Ride Discomfort Index will experience a passenger comfort practically neutral. A gust alleviation system based on closed loop concept as demonstrated in Fig. 5, appears to be attractive to improve the comfort. The investigation indicates that the improvement is dependent to some extent on nonlinear effects in the control loop. Considering realistic parameters the control system could lead to an alleviation factor at least of 50 percent.

7. REFERENCES

/1/ LASCHKA, B.
Interfering Lifting Surfaces in Subsonic Flow
Zeitschrift für Flugwissenschaften, 18, Heft 9/10, 1970

/2/ RODDEN, W. P.
New Developments and Applications of the Subsonic Doublet-Lattice Method for Nonplanar Configurations
AGARD-CP-No. 80, 1971

/3/ Military Specification - Flight Control System
MIL-F-94900 - June 1975

/4/ Military Specification - Flying Qualities of Piloted Airplanes
MIL-F-6785C - November 1980

/5/ BECKER, J.; SENSBURG, O.; WEISS, F.
Active Gust Load Alleviation and Ride Control
International Symposium on Aeroelasticity, Nuremberg, Oct. 5-7, 1981

UNSTEADY THREE-DIMENSIONAL FLOW THEORY VIA MATERIAL FUNCTIONS

by

Dr. W. H. Hui, D.Sc.
Professor of Applied Mathematics
and Mechanical Engineering

H. J. Van Roessel
Graduate Student
Dept. of Applied Mathematics

University of Waterloo

Waterloo, Ontario, Canada N2L 3G1

Abstract

A new Lagrangian formulation for unsteady three dimensional supersonic inviscid flow over rigid bodies is developed. The continuity equation is eliminated by the use of material functions, a generalization of the stream functions for steady flow. This is followed by a transformation to new independent variables, three of which are these material functions. The fourth variable is a Lagrangian time distinct from the Eulerian time. The simultaneous use of both Lagrangian and Eulerian time allows the problem of flow with shock wave to be reduced to a fixed boundary one. In the Newtonian limit it is found possible to obtain analytic solutions for various body shapes.

Consider a rigid aircraft whose motion is characterized by the velocity $\vec{V}_c(t)$ of its centre of mass and its angular velocity $\vec{\Omega}(t)$. Given $\vec{V}_c(t)$ and $\vec{\Omega}(t)$, the central problem in unsteady aerodynamics is to calculate the resulting unsteady flow in terms of $\vec{V}_c(t)$ and $\vec{\Omega}(t)$. The resolution of this problem will also help determine the motion of the aircraft taking into full account the time-history effects.

In a body-fixed curvillinear coordinates $\xi^i (i = 1, 2, 3)$, the Euler equations for the motion of an inviscid, non-heat conducting perfect gas are:

$$\frac{\partial \rho}{\partial t} + \frac{1}{\sqrt{g}} \frac{\partial}{\partial \xi^i} (\sqrt{g}\, \rho\, v^i) = 0 \tag{1}$$

$$\frac{\partial v^i}{\partial t} + v^j \frac{\partial v^i}{\partial \xi^j} + \Gamma^i_{jk} v^j v^k + \frac{1}{\rho} g^{ij} \frac{\partial p}{\partial \xi^j} = F^i , \quad (i = 1,2,3) \tag{2}$$

$$\frac{\partial}{\partial t} \left(\frac{p}{\rho^\gamma}\right) + v^j \frac{\partial}{\partial \xi^j} \left(\frac{p}{\rho^\gamma}\right) = 0 \tag{3}$$

where p is pressure, ρ density, $\vec{v}$ velocity, $\vec{r}$ position vector, t time, γ the ratio of specific heats, and

$$F = -\left[\frac{d\vec{V}_c}{dt} + 2\vec{\Omega} \times \vec{v} + \vec{\Omega} \times (\vec{\Omega} \times \vec{r}) + \frac{d\vec{\Omega}}{dt} \times \vec{r}\right] \tag{4}$$

is the inertial force arising from the motion of the body, $\xi^3 = 0$ defines the body surface, g^{ij} is the inverse of the metric tensor g_{ij}, $g = |g_{ij}|$, and Γ^i_{jk} are the Christoffel symbols.

Letting $v^0 \equiv 1$ and $\xi^0 \equiv t$, and noting the time-independence of g_{ij}, we may replace the continuity equation (1) by introducing three functions $m^i (i = 1,2,3)$ as follows

$$\frac{\sqrt{g}\, \rho v^K}{\lambda(m^i)} = \epsilon^{KLMN} \frac{\partial m^1}{\partial \xi^L} \frac{\partial m^2}{\partial \xi^M} \frac{\partial m^3}{\partial \xi^N} , \quad (K,L,M,N = 0, 1, 2, 3) \tag{5}$$

Using (5), it can easily be shown that

$$\frac{Dm^i}{Dt} = 0 , \qquad (i = 1, 2, 3) \tag{6}$$

implying that m^i $(i = 1, 2, 3)$ are constants following a fluid particle; they are thus called material functions. Material functions in unsteady flow are a generalization of the stream functions in steady flow.

We further introduce a function $m^0(\xi^I) \equiv \tau$ such that

$$\frac{\rho \sqrt{g}}{\lambda} = \frac{\partial(m^0, m^1, m^2, m^3)}{\partial(\xi^0, \xi^1, \xi^2, \xi^3)} \equiv \left(\frac{1}{\Delta}\right) \tag{7}$$

It can also easily be shown that

$$\frac{D}{Dt} = \frac{\partial}{\partial \tau} \tag{8}$$

Thus τ ($\equiv m^0$) is the Lagrangian time variable, in contrast with the Eulerian time variable t ($\equiv \xi^0$) .

We note that the function $m^0(\xi^I)$ (or $\tau(\xi^I)$) introduced above is determined only to an arbitrary function of three independent variables and we can, as we do, impose that the unknown shock surface is given by

$$\tau(\xi^I) = 0 \tag{9}$$

When m^I (I = 0, 1, 2, 3) are regarded as independent variables we obtain the following equations

$$\frac{\partial^2 \xi^i}{(\partial \tau)^2} + \Gamma^i_{jk} \frac{\partial \xi^j}{\partial \tau} \frac{\partial \xi^k}{\partial \tau} + \frac{g^{ij}}{\rho} \frac{\partial m^I}{\partial \xi^j} \frac{\partial p}{\partial m^I} = F^i \ , \quad (i,j,k = 1,2,3) \tag{10}$$

$$\frac{\partial}{\partial \tau} \left(\frac{p}{\rho^\gamma}\right) = 0 \tag{11}$$

$$\frac{\partial t}{\partial \tau} = 1 \tag{12}$$

$$\frac{\lambda}{\rho \sqrt{g}} = \frac{\partial(\xi^0, \xi^1, \xi^2, \xi^3)}{\partial(m^0, m^1, m^2, m^3)} \tag{13}$$

Eq. (12) is integrated to give

$$t = \tau + s(m^1, m^2, m^3) \tag{14}$$

The body surface boundary condition is

$$\xi^3 = 0 \qquad \text{at} \quad m^3 = 0 \tag{15}$$

and the shock jump boundary conditions are of the form

$$f\left(\frac{\partial \xi^i}{\partial \tau}\Big|_{\tau=0}, \ \xi^i\Big|_{\tau=0}, \ p\Big|_{\tau=0}, \ s, \ \nabla s\right) = 0 \tag{16}$$

We thus see that the problem of calculating supersonic flow with shock wave becomes a fixed boundary problem in the m space.

The formulation given above represents a new version of the Lagrangian approach with m^I as Lagrangian variables. It differs from the conventional Lagrangian formulation in that

(a) the material functions m^i (i = 1, 2, 3) are used as Lagrangian variables instead of the particle position (a, b, c) at time t_0 ; the material functions are more closely related to the physics of the flow.

(b) it recognizes the difference between the Eulerian time t and the Lagrangian time τ and utilizes this difference to render the mathematical problem a fixed boundary one,

(c) it simultaneously uses both the Lagrangian variables and the Eulerian variables, making it easier to transform one set to the other; this is helpful in aerodynamic problems for which the pressure is often required in Eulerian form $p(\xi^1, \xi^2, \xi^3, t)$.

The advantages of the new Lagrangian formulation have been exploited in the Newtonian limit which simplifies (10) to

$$\frac{\partial^2 \xi^\alpha}{(\partial \tau)^2} + \bar{\Gamma}^\alpha_{\beta\gamma} \frac{\partial \xi^\beta}{\partial \tau} \frac{\partial \xi^\gamma}{\partial \tau} = \bar{F}^\alpha \qquad (\alpha = 1,2) \tag{17}$$

$$\sqrt{\bar{g}} \ \Lambda \frac{\partial p}{\partial \xi^3} + b_{\alpha\beta} \frac{\partial \xi^\alpha}{\partial \tau} \frac{\partial \xi^\beta}{\partial \tau} = \bar{F}^3 \tag{18}$$

where

$$(\bar{\ \ }) = (\ )_{m^3=0} = (\ )_{\xi^3=0}$$

and $b_{\alpha\beta}$ are the 2nd fundamental form of the body surface. The problem is now to first solve the tangential momentum equations (17) - these are now ordinary differential

equations - for ξ^α ($\alpha = 1,2$) and then to find $p(\xi^1,\xi^2,0,t)$ from (18) by quadrature after a partial transformation to Eulerian coordinates.

For steady flow $F^\alpha = 0$ and (17) become the geodesic equations of the body surface. Exact analytic solutions have been found for families of body shapes including bodies of revolution at arbitrary angles of attack and general conical shapes [1]. For these body shapes the surface pressure are obtained as quadrature in terms of the shape which will be used in conjunction with calculus of variations to determine the optimum conical wing. Finite Mach number flow may be calculated using an iteration scheme starting from the Newtonian flow solution.

Unsteady flow resulting from slow motion of the aircraft relative to its steady flight is calculated by perturbation of Eq. (10-13) from the known steady flow. For the wedge in transient motion an analytic solution is obtained which will be used to study the effects of past motion on the present state of its motion [2], [3].

References

[1] H. J. Van Roessel and W. H. Hui, "Steady Three-Dimensional Hypersonic Flow Theory via Stream Functions" (in preparation).

[2] H. J. Van Roessel and W. H. Hui, "Unsteady Three-Dimensional Hypersonic Flow Theory via Material Functions" (in preparation).

[3] W. H. Hui and H. J. Van Roessel, "Transient Motion of Hypersonic Vehicles Including Time History Effects", AIAA paper 85-0201.

Acknowledgements

This research was financially supported by NASA Grant NAGW-575. The authors thank Drs. Murray Tobak and Gary T. Chapman for their valuable comments on the work.

UNSTEADY INTERACTIONS OF TRANSONIC AIRFOILS WITH GUSTS AND CONCENTRATED VORTICES

W. J. McCroskey*
U.S. Army Aeromechanics Laboratory (AVSCOM)
NASA Ames Research Center, Moffett Field, California 94035, U.S.A.

G. R. Srinivasan†
JAI Associates, Mountain View, California 94042, U.S.A.

SUMMARY

Unsteady interactions of strong concentrated vortices, distributed gusts, and sharp-edged gusts with stationary airfoils have been analyzed in two-dimensional transonic flow. A simple and efficient method for introducing such vortical disturbances has been implemented in numerical codes that range from inviscid, transonic small-disturbance to thin-layer Navier Stokes. The numerical results demonstrate the large distortions in the overall flow field and in the surface air loads that are produced by various vortical interactions. The results of the different codes are in excellent qualitative agreement, but, as might be expected, the transonic small-disturbance calculations are deficient in the important region near the leading edge.

INTRODUCTION

Vortical disturbances can have important effects on the air loads and the aeroacoustics of a variety of aerodynamic devices, such as maneuvering aircraft and missiles, helicopter rotor blades, and turbomachinery. Although the numerical analysis of strong vortical flows has received less attention than the treatment of shock waves over the past decade, compressible flow fields with embedded regions of distributed or concentrated vorticity appear certain to receive increasing attention in the future.

Several methods have already begun to appear in the literature for treating concentrated vorticity in finite-difference computations. Direct approaches, such as those of Rizzi and Ericksson (Ref. 1), Fujii and Kutler (Ref. 2), Krause and Hartwick (Ref. 3), and Srinivasan and Steger (Ref. 4) may be classified as vortex-capturing, by analogy with the familiar shock-capturing methods that are used in many computational fluid dynamics (CFD) codes. As in shock capturing, the details of the actual phenomenon are spread over several grid points. Consequently, the solutions in these high-gradient regions are artificially grid-dependent and are susceptible to the effects of numerical dissipation. In the case of concentrated-tip vortices, for example, numerical dissipation may destroy the simulation of the core structure faster than would physical dissipation (Ref. 4), unless many grid points are clustered in the vortical region.

An alternative approach for modeling vortex flows, the prescribed-disturbance method, is the subject of this note. By analogy with shock-fitting in transonic flows, this method may be thought of as vortex fitting. The essential ideas are due to Steinhoff (Ref. 5) and to Buning and Steger(Ref. 6); the technique was also in the work reported in Refs. 7-9 on potential, Euler, and thin-layer Navier-Stokes analyses of two-dimensional, unsteady airfoil-vortex interactions. In these applications, the structure of the vortex is prescribed, but its path in space can be allowed to develop as part of the solution. The prescribed-disturbance method is also well suited to and has been used for more general vortical flows, such as gusts with distributed vorticity (Ref. 10).

Many of the interesting practical applications, such as blade-vortex interactions of helicopter rotors (e.g., Fig. 1), and gust response of aircraft wings, are three-dimensional unsteady problems that will require enormous computational resources for transonic cases. Therefore, it is useful to study the numerical methods, as well as the general nature of the phenomena, in two dimensions, as indicated in the figure. It is also important to establish the minimum sufficient level of complexity in the governing equations. In the following sections, we review our transonic small-disturbance, Euler, and thin-layer Navier-Stokes analyses, especially the two-dimensional implementation of the prescribed-disturbance approach. Several representative examples are given that illustrate the advantages, capabilities, and limitations of these different formulations, in anticipation of their future extension to real, three-dimensional problems.

NUMERICAL FORMULATIONS

The essence of the prescribed-disturbance (Ref. 5) or perturbation (Ref. 6) method is simply that each of the dependent flow variables is split into a prescribed part, which defines (or is consistent with) the imposed vortical disturbance, and a remaining part, which is obtained from the solution of the governing equation set. Even though the governing equations may be nonlinear, in which case the independent solutions are not superposable, we may still decompose the dependent variables as follows:

$$q = q_v + (q - q_v) \qquad (1)$$

where

$$q = \begin{bmatrix} \rho \\ \rho u \\ \rho v \\ e \end{bmatrix}$$

and where q_v represents the specified vortical disturbance superimposed on a uniform free stream.

The following subsections summarize the development of the governing equations for $(q - q_v)$, and present the methods for solving them numerically. Although the overall concept is essentially the same for the Euler or Navier-Stokes formulations as it is for the transonic small-disturbance (potential) formulation, the actual derivations and solution techniques are rather different; therefore, they are treated separately. The complete details of each are given in Refs. 8 and 9 for the former, and in Refs. 7 and 10 for the latter.

Euler and Thin-Layer Navier-Stokes Equations

In this part of the investigation, we use the unsteady, two-dimensional equations in strong conservation-law form (Ref. 11), including the Baldwin-Lomax (Ref. 12) algebraic eddy-viscosity model for thin-layer turbulent flows. In generalized coordinates (ξ,η,τ) and in the perturbation form of Buning and Steger (Ref. 6), the equations are

$$\partial_\tau(\hat{q} - \hat{q}_v) + \partial_\xi(\hat{E} - \hat{E}_v) + \partial_\eta(\hat{F} - \hat{F}_v) = Re \quad \partial_\eta \hat{S} \tag{2}$$

where the dependent flow-field vector is

$$\hat{q} = J^{-1}\begin{bmatrix} \rho \\ \rho u \\ \rho v \\ e \end{bmatrix}$$

and the flux vectors $\hat{E}$, $\hat{F}$, and $\hat{S}$ are given by

$$\hat{E} = J^{-1}\begin{bmatrix} \rho U \\ \rho u U + \xi_x p \\ \rho v U + \xi_y p \\ (e + p)U - \xi_t p \end{bmatrix}, \quad \hat{F} = J^{-1}\begin{bmatrix} \rho V \\ \rho u V + \eta_x p \\ \rho v V + \eta_y p \\ (e + p)V - \eta_t p \end{bmatrix} \tag{3}$$

$$\hat{S} = J^{-1}\begin{bmatrix} 0 \\ \mu(\eta_x^2 + \eta_y^2)u_\eta + (\mu/3)\eta_x(\eta_x u_\eta + \eta_y v_\eta) \\ \mu(\eta_x^2 + \eta_y^2)v_\eta + (\mu/3)\eta_y(\eta_x u_\eta + \eta_y v_\eta) \\ \kappa Pr^{-1}(\gamma - 1)^{-1}(\eta_x^2 + \eta_y^2)\partial_\eta a^2 \\ \quad + \mu(\eta_x^2 + \eta_y^2)(u^2 + v^2)_\eta/2 \\ \quad + (\mu/3)(\eta_x u + \eta_y v)(\eta_x u + \eta_y v_\eta) \end{bmatrix} \tag{4}$$

Here U and V are the contravariant velocities along the ξ- and η-directions, that is,

$$U = \xi_t + \xi_x u + \xi_y v \tag{5a}$$

$$V = \eta_t + \eta_x u + \eta_y v \tag{5b}$$

and J is the transformation Jacobian (Ref. 11).

In Eq., (2) $\hat{q}_v$ represents any prescribed nonuniformity superimposed on an otherwise uniform free stream. In the present investigation, a concentrated vortex is considered, either fixed in space or moving with the flow. The velocity field of the vortex is specified as

$$v(\theta) = \frac{2\pi\Gamma_v}{|\vec{r}|}\left(1 - e^{-r^2/a^2}\right) \tag{6}$$

where Γ_v is the dimensionless vortex strength, and $\vec{r}(x,t)$ is the instantaneous radial distance from the vortex center. That is, the vortex-induced field $\hat{q}_v$ is irrotational outside a viscous core of radius a. Thus the vector components ρ, (ρu), (ρv), and e are determined from the inviscid (Euler) components of Eq. (2), as discussed in Refs. 8 and 9.

The usual tangency and no-slip boundary conditions on the airfoil are applied at each instant to the total flow-field vector $\hat{q}$. Surface-conforming C-type grids are used, generated by an algebraic method (Ref. 13), with clustering near the leading and trailing edges and in the vicinity of the upper- and lower-surface shock waves. Typical grids for viscous calculations consist of 161 to 181 points in the surface, or ξ, direction, and 52 points in the normal, or η, direction, extending 6 to 10 chords in all directions. Forty-five grid points in the normal direction are generally used for the inviscid cases.

An implicit, spatially factored algorithm with Euler-implicit time-differencing (Ref. 11) is used to solve Eq. (2). The scheme is first-order accurate in time and second-order accurate in space. Second-order implicit smoothing and fourth-order explicit dissipation terms are added to improve the nonlinear stability. Even so, the nondimensional time-steps generally have to be restricted to values of the order of 0.005 during that portion of the interaction when the vortex is close to the airfoil. The CPU solution time on the Ames Cray X-MP computer is approximately 2 sec/time-step. The inviscid cases considered in this paper required 10-15 min each, and the viscous calculations about 25-30 min CPU time, after the initial, steady solution was obtained without the vortex.

The effectiveness of the present prescribed-disturbance scheme is illustrated in Fig. 2 for one of the examples that is discussed in more detail in the next section (Example Results: Unsteady Vortex Interactions). The figure shows the variation in lift on the airfoil as a strong, concentrated vortex passes beneath it, with and without the special treatment outlined above. The "nonperturbation" scheme essentially represents vortex-capturing; that is, the vortex structure is specified only as an initial condition, when the center of the vortex is 5 chords upstream of the leading edge. Subsequently, this initial disturbance convects through the computational domain, and the numerical dissipation associated with the finite grid-spacing progressively weakens the gradients and reduces the effective vortex strength substantially. This numerical error is grid-dependent; however, it is completely absent in the prescribed-disturbance solutions, which are essentially independent of the grid.

Transonic Small-Disturbance Potential Equation

In this case, the approximations are a thin airfoil in an inviscid, isentropic fluid, with either (1) a concentrated potential (irrotational) vortex, or (2) small, distributed vortical disturbances, superimposed on an otherwise uniform, nearly sonic free stream. As in the above formulation, these prescribed vortical disturbances are assumed to be unaltered by the interaction with the airfoil.

The combination of unsteady flow and rotational disturbances in the free stream requires some special attention if potential-flow concepts are to be retained. Under the previously mentioned isentropic, small-disturbance assumptions, however, the continuity and momentum equations can be combined to give (Ref. 10)

$$\frac{\partial Q}{\partial t} + 2u\,\frac{\partial u}{\partial t} + (a^2 - u^2)\,\frac{\partial u}{\partial x} + a^2\,\frac{\partial v}{\partial y} = 0 \tag{7}$$

where

$$Q = \int\left(\frac{\partial \vec{q}}{\partial t} - \vec{q} \times \nabla \times \vec{q}\right) \cdot d\vec{r} - f(t) \tag{8}$$

and where $d\vec{r}$ is an incremental position vector which is integrated over a suitable path from some upstream reference point, and the symbol $\vec{q}$ now represents the velocity field (u,v).

We now go a step beyond Eq. (1) and decompose this total velocity field into the following components: (1) the uniform free stream $\vec{U}_\infty$; (2) the prescribed disturbance field $\vec{q}_v$; and (3) an irrotational perturbation velocity field $\nabla\phi$ produced by the airfoil in the presence of the concentrated vortex or distributed gust. That is,

$$\vec{q} = \vec{U}_\infty + \vec{q}_v + \nabla\phi \tag{9}$$

Then, for example, for a distributed vortical (rotational) gust,

$$Q = \int\left(\frac{\partial \vec{q}_v}{\partial t} - \vec{q} \times \nabla \times \vec{q}_v\right) \cdot d\vec{r} + \frac{\partial \phi}{\partial t} \tag{10a}$$

whereas for an irrotational moving vortex,

$$Q = \frac{\partial \phi_v}{\partial t} + \frac{\partial \phi}{\partial t} \tag{10b}$$

where $\phi_v = 2\pi\Gamma \tan^{-1}[(y - y_1)/(x - x_1)]$, and (x_1, y_1) is the instantaneous position of the center of the concentrated vortex.

It should be emphasized again that the decomposition of the velocity in Eqs. (1) or (9) does not imply linearity. Both the boundary conditions and the governing equation for the airfoil disturbance potential, $\nabla\phi$, are altered by the introduction of $\vec{q}_v$, and independent solutions are not superposable for transonic flows.

The governing equation for ϕ is obtained by substituting first the quantity $\vec{q}_o = \vec{U}_\infty + \vec{q}_v$, and then $\vec{q}$ given by Eq. (9), into Eq. (7). Next, the former resulting equation is subtracted from the latter. Then the quantity

$$\int\left(\frac{\partial\vec{q}_v}{\partial t} - \vec{q}_o \times \nabla \times \vec{q}_v\right) \cdot d\vec{r} \tag{11}$$

which is common to both, drops out. Even if $\nabla \times \vec{q}_v \neq 0$, the quantity $(\nabla\phi \times \nabla \times \vec{q}_v) \cdot d\vec{r}$ vanishes if $d\vec{r}$ is aligned with $\nabla\phi$. Finally, the local speed of sound, a, is evaluated using the isentropic relations, and the usual transonic small-disturbance scaling laws and approximations (Refs. 14,15); this evaluation of the speed of sound assumes that the prescribed disturbances considered in this paper produce only second-order variations in density, pressure, and temperature. This gives the following modified form of the unsteady transonic small-disturbance equation (in strong conservation form)

$$M_\infty^2\phi_{tt} + 2M_\infty^2\phi_{xt} = \frac{\partial}{\partial x}\left[(\beta^2 + C_2\phi_x)(\phi_x + u_v) - \beta^2 u_v\right] + \phi_{yy} \tag{12}$$

where

$$\beta^2 = 1 - M_\infty^2$$

$$C_2 = -\frac{1}{2}(\gamma + 1)M_\infty^2$$

Linear theory can be simulated by setting $C_2 = 0$.

The boundary condition on the airfoil is obtained by simply substituting Eq. (9) into the small-disturbance approximation to flow tangency, giving

$$\left(\frac{\partial\phi}{\partial y}\right)_b = \left(\frac{\partial}{\partial t} + U_\infty\frac{\partial}{\partial x}\right)Y_b - v_v \tag{13}$$

As noted above, neither small-amplitude gusts nor moving concentrated potential vortices produce first-order pressure fluctuations in the free stream. Therefore, consistent with our basic assumption that the prescribed vortical disturbance remains undistorted as it passes by the airfoil, we retain the usual form for the small-disturbance pressure coefficient,

$$C_p = -2(\phi_x + \phi_t) \tag{14}$$

Equation (12) is solved using the alternating-direction-implicit numerical algorithm of the well-exercised transonic code LTRAN2 (Ref. 15), with all of the high-frequency terms included (Ref. 7) and with provisions added for variable time-steps. A rectangular Cartesian grid (113 × 97 or 186 × 97) is used, with clustering near the leading and trailing edges. The CPU solution times on the Ames Cray X-MP computer range from approximately 1 to 4 min.

EXAMPLE RESULTS: UNSTEADY VORTEX INTERACTIONS

For the sake of brevity, we consider only concentrated vortices convecting with the flow past symmetrical airfoils at zero angle of attack. Therefore, all the differences between the flow fields above and below the airfoils are due solely to the vortex interaction. Examples of vortices fixed in space and of airfoils at incidence are given in Refs. 7-9.

The small-disturbance results in Fig. 3 illustrate many of the essential features of transonic airfoil-vortex interactions. For this case of a vortex with clockwise circulation passing beneath the airfoil, the vortex-induced "downwash" effect first appears as an effective negative angle of attack (Figs. 3a and 3d). Unlike the linear results, however, the transonic effects are much larger on the lower surface than they are on the upper surface. Also, the actual shape of the pressure distributions, the shock-wave strengths and positions, and the time-history of the airfoil pressures are quite different, even qualitatively, from the results for airfoil oscillations, or from the results for the sinusoidal gusts considered in the next section (Examples of Airfoil-Gust Interactions).

As the vortex passes beneath the airfoil (Figs. 3b and 3e), the u-component of the vortex-induced velocity field also becomes important in the nonlinear case. After the vortex passes behind the trailing edge (Figs. 3c and 3f), its induced field becomes an effective "upwash" distribution of vertical velocity,

and its horizontal component becomes relatively unimportant again. Throughout the interaction, nonlinear unsteady lag effects are very important, and the return of the flow around the airfoil to its orginal state is extremely slow. The moving-vortex interaction is substantially different from the quasi-steady response that would be obtained by freezing the vortex at different x-positions.

Figures 2 and 4 compare the transonic small-disturbance, Euler, and thin-layer Navier-Stokes results for the NACA 64A006 airfoil at $M_\infty = 0.85$, with the same vortex strength and initial position as before. This airfoil, which has been used in numerous numerical and experimental studies, is not only thinner than the NACA 0012 section, but has a significantly smaller leading-edge radius as well. Therefore, it might be expected to be more sensitive to the vortex-induced downwash than the NACA 0012 profile.

The shock wave in this case is smeared somewhat by the predicted viscous-inviscid interaction, according to the Navier-Stokes calculations. However, no boundary-layer separation is induced. Otherwise, the predictions of all three methods are similar, and the sequence of events is essentially the same as those discussed in connection with Fig. 3. However, larger fluctuations appear in the pressure distributions near the leading edge.

Figure 5 shows the variation with time and space of the pressures on and near the same NACA 64A006 airfoil, but at a slightly lower Mach number. In this case, the flow is subcritical before the vortex approaches the airfoil. The shock wave that forms on the lower surface of the airfoil as a result of the vortex encounter appears to move forward and pass off the leading edge into the oncoming flow, after the vortex convects past the trailing edge. This phenomenon is reminiscent of the "type C" shock-wave motion described by Tijdeman (Ref. 16) on an airfoil with an oscillating flap.

The pressure fluctuations shown in the lower half of Fig. 5 are monitored on a ray extending forward and downward from the leading edge at a 45° angle. These wave-like pressure distrubances suggest that an intense acoustic pulse is radiating to the far-field of the airfoil as a result of the interaction. This phenomenon should be investigated further.

Instabilities usually develop in the small-disturbance calculations when cases with significantly stronger vortex interaction are attempted. The Euler and Navier-Stokes calculations require a reduction in the nondimensional time-step and require special attention to the dissipation and smoothing of parameters. However, solutions have been obtained (Refs. 8.9) for values of Γ_v up to twice the values given in Figs. 2-5.

EXAMPLES OF AIRFOIL-GUST INTERACTIONS

A number of calculations have been performed with the small-disturbance code for transonic flows with sinusoidal and sharp-edged gusts, in which the distributions of vorticity are small in amplitude, but which are not necessarily irrotational (Ref. 10). These correspond to examples that have previously appeared in the literature for incompressible or subsonic flows.

Sinusoidal Transverse Gusts

The first case to be considered is the transonic counterpart of the well-known sinusoidal traveling-wave gust with a transverse velocity,

$$v_G = A_1 \sin(\omega t - \omega \tilde{x}) \tag{15}$$

where $\tilde{x}/c = 2x/c - 1$ is measured from the midchord of the airfoil, and where c is the chord. This case is particularly straightforward within the framework of the transonic small-disturbance approximation, since the gust velocity does not appear explicitly in the governing equation. The effect of the gust is felt through the boundary condition on the airfoil as an effective time- and space-dependent angle of attack (Eq. (13)).

A sketch of this problem and typical results for this type of gust are shown in Fig. 6; the figure shows computations for both the nonlinear and linear mode of Eq. (12) at various "phases" during the passage of the gust. This figure may be compared with Fig. 3, for which the airfoil, Mach number, and mean angle of attack are the same. Here the nondimensional frequency parameter, $K = \omega c/U_\infty$, is inversely proportional to the wavelength λ of the gust; $\lambda = 2\pi U_\infty/\omega = 4\pi c$ in this particular case. The amplitude of the gust corresponds to an effective fluctuating angle of attack of ±1°.

The main distinction of the linear and nonlinear solutions in Fig. 6 is the presence of a shock wave and its unsteady motion as the gust passes by the airfoil. The role of moving shock waves is even more dramatic in some of the examples given in Ref. 10, which include a comparison of the conventional NACA 0012 airfoil and a modern supercritical profile, the Dornier CAST-7.

A Strategy for Gust Alleviation

A number of calculations have also been performed (Ref. 10) to examine the possibility of canceling gust-induced unsteady air loads by the appropriate motion of a simple, trailing-edge flap, using the combined capability of the original LTRAN2 code and the present modifications for calculating the gust response. The basic strategy is outlined in Fig. 7. Starting with a specified gust waveform, we perform

the first iteration as if the problem were linear and superposition were valid. Then a second iteration is performed as necessary. The procedure is described in detail in Ref. 10.

Figure 8 shows the harmonic components of the resultant pressure distributions for the example given previously in Fig. 6, after the first and second iterations of the gust iteration strategy. In this case, the magnitude of the unsteady lift coefficient is reduced by about a factor of 4, from 0.08' to 0.019, after one iteration, although the pitching moment actually increases. The second iteration reduced C_L to 0.0022, and the higher-harmonic content becomes negligible.

The reduction in the magnitude of the unsteady lift by this strategy is shown in Fig. 9 for a range of gust frequencies, or wavelengths. In this figure, C_{L_G} is the basic gust response without the flap, and C_L is the net response with the flap deflected according to the strategy outlined in Fig. 7. The results show that one iteration reduces the lift response by an order of magnitude or more at low and high gust frequencies, but the mid-frequency range requires two iterations.

Figure 8 also shows that even though the lift was essentially canceled, the unsteady pressure fluctuations remained large. Furthermore, this behavior was observed over the entire range of gust frequencies shown in Fig. 9. In fact, these fluctuating pressures produced significantly larger pitching moments with flap oscillation than without, for $K > 0.1$. Conversely, attempts to reduce the pitching moment by the same strategy generally produced larger fluctuating lift. The basic difficulty is that the gust-induced loading tends to be centered close to the quarter chord, whereas trailing-edge flap deflections produce an aft loading. These differences are clearly evident in the figures, and they tend to be even more acute in transonic flow than in purely subsonic flow. This phenomenon amounts to a fundamental difficulty for active control systems that rely solely on trailing-edge flaps, since it appears to be impossible to suppress both C_L and C_M with such a flap.

SUMMARY AND CONCLUSIONS

The prescribed-disturbance method has proven to be a simple and efficient means of introducing vortical disturbances into numerical codes for transonic flow analyses, including inviscid, transonic small-disturbance; Euler; and thin-layer Navier-Stokes formulations. The technique has permitted the interaction of strong concentrated vortices, small-amplitude distributed gusts, and sharp-edged gusts with stationary lifting surfaces to be simulated in two-dimensional transonic flow. The results of the different codes are in excellent qualitative agreement. However, as might be expected, the transonic small-disturbance calculations can be deficient and misleading in the important region near the leading edge, unless special precautions are taken. Also, the small-disturbance code is less robust in coping with very strong vortices and with vortex paths that pass extremely close to the airfoil.

Several important features of the interaction of a concentrated vortex with an airfoil have been established. Detailed examinations of results show that the effect of the vortex is felt primarily through the vertical velocity that it induces, which to first order appears as a time-dependent perturbation in the effective angle of attack, and to a lesser extent through its horizontal induced velocity. Also, unsteady lag effects appear to be very important, especially in the transonic case. Calculations show great differences between quasi-steady and unsteady solutions and between the results for the vortex locations upstream and downstream of the airfoil. Finally, other strong nonlinear effects have been noted at transonic speeds. Even the qualitative pressure variations with respect to time and space differ markedly from the predictions of linear theory, and the vortex distorts the flow on the nearest surface of the body much more than it distorts the flow on the opposite surface.

A vortex with an assumed, invariant structure has been considered thus far. In reality, close encounters with a body alter the vortex core significantly, as shown by Meier and Timm in Paper No. 16 of this Symposium, and may lead to vortex bursting. This aspect of the problem needs to be examined further. For most practical applications, including helicopter rotors, future studies need to be extended to include three dimensions, where it will be even more essential to minimize the level of complexity in the governing equations without sacrificing accuracy.

The transonic small-disturbance formulation has been extended to include distributed vortical disturbances superimposed on a uniform free stream, under the assumption that the prescribed disturbance remains undistorted as it convects past a thin airfoil. A number of unsteady airfoil-gust interactions have been calculated within this framework, and sample results illustrate the essential effects of periodic gusts on the transonic flow around an airfoil. As in the concentrated-vortex interactions, the strength and unsteady motion of the shock wave were found to play major roles in the air loads on the airfoil.

Combined gust response and oscillating control surfaces have also been examined, with the aim of reducing the gust-induced air loads by activating a trailing-edge flap. A simple but effective strategy was developed for suppressing either the gust-induced lift or pitching moment by oscillating the flap with the proper phase and amplitude. However, the chordwise pressure distributions associated with gusts are very different from those produced by trailing-edge flap oscillations. Consequently, this simple device cannot cancel both the fluctuating lift and pitching moments.

REFERENCES

1. Rizzi, A.; Eriksson, L.-E.; Schmidt, W.; and Hitzel, S.: Numerical Solutions of the Euler Equations Simulating Vortex Flows around Wings. Paper No. 21, Aerodynamics of Vortical Type Flows in Three Dimensions, AGARD CP-342, June 1983.

2. Fujii, K.; and Kutler, P.: Numerical Simulation of the Viscous Flow over Three-Dimensional Complicated Geometries. AIAA Paper 84-1550, 1984.

3. Krause, E.; Shi, X.-G.; and Hartwich, P. M.: Computation of Leading Edge Vortices. AIAA Paper 83-1907-CP, 1983.

4. Srinivasan, G. R.; and Steger, J. L.: Computation of Wing-Vortex Interaction in Transonic Flow Using Implicit Finite Difference Algorithm. NASA CR-166251, 1981. (Also AIAA Paper 81-1206, 1981.)

5. Steinhoff, J.: The Treatment of Vortex Sheets in Compressible Potential Flow. AIAA Paper 83-1881-CP, 1983.

6. Buning, P. G.; and Steger, J. L.: Solution of the Two-Dimensional Euler Equations with Generalized Coordinate Transformation Using Flux Vector Splitting. AIAA Paper 82-0971, 1982.

7. McCroskey, W. J.; and Goorjian, P. M.: Interactions of Airfoils with Gusts and Concentrated Vortices in Unsteady Transonic Flow. AIAA Paper 83-1691, 1983.

8. Srinivasan, G. R.; McCroskey, W. J.; and Kutler, P.: Numerical Simulation of a Vortex with a Stationary Airfoil in Transonic Flow. AIAA Paper 84-0254, 1984.

9. Srinivasan, G. R.: Computations of Two-Dimensional Airfoil-Vortex Interactions. NASA CR-3885, 1985.

10. McCroskey, W. J.: The Effects of Gusts on the Fluctuating Airloads of Airfoils in Transonic Flow. J. Aircraft, vol. 22, no. 3, Mar. 1983, pp. 236-243.

11. Steger, J. L.: Implicit Finite-Difference Simulation of Flow about Arbitrary Two-Dimensional Geometries. AIAA J., vol. 16, no. 7, July 1978, pp. 679-686.

12. Baldwin, B. S.; and Lomax, H.: Thin Layer Approximation and Algebraic Model for Separated Turbulent Flows. AIAA Paper 78-257, 1978.

13. Pulliam, T. H.; Jesperson, D. C.; and Childs, R. E.: An Enhanced Version of an Implicit Code for the Euler Equations. AIAA Paper 83-0344, 1983.

14. Landahl, M. T.: Unsteady Transonic Flow. Pergaman Press, New York, 1961, pp. 1-5.

15. Ballhaus, W. F.; and Goorjian, P. M.: Implicit Finite-Difference Computations of Unsteady Transonic Flows about Airfoils. AIAA J., vol. 15, no. 12, Dec. 1977, pp. 1728-1735.

16. Tijdeman, H.; and Seebass, R.: Transonic Flow past Oscillating Airfoils. Annu. Rev. Fluid Mech., vol. 12, 1980, pp. 181-222.

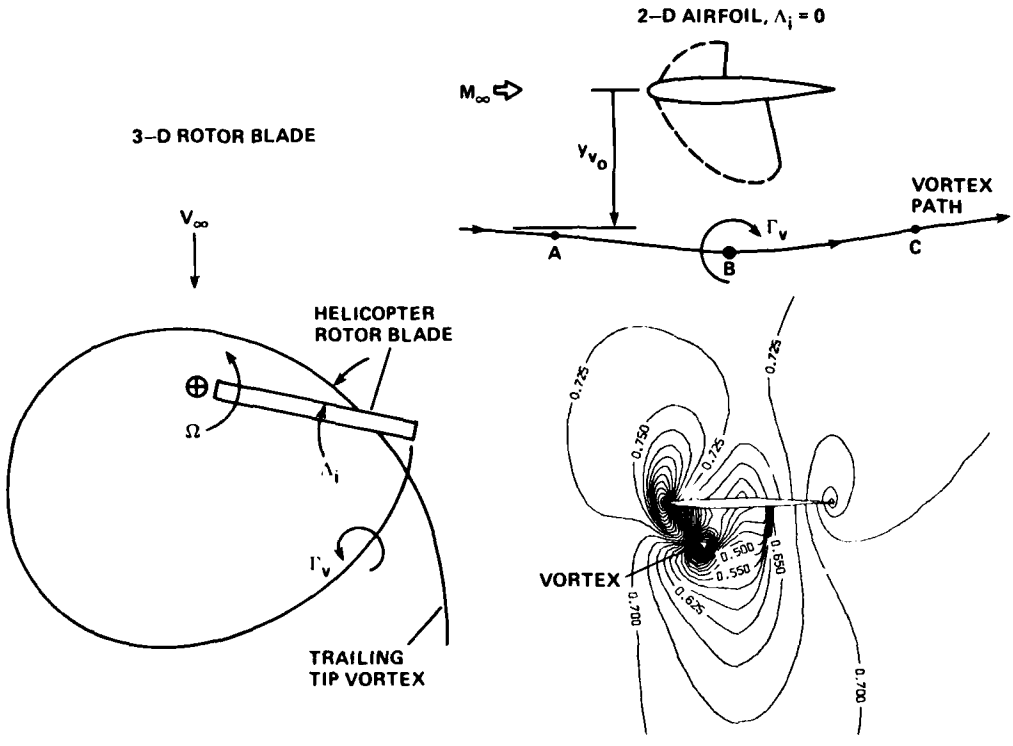

Fig. 1. Two- and three-dimensional unsteady vortex interactions.

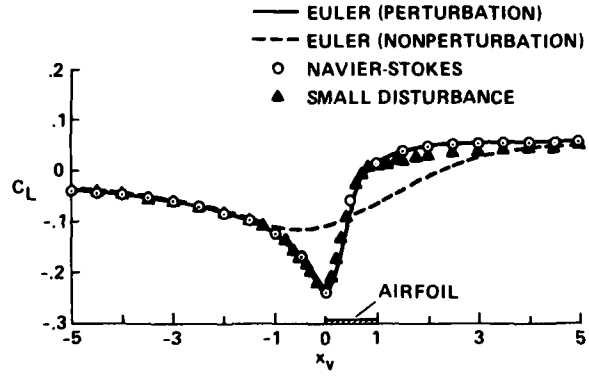

Fig. 2. Effectiveness of the prescribed-disturbance method: NACA 64A006 airfoil, $M_\infty = 0.85$, $\alpha = 0°$, $\Gamma = 0.2$, $y_v = -0.26$.

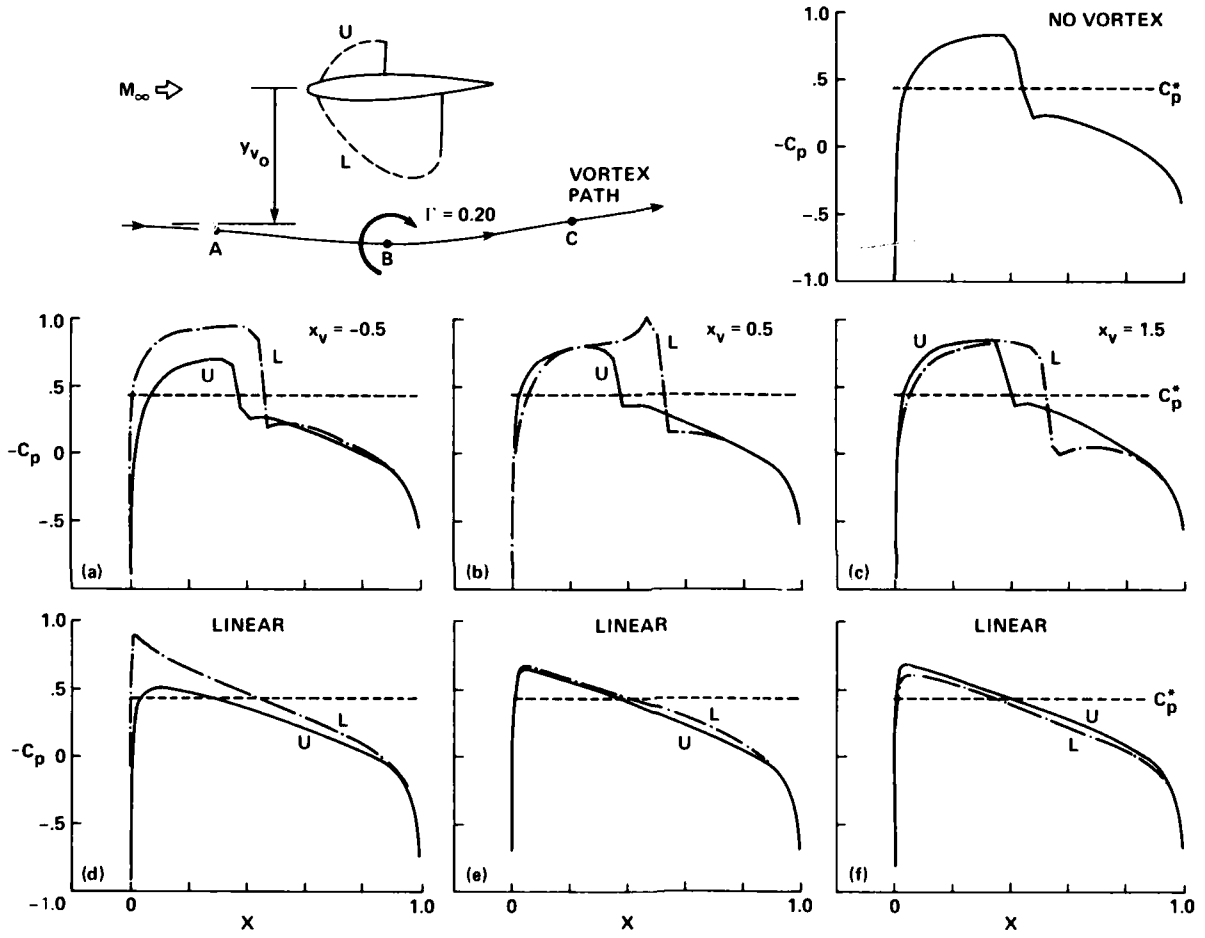

Fig. 3. Transonic airfoil-vortex interaction on the NACA 0012 airfoil at $M_\infty = 0.8$, $\alpha = 0$, $\Gamma_v = 0.20$, $y_{y_0} = -0.26$.

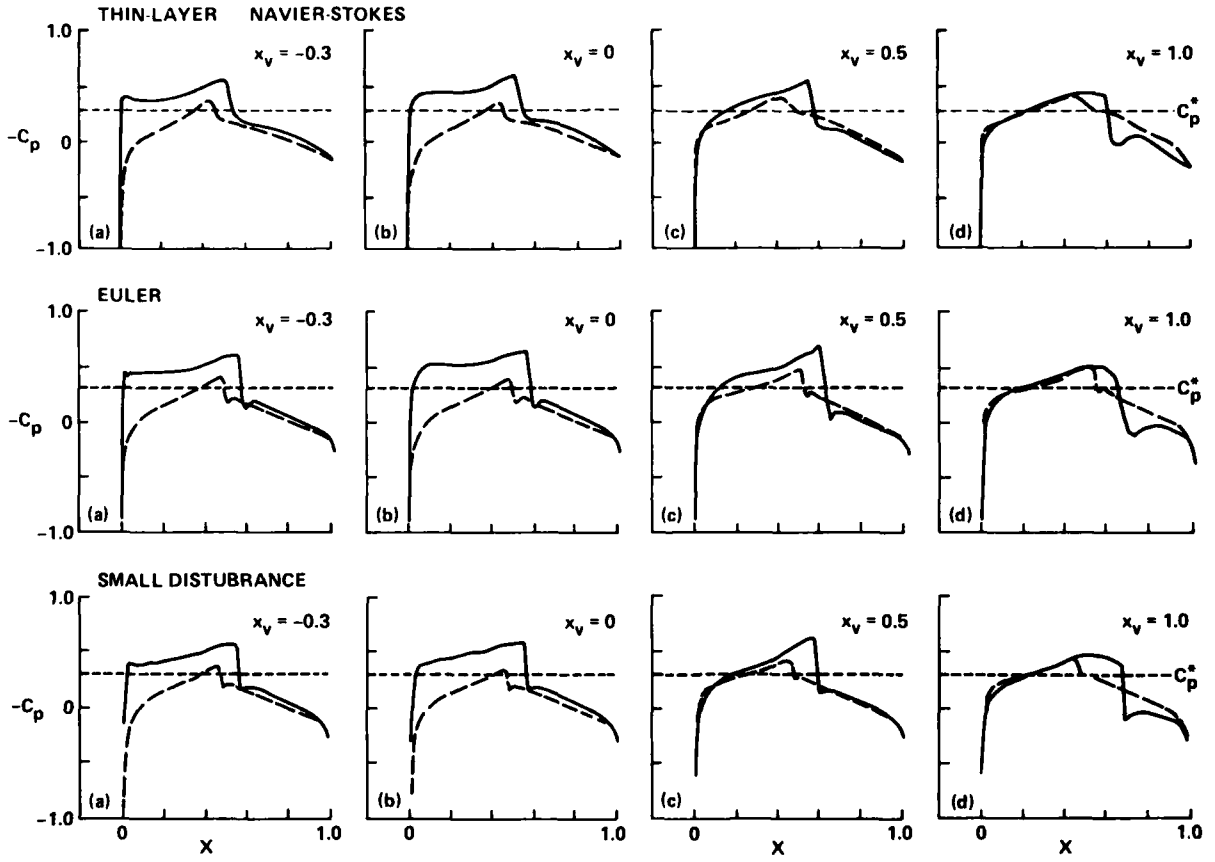

Fig. 4. Airfoil-vortex interaction on the NACA 64A006 airfoil: $M_\infty = 0.85$, $\alpha = 0$, $\Gamma_v = 0.20$, $y_v = -0.26$ = constant, $Re = 6 \times 10^6$.

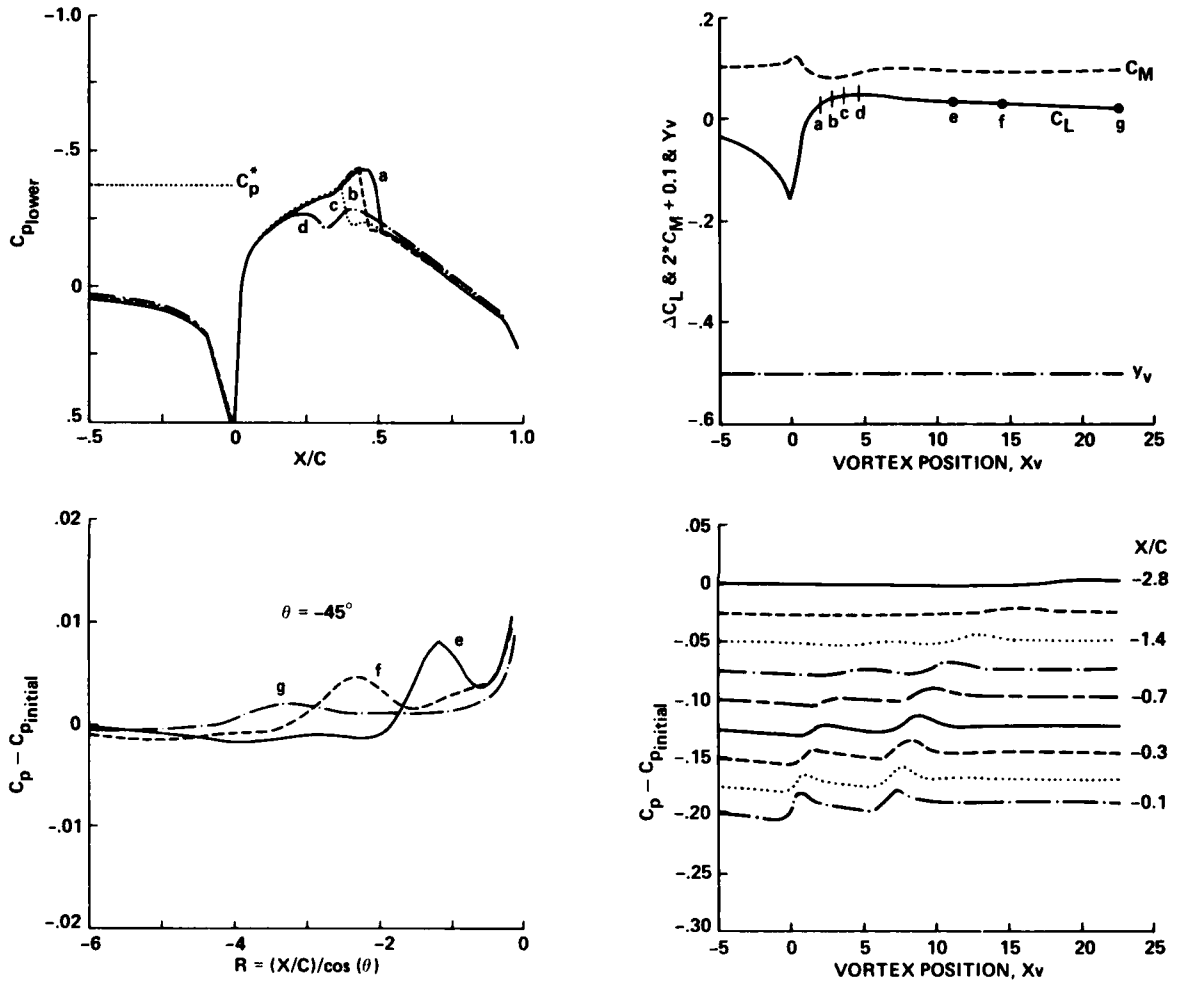

Fig. 5. Airfoil-vortex interaction at M = 0.822: α = 0, Γ = 0.2, y_v = -0.5.

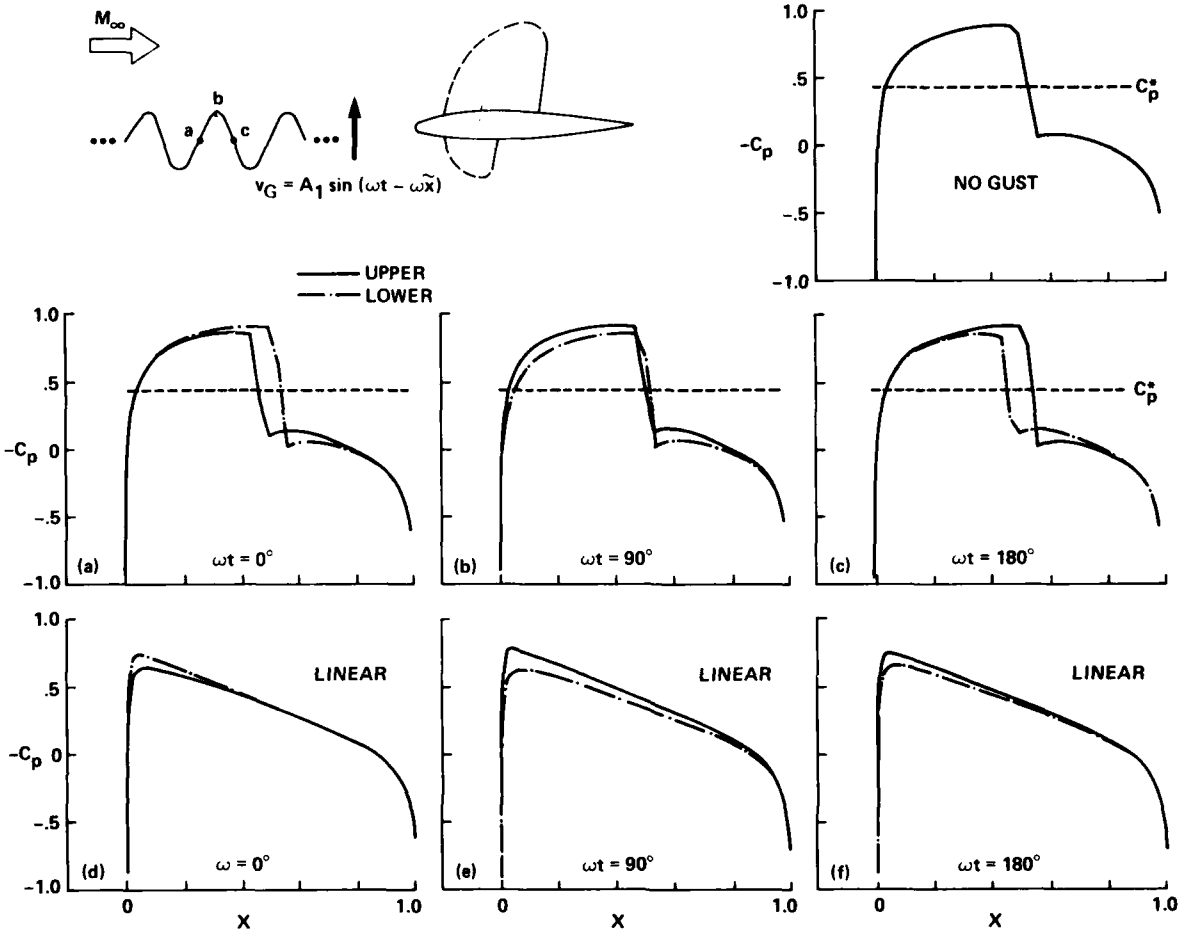

Fig. 6. Transonic airfoil-gust interaction on the NACA 0012 airfoil at $M_\infty = 0.8$, $\alpha = 0$; sinusoidal gust with $A_1 = 0.017$, $\omega c/U_\infty = 0.5$.

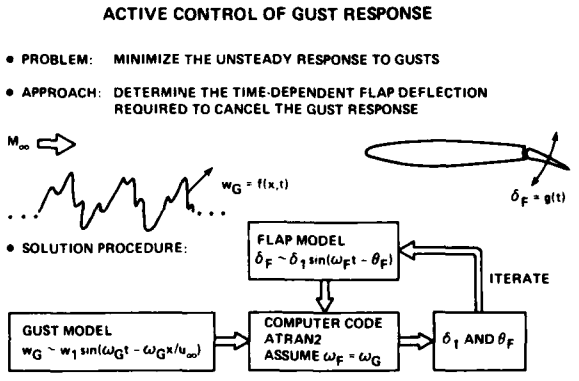

Fig. 7. Reduction of gust-induced air loads by a trailing-edge flap.

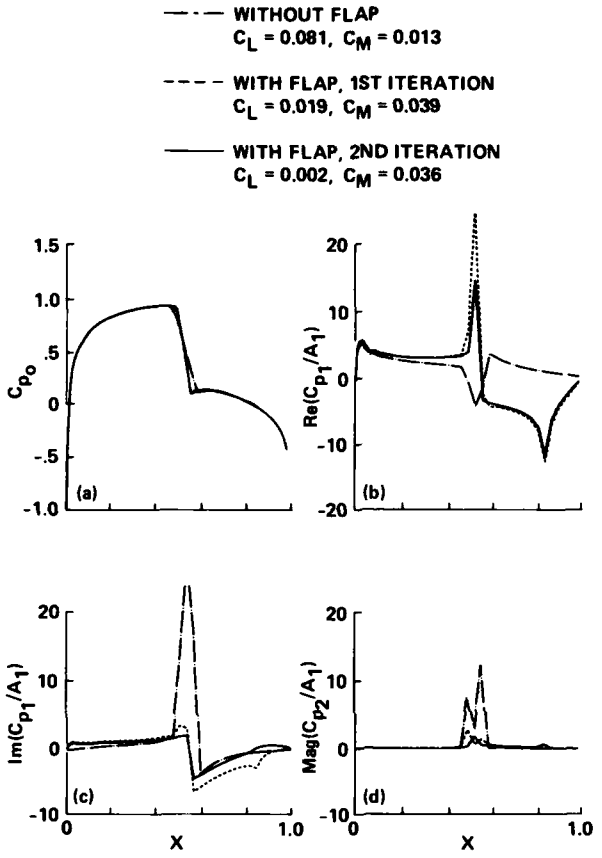

Fig. 8. Gust alleviation by a trailing-edge flap: NACA 0012 airfoil, M_∞ = 0.80, $K_G = \omega c/U_\infty$ = 0.5.

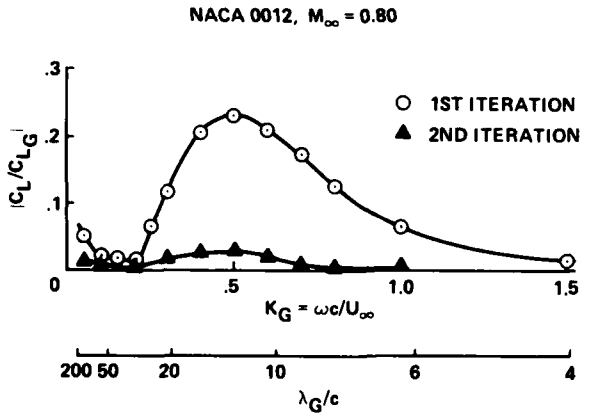

Fig. 9. Gust alleviation as a function of gust wavelength.

MODELLING OF THE VORTEX-AIRFOIL INTERACTION

Argyris G. Panaras
HAF Technology Research Center (KETA)
Palaion Faliron, Athens (77142), Greece

SUMMARY

A modelling of the vortex-airfoil interaction is presented in which the finite-area of the real vortices is taken in consideration. Two vortex models are used. In the first, a disturbed piece of vorticity layer is simulated by four rows of discrete vortices of small strength. In the second, a number of discrete vortices is arranged within a circle. The first model may simulate a shear layer or a wake, while the second, a well-formed vortex. The method has been applied to the calculation of the pressure induced on the surface of the airfoil by the interacting vortex. Both models give similar results. It has been found that for large distances of the vortex from the surface of the airfoil the consideration or not of the finite-area of the vortex is not a significant factor in determining the induced pressure field. However, when the distance of the vortex from the surface is reduced, its shape is distorted and the induced pressure pulses have lower amplitude than the ones induced by an equivalent point vortex. In the limit, where the vortex impinges on the leading edge of the airfoil, it is split into two and the time-dependent pressure coefficient takes even negative values at some time intervals.

1 INTRODUCTION

The interaction of vortices with airfoils is a phenomenon that appears in various applications, such as in the flow about a helicopter rotor, where the tip vortex may interact with the blade, and within the blades of turbomachines. Due to this interaction, aerodynamic noise is generated, while the unsteady flow and, consequently, the aerodynamic forces may be affected considerably, if the vortices pass very near the surface of the airfoils.

The forementioned effects have been demonstrated numerically by Srinivasan and Mc Croskey (1), very recently. In their calculations of the unsteady transonic flow field about an airfoil, by application of the thin-layer Navier-Stokes method, they have embedded a line vortex of given strength. The path of the vortex develops as part of the solution. The concept of the line vortex is also applied by Meier and Timm (2) for comparing the trajectories of laboratory vortices about a symmetrical airfoil, with potential flow calculations and for the estimation of the far-field noise. Other similar studies are reviewed by Meier and Timm.

However, the real vortices have a finite-area. Thus in any vortex-solid body interaction it is expected that during the convection of the vortex within the flow field of the body, its shape will be distorted and strained. The nearer the vortex passes by the surface of the body, the greater this distortion will be. In the limit, the vortex will be diffused within the boundary layer that envelops the body. Very clear evidence of this behaviour has been provided by Rockwell and Knisely (3) for the case of the unsteady cavity flow. A similar behaviour is expected in the vortex-airfoil interaction.

It seems very probable that the intensity of the dynamic effects caused by the presence of a vortex in the flow field of an airfoil, depends on the degree of distortion and straining of the vortex. In order to investigate this hypothesis, a mathematical model of the vortex-airfoil interaction is developed in the present paper, that includes the finite-area character of the real vortices.

The technique of comformal transformations is applied in the case of a family of Joukofski airfoils. A finite number of discrete vortices is used for the simulation of the size of the interacting vortical structure. The term discrete vortex is referred to a point vortex with a core radius necessary for avoiding the singular behaviour that occurs when two vortices come very close.

Concerning the initial distribution of the discrete vortices, there are various possibilities. The simplest evolutionary model is the classical one of Rosenhead (4), according to which, a vortex sheet is represented by a number of point vortices distributed evenly along a sine-wave. The time-dependent positions of the point vortices are estimated by application of the Biot-Savart law. Gradually, the sine-wave is transformed into a vortical structure. Much better results are obtained if a finite thickness is given to the initial vortex sheet, by specifying several rows of point vortices, each identical but with a small separation between the rows (Acton, ref. 5). In this paper, the gradual transformation of a piece of vortex sheet into a vortical structure will be studied, in the presence of an airfoil, while a uniform stream is superimposed.

The assumption of a vortex of circular cross-section, composed by a large number of point vortices, is an alternative model examined in this work. In this model it is assumed that the vortex has been formed far upstream of the airfoil. Then it starts to be convected within the flow field of the airfoil. This model is near to the experimental data by Meier and Timm (2) presented in this Sumposium. Two versions of this model will be used. In the first, the elements of the circular vortical structure have a mutual interaction. Thus, the time development of the structure is affected, both, from the airfoil field and from the internal interaction forces of the elements of the structure. In the second version, the internal interaction forces will be ignored. The vortical structure, in this case, is just a two-dimensional vortex of uniformly distributed vorticity. The changes in its shape are due only to the effect of the local flow field.

Evidently, the first version of the above model is nearer to the physical reality. However, it will be seen that the differences between the two models, in the resulting shape of the vortical structure and in the induced pressure field on the airfoil surface are rather small. Furthermore, the second version is more appropriate for embedding it in a calculation scheme similar to that of Srinivasan and Mc Croskey (1), from the point of view of the simplicity of the calculations.

In the applications of the present model, the vortex will start its trajectory from an initial point upstream of the airfoil. During its motion along the flow field of the airfoil, its shape will be computed periodically, so that an overall picture of its evolution will be given. Besides, the induced pressure pulses on certain points of the airfoil will be calculated. These pressure pulses are useful for giving an impression of the noise field generated by the vortex-airfoil interaction. In addition, they may be considered as a measure of the variation of the vortex strength, because of the distortion of their shape, by comparison to the corresponding pulses induced by a discrete vortex of strength equal to the initial one of the finite-area structure.

2 DESCRIPTION OF THE MODEL

According to the classical wing theory, a Joukofski airfoil may be obtained from the flow about a displaced circle by a single conformal transformation. Referring to figure 1, the following successive transformations transform the flow about the shown airfoil into the one about the line segment of the λ-plane :

$$z = h + \frac{l^2}{h} \qquad (1)$$

$$g = h - be^{i\varphi} \qquad (2)$$

$$\lambda = g + \frac{a^2}{g} \qquad (3)$$

If it is assumed that the vortical structure is composed of N discrete vortices, each of strength $\Gamma(\lambda_n)$, then the complex velocity potential at a point λ in the transformed plane is :

$$F(\lambda) = U_\infty \lambda + \frac{i}{2\pi} \sum_{n=1}^{N} \Gamma(\lambda_n) \ln(\lambda-\lambda_n) - \frac{i}{2\pi} \sum_{n=1}^{N} \Gamma(\lambda_n) \ln(\lambda-\bar{\lambda}_n) \qquad (4)$$

The velocity field induced on a point z in the airfoil plane is given by :

$$u(z) - iv(z) = \frac{dF}{d\lambda} \frac{1}{f'(\lambda)} = \left[1+\frac{i}{2\pi} \sum_{n=1}^{N} K(\lambda_n) \frac{1}{\lambda-\lambda_n} - \frac{i}{2\pi} \sum_{n=1}^{N} K(\lambda_n) \frac{1}{\lambda-\bar{\lambda}_n}\right] \frac{1}{f'(\lambda)} \qquad (5)$$

where the velocities have been non-dimensionalized on U_∞, the lengths on the radius a of the basic circle, $K = \Gamma/U_\infty b$, and the derivative $f'(\lambda)$ is estimated from equations 1, 2, 3 to be equal to :

$$f'(\lambda) = \frac{g^2(h^2-1^2)}{h^2(g^2-1)} \qquad (6)$$

The velocity components of equation 5 are used in this paper for estimating the pressure pulses induced on the surface of the airfoil by the interacting vortical structure. In order to isolate the effect of the elementary discrete vortices from the local pressure field generated by the parallel flow, the following appropriate pressure coefficient is used (Panaras, ref. 6) :

$$c_p = \frac{(p_\mu - p_\infty) - (p - p_\infty)}{p_\infty} = (u^2+v^2) - (u_\mu^2+v_\mu^2) \qquad (7)$$

where the velocity components u, v are estimated from equation 5 assuming that there are no vortices in the flow (K=0), while the components u_μ, v_μ include the vortex terms.

For calculating the velocity of the convected discrete vortices, Routh's rule has to be used, leading to the following equation for a vortex located at a point z_j :

$$u_j - iv_j = \left[1+\frac{i}{2\pi} \sum_{n=1}^{N} K(\lambda_n) \frac{1}{\lambda_j-\lambda_n} - \frac{i}{2\pi} \sum_{n=1}^{N} K(\lambda_n) \frac{1}{\lambda_j-\bar{\lambda}_n} \frac{1}{f'(\lambda_j)}\right] - \frac{iK(\lambda_j)}{4\pi} \frac{f''(\lambda_j)}{[f(\lambda_j)]^2} \qquad (8)$$

The ratio of the derivatives in the above equation is easily estimated. In a non-dimensional form we found that :

$$\frac{f''(\lambda_j)}{[f'(\lambda_j)]^2} = \frac{2h^4}{(h^2-1^2)^2} \left[\frac{1^2}{h^3} - \frac{(h^2-1^2)}{h^2 g(g^2-1)}\right] \qquad (9)$$

In order to have finite velocity at the trailing edge of the airfoil, the Kutta condition has to be fulfilled. For this, in the flow about the basic circle (g-plane) the following potential function has to be introduced :

$$F(g) = \frac{i\Gamma}{2\pi} \ln g \qquad (10)$$

The induced velocity in the airfoil plane is found to be :

$$u_{in}(z) - iv_{in}(z) = \frac{i\Gamma}{2\pi} \frac{h^2}{g(h^2-l^2)} \qquad (11)$$

The non-dimensional circulation is given by : $\Gamma = 4\pi\sin(\beta+\alpha)$, where, in the present, the angle of attack, α, is assumed to be zero. At each vortex, the induced velocity is added to the regular one, given by equ. (8).

3 APPLICATION OF THE METHOD

For the application of the method described in section 2, a family of Zoukofski airfoils will be used, that has a constant chord but variable zero-angle of attack lift. Referring to figure 1, the triangle (TOC) is defined if the radius α, the length l and the angle φ are known. If the length l is given, then the camber of the airfoil and, consequently, the zero-angle of attack lift coefficient depend on the value of the angle φ. For the simplicity of the computer program, in these preliminary results the angle of attack is not examined as a parameter. The airfoils used have the following characteristics :

Airfoil :	A	$l = 0.9\alpha$	$\varphi = 2$ rad	$C_L = 1.14$
	B	0.9α	2.5	0.45
	C	0.9α	3.14	0.00

A typical example of calculation is shown in figure 2. The vortex model consists of one perturbed central-row of clockwise discrete vortices and two external layers of passive tracers, i.e. vortices of zero strength. The tracers have been included for giving a better impression of the evolution of the vortical structure. Various stages of development of the vortex are shown in this figure. The disturbed vorticity layer gradually is transformed into a vortical structure that rotates in a clockwise direction. There is a strong similarity with the development of vortices from perturbed vortex sheets in a bountless still fluid (Acton, ref. 5). But the formed structure is not smooth. It will be seen in section 3.1 that better results are obtained if more rows of discrete vortices are used, and if the total vorticity is distributed uniformly in these vortices.

In figure 2 the numbered lines denote the corresponding value of the pressure coefficient (equ. 7) on the selected points 1, 2, 3 along the upper surface of the airfoil. Also in all the figures, the maximum value of the pressure coefficient, as well as the non-dimensional strength of the vortex are given. It is observed in fig. 2 that the pressure coefficient at each point of the airfoil is equal to zero when the vortex is far upstream or downstream of it. As the vortex approaches a point, the pressure coefficient starts to rise, reaching its maximum value when it is near the point, and then gradually decays. It is also evident in this figure that the pressure amplitude is higher on the forward part of the airfoil.

The value $k = 0.30$ has been assumed for the non-dimensional vortex strength, in most of the applications of this work. It has been found that with this value the pressure pulses induced on the surface of the airfoil, when the vortex is near it, have an amplitude of the same order of magnitude with the maximum suction generated by the free stream on the family of the airfoils that we use.

3.1 The effect of the interaction on the structure of a finite-area vortex.

In this section, the models of finite-area vortices mentioned in the introduction will be applied in some typical configurations. For comparison, similar results of calculation of the simpler model of a point vortex will be presented in each figure. The airfoil B will be used for these illustrations. The distance of an interacting vortex from

is more visible in the circular-vortex model, still the overall dimensions of the structure do not change considerably. In this case the reduction of the amplitude of the pressure pulse is not very impressive.

The extreme case of impingement of the vortex on the leading edge of the airfoil is shown in figure 5. In the case of the finite size models (fig. 5b, c), the vortex is split into two and some of its elements slip along the lower surface of the airfoil. It is evident in this figure that the convection velocity of the vortical elements on the upper surface of the airfoil is greater than on the lower surface. The effect of the two-dimensionality of the vortices on the induced pressure field is really significant in this case. This figure demonstrates how erroneous may be the results of calculations that are based on the point-vortex model, if the distance of the vortex from the surface of the airfoil is very small. The realistic models of fig. 5b, c give pressure pulses of amplitude less than one-fourth of the point vortex model. Even, intervals of negative pressure are observed.

In the cource of the study we tested a simplified version of the circular-section vortex model. In this version the mutual interaction forces of the elementary discrete vortices were ignored. Thus, in this case the changes of the shape of the vortical structure are due only to the effect of the airfoil flow-field and not to the internal forces of the vortex. Results of calculations similar to those of the regular circular-section vortex are shown in figure 6. The observed differences between these two versions are not significant. The distortion of the shape of the vortex and the intensity of the induced pressure pulses are very similar. Differences are observed only when the vortex impinges on the leading edge of the airfoil. Besides, the size of the simplified vortex is not increased. These results support the view that the simplified circular-section model may be used in sophisticated calculation schemes such as that of Srinivasan and Mc Croskey (1).

3.2 The effect of the camber of the airfoil

For examining the effect of the camber of the airfoil in the features of the interaction, calculations with the airfoils A and C were performed. The airfoil A is characterised for the high value of the camber, while airfoil C has a zero camber (symmetrical airfoil). Results of calculations of the interaction of the vorticity-layer model with these airfoils are shown in figure 7. In both cases the initial distance of the vortex from the airfoil is equal to $y = 0.3c$. It is observed in this figure that in both cases the gradual formation of the vortex is similar. However, the vertical elongation of the vortex near the trailing edge is much higher in the case of the airfoil A, which is characterised for the great value of the curvature, than in the case of the airfoil C.

Concerning the effect of the camber on the pressure pulses, it is seen that their amplitude is a little higher in the airfoil A. In addition, the maximum values in the symmetrical airfoil appear on the region of the leading edge, while in the highly cambered airfoil they are shifted to its center.

Calculations similar to the above, but involving the circular-section vortex model are shown in figure 8. Again, the curvature of the flow causes an elongation of the vortex near the trailing edge and slighty greater values of the amplitude of the pressure pulses.

4 DISCUSSION AND CONCLUSIONS

In the present paper the problem of the appropriate simulation of the vortex-airfoil interaction has been addressed. The classical assumption of a point vortex is a useful tool for giving physical insight in many fluid-dynamical phenomena. Still the fact that the real vortices have a finite-area cannot be ignored, especially when the trajectory of

the surface of the airfoil is one of the parameters that affect the distortion of the shape of the vortex and the intensity of the induced pressure pulses. For studying the effect of this distance on the vortex models that will be tested, three cases will be examined. In the first, this distance is large (y = 0.3c) so that the effect of the flow-field on the shape of the vortex is very small. In the second case, the distance is very small (y = 0.06c), so that the vortex is subjected to a severe straining. In the third case the vortex starts its convection from the level of the airfoil axis (y=0) and upon impinging on the leading edge is split into two.

In figure 3 the case of the large distance of the vortex from the surface of the airfoil is shown. In fig. 3a the small circles denote the trajectory of the point vortex. In fig. 3b the vortex layer model is examined. Four rows of discrete vortices are used for the simulation of the disributed vorticity-layer. For a better illustration of the development of the vortical structure, different symbols have been used for denoting the discrete vortices of the upper rows, than for the lower ones. All the discrete vortices have the same strength. The total strength of the vortical structure is equal to the standard value used in the present. Also the initial coordinates of the vorticity layer coinside with the initial position of the point vortex. Thus, a comparison of the induced pressure-fields is possible. The gradual development of the vortical structure is more clear in this figure than in fig. 2. The only difference between this case and that of the formation of a vortex within a bountless still fluid, is the observed small elongation of the vortex when it passes over the trailing edge of the airfoil. Most probably this elongation is due to the effect of the non-uniform airfoil field. More evidence will be provided later.

In figure 3c the circular cross-section model is applied. As we have already mentioned, in this model it is assumed that the vortex has been formed far upstream of the airfoil. Then it starts to be convected within the airfoil flow field. The circular vortex of fig. 3c consists of 33 discrete vortices of equal strength. The total strength of the vortex and the initial coordinates of the center of the circle are equal to the standard values of the previous figures. It is observed, in fig. 3c, that as the vortex is convected downstream, its size is enlarged, its shape gradually becomes elliptical and it rotates (observe the relative position of the upper discrete vortex with the marked center).

The pressure pulses induced on the surface of the airfoil by the above two-dimensional vortex models (fig. 3b, c) are quite similar to the ones induced by a discrete vortex (fig. 3a). Both, the maximum value and the shape of the pulses almost coincide. In view of this observation, it seems that for relatively large distances of the vortical structure from the surface of the airfoil, the effect of its finite area on the induced pressure field is not significant.

In figure 4 the distance of the vortex from the surface of the airfoil is smaller than previously. As expected, from a consideration of the Biot-Savart law, the amplitude of the pressure pulses is decreased, if compared with those of figure 3. However, the observed differences between the pressure pulses induced by the discrete vortex (fig. 4a) and by the two-dimensional vortex models (fig. 4b, c) are the most significant observation in this figure. It is not only the value of the maximum pressure coefficient that has been reduced considerably, it is also the shape of the pressure pulses that has changed, becoming more broad. Evidently, these differences are due to the effect of the two-dimensionality of the vortex and to its distortion as it approaches the surface of the airfoil.

Especially in the case of the vortex-layer model it seems that the differences are mostly due to the consideration of the finite area of the vortex. That, because the observed distortion of the vortex is not large. On the contrary, though the distortion

the vortex passes near the interacting surface. Clear evidence of this argument has been provided in the previous sections.

To this end, in section 3 two models of finite-area vortices have been examined. In the first, a piece of vorticity layer, that consists of a number of rows of discrete vortices of small strength, is subjected to an initial perturbation by giving it a sine-shape. Then it starts to be convected within the flow field of the airfoil. During its motion, gradually the layer is transformed into a vortical structure. The shape of the vortical structure is affected by the non-uniform flow field. The concentrated vorticity-layer model is appropriate for examining the interaction of airfoils with shear layers or wakes. In the case of the interaction with well-formed vortices, the second model that we have tested seems to be more appropriate. This model consists of a number of discrete vortices arranged in a circular formation. It has been found that during the convection of such a structure in the flow field of an airfoil, its size is enlarged and it is subjected, also, to a distortion caused by the non-uniform field.

To our knowledge, the only existing experimental data on the vortex-airfoil interaction are those of Meier and Timm (2) presented in this Symposium. These experiments were obtained by using a symmetrical airfoil and counterclockwise vortices. The conservation of the size and of the circular shape of the vortices is one remarkable feature of the experiments of Meier and Timm. Our model possesses this feature, if counterclockwise vortices are considered. This is very clear in figure 9, where such a vortex has been used. Besides, it is observed in this figure that the induced pressure pulses are negative. The comparison of our prediction with the experiments of Meier and Timm indicate that the circular-section model simulates efficiently the real vortices.

In addition to the examination of the development of the shape of a finite-area vortex, the pressure pulses induced on the surface of the airfoil by it, have been calculated. The results of these calculations provide the means for considering the intensity of the dynamic effects of the vortex on the boundary layer and on the structure of the airfoil, they may be used for the estimation of the noise emitted by the vortex-airfoil interaction, and they may be considered as an indication of the decrease of the actual strength of the vortex due to their distortion and their two-dimensionality.

The results of section 3.1 indicate emphatically the necessity of considering the two-dimensional character of a vortex. More specifically, it has been found that as long as the vortex passes above the surface of the airfoil at a great distance, the assumption of the single point-vortex is a good approximation for estimating the induced pressure field. However, as this distance is decreased, a difference appears between the 2-D model and the point-vortex model. The nearer the vortex passes by the surface the greater this difference becomes. In the limit, where the vortex impinges on the airfoil and is split into two, the actual pressure coefficient is of the order of one - fourth of the corresponding in the point - vortex model.

In all the applications a standard value has been assumed for the strength of the interacting vortex ($k = 0.30$). Obviously, the amplitude of the induced pressure pulses depends on the value of the vortex strength. Furthermore, we have discovered that the temporal evolution of a vortical structure of given size depends also on the value of its strength. In order to illustrate these comments, in figure 10 the typical case of fig. 3b is shown but with a non-dimensional vortex strength equal to $k = 0.2$ and 0.4. It is seen that indeed the formation of the vortical structure is delayed in the case of the small strength, while it is accelerated in the case of the large strength. Also, the amplitude of the pressure pulses is greater in the latter case.

To conclude, we hope that the present analysis has provided strong evidence of the need to consider the finite-area of a vortical structure, when algorithms are developed for treating the vortex-airfoil interaction. We also hope that this work will stimulate

detailed experimental studies.

REFERENCES

1. Srinivasan, G.R., Mc Croskey, W.J. "Numerical simulation of the interaction of a vortex with stationary airfoil in transonic flow". AIAA paper 84-0254, 1985.

2. Meier, G.E.A., Timm, R. "Unsteady vortex airfoil interaction". AGARD Symposium, Unsteady aerodynamics-fundamentals and applications to aircraft dynamics, 6-9 May 1985, Göttingen.

3. Rockwell D., Knisely, G. "The organised nature of flow impingement upon a corner" J. Fluid Mech. 93, pp. 413-432, 1979.

4. Rosenhead, L. "The formation of vortices from a surface of discontinuity". Proc. Roy. Soc. A 134, pp. 170-192, 1932.

5. Acton, E. "The modelling of large eddies in a two-dimensional shear layer". J. Fluid Mech. 76, pp. 561-592, 1976.

6. Panaras, A.G. "Pressure pulses generated by the interaction of a discrete vortex with an edge". J. Fluid Mech., 154, pp. 445-461, 1985.

ACKNOWLEDGEMENT

The author would like to thank Dr W.J.McCroskey for encouraging this work and for his very constructive comments.

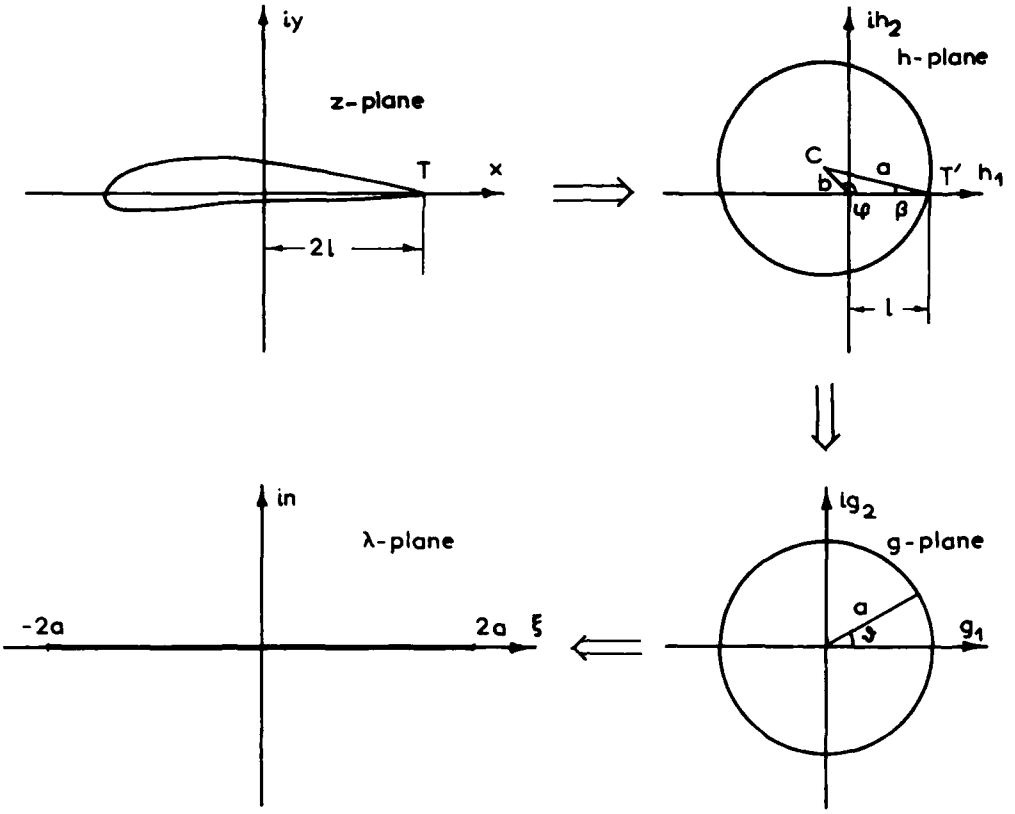

1. Transformation of an airfoil into a line.

VORTEX STRENGTH= 300003
CP-MAX= 4014089

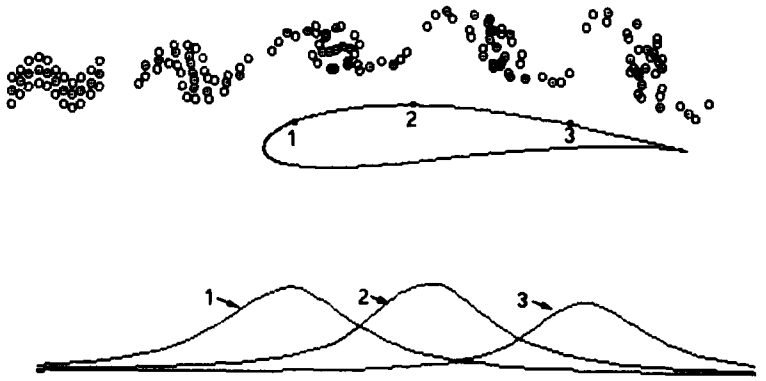

2. A typical example of calculation.

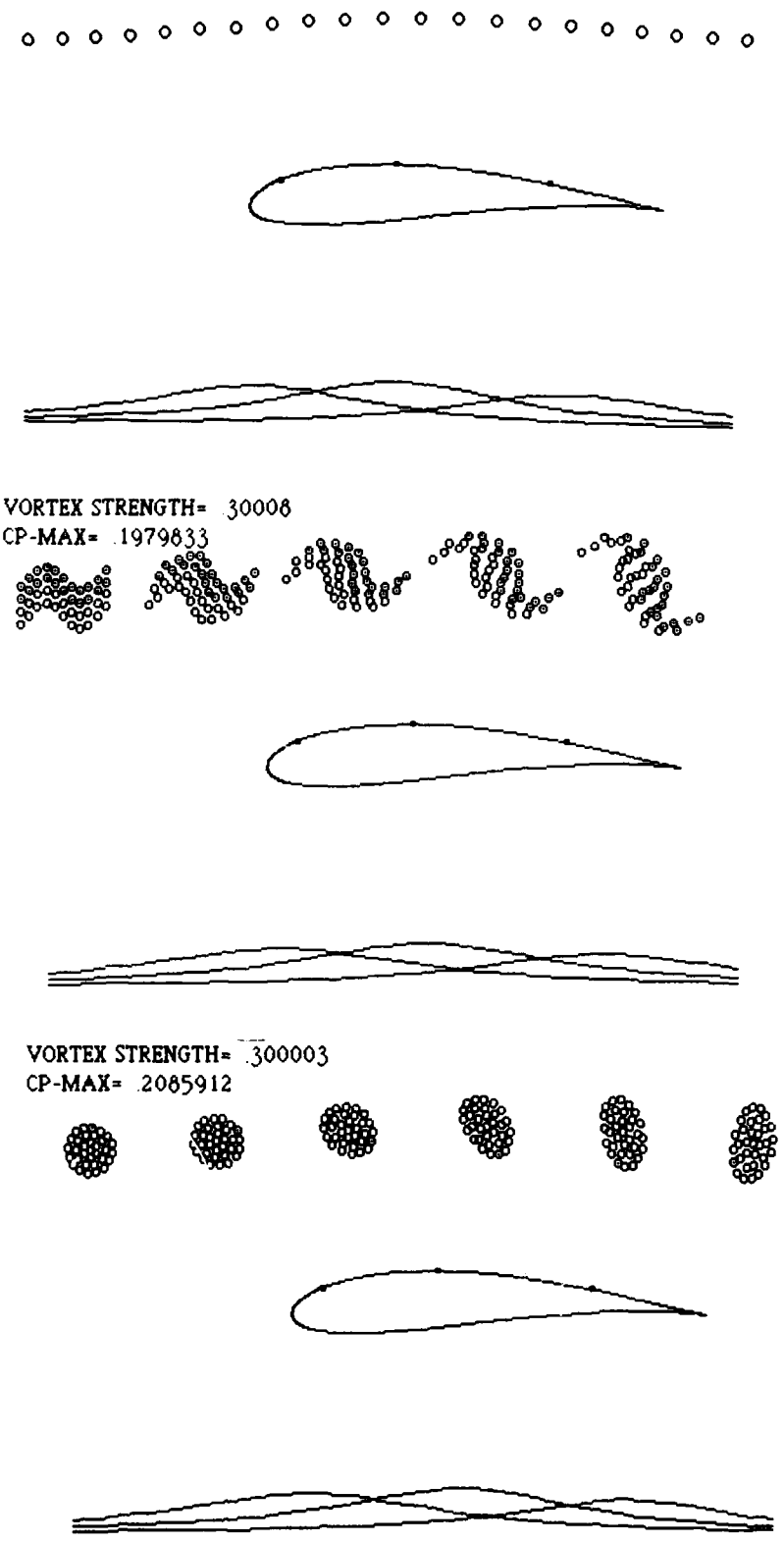

3. Comparison of the vortex models. Large distance from the airfoil.

VORTEX STRENGTH= .3
CP-MAX= 7285317

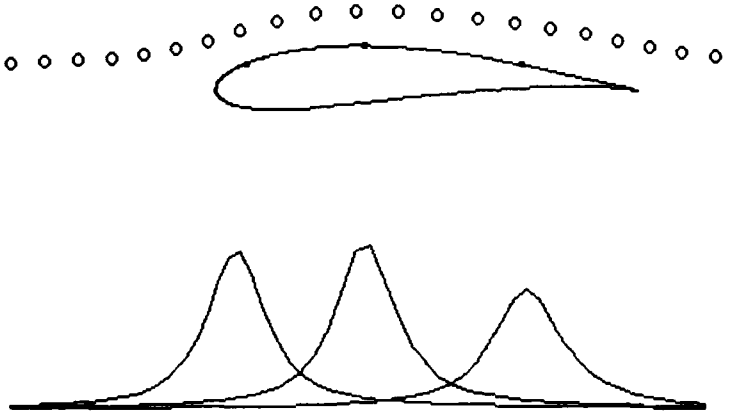

VORTEX STRENGTH= .30008
CP-MAX= 5163009

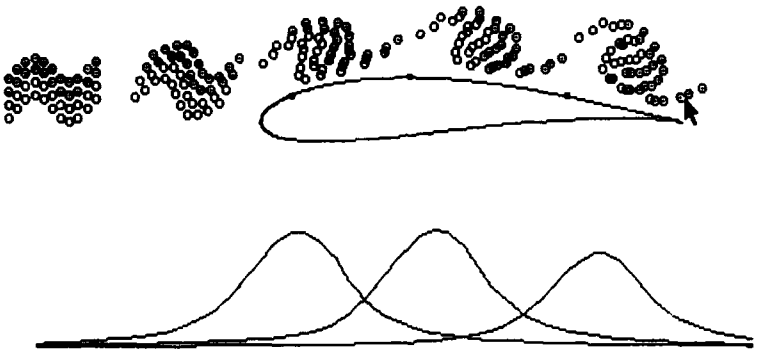

VORTEX STRENGTH= .300003
CP-MAX= 6333108

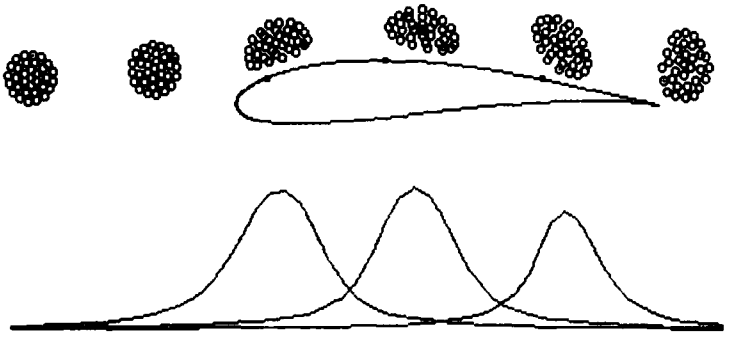

4. Comparison of the vortex models. Small distance from the airfoil.

VORTEX STRENGTH= .3
CP-MAX= 1.179163

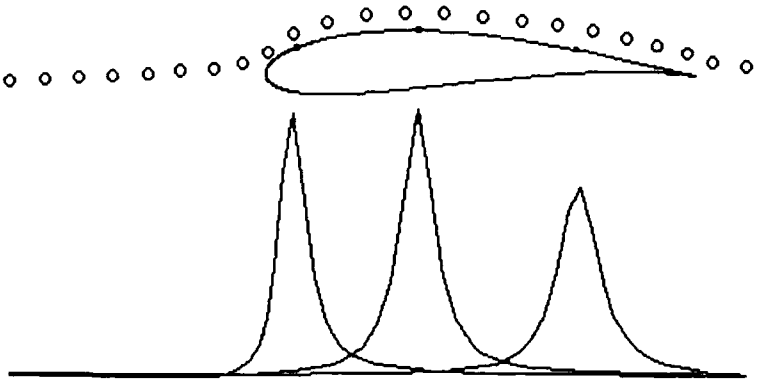

VORTEX STRENGTH= .30008
CP-MAX= .3620368

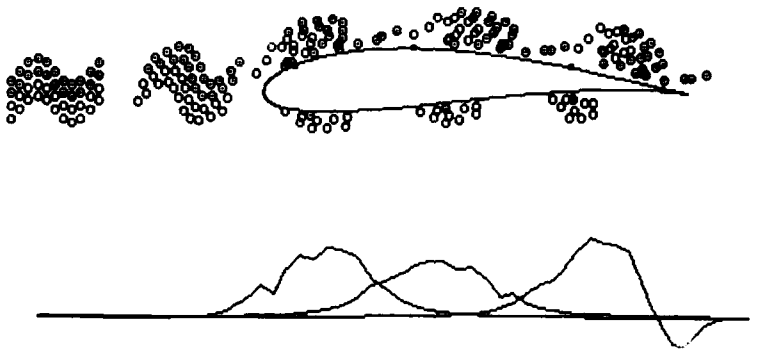

VORTEX STRENGTH= 300003
CP-MAX= 4396065

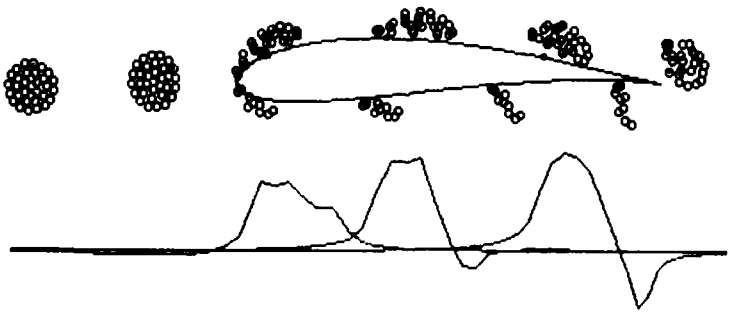

5. Comparison of the vortex models. Split of the vortex.

VORTEX STRENGTH= .300003
CP-MAX= .2075411

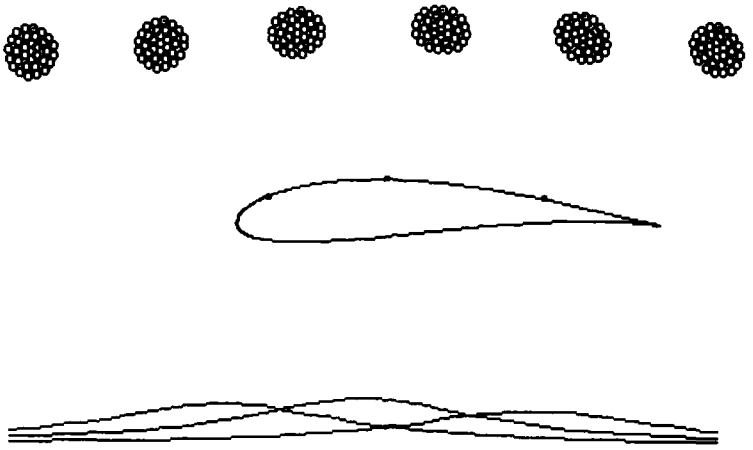

VORTEX STRENGTH= .300003
CP-MAX= 6686923

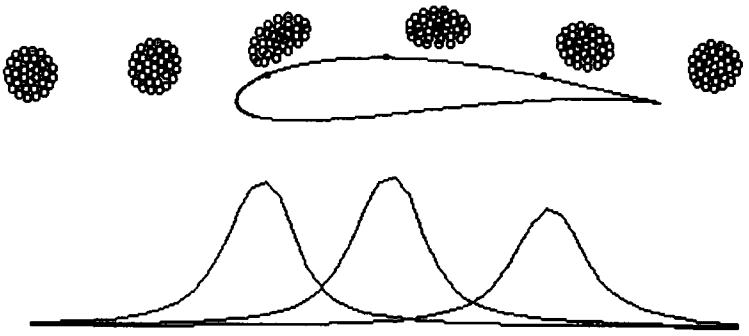

VORTEX STRENGTH= .300003
CP-MAX= .443449

6. Interaction with a simplified vortex model.

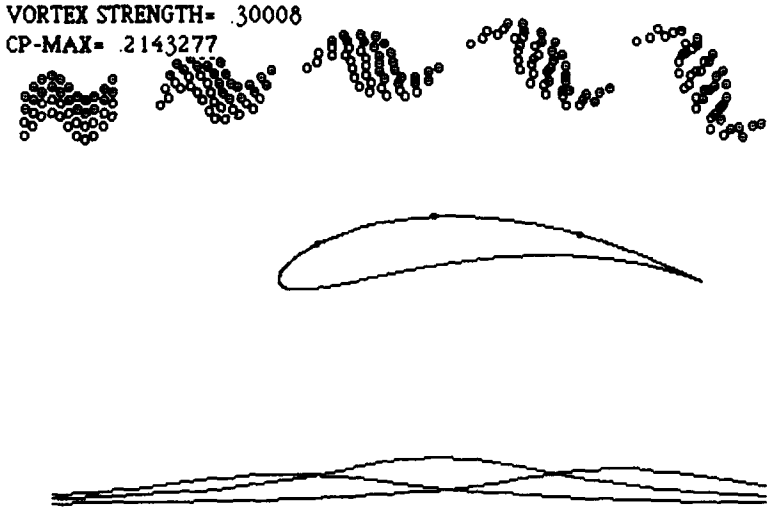

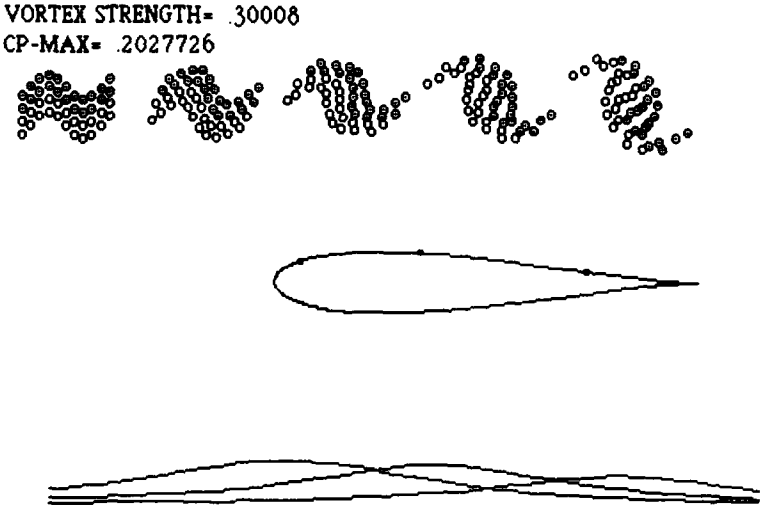

7.The effect of the camber of the airfoil. Distributed vorticity vortex-model.

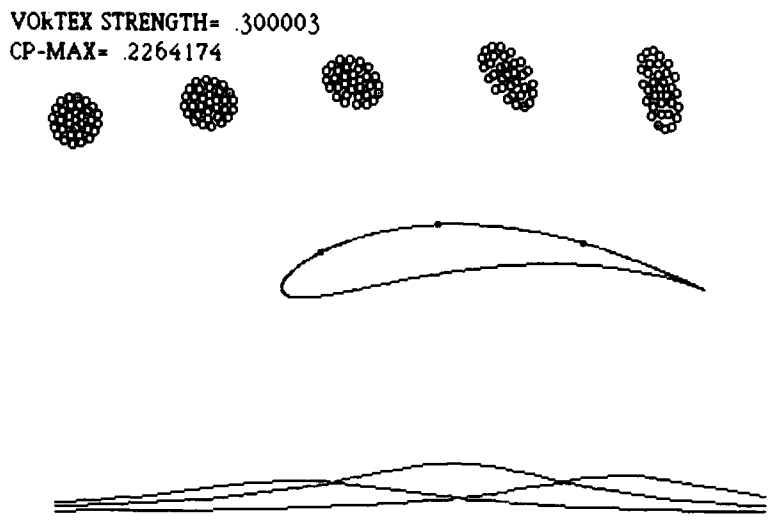

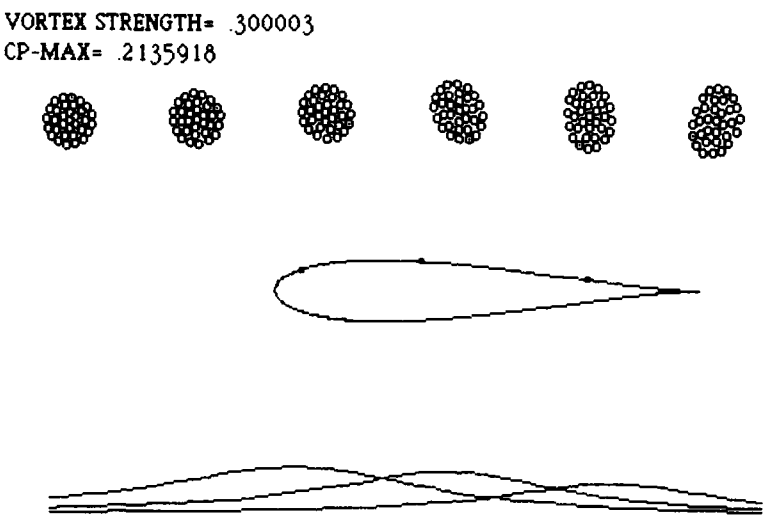

8. The effect of the camber of the airfoil. Circular-section vortex model.

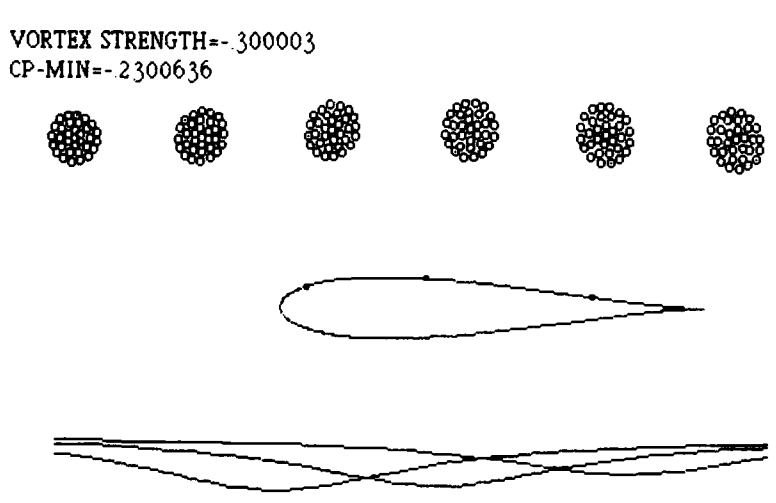

9. Interaction with a counterclockwise vortex.

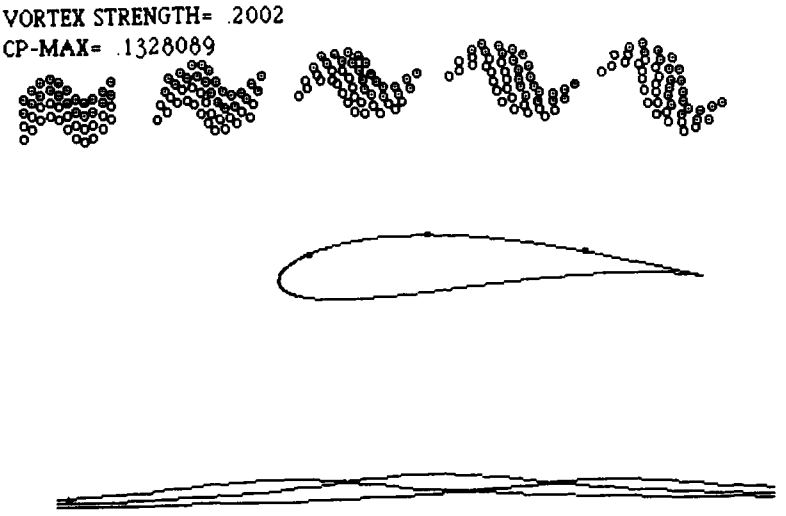

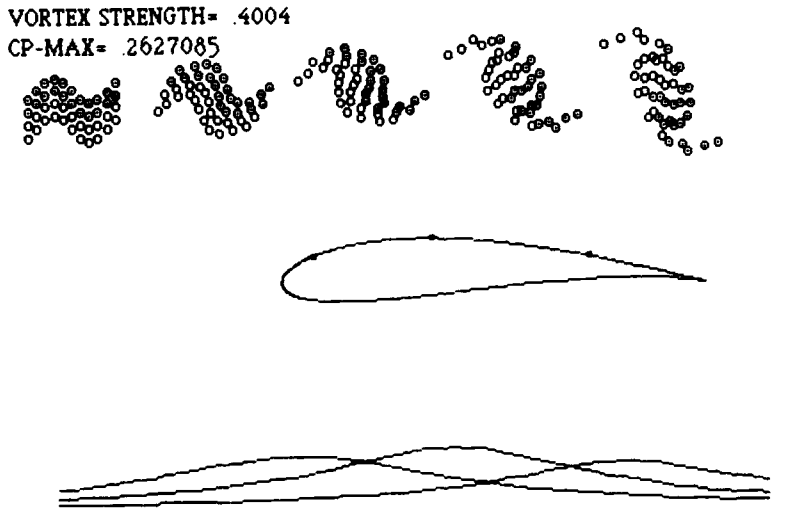

10. The effect of the vortex strength on the interaction.

IDENTIFICATION OF AIRCRAFT CHARACTERISTICS INCLUDING GUST INDUCED DYNAMIC EFFECTS

by

D. Rohlf
Institut für Flugmechanik
Deutsche Forschungs- und Versuchsanstalt
für Luft- und Raumfahrt e.V. (DFVLR)
D 3300 Braunschweig-Flughafen, West Germany

SUMMARY

For the investigation of unsteady aerodynamic effects at low Mach numbers, dynamic tests using controllable models of a light transport aircraft were performed in the Dynamic Simulation Facility in Wind-Tunnels at DFVLR-Braunschweig (Germany) and in the Free Flight Catapult Facility of IMF-Lille (France). These model test techniques have the advantage of laboratory conditions with the possibility of generating reproducible gusts. The achieved flight test data were analyzed in detail applying methods of System Identification. This included the determination of the discrete gust disturbance from onboard measured signals.

The paper presents the special approach using the measured angle of attack and additional calculated dynamic terms which become essential in the presence of fast flow changes due to short-wave gusts or high-frequency control deflections. Measured time histories of model flight tests with excitation by control inputs and gusts are presented and compared with identification results obtained from multi-run evaluation.

1. INTRODUCTION

The increasing demand for Active Control Technology (ACT) to improve aircraft performance and flight characteristics calls for a detailed understanding and mathematical modelling of aerodynamic processes regarding flight mechanics characteristics. Looking at aircraft behaviour in the presence of fast flow changes due to short wave-gusts and high-frequency control surface deflections, it is not sufficient to use only global derivatives. In this case it is necessary to consider aerodynamic delay in lift changes and interference effects.

For the investigation and modellization of these unsteady effects, occuring e.g. when an aircraft with an Active Gust Load Alleviation System encounters turbulence, it is a convenient way to combine Dynamic Model Test Techniques with System Identification Methods for the analysis of the test data. Model tests have the advantage to be less risky and relatively inexpansive compared with flight tests, and they allow systematic tests under laboratory conditions with the possibility of generating reproducible gusts. For the verification of the mathematical modellization two complementary model test techniques were chosen with their particular advantages: Free Flight Catapult Tests and Semi Free Flight Wind-Tunnel Tests.

The investigation is constricted to the longitudinal motion of conventionally configured aircraft at low Mach numbers. The aim is to find a mathematical model which uses the same paramaters for the representation of the response to control inputs and to vertical gusts by the direct use of a measured angle of attack. This includes the determination of the discrete gust.

2. AERODYNAMIC TRANSIENT EFFECTS

2.1 GEOMETRIC PENETRATION EFFECTS

The problem to be considered for a transport aircraft flying in turbulent air with control inputs from an Active Gust Load Alleviation System is illustrated in Fig. 1. Looking at a discrete impulsive gust it is important to describe the penetration process in the correct sequence. First the angle of attack sensor placed at a noseboom or at the aircraft's nose is affected, a short time later the wing and than the horizontal tail. The resulting time-delays are dependent on the airspeed and on the particular geometric distances. Their magnitude is in the order of about 100 ms for light transport aircraft flying with cruising speed, but it increases with decreasing airspeed. Thus the Geometric Penetration Effects should definitely be taken into account regarding e.g. landing approaches with normally high-frequency gust disturbances.

2.2 DELAYED INTERFERENCE EFFECTS

The interference from wing and wing flaps to tail (downwash) and to angle of attack sensor at the aircraft's nose (upwash) are of special importance for flight mechanics investigations. They are approximately included in the quasi-steady system parameters but in fact, the interference effects act with the same time-delays as the ones resulting from the penetration process. The Delayed Interference Effects are important in the case of fast flow changes at the wing due to both short-wave gusts and high-frequency flap deflections.

2.3 INSTATIONARY LIFT DEVELOPMENT

Other important effects due to high-frequency flow changes are the instationary development of lift at wing and tail. They are illustrated by the solid line in Fig. 2 together with the dynamic effects mentioned before. The plotted signals do not include characteristic motion of the aircraft, but only variations caused directly by the local gust disturbance.

The vertical step gust is passing over the aircraft from left to right affecting at first the angle of attack sensor. A short time later the measured angle is increased by the forward acting upwash effect of the wing. When the disturbing gust reaches the leading edge of the wing, the lift begins to develop due to the sudden change of local angle of attack passing over the wing. After a steep initial increase the lift development slowly approaches a steady state value. This is described by the Küssner-Function that depends mainly on the aerodynamic chord, the airspeed and the aspect ratio. A very similar procedure starts some milliseconds later when the gust reaches the leading edge of the horizontal tail. The lift development in this case is somewhat faster because of the smaller chord of the horizontal tail.

2.4 RESULTING ACCELERATIONS

The separated influences of body, wing and tail are combined to the resulting accelerations with respect to their individual sign and magnitude. Longitudinal and vertical acceleration are very similar but with an opposite sign. The longitudinal acceleration is affected in addition by a quadratic angle of attack term. The pitch acceleration shows a change in sign when the gust passes the horizontal tail. Before the stabilizing influence of the horizontal tail becomes effective only the nose-up pitching moment of wing and body is acting. All presented signals reach steady state values after about twice the times that the gust disturbance needs to pass over the aircraft.

2.5 APPROXIMATION OF THE AERODYNAMIC LAGS

The various aerodynamic lags described before are approximated by rough steps (Ref. 1). The shaded areas in Fig. 2 are calculated e.g. from the difference between the measured angle of attack and the same signal shifted in time to the wing position or to the tail position respectively. Thus they are valid only while the angle of attack is varying. Their magnitude is calculated on the assumption that the step signals have just the same influence to the aircraft motion as the approximated instationary transient effects. In both cases the time histories have to reach the same steady state values.

A similar approximation is used to model the instationary effects due to flap deflections. In contrast with Ref. 2 not only the Delayed Downwash Effect to the horizontal tail is to be taken into account but also the Instationary Lift Development.

3. APPLICATION TO SYSTEM IDENTIFICATION

3.1 MODEL CONFIGURATION

The two models one for the IMFL-Free Flight Catapult Tests and the other for the DFVLR-Dynamic Simulation in Wind-Tunnels are 1:8 scaled models of the Do 28 TNT Experimental Aircraft (Fig. 3). This is a light transport aircraft with well separated unswept wing and horizontal tail as required for approximation.

Both models are built from carbon fibre material in the same mould in order to have as little problems as possible concerning both elasticity and weight and to have the same dimensional accuracy. The models are equipped with fast acting flaps and elevator. Sensors such as accelerometers, rate gyros, potentiometers for the control surface deflections, and various angle of attack probes are installed at different locations to measure the motion, the control inputs and the disturbances. In the case of Dynamic Simulation power-supply, control signals, and measured data are transmitted to and from the model via cables. The free flight model, however, is battery operating and contains a microprocessor for control tasks and a PCM-processor for data transmission. More details concerning model configuration and test facilities can be found in Ref. 3.

3.2 SYSTEM IDENTIFICATION TECHNIQUE

System identification provides the basis for the verification of a detailed mathematical modellization of flight mechanics problems by extracting as much information as possible from dynamic wind-tunnel investigations and free flight tests. In particular, it is necessary to include gust induced dynamic effects in the conventional quasi-steady modellization. To maintain a linear identification method the following additional input signals are introduced:

- the measured angle of attack containing both the information about the characteristic motion and the gust disturbance,
- the mentioned dynamic terms calculated from the measured angle of attack and the flap deflections,
- the quadratic terms calculated from the same signals to consider the great changes in local flow.

Furthermore, the identification model is enlarged by an equation for the simultaneous determination of the gust disturbance. In this way the identification procedure includes a dynamic calibration of the angle of attack sensor with respect to time-delay effects concerning the upwash from wing and body.

The following three essential elements of System Identification (Ref. 4) may be repeated because of their special importance for the evaluation of tests with gust induced dynamic effects:

- Proper input signals:
  The input signals must excite all of the aircraft response modes. They have to be optimized to achieve accurate identifications.
- Adequate instrumentation:
  This covers the entire data acquisition process and takes into account the effect of measurement noise and sensor dynamics. The extracted derivatives are a direct function of the accuracy of the instrumentation system.
- Identification procedure:
  This describes the analysis of flight test data including the mathematical model of the dynamic behaviour of the aircraft, and the iterative computational algorithm to minimize the response error and to identify the derivatives.

At DFVLR a maximum likelihood estimation method is used to determine the stability, control and dynamic derivatives from dynamic flight tests. The method is an iterative technique that minimizes a weighted function of the difference between the aircraft's measured and computed response by adjusting the derivative values used in calculating the computed response. A modified Newton-Raphson method is used to attain the minimizations. After each iteration step, the weight factors are automatically updated according to the resulting output errors. The method also takes into account an unknown constant bias in each equation and for each measurement. This method is described in Ref. 5. In addition this method provides uncertainty levels associated with each derivative. Uncertainty levels are proportional to the approximation of the Cramer-Rao bounds and are analogues to standard deviations of the estimated derivatives.

3.3 IMFL-CATAPULT FREE FLIGHT MODEL TESTS

Test Facility

The laboratory Catapult Free Flight Model Test Technique has been developed at IMF-Lille (France) in extension of similar techniques to contribute in dynamic effects and unsteady phenomena investigations (Ref. 3, 6, 7). The main specifications of the technique will be recalled:

Unpropelled models, dynamically scaled, are launched in free flight by means of a catapult system. The flight is performed over 50 meters in a laboratory and the model is recovered. A scheme of the facility is presented in Fig. 4. All initial conditions of the flight can be adjusted. The flights can be performed in still air including inboard or ground based control loop. An optical trajectography system delivers the coordinates of the CG and Euler angles. All the information from inboard transducers (accelerometer, gyro, pressure transducer ...) are transmitted to ground via PCM telemetry system. Gust generators can be slipped into the test section to create various gust profiles.

For gust response tests the nature of the gust was chosen to be critical regarding to the penetration problem and the frequency range for alleviation. The gust length is about 1.5 times the length of the aircraft, the gust intensity up to 6 degrees. The advantage of the test method is that the gust profile is well-known because it is generated by a closed-loop wind-tunnel and the velocity distribution of the gust can be easily adjusted and controlled. The impossibility of generating a large gust field with harmonic or stochastic characteristics is a disadvantage that calls for a complementary test technique.

Free Flight Results

The influence of aerodynamic lags on the longitudinal motion due to a vertical gust is illustrated in Fig. 5 regarding the time histories of the longitudinal, vertical and pitch accelerations (solid lines). They are received from free flight model tests at the catapult facility of IMF-Lille. The model crosses the impulsive gust in about 100 ms with a speed of about 30 m/s.

The following effects may be pointed out:

- the lag between the angle of attack measuring and the wing penetration represented by the steep changes in longitudinal and vertical accelerations,
- the additional lag between the wing penetration and the penetration of the horizontal tail represented by the steep change in pitch acceleration.
- the nose-up pitching moment of wing and body before the stabilizing influence of the horizontal tail becomes effective,
- the relatively smooth transitions caused by the Instationary Lift Development.

The simulated time histories using a mathematical model without taking into account any aerodynamic lag is plotted in the left part of Fig. 5 (dashed lines). This mathematical model corresponds to the conventional quasi-steady modelling for flight mechanics applications. The different phase shifts neglecting the Geometric Penetration Effects and the Delayed Interference Effects are just as evident as the sharp-egded transitions in acceleration signals neglecting the Instationary Lift Developments. In this case it is not possible to reproduce the nose-up pitching moment of wing and body.

The mathematical model, however, that is used to get the identification results at the right part of Fig. 5 includes the aerodynamic lags in the described manner. The fit of the accelerations and of the determined vertical gust is very good. The stepwise approximation of the Instationary Lift Development can be seen when looking carefully at the edges e.g. of longitudinal acceleration. Both simulated time histories were achieved with mathematical models using the same identified parameters in the quasi-steady part. The only difference is the neglecting or the consideration of the introduced dynamic terms approximating the various aerodynamic lags.

To demonstrate the universal applicability of the extended modellization the data of four free flight tests are plotted in Fig. 6 together with the corresponding identification results. The single tests were evaluated in one identification run using a common mathematical model and estimating the initial values of each flight (multi-run evaluation). These specific tests are chosen because their different excitations of characteristic motion lead to proper identified parameters: single inputs of elevator, of symmetric aileron and of vertical gust and at the last test simultaneous use of the three excitation possibilities like it is needed e.g. for gust load alleviation. The good fit of the various signals of these different tests together with small uncertainty levels of all identified parameters is a reliable indication for the applicability of the mathematical modellization.

The peaks in longitudinal acceleration from the first test are a pecularity of these model tests caused by the quick acting flaps in conjunction with their relatively big mass. The high-frequency oscillations especially in the pitch acceleration signal represent elastic vibrations caused by flap deflections and elevator deflections. Elastic modes are not taken into consideration for identification.

The determined vertical gust is compared with the earthfixed measured up-wind. In spite of the measurement noise the sharp-edged impulsive gust is reproduced accurately due to the use of the new dynamic terms which approximate the delayed upwash of the wing to the angle of attack sensor too.

3.4 DFVLR-DYNAMIC SIMULATION IN WIND-TUNNELS

Test Facility

The installation for Dynamic Simulation in Wind-Tunnels (DSW) is an extension of a similar test technique, which is used for testing flutter-models. The facility was designed for the estimation of the aircraft stability derivatives and for the testing of active control systems (Refs. 3, 8, 9, 10). Within certain limitations, portions of the flight envelope can be simulated in the wind-tunnel for a variety of aircraft. These constraints are given by the observance of the laws of similarity and by the limited freedom of movement in the wind-tunnel. The installation for Dynamic Simulation consists of four main parts (Fig. 7): the suspension frame for the model, the control/data processing station, the gust generator system, the model.

The suspension frame consists of a large tubular frame in combination with a vertical rod, which allows freedom of motion in pitch, yaw, heave and to some extent in roll. The frame surrounds the open test section of the 3 m-subsonic wind-tunnel; the distance between frame and airflow is 0.5 m. The resonant frequency of the rod/frame system is about 14 Hz. This value is high enough to allow measurements up to frequencies of 10 Hz. The maximum pitch motion is $\pm$ 10 degrees, the model can heave $\pm$ 0.4 m.

A servo controlled vertical force generator can produce constant vertical forces independent of the vertical model position to compensate a part of the model weight. This is necessary to meet the laws of similarity (Froude number).

The main control station is located in a container next to the test section. This container houses the model control devices, the measurement data processor, and various monitoring devices.

Two movable flaps are installed in the nozzle of the wind-tunnel. They are driven by an electro-hydraulic actuator. This device allows a deflection of the airflow within the test section of up to 10 degrees. The gust generator can generate gusts in the frequency range from zero to 15 Hz. It is possible to generate various types of gust profiles, such as impulsive or stochastic gusts. The properties of the gust generator allow the simulation of a scaled stochastic gust field with special spectral characteristics (e.g. Dryden) over an extended period of time to perform parametric studies.

The conducted wind-tunnel experiments showed that the suspension frame surrounding the test section and the cables for data transmission to and from the model influences the motion of the model (Ref. 11). The nonlinear propagation of the gust dependend on frequency and position is another adverse influence (Ref. 12). The consideration of these effects is a must for System Identification.

Dynamic Simulation Results

The applicability of the established mathematical description of aerodynamic delay effects is demonstrated by another example. Therefore the identification results obtained from multi-run evaluation of four single tests performed in the Dynamic Simulation Facility in Wind-Tunnels are selected (Fig. 8). These tests with excitation by control deflections of elevator and of two types of wing flaps (outboard and inboard) and by wind-tunnel gusts are chosen for the same reasons as in analysis of free flight

tests. The identification model is just the same but without freedom in the horizontal direction and adapted to the specific influences mentioned before.

In contrast to the free flight tests the gust determination was done without recourse to a measured gust signal just as in the case of flights with full-scale aircraft encountering turbulence. In spite of the permanent acting wind-tunnel turbulence aggravated by the presence of the gust flaps the reproduction of vertical acceleration and pitch acceleration by means of system identification is satisfactory too. Only the last test with excitation by gust disturbance shows some discrepancies in the pitch acceleration which might be caused by the nonlinear propagation of the gust in the open test section.

4. CONCLUSIONS

Dynamic terms are introduced to complete the conventional quasi-stationary modellization of longitudinal motion of aircraft with separated wing and horizontal tail at low Mach numbers. The dynamic correction terms are very important for flight mechanics applications including fast flow changes due to both:

- short-wave gust disturbances, and
- high-frequency control deflections.

The dynamic terms represent the following dynamic effects:

- Geometric Penetration Effects,
- Delayed Interference Effects, and
- Instationary Lift Development.

The particularities of the extended linear modellization applied to System Identification are:

- the use of the measured angle of attack as an input signal which contains the information about the characteristic motion as well as the gust disturbance,
- the addition of quadratic and dynamic terms calculated from the measured angle of attack and flap deflections,
- the simultaneous determination of the gust.

The outlined identification method is transferable to flight test analysis of full-scale aircraft. Only onboard measurable signals are used to identify the parameters of the aircraft motion even in the presence of turbulence. This method may be a beneficial tool for the design of high-frequency Active Control Systems, e.g. Gust Load Alleviation Systems.

5. REFERENCES

[1] Rohlf, D., "Ermittlung der Bö und des Böenstörverhaltens aus Flugversuchsdaten am Beispiel Do 28 TNT", DFVLR-FB 84-48, 1984.

[2] Marchand, M., "Bestimmung der Derivative eines Do-28-TNT-Modells aus Freiflugversuchen", DFVLR-FB 82-17, 1982.

[3] Wilhelm, K., Verbrugge, R.A., "Correlation Aspects in the Identification of Dynamic Effects using Complementary Techniques", AGARD-CP-339, 1983.

[4] Hamel, P., "Aircraft Parameter Identification Methods and their Applications - Survey and Future Aspects", AGARD-LS-104, 1979.

[5] Plaetschke, E., "Maximum-Likelihood-Schätzung von Parametern linearer Systeme aus Flugversuchsdaten - Ein FORTRAN-Programm", DFVLR-Mitt. 84-10, 1984.

[6] Charon, W., Verbrugge, R.A., "Nouvelle Technique d'essais sur Maquettes Libres en Laboratoire pour la Determination de Characteristiques Aerodynamiques", AGARD-CP-235, 1978.

[7] Cocquerez, S.L., "Etudes de Mécanique du Vol par Maquettes Catapultées en Laboratoire", Association Aeronautique et Astronautique de France, 16e Colloque, Lille, Novembre 1979.

[8] Subke, H., Krag, B., "Dynamic Simulaion in Wind Tunnels, Part II", AGARD-CP-187, 1975.

[9] Hamel, P., Krag, B., "Dynamic Wind Tunnel Simulation of Active Control Systems", AGARD-CP-260, 1978.

[10] Wilhelm, K., Gmelin, B., "DFVLR-Dynamic Model Testing in Wind Tunnels for Active Controls Research"; 12. ICAS Congress, Munich 1980.

[11] Rohlf, D., "Bewegungsgleichungen und modifiziertes Open-Loop-Böenabminderungssystem für das Do 28 TNT Windkanalmodell", DFVLR-IB 154-79/17, 1979.

[12] Krag, B., "The Wind Tunnel Behaviour of a Scaled Model with a Gust Alleviation System in a Deterministic Gust Field", Symposium on Dynamic Analysis of Vehicle Ride and Manoeuvering Characteristics, London, 1978.

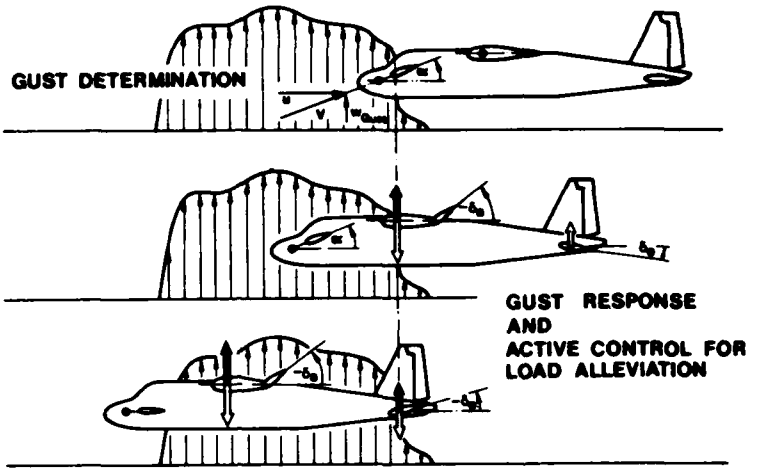

Fig. 1: Gust Penetration with Active Gust Load Alleviation

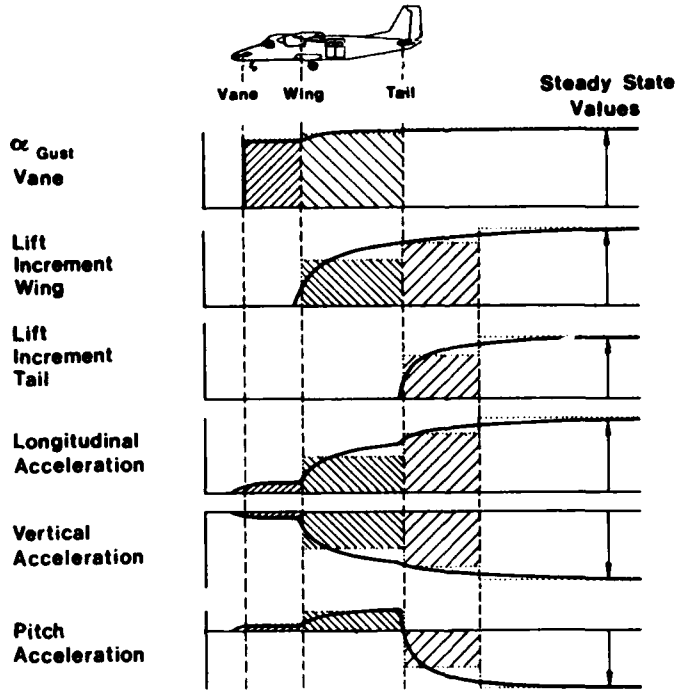

Fig. 2: Instationary Gust Effects

—— Simulation Including Küssner Functions

····· Approximation by Step Signals

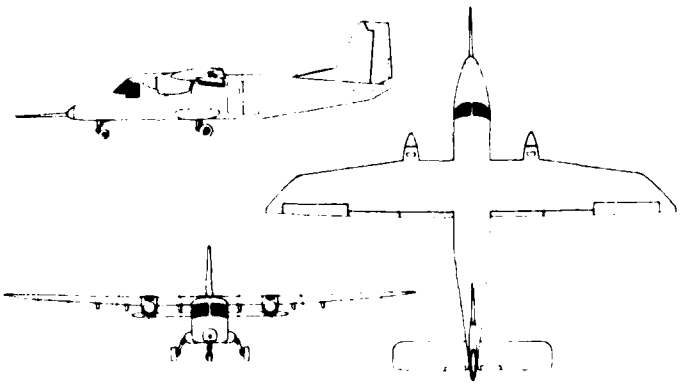

Fig. 3: Dornier Do 28 TNT Experimental Aircraft

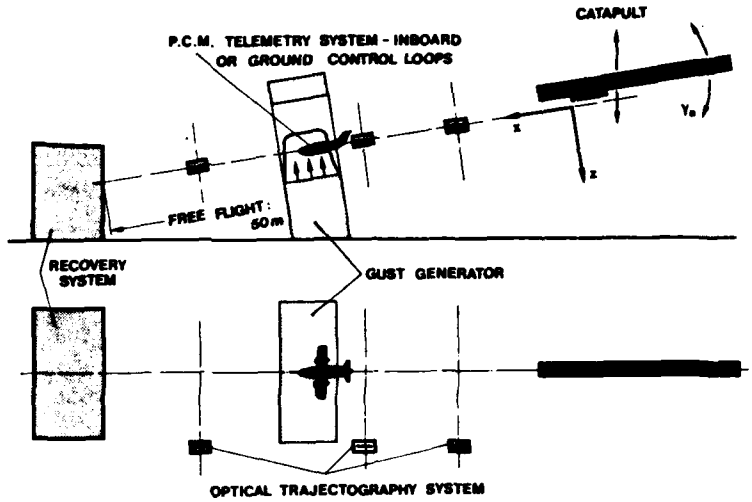

Fig. 4: Schematic of the Catapult Free Flight Facility (IMFL)

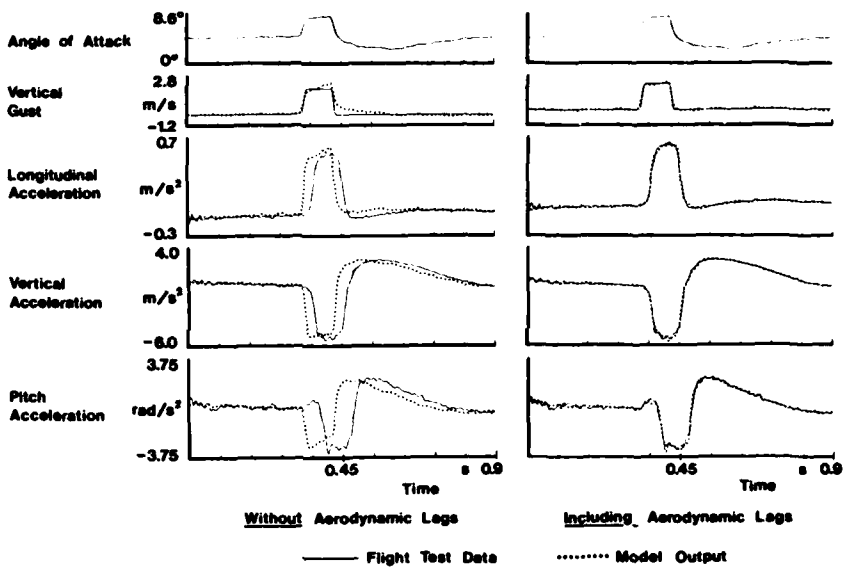

Fig. 5: Influence of Aerodynamic Lags (IMFL)

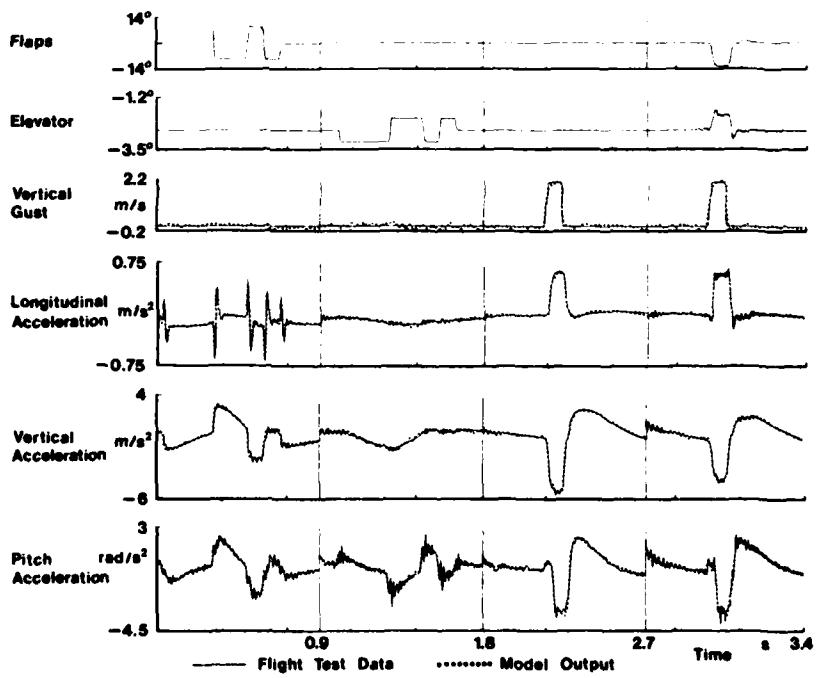

Fig. 6: Common Identification of Control and Gust Behaviour (IMFL)

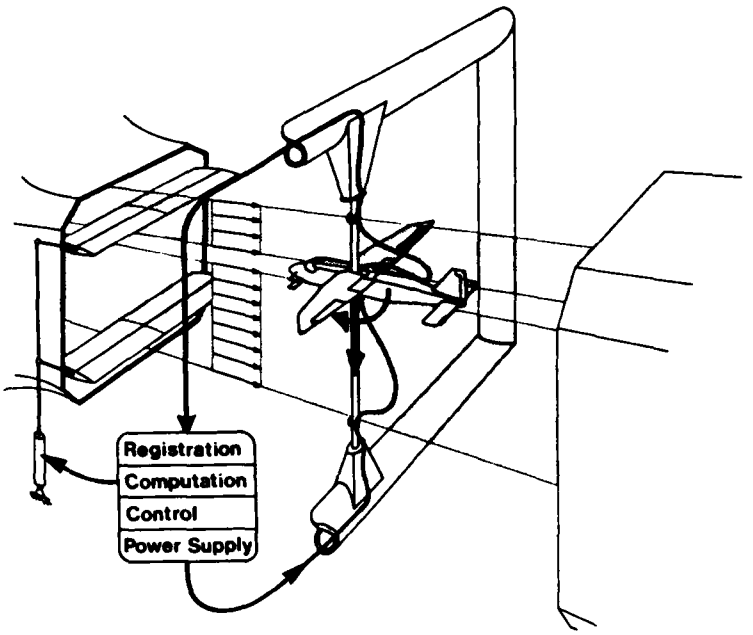

Fig. 7: Schematic of the Dynamic Simulation in Wind-Tunnels (DFVLR)

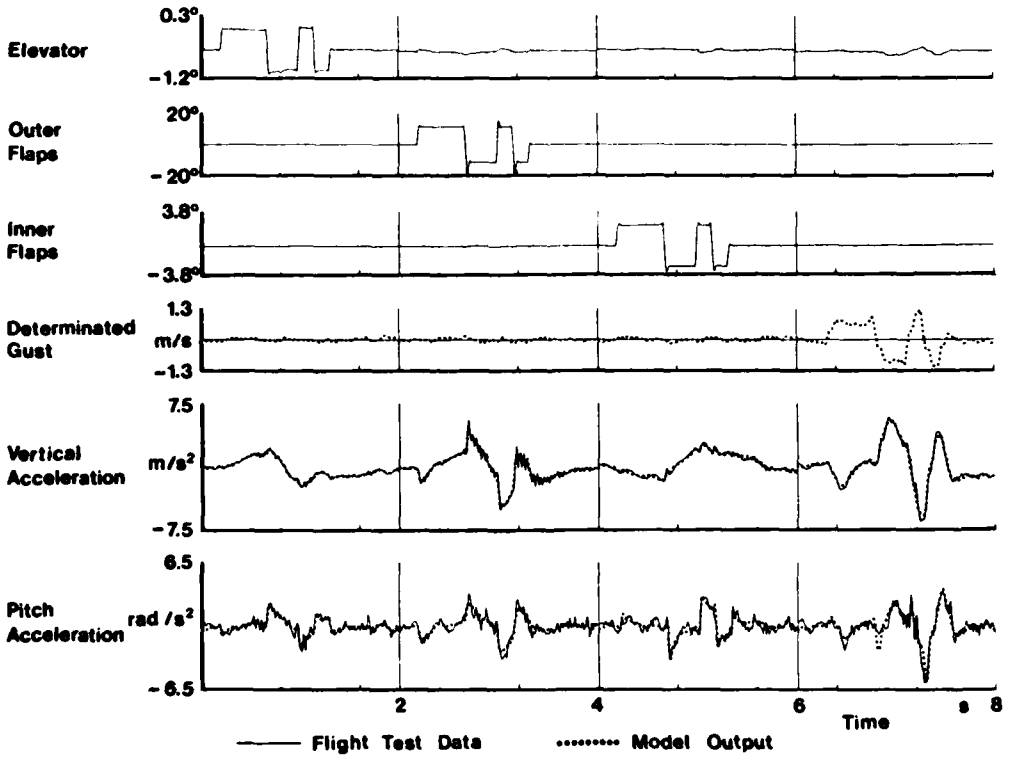

Fig. 8: Common Identification of Control and Gust Behaviour (DFVLR)

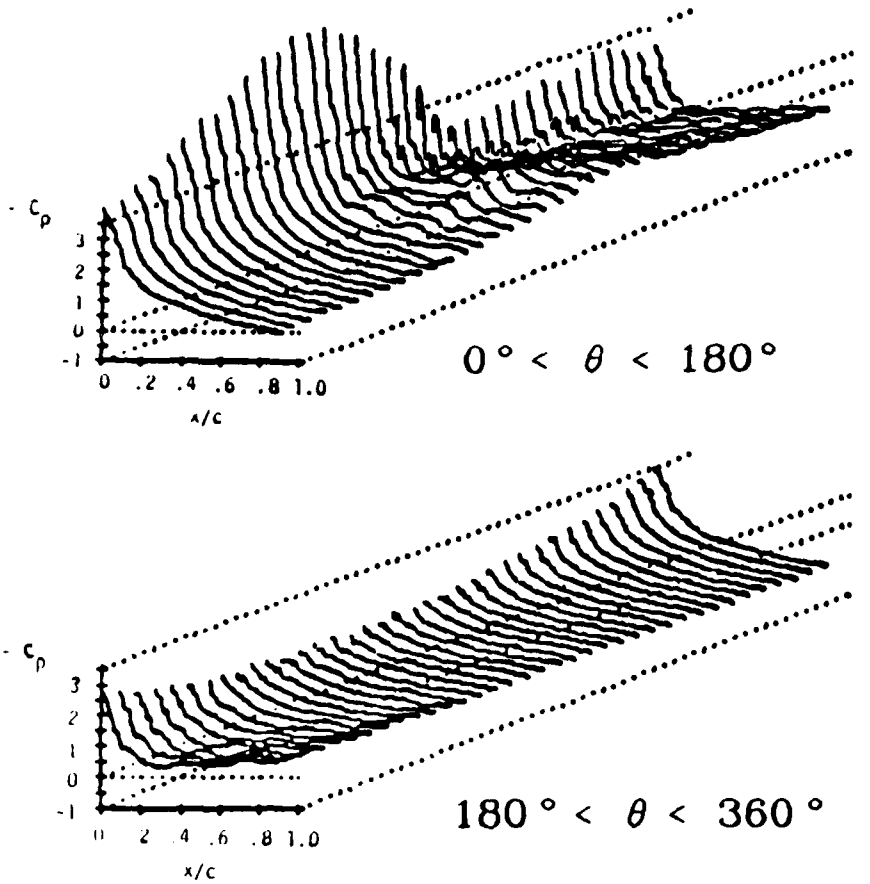

Fig. 5 b) Distribution de pression sur l'extrados à I = 0,15

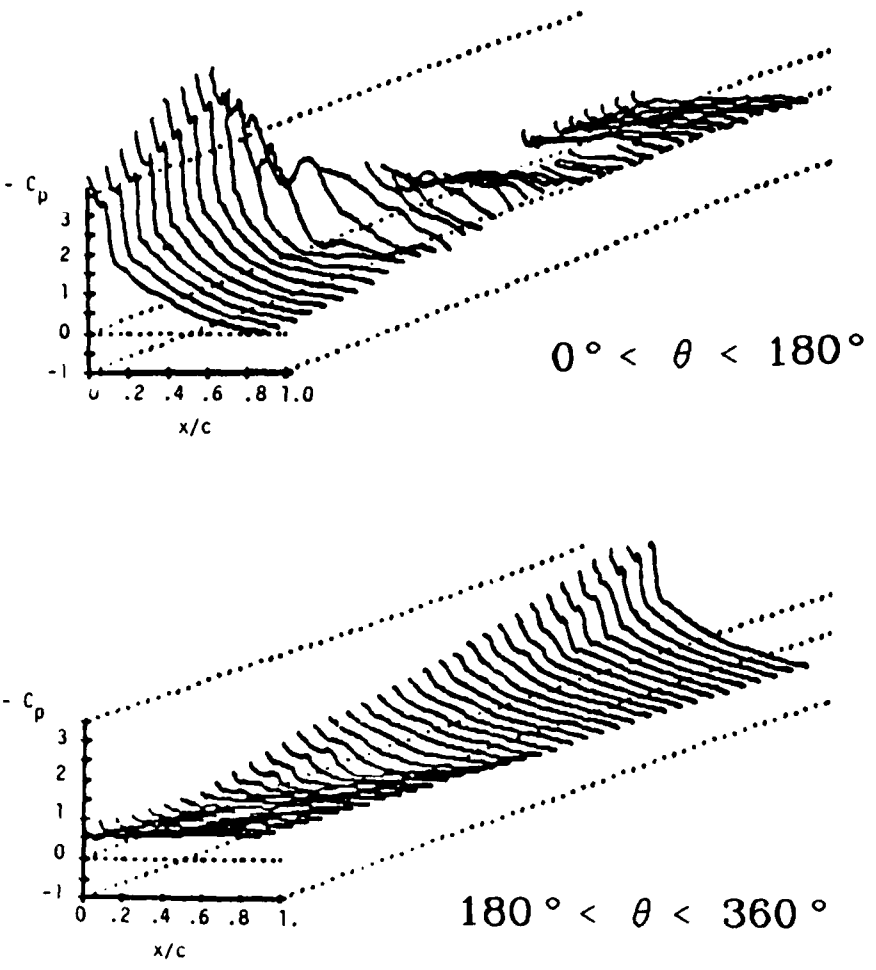

Fig. 5 a) Distribution de pression sur l'extrados à I = 0,007

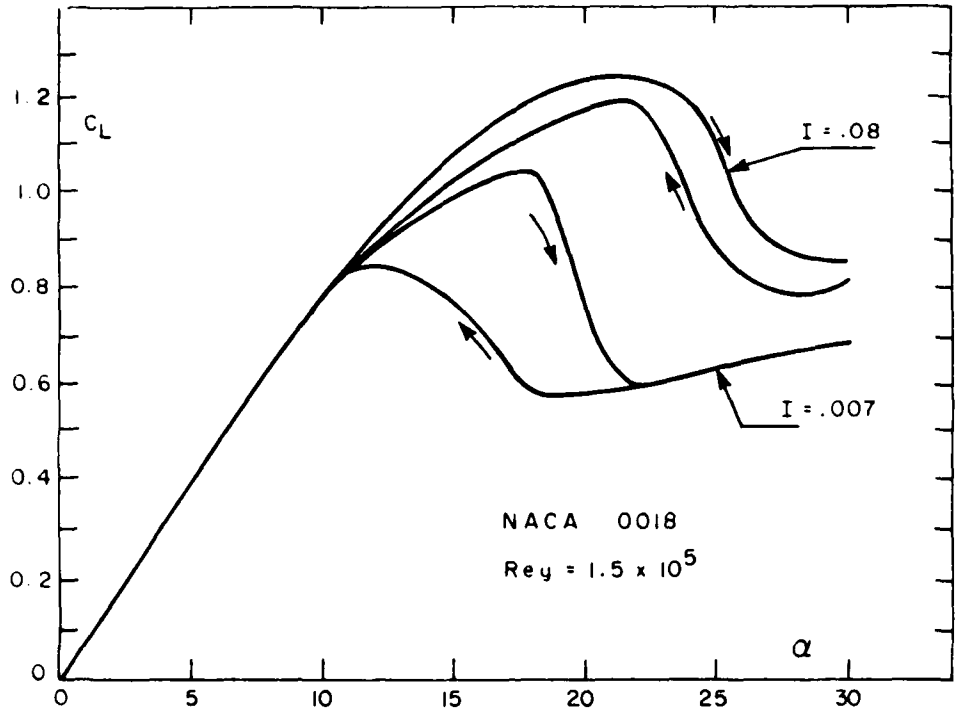

Fig. 3 Coefficients de portance statique.

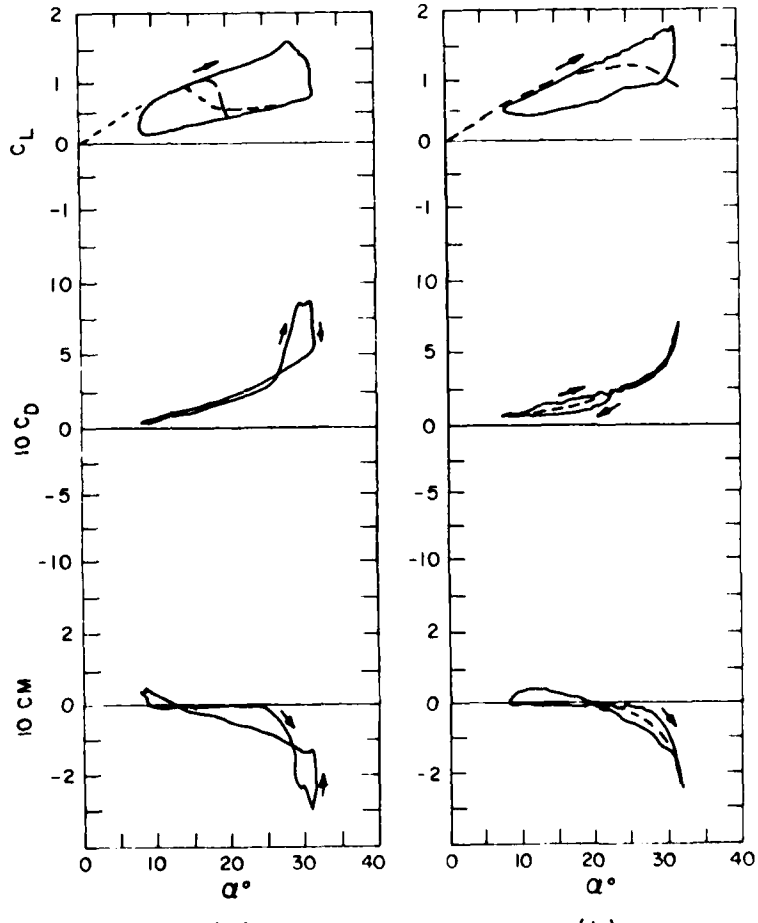

Fig. 4 a) Coefficients aérodynamiques à I = 0,007
b) Coefficients aérodynamiques à I = 0,15

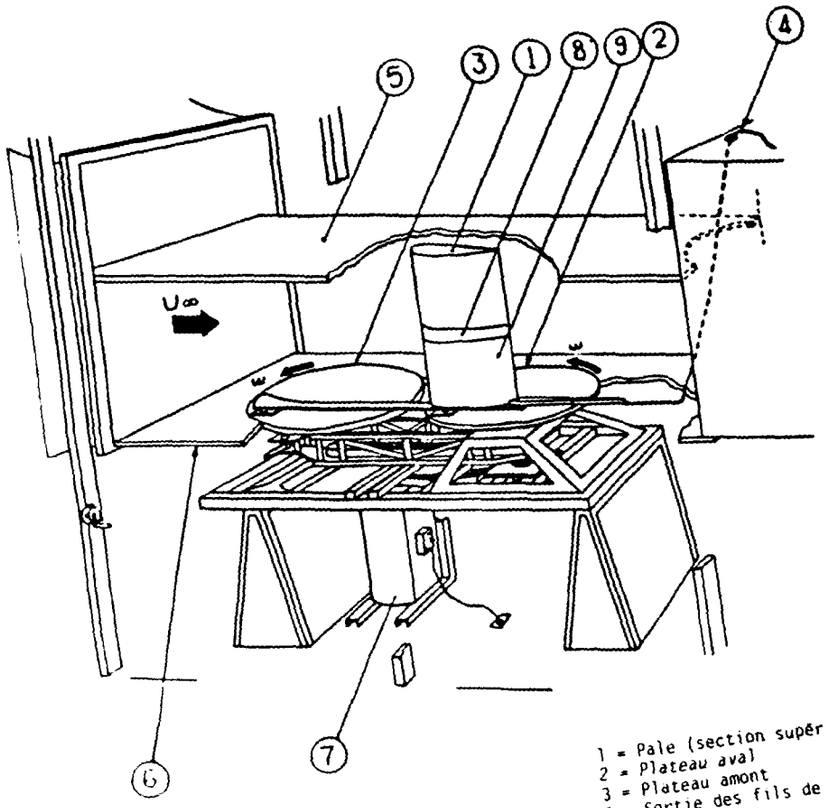

1 = Pale (section supérieure)
2 = Plateau aval
3 = Plateau amont
4 = Sortie des fils de contrôle
5 = Faux plafond
6 = Faux plancher
7 = Moteur Eaton Dynamatic
8 = Prises de pression
9 = Pale (section instrumentée)

Fig. 1 Schéma du montage.

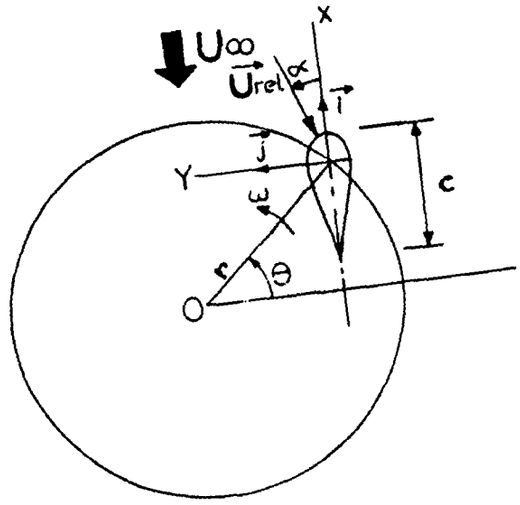

Fig. 2 Cinématique du montage expérimental.

Dans le cas peu turbulent (fig. 4a), la portance, après une croissance linéaire en fonction de α, subit une chute semblable à celle d'un "deep stall". Ceci est confirmé par la courbe du coefficient de moment au quart de corde. Dans le cas de turbulence élevée (fig. 4b), le coefficient de portance atteint une valeur supérieure avant le décrochage et l'hystérésis est moins prononcée que dans le cas de faible turbulence.

Cependant, dans les deux cas, la valeur de C_L chute avec un retard de 2½° sur l'augmentation du C_D et le décrochage du C_M. Il s'agit donc bien, dans les deux cas, du phénomène du "deep stall". La comparaison des courbes de C_D et C_M pour les deux intensités de turbulence semble donc indiquer que la formation du tourbillon sur l'extrados est influencée par la turbulence externe.

La figure 5 compare les distributions de la pression pariétale sur l'extrados d'où ont été tirés les coefficients C_L, C_D et C_M. Les courbes de C_p en fonction de x/c sont présentées pour des valeurs de θ avec un incrément de 5°. Dans le cas de faible turbulence (fig. 5a), on peut noter d'abord à $\theta = 0$ ($\alpha = \alpha_o = 20°$) la présence d'une bulle de séparation au bord d'attaque. Elle débute à un azimuth $\theta = 230°$ ($\alpha \cong 9°$) et s'accentue à $\theta = 325°$ ($\alpha \cong 14°$). Cette bulle de séparation devient le siège d'un tourbillon qui entraîne un affaissement du C_p au bord d'attaque lorsqu'il débute son déplacement sur l'extrados à $\theta = 40°$ ($\alpha = 26.5°$) . A faible turbulence, on retrouve donc la description classique du décrochage dynamique. L'addition de turbulence, comme l'indique la figure 5b change cette description. Le bord d'attaque n'est plus le siège d'une vorticité qui émet un tourbillon. La couche limite reste attachée jusqu'à $\theta = 60°$ ($\alpha = 29.1°$). Au delà de cet angle, une zone de dépression se développe à partir du bord de fuite et remonte vers le bord d'attaque. L'affaissement du C_p se produit à $\theta = 75°$ ($\alpha = 31.0$) et peut être associé au phénomène de séparation. Par ces comparaisons, on peut donc conclure que la turbulence contenue dans l'écoulement amont modifie de façon substantielle le phénomène du décrochage dynamique. Elle stabilise la couche limite permettant ainsi des incidences plus élevées avant le décrochage. De plus, elle altère le développement du tourbillon au bord d'attaque. Elle l'élimine dans le cas observé ($k = 0.15$) et en diminue l'importance dans d'autres cas ($k = 0.35$) qui ne sont pas présentés ici. L'effet de la turbulence externe s'apparente donc à celui de la transition dans la couche limite, transition qui se produit à des nombres de Reynolds plus élevés.

IV. CONCLUSION

Une étude expérimentale portant sur l'effet de la turbulence sur le décrochage dynamique a été réalisée sur un profil NACA 0018 soumis à un mouvement de translation circulaire. Les résultats indiquent que la turbulence stabilise la couche limite et permet aux décrochages statique et dynamique de se produire à des angles d'incidence plus élevés. En régime de "deep stall", la turbulence, selon les résultats, modifie la formation du tourbillon du bord d'attaque, et dans certains cas, l'élimine. Le mécanisme à l'origine de ces modifications semble en être un où la turbulence pénètre dans la couche limite par le point de stagnation et la stabilise d'une façon similaire au mécanisme de la transition.

REMERCIEMENTS

Les auteurs veulent remercier pour leur support les organismes tels que le C.R.S.N.G. et l'I.R.E.Q. de même que R. Rosselli, M. Aubert et V. Mertens pour leur collaboration.

RÉFÉRENCES

[1] Courchesne, J. and Laneville, A., 1982, "An Experimental Evaluation of Drag Coefficient for Rectangular Cylinders Exposed to Grid Turbulence". Trans. ASME, J. Fluids Engrg., Vol. 104, pp. 523-528.

[2] Nakamura, Y. and Ohya, Y., 1984, "The Effects of Turbulence on the Mean Flow Past Two-Dimensional Rectangular Cylinders", J. Fluid Mech., Vol. 149, pp. 255-273.

[3] McCroskey, W.J., 1980, "The Phenomenon of Dynamic Stall", N.A.S.A. Tech. Memo 81264, March 1981.

ties le long du profil de la section de mesure située dans le milieu de la pale. L'acquisition et le traitement des données permettent d'obtenir en fonction du temps la distribution de pression le long du profil ainsi que les coefficients de portance C_L, de moment C_M et de traînée C_D dus à la pression.

II.2 Cinématique du mouvement

Le mécanisme d'entraînement donne au modèle un mouvement de translation circulaire. L'axe du profil garde une orientation constante α_o par rapport à l'axe longitudinal de la soufflerie. L'angle α_o peut prendre les valeurs de 0°, 10°, 15° et 20°.

Le point situé au quart de la corde du profil décrit un cercle de rayon r = 30 cm à une vitesse angulaire ω constante pour chaque essai (voir figure 2).

Lorsque la vitesse moyenne de l'écoulement amont est U_∞, on définit la vitesse spécifique

$$\lambda = U_\infty/\omega r$$

La vitesse relative de l'écoulement est alors

$$U_{rel} = U_\infty[1 + (1/\lambda^2) + (2 \cos \omega t)/\lambda]^{\frac{1}{2}}$$

et l'angle d'incidence calculé est

$$\alpha = \alpha_o + \text{arctg}\ [(\sin \omega t)/(\lambda + \cos \omega t)]$$

D'autre part, la définition de la fréquence réduite devient

$$k = c\ \dot{\alpha}_{max}/[(\alpha_{max} - \alpha_{min})U_\infty]$$

et représente le rapport entre la vitesse $c\ \dot{\alpha}_{max}/(\alpha_{max} - \alpha_{min})$ et celle de l'écoulement amont, U_∞. Pour le cas d'un profil soumis à la loi $\alpha = \alpha_o + \alpha_1 \sin(\omega t)$ dans un écoulement de vitesse U_∞, la fréquence réduite définie en (4) est $\omega c/2U_\infty$, ce qui correspond à la définition traditionnelle pour les pales d'hélicoptères. Dans les conditions des essais présentées ici, l'équation (4) devient

$$k = c/2\lambda r(\lambda-1)\ \text{artg}[(\lambda^2-1)^{-\frac{1}{2}}]$$

ou encore

$$k = \omega c/2U_\infty(\lambda-1)\ \text{artg}[(\lambda^2-1)^{-\frac{1}{2}}]$$

On remarque donc que la variation de la vitesse spécifique λ entraîne simultanément une variation de la fréquence réduite et une variation dans l'amplitude α_{max}.

III. ANALYSE DE QUELQUES RÉSULTATS

L'analyse sera limitée aux résultats obtenus à un nombre de Reynolds moyen de $1.5 * 10^5$. Dans une première section, l'effet de l'intensité de la turbulence sur le coefficient statique de portance sera examiné. Dans une deuxième section, l'effet du niveau de turbulence sur les coefficients aérodynamiques sera étudié pour un angle de calage de 20° (choisi pour assurer la présence du décrochage dynamique) et une même valeur de fréquence réduite.

III-1 Effet de la turbulence sur le C_L statique

La figure 3 permet de comparer les courbes du coefficient de portance à deux intensités de turbulence, soient 0,007 et 0,08. L'envergure équivalente de la pale est de 4,9. Dans cette comparaison, seul le paramètre I a été varié, et on peut constater qu'une augmentation de I entraîne un délai dans l'apparition du décrochage statique, délai accompagné d'un prolongement de la plage de portance supérieure.

Il n'est pas évident à ce stade que la turbulence externe stabilise la couche limite par son introduction à l'intérieur de la couche limite via le point de stagnation ou par l'échange de momentum à l'interface de l'écoulement externe et de la couche limite. Des essais complémentaires avec des anémomètres à fil chaud et affleurant à la paroi permettront de mieux connaître le contenu énergétique de la couche limite. Les essais ont donc permis d'établir que l'angle de décrochage statique varie avec le niveau de turbulence dans l'écoulement externe. Pour les intensités de turbulence de 0.007, 0.08 et 0.15, l'angle de décrochage statique observé est 18°, 22° et 25° respectivement.

III-2 Effet de la turbulence sur les coefficients C_L, C_D et C_M dynamiques

La figure 4 permet de comparer les coefficients aérodynamiques obtenus pour $\alpha_o = +20°$ et k = 0.15 aux intensités de turbulence de 0,007 et 0,15. Dans ces conditions d'essais, la pale est soumise à de fortes incidences et au phénomène de "deep stall" comme en témoignent les courbes C_L, C_D et C_M. Cependant, certaines différences apparaissent avec l'addition de turbulence à l'écoulement externe. D'une part, comme pour les essais statiques en turbulent, le décrochage dynamique se produit avec un délai. Dans le cas où k = 0.15, le début de la chute de portance se produit à $\alpha = 27°$ en peu turbulent (I = 0.008) et à $\alpha = 33°$ en fortement turbulent (I = 0.15). Cet écart de 6° correspond approximativement à celui observé lors des essais statiques. D'autre part, la forme de la boucle du décrochage est altérée en présence de la turbulence.

ÉTUDE EXPÉRIMENTALE DE L'EFFET DE LA TURBULENCE SUR LE DÉCROCHAGE DYNAMIQUE

A. LANEVILLE, P. VITTECOQ, J. CÔTÉ

Département de génie mécanique
Université de Sherbrooke
Sherbrooke (Québec), Canada J1K 2R1

SOMMAIRE

Une étude du décrochage dynamique pour différentes intensités de turbulence contenue dans l'écoulement amont, a été réalisée en soufflerie. La pale avait un profil NACA 0018 et suivait un mouvement différent d'une oscillation sinusoïdale. Pour un angle de calage et une fréquence réduite identiques, les résultats permettent d'établir que la turbulence modifie les phénomènes de décrochage statique et dynamique. La turbulence stabilise la couche limite au bord d'attaque, permet au profil d'atteindre des angles d'incidence plus élevés avant le décrochage et altère la formation du tourbillon du bord d'attaque.

NOTATIONS

c	: corde du profil
C_D	: coefficient de traînée = traînée/$qc\ell$
C_L	: coefficient de portance = portance/$qc\ell$
C_M	: coefficient de moment à c/4 = (moment à c/4)/$qc^2\ell$
C_P	: coefficient de pression = $(P - P_\infty)/q$
I	: intensité longitudinale de la turbulence
k	: fréquence réduite = $c\,\dot{\alpha}_{max}/[(\alpha_{max} - \alpha_{min})U_\infty]$
ℓ	: hauteur de la pale
q	: pression dynamique = $1/2\ \rho U_{rel}^2$
r	: rayon du cercle décrit par la pale
U_{rel}	: vitesse relative définie selon la figure 2
U_∞	: vitesse moyenne de l'écoulement amont
α	: angle d'incidence de la pale
$\dot{\alpha}$	: $d\alpha/dt$
α_o	: angle de calage de la pale
θ	: azimuth de la pale $\theta = \omega t$
ρ	: densité de l'air
ω	: vitesse de rotation de la pale

I INTRODUCTION

Il est généralement admis [1, 2] que la turbulence influence l'écoulement séparé autour de corps non-profilés. Dans le cas de cylindres bidimensionnels, l'effet de l'intensité de la turbulence est relativement plus important que celui de la macro-échelle longitudinale de turbulence. Pour un profil oscillant où le phénomène de séparation ou de décrochage dynamique est présent, l'effet de la turbulence est peu connu [3]. Or les pales d'hélicoptère volant à basse altitude ou dans une manoeuvre près du sol sont exposées à des niveaux de turbulence pouvant atteindre 20%. Dans le domaine de la conversion de l'énergie éolienne, les pales du rotor Darrieus tournant à basse vitesse spécifique subissent des écoulements qui présentent certaines similitudes à ceux des pales d'hélicoptère et sont, elles aussi, exposées à la turbulence atmosphérique. Une campagne d'essais a donc été entreprise dans le laboratoire d'aérodynamique de l'Université de Sherbrooke, campagne où un profil symétrique a été soumis à du décrochage dynamique pour différents niveaux de turbulence.

II. CONDITIONS D'ESSAIS ET MOYENS DE MESURE

Selon les travaux de McCroskey [3], le décrochage dynamique ressenti par une pale oscillant selon une loi sinusoïdale de tangage est influencé en particulier par les paramètres de fréquence réduite k, d'angle de calage α_o et d'amplitude α_{max}. Les travaux présentés ici traitent du même phénomène mais dans des conditions où la pale a un mouvement différent d'une oscillation sinusoïdale et où l'écoulement amont contient une turbulence de grillage.

II.1 Description de l'expérience

Le schéma partiel de l'installation visible sur la figure 1 montre le modèle constitué d'une pale verticale de 60 cm de hauteur, de profil NACA-0018 et de corde c = 35,6 cm. La section de la soufflerie où est placé le modèle a une largeur de 1,20 m. Elle est limitée par un faux plafond qui laisse un espace de 2 mm à la partie supérieure du modèle et par un faux plancher sous le lequel le mécanisme d'entraînement est installé. Les parois latérales de la section d'essais ont un pourcentage d'ouverture de 40% pour minimiser le blocage.

Les essais sont effectués à trois niveaux d'intensité de turbulence dans la zone où évolue le modèle: 0,7%, 8% et 15%, les deux derniers étant obtenus à l'aide de grilles installées en amont du modèle.

La pression pariétale instantanée est mesurée à l'aide d'un Scanivalve qui met successivement en communication son capteur avec l'une des 40 prises de pression répar-

APPLICATION OF CFD TECHNIQUES TOWARD THE VALIDATION OF NONLINEAR AERODYNAMIC MODELS

by

Lewis B. Schiff and Joseph Katz
NASA Ames Research Center
Moffett Field, CA 94035

SUMMARY

Applications of CFD methods to determine the regimes of applicability of nonlinear models describing the unsteady aerodynamic responses to aircraft flight motions are described. The potential advantages of computational methods over experimental methods are discussed and the concepts underlying mathematical modeling are reviewed. The economic and conceptual advantages of the modeling procedure over coupled, simultaneous solutions of the gasdynamic equations and the vehicle's kinematic equations of motion are discussed. The modeling approach, when valid, eliminates the need for costly repetitive computation of flowfield solutions. For the test cases considered, the aerodynamic modeling approach is shown to be valid.

1. INTRODUCTION

Predictions of aircraft flight motions, design of aircraft control systems, and development of realistic piloted flight simulators all hinge on accurate knowledge of the unsteady aerodynamic forces and moments acting on the maneuvering aircraft. Prediction of these unsteady airloads is complicated by the fact that the instantaneous flowfield surrounding the aircraft is not determined solely by the instantaneous values of the motion variables such as angle of attack, pitch rate, and control deflection angles. In general, the instantaneous state of the flowfield, and thus the loading, depends on the history of the motion, that is, on all states experienced by the flowfield during the maneuver prior to the instant in question. Time-history effects are accentuated by requirements for aircraft agility, which lead to flight in the high-angle-of-attack regime and rapid changes in the orientation of the aircraft. As a result, highly-maneuverable aircraft can experience nonlinear and unsteady airloads due to large regions of three-dimensional separated flow, concentrated vortex flows, and the presence and movement of shock waves.

Complete evaluation of time-history effects in wind-tunnel experiments would require the availability of an apparatus capable of simulating, at suitable rates, the complete range of motions the aircraft would experience in flight, and capable of measuring the aerodynamic response to those motions. By coupling this apparatus with a computer, the aircraft's equations of motion could be integrated in time from specified initial conditions. The computed aircraft flight attitude and angular rates would determine the new position of the apparatus, while the measured aerodynamic forces and moments would be input to update the computed aircraft motion. Although, in principle, capable of accounting for all time-history effects, such a general wind-tunnel apparatus is, unfortunately, far more easily envisioned than constructed. As a result the conventional method of predicting aircraft flight motions relies on an alternative approach, that of mathematical modeling.

In the modeling approach, one attempts to specify a *form* for the aerodynamic response that remains the same in the determination of the aerodynamic response to all motions of interest. Ideally, a mathematical model enables one to synthesize the response to a general maneuver from the known aerodynamic responses of the aircraft to a limited number of specific, *characteristic* motions. Wind-tunnel evaluations of the responses to the characteristic motions are, in principle, more easily accomplished than simulations of the general maneuvers. The development of mathematical models capable of accurately describing the variety of aerodynamic phenomena acting on aircraft maneuvering in the nonlinear flight regime has been a subject of ongoing interest (Refs. 1,2), and continues to be addressed in this symposium (Refs. 3,4).

The utility of a proposed mathematical model is dependent upon the range of vehicle motions and aerodynamic phenomena which it can encompass. Determining the range of validity of a candidate mathematical model would require: 1) determining the aerodynamic response of an aircraft to the set of characteristic motions called for by the model, 2) predicting a wide variety of aircraft motion histories using the model and the determined responses, and 3) comparing the predicted motion histories against actual flight histories. The validity of the model would be demonstrated by a match between the predicted and flight motion histories. While such a model validation procedure is straightforward in principle, it is difficult to accomplish in practice. Flight-test data are expensive to obtain, and accurate determination of motion histories during extreme maneuvers is difficult (see Ref. 5 for a discussion of flight-test difficulties). Further, accurate wind-tunnel determination of the unsteady responses to the characteristic motions is itself nontrivial (see Refs. 6,7 for a description of relevant experimental techniques). In addition, in the comparison of motion histories, small changes in the values of the terms of the model may integrate to produce large deviations between the actual and predicted motions. Thus, few, if any, satisfactory model validations have been accomplished for a general set of flight maneuvers.

Fortunately, the remarkable advances which have occurred in computer technology and computational fluid dynamics now offer the aerodynamicist a promising alternative approach. Today, we can envision utilizing CFD techniques to study unsteady three-dimensional flows, both to investigate aerodynamic time-history effects and to validate aerodynamic mathematical models.

A straightforward computational approach to investigating time-history effects (assuming the availability of codes and computer resources adequate to solve suitably modeled equations of turbulent flow around an aircraft) would be to solve the flowfield equations *simultaneously* with the aircraft's equations of motion. Such a coupled approach is shown schematically in Fig. 1a. This is, of course, the CFD analog of the general wind-tunnel apparatus described above, with computation of the instantaneous flowfield replacing the need for measuring the aerodynamic response. By using CFD techniques one avoids the experimental difficulties which hinder wind-tunnel measurements of unsteady flows. Results of these coupled computations would be complete time histories of the aerodynamic response and of the vehicle motion. It is noteworthy that computations involving the coupled-equations approach have recently been carried out for several unsteady two-dimensional inviscid flows (Refs. 8 - 10), and for at least two unsteady two-dimensional viscous flows (Refs. 11,12). However, lack of computational resources has, to date, precluded undertaking the analogous computations for (even steady) three-dimensional viscous flows.

Although coupling of the flowfield equations and the aircraft's inertial equations of motion is, in principle, an exact approach to accounting for aerodynamic time-history effects in predicting the response to arbitrary maneuvers, it inevitably will be a very costly one. This will be particularly true for maneuvers at high incidence, where the airloads depend nonlinearly on the motion variables. Under such conditions the aircraft can experience widely varying motion histories, even if they are started from closely-spaced initial conditions. Thus, to completely evaluate an aircraft's performance envelope, a large number of computational cases, each involving the coupled equations, would be required to cover all possible sets of initial conditions. Since the motion and the aerodynamic response are inextricably linked in the coupled approach, the flowfields must be recomputed for each change in initial conditions.

In contrast to the coupled-equations approach, utilizing mathematical modeling in conjunction with CFD techniques can eliminate the need for repetitive computation of flowfield solutions, and will lead to more efficient use of computational resources. The modeling approach is shown schematically in Fig. 1b. As has been previously mentioned, in formulating a model one attempts to identify a set of characteristic motions from whose aerodynamic response one can generate the response to general maneuvers. Within the regime of validity of the mathematical model, computational evaluation of the aerodynamic terms specified by the model would be required only once, whereupon they could be utilized over a range of motion variables and flight conditions. Flight motions could then be predicted by solving the aircraft's equations of motion independently of the flowfield computations, at far less cost.

Presupposing the availability of codes adequate to solve the equations governing turbulent flows around an aircraft, evaluation of the validity of a candidate aerodynamic mathematical model can itself be easily accomplished with the use of CFD techniques. Two validation procedures can be envisioned. The first method parallels the experimental validation procedure discussed above, that is, by comparing vehicle motion histories. To carry out the validation, the aerodynamic responses to the characteristic motions would be evaluated from flowfield computations. Once obtained, these responses can be used, together with the model, to predict a series of motion histories. On the other hand, by using the coupled-equations approach, motion histories which take exact account of time-history effects can be obtained for the same set of initial conditions. Both series of motion histories are subject to precisely the same set of approximations made in computing the flowfield. Differences, if any, between the motion histories must be attributable to the assumptions made in the modeling process. Thus, the validity of the mathematical model would be demonstrated by agreement between the motion histories. The second computational model validation procedure would involve computing the aerodynamic responses to the characteristic motions, and using the mathematical model and the computed responses to obtain the aerodynamic (rather than the motion) response to a complex, but specified, motion. The response to the complex motion would also be computed directly, and compared to the one obtained using the mathematical model. Here the validity of the model would be demonstrated by agreement between the two aerodynamic response histories.

In this paper we review two mathematical model validation efforts effected with CFD techniques. In the first, Chyu and Schiff (Ref. 10) utilized two-dimensional unsteady-flow computations to validate a nonlinear aerodynamic mathematical model for the case of a freely-deflecting flap hinged to a stationary airfoil and immersed in a transonic flow. Validation of the model was demonstrated by close agreement of flap motion histories obtained with the model and those obtained with the coupled-equations approach. More recently, Katz and Schiff (Ref. 13) investigated the validity of a nonlinear aerodynamic mathematical model for low-rate multi-degree-of-freedom motions of a delta wing maneuvering at large angles of attack. Although computation of three-dimensional unsteady viscous flows by means of modeled equations of turbulent flow is not yet feasible, computation of unsteady three-dimensional inviscid flows by means of potential equations is currently possible. The authors of Ref. 13 employed a nonlinear vortex-lattice method to compute the aerodynamic responses to the characteristic motions called for by the model. Aerodynamic responses to complex specified motions were generated by means of the model and also from direct flowfield computations. The validity of the mathematical modeling concepts for the delta wing maneuvering in the high-angle-of-attack regime was demonstrated by close agreement of the corresponding force histories. In the following sections we discuss the procedures and results of Refs. 10 and 13, focusing in particular on the validation of the mathematical models and on the costs of the modeling approach relative to those of the coupled-equations approach.

2. AERODYNAMIC MATHEMATICAL MODELS

The form that an aerodynamic mathematical model takes depends upon the coordinates used and variables used to describe the motion, and on the types of aerodynamic phenomena that the model can encompass. In a series of papers, Tobak and his colleagues used the concept of a nonlinear indicial

function to derive aerodynamic models to describe, within certain assumptions, nonplanar maneuvers of bodies of revolution (Ref. 14) and of aircraft (Refs. 15,16). In this section an alternative derivation is reviewed which puts clearly into perspective the assumptions made in deriving the models, and the resulting limitations of the resulting models to accommodate certain types of aerodynamic phenomena.

2.1 Model Describing Aircraft Maneuvers

Consider a maneuvering aircraft whose center of mass travels an essentially straight-line path at constant flight velocity. The maneuvers can be described in terms of an aerodynamic axis system, in which the orientation of the aircraft relative to the oncoming wind is specified in terms of pitch and roll coordinates (Fig. 2). In this axis system the resultant angle of attack, σ, is defined as the angle between the body-fixed longitudinal X axis and the flight velocity vector. The plane containing σ is called the resultant-angle-of-attack plane. The roll, or bank, angle ψ is the angle between the normal to the resultant-angle-of-attack plane and a body-fixed axis (normal to the X axis) which lies in the plane of the wing. The resultant-angle-of-attack plane is free to rotate about the velocity vector with a rotation rate, measured relative to an inertia frame, of $\dot{\phi}$. Knowledge of the history of the maneuver is equivalent to knowledge of the histories of σ, ψ, and ϕ.

The aircraft undergoes a maneuver beginning at time zero. The instantaneous aerodynamic response to the maneuver at time t depends, in general, on the entire history of the maneuver. That is, the response depends on the histories of the motion variables over the interval from 0 to t. Mathematically, the response is a *functional* of the motion variables. Thus the pitching-moment coefficient, for example, can be expressed in the square-bracket notation of Volterra, as

$$C_m(t) \quad C_m[\sigma(\xi), \psi(\xi), \dot{\phi}(\xi)], \tag{1}$$

where ξ is a dummy time variable ranging from 0 to t. Note that $\dot{\phi}(\xi)$ appears in Eq. (1), rather than $\phi(\xi)$, because the aerodynamic response is independent of the orientation of the angle-of-attack plane (in contrast to that of the pilot) and depends only on the rate at which the σ plane is rotating.

If the motion is assumed to be differentiable, one can expand each of the variables $\sigma(\xi)$, $\psi(\xi)$, and $\dot{\phi}(\xi)$ in Taylor series about $\xi = t$. Knowledge of the past history of the motion is equivalent to knowing all of the coefficients of the series. Substituting these coefficients for the motion histories in Eq. (1) converts the pitching-moment response from a functional to a function, albeit a function of an infinite number of variables. Thus, the pitching-moment coefficient becomes

$$C_m(t) = C_m(\sigma(t), \dot{\sigma}(t), \ddot{\sigma}(t), \ldots, \psi(t), \dot{\psi}(t), \ddot{\psi}(t), \ldots, \dot{\phi}(t), \ddot{\phi}(t), \ldots) \tag{2}$$

The assumption that the motion history is differentiable immediately restricts the model to cases where the aerodynamic forces and moments are continuous. If sudden jumps in the aerodynamic response occurred, the aircraft would experience discontinuous accelerations, and this would violate the assumption of a differentiable motion history. Restriction to continuous forces rules out the capacity of the resulting mathematical model to treat the bi-valued aerodynamic responses characterizing static hysteresis and both time-invariant and time-dependent subcritical bifurcations (cf. Ref. 3). Within the restriction to continuous, single-valued, aerodynamic responses, one can make a further assumption that, for the slowly-varying motions typifying aircraft rigid-body motions, the aerodynamic response will have only a negligible dependence on the higher-order rate terms such as $\ddot{\sigma}(t), \dot{\sigma}(t), \ddot{\psi}(t), \dot{\psi}(t), \ddot{\phi}(t)$, etc., and thus they may be neglected in Eq. (2). This reduces the pitching-moment response to a function of a finite, rather than an infinite, number of variables. Consistent with the assumption of slow motion, one is justified in expanding Eq. (2) in a Taylor series about $\dot{\sigma}$ 0, $\dot{\psi}$ 0, and $\dot{\phi}$ 0. The resulting model is

$$\begin{aligned} C_m(t) \quad & C_m(\sigma(t), \psi(t), 0, 0, 0) + \frac{\dot{\psi} b}{2U} C_{m_\psi}(\sigma(t), \psi(t), 0, 0, 0) \\ & + \frac{\dot{\sigma} b}{2U} C_{m_\sigma}(\sigma(t), \psi(t), 0, 0, 0) + \frac{\dot{\phi} b}{2U} C_{m_\phi}(\sigma(t), \psi(t), 0, 0, 0) \end{aligned} \tag{3}$$

where b is the wing span, and the zeros refer to the motion rates. Equivalent expressions for the yawing- and rolling-moment coefficients, C_n and C_l, and for the axial-, side-, and normal-force coefficients, C_X, C_Y, C_N, are obtained by substituting these coefficients wherever C_m appears in Eq. (3). Again, the model applies to slowly varying motions of the aircraft, although the values of σ and ψ may be large. The mathematical model is seen to contain four terms, and each term can be identified with a specific, characteristic motion from which it may be evaluated. Thus, $C_m(\sigma(t), \psi(t), 0, 0, 0)$ is the pitching-moment coefficient that would be evaluated in a steady flow with σ and ψ held fixed at $\sigma(t)$, $\psi(t)$. The second term, C_{m_ψ}, is the contribution to the pitching-moment coefficient due to rolling motion, and can be evaluated for small-amplitude oscillations in ψ about ψ = const, with σ held fixed and ϕ fixed at zero. Similarly, the term C_{m_σ} is the contribution to the pitching-moment coefficient due to pitching motions, and can be evaluated for small-amplitude planar oscillations in σ about σ = const, with ψ held fixed and $\dot{\phi}$ fixed at zero. The last term, C_{m_ϕ}, is the rate of change of the pitching-moment coefficient with coning-rate parameter, $\dot{\phi}b/2U$, evaluated at $\dot{\phi}$ = 0, that would be determined from a steady coning motion with σ = const, ψ = const, and $\dot{\phi}$ = const. These characteristic motions are illustrated in Fig. 2.

2.2 Model Describing Flap Motions

Derivation of an aerodynamic mathematical model applicable to slowly-varying motions of a flap on an airfoil parallels that of the model, Eq. (3), describing the response to aircraft maneuvers. For the airfoil flap motions considered in Ref. 10, the coordinates illustrated in Fig. 3 were employed. The airfoil was a NACA 64A010 section hinged at the 75% chord point. The forward portion of the airfoil was held fixed parallel to the oncoming stream, while the flap was free to move about its pivot point. Positive values of the flap deflection angle, σ_f, and of the flap hinge-moment coefficient, C_h, are shown in Fig. 3. As illustrated, a positive value of C_h would tend to increase the flap deflection angle. For the single-degree-of-freedom flap motion, the hinge-moment coefficient is, in general, a functional of the flap deflection angle history, i.e., $C_h(t) = C_h[\sigma_f(\xi)]$. By means of the same logic described above for aircraft maneuvers, the functional can be reduced to the form

$$C_h(t) = C_h(\sigma_f(t),0) + \frac{\dot{\sigma}_f l}{V} C_{h_{\dot{\sigma}_f}}(\sigma_f(t),0) \tag{4}$$

where the reference length l is the chord length. As before, the model applies to slowly-varying motions of the flap, although the values of the flap deflection angle can be large. Again, each of the terms in Eq. (4) is identified with a particular characteristic motion from which it may be evaluated. Thus, the term $C_h(\sigma_f(t),0)$ is the hinge-moment coefficient that would be evaluated in a steady flow with the flap deflection angle held fixed at $\sigma_f(t)$. The remaining term, $C_{h_{\dot{\sigma}_f}}$, is the contribution to the hinge-moment coefficient due to flap motions, and can be evaluated for small-amplitude oscillations of the flap about a mean value of σ_f held fixed at the instantaneous value of $\sigma_f(t)$.

2.3 Issues of Model Applicability

Consistent with the assumptions made in their development, aerodynamic mathematical models at the level of Eqs. (3) and (4) are subject to the following restrictions: 1) the response to a steady motion is itself steady; 2) the response is a single-valued (although allowably nonlinear) function of the orientation of the body; and 3) the responses are linear in the motion rates. Restriction 1 rules out the possibility of modeling time-dependent aerodynamic bifurcations, that is, development of time-varying (periodic, quasi-periodic, or chaotic) responses to a steady motion, e.g., the time-varying flow observed surrounding a stationary circular cylinder in crossflow at Re > 50. However, recent modeling efforts (see Ref. 3), based on the concept of Fréchet differentiability of the aerodynamic response, include treatment of such time-varying flows. Restriction 2 precludes modeling the bi-valued aerodynamic responses characterizing static aerodynamic hysteresis which have been observed in cases of vortex asymmetry on slender bodies of revolution and on slender delta wings. However, this behavior can also be accomodated (see Ref. 1, and more recently, Ref. 3). The third restriction precludes modeling the nonlinear dependence of the aerodynamic response on the motion rates, and in particular, nonlinear dependence on $\dot{\phi}$, the coning rate. Such nonlinear variation with $\dot{\phi}$ has been observed experimentally (see Ref. 17), and can be incorporated in the model by performing the Taylor series expansion about $\dot{\alpha} = 0$, $\dot{\psi} = 0$, and $\dot{\phi} = \dot{\phi}(t)$ rather than about $\dot{\alpha} = \dot{\psi} = \dot{\phi} = 0$, as was done to obtain Eq. (3). This would result in an aerodynamic model equivalent to the one derived previously (Ref. 16) using the nonlinear indicial function approach.

The utility of the aerodynamic modeling approach depends on the ability of the model to treat the aerodynamic phenomena which occur in flight. In applying models analogous to Eq. (3), the general aircraft motion is decomposed into a sum of characteristic motions. The aerodynamic response to the general motion is *modeled* as a sum of responses to the characteristic motions. The actual response to the general motion will differ from the modeled response if aerodynamic phenomena excluded in developing the model are present. The assumption made in developing Eq. (3), that the aerodynamic responses are continuous, single-valued functions of the motion variables, restricts the model to cases where neither hysteresis nor time-dependent aerodynamic bifurcations occur. Within this restriction, the remaining causes for failure of the model to predict a general response would be either 1) significant nonlinear dependence of the aerodynamic responses on rates of motion within the range of rates actually experienced in flight, or 2) presence of significant interactions between responses to pairs characteristic motions. Examples of such interactions include those between responses to pitch oscillations and coning motion or between responses to roll oscillations and coning motion, i.e., terms such as $C_{m_{q\dot{\phi}}}$ or $C_{m_{p\dot{\phi}}}$ which have been excluded in deriving Eq. (3).

2.4 CFD Requirements for Validating Models

As discussed in Sec. 1, validation of a candidate mathematical model with the use of CFD methods involves computation of both the aerodynamic response to characteristic motions and the response to either specified complex motions or coupled-equations responses. From a CFD standpoint, the boundary conditions for the low-rate characteristic pitching, rolling, and coning motions are linear perturbations in $\dot{\alpha}$, $\dot{\psi}$, and $\dot{\phi}$, respectively, about the zero values associated with the steady characteristic motion. If flowfields were governed by linear partial differential equations, the linear boundary conditions guarantee that the responses to the characteristic motions would be linear in the rates. Also, the response to any general motion could be obtained from superposition of the responses to the characteristic motions, for such a solution would satisfy both the PDE's and BC's exactly. In this circumstance, models at the level of Eq. (3) would be exact for all cases.

However, the actual equations governing fluid flow are nonlinear, and the presence of nonlinear convection terms in the momentum equations give rise to the possibility of all the aerodynamic phenomena discussed above. Thus, to be useful in assessing the validity of a model, the computational method must be based on nonlinear flowfield equations. Approximating the flowfield equations with linearized PDE's will clearly be unsatisfactory for validating nonlinear models. Such models will

always appear to be valid, since the linearized flowfield equations cannot capture nonlinear aerodynamic effects. Thus, validation of limited aerodynamic models analogous to those of Eqs. (3) and (4) would require, at a minimum, a CFD method capable of demonstrating nonlinear aerodynamic behavior with the motion rates. In Ref. 10, Chyu and Schiff used a time-accurate method based on the nonlinear Euler equations to demonstrate the validity of the model, Eq. (4), for the case of an oscillating flap. The Euler equations are capable of capturing nonlinear behavior of both the steady and unsteady flowfield responses. Similarly, in Ref. 13, Katz and Schiff utilized a nonlinear vortex-lattice method to investigate the ability of the equivalent model, Eq. (3), to describe the nonlinear aerodynamic response to low-rate maneuvers of a delta wing. In the vortex-lattice technique, the flowfield is assumed to be governed by the incompressible potential equation, $\nabla^2\phi = 0$. Leading-edge separation is modeled by permitting vortex panels to shed from the leading edge of the wing, and the free vortex sheet is allowed to roll up in response to the local velocity fields. Although the PDE which describes the flowfield is linear, the boundary conditions are not. Allowing the free vortex sheets to roll up permits the method to encompass a nonlinear variation, if present, of the aerodynamic response with the rates (see Ref. 18).

Methods based on nonlinear, inviscid flowfield equations would appear adequate to validate aerodynamic models analogous to those of Eqs. (3) and (4). These computational methods cannot, however, incorporate aerodynamic phenomena such as onset of vortex asymmetry, vortex breakdown, and time-varying response to fixed boundary conditions. Thus, validation of aerodynamic models which purport to include these phenomena will require the use of methods based on nonlinear viscous flowfield equations.

3. VALIDATION FOR MANEUVERING DELTA WING

In the study reported in Ref. 13, CFD solutions were carried out for the unsteady three-dimensional flowfield surrounding a sharp-leading-edge delta wing to demonstrate the validity of the multi-degree-of-freedom mathematical model, Eq. (3). The flowfield was assumed to be governed by the potential equations, and a vortex-lattice method (VLM) was applied to solve the time-dependent equations.

3.1 Model Validation Procedure

The particular wing considered in Ref. 13 was a slender delta wing having an aspect ratio of unity (leading-edge sweep angle = 75.96°). The center of mass was fixed at the wing half-chord (x/c = 0.50). The values of the resultant angle of attack and roll angle considered are shown in Fig. 4. The resultant angle of attack σ ranged from 20° to 30°, while the roll angle ψ ranged from 0° (wing level) to 10°. The dimensionless rates $\dot{\sigma}b/2U$, $\dot{\psi}b/2U$, and $\dot{\phi}b/2U$, ranged up to 0.15. The procedure utilized for validating the aerodynamic mathematical model applicable to the wing had three phases. These were

1) Evaluate the aerodynamic responses to the characteristic motions from vortex-lattice computations.

2) Generate aerodynamic force and moment response histories to prescribed complex motions using the aerodynamic mathematical model and the aerodynamic data evaluated in phase 1.

3) Compare the histories obtained in phase 2 with force and moment histories that are, in principle, exact within the framework of the computational technique, namely those obtained by directly the vortex-lattice method to compute the response to the identical complex motions.

Demonstration of the validity of the mathematical modeling approach, as applied to the delta wing maneuvering in the high-angle-of attack regime, hinged on finding close agreement between the force and moment time-histories obtained from the two approaches.

3.2 Numerical Technique

In the computational procedure, the surface of the wing is divided into a number of bound vortex panels. The strengths of the bound panels are determined at each time step during the computation to enforce the boundary condition that there be no flow through the solid wing. Information describing the wing's maneuver enters the computation through the solid-surface boundary condition. Time-evolution of the wake behind the wing is modeled by allowing vortex panels to shed from the trailing edge at each time step. These wake panels have fixed strength and, upon leaving the wing, move with the local fluid velocity.

When a delta wing is maneuvering at high angle of attack, flow separates near the wing leading edges, and the separated fluid rolls up above and behind the wing to form concentrated vortices. For a sharp-edged wing, the separation line is essentially fixed at the sharp leading edge, and does not vary with changes in Reynolds number. In the vortex-lattice method, leading-edge separation is modeled in a manner analogous to that of trailing-edge separation, by allowing vortex panels to shed from lines of separation specified to remain at the leading edges and permitting them to move with the local flow velocity. Specification of the bound vortex strengths and free vortex positions yields the pressure distribution on the wing and, in turn, the nonlinear unsteady airloads (cf. Refs. 18-21). Details of the numerical method and a discussion of the accuracy of the computed results are found in Ref. 18.

3.3 Aerodynamic Response to Characteristic Motions

To obtain the aerodynamic data required by the mathematical model, Eq. (3), computations were carried out for the wing in each of the four characteristic motions shown in Fig. 2 at each value of resultant angle of attack and roll angle shown in Fig. 4. The steady-state term $C_k(\sigma(t),\psi(t))$, where C_k denotes any of the force or moment coefficients, was obtained from a computation in which the resultant angle of attack and roll angle were held fixed, and the flowfield was allowed to evolve until it reached a steady state. In an analogous manner the term $C_{k_\dot{\phi}}(\sigma(t),\psi(t))$ was obtained from a series of computations for steady coning motion in which the resultant angle of attack, roll angle, and coning-rate parameter were fixed, and the flowfield was allowed to evolve to a steady state. Note that to an observer fixed in the moving wing, the flowfield due to a steady coning motion is indeed time-invariant. The coefficient was then determined from the observed rate of change of the moment with coning-rate parameter, $\partial C_k/\partial(\dot{\phi}b/2U)$, evaluated at $\dot{\phi} = 0$.

The aerodynamic coefficient due to pitch oscillations, $C_{k_\alpha}(\sigma(t),\psi(t))$, was evaluated from small-amplitude harmonic pitch oscillations about the mean values of resultant angle of attack and roll angle shown in Fig. 4. The wing was specified to move according to:

$$\begin{aligned} \sigma &= \sigma_0 + \sigma_1 \sin\omega_1 t \\ \psi &= \psi_0 \\ \dot{\phi} &= 0 \end{aligned} \tag{5}$$

The amplitude of the harmonic motion, σ_1, was specified to be less than 2°. The aerodynamic damping coefficient was evaluated from the component of the aerodynamic response that was 90° out of phase with the wing motion. This rationale is easily seen by substituting the conditions describing the pitch oscillations (Eq. (5)) into the aerodynamic model to obtain (after a Taylor-series expansion about $\sigma = \sigma_0$ and omission of terms of $O(\sigma_1^2)$)

$$C_k(t) = C_k(\sigma_0,\psi_0) + \sigma_1 \sin\omega_1 t \frac{\partial C_k(\sigma_0,\psi_0)}{\partial\sigma} + \frac{\omega_1\sigma_1 b}{2U}\cos\omega_1 t C_{k_\alpha}(\sigma_0,\psi_0) \tag{6}$$

The coefficients in Eq. (6) were obtained from a Fourier integration of the response over one cycle of the motion, as shown for the normal-force coefficient response in Fig. 5. Thus

$$C_k(\sigma_0,\psi_0) = \frac{1}{2\pi}\int_0^{2\pi} C_k(t)\,d(\omega_1 t) \tag{7}$$

$$C_{k_\alpha}(\sigma_0,\psi_0) = \frac{1}{\pi\sigma_1}\int_0^{2\pi} C_k(t)\sin\omega_1 t\,d(\omega_1 t) \tag{8}$$

$$C_{k_\alpha}(\sigma_0,\psi_0) = \frac{2U}{\pi b\omega_1\sigma_1}\int_0^{2\pi} C_k(t)\cos\omega_1 t\,d(\omega_1 t) \tag{9}$$

The steady-state coefficient and its slope can be obtained either from the computations of the oscillatory motion (Eqs. (7) and (8)) or, preferably, from the computations of the steady motion described earlier.

In an analogous manner, the coefficient due to roll oscillations, $C_{k_\dot{\phi}}(\sigma(t),\psi(t))$, was evaluated for small-amplitude harmonic roll motions where

$$\begin{aligned} \sigma &= \sigma_0 \\ \psi &= \psi_0 + \psi_1 \sin\omega_2 t \\ \dot{\phi} &= 0 \end{aligned} \tag{10}$$

and the amplitude of the motion, ψ_1, was specified to be less than 2°. The roll damping coefficient was obtained from

$$C_{k_\dot{\phi}}(\sigma_0,\psi_0) = \frac{2U}{\pi b\omega_2\psi_1}\int_0^{2\pi} C_k(t)\cos\omega_2 t\,d(\omega_2 t) \tag{11}$$

The results of the computations for the characteristic motion are shown in Figs. 6-8. Generation of these diagrams of the aerodynamic coefficients required 36 individual computations, one for each of the four characteristic motions at the nine combinations of resultant angle of attack and roll angle shown in Fig. 4. The results confirm that, over the range of angles of attack and roll and over the range of rates considered, the aerodynamic responses to the characteristic motions are linear in the motion rates, and are single-valued functions of the angles. Thus, barring the presence of significant nonlinear interactions between the responses to pairs of characteristic motions, the aerodynamic model, Eq. (3), should prove to be valid.

3.4 Aerodynamic Response to Prescribed Complex Motions

The prescribed complex motions combined pitch oscillations, roll oscillations, and coning motion. The combined motions all had the basic form:

$$\begin{aligned} \sigma &= \sigma_0 + \sigma_1 \sin\omega_1 t, & \dot{\sigma} &= \omega_1\sigma_1 \cos\omega_1 t \\ \psi &= \psi_0 + \psi_1 \sin\omega_2 t, & \dot{\psi} &= \omega_2\psi_1 \cos\omega_2 t \\ \phi &= \omega_3 t, & \dot{\phi} &= \omega_3 \end{aligned} \tag{12}$$

Aerodynamic response histories of the pitching-moment, rolling-moment, and normal-force coefficients were computed from Eq. (3), with the aerodynamic coefficients obtained from table look-ups of the data shown in Figs. 6-8, and values of $\dot{\sigma}$, $\dot{\psi}$, and $\dot{\phi}$ obtained from Eq. (12). The aerodynamic responses to the combined motions were also obtained from direct VLM computations. As was mentioned earlier, the use of the identical vortex-lattice method to evaluate both the nonlinear responses to the characteristic motions and the responses to the general large-amplitude motions ensures a consistent treatment of the time-history effects. Thus discrepancies, if present, between results obtained using the modeling approach and those obtained from the direct VLM computations must be attributed to the inadequacy of the aerodynamic model.

3.5 Validation of the Mathematical Model

The motions considered in Figs. 9 and 10 combine pitch and roll oscillations, having amplitudes of 3° and reduced frequencies ranging up to 0.15, superimposed on a steady coning motion in which σ_0 = 25° and ψ_0 = 5°. Typical responses of the pitching-moment, rolling-moment, and normal-force coefficients to these motions are shown in Figs. 9 and 10 as functions of wing-chord lengths of travel, Ut/c. In each figure the dotted lines show the histories obtained from the mathematical model, Eq. (3), while the solid lines indicate the results obtained from direct VLM computations. For the direct computations, the overshoot indicated at the beginning of each time-history occurs because the motion was started impulsively from rest. It will be recalled that the mathematical models described in Sec. 2 were obtained under the assumption of slowly-varying motions, and are not expected to model the impulsive start. If the short initial transient period is excluded, in both cases the aerodynamic responses obtained from the model show reasonable agreement with those obtained from direct computation. The differences between the results obtained from the model and those from direct VLM computation can be attributed to errors in the interpolations in the table look-ups based on Figs. 6-8 that were required to obtain the coefficients of the model. This would indicate that, for these cases, no significant interactions existed between responses to pairs of characteristic motions, such as the interaction between the responses to the pitch oscillation and coning motion, or between the responses to the roll oscillation and coning motions.

The agreement shown in Figs. 9 and 10 would tend to indicate that, over the range of angles and motion rates considered in Ref. 13, the mathematical model presented in Eq. (3) is adequate to describe the aerodynamic response to complex motions of the delta wing. In actuality, for the range of pitch and roll rates considered, the contributions of the pitch-damping and roll-damping terms in Eq. (3) were almost negligible. As a result, the aerodynamic interactions between pairs of the characteristic motions, which are of higher order than the damping terms, must be negligible. In these circumstances it is not surprising that the mathematical model would appear to be validated. Thus, while the VLM computations confirm the validity of the model for the cases considered, the cases themselves do not conclusively demonstrate the limits of the range of motions and rates for which the model is valid. Nevertheless, the procedure discussed indicates the way in which CFD methods can be used to validate a candidate mathematical model.

4. VALIDATION FOR FLAP MOTIONS

In the study reported in Ref. 10, CFD solutions were obtained for the two-dimensional unsteady transonic flowfield surrounding a wing and moving flap (Fig. 3) to demonstrate the validity of the nonlinear mathematical modeling concepts. The flowfield was assumed to be governed by the time-dependent inviscid Euler equations, and an implicit time-accurate finite-difference technique was applied to obtain the solutions. The flowfield equations were solved on a moving body-conforming computational mesh, which deformed in response to the flap motion (Fig. 11). Details of the numerical technique, boundary conditions, and mesh-generation method are found in Ref. 10.

4.1 Model Validation Procedure

The airfoil considered in Ref. 10 was a NACA 64A010 section, hinged at the 75% chord point. The forward portion of the airfoil was held fixed parallel to the oncoming stream, while the flap was free to pivot about its hinge point with deflection angles ranging up to 20°. The free-stream Mach number was held fixed at 0.8. Validation of the aerodynamic mathematical model involved:

1) evaluating the aerodynamic response to the characteristic motions from Euler-equation computations.

2) utilizing the equation governing mechanically unconstrained motions of the flap,

$$I\ddot{\sigma}_f(t) \quad qSlC_h(t) \tag{13}$$

together with the aerodynamic mathematical model, Eq. (4), to predict a series of flap motion histories.

3) simultaneously solving the flowfield equations and flap-motion equation to obtain "exact" flap motion histories with the same initial conditions.

The validity of the modeling approach for this nonlinear, transonic flow case was demonstrated by close agreement of the motion histories obtained from the two approaches.

4.2 Hinge-Moment Response to Characteristic Motions

To obtain the hinge-moment coefficients required by the mathematical model, computations were carried out for the flap in both required characteristic motions. The steady-state term $C_h(\sigma_f)$ was obtained from a computation in which the flap deflection angle was held fixed. A time-invariant mesh was employed, and the flowfield was allowed to evolve until it reached a steady state. The resulting static hinge-moment coefficient, obtained from spatial integration of the surface-pressure distributions, is shown in Fig. 12. The hinge moment is statically stabilizing, tending to oppose the flap deflection. The nonlinear behavior of the static hinge moment is associated with rearward movement and increase in strength of the upper-surface shock wave with increasing flap deflection. For low flap deflection angles, at the Mach number considered, the shock wave was located ahead of the flap hinge point. As the flap deflection was increased beyond 3°, the shock moved onto the flap, and its rearward movement along the flap, for $3° \leq \sigma_f \leq 10°$, caused the greatly increased slope of the hinge-moment curve. For values of $\sigma_f > 17°$, the shock wave was essentially fixed at the trailing edge.

The contribution to the hinge-moment coefficient due to flap oscillations, $C_{h_{\dot{\sigma}_f}}$, were evaluated from the periodic response to small-amplitude harmonic flap oscillations. The flap motion was specified as

$$\sigma_f(t) = \sigma_{f_m} + \sigma_{f_1} \sin \omega t \tag{14}$$

where σ_{f_m} ranged from 0° to 20°, and σ_{f_1} was small, usually 0.5°. The reduced frequency of the motion, $k = \omega l / V$, was held fixed at 0.15 for all cases. Starting from an initial steady solution obtained at $\sigma_f = \sigma_{f_m}$, computations were carried out for three cycles of the motion to ensure that a periodic solution had been obtained. The hinge-moment damping coefficient was evaluated from the component of the aerodynamic response that was 90° out of phase with the flap motion. The results are shown in Fig. 13 as a function of the mean flap deflection angle. Note that at the transonic flow conditions considered in Ref. 10, the damping coefficient is a highly nonlinear function of the flap deflection. For values of $\sigma_{f_m} \leq 3°$ the coefficient is negative, or dynamically stabilizing. However, for mean flap deflections ranging between 3° and 17°, the coefficient is positive (dynamically destabilizing) and would cause an unconstrained flap oscillation to increase in amplitude. The nonlinear behavior of the damping coefficient is qualitatively related to the behavior of the static hinge moment. In particular, the decrease in dynamic stability is linked to the increase in slope of the static hinge-moment curve (see Ref. 22 for a detailed discussion).

4.3 Flap Motion Histories

Oscillatory time-histories of the flap motion were generated using the flap equation of motion, Eq. (13), with the instantaneous hinge-moment coefficient specified by the nonlinear aerodynamic model. In these computations, the flap moment of inertia was chosen to give a value of reduced frequency close to the one specified for the characteristic-motion computations. After initial values of the flap deflection angle and velocity were specified, the equation of motion was solved numerically to obtain the motion histories. At each time step the hinge-moment coefficient was specified by Eq. (4), where the terms $C_h(\sigma_f(t))$ and $C_{h_{\dot{\sigma}_f}}(\sigma_f(t))$ were obtained from table look-ups in Figs. 12 and 13, respectively. Corresponding histories of the flap motion were also predicted using the coupled-equations approach.

Time-histories of flap motion, generated with both the modeling approach and the coupled-equations approach are shown in Figs. 14 and 15. The motion resulting when the flap was released from rest with an initial deflection angle $\sigma_{f_0} = 4.0°$ is shown in Fig. 14. In this case the stabilizing portion of the hinge-moment damping curve governed the motion, and the amplitude of the oscillation decayed smoothly. In contrast, when the flap was released with a slightly larger initial deflection, $\sigma_{f_0} = 4.5°$, the dynamically destabilizing portion of the damping curve caused the amplitude of the oscillation to grow rapidly (Fig. 15). In both cases, however, the motion histories obtained using the aerodynamic mathematical model were in good agreement with the "exact" motion histories obtained from the coupled equations. This confirmed the ability of the mathematical model, Eq. (4), to describe the unsteady aerodynamic response in this highly nonlinear transonic flow. On the other hand, a motion history generated with an aerodynamic model which does not account for nonlinear unsteady aerodynamic contributions (i.e., Eq. (4), but with the value of the damping term $C_{h_{\dot{\sigma}_f}}$ held fixed for all σ_f at the value obtained at $\sigma_f = 0°$) failed to predict the undamped growth of the of the flap oscillation (Fig. 15).

5. DISCUSSION

The agreement between the force and moment histories obtained for the delta wing using the modeling approach and those obtained from direct CFD computations confirmed the ability of the model to describe the unsteady aerodynamic response to complex motions, at least within the limited range of motions and rates considered. Similarly, the agreement between the flap motion histories obtained with the coupled-equations approach and those generated with the model confirmed the capacity of the model to adequately describe the unsteady, nonlinear aerodynamic response to arbitrary flap motions. The success of the modeling approach in this case points the way to approach future problems involving unsteady motions. In our view, for cases where mathematical models are valid, the modeling approach will be more economical and more versatile than the coupled-equations approach. Further, use

of the modeling approach will give better insight into the underlying physics than can be obtained through use of the coupled-equations approach.

First, regarding costs, we note that the computation of motion histories from the vehicle equations of motion requires negligible computational effort in comparison with that needed for computations of time-dependent flowfields. Consequently, with the modeling approach, once the initial effort of evaluating the aerodynamic responses to the characteristic motions is expended, computation of motion histories would be relatively inexpensive. Regarding versatility, the modeling approach makes it easy to introduce changes into the aircraft's equations of motion (e.g., changes in vehicle mass or moment of inertia, or inclusion of a model of a control system) and to evaluate their effects at low cost, since the aerodynamic data within the mathematical model will remain unchanged. In contrast, in the coupled-equations approach the simplest change in the aircraft's equations of motion would require a complete reevaluation of the flowfield and motion response.

Second, the modeling approach would appear to give better insight into the physics governing the unsteady flow than would the coupled- equations approach. If an undamped or divergent motion results from coupled-equations computations, it would be difficult to identify the aerodynamic phenomena causing the instability. On the other hand, computations carried out in terms of the characteristic motions permit an investigation of the underlying aerodynamic mechanisms. For the transonic flap motions considered in Ref. 10, these computations indicated that it was the rearward movement of the upper-surface shock wave that caused the large change on the slope of the static hinge-moment curve. It was also possible to show how the change in the static hinge-moment coefficient was related to the destabilizing behavior of the hinge-moment damping coefficient. Further, the modeling approach is compatible with established methods for determining the stability of motions. In the case of the flap, knowledge of the behavior of the damping coefficient with increasing deflection, obtained from the characteristic motion computations, permitted prediction of the change from a damped to an undamped oscillation with increased initial deflection angle that was subsequently observed. Thus, the nonlinear modeling approach would appear to be the method of choice in the design of flight control systems and in flight simulations.

6. CONCLUDING REMARKS

Applications of CFD methods to demonstrate the regimes of validity of nonlinear aerodynamic mathematical models for the case of a maneuvering delta wing, and for the case of an oscillating flap on an airfoil in transonic flow, are discussed. The assumptions underlying the development of the models are reviewed, and the ensuing limitations on the aerodynamic phenomena that the resulting models can accommodate are discussed. The class of mathematical models considered, where the nonlinear aerodynamic responses are continuous single-valued functions of the motion variables, was found to be adequate for the types of aerodynamic phenomena that were in play. Extension of the mathematical models to encompass a wider variety of possible aerodynamic phenomena, including bi-valued aerodynamic responses and time-varying responses to steady motions is currently being pursued.

The economic and conceptual advantages of the modeling approach over that of coupled, simultaneous, solutions of the flowfield and kinematic equations of motion in predicting flight vehicle motion histories are illustrated. The modeling approach, when valid, eliminates the need for costly repetitive computation of flowfield solutions when multiple motion histories must be determined.

REFERENCES

1. Tobak, M. and Schiff, L. B., "Aerodynamic Mathematical Modeling - Basic Concepts," AGARD Lecture Series No. 114 on Dynamic Stability Parameters, Paper No. 1, March 1981.

2. Tobak, M. and Schiff, L. B., "The Role of Time-History Effects in the Formulation of the Aerodynamics of Aircraft Dynamics," AGARD CP-235, Dynamic Stability Parameters, Paper No. 26, May 1978.

3. Tobak, M. and Chapman, G. T., "Problems in Nonlinear Flight Dynamics Involving Aerodynamic Bifurcations," AGARD Symposium on Unsteady Aerodynamics - Fundamentals and Applications to Aircraft Dynamics, Paper No. 25, May, 1985.

4. Hui, W. H. and Tobak, M., "Applications of Bifurcation Theory to Aircraft Dynamics," AGARD Symposium on Unsteady Aerodynamics - Fundamentals and Applications to Aircraft Dynamics, Paper No. 26, May, 1985.

5. Iliff, K. W., "Extraction of Aerodynamic Parameters for Aircraft at Extreme Flight Conditions," AGARD Symposium on Unsteady Aerodynamics - Fundamentals and Applications to Aircraft Dynamics, Paper No. 24, May, 1985.

6. Malcolm, G. N., "Rotary and Magnus Balances," AGARD Lecture Series No. 114 on Dynamic Stability Parameters, Paper No. 6, March, 1981.

7. Hanff, E. S., "Dynamic Nonlinear Airloads - Representation and Measurement," AGARD Symposium on Unsteady Aerodynamics - Fundamentals and Applications to Aircraft Dynamics, Paper No. 27, May, 1985.

8. Ballhaus, W. F. and Goorjian, P. M., "Computation of Unsteady Transonic Flow by the Indicial Method," AIAA Journal, Vol. 16, No. 2, Feb. 1978, pp. 117-124.

9. Rizzetta, D. P., "Time-Dependent Response of a Two-Dimensional Airfoil in Transonic Flow," AIAA Journal, Vol. 17, No. 1, Jan. 1979, pp. 26-32.

10. Chyu, W. J. and Schiff, L. B., "Nonlinear Aerodynamic Modeling of Flap Oscillations in Transonic Flow - A Numerical Validation," AIAA Journal, Vol. 21, No. 1, Jan. 1983, pp. 106-113.

11. Steger, J. L. and Bailey, H. E., "Calculation of Transonic Aileron Buzz," AIAA Journal, Vol. 18, No. 3, March 1980, pp. 249-255.

12. Gallaway, C. R. and Hankey, W. L., "Free-Falling Autorotating Plate," AIAA Paper 84-2080, August, 1984.

13. Katz, J. and Schiff, L. B., "Modeling of the Aerodynamic Response to Arbitrary Aircraft Maneuvers - A Numerical Validation," AIAA Paper 84-2079, August, 1984.

14. Levy, L. L. and Tobak, M., "Nonlinear Aerodynamics of Bodies of Revolution in Free Flight," AIAA Journal, Vol. 8, No. 12, Dec. 1970, pp. 2168-2171.

15. Tobak, M. and Schiff, L. B., "Generalized Formulation of Nonlinear Pitch-Yaw-Roll Coupling: Part 1 - Nonaxisymmetric Bodies," AIAA Journal, Vol. 13, No. 3, March 1975, pp. 323-326.

16. Tobak, M. and Schiff, L. B., "Generalized Formulation of Nonlinear Pitch-Yaw-Roll Coupling: Part 2 - Nonlinear Coning-Rate Dependence," AIAA Journal, Vol. 13, No. 3, March 1975, pp. 327-332.

17. Malcolm, G. N., "New Rotation-Balance Apparatus for Measuring Airplane Spin Aerodynamics in the Wind Tunnel," J. Aircraft, Vol. 16, No. 4, April 1979, pp. 264-268.

18. Katz, J., "Lateral Aerodynamics of Delta Wings with Leading-Edge Separation," AIAA Journal, Vol. 22, No. 3, March 1984, pp. 323-328.

19. Levin, D. and Katz, J., "A Vortex-Lattice Method for the Calculation of the Nonsteady Separated Flow over Delta Wings," AIAA Paper 80-1803, August, 1980.

20. Katz, J., "Method for Calculating Wing Loading During Maneuvering Flight Along a Three-Dimensional Curved Path," J. Aircraft, Vol. 16, No. 11, Nov. 1979, pp. 739-741.

21. Levin, D., "A Vortex Lattice Method which Predicts the Longitudinal Dynamic Stability Derivatives of Oscillating Delta Wings," AIAA Paper 81-1876, August 1981.

22. Schiff, L. B. and Tobak, M., "Some Applications of Aerodynamic Formulations to Problems in Aircraft Dynamics," AGARD Lecture Series No. 114 on Dynamic Stability Parameters, Paper No. 16, March 1981.

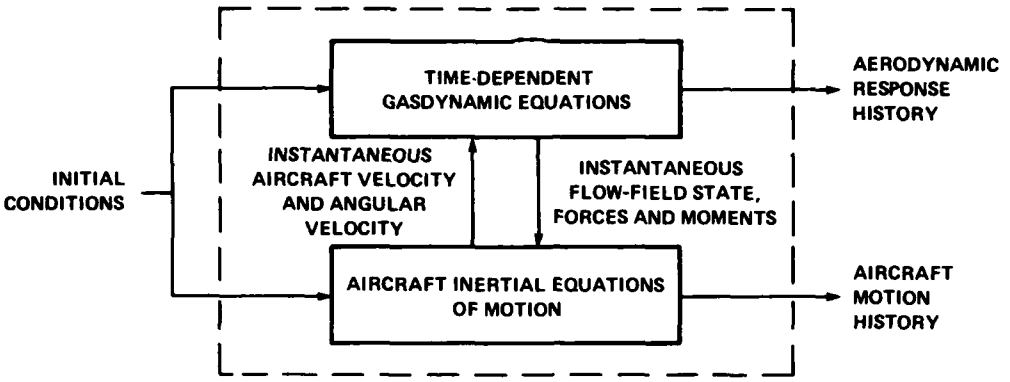

(a) Coupled flowfield and inertial equations approach.

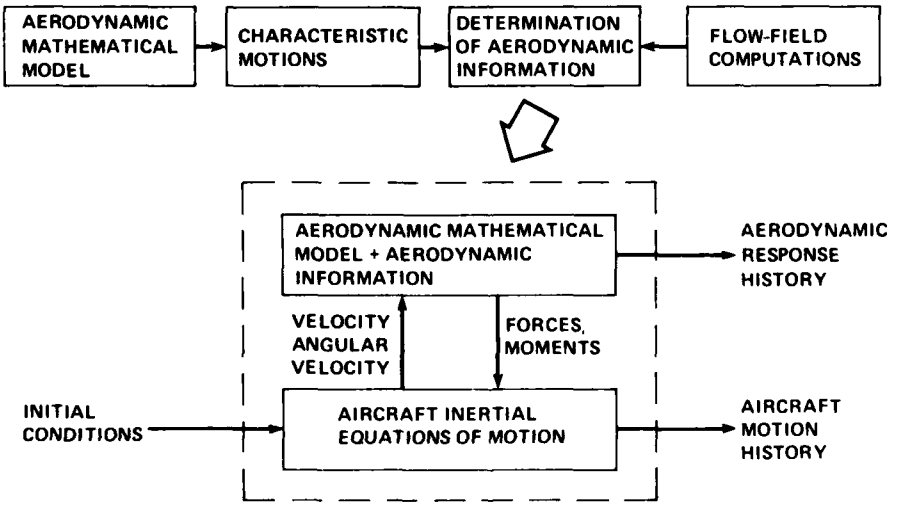

(b) Aerodynamic mathematical modeling approach.

Fig. 1. Approaches to applying CFD methods to predict aerodynamic responses and aircraft motion histories.

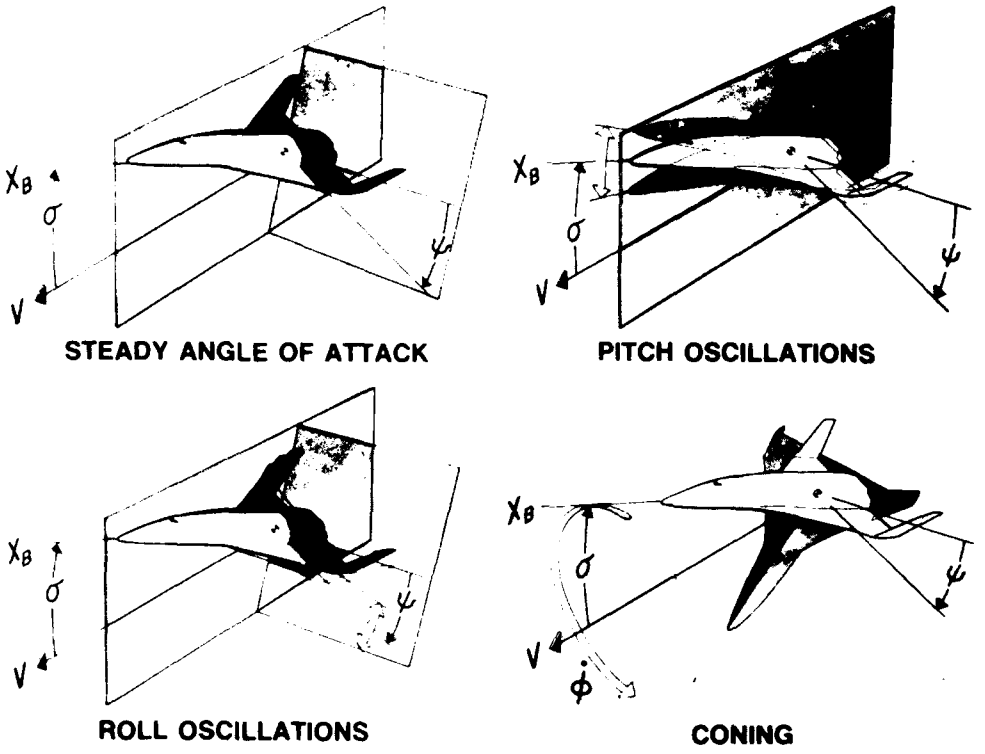

Fig. 2. Aerodynamic axis system and characteristic motions obtained assuming linear variation of the response on the motion rates.

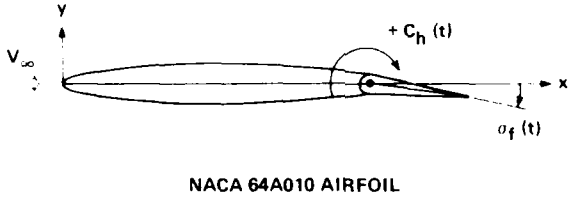

Fig. 3. Coordinates and notation for flap motion.

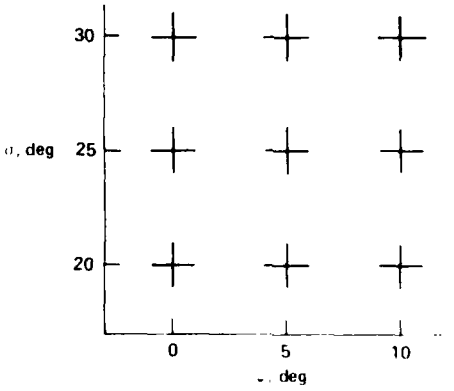

Fig. 4. Range of angle of attack σ and roll angle φ considered in determining the stability and control coefficients for the mathematical model (Ref. [ ]).

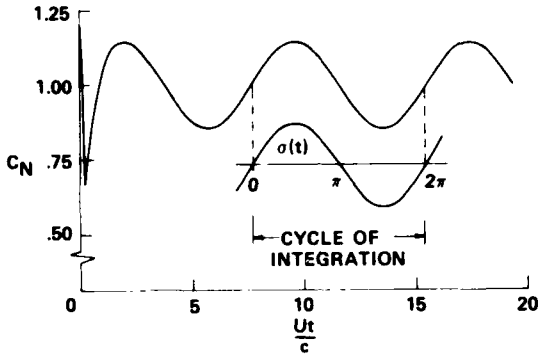

Fig. 5. Fourier integration of the normal-force response to evaluate the aerodynamic coefficients from Equations (7)-(9) (Ref. 13).

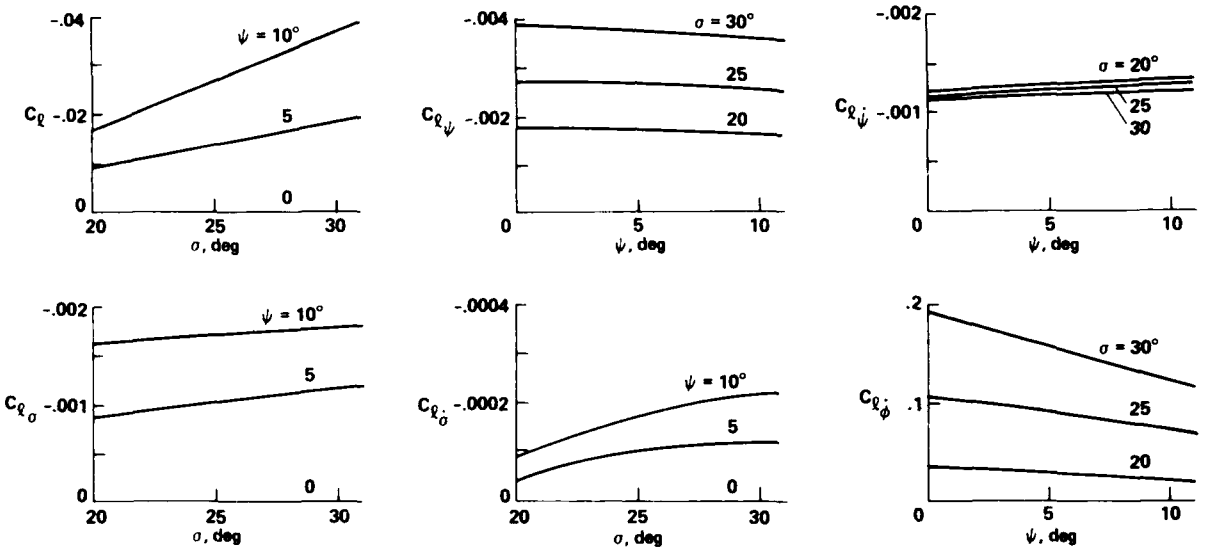

Fig. 6. Rolling-moment coefficients of delta wing evaluated from characteristic motions (Ref. 13).

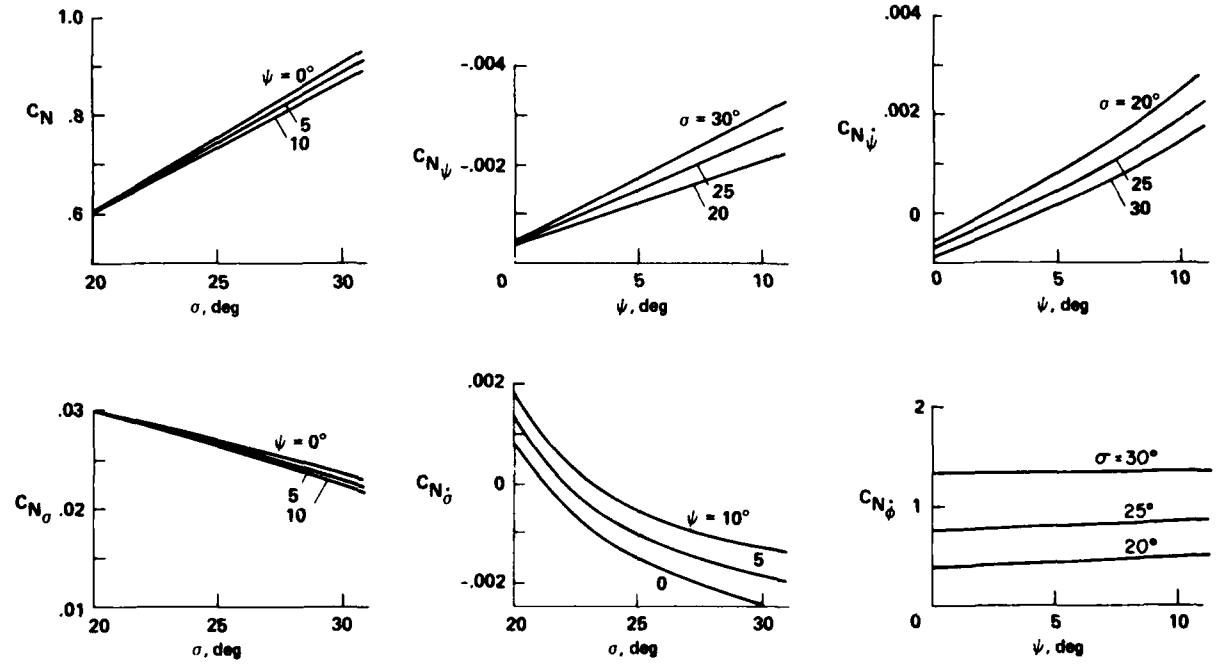

Fig. 7. Normal-force coefficients of d lta wing evaluated from characteristic motions (Ref. 13).

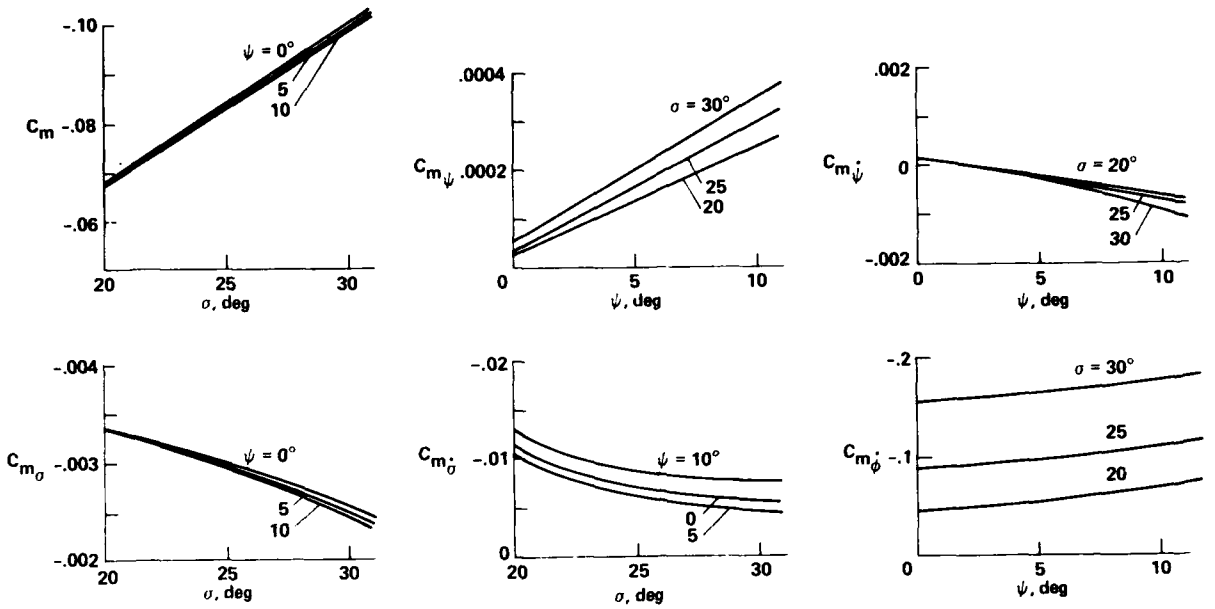

Fig. 8. Pitching-moment coefficients of delta wing evaluated from characteristic motions (Ref. 13).

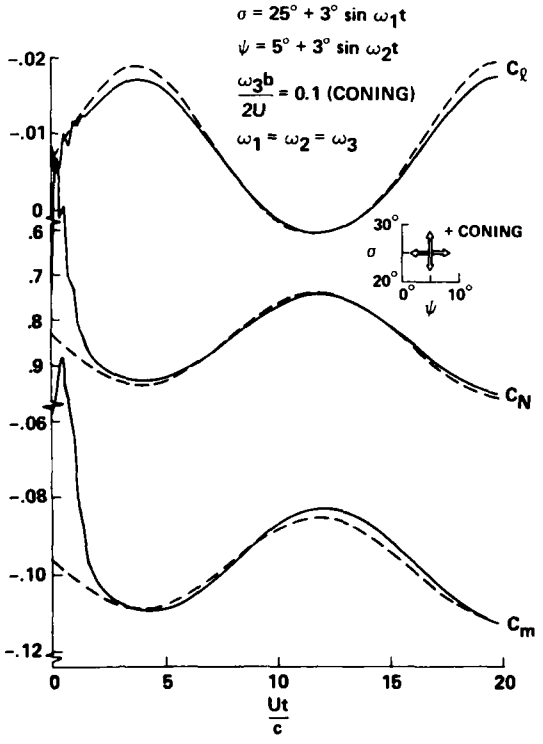

Fig. 9. Aerodynamic response of delta wing to combined pitch oscillations, roll oscillations, and coning motion (Ref. 13).

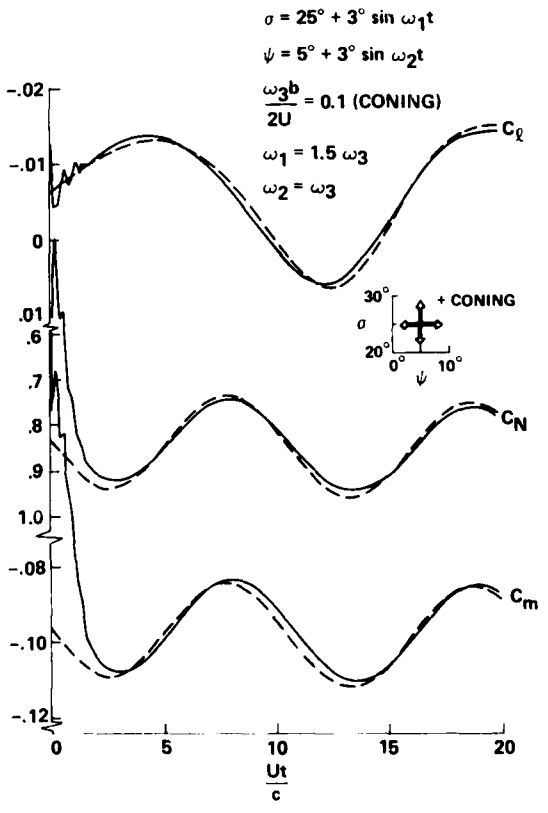

Fig. 10. Aerodynamic response of delta wing to combined pitch oscillations, roll oscillations, and coning motion (Ref. 13).

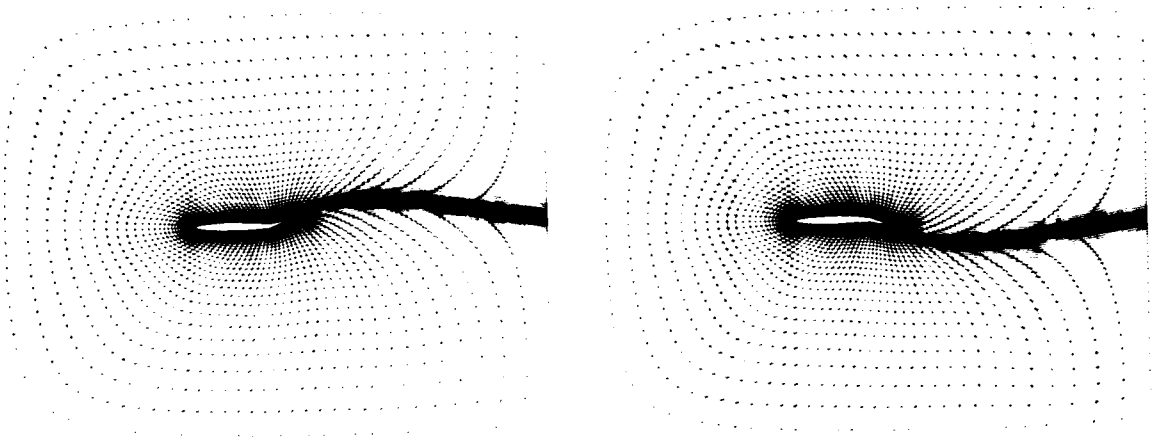

Fig. 11. Typical body-conforming grids with flap at extreme deflection angles (Ref. 10).

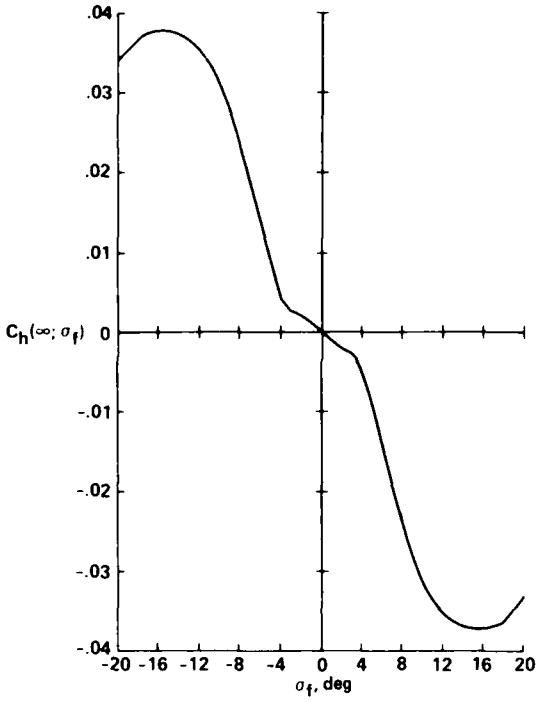

Fig. 12. Static hinge-moment coefficient: M = 0.8 (Ref. 10).

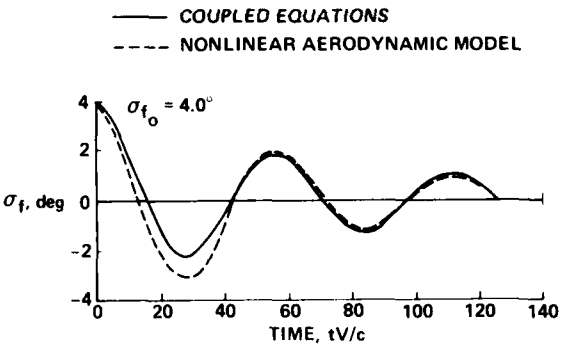

Fig. 14. Time-history of flap deflection; σ_{f_o} = 4.0° (Ref. 10).

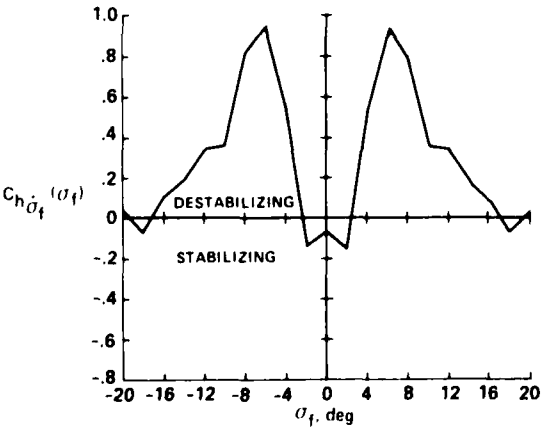

Fig. 13. Hinge-moment damping coefficient: M = 0.8 (Ref. 10).

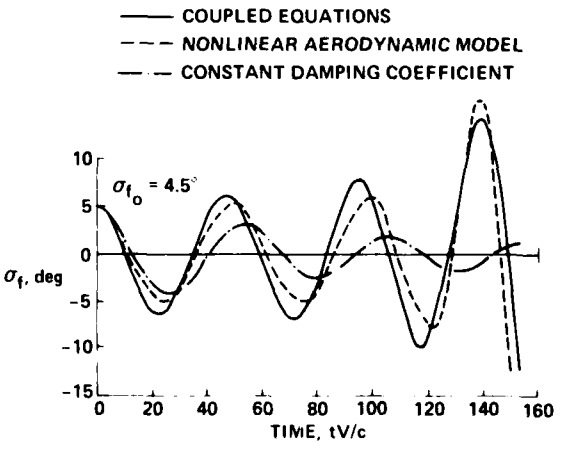

Fig. 15. Time-history of flap deflection; σ_{f_o} = 4.5° (Ref. 10).

ETUDE DU COMPORTEMENT TRANSITOIRE D'UN AVION AU VOISINAGE DE POINTS DE BIFURCATION

par
P. GUICHETEAU

O.N.E.R.A.
29, Avenue de la Division Leclerc - 92322 CHATILLON CEDEX
France

RESUME

Le comportement transitoire d'un avion au voisinage de points de bifurcation peut être étudié par l'application de la méthode des projections sur un système différentiel réduit dont on connaît analytiquement toutes les non-linéarités [1] .

En utilisant le même principe, la méthode proposée ici s'affranchit de la connaissance explicite des non-linéarités et ne nécessite pas la réduction du système différentiel étudié. Plusieurs applications à un avion de combat typique montrent l'intérêt de cette dernière approche.

1. INTRODUCTION

Depuis plusieurs années, l'ONERA élabore une méthodologie d'étude des pertes de contrôle à grande incidence ou en mouvement de roulis rapide basée sur la théorie des bifurcations. Les codes numériques développés permettent le calcul des surfaces d'équilibre et de bifurcation d'un avion complet. L'interprétation de ces résultats conduit à la prédiction du comportement global de l'avion [2] .

Les points de bifurcation usuellement rencontrés sont soit des points de retournement, soit des points de bifurcation de Hopf. En un point de retournement une valeur propre du système linéarisé est nulle. La surface d'équilibre présente un pli et, en simulation, un phénomène de saut peut être observé lors du franchissement de ce point limite de stabilité (fig. 1). En un point de bifurcation de Hopf, deux valeurs propres du système linéarisé sont imaginaires pures. Suivant la nature des non-linéarités du système, la bifurcation de Hopf peut être soit subcritique soit supercritique. Dans le premier cas, le point de bifurcation est instable et une perturbation de celui-ci conduit à l'apparition d'un cycle limite de grande amplitude (fig. 2a). Dans le deuxième cas, le point de bifurcation est stable et seul son franchissement peut faire apparaitre un cycle limite dont l'amplitude est proportionnelle à la valeur du franchissement (fig. 2b).

En simulation il a été observé que le franchissement des bifurcations n'entrainait pas toujours une brusque variation des paramètres en vol. Il est donc apparu nécessaire de rechercher un moyen susceptible de caractériser le mouvement transitoire au voisinage des points de bifurcation afin de pouvoir classer ces derniers suivant leur "degré de gravité" : lent ou rapide, convergent ou divergent.

Généralement, le comportement transitoire des systèmes différentiels au voisinage des points de bifurcation est étudié en effectuant un développement asymptotique de la solution d'un système différentiel réduit, approchant les équations initiales, dont on suppose connues explicitement toutes les non-linéarités.

S'agissant ici d'une application au système complet des équations de la mécanique du vol, la connaissance a priori des non-linéarités et en particulier des non-linéarités du modèle aérodynamique de l'avion étudié n'est pas envisageable. La méthode proposée ici s'affranchit de cette contrainte, et procède en deux étapes. La première consiste à réduire la dimension du problème en effectuant tout d'abord la projection du mouvement dans le sous-espace associé à la(aux) valeur(s) propre(s) critique(s). Ensuite, l'association de l'approximation au 1er ordre de la solution et d'un lissage polynomial ou bi-polynomial permet de ramener le système à la dimension 1 pour l'étude des points de retournement et à la dimension 2 pour la bifurcation de Hopf. Dans la 2ème étape, la stabilité du point de bifurcation est qualifiée en testant des grandeurs caractéristiques issues de l'étude asymptotique du système différentiel réduit précédemment déterminé. Ainsi, il est loisible de prédire la stabilité ou l'instabilité des points de retournement et de qualifier le mouvement du système complet dans leur voisinage. De même, il est possible de déterminer le caractère subcritique ou supercritique des points de bifurcation de Hopf.

2. SYSTEME D'EQUATIONS ETUDIE

Le système différentiel non linéaire des équations complètes de la mécanique du vol est ramené à la forme générale :

$$\dot{x} = F(x, u)$$

dans laquelle

x est un vecteur de dimension 8 appelé vecteur d'état

$$x^T : (\alpha\ \beta\ V\ p\ q\ r\ \theta\ \varphi)$$

u est un vecteur de dimension 4 appelé vecteur de commande

$$u^T : (\delta l\ \delta m\ \delta n\ \delta_x)$$

F est un ensemble de 8 fonctions, continues dérivables non linéaires dépendant à la fois de l'état et de la commande, issues des équations du mouvement.

$$m[\dot{V}\cos\alpha\cos\beta - V(\sin\alpha\cos\beta\,\dot{\alpha} + \cos\alpha\sin\beta\,\dot{\beta}) + V(q\sin\alpha\cos\beta - r\sin\beta)]$$
$$= -mg\sin\theta + \frac{1}{2}\rho S V^2 C_x + F_x$$
$$m[\dot{V}\sin\beta + V\cos\beta\,\dot{\beta} + V(r\cos\alpha\cos\beta - p\sin\alpha\cos\beta)]$$
$$= mg\cos\theta\sin\phi + \frac{1}{2}\rho S V^2 C_y$$
$$m[\dot{V}\sin\alpha\cos\beta + V(\cos\alpha\cos\beta\,\dot{\alpha} - \sin\alpha\sin\beta\,\dot{\beta}) + V(p\sin\beta - q\cos\alpha\cos\beta)]$$
$$= mg\cos\theta\cos\phi + \frac{1}{2}\rho S V^2 C_z + F_z$$
$$A\dot{p} - E\dot{r} + (C-B)qr - Epq = \frac{1}{2}\rho S\ell V^2 C_\ell$$
$$B\dot{q} + (A-C)rp + E(r^2 - p^2) = \frac{1}{2}\rho S\ell V^2 C_m$$
$$C\dot{r} - E\dot{p} + (B-A)pq + Erq = \frac{1}{2}\rho S\ell V^2 C_n$$
$$\dot{\phi} = p + tg\theta(q\sin\phi + r\cos\phi)$$
$$\dot{\theta} = q\cos\phi - r\sin\phi$$

Les non-linéarités de ce système sont nombreuses et peuvent être classées en deux catégories :

- la première renferme celles qui sont intrinsèques au système et qui sont dues à l'écriture des équations d'un solide dans l'espace (lignes trigonométriques et couples gyroscopiques)

- la seconde contient celles qui proviennent du modèle aérodynamique de l'avion considéré.

Le modèle d'avion utilisé est celui d'un avion de combat fictif à aile haute et empennage arrière. Son modèle aérodynamique, dont la validité s'étend à des incidences $-10° \leq \alpha \leq 90°$ et des dérapages $-40° \leq \beta \leq 40°$ ne comporte pas d'hystérésis.

Chacun des six coefficients globaux $C_x, C_y, C_z, C_\ell, C_m, C_n$, s'exprime de façon indépendante en fonction des paramètres d'influence : α, β, p, q, r, gouvernes.

Ainsi les non-linéarités et les couplages aérodynamiques s'expriment dans un développement en série de Taylor autour des valeurs de référence (état nominal) définies de la façon suivante :

$$\alpha, \beta = 0, \quad p = q = r = 0., \quad \delta\ell = \delta m = \delta n = 0.$$

L'expression générale des coefficients est de la forme :

$$C = C_o(\alpha, \beta = 0, p = q = r = 0, \delta\ell = \delta m = \delta n = 0) + \Delta C(\alpha, \beta) + \Delta C(\alpha, \delta\ell) + \cdots + \Delta C(\alpha, p) + \cdots$$

- les coefficients C_o sont appelés coefficients nominaux. Ils sont non linéaires en fonction de l'incidence

- les termes $\Delta C(\alpha, x)$ expriment la variation par rapport à sa courbe nominale, du coefficient C, en fonction du paramètre x. Ce sont des fonctions paires ou impaires du paramètre x suivant la nature du coefficient ΔC et de x.

3. QUALIFICATION DES BIFURCATIONS A L'AIDE DE LA METHODE DES PROJECTIONS

Le principe de la méthode consiste à étudier la projection du mouvement du système dans l'espace engendré par le (s) vecteur (s) propre (s) associé (s) aux valeurs propres critiques (à partie réelle nulle) [3].

Les autres valeurs propres du système étant supposées à partie réelle négative, après une perturbation et lorsque les modes stables seront amortis, le système évoluera dans un voisinage de l'espace engendré par les vecteurs propres associés aux valeurs propres critiques.

Soit (x_o, μ_o) un point d'équilibre du système ($F(x, \mu) = 0$). La stabilité du point d'équilibre vis-à-vis de perturbations sur l'état peut être étudiée en effectuant un développement de $F(x, \mu)$ autour du point (x_o, μ_o).

(1) $$\Delta\dot{x} = Q\Delta x + h(\Delta x)$$

dans lequel $\Delta x \triangleq x - x_o$: vecteur de dimension n,
Q : matrice (n x n) à coefficients constants,
h : vecteur de dimension n de fonctions non linéaires de Δx

3.1. Cas d'une valeur propre réelle nulle

Supposons qu'une valeur propre réelle de la matrice Q soit nulle, les autres étant à partie réelle négative.

Soit X, de composantes $(X_1, X_2, \ldots, X_n)^T$, le vecteur propre à gauche correspondant à la valeur propre nulle ($X^T . Q = 0^T$) et définissons une nouvelle variable ε, projection de Δx sur le vecteur propre X :

$$\varepsilon = \langle X^T, \Delta x \rangle = X^T . \Delta x$$

Il s'ensuit que : $\dot{\varepsilon} = \langle X^T, h(\Delta x) \rangle$

Les vecteurs propres étant définis à un facteur constant près, il est possible de supposer $X_n = 1$ et de remplacer l'équation (1) par le système équivalent :

$$\begin{cases} \Delta x_2 = [\Delta x_1, \ldots, \Delta x_{n-1}]^T \\ h_2 = [h_1, \ldots, h_{n-1}]^T \end{cases}$$

(2a) $$\Delta \dot{x}_2 = P \Delta x_2 + B\varepsilon + h_2(\Delta x_2, \varepsilon)$$

(2b) $$\dot{\varepsilon} = \langle X^T, h(\Delta x_2, \varepsilon) \rangle$$

possédant les mêmes propriétés que le système initial (en particulier, la matrice P n'est pas singulière). Pour résoudre ce système, on cherche une solution particulière de l'équation (2a) de la forme :

$$\Delta x_i = w_i(\varepsilon)$$

sachant que l'évolution de ε au cours du temps est donnée par l'équation (2b).

Une façon de procéder consiste à exprimer $w_i(\varepsilon)$ sous la forme d'un développement en série de Taylor :

$$w_i(\varepsilon) = \sum_{k=1}^{m} w_i^{(k)} \frac{\varepsilon^k}{k!} \triangleq \sum_{k=1}^{m} a_{ik} \varepsilon^k$$

Il s'ensuit :

$$[P_{ij}] \sum_{k=1}^{m} a_{ik} \varepsilon^k + B_j \varepsilon = \left(\sum_{k=1}^{m} k a_{ik} \varepsilon^{k-1}\right) \langle X^T, h\left(\sum_{k=1}^{m} a_{ik} \varepsilon^k, \varepsilon\right) \rangle - h_j\left(\sum_{k=1}^{m} a_{ik} \varepsilon^k, \varepsilon\right)$$

$i, j \in [1, m-1]$

Si l'on décompose le second membre de la relation précédente sous la forme :

$$H_j(\varepsilon) = H_{j2} \varepsilon^2 + H_{j3} \varepsilon^3 + \cdots + H_{jp} \varepsilon^p \qquad \text{avec } H_{jk} = H_{jk}(a_{ik})$$

les coefficients a_{ik} sont déterminés en identifiant les termes de même degré en ε

$$a_{i1} = -P^{-1} B$$

$$a_{ik} = P^{-1} H_{jk} \qquad k = 1, m$$

Au premier ordre $\Delta x_i = a_{i1} \varepsilon$ et, pour ε donné, il est possible de calculer Δx_i et d'en déduire $\dot{\varepsilon}$ par la relation $\dot{\varepsilon} = \langle x^T, \Delta \dot{x} \rangle$ sans connaître explicitement les non-linéarités du système. Puis, à partir de plusieurs couples (ε, $\dot{\varepsilon}$), l'utilisation d'un code numérique de lissage polynomial permet d'écrire l'évolution de ε sous la forme

(3) $$\dot{\varepsilon} = \alpha_m \varepsilon^m + \alpha_{m+1} \varepsilon^{m+1} + \cdots \qquad m \geq 2$$

Le problème de la stabilité de l'équilibre est ainsi ramené à l'étude de la stabilité de l'équation ci-dessus au voisinage de $\varepsilon = 0$. L'application de la théorie de Liapounov amène les conclusions suivantes :

1) Si m est pair, le système est instable quel que soit le signe de α_m

2) Si m est impair et si $\alpha_m > 0$, le système est instable,

3) Si m est impair et si $\alpha_m < 0$, le système est stable.

De plus, en approximant l'équation (3) par son terme de plus bas degré, il est loisible de calculer le temps (t_2) mis par ε pour passer de ε_0 à t = 0 à $2\varepsilon_0$.

(4) $$t_2 = \frac{2^{1-m} - 1}{(1-m)\alpha_m} \varepsilon_0^{1-m}$$

Il est à noter que contrairement aux systèmes linéaires, le temps mis par une perturbation pour doubler est proportionnel à sa valeur initiale.

L'expérience montre que l'approximation de t_2 donnée par (4) est généralement grossière. Il est préférable de tenir compte des termes d'ordre m + 1 et m + 2 qui conduisent à une meilleure estimation de t_2 moyennant des relations plus compliquées.

3.2. Cas de deux valeurs propres imaginaires pures

En reprenant les mêmes notations qu'au paragraphe 1, on suppose que deux valeurs propres de la matrice Q sont imaginaires pures, les autres étant à partie réelle négative [1,3].

Soient $X_{1,2}^T = \xi^T \pm i\mu^T$ les deux vecteurs propres à gauche de Q associés aux valeurs propres critiques $\lambda_{1,2} = \pm i\omega$ et les nouvelles variables ε_1 et ε_2 définies de la façon suivante :

$$\varepsilon_1 = \frac{1}{2} \langle (X_1^T + X_2^T), \Delta x \rangle = \langle \xi^T, \Delta x \rangle$$

$$\varepsilon_2 = \frac{-i}{2} \langle (X_1^T - X_2^T), \Delta x \rangle = \langle \mu^T, \Delta x \rangle$$

Il s'ensuit que :

$$\dot{\varepsilon}_1 = -\omega \varepsilon_2 + \langle \xi^T, h(\Delta x) \rangle$$

$$\dot{\varepsilon}_2 = \omega \varepsilon_1 + \langle \mu^T, h(\Delta x) \rangle$$

Par un raisonnement analogue à celui du paragraphe précédent, le système (1) peut être remplacé par un système équivalent, possédant les mêmes particularités que le système (2) :

(5a) $$\Delta \dot{x}_2 = P \Delta x_2 + B\varepsilon + h_2(\Delta x_2, \varepsilon)$$

$$\begin{cases} \Delta x_2 : [\Delta x_1, \dots, \Delta x_{m-2}]^T \\ h_2 : [h_1, \dots, h_{m-2}]^T \\ \varepsilon : [\varepsilon_1, \varepsilon_2]^T \end{cases}$$

(5b) $$\dot{\varepsilon}_1 = -\omega \varepsilon_2 + \langle \lambda^T, h(\Delta x_2, \varepsilon) \rangle$$

(5c) $$\dot{\varepsilon}_2 = \omega \varepsilon_1 + \langle \mu^T, h(\Delta x_2, \varepsilon) \rangle$$

dont on cherche une solution particulière de l'équation (5a) sous la forme :

$$\Delta x_i = w_i(\varepsilon_1, \varepsilon_2)$$

$w_i(\varepsilon_1, \varepsilon_2)$ étant une somme de polynomes homogènes en ε_1 et ε_2 de degré croissant

$$w_i(\varepsilon_1, \varepsilon_2) = \sum_{j=1}^{m} W_{ij}(\varepsilon_1, \varepsilon_2)$$

Au premier ordre, $\Delta x_i = a_{i1}\varepsilon_1 + b_{i1}\varepsilon_2$ et les coefficients a_{i1} et b_{i1} sont donnés par

$$a_{i1} = -[\omega^2 I + P^2]^{-1} \cdot [P B_{i1} + \omega B_{i2}]$$

$$b_{i1} = -[\omega^2 I + P^2]^{-1} \cdot [P B_{i2} - \omega B_{i1}]$$

Pour des combinaisons $(\varepsilon_1, \varepsilon_2)$ il est possible de calculer les valeurs de $\dot{\varepsilon}_1$ et $\dot{\varepsilon}_2$ et d'obtenir par lissage bi-polynomial les équations d'évolutions de ε_1 et ε_2 sous la forme

(6)
$$\dot{\varepsilon}_1 + \omega \varepsilon_2 = \sum_{i=1}^{m_1} \sum_{j=1}^{m_2} \alpha_{ij} \varepsilon_1^{i-1} \varepsilon_2^{j-1} \qquad \alpha_{11} = \alpha_{12} = \alpha_{21} = 0$$

$$\dot{\varepsilon}_2 - \omega \varepsilon_1 = \sum_{i=1}^{m_1} \sum_{j=1}^{m_2} \beta_{ij} \varepsilon_1^{i-1} \varepsilon_2^{j-1} \qquad \beta_{11} = \beta_{12} = \beta_{21} = 0$$

Le problème de la stabilité du système est alors ramené à l'étude de la stabilité du système différentiel (6) dont la solution est une oscillation non linéaire qui est développée jusqu'à l'ordre m en fonction de la condition initiale c $(\varepsilon_1(\omega) = c\ ,\ \varepsilon_2(\omega) = 0)$:

(7a)
$$\varepsilon_1(\tau) = \sum_{k=1}^{m} c^k \varepsilon_{k1}(\tau)$$

$$\varepsilon_2(\tau) = \sum_{k=1}^{m} c^k \varepsilon_{k2}(\tau)$$

dans laquelle $\varepsilon_{k1}(\tau)$ et $\varepsilon_{k2}(\tau)$ représentent les coefficients du développement, fonctions de τ, et τ représente une nouvelle variable introduite dans les équations pour exprimer le caractère non linéaire de l'équation (12)

(7b) $$\tau = \frac{\omega t}{1 + s_1 c + \dots + s_p c^p}$$

s_i étant des constantes arbitraires destinées à faire disparaître les termes séculaires qui pourraient apparaître dans la solution.

En introduisant les relations (7) dans les équations 5b et 5c, la résolution des équations différentielles pour les termes de même degré en C donne les approximations successives qui sont de la forme :

$$\varepsilon_{k1}(\tau) = A_k(\tau)\cos\tau + B_k(\tau)\sin\tau$$

$$\varepsilon_{k2}(\tau) = A_k(\tau)\sin\tau - B_k(\tau)\cos\tau$$

dans lesquelles :

$$A_k(\tau) = \int_0^\tau (P_k(\tau)\cos\tau + Q_k(\tau)\sin\tau)\, d\tau$$

$$B_k(\tau) = \int_0^\tau (P_k(\tau)\sin\tau - Q_k(\tau)\cos\tau - s_{k-1})\, d\tau$$

$P_k(\tau)$ et $Q_k(\tau)$ étant les termes de degré k dans les équations 5b et 5c modifiées.
De ces dernières relations il vient que si $A_k(2\pi) = 0$, alors $A_k(\tau)$ est périodique en τ et on peut choisir s_{k-1} tel que $B_k(\tau)$ soit également périodique. Il s'ensuit que l'étude de la stabilité du système est ramenée à l'étude du signe de $A_k(2\pi)$

- Si quelque soit k, $A_k(2\pi) = 0$, le système est stable
- dès qu'il existe $k_1 > k$ tel que $A_{k_1}(2\pi) \neq 0$,
  - si $A_{k_1}(2\pi)$ est positif, le système est instable
  - si $A_{k_1}(2\pi)$ est négatif, le système est asymptotiquement stable

L'analyse du comportement asymptotique du système (6) au 1er et au 2ème ordre ne permet pas de conclure sur le caractère de l'oscillation. En revanche, l'approximation au 3ème ordre conduit à

$$A_3(2\pi) = \frac{\pi}{4\omega}[3(\alpha_{41} + \beta_{14}) + \alpha_{23} + \beta_{32}]$$

qui est en général différent de zéro.

3.3. Application à l'avion

3.3.1. Cas d'une valeur propre réelle nulle

On se propose de prédire le comportement de l'avion au voisinage d'un point de bifurcation déjà observé dans [2].

Autour du vol en palier stabilisé à dérapage nul à une incidence de 13°, la figure 3 représente la surface d'équilibre du système lorsque la direction varie, gauchissement au neutre. Le point de bifurcation étudié a les caractéristiques suivantes :

$\alpha_0 = 19.3°$ $\beta_0 = 7°$ $V_0 = 140.6\,m/s$ $p_0 = -70.5°/s$ $q_0 = 4.9°/s$ $r_0 = -26.8°/s$
$\theta_0 = -68.9°$ $\varphi_0 = -10.5°$
$\delta_{x_0} = 0.42$ $\delta l_0 = 0.$ $\delta_{m_0} = -0.4°$ $\delta_{n_0} = 10.1°$

L'analyse linéarisée autour de ce point d'équilibre conduit aux valeurs propres

$\lambda_1 = -0.18$ $\lambda_2 = 0$ $\lambda_{3,4} = -0.07 \pm 1.33\,i$
$\lambda_{5,6} = -1.5 \pm 1.5\,i$ $\lambda_{7,8} = -1.1 \pm 3.77\,i$

et au vecteur propre critique :

$X^T : [55.4 \quad 13.8 \quad 2.0 \quad 0.3 \quad 6.8 \quad -42.3 \quad -12.6 \quad 1.0]$

L'approximation des composantes $\Delta\alpha_i$ au premier ordre :

$a_1^T : [10^{-2} \quad 2.7\,10^{-3} \quad 4.10^{-4} \quad 5.1\,10^{-5} \quad 1.3\,10^{-3} \quad -8.3\,10^{-2} \quad -2.5\,10^{-4} \quad 2\,10^{-4}]$

associée au lissage polynomial permet d'obtenir l'équation

$\dot{\varepsilon} = 3.98\,10^{-4}\varepsilon^2 + 6.44\,10^{-9}\varepsilon^3 + 8.7\,10^{-9}\varepsilon^4 + \cdots$

La simulation d'une perturbation de 3° sur l'incidence ($\varepsilon_0 = X_1 \cdot \Delta\alpha_0$) montre que la divergence du mouvement (après disparition des modes amortis) conduit à un temps pour doubler de l'ordre de 3s très proche de la valeur calculée (t_2 = 3,07s) (fig. 4).

3.3.2. Cas de deux valeurs propres imaginaires pures

Gouvernes transversales au neutre. lorsque l'on fait varier la profondeur à partir du vol rectiligne équilibré à α_0 = 13° et dérapage nul, la surface d'equilibre à vitesse angulaire nulle présente un point de bifurcation correspondant à 2 valeurs propres imaginaires pures (fig. 5).

L'analyse de la stabilité des petits mouvements autour de ce point d'équilibre particulier

$\alpha_0 = 23.3°$ $\beta_0 = 0.$ $V_0 = 69.7\,m/s$ $p_0 = q_0 = r_0 = 0.$ $\theta_0 = 14.7°$ $\varphi_0 = 0.$
$\delta_{x_0} = 0.42$ $\delta l_0 = \delta_{n_0} = 0.$ $\delta_{m_0} = -6.8°$

conduit aux valeurs propres suivantes.

$\lambda_{1,2} = \pm 0.4\,i$ $\lambda_{3,4} = -0.06 \pm 0.2\,i$ $\lambda_5 = -0.64$ $\lambda_6 = -1.72$ $\lambda_{7,8} = -0.35 \pm 1.7\,i$

En utilisant la même méthode qu'au paragraphe précédent, le système (6) s'écrit

$\dot{\varepsilon}_1 + 0.4\,\varepsilon_2 = 1.115\,\varepsilon_1^2 + 7.13\,10^{-4}\,\varepsilon_1\varepsilon_2 + 0.61\,\varepsilon_2^2 + \cdots$
$\dot{\varepsilon}_2 - 0.4\,\varepsilon_1 = 6.01\,\varepsilon_1^2 + 1.3\,10^{-4}\,\varepsilon_1\varepsilon_2 + 18.5\,\varepsilon_2^2 + \cdots$

d'où l'on tire $A_3(2\pi) = -99.4$; l'oscillation sera convergente et la bifurcation supercritique. La simulation du mouvement du système soumis à une perturbation de 2° sur l'incidence présente bien un mouvement oscillatoire de faible amplitude et convergent (fig. 6). Cette frontière de stabilité ne présente donc pas de danger.

A partir du point de bifurcation ci-dessous, si l'on se déplace sur la surface de bifurcation correspondant à 2 valeurs propres imaginaires pures, on observe que pour le point :

$\alpha_0 = 23.3°$ $\beta_0 = -2.2°$ $V_0 = 69.9\,m/s$ $p_0 = 0.24°/s$ $q_0 = 0.15°/s$ $r_0 = -0.9°/s$
$\theta_0 = 14.5°$ $\varphi_0 = -9.6°$ $\delta_{x_0} = 0.42$ $\delta l_0 = 0$ $\delta_{m_0} = -6.9°$ $\delta_{n_0} = 1.1°$

le système (6) s'écrit

$\dot{\varepsilon}_1 + 0.41\,\varepsilon_2 = -1.2\,\varepsilon_1^2 + 0.11\,\varepsilon_1\varepsilon_2 - 0.18\,\varepsilon_2^2 + \cdots$
$\dot{\varepsilon}_2 - 0.41\,\varepsilon_1 = 1.14\,\varepsilon_1^2 - 0.08\,\varepsilon_1\varepsilon_2 + 0.07\,\varepsilon_2^2 + \cdots$

et conduit à $A_3(2\pi) = 3.35$; le mouvement oscillatoire est donc divergent et la bifurcation subcritique. En simulation, une perturbation de 2° sur l'incidence, met en évidence l'existence d'un mouvement oscillatoire entretenu, en particulier sur les paramètres latéraux, dont l'amplitude n'est pas négligeable (fig. 7). Bien que dans ce cas favorable le mouvement oscillatoire n'entraine pas une variation très importante du comportement de l'avion, il n'en reste pas moins que l'apparition de ce cycle limite peut surprendre.

4. CONCLUSION

Les résultats présentés dans cette communication affinent les renseignements fournis par l'application de la théorie des bifurcations à la mécanique du vol exposés dans [2] .

Par opposition aux méthodes usuellement utilisées pour prédire le comportement transitoire d'un système différentiel non linéaire au voisinage de points de retournement et de points de bifurcation de Hopf, la méthode proposée ici opère sur le système complet sans la connaissance a priori des non-linéarités. L'utilisation conjointe de la méthode des projections, du développement asymptotique de la solution et des techniques de lissage conduit à un traitement numérique rapide et précis du régime transitoire autour de chaque point de bifurcation calculé. La corrélation avec les simulations numériques est satisfaisante.

Comme toute méthode, celle-ci a des limites. Elle est moins précise lorsque plusieurs valeurs propres ont une petite partie réelle et ne traite pas le cas des points de bifurcation tels que $\lambda_1 = 0$ et $\lambda_{2,3} = \pm i\omega$. Ces derniers entrainent une interaction entre un mouvement divergent et un mouvement oscillatoire éventuellement convergent qui peut conduire à des comportements très complexes en cours d'étude actuellement.

Plus généralement, la méthodologie de prédiction du comportement d'un avion basée sur la théorie des bifurcations et développée à l'ONERA est à un stade avancé. Mis à part la prédiction globale du comportement issue de l'interprétation de la surface d'équilibre et des surfaces de bifurcation, elle vient de s'enrichir de la caractérisation du transitoire au voisinage des frontières de stabilité. Des comparaisons qualitatives entre essais en vol et prédiction ont montré que même un modèle aérodynamique stationnaire était capable de reproduire de nombreux phénomènes observés en vol.

Enfin, jusqu'à présent cette méthode a été mise à l'épreuve sur des avions de combat fictif ou existant. Au stade actuel de son développement elle pourra, dans le futur, être utilisée aussitôt après la caractérisation aérodynamique de nouveaux avions de façon d'une part à prédire leurs comportements et préparer les programmes d'essais en vol et d'autre part à définir les lois de commande appropriées à éviter les pertes de contrôle.

REFERENCES

[1] Stability of Aircraft motion in critical cases
J.E. COCHRAN Jr et C.S. HO
J. of Aircraft (Juillet-Août 1983)

[2] Application de la théorie des bifurcations à l'étude de pertes de contrôle sur avion de combat
P. GUICHETEAU
AGARD CP 319

[3] Elementary Stability and Bifurcation Theory
G. IOOS et D.D. JOSEPH
Springer Verlag.

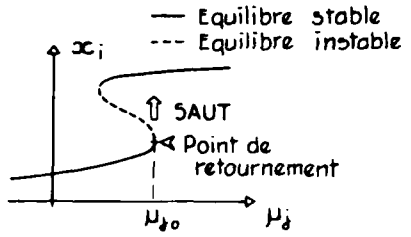

Fig 1. Point de retournement.

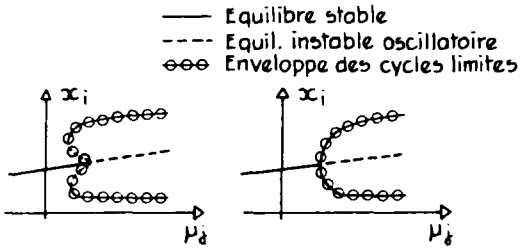

Fig. 2. Bifurcation de Hopf

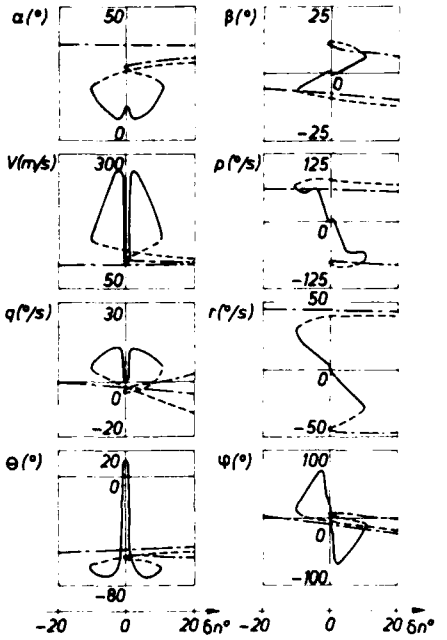

Fig 3. Extrait de la surface d'équilibre
($\delta_m = 0{,}4°$, $\delta_\ell = 0$)
— Stable
--- Instable
— · — Instable oscillatoire

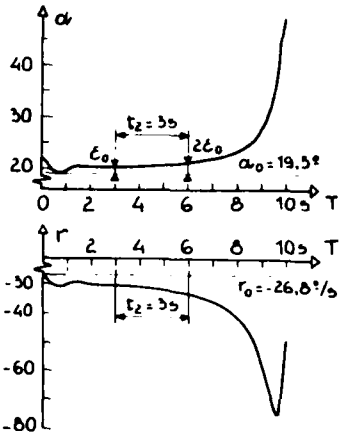

Fig 4. Evolution en fonction du temps
($\Delta\alpha_0 = 3°$, t_2 prédit $\approx 3s$)

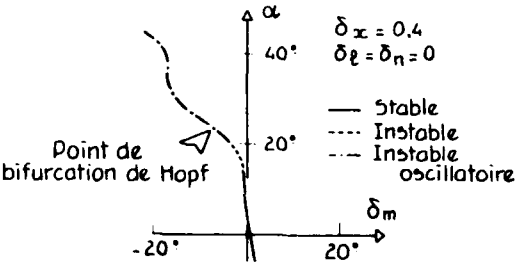

Fig 5. Incidence d'équilibre en fonction du braquage de la gouverne de profondeur

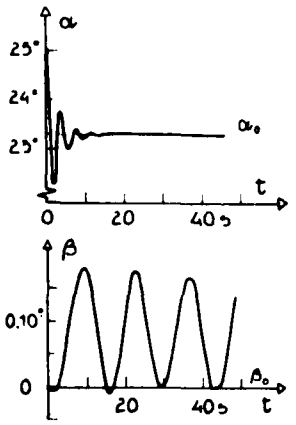

Fig 6. Bifurcation supercritique.
Mouvement oscillatoire convergent
($\Delta\alpha_0 = 2°$)

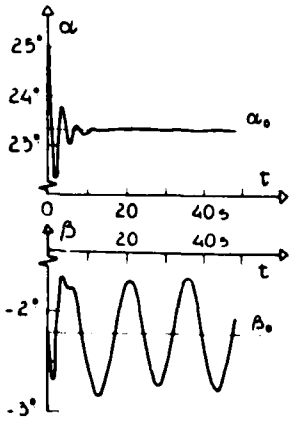

Fig 7. Bifurcation subcritique.
Cycle limite visible essentiellement sur le dérapage. ($\Delta\alpha_0 = 2°$).

ROUND TABLE DISCUSSION

Dr. Orlik-Rückemann

We have now come to the final session of the Symposium, which is the Summary Discussion. We will first have some remarks from our Technical Evaluators, after which there will be time for discussions and comments from the floor. Since this meeting has dealt with a rather wide range of subjects, we have this time arranged for having two Technical Evaluators. They are: Mr. Dennis Mabey from RAE, who is evaluating Part 1, and Mr. Joseph Chambers from NASA Langley, who is covering Parts 2 and 3. You have not heard very much from these gentlemen during the meeting because they were busy watching, listening, assessing and making notes. They will now go home and sift through all this material and all their notes, and then they will write the technical evaluation report which will be available as an AGARD publication at about the same time as the proceedings from this meeting.

These two gentlemen were kind enough to agree to share with us at this time their unedited first impressions of this meeting. I hope that you appreciate the difficulty involved in preparing such instantaneous comments, as well as the fact that, while the rest of us have been enjoying our dinners in the excellent restaurants in Göttingen, Mr. Mabey and Mr. Chambers have probably been working many hours in the evening, preparing their notes. So I would like once more to express my appreciation of their efforts. I will come back to this in a moment, in the meantime, I would like to introduce Mr. Dennis Mabey.

Mr. Mabey

This is a very difficult task. First I would like to give you the good news, and in the historic town of Göttingen, I think I should refer to the seven universal virtues known to medieval theologians. I take three of these virtues, the first three, from Dr. Laschka's paper. He reminded us that any time-dependent measurement is compounded of a steady term, a time-dependent term that is associated very often with a motion, and then a random term that most of us would prefer not to exist, because it plagues our measurements. You may argue that this is a very obvious statement, and so it is, but in so many experimental investigations, its existence is ignored. In particular, to attempt a time-dependent experiment with instrumentation that doesn't simultaneously measure the mean value and these two other terms that Dr. Laschka referred to, is inviting disaster. Let me just give you an example. We have seen many loops of lift and drag from helicopter sections. Those were obtained mostly with Kulite pressure transducers. For each of those aerofoil sections with the model at fixed static angles of incidence, the fluctuating normal force could have been measured very easily, coming from that random term that we would prefer not to be there. In fact this is very rarely being done. Secondly, Dr. Laschka reminded us of the importance of boundary conditions for some flows and indicated how the singularities moved away from the surface when the wall was in motion. Now there are a number of problems that are not sensitive to the boundary condition such as the calculation of the resonance frequencies in ventilated wind tunnels. It may shock you to learn that you can make almost any old boundary condition (as long as you include the plenum chamber) and get almost the right answer. This is a problem that is insensitive to boundary conditions. However, if you have an aerofoil with a moving leading edge (as discussed by Lars Ericsson) then you will have a flow that is very sensitive to the boundary condition.

Thirdly, Dr. Laschka discussed Prandtl's concept of steady separation. Gentlemen, I believe that the concept of steady separation is a misconcept and that there is really no such thing. If you start measuring with Kulites, you will find that all sorts of dreadful things happen. Steady separation may exist in laminar flow, but certainly for turbulent flow the concept of steady separation is a misconcept. I would like time to develop that but I won't.

The fourth virtue: I was very impressed with Dr. Geissler's calculations which show that the separation loops on the oscillating aerofoil were reduced as the frequency of oscillation was increased. I believe that to be a general trend in nature, and very, very significant for all sorts of aircraft buffeting problems. One would hope that in the future one would see more calculations of that type and see if, indeed, that is a general trend. The fifth virtue I found in Brereton's paper, "Study of the Turbulence Characteristics of Separated Flows". Towards the end he remarks on the long time it takes to get a separation established and the very short time in which the separation is blown away. I believe that to be profoundly true and very important. It certainly squares with our own experience on a rapidly deployed spoiler where a separated flow takes a very long time to develop. In contrast when you retract the spoiler, the separation goes away very quickly. I think that is a general trend, worthy of our attention. The sixth virtue: for attached boundary layers, only the wake region is influenced by free stream variations. We had many references to a slug of flow. The implications of that are really quite spectacular. The implication is that quasi-steady methods of turbulent boundary layer modelling should really be very good, because the wake region, as you all know, comprises much the largest portion of the turbulent boundary layer. The seventh, the most rewarding virtue, must be the gleaming horizon revealed to us by the work of Houwink and Le Balleur of having some kind of boundary layer solution valid beyond separation linked to an outer inviscid solution.

Now for the bad news. The seven universal virtues are balanced, I am afraid, by the seven deadly sins. Because medieval art was more successful in depicting these than the seven universal virtues, I have prepared some viewgraphs. The cardinal sin is the number of tests reported that were made with free transition, and in addition were made on NACA 0012 aerofoils with low Reynolds number. Gentlemen, I could produce a roll of dishonor of all the people that used NACA 0012 aerofoils at free transition at low Reynolds number, but I won't do that. Rather, I would refer you to Figure 17 of Lars E. Ericsson's paper, and you will see there why I think the use of this particular airfoil at low Reynold number with free transition is so unwise as to be unbelievable. I am not going to develop that, but watch out Gentlemen,

for the written evaluation. There is no discussion at all of transonic shock motion. I think that that is a great pity, because in the light of Dr. Tijdeman's work, one would hope now that the CFD community would be busily applying their methods and trying to predict the three kinds of motion, type A, type B, type C motions of Tijdeman. (I didn't explain that this funny symbol on the top left is supposed to be a gauntlet I am throwing down) So in shock motions, the challenge for the CFD community is to predict the type B oscillation of Tijdemans which occurs on 14% thick biconvex aerofoils in the narrow Mach number range from 0.82 - 0.86 with transition fixed. If you have an 18% thick convex bi-aerofoil, then the Mach number range is slightly different, a little bit lower and the oscillation changes to Tijdeman type C. I want to use the bottom half of that graph to illustrate the folly and danger of testing with free transition at transonic speeds. These are my own measurements, so I stand condemned by my own mouth. If you increase the Reynolds number with free transition, you will find to your dismay that the region of periodic flow disappears, and by three and a half million, it is gone. If you tested at 4 million, you would have lost this region of periodic flow, and you would conclude, quite wrongly, that this phenomenon does not occur at full scale. If, however, you have the courage of your convictions and increase the Reynolds number further, then it reappears at a Reynolds number of 5 million. I don't need to remind you that many transonic wind tunnels currently available are restricted to Reynolds numbers of about 3 to 5 million. If you had been testing a bi-convex aerofoil with free transition in one of these facilities, you would have been in trouble.

Buffeting is a subject dear to my heart. We only had one paper on buffeting, and here I confused the speaker in the discussion by making a remark about stopping the train short of the station. I am sorry about that, but this is exactly what had been done in that particular experiment. Everything was available to get the buffet excitation parameter. The generalized mass M, the tip accelerations as determined from the accelerometers, the kinetic pressure Q, the wing area S, were all certainly known; I believe that there may have been some doubt about the total damping coefficient. But you must work through to non-dimensional numbers, and it is very important to realize that this can be done for all modes. In our youth it was sufficient to think about accelerations of 0.2 G at the pilot's seat. But in our old age, we have to think of a missile sitting out at the wingtip and being shaken up and down, and not merely at first bending mode but also in torsional modes. (The same equation is valid for the torsional modes.)

We had a question about the use of cryogenic wind tunnels, and it was framed specifically to the NTF. I believe and have believed since 1975 that cryogenic tunnels are going to open a whole new avenue of research into unsteady aerodynamics. I would like to show you what actually happens in a cryogenic tunnel. If you are measuring any response, for example, unsteady wing root strain or normal force fluctuation or an axial force fluctuation, you will find that the response y varies with Reynolds number according to a law of $R^{-1/5}$. This is quite a normal mode of operation of a cryogenic tunnel, constant Mach number, constant total pressure and total temperature varying. The response is a consequence of the fact that the aerodynamic damping gamma is k, (different for every mode) times the freestream density and the velocity. That's all I've assumed to get that relationship. You will notice the dotted portion in the middle: for the purposes of this educational talk, I am testing this model with free transition. The peak that you may see sometimes is the effect of transition. It is a happy accident, gentlemen, that any response measured in a cryogenic tunnel, whether it comes from a balance or from a wing, will scale that way, because you will recognize that that variation with Reynolds number is very close to the variation of skin friction with a turbulent boundary layer.

No investigation of boundary conditions is the fourth sin. Dr. Laschka shows us how important they are, and I believe that the modification of time-dependent boundary conditions is going to be one of the great areas of advance in the next few years. We had no discussion of dynamic wall interference, except in the experiment of the gust tunnel. There what you should notice is that the wall effects were very large at the low frequency. In contrast at the very high frequencies all these wind tunnels behave much the same. That is a very significant and important result. Finally, the experiments on gust tunnels are very interesting as far as they go. I don't wish to spoil the party, but as Dr. McCroskey pointed out this morning, the gust lengths of interest are such that the parameter $\omega c/u$ should be about a half. That is the gust that is most important. A model chord of about 0.3 meter could be used in a 1 meter tunnel. That gust length parameter then corresponds to a frequency of 10 Hz at 30 meters per second on that chord. It actually corresponds with 100 Hz at a velocity of 300 meters a second, which is where these systems are going to be used, that is $M_{infinity} = 0.8$. The practical problem is testing such a system at a Mach number of 0.8 or 0.9, and for that you are looking for a system that has got a frequency of 100 Hz. I don't believe you'll ever get that with flapping vanes. If anyone is interested in generating strong gusts at frequencies of up to 500 Hz in a transonic wind tunnel, they should send me a postcard. Thank you.

Dr. Orlik-Ruckemann

Thank you very much Mr. Mabey. We will continue directly with the second evaluator, Mr. Chambers, and then we will open the general discussion.

Mr. Chambers

I thank AGARD for the opportunity of being an evaluator for this meeting. With Dennis' introductory remarks and their religious overtones, I thought perhaps we would all retire to a mass confession this afternoon to rid ourselves of those sins.

In the ten minutes or so that I have available, I would like to take a critical look at the meeting. It would be very easy to sit here and pat everyone on the back. All the papers were obviously very good technical contributions, but I think that it might be helpful to look at the meeting in the context again of good news and bad news, and recognize where we are really falling short in this area of unsteady aerodynamics. First, to take a look at this from a personal perspective, I would like to look at the meeting in a manner intended to complement Dennis' observations as a fundamental aerodynamicist, with my comments from a flight mechanics viewpoint. Let me start with the first viewgraph and a few comments here

which I have observed in working in the area of dynamic stability parameters and aircraft applications, with a few thoughts regarding the relative importance of unsteady flows. With the exception of the classical flutter structural load area, and especially when we look only at the stability and control area, I think it is fair to say that the unsteady aerodynamics area has been one of secondary interest to aircraft designers, particularly in the United States. They have regarded it predominantly as textbook material, within the normal attached-flow flight regime. This neglect is evidenced to a large extent in the U.S. by the lack of industrial facilities and research in the area of unsteady flows. That, however, is past history. Current aircraft such as the F-16 and F-18 have stimulated the interest in this area, and as a result we see a perspective now which calls in the future for increased importance of unsteady aerodynamics due to a number of reasons which were cited in Jim Lang's outstanding paper. The need for agility, that is, the ability to rapidly move the airplane in the sky, to routinely use high angle of attack and the associated separated flows, the use of relaxed stability that we are now incorporating in fighters to a very high degree, require that we determine such unsteady affects to a very high degree of accuracy. We haven't talked much about configuration effects at this meeting, but it is quite obvious that combat aircraft of the future may be radically different in terms of geometric shapes, which will require us to determine to some accuracy all of the unconventional aerodynamic effects; and in particular the unsteady characteristics.

The next viewgraph gives a few general comments about the overall meeting and results. It was interesting that most all of the papers dealing with applications dealt with non-linear separated flow conditions. Obviously, we are very interested these days in high angle of attack flight conditions. I was very encouraged by the experience being gained, especially the checking out of new facilities and analysis methods for unprecedented capability for analyzing unsteady flow conditions. However, I was at the same time very troubled by the fact that we lack validation, and by that I mean flight validation, of many of the theories that were expounded at the meeting. Wing rock, hysteresis, and dynamic stall have many, many theories yet to be validated for actual aircraft. There is a challenge, of course, facing us in terms of the new combat requirements, as I mentioned earlier. Aircraft are going to be challenging the state-of-the-art beyond our capabilities. Aircraft unfortunately are three-dimensional objects; they are not two-dimensional cylinders, they are not two-dimensional airfoils, they have highly non-linear response characteristics at high angles of attack and separated flows, and of course, they have multi degrees of freedom. So we as technologists are going to be taxed to the fullest to meet this challenge.

There are several important areas dealing with separated flows which weren't discussed at all in this meeting.

One which is of great interest to us in the United States today has resulted because of our fighter aircraft which have twin vertical tails and strong vortex flows - that is, the tail loads which occur due to separated flows at high angles of attack. We didn't talk very much in the meeting about solutions for some of our unsteady flow phenomena, such as wing rock. Jim Lang brought up the subject of active control of separated flows to enhance stability control or performance, and we didn't talk very much about that. One subject area which I feel the meeting was very remiss in was that we didn't talk much about flight validation, or didn't have much in terms of flight results. There is one additional point to be talked about in terms of the meeting. I have been talking to some of my colleagues here who feel that technology transfer constraints within various countries have hampered us a bit in exchanging some of the data that we have in hand. I will come back to this subject a little bit later as a recommendation.

The next slide takes a look in particular at part 2 of this meeting which dealt with dynamic stability parameters, the measurement and use thereof. I am very impressed with the progress that has been made in the last five to eight years in terms of our ground-based experimental test rigs to measure these parameters, and of course, the analyses that are being developed are quite impressive. As a result of these improved capabilities, we now have the ability to examine very important Mach and Reynolds number effects which were heretofore not possible. Our friends at Lille have shown us innovative methods to measure some of the troublesome parameters such as the $\dot{\beta}$ derivatives. We heard about some of the advanced flight parameter identification techniques which are being exploited. Taking a look at these areas critically, it is obvious that at this point we very urgently need flight validation of the ground-based facilities so that we can move on beyond the state-of-the-art and get to the point of really interactively developing our predictive methods. What is needed is the systematic development of the flow diagnostics which lead hopefully to valid computational methods such that we can begin to predict some of these phenomena, rather than continuing to "bandaid" our aircraft.

The next slide takes a look at Part 3 of the meeting which was the applications area. We covered quite a few topics in this discussion. The analysis techniques which we heard about for non-linear phenomena are very rapidly developing. I was very impressed by the lucid presentations that were given in those areas. The anticipated combat mission requirements for aircraft and flight at high angles of attack demand that we have a much better fundamental understanding of the control of unsteady flows. The correlation of predicted motions for the sub-scale models as presented by Jean Ross was quite satisfactory, although I caution all of us to not make generalizations. Experience has shown that this can be very dependent on the phenomena we are trying to analyze and to configuration effects. This topic of configurations again is of great concern to us because we do feel that tomorrow's combat aircraft may be radically different from contemporary fighters. We are encouraged by the aero estimation methods, such as Eddy Lan's paper which estimated both static and dynamic aero characteristics. I thought that it was a very impressive piece of work, especially the fact that it looks like some preliminary design methods are being formulated which would be a tremendous stride forward. The non-linear high-alpha characteristics being accommodated by advanced control systems is another very encouraging development. However, the bottom line area of concern in the application to aircraft dynamics is that we must accelerate the development, and in particular, the applications of this technology to representative aircraft configurations rather than paper studies or unrepresentative configurations for which there is not enough flight data to sufficiently validate the techniques and analysis methods. As usual, as we usually say at all AGARD meetings, it is obvious that we are going to need a very coordinated effort by the analytical, experimental and dynamics personnel to be able to accomplish this task.

The next chart gives two preliminary recommendations that occurred to me while listening to the program. The first recommendation is an opportunity which I think could be a valuable contribution of the meeting. I would make this recommendation to the Fluid Dynamics Panel. It is obvious that we now have rotary balance testing being conducted in at least five countries. A great deal of information is being produced. Personally, I feel that it would be extremely significant to be able to document, consolidate and correlate our rotary testing, hopefully, as a Working Group type of activity such that we could produce a report for everyone's benefit within the AGARD community. I think that this would be an extremely beneficial output of the meeting. The second area is a general observation to all present that we need efforts, very consolidated efforts, to validate our theories and ground tests with flight studies. I would like, for the information of both the Flight Mechanics Panel members and the Fluid Dynamics Panel members, to provide a little information about what we are attempting to do within NASA to provide some information.

The next chart shows a photograph of an F-18 airplane. We within NASA recognize that the problem of verification and validation of theory has been hampered in the high angle of attack area for some years. NASA has not been in a position of having an adequate test vehicle to close the loop on that problem. We have recently acquired an F-18 high angle of attack research vehicle from the Navy. This airplane is currently being instrumented at our Dryden Flight Research facility for testing. We have drawn together an intercenter NASA program which will exercise our ground based facilities and analysis techniques, and we plan to validate these with the airplane. This airplane, for those of you who are not familiar with the F-18, is an outstanding candidate for high angle of attack research. The airplane is capable of being flown and trimmed up to angles of attack of 60 degrees. The airplane exhibits virtually all aerodynamic phenomena that we are interested in, including strong vortex flows. By reconfiguring the leading and trailing edge flaps, the airplane will exhibit wing rock, it will exhibit a violent yaw departure, or virtually any other high angle of attack phenomenon of interest to flight dynamicists. The airplane utilizes a very versatile flight control system. The airplane has 14 individually controlled surfaces, and for those of you not familiar with the aircraft, as an example, the airplane utilizes the rudders for longitudinal stability augmentation for certain configurations. The airplane, as I mentioned, is being outfitted and we plan a number of aerodynamic experiments which will be of interest to this group. We plan to do very detailed boundary layer and vortex interaction studies. We will provide an actively controlled deflectable wing-body strake for control of unsteady aerodynamics at high angles of attack, and we will be studying the vertical tail unsteady airload buffeting problems with the airplane.

The next chart lists some of the objectives within the area of configuration aerodynamics, including forebody/wing interaction activity, the importance of establishing the validation and correlation between tunnel, theory, and flight. Wind tunnels used will include the NTF, the Ames 12 foot Pressure Tunnel and some of our lower Reynolds number facilities, together with extensive computational work. The development of inflight flow visualization and measurement will also be done with this aircraft. At Langley we are currently flying an F-106 airplane using a sheet light process and flying the aircraft at night to visualize vortex flows. On the F-18 we intend to expand this to include LDV measurements of the airplane off-surface in flight. The dynamic lift potential both in terms of aerodynamically what is there, as well as the tactical utilization and benefit of using dynamic lift, will also be studied with this airplane. So this is a list of some of the things that we plan to do with the aircraft. I would like to end my 10 minutes here by encouraging us all to accept the fact that the challenge for unsteady aerodynamics will intensify in the combat aircraft arena in the very near future. I hope that the state of the art can indeed be accelerated and validated quickly enough to meet that challenge.

Dr. Orlik-Rückemann

Thank you very much. Again I would like to thank the two technical evaluators for their outstanding comments. I think that they were very thought provoking. I would like to hear now what the audience has to say about these and maybe other things. So at this time I would like to open the floor for general comments and discussion. Please identify yourself and go to the mike. This is being recorded and it is also being translated.

Prof. E. Laitone

I would like to make another complementary remark about the Prandtl Göttingen wind tunnels here. In fact, this is very appropriate to this concept of the super manoeuverable fighter, because the same thing happened way back in 1916 when the Fokker D7 first came out. The Prandtl wind tunnel was the first one to run at a Reynolds number of over a million. They found that a thicker wing with a rounded leading edge was actually more efficient than the razor blades they were using on all the Allied fighters. The Fokker D7 came out with an 18% thick wing with a nicely rounded leading edge and was able to do a fantastic manoeuver that is almost tied up with this concept of super manoeuverability. They were able to control the Fokker D7 in stalled flight. They would raise the fuselage up to the angle of attack over 20° and the German pilots found that by just using rudder kick and not touching the ailerons at all, they could actually maintain this stall position. In those days they had no missiles, they just had the straight ahead machine guns, so the typical position was the fighting on the tail, and when a Fokker D7 would raise its fuselage up like that, they were able to put a nice burst into the fighter that had been on the tail. Because of this manoeuver the Fokker D7 was so feared and so respected that it was the only one that was included in the treaty of Versailles ending World War I.

Mr. Aulehla

I would like to comment on some of the results which showed the Reynolds number effects obtained from variable density wind tunnels and on data from rotating stings. I am concerned about these results because I feel that the Reynolds number dependent changes of the wall interference, and also the interference of the rotating balances have not sufficiently been taken into account. As regards Reynolds number effects, I would like to suggest that if you cannot take into account the Reynolds number dependent changes of the wall interferences, you should at least make sure that the empty tunnel calibration was made for all total pressures and Reynolds number respectively. To my knowledge there are still quite a

number of wind tunnels which either do not have such calibrations or do not use them. On boundary layer transition, I think Mr. Mabey made a very good comment, so I'll skip this one. As regards rotating stings, especially for the huge constructions, there should be a clear upstream influence. One way of assessing this effect could be at first to increase this upstream influence stepwise in order to exaggerate the swirling interference and then to eliminate this interference by extrapolation to zero sting volume.

Dr. Orlik-Ruckemann

Thank you. Would anybody who performs experiments in wind tunnels on rotary or oscillatory balances care to comment on this?

Mr. O'Leary

I am sure that the last speaker has a valid point, but it is all a question of degree. We have tested the same configuration in three different wind tunnels with two different sizes of models, and we can't detect any significant differences in the results. I am sure that constraint effects, blockage effects, and wall effects do have some significance, but it is a matter of whether these are significant in the context of what we are trying to measure.

Mr. Aulehla, Munich

In my first comment I was not addressing the method of testing one model in different wind tunnels, but rather of testing a model in the same wind tunnel in which you vary the density. In doing so, you also vary inadvertently the wall interference, in addition and even more important, the empty tunnel calibration - if conducted only at one total pressure - is no longer applicable in sensitive measurements. As a result, spurious Reynolds number effects will be obtained. This could explain some of the unexpected Reynolds number effects presented yesterday morning.

Testing a model in a variable density wind tunnel is quite different from what you have done in testing models of different sizes in different tunnels.

Mr. O'Leary

No, but all I can say is that the significance of these effects is not really important as far as I am concerned. We haven't been able to detect any difference by using different wind tunnels.

Dr. Orlik-Rückemann

I think that what Mr. O'Leary is trying to say is that when testing in wind tunnels, there is no ideal situation that will deal with all kinds of interference effects such as sting interference and wall interference, and this is one more thing that we have to deal with. However, the point is well taken that one should be careful and maybe examine from time to time these things.

Are there any other subjects.

Prof. Reshotko

I would like to make a comment on the use of modelling by bifurcation theory. The equation

$$x_{n+1} = Ax_n(1-x_n)$$

is a well known algebraic iteration equation that displays befurcation at a value of A of about 3.2. A is a type of damping coefficient, the damping is inverse to A. For A less than 3.2 the equilibrium value is resumably obtained. The equilibrium value is that for which $X_{n+1} = x_n$, and is equal to (1 - 1/A).

I have been playing around on my programmable pocket calculator with this equation using the value A = 3, which is presumably in the stable range. But the damping rates are so small at A = 3 that I cannot reach the equilibrium value 'within my battery lifetime'. This means that in the use of bifurcation theory, one should exercise care that the mathematical criteria are not strictly interpreted when applied to a real airplane. A value of A = 3 which is mathematically damped has such a low damping rate that a pilot may not regard it as damped. The interpretation of results using the bifurcation theory should be examined very carefully.

Dr. Orlik-Rückemann

Thank you very much, Eli. Would any of our bifurcation experts present here today care to comment. Mr. Tobak of Ames is nodding his head, indicating that he agrees with you.

Are there any other comments on other subjects?

Dr. McCroskey

I am always concerned about the gap between fundamental research and applied research, and to that end I would like to return to the viewgraph that I showed at the beginning of the Symposium, originally prepared, as you see, with regard to this basic subject of unsteady separation and dynamic stall. As I thought about this ahead of time, it seemed to me the key issues were, from the point of view of the basic research, how to simulate these phenomena and whether we can do meaningful experiments. In fact, this turns out to be where almost all our information comes from and where most of the progress is made. What about simulation with theoretical computations? I must say that I am a little disappointed in the progress that has been made there. On this subject, what is the relevance of the basic two-dimensional

studies, which are so attractive from a basic point of view, to the three-dimensional aerodynamics, which is so important in the applied world? We have seen some interesting papers on these subjects, although I must say in general it looks not so much different from our meeting in 1977 on this area. I am a little disappointed not to have seen more of a connection made between things like the dynamic stall overshoot and how it could be used in flight mechanics implications. But I should also like our technical evaluators to say whether or not they have any strong feelings along these lines. Do you feel that we are bridging the gap between the basic and applied research on this important topic, or are there things that are obviously being ignored which should be considered more. How do you see these, are these key issues and how do you see them from your viewpoint as technical evaluators. I might ask others in the audience if they have similar comments to make as well.

KEY ISSUES

- How to Simulate the Aerodynamic Phenomena
  - experiment
  - theory / computations
- Relevance of Basic 2–D Studies to 3–D Aerodynamics
- Performance and Flight Mechanics Implications
  - how to utilize "superlift" ?
  - adverse aircraft dynamics ?

Fig.1 Unsteady separation and dynamic stall

Mr. Chambers

The comments Jim's just made are exactly in line with my thoughts as I sat here this week and listened to the presentations. The dynamic stability parameter meeting, and I presume the unsteady meeting earlier, it is difficult to see that we have come a long way toward addressing the questions in your third bullet there, particularly in terms of utilization of unsteady aerodynamics for improved manoeuvering of combat aircraft. I think that my comments probably summarize my feelings that are in line with the comments that you have just made. This is a tremendous challenge. There is a tremendous potential benefit. However, we haven't begun to scratch the surface even in terms of defining quantitatively what that benefit might be. Let us hope that we don't wait another five years before we have answers to the questions that we have posed here.

Dr. Orlik-Rückemann

I think that there is maybe some hope to be derived from the fact that back in 1977 and 1978 aircraft dynamics and unsteady aerodynamics, as you said, were not considered particularly important. Nowadays the momentum is steadily increasing, and if we have another meeting like this in 3, 4 or 5 years, hopefully we will have much more to report on.

Dr. Schiff

Looking at the question you show on your slide Jim, under performance and flight mechanics implications. The question of how to utilize superlift. First of all, I am not so sure that superlift is the only element that people should focus on in the near future. I think that there is a large variety of high-angle-of-attack phenomena and highly manoeuverable types of combat manoeuvers that can be addressed in addition to this one question of superlift. For example, people are interested in such things as pointing the fuselage of the airplane in some specified direction while continuing to fly in another direction. That doesn't necessarily need superlift, it needs perhaps supermoment. Another thing people are interested in is the ability to put the airplane up to high angle of attack, then roll around the velocity vector and then drop the airplane down and then go off in a different direction. It is another aerodynamic phenomenon which has to be looked at as well as superlift. To put only superlift up there, that is, the transient overshoot in the lift observed in two-dimensional dynamic stall experiments, may be focussing people's attention down to too great a degree.

Mr. Mabey

Yes, I would like to comment on one of the basic questions of fluid dynamics. I find it very surprising that the unsteady trailing edge condition wasn't mentioned at all in the course of this meeting. I think that this has great practical importance. Recently we made our first measurements of unsteady trailing edge pressure at RAE, Bedford, together with the static trailing edge pressure, and they pose some very interesting philosophical problems. We would certainly like to stimulate interest in this. Some of you may remember that there was a paper by Roos (AIAA J. Aircraft, Vol 17, No 11) a few years ago on the direction of propagation of disturbances at transonic speeds. He found that as long as the flow was attached, then the disturbances were propagating upstream from the trailing edge to the shock. Once the flow was separated the predominant disturbance went the other way. That result was only for a couple of aerofoils. The implications, for example, for computational fluid dynamics, are really quite horrendous. This is indicative of the change of the trailing edge condition. I would hope that this is a question that will be addressed in the future.

Prof. Hornung

I would like to level mild criticism at some of the papers, which to people who are not experts in flight mechanics and plot such things as CLB and CLPP against other parameters follow the unfortunate trend of later years of lacking or omitting to try to relate the effects of such curves to the physical features of the flow.

Prof. Hancock

I was hoping that from this Symposium I would get a clearer impression of what is meant by unsteady aerodynamics in the context of aircraft dynamics. There seems to be some confusion between unsteady aerodynamics and the unsteady dynamic loads which appear in all these complicated manoeuvers that we have been hearing about. Unsteady aerodynamics, as I understand it, happen in the order of aerodynamic time, which is usually thought of in terms of the time it takes the air to go one chord. Now traditionally, aircraft dynamics has been extremely slow in terms of aerodynamic time so we have been able to think in terms of the aerodynamics essentially going through a series of steady states as the airplane goes through its manoeuvers.

In the extremely complicated aerodynamic models described in the Symposium, most of the derivatives are literally steady and all of the measured rotary derivatives are, I would suggest, also steady. I would like some guidance on exactly where unsteady effects according to my definition appear in aircraft dynamics so that we can concentrate on those unsteady aerodynamic aspects.

Another point that I would like to reiterate is one I made in my lecture. I think that we have got to bring the control man into our discussions because the way the control man uses unsteady aerodynamics is not altogether compatible with what we have been saying here.

Dr. Orlik-Rückemann

Thank you, Prof. Hancock, would anybody care to answer the challenge; what is unsteady, what is quasi-steady?

Off hand, I would say, Professor Hancock, that effects such as alpha dot, beta dot and so on would normally be considered unsteady. Rotary derivatives such as those due to p, q or r are steady or quasi-steady, if you prefer. But, of course, you already know all that. I apologize if the meeting did not provide the definition of unsteady aerodynamics that you have been expecting. However, it is very difficult to cover everything in a meeting like this.

Dr. G.E.A. Meier

Maybe I can comment a little about it because it is a problem which arose also in our research with the vortices. The main thing to compare is the chord length of the airfoil and the extension of the distortion. If this is in the order of one, I think that you have to go from the quasi-steady case to the unsteady case. This brings me to another point on which I would like to comment: the meaning of the Reynolds number in unsteady aerodynamics. I would like to come back to the sin number 1 of Mabey: I feel a little bit like a sinner having not fixed a transition on our airfoil in the experiment. This is really the question, what is the meaning of the Reynolds number in unsteady aerodynamics? Reynolds number is a definition which comes from the steady aerodynamics. If you have flow velocities which are in the order of the free stream velocity inside the distortion, I think it is not very meaningful to take the Reynolds number as a characteristic parameter for the unsteady problem. So this is the question, maybe someone else can answer this.

Dr. Ericsson

The question about boundary layer transition, whether or not to fix transition, has been raised before. Whereas it used to be allowable to fix transition in the past in regard to steady aerodynamics, I think it is fair to say that this is no longer the case, especially not in the dynamic case. There is a very strong coupling between the vehicle motion and boundary layer transition. Even in the full scale flight where the flow is 90% turbulent, there is a point on the wing, for instance, where transition occurs. If you fix transition where transition occurs in flight, you get too thick a boundary layer, and the shock induced separation occurs very far forward. You can fix transition at some other place, so you get the correct boundary layer thickness at the shock location; then, for that particular condition, you get scaling or the full scale flight conditions. However, the trip will have to be moved around with angle of attack. Maybe you can do that in the static case and get correct aerodynamics, but you can see the problem you have to simulate the full scale flight dynamics. Boundary layer transition has a very strong effect on the aerodynamics, so there is no easy fix for this, as far as I can see. Dynamic simulation in the wind tunnel test is only possible if you have full scale Reynolds number. I don't think we are today very close to making a CFD simulation of it either, the coupling between boundary layer transition and vehicle dynamics. The solution we have been using in the missile industry is to provide a mathematical relationship between the static and the dynamic characteristics. Then, by having the static characteristics up to full scale Reynolds number, you can extrapolate analytically to the full-scale dynamic condition from subscale dynamic test data.

Dr. Orlik-Rückemann

We can take one or two more questions after which I will have to bring the meeting to a close. I see that the translators are leaving.

Prof. Campos

Well, I won't delay the translators for very long. I would like to return to the matter of the bifurcation theory. I think in principle the bifurcation theory has two advantages. It can predict all the states an aircraft can reach, and in principle, also all transitions between these various states.

There are, I think, two limitations, one has been mentioned already, that it does not give parameters for a state. For example, the example that was given was a stable state with very low damping which in practice would not be noticed by the pilot. Another issue, I have the impression that in some complicated bifurcation diagrams more than one transition between states is possible. I have the impression that bifurcation theory cannot tell us which of the various possible transitions is likely to occur in a particular flight condition. In other words, it gives all possible states, but not so much likelihood of finding each of these in flight. Also it does not indicate the appropriate recovery action to get out of a state.

Dr. Orlik-Rückemann

For the record, Professor Hui agrees with you. Prof. Ciray?

Prof. Ciray

One thing that I observed is that there was not much about the turbulence behavior of these unsteady flows, with the exception perhaps of the paper by Prof. Cebeci in which he was stating that he was perfectly happy with the steady models and to put it into the unsteady problem. If it is the case there is no problem. But I didn't hear much discussion about this.

Dr. Orlik-Rückemann

Thank you very much Prof. Ciray. I think the time has come to bring this meeting to a close. At the very outset we had at least two different purposes, and the main one, of course, was to review the progress in our understanding of unsteady flows and unsteady boundary layers, to discuss the methods for obtaining various dynamic stability information in wind tunnels or through flight testing and to apply all this knowledge to improve our abilities to predict correctly the dynamic behavior of an aircraft. However, there was also a secondary purpose for this meeting which I believe was just as important maybe as the first one. This was to get in one meeting room specialists representing these various walks of life. I think that maybe at times the vehicle dynamics people may have been a little bit lost when listening to details of unsteady boundary layer analysis, but I am sure that they now appreciate better the problems and the difficulties involved in such a fundamental topic. Conversely, the specialist dealing with basic research may have felt left out when the discussions turned to things such as wing rock or supermanoeuverability. But this surely must have increased their appreciation of the real world around them, so to speak, and of the flight conditions for which their basic work has to be applied. For instance, one thing that came out loud and clear yesterday was the fact that in the future we may be interested in manoeuvers involving much higher than before angular rates. So we have to expand our research in unsteady aerodynamics to cover such conditions, which maybe we haven't covered before. I wish I could say that we have now learned to speak the same language. But this is certainly not true, at least not yet. But we are learning fast to at least understand the language of our colleagues representing the other side of the house, and that in itself is already an important step forward.

At this point, I would like to thank, on behalf of the Program Committee, all the speakers, both in the regular and the open sessions, for the efforts which they have put into the preparation and the presentation of their papers. I would like to thank all the session chairmen for their attempts to keep the meeting on schedule, which on the whole was quite successful. I would also like to specially thank the two technical evaluators for sharing with us in such an excellent way their first impressions of the meeting, and in doing so, triggering this period of discussion. Last but not least, I would like to thank all of you, the audience, for being here with us these four days and for participating actively in all the discussions and questions. With this I would like to turn the meeting over to the two panel chairmen, first Dr. Hamel of the Flight Mechanics Panel and then Dr. Roberts of the Fluid Dynamics Panel.

Dr. Hamel

Mr. Chairman, I think that we have not left very much time for additional technical comments, but I would like to refer to your comments about speaking to the same languages. I think that I have one type of solution:

This is a mouth from a Chinese viewpoint. This is a triangle which is in balance. The combination of mouth and balanced triangle is called in China "He". This word means more or less "unification" or "harmonization". If three men speak the same language, as the Chinese saying is, they can golden the world. With this tutorial I am coming to my conclusions. I would like to talk about the golden FDP/FMP triangle. We have in the upper part of the figure one aspect which we tackled not at all. I am talking about the human being, which could be, for example the pilot. Continuing to the left corner we see aerodynamics or unsteady aerodynamics; these are the so-called external problems, if you keep in mind that the flight vehicle is immersed in some kind of unsteady airflow. This is really the visual external problem. We talked about this in this meeting in Göttingen. Some typical problem areas are stability, controllability, sensitivity, not only with respect to gusts sensitivity, but also with respect to the sensitivity of aerodynamics theories. On the right hand side you can see the system dynamics corner which one can define as the internal problem of the flight vehicle. Here we talk about sub-systems built into the aircraft. For example, there are three main components for the so-called fly-by-wire or light systems: Sensors, computers and actuators. What is the message of the figure? WE have three critical problems areas: we have in the upper part the flight critical work load problem. Is the pilot in the future able to cure these problems from the stability/controllability standpoint, is the pilot really willing or able to fly extremely exotic manoeuvers? Perhaps we can think about the 180 degree tumbling turn in addition to a 180 degree roll, and then we have something like an inverted "Goofy"-manoeuver. We have on the lower left the flight critical envelope where the aerodynamics provide the limits to the plane although we are looking for "forgiving" airplanes. Finally, on the right hand side we are confronted with the flight critical systems. I am talking about the redundancy of the systems. The issue to be addressed is: to what extent do we desire or need "flight critical systems" to cure our aerodynamic problems? We must be ever mindful that there is a brigade of avionics experts challenging our perogative in this area. They would wish to sell us all kinds of nice little black boxes to cure our aerodynamic and handling

problems. Finally, the question must be raised as to whether we need Avionics expertise to solve the aerodynamic problems that are central to the Fluid Dynamics and Flight Mechanics fields. In my opinion, the answer is firmly - NO!
Dr. Roberts

An AGARD symposium attempts to treat a topic that will attract good informative technical papers of interest to a broad audience. In the present symposium involving a cooperative effort between two AGARD panels, the problem of keeping the interest of the entire audience is obviously compounded. We have probably succeeded only partially in this respect. We were certainly successful in having a large audience, almost 250 people, and this is probably something of a record for an AGARD symposium. I hope that all of you have found the Symposium to be worthwhile.

A successful meeting requires not only an interested audience, but a great deal of preparation on the part of the organizers. I would like you to join me in congratulating and thanking Dr. Kazik Orlik-Ruckemann as program chairman and his joint FDP/FMP program committee for providing us with such a fine program covering so much ground in such a short time.

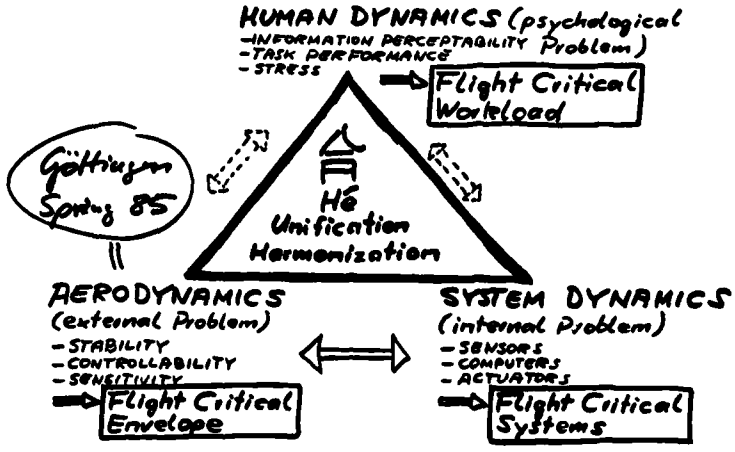

Fig.2 The golden FDP—FMP triangle

REPORT DOCUMENTATION PAGE

1. Recipient's Reference	2. Originator's Reference	3. Further Reference	4. Security Classification of Document
	AGARD-CP-386	ISBN 92-835-0382-1	UNCLASSIFIED

5. Originator Advisory Group for Aerospace Research and Development
North Atlantic Treaty Organization
7 rue Ancelle, 92200 Neuilly sur Seine, France

6. Title

UNSTEADY AERODYNAMICS-FUNDAMENTALS AND APPLICATIONS TO AIRCRAFT DYNAMICS

7. Presented at

the joint Symposium of the Fluid Dynamics and Flight Mechanics Panels held in Göttingen, Federal Republic of Germany, 6—9 May 1985.

8. Author(s)/Editor(s)	9. Date
Various	November 1985
10. Author's/Editor's Address	**11. Pages**
Various	644

12. Distribution Statement This document is distributed in accordance with AGARD policies and regulations, which are outlined on the Outside Back Covers of all AGARD publications.

13. Keywords/Descriptors

Vortices	Turbulent flow
Boundary layer	Turbulence
Aerodynamics	

14. Abstract

The dynamic behaviour of aircraft in high performance manoeuvres is greatly affected by various unsteady flow phenomena, particularly at high angles of attack, where extensive regions of separated flow and several systems of symmetric or asymmetric vortices are often present. Such flows, already rather complex in steady flight, become even more involved in oscillatory or high rate-of-turn flight, where the time lags associated with the various vortical and separated flows become a significant factor affecting profoundly both the static and the dynamic aerodynamic parameters of the aircraft. A good understanding of the unsteady aerodynamics is also important for design of advanced flight control systems, prediction of wing structural and manoeuvre loads and buffet prediction.

The aim of this symposium was to examine the recent advances in many countries in the methods for experimental and computational prediction of non-linear flow phenomena in unsteady aerodynamics and of stability parameters required to describe adequately the dynamic behaviour of aircraft with special emphasis on high-angle-of-attack situations. The programme comprised parts on (1) Unsteady Aerodynamics, (2) Dynamic Stability Parameters, and (3) Applications to Aircraft Dynamis. In the first part, topics such as unsteady boundary layers, unsteady separation and stall, buffeting and unsteady airloads were discussed. The second part covered wind-tunnel and flight-test techniques, with special emphasis on the measurement of non-linearities, aerodynamic cross-coupling, hysteresis and time-dependent effects. Finally, in part three, the various applications of the above to the actual prediction of aircraft dynamics were described, including topics such as mathematical modelling, bifurcation theory, prediction of wing rock, advanced control systems, etc.

AGARD Conference Proceedings No.386 Advisory Group for Aerospace Research and Development, NATO UNSTEADY AERODYNAMICS – FUNDAMENTALS AND APPLICATIONS TO AIRCRAFT DYNAMICS Published November 1985 644 pages The dynamic behaviour of aircraft in high performance manoeuvres is greatly affected by various unsteady flow phenomena, particularly at high angles of attack, where extensive regions of separated flow and several systems of symmetric or asymmetric vortices are often present. Such flows, already rather complex in steady flight, become even more involved in oscillatory or high rate-of-turn flight, where the time lags associated with the various vortical and separated flows become a significant factor affecting profoundly both the static P.T.O	AGARD-CP-386 Vortices Boundary layer Aerodynamics Turbulent flow Turbulence	AGARD Conference Proceedings No.386 Advisory Group for Aerospace Research and Development, NATO UNSTEADY AERODYNAMICS – FUNDAMENTALS AND APPLICATIONS TO AIRCRAFT DYNAMICS Published November 1985 644 pages The dynamic behaviour of aircraft in high performance manoeuvres is greatly affected by various unsteady flow phenomena, particularly at high angles of attack, where extensive regions of separated flow and several systems of symmetric or asymmetric vortices are often present. Such flows, already rather complex in steady flight, become even more involved in oscillatory or high rate-of-turn flight, where the time lags associated with the various vortical and separated flows become a significant factor affecting profoundly both the static P.T.O	AGARD-CP-386 Vortices Boundary layer Aerodynamics Turbulent flow Turbulence
AGARD Conference Proceedings No.386 Advisory Group for Aerospace Research and Development, NATO UNSTEADY AERODYNAMICS – FUNDAMENTALS AND APPLICATIONS TO AIRCRAFT DYNAMICS Published November 1985 644 pages The dynamic behaviour of aircraft in high performance manoeuvres is greatly affected by various unsteady flow phenomena, particularly at high angles of attack, where extensive regions of separated flow and several systems of symmetric or asymmetric vortices are often present. Such flows, already rather complex in steady flight, become even more involved in oscillatory or high rate-of-turn flight, where the time lags associated with the various vortical and separated flows become a significant factor affecting profoundly both the static P.T.O	AGARD-CP-386 Vortices Boundary layer Aerodynamics Turbulent flow Turbulence	AGARD Conference Proceedings No.386 Advisory Group for Aerospace Research and Development, NATO UNSTEADY AERODYNAMICS – FUNDAMENTALS AND APPLICATIONS TO AIRCRAFT DYNAMICS Published November 1985 644 pages The dynamic behaviour of aircraft in high performance manoeuvres is greatly affected by various unsteady flow phenomena, particularly at high angles of attack, where extensive regions of separated flow and several systems of symmetric or asymmetric vortices are often present. Such flows, already rather complex in steady flight, become even more involved in oscillatory or high rate-of-turn flight, where the time lags associated with the various vortical and separated flows become a significant factor affecting profoundly both the static P.T.O	AGARD-CP-386 Vortices Boundary layer Aerodynamics Turbulent flow Turbulence

and the dynamic aerodynamic parameters of the aircraft. A good understanding of the unsteady aerodynamics is also important for design of advanced flight control systems, prediction of wing structural and manoeuvre loads and buffet prediction.

The aim of this symposium was to examine the recent advances, in many countries, in the methods for experimental and computational prediction of non-linear flow phenomena in unsteady aerodynamics and of stability parameters required to describe adequately the dynamic behaviour of aircraft with special emphasis on high-angle-of-attack situations. The programme comprised parts on (1) Unsteady Aerodynamics, (2) Dynamic Stability Parameters, and (3) Applications to Aircraft Dynamics. In the first part, topics such as unsteady boundary layers, unsteady separation and stall, buffeting and unsteady airloads were discussed. The second part covered wind-tunnel and flight-test techniques, with special emphasis on the measurement of non-linearities, aerodynamic cross-coupling, hysteresis and time-dependent effects. Finally, in part three, the various applications of the above to the actual prediction of aircraft dynamics were described, including topics such as mathematical modelling, bifurcation theory, prediction of wing rock, advanced control systems, etc.

Papers presented and discussions held at the joint Symposium of the Fluid Dynamic and Flight Mechanics Panels held in Göttingen, Federal Republic of Germany, 6—9 May 1985.

ISBN 92-835-0382-1

and the dynamic aerodynamic parameters of the aircraft. A good understanding of the unsteady aerodynamics is also important for design of advanced flight control systems, prediction of wing structural and manoeuvre loads and buffet prediction.

The aim of this symposium was to examine the recent advances, in many countries, in the methods for experimental and computational prediction of non-linear flow phenomena in unsteady aerodynamics and of stability parameters required to describe adequately the dynamic behaviour of aircraft with special emphasis on high-angle-of-attack situations. The programme comprised parts on (1) Unsteady Aerodynamics, (2) Dynamic Stability Parameters, and (3) Applications to Aircraft Dynamics. In the first part, topics such as unsteady boundary layers, unsteady separation and stall, buffeting and unsteady airloads were discussed. The second part covered wind-tunnel and flight-test techniques, with special emphasis on the measurement of non-linearities, aerodynamic cross-coupling, hysteresis and time-dependent effects. Finally, in part three, the various applications of the above to the actual prediction of aircraft dynamics were described, including topics such as mathematical modelling, bifurcation theory, prediction of wing rock, advanced control systems, etc.

Papers presented and discussions held at the joint Symposium of the Fluid Dynamic and Flight Mechanics Panels held in Göttingen, Federal Republic of Germany, 6—9 May 1985.

ISBN 92-835-0382-1

and the dynamic aerodynamic parameters of the aircraft. A good understanding of the unsteady aerodynamics is also important for design of advanced flight control systems, prediction of wing structural and manoeuvre loads and buffet prediction.

The aim of this symposium was to examine the recent advances, in many countries, in the methods for experimental and computational prediction of non-linear flow phenomena in unsteady aerodynamics and of stability parameters required to describe adequately the dynamic behaviour of aircraft with special emphasis on high-angle-of-attack situations. The programme comprised parts on (1) Unsteady Aerodynamics, (2) Dynamic Stability Parameters, and (3) Applications to Aircraft Dynamics. In the first part, topics such as unsteady boundary layers, unsteady separation and stall, buffeting and unsteady airloads were discussed. The second part covered wind-tunnel and flight-test techniques, with special emphasis on the measurement of non-linearities, aerodynamic cross-coupling, hysteresis and time-dependent effects. Finally, in part three, the various applications of the above to the actual prediction of aircraft dynamics were described, including topics such as mathematical modelling, bifurcation theory, prediction of wing rock, advanced control systems, etc.

Papers presented and discussions held at the joint Symposium of the Fluid Dynamic and Flight Mechanics Panels held in Göttingen, Federal Republic of Germany, 6—9 May 1985.

ISBN 92-835-0382-1

and the dynamic aerodynamic parameters of the aircraft. A good understanding of the unsteady aerodynamics is also important for design of advanced flight control systems, prediction of wing structural and manoeuvre loads and buffet prediction.

The aim of this symposium was to examine the recent advances, in many countries, in the methods for experimental and computational prediction of non-linear flow phenomena in unsteady aerodynamics and of stability parameters required to describe adequately the dynamic behaviour of aircraft with special emphasis on high-angle-of-attack situations. The programme comprised parts on (1) Unsteady Aerodynamics, (2) Dynamic Stability Parameters, and (3) Applications to Aircraft Dynamics. In the first part, topics such as unsteady boundary layers, unsteady separation and stall, buffeting and unsteady airloads were discussed. The second part covered wind-tunnel and flight-test techniques, with special emphasis on the measurement of non-linearities, aerodynamic cross-coupling, hysteresis and time-dependent effects. Finally, in part three, the various applications of the above to the actual prediction of aircraft dynamics were described, including topics such as mathematical modelling, bifurcation theory, prediction of wing rock, advanced control systems, etc.

Papers presented and discussions held at the joint Symposium of the Fluid Dynamic and Flight Mechanics Panels held in Göttingen, Federal Republic of Germany, 6—9 May 1985.

ISBN 92-835-0382-1

AGARD
NATO OTAN
7 RUE ANCELLE · 92200 NEUILLY-SUR-SEINE
FRANCE
Telephone 47.45.08.10 · Telex 610176

DISTRIBUTION OF UNCLASSIFIED AGARD PUBLICATIONS

AGARD does NOT hold stocks of AGARD publications at the above address for general distribution. Initial distribution of AGARD publications is made to AGARD Member Nations through the following National Distribution Centres.Further copies are sometimes available from these Centres, but if not may be purchased in Microfiche or Photocopy form from the Purchase Agencies listed below.

NATIONAL DISTRIBUTION CENTRES

BELGIUM
Coordonnateur AGARD – VSL
Etat-Major de la Force Aérienne
Quartier Reine Elisabeth
Rue d'Evere, 1140 Bruxelles

CANADA
Defence Scientific Information Services
Dept of National Defence
Ottawa, Ontario K1A 0K2

DENMARK
Danish Defence Research Board
Ved Idraetsparken 4
2100 Copenhagen Ø

FRANCE
O.N.E.R.A. (Direction)
29 Avenue de la Division Leclerc
92320 Châtillon

GERMANY
Fachinformationszentrum Energie,
Physik, Mathematik GmbH
Kernforschungszentrum
D-7514 Eggenstein-Leopoldshafen

GREECE
Hellenic Air Force General Staff
Research and Development Directorate
Holargos, Athens

ICELAND
Director of Aviation
c/o Flugrad
Reyjavik

ITALY
Aeronautica Militare
Ufficio del Delegato Nazionale all'AGARD
3 Piazzale Adenauer
00144 Roma/EUR

LUXEMBOURG
See Belgium

NETHERLANDS
Netherlands Delegation to AGARD
National Aerospace Laboratory, NLR
P.O. Box 126
2600 AC Delft

NORWAY
Norwegian Defence Research Establishment
Attn: Biblioteket
P.O. Box 25
N-2007 Kjeller

PORTUGAL
Portuguese National Coordinator to AGARD
Gabinete de Estudos e Programas
CLAFA
Base de Alfragide
Alfragide
2700 Amadora

TURKEY
Department of Research and Development (ARGE)
Ministry of National Defence, Ankara

UNITED KINGDOM
Defence Research Information Centre
Station Square House
St Mary Cray
Orpington, Kent BR5 3RE

UNITED STATES
National Aeronautics and Space Administration (NASA)
Langley Research Center
M/S 180
Hampton, Virginia 23665

THE UNITED STATES NATIONAL DISTRIBUTION CENTRE (NASA) DOES NOT HOLD STOCKS OF AGARD PUBLICATIONS, AND APPLICATIONS FOR COPIES SHOULD BE MADE DIRECT TO THE NATIONAL TECHNICAL INFORMATION SERVICE (NTIS) AT THE ADDRESS BELOW.

PURCHASE AGENCIES

Microfiche or Photocopy
National Technical
Information Service (NTIS)
5285 Port Royal Road
Springfield
Virginia 22161, USA

Microfiche
ESA/Information Retrieval Service
European Space Agency
10, rue Mario Nikis
75015 Paris, France

Microfiche or Photocopy
British Library Lending
Division
Boston Spa, Wetherby
West Yorkshire LS23 7BQ
England

Requests for microfiche or photocopies of AGARD documents should include the AGARD serial number, title, author or editor, and publication date. Requests to NTIS should include the NASA accession report number. Full bibliographical references and abstracts of AGARD publications are given in the following journals:

Scientific and Technical Aerospace Reports (STAR)
published by NASA Scientific and Technical
Information Branch
NASA Headquarters (NIT-40)
Washington D.C. 20546, USA

Government Reports Announcements (GRA)
published by the National Technical
Information Services, Springfield
Virginia 22161, USA

Printed by Specialised Printing Services Limited
40 Chigwell Lane, Loughton, Essex IG10 3TZ

ISBN 92-835-0382-1

NATO OTAN
7 RUE ANCELLE · 92200 NEUILLY-SUR-SEINE
FRANCE
Telephone 47.45.08.10 · Telex 610176

DISTRIBUTION OF UNCLASSIFIED AGARD PUBLICATIONS

AGARD does NOT hold stocks of AGARD publications at the above address for general distribution. Initial distribution of AGARD publications is made to AGARD Member Nations through the following National Distribution Centres.Further copies are sometimes available from these Centres, but if not may be purchased in Microfiche or Photocopy form from the Purchase Agencies listed below.

NATIONAL DISTRIBUTION CENTRES

BELGIUM
Coordonnateur AGARD – VSL
Etat-Major de la Force Aérienne
Quartier Reine Elisabeth
Rue d'Evere, 1140 Bruxelles

CANADA
Defence Scientific Information Services
Dept of National Defence
Ottawa, Ontario K1A 0K2

DENMARK
Danish Defence Research Board
Ved Idraetsparken 4
2100 Copenhagen O

FRANCE
O.N.E.R.A. (Direction)
29 Avenue de la Division Leclerc
92320 Châtillon

GERMANY
Fachinformationszentrum Energie,
Physik, Mathematik GmbH
Kernforschungszentrum
D-7514 Eggenstein-Leopoldshafen

GREECE
Hellenic Air Force General Staff
Research and Development Directorate
Holargos, Athens

ICELAND
Director of Aviation
c/o Flugrad
Reyjavik

ITALY
Aeronautica Militare
Ufficio del Delegato Nazionale all'AGARD
3 Piazzale Adenauer
00144 Roma/EUR

LUXEMBOURG
See Belgium

NETHERLANDS
Netherlands Delegation to AGARD
National Aerospace Laboratory, NLR
P.O. Box 126
2600 AC Delft

NORWAY
Norwegian Defence Research Establishment
Attn: Biblioteket
P.O. Box 25
N-2007 Kjeller

PORTUGAL
Portuguese National Coordinator to AGARD
Gabinete de Estudos e Programas
CLAFA
Base de Alfragide
Alfragide
2700 Amadora

TURKEY
Department of Research and Development (ARGE)
Ministry of National Defence, Ankara

UNITED KINGDOM
Defence Research Information Centre
Station Square House
St Mary Cray
Orpington, Kent BR5 3RE

UNITED STATES
National Aeronautics and Space Administration (NASA)
Langley Research Center
M/S 180
Hampton, Virginia 23665

THE UNITED STATES NATIONAL DISTRIBUTION CENTRE (NASA) DOES NOT HOLD STOCKS OF AGARD PUBLICATIONS, AND APPLICATIONS FOR COPIES SHOULD BE MADE DIRECT TO THE NATIONAL TECHNICAL INFORMATION SERVICE (NTIS) AT THE ADDRESS BELOW.

PURCHASE AGENCIES

Microfiche or Photocopy
National Technical
Information Service (NTIS)
5285 Port Royal Road
Springfield
Virginia 22161, USA

Microfiche
ESA Information Retrieval Service
European Space Agency
10, rue Mario Nikis
75015 Paris, France

Microfiche or Photocopy
British Library Lending
Division
Boston Spa, Wetherby
West Yorkshire LS23 7BQ
England

Requests for microfiche or photocopies of AGARD documents should include the AGARD serial number, title, author or editor, and publication date. Requests to NTIS should include the NASA accession report number. Full bibliographical references and abstracts of AGARD publications are given in the following journals:

Scientific and Technical Aerospace Reports (STAR)
published by NASA Scientific and Technical
Information Branch
NASA Headquarters (NIT-40)
Washington D.C. 20546, USA

Government Reports Announcements (GRA)
published by the National Technical
Information Services, Springfield
Virginia 22161, USA

Printed by Specialised Printing Services Limited
40 Chigwell Lane, Loughton, Essex IG10 3TZ

ISBN 92-835-0382-1